



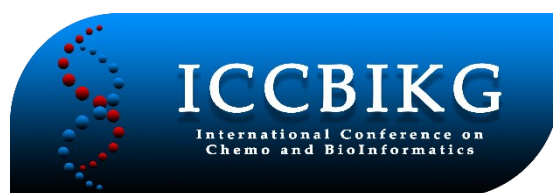
28-29 September 2023,

Kragujevac, Serbia

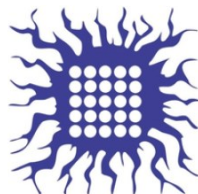
www.iccbikg2023.kg.ac.rs

2nd International Conference on Chemo and Bioinformatics

ICCBIKG_2023



BOOK OF PROCEEDINGS





2nd International Conference on Chemo and Bioinformatics
ICCBIKG 2023

BOOK OF PROCEEDINGS

September 28-29, 2023
Kragujevac, Serbia

Sponsored by



2nd International Conference on Chemo and BioInformatics, Kragujevac, September 28-29, 2023, Serbia.

Editors:

Professor Dr. Zoran Marković

Professor Dr. Nenad Filipović

Technical Editors:

Jelena Živković

Marko Antonijević

Dr. Žiko Milanović

Dr. Vladimir Simić

Proofreading:

Marijana Dimović

Publisher:

Institute for Information Technologies, University of Kragujevac, Serbia, Jovana Cvijića bb, 2023

Press:

„Grafo Ink“, Kragujevac

Impression:

120 copies

CIP - Каталогизacija u publikaciji - Narodna biblioteka Srbije, Beograd

54:004(048)(0.034.2)

57+61]:004(082)(0.034.2)

INTERNATIONAL Conference on Chemo and BioInformatics (2 ; 2023 ; Kragujevac) Book of Proceedings [Elektronski izvor] / 2nd International Conference on Chemo and BioInformatics, ICCBIKG 2023, September 28-29, 2023 Kragujevac, Serbia ; [editors Zoran Marković, Nenad Filipović]. - Kragujevac : University, Institute for Information Technologies, 2023 (Kragujevac : Grafo Ink). - 1 USB fleš memorija ; 1 x 2 x 6 cm

Sistemski zahtevi: Nisu navedeni. - Nasl. sa naslovne strane dokumenta. - Tiraž 120. - Bibliografija uz svaki rad.

ISBN 978-86-82172-02-4

a) Хемија -- Информациона технологија -- Зборници b) Биомедицина -- Информациона технологија -- Зборници

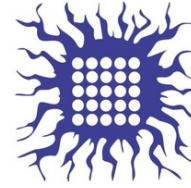
COBISS.SR-ID 125908489

Organized by:

Institute for Information Technologies,
University of Kragujevac, **Organizer**



Institute of Nuclear Science,
University of Belgrade, *Suborganizer*



Faculty of Science, University of Kragujevac,
Suborganizer



The Ministry of Science,
Technological Development and
Innovation of The Republic of Serbia,
Supporting organization



Faculty of Technical Science, University of
Kragujevac, *Suborganizer*



University of Kragujevac, *Supporting organization*



State University of Novi Pazar, *Suborganizer*



Committees

International Organizing Committee:

Chairman:	Prof. Dr Zoran Marković (Serbia)
Vice-chairmans:	Prof. Miloš Kojić (USA)
	Prof. Dr. Mimoza Ristova (North Macedonia)

Members:

Dr Dejan Milenković (Serbia), Dr Marijana Petković (Serbia), Dr. Jasmina Grbović Novaković (Serbia), Prof. Dr. Aleksandar Ostojić (Serbia), Dr Jovana Sekulić (Serbia), Dr Edina Avdović (Serbia), Dr Dušica Simijonović (Serbia), Dr Tijana Geroski (Serbia), Doc. Dr Dušan Dimić (Serbia), Dr Ana Kesić (Serbia), Doc. Dr Svetlana Jeremić (Serbia), Dr Marija Ristić (Serbia), Dr Vladimir Simić (Serbia), Dr Žiko Milanović (Serbia), Marko Antonijević (Serbia).

International Scientific Committee:

Chairman:	Prof. Dr Nenad Filipović (Serbia)
Vice-chairmans:	Prof. Dr Snežana Pajović (Serbia)
	Prof. Dr Zlatan Car (Croatia)

Members:

Prof. Zoran Marković (Serbia), Prof. Ivan Gutman (Serbia), Prof. Miloš Kojić (USA), Prof. Miloš Đuran (Serbia), Prof. Nenad Kostić (USA), Prof. Ljiljana Kolar-Anić (Serbia), Prof. Svetlana Marković (Serbia), Prof. Snežana Zarić (Serbia), Prof. Marija Stanić (Serbia), Prof. Miroslav Živković (Serbia), Prof. Dr Nino Russo (Italy), Prof. Nenad Grujović (Serbia), Prof. Luciano Saso (Italy), Jasmina Dimitrić-Marković (Serbia), Prof. Dražen Vikić-Topić (Croatia), Prof. Zana Dolićanin (Serbia), Prof. Bakhtiyor Rasulev (USA), Prof. Enver Karahmet (Bosnia and Herzegovina), Prof. Themis Exarchos (Greece), Dr. Sc. Mario Vazdar (Czech Republic), Prof. Dr. Goran Kaluđerović (Germany), Prof. Dr. Jasmina Stevanović (Serbia), Prof. Dr Rudolf Bauer (Austria), Prof. Dr Slobodan Savić (Serbia), Prof. Dr. Petar Uskoković (Serbia), Prof. Dr. Danijela Milošević (Serbia), Prof Dr Janez Konc (Slovenia), Prof. Dr. Bartosz Trzaskowski (Poland), Prof. Dr Miljan Milošević (Serbia), Dr Edina Avdović (Serbia), Dr Katarina Marković (Serbia).

Local Executive Committee:

Chairman: Prof. Dr Miljan Milošević (Serbia)

Vice-chairmans: Dr Marina Kostić (Serbia)

Dr Jasmina Obradović (Serbia)

Members:

Jelena Živković (Serbia), Bogdan Milićević (Serbia), Nevena Veselinović (Serbia), Momčilo Prodanović (Serbia), Emilija Milović (Serbia), Sandra Jovičić Milić (Serbia).

Table of contents

PLENARY LECTURERS	1
THE IMPORTANCE OF CHEMOMETRICS IN DRUG DISCOVERY FROM MEDICINAL PLANTS	2
A REVIEW OF THE APPLICATION OF THE FINITE ELEMENT SMEARED CONCEPT TO BIOMEDICAL ENGINEERING PROBLEMS	6
IS DEUTERIUM BIOLOGICALLY SIGNIFICANT? SOME UNEXPECTED DEUTERIUM SPECTROSCOPIC DATA	7
TARGETING DEPRESSION VIA COMPUTATIONAL APPROACHES TO DESIGN NEW COUMARIN-BASED SEROTONIN RECEPTOR ANTAGONISTS/AGONISTS AND DEVELOP RELIABLE MODELS OF G PROTEIN-COUPLED RECEPTORS.....	10
ALGORITHMS AND WEB SERVERS FOR PROTEIN BINDING SITES DETECTION IN DRUG DISCOVERY	14
TOWARD QUANTITATIVE RAMAN SPECTROSCOPY.....	22
SYNTHETIC DATA GENERATION FOR BIOMEDICAL DEEP LEARNING: METHODS, CHALLENGES, AND OPPORTUNITIES	26
SECTION LECTURERS	34
BENZENE AND WATER – DIFFERENT OR SIMILAR?	35
THE HYDROGEN ECONOMY: CHALLENGES AND PROSPECTIVES	39
MULTIPARAMETER MONITORING OF CARDIOVASCULAR FUNCTION	43
DB.3D-QSAR.COM. THE FIRST 3D QSAR MODELS DATABASE.....	51
IRM@Be ²⁺ - QUANTUM CHEMISTRY BETWEEN BAVARIA AND ŠUMADIJA.....	53
APPLICATION OF CARBON-BASED NANOCOMPOSITE SYSTEMS AS PHOTOSENSITIZERS FOR PHOTODYNAMIC THERAPY.....	61
CONFUSION ABOUT THE CHOICE OF EVALUATION METRICS FOR MODEL PERFORMANCE ASSESMENT IN CHEMOINFORMATICS, BIOINFORMATICS AND IN GENERAL	67
HISTORY OF RADIOLOGICAL PROTECTION AND EVOLUTION OF DOSIMETRIC QUANTITIES	73
APPLIED SCIENCE AND TECHNOLOGY	81
ENTROPY DYNAMICS FOR A PROPELLER-SHAPED QUANTUM BROWNIAN MOLECULAR ROTATOR	82
BIOCORROSION, BIOFOULING AND HEALTH RISK: BIOLOGICAL ACTIVITY REACTION TESTS OF SELECTED BRACKISH GROUNDWATER OCCURRENCES IN SERBIA.....	86
BACTERIA IN DRINKING AND BATHING MINERAL WATERS OF SERBIA WITH POLYMER-DEGRADING POTENTIAL	91
MODELING AND SIMULATION OF A POLYMER OPTICAL FIBER HUMIDITY SENSOR FOR THE SKIN MICROENVIRONMENT	96
COMPARISON OF ORGANIC SUBSTANCE CONTENT IN PELOIDS FROM SUTOMORE AND IGALO (MONTENEGRO)	100
DRIFT SPECTROSCOPY AND PERMUTATION IMPORTANCE ALGORITHM IN QUANTITATIVE ANALYSIS OF ORGANIC MATTER IN SOIL MODEL SYSTEMS	104
THE INFLUENCE OF PYROCATECHOL ADDED IN PRE-OSCILLATORY PERIOD ON THE DYNAMICS OF THE BRAY-LIEBHAFSKY REACTION.....	108
ENVIRONMENTAL IMPLICATIONS OF FINANCIAL DEVELOPMENT IN CEE COUNTRIES.....	112
GREENHOUSE GAS EMISSIONS AND DIGITAL COMPETITIVENESS IN CEE COUNTRIES	116
ANTIFREEZE WITH COFFEE TASTE	120
THE HYDRATION AND ANTIMICROBIAL PROPERTIES OF SELECTED IMIDAZOLE-BASED IONIC LIQUIDS WITH A HOMOLOGOUS SERIES OF CHLORIDE OXYANIONS	124
INFLUENCE OF THE IONIC LIQUIDS-BASED ELECTROLYTES ON THE TOMATO (<i>SOLANUM LYCOPERSICUM</i> L.) AND CUCUMBER (<i>CUCUMIS SATIVUS</i> L.) GROWTH, DEVELOPMENT AND OXIDATIVE STRESS	128
SOLUBILITY AND STRUCTURAL ORGANIZATION OF TAURINE MOLECULES IN WATER	132
SELECTING CRITICAL FEATURES FOR BIOMEDICAL DATA CLASSIFICATION	136
THROMBOPHILIA PREDICTION USING MACHINE LEARNING ALGORITHMS	140
SIMULATION OF DNA DAMAGE USING THE “MOLECULARDNA” EXAMPLE APPLICATION OF GEANT4-DNA.....	144
DEVELOPMENT OF NANOMATERIALS FOR SUSTAINABLE FOOD PACKAGING APPLICATIONS.....	148
BIOACCUMULATION POTENTIAL OF 'MEEKER' AND 'WILLAMETTE' RASPBERRY (<i>RUBUS IDAEUS</i> L.) FRUITS TOWARDS MACRO- AND MICROELEMENTS AND THEIR NUTRITIONAL EVALUATION	152
<i>IN VITRO</i> AND <i>IN SILICO</i> ASSESSMENT OF ANTI-INFLAMMATORY ACTIVITY OF COCOA POWDERS	156

COMPARISON OF THE LUMINESCENCE PROPERTIES OF PHOSPHATE-TUNGSTEN BRONZE AND CERIUM DOPED PHOSPHATE-TUNGSTEN BRONZE	160
THE COMPARISON OF TWO METHODS USED TO OBSERVE A NONLINEAR SYSTEM: POTENTIOMETRY AND HOLOGRAPHY	164
RADIOACTIVITY LEVELS AND HEALTH RISKS ASSOCIATED WITH HIMALAYAN SALT CONSUMPTION	168
PREVALENCE OF RADON AND METALS IN NATURAL SPRINGS IN THE SOKOBANJA AREA	172
INVESTIGATION OF THE POSSIBILITY OF INTERACTION BETWEEN LITHIUM FLUORIDE CLUSTERS AND BORON USING LDI MS.....	176
<i>IN VITRO</i> BIOLOGICAL EFFECTS OF CLONAL RED WINES	180
APPLIED MACHINE LEARNING IN EXPLORING KEY FEATURES OF CRAYFISH POPULATIONS	184
DOSE COMPENSATION ALGORITHM IN RADIOTHERAPY PLANNING.....	188
A PROTOCOL FOR THORACIC RADIATION THERAPY IN PATIENTS WITH CARDIAC IMPLANTABLE ELECTRONIC DEVICES.....	193
DISTRIBUTION OF DOSES TO ORGANS AT RISK IN CERVICAL CANCER HIGH DOSE RATE BRACHYTHERAPY USING TANDEM AND OVOIDS OR VAGINAL CYLINDER.....	197
ASSESSMENT OF RADIOACTIVITY LEVELS IN SOIL SAMPLES ON ZLATIBOR MOUNTAIN.....	201
INFLUENCE OF DIFFERENT PRODUCTION SYSTEMS AND TOMATO GENOTYPES ON THE	205
CHALLENGES IN RADIOTHERAPY PLANNING IN PATIENTS WITH SYNCHRONOUS RECTAL AND PROSTATE CANCER AND HIP PROSTHESIS..	209
EXPLORING THE PHARMACOKINETIC PROPERTIES OF (NH ₄) ₄ [Fe(1DADTC) ₂]: <i>IN SILICO</i> BIOLOGICAL SCREENING AND ADMET ANALYSIS	213
THE INFLUENCE OF DIFFERENT PLASTICIZERS ON THE MECHANICAL PROPERTIES OF ACTIVE EDIBLE BILAYER FILMS	217
PATCH CLAMP PIPETTE GIGA SEAL FORMING SUCCESS ON THE NANOSURGERY-OBTAINED FILAMENTOUS FUNGI PROTOPLASTS.....	221
ANALYSIS OF HEAVY METALS IN THE SOIL IN THE IBAR RIVER VALLEY IN THE DISTRICT OF KOSOVSKA MITROVICA	225
WATER QUALITY ANALYSIS IN THE DISTRICT OF KOSOVSKA MITROVICA.....	229
THE EFFECT OF CONSUMER ETHNOCENTRISM ON THE COMPETITIVENESS OF THE ECONOMY OF THE REPUBLIC OF SERBIA.....	232
THE ROLE OF SOCIALLY RESPONSIBLE BUSINESS IN IMPROVING THE COMPANY'S MARKET POSITIONING	236
CHEMOMETRIC APPROACH TO THE INVESTIGATION OF MICROELEMENTS AND POTENTIALLY TOXIC ELEMENTS IN THE SOIL.....	241
APPLICATION OF CHEMOMETRICS IN MONITORING OF SPATIAL AND TEMPORAL VARIATIONS IN RIVER WATER QUALITY AND WATER CLASSIFICATION	245
MECHANOCHEMISTRY: OPTIMIZATION OF THE SYNTHESIS OF DITHIOCARBAMATE DERIVATIVES.....	249
CAPACITIVE BEHAVIOUR OF BIOMASS-DERIVED ACTIVATED CARBON IN AL-ION-CONTAINING ELECTROLYTES	253
THE INTERDEPENDENCE OF STRUCTURAL PROPERTIES AND PSEUDOCAPACITIVE BEHAVIOR OF BIOMASS-DERIVED ACTIVATED CARBON	257
ELUCIDATING HEALTH-ENHANCING PROPERTIES OF NATURAL PRODUCTS: A JOURNEY FROM EXTRACT ISOLATION TO QUANTUM MECHANICS (QM) CALCULATIONS.....	261
A COMPUTATIONAL MODEL OF THE LEFT VENTRICLE – APPLICATION IN CARDIOMYOPATHY DISEASE	265
STATUS AND QUALITY OF LIFE OF PEOPLE WITH CELIAC AND PEOPLE ON A GLUTEN-FREE DIET	269
MODELING OF CIRCULATING TUMOR CELL (CTC) AND PLATELET INTERACTION IN CAPILLARIES.....	274
BIOINFORMATICS AND APPLIED BIOLOGY	279
ABUNDANCE, SPECIES RICHNESS AND DIVERSITY OF EARTHWORMS (LUMBRICIDAE) IN SEVERAL HABITATS OF THE NORTHERN PART OF JASTREBAC MOUNTAIN	280
A NEW RECORD OF <i>DENDROBAENA SERBICA</i> KARAMAN, 1973 (CLITELLATA; LUMBRICIDAE) FROM SERBIA.....	284
POTENTIALLY TOXIC ELEMENTS IN THE EDIBLE PART OF TROUT (<i>SALMO TRUTTA</i> L.) FROM THE UPPER REACHES OF THE RAŠKA AND STUDENICA RIVERS	288
DIET COMPOSITION AND FEEDING HABITS OF COMMON BLEAK (<i>ALBURNUS ALBURNUS</i> L.) IN THE GRUŽA AND GAZIVODE RESERVOIRS	292
IDENTIFICATION OF PROTEIN TARGET MOLECULES FOR [Pd(DACH)Cl ₂] COMPLEX IN HELA CERVICAL CARCINOMA CELLS	296
EDIBLE MUSHROOMS AS PROMISING ANTIOXIDANTS	300
ANTIMICROBIAL POTENTIAL OF MUSHROOMS <i>MACROLEPIOTA PROCERA</i> AND <i>CHLOROPHYLLUM RHACODES</i>	304
OBESITY AS A RISK FACTOR FOR COVID- 19 MORTALITY: AN OVERVIEW OF PUBLISHED META-ANALYSES	308
CLASSIFICATION AND ANALYSIS OF KEY PARAMETERS IN PREDICTING THE STATE OF FACULTATIVE OLIGOTROPHS IN TWO DIFFERENT RESERVOIRS	312

ECOLOGICAL APPLICATIONS BASED ON BACTERIAL COMMUNITY ABUNDANCE IN RESERVOIRS USING AN ARTIFICIAL NEURAL NETWORK APPROACH.....	317
OXIDATIVE DNA DAMAGE PREVENTIVE ACTIVITY OF ESSENTIAL OILS OF THREE <i>PINUS</i> SPECIES: <i>P. MUGO</i> , <i>P. SIBIRICA</i> , AND <i>P. SILVESTRE</i>	321
COMPARATIVE ASSESSMENT OF FISH DIVERSITY INDICES IN PROTECTED VLASINA RESERVOIR AND UNPROTECTED GRUŽA RESERVOIR	326
ASSESSMENT OF DIFFERENT MACHINE LEARNING TOOLS EMPLOYED IN LIPIDOMICS	330
SLIGHT COOLING DURING GROWTH INDUCED CHANGES IN FILAMENTOUS FUNGI HYPHA MITOCHONDRIAL MORPHOLOGY	334
STRUCTURAL SIMULATIONS PREDICTING PROTEIN FOLDING IN ALZHEIMER'S DISEASE	338
A MACHINE LEARNING APPROACH COMBINING OMICS DATA FOR ALZHEIMER'S DISEASE ANALYSIS	342
BIOMEDICAL ENGINEERING	346
NUMERICAL MODELING OF NEW 4,7-DIHYDROXYCOUMARIN DERIVATIVE DIFFUSION WITHIN FINITE ELEMENT LIVER MODEL.....	347
UV-BLOCKING SUSTAINABLE FOOD PACKAGING BASED ON POLYHYDROXYALKANOATE AND BACTERIAL PIGMENT PRODIGIOSIN	351
USING NUMERICAL MODELING TO ANALYZE THE BEHAVIOR OF CANCER CELLS AFTER DIVERSE CO-TREATMENTS.....	355
OVERVIEW OF LEFT VENTRICULAR SEGMENTATION IN ULTRASOUND IMAGES	359
FINITE ELEMENT ANALYSIS OF STRESS DISTRIBUTION IN 3D TOOTH MODEL WITH EXTENSIVE CAVITIES RESTORED WITH DIRECT AND INDIRECT COMPOSITE RESTORATION	363
MULTISCALE MODELLING OF THE EFFECTS OF TEMPERATURE ON CARDIAC TWITCHES	367
ANALYTICALLY COMPUTED FRACTIONAL FLOW RESERVE BASED ON CORONARY CT ANGIOGRAPHY.....	371
A FINITE ELEMENT MODEL FOR STRUCTURAL OPTIMIZATION OF PARAMETRIZED LATTICE SCAFFOLDS	375
APPLICATION OF MACHINE LEARNING ALGORITHMS IN MEDICAL DATA PROCESSING	379
BIOORGANIC, BIOINORGANIC AND MEDICINAL CHEMISTRY.....	382
STRUCTURAL, SPECTROSCOPIC, AND MOLECULAR DOCKING ANALYSIS OF ISOPROTERENOL.....	383
MOLECULAR DOCKING STUDY OF RUTHENIUM- <i>p</i> -CYMENE COMPLEXES WITH ISOTHIAZOLE DERIVATIVES AS SARS-COV-2 MAIN PROTEASE INHIBITORS	387
SYNTHESIS, SPECTROSCOPIC, AND QUANTUM-CHEMICAL ANALYSIS OF MONONUCLEAR Ru(II)-NAPHTHYLHYDRAZINE COMPLEX	391
SYNTHESIS, SPECTROSCOPIC, AND THEORETICAL ANALYSIS OF Ru(II)-PHENYLHYDRAZINE COMPLEX	395
DNA/BSA BINDING STUDY OF MONONUCLEAR GOLD(III) COMPLEXES WITH CLINICALLY USED AZOLES.....	399
DNA/BSA INTERACTION OF PLATINUM(II) COMPLEXES WITH PHENOTHIAZINE AND <i>N</i> -METHYLPHENOTHIAZINE	403
THE INTERACTION STUDIES OF NOVEL DIAMINOPHENAZINE GOLD(III) COMPLEX AND BOVINE SERUM ALBUMIN (BSA-IBUPROFEN AND BSA-EOZINE Y)	407
THE INFLUENCE OF STRUCTURAL MODIFICATION OF Pd(II) Pincer-TYPE COMPLEXES ON THE KINETICS OF SUBSTITUTION REACTIONS.	411
<i>IN VITRO</i> CYTOTOXIC ACTIVITY OF A MONOLACUNARY WELLS-DAWSON NANOCUSTER AGAINST CERVICAL CARCINOMA HELA CELLS	415
THE INFLUENCE OF Fe(III) INCORPORATION ON ANTI-CANCER POTENTIAL OF A WELLS-DAWSON NANOCUSTER	419
DFT APPROACH OF THE REDOX PROPERTIES OF BRIMONIDINE AND VARENICLINE.....	423
THEORETICAL AND EXPERIMENTAL STUDY OF BILASTINE IONIZATION	427
NEW VANADIUM COMPLEXES WITH POTENTIAL BIOLOGICAL ACTIVITY.....	431
SYNTHESIS OF SCHIFF BASES BETWEEN SOME FIVE-MEMBERED HETEROCYCLIC ALDEHYDES AND THIOCARBOHYDRAZIDE (TCH) AND OPTIMIZATION OF REACTION CONDITIONS	435
SYNTHESIS, STRUCTURE AND ANTICANCER ACTIVITY OF Zr(IV) COMPLEXES WITH SCHIFF BASES DERIVED FROM 8-HYDROXYQUINOLINE	439
IONIC PALLADIUM(II) COMPLEXES WITH NITRO AND HALOGEN DERIVATIVES OF 8-HYDROXYQUINOLINE	443
A NOVEL SILVER COMPLEX WITH 4-HYDROXYCOUMARIN DERIVATIVE: SYNTHESIS, STRUCTURE, AND BIOLOGICAL ACTIVITY	447
ANTICANCER GALLIUM(III) COMPLEXES WITH HALOGEN- AND NITRODERIVATIVES OF 8-HYDROXYQUINOLINE.....	451
<i>IN SILICO</i> DRUG-LIKENESS, PHARMACOKINETIC AND OTHER ADME PROPERTIES OF 2-(AMINOMETHYL)CYCLOPROPANE-1,1-DICARBOXYLIC ACID.....	455
BSA BINDING OF 2-(AMINOMETHYL)CYCLOPROPANE-1,1-DICARBOXYLIC ACID	459
INVESTIGATION OF BINDING MODE OF NOVEL 2,4-DIKETO ESTERS TO BSA	463

SR FTIR SPECTROSCOPY INVESTIGATION OF Pd@S-CD NANOCOMPOSITE SYSTEM EFFECTS ON BIOMOLECULES IN CERVICAL CARCINOMA CELLS	467
THE EFFECTS OF A SELECTED METHOXY SUBSTITUTED CHALCONE IN HUMAN MELANOMA CELLS IRRADIATED WITH γ -RAYS	471
<i>IN SILICO</i> ESTIMATION OF COX-2 AND 5-LOX INHIBITORY POTENTIAL OF SOME NOVEL THIOUREA DERIVATIVES OF NAPROXEN	475
MOLECULAR DOCKING STUDY OF DESIGNED N-MYRISTOYL TRANSFERASE INHIBITORS.....	479
PLATINUM(II) COMPLEXES WITH EPOXIDE DERIVATIVE OF 1,10-PHENANTHROLINE IN INTERACTION WITH HUMAN SERUM ALBUMIN .	483
ANALYTICAL VALUES OF BEESWAX FROM MONTENEGRO AND DETECTION OF ADULTERATION	487
PHENOLIC <i>N</i> -ACYL HYDRAZONE DERIVATIVES: <i>IN SILICO</i> ASSESSMENT OF POTENTIAL ANTIBACTERIAL ACTIVITY AGAINST SELECTED G ⁺ AND G ⁻ STRAINS	491
<i>IN SILICO</i> ANTIBIOFILM POTENCY OF PHENOLIC <i>N</i> -ACYL HYDRAZONES AGAINST SELECTED BACTERIAL STRAINS	495
TiO ₂ NANOPARTICLES AND TiO ₂ NANOPARTICLES SURFACE MODIFIED WITH SALICYLIC ACID AFFECT NEUROLOGICAL FUNCTIONS AND OXIDATIVE STRESS MARKERS IN THE EYES OF ADULT RATS	499
SYNTHESIS AND CYTOTOXIC ACTIVITY OF SELECTED DUAL COX-2 AND 5-LOX INHIBITORS IN HELA AND MIA PaCa-2 HUMAN CANCER CELL LINES	503
SYNTHESIS, CHARACTERIZATION AND HSA INTERACTIONS OF A NEW PIANO-STOOL RUTHENIUM(II) COMPLEX CONTAINING A THIOAMIDE-TYPE LIGAND	507
HPLC/UV PROFILE AND DETERMINATION OF TOTAL PHENOLIC AND FLAVONOID CONTENTS OF LICHEN <i>UMBILICARIA CRUSTULOSA</i> GROWING IN SERBIA	511
LICHENO-CHEMICAL ANALYSIS AND <i>IN VITRO</i> ANTIOXIDANT ACTIVITY OF EXTRACTS AND GYROPHORIC ACID FROM LICHEN <i>UMBILICARIA GRISEA</i>	515
BIOLOGICAL ACTIVITY OF THIENYL-TERPYRIDINE Ru(II) COMPLEX IN THE PRESENCE OF BIOCOMPATIBLE IONIC LIQUIDS	519
KINETIC STUDIES OF THE Ru(II) POLYPYRIDYL COMPLEX WITH BIOLOGICALLY RELEVANT LIGANDS	523
SYNTHESIS AND PHYSICO-CHEMICAL CHARACTERISATION OF THE Ni(II) COMPLEX WITH 3-(4-CHLOROPHENYL)-1H-PYRAZOLE LIGAND	527
NORMAL AND REVERSED PHASES THIN-LAYER CHROMATOGRAPHY OF ARYLIDENE 2-THIOHYDANTOIN DERIVATIVES	531
INVESTIGATION OF THE ANTICANCER ACTIVITY OF 2-AMINO-6-METHYLBENZOTHAZOLE AND CORRESPONDING Pd(II) COMPLEX USING MOLECULAR DOCKING SIMULATIONS	535
DNA BINDING AND MOLECULAR DOCKING OF FOUR PALLADIUM(II) COMPLEXES WITH <i>O,O'</i> -DIALKYL ESTERS OF (<i>S,S</i>)-PROPYLENEDIAMINE- <i>N,N'</i> -DI-2-(2-BENZYL) ACETIC ACID	539
MACRO AND MICROELEMENTS IN THE LEAF AND EXTRACT OF NETTLE FROM DIFFERENT LOCALITIES OF MONTENEGRO	543
SYNTHESIS AND ANTIOXIDANT ACTIVITY OF NOVEL VANILLIN-BASED FERROCENYL CHALCONES	547
A CONTRIBUTION TO THE KNOWLEDGE OF THE SPECIES <i>DIPSACUS SYLVESTRIS</i> HUDS.	551
QUALITATIVE CONTENT OF SELECTED PHENOLIC COMPOUNDS IN DIFFERENT EXTRACTS OF PLANT SPECIES <i>IRIS PUMILA</i> L.	555
BUILDING A 3D QSAR MODEL WITH ISOPROPYLIDENE ANALOGS OF CYTOTOXIC STYRYL-LACTONES	559
VALIDATION OF GRAVIMETRIC METHOD FOR DETERMINATION OF CLAY IN SOIL	563
PYRAZOLE/TACRINE DERIVATIVES AS POTENTIAL CHOLINESTERASE INHIBITORS.....	567
THE INFLUENCE OF THE METHANOL EXTRACT OF <i>GALIUM VERUM</i> ON CARDIAC OXIDATIVE DAMAGE IN HYPERTENSIVE RATS IN A MODEL OF GLOBAL ISCHEMIA	571
CAN A THREE-WEEK ADMINISTRATION OF METHANOL EXTRACT OF WILD GARLIC MODULATE SYSTEMIC REDOX STATE IN HYPERTENSIVE RATS?	575
CHEMOINFORMATICS, CHEMOGENOMICS AND MOLECULAR DESIGN	579
HIGH-THROUGHPUT SCREENING OF NOVEL HYDROGEN STORAGE MATERIALS – ML APPROACH	580
3D-QUANTITATIVE STRUCTURE-ACTIVITY RELATIONSHIP AND DESIGN OF NOVEL RHO-ASSOCIATED PROTEIN KINASES-1 (ROCK1) INHIBITORS	584
VIRTUAL DOCKING, DESIGN AND <i>IN SILICO</i> ADMET PROFILING OF NOVEL RHO-ASSOCIATED PROTEIN KINASES-1 (ROCK1) INHIBITORS	589
A METRIC FOR PAIRWISE SIMILARITY ANALYSIS OF BINARY CHEMINFORMATICS DATA.....	593
COUMARINS AS PROMISING PPAR α AGONISTS. NOVEL <i>IN SILICO</i> INSIGHTS	597
COMBINED <i>IN SILICO</i> APPROACH TO IDENTIFY NEW TERPENOID PPAR α AGONISTS.....	601

<i>IN SILICO</i> SCREENING OF <i>SOLANUM LYCOPERSICUM</i> CAROTENOIDS FROM CAROTENOIDS DATABASE FOR CANDIDATES PPARA AGONISTS	605
NUMERICAL SIMULATIONS OF THE OSCILLATORY DYNAMICS IN THE BRAY-LIEBHAFSKY REACTION PERTURBED BY L-TYROSINE.....	609
THE ASSESSMENT OF THE ANTIOXIDANT CAPACITY OF THE SELECTED VANILLIN-BASED PYRIDO-DIPYRIMIDINES USING DPPH ASSAY: <i>IN SILICO</i> APPROACH	613
INHIBITORY POTENTIAL OF BARBARIN AND ITS PLATINUM(II) COMPLEX TOWARDS PBP1A PROTEIN	617
MODELING ION- π INTERACTIONS OF TRANSITION METAL COMPLEXES	621
SUBSTITUENT EFFECTS ON STACKING INTERACTIONS OF AROMATIC LIGANDS IN ORGANOMETALLIC COMPOUNDS – CHEMOINFORMATICS AND QUANTUM CHEMICAL STUDY	625
COMPUTATIONAL STUDY ON THE INTERACTIONS OF QUERCETIN 3-O-RUTINOSIDE WITH HUMAN DPP III	629
NONCOVALENT INTERACTIONS OF HALOGEN ATOMS IN HALOGENATED BIPYRIDINES	633
REPULSIVE WATER-WATER CONTACTS FROM CAMBRIDGE STRUCTURAL DATABASE	637
COMPUTER-AIDED DESIGN OF NEW DRUGS AGAINST BREAST CANCER.....	641
STACKING INTERACTIONS AT LARGE HORIZONTAL DISPLACEMENTS—COMPARISON OF VARIOUS RING TYPES.....	645
INFLUENCE OF COORDINATION ON OH/ π AND NH/ π INTERACTIONS	649
RELATIVISTIC DFT CALCULATION AND THEIR EFFECT ON THE ACCURACY OF RESULTS	653
ANALYSIS OF PREDICTION OF WATER SOLUBILITY AND LIPOPHILICITY OF COUMARINS BY FREE CHEMINFORMATICS TOOLS	657
INFLUENCE OF PHTHALIMIDE SUBSTITUTION ON THE INTERACTION WITH CARBON NANOTUBE	662
INTERACTION ENERGY AND DECOMPOSITION OF INTERACTION ENERGY OF HALO-SUBSTITUTED PHTHALIMIDE WITH CARBON NANOTUBE	666
IDENTIFICATION OF SMALL MOLECULE BINDING SITES USING CMDOCK	670
A COMPREHENSIVE <i>IN SILICO</i> PROTOCOL FOR FAST AUTOMATED MUTAGENESIS AND BINDING AFFINITY SCORING OF PROTEIN-LIGAND COMPLEXES	674
WORKFLOW AUTOMATION OF HIGH-THROUGHPUT INVERSE DOCKING USING PHARMMAPPER	678
INVESTIGATING THE POTENTIAL INHIBITORY EFFECT OF THE MEGAPHONE (MOLECULE) ON NASOPHARYNGEAL CANCER GROWTH FACTOR RECEPTORS	682
GREEN SYNTHESIS OF CHROMENO-PYRIMIDINE DERIVATIVES – PART I.....	686
CHROMENO-PYRIMIDINE-TYPE COMPOUNDS (PART II): <i>IN VITRO</i> EVALUATION OF ANTIOXIDANT POTENTIAL	690

Plenary Lecturers

The Importance of Chemometrics in Drug Discovery from Medicinal Plants

Rudolf Bauer*

University of Graz, Institute of Pharmaceutical Sciences, Department of Pharmacognosy,
Beethovenstrasse 8, Graz, Austria

* Corresponding author

DOI: 10.46793/ICCB23.002B

Abstract: Drug discovery from medicinal plants has always been a longstanding and fruitful endeavor in the quest for novel therapeutic agents. Chemometric techniques, such as multivariate data analysis, enable the systematic analysis of complex chemical profiles obtained from plant extracts and correlation with activity. Compounds exhibiting high correlations in orthogonal projections to latent structures discriminant analysis (OPLS-DA) of pharmacological and MS data, are most promising for the identification of active constituents. Feature-based molecular networking within the Global Natural Product Social Molecular Networking (GNPS) helps to identify interesting compound clusters. Several examples are presented which demonstrate how these methods can be applied in drug discovery from medicinal plants.

Keywords: Medicinal plants, LC-MS, metabolomics, chemometrics, drug discovery

1. Introduction

According to a recent evaluation, about two-thirds of all therapeutic agents are directly or indirectly derived from nature [1]. Therefore, drug discovery from medicinal plants has been a longstanding and fruitful endeavor. However, the chemical complexity of plant extracts, coupled with the intricate bioactivity profiles, poses considerable challenges in the identification and development of effective drug candidates. In recent years, chemometrics, a multidisciplinary approach combining analytical chemistry, statistics, and computer science, has emerged as an indispensable tool in the field of drug discovery from medicinal plants [2].

2. Using Metabolomics Methods for Analyzing Complex Chemical Profiles

Medicinal plants often contain hundreds to thousands of chemical constituents, each potentially contributing to their therapeutic effects. It is compared with an orchestra, in which each instrument somehow contributes to the overall effect. Therefore, "holistic methods", which cover as many constituents as possible, are needed for analyzing the constituents and effects of medicinal plants [3]. Plant metabolomics has now become more and more used [4]. Infrared spectroscopy, NMR, HPTLC, and HPLC-MS are the

most often used technique for this type of “fingerprint analysis”. Chemometric techniques, such as multivariate data analysis, enable the systematic analysis of complex chemical profiles obtained from plant extracts. Through techniques like principal component analysis (PCA) and hierarchical clustering, chemometrics allows researchers to uncover hidden relationships and patterns within these profiles, aiding in the selection of plants with promising bioactivity for further investigation. In this way, plant metabolomics can be applied for plant taxonomy, quality control, and identification of active constituents for drug discovery.

3. Using Metabolomics Methods for Identifying Bioactive Compounds

One of the challenging goals of drug discovery from medicinal plants is the identification of the bioactive compounds responsible for their therapeutic effects. LC-mass spectrometry-based metabolomics is certainly the most widely used method for discovering the active ingredients of medicinal plants [5]. Chemometrics assists in dereplication, a process that involves identifying known compounds in complex mixtures. By comparing experimental data with databases of known natural products, chemometric tools are very powerful in pinpointing bioactive compounds, saving time and resources. Moreover, chemometrics can aid in prioritizing compounds for isolation and characterization, streamlining the identification of novel lead compounds.

Within the Austrian research network project “Drugs from nature targeting inflammation”, we have successfully applied such LC-MS based methods [6]. Extracts from *Lonicera* species were subjected to UHPLC-HRMS analysis and to pharmacological testing in three anti-inflammatory assays. Compounds exhibiting high correlations in orthogonal projections to latent structures discriminant analysis (OPLS-DA) of pharmacological and MS data were considered as potentially activity-related candidates. 65 compounds were tentatively or unambiguously annotated. Of the potentially active candidate compounds, 15 were subsequently subjected to pharmacological testing and their activities were experimentally verified, confirming the relevance of *Lonicera* species as a source of anti-inflammatory active constituents. The flavone aglycone luteolin was correlated with inhibitory activity in the NF- κ B and IL-8 assays, and apigenin was identified as an NF- κ B inhibitor. 7-hydroxy-5,3',4',5'-tetramethoxyflavone was found as a potential IL-8 and NO inhibitor. Luteolin and apigenin potently inhibited NF- κ B activation and moderately inhibited IL-8 production. Luteolin was moderately active in the NO assay [7]. Therefore, this approach can assist in prioritizing compounds for specific pharmacological assays, ultimately guiding the selection of candidates with the highest likelihood of success in drug discovery.

Chemometric techniques can also contribute to predicting the pharmacological activities of plant extracts. We investigated the use of Attenuated Total Reflectance Fourier Transform Infrared (ATR-FTIR) spectroscopy as a tool for rapid and non-destructive assessment and prediction of anti-inflammatory properties of extracts from

Lonicera species. The extracts were tested for effects on four key players of inflammation: Nitric oxide (NO), interleukin 8 (IL-8), peroxisome proliferator-activated receptor β/δ (PPAR β/δ), and nuclear factor kappa-light-chain-enhancer of activated B-cells (NF- κ B). Multivariate analysis of variance (MANOVA) revealed a statistically significant, quantitative pattern-activity relationship between the ATR-FTIR spectra of the extracts and their ability to modulate these targets. OPLS discriminant models were used for the identification of extracts exhibiting high and low activity. Predictions made on an independent test set revealed good generalizability of the models. Partial least squares (PLS) regression models were successfully established to predict the ability of the extracts to suppress NO production and NF- κ B activity [8].

We have also applied a chemometrics and LC-MS based approach for identifying the constituents contributing to the bioactivity of Huangqi Jianzhong Tang (HJZT), a TCM herbal formula, which has been used for the treatment of various chronic inflammatory gastrointestinal diseases. Extracts of different polarities were prepared from every single herbal component and from HJZT decoction. These extracts were analyzed by means of UPLC-QTOF-MS/MS and the inhibitory effects of the extracts on TNF- α , IL-1 β and IFN- γ production were investigated in U937 cells. Phytochemical and pharmacological bioactivity data were correlated by OPLS-DA. 16 HJZT constituents were identified which are likely to contribute to the activities, including calycosin, formononetin, astragaloside I, liquiritigenin, 18 β -glycyrrhetic acid, paeoniflorin and albiflorin. The predicted results were verified in the corresponding pharmacological assays [10].

The TCM formula Hanshiyi (HSYF) has significantly reduced the number of severe cases of COVID-19 [10]. We applied Feature-based molecular networking within the Global Natural Product Social Molecular Networking (GNPS) [11], a web-enabled mass spectrometry knowledge capture and analysis platform, to identify compound clusters present in the mixture, which may be relevant for activity.

4. Conclusions

In conclusion, chemometrics has revolutionized the field of drug discovery from medicinal plants by providing analytical, predictive, and optimization tools that streamline the process of identifying bioactive compounds. Chemometrics will continue to play a pivotal role in unlocking nature's treasure trove of potential therapeutic agents, thereby contributing to the development of safer, more effective medicines derived from traditional herbal sources.

Acknowledgment

This research has been supported by the Austrian Science Funds (FWF projects S 10705 and S 10704), the China State-Funded Postgraduate Overseas Study Program, WTZ

Project CN 03/2013, and Eurasia-Pacific Uninet, funded by the Austrian Federal Ministry of Education, Science and Research (BMBWF) (EPU 15/2020).

References

- [1] Newman DJ, Cragg GM. *Natural Products as Sources of New Drugs over the Nearly Four Decades from 01/1981 to 09/2019*. J Nat Prod. 83(3) (2020) 770-803.
- [2] Sharma B, Yadav DK. *Metabolomics and Network Pharmacology in the Exploration of the Multi-Targeted Therapeutic Approach of Traditional Medicinal Plants*. Plants 11(23) (2022) 3243.
- [3] Ren, J. L., Yang, L., Qiu, S., Zhang, A. H., Wang, X. J. *Efficacy evaluation, active ingredients, and multitarget exploration of herbal medicine*. Trends in endocrinology and metabolism: TEM, 34(3) (2023) 146–157.
- [4] Guy, C., Kopka, J., Moritz, T. *Plant metabolomics coming of age*. Physiologia plantarum, 132(2) (2008) 113–116.
- [5] Guo, S., Qiu, S., Cai, Y., Wang, Z., Yang, Q., Tang, S., Xie, Y., Zhang, A. *Mass spectrometry-based metabolomics for discovering active ingredients and exploring action mechanism of herbal medicine*. Frontiers in chemistry 11 (2023) 1142287.
- [6] Waltenberger, B., Atanasov, A. G., Heiss, E. H., Bernhard, D., Rollinger, J. M., Breuss, J. M., Schuster, D., Bauer, R., Kopp, B., Franz, C., Bochkov, V., Mihovilovic, M. D., Dirsch, V. M., Stuppner, H. *Drugs from nature targeting inflammation (DNIT): a successful Austrian interdisciplinary network project*. Monatsh Chemie, 147 (2016) 479-491.
- [7] Pferschy-Wenzig, E. M., Ortmann, S., Atanasov, A. G., Hellauer, K., Hartler, J., Kunert, O., Gold-Binder, M., Ladurner, A., Heiß, E. H., Latkolik, S., Zhao, Y. M., Raab, P., Monschein, M., Trummer, N., Samuel, B., Crockett, S., Miao, J. H., Thallinger, G. G., Bochkov, V., Dirsch, V. M., Bauer, R. *Characterization of Constituents with Potential Anti-Inflammatory Activity in Chinese Lonicera Species by UHPLC-HRMS Based Metabolite Profiling*. Metabolites, 12(4) (2022) 288.
- [8] Nikzad-Langerodi, R., Ortmann, S., Pferschy-Wenzig, E. M., Bochkov, V., Zhao, Y. M., Miao, J. H., Saukel, J., Ladurner, A., Heiss, E. H., Dirsch, V. M., Bauer, R., Atanasov, A. G. *Assessment of anti-inflammatory properties of extracts from Honeysuckle (Lonicera sp. L., Caprifoliaceae) by ATR-FTIR spectroscopy*. Talanta 175 (2017) 264–272.
- [9] Nöst, X., Pferschy-Wenzig, E. M., Nikles, S., He, X., Fan, D., Lu, A., Yuk, J., Yu, K., Isaac, G., Bauer, R. *Identification of Constituents Affecting the Secretion of Pro-Inflammatory Cytokines in LPS-Induced U937 Cells by UHPLC-HRMS-Based Metabolic Profiling of the Traditional Chinese Medicine Formulation Huangqi Jianzhong Tang*. Molecules (Basel, Switzerland), 24(17) (2019). 3116.
- [10] Tian J, Yan S, Wang H, Zhang Y, Zheng Y, Wu H, Li X, Gao Z, Ai Y, Gou X, Zhang L, He L, Lian F, Liu B, Tong X. *Hanshiyi Formula, a medicine for Sars-CoV2 infection in China, reduced the proportion of mild and moderate COVID-19 patients turning to severe status: A cohort study*. Pharmacological research 161 (2020) 105127.
- [11] Nothias, L. F., Petras, D., Schmid, R., Dührkop, K., Rainer, J., Sarvepalli, A., Protsyuk, I., Ernst, M., Tsugawa, H., Fleischauer, M., Aicheler, F., Aksenov, A. A., Alka, O., Allard, P. M., Barsch, A., Cachet, X., Caraballo-Rodriguez, A. M., Da Silva, R. R., Dang, T., Garg, N., ... Dorrestein, P. C. *Feature-based molecular networking in the GNPS analysis environment*. Nature methods, 17(9) (2020) 905–908.

A review of the application of the finite element smeared concept to biomedical engineering problems

Miloš Kojić^{1,2,3}

¹ Bioengineering Research and Development Center (BioIRC), Prvoslava Stojanovića 6, 34000 Kragujevac, Serbia; e-mail: mkojic42@gmail.com

² Serbian Academy of Sciences and Arts, Knez Mihailova 35, 11000 Belgrade, Serbia

³ Houston Methodist Research Institute, The Department of Nanomedicine, 6670 Bertner Ave., R7 117, Houston, TX 77030

DOI: 10.46793/ICCB23.006K

Abstract: The biomechanical and biochemical processes in the biological systems of living organisms are extremely complex. Advances in understanding these processes are mainly achieved by laboratory and clinical investigations, but in recent decades they are supported by computational modeling. Besides enormous efforts and achievements in this modeling, there still is a need for new methods which can be used in everyday research and medical practice. In this review, first are presented the basic assumptions in the formulation of the smeared concept, termed as Kojic Transport Model (KTM) model - introduced by the author several years ago. Then, it is demonstrated the distinction and advantages of the KTM by referring to selected publications in the literature. Application of the KTM is illustrated on several examples which include drug delivery in tumors, heart electrophysiology, and lung airflow and molecular transport by diffusion.

Keywords: smeared finite element, Kojic Transport Model, biomechanics, engineering

Is Deuterium biologically significant? Some unexpected Deuterium spectroscopic data

Dražen Vikić-Topić^{1*}

¹Juraj Dobrila University of Pula, Croatia and Ruđer Bošković Institute, Zagreb, Croatia

* *Corresponding author*

DOI: 10.46793/ICCB23.007VT

It is well known that hydrogen plays an important role in biological processes. The structures of nucleic acids and proteins are highly dependent on pH and hydrogen bonding. It was experimentally observed and theoretically calculated that the deuterium (D) bonds are somewhat shorter and hence stronger than the hydrogen (H) bonds. Consequently, the changing of H/D ratio induces differences in biomolecular structure. Although such differences between H and D structures are often minor they are not necessarily irrelevant since they depend on the degree of deuteration *i.e.* on cumulative D-effects. Anyway, the role of D in the evolution of biological systems is still unclear.

Due to the relatively easy of incorporation of D into the molecules and 100% fractional mass changing upon going from H to D, which causes peculiar effects, there is still a lot of interest in deuterium research.

Harold C. Urey¹ discovered deuterium in 1931 and gave its name. Deuterium is produced in stars in high amounts. On planet Jupiter abundance of D is 26 ppm, while on planet Venus is even 16.000 ppm. On Earth, the average natural abundance of D is 156 ppm (0.0156%), which means that only one atom of D is present in 6420 atoms of H. More precisely the natural abundance of D on Earth in water varies from 90 ppm at the South Pole to 180 ppm at the Equator.

Substitution of 20% of H₂O with D₂O causes the death of plants. In animals if one substitutes 25% of body H₂O with D₂O cell division problems occur and sterility arises. Substitution of 50% H₂O with D₂O in animals causes death by cytotoxic syndrome, bone marrow failure and gastrointestinal lining failure. Contrary to it, prokaryotic organisms can survive and even grow, although very slowly, in pure D₂O.

It seems that small amounts of D are needed in some biological processes. G. Somlyai et al. [2] revealed that deuterium-depleted water (30-40 ppm D), instead of water containing the natural abundance of D (156 ppm), significantly decreased the growth rate of the L₉₂₉ fibroblast cell line. Also, deuterium-depleted water inhibited the tumor

growth in xenotransplanted mice, since eighty days after transplantation in 10 tumourous mice (out of 17) the growing tumor regressed and disappeared.

On the molecular level D substitution gives rise to some unexpected effects *i.e.* optical activity in CXYHD. Also, small dipole moments (10^{-2} - 10^{-4} D) in monodeuterated benzene and acetylene are present enabling the measurements of pure rotational spectra of these otherwise symmetrical compounds. In addition, an unusual feature of deuterium labeling is the existence of long-range deuterium isotope effects (LRDIE) on ^{13}C NMR chemical shifts. The high magnetic field NMR spectrometers (400-600 MHz) have enabled the detection of very subtle LRDIE, as small as 0.1 Hz, even through 12 C-C bonds in extended π -electron systems. The exact calculations of LRDIE are still challenging because of their rather low magnitude (from 0,5 ppb up) and lack of reliable theoretical underpinning for isotope interactions through more than one and two bonds. The isotope effects on chemical shifts in NMR spectroscopy are interpreted in terms of vibrational and rotational averaging of nuclear shielding. Changes in nuclear shielding with bond extension and / or bond angle deformation are accompanying deuteration processes. In the theoretical approach to LRDIE at least two contributions have to be taken into account: (1) the secondary change in shielding at remote C-atom due to shorter C-D than C-H mean bond length at the site of deuteration and (2) the primary change in remote C-atom shielding, due to change in mean bond length at this remote site. We have postulated that LRDIE predominantly arises from (1), *i.e.* primary change of bond length at the site of deuteration, since vibrational differences at remote C-atoms in isotopomers are extremely small. The C-D bond was modeled by reduction of the corresponding C-H bond in the range 0.003-0.018 Å, since there is a great deal of experimental data on this reduction in the range of 0.001-0.020 Å. Nuclear shieldings (GIAO) and atomic charges (Löwdin, Mulliken) were calculated for fully optimized structure by different *ab initio* basis sets. For C-atoms more than 4 bonds away from the deuteration site, the differences of theoretically calculated shieldings and charges between protonated and deuterated molecules correlate fairly well with experimental LRDIE data. By this approach experimentally measured LRDIE can be successfully theoretically reproduced even over 10 and 12 C-C bonds, in our deuterated molecules and deuterated molecules published in literature by other investigators. All deuterated molecules were synthesized at Ruđer Bošković Institute, University of Pula and Faculty of Chemical Engineering and Technology, University of Zagreb as well as through collaborative projects with National Institutes of Health, Bethesda, MD, USA and Kernforschungszentrum Karlsruhe, Germany and National Institute of Chemistry, Ljubljana, Slovenia.

On the basis of here obtained experimental and theoretical data we shall discuss on the peculiar behaviour of deuterium in these model compounds and possibility of use and transfer these knowledge to biological systems.

As a short conclusion our results on model molecules do not mean that D-atom has different electronic properties than the H-atom, but it reveals that due to 100% of fractional mass change on going from H to D, subtle electronic redistribution of charges in deuterated molecules in comparison to H-ones occurs, which is due to disturbance of vibrational and rotational molecular modes upon deuteration. This redistribution of charges is just enough significant to affect various physical and chemical properties of deuterated molecules in comparison with hydrogenated ones, giving one set of data which could help in understanding the biological meaning of deuterium.

References

- [1] Urey, H. C., Brickwedde, F. G., Murphy, G. M., *A hydrogen isotope of mass 2 and its concentration*, Phys. Rev, **1932**, 40, 1-15
- [2] Somlyai, G., Jancso, G., Jakli, G., Vass, K., Barna, B., Lakics, V., Gaal, T., *Naturally occurring deuterium is essential for the normal growth rate of cells*, FEBS Letters, **1993**, 317, 278.

Targeting depression via computational approaches to design new coumarin-based serotonin receptor antagonists/agonists and develop reliable models of G protein-coupled receptors

Bartosz Trzaskowski^{1*}, Kinga Ostrowska²

¹ University of Warsaw, Centre of New Technologies, Warszawa, 2c Banacha Str., 02-097 Poland; e-mail: b.trzaskowski@cent.uw.edu.pl

² Medical University of Warsaw, Department of Organic Chemistry, Faculty of Pharmacy, 1 Banacha Str., 02-097 Warsaw, Poland e-mail: kostrowska@wum.edu.pl

DOI: 10.46793/ICCBi23.010T

Abstract: It has been over 60 years since the pharmacological mechanisms of action of antidepressant drugs and the role of serotonin, norepinephrine, and dopamine in depression and other neurological disorders have been established. Since then, a very large number of chemical compounds targeting among others, serotonin and dopamine receptors have been developed. Here we present the most recent approaches to design and develop a new class of coumarin-based candidates for antidepressants with the help of computational studies.

Keywords: serotonin, G protein-coupled receptors, modelling, depression, coumarins

1. Introduction

Among the most significant classes of natural compounds, an important position is occupied by coumarin-related drugs [1]. Both natural and synthetic coumarin derivatives can be used in the therapy of neurodegenerative mental disorders such as Alzheimer's and Parkinson's disease, schizophrenia, epilepsy or depression. The medical interest in coumarins is related to their effects on the central nervous system, in particular on the serotonergic and dopaminergic systems. Since that serotonin (5-HT) and dopamine (DA) receptors, members of the G protein-coupled receptor (GPCR) family, are involved in the mechanisms of many neurological and psychiatric disorders, research on chemicals that affect these systems is a huge branch of drug chemistry [2]. Natural coumarins such as scopoletin isolated from *Polygala sabulosa* and psoralen isolated from *Psoralea corylifolia* seeds have antidepressant activity that is a result of the activation of serotonergic neurotransmission and dopaminergic receptors [3], while scoparone from *Artemisia scoparia*, as well as licopyranocoumarin and glycyrurol, isolated from a *Glycyrrhiza sp.*, showed neuroprotection by reducing L-DOPA induced cytotoxicity in PC12 cells or inhibiting MPP⁺-induced neuronal PC12D cell death [4]. There are also numerous examples of coumarin derivatives, particularly 7-, 6- and 5-hydroxycoumarins, acting on the central nervous system and with high affinities to serotonin and dopamine receptors [5].

The search for new coumarin derivatives acting on the central nervous system is often a daunting hit-or-miss task, particularly if no design phase is planned. As a result, various computational approaches have been used to aid in this important task. Here we will review more than 10 years of our research in this field which led to the development of over 200 active compounds interacting with serotonin and dopamine receptors.

2. Results

The first literature reports on the action of N-phenylpiperazinyl derivatives of coumarin appeared in 1998. The authors described four compounds containing N-aryl piperazinyl moiety which is very important for CNS-activity, especially for serotonergic and dopaminergic activity [6]. The idea to study coumarin piperazine derivatives was later expanded by Chen et al. in a series of investigations [5,7]. Chen's and Santana's strategy was continued by the Ostrowska group, which first designed a series of biologically active compounds based on 7-hydroxy-4-methylcoumarin as the leading structure. It was found that the additional acetyl moiety with the ability to form hydrogen bonds, was more potent in binding additional residues in the 5-HT_{1A} receptor pocket, compared to compounds with methyl or chlorine group in C-8 position. As previously mentioned,, the action on 5-HT_{1A} and 5-HT_{2A} serotonin receptors has also been tested for a series of new derivatives with structural differences in the arylpiperazine moiety and different link lengths between the piperazinyl ring and coumarin [8-11]. Biological investigations were carried out on 5-HT_{1A/2A} receptors, which are known as important factors in the pathogenesis and treatment of depression.

In some of these studies, the design phase was based solely on scarce experimental data available with no computational modelling support. However, for several serotonin and dopamine receptors, there are available crystal structures, allowing one to incorporate the computational design phase to improve the process of obtaining novel compounds with the coumarin core. In order to do that in our next studies we extensively use computational modelling to provide rational design of novel compounds. In most cases we used homology modelling to the most similar GPCRs available in the crystal structures database. In our first studies we used the human dopamine D3 receptor to obtain a model of the 5-HT_{1A} receptor [8] and obtained binding affinities which were in good agreement with the experimental data. However, studying binding affinities to only one protein in the context of potential antidepressant design is suboptimal, as most of active compounds interact with several different serotonin and/or dopamine receptors. Therefore, in the next study, we expanded the scope of the studies by investigating the affinity of new coumarin derivatives to both 5-HT_{1A} and 5-HT_{2A} receptors. Previously 5-HT_{1A} homology model was obtained using the D3 receptor as the scaffold, while to obtain a homology model of 5-HT_{2A} receptor we used turkey b1 adrenergic receptor [10]. As in the previous work, computational docking studies allowed us to shed more light onto the binding modes of new derivatives and design next series of potential active compounds. In the following study, we further expanded the scope by including experimental binding affinities of protein-ligand complex

modelling for D2 dopamine receptor, whose crystal structure was recently solved [12]. It is worth noting, however, that in selected cases the agreement between the experimental and computational binding affinities was rather moderate [13]. The most likely explanation of these discrepancies is the combination of the imperfection of our computational model of the 5HT_{2A} receptor, particularly in the binding site part and the limited accuracy of the computational methods. The second problem is very well-known in the scientific community, as it has been shown that while Autodock and other similar programs can identify the correct binding poses, they often have a problem predicting correct binding affinities [14]. As for the accuracy of homology models of GPCRs, they certainly can be improved by resorting to more sophisticated methods, such as e.g., using multiple templates or going beyond the homology modelling, and we are planning to make use of these new methods in the future [15].

3. Conclusions

Coumarins have a wide range of biological activities, and many of them occur in traditional medicinal plants that are still used around the world. Coumarin-piperazinyl derivatives have been shown to possess activity as antidepressants, anticancer, antibacterial agents and as α -adrenergic antagonists. Due to the potential widespread use of these structures, they can be treated as scaffolds to develop new leading structures and, as a result, can be considered as future therapeutic agents for use in a variety of important diseases. As we are currently in the decade of an unprecedented rise of coumarin-related studies but also the rise of new powerful computational approaches to modelling both structures of proteins and protein-ligand complexes, combining the expertise of experimental and computational scientists and groups should lead to faster development of even more potent compounds.

References

- [1] K. Ostrowska, E. Hejchman, D. Grzeszczuk, N. Kruk., *Leki kumarynowe*, *Farmacja Polska* 6 (2013), 303-310.
- [2] M. Jaber, S.W. Robinson, C. Missale, M.G. Caron., *Dopamine receptors and brain function*. *Neuropharmacology* 35 (1996), 1503-1519.
- [3] J.C. Capra, M.P. Cunha, D.G. Machado, A.D. Zomkowski, B.G. Mendes, A.R. Santos, M.G. Pizzolatti, A.L. Rodrigues., *Antidepressant-like effect of scopoletin, a coumarin isolated from Polygala sabulosa (Polygalaceae) in mice: evidence for the involvement of monoaminergic systems*, *Eur. J.Pharmacol.* 643 (2010), 232-238.
- [4] T. Fujimaki, S. Saiki, E. Tashiro, D. Yamada, M. Kitagawa, N. Hattori, M. Imoto., *Identification of licopyranocoumarin and glycyrurol from herbal medicines as neuroprotective compounds for Parkinson's disease*, *PLoS One.* 9 (2014), 100395-100412.
- [5] Y. Chen, S. Wang, X. Xu, X. Liu, M. Yu, S. Zhao, S. Liu, Y. Qiu, T. Zhang, B.F. Liu, G. Zhang., *Synthesis and biological investigation of coumarin piperazine (piperidine) derivatives as potential multireceptor atypical antipsychotics*, *J. Med. Chem.* 56 (2013), 4671-4690.
- [6] C. Teran, L. Santana, E. Uriarte, Y. Fall, L. Unelius, B.R. Tolf., *Phenylpiperazine derivatives with strong affinity for 5-HT_{1A}, D_{2A} and D₃ receptors*, *Bioorg. Med. Chem. Lett.*, 8 (1998), 3567-3570.

- [7] Y. Chen, Y. Lan, S. Wang, H. Zhang, X. Xu, X. Liu, M. Yu, B.F. Liu, G. Zhang, .*Synthesis and evaluation of new coumarin derivatives as potential atypical antipsychotics.*, Eur. J. Med. Chem. 74 (2014), 427-439.
- [8] K. Ostrowska, D. Grzeszczuk, M. Głuch-Lutwin, A. Gryboś, A. Siwek, Ł. Dobrzycki, B. Trzaskowski., *Development of selective agents targeting serotonin 5HT_{1A} receptors with subnanomolar activities based on a coumarin core*, Med. Chem. Comm., 8 (2017), 1690-1696.
- [9] K. Ostrowska, K. Młodzikowska, M. Głuch-Lutwin, A. Gryboś, A. Siwek, *Synthesis of a new series of aryl/heteroarylpiperazinyl derivatives of 8-acetyl-7-hydroxy-4-methylcoumarin with low nanomolar 5-HT_{1A} affinities*, Eur. J. Med. Chem., 137 (2017), 108-116.
- [10] K. Ostrowska, D. Grzeszczuk, M. Głuch-Lutwin, A. Gryboś, A. Siwek, A. Leśniak, M. Sacharczuk, B. Trzaskowski., *5-HT_{1A} and 5-HT_{2A} receptors affinity, docking studies and pharmacological evaluation of a series of 8-acetyl-7-hydroxy-4-methylcoumarin derivatives.*, Bioorg. Med. Chem., 26 (2018), 527-535.
- [11] T. Żółek, O. Dömötör, K. Ostrowska, E.A. Enyedy, D. Maciejewska., *Evaluation of blood-brain barrier penetration and examination of binding to human serum albumin of 7-O-arylpiperazinylcoumarins as potential antipsychotic agents*, Bioorg. Chem., 84 (2019), 211-225.
- [12] K. Ostrowska, A. Leśniak, U. Karczyńska, P. Jeleniewicz, M. Głuch-Lutwin, B. Mordyl, A. Siwek, B. Trzaskowski, B. Sacharczuk, M. Bujalska-Zadrozny., *6-Acetyl-5-hydroxy-4,7-dimethylcoumarin derivatives: Design, synthesis, modeling studies, 5-HT_{1A}, 5-HT_{2A} and D₂ receptors affinity*, Bioorg. Chem. (2020), 100, 103912.
- [13] K. Ostrowska, A. Leśniak, Z. Czarnocka, J. Chmiel, M. Bujalska-Zadrozny, B. Trzaskowski., *Design, Synthesis and Biological Evaluation of a Series of 5- and 7-hydroxycoumarin Derivatives as 5-HT_{1A} Serotonin Receptor Antagonists*, Pharmaceuticals, 14 (2021), 179.
- [14] Z. Wang, H. Sun, X. Yao, D. Li, L. Xu, Y. Li, S. Tian, T. Hou., *Comprehensive evaluation of ten docking programs on a diverse set of protein–ligand complexes: The prediction accuracy of sampling power and scoring power*. Phys. Chem. Chem. Phys., 18 (2016), 12964–12975.
- [15] J. K. Bray, R. Abrol, W. A. Goddard, B. Trzaskowski, C. E. Scott, *SuperBiHelix method for predicting the pleiotropic ensemble of G-protein–coupled receptor conformations.*, Proc. Nat. Acad. Sci. USA, 111 (2014), E72–E78.

Algorithms and web servers for protein binding sites detection in drug discovery

Janez Konc^{1,2,3,*}, Dušanka Janežič²

¹ National Institute of Chemistry, Theory Department, Hajdrihova 19, SI-1000 Ljubljana, Slovenia; e-mail: konc@cmm.ki.si

² University of Primorska, Faculty of Mathematics, Natural Sciences and Information Technologies, Glagoljaška ulica 8, SI-6000 Koper, Slovenia; e-mail: dusanka.janezic@upr.si

³ University of Ljubljana, Faculty of Pharmacy, Aškerčeva 7, SI-1000 Ljubljana, Slovenia

* *Corresponding author*

DOI: 10.46793/ICCBi23.014K

Abstract: Drug discovery is a protracted and demanding process, which can be expedited during its early stages through novel mathematical approaches and modern computing. To tackle this crucial issue, we are developing fresh mathematical solutions aimed at detecting and characterizing protein binding sites, pivotal for new drug discovery. This paper introduces algorithms founded on graph theory which we have devised to scrutinize target biological proteins. These algorithms yield vital data, facilitating the optimization of initial phases in novel drug development. A particular emphasis lies in the creation of pioneering protein binding site prediction algorithms (ProBiS) and innovative web tools for modeling pharmaceutically intriguing molecules—ProBiS tools. These tools have matured into comprehensive graphical resources for the study of proteins in the proteome. ProBiS stands apart from other structural algorithms due to its ability to align proteins with disparate folds, all without prior knowledge of the binding sites. This unique capability enables the identification of analogous binding sites and the prediction of molecular ligands of diverse pharmaceutical relevance. These ligands could potentially progress into drug candidates for treating diseases. Notably, this prediction is based on data sourced from the complete Protein Data Bank (PDB) and the AlphaFold database, encompassing proteins not yet cataloged in the PDB. All ProBiS tools are made available without charge to the academic community through <http://insilab.org> and <https://probis.nih.gov>.

Keywords: structural biology, protein binding sites, clique algorithm, ProBiS

1. Introduction

Proteins have functional regions on their surface called protein binding sites (ProBiS), which allow them to interact with other molecules. Each binding site typically binds one or a few specific molecules known as ligands. These ligands can take many forms, such as ions, proteins, nucleic acids, small molecules, and water molecules that bind to specific sites on protein structures. Detecting protein binding sites is important for gaining insight into protein functionality and is therefore essential for drug design.

We have developed a suite of protein binding site tools, collectively known as ProBiS tools shown in Figure 1, which includes algorithms, web servers, and databases for predicting protein binding sites and ligands [1]. These tools are based on a graph theoretic algorithm that we developed, which uses a fast and improved maximum clique algorithm to identify the largest fully connected subgraph in a protein graph [2–4].

We have made significant progress in addressing several pharmaceutical issues using our existing ProBiS tools based on our protein graph theory algorithms. These tools are currently the most precise and efficient available.

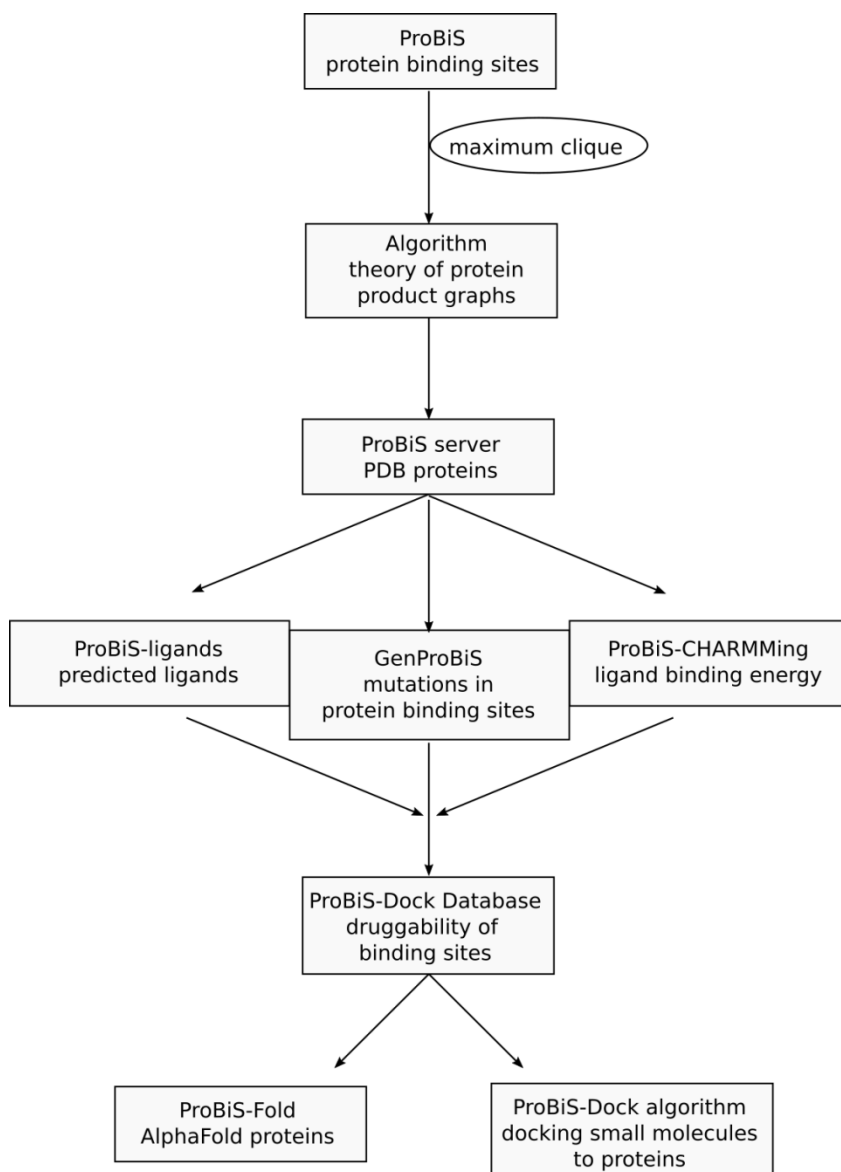


Figure 1. Evolution of Protein Binding Sites (ProBiS) tools.

2. Protein Binding Site (ProBiS) tools

The developed Protein Binding Site (ProBiS) tools (algorithms, web servers and databases) enable the detection of protein binding sites and ligands on experimental and modeled structures of pharmaceutically interesting proteins from the Protein Data Bank (PDB) or AlphaFold databases that could become targets for next-generation drugs. Recently developed tools include the following.

2.1 Graph theoretic algorithms for clique search

Heuristic and exact graph-theoretic algorithms for NP-hard problems in bioinformatics (<http://insilab.org/maxclique>). We have developed MaxCliqueDyn, a fast exact algorithm for finding a maximum clique in an undirected graph [2,3]. A clique is a fully connected subgraph of a graph, and a maximum clique is a clique with the largest number of vertices in a given graph.

Maximum clique algorithms differ from maximal clique algorithms, e.g., Bron-Kerbosch algorithm. The maximal search is for all maximal cliques in a graph (cliques that cannot be enlarged), while the maximum clique algorithms find a maximum clique (a clique with the largest number of vertices). This makes maximum clique algorithms about an order of magnitude faster.

The MaxCliqueDyn algorithm has two new features compared to the previous algorithms to increase its performance of maximum clique calculation.

It features an improved approximate coloring algorithm (ColorSort), which maintains the vertices in the candidate set R in the favorable decreasing order according to their degrees. This is based on the realization that the assignation of vertices into color classes (which disrupts the order) is only needed above a certain threshold, which we calculate as $K_{min} = |Q_{max}| - |Q| + 1$, where $|Q_{max}|$ is the size of the current maximum clique and $|Q|$ is the size of the clique found on the current branch of the search tree. Vertices with their colors below K_{min} can remain in their original order. This idea consistently reduces the number of steps needed to find a maximum clique as well as the time required to find a maximum clique.

Another distinguishing feature of the algorithm is that it is dynamic (indicated by the “Dyn” in its name), which indicates that it applies tighter, more computationally expensive upper bounds on a fraction of the search space. By doing this it is possible to reduce the time to find the maximum clique. Thus, we re-sort vertices in R by their degrees (DegreeSort) on the lower branches of the search tree enabled by a counter (S) and parameter ($Tlimit$) that turns on/off the sorting during the algorithm's execution dynamically. This heuristics increases the overall performance of the algorithm on a large number of DIMACS and random graphs, and can be tuned to specific graphs by changing the $Tlimit$ parameter.

2.2 ProBiS algorithm

ProBiS algorithm for detecting structurally similar binding sites in proteins using protein graph theory (<http://insilab.org/probis-algorithm>) [5]. Exploitation of locally similar 3D patterns of physicochemical properties on the surface of a protein for detection of binding sites that may lack sequence and global structural conservation.

ProBiS detects structurally similar sites on protein surfaces by local surface structure alignment. It compares the query protein to members of a database of protein 3D structures and detects with sub-residue precision structurally similar sites as patterns of physicochemical properties on the protein surface. Using an efficient maximum clique algorithm, the program identifies proteins that share local structural similarities with the query protein and generates structure-based alignments of these proteins with the query. Structural similarity scores are calculated for the query protein's surface residues and are expressed as different colors on the query protein surface. The algorithm has been used successfully for the detection of protein-protein, protein-small ligand and protein-DNA binding sites.

2.3 ProBiS-ligands web server

ProBiS-ligands web server is open and free to all users at (<http://probis.cmm.ki.si>) that predicts molecular ligands and their positions for a given protein based on the detection of similarities in protein binding sites in the PDB [6]. The server predicts the binding of ligands to a protein structure. Starting with a protein structure or binding site, ProBiS-ligands first identifies template proteins in the PDB that share similar binding sites. Based on the superimpositions of the query protein and the similar binding sites found, the server then transposes the ligand structures from those sites to the query protein. Such ligand prediction supports many activities, e.g., drug repurposing.

2.4 ProBiS-CHARMMing web server

Proteins often exist only as apo structures (unligated) in the PDB, with their corresponding holo-structures (with ligands) unavailable. However, apoproteins may not represent the amino-acid residue arrangement upon ligand binding well, which is especially problematic for molecular docking.

We developed the ProBiS-CHARMMing web interface freely available for academic users at <https://probis.nih.gov> [7]. We connected the ProBiS (<http://probis.cmm.ki.si>) and CHARMMing (<http://www.charmming.org>) web servers into one functional unit that enables the prediction of protein-ligand complexes and allows for their geometry optimization and interaction energy calculation.

The ProBiS web server predicts ligands (small compounds, proteins, nucleic acids, and single-atom ligands) that may bind to a query protein. This is achieved by comparing its surface structure against a nonredundant database of protein structures and finding those that have binding sites similar to that of the query protein. Existing

ligands found in similar binding sites are then transposed to the query according to predictions from ProBiS.

The CHARMMing web server enables, among other things, minimization and potential energy calculation for a wide variety of biomolecular systems, and it is used here to optimize the geometry of the predicted protein–ligand complex structures using the CHARMM force field and to calculate their interaction energies with the corresponding query proteins.

We showed how ProBiS-CHARMMing can be used to predict ligands and their poses for a particular binding site, and minimize the predicted protein–ligand complexes to obtain representations of holoproteins.

2.5 GenProBiS web server

GenProBiS web server (<http://genprobis.insilab.org>) maps sequence variants to binding sites to enable the detection of potentially harmful sequence variants in drug discovery [8]. Discovery of potentially deleterious sequence variants is important and has wide implications for research and generation of new hypotheses in human and veterinary medicine, and drug discovery.

The GenProBiS web server maps sequence variants to protein structures from the PDB, and further to protein–protein, protein–nucleic acid, protein–compound, and protein–metal ion binding sites. The concept of a protein–compound binding site is understood in the broadest sense, which includes glycosylation and other post-translational modification sites.

Binding sites were defined by local structural comparisons of whole protein structures using the Protein Binding Sites (ProBiS) algorithm and transposition of ligands from the similar binding sites found to the query protein using the ProBiS–ligands approach with new improvements introduced in GenProBiS. Binding site surfaces were generated as three-dimensional grids encompassing the space occupied by predicted ligands.

The server allows intuitive visual exploration of comprehensively mapped variants, such as human somatic missense mutations related to cancer and non-synonymous single nucleotide polymorphisms from 21 species, within the predicted binding sites regions for about 80 000 PDB protein structures using fast WebGL graphics.

2.6 ProBiS-Dock database

We have developed a new system, ProBiS-Dock, which can be used to determine the different types of protein binding sites for small ligands [9]. The binding sites identified this way are then used to construct a new binding site database, the ProBiS-Dock Database, that allows for the ranking of binding sites according to their utility for drug development. The newly constructed database currently has more than 1.4 million binding sites and offers the possibility to investigate potential drug targets originating from different biological species. The interactive ProBiS-Dock Database, a web server

and repository that consists of all small-molecule ligand binding sites in all of the protein structures in the PDB, is freely available at <http://probis-dock-database.insilab.org>.

The main goals of the newly developed database and web server are to facilitate drug discovery and selectivity prediction through the provision of downloadable binding sites ready for docking and inverse docking, which include all available PDBs. Additionally, the system aims to classify binding sites as orthosteric or allosteric and rank them based on their druggability, allowing for PDB-wide analysis. These goals are paramount to the success of the database and web-server and will greatly enhance the efficiency and accuracy of drug discovery efforts.

2.7 ProBiS Fold web server

ProBiS-Fold web server (<http://probis-fold.insilab.org>) determines protein binding sites for all ligand types for the entire human structural proteome from the AlphaFold database [10]. The server annotates human structures from the AlphaFold database with or without a corresponding structure in the PDB to discover new druggable binding sites. The ProBiS algorithm is used to compare each query protein structure predicted by the AlphaFold approach with the protein structures from the PDB to identify similarities between known binding sites found in the PDB and yet unknown binding sites in the AlphaFold database.

Ligands bound in these identified similar PDB sites are then transferred to each query protein from the AlphaFold database, and binding sites are identified as ligand clusters on an AlphaFold protein. Small molecule binding sites are assigned druggability scores based on the similarity of their ligands to known drugs, allowing them to be ranked according to their perceived and actual potential for drug development.

ProBiS-Fold provides interactive and downloadable binding sites for the entire human structural proteome, including more than 3000 new druggable binding sites that have no corresponding structure in the PDB, taking into account AlphaFold's model quality, to enable protein structure–function relationship studies and pharmaceutical drug discovery research.

This newly developed web server is groundbreaking as it enables the identification of interactions between a vast majority of human protein structures, not just those from the PDB. This enables the exploration of binding sites throughout the entire human proteome. The web server also provides interactive and downloadable data on binding sites that can be used for functional studies and drug discovery. It also facilitates structure-based virtual screening to predict drug selectivity across the human proteome.

3. Conclusions

We have developed the ProBiS Tools for the detection of protein binding sites, as well as the prediction and characterization of ligands. The latest addition to this suite of tools is the newly developed ProBiS-Fold web server. This innovative server annotates

the AlphaFold human protein structure database, which comprises over 24,000 predicted protein structures. It achieves this by identifying ligand binding sites and sites for post-translational modifications. Additionally, it provides the 3D structures of ligands that bind to these sites. Utilizing a structure-based comparative approach, the ProBiS-Fold web server offers a groundbreaking capability: it enables the examination of structures within the AlphaFold Database that lack corresponding structures in the PDB. This tool predicts the precise locations of binding sites, identifies the ligands they bind to, and assesses the suitability of these binding sites for drug development. Notably, the ProBiS-Fold web server also assesses the reliability of AlphaFold structures, particularly in relation to binding sites. A remarkable achievement of the ProBiS-Fold web server is the categorization of binding sites into various types, including protein, peptide, nucleic acid, small molecule (substrate and cofactor competitive), metal ion, conserved water, and glycan categories. This categorization is dependent on the specific ligands that these binding sites interact with. We are pleased to make all of our past, present, and future web servers and tools freely accessible to academic users. You can access them at two primary URLs: <http://insilab.org> and <https://probis.nih.gov>.

Acknowledgment

This work was supported by the Slovenian Research Agency project grants N1-0142, L7-8269, J1-1715 and J1-9186 as well as the bilateral grant BI-RS/23–25-020.

References

- (1) Konc, J.; Janežič, D. Protein Binding Sites for Drug Design. *Biophys Rev* **2022**, *14* (6), 1413–1421. <https://doi.org/10.1007/s12551-022-01028-3>.
- (2) Konc, J.; Janežič, D. An Improved Branch and Bound Algorithm for the Maximum Clique Problem. *MATCH Commun. Math. Comput. Chem.* **2007**, *58* (5), 569–590.
- (3) Depolli, M.; Konc, J.; Rozman, K.; Trobec, R.; Janežič, D. Exact Parallel Maximum Clique Algorithm for General and Protein Graphs. *J. Chem. Inf. Model.* **2013**, *53* (9), 2217–2228. <https://doi.org/10.1021/ci4002525>.
- (4) Reba, K.; Guid, M.; Rozman, K.; Janežič, D.; Konc, J. Exact Maximum Clique Algorithm for Different Graph Types Using Machine Learning. *Mathematics* **2022**, *10* (1), 97. <https://doi.org/10.3390/math10010097>.
- (5) Konc, J.; Janežič, D. ProBiS Algorithm for Detection of Structurally Similar Protein Binding Sites by Local Structural Alignment. *Bioinformatics* **2010**, *26* (9), 1160–1168. <https://doi.org/10.1093/bioinformatics/btq100>.
- (6) Konc, J.; Janežič, D. ProBiS-Ligands: A Web Server for Prediction of Ligands by Examination of Protein Binding Sites. *Nucleic Acids Res.* **2014**, *42* (W1), W215–W220. <https://doi.org/10.1093/nar/gku460>.
- (7) Konc, J.; Miller, B. T.; Štular, T.; Lešnik, S.; Woodcock, H. L.; Brooks, B. R.; Janežič, D. ProBiS-CHARMMing: Web Interface for Prediction and Optimization of Ligands in Protein Binding Sites. *J. Chem. Inf. Model.* **2015**, *55* (11), 2308–2314. <https://doi.org/10.1021/acs.jcim.5b00534>.

- (8) Konc, J.; Skrlj, B.; Erzen, N.; Kunej, T.; Janezic, D. GenProBiS: Web Server for Mapping of Sequence Variants to Protein Binding Sites. *Nucleic Acids Res.* **2017**, *45* (W1), W253–W259. <https://doi.org/10.1093/nar/gkx420>.
- (9) Konc, J.; Lešnik, S.; Škrlj, B.; Janežič, D. ProBiS-Dock Database: A Web Server and Interactive Web Repository of Small Ligand–Protein Binding Sites for Drug Design. *J. Chem. Inf. Model.* **2021**, *61* (8), 4097–4107. <https://doi.org/10.1021/acs.jcim.1c00454>.
- (10) Konc, J.; Janežič, D. ProBiS-Fold Approach for Annotation of Human Structures from the AlphaFold Database with No Corresponding Structure in the PDB to Discover New Druggable Binding Sites. *J. Chem. Inf. Model.* **2022**, *62* (22), 5821–5829. <https://doi.org/10.1021/acs.jcim.2c00947>.

Toward quantitative Raman spectroscopy

Henryk A. Witek^{1,2,3,*}, Ankit Raj^{1,4}, Yen-Bang Chao¹

¹ National Yang Ming Chiao Tung University, College of Science, Department of Applied Chemistry, Hsinchu 30010, Ta Hsueh Rd. 1001, Taiwan, email: hwitek@nycu.edu.tw, ankit@nycu.edu.tw, brown0403.ac07g@nctu.edu.tw

² National Yang Ming Chiao Tung University, College of Science, Institute of Molecular Science, Hsinchu 30010, Ta Hsueh Rd. 1001, Taiwan

³ National Yang Ming Chiao Tung University, College of Science, Center of Emergent Functional Matter Science, Hsinchu 30010, Ta Hsueh Rd. 1001, Taiwan

⁴ Current address: Gakushuin University, Department of Chemistry, Tokyo 171-8588, Mejiro 1-5-1, Japan

* Corresponding author

DOI: 10.46793/ICCBi23.022W

Abstract: Raman spectra recorded using various Raman spectrometers can be quite different. The main reason for those discrepancies is the lack of a consistent calibration scheme. Our work over the past few years was devoted to finding a universal absolute calibration scheme of Raman apparatuses that would allow us to report consistent Raman spectra of molecules with an absolute intensity scale. The reported scheme is based on a carefully designed home-built Raman spectrometer, for which the conceivable sources of experimental errors have been included in the analysis, and hence eliminated. The experimental rotational and rovibrational Raman spectra of various isotopologues of molecular hydrogen (H₂, HD, and D₂) recorded on our apparatus are then compared to very accurate, state-of-the-art calculations of Raman cross-sections, and the comparison is used to design the final correction to the Raman intensity scale of our apparatus. The Raman spectrometer calibrated in this way is subsequently used to measure standardized Raman spectra of organic molecules, which can serve as benchmarks in the calibration of the plethora of Raman spectrometers used in chemical laboratories. Most of the experimental details of our work were already published previously (for detailed information, see the attached reference list); the current contribution focuses on theoretical aspects of our work.

Keywords: Raman spectroscopy, absolute intensity scale, calibration scheme, Raman cross-sections

1. Introduction

The theoretical foundations of molecular Raman spectroscopy were developed by Placzek [1], who used the invariants of the molecular polarizability tensor and the molecular vibrational wave functions as the basic building blocks of his theory. In principle, the molecular geometry-dependent mean polarizability $\bar{\alpha} = \bar{\alpha}(\vec{R})$ and polarizability anisotropy $\gamma = \gamma(\vec{R})$ together with the molecular geometry-dependent

rovibrational wave functions $\varphi_{\nu j} = \varphi_{\nu j}(\vec{\mathbf{R}})$ are sufficient to predict Raman spectra associated with molecular rovibrational transitions, $(\nu'j') \rightarrow (\nu''j'')$, where ν is the quantum number enumerating vibrational levels and j is the quantum number labelling rotational levels. In practice, the determination of these quantities is quite cumbersome, and a number of approximations are usually performed in quantum chemistry codes typically employed in such calculations. In particular, it is assumed that the vibrational potential is harmonic around the molecular equilibrium geometry $\vec{\mathbf{R}}_{\text{eq}}$ and that the polarizability invariants $\bar{\alpha}$ and γ are slowly varying functions of molecular geometry $\vec{\mathbf{R}}$, allowing one to retain only the first derivative terms in the Taylor expansion of $\bar{\alpha}$ and γ around the equilibrium geometry $\vec{\mathbf{R}}_{\text{eq}}$. The resulting double harmonic approximation [2] became a golden standard in theoretical determination of Raman intensities.

A typical Raman spectrometer consists of a large number of optical elements, such as lenses, lasers, filters, polarizers, pinholes, mirrors, polychromators, CCD cameras, etc. Each of these optical elements has its own, quite complicated spectral characteristic, which contributes to the distortions in the recorded Raman spectra. Consequently, each Raman spectrometer produces a different spectrum of the same compound, often with surprisingly large differences. A consistent calibration procedure, allowing one to post-process the recorded Raman spectrum using some corrective spectral envelope, could cast the recorded spectrum in a standard form. In general, no such procedure is available.

Our dream was to design standardized Raman spectra of a series of organic compounds that could help any experimentalist to design a post-processing correction scheme allowing him/her to cast the recorded Raman spectrum in a standard form. Our plan went one step further: We wanted to design benchmark spectra with accurate calibration of the intensity scale, which can be considered as an ultimate calibration. To this end, we had to eliminate all the sources of errors in both the experimental and theoretical procedures usually used to determine Raman spectra of molecules. A detailed sequence of steps used for this purpose is discussed in the next Section.

2. Calibration procedure

The procedure consisted of three steps described briefly below: (i) theoretical determination of very accurate spectral standards, (ii) experimental characterization and elimination of spectral distortions, and (iii) using the calibrated Raman spectrometer with accurate intensity scale to generate a series of absolute benchmark Raman spectra to be used as a calibration standard in the future.

2.1 Theoretical calculations of absolute Raman cross-sections

To eliminate the drawbacks of the double-harmonic approximation, we have decided to employ in the calibration process the isotopologues of molecular hydrogen (H_2 , HD, and D_2) and oxygen (O_2). For those systems, we performed very accurate calculations of polarizability invariants of molecular hydrogen as a function of the

molecular geometry and the excitation laser wavelength [3,4]. The rovibrational wave functions of molecular hydrogen were obtained by numerical solution to the rovibrational Schrödinger equation with centrifugal rotational potentials and very accurate vibrational potential including adiabatic, relativistic and radiative corrections [5]. The polarizability invariants, needed to compute the Raman cross-sections via Placzek's formalism, were obtained by numerical integration over the vibrational coordinate. This accurate procedure demonstrated that the error in the theoretical cross-sections due to double harmonic approximation is about 3% [6].

2.2 Identification and elimination of experimental uncertainties

To eliminate the experimental uncertainties, a general multistep procedure for sensitivity analysis or Raman spectrometers has been designed, which consisted of three corrections allowing to eliminate various sources of experimental errors. The first correction accounted for the photons-per-wavenumber conversion factor. The second correction accounted for the various sensitivity offsets in the employed channels of the CCD camera. The third, final correction was based on the theoretically determined absolute Raman cross-sections of selected rovibrational transitions [7,8,9]. In addition to these developments, we have evaluated the variability of the recorded Raman spectra of selected molecular transition in long-lasting Raman experiments, showing that the fluctuations in the position and the intensity of Raman bands can be quite sizable [10].

2.2 Benchmark Raman spectra with absolute intensities

The Raman spectrometer calibrated using predicted Raman spectra of hydrogen was first used to generate gas-phase and liquid-phase benchmark Raman spectra of benzene and cyclohexane. [9] The latter were subsequently used to record (using absolute intensity scale) liquid-phase spectra of over 100 organic compounds to be used in the future as a benchmark for calibrating other Raman spectrometers.

3. Conclusions

A standardized Raman spectra of a series of organic compounds were obtained with an accurate intensity scale on a home-built Raman spectrometer calibrated using theoretically determined accurate Raman cross-sections of rovibrational transitions in molecular hydrogen. The spectra determined in such a way will serve as benchmarks for calibration (relative and absolute) of other Raman spectrometers as well as comparison with theoretical estimations.

Acknowledgment

This research was funded by the Ministry of Science and Technology, Taiwan (multiple grants) and the Center for Emergent Functional Matter Science of National Yang Ming

Chiao Tung University from the Featured Areas Research Center Program within the framework of the Higher Education Sprout Project by the Ministry of Education (MOE), Taiwan.

References

- [1] G. Placzek, *Rayleigh-Streuung und Raman-Effekt*, in *Handbuch der Radiologie*, (E. Marx (Ed.), Akademische Verlagsgesellschaft, Leipzig, vol. 6, 2 (1934), 209-374.
- [2] E. B. Wilson, J. C. Decius, P. C. Cross, *Molecular Vibrations: The Theory of Infrared and Raman Vibrational Spectra*, Dover Publications, New York, (1955).
- [3] A. Raj, H. Hamaguchi, H. A. Witek, *Polarizability tensor invariants of H_2 , HD, and D_2* , J. Chem. Phys., 148 (2018) 104308 (11 pages).
- [4] A. Raj, H. A. Witek, H. Hamaguchi, *Vibration-rotation interactions in H_2 , HD and D_2 : centrifugal distortion factors and the derivatives of polarisability invariants*, Mol. Phys., 118 (2020) e1632950 (13 pages).
- [5] L. Wolniewicz, *Relativistic energies of the ground state of the hydrogen molecule*, J. Chem. Phys., 99 (1993) 1851-1868.
- [6] A. Raj, Y. B. Chao, H. A. Witek, *Testing the limitations of harmonic approximation in the determination of Raman intensities*, Mol. Phys., 120 (2022) e2069613 (19 pages).
- [7] A. Raj, C. Kato, H. A. Witek, H. Hamaguchi, *Toward standardization of Raman Spectroscopy: Wavenumber and intensity calibration using rotational Raman spectra of H_2 , HD, D_2 and vibration-rotation spectrum of O_2 as primary standards*, J. Raman Spectrosc., 51 (2020) 2066–2082.
- [8] A. Raj, C. Kato, H. A. Witek, H. Hamaguchi, *Accurate intensity calibration of multichannel detectors using Raman intensity ratios*, J. Raman Spectrosc., 52 (2021) 2038–2050.
- [9] A. Raj, H. A. Witek, H. Hamaguchi, *Determination of accurate absolute Raman cross-sections of benzene and cyclohexane in the gas phase*, Asian J. Phys., 30 (2021) 321–335.
- [10] A. Raj, H. A. Witek, H. Hamaguchi, *Evaluating stability of a Raman spectrometer for long-time experiments*, J. Raman Spectrosc., 52 (2021) 1032–1047.

Synthetic Data Generation for Biomedical Deep Learning: Methods, Challenges, and Opportunities

Zlatan Car^{1,*}, Sandi Baressi Šegota¹, Branka Dobraš²

¹ Faculty of Engineering - University of Rijeka, Department of Automation and Electronics, Vukovarska 58, 51000 Rijeka, Croatia; e-mail: car@riteh.hr and sandibaressisegota@riteh.hr

² Faculty of Engineering - University of Rijeka, Department of Electric Power Systems, Vukovarska 58, 51000 Rijeka, Croatia; e-mail: branka.dobras@riteh.hr

* *Corresponding author*

DOI: 10.46793/ICCB23.026C

Abstract: With the proliferation of deep learning (DL) techniques in biomedical applications, the need for large-scale and diverse datasets has become more and more apparent. However, obtaining labeled biomedical data is often challenging. Concerns such as patient privacy, data sharing issues, ethical questions, and the lack of data - either due to the bias towards patients affected by an illness in medical examinations or due to the rarity of the investigated disease, can cause significant issues in the data collection process. In addition, manual annotation of collected data is time-intensive and requires trained personnel. One of the potential solutions discussed in the area of data science is the application of synthetically generated data, with the goal of creating artificial data points, based on previously collected data, which can aid in model training. A look into the existing synthetic data applications and generation methods, for both numeric and image data is provided by the authors. This paper explores the potential of synthetic data generation as a solution to this data scarcity, with the focus given on current state-of-the-art methods, standard approaches and challenges introduced by the application of the synthetic data in DL methodologies, and future opportunities in the field.

Keywords: biomedical data, data science, deep learning, generative data methods, synthetic data

1. Introduction

Deep learning (DL) is a subset of machine learning (ML) which focuses on model training on pure, unprocessed data [1]. This approach significantly simplifies the process of model training for researchers, as the algorithms can be applied directly to the collected (labeled) data. As there is no need for preprocessing, the modeling process is significantly sped up, as a large number of DL algorithms are available for direct application [2]. Despite the simpler approach, DL-based models have been shown to

have a higher performance ceiling in comparison to deterministic or classical ML approaches [3]. Still, the trade-off is the need for a much higher amount of training data points – while traditional deterministic approaches may be based on less than a hundred data points, and ML approaches may need less than a thousand; DL approaches will often require thousands of data points, if not tens of thousands of data points, in order to achieve a high-performing and well-generalizing model [4].

This need for a larger amount of data points is only exacerbated in fields in which data collection is already complicated, due to the complexity of the needed approaches or data scarcity. One of the fields in which this issue is most apparent is biomedicine. There are multiple issues which increase the complexity of collecting enough data to apply DL methods, the first of which is simply the lack of data [5]. Studying certain ailments which rarely appear in the population is a significant issue. Even when the data can be collected, it is rarely well-balanced, due to biases inherently present in the biomedical data [6]. Most of the patients who suffer from the ailments are the ones who fall into comorbidities, common to the ailment that is being investigated. Additionally, medical examinations are usually performed on patients which exhibit symptoms related to the investigated disease - because of which the patients which do not suffer from the investigated ailment may suffer from other diseases which can muddle the data. Finally, the ethical issues of data privacy make data collection complex [7]. Sharing the data between hospitals and research centers can be slowed down by the need for approvals from different levels of committees. This point is even more apparent when researchers attempt to alleviate the data collection issues by collecting data from multiple sources, especially when the hospitals included in the study originate from different countries [8].

One of the possible approaches which may be used to address the issue of the need for large data amounts is the application of synthetic data generation. This type of data collection is also commonly referred to as *in-silico* (compared to *in-vivo* and *in-vitro*) data collection [9]. While *in-silico* modeling and studies have been accepted as valid data study types, *in-silico* data generation for further studies is a newer field [10]. Synthetic data is based on simulation, statistics or heuristics of existing data, and allows for a very rapid generation of data points - provided that some data was already collected. Various methods for data generation exist and are commonly split into simulation and statistical approaches. Simulation approaches aim at the creation of simulated environments and data collection from executing the created simulations under different conditions, while statistical data generation includes statistical and heuristic methods which are trained on already collected data [11].

2. Research trends

Observing the trends for publications within the topic of DL in biomedicine can be performed by researching the number of publications focusing on the publications which include appropriate keywords. Figure 1 shows the number of papers which include the keywords “Deep Learning” and “Biomedicine” since 1991, as published in

Web of Science Core Collection indexed journals. Figure 1 shows an exponential growth in the number of papers published targeting the topics, indicating an interest in the application.

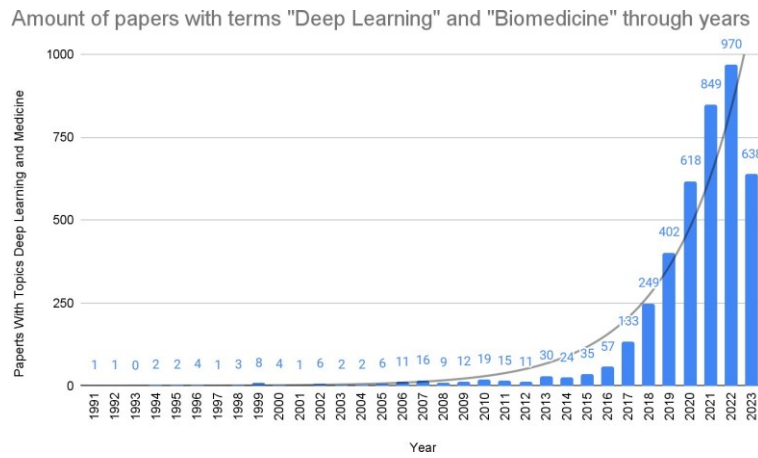


Figure 1. Publications which include keywords “Biomedicine” and “Deep Learning”, per year. From the Web of Science Core Collection. Includes related keywords and variations.

The same methodology can be applied to synthetic data, as shown in Figure 2. It can be seen that synthetic data has a significantly smaller number of publications, in conjunction with biomedicine. Such a discrepancy is significantly smaller when searching for synthetic data in all topics - which indicates less use of synthetic data compared to other fields. Still, a significant growth in the application of synthetic data in biomedicine is apparent since 2017. The point of note is the current year - this year's number of new publications is around 65% of the previous years, while for synthetic data the number is 93.75% (data collected August 2023). This indicates that the number of publications including synthetic data in biomedicine can be expected to experience a significant increase in this and upcoming years.

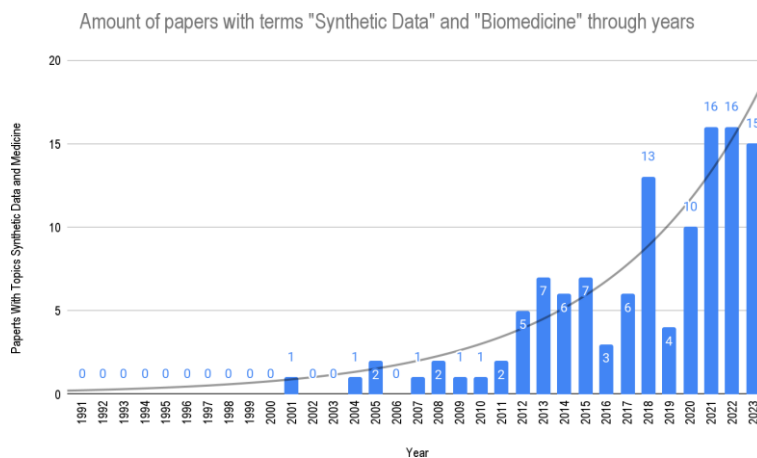


Figure 2. Publications which include keywords “Biomedicine” and “Synthetic data”, per year. From the Web of Science Core Collection. Includes related keywords and variations.

3. Synthetic data generation methods

3.1. Methods for generating synthetic image data

The process of generating image data is almost exclusively done with the application of generative adversarial networks (GANs). These networks consist of two separate but connected networks - the generator and differentiator. The process of training the GAN starts by training the differentiator. It is trained to classify the input images into two classes - 'real' and 'fake', which is accomplished by automatically labeling the images from the dataset as 'real' and generating random noise in the shape equal to the images and labeling it as 'fake' data. The second network - the generator, is trained to generate images from the random noise vector used as the output. The output of this network is then fed into the differentiator. If the differentiator notes the image as 'fake' this is used as the error and, using the standard backpropagation process, trains the generator. If the generated image is instead classified as real, this is in turn used as a differentiator error and backpropagated adjusting the weights. This process is repeated over the course of multiple iterations until a quality model is achieved [12].

The second manner in which image data can be generated is the use of generative pre-trained transformers (GPT) models. These models, commonly commercially available - such as DALL-E, can be used to generate high-quality images based on imputed textual prompts. Still, since they are trained on the general data - unlike GANs which are commonly developed on a specific targeted dataset, such models do not generate precise images in the context of medical applications yet [13].

3.2. Methods for generating numeric synthetic data

There are two main approaches in numeric data generation - heuristical and statistical. The heuristic approach is based on the same principle as the aforementioned GANs. Conditional Tabular GAN (CTGAN) is a method which works in nearly the same manner as GAN - through the training of adversarial networks, with the added conditionals which keep the generated data within desired ranges, based on the original data vectors. Other methods, such as Triplet-Encoded Variable Autoencoder (TVAE) use the same principle while replacing the neural network with a different ML-based algorithm as the foundation [14].

Statistical methods focus on modeling the descriptive statistics and distributions of data, and then generate the data that falls within such defined limits. One of the most commonly used methods are the copula-based methods. Copulas are equations which allow the mapping of one distribution to another. They are commonly applied by generating a hypercube with ranges $\langle 0,1 \rangle$, and dimensions equal to the number of variables. Then, the copula is determined, as a function that transforms the data vector of the input to the data of the uniform distribution. Then, randomly generated points within the hypercube can be transferred back using the inverse copula function - generating a new

data point [15]. It is common to combine these two types of methods - such as CopulaGAN which uses GANs to determine the copula functions for the dataset [16].

3.3. Simulation based synthetic data

Simulation based synthetic data refers to the process of creating a computational simulation of a certain process [14]. The created simulation must be verified against real data - with the common approach being the creation of testing sets, similar to ML. There are significant shortcomings of this approach - the researchers creating the model must be extremely familiar with the underlying intricacies of the problem (e.g., the anatomy), in addition to possessing the modeling knowledge. Additionally, the created models do not necessarily share the benefits associated with ML- and statistics-based models: most complex modeling parts are done by humans instead of automated software, rapid generation of results due to low computational cost is not present (depending on the simulation, the computational cost may be extremely high) and may be created in paid, domain-specific, software which can raise the barrier of use. The main benefit of such an approach is the possibility of clear model exploration - in other words, this approach avoids the “black-box” problem associated with ML-based models [17].

4. Challenges and best practices.

The goal of this chapter is to address the challenges with the use of synthetic data in biomedicine, split into three main groups - methodological, technical and ethical.

One of the main methodological concerns, currently largely unaddressed, is the so-called “mode collapse” [18], which presents itself as a low variety within the generated samples. The best manner of addressing this is to continually test the variety of the generated samples during the generator training. The second large issue is the problem of inherited bias [19]. Generated data is based on the original datasets, and it may include any of the biases that were present in the original data. The synthetization methods cannot address this issue by themselves, and because of that it is important to ensure that the original datasets do not contain biased data. Due to the lower amount of data necessary, this is more easily accomplished, and it can be addressed along with the generalization issue through the use of diverse data sources. Finally, there are the issues of overfitting the data and overgeneration. Data overfitting results from over-trained models which generate data that does not contain any variability and information not present in the original data - meaning that from the perspective of the training model algorithm used at the later stages of research, the new data points do not advance the modeling performance. This issue is commonly addressed through continual analysis of the generated data in comparison to the original data using entropy and variability measuring techniques [20]. Overgeneration can be addressed in the same manner. It refers to the mistake of generating a vast amount of data points, which do not introduce any new information (this can be thought of as a forced mode collapse due to large amounts of data), and only negatively affect the training times.

Technical issues also arise - such as the issue of training and storing the generated data. The generator models are more complex than the classification/regression models used in the later stages of research, and as such require high computing power [21].

Finally, ethical issues are the most commonly discussed issues pertaining to the use of synthetic data in biomedical applications. Two main concerns are patient protection and misrepresentation. Misrepresentation refers to the usage of synthetic data in lieu of real data without disclosing it. Data differentiation should be used on any datasets of questionable origin [11]. As for patient protection, two main issues arise. Consent for synthetic data use is questioned at large, in various fields [22] - while the data used in the study may not be the actual patient data, it is still based on it. The question of patient rights in this type of situation is largely unanswered. This is exacerbated by the pseudonymization issue, which posits that it may be possible to back-map the original data from the synthetic data, as that data is not completely anonymized. For this reason, it is important to perform proper anonymization procedures on the data prior to the use for data synthesization.

5. Future approaches

As mentioned previously, synthetic data is a hot-topic field. Due to this, methodological improvements can be expected. ML-based synthetization methods can benefit from any improvements related to improving the speed of ML-training, such as distributed training algorithms or advanced architectures [23]. This speed-up will allow for rapid synthesization of models, and allow the online training feedback loops which can continually update and test the models in an automated manner [24].

In addition to DL-model training there are plans for using the synthetic data in other manners, such as training. Generating synthetic data for the purposes of medical expert training can be valuable, especially in cases of rare diseases or atypical symptoms which may appear in synthetic data. This will allow the trainees to learn from a wider set of examples compared to possibly limited learning opportunities [25].

Finally, one of the larger issues which must be addressed in the future is the issue of oversight. The creation of national- or international-level bodies which will provide guidelines on the use and application of synthetic data may be key in the protection of patient privacy and the assurance of proper data use, to avoid issues of unreliable models being used [26]. Another manner of addressing issues related to synthetic data is the creation of data authenticity standards or proper synthetic data standards. Such standards will allow for the researchers to be certain that the data which they use in their study is original or generated using proper procedures [27].

6. Conclusions

The use of synthetic data in biomedical applications, especially for the development of DL-based prediction models is a highly researched topic, with many different methods being presented. Still, with the growing use of generated data points for model

training, it is important to continuously consider the possible issues and best practices that allow for the avoidance of negative consequences.

Acknowledgment

This research has been (partly) supported by the CEEPUS network CIII-HR-0108, European Regional Development Fund under the grant KK.01.1.1.01.0009 (DATACROSS), project CEKOM under the grant KK.01.2.2.03.0004, Erasmus+ project WICT under the grant 2021-1-HR01-KA220-HED-000031177 and University of Rijeka scientific grant uniri-tehnic-18-275-1447 and uniri-mladi-technic-22-61.

References

- [1] I. Goodfellow, Y. Bengio, and A. Courville. *Deep learning*. MIT press, 2016.
- [2] Y. LeCun, Y. Bengio, and G. Hinton. "Deep learning." *nature* 521, no. 7553 (2015): 436-444.
- [3] Y. Matsuo, Y. LeCun, M. Sahani, D. Precup, D. Silver, M. Sugiyama, E. Uchibe, and J. Morimoto. "Deep learning, reinforcement learning, and world models." *Neural Networks* 152 (2022): 267-275.
- [4] S. Dong, P. Wang, and K. Abbas. "A survey on deep learning and its applications." *Computer Science Review* 40 (2021): 100379.
- [5] P. Rajpurkar, E. Chen, O. Banerjee, and E.J. Topol. "AI in health and medicine." *Nature medicine* 28, no. 1 (2022): 31-38.
- [6] G.S. Nelson, 2019. Bias in artificial intelligence. *North Carolina medical journal*, 80(4), pp.220-222.
- [7] N.W. Price, and G. Cohen. "Privacy in the age of medical big data." *Nature medicine* 25, no. 1 (2019): 37-43.
- [8] J. Morley, C. Machado, C. Burr, J. Cowls, I. Joshi, M. Taddeo, and L. Floridi. "The ethics of AI in health care: a mapping review." *Social Science & Medicine* 260 (2020)
- [9] B. Shaker, S. Ahmad, J. Lee, C. Jung, and D. Na. "In silico methods and tools for drug discovery." *Computers in biology and medicine* 137 (2021): 104851.
- [10] S. Kar, and J- Leszczynski. "Open access in silico tools to predict the ADMET profiling of drug candidates." *Expert opinion on drug discovery* 15, no. 12 (2020): 1473-1487.
- [11] S. Baressi Šegota, N. Anđelić, D. Štifanić, J. Štifanić, and Z. Car. "On differentiating synthetic and real data in medical applications." (2023): 1-4.
- [12] I. Lorencin, S. Baressi Šegota, N. Anđelić, V. Mrzljak, T. Čabov, J. Španjol, and Z. Car. "On urinary bladder cancer diagnosis: Utilization of deep convolutional generative adversarial networks for data augmentation." *Biology* 10, no. 3 (2021): 175.
- [13] L. Adams, F. Busch, D. Truhn, M. Makowski, H. Aerts, and K. Bressemer. "What Does DALL-E 2 Know About Radiology?." *Journal of Medical Internet Research* 25 (2023): e43110.

- [14] S. Baressi Šegota, N. Anđelić, M. Šercer, and H. Meštrić. "Dynamics Modeling of Industrial Robotic Manipulators: A Machine Learning Approach Based on Synthetic Data." *Mathematics* 10, no. 7 (2022): 1174.
- [15] Z. Li, Y. Zhao, and J. Fu. "Sync: A copula based framework for generating synthetic data from aggregated sources." In *2020 International Conference on Data Mining Workshops (ICDMW)*, pp. 571-578. IEEE, 2020.
- [16] A. Shafquat, J. Mezey, M. Beigi, J. Sun, A. Gao, and J. Aptekar. "An interpretable data augmentation framework for improving generative modeling of synthetic clinical trial data." In *ICML 3rd Workshop on Interpretable Machine Learning in Healthcare (IMLH)*. 2023.
- [17] S. Baressi Šegota, I. Lorencin, Z. Kovač, and Z. Car. "On Approximating the pIC 50 Value of COVID-19 Medicines In Silico with Artificial Neural Networks." *Biomedicines* 11, no. 2 (2023): 284.
- [18] H. Thanh-Tung, and T. Tran. "Catastrophic forgetting and mode collapse inGANs." In *2020 international joint conference on neural networks (ijcnn)*, pp. 1-10. IEEE, 2020.
- [19] F. Jacobs, S. D'Amico, C. Benvenuti, M. Gaudio, G. Saltalamacchia, C. Miggianno, R. De Sanctis, M. Giovanni Della Porta, A. Santoro, and A. Zambelli. "Opportunities and Challenges of Synthetic Data Generation in Oncology." *JCO Clinical Cancer Informatics* 7 (2023): e2300045.
- [20] R. Chen, M. Lu, T. Chen, D. Williamson, and F. Mahmood. "Synthetic data in machine learning for medicine and healthcare." *Nature Biomedical Engineering* 5, no. 6 (2021): 493-497.
- [21] S. Nikolenko. *Synthetic data for deep learning*. Vol. 174. Springer Nature, 2021.
- [22] M. Lacasa, F. Prados, J. Alegre, and J. Casas-Roma. "A synthetic data generation system for myalgic encephalomyelitis/chronic fatigue syndrome questionnaires." *Scientific Reports* 13, no. 1 (2023): 14256.
- [23] M. Guillaudeux, O. Rousseau, J. Petot, Z. Bennis, C. Dein, T. Goronflot, N. Vince et al. "Patient-centric synthetic data generation, no reason to risk re-identification in biomedical data analysis." *NPJ Digital Medicine* 6, no. 1 (2023): 37.
- [24] S. Baressi Šegota, I. Lorencin, N. Anđelić, D. Štifanić, J. Musulin, S. Vlahinić, T. Šušteršič, A. Blagojević, and Z. Car. "Automated pipeline for continual data gathering and retraining of the machine learning-based COVID-19 spread models." *EAI Endorsed Transactions on Bioengineering and Bioinformatics* 1, no. 21 (2021)
- [25] K. Theodora, and K. Harron. "Synthetic data in medical research." *BMJ medicine* 1, no. 1 (2022).
- [26] A. Lal, J. Dang, C. Nabzdyk, O. Gajic, and V. Herasevich. "Regulatory oversight and ethical concerns surrounding software as medical device (SaMD) and digital twin technology in healthcare." *Annals of Translational Medicine* 10, no. 18 (2022).
- [27] R. Foraker, S. Yu, A. Gupta, A. Michelson, J. Pineda Soto, R. Colvin, F. Loh et al. "Spot the difference: comparing results of analyses from real patient data and synthetic derivatives." *JAMIA open* 3, no. 4 (2020): 557-566.

Section Lecturers

Benzene and water – different or similar?

Milan R. Milovanovic¹, Jelena M. Zivković¹, Dragan B. Ninković¹, Jelena P. Blagojević¹, Snežana D. Zarić^{2,*}

¹ Innovation Center of the Faculty of Chemistry in Belgrade, Studentski trg 12-16, Belgrade 11001, Serbia); e-mail: milovanovicmilan11@gmail.com, jelenaandric.chem@gmail.com, dragannin@yahoo.com, blagojevicj3@gmail.com

² University of Belgrade, Faculty of Chemistry, Studentski trg 12-16, Belgrade 11000, Serbia; e-mail: szaric@chem.bg.ac.rs

* Corresponding author

DOI: 10.46793/ICCB23.035M

Abstract: Considering the properties of water and benzene molecules, one can expect very different benzene/benzene and water/water interactions. Benzene does not have a dipole moment, while water does. Analysis of the data in the crystal structures in the Cambridge Structural Database (CSD) revealed the most frequent benzene/benzene and water/water geometries. The majority of the benzene/benzene interactions in the crystal structures in the CSD are stacking interactions with large horizontal displacements, and not geometries that are minima on benzene/benzene potential surface. A large number of the water/water contacts in the CSD are hydrogen bonds, 70% of all attractive water/water interactions. In addition, water/water contacts with two water forming antiparallel interactions are 20% of all attractive water/water contacts. In these contacts, the O-H bonds of water molecules are in antiparallel orientation. In benzene/benzene interactions at large horizontal displacements, two C-H bonds also are in the antiparallel orientation. This shows that although the two molecules are different, both of them form antiparallel interactions with a local O-H and C-H dipole moments.

Keywords: H-bond, T-shaped, stacking, noncovalent

1. Introduction

Both benzene and water are liquids at room temperature, and it is their common property. It means that intermolecular interactions are strong to keep molecules in the liquid phase, however, not strong enough to form a solid phase. It raises the interesting question of the intermolecular interactions among water molecules and among benzene molecules.

Water is a polar solvent. It has been well known, for over a hundred years, that water molecule is polar and forms hydrogen bonds, while hydrogen bonds define many properties of water as a substance. For example: melting and boiling temperatures, density of liquid water and ice, snowflakes and shapes of snowflakes. On the other hand, benzene is a non-polar solvent. Benzene boils at 80.1 °C, indicating that

interactions among benzene molecules are weaker than interactions among water molecules.

A large number of papers has been published on water hydrogen bonds and on interactions between benzene molecules. Quantum chemical calculations in the gas phase showed that the minimum on the potential surface of water/water dimer is the hydrogen bond, where the dipole moment of water plays an important role (Figure 1a). The calculations show that the minima on the potential surface for benzene/benzene are stacking (parallel displaced) geometry and T-shaped geometry (Figure 1).

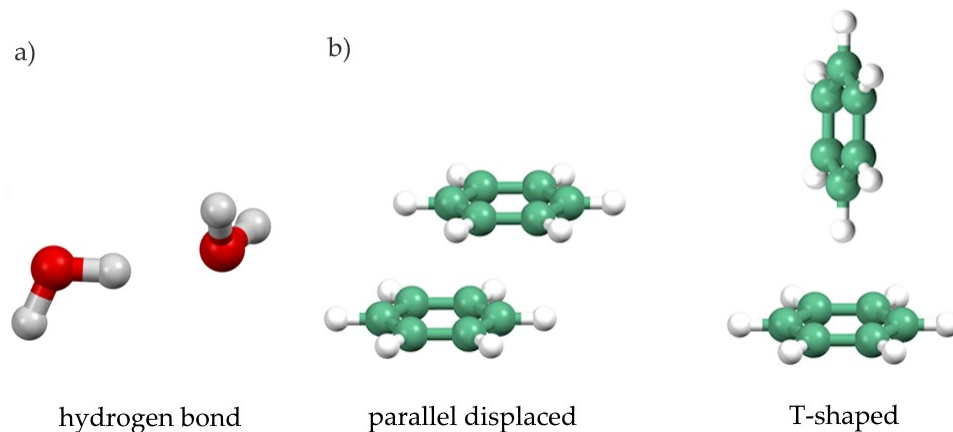


Figure 1. Minimum on potential surface for water/water dimer (hydrogen bond) and minima on potential surface for benzene/benzene dimer (parallel displaced and T-shaped geometry).

In this work, we compare the data on the water/water and benzene/benzene interactions in the crystal structures from the Cambridge Structural Database (CSD) and we show the common properties of these interactions.

2. Results and discussion

The analysis of all crystal structures in the Cambridge Structural Database (CSD) showed that the most frequent interaction between two water molecules is the hydrogen bond, in agreement with the calculated minimum on the potential surface in the gas phase (Figure 1a). However, the most frequent interaction of two benzene molecules is not in agreement with the calculated potential energy surface, it is stacking geometry (parallel displaced) with very large horizontal displacement (Figure 2b).

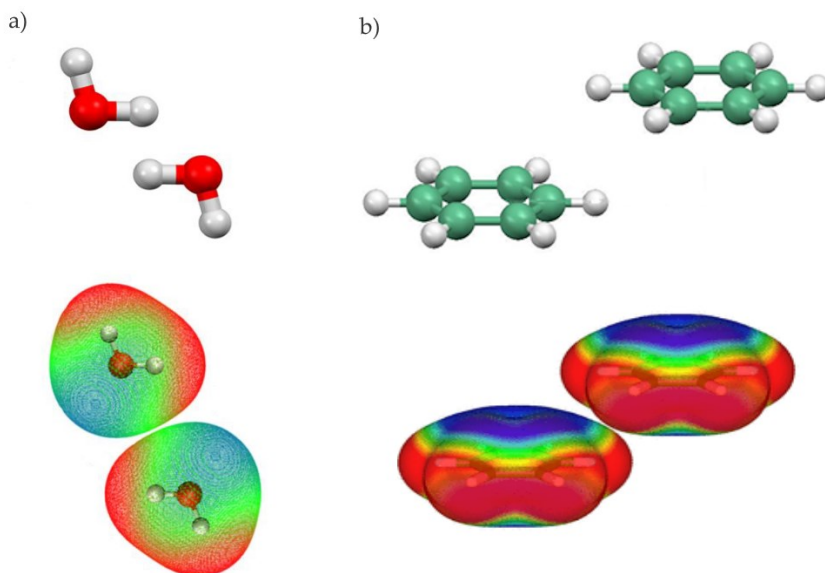


Figure 2. The water/water antiparallel interaction (a), benzene/benzene interaction at large horizontal displacement (b) and their corresponding overlaid electrostatic potentials.

The quantum chemical calculations of potential surface of water/water interactions showed that the minimum is a hydrogen bond. Analysis of the data in the crystal structures in the Cambridge Structural Database (CSD) revealed antiparallel water/water interactions, in addition to classical hydrogen bonds [1]. The geometries of all water/water contacts in the CSD were analyzed and for all contacts interaction energies were calculated at accurate CCSD(T)/CBS level. The results showed that the most frequent water/water contacts are hydrogen bonds; hydrogen bonds are 70% of all attractive water/water interactions. In addition, water/water contacts with antiparallel interactions are 20% of all attractive water/water contacts. In these contacts, O-H bonds of water molecules are in antiparallel orientation (Figure 2a).

The quantum chemical calculations of potential surface of benzene/benzene interactions showed two minima stacking (parallel displaced) geometry and T-shaped geometry. Analysis of all benzene/benzene contacts in the crystal structures in the CSD revealed the most frequent benzene/benzene geometries [2]. The majority of the benzene/benzene interactions in the CSD are stacking interactions with large horizontal displacements, and not geometries that are minima on benzene/benzene potential surface. In benzene/benzene interactions at large horizontal displacements two C-H bonds are in the antiparallel orientation (Figure 2b).

In these O-H and C-H antiparallel interactions, two dipoles are in antiparallel orientation enabling close contact of positive and negative regions of the dipoles (Figure 2). Symmetry Adapted Perturbation Theory (SAPT) analysis showed that electrostatic is the largest attractive force in antiparallel interactions. Antiparallel interactions are also possible between O-H and C-H bonds; in the crystal structures from the CSD these interactions are observed as one of the types of water benzene interactions [3].

3. Conclusions

In spite of being quite different substances, benzene and water can form similar noncovalent interactions. Analysis of the data in the crystal structures in the CSD revealed similarities in benzene/benzene and water/water interactions since both can form antiparallel interactions.

The analysis of the crystal structures from the CSD shows that the majority of the benzene/benzene interaction are stacking interactions with large horizontal displacements in which the dipole moment of the C-H bond plays an important role. A significant number of water/water interactions are antiparallel interactions, namely 20% of all attractive water/water contacts in the CSD are antiparallel interactions. These antiparallel interactions are a consequence of the interaction of two O-H bonds in which dipoles are in antiparallel orientation.

This shows that although these two molecules are very different, they can have similar interactions with respect to the local dipole moment. The deciding factor for these two important interactions is the antiparallel dipole moments of the O-H and C-H bonds.

Acknowledgment

This research is funded by the Ministry of Education and Ministry of Science, Technological Development and Innovation, Republic of Serbia, Grants: No. 451-03-47/2023-01/200168 and 451-03-47/2023-01/200288.

References

- [1] M. R. Milovanović, I. M. Stanković, J. M. Živković, D. B. Ninković, M. B. Hall, S. D. Zarić., *Water: new aspect of hydrogen bonding in the solid state*. IUCrJ, 9 (2022), 639-647.
- [2] D. B. Ninković, J. P. Blagojević Filipović, M. B. Hall, E. N. Brothers, S. D. Zarić., *What is Special about Aromatic–Aromatic Interactions? Significant Attraction at Large Horizontal Displacement.*, ACS Central Science, 6 (2020), 420-425.
- [3] G. V. Janjić, D. Ž. Veljković, S. D. Zarić., *Water/aromatic parallel alignment interactions. Significant interactions at large horizontal displacements*, Crystal Growth & Design, 11 (2011), 2680–2683.

The hydrogen economy: challenges and prospectives

Jasmina Grbović Novaković^{1*}, Sanja Milošević Govedarović¹, Igor Milanović¹, Tijana Pantić¹, Jelena Rmuš Mravik¹, Andjela Mitrović Rajić¹, Katarina Tošić¹, Milica Prvulović¹, Bojana Babić¹, Ana Vujačić Nikezić¹, Sandra Kurko¹, Nikola Novaković¹

¹The University of Belgrade, National Institute of Republic of Serbia, Vinča Institute of Nuclear Sciences, Centre of Excellence for Renewable and Hydrogen Energy, POB 522, 11000 Belgrade, Serbia

* *Corresponding author*

DOI: 10.46793/ICCB23.039GN

Abstract. The fossil fuels-based economy led to considerable growth in CO₂ footprint and air pollution. The shift toward renewable and green energy sources is necessary and a hydrogen-based economy may be a solution for both climate change and the need for a secure energy supply. To make the transition from the present carbon-based economy to the hydrogen economy several problems have to be solved, regarding the production, safety issues, and the storage of hydrogen. Hydrogen has high gravimetric chemical energy (142 MJ/kg) and its electrochemical reaction with oxygen in the fuel cell leads to zero carbon emission. It is abundant, but in the bonded form in water, hydrocarbons, and other organic compounds. The most of hydrogen is produced by the steam reforming of hydrocarbons. However, this is so-called “grey hydrogen”, as a considerable amount of CO₂ and CO is released during the process. To meet the sustainability criteria, it is necessary to make the methods of “green hydrogen” generation, like water electrolysis, more affordable and energy efficient. Thus, the development of low-cost, stable electrocatalysts with high activity for the hydrogen evolution reaction (HER) without noble metals, is a considerable challenge.

Among all possible solutions for hydrogen storage (gas cylinders, liquid tank, solid-state storage), the one which relies upon storage in solid media such as hydrides, is the most attractive. Solid-state storage implies hydrides such as metal/intermetallic and complex-chemical hydrides. Since the release of hydrogen from hydrides takes place via an endothermic process, this method of storage is the safest of all mentioned, but the problem of the slow sorption process and high temperature of desorption has to be solved if hydrogen is to be used as an energy carrier. In the last three decades, many studies have been performed, both experimental and theoretical, on the same subject - how to overcome these drawbacks. Sluggish thermodynamics and slow sorption/desorption kinetics can be altered by MgH₂ destabilization through surface modification and structural deformation.

To improve the diffusivity of hydrogen in the metal hydride, various techniques such as ball milling and ion bombardment are applied, which in turn reduces the particle size,

increases the defect concentration and shortens the diffusion path for hydrogen. Also, sufficiently fast hydrogen sorption kinetics has been achieved by using metals, metal oxides, transition metals, and transition metal oxides as additives in the process of milling. In this short review, we have summarized the possibilities for the storage and production of hydrogen by green synthesis methods.

Keywords: hydrogen economy, storage, hydrogen production, metal hydrides

1. Introduction

1.1 Hydrogen production – hydrogen colors

Hydrogen itself is a colorless gas, but there are nine color codes to identify hydrogen. The color codes of hydrogen refer to the source or the process used to make hydrogen. These codes are green, blue, grey, brown or black, turquoise, purple, pink, red, white, and gold.

- Green hydrogen is produced through the water electrolysis process by employing renewable electricity. The reason it is called green is that there is no CO₂ emission during the production process. Water electrolysis is a process that uses electricity to decompose water into hydrogen gas and oxygen. The main challenge is to find good catalyst for water splitting. A material with the most desirable properties for catalytic water splitting is molybdenum disulfide (MoS₂) [1]. Molybdenum disulfide (MoS₂), as a representative of the broad class of transition metal dichalcogenides (TMDC) attracts significant attention as a catalyst due to its high efficiency and abundance, noble metal-free composition, and consequently low cost [1]. Whereas bulk MoS₂ is not considerably catalytically active, various nanostructures express excellent HER activity and outstanding performance in charge storage. Most of the activities in our lab are based on the development of different nanostructures and their composites [1].
- Blue hydrogen is sourced from fossil fuels. However, the CO₂ is captured and stored underground (carbon sequestration). Involved companies are also trying to utilize it through Carbon Capture, Storage, and Utilization (CCSU) process. Utilization is not essential to qualify for blue hydrogen. As no CO₂ is emitted, the blue hydrogen production process is categorized as carbon neutral.
- Gray hydrogen is produced from fossil fuels and commonly uses the steam methane reforming (SMR) method. During this process, CO₂ is produced and eventually released into the atmosphere.
- Black or brown hydrogen is produced from coal. The black and brown colors refer to the type of bituminous (black) and lignite (brown) coal. The gasification of coal is a method used to produce hydrogen. However, it is a very polluting process, and CO₂

and carbon monoxide are produced as by-products and released into the atmosphere.

- Turquoise hydrogen can be extracted by using the thermal splitting of methane via methane pyrolysis. The process, though at the experimental stage, removes the carbon in a solid form instead of CO₂ gas.
- Purple hydrogen is made using nuclear power and heat through combined chemothermal electrolysis splitting of water.
- Pink hydrogen is generated through the electrolysis of water by using electricity from a nuclear power plant.
- Red hydrogen is produced through the high-temperature catalytic splitting of water using nuclear power thermal as an energy source.
- White hydrogen refers to naturally occurring hydrogen.
- Gold hydrogen is made by injecting bacteria that convert residual hydrocarbons located within depleted, abandoned oil wells into CO₂ and H₂ gases. While the H₂ is collected for use, the CO₂ is sequestered, making gold hydrogen a zero to negative carbon emission process. Through this method, golden hydrogen allows oil and gas companies to make “second use” of old oil and natural gas assets, extending the profitability of drilling projects.

1.2 Hydrogen storage

Hydrogen storage is a key enabling technology for the improvement of hydrogen and fuel cell technologies in applications for both stationary and portable power and transportation. To store 1 kg of hydrogen, a volume of about 11 m³ is needed. Given that this quantity can allow a hydrogen-powered vehicle to travel 100 km, it is easy to see why storing it in its natural form is so complicated. Hydrogen has the highest energy per mass of any fuel; however, its low ambient temperature density results in a low energy per unit volume, therefore requiring the development of advanced storage methods that have the potential for higher energy density. Hydrogen can be stored physically as either a gas or a liquid. Storage of hydrogen as a gas typically requires high-pressure tanks (350–700 bar tank pressure). Storage of hydrogen as a liquid requires cryogenic temperatures because the boiling point of hydrogen at standard pressure is -252.8°C. Hydrogen can also be stored on the surfaces of solids (by adsorption) or within solids (by absorption). Compressed hydrogen storage involves the physical storage of compressed hydrogen gas in high-pressure vessels. The current near-term technology for onboard automotive physical hydrogen storage is 350 and 700 bar nominal working-pressure compressed gas vessels — that is, “tanks.”

Liquid hydrogen storage requires refrigeration to a temperature of 20 K, and the liquefaction process requires an industrial facility expending a minimum of 15.1 MJ/kg. On the other hand, hydrogen storage in the form of hydrogen-containing liquids (HCL) can be classified into two categories: organic-based and not-organic-based liquids. The organic-based-hydrogen-containing liquids are essentially hydrocarbons (gasoline or

diesel). Methanol, ethanol, isopropanol, or formic acid are also HCL but to contribute positively to the energy transition, these vectors cannot be obtained from fossil origin.

In materials-based storage, hydrogen is stored in materials such as metal or chemical hydrides. The binding energy between hydrogen molecules and the materials varies depending on the type of their interaction. Metal hydrides can be defined as concentrated single-phase compounds between a host metal and hydrogen. For most uses, the sorption of hydrogen has to be done in a small temperature/pressure interval; this is one of the main advantages of metal hydrides over high-pressure tanks which shows that the system should present a flat plateau and small hysteresis. Among metal hydride-based hydrogen storage materials, magnesium and magnesium-based hydrides have been considered feasible materials to store hydrogen and have attracted huge attention in recent years. This is mainly due to the great abundance of magnesium in the Earth's crust as well as the high hydrogen gravimetric and volumetric density of magnesium hydride (MgH_2) [2].

3. Conclusions

Decarbonizing the planet is one of the goals that countries around the world have set for 2050. To achieve this, decarbonizing hydrogen production, giving rise to green hydrogen is one of the keys as this is currently responsible for more than 2% of total global CO_2 emissions. Finding out how this is to be achieved and what is its impact, is a crucial task in the coming decades.

Acknowledgment

This research is funded by the Ministry of Education and Ministry of Science, Technological Development and Innovation, Republic of Serbia, Grants: No. 451-03-47/2023-01/200017.

References

- [1] J.Rmuš, B. Belec, I. Milanović, M. Fanetti, S. Gardonio, M. Valant, S. Kurko, *Composites of transition metal dichalcogenides and topological insulators as catalytic materials for HER*, *Journal of Energy Storage* 68 (2023) 107719
- [2] S. Kurko, A.Aurora. D. Mirabile Gattia, V.Contini, A.Montone, Ž.Rašković -Lovre, J. Grbović Novaković, *Hydrogen sorption properties of $MgH_2/NaBH_4$ composites*, *International Journal of Hydrogen Energy* 38(27) (2013) 12140-12145

Multiparameter monitoring of cardiovascular function

Aleksandar Lazović^{1,2}, Natalija Đorđević³, Predrag Tadić³, Marija Ivanović¹, Vladimir Atanasoski¹, Marjan Miletić¹, Ljupčo Hadžievski¹, Arsen Ristić⁴, Vladan Vukčević⁴, Jovana Petrović¹

¹ University of Belgrade, National Institute of Republic of Serbia, Vinča Institute of Nuclear Sciences, Mike Petrovića Alasa 12-14, 11000 Belgrade, Serbia

² IMTEL Komunikacije a.d., Bulevar Mihaila Pupina 165b, 11070 Belgrade, Serbia

³ University of Belgrade, School of Electrical Engineering, Bulevar kralja Aleksandra 73, 11000 Belgrade, Serbia

⁴ University of Belgrade, Faculty of Medicine, University Clinical Center of Serbia, Department of Cardiology, Dr. Subotića 8, 11000 Belgrade, Serbia

* *Corresponding author*

DOI: 10.46793/ICCB23.043L

Abstract: We report the preliminary results of a laboratory validation study of a new polycardiographic device for the assessment of cardiovascular function (SensSmartTech). The main principle behind polycardiography is a synchronized measurement of multiple electro-mechanical parameters of the cardiovascular system. The assessment is non-invasive and entails electrocardiography, photoplethysmography, phonography and seismography. The study's results validate the use of the proposed polycardiograph implementation in settings with varying measurement and physiological conditions in both clinical and homecare settings. A simple signal analysis shows that the method is suitable for automated determination of diagnostically relevant features including the heart rhythm, openings and closures of heart valves, heart sounds, and systolic intervals generated as a combination of electrical and mechanical observables.

Keywords: polycardiography, cardiovascular, signal processing

1. Introduction

Polycardiography was proposed in 1940 [1] and was heavily studied in the 1970s [2]. A polycardiograph recorded ECG, heart sounds, and carotid pulses, which were subsequently analyzed to determine the coupled electromechanical properties of the cardiovascular system. Its notable uses are in determining the cardiovascular performance of astronauts and athletes [3] and the status of heart failure (HF) patients [4]. The latter relied on the determination of systolic time intervals and it has been shown that the shortening of the left ventricular ejection time (LVET) and lengthening of the pre-ejection period (PEP) are associated with the development of HF [5-10]. However, technological constraints such as poor signal reproducibility, signal dependence on the operator, insufficiently fast synchronization of different recordings,

and modest data processing capabilities, impeded a wider application of polycardiography [11, 12]. In particular, the interest in recording heart sounds gradually decreased since obtaining high-quality recordings of heart sounds was difficult, apparatus-dependent, and insufficiently quantitative for a high level of standardization [11]. Even more impairing was the inability of sphygmographs and tonnographs to produce reproducible and operator-independent measurements of carotid pulses due to the operator-dependent compulsory pressing (applanation) of the blood vessel. In addition, the mandatory synchronous data acquisition required a non-trivial optimization of the recording tape speed to accommodate multiple time scales of different measured parameters [12]. At the same time, ultrasound investigations (echocardiography) became available and gradually improved, providing information more closely related to heart action in terms of heart valve and wall movement and blood velocity. Nowadays, echocardiography and cardiac imaging techniques are established as the gold standard for the diagnosis of HF (sensitivity of 95% and specificity 88% [13]) and other conditions. However, despite good diagnostic parameters, echocardiography requires a highly-trained specialist and 20-30 min test duration. The corresponding high cost and operator dependence make it unsuitable for use in screening and primary care. As a consequence, HF is usually diagnosed at a very late stage of the disease, while a substantial number of patients remain undiagnosed and without adequate treatment [14].

Technical developments of the last half century have enabled the major drawbacks of polycardiography from the 1970s to be overcome [15, 16]. Here, we take advantage of modern sensing technology and construct a multisensory system that eliminates the aforementioned disadvantages and enables non-invasive multi-parameter measurement of electrical and mechanical signals of the heart suitable for primary care utilization and big data collection. The paper reports on the laboratory validation study of this system and its early results.

2. Method

2.1 Acquisition device

The acquisition device is battery-operated and connected to a portable notebook computer equipped with a user interface that controls the recording sequence, data acquisition, processing, and storage, and displays the signals in real-time. The device has a modular structure with 3 modules (Fig. 1):

- Module for the acquisition of heart sounds (PCG module)
- Module for the acquisition of 12-lead ECG signals (ECG module)
- Module for the acquisition of mechanical arterial/heart pulses from accelerometer sensors and photoplethysmograph sensors (ACC/PPG module).

PCG module is a module for recording the data from two stethoscopes. The module is based on STM32F407 microcontroller which acquires data from analogue microphone sensors. The acquisition sample rate is 1 kHz with 16-bit A/D conversion. Microphone sensors are low-noise MEMS microphones ICS-40300 with extended low-frequency response below 50 Hz. The microphone is encapsulated down the pipe of the

stethoscope in order to fully maintain the resonant characteristics of the stethoscope bell and thus provide good quality heart sound signals. As major frequency components of heart sounds are below 200 Hz, the sampling frequency of 1 kHz is sufficient. MEMS microphones are chosen to have high sensibility and wide frequency bandwidth. The PCG module is a master module for control of synchronization. This module transmits data to a PC over Ethernet. The patient is interfaced via the membrane head of the cardiology stethoscope SPIRIT CK-S4748PF63. In the measurements in a supine position the stethoscope is not fixed, while in the measurements in a standing or sitting position it is fixed by an elastic tape.

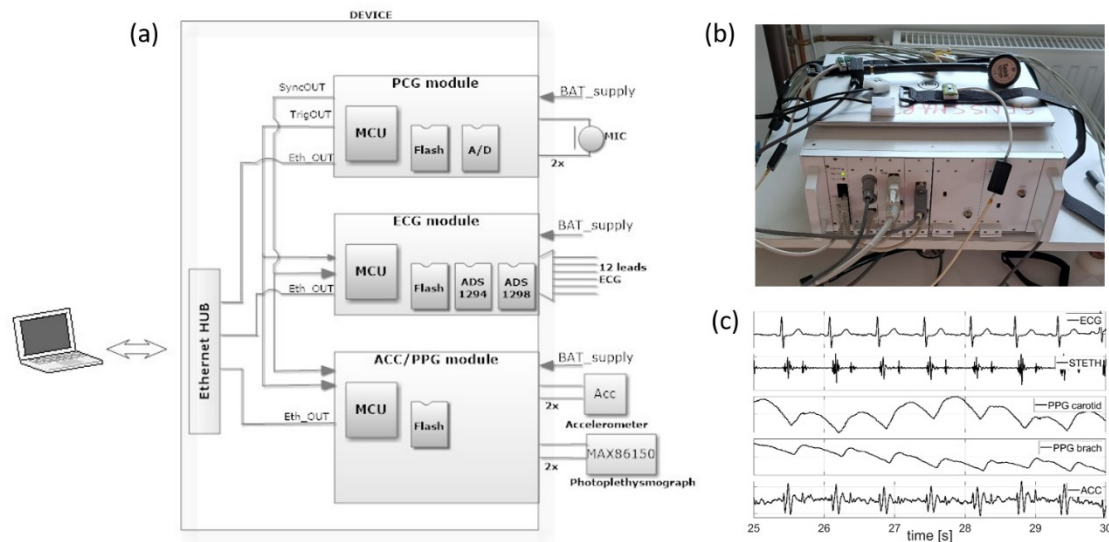


Figure 1. Polycardiography. (a) Schematics of a polycardiograph unit with 3 modules: phonocardiograph as a master module, electrocardiograph and a module for acquisition of acceleration and plethysmographic data. (b) Polycardiograph device with sensors. (c) Typical polycardiographic signals.

ECG module is mainly based on Texas Instruments chip ADS1298. This chip has advanced functionalities that allow for a straightforward acquisition of ECG signals. It consists of 8 channels with 8 differential amplifiers and a 24-bit A/D converter with a maximum sampling frequency of 32 KHz. The ECG module samples the ECG signal with a 500 Hz sampling frequency. ECG chip is controlled by a microcontroller (STM32F407) over SPI. Data is acquired in real-time and transmitted to the PC over Ethernet. Electrodes are DC coupled to the inputs of the ECG chip. The patient is interfaced via the commercially attested self-adhesive electrodes (in the SensSmartTech study, NM 2844 RFS Ceracarta).

ACC/PPG module is one common module for data acquisition from both accelerometer and PPG sensors. It consists of one microcontroller STM32F407 which acquires data from sensors over I2C. The accelerometer sampling rate is 500 Hz with an acceleration range of ± 1 g. It is possible to use up to 2 sensors from each group of sensors. PPG sensor chip MAX86150EFF+T is a Maxim Integrated chip with integrated

all necessary components for reflective photoplethysmography measurement. It has integrated photodiodes, one red and one near infrared LED. Ambient light and offset rejection, photodiode amplifier gain control and LED intensity control are built-in features of the sensor that simplify its usage and eliminate the need for processing when data is acquired. The sampling frequency of the photodiode A/D converter is 100 Hz. Data is synchronously acquired from both groups of sensors and transmitted to the PC over Ethernet. ACC sensors are mounted via a self-adhesive electrode. PPG sensors are mounted using the non-elastic Velcro tapes, allowing for controlled positioning and pressure.

Crucial design constraints of the multi-sensor device are the sampling frequency of each module and the synchronization of the modules. In the used timestamp method, the time difference between modules originates from the limited accuracy of the crystal oscillators. Considering that each module is equipped with an MHz oscillator of 20 ppm accuracy, the time shift accumulates to 1.5 μ s for a 30s recording. This is small compared to the sample periods of each module and diagnostically significant time intervals. Multiple built-in synchro tests and a detailed analysis of the difference between signal peaks proved this estimate correct.

All elements of the multi-sensor device and system software comply with the harmonized standard EN ISO 14155. The sensors are commercially available, electrically and radiation safe, and in biocompatible housings.

2.2 Measurement protocol

The aim of the SensSmartTech study was to test the polycardiographic measurements under different conditions and to examine the possibility of detection of characteristic signal features. The measurement in laboratory conditions before and after the activity, hence under the varying heart rate, suited this purpose. The subjects were first measured three times in standing position (reference measurements) and then they were asked to run on a training track to their personal limit of being comfortable. As soon as they reached the stationary standing position again, the measurement was repeated several times until the heart rate decrease levelled off. Each measurement lasted 30 s. We used a subset of sensors: 6 ECG electrodes (4 limb and precordial V3 and V4), 1 accelerometer placed between V3 and V4, 1 stethoscope placed at the xiphoid, and 2 PPG sensors placed above the carotid and brachial arteries. Recorded signals were encrypted to ensure the anonymity of the subjects in relation to researchers who process the data and other potential users of the database. The SensSmartTech study was approved by the Ethical Committee of the Vinca Institute of Nuclear Sciences, University of Belgrade (approval number 116-18-2/2022-000).

3. Preliminary Results

3.1 SensSmartTech Database

The database contains 348 recordings taken on 34 healthy volunteers with an average age of 35.3 ± 9.4 years and a BMI 25.0 ± 4.2 . Upon removal of recordings with insufficient

signal quality or interruptions, the data set used in the further analysis contained 342 recordings, out of which 102 reference recordings and 140 recordings at increased HR.

3.2 Signal quality analysis

Table 1. Signal-to-noise ratio of signals from different sensors on the whole set.

SNR [dB]	ECG	MIC	PPG1	PPG2	ACC
$\langle \text{SNR} \rangle \pm \text{std}(\text{SNR})$	15.8±3.0	3.7±1.55	9.1±3.5	9.3±3.5	4.7±1.8
SNRmin	6.7	0.4	1.3	0.46	0.5
SNRmax	24.4	8.2	18.43	17.8	9.0

Signal quality was assessed in terms of the signal-to-noise ratio (SNR), which was calculated as the ratio of the filtered signal and noise energy (MATLAB, Mathworks). The filtered signal was obtained by applying a high-pass filter with a cut-off of 1 Hz to eliminate the baseline wander and respiration and a low-pass filter with a cut-off of 100 Hz to eliminate noises. Additionally, a 50 Hz notch filter was applied to ECG signals to eliminate the power line interference. The noise was estimated under the assumption that the median beat is a noise-free signal. SNR of each signal was calculated in four steps: division of the filtered signal into pulses, calculation of the median, estimation of the SNR for each pulse with respect to the median, and averaging of the SNRs across all pulses. Table 1 shows statistics on the whole set.

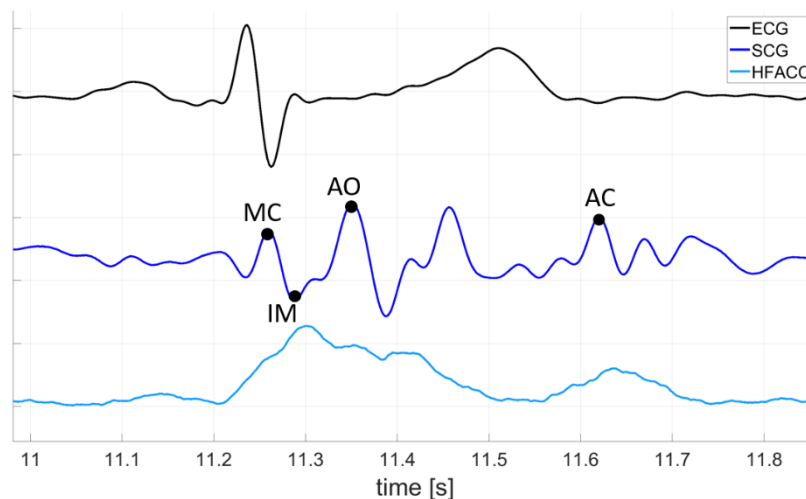


Figure 2. ACC signal decomposed into seismograph and high frequency signal. Shown is the envelope of the high frequency component. The annotated points are MC- mitral valve closure, IM – isovolumetic moment, AO – aortic valve opening, AC – aortic valve closure.

Expectedly, the most robust signal is the ECG signal with the set average SNR > 15 dB. Mechanical signals are clearly more affected by noise. We can explain this by their dependency on sensor position, pressure applied when mounting and underlying tissues. The slow signals, PPG1 and PPG2, have a respectable SNR > 9 dB. Faster, oscillatory, signals, MIC and ACC, were more susceptible to noise with the set average SNR < 5 dB. However, their components were robust to noise and displayed

physiologically relevant features on the beat-by-beat basis. An example in Fig. 2 shows semismographic component (<25 Hz) and the envelope of the high-frequency component (>25 Hz) of a typical ACC signal. Both signals contain clear systolic and diastolic parts with recognizable points that can be annotated according to the definitions in the literature [17].

Remarkably, SNR did not have any correlation with HR and was not affected by varying HR (in the first signals measured after running the HR often decreased for 20 bps in 30 s), meaning that the polycardiograph can be used in the presence of arrhythmias.

3.3 Automated feature detection

Polycardiographic combination of electrical and mechanical signals enables the determination of characteristic intervals in the cardiac cycle, such as electro-mechanical systole ($QS2 = S2 - Q$), left ventricular ejection time ($LVET = S2 - \text{the onset of PPG}$) and pre-ejection period ($PEP = QS2 - LVET$), which are not easily observable by a single electrical or mechanical sensor. Typically used electromechanical measurement in the standard clinical praxis is the application of an ECG electrode during echocardiographic assessment; thus inheriting the practical insufficiencies of the echocardiography.

Figure 3 shows an example of automated detection of the characteristic electrical and mechanical events in the recorded polycardiographic sequence. In particular, we detect the depolarization of ventricles as the QRS complex in the ECG signal, the onset of systole, systolic and diastolic peaks, and aortic notch in PPG signals, the 1st and the 2nd heart sound in the PCG signal. Importantly, the points are derived by the beat-by-beat analysis upon the rudimentary low- and high-pass filtering. Further processing of polycardiographic signals will without doubt unravel more information on the cardiac cycle. An obvious example is the information stored in the fine fast oscillating structures of the PCG and ACC signals, which is accessible by more aggressive averaging and filtering.

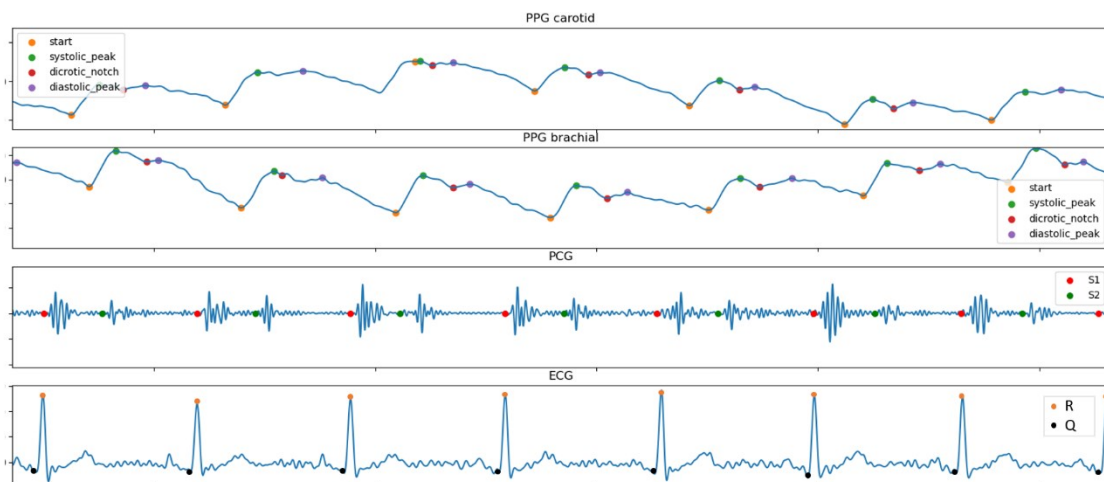


Figure 3. Automated detection of characteristic events in the cardiac cycle.

4. Conclusions

We have described the laboratory validation study of the new polycardiographic method constructed for the purposes of advanced detection of heart failure. The method is based on the simultaneous acquisition of the electrocardiogram, phonocardiogram, photoplethysmograph of large arteries, and apexcardiogram recorded by an accelerometer. Our results show a good signal quality and robustness of the measurement in nonclinical settings, before and after the activity, in standing and supine positions. They are assessed in terms of the ability to automatically detect the characteristic events in the cardiac cycle without extensive signal processing. The independence of the signal-to-noise on the heart rate gives us confidence that the polycardiograph can be applied in patients with arrhythmias. Finally, the low-frequency components of the polycardiographic signals (< 1 Hz), which were not considered here, may be used to study the cardio-respiratory coupling during the activity or in patients with mutually related cardio-respiratory problems, such as the pulmonary congestion in heart failure patients.

Acknowledgment

We are grateful to our volunteers.

This research is supported by the Science Fund of the Republic of Serbia, Grant. No. 7754338, Multi-SENSor System and ARTificial intelligence in service of heart failure diagnosis – SensSmart. We acknowledge the support from the Ministry of Science RS, Grants No. 451-03-47/2023-01/200017 and 451-03-47/2023-01/200103.

References

- [1] K. Blumberger, *Die Anspannungszeit und Austreibungszeit beim Menschen*. Arch. Kreisl.-Forsch. 6 (1940) 203
- [2] A. M. Weissler, W. S. Harris and C. D. Schoenfeld, *Systolic time intervals — correction for heart rate*, Circulation 37 (1968) 149–159
- [3] *The Heart and Sports, Essays on Cardiology in Sports*, Ed. by V. L. Karpman and G. M. Kukolevskiy, NASA TT F-662 Translation of „Serdtshe i sport; Ocherki Spotivnoy Karidiologii“, "Meditshina" Press, Moscow (1968) 74-105
- [4] V. Eliseo, V. Albano, M. Biagi, G. Clemente, U. Nardi, A. Romano, D. Romeo and L. Piccenna, *La polycardiografia nell'adiagnostica della insufficienza cardiaca latente*, Min. Med. 73 (1982) 2311-2318
- [5] F. C. Basilio, E. D. Folland, S. Karaffa, D. E. Tow and A. F. Parisi, *Non-invasive measurement of left ventricular function in coronary artery disease*, Br. Heart J. 45 (1981) 369-375
- [6] C. L. Garrard, A. M. Weissler and H. T. Dodge, *The Relationship of Alterations in Systolic Time Intervals to Ejection Fraction in Patients with Cardiac Disease*, Circulation 42 (1970) 455-462
- [7] J. C. Ghose, S. K. Mitra and M. K. Chhetri, *Systolic time intervals in the differential diagnosis of constrictive pericarditis and cardiomyopathy*, Brit. Heart J. 38 (1976) 47-50
- [8] P. Reant, M. Dijos, E. Donal, A. Mignot, P. Pitter, P. Bordachar, P. Dos Santos, C. Leclercq, R. Roudaut, G. Habib and S. Lafitte, *Systolic time intervals as simple echocardiographic parameters of left ventricular performance: correlation with ejection fraction and longitudinal two-dimensional strain*, Eur. J. Echocardiogr. 11 (2010) 834-844

- [9] D. R. McConahay, C. M. Martin and M. D. Cheitlin, *Resting and Exercise Systolic Time Intervals: Correlations with Ventricular Performance in Patients with Coronary Artery Disease*, *Circulation* 45 (1972) 592-601
- [10] S. Modak and P. K. Banerjee, *Studies of left ventricular functions by systolic time intervals on exposure to dry immersion*, *Ind. J. Aerospace Med.* 48 (2004) 48-56
- [11] A. K. Abbas and R. Bassam, *Phonocardiography Signal Processing*, ed. J. D. Enderle, Morgan and Claypool publishers
- [12] D. H. Spodick, H. G. Ball, and V. M. Pigott, *Effects of recording speed on precision of time-based polycardiographic measurements. Optimal paper speeds for measuring points and intervals*. *Br. Heart. J.* 40 (1978) 1344–1348
- [13] P. Ponikowski, S. D. Anker et al. *Heart failure: preventing disease and death worldwide*, *ECS Heart Failure*, 1 (2014) 4-25
- [14] H. Dokainish, W. A. Zoghbi, et al., *Comparative accuracy of B-type natriuretic peptide and tissue Doppler echocardiography in the diagnosis of congestive heart failure*, *Am. J Cardiol.* 93, 1130 (2004) 844
- [15] J. N. Njoroge, J. R. Teerlink, *Systolic time intervals in patients with heart failure: time to teach new dogs old tricks*, *Eur. J Heart Fail.* 22 (2020) 1183–1185
- [16] M. A. Nogueira, S. Calcagno, N. Campbell, A. Zaman, G. Koulaouzidis, A. Jalil, F. Alam, T. Stankovic, E. Szabo, A. B. Szabo, I. Kecskes, *Detecting heart failure using novel bio-signals and a knowledge enhanced neural network*, *Comp. Biol. Med.* 154 (2023) 106547
- [17] F. Khosrow-Khavar, K. Tavakolian, A. P. Blaber, J. M. Zanetti, R. Fazel-Rezai, C. Menon, *Automatic Annotation of Seismocardiogram With High-Frequency Precordial Accelerations*, *IEEE J Biomed. Health Inf.*, 19 (2015) 1428-1434

db.3d-qsar.com. The first 3D QSAR models database

Rino Ragno^{1,*} and Alessio Ragno²

¹ Sapienza University of Rome, Department of Drug chemistry and Technology, Piazzale Aldo Moro 5 00185 Roma, Italy e-mail: rino.ragno@uniroma1.it

² Sapienza University, Department of Computer, Control, and Management Engineering "Antonio Ruberti", 00185 Rome, Italy; alessio.ragno@uniroma1.it

* *Presenting author*

DOI: 10.46793/ICCB23.051R

Abstract: Field-Based Three-Dimensional Quantitative Structure-Activity Relationships (FB 3D QSAR) comprise computational approaches used in drug design and molecular modeling to analyze the relationship between the three-dimensional structure of a list of molecules (described by molecular interaction fields) and their associated biological activities (BAs). It aims to understand how different structural features of the molecules contribute to enhancing or lowering the biological potency. The process of FB 3D QSAR involves several steps. First, a dataset of structurally diverse molecules with known BAs is selected. Then, their three-dimensional structures are generated using computational methods. Next, in the classical form of Cramer [1], sterical and electrostatic molecular interaction fields (MIFs) are calculated and as a final step a mathematical model is built through the correlation of BAs with MIFs by means of projection of latent structures (PLS) algorithm. With our interest in making 3D QSAR accessible to all as done with the www.3d-qsar.com [2] db.3d-qsar.com, the first publicly available database of 3D QSAR models, is presented in which the user can insert or draw a molecule and predict its potency against an available target. All the models available on db.3d-qsar.com have been heavily optimized in prediction power through a semi-systematic pretreatment and parameter selection procedure by initially dividing the datasets into training (80%) and prediction (20%) sets. Each published model was and will be prepared by a selection among thousands of alignment trials. The selected models were finally characterized using a validation set compiled with molecules taken from the ChEMBL database. At the time of writing more than 40 models associated to more than 30 different pharmacological targets have been prepared and are ready to be used. At the time of the presentation db.3d-qsar.com will be accessible to the public and during the presentation its features will be shown.

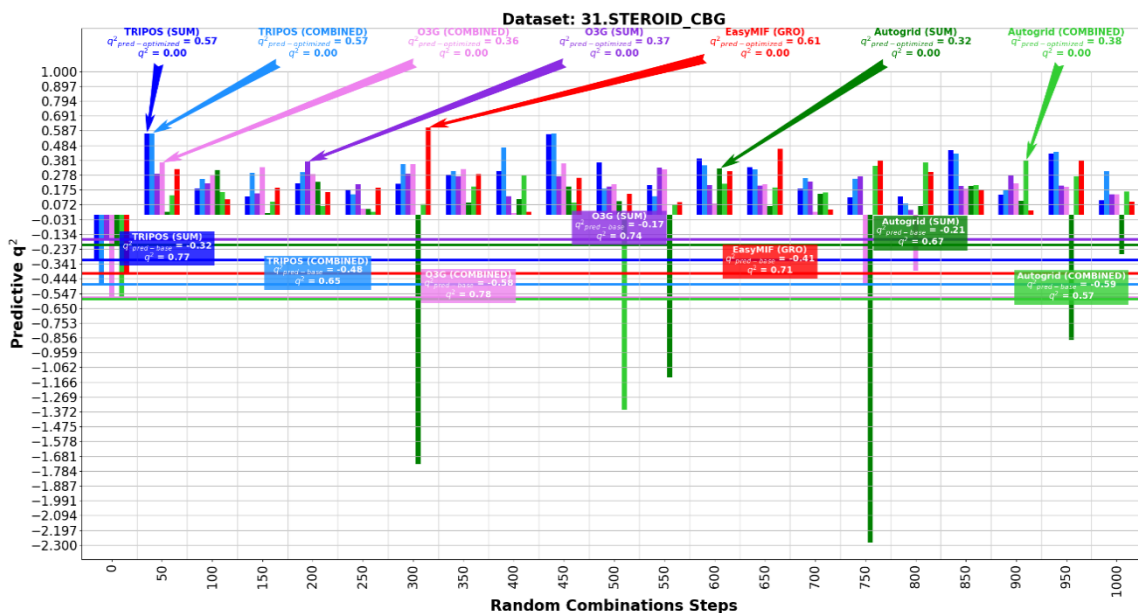


Figure1. Example of variable optimization pretreatment for the predictive ability optimization on the STEROIDS_CBG dataset.

Keywords: 3D QSAR, Prediction of activity, db.3d-qsar.com, www.3d-qsar.com

References

- [1]. Cramer, R.D.; Patterson, D.E.; Bunce, J.D.; Comparative molecular field analysis (CoMFA). 1. Effect of shape on binding of steroids to carrier proteins. *J. Am. Chem. Soc.* 1988, 110, 5959-67
- [2]. Ragno, R. www.3d-qsar.com: a web portal that brings 3-D QSAR to all electronic devices- the Py-CoMFA web application as tool to build models from pre-aligned datasets. *J. Comput., Aided Mol. Des.* 2019, 33, 855-864.

IRM@Be²⁺ - quantum chemistry between Bavaria and Šumadija

Ralph Puchta^{1*}, Dušan Čović²

¹Friedrich-Alexander Universität Erlangen-Nürnberg, Department Chemie und Pharmazie, 91058 Erlangen, Bayern, Germany; e-mail: Ralph.Puchta@fau.de

²University of Kragujevac, Faculty of Science, Department of Chemistry, Radoja Domanović ca 12, P.O. Box 60, 34000 Kragujevac, Serbia; e-mail: dusan.cocic@pmf.kg.ac.rs

* Corresponding author

DOI: 10.46793/ICCB23.053P

Abstract: Quantum chemical (density functional theory) mechanistic investigations on ligand exchange reactions at a tetrahedrally-coordinated dicationic Beryllium center offer a harmless and alternative way to learn about the traversed reaction pathways compared to experimental studies. Calculations for solvent exchange at [Be(H₂O)₄]²⁺, [Be(NH₃)₄]²⁺, and [Be(HCN)₄]²⁺ showed interchange (I) type mechanisms. To learn about the potential influences of spectator ligands we calculated the water exchange at [Be(L)(H₂O)₃]ⁿ⁺ (L: neutral ligands, mono-anionic ligands or cationic ligands) and got again consequently I-type paths. The activation energies depend strongly on the starting complexes, e.g., if hydrogen bonds have to be broken. The influence of spectator ligands is limited to the charge of the ligand and therefore the overall charge of the beryllium complex.

The small size of the beryllium solvent complexes allows to test tools like AIM to dissect between pure interchange mechanisms, associative mechanisms and dissociative interchange mechanisms based on electron density along the reaction pathway.

Keywords: inorganic reaction mechanism, beryllium, quantum chemistry

1. Introduction

Compared to the neighboring elements the element Beryllium is barely investigated, as a simple Google search demonstrates. Experimental research on Be²⁺ cations is a severe challenge due to the widely known potential toxicological aspects.[1]

Computational chemistry on Beryllium cations benefits from:

- i) the closed shell character of Be²⁺
- ii) Beryllium is included in most quantum chemical methods
- iii) The maximal tetrahedral coordination of Be²⁺.

Coordination number four and solvation with standard solvent molecules makes the smallest cation perfectly suited for mechanistic investigations, especially to be used as

“guinea pigs” to investigate and explore different mechanistic influences and computational methods.

In this contribution, we will report on the recent status of quantum chemical studies on $[\text{Be}(\text{L})_4]^{n+}$ done in cooperation between the University of Kragujevac and Erlangen.

2. Results and Discussion

The first systems we investigated were water exchange at $[\text{Be}(\text{H}_2\text{O})_4]^{2+}$, the ammonia exchange on $[\text{Be}(\text{NH}_3)_4]^{2+}$ and the hydrogen cyanide exchange on $[\text{Be}(\text{NCH})_4]^{2+}$. NH_3 and HCN are so-called water-like solvents and are still used in experimental chemistry [2].

Before we became interested in Be^{2+} , detailed studies on solvent-exchange reactions were performed by means of NMR techniques, [3,4] including high-pressure NMR techniques [5], from which activation-volume data of such processes could be obtained. Our goal was to obtain a reliable mechanistic model, that enabled an accurate description of the solvent-exchange mechanisms [6]. Merbach et al. interpreted obtained activation volumes as a limiting associative (A) or associative-interchange (Ia) mechanism based on analogues values established by Swaddle on octahedral complexes [7]; a linkage that may not be completely justified as our quantum chemical calculations challenged.

In all investigations of solvent exchange studies, we applied the same approach starting with the addition of an extra solvent molecule, to indicate in the calculations the second coordination sphere. Of course, this is a highly artificial step for any ion solvation, but one can learn about the system already before looking for transition states. Note, this first step is without an implicit solvent model (e.g., CPCM or PCM in the gas phase) clearly dominated by the overall charge of the complex, independently from the nature of the metal ion, more depending on the nature of the solvent molecule.

The hydrated $[\text{Be}(\text{H}_2\text{O})_4]^{2+}$ shows tetrahedral structure with H_2O ligands in local C_{2v} symmetry indicating the domination of electrostatic ion-dipole interactions with negligible charge transfer from the O-atoms of H_2O to the dication. The effect of the two positive charges on the metal center is clearly prominent, resulting in short Be-ligand bonds. There was no evidence of a fifth solvent molecule coordinated to the smallest cation Be^{2+} , in all calculations the second coordination sphere was preferred (Figure 1)

The binding of the fifth H_2O in the second coordination sphere, liberates 29 kcal/mol, (exaggerated in the gas phase, molten to 10% by application of the IPCM solvent model), but a clear sign of strong hydrogen bonding and leading to an activation energy of 16 kcal/mol, around the half energy liberated by the addition of the fifth water molecule. Contrary to the expectation of an associative (A) mechanism, no evidence was found of a five-fold coordinated Be^{2+} intermediate. In all cases, a transition state typical for an interchange (I)-type of mechanism was calculated [8].

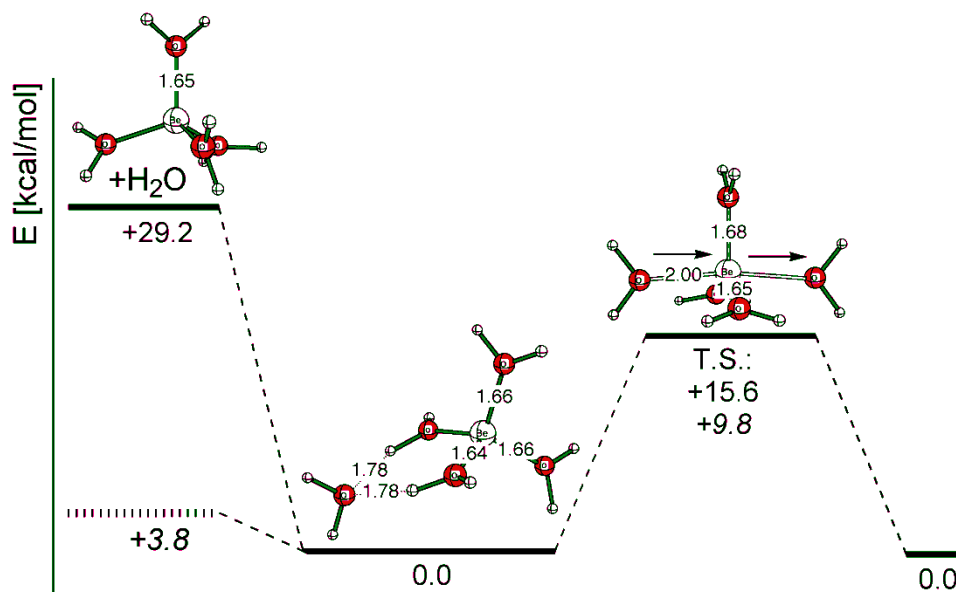


Figure 1. Calculated water exchange at $[\text{Be}(\text{H}_2\text{O})_4]^{2+}$ (values; B3LYP/6-311+G** + ZPE(B3LYP/6-311+G**), italic: B3LYP/6-311+G*(ICPM)// B3LYP/6-311+G** + ZPE(B3LYP/6-311+G*)) [8].

For the water-like solvent NH_3 the ligand exchange was investigated. Again an interchange mechanism for NH_3 exchange at the $[\text{Be}(\text{NH}_3)_4]^{2+}$ center was observed. Due to the different way of binding the fifth NH_3 molecule in the second coordination sphere by one hydrogen bond, the addition of this molecule to $[\text{Be}(\text{NH}_3)_4]^{2+}$ liberates only 21 kcal/mol, again this decreases dramatically by application of the ICPM solvent model. The activation barrier in $[\text{Be}(\text{NH}_3)_4]^{2+}$ is 18.8 kcal/mol (i.e. 3.2 kcal/mol higher than in $[\text{Be}(\text{H}_2\text{O})_4]^{2+}$) most probably due to the more sterically demanding NH_3 -ligand in comparison (Figure 2) [8].

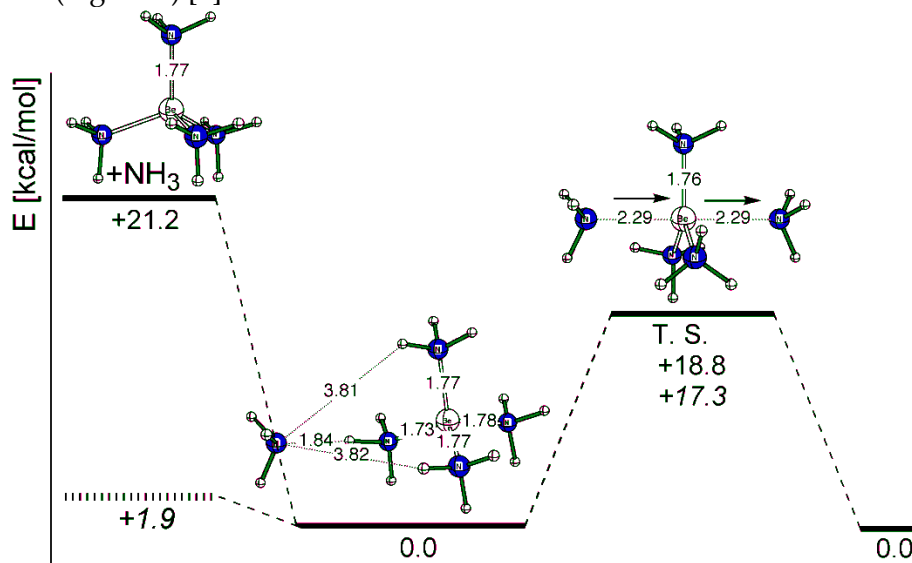


Figure 2. Calculated ammonia exchange at $[\text{Be}(\text{NH}_3)_4]^{2+}$ (values; B3LYP/6-311+G** + ZPE(B3LYP/6-311+G**), italic: B3LYP/6-311+G*(ICPM)// B3LYP/6-311+G** + ZPE(B3LYP/6-311+G*)) [8].

Hydrogen cyanide is also a water-like solvent and sterically non-demanding. Investigation of the HCN exchange at $[\text{Be}(\text{NCH})_4]^{2+}$ illustrates impressively the consequences of missing H-bonds in the reactant state $[\text{Be}(\text{NCH})_4\text{HCN}]^{2+}$ (Figure 3). Immediately the energy liberated by the addition of the solvent molecule number five decreases to less than 50% compared to the water and ammonia exchange; the activation energies are only around 30% of those for NH_3 and H_2O . The difference between the H-bonded and the ligand exchange process of those starting structures at $[\text{Be}(\text{NCH})_4]^{2+}$ is 7.4 kcal/mol.

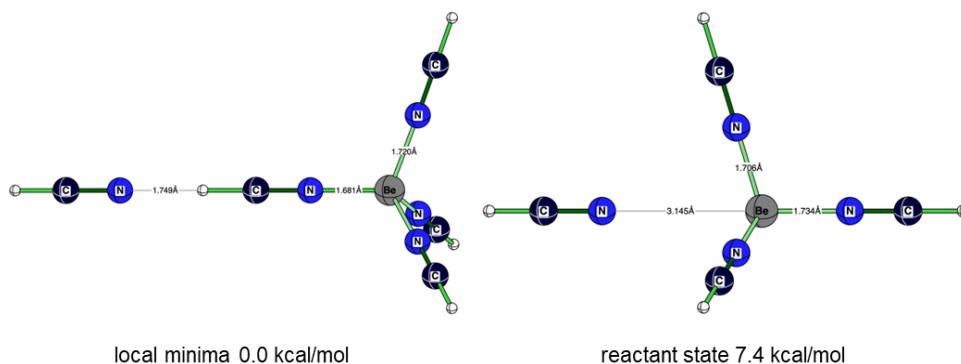


Figure 3. Energetic comparison (B3LYP/6-311+G**) of the hydrogen bound HCN and the starting structure for the ligand exchange at $[\text{Be}(\text{NCH})_4]^{2+}$.

A general problem while calculating solvent exchange reactions is the treatment of the bulk solvents. Our goal is to investigate these types of reactions in a simple and clear way, so we apply non-dynamic techniques. The simplest way including the influence of solvent effects in our calculations, is the use of implicit solvent models.

While energy calculations on the exact characterised gas-phase structures work, we could not get local minima for the reactant state. This situation is not acceptable. An alternative approach is to concatenate the entering and the leaving ligands in $[\text{Be}(\text{H}_2\text{O})_4]^{2+}$ by five H_2O (see Figure 4).[9] Independently, if simple gas phase calculations were applied with 4+1 water molecules, if DFT or Post-HF-techniques were applied, including different sorts of implicit solvent models or if we added another five H_2O molecules to concatenate the entering and the leaving H_2O , an I_a mechanism was always obtained; of course, the activation energy varied as expected. As all approaches consistently reproduce the I -mechanism, we are sure that our simple and small model applied is suitable for our purpose.[9]

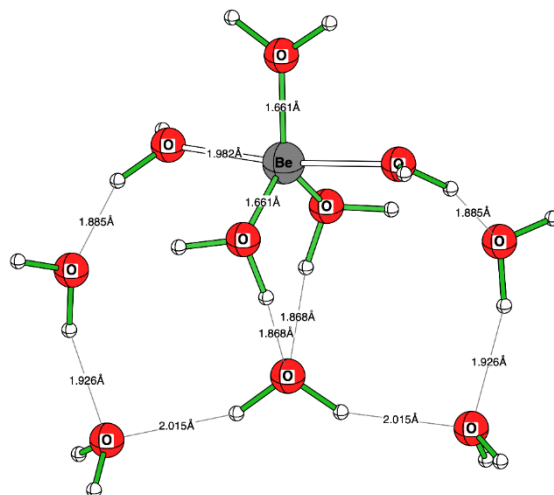


Figure 4. Calculated transition state (B3LYP/6-311+G**) for the water exchange at $[\text{Be}(\text{H}_2\text{O})_4]^{2+}$ with concatenated entering and leaving water ligands [9].

The next step was to investigate the influence on solvent exchange of spectator ligands. Three sorts of mono-dentate ligands neutral, [10] anionic[11] and cationic[12], that serve as spectator ligands coordinated to Be^{2+} were investigated.

To learn about the influence of neutral ligands, the water exchange for $[\text{BeL}(\text{H}_2\text{O})_3]^{2+}$ was calculated. As ligands, L around 35 neutral ligands with donors from the main group V and VI, and different hybridization, were chosen. In all cases, a similar picture can be drawn. The addition of the fourth water molecule liberated yielded on average -27 kcal/mol, while the activation energy was averaged at 17 kcal/mol (all values B3LYP/6-311+G**). The great deviations due to the trans-influence and trans-effect observed in square-planar complexes compared to tetrahedrally coordinated cases, are understandable since there are no joined orbitals that are affected by the spectator ligand [10].

To test the influence of a negative charge on the water exchange mechanism, neutral ligands were substituted by monoanionic. This reduced the overall charge from $2+$ to $1+$. Therefore, L: H, F, Cl, Br, OH, NC-N-CN were introduced, and the effect on H_2O exchange at $[\text{BeL}(\text{H}_2\text{O})_3]^+$ was tested. As expected, the energy set free by binding an additional water molecule to $[\text{BeL}(\text{H}_2\text{O})_3]^+$ to obtain $[\text{BeL}(\text{H}_2\text{O})_3\text{H}_2\text{O}]^+$ decreased to 60% (17 kcal/mol (B3LYP/6-311+G**)) of the value of the dicationic species [8]. The averaged transition state passed during the water exchange at $[\text{BeL}(\text{H}_2\text{O})_3]^+$ is, with 12 kcal/mol (B3LYP/6-311+G**) also reduced (20%) from the value for $[\text{Be}(\text{H}_2\text{O})_4]^{2+}$. We attributed this to the higher electron density at the beryllium cation due to the anionic ligand L [11].

If anionic ligands L decrease the accretion energy of the extra water molecule and to a smaller degree the activation energy, then cationic ligands should increase these energies. A special group of ligands was designed, inspired by the SASAPOS protocol [13]; starting from deprotonated para-hydroxypyridine and pyridine, up to three pyridinium moieties were added to pyridine. In this way, we were able to get a series of ligands L from monoanionic to tricationic systems allowing the range from $[\text{BeL}(\text{H}_2\text{O})_3]^+$

to [BeL(H₂O)₃]⁵⁺. As expected, a linear correlation between the charge of the complex and the accretion energy of the extra H₂O was obtained, and the activation energy increased linearly [12].

Besides interesting modifications of the coordination sphere, [Be(Sol)₄]²⁺ can be used to challenge quantum chemical methods. While theoretical-oriented chemistry can often reach similar conclusions as experimental-oriented chemistry by different methods, the discrimination between *I_a*, *I*, and *I_d* mechanisms is still a problem. As test cases, we calculated the solvent exchange at [Be(Sol)₄]²⁺ (Sol: H₂O, H₂S, H₂Se, HCN, pyridine and NH₃) to have different hybridized N-atoms and coordinating lone pairs of different quantum numbers. The expectation from orientating simulations is that these factors can shift a mechanism from *I_a* to *I_d*.

While experimentalists differentiate between *I_a* and *I_d* by the activation volume, quantum chemical studies traditionally utilize differences in bond length as descriptors [14,15]. Analysing the electron density (⊙) between Be²⁺ and the donor atom of the entering or leaving ligand offers a quantum chemical bond approach to discrimination between an *I_a* and *I_d* mechanism. Analogous to the increasing bond length the electron density (⊙) decreases, a clear sign of a more dissociative character (Figure 5).

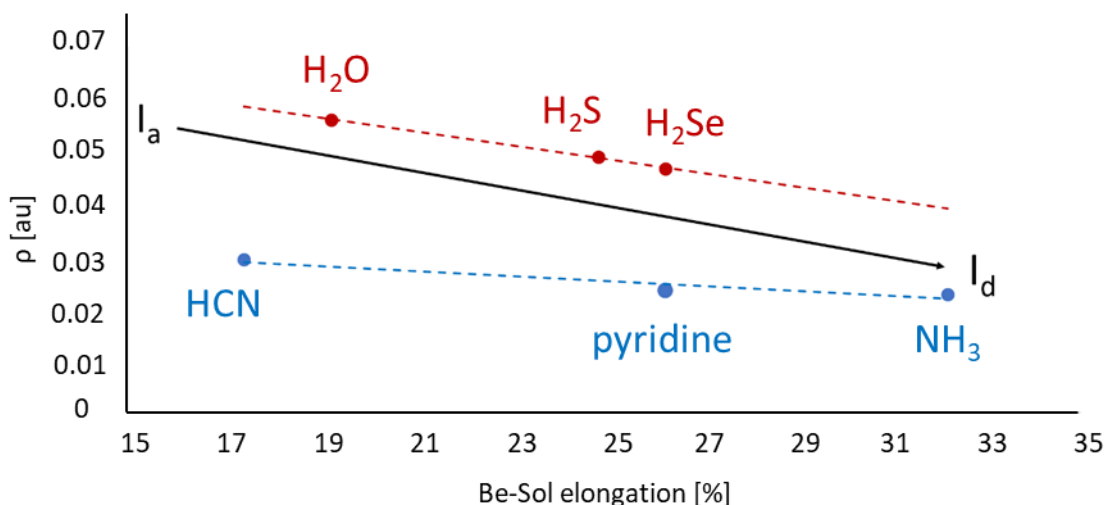


Figure 5. AIM based analysis of the electron density ρ for solvent exchange reactions at [Be(Sol)₄]²⁺ (Sol: H₂O, H₂S, H₂Se, HCN, pyridine, NH₃) (ω B97XD/6-311+G**) AIMAll V17.[16]

A central question while studying chemical reactions: when does bond formation start? A challenge for Atoms In Molecules (AIM). Here we used the HCN exchange on [Be(NCH)₄]²⁺. After optimization at 0.05 Å steps along the reaction coordinate, topological analysis using QTAIM demonstrates the change in electron density ρ at the transition from a coordinating interaction (presence of bond critical points BCP) to a non-coordinative interaction (presence of cage critical points CCP to equatorial HCN). At approximately 2.3 Å an interaction between Be²⁺ and the incoming/leaving NCH ligand is observed. At this distance, the CCPs between Be²⁺ and NCH molecules change

into BCPs. Therefore, this distance could be best addressed as the first contact point (FCP) of this reaction (see Figure 6) [16].

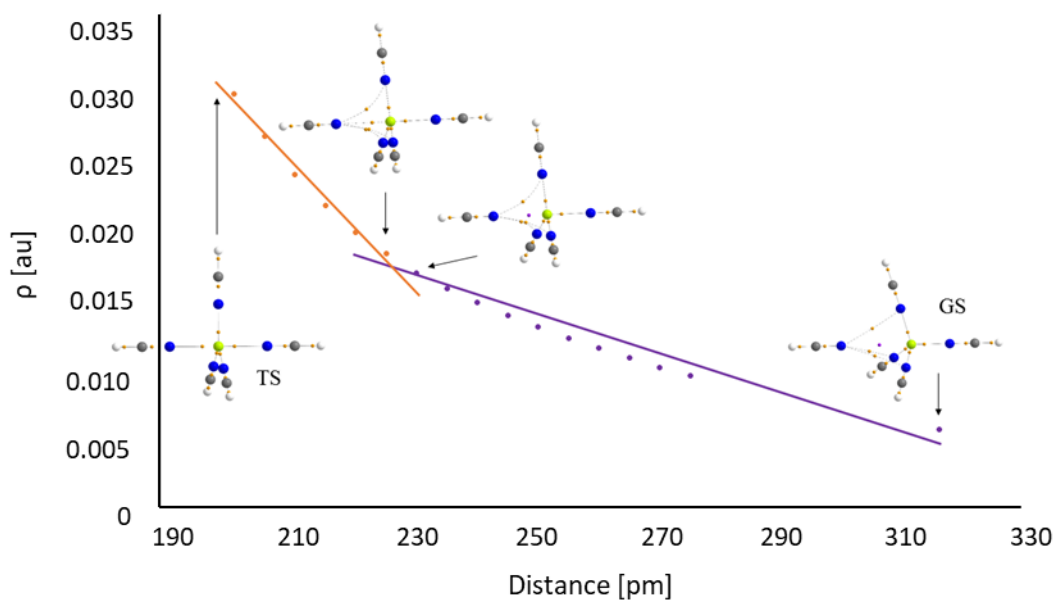


Figure 6. AIM analysis of the HCN exchange at $[\text{Be}(\text{NCH})_4]^{2+}$ (BCP: orange dots, CCP: violet dots) ($\omega\text{B97XD/6-311+G}^{**}$) AIMAll V17.[16]

3. Conclusions

Solvent complexes of Be^{2+} $[\text{Be}(\text{Sol})_4]^{2+}$ (Sol: H_2O , NH_3 , HCN) are perfect test cases for investigating reaction mechanisms at tetrahedrally coordinated metal cations by quantum chemical methods. We found always an I-type of mechanism independent from the selected solvents (Sol) or the nature of the spectator ligands (L) in the case of $[\text{Be}(\text{L})(\text{Sol})_3]^{2+}$. The main influence of the spectator ligand is its charge that dominates the overall charge of the Be-complex influencing the accretion energy and the activation energy. A linear correlation between the charge of the complex and these energies is observed.

Additionally, these quantum chemical investigations of ligand exchange mechanisms at tetrahedrally coordinated Be^{2+} allow us to test concepts like AIM as tools for analysing and understanding reaction mechanisms.

Acknowledgment

We would like to thank Prof. Dr. Dr. hc. mult. Rudi van Eldik, Dr. Nico van Eikema Hommes, Dr. Markus Walther, Dr. Holger Elsen and Prof. Dr. Colin Hubbard for friendly discussion, continuous scientific input and their friendship. The FAU Erlangen-Nürnberg, the TH Nürnberg and the University of Kragujevac for a generous allotment of computer time. D. Ć. Thanks the Ministry of Education and Ministry of Science, Technological Development and Innovation, Republic of Serbia for constant support (Grant number No. 451-03-47/2023-01/200122).

References

- [1] M. D. Rossman, M. B. Powers, O. P. Preuss, *Beryllium: Biomedical and Environmental Aspects*, Williams & Wilkins, Philadelphia, (1991).
- [2] J. Jander, Ch Lafrenz, *Wasserähnliche Lösungsmittel*, Verlag Chemie, (1968).
- [3] S. F. Lincoln, M. N. Tkaczuk, *A Proton NMR Study of the Dynamics of Ligand Exchange on Tetrakis(1,1,3,3-Tetramethylurea)Beryllium(II) and its Dimethyl Sulphoxide Analogue*, Ber. Bunsenges. Phys. Chem., 85 (1981) 433–437.
- [4] S. F. Lincoln, M. N. Tkaczuk, *A Proton Magnetic Resonance Study of Ligand Exchange on Tetrakis (N,N-Dimethylacetamide) Beryllium(II) and its N-Methylacetamide, and N,N-Dimethylformamide Analogues*, Ber. Bunsenges. Phys. Chem., 86 (1982) 221–225.
- [5] P. A. Pittet, G. Elbaze, L. Helm, A. E. Merbach, *Tetrasolventoberyllium(II): high-pressure evidence for a sterically controlled solvent-exchange mechanism crossover*, Inorg. Chem., 29, (1990) 1936–1942.
- [6] F. A. Dunand, L. Helm, A. E. Merbach, *Solvent exchange on metal ions*, Adv. Inorg. Chem. 54 (2003) 1.
- [7] T. W. Swaddle, *A model for the prediction of the molar volume effects accompanying changes in the primary coordination number of aqueous metal ions*, Inorg. Chem. 22 (1983) 2663–2665.
- [8] R. Puchta, N. J. R. van Eikema Hommes, R. van Eldik, *Evidence for Interchange Ligand-Exchange Processes on Solvated Beryllium Cations*, Helv. Chim. Acta, 88 (2005) 911–922.
- [9] R. Puchta, R. van Eldik, *Which Model Reaction is Preferable for Quantum-Chemical Investigations of a Water-Exchange Mechanism?*, Helv Chim Acta, 91 (2008) 1063–1071
- [10] M. Walther, A. Budimir, R. Puchta, *Water exchange on beryllium complexes: part VIII - influence of neutral electron pair donors* J. Coord. Chem., 65 (2012) 4359–4374.
- [11] A. Budimir, M. Walther, R. Puchta, R. van Eldik, *Water Exchange on [Be(X)(H₂O)₃]⁺ (X: H, F, Cl, Br, OH, CN, NCNCN)*, Z. Anorg. Allg. Chem. 637 (2011) 515–522.
- [12] M. Walther, R. Puchta, *Ligand exchange processes on solvated beryllium cations VII - water exchange on cationic [Be(H₂O)₃(Lⁿ)]²⁺ⁿ (Lⁿ: 4-O-Py, Py, 4-(Py)-Py⁺, 3,5-(Py)₂-Py²⁺, 3,4,5-(Py)₃-Py³⁺)*, RSC Adv., 2, (2012) 5815–5821.
- [13] R. Weiss, F. Pühlhofer, N. Jux, K. Merz, *SASAPOS statt Sisypfos: Hocheffiziente 20-stufige Eintopfsynthese eines diskreten organisch-anorganischen Ionenclusters mit Porphyrinkern*, Angew. Chem., 114 (2002) 2696–2971.
- [14] F. P. Rotzinger, *Structure of the Transition States and Intermediates Formed in the Water-Exchange of Metal Hexaaqua Ions of the First Transition Series*, J. Am. Chem. Soc., 118 (1996) 6760–6766.
- [15] F. P. Rotzinger, *Mechanism of water exchange for the di- and trivalent metal hexaaqua ions of the first transition series*, J. Am. Chem. Soc., 119 (1997) 5230–5238.
- [16] D. Čović H. Elsen, R. Puchta, *in preparation*.

Application of Carbon-Based Nanocomposite Systems as Photosensitizers for Photodynamic Therapy

Marijana Petković^{1*}, Milutin Stepić,¹ Iva Popović,¹ Manuel Algarra,² Tanja Dučić,³
Anamarija Abu el Rub,¹ Vanja Ralić,¹ Lela Korićanac,¹ Jelena Žakula,¹ Jelena
Filipović Tričković,¹ Ana Valenta Šobot,¹ Maja D. Nešić¹

¹ University of Belgrade, National Institute of the Republic of Serbia, VINČA Institute of Nuclear Sciences, Mike Petrovića Alasa 12-14, 11 000 Belgrade, Serbia; e-mail: petkovic.marijana.71@gmail.com (M.P.), mstepic@vin.bg.ac.rs (M.S.), ivavukicevic@vin.bg.ac.rs (I.P.), anamarija.aburub@gmail.com (A.A.R.), vanja.ralic@live.com (V.R.), lela@vin.bg.ac.rs (L.K.), pozegaj@vin.bg.ac.rs (J.Ž) filipovicj@vin.bg.ac.rs (J.F.T.), ana_v.s@vin.bg.ac.rs (A.V.Š.), maki@vin.bg.ac.rs (M.N.)

² INAMAT²-Public University of Navarre, Edificio Jeronimo de Ayanz, Campus Arrosadia, 31006 Pamplona, Spain; e-mail: manuel.algarra@unavarra.es

³ ALBA CELLS Synchrotron, Carrer de la Llum 2-26 08290 Cerdanyola del Vallès, Barcelona, Spain

* Corresponding author

DOI: 10.46793/ICCB23.061P

Abstract: Small, carbon-based nanoparticles, carbon dots (CDs), are investigated as photosensitizers (PSs) for photodynamic therapy of cancers. The results presented here show biochemical changes in cancer cells treated with surface-modified CDs, which are augmented by illumination, indicating a high potential of CDs as selective drug carriers and potent PSs. In addition, we will show that CDs produced from black carrot extract (biomass) can be exploited for image-guided therapy and be cytotoxic for cancer cells, thanks to their fluorescence properties. Finally, since biomass-fabricated CDs interact strongly with nucleic acids, they can be further developed for cell cycle sensing purposes.

Keywords: Carbon dots, Photodynamic therapy, cancer, theranostic, biomass

1. Introduction

Carbon dots (CDs) are small carbon-based materials with dimensions mostly less than 10 nm, but for some synthetic processes and applications, their diameter can be around 70 nm as well [1]. These nanoparticles can be fabricated from isolated chemicals or extracts of natural products (biomass). CDs have a high potential for biomedical applications. CDs have been reported to efficiently suppress cancer cell growth *in vitro*, for instance, Hep G2 liver cancer cells or breast cancer cell lines (MDA-MB-231 and MCF-7) [2]. Their mechanism of action is related to the stimulation of the generation of a large amount of reactive oxygen species (ROS) [2]. Apart from the cytotoxic effect, the

excellent optical properties of CDs and high efficiency for ROS generation enable their application as photosensitizers (PSs) in photodynamic therapy (PDT), [3] in which doping of CDs with heteroatoms, such as N, S or B, can improve the quantum yield and their function as PSs [4]. CDs' fluorescence properties enable their application for bioimaging [5], and their functionalization with medicaments, including those based on transition metal complexes, proves that they can also be considered nanocarriers.

CDs and many other nanoparticles, as drug carriers, reach the tumor sites thanks to the so-called enhanced permeability and retention effect. However, upon cellular uptake, they can mainly be found in the organelles in the cytoplasm [6]. CDs' surface modification can result in their accumulation in the cell nucleus. The cell nucleus is the primary site of action in cancer treatment since the attached drug can be released in the nucleus directly and damage genes resulting in the termination of cancer cell proliferation [7].

In this work, we will present our recent results on the application of biomass-produced CDs as imaging and anti-cancer agents and discuss intracellular biochemical changes that occur upon the action of light on the CD-treated ovarian cancer and osteosarcoma cells.

2. Materials and Methods

2.1. Synthesis and characterization of CDs

CDs were obtained by an acid hydrothermal approach, in which lactose or black carrot extract was the starting material. CDs enriched with nitrogen (N-CDs) were obtained by mixing previously acquired CDs and 1,6-hexanediamine. Cervical cancer-HeLa, ovarian cancer-A2780, melanoma-A375, osteosarcoma-CAL72, pancreatic cancer-PANC1, and lung fibroblasts MRC-5 cells were grown in the corresponding medium and treated with increasing concentrations of either (N-)CD, (N-) CDs@Ru-complex or CDs produced from black carrots; the treatment was conducted in the dark or upon UV [8]. For fluorescence imaging, after the treatment with CDs, cells were fixed, dehydrated, and counterstained with a fluorescence dye (DAPI, that binds to double-stranded DNA).

Intracellular changes in biomolecules were analyzed by the Synchrotron Radiation-Fourier Transform Infrared Spectroscopy (SR-FTIR spectroscopy) (Synchrotron ALBA, MIRAS beamline, Barcelona, Spain), [9] and technical details were the same as described in our publications. [8] SR FTIR spectra were processed using the Orange Spectroscopy tools, allowing multimodal spectral analysis involving Principal Component Analysis (PCA). The bands with the highest differences in position and intensity were identified as outliers (maximum three per sample) and excluded from further calculations.

3. Results and Discussion

3.1. Biochemical changes in cancer cells induced by (N-)CDs@Ru-complex

In this work, intracellular biomolecular changes in A2780 (ovarian cancer cells) and CAL72 (osteosarcoma) cells treated with nanocomposite system (N-)CDs@Ru-complex

are studied in the dark and upon light illumination. Changes in the position and intensity of bands that arise from major functional groups of biomolecules are investigated. Treating cells with (N-)CDs@Ru-complex induces significant biomolecular structural changes in the A2780 and CAL72 cells, as detectable by SR FTIR spectroscopy. The structure and conformation changes are observed in proteins, lipids, and nucleic acids. The treatment of ovarian cancer cells with N-CDs@RuCN/UV light shows more pronounced changes than treatment with CDs@RuCN/UV light, whereas the opposite is detected in CAL72 cells.

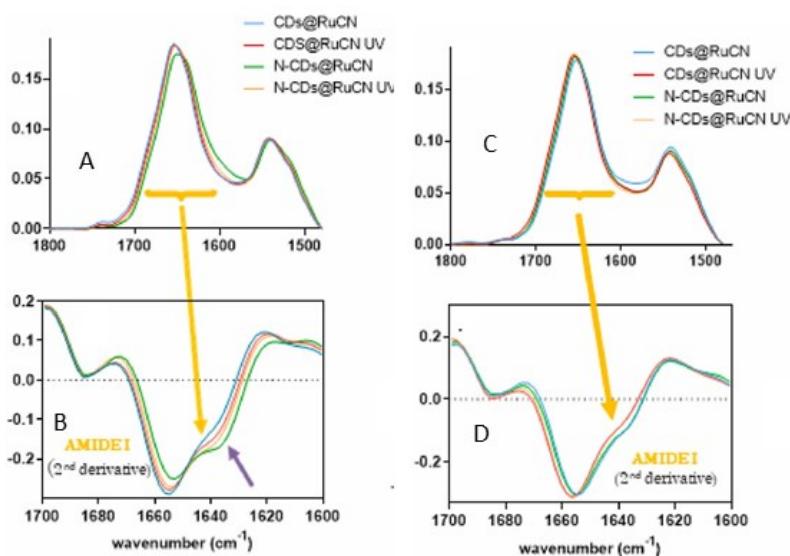


Figure 1. SR-FTIR spectra (A, C) of the protein region and the second derivative of the Amide I regions (B, D) of A2780 and CAL72 cells, respectively, treated with CDs@RuCN and N-CDs@RuCN. An arrow indicates the β -secondary structure changed upon the cell treatment.

Figure 1 shows the average FTIR spectra of the protein region (Amide I and Amide II bands, 1480 cm^{-1} to 1800 cm^{-1}) along with the second derivative of the Amide I band. The second derivative of the same region showed a shift of the Amide I band to the maximum at $\sim 1655\text{ cm}^{-1}$ after interaction with N-CDs@RuCN/UV light with A2780 cells. This shift is most likely due to the interaction of proteins with the RuCN moiety of the nanocomposite system. Similarly, this shift was also detected in the FTIR spectra of bovine serum albumin interaction with Ru-ion [10]. The band at $\sim 1630\text{ cm}^{-1}$, corresponding to the β -secondary structure, changed upon the treatments, especially for A2780 (an arrow in **Figure 1**). In CAL72, changes were similar, but for these cells, the CDs@RuCN treatment was more efficient in inducing changes in the protein region after the illumination. The changes in the lipid region in both cell lines indicate a cell-specific response to the treatment. UV illumination does not induce significant changes in the lipid region in the A2780 cells treated with CDs@RuCN. In contrast, in the presence of N-CDs@RuCN in these cells, illumination leads to an increase in the intensity of CH_2 -asymmetric and symmetric stretching bands ($\sim 2920\text{ cm}^{-1}$ and $\sim 2850\text{ cm}^{-1}$, respectively) [11], which might indicate an increased level of oxidative stress. The carbonyl band corresponding to the C=O group also has a moderately higher intensity in the case of N-

CDs@RuCN treated and illuminated A2780 cells than the corresponding unilluminated analog. It is possible that N-CDs@RuCN interacts more readily with the membrane phospholipids and therefore acts locally after the light illumination.

A shift of the bands corresponding to the CH₃ and CH₂ vibrations towards higher wavenumbers might indicate the interactions of CDs@RuCN with the lipids of CAL72 cells, and consequently, changes in membrane fluidity. [12] These changes can be triggered by the oxidative modification of lipids or lipids fluidity changes caused by ROS, initiated by the light catalyzed by CDs@RuCN and N-CDs@RuCN. Also, the photosubstitution reactions of RuCN, [13] can play a role in indicated changes. In the region where functional groups of nucleic acids (NAs) are detectable, there are changes in the position and intensity of the signal at ~1240 cm⁻¹ and 1080 cm⁻¹, corresponding to asymmetric and symmetric P=O vibrations of NAs. In the A2780 cells exposed to CDs@RuCN, we observed that the asymmetric P=O band is shifted toward higher wavenumbers. A decrease of the same band intensity of about 10% is observed upon illumination compared to the results collected in the dark. The illumination of the N-CDs@RuCN-treated cells did not lead to a shift in the wavenumbers, but there is an increased intensity of the P=O bands for about 30%. In the case of CAL72 cells, the phosphate band is also changed. The band at ~1240 cm⁻¹ shifted towards higher wavenumbers when the cells were treated with CDs@RuCN and N-CDs@RuCN. Moreover, in both cases, the intensity of this band increased, implying the changes in the NA structure, especially in DNA [14]. These data are consistent with the findings of Havrdova et al., who found that the negatively charged CDs entered the cell nucleus to a lesser extent than those with positively charged functional groups, which interact better with DNA.

3.2. CDs as imaging agents

After demonstrating a significant cytotoxic effect of CDs synthesized from black carrots against several cancer cell lines, in particular against melanoma (A375 cells), and lower cytotoxicity against healthy cells, we have also studied the potential of CDs to be used for bioimaging purposes. Namely, black carrot extract is rich in anthocyanins. CDs have a high content of a flavylum cation on the surface, which is responsible for the cytotoxic effect, but also enables the fluorescence of used carbon dots. Namely, the black carrot-derived CDs emit green fluorescence upon illumination with the UV light, and in this case, the emission wavelength is independent of the excitation light. This property makes them convenient for bioimaging and demonstrates their potential for further development as theranostic agents (both diagnostic and therapeutic).

Upon the cell treatment with CDs, a solid green fluorescence appeared in the cytoplasm and the nucleus, thus demonstrating their ability to cross both the plasma and nuclear membranes and stain the whole cell (**Figure 2**). The size and positive charge enable CDs to enter the cells efficiently. Specifically, these CDs enter the cell nuclei and sub-nuclear compartments such as nucleoli. Havrdova and co-workers observed this CD localization on a mouse [15] and human cells [16]. The DAPI stain was visible as a blue light in the cell nucleus. Our results also suggest that CDs, produced from biomass, have a solid

affinity for both DNA and RNA molecules. Moreover, cells with a higher intensity of green fluorescence in the nucleus were the cells in cell cycle's mitotic phase, indicating that CDs interact with chromatin and that they could be used as markers of cell mitosis and proliferation.

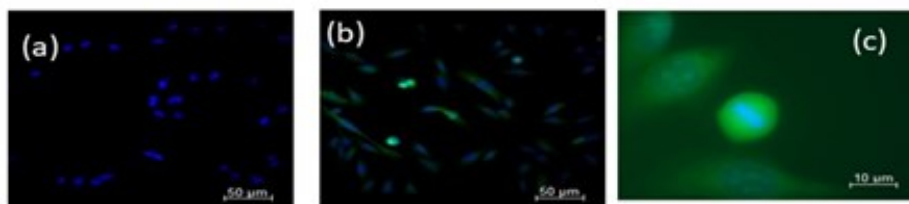


Figure 2. Photomicrograph of A375 untreated control cells stained with DAPI (a). In (b), the fluorescence photomicrograph of cells treated with CDs and stained with DAPI (merged blue and green channel, 20x magnification). (c) 100x magnified region of the image acquired in (b).

4. Conclusions

Intracellular biochemical changes, specific for cell type and surface modification of CDs, were documented in A2780 and CAL72 cells treated with (N-)CDs@RuCN system. These changes are augmented by illumination, promoting structural changes in biomolecules. In addition, our results demonstrate the potential of biomass-derived CDs to be used for imaging by the conventional fluorescence microscopy analysis, thus opening the possibilities to develop novel strategies for targeted photosensitive theranostics.

Acknowledgment

The research was funded by the Ministry of Science, Technological Development and Innovation of the Republic of Serbia (451-03-47/2023-01/200017), the Spanish Ministry of Science and Innovation (MCIN/AEI/10.13039/501100011033) through project PID2021-122613OB-I00. SR FTIR experiment was granted at the MIRAS beamline at ALBA Synchrotron with the collaboration of ALBA staff (experiment No. 2022025758).

References

- [1] J. Liu, R. Li, B. Yang., *Carbon Dots: A New Type of Carbon-Based Nanomaterial with Wide Applications*, *ACS Central Science*, 6 (2020) 2179–2195.
- [2] P.-C. Hsu, P.-C. Chen, C.-M. Ou, H.-Y. Chang, H.-T. Chang, *Extremely high inhibition activity of photoluminescent carbon nanodots toward cancer cells*, *Journal of Materials Chemistry B*, 1 (2013) 1774.
- [3] M. Lan, G. Liang, Z. Shaojing, Z. Zhenyu, J. Qingyan, Y. Li, X. Jing, Z. Hongyan, W. Pengfei, Z. Wenjun, *Carbon Dots as Multifunctional Phototheranostic Agents for Photoacoustic/Fluorescence Imaging and Photothermal/Photodynamic Synergistic Cancer Therapy*, *Advanced Therapeutics*, 1 (2018) 1800077.
- [4] B. B. Campos, R. Contreras-Cáceres, T.J. Bandosz, J. Jiménez-Jiménez, E. Rodríguez-Castellón, J.C.G.E. da Silva, M. Algarra., *Fluorescent chemosensor for pyridine based on N-doped carbon dots*, *Journal of Colloid and Interface Science*, 458 (2015) 209–216.
- [5] L. Cui, X. Ren, M. Sun, H. Liu, L. Xia, *Carbon Dots: Synthesis, Properties and Applications*, *Nanomaterials*, 11 (2021) 3419.

- [6] P. Pierrat, R. Wang, D. Kereselidze, M. Lux, P. Didier, A. Kichler, F. Pons, L. Lebeau, *Efficient in vitro and in vivo pulmonary delivery of nucleic acid by carbon dot-based nanocarriers*, *Biomaterials*, 51 (2015) 290–302.
- [7] Y. K. Jung, E. Shin, B.-S. Kim, *Cell Nucleus-Targeting Zwitterionic Carbon Dots*, *Scientific Reports*, 5 (2015) 18807.
- [8] M. D. Nešić, T. Dučić, M. Gonçalves, M. Stepić, M. Algarra, J. Soto, B. Gemović, T.J. Bandosz, M. Petković, *Biochemical changes in cancer cells induced by photoactive nanosystem based on carbon dots loaded with Ru-complex*, *Chemico Biological Interactions*, 360 (52022) 109950.
- [9] I. Yousef, L. Ribó, A. Crisol, I. Šics, G. Ellis, T. Ducic, M. Kreuzer, N. Benseny-Cases, M. Quispe, P. Dumas, S. Lefrançois, T. Moreno, G. García, S. Ferrer, J. Nicolas, M.A.G. Aranda, *MIRAS: The Infrared Synchrotron Radiation Beamline at ALBA*, *Synchrotron Radiation News*, 30 (2017) pp. 4–6.
- [10] H. Alhazmi, *FT-IR Spectroscopy for the Identification of Binding Sites and Measurements of the Binding Interactions of Important Metal Ions with Bovine Serum Albumin*, *Scientia Pharmaceutica*, 87 (2019) 5.
- [11] S. Sirikwanpong, D. Dahlan, S. Ngamukote, S. Sangsuthum, S. Adisakwattana, V. Nopponpunth, T. Himathongkam, *The Alterations of Erythrocyte Phospholipids in Type 2 Diabetes Observed after Oral High-Fat Meal Loading: The FTIR Spectroscopic and Mass Spectrometric Studies*, *Journal of Clinical Biochemistry and Nutrition*, 47 (2010) 111–120.
- [12] M. Kreuzer, S. Stamenković, S. Chen, P. Andjus, T. Dučić, *Lipids status and copper in a single astrocyte of the rat model for amyotrophic lateral sclerosis: Correlative synchrotron-based X-ray and infrared imaging*, *Journal of Biophotonics*, 13 (2020) e202000069.
- [13] L. Lilge, *Use of Ruthenium Complexes as Photosensitizers in Photodynamic Therapy*, in *Ruthenium Complexes*, W. R. Browne, A. A. Holder, M. A. Lawrence, J. L. Bullock Jr, L. Lilge, Eds., Weinheim, Germany: Wiley-VCH Verlag GmbH & Co. KGaA, 2017, pp. 117–137.
- [14] M. Havrdova, K. Hola, J. Skopalik, K. Tomankova, M. Petr, K. Cepe, K. Polakova, J. Tucek, A.B. Bourlinos, R. Zboril, *Toxicity of carbon dots – Effect of surface functionalization on the cell viability, reactive oxygen species generation and cell cycle*, *Carbon*, 99 (2016) 238–248.
- [15] M. Havrdová, I. Urbančič, K. Bartoň Tománková, L. Malina, J. Štrancar, A. B. Bourlinos, *Self-Targeting of Carbon Dots into the Cell Nucleus: Diverse Mechanisms of Toxicity in NIH/3T3 and L929 Cells*, *International Journal of Molecular Sciences*, 22 (2021) 5608.
- [16] M. Havrdová, I. Urbančič, K. B. Tománková, L. Malina, K. Poláková, J. Štrancar, A.B. Bourlinos, *Intracellular Trafficking of Cationic Carbon Dots in Cancer Cell Lines MCF-7 and HeLa—Time Lapse Microscopy, Concentration-Dependent Uptake, Viability, DNA Damage, and Cell Cycle Profile*, *International Journal of Molecular Sciences*, 23 (2022) 1077.

Confusion about the choice of evaluation metrics for model performance assesment in chemoinformatics, bioinformatics and in general

Bono Lučić^{1*}, Viktor Bojović¹, Antonija Kraljević², Jadranko Batista³

¹ Ruđer Bošković Institute, Bijenička cesta 54, HR 10000 Zagreb, Croatia; e-mails: lucic@irb.hr, vbojovic@irb.hr

² University of Mostar, Faculty of Mechanical Engineering, Computing and Electrical Engineering, Mostar, Bosnia and Herzegovina; e-mail: antonija.kraljevic@fsre.sum.ba

³ University of Mostar, Mostar, Faculty of Science and Education, Bosnia and Herzegovina; e-mail: jadranko.batista@fpmoz.sum.ba

* Corresponding author

DOI: 10.46793/ICCBi23.067L

Abstract: In chemo/bioinformatics, we evaluate the quality of models using model performance parameters/metrics. A large group of models in this field are binary classification models, which are a consequence of the general digitization of information and data in chemistry and life sciences. When classifying different models developed with different methods and by different research groups for the same data sets, we try to classify the models according to their quality. In this case, the question of selecting appropriate metrics arises, leading to incorrect (non-optimal) application of inappropriate metrics and thus incorrect assessment of the quality of the models and their incorrect (non-optimal) ranking. The article addresses the limitations and problems of using the Matthews correlation coefficient (*MCC*) and the *F1* parameter to describe the quality of classification models. To overcome these difficulties, it is proposed to use the parameter that estimates the real accuracy of the model above the accuracy level of the random model. Its use is suggested as an additional baseline test that confirms that the developed model is better than the corresponding random model. Finally, the use of the parameter called real accuracy and the well-known parameter Cohen's kappa (κ) should be preferred to the parameters *MCC* and *F1*, since they can be derived as special cases of κ .

Keywords: chemo/bioinformatics, evaluation metrics, real model accuracy, Cohen's kappa

1. Introduction

Computational modelling is used extensively in many fields, including chemistry and the life sciences. When it involves models developed using knowledge extraction (or learning, machine learning) methods from sets of molecules or biomolecules and their measured or calculated properties (features, descriptors), such models are classified as belonging to the field of chemoinformatics or bioinformatics.

The main goal of modelling in chemo/bioinformatics is to extract useful information or regularities in the form of a functional relationship between:

(1) dependent (Y) variables (*i.e.*, the measured property or activity) and
(2) a set of independent (X) variables (descriptors), usually calculated by available computer programmes based on the structures of molecules/biomolecules.

Due to the widespread digitization of data, a large number of properties modelled today are binary classification problems, *i.e.*, the values of the Y variables take only the values 1 or 0 (active/inactive, toxic/non-toxic, etc.). This paper addresses the problem of calculating the accuracy of binary classification models and selecting the best (optimal) statistical parameters to evaluate the quality of these models.

The dynamism of the field and the availability of large databases are attracting researchers from various fields such as scientific computing, machine learning or deep learning, etc., who are working intensively on modelling in chemo/bioinformatics. Predictive challenge organizations contribute significantly to accelerating the development and application of computational methods in chemo-bioinformatics. Thus, the DREAM consortium [1] has many years of experience in organising various Challenges since 2006 and is an interdisciplinary team composed of researchers from biotechnology, pharmaceutical and engineering and technology companies. One of these Challenges we participated in aimed to predict the binding efficiency of drug-like compounds to protein kinases in order to find successful inhibitors for cancer treatment [2]. In these competitions, the methods are evaluated/ranked according to predefined parameters. Therefore, the ranking of the best methods always depends on these selected parameters.

Using the examples of challenge models in the prediction of the set of structure of disordered proteins [3] described by confusion matrices (*TP*, *FN*, *FP*, *TN* values – explained in part 2), we will demonstrate the usefulness of evaluating the quality of models with parameters that include the random accuracy (error).

2. Materials and methods

All important measures of the quality of the classification models are calculated using the values of the confusion matrix (Table 1) [4]:

Table 1. Elements of a general confusion matrix.

		Model Class = 1	Model Class = 0	Σ rows
Exp. Class = 1		<i>TP</i>	<i>FN</i>	<i>TP + FN</i>
Exp. Class = 0		<i>FP</i>	<i>TN</i>	<i>TN + FP</i>
Σ columns		<i>TP + FP</i>	<i>TN + FN</i>	<i>N</i>

*F*₁score is defined as [4,5]:

$$F_1score = F1 = \frac{2 \cdot TP}{2 \cdot TP + FN + FP}.$$

The correlation coefficient, *i.e.* Matthews correlation coefficient (*MCC*), is calculated as:

$$R = MCC = \frac{TP \cdot TN - FN \cdot FP}{\sqrt{(TP + FN)(TP + FP)(TN + FN)(TN + FP)}}$$

and is often used in research and cited in the literature [6] (~5600 times in Google Scholar). It is simply a correlation coefficient adapted for the correlation analysis of classification variables and expressed by the elements of the confusion matrix (Table 1). The Accuracy parameter is simply defined as:

$$Accuracy = \frac{TP + TN}{TP + TN + FN + FP} = \frac{TP + TN}{N}.$$

The random (chance) accuracy can be calculated as:

$$Accuracy_{rnd} = \frac{(TP + FN)(TP + FP) + (TN + FP)(TN + FN)}{N^2}.$$

The 'delta accuracy' or 'real accuracy' is the contribution of a model to the *Accuracy* above the level of random accuracy [4]:

$$\Delta Accuracy = \Delta Acc = 100(Accuracy - Accuracy_{rnd})$$

Expressed in (%), this parameter ΔAcc represents the "real accuracy of the model/prediction", *i.e.*, "accuracy of the model/prediction above the corresponding random accuracy". Thus, this parameter is an indicator of the contribution of the model in relation to the corresponding random model, *i.e.*, random prediction. The value of this parameter can also be negative, indicating that the model performs worse than the corresponding random one.

The overview of evaluation metrics of classification models is given in the highly cited paper by Powers [5] (~8800 times in Google Scholar). An extremely frequently used parameter in the literature is Cohen's kappa [7] (cited ~48700 times in Google Scholar):

$$Cohen's - \kappa = \kappa = \frac{Accuracy - Accuracy_{rnd}}{1 - Accuracy_{rnd}} = \frac{\Delta Accuracy}{1 - Accuracy_{rnd}}$$

This parameter was originally developed and primarily used to assess the consistency of diagnoses by medical doctors and psychologists. It has also found applications in sociology and the social sciences, as well as in modelling in technical and natural sciences, life sciences and engineering.

3. Results and discussion

3.1. Analysis and comparison of parameters in special cases of confusion matrices

Most datasets in chemo/bioinformatics modelling are highly imbalanced. Six examples of extremely imbalanced data sets in Table 2 are constructed and suggested to test the suitability of statistical parameters in the estimation of the quality of classification models [4].

Table 2. Comparison of quality parameters of binary classification models. ^a

<i>Model</i>	<i>TP</i>	<i>FN</i>	<i>TN</i>	<i>FP</i>	<i>N</i>	<i>Acc, %</i>	<i>F1</i>	<i>MCC</i>	$\Delta Acc., \%$	<i>Cohen's κ</i>
<i>M</i> ₁	0	5	9995	0	10000	99.95	0.00	n.d.	0.00	0.00
<i>M</i> ₂	1	4	9994	1	10000	99.95	0.29	0.32	0.02	0.29
<i>M</i> ₃	2	3	9993	2	10000	99.95	0.44	0.45	0.04	0.44
<i>M</i> ₄	3	2	9992	3	10000	99.95	0.55	0.55	0.06	0.55
<i>M</i> ₅	4	1	9991	4	10000	99.95	0.62	0.63	0.08	0.62
<i>M</i> ₆	5	0	9990	5	10000	99.95	0.67	0.71	0.10	0.67
<i>M</i> ₇	5	0	5	9990	10000	0.1	0.001	0.0005	0.0001	0.0000
<i>M</i> ₈	4	1	4	9991	10000	0.08	0.0008	-0.20	-0.02	-0.0002

^a*M*₁, ..., *M*₉, are confusion matrices of different models; *Acc.* – *Accuracy*; n.d. – not defined.

The authors suggested that the correct ranking of models based on their quality should be $M_6 \rightarrow M_5 \rightarrow M_4 \rightarrow M_3 \rightarrow M_2 \rightarrow M_1$. The last four parameters from Table 2 are ordered that way, and *Accuracy* is not sensitive to variation of values *TP*, *FN*, *FN* and *FP* values. Only the parameter $\Delta Accuracy$ defined in the Methods section shows a uniform difference in the quality of the first six models, which corresponds to reality. The remaining three parameters (except *Accuracy*, which remains constant) exhibit uneven variation with respect to uniform changes of elements of the confusion matrix - which is not a desirable property of model evaluation metrics.

We find that the values of $\Delta Accuracy$ for the first six models are very small (and the same is true for the last two models in Table 2), which corresponds to reality and indicates that the real contribution of the model is *minimal* (almost less than 0.1%). The reason for this is the high imbalance of the data sets (*i.e.*, only 5 values are in class 1, and 9995 values are in class 0), so the accuracy of the random model is already very high. Therefore, random guessing with such a highly unbalanced set achieves high accuracy (matching). This information is provided only by the parameter $\Delta Accuracy$.

Of the remaining parameters, preference should be given to *Cohen's κ* since the *MCC* parameter can be derived from it as a special case with the transition $FN = FP$. As we know from statistical theory, especially when calculating the *MCC* parameter and testing its significance, the most important prerequisite is that the distributions of the two variables to be compared (experimental versus predicted) are similar (almost identical), *i.e.*, normal. This similarity is achieved in binary classification modelling when the model is optimized to achieve $FN = FP$.

Furthermore, the *F1* parameter is a special case of κ in the limiting case when $TN \gg TP, FN, FP$ (*i.e.*, $TN \rightarrow \infty$). This implies that the use of the *F1* parameter is only justified when the ratios TP/TN , FN/TN and FP/TN are close to zero, and in the literature, it is often used when these conditions are not met. It seems that it is easy to forget to check whether the use of a particular parameter is justified in a particular case.

3.2. Application of parameters in ranking models developed for the prediction of disorder in proteins

A total of 35 methods were evaluated using a dataset of 646 proteins from DisProt [3]. Depending on the parameters chosen to evaluate the models, the best performing methods use deep learning techniques in model development and optimisation and outperform physicochemical prediction methods. However, the selection of $F1$ and MCC for model validation is not an optimal choice, as these two parameters are only special cases of the *Cohen's* κ parameter, which should be preferred in this case. Moreover, in almost all models, the condition $FN = FP$ is not met, nor can all the ratios TP/TN , FN/TN and FP/TN be considered equal to zero.

The agreement and disagreement of the ranks when comparing the $F1$ and MCC parameters with *Cohen's* κ is shown in Figure 1 (parts A) and B)). Similarly, in Figure 2 we have shown the scatter plot between the ranks based on $\Delta Accuracy$ on one side and $F1$ and MCC on the other. Here we observe that the dispersions (mismatch of ranks) are significantly higher than in the case of *Cohen's* κ .

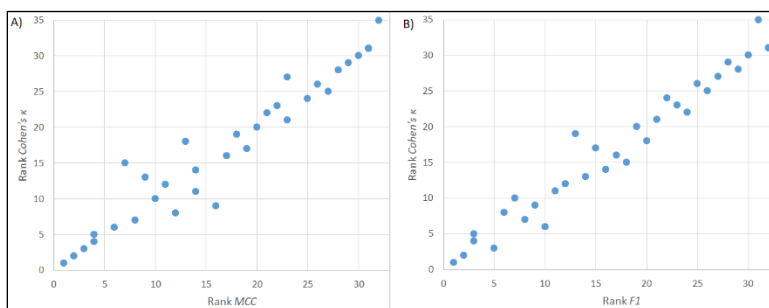


Figure 1. Correlation between the ranks of 35 sequence-based models for the prediction of disordered proteins. Comparison of ranks was performed between *Cohen's* κ and MCC parameters (part A)) and between *Cohen's* κ and $F1$ (part B)).

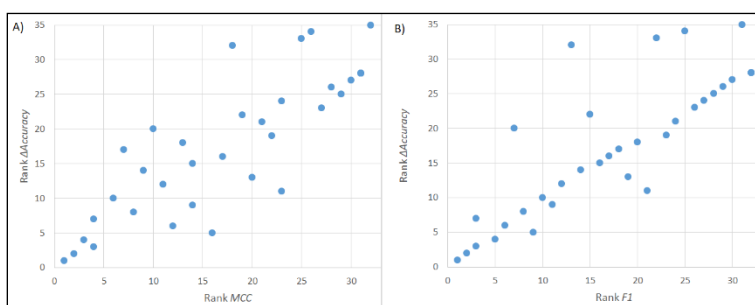


Figure 2. Correlation between the ranks of 35 sequence-based models for the prediction of disordered proteins. Comparison of ranks was performed between $\Delta Accuracy$ and MCC parameters (part A)) and between $\Delta Accuracy$ and $F1$ (part B)).

From these figures it is clear that the evaluation of model quality in prediction competitions or literature methods developed on identical datasets leads to a different ranking of the models when *Cohen's* κ or the actual accuracy (contribution) of the $\Delta Accuracy$ model is used as a criterion for comparing the models. The latter is also

highly informative and gives an intuitively clear idea of the quality of the model compared to a random model.

4. Conclusion

The analysis carried out shows that the assessment of model quality can be improved by introducing new statistical measures (parameters) of model quality. Commonly used parameters such as *F1* and *MCC* are less general, highly dependent on data distribution and less intuitive than the *Cohen's κ* parameter and the newly proposed additional parameter *$\Delta Accuracy$* , which has a clear meaning. We suggest that *Cohen's κ* and *$\Delta Accuracy$* should be preferred. The former is widely used in the literature, while the latter parameter is very informative and easy to understand when assessing model quality, and both take into account the accuracy of the corresponding random model. Therefore, we suggest their use when comparing the quality of models as a substitute or at least as a complement to the existing parameters.

Acknowledgment

This research is funded by the Ministry of Science and Education of the Republic of Croatia through a basic grant to the Ruđer Bošković Institute, Zagreb, Croatia and by the EU through the ERD Fund - Competitiveness and Cohesion Operational Programme (KK.01.1.1.01) The Scientific Centre of Excellence for Marine Bioprospecting – BioProCro, as well as by the Ministry of Science and Education of the Republic of Croatia and the German Academic Exchange Service (DAAD) for the ChemInf4Biosciences project. V. Bojović's work is partly supported by the project "Young researchers' career development project – training of doctoral students" funded by the EU through the European Social Fund and the Croatian Science Foundation (DOK-2018).

References

- [1] The DREAM Consortium, 2019, <https://dreamchallenges.org>, (Sept 31, 2023).
- [2] A. Cichońska, et al. *Crowdsourced mapping of unexplored target space of kinase inhibitors*, Nature Communications, 12 (2021) no. 3307 (18 pages).
- [3] M. Necci, et al., *Critical assessment of protein intrinsic disorder prediction*, Nature Methods, 18 (2021) 472–481.
- [4] B. Lučić, et al, *Estimation of random accuracy and its use in validation of predictive quality of classification models within predictive challenges*, Croatica Chemica Acta, 92 (2019) 379–391.
- [5] D.M. Powers, *Evaluation: from precision, recall and F-measure to ROC, informedness, markedness and correlation*, Journal of Machine Learning Technologies, 2 (2011) 37-63.
- [6] B.W. Matthews, *Comparison of the predicted and observed secondary structure of T4 phage lysozyme*, Biochimica et Biophysica Acta (BBA) - Protein Structure, 405 (1975) 442–451.
- [7] J. Cohen, *A coefficient of agreement for nominal scales*, Educational and Psychological Measurement, 20 (1960) 37–46.

History of radiological protection and evolution of dosimetric quantities

Dragana Ž. Krstić^{1*}, Dragoslav R. Nikezić^{1,2}

¹University of Kragujevac, Faculty of Science, R. Domanovica 12, 34000 Kragujevac, Serbia);
e-mail: dragana@kg.ac.rs; dragana.krstic@pmf.kg.ac.rs

²State University of Novi Pazar, Vuka Karadzic 2, Novi Pazar, Serbia;
e-mail: nikezic@kg.ac.rs

* *Corresponding author*

DOI: 10.46793/ICCBi23.073K

Abstract: The paper presents a brief history of radiation protection and the evolution of radiation quantities. Special attention is given to the history of tissue weight factors. The internationally adopted system of radiation quantities is presented.

Keywords: ionising radiation, radiation protection, radiation quantities, tissue weighting factors

1. Introduction

Ionizing radiation was discovered at the end of the 19th century. X-ray radiation, which is used extremely widely in medicine, but also in other fields, was discovered by Wilhelm Roentgen in 1895. Shortly after this invention, in 1896, radioactivity was discovered (Henri Becquerel), which represents the spontaneous transmutation of the atomic nucleus, with the emission of one or more particles or electromagnetic radiation. This was followed by discoveries of other types of ionizing radiation, such as, for example, neutron radiation.

The main characteristic of ionizing radiation is that it can ionize atoms and molecules of matter with which they interact when one or more electrons are ejected from the atom, leading to the creation of free electrons and positively charged atoms and molecules. For biology and medicine, the most important process is the ionization of water molecules, because there are many of these molecules in human cells. After ionization, the water molecule dissociates into H⁺ and OH⁻, which further interact with the present atoms and molecules. This process is called "radiolysis of water", and as a final result, it leads to the creation of free chemical radicals, which by diffusion can reach the DNA molecule and damage it with its chemical aggressiveness. Non-ionizing radiation cannot cause the ionization of water molecules, nor damage to DNA molecules, and that is the main difference between the two types of radiation. The text presented below is related only to ionizing radiation.

2. History of radiation protection

After the discovery of ionizing radiation, it was not known that it could cause damage to the tissue. Some great scientists sensed that radiation could be harmful or dangerous and issued some warnings. There is a record that Nikola Tesla, who was among the first to warn of the danger of X-ray radiation, expressed the thought "Experimenters should not get too close to the X-ray tube" in June 1896. On December 12, 1896, in the *Western Electrician* magazine, Wolfram Fush published a recommendation on how to reduce the effect of radiation in three points:

- a) shorten the irradiation time as much as possible;
- b) do not bring the x-ray tube closer than 12 inches to the body;
- c) rub out the irradiated part of the skin gently with Vaseline.

It is not known whether he was aware of Nikola Tesla's opinion when making these recommendations, but the first two recommendations have become the basis of radiation protection. Despite these warnings, there was almost no radiation protection, and it was completely disorganized. Organized protection against ionizing radiation began only in 1925.

Until the twenties of the last century, it was not known that ionizing radiation could cause cancer and genetic effects. It was known that radiation could cause reddening of the skin. The connection between leukemia and radiation was discovered in a strange way, almost by accident. At that time, the watch industry was developed in the USA in New York. Clocks with hands and dials that glow in the dark were made by mixing some fluorescent substance with radium or thorium; such a mixture was applied in the form of paint with brushes on certain surfaces. Workers who worked in such factories were exposed to an increased dose of radiation due to significant internal contamination, and soon a higher incidence of leukemia was discovered among them than among the rest of the population. Leukemia is the first cancer that appears after radiation, a year and a half to two years. This fact contributed to the understanding of the connection between radiation and cancer. Other cancers appear much later after radiation, ten or more years, and it has been difficult to establish a connection between radiation and the effect.

2.1 Organized radiation protection

An organized approach to ionizing radiation protection dates back to 1925, when the first congress of radiologists was held in London. At this congress, a body was established which was called the "International Committee on the X Radiation Unit", which was later renamed the "International Commission on Radiological Units". Three years later, in 1928, another international body was formed, called the "International Commission on Radiological Protection". The Commission had seven members and the first president was Ralf Sievert, from its host country, Sweden.

The Commission soon began its work, and in 1934 they proposed a permissible, tolerable level of radiation exposure of 0.2 R/d; according to current measures, this

corresponds to 500 mSv/year. This was three times less than the previously recommended value of 0.6 R/d which was independently proposed by Sievert and Arthur Marceller (1925). Sievert and Marceller's recommendation was based on the idea of preventing reddening of the skin, which is one of the first effects that appear after radiation. The ICRP Commission met once more before the Second World War, in 1937, and only after the war, in 1950, in London. At that meeting, a maximum permissible dose of 0.3 R per week, which corresponds to 150 mSv/year, was proposed for professionally employed persons.

At the beginning of the fifties of the last century, an intensive study of the effects of ionizing radiation on living tissue began. The survivors of the atomic bombings in Hiroshima and Nagasaki were studied and monitored in detail - it was a living laboratory. It has been discovered that in addition to leukemia, radiation can cause other types of cancer as well as genetic effects. It was considered that there is no dose threshold for genetic effects, and the Commission, at a meeting held in 1956, proposed reducing the maximum permissible dose for professionals from 0.3 R per week to 0.1 R per week, which in today's terminology amounts to 50 mSv/year. In addition, at the same meeting, a new concept was introduced, the protection of the population that does not work with radiation sources, and 1/10 of the dose for professionally employed persons was proposed for them.

Also, in the fifties of the last century, two more international institutions dealing with radiation protection and related problems were founded. The first of them was founded in 1956 by the United Nations, and was called the "United Nations Scientific Committee on the Effects of Atomic Radiation", abbreviated UNSCEAR. A year later, in 1957, the International Agency for Atomic Energy (IAEA) was founded, with headquarters in Vienna, Austria.

By the end of the fifties of the last century, numerous nuclear reactors were built - research, energy and other, and in addition to Hiroshima and Nagasaki, numerous test nuclear explosions took place, as well as two major nuclear accidents. The first of them occurred in England in Windscale, and the second in Kishtim near Chelyabinsk in the former USSR (current Russia). Both accidents led to significant environmental contamination in the wider area around the reactor. A significant accident occurred in Vinca Institute on October 15, 1958, which resulted in the irradiation of six people (one of whom died), but without contaminating the reactor environment. This accident led to the formation of an organized service for radiation protection at the Vinca Institute and soon to the adoption of the Law on Radiation Protection. Thus, the former Yugoslavia became one of the first countries in the world to have such a law. Atmospheric and other nuclear tests carried out in the fifties and sixties led to the global contamination of the world with radioactive fission products. In this situation, the influence of the ICRP and other agencies grew in this field. The main activity of the ICRP (and UNSCEAR) at that time was the collection, systematization and analysis of data on the sources and effects of radiation. On that basis, recommendations regarding radiation protection were issued in the form of publications - most countries in the world follow these recommendations, incorporate them into their legislation and represent the basis of radiation protection.

The recommendations issued in 1977 and 1991 [1,2] are particularly significant. The maximum permissible doses were reduced for the last time in the recommendations of 1991, and 20 mSv/year, averaged over 5 years, was recommended, with the condition that in one year the effective dose must not exceed 50 mSv. The annual maximum dose for the population is proposed to be 1 mSv.

2.2 Concepts adopted in ICRP publication no. 60, from 1991

After publication 26 [1], work continued on the adoption and further development of radiation protection. Special attention was paid to the ALARA principle because for its application it was necessary to adopt the monetary equivalent of a human life, which caused ethical discussions in which even the Vatican became involved. Also, for the first time, the radon problem is taken into consideration. As a consequence of the new development, the Commission adopted in 1990, and in 1991 published the new recommendations number 60 [2]. The most important is the reduction of the annual limit dose from 50 to 20 mSv averaged over 5 years. Also, the previous quantity, the *effective dose equivalent*, has been replaced by the *effective dose*. Instead of radiation quality factors, radiation weighting factors with the same numerical values for various types of radiation were introduced.

3. Evolution of radiation units

From the very beginning, the problem of determining how much an individual was irradiated appeared. This problem, in the opinion of the authors of this text, has not been fully resolved even today. It is necessary to define physical quantities (and units) that represent a person's exposure to radiation. At that time, it was well known that radiation, ionizing the air, creates a certain amount of charge in the air. It was logical to define a physical quantity that describes air ionization. This was the exposure dose (or just exposure), denoted by X , and was defined as the quotient of the charge, dQ created by the radiation (X and gamma) and the mass of air, dm , in which that charge was created:

$$X = \frac{dQ}{dm} \quad (1)$$

The exposure dose unit was defined as 1 R (one Rendgen, used above) and represents one electrostatic charge created in 1 gram of air. In parallel with this quantity, the rate of the exposure dose was defined, and the unit is 1 R/h. As a measure of irradiance, 1 R has been used for a long time. For example, if in some space the rate of the exposure dose is 0.1 R/h, and a person spends 10 hours in that place, then he "received a dose" of 1 R. This is a rough estimate of the actual exposure. For a better assessment of radiation, it is necessary to use more precise and better-defined sizes.

Ionization in the air, i.e., the amount of charge created, can be connected to the energy absorbed in the mass of air because an average of 34 eV is spent for one ionization event in the air. It was soon shown that the final biological effect is

determined by the absorbed energy, and therefore a quantity called the absorbed dose, D , was introduced and defined as the quotient of the energy, dE , and the mass of matter, dm , in which the absorption occurred:

$$D = \frac{dE}{dm} \quad (2)$$

The unit for absorbed dose is 1 Gray, i.e., 1 Gy=J/kg.

Over time, it became clear that different types of radiation cause different damage and cause different effects. For example, comparing alpha radiation and gamma radiation reveals this difference. Gamma (as well as X) radiation creates spatially scattered, rare damage. On the other hand, alpha radiation creates very dense damage, and can, for example, at a distance of less than 100 μm create more than 100,000 ionizations. It is clear that the latter case is much more difficult to repair, which normally happens in the human body. In order to account for this difference, a physical quantity, the equivalent dose, was introduced, which was originally defined as

$$H = QND \quad (3)$$

where D is absorbed dose, Q quality factor of radiation, and N is the product of all other modifying factors. This definition was modified later, and it is as follows

$$H = \sum_R w_R D_R \quad (4)$$

where D_R is absorbed dose due to the radiation type R , w_R are radiation weighting factors and they are 1 for X and gamma radiation, 5 to 15 for neutrons and 20 for alpha radiation.

It was later shown that various organs and tissues in the human body are differently sensitive to radiation. To account for this difference, a new quantity was introduced called the effective dose, E , and is defined as

$$E = \sum_T w_T H_T \quad (5)$$

where H_T is the equivalent dose in the organ/tissue marked with T , and w_T is the so-called tissue weighting factor for the organ/tissue T : it represents the probability that cancer will appear in a given organ if the whole human body is uniformly irradiated. Tissue weighting factors were derived from studies of the surviving population irradiated in Hiroshima and Nagasaki at the end of World War II. Since this population has been followed since World War II, there has been some change and evolution of tissue weighting factors. Tissue weighting factors are shown in Table 1.

Table 1. Tissue weighting factors according ICRP 26 (1977), ICRP 60 (1991) and ICRP 103(2007) [1,2,3]

Main organs or tissue	Tissue weighting factors, w_T		
	ICRP26	ICRP60	ICRP103
Gonads	0.25	0.20	0.08
Red bone marrow	0.12	0.12	0.12
Colon	-	0.12	0.12
Lungs	0.12	0.12	0.12
Stomach	-	0.12	0.04
Bladder	-	0.05	0.12
Breast	0.15	0.05	0.12
Esophagus	-	0.05	0.04
Liver	-	0.05	0.04
Thyroid	0.03	0.05	0.04
Brain	-	-	0.01
Salivary glands	-	-	0.01
Skin	-	0.01	0.01
Endosteum	0.03	0.01	0.01
Remainder	0.30	0.05	0.12

In the last column of Table 1, the newly adopted numerical values for tissue factors for the specified tissue and organs are given, which range from 0.01 to 0.12 according to the recommendations in ICRP publication 103 from 2007 [3]. These recommendations have updated the tissue factors, based on the latest available scientific data on exposure to ionizing radiation.

The first group of organs/tissues with the highest individual weight factor of 0.12 consists of bone marrow (red), colon, lung, stomach, breast, bladder and tissue of the "remainder". The remainder of the body consists of 13 organs: adrenal glands, extrathoracic region, gall bladder, heart, kidneys, lymph glands, oral mucosa, prostate (male), small intestine, spleen, pancreas, thymus, and uterus/cervix (female). All organs of the remainder are treated as one organ with a weighting factor of 0.12. The second group with a factor of 0.08 consists only of gonads. The new weighting factor for gonads is 2.5 times lower than the previous one, which was 0.20, which represents one of the biggest changes compared to the old recommendations. The third group with an individual factor of 0.04 consists of the esophagus, liver and thyroid. Finally, the tissue group with the smallest individual factor of 0.01 follows: skin, brain, salivary glands, and endosteum. Organs which have a probability smaller than 1 % are in the group remainder.

3.1 Current system of radiation units

According to current international standards, there are three groups of radiation quantities. The first group consists of physical quantities, Fluence, Kerma and Absorbed dose. The second group is the protective quantities, mean absorbed dose in an organ or tissue, equivalent dose and effective dose according to the definitions given in the previous text. The effective dose defined according to equation (5) requires knowledge of the equivalent (that is, the absorbed dose) by the organs of the human body, which means that it is not a measurable quantity. For this reason, a third set of quantities that are measurable and called operational quantities has been defined. Ambient dose equivalent, $H^*(d)$ and directional dose equivalent $H'(d, \Omega)$ are used for area monitoring. Personal dose equivalent, $H_p(d)$, is used for monitoring the exposure of individuals. The relationship between these quantities is given in Figure 1.

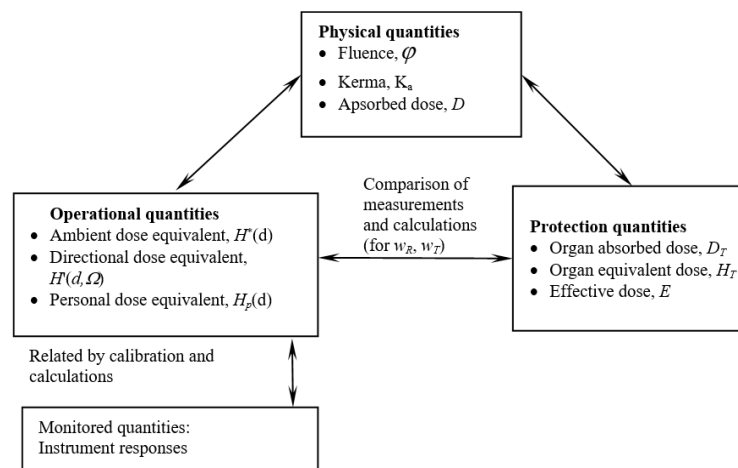


Fig. 1. The relationship between physical, protective and operational quantities

However, the current system has its drawbacks. Based on the joint ICRP/ICRU Report 95, it was proposed to significantly modify the more than 30-year-old approach to measuring quantities in radiation protection, based in part on the ICRU sphere concept.

Consequently, the ICRU, in collaboration with the ICRP, developed new operational quantities (ICRU, 2020) [4], which are shown in Figure 2. The main philosophical change is that the operational quantities are now defined as the product of fluence at a point in space with conversion coefficients which are defined in the same reference phantoms (ICRP110, 2009) [5] used to calculate protective sizes. In addition, the range of energies and types of radiation for which conversion coefficients are available has been expanded.

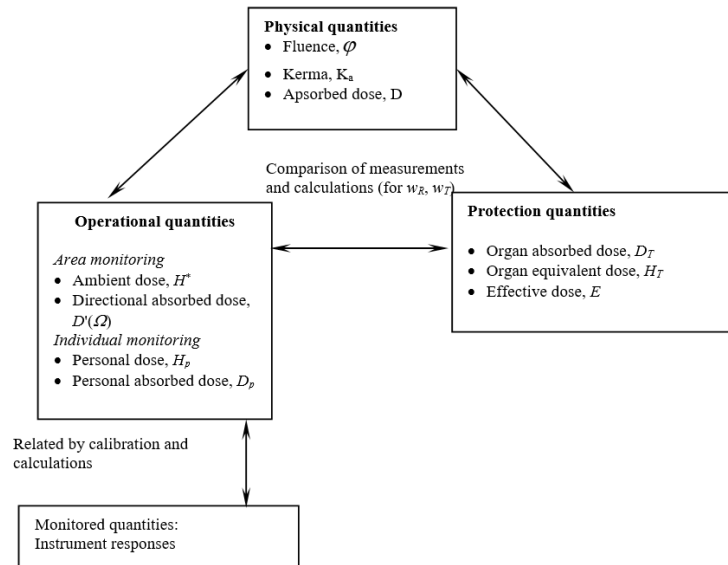


Figure 2. Relationship between radiation protection quantities and new operational quantities according to recommendations of ICRU Report 95 (ICRU, 2020)

4. Conclusions

Defining radiation quantities is a field that has been developing for almost 100 years. The target size is the Effective Dose, which best reflects how much a person is irradiated, but it is unmeasurable. That is why a set of measurable quantities is defined, which are translated into an equivalent and effective dose through the appropriate conversion coefficients.

Acknowledgment

This research is funded by the Ministry of Education and Ministry of Science, Technological Development and Innovation, Republic of Serbia, Grants: No. 451-03-47/2023-01/ 200122.

References

- [1] ICRP 26, Recommendations of the International Commission on Radiological Protection. Pergamon Press, Oxford (1977), Vol 1, Issue 3: 1-53.
- [2] ICRP 60, Recommendations of the International Commission on Radiological Protection. Pergamon Press, Oxford (1991) Vol 21, Issues 1-3: 1-201.
- [3] ICRP 103, Recommendations of the International Commission on Radiological Protection. ICRP Publication 103 (2007). Ann. ICRP 37 (2-4).
- [4] ICRU Report 95, Operational Quantities for External Radiation Exposure (2020) Vol 20, Issue 1.
- [5] ICRP 110, Adult Reference Computational Phantoms. Realistic reference phantoms. ICRP Publication 110 (2009). Ann. ICRP 39 (2).

Applied Science and Technology

Entropy dynamics for a propeller-shaped quantum Brownian molecular rotator

J. Jeknic-Dugic^{1*}, I. Petrovic¹, K. Kojic¹, M. Arsenijevic², M. Dugic²

¹ University of Nis, Faculty of Science and Mathematics, Visegradska 33, 18000 Nis, Serbia; e-mail: jjeknic@pmf.ni.ac.rs, igorpetrovicsb@gmail.com, kristina.kojic@pmf.edu.rs

² University of Kragujevac, Faculty of Science, University of Kragujevac, Radoja Domanovica 12, 34000 Kragujevac; fajnman@gmail.com, mdugic18@sbb.rs

* Corresponding author

DOI: 10.46793/ICCB23.082JD

Abstract: We investigate and analyze the time dependence of the so-called differential entropy as a measure of the dynamical stability of a one-dimensional, propeller-shaped quantum Brownian molecular rotator. The larger the entropy change, the more profound the instability (lower control) of the rotator. The quantum molecular rotator is modelled by the quantum Caldeira-Leggett master equation while assuming the external harmonic field for the rotator. Rotational stability is found relatively high for the constructed Gaussian states, especially for molecules with a larger number of blades.

Keywords: molecular cogwheels, entropy, open quantum systems, Brownian motion

1. Introduction

Achieving the goals of molecular nanotechnology requires a multidisciplinary approach [1-4]. Theoretical results are often instrumental for applications. The propeller-shaped molecular rotators (molecular cogwheels) are among the basic elements of molecular nanomachinery [1-5]. Exposed to the environmental influence, molecular cogwheels (MC) exhibit stochastic, dynamically unstable behavior; in general, the molecules suffer from decoherence, diffusion, friction, state relaxation or even thermalization [1-6]. The expected realistic situations are characteristic of the short and rather frequent external actions applied on the rotator thus raising a question of the possibly non-negligible quantum-mechanical corrections (much before the possible relaxation or thermalization of the rotator). Only recently similar analyzes have been systematically performed [7-13]. The nonexistence of a canonical quantifier imposes the task of comparing the different methods of statistical inference in order to improve stability and therefore the desired dynamical control of the molecular rotators [1-3,8,11].

In this paper, we perform an analysis of the MC dynamical stability via the use of *entropy*. To this end, entropy as a quantifier of information is not very informative per se [14]. The larger the *change* of entropy the less stable—the less predictable, and therefore the less controllable—are the molecular rotations. We utilize a quantum model of the

Brownian motion [6,15] for small rotations of a propeller-shaped molecule while assuming that the molecule is exposed to a constant external harmonic field.

2. Model and methods

The so-called Caldeira-Leggett (CL) master equation is a proper quantum-mechanical counterpart of the classical Brownian motion model [6,15]. It is suited well also for investigating the dynamics of a planar rotator with the assumption of a very small angle of rotation [8,11]. Interestingly, it is possible to account for the *size* of the propeller-shaped molecules by re-scaling the molecule moment of inertia ($I = nI_0$) and the so-called damping factor ($\gamma = n\gamma_0$) for a molecule with the number n of blades [8,11]. Denoting the angle of rotation by φ and the angular momentum by L , the CL master equation in the Schrodinger picture and in the position representation reads [6,8,11]:

$$\frac{\partial \rho(\varphi, \varphi', t)}{\partial t} = \left[\frac{i\hbar}{2nI_0} \left(\frac{\partial^2}{\partial \varphi^2} - \frac{\partial^2}{\partial \varphi'^2} \right) - \frac{i}{\hbar} (V(\varphi) - V(\varphi')) - n\gamma_0(\varphi - \varphi') \left(\frac{\partial}{\partial \varphi} - \frac{\partial}{\partial \varphi'} \right) - \frac{2n^2 I_0 \gamma_0 kT}{\hbar^2} (\varphi - \varphi')^2 \right] \rho(\varphi, \varphi', t), \quad (1)$$

where I_0 is the average moment of inertia and γ_0 the average damping factor for the set of n blades, while k is the Boltzmann's constant, T is the environment temperature and the external field $V(x)$. The unknown function is the so-called "kernel" of the "density matrix" (statistical operator) $\hat{\rho}(t)$, $\rho(\varphi, \varphi', t) \equiv \langle \varphi | \hat{\rho}(t) | \varphi' \rangle$, which for $\varphi = \varphi'$ becomes the probability distribution $\rho(\varphi, t)$.

The general solution to equation (1) is not known. The process described by equation (1) is known to have a (dynamically inaccessible) *stationary state*, $\hat{\rho}(t) = \int d\varphi d\varphi' \rho(\varphi, \varphi', t) |\varphi\rangle \langle \varphi'|$, with the kernel [6]:

$$\rho(\varphi, \varphi', t) = \frac{1}{\sqrt{\sigma_\varphi^2 2\pi}} \exp \left\{ -\frac{1}{2\sigma_\varphi^2} \left(\frac{\varphi + \varphi'}{2} \right)^2 - \frac{\sigma_L^2}{2\hbar^2} (\varphi - \varphi')^2 \right\} \quad (2)$$

for the external harmonic potential $V(\varphi) = nI_0\omega^2\varphi^2/2$ and the circular frequency ω , while by σ_s we denote the standard deviations.

On the other hand, the approximate stationary state(s) may produce the least change of entropy. That is, preparation of the rotator in that state is expected to lead to a relatively stable rotation. Hence, we "equip" the time-independent stationary state (2) with the following *ansatz*: instead of the time-independent standard deviations σ_φ^2 and σ_L^2 , in equation (2), we place the known time-dependent standard deviations [8],

$$\begin{aligned} \sigma_\varphi^2(t) &= e^{-2n\gamma_0 t} \left(\sigma_\varphi^2(0)(\cos \omega t)^2 + \frac{\sigma_L^2(0)}{(nI_0\omega)^2} (\sin \omega t)^2 + \frac{\sigma(0)}{2nI_0\omega} \sin 2\omega t \right) + \frac{kT}{nI_0\omega^2} (1 - e^{-2n\gamma_0 t}), \\ \sigma_L^2(t) &= e^{-2n\gamma_0 t} \left(\sigma_L^2(0)(\cos \omega t)^2 + (nI_0\omega)^2 \sigma_\varphi^2(0)(\sin \omega t)^2 - \frac{nI_0\omega}{2} \sigma(0) \sin 2\omega t \right) + \\ & nI_0 kT (1 - e^{-2n\gamma_0 t}), \end{aligned} \quad (3)$$

where $\sigma(0)$ is the initial value of the correlation between the angle and the angular momentum. Now, we can calculate the time change of entropy.

3. Results

For the "equipped" initial states, we perform study of the so-called *differential*

entropy, S_d , that is defined as [16]:

$$S_d(t) = - \int d\varphi \rho(\varphi, t) \ln \rho(\varphi, t), \quad (4)$$

with the range $\varphi \in [-\pi, \pi]$ of integration.

The results for the absolute value of the relative change of entropy (quantum versus classical), $\delta S_d = |(S_d(t) - S_d(0))/S_d(0)|$, are graphically presented in Figure 1 for small angle of rotation (i.e., small time interval $t \in [0, 0.1]$). The rotator/bath parameters are chosen: $\sigma_\varphi(0) = 0.1, \sigma_L(0) = 10, \sigma(0) = 0, \gamma_0 = 0.001, \omega = 1, kT = 10, I_0 = 1 = \hbar$.

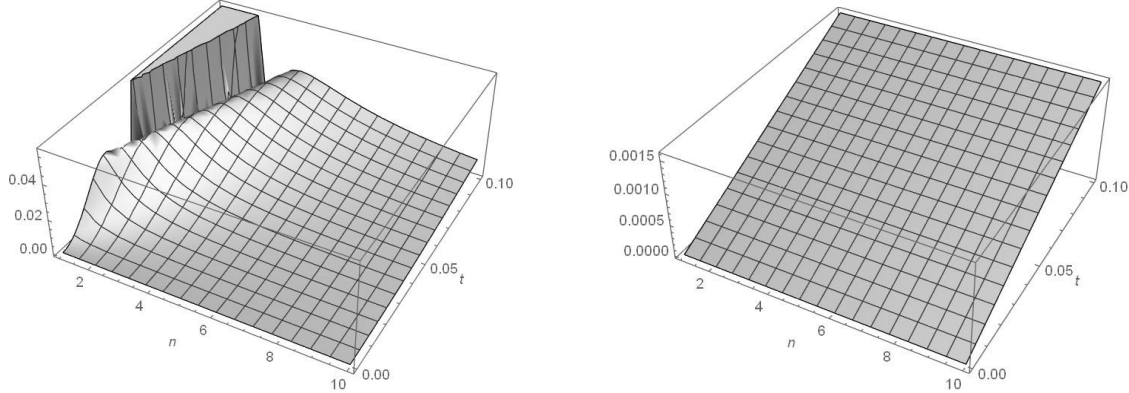


Figure 1. Time change of the absolute value of the relative differential entropy δS_d : (left) quantum and (right) classical case. The classical expression follows from the classically allowed zero standard deviations in equation (3).

3. Conclusions

From Figure 1, we can detect both relatively stable rotation ($\delta S_d \sim 0.15 - 4\%$ for $n > 1$) and significant quantum contributions already for short time intervals for the underdamped regime ($kT = 10$). Better dynamical stability is found for larger number n of blades for the quantum case. Overall, small change of δS_d even for the quantum case is encouraging in search for better stability of the molecular rotations – that deserves more detailed and comprehensive study to be presented elsewhere [17].

Acknowledgment

This research is funded by the Ministry of Education and Ministry of Science, Technological Development and Innovation, Republic of Serbia, Grants: No. 451-03-47/2023-01/200124 and 451-03-47/2023-01/200122.

References

- [1] R. A. L. Jones, *Soft machines, Nanotechnology, and Life*, Oxford University Press, Oxford, 2004.
- [2] M. Kurzinski, *The thermodynamic machinery of life*, Springer, Berlin, 2006.
- [3] G. S. Kottas, L. I. Clarke, D. Horinek, and J. Michl, *Artificial molecular rotors*, *Chemical Reviews*, 105 (2005) 1281-1376.

- [4] *Nanoscience and Technology: A Collection of Reviews from Nature Journals*, Ed., Peter Rogers, World Scientific, Singapore, 2009.
- [5] T. Kudernac, N. Ruangsapapichat, M. Parschau, B. Macia, N. Katsonis, S. R. Harutyunyan, K.-H. Ernst, and B. L. Feringa, *Electrically driven directional motion of a four-wheeled molecule on a metal surface*, *Nature*, 479 (2011) 208-211.
- [6] H.-P. Breuer, and F. Petruccione, *The theory of open quantum systems*, Clarendon Press, Oxford, 2002.
- [7] A. Roulet, S. Nimmrichter, J. M. Arrazola, S. Seah, and V. Scarani, *Autonomous rotor heat engine*, *Physical Review E*, 95 (2017) 062131.
- [8] J. Jeknic-Dugic, I. Petrovic, M. Arsenijevic, and M. Dugic, *Dynamical stability of the one-dimensional rigid Brownian rotator: The role of the rotator's spatial size and shape*, *Journal of Physics: Condensed Matter*, 30 (2018) 195304.
- [9] B. A. Stickler, B. Schrintski, and K. Hornberger, *Rotational friction and diffusion of quantum rotors*, *Physical Review Letters*, 121 (2018) 040401.
- [10] D. Dattler, G. Fuks, J. Heiser, E. Moulin, A. Perrot, X. Yao, and N. Giuseppone, *Design of collective motions from synthetic molecular switches, rotors, and motors*, *Chemical Reviews*, 120 (2019) 310-433.
- [11] I. Petrovic, J. Jeknic-Dugic, M. Arsenijevic, and M. Dugic, *Dynamical stability of the weakly nonharmonic propeller-shaped planar Brownian rotator*, *Physical Review E*, 101 (2020) 012105.
- [12] C. Gonzalez-Ballester, M. Aspelmeyer, L. Novotny, R. Quidant, and O. Romero-Isart, *Levitodynamics: Levitation and control of microscopic objects in vacuum*, *Science*, 374 (2021) eabg3027.
- [13] B. Schrintski, Y. J. Chan, B. Schrintski, *Thermalization of the Quantum Planar Rotor with external potential*, E-print [arXiv:2207.04810](https://arxiv.org/abs/2207.04810) [quant-ph].
- [14] M. A. Nielsen, and I. L. Chuang, *Quantum computation and Quantum information*, Cambridge University Press, Cambridge, 2000.
- [15] A. O. Caldeira and A. J. Leggett, *Path integral approach to quantum Brownian motion*, *Physica A*, 46 (1983) 587-616.
- [16] P. Garbaczewski, *Differential Entropy and Dynamics of Uncertainty*, *Journal of Statistical Physics*, 123 (2006) 315-355.
- [17] J. Jeknic-Dugic, K. Kojic, I. Petrovic, M. Arsenijevic, M. Dugic, *Entropy production for a harmonic propeller-shaped planar molecular quantum Brownian rotator* (work in progress).

Biocorrosion, biofouling and health risk: biological activity reaction tests of selected brackish groundwater occurrences in Serbia

Vladimir Šaraba^{1*}, Jasmina Nikodinovic-Runic¹, Vesna Obradović², Ivica Dimkić³, Tamara Janakiev³, Veselin Dragišić⁴, Milica Ciric¹

¹University of Belgrade, Institute of Molecular Genetics and Genetic Engineering, Laboratory for Molecular Genetics and Ecology of Microorganisms, Belgrade, Serbia; e-mail: vsaraba@imgge.bg.ac.rs , jasmina.nikodinovic@imgge.bg.ac.rs , milica.ciric@imgge.bg.ac.rs

²Jaroslav Černi Water Institute, Laboratory Jaroslav Černi, Belgrade, Serbia; e-mail: vesna.obradovic@jcerni.rs

³University of Belgrade, Faculty of Biology, Chair of Biochemistry and Molecular Biology, Belgrade, Serbia; e-mail: ivicad@bio.bg.ac.rs , tamara.janakiev@bio.bg.ac.rs

⁴University of Belgrade, Faculty of Mining and Geology, Department of Hydrogeology, Belgrade, Serbia, e-mail: veselin.dragisic@rgf.bg.ac.rs

* Corresponding author

DOI: 10.46793/ICCB23.086S

Abstract: Targeted physiological groups of bacteria were cultivated and identified in the brackish groundwaters of Obrenovačka Barja (OB), Lomnički Kiseljak (LK) and Velika Vrbnica (VV) using biological activity reaction tests (BARTs) to assess the biocorrosion, biofouling and health risks. The highest density of iron-related, sulfate-reducing, slime-forming, facultatively anaerobic heterotrophic, denitrifying bacteria and representatives of *Pseudomonas* spp. was recorded in the OB sample, while the lowest density of the same physiological groups of bacteria was recorded in the LK sample. Facultatively anaerobic heterotrophic bacteria were the most abundant in the OB and LK samples, while, in contrast, heterotrophic aerobic bacteria were the most abundant in the VV sample. All tested samples were characterized by a high degree of biochemical activity associated with iron-related, sulfate-reducing, slime-forming, heterotrophic aerobic and facultatively anaerobic bacteria. Also, high biochemical activity of denitrifying bacteria was recorded in the OB sample, and the same activity of *Pseudomonas* species was recorded in the OB and VV samples. For OB and LK groundwaters, the highest degree of risk was estimated for biocorrosion process, while for the OB and VV occurrences, the highest degree of risk was estimated for biofouling process. The health risk was present for all examined groundwaters. Caution is warranted in further use of all investigated occurrences due to the established public health risk and an immediate revitalization of the OB, LK and VV wells is necessary.

Keywords: brackish groundwaters, biological activity reaction tests, Serbia.

1. Introduction

Wells, like any other part of the plumbing system, require preventive maintenance treatments and appropriate periodic cleaning [1], taking into account that bacteria are ubiquitous in wells [2]. In order for groundwater to have a satisfactory qualitative status, it is of the highest importance to prevent the occurrence of biofouling of wells. The development of biofouling contributes to the reduction of well capacity [1] and it is reported in North America as the major, most costly factor in the deterioration of groundwater system characteristics [3, 4]. Also, biofouling can represent a

source of pathogenic bacteria that can cause water-borne infections [5]. With its further development, a microenvironment contributing to the progress of biocorrosive processes is formed [6]. About 20% of all corrosive processes in various branches of industry, including the water industry, are the result of bacteriological activity, which amounts every year to billions of dollars in the US [7] and to 30-50 billion dollars worldwide [8]. Three occurrences, which are used for health-and-recreation and drinking purposes, which belong to the group of brackish groundwaters [9] and are captured by wells with a depth of 6.5-442.5 m [10, 11], were selected for cultivation and identification of targeted physiological groups of bacteria that can contribute to the development of biocorrosion and biofouling processes and may pose a health risk for groundwater users. Although bacteriological contamination of LK groundwaters was previously confirmed [12], continuous monitoring of its bacterial diversity and prediction of the risk of aging for LK well is warranted.

2. Methods

Sampling of studied groundwaters and transport of the three samples, each collected from corresponding wells was carried out in accordance with SRPS EN ISO - 19458:2009 standards during January 2020. The presence of targeted physiological groups of bacteria was determined using Iron-Related Bacteria (IRB), Sulfate-Reducing Bacteria (SRB), Slime-Forming Bacteria (SLYM), Heterotrophic Aerobic Bacteria (HAB), Denitrifying Bacteria (DN) and Fluorescent *Pseudomonas* (FLOR) Biological Activity Reaction Tests (BARTs). Portions of well-mixed, undiluted groundwater samples (7.5 mL) were carefully transferred *via* flotation ball to the inner test vial of the different BART biotectors under sterile conditions and incubated at 22°C for a period of time standard for each type of BART test (5, 10 or up to 15 days). Protocols available from the manufacturer (DBI, Saskatchewan, Canada) were used. During the sample incubation period signature reactions of bacterial activity and their metabolic products were monitored daily (lag period) and photo-documented. Based on the time of occurrence of all recognized signature reactions in the applied BART system, the probable risks of biocorrosion, biofouling and public health risk were calculated using the BART-Soft v6 software and results were expressed as high, medium, and low aggressivity (HA, MA, and LA). For all examined occurrences, an assesment for each type of risk (biocorrosion, biofouling and health risk) was given numerically and it ranged from 0 (no risk) to 9 (maximum risk) [13].

3. Results and discussion

BART analysis recorded the highest bacterial density in the OB sample and the lowest in the LK sample. Facultatively anaerobic heterotrophic bacteria were the most abundant in the OB and LK samples, while heterotrophic aerobic bacteria were the most abundant in the VV sample. All examined occurrences exhibited a high degree of biochemical activity associated with iron-related, sulfate-reducing, slime-forming, heterotrophic aerobic and facultatively anaerobic bacteria, as well as the same degree of biochemical activity of denitrifying bacteria was recorded in the OB sample. It is important to note that high biochemical activity of fluorescent *Pseudomonas* species was recorded in the VV sample and the non-fluorescent pseudomonads, with the same degree of

biochemical activity, were detected in the OB sample. The calculated biocorrosion risk was highest for the OB and LK groundwaters, while the calculated biofouling risk was highest for the OB and VV occurrences. For all examined occurrences, health risk was present (Table 1).

Table 1. Density of populations of target physiological groups of bacteria in the studied groundwater occurrences.

Investigated groundwaters	Population estimate (CFU/mL)						Total	Biocorrosion risk Biofouling risk Health risk
	IRB	SRB	SLYM	HAB	DN	FLOR		
	Aggressivity							
Obrenovačka Banja	35.300	731.000	70.000	6.890.000	17.200	4.000**	7.747.500	8.1
	HA	HA	HA	HA	HA	HA		6.3
Lomnički Kiseljak	8.820	731.000	70.000	454.000	2.140	400*	1.266.360	8.1
	HA	HA	HA	HA	MA	MA		4.5
Velika Vrbnica	35.300	910	632.000	6.890.000	417	4.000*	7.562.627	5.4
	HA	HA	HA	HA	LA	HA		7.0
								5.4

**P. aeruginosa* confirmed as a result of detection of signature reaction PB (Pale blue); **Non-fluorescent pseudomonads confirmed as a result of detection of signature reaction CL (Cloudy).

Based on the detected level of biochemical activity of iron-related, sulfate-reducing, slime-forming and heterotrophic aerobic bacteria, and taking into account the manufacturer's recommendations, revitalization of the OB, LK and VV wells is necessary in the shortest possible period. Due to the complexity of bacterial communities in groundwater and their tendency to grow in the form of biofilms, revitalization may include all or a combination of recommended treatments, such as the implementation of biocides, physical and chemical treatments [13]. According to the Rulebook on the quality and other requirements for natural mineral, spring, and table waters of Serbia [14], the presence of *P. aeruginosa* is not allowed. In contrast, the World Health Organization [15] and the United States Environmental Protection Agency [16] set no criteria for the acceptable level of *P. aeruginosa* in drinking water. *P. aeruginosa* does not pose a risk for gastrointestinal infections in the general human population using drinking water containing this bacteria. However, in vulnerable populations, e.g., patients with large wounds or burns, very young or elderly people, patients with acquired immunodeficiency syndrome (AIDS), or those undergoing immunosuppressive therapy, the presence of these bacteria in drinking or bathing groundwater may pose a health risk and may be associated with various infections of the ear, nose, throat, skin and the eye [15].

4. Conclusions

BARTs have a valuable place in informing water quality recommendations. Due to the established public health risk, caution is warranted in further use of the OB, LK and VV groundwaters. We recommend urgent revitalization of these wells, which will enable the

unhindered use of groundwater resources without negative indications on the service life of the wells and the health and safety of their users.

Acknowledgment

This research was funded by the Ministry of Education, Science and Technological Development of Republic of Serbia (Agreement Nos. 451-03-47/2023-01/200042 and 451-03-47/2023-01/200178).

References

- [1] N. Mansuy., *Water well rehabilitation: A practical guide to understanding well problems and solutions*, USA: CRC Press, (2017).
- [2] K.E. Murray, E.I. Manitou-Alvarez, E.C. Inness, F.G. Healy, A.A. Bodour., *Assessment of oxidative and UV-C treatments for inactivating bacterial biofilms from groundwater wells*, *Frontiers of Environmental Science & Engineering*, 9 (2015), 39-49.
- [3] S.A. Smith., *Biofouling in Water Wells*, In: J.H. Lehr, J. Keeley., (Ed.), *Water Encyclopedia: Ground Water* (pp. 35-38), John Wiley & Sons, Inc., (2005).
- [4] V. Šaraba, V. Dragišić, T. Janakiev, V. Obradović, M. Čopić, B. Knežević, I. Dimkić., *Bacteriome composition analysis of selected mineral water occurrences in Serbia*, *Archives of Biological Sciences*, 74 (2022), 67-79.
- [5] L.C. Simões., *Biofilms in drinking water*, In: M. Simões, F. Mergulhão (Ed.), *Biofilms in Bioengineering* (pp. 157-189), USA, NY: Nova Science Publishers, Inc., (2013).
- [6] J. Liu., *Mechanism of biocorrosion caused by biofilms and its mitigation (Doctoral dissertation)*, USA: Ohio University, (2017).
- [7] W. Dou, D. Xu, T. Gu., *Biocorrosion caused by microbial biofilms is ubiquitous around us*. *Microbial Biotechnology*, 14 (2021), 803-805.
- [8] J. Guo, S. Yuan, W. Jiang, L. Lv, B. Liang, S.O. Pehkonen., *Polymers for combating biocorrosion*. *Frontiers in Materials*, 5 (2018), 10.
- [9] B. Filipović., *Mineralne, termalne i termomineralne vode Srbije*, Belgrade: University of Belgrade, Faculty of Mining and Geology, (2003).
- [10] D. Stojadinović, D. Isaković., *Uticaj klimatskih promena na temperaturni režim mineralne vode Lomničkog kiseljaka kod Kruševca*, In: S. Popović (Ed.), *Water for the 21st century*, Belgrade: Association for Water Technology and Sanitary Engineering (pp. 679-84), (1999).
- [11] I. Đinđić, D. Drašković, S. Špadijer, S. Drobac, T. Vinčić, Lj. Mrkonja., *Analysis of thermo-mineral water regime of „New Obrenovac Spa“ and possibility for the use of thermal water*, In: A. Vranješ (Ed.), *XVI Serbian Symposium on Hydrogeology* (pp. 171-7), Belgrade: University of Belgrade, Faculty of Mining and Geology, (2022).
- [12] D. Stojadinović, G. Rašula., *Sadašnje stanje u pogledu mogućnosti korišćenja mineralne vode Lomničkog kiseljaka kod Kruševca*, In: Z. Stevanović (Ed.), *100 years of hydrogeology in Yugoslavia*, Belgrade: University of Belgrade, Faculty of Mining and Geology (pp. 197-201), (1997).
- [13] Drycon Bioconcepts Inc (DBI), *Biological Activity Reaction Tests – BART™*, (2004). Available at: <http://www.dbi.ca/BARTs/PDFs/Manual.pdf>
- [14] Official Gazette., *Rulebook on quality and other requirements for natural mineral water, natural spring water and table water 53/2005 and 43/2013*, (2005/2013). Available at: <http://www.pravno-informacioni-sistem.rs/SlGlasnikPortal/eli/rep/slscg/ministarstva/pravilnik/2005/53/1/reg>
- [15] World Health Organization (WHO)., *Guidelines for drinking-water quality (4th edition)*, Geneva, Switzerland: World Health Organization, 541 p., (2011).

[16] National Primary Drinking Water Regulations (NPDWR) – Microorganisms, Washington, D.C: United States Environmental Protection Agency. Available at: <https://www.epa.gov/ground-waterand-drinking-water/national-primary-drinking-waterregulations#Microorganisms>.

Bacteria in drinking and bathing mineral waters of Serbia with polymer-degrading potential

Milica Ciric¹, Vladimir Šaraba^{1*}, Clémence Budin², Tjalf de Boer², Jelena Milovanovic¹, Jasmina Nikodinovic-Runic¹

¹University of Belgrade, Institute of Molecular Genetics and Genetic Engineering, Laboratory for Molecular Genetics and Ecology of Microorganisms, Belgrade, Serbia; e-mail: milica.ciric@imgge.bg.ac.rs, vsaraba@imgge.bg.ac.rs, jasmina.nikodinovic@imgge.bg.ac.rs

²Microlife Solutions, Amsterdam, The Netherlands, e-mail: Clemence.Budin@microlifesolutions.nl, Tjalf.deBoer@microlifesolutions.nl

* Corresponding author

DOI: 10.46793/ICCB23.091C

Abstract: Three mineral water occurrences, captured by wells with a depth of 6.5-442.5 m and used for drinking and bathing purposes, were sampled and cultivated under conditions favouring the growth of anaerobic, microaerophilic or CO₂ bacteria, in order to capture predominantly anaerobic portion of the bacteriome, which is dominant in water and soils. Cultivated bacteria were identified by next-generation 16S sequencing and their biotechnological potential in plastics and lignocellulose degradation was explored. Most abundant genera detected in examined samples mainly belong to facultative anaerobes that are common representatives of water and soil environments. In total, 17 genera were detected with a relative abundance over 1% in all three samples, including *Aeromonas*, *Exiguobacterium*, *Comamonas* and *Acinetobacter*. Half of the screened isolates demonstrated growth on at least one plastic or lignocellulosic polymer, with one isolate demonstrating growth on all tested substrates, one demonstrating carboxymethyl cellulose- and one arabinoxylan-degrading ability. Some of the representatives of genera identified with high relative abundance in mineral water samples, such as *Aeromonas*, *Klebsiella*, *Escherichia*, *Salmonella*, *Enterobacter*, *Pseudomonas* and *Staphylococcus*, have been previously documented to have pathogenic potential. Due to the use of investigated mineral waters for drinking and bathing, the health risk from such bacteria in these occurrences needs to be continuously monitored, while, on the other hand, mineral waters deserve special attention in the future from the aspect of screening for biotechnologically relevant enzymes.

Keywords: mineral water, bacteria, 16S rDNA sequencing, Serbia.

1. Introduction

Mineral water usually refers to groundwater with chemical characteristics that differ from water for public water supply. They are characterized by a content of dissolved mineral substances above 1000 mg/L or an increased content of certain specific components (CO₂, H₂S, Br, Rn, J, Rb, etc.), with a pharmacological effect on the human body, or by a higher temperature compared to ordinary low-mineralized waters [1]. There are approximately 230 recorded mineral water occurrences in Serbia, with reserves estimated at around 1000 L/s, positioning Serbia as one of the most promising countries in the region in terms of the richness of this natural resource. Mineral waters are used, to a certain extent, for drinking (as table bottled water) and bathing purposes (as spa water) [2]. Water,

while essential for all forms of life, can also act as a vector for pathogens and chemicals, and thus be associated with diseases. Exposure to pathogens, which are in mineral water most often of allochthonous origin [3], may have serious health consequences [4, 5]. Hydric infections caused by bacterial pathogens and opportunistic pathogens have been documented for drinking and bathing waters [5] and for the latter the risk of colonization by certain pathogens is significantly higher due to inhalation of aerosols or skin colonization than due to the digestive tract colonization [6]. Ecological data, especially the diversity of bacterial communities, are essential for the health risk assessment of mineral waters [7]. In addition, mineral waters can represent untapped reservoir of enzymes with possible biotechnological application [8]. Therefore, three mineral water occurrences in Serbia, captured by wells with depth of 6.5-442.5 m [9, 10] and used for bathing and drinking purposes, were selected for cultivation and identification of bacteria and evaluation of their biotechnological potential.

2. Methods

Mineral water occurrences of Obrenovačka Banja (OB), Velika Vrbnica (VV) and Lomnički Kiseljak (LK) were sampled and cultivated during September 2022. For each occurrence, both direct mineral water samples and pellets were cultivated on 3 different solid media: Luria Agar (LA), Yeast Extract-Malt Extract (ISP-2) and Mannitol-Soy Flour (MSF). Plates were incubated for 72 h in accordance with temperatures of the sampled occurrence using the GasPak™ EZ System to capture the predominantly anaerobic portion of the bacteriome. Full-length 16S rDNA next-generation sequencing was performed on DNA from cultivated OB, LK and VV samples using the MinION platform to assess the diversity of bacteria captured under applied cultivation conditions. Several isolates representative of distinct observed morphologies from OB occurrence, which is unique due to its depth (442.5 m) and temperature (22.8-31.3°C) [9], were screened for growth and/or enzymatic activity in the GasPak™ EZ System using plastic and lignocellulosic polymeric substrates as sole C source to assess their biotechnological potential. The Minimal Salt Medium agar was supplemented with different plastic polymers Impranal® DLN-SD and DL 2077, polycaprolactone diol and bis(2-hydroxyethyl) terephthalate and lignocellulosic polymers carboxymethyl cellulose (CMC), arabinoxylan (AXYL) and lignin for screening.

3. Results

For each cultivated mineral water sample, plate counts were in the range of $2 \times 10^2 - 1 \times 10^3$ CFU/mL and similar morphologies were observed across all three types of cultivation media used and between pellet and whole mineral water samples. In total, 17 genera were detected with a relative abundance over 1% in three cultivated samples. Of these, 13 and 11 genera were detected in VV and LK samples, while only 3 genera were detected in the OB sample (Table 1). Two genera (*Aeromonas* and *Acinetobacter*) are shared among all three samples, while 5 and 4 genera were unique for LK and VV cultivated samples, respectively.

In OB and LK samples, *Aeromonas* was the most abundant genus, while *Exiguobacterium* was detected at the highest relative abundance in the cultivated VV sample. In the OB sample, genera *Acinetobacter* and *Comamonas* were also detected with relative abundance >1%. *Aeromonas*, *Pseudomonas*, *Acinetobacter*, *Stenotrophomonas*, *Escherichia*, *Klebsiella* and *Salmonella* are shared

between LK and VV samples. In addition, in LK sample representatives of genera *Flavobacterium*, *Staphylococcus*, *Pantoea*, *Comamonas*, *Mammaliicoccus* and *Microbacterium* and in VV sample, representatives of genera *Exiguobacterium*, *Enterobacter*, *Proteus* and *Bacillus*, were also detected at relative abundance >1%. Four out of 8 screened isolates demonstrated growth on at least one plastic or lignocellulosic polymeric substrate. All 4 demonstrated growth on SD, 3 on DL and 2 on PCL, CMC and AXYL. One isolate had growth on all tested polymers; one demonstrated CMC- and one AXYL-degrading ability.

Table 1. Bacterial genera detected by 16S rDNA sequencing in cultivated mineral water samples.

Genus	OB	LK	VV
<i>Aeromonas</i>	88.2	52.3	1.7
<i>Pseudomonas</i>	0.0	10.1	3.0
<i>Acinetobacter</i>	6.2	7.6	24.1
<i>Stenotrophomonas</i>	0.0	4.2	3.7
<i>Escherichia</i>	0.4	4.2	13.3
<i>Flavobacterium</i>	0.0	3.7	0.0
<i>Klebsiella</i>	0.5	3.0	8.6
<i>Staphylococcus</i>	0.0	2.2	0.0
<i>Pantoea</i>	0.0	1.8	0.3
<i>Comamonas</i>	3.6	1.7	0.0
<i>Salmonella</i>	0.3	1.4	3.7
<i>Mammaliicoccus</i>	0.0	1.3	0.0
<i>Microbacterium</i>	0.0	1.1	0.1
<i>Bacillus</i>	0.0	0.7	1.3
<i>Exiguobacterium</i>	0.1	0.5	25.7
<i>Enterobacter</i>	0.0	0.4	8.2
<i>Proteus</i>	0.1	0.1	2.0

Genera detected with relative abundance >1% for all samples are included. Lowest Value – red, Percentile (50) – yellow, Highest Value – green. Mineral water samples: OB – Obrenovačka Banja; LK – Lomnički Kiseljak; VV – Velika Vrbnica.

Most abundant genera detected in examined samples mainly belong to facultative anaerobes that are common representatives of water and soil environments. Applied cultivation conditions seemed to favor the growth of facultative anaerobes over obligate anaerobic bacteria. Some representatives of genera identified at the highest relative abundance in three mineral water samples, such as *Aeromonas*, *Klebsiella*, *Escherichia*, *Salmonella*, *Enterobacter*, *Pseudomonas*, *Staphylococcus*, *Acinetobacter*, *Stenotrophomonas*, *Proteus* and *Bacillus* have been previously documented to have pathogenic potential [5]. Some of the detected representatives, such as *Proteus* [11], *Stenotrophomonas* [12], *Pseudomonas* [13], *Aeromonas* [14] and *Microbacterium* [15], have a documented biotechnological potential in degradation of plastic or lignocellulose polymeric materials.

4. Conclusions

Since examined mineral waters are used for bathing and drinking purposes, the health risk from bacteria with pathogenic potential detected in these occurrences needs to be continuously monitored. On the other hand, two of the cultivable isolates demonstrated CMC- and AXYL-degrading ability and, in the future, mineral waters deserve special attention from the aspect of screening for biotechnologically relevant enzymes.

Acknowledgment

This work was supported by the EU H2020 Research and Innovation Programme (grant agreement No. 870292, BioICEP) and by the Ministry of Science, Innovation and Technological Development of the Republic of Serbia (agreement No. 451-03-47/2023-01/ 200042). The 16S rDNA sequence datasets for cultivated groundwater samples are deposited in the NCBI BioProject database (PRJNA977830).

References

- [1] V. Dragišić, V. Živanović., *Opšta hidrogeologija*, Belgrade: University of Belgrade, Faculty of Mining and Geology, (2014).
- [2] Z. Stevanović., *Menadžment podzemnih vodnih resursa*, Belgrade: University of Belgrade, Faculty of Mining and Geology, (2011).
- [3] N. Goldscheider, D. Hunkeler, P. Rossi., *Microbial biocenoses in pristine aquifers and an assessment of investigative methods*, Hydrogeology Journal, 14 (2006), 926-941.
- [4] C. Curutiu, F. Iordache, P. Gurban, V. Lazar, M. C. Chifiriuc., *Main microbiological pollutants of bottled waters and beverages*, In: Bottled and packaged water (pp. 403-422), Woodhead Publishing, (2019).
- [5] J. Stec, U. Kosikowska, M. Mendrycka, D. Stepień-Pyśniak, P. Niedźwiedzka-Rystwej, D. Bębnowska, R. Hryniewicz, J. Ziętara-Wysocka, E. Grywalska., *Opportunistic Pathogens of Recreational Waters with Emphasis on Antimicrobial Resistance—A Possible Subject of Human Health Concern*, International Journal of Environmental Research and Public Health, 19 (2022).
- [6] K. D. Mena, C. P. Gerba, *Risk assessment of Pseudomonas aeruginosa in water*, Reviews of environmental contamination and toxicology, 201 (2009), 71-115.
- [7] H. Leclerc, A. Moreau., *Microbiological safety of natural mineral water*, FEMS Microbiology Reviews, 2(2002), 207-222.
- [8] M. T. Madigan, J. M. Martinko, D. A. Stahl, D. P. Clark., *Brock biology of microorganisms* (13th edition), San Francisco: Pearson Benjamin-Cummings, (2010).
- [9] I. Đinđić, D. Drašković, S. Špadijer, S. Drobac, T. Vinčić, Lj. Mrkonja., *Analysis of thermo-mineral water regime of „New Obrenovac Spa“ and possibility for the use of thermal water*, In: A. Vranješ (Ed.), XVI Serbian Symposium on Hydrogeology (pp. 171-7), Belgrade: University of Belgrade, Faculty of Mining and Geology, (2022).
- [10] D. Stojadinović, D. Isaković., *Uticaj klimatskih promena na temperaturni režim mineralne vode Lomničkog kiseljaka kod Kruševca*, In: S. Popović (Ed.), Water for the 21st century, Belgrade: Association for Water Technology and Sanitary Engineering (pp. 679-84), (1999).
- [11] B. O. Ojiego, O. P. Ilo, F. Dantanko, S. A. Abdullahi, I. M. K. Gadzama, P. Bolorunduro, E. Ella, G. I. Ogu, *Biodegradation of plastic materials obtained from solid waste dumpsites in Nigeria, using native bacterial strains*, Novel Research in Microbiology Journal, 6(2022), 1713-1724.
- [12] S. Dey, U. Anand, V. Kumar, S. Kumar, M. Ghorai, A. Ghosh, N. Kant, S. Suresh, S. Bhattacharya, E. Bontempi, S. A. Bhat, A. Dey., *Microbial strategies for degradation of microplastics generated from COVID-19 healthcare waste*, Environmental Research, 216 (2023).

[13] G. Badahit, *Screening of plastic degrading Pseudomonas spp. from soil* (Doctoral dissertation), Kathmandu, Nepal: Tribhuvan University, Department of Microbiology, (2018).

[14] O. E. Urgessa, Y. A. Sima, M. M. Adem, A. K. Ayele, Isolation of cellulose degrading bacteria from rumen and evaluation of cellulase production by the isolate using lignocellulosic substrate, *Ethiopian Journal of Science and Sustainable Development*, 7(2020), 8-17.

[15] V. Ventorino, A. Aliberti, V. Faraco, A. Robertiello, S. Giacobbe, D. Ercolini, A. Amore, M. Fagnano, O. Pepe., *Exploring the microbiota dynamics related to vegetable biomasses degradation and study of lignocellulose-degrading bacteria for industrial biotechnological application*, *Scientific Reports*, 5 (2015).

Modeling and simulation of a polymer optical fiber humidity sensor for the skin microenvironment

Milan S. Kovačević^{1*}, Marko M. Milošević¹, Ljubica Kuzmanović¹, Daniele Tosi²,
Alexandar Djordjevich³

¹ University of Kragujevac, Faculty of Science, Department of Physics, Kragujevac, Serbia,
kovac@kg.ac.rs, marko.milosevic@pmf.kg.ac.rs, ljubica.kuzmanovic@pmf.kg.ac.rs

² Nazarbayev University, School of Engineering, Astana, Kazakhstan, daniele.tosi@nu.edu.kz

³ City University of Hong Kong, Department of Mechanical Engineering, 83 Tat Chee Avenue,
Hong Kong, China, mealex@cityu.edu.hk

DOI: 10.46793/ICCB23.096K

Abstract: A polymer optical fiber (POF) humidity sensor to monitor the humidity of a skin microenvironment of wounds without removing the wound dressing is modelled by ray tracing based on Monte Carlo simulation. To produce the sensor, a sensitive zone is made by removing the cladding from a segment of POF and mesoporous SiO₂ nanoparticles are deposited layer-by-layer. In this paper, there is a report that applied the ray tracing model to simulate POF humidity sensor characteristics and compared the experimental results that have been reported earlier. This sensor which is based on plastic optical fiber was easily fabricated and could be used for real-time humidity monitoring of wound status.

Keywords: polymer optical fiber, humidity sensor, ray tracing, relative humidity

1. Introduction

Control of humidity in many fields, such as industry, medical facilities, farming and the home environment, is becoming very important. Therefore, the development of a low-cost humidity sensor with fast response is very much required. An overview of fiber-optic-based methods for humidity sensing is given in [1]. Compared to their glass counterparts, they are less costly and easier to handle. POF humidity sensor (POFHS) has been proposed [2]. The various accurate methods of multimode fibers modal analysis are exploited. For example, the method that relies on solving power flow equations was described in [3–6]. In this paper, there is a report that applied the ray tracing model to simulate POF humidity sensor characteristics and compared the experimental result that has been reported in [2].

2. The structure of POF humidity sensor – an overview

Commercial fiber ESKA SK-10 (by Mitsubishi Rayon Co., Ltd.) was used to build the sensor. This multimode (step index) polymer fiber has the polymethyl-methacrylate

resin core with the diameter of 240 μm . Its index of refraction is 1.49 and numerical aperture is 0.5. Its core is cladded in a 5 μm fluorinated polymer. The optical fiber of the humidity sensor is specially sensitized by precision machining into the cladding of a selected fiber segment. This removed the cladding and a portion of the fiber core along a selected fiber segment as illustrated in Fig. 1.

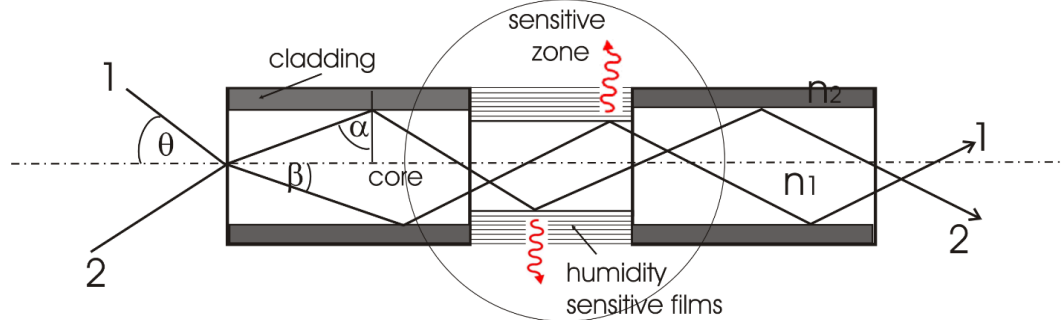


Figure 1. POFHS structure and the light propagation along the sensitive zone of the POF.

Once the cladding and a part of the core are removed, a film sensitive to humidity is deposited using the LbL method. It consists of SiO_2 mesoporous nanoparticles (SNOWTEX 20L, 40–50 nm diameter, Nissan Chemical, Japan). They were deposited with poly(allylamine hydrochloride) (PAH) to form a PAH/ SiO_2 hydrophilic material. This combination provided a higher sensitivity to humidity [7]. The deposition of the PAH/ SiO_2 layers was in three stages [8]. The resulting cut-out of POF cladding/core introduced light transmission loss that is related to relative humidity.

3. Modeling by three-dimensional ray tracing

Using Monte Carlo (MC) simulation, the basic idea is to trace rays propagating along the fiber that has the sensitised zone. Using MC more than 10^6 random directions for many input rays were generated. Each such launch is traced as it propagates along the POF until either contributing to a radiation loss or reaching the output fiber end. Rays radiated through the sensitive zone represent a modulation loss induced by the sensor – for the particular level of relative humidity taken as a reference. At different humidity, the ratio of this light loss to that in the sensitive zone at the reference humidity level is then calculated (under equal other conditions). The magnitude of this relative loss characterises the device sensitivity for the particular set of the sensitive zone's features, chiefly the zone length, depth and the number/type of deposited layers. Because it would be difficult to optimise these multiple sensor-features experimentally, a computer optimisation is performed by ray tracing. Further ray trajectories with distance from the input fiber-end are traced by the method described previously [9, 10].

3. Results

The important part of the simulation is to trace rays as they propagate along the sensitized zone of the multimode POF (ESKA SK-10 multimode POF, Mitsubishi Rayon

Co. Ltd. with the core diameter of 240 μm , 1.49 core refractive index and 5 μm thick fluorinated polymer cladding; NA = 0.5). A 125 mW point source was situated at a distance of 100 μm from the input fiber end. The axial location at the start of the zone is specified as an input parameter $z = z_1$ along the fiber axis. The zone is rough, and the depth of the zone is fixed. The sensing region's lengths of 5, 10, 20 and 30 mm were modelled for the core diameter reduced to 190 μm . The condition for total reflection was examined for each ray at every reflection. The program recorded the outcomes. If a ray reached the sensitized zone, its transmission loss was also recorded. To compare the interaction of the evanescent wave with different lengths of the sensitive zone, the transmittance at the wavelength of 611 nm was calculated as a function of the length of the unclad section of the POF. The transmittance is simply calculated as the ratio $(P_{\text{out}}/P_{\text{in}}) \times 100\%$ where P_{out} is the total optical power at the end face of the fiber, and P_{in} is the total initial power at the fiber origin.

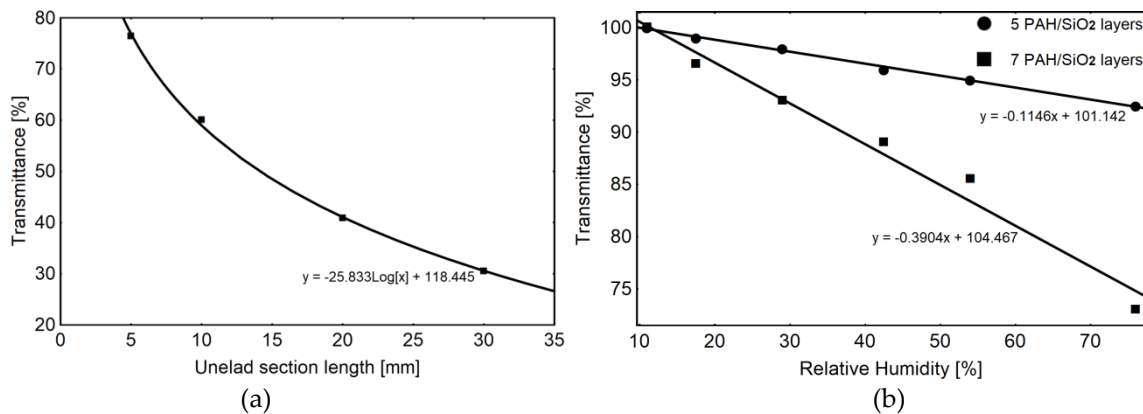


Figure 2. (a) Transmittance vs. the length of the unclad section of the, (b) Transmittance vs. relative humidity. The curves of a POFHS coated with five and seven PAH/SiO₂ layers.

Figure 2(a) shows transmittance as a function of the number of PAH/SiO₂ layers deposited. The hydrophilic mesoporous films are deposited layer by layer on the unclad central region of the POF. The light intensity change in the interaction of the evanescent wave with the hydrophilic film is calculated as well. Figure 2(b) shows the calculations with POFHS coated with five and seven PAH/SiO₂ layers. Calculations are for the wavelength of 611 nm for both sensors (190 μm core diameter and 30 mm length of the sensitive region).

3. Conclusions

Plastic fibers' use as sensors often requires not much more than basic (inexpensive) devices such as light emitting and photodiodes. In this paper, a three-dimensional analysis of light propagation through the optical fiber humidity sensor is reported. The sensor characteristics are simulated in order to analyze and compare the experimental results. All major cases that may appear when light interacts with the device's sensitive zone have been considered. This simulation includes different lengths of the sensitive

zone of the POF. In the computer experiment, the penetration depth of the evanescent wave and its interaction with the hydrophilic film is related to the light loss that reaches the sensitized region. The refractive index of PAH/SiO₂ layers was altered, and the fiber transmittance was calculated as a function of relative humidity. These results are in good agreement with previous experimental results [2]. This new approach for humidity sensing is potentially extremely helpful for providing improved monitoring of wound status. If successful it will be of increased benefit for patients and offers the potential to allow a better understanding about the process of wound healing itself.

Acknowledgment

This research is funded by the Ministry of Education and Ministry of Science, Technological Development and Innovation, Republic of Serbia, Agreement: No. 451-03-47/2023-01/ 200122.

References

- [1] T. L. Yeo, T. Sun, K. T. V. Grattan., *Fibre-optic sensor technologies for humidity and moisture measurement*, *Sensors and Actuators A*, 144 (2008) 280–295.
- [2] D. Gomez, S. P. Morgan, B. R. Hayes-Gill, R. G. Correia, S. Korposh., *Polymeric optical fibre sensor coated by SiO₂ nanoparticles for humidity sensing in the skin microenvironment*, *Sensors and Actuators B*, 254 (2018) 887–895.
- [3] B. Drljaca, S. Savovic, A. Djordjevich, *Calculation of the frequency response and bandwidth in step-index plastic optical fibres using the time-dependent power flow equation*, *Physics Scripta T149* (2012) 014028.
- [4] S. Savovic, A. Djordjevich, A. Simovic, B. Drljaca, *Influence of mode coupling on three, four and five spatially multiplexed channels in multimode step-index plastic optical fibers*, *Optics and Laser Technology* 106 (2018) 18–21.
- [5] S. Savovic, B. Drljaca, A. Djordjevich, *Influence of launch-beam distribution on bandwidth in step-index plastic optical fibers*, *Applied Optics* 52 (6) (2013) 1117–1121.
- [6] J. Mateo, M. A. Losada, J. Zubia, *Frequency response in step index plastic optical fibers obtained from the generalized power flow equation*, *Optics Express* 17(4) (2009) 2850–2860.
- [7] D. Viegas, J. Goicoechea, J. L. Santos, F.M. Araujo, L. A. Ferreira, F. J. Arregui, I. R. Matias., *Sensitivity improvement of a humidity sensor based on silica nanospheres on a long-period fiber grating*, *Sensors*, 9 (2009) 519–527.
- [8] S. Korposh, S. James, R. Tatam, L. Seung-Woo., *Fibre-optic chemical sensor approaches based on nano assembled thin films: a challenge to future sensor technology*, *Curr. Dev. Opt. Fiber Technol.*, (2013) 237–264.
- [9] M. S. Kovacevic, D. Nikezic, A. Djordjevich., *Modeling of the loss and mode coupling due to an irregular core-cladding interface in step-index plastic optical fibers*, *Applied Optics*, 44 (2005) 3898–3903.
- [10] M. Kovačević, D. Nikezić, A. Djordjevich., *Monte Carlo simulation of curvature gauges by ray tracing*, *Meas. Sci. Technol.*, 15 (2004) 1756–1761.

Comparison of organic substance content in peloids from Sutomore and Igalo (Montenegro)

Miljan Bigović^{1*}, Marija Kaluđerović², Jovana Jovanović³, Dijana Đurović⁴, Željko Jaćimović⁵

¹ University of Montenegro, Faculty of Natural Sciences and Mathematics, G. Washington Street bb, 81 000 Podgorica, Montenegro.; e-mail: miljan@ucg.ac.me

² University of Montenegro, Faculty of Natural Sciences and Mathematics, G. Washington Street bb, 81 000 Podgorica, Montenegro. e-mail: marijakaludjerovic.9@gmail.com

³ University of Montenegro, Faculty of Medicine, Krusevac bb, 81 000 Podgorica, Montenegro, e-mail: jokicajoka1212@gmail.com

⁴ Institute for Public Health of Montenegro, Ljubljanska bb, 81000, Podgorica, Montenegro, e-mail: dijana.djurovic@ijzcg.me

⁵ University of Montenegro, Faculty for Technology and Metallurgy, G. Washington Street bb, 81 000 Podgorica, Montenegro, e-mail: zeljkoj@ucg.ac.me

* *Corresponding author*

DOI: 10.46793/ICCB23.100B

Abstract: The presence of organic substances in soil or peloid and their concentration are very important parameters of the features and qualities of peloid. The peloid from Sutomore turned out to be particularly interesting because so far no similar research has been done with it, nor has it been used on a larger scale for the treatment of patients compared to the other two peloids from Montenegro – from Igalo and Ulcinj. As it is known that the medicinal composition of peloid is influenced by the content of organic components in it, we determined the total organic matter content in two peloids – from Sutomore and Igalo. Based on the determination of the total organic substance, it is possible to determine the content of the total organic carbon, which we also did and concluded that both peloids according to the content of organic substances are classified as peloids with a high content of organic matter.

Keywords: peloid, organic carbon, organic substances

1. Introduction

Peloids or thermal muds are hydrothermal inorganic gels with optimal rheological and thermal properties, produced by process of mixing of clay minerals and mineral-medicinal waters. It has been used for recovering muscle–bone–skin pathologies and now such old practice has received applications also for wellness and relaxation purposes [1]. Their structure is complex and with changeable matrixes, so their chemical compositions depend on different factors (mineralogical composition of clay (geomaterials), organic matter, type of water, and micro-organisms involved in the

maturation process) [2]. The final characteristics of peloids depend on a) the chemical and mineral composition; b) the properties of water that participates in the processes of maturation and formation of peloids; c) the maturation process which is conditioned by numerous microbiological activities and the presence of organic matter. Peloid or thermal mud is one of the examples of natural products that contain significant amounts of organic compounds with exceptional biological activity, so they have found application in the treatment of a large number of diseases. Such natural products are also precursors for drug synthesis and in the treatment of various pathologies. More recently, these thermal muds have found an increasing use in relaxation therapies in health spas [3].

Depending on the overall chemical composition, natural peloids are divided into three categories: essentially inorganic, essentially organic, and mixed inorganic/organic peloids [4]. Based on the content of organic matter, peloids can be classified into two groups: with high mineral composition and low organic matter (1-5%), and with higher content of the organic matter [3,5].

2. Material and Methods

Sutomore peloid is formed at the point of contact of salty sea water with clayey rocks in the coastal area of the Strbina bay while the peloid from Igalo is formed at the mouth of the river Suturina into the bay as shown in Figure 1.



Figure 1. The location from which peloid from Sutomore (a) and Igalo (b) is exploited.

Samples for analysis were collected at the locations where they originate and three samples were taken, and then compost was made - they were mixed. The samples were collected in February 2020. The temperature was measured in situ, while the pH-values, conductivity of each sample and density were measured in a laboratory (the sample is immediately closed in polypropylene tubes after collecting to prevent losses of potentially volatile components, water and possible pollution). The determination of these two parameters is important because it is a clear indicator of the content of organic compounds in soil samples, soil or, as in our case, peloids. In our research, we determined the content of total organic matter (TOM) based on two different methods [6].

Method 1: The basic principle of this method is based on the combustion of organic materials at high temperatures. It is known that most organic compounds decompose at temperatures higher than 400 °C and that carbon dioxide and water vapor are produced as products of this decomposition. First, we lyophilized a certain amount of raw peloid and then heated a certain amount to 800 °C for one hour. After cooling the samples in a desiccator for half an hour, we measured the mass. The measurements were made on three samples.

Method 2: This method is based on the measurement of the difference in the content of inorganic carbon (carbonates, bicarbonates) and organic carbon, included in the composition of organic matter in the sample [7]. Organic matter is oxidized with 10% hydrogen peroxide (H₂O₂) while heating to a gentle boil. Namely, a hydrogen peroxide solution (1:3, v/v) was added to the measured mass of the peloid sample (around 1.0 g) until the moment when bubbles cease to emerge after the next addition of this solution. After that, the resulting mixture was heated to 60 °C for two hours. After cooling, the resulting mixture is allowed to settle into a solid phase, after which it is separated by decantation. The solid phase is transferred to porcelain salt and heated in dryer at 110 °C until complete evaporation of water and constant mass.

Based on the obtained experimental values for the content of total organic carbon, the amount total organic carbon obtained computationally (TOC) is calculated using the following equation:

$$\text{TOC} = \text{TOM}/1.72$$

3. Results and discussion

The results of measuring of total organic matter (TOM) and computational determination of total organic carbon (TOC) for samples of both peloids are shown in Table 1.

Table 1. TOM and TOC determination results for peloids from Sutomore and Igalo.

		Sutomore	Igalo
Total organic matter (TOM) experimentally obtained	<i>Method 1</i>	14.36%	8.81%
	<i>Method 2</i>	15.01%	8.70%
Total organic carbon (TOC) obtained computationally	<i>Method 1</i>	8.35%	5.12%
	<i>Method 2</i>	8.72%	5.05%

Both Montenegrin peloids contain large amounts of organic matter and therefore belong to second group of peloids, according to the classification based on the content of organic matter [3,5]. With a content from about 15% of total organic matter, peloid from Sutomore is very rich in the content of organic matter, almost twice as much compared to the peloid from Igalo, which also has a high content of organic matter in its composition.

4. Conclusions

The content of organic matter in the peloid is very important for its application for medical purposes. From organic matter, more fatty acids, carbohydrates and proteins dominate. The total content of organic matter can be determined experimentally, which is what we did in our research. We concluded that the investigated peloids from the Montenegrin coast are rich in organic matter content.

References

- [1] F. Veniale, A. Better, P. Jobstraibiyer, M. Setti, *Thermal muds: perspectives of innovations*, Applied Clay Science, 36, (2007) 141-147.
- [2] M. Centini, M. R. Tredici, N. Biondi, A. Buonocore, R. M. Facino, C. Anselmi, *Thermal mud maturation: organic matter and biological activity*, International Journal of Cosmetic Science, 37 (2015) 339-347.
- [3] M. Suárez, P. González, R. Domínguez, A. Bravo, C. Melian, M. Pérez, I. Herrera, D. Blanco, R. Hernández, J. R. Fagundo, *Identification of organic compounds in San Diego de los Baños Peloid (Pinar del Río, Cuba)*, Journal of Alternative and Complementary Medicine, 17 (2011), 155-165.
- [4] C. Gomes, M. I. Carretero, M. Pozo, F. Maravera, P. Cantista, F. Armijo, J. L. Legido, F. Teixeira, M. Rautereau, R. Delgado, *Peloids and pelotherapy: Historical evolution, classification and glossary*, Applied Clay Science 75-76 (2013) 28-38.
- [5] M. Bigovic, S. Pantovic, I. Milasevic, Lj. Ivanovic, D. Djurovic, V. Slavic, M. Popovic. M. Vrvic, M. Roganovic, *Organic composition og Igalo bay peloid (Montenegro)*, Indian Journal of Traditional Knowledge, 18 (2019) 837-848.
- [6] B. Schumaster, *Methods for the determination of total organic carbon (TOC) in solis and sedminets*, US. Envinronmental Protection Agency, Las Vegas, Unites States, 2002, 1-23.
- [7] D. Florescu, A. M. Iordache, D. Costinel, E. Horj, R. E. Ionete, M. Culea, *Validation procedure for assessing the total organic carbon in water samples*, Romanian Journal of Physics, 58 (2013) 211-219.

DRIFT spectroscopy and permutation importance algorithm in quantitative analysis of organic matter in soil model systems

Branislav D. Jović^{1*}, Marko N. Panić²

¹ University of Novi Sad, Faculty of Sciences, Department of Chemistry Biochemistry and Environmental protection, Novi Sad, Serbia; e-mail: branislav.jovic@dh.uns.ac.rs

² University of Novi Sad, Biosense Institute, Novi Sad, Serbia; e-mail: panic@biosense.com

* Corresponding author

DOI: 10.46793/ICCB23.104J

Abstract In order to obtain useful MIR spectrochemical data of soil organic matter for the development of remote sensing methods, synthetically prepared soils with artificial precisely defined organic matter fractions, DRIFT spectroscopy and permutation importance algorithm were used in this paper. In terms of imitation of soil organic matter, sample model systems were prepared with precisely defined added values of added organic components. After MSC and SNV spectral treatments using PCA and LDA techniques and DRIFT spectra, the soil was classified according to the percentage of organic matter. Using the KDE+permutation importance algorithm, three significant MIR spectral regions were obtained for percentage grouping: 600-1000cm⁻¹ (skeletal vibrations of organic matter); 1750-2250cm⁻¹ (Total reflectance+quartz overtones) and 3250-3950cm⁻¹ (Hydroxyl groups). In terms of the potential for quantitative analysis, the calculated wavelength ranges match well with the classical spectrochemical theoretical basis of analytical methodologies. Also, extracted useful spectrochemical data can be potentially used in the development of new remote-satellite detection methods (ASTER satellite in SWIR and MIR range).

Keywords: FTIR spectroscopy, Soil organic matter, PCA, Feature permutation algorithm

1. Introduction

In recent times, the need for analysis of soil organic matter for many samples at a field scale has emerged, especially for the purpose of precision agriculture implementation. Soil organic matter has great implications on all physical and plenty of chemical soil properties and thus characterizes fertility and other potentials of this valuable natural resource. Standard laboratory analysis of soil organic matter is complex, expensive and time-consuming compared to possible indirect measurement by reflectance spectroscopy. Diffuse Reflectance Infrared Fourier Transform *Spectroscopy* (DRIFTS) is a method widely used in different fields of soil studies. Examination of structural differences of humic acids [1], and vertical distribution of coal [2] are just some of the many beneficial uses of the DRIFT method. In this research, the aim was to explore the possibilities of using DRIFT spectroscopy in the determination of organic

matter. In this sense, model systems were created by adding a precisely defined amount of organic matter to the soil samples. About six hundred DRIFT spectra were recorded and subjected to multivariate analysis methods (LDA, Feature permutation algorithm) and useful information was extracted for the development of further remote sensing methods. This paper is a part of our continuing and systematic investigation of the application of spectroscopic-chemometric methods in soil analysis [3,4].

2. Experimental

To imitate soil organic matter, a mixture of humic acid, starch and nicotinamide was used. These model systems were prepared due to the presence of characteristic functional groups of organic molecules (aliphatic, aromatic, Hydroxyl, nitrogenous...). To examine and influence the soil type and obtain a robust model mixture of the most common soil types from northern Serbia was used. A total of 5 grams of soil with a percentage of organic matter of 0.5 to 4% was prepared for each sample of the system model. Infrared spectra were obtained using the Thermo-Nicolet Nexus iS20 instrument on the diffuse reflectance module. The spectral range was 4000-400 cm^{-1} , a total of 32 scans per spectrum were recorded at a resolution of 4 cm^{-1} . Savitzky-Golay digital filter, multiplicative scatter correction (MSC) and standard normal variate (SNV) techniques are utilized for the removal of (physical) variability among the data samples due to scatter caused by variations in sample positioning, irregularities in its surface and differences in particle size.

3. Results and discussion

3.1. Classification of samples based on the concentration of organic matter

Linear dimensionality reduction technique LDA achieve moderately good separation in latent space among four groups with different concentration of organic matter denoted as G05, G1, G2 and G4. MSC preprocessing yields significantly better classification model performance than SNV treatment. ROC stands for receiver operating characteristic presented with a curve, defined by true positive rate (TPR) against the false positive rate (FPR), and serves as a visual diagnostic tool for the evaluation of the binary classifier.

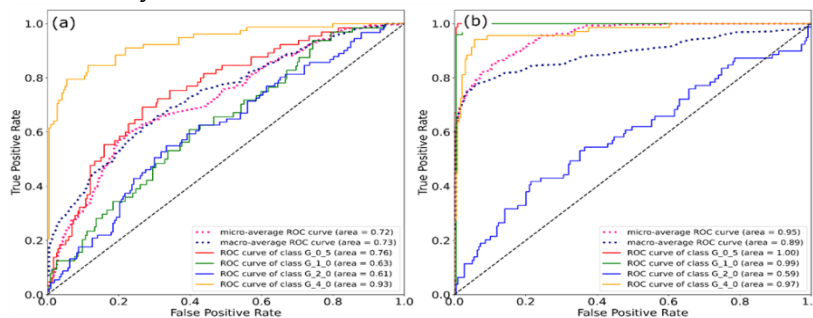


Figure 1. ROC curves of binary models for classification of samples into four groups preprocessed with (a) SNV and (b) MSC correction techniques.

One-vs-all strategy for fitting the model for the classification of fractions is used during the training procedure and the LDA with one component is selected as the model to be fitted using 50% of data within the dataset. These results in trained for binary classifiers (models) whose ROC curves are estimated from predictions on the test set, are presented in Figure 1.

3.2. Analysis of feature importance for classification

The permutation importance algorithm is applied to the created dataset using trained binary models to evaluate which wavelengths (features) or part of the spectrum has influenced the most model performances.

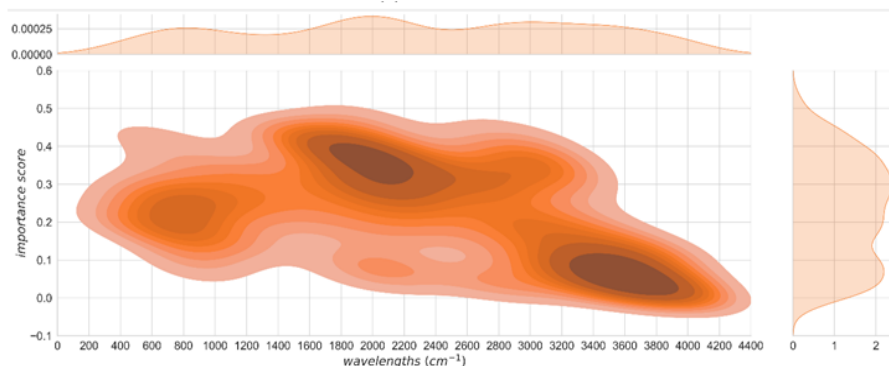


Figure 2 Estimated bivariate probability density functions (pdfs) of an importance score and wavelength from a list of scores and selected wavelengths obtained from a permutation importance algorithm runs.

Starting with the condensed distance matrix, obtained from Spearman rank-order correlations a Ward's linkage matrix is calculated, and a hierarchical clustering is performed on the predefined train dataset for creation of models for the classification of percent of organic matter. Visualizing the dendrogram of obtained clusters the following range of values are selected for the threshold of [0.1, 5.0] for the percent dedicated train dataset used for building corresponding models for classification. Importance scores show how much trained binary model performance decreased in accuracy with a random shuffling of features. Presenting the importance scores for the representative wavelengths together with their frequency of occurrences in the form of a pdf, give more insight into important part of the spectrum for classification than that only importance scores are used. Models for classification of samples according to percent of organic matter divide the wavelength-score region into three regions: (600 - 1000, 0.18 - 0.26), (1750 - 2250, 0.30 - 0.41) and (3250 - 3950, 0.01 - 0.11). In the research of Demate et al, [5] after high correlations of extracted spectral MIR regions and ASTER simulated spectral bands were determined. Namely, in this research the following potential spectral regions for future satellite sensors were suggested: 2760 – 2500 cm^{-1} , 2150–1875 cm^{-1} and 840 – 740 cm^{-1} . In our research, using a completely different approach in laboratory conditions, very similar data were obtained. We believe that the obtained wavelength

ranges lead to the convergence of useful data necessary for the calibration of existing and the development of new sensors and remote sensing methods.

4. Conclusions

Obtained wavelength ranges indicate the importance of the aliphatic (CH_x) and aromatic (C=C) vibration MIR region as well as the soil color (total reflectance related to the mineral content, quartz) for the potential quantification of soil organic matter. In terms of the potential for quantitative analysis, the calculated wavelength ranges match well with the classical spectrochemical theoretical basis of analytical methodologies. Obtained MIR wavelength ranges can be potentially used in the development of satellite detection methods (ASTER satellite).

Acknowledgment

This work was supported by the Provincial Secretariat for Science and Technological Development, Autonomous Province of Vojvodina, project no. 142-451-2198/2022-01.

References

- [1] Francioso O., Montecchio D., Gioacchini P., Cavani L., Ciavatta C., Trubetskoj O., Trubetskaya O., 2009. *Structural differences of Chernozem soil humic acids SEC-PAGE fractions revealed by thermal (TG-DTA) and spectroscopic (DRIFT) analyses*, *Geoderma*, 152; 264-268
- [2] Hobley E., Willgoose G.R., Frisia S., Jacobsen G., 2014. *Vertical distribution of charcoal in a sandy soil: evidence from DRIFT spectra and field emission scanning electron microscopy*, *European Journal of Soil Science*, 65; 751-762
- [3] Jović, B., Ćirić, V., Kovačević, M., Šeremešić, S., et al. *Empirical equation for preliminary assessment of soil texture*. *Spectrochim. Acta A Mol. Biomol. Spectrosc.* 2019. 206: 506-511.
- [4] Jović, B., Maletić, S., Kordić, B., Beljin, J. *DRIFT spectroscopic determination of clay and organic matter in sediment by mixed soil-sediment calibration approach*, *Environmental Monitoring and Assessment*. Volume 195, 3 2023
- [5] N. E. Q. Silvero, L. A. Di Loreto Di Raimo, G. Silva Pereira, L. P. de Magalhães, F. da Silva Terra, M. A. Ananias Dassan, D. F. Urbina Salazar, José A.M. Demattê, *Effects of water, organic matter, and iron forms in mid-IR spectra of soils: Assessments from laboratory to satellite-simulated data* *Geoderma*. 2020. 375:114480

The influence of pyrocatechol added in pre-oscillatory period on the dynamics of the Bray-Liebhafsky reaction

Jelena Maksimović¹, Kristina Stevanović^{2,*}, Marina Simović-Pavlović³, Maja Pagnacco⁴

¹ University of Belgrade, Faculty for Physical Chemistry, Studentski trg 12-14, 11158 Belgrade, Serbia; e-mail: jelena.maksimovic@ffh.bg.ac.rs

² University of Belgrade, Institute of Nuclear Sciences Vinča, Department for Bioinformatics and Computational Chemistry, Mike Petrovića Alasa 12-14, 11351 Vinča, Belgrade, Serbia; e-mail: kristina.stevanovic@vin.bg.ac.rs

³ University of Belgrade, Faculty of Mechanical Engineering, Kraljice Marije 12-16, 11120 Belgrade, Serbia; e-mail: simovicmarina99@gmail.com

⁴ University of Belgrade, Institute of Chemistry, Technology and Metallurgy, Center of Catalysis and Chemical Engineering, Njegoseva 12 11000 Belgrade, Serbia; e-mail: maja.pagnacco@ihtm.bg.ac.rs

* *Corresponding author*

DOI: 10.46793/ICCB23.108M

Abstract: In the past two decades, chemical oscillators have emerged as a popular tool for the determination of “reactive” analytes due to their great sensitivity toward any kind of external perturbations. They have found application in many fields of applied science enabling relatively easy quantitative and qualitative analyses. In this study influence of pyrocatechol, an important precursor in many organic syntheses, on the pre-oscillatory period of the Bray-Liebhafsky (BL) reaction was examined. The BL reaction was followed by the potentiometric method. In a series of experiments (in a concentration range from 1.5×10^{-5} M to 3×10^{-5} M), pyrocatechol was added 45 minutes after the start of the reaction, causing an immediate appearance of oscillations. For these experimental conditions, the period between the first and second oscillation increases linearly with the added pyrocatechol concentration. The obtained results can be useful for analytical purposes and accordingly, potential determination of unknown pyrocatechol concentration..

Keywords: Bray-Liebhafsky reaction, oscillatory reaction, pyrocatechol, electrochemical measurements, environmental protection

1. Introduction

A chemical system containing only three reactants: hydrogen peroxide, iodate, and sulfuric acid may at first seem very simple, but still the Bray - Liebhavski (BL) reaction is one of the most studied phenomena of nonlinear dynamics [1, 2]. It is an oscillatory reaction, which means that intermediate concentrations oscillate in time, while concentrations of reactants and products change cascadingly. BL represents the catalytic

(in the presence of hydrogen and iodate ions) decomposition of hydrogen peroxide into water and oxygen [1]:



However, the very complex mechanism of this chemical reaction abounds in plenty of intermediates, many of which are short-lived and highly reactive [3]. The dynamics of such a system is very specific and, depending on the initial conditions, different dynamic states can be obtained. External perturbators can significantly affect the course of the reaction and their effects can be used to investigate the reaction mechanism, but also in analytical purposes where different (“reactive”) analytes are added. Here we investigated the influence of pyrocatechol, a typical phenolic compound that is an important precursor for manufacturing pesticides, flavors, fragrances, and paints. High levels of pyrocatechol in wastewater can be a serious health issue due to its reactivity and toxicity [4]. Pyrocatechol has been already tested in the BL oscillatory system [5, 6], but this is the first time that it has been added in the pre-oscillatory period of the reaction. This can give additional insights into its mechanism of action which can be of particular interest for environmental chemistry.

2. Experimental section

In this study, BL experiments were performed in a well-stirred ($\sigma = 900$ rpm) batch reactor and thermostated at (60.0 ± 0.2) °C. The total reaction volume was 55 ml and the initial concentrations of reactants were: $[\text{KIO}_3]_0 = 7.35 \times 10^{-2}$ M, $[\text{H}_2\text{SO}_4]_0 = 4.79 \times 10^{-2}$ M, $[\text{H}_2\text{O}_2]_0 = 7 \times 10^{-3}$ M. All used chemicals were pro analysis grade, and their solutions were prepared with deionized water (18 M Ω cm). The moment when H_2O_2 was added to the vessel was taken as the beginning of the reaction. Different concentrations of the pyrocatechol were added (100 μl aliquot) into the reaction 45 minutes after the reaction started (see Figure 1.). The reaction was followed by the potentiometric method. The working iodide ion-selective electrode was connected to a double-junction Ag/AgCl reference electrode and potential-time evolution of the BL reaction was followed in time.

3. Results and Discussion

The potential-time curve for the BL reaction without pyrocatechol addition for these experimental conditions is reported in our previous work [5,6]. Here it is important to emphasize that reaction is preceded by the induction period $\tau_{\text{ind}} = 55$ min, after which six regular oscillations take place. As it can be seen on Figure 1 the pyrocatechol addition in the pre-oscillatory period (45 min after the reaction beginning) caused an instantaneous oscillation thereby shortening the induction period of the reaction. We measured the time between the first and the second oscillation (denoted as τ_{1-2}) and compared it to the value reported previously for the system without pyrocatechol [5, 6]. For the concentration range from 1.5×10^{-5} M to 3×10^{-5} M parameter τ_{1-2} showed linear dependence on pyrocatechol concentration (Figure 2), with the regression equation:

$$\tau_{1-2} = 1.04 \times 10^6 \times C_{\text{Pyrocatechol}} + 32.5 \quad (2)$$

where C is the concentration of pyrocatechol in BL system in M.

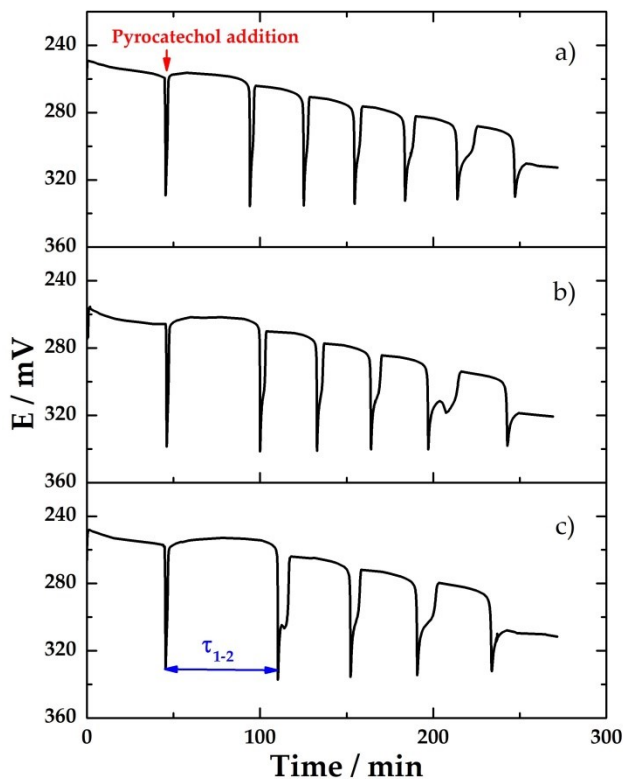


Figure 1. Oscillograms of the BL reaction with different concentrations of pyrocatechol, added 45 minutes after the beginning of the reaction: 3.0×10^{-5} M (a), 9.0×10^{-5} M (b) and 1.2×10^{-4} M (c).

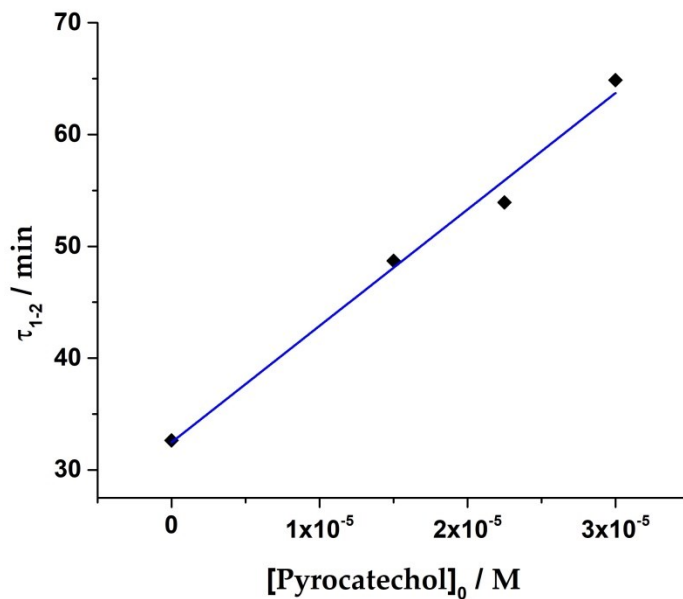


Figure 2. The period between the first and the second oscillations dependence on pyrocatechol concentrations.

Compared to our previous results (where the pyrocatechol was added in and after the oscillatory regime), the slope of the obtained regression equation is slightly lower indicating lower sensitivity of measurement [5,6]. Although different parameters were measured, the experimental conditions and composition of the BL matrix are the same, allowing comparison. Nevertheless, in the specified concentration range, pyrocatechol concentrations can be determined with satisfactory accuracy in the manner presented here.

4. Conclusions

The influence of the pyrocatechol addition in the pre-oscillatory period on the dynamics of the Bray-Liebhaftsky (BL) reaction was investigated. Obtained potential-time curves show that pyrocatechol provokes an oscillatory regime immediately. The period between the first and second oscillation, τ_{1-2} , was chosen as a parameter for comparing the results. In the examined concentration range (1.5×10^{-5} M - 3×10^{-5} M) τ_{1-2} linearly increases with the pyrocatechol concentration. This linear dependence can be very useful in future analytical determinations.

Acknowledgment

This research is funded by the Ministry of Education and Ministry of Science, Technological Development and Innovation, Republic of Serbia, Grants: Nos. 451-03-47/2023-01/200146, 451-03-47/2023-01/200017, and 451-03-47/2023-01/200026.

References

- [1] W.C. Bray., *A Periodic Reaction in Homogeneous Solution and Its Relation to Catalysis*, Journal of American Society, 43 (1921) 1262-1267.
- [2] L. Treindl, R.M. Noyes., *A New Explanation of the Oscillations in the Bray-Liebhaftsky Reaction*, The Journal of Physical Chemistry A, 97 (1993) 11354-11362.
- [3] D.R. Stanisavljev, M.C. Milenković, A.D. Popović-Bijelić, M.D. Mojović., *Radicals in the Bray-Liebhaftsky Oscillatory Reaction*, The Journal of Physical Chemistry A, 117 (2013) 3292-3295.
- [4] K. Shakir, H.F. Ghoneimy, A.F. Elkafrawy, Sh.G. Beheir, M. Refaat., *Removal of Catechol from Aqueous Solutions by Adsorption onto Organophilic-Bentonite*, Journal of Hazardous Materials, 150 (2008) 765-773.
- [5] J. Maksimović, J. Tošović, M.C. Pagnacco., *Insight into the Origin of Pyrocatechol Inhibition on Oscillating Bray-Liebhaftsky Reaction: Combined Experimental and Theoretical Study*, Bulletin of the Chemical Society of Japan, 93 (2020), 676-684.
- [6] J. Maksimović, M.C. Pagnacco., *Electrochemical Examination of the Pyrocatechol Influence on the Bray-Liebhaftsky Reaction after the Oscillatory period*, XXII YuCorr Proceedings, September 13-16, 2021, Tara Mountain, Serbia.

Environmental Implications of Financial Development in CEE countries

Nevena Veselinović^{1*}, Jelena Živković¹

¹ University of Kragujevac, Institute for Information Technologies Kragujevac, Jovana Cvijića bb, 34000 Kragujevac, Republic of Serbia, e-mail: nveselinovic@uni.kg.ac.rs, jelenazivkovic@uni.kg.ac.rs

DOI: 10.46793/ICCB23.112V

Abstract: The examination considers the causality between financial development and carbon dioxide (CO₂) emissions in the sample of six Central and Eastern European (CEE) countries in the period range between 2000 to 2020. Utilizing the Dumitrescu and Hurlin panel causality test, the results confirmed a one-way causality, where financial development precedes changes in CO₂ emissions. The observed one-way causality suggests that improvements or advancements in financial development might have implications for environmental sustainability. Additionally, the Westerlund error-correction-based panel cointegration tests reveal cointegration between the variables, indicating a stable equilibrium association among them in the complete sample of countries. As countries strive for economic growth and development, it becomes crucial to consider the environmental consequences and adopt measures that promote sustainable practices. Policymakers and stakeholders must proactively recognize the potentially important role of financial development in shaping environmental outcomes and identify opportunities to effectively integrate sustainable practices into financial and economic strategies.

Keywords: financial development, CO₂ emissions, CEE countries

1. Introduction

The European Union (EU) has set an ambitious goal to achieve climate neutrality by 2050. This means creating an economy where the total greenhouse gas emissions produced are balanced by the amount removed from the atmosphere, effectively resulting in zero net emissions. This commitment forms the core of the European Green Deal, which outlines the EU's comprehensive plan to address climate change and promote sustainability [1]. Achieving carbon neutrality by 2050 poses a significant and complex challenge for the Central and Eastern European (CEE) countries. Unlike their more developed counterparts in Western Europe, CEE countries cannot simply replicate the strategies employed by them. Instead, they must chart a unique path toward carbon neutrality that aligns with their specific circumstances and capabilities.

While numerous studies have shed light on the impact of economic development on carbon dioxide emissions, the relationship between financial development and emissions has been relatively understudied, leading to inconsistent findings. Interestingly, the period between 2007 and 2009 witnessed a significant reduction in global per capita CO₂ emissions [2], indicating a subtle correlation with the global

financial crisis of 2007-2008. This observation underscores the potential influence of financial factors on carbon emissions.

The prevailing mainstream viewpoint regarding the relations between financial development and CO₂ emissions can be categorized into three main perspectives. First, a majority of studies have concluded that financial development has a detrimental effect on CO₂, as demonstrated by research conducted by [3]. Second, there are some studies that have highlighted the possibility of financial development leading to an increase in CO₂, as observed in [4]. Finally, thirdly, certain studies have found no significant correlation between financial development and CO₂, suggesting a lack of substantial connection between these two factors [5].

The primary objective of the paper is to investigate the causal relationship between financial development and CO₂ emissions in the CEE countries. The study aims to delve deeply into this subject to determine whether financial development plays a causal role in influencing CO₂ emissions in these countries. The primary contribution of the research is to empirically uncover the causal connection between financial development and CO₂ emissions in selected CEE countries, complementing the existing literature with valuable insights. To achieve this research objective, the paper employs the Dumitrescu and Hurlin panel Granger causality test (DH test) [6], which is particularly suitable for examining causality when cross-sectional dependence is present.

2. Data and methodology

The analysis in the study utilizes annual data spanning the period from 2000 to 2020. The research focuses on six CEE countries, namely Bulgaria, Croatia, the Czech Republic, Hungary, Poland, and Romania, as the sample for examination.

Financial development is presented by the financial development index provided by the International Monetary Fund – variable FD. This index comprises nine individual indicators that collectively measure the depth, accessibility, and efficiency of financial institutions and financial markets. The CO₂ emissions are presented as the yearly percentage increase in total production-based carbon dioxide (CO₂) emissions, excluding emissions resulting from land-use changes – variable CO₂ emissions. Data on CO₂ emissions were taken from the Global Change Data Lab (Our World in Data).

Given the high level of interactivity and interconnectedness in the economies of the analyzed countries, the occurrence of spatial spillover consequences becomes more probable. These spillover effects can be a fundamental cause of cross-sectional dependence in the data. Two tests, the Breusch-Pagan LM test and Pesaran-scaled LM test, are used to examine cross-sectional dependence among the units in the data. The Breusch-Pagan test detects heteroskedasticity, while the Pesaran-scaled LM test specifically identifies cross-sectional correlation in panel data, indicating potential spatial spillover effects [7]. These tests ensure the reliability of the research findings on the relationship between FD and CO₂ emissions in the CEE countries. The article also utilizes the error-correction-based panel cointegration tests proposed by Westerlund [8]. Two group statistics (Gt, Ga) test whether at least one unit is cointegrated, while two panel statistics (Pt, Pa) test whether the entire panel is cointegrated. Lastly, to assess the

causality between financial development and CO₂ emissions, the study employs the DH test. This test is well-suited for yielding reliable results in both large and small heterogeneous panels, while also considering cross-sectional dependence. The DH test utilizes bootstrapping to enhance the statistical validity of the panel-causality test by reducing the impact of cross-sectional dependence [6].

3. Results and Discussion

Table 1 displays the results of the cross-sectional dependence tests, indicating that there is indeed cross-sectional dependence among the examined countries. The presence of cross-sectional dependence supports the appropriateness of using the DH test to examine the causality between financial development and CO₂ emissions.

Table 1. Cross-sectional dependence tests results

Variable	FD	CO ₂ emissions
Breusch–Pagan LM	145.3339 (0.0000)	92.65646 (0.0000)
Pesaran-scaled LM	23.79561 (0.0000)	14.17806 (0.0000)

Source: Authors' calculations

Table 2 presents the results of the robust Westerlund error-correction-based panel cointegration tests. The robust p-values for Gt, Ga, Pt, and Pa statistics lead to the rejection of the null hypothesis of no cointegration at a 1% significance level, indicating the presence of a cointegration relationship between financial development and CO₂ emissions in the complete sample of countries.

Table 2. The Westerlund cointegration test results

Westerlund's Test	Value	Z-value	P-value	Robust P-value
Gt	-3.405	-5.719	0.0000	0.0000
Ga	-13.185	-5.053	0.0000	0.0000
Pt	-9.658	-7.203	0.0000	0.0000
Pa	-14.785	-11.640	0.0000	0.0000

Source: Authors' calculations

The results of the short-run dynamic bidimensional causality between the variables presented in Table 3. reveal a one-way causality, where financial development influences CO₂ emissions. This finding indicates that changes in financial development precede changes in air pollution, implying that improvements or alterations in financial development may have an impact on CO₂ emissions in CEE countries.

Table 3. The Dumitrescu-Hurlin panel causality test results

Variable	FD	CO ₂ emissions
FD	-	-1.1256
CO ₂ emissions	5.4701**	-

Notes: The values are the Z-bar statistics. ** Indicate significance at 5% P-values are computed using bootstrap replication

Source: Authors' calculations

4. Conclusions

The analysis demonstrates a one-way causality from financial development to CO₂ emissions, indicating that changes in financial development precede changes in air pollution levels in CEE countries. The finding emphasizes the potential role of financial development as a driver of environmental outcomes, underscoring the need for integrating sustainability considerations into economic and financial strategies.

One possible limitation of the examination is that while the DH test showed causality between FD and CO₂ emissions, it did not provide insights into the specific positive or negative impacts of this relationship. To address this limitation, future research can use appropriate panel models to better understand the magnitude and direction of the effects between FD and CO₂ emissions, thus improving the examination's comprehensiveness.

Acknowledgment

This research is funded by the Ministry of Education and Ministry of Science, Technological Development and Innovation, Republic of Serbia, Grants: No. 451-03-47/2023-01/200378.

References

- [1] European Commission. (n.d.). 2050 long-term strategy. Retrieved from https://climate.ec.europa.eu/eu-action/climate-strategies-targets/2050-long-term-strategy_en
- [2] Sadorsky, P. (2020). Energy Related CO₂ Emissions before and after the Financial Crisis. *Sustainability*, 12(9), 3867. doi:10.3390/su12093867
- [3] Al-mulali, U., Tang, C. F., & Ozturk, I. (2015). Does financial development reduce environmental degradation? Evidence from a panel study of 129 countries. *Environmental Science and Pollution Research*, 22(19), 14891–14900. doi:10.1007/s11356-015-4726-x
- [4] Sehrawat, M., Giri, A. K., & Mohapatra, G. (2015). The impact of financial development, economic growth and energy consumption on environmental degradation. *Management of Environmental Quality: An International Journal*, 26(5), 666–682. doi:10.1108/meq-05-2014-0063
- [5] Maji, I. K., Habibullah, M. S., & Saari, M. Y. (2017). Financial development and sectoral CO₂ emissions in Malaysia. *Environmental Science and Pollution Research*, 24(8), 7160–7176. doi:10.1007/s11356-016-8326-1
- [6] Dumitrescu, E.-I., & Hurlin, C. (2012). Testing for Granger non-causality in heterogeneous panels. *Economic Modelling*, 29(4), 1450–1460. doi:10.1016/j.econmod.2012.02.014
- [7] Baltagi, B. H., Feng, Q., & Kao, C. (2012). A Lagrange Multiplier test for cross-sectional dependence in a fixed effects panel data model. *Journal of Econometrics*, 170(1), 164–177. doi:10.1016/j.jeconom.2012.04.004
- [8] Westerlund, J. (2007). Testing for Error Correction in Panel Data. *Oxford Bulletin of Economics and Statistics*, 69(6), 709–748. doi:10.1111/j.1468-0084.2007.00477.x

Greenhouse Gas Emissions and Digital Competitiveness in CEE countries

Jelena Živković^{1*}, Nevena Veselinović¹

¹ University of Kragujevac, Institute for Information Technologies Kragujevac, Jovana Cvijića bb, 34000 Kragujevac, Republic of Serbia, e-mail: jelenazivkovic@uni.kg.ac.rs, nveselinovic@uni.kg.ac.rs

DOI: 10.46793/ICCB23.116Z

Abstract: This research is focused on the relationship between greenhouse gas emissions and digital competitiveness at the macro level because of the importance of climate conditions and the use of new technologies, especially digital technologies. Greenhouse gas emissions were measured using the composite index (CI) conducted by the DEA method. Digital competitiveness is measured using the Digital Competitiveness Index (DCI) calculated by the International Institute for Management Development (IMD). The research covered 11 CEE countries: The latest available data on greenhouse gas emissions were from 2019. Correlation analysis results showed that there was no correlation between these variables. Explanations for these results can be found at the DCI level. These index values show that CEE countries do not have a high value of digital competitiveness, which indicates that digital technology adoption is not at a high level, so it still has effects on gas emissions, the environment, and climate change.

Keywords: greenhouse gas emissions, digital competitiveness, composite index, DEA approach

1. Introduction

To protect the earth's ecological security, the Paris Agreement established the following target for managing the global temperature increase: achieving the objective of decreasing the global average temperature rise to no more than 2 °C and attempting to maintain it at 1.5 °C [1]. Countries must immediately lower emitting greenhouse gases to achieve this long-term objective, and they must help the world achieve carbon neutrality.

By acting as a less formal type of environmental regulation, the digital economy has a positive impact on environmental pollution control and is creating innovative stimulation for intelligent management of the environment with information technology at its core [2,3]. The extrusion impact of the digital economy can effectively encourage the transformation and modernization of the regional industrial structure and further constrain the growth of high-energy and high-polluting industries, thereby improving environmental quality [4]. On the other hand, the growing importance of the digital economy has increased, rather than decreased, energy consumption and the energy growth effect, increasing gas emissions [5].

Because of the opposite views in the literature, the paper aims to analyse correlation between greenhouse gas emissions measured by composite index and digital competitiveness on macro level measured by Digital Competitiveness Index.

2. Data and methodology

The research covers 11 CEE countries. The variables for researching gas emissions are CO₂ emissions (kg per 2017 ppp \$ of GDP), methane emissions (kt of CO₂ equivalent) and nitrous oxide emissions (thousand metric tons of CO₂ equivalent) in 2019. Data are retrieved from World Bank database [6]. The Digital Competitiveness Index is used from the IMD World Digital Competitiveness Ranking report by the International Institute for Management Development (IMD) [7].

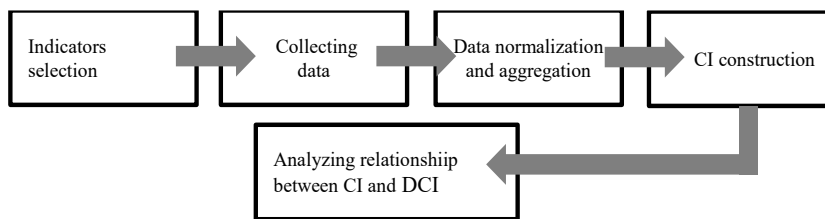


Figure 1. Research framework

Source: Authors' illustration

In order to maximize the value of the composite index for each country, the basic DEA (Data Envelopment Analysis) model posits that composite index for each country j ($j=0,1,\dots,m$) are calculated as the weighted sum of m indicators [8, 9, 10]. Normalization was performed in the range of 0 – 1. This results in the linear programming issue shown below for each country j [11]:

$$CI_j = \max_{w_i} \sum_{i=1}^m y_{ij} w_i$$

In line with the sum of $y_{ik} w_i \leq 1$ and $w_i \geq 0$, where is: $i = 0,1,\dots,m$; $j = 0,1,\dots,m$; and $k = 0,1,\dots,n$; CI composite index, y_{ij} is indicator i for the country j , w is ponder used for aggregation and it is used m indicators for n countries.

After calculating the CI for gas emissions, the relationship between the CI and DCI was examined by correlation analysis with visualization of the results.

2. Results and Discussion

There is a positive correlation between the selected variables. There was a weak correlation between CO₂ emissions and methane emissions and between CO₂ emission and nitrous oxide emission, with Person coefficient of 0.382 and 0.353, respectively. Methane and nitrous oxide emissions showed a statistically significant positive correlation, with a Pearson coefficient of correlation of 0.964. Figure 2 shows the data distribution with scatter graphs.

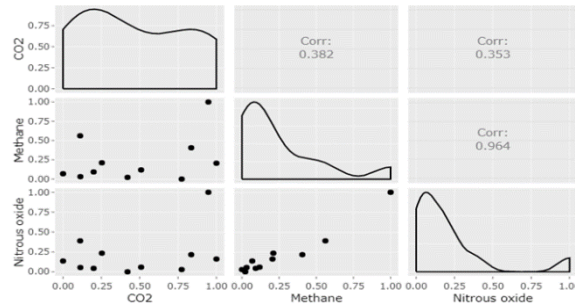


Figure 2. Correlation between individual indicators
Source: Authors

The countries with least greenhouse gas emissions measured by CI are Slovenia, Lithuania and Estonia with the highest value of CI. The worst result is achieved by Poland (CI=0). The most countries from the sample has CI value higher than 0.50. For the purposes of correlation analysis, the DCI was normalized. DCI shows that 5 countries have an index higher than 0.5. (Czech Republic, Estonia, Lithuania, Latvia, Poland and Slovenia) and 3 countries with index lower than 0.2 (Bulgaria, Croatia and Slovak Republic).

Table 1. Normalized data of selected indicators, CI and DCI

	BGR	HRV	CZE	EST	HUN	LTU	LVA	POL	ROU	SVN	SVK
CO2	1.00	0.20	0.84	0.77	0.25	0.00	0.11	0.95	0.01	0.42	0.51
Methane	0.21	0.09	0.41	0.00	0.21	0.07	0.03	1.00	0.56	0.02	0.12
N. oxide	0.16	0.04	0.22	0.03	0.23	0.14	0.05	1.00	0.39	0.00	0.06
CI	0.46	0.86	0.38	1.00	0.74	1.00	0.91	0.00	0.60	1.00	0.75
DCI	0.20	0.00	0.63	1.00	0.29	0.94	0.67	0.73	0.47	0.81	0.14

Source: Authors' calculation

The results of correlation analysis show that there is no statistically significant correlation relationship between CI and DCI in selected countries. The matrix of results for selected countries is shown in Figure 3. The calculated values of CI and DCI divided the economies into four categories, with the most prosperous nations in the top-right corner.

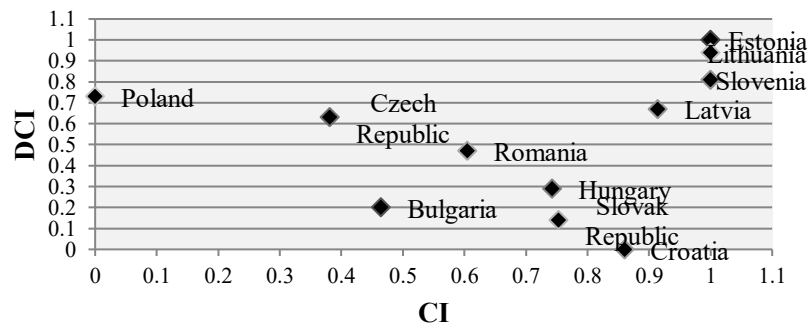


Figure 3. CI and DCI for selected CEE countries in 2019
Source: Authors

3. Conclusions

Based on the presented results, it can be concluded that there is no relationship between greenhouse gas emissions and digital competitiveness in CEE countries. This can be explained by the level of digital technology adoption. In other words, digital technology applications are not at a high level in these countries, so they have not yet affected gas emissions or the environment.

Acknowledgment

This research is funded by the Ministry of Education and Ministry of Science, Technological Development and Innovation, Republic of Serbia, Grants: No. 451-03-47/2023-01/200378.

References

- [1] United Nations Framework Convention on Climate Change (UNFCCC). The Paris Agreement.
- [2] Usman, A., Ozturk, I., Hassan, A., Zafar, S.M., Ullah, S. (2021). The Effect of ICT on Energy Consumption and Economic Growth in South Asian Economies: An Empirical Analysis. *Telematics and Informatics*, 58(29), 101537.
- [3] Li, L., Zheng, Y., Zheng, S., Ke, H. (2020). The New Smart City Programme: Evaluating the Effect of the Internet of Energy on Air Quality in China. *The Science of the total environment*, 714, 136380
- [4] Lin, R., Xie, Z., Hao, Y., Wang, J. (2020). Improving High-Tech Enterprise Innovation in Big Data Environment: A Combinative View of Internal and External Governance. *International Journal of Information Management: The Journal for Information Professionals*, 50, 575–585.
- [5] Lange, S., Pohl, J., Santarius, T. (2020). Digitalization and Energy Consumption. Does ICT Reduce Energy Demand? *Ecological Economics*, 176, 106760
- [6] <https://databank.worldbank.org/source/world-development-indicators#>
- [7] IMD (2019). *IMD World Digital Competitiveness Ranking 2019*. International Institute for Management Development
- [8] Zhou, P., Ang B. W., & Poh, K.L. (2007). A mathematical programming approach to constructing composite indicators. *Ecological Economics*, 62(2), 291-297.
- [9] Cherchye, L., Moesen W., Rogge, N. & Puyenbroeck, T. V. (2007). An introduction to 'benefit of the doubt' composite indicators. *Social Indicators Research*, 82(1), 111-145.
- [10] Fusco, E. (2015). Enhancing non-compensatory composite indicators: A directional proposal. *European Journal of Operational Research*, 242(2), 620-630.
- [11] Cherchye, L., Moesen W., Rogge, N., Puyenbroeck, T. V., Saisana, M., Saltelli, A., Liska R. & Tarantola, S. (2008). Creating composite indicators with DEA and robustness analysis: The case of technology achievement index. *The Journal of Operational Research Society*, 59 (2), 239-251.

Antifreeze with coffee taste

Milan B. Vraneš^{1*}, Snežana M. Papović¹, Jovana J. Panić¹, Teona Teodora V. Borović¹,
Nikolet A. Cako Baganj¹, Sanja D. Belić¹, Sanja Rackov², Slobodan B. Gadžurić¹

¹ Faculty of Sciences, Department of Chemistry, Biochemistry and Environmental Protection,
University of Novi Sad, Trg Dositeja Obradovića 3, 21000 Novi Sad City, Serbia

² Faculty of Technology Novi Sad, University of Novi Sad, Bulevar cara Lazara 1, 21000 Novi Sad,
Serbia

e-mail: milan.vranes@dh.uns.ac.rs, snezana.papovic@dh.uns.ac.rs, jovanap@dh.uns.ac.rs,
teona@dh.uns.ac.rs, nikolet.baganj@dh.uns.ac.rs, sanja.belic@dh.uns.ac.rs, sanja.rackov@uns.ac.rs,
slobodan.gadzuric@dh.uns.ac.rs

DOI: 10.46793/ICCBi23.120V

Abstract: This study presents the results of volumetric and viscometric measurements of caffeine solutions in an equimolar mixture of ethylene glycol - water, known as antifreeze. Measurements were made in the temperature range $T = (283.15 - 313.15)$ K and up to a caffeine molality of $0.12 \text{ mol}\cdot\text{kg}^{-1}$. Experimental results are supported by molecular dynamics (MD) computer simulations. The obtained results indicate that water molecules have a dominant role in the solvation of caffeine. At the same time, ethylene glycol acts as a dehydrating agent and promotes the self-aggregation of caffeine and the investigated mixture.

Keywords: caffeine, water, ethylene glycol, antifreeze, self-aggregation, structure organization

1. Introduction

Caffeine is one of the most widely consumed stimulants globally and is a primary ingredient in many beverages. Coffee and tea are the most popular caffeine-containing beverages, but it is also found in energy drinks, soft drinks, and some flavored water products. Caffeine is used as an active ingredient in some over-the-counter and prescription medications. It is often combined with other drugs to enhance their effects or to relieve headaches, migraines, and certain respiratory conditions. In addition to its use as a pharmaceutically active substance, caffeine is widely used today in numerous other industrial branches, such as the food industry, cosmetics and personal care industry, agriculture and many others. Our previous research has shown that caffeine reduces the viscosity of ethylene glycol (EG) and that combining them produces a heat transport fluid with improved properties [1]. However, ethylene glycol is always used as a heat transfer fluid in an equimolar water mixture known as antifreeze. Caffeine behaves quite differently in water [2] and ethylene glycol from the point of view of influence on the structural organization of the solvent. Caffeine in water increases its viscosity and the structural order of the solvent, while caffeine in ethylene glycol reduces viscosity and acts as a structure-breaker on the solvent. In addition, caffeine's tendency to self-aggregate is much more pronounced in ethylene glycol than in water.

Therefore, it is important to examine which solvent will significantly influence caffeine's solvation when added to their equimolar mixture - antifreeze.

2. Results and Discussion

Density and viscosity measurements of the solutions were made up to a caffeine molality of up to 0.12 mol·kg⁻¹ and in the temperature range from $T = (283.15 \text{ to } 313.15) \text{ K}$ to obtain information about the structural organization of solvent molecules around caffeine.

2.1 Volumetric results

From densities data, the apparent molar volumes, V_ϕ at given molality and temperature were calculated using the following relation:

$$V_\phi = \frac{1000(d_1 - d)}{m d d_1} + \frac{M_2}{d}$$

where m is the molality of the solution, d and d_1 are the density of the mixture and the pure solvent (water+EG), while M_2 is the molar mass of the caffeine. The V_ϕ values are fitted with Masson's equation modified for non-electrolytes:

$$V_\phi = V_\phi^\circ + S_v m,$$

where V_ϕ° value represents the apparent molar volume of solute at infinite dilution and S_v is the experimental slope, which is a measure of solute-solute interactions. The obtained values of V_ϕ° and S_v are listed in Table 1, along with results for caffeine in pure water and ethylene glycol.

Table 1. Fitting parameters Masson's equation in ethylene glycol – water (EG+H₂O), pure EG and pure water (H₂O) in the temperature range from $T = (283.15 \text{ to } 313.15) \text{ K}$.

$T \text{ (K)}$	$V_\phi^\circ \text{ (cm}^3\cdot\text{mol}^{-1}\text{)}$			$S_v \text{ (cm}^3\cdot\text{kg}\cdot\text{mol}^{-2}\text{)}$		
	EG+H ₂ O	EG	H ₂ O	EG+H ₂ O	EG	H ₂ O
283.15	142.85	/	141.05	-1.01	/	-10.44
288.15	143.03	145.46	141.99	1.74	1.27	-12.34
293.15	143.25	145.64	142.93	2.75	3.19	-14.85
298.15	143.34	145.72	143.59	5.17	6.24	-13.60
303.15	143.56	146.23	144.45	6.56	6.63	-15.35
308.15	143.88	146.76	145.20	8.09	4.96	-15.69
313.15	144.06	147.10	145.91	11.6	5.48	-15.46

Lower values V_ϕ° and higher values of S_v at higher temperatures in the EG+water mixture than pure solvents indicate that the aggregation of caffeine molecules is pronounced in antifreeze at higher temperatures. These results are a consequence of the dehydrating property of the EG molecule. Interactions between water and EG are strong

and are realized primarily through dipole-dipole interactions and H-bonds. As a result, the hydration of caffeine is reduced, leading to its self-aggregation.

It is possible to estimate the taste of a substance in an aqueous solution from the ratio of the apparent molar volume at infinite dilution and the molar mass of the solute. The obtained quantity is called apparent specific volume at infinite dilution, and its values correlate with taste according to the following scale: salty ($0.1\text{--}0.3\text{ cm}^3\cdot\text{g}^{-1}$) < sour ($0.3\text{--}0.5\text{ cm}^3\cdot\text{g}^{-1}$) < sweet ($0.5\text{--}0.7\text{ cm}^3\cdot\text{g}^{-1}$) < bitter ($0.7\text{--}0.9\text{ cm}^3\cdot\text{g}^{-1}$). In our system, calculated values were placed around 0.736 and $0.742\text{ cm}^3\cdot\text{g}^{-1}$ in the temperature range $283.15\text{--}313.15\text{ K}$, indicating a bitter taste.

2.2 Viscosimetry results

Measured values of viscosity were used to calculate B -coefficient from Jones-Dole equation:

$$\frac{\eta}{\eta_0} - 1 = Bc.$$

The ratio of the viscosity of the solution (η) and the solvent (η_0) represents the reduced viscosity, c is a molar concentration of caffeine, and B is a coefficient that characterises the solute-solvent interactions at a defined temperature and pressure. According to Jones-Dole's equation, the reduced viscosity (η/η_0) dependence on the concentration was linear (Figure 1).

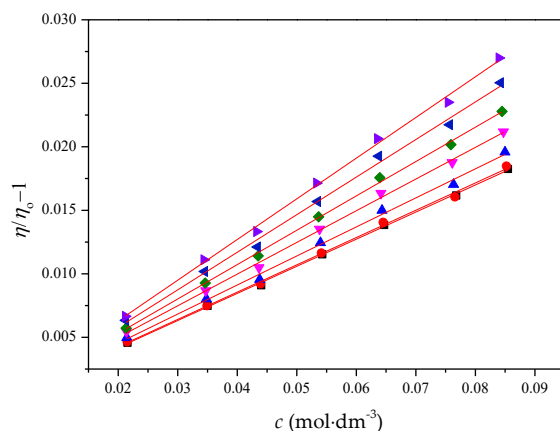


Figure 1. The plot of reduced viscosity ($\eta/\eta_0 - 1$) versus concentration (c) of the caffeine in EG+water at different temperatures, (T): = (■) 283.15; (●) 288.15; (▲) 293.15; (▼) 298.15; (◆) 303.15; (◄) 308.15 and (►) 313.15

Calculated B -coefficients are shown in Table 2.

Table 2. Values of viscosity B -coefficients obtained from the Jones-Dole equation for caffeine in EG+water mixtures in the temperature range from $T = (283.15\text{ to }313.15)\text{ K}$.

T (K)						
283.15	288.15	293.15	298.15	303.15	308.15	313.15
B ($\text{dm}^3\cdot\text{mol}^{-1}$)						
0.213	0.215	0.229	0.249	0.270	0.296	0.320

B -coefficients for caffeine in the EG+water system have positive values and increase with the temperature, so in EG+H₂O system, caffeine behaves as an atypical structure-maker.

2.3 Computational results

To gain a thorough understanding of how caffeine is structured in EG+water equimolar mixtures, molecular dynamic simulations were conducted. The simulation was carried out under specific conditions: caffeine molality $m = 0.06 \text{ mol}\cdot\text{kg}^{-1}$ and at $T = 298.15 \text{ K}$. The results, depicted in Figure 2, demonstrate that caffeine molecules undergo self-aggregation through pi-pi interactions. Furthermore, the radial distribution function of caffeine-caffeine centers of mass indicates that the distance between caffeine molecules in the self-aggregate measures approximately 4 \AA .

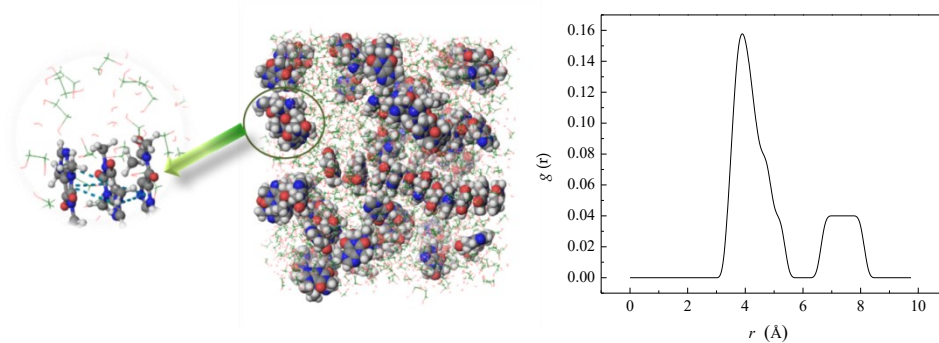


Figure 2. Evidence for self-aggregation of caffeine in the ethylene glycol+water mixture from MD computational simulations: a visual representation and selected part with pi-pi caffeine interactions (left) and RDF function of the centers of mass of caffeine molecules (right).

3. Conclusions

When caffeine is added to a mixture of ethylene glycol and water (which is used in antifreeze), it makes the solvent more organized and gives it a bitter taste. Caffeine is surrounded only by water molecules in its hydration sphere. The strong interaction between ethylene glycol and water reduces the solvent's ability to dissolve substances, causing caffeine self-aggregation.

Acknowledgement

The authors acknowledge the financial support of the Ministry of Education, Science and Technological Development of the Republic of Serbia (Grant No. 451-03-9/2021-14/200125), the Secretariat for Higher Education and Scientific Research of the Autonomous Province of Vojvodina, Serbia (Grant No. 142-451-2545/2021-01/2).

References

- [1] M. Vraneš, I. Radović, S. Bikić, A. Tot, M. Kijevčanin, T. T. Borović, S. Papović, *Improving ethylene glycol transport properties by caffeine-Thermodynamic and computational evidence*, Journal of Molecular Liquids 333 (2021) 115918.
- [2] M. Vraneš, J. Panić, A. Tot, S. Gadžurić, Č. Podlipnik, M. Bešter-Rogač, *How does the presence of ATP affect caffeine hydration and self-aggregation?*, Journal of Molecular Liquids 318 (2020) 113885.

The hydration and antimicrobial properties of selected imidazole-based ionic liquids with a homologous series of chloride oxyanions

Jovana J. Panić*, Snežana M. Papović, Teona Teodora V. Borović, Nikolet A. Cako Baganj, Sanja D. Belić, Slobodan B. Gadžurić, Milan B. Vraneš

University of Novi Sad, Faculty of Sciences, Department of Chemistry, Biochemistry and Environmental Protection, Trg Dositeja Obradovića 3, 21000 Novi Sad, Serbia;

e-mail: jovanap@dh.uns.ac.rs, snezana.papovic@dh.uns.ac.rs, teona@dh.uns.ac.rs,
nikolet.baganj@dh.uns.ac.rs, sanja.belic@dh.uns.ac.rs, slobodan.gadzuric@dh.uns.ac.rs,
milan.vranes@dh.uns.ac.rs

* Corresponding author

DOI: 10.46793/ICCBi23.124P

Abstract: The aim of this work was to get a detailed insight into the ion's interactions along with the structure-making/structure-breaking tendency that has been retrieved through the perusal of calculated parameters from volumetric measurements for aqueous solutions of three newly synthesized ionic liquids: 1-butyl-3-methylimidazolium chlorite, 1-butyl-3-methylimidazolium chlorate and 1-butyl-3-methylimidazolium perchlorate. Further, the antimicrobial activity of synthesized and commercial (1-butyl-3-methylimidazolium chloride) ionic liquids on certain strains of bacteria and fungi was obtained. Antimicrobial tests were performed using the *in vitro* microdilution method against isolated strains of *Escherichia coli*, *Staphylococcus aureus*, *Bacillus cereus* bacteria, and the fungus *Candida guilliermondii*. This method is a rapid, quantitative method for the determination of minimum inhibitory concentration (MIC) and minimum bactericidal concentration (MBC) using small amounts of samples (μl) and test compound. Based on the obtained results, the influence of the homologous series of chloride oxyanions on hydration and antimicrobial properties of imidazole-based ionic liquids will be discussed.

Keywords: ionic liquid, hydration, antimicrobial properties

1. Introduction

Ionic liquids (ILs) are defined as organic salts that melt below the boiling point of water. Thanks to unique properties such as negligible vapor pressure, high thermal stability, and biodegradability, as well as the possibility of modifying physical, chemical and biological properties by changing cations, anions or substituents on them, they have found wide applications [1]. Ionic liquids usually consist of large asymmetric cations and organic/inorganic anions. For the purposes of this research, 1-butyl-3-methylimidazolium ion was chosen as a cation, and known oxidants chlorine oxyanions, chlorite (ClO_2^-), chlorate (ClO_3^-) and perchlorate (ClO_4^-), were used as anions in the

synthesis to obtain 1-butyl-3-methylimidazolium chlorite [Bmim][ClO₂], 1-butyl-3-methylimidazolium chlorate [Bmim][ClO₃] and 1-butyl-3-methylimidazolium perchlorate [Bmim][ClO₄]. Their oxidation potential gives them antibacterial and antiviral activity and is responsible for their wide application as disinfectants.

To estimate ILs hydration properties, aqueous solutions of [Bmim][ClO₂], [Bmim][ClO₃] and [Bmim][ClO₄] were prepared with ultrapure water and solutions density was measured. The determination of antimicrobial activity by estimation of MIC and MBC was carried out by mixing a series of diluted test ILs with a liquid medium previously inoculated with the test organism: *Escherichia coli*, *Staphylococcus aureus*, *Bacillus cereus* bacteria, and the fungus *Candida guilliermondii*.

2. Results and discussions

2.1 Hydration properties

Densities (d) of aqueous solutions of [Bmim][ClO₂], [Bmim][ClO₃] and [Bmim][ClO₄] were measured in the temperature interval from 293.15 K to 313.15 K in the molality range (m) of 0.02 up to 0.12 mol/kg. The measured densities of the aqueous solutions were used to calculate apparent molar volumes, V_ϕ , for given temperatures. The obtained values of the apparent molar volumes were fitted depending on the root of the concentration of the ionic liquid by Masson's equation:

$$V_\phi = V_\phi^\circ + S_V c^{1/2} \quad (1)$$

where V_ϕ° is the apparent molar volume at infinite dilution and S_V is the experimentally obtained slope. V_ϕ is defined as the change in volume of solution per addition of one mole of solute to an infinitely large volume of solvent, and the slope S_V represents the intensity of interactions between the ions of the solution. The obtained values of V_ϕ° and S_V are given in Table 1, from which V_ϕ° of aqueous solutions of all three ionic liquids are positive and increase with increasing temperature. The obtained positive S_V values indicate strong interactions between ions of ionic liquids and increase with increasing temperature. The increase in S_V with temperature is most pronounced for [Bmim][ClO₄]. As the oxygen content of the anion increases, ion-ion interactions also rise.

To calculate the limiting molar expansibility, E_ϕ° , V_ϕ° values were fitted as a function of temperature by a second-order polynomial equation. From the obtained coefficients, E_ϕ° was calculated using equation (2), and the obtained E_ϕ° values are given in Table 1.

$$E_\phi^\circ = \left(\frac{\partial V_\phi^\circ}{\partial T} \right)_p = a_1 + 2a_2 T \quad (2)$$

The limiting molar expansibility represents the expansion of the solution in relation to the pure solvent, so the fact that for all three ionic liquids, the expansibility values decrease with increasing temperature indicates that there are stronger interactions between the water molecules and the ionic liquid than between the water molecules themselves.

Using the Hepler equation:

$$\left(\frac{\partial E_{\phi}^{\circ}}{\partial T}\right)_p = \left(\frac{\partial^2 V_{\phi}^{\circ}}{\partial T^2}\right)_p = 2a_2 \quad (3)$$

Hepler's coefficient, often used to determine the structure making/breaking properties of compounds, was calculated. Positive values indicate structure making properties, while negative values indicate structure breaking properties. The obtained values and whether the given ionic liquid is chaotropic or kosmotropic are shown in Table 1.

Table 1. Estimated volumetric parameters from equation (1) and calculated limiting apparent molar expansibility (E_{ϕ}°) and Hepler's coefficients for ionic liquids aqueous solutions.

Ionic liquid	T (K)	V_{ϕ}° (cm ³ /mol)	S_v (cm ³ ·dm ^{3/2} /mol ^{3/2})	E_{ϕ}° (cm ³ /mol·K)	Hepler's coefficient
[Bmim][ClO ₂]	293.15	195.60	6.16	-0.0061	-0.141 structure breaker
	298.15	193.85	7.95	-0.7134	
	303.15	188.87	16.8	-1.4207	
	308.15	179.20	24.7	-2.1280	
	313.15	167.41	55.2	-2.8353	
[Bmim][ClO ₃]	293.15	178.42	15.5	-0.0691	-0.118 structure breaker
	298.15	175.26	30.1	-0.6611	
	303.15	171.82	35.6	-1.2531	
	308.15	164.04	63.1	-1.8452	
	313.15	152.70	91.1	-2.4372	
[Bmim][ClO ₄]	293.15	201.08	17.8	0.4893	-0.235 structure breaker
	298.15	200.34	20.8	-0.6870	
	303.15	193.86	44.5	-1.8634	
	308.15	182.31	79.5	-3.0397	
	313.15	163.51	135	-4.2160	

2.2 Antimicrobial properties

Based on the results shown in Figure 1, it was revealed that the presence of oxygen in the structure of the anion increases toxicity. Namely, ionic liquids containing chlorine as part of the anion are more toxic to all tested organisms if the anion is in the form of chlorite, chlorate or perchlorate than in the form of chloride. [Bmim][Cl] exhibited toxicity only to *E. coli* at a MIC value of 5.9 mg/mL, with no MBC recorded. Other bacterial strains and tested fungi are resistant to [Bmim][Cl]. 1-butyl-3-methylimidazolium ionic liquids with chlorine and oxygen as an anion exhibited toxicity at comparable concentrations. Based on the MIC and MBC/MFC values, it can be concluded that [Bmim][ClO₂] has shown the highest level of toxicity among all the tested bacterial strains and *C. guilliermondii* fungus. As the amount of oxygen in the anion increases, the antimicrobial effect on the bacterial strains of *E. coli* and *B. Cereus* decreases. On the other hand, [Bmim][ClO₃] shows the weakest antimicrobial effect on

the bacterial strain *S. aureus* and the fungus *C. guilliermondii*. Observing MIC and MBC/MFC values, slight differences in values may come from the oxidizing ability of these ions to oxidize certain components of the cell membrane and thus cause death or prevent further reproduction of the bacterial cell. As the anion's oxygen content increases, the ion's oxidising ability decreases as it becomes kinetically poorer oxidizers. More oxygenated anions are more stable with respect to oxidation and reduction.

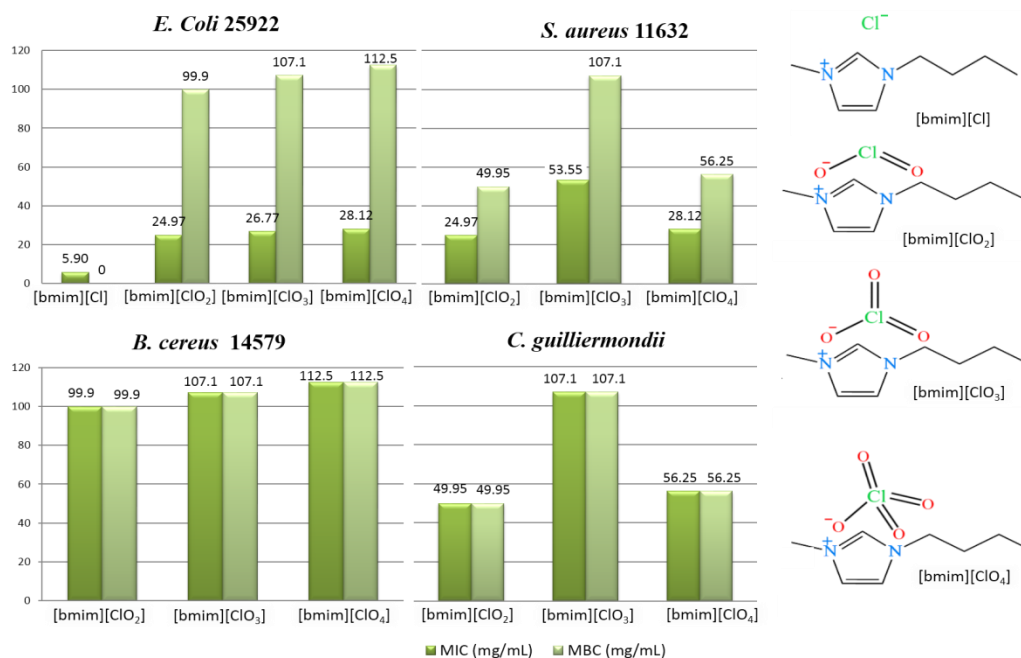


Figure 1. The structures and effect of used ionic liquids on the tested organisms.

3. Conclusions

Based on the outcomes presented, it can be deduced that the interactions between the ionic liquid and water are relatively weak, and their strength diminishes as the oxygen content in the anion increases. Additionally, the ionic liquid [Bmim][ClO₂] has been identified as the most efficacious structure breaker and antimicrobial agent, possessing the highest oxidizing potential among all investigated anions.

Acknowledgment

This research is funded by the Secretariat for Higher Education and Scientific Research of the Autonomous Province of Vojvodina, Republic of Serbia, Grants: No. 142-451-2545/2021-01/2.

References

- [1] N. Nasirpour, M. Mohammadpourfard, S. Zeinali Heris., *Ionic liquids: Promising compounds for sustainable chemical processes and applications*, *Chemical Engineering Research and Design*, 60 (2020),264-300.

Influence of the ionic liquids-based electrolytes on the tomato (*Solanum lycopersicum* L.) and cucumber (*Cucumis sativus* L.) growth, development and oxidative stress

Snežana Papović^{1*}, Jovana Panić¹, Teona Teodora Borović¹, Nikolet Cako Baganj¹, Sanja Belić¹, Ivana Maksimović², Marina Putnik Delić², Slobodan Gadžurić¹, Milan Vranes¹

DOI: 10.46793/ICCB23.128P

¹ University of Novi Sad, Faculty of Sciences, Department of Chemistry, Biochemistry and Environmental Protection, Trg Dositeja Obradovića 3, 21000 Novi Sad, Serbia
e-mail: snezana.papovic@dh.uns.ac.rs*, teona@dh.uns.ac.rs, jovanap@dh.uns.ac.rs, nikolet.baganj@dh.uns.ac.rs, sanja.belic@dh.uns.ac.rs, slobodan.gadzuric@dh.uns.ac.rs, milan.vranes@dh.uns.ac.rs

² University of Novi Sad, Faculty of Agriculture, Trg Dositeja Obradovića 3, 21000 Novi Sad, Serbia; e-mail: ivana.maksimovic@polj.uns.ac.rs , putnikdelic@polj.uns.ac.rs

Abstract: The increasingly frequent improper disposal of lithium-ion batteries (LIB) is leading to concerns about the environmental consequences. When they are poured out, the flammable solvents from the electrolytes in LIBs are the threatening soil and plant contamination. If these liquids spill or leak from batteries, they could enter the soil through various pathways and contaminate crops such as cucumber and tomato plants, which have extensive root systems that may facilitate the absorption of ILs. After absorption, some electrolyte components could accumulate inside the plants and have toxic effects, potentially harming plant growth and crop fields. This study investigated how spilling electrolytes with varying combinations of ILs, organic solvents, and lithium salts in different concentrations affects the growth and development of tomatoes and cucumbers. Special attention was paid to examining the influence of electrolyte components on aerial parts and/or fruits of these plants and the levels of metabolites involved in antioxidant protection under stressful conditions, such as malonyldialdehyde (MDA). In this work, certain ILs with *bis*(trifluoromethylsulfonyl)imide, NTf₂⁻ anion have a phytotoxic effect, which negatively affects cucumber and tomato growth and development.

Keywords: lithium-ion batteries, ionic liquids, environment, tomato, cucumber

1. Introduction

The electrolyte plays a crucial role in a lithium-ion battery (LIB), facilitating the movement of lithium ions between the electrodes during charge and discharge cycles. While ionic liquids (ILs) have the potential to improve battery efficiency and stability, their use in electrolytes for LIBs raises concerns about their impact on the environment, particularly in terms of soil and plant contamination. If not properly managed, spills or leaks during battery manufacturing, recycling, or disposal processes could result in ILs entering the soil [1]. Once in the soil, some ILs may resist biodegradation and

accumulate, potentially affecting soil microorganisms and disrupting the ecological balance. Cucumber and tomato crops are specifically relevant due to their importance in agriculture and human nutrition. As widely grown and consumed crops, they are important indicators of potential environmental contamination. The uptake of ILs by plants depends on various factors, such as the type of IL, soil characteristics, and plant species. After accumulation, they may also transfer to the fruits, posing a potential risk to human health if consumed. Therefore, research on the potential impact of LIB electrolyte components, both hydrophilic and hydrophobic electrolyte components, on plants widely used in human nutrition is very important. Different mixtures are used for electrolytes in lithium-ion batteries, with combinations of ILs and lithium salts with identical anions. The propylene-carbonate (PC) is added to that mixture as a common solvent for LIBs, in the previously described way [2,3]. This study has shown that cucumber and tomato can take up certain hydrophobic ILs (such these with *bis*(trifluoromethylsulfonyl) imide, NTf₂, anion) and accumulate in their tissues, potentially affecting plant growth and development.

2. Results and Discussion

2.1. Average mass of the fresh cucumber and tomato

While treating cucumber with electrolytes [bmpyrr][DCA]/PC/LiDCA and [bmim][DCA]/PC/LiDCA, $c = 100 \text{ mg}\cdot\text{L}^{-1}$, it is observed that the average weight of fresh fruit is equal to the weight of fresh control fruit. With the same electrolytes, $c = 1000 \text{ mg}\cdot\text{L}^{-1}$, a decrease can be seen in the average mass of fresh fruit of about 30-40% compared to the control.

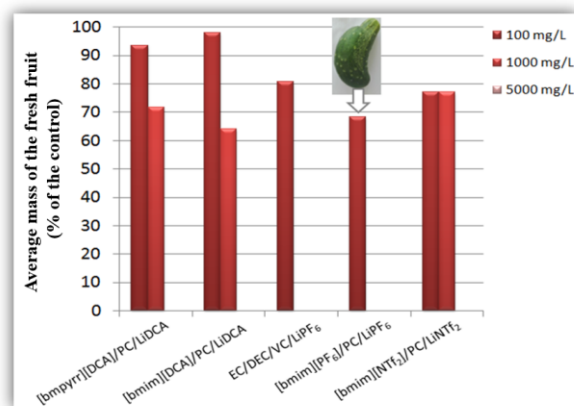


Figure 1. The average mass of fresh cucumber *Cucumis sativus* L. fruit depending on the type and concentration of electrolytes (% of control) and the picture of the appearance of the fruits.

The lowest mass is observed in the electrolyte treatment [bmim][DCA]/PC/LiDCA at $c = 1000 \text{ mg}\cdot\text{L}^{-1}$. After treatment with a commercial electrolyte, EC/DEC/VC/LiPF₆, concentration $c = 100 \text{ mg}\cdot\text{L}^{-1}$, the average fruit weight compared to the control was reduced by some 20%. Cucumber treated with this electrolyte of higher concentrations, $c = 1000 \text{ mg}\cdot\text{L}^{-1}$ and $c = 5000 \text{ mg}\cdot\text{L}^{-1}$, had no fruits, and the growing season ended 23 days after the treatment and the same was with with the electrolyte [bmim][PF₆]/PC/LiPF₆, $c =$

1000 mg·L⁻¹. At the end of the growing season, the cucumber treated with this electrolyte at a concentration of $c = 1000 \text{ mg}\cdot\text{L}^{-1}$ had many flowers.

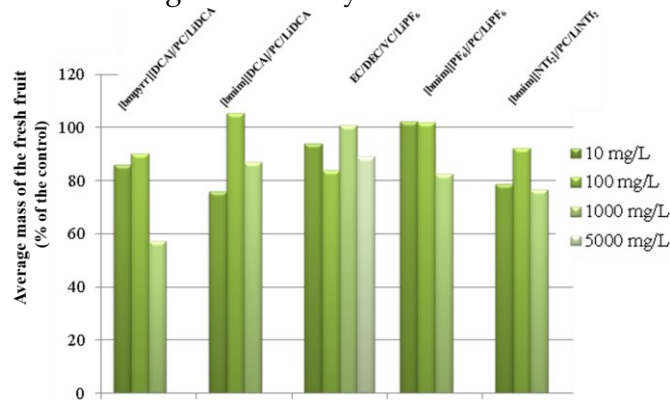


Figure 2. The average mass of fresh tomato *Solanum lycopersicum* L. fruit depending on the type and concentration of electrolytes (% of control)

The average mass of fresh tomato fruit is lower in almost all treatments compared to the control (Figure 2). In all cases, the average mass of fresh tomato fruits is lower than the control by 10 to 40-50%. The smallest mass is observed in the treatment with electrolyte [bmim][DCA]/PC/LiDCA at $c = 1000 \text{ mg}\cdot\text{L}^{-1}$. It can be noted that with each electrolyte, except for the commercial one (EC/DEC/LiPF₆), the concentration of $c = 100 \text{ mg}\cdot\text{L}^{-1}$ had a 10-30% higher average mass fruits in relation to the concentration of $c = 1000 \text{ mg}\cdot\text{L}^{-1}$.

2.2 Degree of lipid peroxidation of the cucumber and tomato

The content of MDA in the leaves of most plants treated with electrolytes was higher compared to the control. The only case of a lower concentration of MDA compared to the control was observed when plants were treated with the electrolyte [bmim][DCA]/PC/LiDCA, $c = 1000 \text{ mg}\cdot\text{L}^{-1}$ (Figure 3).

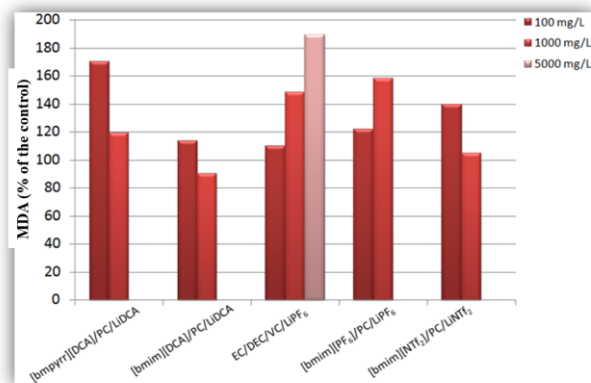


Figure 3. MDA content in cucumber leaves depending on the type and concentration of tested electrolytes (% of control).

Commercial electrolyte, EC/DEC/VC/LiPF₆, concentrations $c = 5000 \text{ mg}\cdot\text{L}^{-1}$, as well as electrolyte, [bmim][PF₆]/PC/LiPF₆, $c = 1000 \text{ mg}\cdot\text{L}^{-1}$, show a trend of increasing MDA content with increasing electrolyte concentration. The measured content of MDA in

tomato and cucumber leaves for all concentrations of tested electrolytes was lower compared to the control, except for the electrolyte [bmpyrr][DCA]/PC/LiDCA (Figure 4).

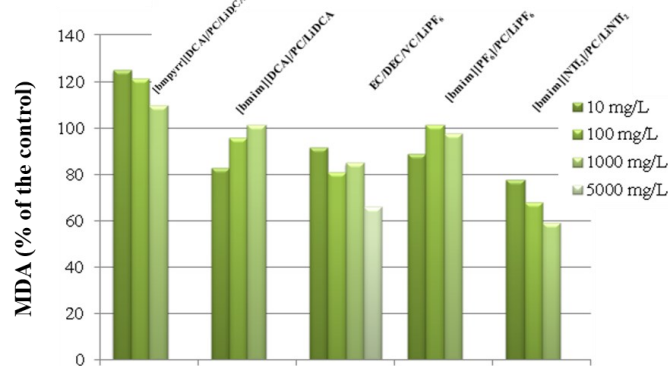


Figure 4. MDA content in cucumber leaves depending on the type and concentration of tested electrolytes (% of control)

3. Conclusions

It can be noted that in cucumbers treated with an electrolyte based on dicyanamide anion there is the same trend of reduction in the weight of fresh cucumber fruits compared to the control. Higher concentrations of electrolytes showed the greatest negative impact on the growth and development of cucumber [bmim][PF₆]/PC/LiPF₆ i EC/DEC/VC/LiPF₆. The higher concentration of MDA in most cucumber leaves treated with electrolytes can be explained by the fact that the plant survived the stress. More hydrophobic electrolytes such as [bmim][NTf₂]/PC/LiNTf₂, had a greater negative impact on the growth and development of the generative organs of tomato, without having almost any negative impact on the cucumber fruit.

Acknowledgement

The authors acknowledge the financial support of the Ministry of Education, Science and Technological Development of the Republic of Serbia (Grant No. 451-03-9/2021-14/200125), the Secretariat for Higher Education and Scientific Research of the Autonomous Province of Vojvodina, Serbia (Grant No. 142-451-2545/2021-01/2).

References

- [1] M. Contestabile, S. Panero i B. Scrosati, *A laboratory-scale lithium-ion battery recycling process*. Journal of Power Sources, 92, (2001) 64-69.
- [2] S. Papović, N. Cvjetičanin, S. Gadžurić, M. Bešter-Rogač, M. Vraneš, *Physicochemical and electrochemical characterisation of imidazolium based IL + GBL mixtures as electrolytes for lithium-ion batteries*, Physical Chemistry Chemical Physics, 19, (2017) 28139-28519.
- [3] M. Vraneš, N. Cvjetičanin, S. Papović, S. Gadžurić, M. Bešter-Rogač, *Physicochemical and electrochemical characterisation of imidazolium based IL + GBL mixtures as electrolytes for lithium-ion batteries*, Journal of Molecular Liquids, 243, (2017) 52-60.

Solubility and structural organization of taurine molecules in water

Teona Teodora V. Borović¹, Snežana M. Papović^{1*}, Jovana J. Panić¹, Nikolet A. Cako Baganj¹, Sanja D. Belić¹, Slobodan B. Gadžurić¹, Milan B. Vranes¹

¹ University of Novi Sad, Faculty of Sciences, Department of Chemistry, Biochemistry and Environmental Protection, Trg Dositeja Obradovića 3, 21000 Novi Sad City, Serbia
e-mail : teona@dh.uns.ac.rs, snezana.papovic@dh.uns.ac.rs*, jovanap@dh.uns.ac.rs, nikolet.baganj@dh.uns.ac.rs, sanja.belic@dh.uns.ac.rs, slobodan.gadzuric@dh.uns.ac.rs, milan.vranes@dh.uns.ac.rs

DOI: 10.46793/ICCB23.132B

Abstract: In this study, a detailed physicochemical characterization of taurine in water is performed based on density and viscosity measurements in the temperature range from $T=(293.15 - 313.15)$ K. Solubility of taurine increases with the temperature increasing. Data obtained from the volumetric and viscosimetric measurements indicate that taurine does not self-aggregate in water. Molecular dynamic simulations provided insight into how taurine molecules behave in water.

Keywords: taurine, water, structure organization, solubility

1. Introduction

Taurine or 2-aminoethanesulfonic acid (from the Latin word *taurus*, meaning bull) is an organic acid widely distributed in animal and human tissues and was first isolated from bull bile [1]. Taurine is an essential substance that regulates various biological processes in the body. Additionally, it impacts cardiovascular functions, skeletal muscle development and function, retina function, and the central nervous system. Within the nervous system, it plays the role of neurotransmitter and neuromodulator. The average intake of taurine varies significantly by diet. However, this figure varies between 40 and 400 mg of taurine daily. Such variations are not problematic because of the body's ability to compensate for taurine deficiencies by synthesising from cysteine. Due to its influence on the functioning of cardiac and skeletal muscles, athletes often use it as a supplement. Taurine is one of the main constituents of energy drinks [2]. The greater demand for taurine from the food additives market currently calls for its chemical synthesis. The solubility of taurine in water is significant from the food industry aspect. Both Wu et al. and Yang et al. published taurine's solubility in different binary solvent systems, while the solubility of taurine in water has not been tested [3].

Therefore, this paper aims to discuss solubility and structure organization of taurine molecules in water from volumetric and viscosimetric measurements, solubility determination, and computational simulations.

2. Results and Discussion

2.1 Solubility results

Experimental data for the solubility of taurine in water was obtained experimentally and presented in Table 1. As can be seen, the solubility of taurine increases with temperature increasing.

Table 1. Determined solubility of taurine in water in the temperature range from $T=(293.15$ to $313.15)$ K.

$T / (\text{K})$	Taurine Solubility / ($\text{g} (1000 \text{ L}_{\text{water}})^{-1}$)
293.15	85.91
298.15	102.74
303.15	122.57
308.15	145.12
313.15	167.79

2.2 Volumetric results

To determine taurine volumetric properties in the water, data obtained from experimental measurements of solution densities were collected and used to calculate the apparent molar volume (V_{ϕ}) of taurine. Obtained values are shown in Figure 1.

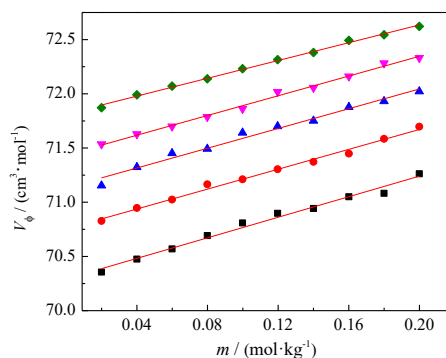


Figure 1. The dependence of the apparent molar volume (V_{ϕ}) on taurine molality (m) in water at different temperatures, (T): = (\square) 293.15; (\circ) 298.15; (\triangle) 303.15; (∇) 308.15; (\diamond) 313.15 K.

The linear trend of increasing the V_{ϕ} values with taurine concentration can be described by *Masson's* equation modified for non-electrolytes [4]:

$$V_{\phi} = V_{\phi}^{\circ} + S_v \cdot m$$

Table 2. Fitting parameters obtained using *Masson's* equation modified for taurine in water in the temperature range from $T=(293.15$ to $313.15)$ K.

$T / (\text{K})$	$V_{\phi}^{\circ} / (\text{cm}^3 \cdot \text{mol}^{-1})$	$S_v / (\text{cm}^3 \cdot \text{kg} \cdot \text{mol}^{-2})$
293.15	70.29	4.74
298.15	70.75	4.58

303.15	71.13	4.56
308.15	71.44	4.55
313.15	71.81	4.10

The value V_{ϕ}° represents (Table 2) the apparent molar volume of solute at infinite dilution. It shows the change in solution volumes (in cm^3 units) after adding 1 mole of taurine to an infinitely large solvent volume. The slope of *Masson's* equation, S_v , gives information about solute-solute interactions. The positive S_v values indicate the existence of strong taurine–taurine interactions in water.

2.3 Viscosimetry results

The viscosity of taurine in water was measured up to molality of taurine $m = 0.1999 \text{ mol}\cdot\text{kg}^{-1}$ in the temperature range from $T=(293.15 \text{ to } 313.15) \text{ K}$. Measured viscosity was used to calculate B -coefficient from *Jones-Dole* equation [5]:

$$\frac{\eta}{\eta_0} - 1 = Bc.$$

The ratio of the viscosity of the solution (η) and the solvent (η_0) represents the reduced viscosity, c is a molar concentration of taurine, and B is a coefficient that characterises the solute-solvent interactions at a defined temperature and pressure. According to *Jones-Dole's* equation, the reduced viscosity (η/η_0) dependence on the concentration was linear (Figure 2). Calculated B -coefficients are shown in Table 3.

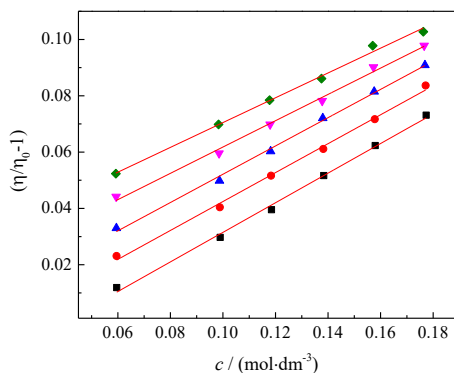


Figure 2. The plot of reduced viscosity ($\eta/\eta_0 - 1$) versus concentration (c) of the taurine water at different temperatures, (T): = (\square) 293.15; (\bullet) 298.15; (\blacktriangle) 303.15; (\blacktriangledown) 308.15; (\blacklozenge) 313.15 K.

Table 3. Values of viscosity B -coefficients obtained from the *Jones-Dole's* equation for taurine in water in the temperature range from $T=(293.15 \text{ to } 313.15) \text{ K}$.

$T / (\text{K})$				
293.15	298.15	303.15	308.15	313.15
$B / (\text{dm}^3\cdot\text{mol}^{-1})$				
0.526	0.514	0.502	0.467	0.440

From Table 3, it can be seen that B -coefficients for taurine in water have positive values and decrease with the temperature increase. Thus, both conditions ($B > 0$ and $\text{d}B/\text{d}T < 0$) were satisfied, and the taurine molecule in water can be declared a structure-maker.

2.4 Computational results

Molecular dynamic simulations were performed to have a complete picture of the structural organization of taurine in water. MD simulation was performed at taurine molality $m = 0.08 \text{ mol}\cdot\text{kg}^{-1}$ and at $T=298.15 \text{ K}$, where eight molecules of taurine and 5555 molecules of water were used. Figure 3 shows a snapshot of the distribution after reaching the equilibrium of taurine in water. This figure indicates that taurine molecules do not self-aggregate in water.

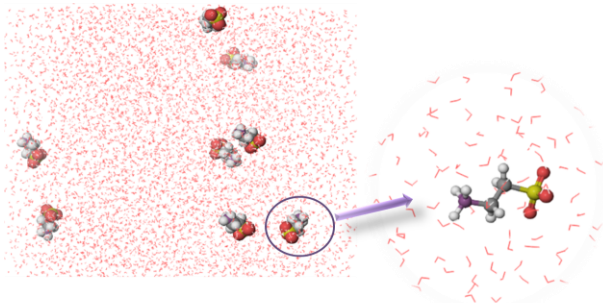


Figure 3. Visual representation obtained from the YASARA program of taurine organisation in water at $T=298.15 \text{ K}$.

3. Conclusions

1. Solubility values of taurine in water increase as temperature increases.
2. Based on the analysis of the *Jones-Dole* equation, taurine behaves as a *structure-maker* in water.
3. The positive S_v values indicate strong taurine–taurine interactions in water
4. Based on the MD simulations it can be concluded that there is no self-aggregation of taurine in water

Acknowledgement

The authors acknowledge the financial support of the Ministry of Education, Science and Technological Development of the Republic of Serbia (Grant No. 451-03-9/2021-14/200125), the Secretariat for Higher Education and Scientific Research of the Autonomous Province of Vojvodina, Serbia (Grant No. 142-451-2545/2021-01/2).

References

- [1] Tiedemann F., Gmelin L., *Annalen der Physik.*, 85 (2006) 326-337.
- [2] K. Parker, L. Brunton, G. Louis Sanford, S.L. John, G. Alfred, *Goodman & Gilman's The Pharmacological Basis of Therapeutics (11 ed.)*, New York: McGraw-Hill (2006).
- [3] W. Gong, P.Li, S. Rohani, *Taurine in several aqueous binary solvents: Solubility prediction, measurement, modelling, solvent effect, and thermodynamics*, *Journal of Molecular Liquids* 367 (2022) 120522.
- [4] D.O. Masson, XXVIII. *Solute molar volumes in relation to solvation and ionisation*, *The London, Edinburgh, and Dublin Philosophical Magazine and Journal of Science* 8 (1929) 218-235.
- [5] G. Jones, M. Dole, *The viscosity of aqueous solutions of strong electrolytes with special reference to barium chloride*, *J. Am. Chem. Soc.* 51 (1929) 2950–2964.

Selecting critical features for biomedical data classification

Ulfeta A. Marovac^{1*}, Lejlija M. Memić¹, Aldina R. Avdić¹, Natasa Z. Djordjević², Zana Ć. Dolićanin³, Goran M. Babić⁴

¹ State University of Novi Pazar, Department of Technical and Technological Sciences, Vuka Karadžića 9, 36300 Novi Pazar, Serbia, e-mail: apljaskovic@np.ac.rs, umarovac@np.ac.rs, lmemic@np.ac.rs

² State University of Novi Pazar, Department of Natural and Mathematical Sciences, Vuka Karadžića 9, 36300 Novi Pazar, Serbia e-mail: natasadj@np.ac.rs

³ State University of Novi Pazar, Department of Biomedical Sciences, Vuka Karadžića 9, 36300 Novi Pazar, Serbia, e-mail: zdolicanin@np.ac.rs

⁴ University of Kragujevac, Faculty of Medical Sciences, Svetozara Markovića 69, 34000 Kragujevac, Serbia, e-mail: ginbabic@medf.kg.ac.rs

* *Corresponding author*

DOI: 10.46793/ICCBi23.136M

Abstract: In this paper, the application of machine learning methods on large data sets with numerous features was investigated, with a focus on the identification of critical features in order to reduce the data and produce more accurate results. The research discusses feature extraction techniques for classifying two biomedical data sets with 62 and 71 features, respectively. The results were compared and presented using four classification techniques. The acquired results demonstrate that the selected important features typically produce more accurate results, or at least the same results while reducing the size of the data set and making data collecting easier.

Keywords: feature selection, machine learning, biomedical data classification, pregnant women

1. Introduction

Prior to applying machine learning techniques to huge datasets with numerous features, it is crucial to prioritize the most significant ones in order to reduce the size of the dataset and produce more accurate results. Choosing good features means choosing only the important features and not leaving out any essential features [1]. High dimension biomedical data usually contains a large number of weak relevant or irrelevant features. Therefore, feature selection is considered to be an essential step in the diagnosis of related diseases using high dimension biomedical data [2]. In classification models for colorectal cancer cases phenotypic [3] as well as for the classification of high-dimensional biomedical data [4], attribute selection produced

positive outcomes. This research deals with the problem of determining diagnostic biomarkers in pregnancy. Thrombophilia in pregnancy, preeclampsia and gestational diabetes are a few of the issues that could occur during pregnancy. This study aims to develop a more accurate method of determining whether a pregnant woman has any of the issues above. For this study, biomedical and demographic information was gathered. The research task is to single out the most significant attributes that provide an equally good model for predicting possible problems in pregnancy as a model built on all available attributes. To check the correctness, the classification of pregnant women was applied based on the available biomedical and demographic data using four classification methods and the obtained models were compared with the classification models obtained on a separate set of attributes.

2. Materials and Methods

Subjects were selected from pregnant women who are accommodated at the Gynecology-Obstetrics Clinic of the University Clinical Center Kragujevac for treatment or labor. Four categories of pregnant women were included in the study: 1) healthy pregnant women (control group); 2) women with preeclampsia; 3) pregnant women with thrombophilia; 4) women with gestational diabetes, controlled by diet. Ethics Committee of the University Clinical Center Kragujevac approved the study protocol, and all patients gave informed consent. For the purposes of this research, two sets of data were selected. The first data set contains information on demographic data for 65 women, of which 27 women have biomedical data. These women are from all four categories. The second set of data consists of demographic and biomedical data of 35 who belong to the group of healthy pregnant women or pregnant women with thrombophilia. Biomedical data consists of clinical data obtained by taking an anamnesis, blood and urine analysis, and via ultrasound examination of pregnant women. Demographic data were collected using a questionnaire on demographic and lifestyle issues. The aim of this study is to enhance the model and categorize pregnant women into one of the four or one of the two groups found in the initial data set. Before applying the modeling, we completed identifying the associated features from a collection of data and removing the irrelevant or less significant features. The `SelectKBest` class (from the Python `scikit-learn` library) is used to choose 10 of the best features. The chi-squared (χ^2) statistical test was performed to determine the most important categorical features (demographic) and ANOVA for numerical data (biomedical analysis). This study compares the performance of K-nearest neighbors (KNN), Random Forest (RF), Support Vector Machines (SVM), and Naive Bayes (NB) machine learning methods for classification on the described datasets. Comparisons were made between the classification outcomes obtained using the set of attributes chosen through univariate selection and the outcomes of applying the methods to all available attributes. The implementation of the proposed machine learning methods is done using Python and corresponding ML packages (`pandas`, `numpy`). To compare classification results, the accuracy measure was used.

3. Results and discussion

The proposed method for the selection of attributes for the classification of biomedical data sets was applied to both described sets. The extracted demographic and biomedical features for the two datasets are displayed in Figure 1.

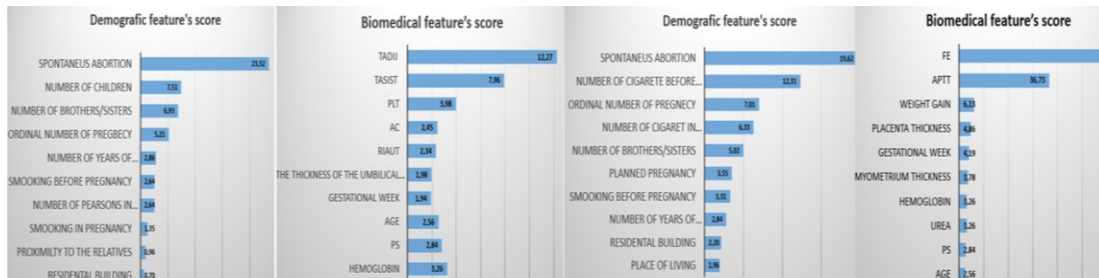


Figure 1. Demographic and biomedical feature's score for the first (left) and the second (right) data set.

A classification using all demographic (biomedical) variables was carried out and the results were compared with those when the classification was carried out just on the basis of 10 selected ones. This was done in order to assess the significance of the selected features on both sets of data. The proposed strategy was evaluated using five-field cross-validation. The first set of data contains four groups of pregnant women, and the classification of this set was made into 4 classes. Four classification methods were applied, and the obtained results are shown in Table 1.

Table 1. Results of 4-class classification on the first data set when using demographic (left) and biomedical (right) data with all attributes and reduced data.

Demographic features					Biomedical features				
#Features	KNN	RF	SVM	NB	#Features	KNN	RF	SVM	NB
Top 10	0.39	0.39	0.39	0.30	Top 10	0.7	0.63	0.51	0.58
All (25)	0.39	0.29	0.37	0.25	All (37)	0.37	0.45	0.44	0.45

The best classification results for both demographic and biomedical features are obtained using the top 10 extracted features, using the KNN method: 0.39 for demographic and 0.7 for biomedical (Table 1). For all four methods, attribute reduction gave better or at least the same accuracy. The low precision is due to the large number of classes and the small sample. The second set of data shows the results of applying this method when we have only two classes of healthy pregnant women and pregnant women with thrombophilia. Table 2 shows the results obtained by applying the classification to all attributes compared to the classification only to the selected ones. As for demographic attributes, the RF method applied to the selected 10 attributes gave the best results. Again, in all cases, the classification is of the same or better accuracy compared to the reduced attributes.

Table 2. Results of binary classification on the second data set when using demographic (left) and biomedical (right) data with all attributes and reduced data.

Demographic features					Biomedical features				
#Features	KNN	RF	SVM	NB	#Features	KNN	RF	SVM	NB
Top 10	0.80	0.83	0.80	0.63	Top 10	0.83	0.91	0.63	1.00
All (34)	0.66	0.83	0.63	0.57	All (37)	0.46	0.94	0.63	0.97

The classification using biomedical attributes is shown in Table 2, where the best results were given by the NB method using 10 selected attributes. Only in the case of the RF method, less precise results were obtained on the reduced data set compared to the whole set. In all other and global classification methods when applied over 10 attributes give the same or better precision. These results justify the application of the attribute extraction method before creating the classification model. The selection of attributes that are correlated with one disease gave much better results.

4. Conclusions

Based on the presented results, it can be concluded that the application of attribute extraction on biomedical data improves classification results. It has been shown that binary classification gives better results and that, in general, it is necessary to expand the data set. Future studies will focus on data preparation and training set enlargement in order to obtain more precise results.

References

- [1] Y. Lyu, Y. Feng, K. Sakurai., *A survey on feature selection techniques based on filtering methods for cyber attack detection*, Information, 14.3 (2023) 191.
- [2] J. Tao, Y. Kang., *Features importance analysis for emotional speech classification*, Lecture Notes Comput Sci, 3784 (2015) 449–57.
- [3] T. W. Cenggoro, B. Mahesworo, A. Budiarto, J. Baurley, T. Suparyanto, B.Pardamean *Features importance in classification models for colorectal cancer cases phenotype in Indonesia*, Procedia Comput Science, 157 (2019) 313–320.
- [4] B. Zhang, C. Peng., *Classification of high dimensional biomedical data based on feature selection using redundant removal*, PloS one, 14.4 (2019) e0214406.

Thrombophilia Prediction Using Machine Learning Algorithms

Aldina R. Avdić¹, Natasa Z. Djordjević², Ulfeta A. Marovac^{1*}, Lejlja M. Memić¹, Zana Ć. Dolićanin³, Goran M. Babić⁴

¹ State University of Novi Pazar, Department of Technical and Technological Sciences, Vuka Karadžića 9, 36300 Novi Pazar, Serbia, e-mail: apljaskovic@np.ac.rs, umarovac@np.ac.rs, lmemic@np.ac.rs

² State University of Novi Pazar, Department of Natural and Mathematical Sciences, Vuka Karadžića 9, 36300 Novi Pazar, Serbia, e-mail: natasadj@np.ac.rs

³ State University of Novi Pazar, Department of Biomedical Sciences, Vuka Karadžića 9, 36300 Novi Pazar, Serbia, e-mail: zdolicanin@np.ac.rs

⁴ University of Kragujevac, Faculty of Medical Sciences, Svetozara Markovića 69, 34000 Kragujevac, Serbia, e-mail: ginbabic@medf.kg.ac.rs

* *Corresponding author*

DOI: 10.46793/ICCBIG23.140A

Abstract: Thrombophilia in pregnancy is the result of a complex interaction of inherited and acquired factors, which increase blood coagulation and consequently placental ischemic conditions. Early identification of risk of developing thrombophilia in pregnancy is crucial for implementing preventive measures and personalized therapy. In this study, we propose a novel approach for prediction of thrombophilia in pregnancy utilizing machine learning (ML) algorithms with a particular focus on neural networks. The research is done using a dataset consisting of demographic, lifestyle, and clinical information from a 35 pregnant woman (22 healthy and 13 with thrombophilia). These features are used to train and evaluate different ML models with neural networks and decision trees. The evaluation of the proposed approach involves cross-validation and performance metrics assessment. The results highlight the effectiveness of decision trees and neural networks in accurately predicting thrombophilia in pregnancy risk.

Keywords: neural networks, decision trees, machine learning, thrombophilia in pregnancy, prediction

1. Introduction

Thrombophilia is inherited or acquired disorder of hemostasis and represents condition of increased hypercoagulability that predisposes patients to thromboembolic events. In normal pregnancy, hormonal changes induce hypercoagulability state, which is adaptive mechanism to reduce the risk of hemorrhage during and after the delivery. The risk of thromboembolic events in pregnancy and postpartum period is 5 times greater compared to non-pregnant women. Thrombophilia in pregnancy is the result of a

complex interaction of inherited and acquired factors, which increase blood coagulation. It is characterized by the generation of microthrombi, which causes reduction in uteroplacental blood flow and consequently placental ischemic conditions. Mutations FV Leiden (G1691A), FII (G20210A), MTHFR (C677T) and PAI-1 are the most common genetic risk factors for thromboembolism. Several environmental factors and stress are associated with the occurrence of thrombophilia in pregnancy. However, many environmental factors are not considered in the assessment of the risk of developing thrombophilia in pregnancy due to their still unknown influence on the etiology of this disease. Identification of environmental risk factors associated with genetic predisposition to thrombophilia in pregnancy would enable individual assessment of the risk of developing this disease, and therefore more adequate prevention and therapy [1].

Machine learning (ML) algorithms have emerged as powerful tools for analyzing complex clinical data and making accurate predictions. By leveraging ML techniques, researchers have made significant progress in various medical domains, including disease diagnosis, prognosis, and risk prediction [2-3]. The aim of this research was to develop a new approach to identify environmental risk factors in pregnant women with thrombophilia using ML algorithms, with a special focus on decision trees and neural networks. Accurately predicting the risk of developing thrombophilia can enable healthcare professionals to identify high-risk pregnant women early, which leads to the improvement of preventive measures, such as lifestyle modifications and the use of therapeutic prophylaxis. In the following sections, we will detail the methodology, results, and discussion of our study, presenting the effectiveness of machine learning algorithms in thrombophilia prediction.

2. Materials and Methods

The studied population consisted of 35 pregnant women who are accommodated at the Gynecology and Obstetrics Clinic of the University Clinical Center Kragujevac for treatment or delivery, and 13 of whom had a diagnosis of thrombophilia. Thrombophilia in pregnant women was diagnosed based on confirmed mutations: FV Leiden (G1691A), FII (G20210A), MTHFR (C677T) and PAI-1. Clinical (spontaneous abortion, method of conception, week of pregnancy, systolic blood pressure, number of erythrocytes, myometrial thickness, fetal femur length) and demographic (smoking in pregnancy, number of cigarettes before pregnancy, place of residence, family relative (brothers and sisters), number of persons in the household, assessment of a healthy lifestyle) data were collected for each participant. The data on the way emotions regulated were collected from each pregnant woman using the Affective styles questionnaire. The Ethics Committee of the University Clinical Center Kragujevac approved the study protocol, and all patients gave informed consent before data collection.

The raw data is transformed into a suitable format for ML algorithms: decision Trees, recurrent (RNN) and convolutional (CNN) neural networks [2-3]. To evaluate the performance of the model, multiple metrics were utilized, including precision, recall, accuracy and F1 score. The entire study was implemented using Weka and Python.

Python libraries such as TensorFlow, Keras, and scikit-learn were employed for implementing neural networks, deep learning techniques, and performance metric calculations. To ensure the reliability and robustness of the model, a cross-validation technique, such as 10-fold cross-validation, was employed. By following these materials and methods, we aimed to develop a predictive model for thrombophilia in pregnancy using neural networks and decision trees.

3. Experiments

The following ML algorithms based on decision trees were applied to the demographic, lifestyle and clinical data: a DecisionTree classification in Python, and a RandomTree classification in Weka. Since the demographic and lifestyle data contained textual attributes, it was necessary to encode them using the OneHotEncoder package from the sklearn library, for DecisionTree classification. In Weka, it was necessary to use a filter for clinical data, ie. for the last class, NumericToNominal, to apply the RandomTree classification. The examples of following decision tree rules for demographic and lifestyle data were obtained and shown in Table 1.

Table 1. The decision tree rules

Demographic and lifestyle data	Clinical data
--- SpontaneousAbortion <= 1.50	WeekOfPregnancy < 39.52
---	SystolicBloodPressure < 122.5
CigarettesNumberBeforePregnancy <= 7.50	MyometrialThickness < 0.77
--- class: 2	FetalFemurLength < 7.78 : 2 (10/0)
---	FetalFemurLength >= 7.78 : 0 (1/0)
CigarettesNumberBeforePregnancy > 7.50	MyometrialThickness >= 0.77
--- class: 0	FetalFemurLength < 7.71
--- SpontaneousAbortion > 1.50	ErythrocytesNumber < 4.69 : 0 (6/0)
--- class: 2	ErythrocytesNumber >= 4.69 : 2 (1/0)
	FetalFemurLength >= 7.71 : 2 (2/0)
	SystolicBloodPressure >= 122.5 : 0 (3/0)
	WeekOfPregnancy >= 39.52 : 0 (12/0)

Table 2. Classification results on demographic and lifestyle data.

	Classifier	Accuracy	Precision	Recall	F1-score
Demographic and lifestyle data	DecisionTree	71.67%	62.92%	70.83%	62.67%
	RandomTree	62.86%	62.30%	62.90%	62.50%
Clinical data	DecisionTree	85.83%	82.08%	85.00%	81.45%
	RandomTree	82.86%	82.80%	82.90%	82.50%

Both trees take smoking during pregnancy and previous spontaneous abortions as key factors for predicting thrombophilia in pregnancy, while RandomTree considers the living environment as important factors. The methods were applied to clinical data in the same way, and again a simpler tree was obtained for the DecisionTree classifier,

where Fe level is crucial, while RandomTree showed that week of pregnancy, systolic blood pressure, myometrial thickness, fetal femur length and number of erythrocytes are important. There are very good classification results, over 80%, which means that clinical factors give us a more accurate prediction than demographic ones (Table 1 and 2).

Algorithms based on neural networks were applied to demographic and clinical data, namely MultilayerPerception in Weka, then using CNN and RNN in Python. Classification results for demographic and clinical data using the MultilayerPerception algorithm and classification accuracy using CNN and RNN are in Table 3. The results show that good prediction (above 85%) is achieved using MultilayerPerception (MP) on clinical data, and that RNN is more suitable for this data, which is expected considering its application. CNN should rather be used in future if the dataset will be enlarged using some images (some health recording, for example ultrasound etc.).

Table 3. Classification results on clinical and demographic data using MP, CNN and RNN

Data	Accuracy MP	Precision MP	Recall MP	F1-score MP	Accuracy CNN	Accuracy RNN
Clinical	85.71%	87.4%	85.7%	85.9%	66.67%	79.17%
Demographic	74.29%	74.8%	74.3%	74.5%	32.5%	24.85%

4. Conclusions

In this study, we developed a prediction model of thrombophilia in pregnancy using decision trees and neural network techniques based on a comprehensive data set consisting of clinical, lifestyle and demographic information. Through our experiments, we demonstrated the potential of decision trees and neural networks in predicting thrombophilia in pregnancy. The model achieved promising results, outperforming the baseline models, and showing high precision, recall, accuracy and F1 score. These findings highlight the effectiveness of ML algorithms, with over 85% accuracy achieved on clinical data in identifying women at risk of developing thrombophilia in pregnancy. Despite the promising results, there are several areas for future research. We can expect better results using FE techniques, other ML algorithms or enlarging the dataset. The developed model is promising in the precise identification of women with risk of developing thrombophilia during pregnancy, which leads to the development of personalized preventive and therapeutic measures.

References

- [1] M. J. Kupferminc, *Thrombophilia and pregnancy*, *Curr Pharm Des.*, 11(2005) 735-748.
- [2] F. Shamout, T. Zhu, D. A. Clifton, *Machine learning for clinical outcome prediction*, *IEEE Rev. Biomed. Eng.*, 14 (2021) 116–126.
- [3] M. Chen, Y. Hao, K. Hwang, L. Wang, L. Wang, *Disease prediction by machine learning over big data from healthcare communities*, *IEEE Access*, 5 (2017) 8869–8879.

Simulation of DNA damage using the “molecularDNA” example application of Geant4-DNA

Milos Dordevic^{1,*}, Konstantinos Chatzipapas², Ngoc Hoang Tran², Dousatsu Sakata³, Ivan Petrovic¹, Aleksandra Ristic-Fira¹, Sara Zein², Jeremy M.C. Brown⁴, Ioanna Kyriakou⁵, Dimitris Emfietzoglou⁵, Susanna Guatelli⁶, Sebastien Incerti²

¹ University of Belgrade, National Institute of the Republic of Serbia, Vinca Institute of Nuclear Sciences, Mike Petrovica Alasa 12-14, 11351 Vinca, Belgrade, Serbia; e-mail: mdjordjevic@vin.bg.ac.rs, ipetrov@vin.bg.ac.rs, aristic@vin.bg.ac.rs

² University of Bordeaux, CNRS, LP2i, UMR5797, F-33170 Gradignan, France; e-mail: chatzipa@lp2ib.in2p3.fr, tran@lp2ib.in2p3.fr, zein@lp2ib.in2p3.fr, incerti@lp2ib.in2p3.fr

³ Osaka University, Division of Health Sciences, Osaka 565-0871, Japan; e-mail: dousatsu@sahs.med.osaka-u.ac.jp

⁴ Swinburne University of Technology, Optical Sciences Centre, Department of Physics and Astronomy, Hawthorn 3122, Australia; e-mail: jeremy.brown@cern.ch

⁵ University of Ioannina, Medical Physics Laboratory, Department of Medicine, 45110 Ioannina, Greece; e-mail: ikyriak@uoi.gr, dempfietz@uoi.gr

⁶ University of Wollongong, Centre for Medical Radiation Physics, Wollongong, NSW 2522, Australia; e-mail: susanna@uow.edu.au

* Corresponding author

DOI: 10.46793/ICCBi23.144D

Abstract: The scientific community has a large interest in the studies of DNA damage and response after exposure to ionizing radiation. Several in-silico methods have been proposed so far to model and study the mechanisms of DNA damage using Monte Carlo simulations. The “molecularDNA” example is one of the most recent applications to simulate the irradiation of human cancer cells and bacteria using Geant4-DNA. This example enables the simulation of the physical, physico-chemical and chemical stages of liquid water irradiation, including radiolytic processes following the particle irradiation of the pre-defined human cell geometries and it can be used to calculate the early direct and non-direct DNA damage such as single (SSB) and double strand breaks (DSB) as well as DNA fragment distribution. The application is user friendly and can be used following simple macro commands. The results of the Monte Carlo simulation are compared to experimental data of DSB yields, as well as with previously published simulation data.

Keywords: Geant4-DNA, Monte Carlo simulation, cancer, protons, helium ions

1. Introduction

There are large efforts worldwide to perform accurate modelling and validation of radiobiological measurements of radio-induced DNA damage. The main goal is to understand cancer formation. The first software toolkit that was made available to the user community in full open access and able to model DNA damage and repair is the Geant4-DNA (<http://geant4-dna.org/>). The Geant4-DNA toolkit can simulate the physical interaction of radiation at the DNA scale, as well as the physico-chemical and chemical stages of water radiolysis. A new "molecularDNA" example of Geant4-DNA, publicly released in December 2022 in the Geant4 toolkit version 11.1, is presented in this manuscript [1 - 8].

2. Materials and Methods

The "molecularDNA" example incorporates a geometrical model of a human cell, consisting of a continuous Hilbert curve that produces a fractal-based DNA chain, made of straight and turned chromatin sections including nucleosomes, and placed inside an ellipsoid imitating the human cell nucleus. It enables the simulation of the direct and non-direct early DNA damage induction and a quantitative measure of this damage through counting the number of single strand breaks, SSB, DSB and DNA fragments distribution. The "human cell" geometrical configuration was irradiated with protons of energies in the range of 0.15 to 66.5 MeV, corresponding to the LET range from 73.5 to 1 keV/ μm and both SSB and DSB yields, as well as their ratio, were calculated [1]. The SSB/DSB ratio, the DNA fragment length frequency distribution for 1 MeV incident protons, the damage kinetics as a function of DNA repair time and also the surviving fraction curves of NB1RGB cells as a function of delivered dose are also reported in [1]. The lung carcinoma, HTB-177, and breast adenocarcinoma MCF-7, cancer cell lines were modelled and incorporated into the "molecularDNA" example, starting from the default "human cell" geometry. The simulation of the irradiation with alpha particle beams was performed in the LET range up to 80.3 keV/ μm and compared to experimental data [2].

3. Results

The "molecularDNA" example application of the Geant4-DNA was used to quantify early DNA damage in human cancer cells upon irradiation with alpha particle beams, as a function of linear energy transfer (LET), as described in [2]. Considering the difference in size for the different types of nuclei for HTB-177 and MCF-7 cell lines used, with respect to the "molecularDNA" default human cell geometry, subtle modifications to the voxel size and the number of nucleosomes were used to maintain the number of 6.4 Gbp in each DNA molecule. In Figure 1, the number of DSBs is normalised to the dose and the number of base pairs and is plotted as a function of LET. For both cell lines studied, the simulation results are within the experimental uncertainties, except for the

highest LET of 39.1 ± 1.1 keV/ μm , due to the limitation of the experimental method of DSB evaluation as described in [2].

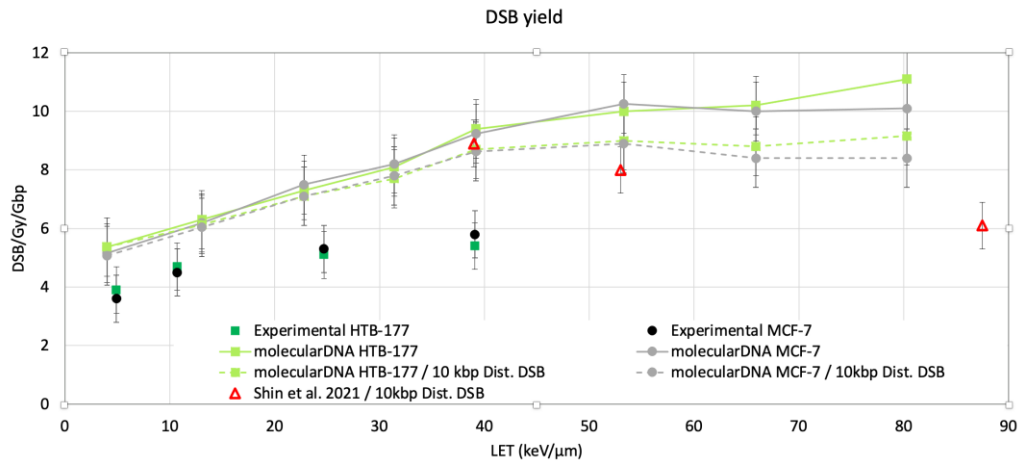


Figure 1. DSB yield as a function of LET, shown in light green and grey lines, for the HTB-177 and MCF-7 cells, respectively. The previous results [7] are shown as red triangles. Experimental data are shown in green squares and black dots, for HTB-177 and MCF-7 cell lines, respectively. This figure was reprinted from *Physica Medica*, 112, K. Chatzipapas, M. Dordevic, S. Zivkovic, N.H. Tran, N. Lampe, D. Sakata, I. Petrovic, A. Ristic-Fira, W.-G. Shin, S. Zein, J. M.C. Brown, I. Kyriakou, D. Emfietzoglou, S. Guatelli, S. Incerti, *Geant4-DNA simulation of human cancer cells irradiation with helium ion beams*, 102613, Copyright (2023), with permission from Elsevier.

4. Conclusions

The "molecularDNA" example application of Geant4-DNA has extensive possibilities for the modeling of DNA damage following irradiation with particles of different types, such as protons and alpha particles, as summarized in this manuscript. The simulation incorporates physical, physicochemical and chemical stages of liquid water irradiation, including radiolytic processes and is used to calculate direct and non-direct DNA damage. The "molecularDNA" application was benchmarked with respect to previous studies of the Geant4-DNA collaboration, as well as to experimental data available, for both proton and alpha particle irradiation. To achieve a more conclusive understanding of radiation induced damage in cells, more experimental data will be collected in a higher LET range. The simulation parameters will be adjusted as well.

Acknowledgment

This research is funded by the Ministry of Education and Ministry of Science, Technological Development and Innovation, Republic of Serbia, Grants: 451-03-47/2023-01/ 200017). The authors also thank the European Space Agency for its support to Geant4-DNA through the "BioRad3" project (contract 4000132935/21/NL/CRS, 2021-2023). The authors wish also to acknowledge financial support obtained from CNRS

through PICS "DAMOCLES" (2018-2020) and IEA "TOLERANCE" (2023-2024) and Hubert Curien Pavle Savic (PHC) "Monte Carlo simulation of irradiation with hadron beams" (grant number 337-00-93/2023-05/18) (2023-2024) France-Serbia projects.

References

- [1] K. Chatzipapas, N. H. Tran, M. Dordevic, S. Zivkovic, S. Zein, W.-G. Shin, D. Sakata, N. Lampe, J. M. Brown, A. Ristic-Fira, I. Petrovic, I. Kyriakou, D. Emfietzoglou, S. Guatelli, S. Incerti, *Simulation of DNA damage using Geant4-DNA: an overview of the "molecularDNA" example application*, Precision Radiation Oncology, 7 (2023) 4-14.
- [2] K. Chatzipapas, M. Dordevic, S. Zivkovic, N. H. Tran, N. Lampe, D. Sakata, I. Petrovic, A. Ristic-Fira, W.-G. Shin, S. Zein, J. M.C. Brown, I. Kyriakou, D. Emfietzoglou, S. Guatelli, S. Incerti, *Geant4 simulation of human cancer cells irradiation with helium ion beams*, Physica Medica: European Journal of Medical Physics 112 (2023) 102613.
- [3] D. Sakata, M. Suzuki, R. Hirayama, Y. Abe, M. Muramatsu, S. Sato, O. Belov, I. Kyriakou, D. Emfietzoglou, S. Guatelli, S. Incerti, T. Inaniwa, *Performance evaluation for repair of HSGc-C5 carcinoma cell using Geant4-DNA*, Cancers 13 (2021) 6046.
- [4] D. Sakata, O. Belov, M.-C. Bordage, D. Emfietzoglou, S. Guatelli, T. Inaniwa, V. Ivanchenko, M. Karamitros, I. Kyriakou, N. Lampe, I. Petrovic, A. Ristic-Fira, W.-G. Shin, S. Incerti, *Fully integrated Monte Carlo simulation for evaluating radiation induced DNA damage and subsequent repair using Geant4-DNA*, Scientific Reports 10 (2020) 20788.
- [5] D. Sakata, N. Lampe, M. Karamitros, I. Kyriakou, O. Belov, M. A. Bernal, D. Bolst, M.- C. Bordage, V. Breton, J. M. Brown, Z. Francis, V. Ivanchenko, S. Meylan, K. Murakami, S. Okada, I. Petrovic, A. Ristic-Fira, G. Santin, D. Sarramia, T. Sasaki, W.-G. Shin, N. Tang, H. N. Tran, C. Villagrasa, D. Emfietzoglou, P. Nieminen, S. Guatelli, S. Incerti, *Evaluation of early radiation DNA damage in a fractal cell nucleus model using Geant4-DNA*, Physica Medica 62 (2019) 152–157.
- [6] D. Sakata, R. Hirayama, W.-G. Shin, M. Belli, M. A. Tabocchini, R. D. Stewart, O. Belov, M. A. Bernal, M.-C. Bordage, J. M.C. Brown, M. Dordevic, D. Emfietzoglou, Z. Francis, S. Guatelli, T. Inaniwa, V. Ivanchenko, M. Karamitros, I. Kyriakou, N. Lampe, Z. Li, S. Meylan, C. Michelet, P. Nieminen, Y. Perrot, I. Petrovic, J. Ramos-Mendez, A. Ristic-Fira, G. Santin, J. Schuemann, H. N. Tran, C. Villagrasa, S. Incerti, *Prediction of DNA rejoining kinetics and cell survival after proton irradiation for V79 cells using Geant4-DNA*, Physica Medica 105 (2023) 102508.
- [7] W.-G. Shin, D. Sakata, N. Lampe, O. Belov, N. H. Tran, I. Petrovic, A. Ristic-Fira, M. Dordevic, M. A. Bernal, M.-C. Bordage, Z. Francis, I. Kyriakou, Y. Perrot, T. Sasaki, C. Villagrasa, S. Guatelli, V. Breton, D. Emfietzoglou, S. Incerti, *A Geant4-DNA evaluation of radiation-induced DNA damage on a human fibroblast*, Cancers 13 (2021) 4940.
- [8] W.-G. Shin, J. Ramos-Mendez, N. H. Tran, S. Okada, Y. Perrot, C. Villagrasa, S. Incerti, *Geant4-DNA simulation of the pre-chemical stage of water radiolysis and its impact on initial radiochemical yields*, Physica Medica 88 (2021) 86–90.

Development of Nanomaterials for Sustainable Food Packaging Applications

Sanja Rackov^{1,*}, Milan Vraneš², Tamara Erceg¹, Branka Pilić¹

¹ Faculty of Tehnology, Department of Materials Engineering, Bulevar cara Lazara 1, 21000 Novi Sad, Serbia; e-mail: sanja.rackov@uns.ac.rs, tamara.erceg@uns.ac.rs, brapi@uns.ac.rs

² Faculty of Sciences, Trg Dositeja Obradovića 3, 21000 Novi Sad, Serbia; e-mail: milan.vranes@dh.uns.ac.rs

* *Corresponding author*

DOI: 10.46793/ICCB23.148R

Abstract: The use of biodegradable polymers from renewable resources in polymer manufacturing, food packaging and for medical application is becoming a favorable option over petroleum-based plastics. Among all biopolymers, biopolyesters poly(lactic acid) (PLA) and poly(hydroxyalkanoates) (PHAs) are considered as the most commercially promising bioplastics. PLA is a biopolyester produced by polymerization of D-, L- lactic acids originating through fermentation of simple sugars from agricultural sources (corn, potato, sugar cane, sugar beet, etc.). PHA is a generic designation for biopolyesters produced by controlled microbial fermentation in the presence of an abundant source of sugars or lipids. The focus of this study was to prepare fully biodegradable flexible nanomaterials using PLA and poly(hydroxybutyrate) (PHB) polymer blend solution by means of electrospinning technique. Since PHB possesses low resistance to thermal degradation with melting temperatures close to degradation and narrowing the processing window, the electrospinning technique reduces energy consumption and avoids thermal degradation during processing. A complete morphological, structural and thermal characterization of the developed materials was conducted at the same time.

Keywords: electrospinning, nanomaterials, biopolymers, sustainable materials and technologies

1. Introduction

Current strategies to solve the growing ecological concern for petroleum-based materials waste disposal include the development of bio-based materials obtained from renewable resources. Short-shelf life and high consumption generate a significant amount of packaging materials waste having a huge environmental impact. Consequently, scientists' attention is focused on the reduction of petroleum residues and replacing them with alternative packaging materials in bio-based packaging, in particular derived from agro-industrial resources. As they are mainly produced by direct extraction from biomass or by the activity of microorganisms, these biopolymers lower the total carbon footprint. In this sense, poly(lactic acid) (PLA) obtained by fermentation of renewable resources (corn, starch, potatoes, other polysaccharides) and poly(hydroxyalkanoates) (PHAs) synthesized by controlled bacterial fermentation are

both economically and environmentally attractive [1]. These biopolymers exhibit the highest potential to substitute conventional polymeric materials in packaging applications, nevertheless, they still show certain limitations.

Electrospinning is a versatile and sophisticated technique which allows scalable and low-cost production of fibrous materials with diameters ranging from the micro to the nanoscale. The electrospinning technique is based on the formation of nanofibers after the high voltage is applied to a polymer solution. Electrostatic repulsions of the solution molecules cause stretching of the polymer solution jet until it finally solidifies and reaches the collector in the form of fibers. These continuous, interconnected ultrathin materials can be produced from a variety of synthetic and natural polymers responding to the packaging industry's demands. Electrospun fibers have a strong tendency to adhere offering a wide range of promising possibilities suitable for packaging material applications, particularly in the design of adhesive interlayers [2], superabsorbent patches [3], barrier layers and coatings [4].

In this scope, the main objective of this work is to develop flexible PLA-PHB thin nanomaterials for sustainable food packaging applications by means of electrospinning technique. The resulting product is intended for food packaging applications and therefore structural, thermal and morphological properties of these materials were evaluated.

2. Experimentar Section

Polymer blend solution is prepared by mixing PLA and PHB pellets (80:20 wt.% ratio) by dissolving in chloroform under continuous stirring for 6 hours at elevated temperatures. The electrospinning process was carried out by Fluidnatek LE-10 setup after optimization. The experiment is performed at room conditions in a controlled closed chamber (relative humidity 40 ± 4 % and temperature 25 ± 2 °C). The solution is electrospun for 2 hours under a constant flow rate of 0.5 ml/h at 15 kV applied voltage and injector to collector distance of 8 cm.

The chemical structure of the sample was examined with Shimadzu IRAffinity-1s Fourier Transform Infrared Spectrometer in the wavelength range 4000 to 400 cm^{-1} by averaging 40 scans at a spectral resolution of 4 cm^{-1} .

Thermal properties were investigated by differential scanning calorimeter, DSC TA Instruments Q20, under a nitrogen atmosphere.

Scanning Electron Microscopy allowed the investigation of the morphology of the nanofibers using Hitachi Tabletop TM3030.

3. Results and Discussion

The overlap of spectra of neat components PLA (blue spectral line), PHB (orange spectral line) together with their electrospun blend PLA-PHB (red spectral line) is displayed in Figure 1. a). All the spectra show strong conformationally sensitive band at around 1760 cm^{-1} assigned to a carbonyl group (C=O) stretching vibration of PHB, PLA and their electrospun blend. A peak at around 1450 cm^{-1} originates from symmetric

wagging of the $-\text{CH}_3$ group, while C-O-C stretching vibration peaks at around 1230 and 1190 cm^{-1} with small shoulder peaks can be seen for the neat PHB and PLA-PHB blend as a typical fingerprint vibrations of PHB.

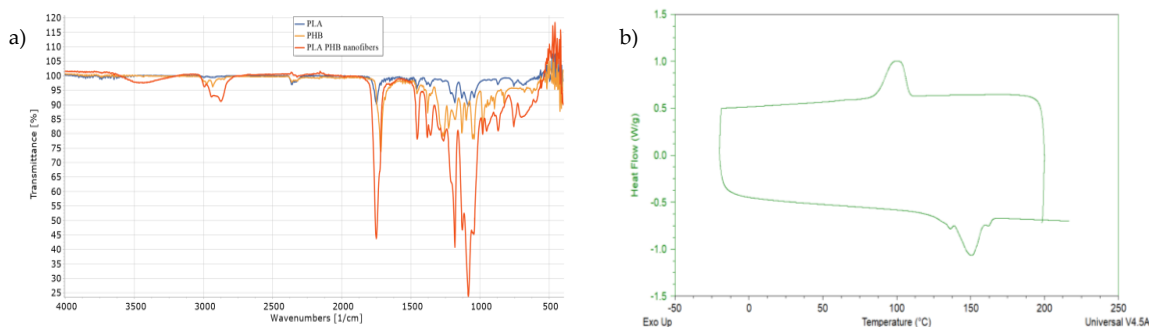


Figure 1. a) Vibrational spectra of neat PHB, PLA and PLA-PHB nanomat; b) Thermogram of cooling and reheating cycles.

The thermogram was recorded during the cooling and second heating step shown in Figure 1. b). The range covers the temperatures of the manipulation of the potential final product and the application conditions. At the examined heating cycle, overlapped endothermic peaks were observed concerning the onset of melting phase changes of the PLA-PHB blend at around $140\text{ }^{\circ}\text{C}$ which is slightly lower than the melting temperatures of the pure constituents of the blend. An exothermic peak that appeared with a maximum of $102\text{ }^{\circ}\text{C}$ corresponds to crystallization. The presented results indicate that the constituents of the blend are well mixed and the homogeneity of the resulting nanomaterial is achieved. The prepared blend does not undergo any phase transformations during heating up to $140\text{ }^{\circ}\text{C}$, therefore the resulting flexible thin film can be safely used at ambient conditions as well as at elevated temperatures.

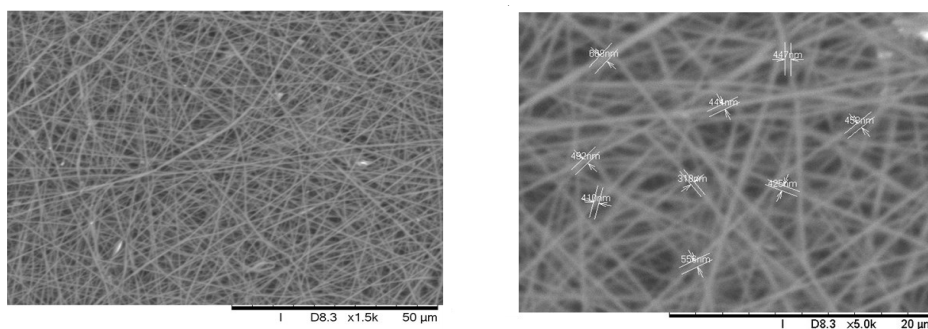


Figure 2. SEM micrographs of PLA-PHB nanofibers under two magnifications ($1500\times$ and $5000\times$).

Figure 2. displays SEM images of the electrospun solution of PLA-PHB blend at different magnifications ($1500\times$; $5000\times$) and the correspondingly determined fiber diameters. Uniformly interconnected and well-defined cylindrical nanofibers were obtained with average diameters varying from 318 ± 23 to $668 \pm 8\text{ nm}$. The smooth surface without a formation of beads and other disproportions with a relatively narrow diameter variation suggests that no phase separation manifested at the selected PLA-PHB polymer blend ratio (80:20).

4. Conclusions

PLA and PHB blend nanofibers were successfully prepared to obtain a flexible porous nanomaterial. In brief, electrospun nanofibers made of biodegradable polymers are outstanding and promising materials for a variety of applications thanks to the combination of unique properties of electrospun nanofibers and non-toxic and eco-friendly nature of biodegradable polymers. The performed structural, thermal and morphological characterization suggests regular orientation and shape of the obtained nanofibers with uniform diameters showing good thermal stability within the range of their potential use as well as good miscibility between the two biopolymers. According to these results, it can be concluded that the combination of PLA-PHB blend at the proposed ratio (80:20) represents a promising flexible nanofibrous material suitable for biodegradable food packaging solutions. Future work will be oriented towards producing electrospun PLA-PHB nanofibers that are able to deliver naturally-derived plant compounds in a controlled way, prevent their degradation, and provide antimicrobial and anti-oxidant activity thus delaying the spoilage of the packaged products.

Acknowledgment

This research is funded by the Ministry of Science, Technological Development and Innovation, Republic of Serbia, Grants: No. 451-03-47/2023-01/200134 and Provincial Secretariat for Higher Education and Scientific Research, Autonomous Province of Vojvodina, Republic of Serbia, 142-451-3106/2022-01/02.

References

- [1] D. Briassoulis, C. Dejean, *Viscous resistance to blood flow in solid tumors: Effect of hematocrit on intratumor blood viscosity Critical Review of Norms and Standards for Biodegradable Agricultural Plastics Part I. Biodegradation in Soil*, Journal of Polymers and The Environment, 18 (2010) 384-400.
- [2] M. J. Fabra, J. M. Lagaron, *On the use of different hydrocolloids as electrospun adhesive interlayers to enhance the barrier properties of polyhydroxyalcanoates of interest in fully renewable food packaging concepts*, Food Hydrocolloids, 9 (2014) 77-84.
- [3] Md. S. Islam, Md. S. Rahaman, J. H. Yeum, *Electrospun novel super-absorbent based on polysaccharide-polyvinyl alcohol-montmorillonite clay nanocomposites*, Carbohydrate Polymers, 115 (2015) 69-77.
- [4] A. Cherpinski, S. Torres-Giner, L. Cabedo, J. A. Mendez, J. M. Lagaron, *Multilayer structures based on annealed electrospun biopolymer coatings of interest in water and aroma barrier fiber-based food packaging applications*, Journal of Applied Polymer Science, 135 (2018),45501.

Bioaccumulation potential of 'Meeker' and 'Willamette' raspberry (*Rubus idaeus* L.) fruits towards macro- and microelements and their nutritional evaluation

Stefan Jevremović¹, Jasminka Milivojević¹, Jelena S. Katanić Stanković², Jelena Popović-Đorđević^{1*}

¹ University of Belgrade, Faculty of Agriculture, Nemanjina 6, 11080 Belgrade, Serbia; e-mail: jelenadj@agrif.bg.ac.rs*

² University of Kragujevac, Institute for Information Technologies Kragujevac, Department of Science, Jovana Cvijića bb, 34 000 Kragujevac, Serbia

* Corresponding author

DOI: 10.46793/ICCBi23.152J

Abstract: Raspberry (*Rubus idaeus* L.) is the most important type of berry fruit in the Republic of Serbia. The bioaccumulation factor (BF) for the elements detected in the fruits of the raspberry cultivars 'Willamette' and 'Meeker' was calculated to determine their bioaccumulation potential. In addition, the nutritional quality of fruits in relation to nutritionally essential elements was evaluated and compared with the recommended daily intake. For determining the concentrations of 19 macro- and microelements in fruits and the soil, the analytical technique of optical emission spectrometry with inductively coupled plasma was used. Among the analyzed elements, As, Cd, Co, Cr, Li and Mo were below the limit of detection in the fruits of both raspberry cultivars, whereas Na and Ni were detected only in fruits of the 'Meeker' cultivar. All analyzed elements were detected in the soil. The results of the work indicated the high potential of the studied cultivars to accumulate nutritional elements K and Ca. In both raspberry cultivars, there were no substantial differences in the bioaccumulation of most elements. However, two elements (B and Mn) can be singled out; the BF for B in the 'Willamette' fruit was 3 times lower compared to the BF in the 'Meeker' fruit, whereas the BF value for Mn in the 'Willamette' fruit was almost 8 times higher compared to the BF value for the 'Meeker' fruit. Furthermore, the cultivars did not tend to accumulate potentially toxic elements such as Ba, Co, Cu and Ni. The nutritional evaluation revealed that the studied raspberry fruits are a good source of K, Ca, Mg, Fe, Mn and Cu. Based on the BF values, differences observed in the accumulation of B, Ba, Na, Ni and Mn may be attributed to the characteristics of the cultivars.

Keywords: raspberry fruit, 'Willamette', 'Meeker', soil, bioaccumulation

1. Introduction

Raspberry (*Rubus idaeus* L.) is the most important type of berry fruit in the Republic of Serbia, taking into account the volume of production, total production area and realized export [1]. In addition, the Republic of Serbia is one of the largest producers and exporters of frozen raspberries in the world, while domestic consumption and export of

fresh raspberries from Serbia are quite limited. Dehydrated fruits are used for fruit mixes, as well as for long-distance transport, whereas fresh fruits are used processed into jam, jelly, topping for desserts, ice cream and yogurt [2]. About 30 chemical elements (called biogenic elements) are involved in physiological and biochemical activities in the human body, so they must be present in a regular daily diet [3]. Besides, non-essential elements (Al, As, Ba, Cd, Hg, Ni, Pb, Sb) could be also found in the food and are considered food contaminants. Due to cumulative properties, these elements are harmful to humans [3,4]. The bioaccumulation factor (BF) indicates the ability of plants to accumulate elements and tolerate toxic elements, depending on the concentration of elements and their bioavailability in the soil, and BF is used to calculate the transfer of elements from the soil to different parts of the plant. [5]. The study aimed to determine the bioaccumulation factor in fruits of raspberry cultivars 'Willamette' and 'Meeker' grown in the Toplica district (Serbia), based on the content of 19 elements analyzed in the fruits and in the soil. In addition, the nutritional quality of the fruits concerning the content of nutritionally essential elements was evaluated.

2. Materials and Methods

Plant material - Raspberry plantations of the 'Willamette' and 'Meeker' cultivars are located in the village of Igrište (on the administrative border with Kosovo), municipality of Kuršumljia, southern Serbia (coordinates 43° 11' N/ 21° 08' E, at an altitude of 938 m). The fruits of the examined cultivars (approx. 200 grams for each) were harvested at the maturity stage and then frozen at -20 °C.

Instrumental analysis - To determine the content of 19 elements in raspberry fruits and the soil, the analytical technique of inductively coupled plasma with optical emission spectrometry (ICP-OES) was applied as described in the literature [6]. The content of the elements in the fruits was expressed as milligrams per kg (mg/kg) of fresh weight.

Calculation of the bioaccumulation factor - The bioaccumulation factor (BF) of the analyzed elements in the fruits of the examined cultivars was calculated according to the literature [6], using the equation $BF = C_{\text{fruit}}/C_{\text{soil}}$ (1)

where C_{fruit} and C_{soil} represent the concentration of the element in the raspberry fruit and in the soil, respectively.

Nutritional assessment of fruit quality - The nutritional quality of the studied cultivars' fruits was evaluated for Ca, Cu, Fe, K, Mg, Mn and Zn, as previously reported [3].

3. Results and Discussion

Content of aluminum (Al), arsenic (As), barium (Ba), boron (B), calcium (Ca), cadmium (Cd), cobalt (Co), chromium (Cr), copper (Cu), iron (Fe), potassium (K), lithium (Li), magnesium (Mg), manganese (Mn), molybdenum (Mo), sodium (Na), nickel (Ni), lead (Pb) and zinc (Zn) was measured in the samples of studied raspberry cultivars and in the soil. The concentrations of As, Cd, Co, Cr, Li and Mo were below the limit of detection (LD) in the raspberry fruits of the cultivars 'Willamette' and 'Meeker'. In

addition, concentrations of Na and Ni in the fruit of the cultivar 'Willamette' were below the LD. The lowest concentration in fruits of the cultivars 'Willamette' and 'Meeker' was measured for Ba (0.005 mg/kg) and Pb (0.498 mg/kg), respectively. On the other hand, K was measured in the highest concentration of both cultivars' fruits; 1877.701 mg/kg - 'Willamette' and 2019.861 mg/kg - 'Meeker'. The content of elements in raspberry fruits may depend on the cultivar and/or cultivation practice (conventional, organic, wild-growing) [7]. All tested elements were detected in the soil (data are not shown).

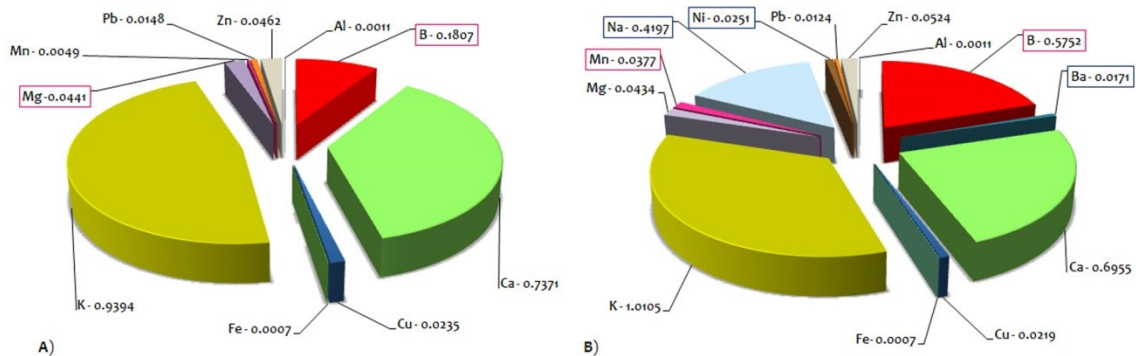


Figure 1. Bioaccumulation factor values for 'Willamette' (A) and 'Meeker' (B) fruits.

The results were used for the calculation of the bioaccumulation factor (BF) of the analyzed elements for both raspberry cultivars, Figure 1. The BF values in the fruits were in the following order: 'Willamette': K > Ca > B > Zn > Mg > Cu > Pb > Mn > Al > Fe; 'Meeker': K > Ca > B > Na > Zn > Mg > Mn > Ni > Cu > Ba > Pb > Al > Fe.

In fruits of both raspberry cultivars, there were no significant deviations in the bioaccumulation of most elements. Values of BF > 1 indicate that the accumulation in the plant is greater than the accumulation of the medium (e.g. soil or water) from which the element is taken [5]. In this study, only BF for K in 'Meeker' fruits was > 1. Boron and manganese can be singled out, with the BF values substantially lower in fruits of the cultivar 'Willamette' than in the cultivar 'Meeker', Figure 1.

Table 1. Daily recommended intake (DRI) of essential elements (mg/day), the content in 100 g of fruits (mg/100 g) and the percentage of DRI in fruits of 'Willamette' and 'Meeker' cultivars.

	DRI* (mg/day)	'Willamette' (mg/100 g)	% of DRI**	'Meeker' (mg/100)	% of DRI
Ca	2000	187.77	9.4	201.99	10.1
K	800	32.89	4.1	31.03	3.9
Mg	375	27.98	7.5	27.54	7.3
Fe	14	1.78	12.7	1.79	12.8
Zn	10	0.54	5.4	0.62	0.6
Mn	2	0.43	21.3	3.24	162.1
Cu	1	0.11	10.7	0.10	10.0

* DRI - Daily recommended intake [8]; ** Percentage of DRI expressed in 100 g of fruits

The content in 100 g of fruits was expressed as a percentage in relation to the recommended daily intake (RDI) of elements, Table 1. Based on the obtained results it can be noted that the fruits of the cultivars 'Willamette' and 'Meeker' are a good source

of essential elements. Consumption of 100 g of the fruits of examined raspberry cultivars can cover the RDI of Mg, K, Fe, Cu and Mn to a significant percentage (7.3-21.3%).

3. Conclusions

The results indicated a high potential of the tested cultivars to accumulate nutritional elements K and Ca. On the other side, fruits did not tend to accumulate potentially toxic elements such as Ba, Co, Cu and Ni. Differences observed in the accumulation of B, Ba, Na, Ni and Mn may be attributed to the characteristics of the cultivars.

Acknowledgment

This research is funded by the Ministry of Science, Technological Development and Innovation of the Republic of Serbia, grants Nos. 451-03-68/2023-14/200116 and 451-03-47/2023-01/200378.

References

- [1] J. Milivojević, *Posebno voćarstvo 3 - Jagodaste voćke*, (2022) Poljoprivredni fakultet, Beograd.
- [2] A.L. Vara, J. Pinela, M.I. Dias, J. Petrović, A. Nogueira, M. Soković, I.C.F.R. Ferreira, L. Barros, *Compositional features of the "Kweli" red raspberry and its antioxidant and antimicrobial activities*, *Foods* 9 (2020) 1522.
- [3] J.B. Popović-Djordjević, A.Ž. Kostić, M.B. Rajković, I. Miljković, Đ. Krstić, G. Caruso, S. Siavash Moghaddam, I. Brčeski, *Organically vs. conventionally grown vegetables: multi-elemental analysis and nutritional evaluation*, *Biological Trace Element Research* 200 (2022) 426–436.
- [4] N. Zand, T. Christides, E. Loughrill, *Dietary intake of minerals*. In: Handbook of mineral elements in food. Editors: de la Guardia M., Garrigues S. (2015) 41–68, John Wiley & Sons. Chichester, UK.
- [5] B. Balabanova, T. Stafilov, *Bio-accumulation of essential and heavy metals in plant food – multielements characterization of plant food*, (2017) Lap Lambert Academic Publishing: Saarbrücken, Germany.
- [6] J. Popović-Djordjević, S.Ž. Marjanović, N. Gršić, T. Adžić, B. Popović, J. Bogosavljević, I. Brčeski, *Essential elements may be distinguishing factors between mycorrhizal potentials of *Tuber magnatum* Pico and *Tuber brumale* Vitt. as cohabiting truffle species in riparian forest habitat in Serbia*. *Chemistry and Biodiversity* 16 (2019) e1800693.
- [7] M. Kotuła, J. Kapusta-Duch, S. Smoleń, *Evaluation of selected heavy metals contaminants in the fruits and leaves of organic, conventional and wild raspberry (*Rubus idaeus* L.)*. *Applied Sciences* 12 (2022) 7610.
- [8] *Pravilnik o deklarisanju, označavanju i reklamiranju hrane* ("Sl. glasnik RS". No. 19/2017, 16/2018, 17/2020, 118/2020, 17/2022, 23/2022 i 30/2022).

In vitro and *in silico* assessment of anti-inflammatory activity of cocoa powders

Jelena S. Katanić Stanković^{1*}, Vanja Todorović², Jelena Đorović Jovanović¹, Zoran Marković¹, Sanja Krstić³, Nevena Dabetić², Slađana Šobajić², Agnieszka Bartoszek⁴, Zoran Maksimović⁵, Rudolf Bauer³

¹ University of Kragujevac, Institute for Information Technologies Kragujevac, Department of Science, Jovana Cvijića bb, Kragujevac, Serbia; e-mail: jkatanic@kg.ac.rs

² University of Belgrade - Faculty of Pharmacy, Department of Bromatology, Vojvode Stepe 450, Belgrade, Serbia

³ University of Graz, Institute of Pharmaceutical Sciences, Department of Pharmacognosy, Beethovenstraße 8, Graz, Austria

⁴ Gdansk University of Technology, Faculty of Chemistry, Department of Food Chemistry, Technology and Biotechnology, Gabriela Narutowicza 11/12, 80-233 Gdańsk, Poland

⁵ University of Belgrade - Faculty of Pharmacy, Department of Pharmacognosy, Vojvode Stepe 450, Belgrade, Serbia

* Corresponding author

DOI: 10.46793/ICCBi23.156KS

Abstract: Plants are considered the major sources of biologically active compounds, which provide unlimited opportunities for their use either as medical treatments or as novel drug formulations. Cocoa powder is frequently used in nutrition and is known to have many benefits thanks to its wide range of biological activities. The presented study was focused on the evaluation of the anti-inflammatory potential of extracts obtained from cocoa powder. *In vitro* assays were employed to evaluate the level of inhibition of cyclooxygenases-1 and -2 activities (COX-1 and COX-2) by tested extracts. Molecular docking was used for *in silico* prediction of cyclooxygenase isoforms inhibition by selected cocoa powder constituents. The results showed that all tested extracts exerted much higher potential in inhibiting COX-2 activity and may be considered in use as selective inhibitors of COX-2 enzyme. On the other hand, *in silico* study shows quercetin and clovamide as the compounds with the highest potential to inhibit both COX-1 and COX-2.

Keywords: *Theobroma cacao* L., cocoa powder, inflammation, anti-inflammatory activity, *in vitro*, *in silico*

1. Introduction

The interest in the utilization of plants with outstanding nutritional properties, such as cocoa, is rapidly increasing and is in line with the recognition of the necessity to prevent and manage ubiquitous and numerous noncommunicable diseases. Cocoa powder, obtained from the seeds of *Theobroma cacao* L. (Malvaceae), is a rich source of compounds possessing a spectrum of biological activities. Among the most important bioactive compounds found in cocoa powder are methylxanthines and flavonoids [1, 2]. The alkalization process is optionally used to change the flavor and color of cocoa powder [3]. Cocoa powder has a specific and unique chemical composition of bioactive compounds and is therefore associated with various health benefits. In particular, some cocoa compounds are considered to be anti-inflammatory agents that can have a positive effect on general health and the prevention of chronic diseases.

This study aimed to evaluate the anti-inflammatory properties of cocoa powder extracts (CPE) towards the inhibition of cyclooxygenases-1 and -2 (COX-1 and COX-2) *in vitro* and *in silico* prediction of COX-1 and COX-2 inhibition by selected compounds contained in the CPE.

2. Materials and Methods

2.1 Preparation of the cocoa samples

Six natural and five alkalized cocoa powders were obtained from three companies: Gerkens, Netherlands; De Zaan Company, USA; Nederland, Spain. To obtain the CPE, 3 g of cocoa powder was suspended in 30 mL of 70% ethanol (v/v). The suspension was mixed for 24 h on a shaker at room temperature and centrifuged (4 000 rcf, 10 min, 25°C). The collected supernatants were lyophilized, and the extracts were stored as such and used for further analyses.

2.2 Anti-inflammatory activity *in vitro*

The anti-inflammatory effects of CPE were analyzed regarding the inhibition of the activity of cyclooxygenases-1 and -2 enzymes using *in vitro* assays. Inhibition assays for COX-1 and COX-2 were conducted per the modified methodology delineated in Mićović et al. [4]. The extracts were solubilized in DMSO, while indomethacin (purity $\geq 99\%$, MP Biochemicals, 190217) and celecoxib (purity $\geq 98\%$, Sigma, PZ 0008), serving as positive control substances, were dissolved in ethanol and DMSO respectively. The extract solutions were prepared at a concentration of 50 $\mu\text{g}/\text{mL}$; indomethacin at 1.25 μM concentration; and celecoxib at a concentration of 8.8 μM .

2.3 Anti-inflammatory activity *in silico*

For the *in silico* analysis of the selected compounds present in CPE, molecular docking simulations were applied. They were used for *in silico* prediction of the inhibitory potency of theobromine, caffeine, epicatechin, catechin, gallic acid, procyanidin B1,

procyanidin C1, caffeoyl-aspartic acid, procatechuic acid, clovamide, dideoxyclovamide, and quercetin toward COX-1 and COX-2 receptors. All simulations are performed according to the methodology from Katanić Stanković et al. [5].

3. Results

According to the obtained results of the *in vitro* tests (Figure 1), all tested CPE showed quite low inhibition of COX-1 enzyme activity. The values ranged from 2.29% of COX-1 inhibition for extract 2 to 10.66% for extract 8. In comparison with the positive control indomethacin with 40.25% of COX-1 inhibition, the COX-1 inhibitory effects of the CPE are negligible. On the other hand, the results of COX-2 inhibition were much more prominent. Extracts 1, 2, 9, 10, and 11 stood out in particular with COX-2 inhibitory activity of 88.91, 58.19, 60.02, 62.09, and 61.17%, respectively. These results are even higher than those of Celecoxib as a positive control (46.09%). Generally, non-selective COX inhibitors (non-steroidal anti-inflammatory drugs-NSAIDs) are known for their adverse effects, particularly present in the gastrointestinal tract. In this case, the cocoa powder extracts showed much higher inhibition towards COX-2 activity in comparison to COX-1 inhibition, which actually represents a great advantage in terms of protection of the gastrointestinal tract. Based on the obtained results, it can be concluded that CPE may be used for the inhibition of COX-2 activity particularly.

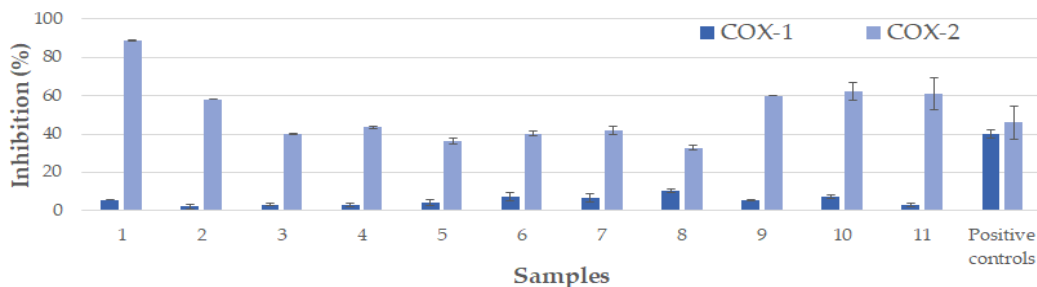


Figure 1. The inhibition of cocoa extract (50 $\mu\text{g/mL}$) towards COX-1 and COX-2 activities. The results are from two independent experiments ($n = 4$, mean \pm SD). Positive controls: indomethacin (1.25 μM) for COX-1 and celecoxib (8.8 μM) for COX-2.

The influence of the selected compounds from the cocoa extracts (theobromine, caffeine, epicatechin, catechin, gallic acid, procyanidin B1, procyanidin C1, caffeoyl-aspartic acid, procatechuic acid, clovamide, dideoxyclovamide, and quercetin) on the activity of COX-1 and COX-2 enzymes was tested *in silico*. A careful inspection of the recognized interactions revealed the inhibitory potency of the tested compounds treated as ligands in molecular docking simulations towards COX-1 and COX-2. The obtained results indicate quercetin and clovamide as the most important compounds. Of all tested compounds, quercetin possessed the lowest values of the ΔG_{bind} and K_i and it has the highest inhibitory potency toward COX-1 and COX-2 ($\Delta G_{\text{bind}} = -9.02$ kcal/mol and $K_i =$

0.24 μM , and $\Delta G_{\text{bind}} = -9.85$ kcal/mol and $K_i = 0.06$ μM , respectively). Clovamide followed the quercetin results and the obtained values of ΔG_{bind} and K_i were almost the same as those of quercetin ($\Delta G_{\text{bind}} = -8.91$ kcal/mol and $K_i = 0.29$ μM towards COX-1 and $\Delta G_{\text{bind}} = -9.82$ kcal/mol and $K_i = 0.06$ μM towards COX-2). In addition, it seems that both quercetin and clovamide have the same inhibitory potency against COX-2. In the case of inhibition of COX-1, quercetin showed a slightly higher inhibition potency than clovamide.

4. Conclusions

The *in vitro* assessment of the anti-inflammatory activity of the extracts from six natural and five alkalized cocoa powders showed much higher inhibitory potential towards COX-2 activity. There was no clear difference in the activity of alkalized and non-alkalized compounds. Based on the results of the *in silico* study, quercetin and clovamide stand out significantly for their inhibitory potential of both isoforms of cyclooxygenase. Further qualitative and quantitative evaluation of the phytochemical composition of tested extracts is needed in order to define active principles and propose the mechanism of anti-inflammatory action.

Acknowledgment

This study was supported by the Ministry of Science, Technological Development and Innovation (Grants No. 451-03-47/2023-01/200378 and 451-03-47/2023-01/200161) and the bilateral project of scientific and technological cooperation between the Republic of Serbia and the Republic of Austria (Grant No. 337-00-577/2021-09/9).

References

- [1] L. Dugo, G. Tripodo, L. Santi, C. Fanali, *Cocoa Polyphenols: Chemistry, Bioavailability and Effects on Cardiovascular Performance*, *Current Medicinal Chemistry* 25 (2018), 4903 – 4917.
- [2] V. Sorrenti, S. Ali, L. Mancin, S. Davinelli, A. Paoli, G. Scapagnini, *Cocoa Polyphenols and Gut Microbiota Interplay: Bioavailability, Prebiotic Effect, and Impact on Human Health*, *Nutrients* 12(7) (2020) 1908.
- [3] K.B. Miller, W.J. Hurst, M.J. Payne, D. A. Stuart, J. Apgar, D.S. Sweigart, B. Ou, *Impact of Alkalization on the Antioxidant and Flavanol Content of Commercial Cocoa Powders*, *Journal of Agricultural and Food Chemistry*, 56 (2008) 8527–8533.
- [4] T. Mićović, J.S. Katanić Stanković, R. Bauer, X. Nöst, Z. Marković, D. Milenković, V. Jakovljević, M. Tomović, J. Bradić, D. Stešević, D. Stojanović, Z. Maksimović, *In vitro, in vivo and in silico evaluation of the anti-inflammatory potential of Hyssopus officinalis L. subsp. aristatus (Godr.) Nyman (Lamiaceae)*, *Journal of Ethnopharmacology* 293 (2022) 115201.
- [5] J.S. Katanić Stanković, J. Đorović Jovanović, D. Mišić, U. Gašić, S. Nikles, Z. Marković, R. Bauer, *UHPLC-MS Phytochemical Profiling and Insight into Bioactivity of Rabelera holostea (Greater Stitchwort) Extract*, *Molecules*, 28, (2023).

Comparison of the luminescence properties of phosphate-tungsten bronze and cerium doped phosphate-tungsten bronze

Tijana V. Maksimović^{1*}, Ljubinka G. Joksović¹, Dimitrije Mara^{2,3}, Rik Van Deun⁴,
Zoran P. Nedić⁵, Marina Simović-Pavlović⁶, Maja C. Pagnacco⁷

¹ University of Kragujevac, Faculty of Science, Department of Chemistry, 34000 Kragujevac (Radoja Domanovića 12), Serbia

² University of Belgrade, Institute of General and Physical Chemistry, 11 158 Belgrade (Studentski trg 12/V P.O. Box 45), Serbia

³ KU Leuven, Molecular Imaging and Photonics, Department of Chemistry, Leuven (Celestijnenlaan 200 D, box 2425, B-3001), Belgium

⁴ Ghent University, L³-Luminescent Lanthanide Lab, Department of Chemistry, Ghent (Krijgslaan 281-S3, B-9000), Belgium

⁵ University of Belgrade, Faculty of Mining and Geology, 11 120 Belgrade (Đušina 7), Serbia

⁶ University of Belgrade, Faculty of Mechanical Engineering, Belgrade (Kraljice Marije 16), Serbia

* Corresponding author

DOI: 10.46793/ICCB23.160M

Abstract: Phosphate-tungsten bronzes (PWBs) constantly attract a lot of attention owing to their interesting chemical, mechanical, and optical properties. Furthermore, tungsten bronzes as inert inorganic solids, exhibit interesting and useful electronic properties when rare-earth ions are incorporated into their structure. Cerium doped phosphate-tungsten bronze (Ce-PWB) is obtained in the process of phase transformations of $\text{CePW}_{12}\text{O}_{40}\times 6\text{H}_2\text{O}$ (Ce-PWA) salt. The brown crystals of Ce-PWB are formed after heating of Ce-PWA in a furnace, in a temperature range from room temperature to 650 °C. In the present paper the luminescence properties of undoped PWB and Ce-PWB are analyzed and compared. Regarding the characterized luminescence properties of PWB and Ce-PWB, only PWB matrix showed luminescence, while dopant Ce^{3+} had no significant influence on the change of the emission spectra with characteristic spectra for this ion. The obtained CIE chromaticity diagrams showed that both samples emit in the deep blue region, suggesting their possible use as a blue emitting source for white light-emitting diodes (LEDs).

Keywords: phosphate-tungsten bronze, cerium doped phosphate-tungsten bronze, luminescence properties

1. Introduction

Heteropoly acids (HPAs) are acids made of hydrogen, oxygen, and specific metals and non-metals. They have attracted interest in scientific research for over a century due to their high protonic conductivity at room temperature [1-3]. Keggin's type HPAs have a general formula of $\text{H}_{(8-x)}\text{XM}_{12}\text{O}_{40}\times n\text{H}_2\text{O}$, where X represents heteroatoms like P^{5+} , Si^{4+} , As^{5+} , Ce^{4+} , Ge^{4+} , Th^{4+} , and M represents metal addenda atoms like W, Mo, V, Nb. One particular

HPA, 29-PWA ($\text{H}_3\text{PW}_{12}\text{O}_{40}\times 29\text{H}_2\text{O}$), has been found to be a suitable precursor for synthesizing phosphate-tungsten bronze (PWB) and cerium-doped phosphate tungsten bronze (Ce-PWB) [4-7]. PWBs have distinct structural features with different types of canals, leading to monophosphate tungsten bronzes and diphosphate tungsten bronzes [8]. These compounds possess unique properties in mechanics, electronics, and optics, making them valuable for photonics and optoelectronics applications such as LEDs, lasers, and photodetectors. PWBs also exhibit intriguing electronic and magnetic characteristics when alkali, alkaline earth, or rare earth ions are incorporated into their structure [9]. This study focuses on Ce-PWB, which is a monophosphate tungsten bronze doped with cerium ions from the rare earth group. The luminescence properties of undoped PWB and doped Ce-PWB, are analyzed and compared to gain insights into their behavior and potential practical applications.

2. Experimental

2.1 Synthesis of heteropoly acid hydrate $\text{H}_3\text{PW}_{12}\text{O}_{40}\times 6\text{H}_2\text{O}$ (6-PWA)

Synthesis of the heteropoly acid hydrate $\text{H}_3\text{PW}_{12}\text{O}_{40}\times 6\text{H}_2\text{O}$ (6-PWA) was done the same way as described in references [4,10]. Afterward, 6-PWA was used as the initial compound for the synthesis of doped PWB.

2.2 Synthesis of Ce-PWA and Ce-PWB

Ce-PWA was prepared by mixing the aqueous solution of 6-PWA, prepared by dissolving in distilled water, with an aqueous solution $\text{CeCl}_3\times 7\text{H}_2\text{O}$ solution, prepared by dissolving 0.9975 g of $\text{CeCl}_3\times 7\text{H}_2\text{O}$ (Acros Organics, Belgium) in distilled water. The obtained solution was slightly heated and left over night at room temperature to complete the crystallization process. Subsequently, the synthesized Ce-PWA salt was heated in a furnace in a temperature range from room temperature to 650 °C (at 10 °C min^{-1}), and brown crystals of Ce-PWB were formed.

2.3 Characterization

Luminescence measurements were conducted using an Edinburgh Instruments FLSP920 UV-Vis-NIR spectrometer. To induce excitation, a stationary 450W Xe lamp was used. Time-resolved measurements were captured using a 60 W Xe lamp, operating at a frequency of 100 Hz. The emitted signals within the visible region were recorded using a Hamamatsu R928P photomultiplier tube. All luminescence measurements were performed under ambient room temperature conditions. For powder samples, the powders were carefully positioned between quartz plates, specifically Starna cells of type 20/C/Q/0.2. The time-resolved measurements were then fitted with a monoexponential function for analysis.

3. Results and discussion

The photoluminescence (PL) properties of PWB and Ce-PWB have shown only the luminescence of the matrix PWB, while the dopant Ce^{3+} has no significant effect on the change of the emission spectra with characteristic emission for this ion. The emission and excitation spectra of PWB and Ce-PWB are shown in Figure 1. The Ce^{3+} emission was not observed when excited in one of the $\text{W}=\text{O}$ charge transfer bands, possibly due to a low doping fraction of this lanthanide ion or its inability to integrate into the PWB matrix, preventing successful excitation. The matrix displays fluorescence properties with broadband emission spanning from 400 to 500 nm. The addition of Ce^{3+} to the matrix does not exhibit the typical emission peaks found in the Ce^{3+} ion emission spectrum.

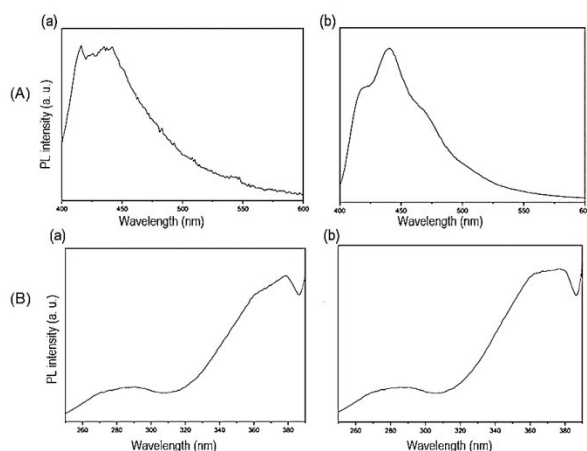


Figure 1. (A) Emission spectra of: (a) PWB and (b) Ce-PWB excited at 376 nm at room temperature; (B) Excitation spectra of: (a) PWB and (b) Ce-PWB monitored at the emission peak maximum ~ 430 nm at room temperature.

According to the CIE chromaticity diagrams, presented in Figure 2, both samples, PWB and Ce-PWB, emit light in the deep blue region, suggesting their potential application as a blue-emitting source for white light LEDs.

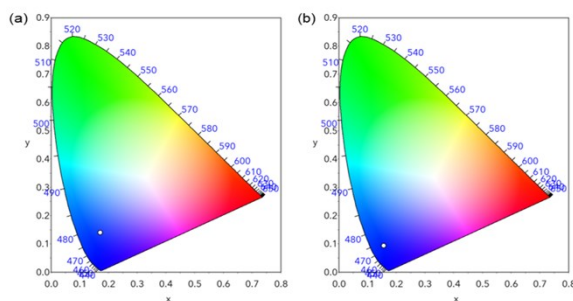


Figure 2. The CIE chromaticity diagrams of: (a) PWB and (b) Ce-PWB excited at 376 nm.

4. Conclusions

In this research, Ce-PWB is synthesized through the thermal conversion of Ce-PWA, derived from 12-tungstophosphoric heteropolyacid as the precursor. Notably, cerium, a rare earth metal lanthanide ion, is introduced as a novel dopant for PWB. The

resulting brown crystals of Ce-PWB are formed by heating Ce-PWA in a furnace, with temperatures ranging from room temperature to 650 °C. The obtained results indicate that

doping PWB with Ce³⁺ ions, resulting in Ce-PWB, shifts the emission towards the red region. Additionally, both samples, PWB matrix, and Ce-PWB, emit light in the deep blue range, which indicates their potential application as a blue-emitting source for white light LEDs.

Acknowledgment

This research is funded by the Ministry of Education and Ministry of Science, Technological Development and Innovation, Republic of Serbia, Grants No. 451-03-47/2023-01/200122, 451-03-47/2023-01/200051, 451-03-47/2023-01/200026).

References

- [1] O. Nakamura, J. Kodama, J. Ogino, I. Miyake., *High-conductivity solid proton conductors: dodecamolybdophosphoric acid and dodecatungstophosphoric acid crystals*, Chemistry Letters, 8 (1979) 17-18.
- [2] K.D. Kreuer, M. Hampele, K. Dolde, A. Rabenau., *Proton transport in some heteropolyacidhydrates a single crystal PFG-NMR and conductivity study*, Solid State Ionics, 28-30 (1988) 589–593.
- [3] U.B. Mioč, M.R. Todorović, M. Davidović, Ph. Colomban, I. Holclajtner-Antunović., *Heteropoly compounds-From proton conductors to biomedical agents*, Solid State Ionics 176 (2005) 3005–3017.
- [4] U.B. Mioč, R.Ž. Dimitrijević, M. Davidović, Z.P. Nedić, M.M. Mitrović, Ph. Colomban., *Thermally induced phase transformations of 12-tungstophosphoric acid 29-hydrate: synthesis and characterization of PW₈O₂₆-type bronzes*, Journal of Materials Science, 29 (1994) 3705–3718.
- [5] R.Ž. Dimitrijević, Ph. Colomban, U.B. Mioč, Z. Nedić, M.R. Todorović, N. Tjapkin, M. Davidović., *Synthesis, conductivity and structural characterization of phosphorous bronzes originating from heteropolyacids. Relation with similar proton containing phases*, Solid State Ionics, 77 (1995) 250–256.
- [6] T. Maksimović, J. Maksimović, Lj. Joksović, Z. Nedić, M. Pagnacco., *Oscillatory reaction as a system detector for doped and undoped phosphate tungsten bronzes*, Hemijska Industrija, 72 (2018) 275-283.
- [7] T.V. Maksimović, J.P. Maksimović, P.I. Tančić, N.I. Potkonjak, Z.P. Nedić, Lj.G. Joksović, M.C. Pagnacco., *A Possible Connection between Phosphate Tungsten Bronzes Properties and Briggs-Rauscher Oscillatory Reaction Response*, Science of Sintering, 53 (2021) 223-235.
- [8] P. Roussel, O. Pérez, Ph.Labbé., *Phosphate tungsten bronze series: crystallographic and structural properties of low-dimensional conductors*, Acta Crystallographica Section B, 57 (2005) 603–632.
- [9] K. Wasserman, M.T. Pope, M. Salmen, J.N. Dann, H.J. Lunk., *Thermal Degradation of Polyoxotungstates - An Effective Method for the Preparation of Tungsten Bronzes*, Journal of Solid State Chemistry, 149 (2000) 378–383.
- [10] U. Mioč, Ph. Colomban, A. Novak., *Infrared and Raman study of some heteropoly acid hydrates*, Journal of Molecular Structure, 218 (1990) 123-128.

The comparison of two methods used to observe a nonlinear system: potentiometry and holography

Marina Simović Pavlović¹, Tijana Maksimović^{2,*}, Jelena Maksimović³, Maja Pagnacco⁴

¹ University of Belgrade, Faculty of Mechanical Engineering, Kraljice Marije 16, Belgrade, Serbia; e-mail: simovicmarina99@gmail.com

² University of Kragujevac, Faculty of science, Radoja Domanovića 12, Kragujevac, Serbia; e-mail: tijana.maksimovic@pmf.kg.ac.rs

³ University of Belgrade, Faculty of physical chemistry, Studentski trg 12-16, Belgrade, Serbia; e-mail: jelena.maksimovic@ffh.bg.ac.rs

⁴ University of Belgrade, Institute of Chemistry, Technology and Metallurgy, Njegoševa 12, Belgrade, Serbia; e-mail: maja.pagnacco@ihmtm.bg.ac.rs

* Corresponding author

DOI: 10.46793/ICCB23.164SP

Abstract: The transition from state I (characterized by low iodide and iodine concentration) to state II (high iodide and iodine concentration) occurs in a nonlinear Briggs-Rauscher (BR) oscillatory reaction. This transition was studied by two methods: potentiometric and holographic. The first derivative technique was applied to the obtained electrochemical and holographic curves of the transition state I→state II to obtain the corresponding slopes. Based on these slopes, the results of the two methods are compared. The obtained holographic slope for the transition from state I to state II is higher than the potentiometric one in all selected reaction sections. In the initial phase of the transition from state I to state II, it is clear that the velocity of the holographic method is twice that of the potentiometric method. While this trend shows a twofold increase at the beginning of the phase transition, it deviates in the other phases, where the holographic measurements show a 1.5-fold higher rate in the middle. The obtained results could have a strong impact on the study of nonlinear systems in the future.

Keywords: oscillatory reaction, nonlinear chemical system, state I to state II transition, potentiometry, holography

1. Introduction

Some established methods are used to measure nonlinear systems, such as chemical oscillatory reactions. One of the commonly used methods is the potentiometric method [1], which measures the electric potential (and throughout the Nernst equation concentration of certain species). This is of particular importance in terms of the Briggs-Rauscher (BR) oscillatory chemical reaction [2] and therein state I to state II transitions, which are followed by phase transition - solid iodine observation [3]. Due to BR oscillatory reaction having plenty of oxide-redox species, there is no general agreement

concerning the potential determining redox pair for a working electrode in the BR reaction [4].

The researchers compared the commonly used method with the innovative possibility of holographic monitoring of the state I to state II transitions in BR oscillatory reaction [5,6]. The holographic method uses laser light to monitor nano-level system dynamics. Depending on the laser wavelength, the classical disturbance of the system could be avoided, which is one of the advantages of this method.

This work uses math to measure outcomes from both potentiometric and holographic methods.

2. Methods

For the investigation of the BR reaction, two completely different methods were used: a potentiometric method as a representative for methods to observe state I to state II transition in BR reaction, and holography as a contemporary method for monitoring this kind of nonlinear systems.

2.1 Potentiometric method

The potentiometric method measures and compares the potential between two electrodes, namely the reference electrode with a known potential and the working electrode (usually Pt or iodide ion-selective electrode) immersed in BR solution. See Figure 1.

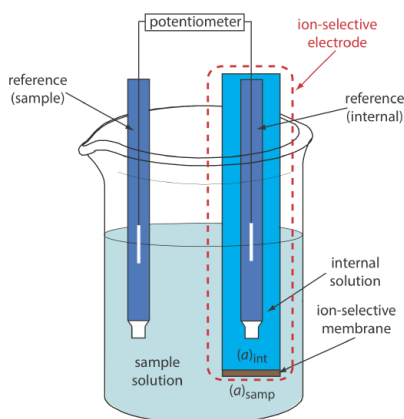


Figure 1. The potentiometric method with iodide ion-selective and reference electrodes immersed. In this investigation iodide ion-selective and Ag/AgCl, as working and reference electrodes are used, respectively.

The concentrations of BR reactants and reaction volume are the same as in reference [3], with one exception, the temperature is maintained at 25 °C.

2.2 Holographic method

The researchers outline the optical scheme and detailed procedure for monitoring the state I to state II transition in BR reaction by the holographic method elsewhere [5,6].

3. Results and discussion

The comparison of different methods (potentiometric and holographic) at the beginning, and in the middle of state I→state II phase transition, is done. Below is a palette of standardized diagrams to provide the possibility of comparing two methods for phase transition - solid iodine observation. To compare the rate of overall process measuring, we simply applied the first derivate technique (and determined the slope) for both (Figure 2). To be precise, we compared the tangent slopes gained with two described methods in different parts of the reaction. Figures 2A-2D for the state I to state II transitions in BR reaction are obtained from the conversion of potentiometric and holographic diagrams explained in detail in reference [6].

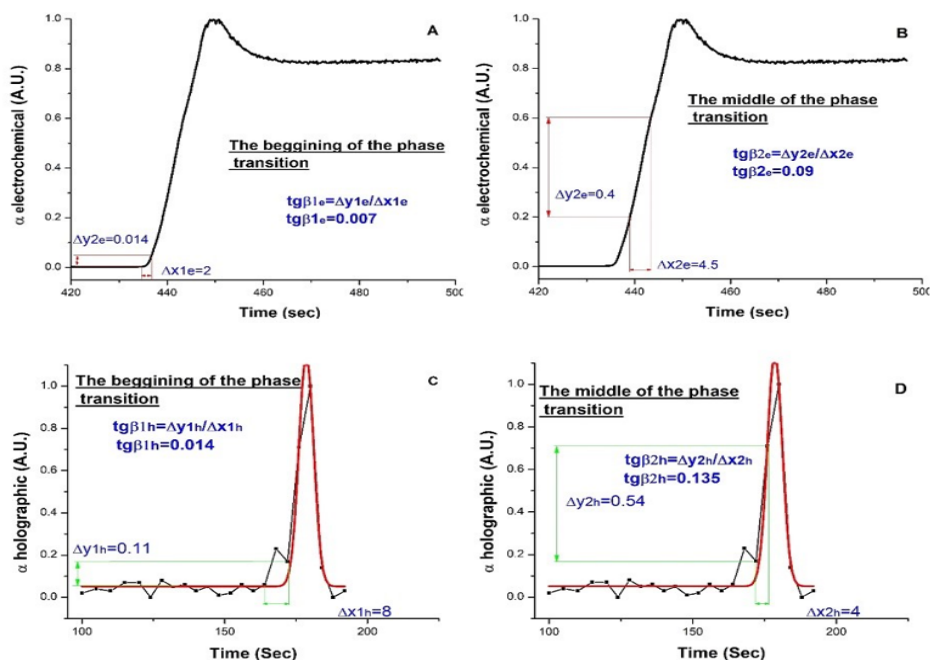


Figure 2. Graphical representation of the comparative use of two measurement methods: Potentiometric measurement of the beginning (A) and the middle (B) of the phase transition; Holographic measurement of the beginning (C) and the middle (D) of the phase transition. As it is known the transition is irreproducible and therefore does not start at the same time for both methods applied.

Here, we see that the speed of the holographic method is twice as high as the potentiometric method in the beginning of the state I to state II transition. This trend is not preserved during all phase transition (at the beginning it is twice as high, while in the middle this rate is 1.5 higher for holographic measurements). However, the holographic method during all stages of reaction (state I→state II transition) has a larger slope. The results obtained surely open new questions. What is monitored by a holographic method? Do these two methods measure the concentration of the identical reaction species?

Moreover, the holographic method is more sensitive and faster, which could have the strong influence in the investigation of oscillatory reactions and, in general, nonlinear systems, in the future.

4. Conclusions

Sometimes, it is very important to implement different scientific techniques to get more information about the investigated system. In this paper, the state I to state II transition in nonlinear Briggs-Rauscher oscillatory reaction was followed by two different methods: potentiometric and holographic. The technique of the first derivative was applied on obtained electrochemical and holographic curves of the state I→state II transition. The holographic curves during all stages of the transition have a larger slope, indicating a more sensitive and faster technique. Results found could have strong influence in the investigation of nonlinear systems in the future and require further investigations.

Acknowledgment

M.S.P. and M.P. acknowledge the support of the Office of Naval Research Global through the Research Grant N62902-22-1-2024. Authors acknowledges support from the Ministry of Education, Science and Technological Development of the Republic of Serbia (Grant No.451-03-47/2023-01/200026, 451-03-47/2023-01/200146,451-03-47/2023-01/200122).

References

- [1] E. Lindner, B.D. Pendley., *A tutorial on the application of ion-selective electrode potentiometry: An analytical method with unique qualities, unexplored opportunities and potential pitfalls*; *Tutorial, Analytica Chimica Acta*, 762 (2013) 1-13.
- [2] T. Briggs, W. Rauscher, Warren, *An Oscillating Iodine Clock*, *J. Chem. Educ.* 50 (1973): 496-496.
- [3] M.C. Pagnacco, J. P. Maksimovic, N.I. Potkonjak, B.Đ. Božič, A.K. Horvath., *Transition from Low to High Iodide and Iodine Concentration States in the Briggs–Rauscher Reaction: Evidence on Crazy Clock Behavior*, *The Journal of Physical Chemistry A*, 122 (2018) 482-491.
- [4] Gábor Holló, Kristóf Kály-Kullai, Thuy Bich Lawson, Zoltan Noszticzius, Maria Wittmann, Norbert Thomas Muntean, Stanley D. Furrow, and Guy E. Schmitz, *Platinum as a HOI/I₂ Redox Electrode and its Mixed Potential in the Oscillatory Briggs-Rauscher Reaction*, *J.Phys.Chem* 121 (2017) 429-439.
- [5] M. Simovic-Pavlovic, M.C. Pagnacco, D. Grujic, B. Bokic, D. Vasiljevic, S. Mouchet, T. Verbiest, B. Kolaric., *Uncovering Hidden Dynamics of Natural Photonic Structures using Holographic Imaging*, *J. Vis. Exp.* (2022) No. e63676.
- [6] M.C. Pagnacco, M. Simovic-Pavlovic, D. Grujic, D. Vasiljevic, B. Bokic, S. Mouchet, T. Verbiest, Y. Caudano, B. Kolaric., *Stochastic Phase Transition Dynamics in Nonequilibrium System: Holographic Study*, *The Journal of Physical Chemistry C*, 127, (2023) 10821-10825.

Radioactivity levels and health risks associated with Himalayan salt consumption

Jelena M. Stajić^{1*}, Biljana Nikić¹, Sofija Forkapić², Jan Hansman², Emina Mrkalić¹

¹ University of Kragujevac, Institute for Information Technologies, Kragujevac, Department of Science, Jovana Cvijića bb, 34000 Kragujevac, Serbia; e-mail: stajicjelena11052012@gmail.com, bmilenkovic@kg.ac.rs, emina.mrkalic@pmf.kg.ac.rs

² University of Novi Sad, Faculty of Sciences, Department of Physics, Trg Dositeja Obradovića 4, 21000 Novi Sad, Serbia; e-mail: sofija@df.uns.ac.rs, jan.hansman@df.uns.ac.rs

* Corresponding author

DOI: 10.46793/ICCB23.168S

Abstract: Table salt commonly refers to a refined salt containing primarily sodium chloride. During the refining process, salt is often treated with chemicals to remove all impurities and also to achieve the desired color and structure of the final product. Himalayan salt is usually less processed than regular refined table salt and may contain trace nutrients and minerals which are assumed to provide various health benefits. However, some of these impurities (such as radionuclides and heavy metals) may also lead to potentially harmful effects. This study was conducted to investigate specific activities of natural radionuclides in five different samples of Himalayan salt available in Serbian markets. Average specific activities \pm standard deviations of ²²⁶Ra, ²³²Th, and ⁴⁰K were 1.4 ± 0.2 , 0.5 ± 0.3 , and 113 ± 48 Bq kg⁻¹, respectively. The annual effective doses from radionuclides and radiological risks were estimated. The results indicate that Himalayan salt consumption is radiologically safe in all age groups.

Keywords: Himalayan salt, natural radionuclides, annual effective doses, lifetime cancer risk

1. Introduction

Himalayan salt extracted from mines in the Himalayas is often promoted as being healthier than conventional refined table salt due to the higher content of trace nutrients and minerals which are beneficial for the human body. However, health benefits of Himalayan salt have been brought to question due to the potential presence of certain impurities such as radioactive elements. This study aims to estimate radiological health risks associated with Himalayan salt consumed in Serbia.

2. Materials and methods

Samples of the five most frequently consumed types of Himalayan salt (provided by different suppliers) were purchased from well-known markets in Kragujevac City. Samples were sealed in 450 mL Marinelli beakers for a month to achieve radioactive equilibrium between ²²⁶Ra and its progeny. Specific activities were measured using

coaxial HPGe detector (GEM30-70 ORTEC with 30% relative efficiency and 1.65 keV FWHM for ⁶⁰Co at 1.33 MeV) enclosed in a 10 cm lead shield to reduce the background. Measurement of each salt sample lasted for 48 h. The energies of photopeaks used for the estimation of specific activities of radionuclides are listed in Table 1.

Table 1. Gamma lines commonly used for measurement of specific activities of radionuclides.

Radionuclide	Progeny	Gamma energy [keV]	Intensity [%]
²²⁶ Ra	²¹⁴ Pb	351.9	37.1
	²¹⁴ Bi	609.3	46.1
	²¹⁴ Bi	1764.5	15.9
²³² Th	²²⁸ Ac	338.3	12
	²²⁸ Ac	911.1	29
	²²⁸ Ac	968.9	17.5
	²⁰⁸ Tl	338.3	86
	²⁰⁸ Tl	860.6	12
⁴⁰ K		1460.7	10.7

3. Results and discussion

Specific activities of natural radionuclides measured in salt are presented in Fig. 1. The average values obtained for ²²⁶Ra, ²³²Th, and ⁴⁰K were 1.4, 0.5, and 113 Bq kg⁻¹, respectively. Specific activities of ²²⁶Ra were slightly higher than those of ²³²Th in all samples, but both these radionuclides were detected in rather low concentrations. On the contrary, specific activity of ⁴⁰K ranged between 78 and 195 Bq kg⁻¹.

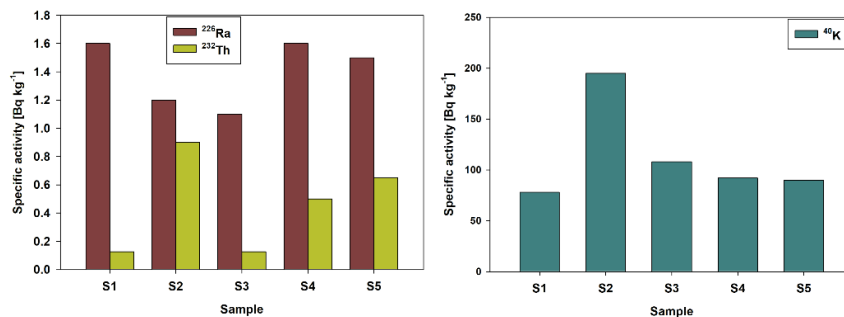


Figure 1. Specific activities of natural radionuclides in Himalayan salts.

Annual effective dose (AED) due to ingestion of natural radionuclide R in salt was calculated using the following equation [1-3]:

$$AED_R = A_R \times I \times F_R \tag{1}$$

where A_R is the specific activity of radionuclide R (in Bq kg⁻¹), I is the annual intake of salt, and F_R is the dose conversion factor (Sv Bq⁻¹) for ²²⁶Ra, ²³²Th, and ⁴⁰K given in [2, 4] for four age groups (children: 2–7y, 7–12y, 12–17y; adults: >17y). The results of calculating AED are presented in Table 2 for ²²⁶Ra, ²³²Th, and ⁴⁰K as well as total AED obtained by summing individual contributions of all three radionuclides. Although specific activities of ⁴⁰K are rather high compared to ²²⁶Ra, the annual effective doses from ²²⁶Ra are higher than those from ⁴⁰K in certain age groups. The lowest values of total AED were estimated for adults (>17y).

The radiological risk associated with consumption of radionuclide R in salt was calculated using the following equation [1-3]:

$$Risk_R = D_{intR} \times SF_R \times t \tag{2}$$

where D_{intR} is the average daily intake of radionuclide R (in pCi day⁻¹), SF is the slope risk factor of each radionuclide (in pCi⁻¹), and t is exposure duration (in days). The slope risk factors used for ²²⁶Ra, ²³²Th and ⁴⁰K were 5.14×10⁻¹⁰, 1.33×10⁻¹⁰ and 3.43×10⁻¹¹ pCi⁻¹, respectively [2, 5]. The exposure duration was taken as 5 y (= 1825 days) for 2-7 years group, 10 years (= 3650 days) for 7-12 y group, 15 years (= 5475 days) for 12-17 y group, and 70 years (= 25550 days) for adults (>17y) [2, 4]. The average daily intake of radionuclide R can be obtained by the following equation [2]:

$$D_{intR} \left(\frac{pCi}{day} \right) = \frac{A_R \times I}{365} \times 27.027 \tag{3}$$

where factor 27.027 appears due to the conversion from Bq to pCi; A_R and I have already been defined above.

Table 2. Annual effective doses, total annual effective doses, and total radiological health risk.

		S1	S2	S3	S4	S5	
AED [μSv y ⁻¹]	2 - 7 y	²²⁶ Ra	1.81	1.36	1.24	1.81	1.70
		²³² Th	0.08	0.57	0.08	0.32	0.42
		⁴⁰ K	2.99	7.47	4.14	3.53	3.45
	7 - 12 y	²²⁶ Ra	2.34	1.75	1.61	2.34	2.19
		²³² Th	0.07	0.48	0.07	0.26	0.34
		⁴⁰ K	1.85	4.63	2.56	2.18	2.14
	12 - 17 y	²²⁶ Ra	4.38	3.29	3.01	4.38	4.11
		²³² Th	0.06	0.41	0.06	0.23	0.30
		⁴⁰ K	1.08	2.70	1.50	1.28	1.25
	>17 y	²²⁶ Ra	0.82	0.61	0.56	0.82	0.77
		²³² Th	0.05	0.38	0.05	0.21	0.27
		⁴⁰ K	0.88	2.21	1.22	1.04	1.02
Total AED [μSv y ⁻¹]	2 - 7 y	4.88	9.41	5.46	5.66	5.56	
	7 - 12 y	4.25	6.85	4.23	4.78	4.67	
	12 - 17 y	5.52	6.40	4.57	5.88	5.65	
	>17 y	1.75	3.20	1.84	2.07	2.06	
Total Risk [×10 ⁻⁶]	2 - 7 y	0.87	1.83	1.06	1.00	0.97	
	7 - 12 y	1.73	3.66	2.11	1.99	1.95	
	12 - 17 y	2.60	5.49	3.17	2.99	2.92	
	>17 y	12.13	25.64	14.80	13.96	13.62	

Table 2 presents the values of total risk from radionuclides in salt. Average total risk is 1.15×10⁻⁶ (for 2-7y age group), 2.29×10⁻⁶ (for 7-12y age group), 3.44×10⁻⁶ (for 12-17y age group), and 16.03×10⁻⁶ (for adults). All these values are lower than the recommended limit of 1×10⁻⁴ – 1×10⁻⁶ reported by USEPA [6]. It is important to indicate that all doses and risks presented here were calculated assuming salt intake of 5 g per day (i.e., 1.825 kg y⁻¹) which is recommended by The World Health Organization [7]. However, the studies conducted by Jovičić-Bata in Novi Sad [8] indicate that the real intake of salt in the Serbian population exceeds the WHO recommendation by double (or even more). Therefore, the real radiological risk from

Himalayan salt consumption can be higher than the estimated values, but probably still within the acceptable limits.

3. Conclusions

The Himalayan salts investigated in the study contain low levels of natural radionuclides and their consumption can be considered radiologically safe in all age groups.

Acknowledgment

This research is funded by Ministry of Science, Technological Development and Innovation of the Republic of Serbia, Grants: No. 451-03-47/2023-01/200378.

References

- [1] E. Jemii, T. Alharbi, *Measurements of natural radioactivity in infant formula and radiological risk assessment*, *Journal of Radioanalytical and Nuclear Chemistry*, **315** (2018) 157-161.
- [2] O.S. Ameh, H. Tuwilika, C. Kamunda, A. James, H. Markus, J. Kennedy, *Annual effective dose and radiological risk assessment from selected salt pans from the lagoon of Erongo region, Namibia*. *International Journal of Applied Science and Engineering*, 19 (2022) 2021067.
- [3] W. Poltabtim, K. Saenboonruang, *Assessment of activity concentrations and their associated radiological health risks in commercial infant formulas in Thailand*. *Chiang Mai Journal of Science*, 46 (2019) 778-786.
- [4] ICRP, 2012. *Compendium of dose coefficients based on ICRP Publication 60*. ICRP Publication 119. Ann. ICRP 41(Suppl.).
- [5] O.B. Uwatse, M.A. Olatunji, M.U. Khandaker, Y.M. Amin, D.A. Bradley, M.K. Alkhorayef, K. Alzimami, *Measurement of natural and artificial radioactivity in infant powdered milk and estimation of the corresponding annual effective dose*. *Environmental Engineering Science* 32 (2015) 838-846.
- [6] USEPA. 1991. *Role of the Baseline Risk Assessment in Superfund Remedy Selection Decisions* (Memorandum from D. R. Clay, OSWER 9355.0-30, April 1991). Washington DC: US Environmental Protection Agency.
- [7] WHO. 2012. *Guideline: Sodium intake for adults and children*. Geneva, World Health Organization.
- [8] J. Jovičić-Bata, M. Grujičić, S. Rađen, B. Novaković, *Sodium intake and dietary sources of sodium in a sample of undergraduate students from Novi Sad, Serbia*. *Vojnosanitetski Pregled* 73 (2016) 651-656.

Prevalence of radon and metals in natural springs in the Sokobanja area

Biljana Vučković¹, Ivana Penjišević², Nataša Todorović³, Jovana Nikolov³, Ljiljana Gulan¹, Jelena M. Stajić^{4*}, Biljana Nikić⁴

¹University of Pristina in Kosovska Mitrovica, Faculty of Sciences and Mathematics, Department of Physics, Lole Ribara 29, 38220 Kosovska Mitrovica, Serbia; e-mail: biljana.vuckovic@pr.ac.rs, ljiljana.gulan@pr.ac.rs

²University of Pristina in Kosovska Mitrovica, Faculty of Sciences and Mathematics, Department of Geography, Lole Ribara 29, 38220 Kosovska Mitrovica, Serbia; e-mail: ivana.penjisevic@pr.ac.rs

³University of Novi Sad, Faculty of Science, Department of Physics, Trg Dositeja Obradovica 4, 21000 Novi Sad, Serbia; e-mail: natasa.todorovic@df.uns.ac.rs, jovana.nikolov@df.uns.ac.rs

⁴Institute for Information Technologies Kragujevac, Jovana Cvijića bb, 34000 Kragujevac, Serbia; e-mail: stajicjelena11052012@gmail.com, bmilenkovic@kg.ac.rs

* Corresponding author

DOI: 10.46793/ICCB23.172V

Abstract: In this study, radon concentrations in natural springs were measured at 9 locations in the area of Sokobanja, using a RAD-7 radon monitoring system (DURRIDGE Co., USA). The average value of radon concentration was 19.6 Bq/l. Annual effective doses due to ingestion and inhalation of radon in water were calculated. Concentrations of metals were measured using the ICP OES technique by EPA 200.7:1994 method and their mean values were: Ca - 80.8 mg/l, Na - 8.7 mg/l, Mg - 8.6 mg/l, K - 1.8 mg/l and Pb - 0.002 mg/l. Based on the results obtained in the study and the reference levels recommended for the parameters under consideration, water from Sokobanja natural sources can be considered safe for drinking.

Keywords: water, radon, heavy metals, health risk, Sokobanja

1. Introduction

Radioactive gas radon is a direct product of the decay of radium, characterized by its high solubility in water. According to the decision of the World Health Organization, the reference level of radon in drinking water is 100 Bq/l [1], while the reference level of radon in drinking water set by the United States Environmental Protection Agency is 11.1 Bq/l [2]. Heavy metals exist in the environment naturally as trace elements in rocks and soils and also in natural waters. When taken into the organism, they adhere to

enzymes, inhibiting their function, where they can cause numerous physiological and neurological consequences [3].

This paper presents the results of testing the presence of radon and metals in natural mineral spring waters at 9 locations in the Sokobanja area, in order to assess whether their levels can have a negative impact on public health.

2. Material and methods

Sampling waters. Water was sampled in two bottles from each site, one for radon detection and the other for heavy metals detection. The bottles were closed and the exact time, date and place of sampling were marked following the recommendation rules from the Policy book of the Republic of Serbia [4].

Detection of radon. Detection of radon was conducted at the Laboratory for Testing Radioactivity of Samples and Doses of Ionizing and Non-Ionizing Radiation, at the Faculty of Sciences, University of Novi Sad. Radon concentration in mineral water samples was determined using the RAD H₂O system (Durrige Co.) [5].

Detection of metals. Analysis of metals in water samples was carried out in the laboratory for testing the quality and healthiness of foodstuffs and items of general use „Institute Topčider“, Jugoinspekt Beograd ad. Concentrations of metals were measured using ICP OES technique by EPA 200.7:1994 method [6].

3. Results and discussion

Table 1 presents the summarized values of the investigated parameters in this area, as well as their maximum allowed values.

Table 1. Summarized results of this research in the Sokobanja area.

	C _{Rn} (Bq/l)	Ca (mg/l)	K (mg/l)	Mg (mg/l)	Na (mg/l)	Pb (mg/l)
Max	111	92.0	5.8	14.0	25.1	0.005
Average value	19.6	80.8	1.8	8.6	8.7	0.002
Min	1.2	75.3	0.5	1.8	1.3	0.001
Refer. levels	100	Max 200	Max 12	Max 50	Max 200	Max 0.01

Metals. Based on the summarized results, the mean values of measured elements are as follows: for calcium - 80.8 mg/l, for potassium - 1.8 mg/l, for magnesium - 8.6 mg/l, for sodium - 8.7 mg/l and for lead - 0.002 mg/l. The values of analyzed contents of metals were far below in terms of values given by the EU Directive [7] and related to the Policy about the quality and other requests for natural, mineral, and table water [4].

Radon. The mean value of radon concentration in water from 9 selected locations is 19.6±4.5 Bq/l, which is below the recommended value of 100 Bq/l. The recommended value of 100 Bq/l was slightly exceeded in only one sample. However, EU Council Directive [8] establishes parametric values between 100 and 1000 Bq l⁻¹ in the EU

countries. Therefore, it can be considered that the water from Sokobanja natural sources is radiologically safe and can be used for drinking.

Doses from radon. Annual effective doses due to ingestion and inhalation of radon in water were calculated using the following two equations, respectively [9, 10]:

$$AED_{ing} = C_{Rn} \times A_i \times D_{f(ing)} \quad (1)$$

$$AED_{inh} = C_{Rn} \times R \times T \times F \times D_{f(inh)} \quad (2)$$

where C_{Rn} is radon activity concentration in water; $D_{f(ing)}$ and $D_{f(inh)}$ are dose conversion factors for radon ingestion and radon inhalation, respectively; A_i is the annual water intake; T is indoor occupancy time, R is the ratio of radon in air to radon in water, F is the equilibrium factor between radon and its progeny.

The results of radon dose calculation are presented in Table 2. Average annual effective doses from radon ingestion were estimated to be in the range of 6 – 590 $\mu\text{Sv/y}$ for infants, 2 – 216 $\mu\text{Sv/y}$ for children, and 3 – 284 $\mu\text{Sv/y}$ for adults. Annual effective doses from radon inhalation ranged between 3 and 280 $\mu\text{Sv/y}$.

Table 2. Annual effective doses from radon ingestion and inhalation.

Sample	AED_{ing} [$\mu\text{Sv/y}$]			AED_{inh} [$\mu\text{Sv/y}$]
	Infants	Children	Adults	
1	590	216	284	280
2	93	34	45	44
3	6	2	3	3
4	37	14	18	18
5	17	6	8	8
6	47	17	22	22
7	74	27	36	35
8	16	6	8	8
9	54	20	26	26

4. Conclusions

The mean value of radon concentration in water from 9 selected locations is 19.6 ± 4.5 Bq/l, which is below the recommended value of 100 Bq/l. The concentrations of heavy metals are below the recommended values and their mean values are as follows: Ca - 80.8 mg/l, K - 1.8 mg/l, Mg - 8.6 mg/l, Na - 8.7 mg/l, and Pb - 0.002 mg/l. Average annual effective doses from radon ingestion were 103.5, 38.1, and 50 $\mu\text{Sv/y}$ for infants, children, and adults, respectively, while the average annual effective dose from inhalation was estimated to be 49.3 $\mu\text{Sv/y}$. Accordingly, water from Sokobanja natural sources is radiologically safe and can be used for drinking.

Acknowledgment

The authors wish to thank the Faculty of Sciences and Mathematics, University of Pristina in Kosovska Mitrovica for the support to realize this research. The work was supported by The Ministry of Science, Technological Development and Innovation of the Republic of Serbia (451-03-47/2023-01/200378, 451-03-47/2023-01/200123).

References

- [1] WHO, World Health Organization. (2004). Guidelines for drinking water quality. 3rd ed. WHO Press, Geneva.
- [2] USEPA, US Environmental Protection Agency (1999). Radon in drinking water health risk reduction and cost analysis. EPA Federal Register 64 (USEPA, Office of Radiation Programs), Washington, DC.
- [3] F. Zhang, Z. Wang, H. Cheng, X. Ly, W. Gong, X. Wang, G. Zhang., *Seasonal variations and chemical characteristics of PM_{2.5} in Wuhan, central China*, Science of The Total Environment, 518–519 (2015) 97–105.
- [4] Official Gazette Regulation on hygienic quality of drinking water 42/98, 44/99 and 28/2019. <https://www.pravno-informacionisistem.rs/SlGlasnikPortal/eli/rep/slsrj/ministarstva/pravilnik/1998/42/2/reg> (in Serbian)
- [5] RAD7 RAD H₂O, Radon in Water Accessory (DURRIDGE Co., USA, 2012).
- [6] USEPA, US Environmental Protection Agency (1982). Inductively Coupled Plasma- Atomic Emission Spectrometric Method for Trace Element Analysis of Water and Wastes-Method 200.7, Dec. 1982. EPA-600/4-79-020, Determination of metals and trace elements in water and wates by inductively coupled plasma – atomic emission spectrometry Methods 200.7
- [7] EU Directive 98/83/EC. Council Directive of 3 November 1998 on the quality of water intended for human consumption. Of. J. Eur. Union L330/32 5/12/1998 (1998).
- [8] Council Directive 2013/51/EUROATOM laying down requirements for the protection of the health of the general public with regard to radioactive substances in water intended for human consumption, Official Journal of the European Union, European Commission, Brussels, 2013. <https://www.fao.org/faolex/results/details/en/c/LEX-FAOC128382/>
- [9] UNSCEAR, 2000. United Nations Scientific Committee on the Effects of Atomic Radiations. Sources and Effects of Ionizing Radiation, Report to the General Assembly, with Scientific Annexes, Volume I: Sources. United Nations, New York.
- [10] V. Duggal, S. Sharma, R. Mehra. *Risk assessment of radon in drinking water in Khetri Copper Belt of Rajasthan, India*. Chemosphere 239 (2020) 124782.

Investigation of the possibility of interaction between lithium fluoride clusters and boron using LDI MS

F. Veljkovic¹, D. Drakulic², A. Todorovic², S. Pejic², K. Bobic^{2*}, I. Stajcic¹, S. Pajovic², S. Velickovic¹

¹ University of Belgrade, Department for Physical Chemistry, VINČA Institute of Nuclear Sciences - National Institute of the Republic of Serbia, Mike Petrovića Alasa 12-14, Belgrade, Republic of Serbia; e-mail: filipveljkovic@vin.bg.ac.rs, vsuzana@vin.bg.ac.rs, ivana_r@vin.bg.ac.rs

² University of Belgrade, Department for Molecular Biology and Endocrinology, VINČA Institute of Nuclear Sciences - National Institute of the Republic of Serbia, Mike Petrovića Alasa 12-14, Belgrade, Republic of Serbia; e-mail: drakulic@vin.bg.ac.rs, anato@vin.bg.ac.rs, katarina.bobic@vin.bg.ac.rs, snezana@vin.bg.ac.rs, pajovic@vin.bg.ac.rs

* Corresponding author

DOI: 10.46793/ICCB23.176V

Abstract: It is known that the “superalkali” cluster Li_2F can significantly improve the hydrogen storage capabilities in carbon materials; boron compounds play a similar role. However, the possibility of interactions of lithium fluoride clusters with boron and hydrogen has not been investigated so far. In this work, a laser desorption/ionization mass spectrometry (LDI MS) was used for this purpose. Preliminary results showed that the interaction between the “superalkali” Li_3F cluster, boron and six hydrogen atoms is possible; the ion $\text{Li}_3\text{FBH}_6^+$ was detected. Non-stoichiometric clusters of lithium fluoride can also combine with boron and hydrogen in the following manner: $\text{Li}_5\text{F}_2\text{BH}_5^+$, $\text{Li}_5\text{F}_3\text{BH}_2^+$, $\text{Li}_4\text{F}_5\text{BH}_4^+$, $\text{Li}_6\text{F}_2\text{B}_6\text{H}^+$, and $\text{Li}_8\text{F}_6\text{H}^+$.

Keywords: “superalkali” clusters, LDI MS, hydrogen storage, boron

1. Introduction

The search for alternative energy sources that do not have a negative impact on environmental pollution is one of the most important issues for humanity today. Hydrogen is recognized as a new economic energy model [1-4]. However, there are many problems that must be overcome to make hydrogen available as a fuel (hydrogen extraction, hydrogen is a highly flammable fuel source, high cost of a unit of hydrogen fuel cell power, regulatory issues related to the framework that defines commercial deployment models, cost of feedstock, new infrastructure). In the area of basic research, hydrogen storage should be first.

Theoretical and experimental studies have shown that various materials can be used as hydrogen storage, such as nanostructured carbon clusters, boron-based materials,

hydrides and liquid organic carriers, zeolites, clathrates, and others [5-10]. Previous studies have also shown that metal-decorated carbon fullerenes and their boron-substituted nanostructures could be good candidates for the storage of H₂ molecules. For example, it has been discovered that lithium-doped fullerenes, Li_x-C₆₀, with x= 6, 9, 12 efficiently reversibly adsorb H₂. It was also shown that the reversible hydrogen storage of C₆₀ and C₄₈B₁₂ coated with transition metals can be as high as 9 wt%. Additions to the fullerene play a crucial role in the interaction with H₂. The electrostatic interaction between Li (with low ionization energy of 5.39 eV) and H₂ is believed to play an important role in this process [11-13]. Compounds that have lower ionization energy than lithium are "superalkali" clusters of the Li_nF_m type. "Superalkali" clusters are successfully obtained by evaporation of LiF salt in mass spectrometers of various types. Thanks to their low ionization energy, the electrostatic interaction between "superalkali" clusters and hydrogen is expected to be stronger than that of alkali metals [14]. In accordance with that theoretical studies have shown that fullerene doped with Li₂F-type "superalkali" clusters (10.86 wt%) is more efficient than Li_x-C₆₀ in hydrogen storage [15]. On the other hand, lithium-decorated diborene and diboryne clusters can trap H₂ molecules by ion-quadrupole and ion-induced dipole interactions, making these systems well suited for hydrogen storage [16]. However, the interaction between "superalkali" clusters, B and hydrogen has not yet been studied. Therefore, in this work we have investigated the LiF/B system using the LDI MS.

2. Experimental

Results were obtained using a commercially available matrix-assisted laser desorption/ionization mass spectrometer (MALDI MS), Voyager- DE PRO (Sciex, USA) equipped with a time-of-flight (TOF) mass analyzer and operating in linear or reflector mode as standard. A nitrogen laser (with 20 Hz pulse frequency, a wavelength of 337 nm, and pulse duration of 3 ns) was installed in this mass spectrometer. Other instrumental parameters were: Accelerating voltage 25000 V, grid voltage 85%, laser intensity 3300 a.u. and number of laser beats 200, with a delayed extraction time of 100 ns. Mass spectra were recorded in positive reflectron mode.

The sample was a suspension of LiF:B (1:5 ratio) in 50 µl of deionized water; 1 µl of the sample was applied directly to a stainless steel plate and dried at room temperature before being introduced to the mass spectrometer. No additional hydrogen source was used in these experimental conditions.

3. Results and discussion

The LDI mass spectrum of LiF/B in positive mode is shown in Figure 1. The identification of the peaks recorded in Figure 1 was done in the following way: *m/z* 55.17, 56.17, 57.17 correspond to Li₃FBH₆⁺ (calculated 55.10, 56.11, 57.10); *m/z* 87.15 88.17, 89.17 correspond to Li₅F₂BH₅⁺ (calculated 87.13, 88.12, 89.12); *m/z* 103.13, 104.13, 105.13

correspond to $\text{Li}_5\text{F}_3\text{BH}_2^+$ (calculated 103.10, 104.10, 105.10); m/z 136.13, 137.12, 138.12 correspond to $\text{Li}_4\text{F}_5\text{BH}_4^+$ (calculated 136.10, 137.10, 138.10), m/z 144.17, 145.17, 146.17, 147.17, correspond to $\text{Li}_6\text{F}_2\text{B}_6\text{H}^+$ (calculated 144.16, 145.16, 146.16, 147.16); m/z 169.22, 170.18, 171.18 correspond to $\text{Li}_8\text{F}_6\text{H}^+$ (calculated 169.13, 170.13, 171.13).

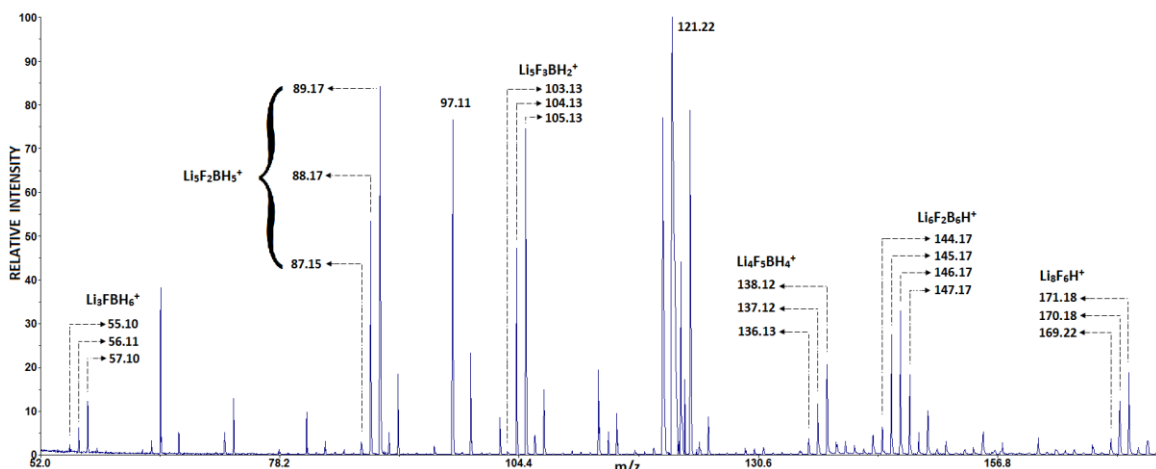


Figure 1. The positive mod LDI mass spectrum of LiF/B.

Preliminary results show that an interaction can occur between the “superalkali” Li_3F cluster and a boron atom and 6 hydrogen atoms. Other lithium fluoride clusters such as Li_5F_2 , Li_5F_3 , and Li_4F_5 also interact with a boron atom and a different number of hydrogen atoms. The Li_6F_2 cluster interacts with 6 boron atoms, while the Li_8F_6 cluster interacts directly with one hydrogen atom.

4. Conclusions

The LDI MS was used to investigate possibilities interaction between clusters lithium fluoride with boron and hydrogen. In this work clusters are detected: $\text{Li}_3\text{FBH}_6^+$ $\text{Li}_5\text{F}_2\text{BH}_5^+$ $\text{Li}_5\text{F}_3\text{BH}_2^+$ $\text{Li}_4\text{F}_5\text{BH}_4^+$ $\text{Li}_6\text{F}_2\text{B}_6\text{H}^+$, and $\text{Li}_8\text{F}_6\text{H}^+$. The results show that “superalkali” clusters Li_3F and non-stoichiometric lithium fluoride clusters can interact with boron and hydrogen atoms.

Acknowledgment

This research is funded by the Ministry of Education and Ministry of Science, Technological Development and Innovation, Republic of Serbia, Grant: No. 451-03-47/2023-01/200017.

References

- [1] W. Lubitz, W. Tumas., *Hydrogen: an overview*, Chemical Reviews., 107 (2007) 3900-3903.
- [2] R. Coontz, B. Hanson., *Not So Simple*, Science, 305 (2004) 957.

- [3] L. Schlapbach, A. Züttel., *Hydrogen-storage materials for mobile applications*, Nature, 414 (2001) 353-358.
- [4] G. W. Crabtree, M. S. Dresselhaus, V. Buchanan., *The hydrogen economy*, Physics Today, 57 (2004) 39-44.
- [5] K.K. Gangu, S. Maddila, S.B.Mukkamala, S.B. Jonnalagadda., *Characteristics of MOF, MWCNT and graphene containing materials for hydrogen storage: A review*, Journal of Energy Chemistry, 30 (2019) 132-144.
- [6] P.C. Rao, M. Yoon., *Potential liquid-organic hydrogen carrier (LOHC) systems: A review on recent progress*, Energies, 13 (2020) 6040.
- [7] X. Yu, Z. Tang, D. Sun, L. Ouyang, M. Zhu., *Recent advances and remaining challenges of nanostructured materials for hydrogen storage applications*, Progress in Materials Science, 88 (2017) 1-48.
- [8] A. Gupta, G.V. Baron, P. Perreault, S. Lenaerts, R.G. Ciocarlan, P. Cool, P.G.M. Mileo, S. Rogge, V. Van Speybroeck, G. Watson, P.V.D. Voort, M. Houllberghs, E. Breynaert, J. Martens, J.F.M. Denayer., *Hydrogen clathrates: Next generation hydrogen storage materials*, Energy Storage Mater, 41 (2021) 69-107.
- [9] G. Moussa, R. Moury, U.B. Demirci, T. Sener, P. Miele., *Boron-based hydrides for chemical hydrogen storage*, International Journal of Energy Research, 37 (2013) 825-842.
- [10] Y. Kojima., *Hydrogen storage materials for hydrogen and energy carriers*, International Journal of Hydrogen Energy, 44 (2019) 18179-18192.
- [11] Q. Sun, P. Jena, Q. Wang, M. Marquez., *First-principles study of hydrogen storage on $Li_{12}C_{60}$* , Journal of the American Chemical Society, 128 (2006) 9741-9745.
- [12] J. A. Teprovich Jr, M. S. Wellons, R. Lascola, S. J. Hwang, P. A. Ward, R. N. Compton, R. Zidan., *Synthesis and characterization of a lithium-doped fullerane ($Li_x-C_{60}-Hy$) for reversible hydrogen storage*, Nano Letters, 12 (2012) 582-589.
- [13] A. Yoshida, T. Okuyama, T. Terada, S. Naito., *Reversible hydrogen storage/release phenomena on lithium fulleride (Li_nC_{60}) and their mechanistic investigation by solid-state NMR spectroscopy*, Journal of Materials Chemistry, 21 (2011) 9480-9482.
- [14] S. Veličković, V. Koteski, J. Belošević Čavor, V. Đorđević, J. Cvetićanin, J. Đustebek, M. Veljković, O. Nešković., *Experimental and theoretical investigation of new hypervalent molecules Li_nF ($n=2-4$)*, Chemical Physics Letters, 448 (2007) 151-155.
- [15] K. Wang, Z. Liu, X. Wang, X. Cui., *Enhancement of hydrogen binding affinity with low ionization energy Li_2F coating on C_{60} to improve hydrogen storage capacity*, International Journal of Hydrogen Energy, 39 (2014) 15639-15645.
- [16] K. Srinivasu, S.K. Ghosh., *Theoretical studies on hydrogen adsorption properties of lithium decorated diborane (B_2H_4Li) and diboryne ($B_2H_2Li_2$)*, International Journal of Hydrogen Energy, 36 (2011) 15681-15688.

In vitro biological effects of clonal red wines

N. Đorđević^{1*}, O. Keta¹, V. Petković¹, N. Todorović Vukotić¹, D. Stanković², V. Tešević³, S. B. Pajović¹

¹ University of Belgrade, Department of Molecular Biology and Endocrinology, “Vinča” Institute of Nuclear Sciences, National Institute of the Republic of Serbia, 12-14 Mike Petrovića Alasa, P.O. Box 522-090, 11000 Belgrade, Serbia; e-mail: neda@vin.bg.ac.rs, otilijak@vin.bg.ac.rs, vladana@vin.bg.ac.rs, nevenat@vin.bg.ac.rs, pajovic@vin.bg.ac.rs

² University of Belgrade, Faculty of Chemistry, Department of Analytical Chemistry, Studentski trg 12-16, 11000 Belgrade, Serbia; e-mail: dalibors@chem.bg.ac.rs

³ University of Belgrade, Faculty of Chemistry, Department of Organic Chemistry, Studentski trg 12-16, 11000 Belgrade, Serbia; e-mail: ytesevic@chem.bg.ac.rs

* Corresponding author

DOI: 10.46793/ICCB23.180DJ

Abstract: This study aimed to determine the phenolic compound content, *in vitro* antioxidative potential, and cytotoxic effects of four red wine samples: a commercial (V) and three clonal wines (V1, V2, and V3). LC/MS-MS, cyclic voltammetry, and MTT assay techniques were employed for this purpose. Results revealed that all wines were rich in phenolic compounds. Clonal wines outperformed the commercial ones in most phenolic compounds (except myricetin). Notably, V2 and V3 showed the highest levels of gallic acid, catechin, and epicatechin. Among them, V3 exhibited superior antioxidative activity. The MTT assay demonstrated stronger cytotoxic effects of the wine samples on pancreas (Bx-PC3) and colon (HT29) carcinoma cells (47% to 16% and 27% to 7% compared to control, respectively) than on the normal lung fibroblasts (MRC-5) cell line (106% to 77%). It can be concluded that HT29 cells were more sensitive than Bx-PC3 cells. Finally, both clonal and commercial wines serve as valuable sources of polyphenolic compounds, which could have a significant role in preventing cancer and diseases related to oxidative stress.

Keywords: red wine, polyphenols, LC-MS/MS, cyclic voltammetry, cytotoxic activity

1. Introduction

Red wine, an enchanting elixir crafted from dark-colored grape varieties, holds a rich history in human culture, spanning millennia. Within this exquisite beverage lie wine polyphenols, a diverse group of compounds found in grapes and thus, infused into wine. These compounds play pivotal roles in shaping the wine's color, flavor, mouthfeel, and potential health benefits. Major categories of wine polyphenols encompass flavonoids (like anthocyanins and flavonols), phenolic acids, stilbenes (including the renowned resveratrol), and tannins [1]. Their composition varies based on grape variety, winemaking techniques, and aging processes. An important facet of these polyphenols is

their antioxidant function in wine, which aids in countering free radicals and mitigating oxidative stress [2]. This contributes to wine's potential health advantages. Despite advancements in cancer therapies, cancer remains a leading cause of death with limited lifespan extensions and significant side effects. This underscores the urgency of exploring effective cancer prevention strategies, where natural products like red wine have gained attention for their potential in cancer prevention [3]. Research focuses on wine polyphenols, particularly resveratrol, to comprehend their impact on carcinogenesis stages and anticancer efficacy.

The objective of this paper was to examine phenolic content and *in vitro* antioxidative activity of commercial and clonal Vranac red wine, vintage 2010. Furthermore, this paper analyses cytotoxic activity of the mentioned samples against normal lung fibroblasts (MRC5), as well as two carcinoma cell lines, pancreas and colon (Bx-PC3 and HT29, respectively).

2. Materials and methods

The samples of Montenegrin Vranac wines, commercial wine (V) and three clonal wines (V1, V2 and V3) vintage 2010, were analysed. The content of nine phenolic compounds was determined by liquid chromatography – tandem mass spectrometry (LC–MS/MS) using LC system (Waters Acquity UPLC H-Class; WAT176015007; Milford, MA USA) with ultraviolet detector (Waters 2998 PDA), coupled to MS (Waters TQ, WAT-176001263) [4]. Quantification of phenolic compounds was done using appropriate standards. *In vitro* antioxidant capacity was assessed by cyclic voltammetry using a CHI760 B instrument (CHIInstruments, Austin, Texas, USA) [5]. Cytotoxic activity of analysed wines on MRC5, Bx-PC3 and HT29 cell lines was determined using MTT (3-(4,5-dimethylthiazol-2-yl)-2,5-diphenyltetrazolium bromide) tetrazolium reduction assay after 72h of treatment with different wine volume percentage (2.5, 5 and 10%). Absorbance was measured in an ELISA plate reader (Victor2 1420 Multilabel counter, Wallac, Turku, Finland), at a wavelength of 550 nm, and the obtained results were expressed as percentage of control.

2. Results and discussion

The primary phenolic compound present in all examined wines is gallic acid. As demonstrated in Table 1, the samples labeled as V2 and V3 exhibit the highest concentrations of gallic acid. The observation indicates that, except for myricetin, clonal wines outperform commercial wine as a source of analyzed phenolic compounds. Among these, V2 and V3 samples exhibit the highest concentrations of gallic acid, catechin, and epicatechin. Notably, the cumulative resveratrol content in V1 and V3 wines is nearly twice that found in the commercial wine, as indicated in Table 1.

Table 1. Content of phenolic compounds in analyzed wine samples determined by LC-MS/MS

Phenolic compound	V	V1	V2	V3
Gallic acid	16,41 ± 0,41 ^A	20,81 ± 0,38 ^B	26,48 ± 0,37 ^C	25,87 ± 0,41 ^C
Catechin	7,41 ± 0,22 ^A	9,27 ± 0,14 ^B	12,74 ± 0,10 ^D	11,24 ± 0,15 ^C
Epicatechin	2,96 ± 0,04 ^A	5,69 ± 0,15 ^B	7,09 ± 0,15 ^C	7,16 ± 0,15 ^C
<i>trans</i> -Resveratrol	0,46 ± 0,02 ^A	0,74 ± 0,05 ^B	0,65 ± 0,02 ^B	0,51 ± 0,04 ^A
<i>cis</i> -Resveratrol	0,11 ± 0,01 ^A	0,36 ± 0,01 ^C	0,43 ± 0,02 ^D	0,26 ± 0,02 ^B
<i>trans</i> -Piceid	2,08 ± 0,07 ^A	4,36 ± 0,01 ^C	3,11 ± 0,02 ^B	3,04 ± 0,15 ^B
<i>cis</i> -Piceid	1,84 ± 0,04 ^A	3,31 ± 0,03 ^C	2,89 ± 0,02 ^B	4,81 ± 0,15 ^D
Myricetin	1,32 ± 0,05 ^C	0,58 ± 0,03 ^A	0,92 ± 0,05 ^B	0,99 ± 0,02 ^B
Quercetin	0,82 ± 0,03 ^C	0,27 ± 0,01 ^A	0,40 ± 0,03 ^B	1,06 ± 0,03 ^D

Comm – commercial wine; CI/II/III – clonal wines. All values are represented as mean ± SD (in triplicate). Different letters within each column show statistically significant differences at the level of $p < 0.05$, according to HSD Tukey's test.

In Figure 1(A), the cyclic voltammograms depict the characteristics of the examined wine samples. The cyclic voltammogram of the commercial wine sample displays two distinct anodic peaks occurring at approximately +0.67 and +0.92 V, with a Q600 factor of 2.871. The voltammograms of V1 and V3 wines show an increase in the oxidation current of the second anodic peak with a slight displacement of the peak toward more positive values.

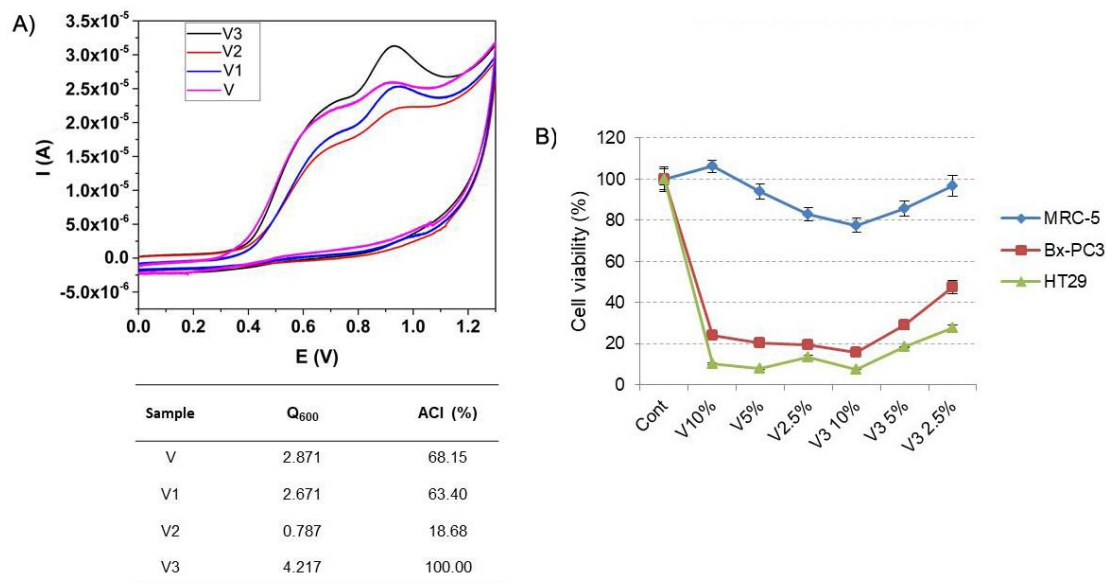


Figure 1. A) Cyclic voltammograms obtained for the analysed wine samples (V, V1, V2 and V3) and B) Cell viability after treatment with different wine volume ratio of commercial wine (V) and clonal wine (V3).

For sample V1, a slight decrease in both the Q600 factor and the ACI index is noticeable. In contrast, the voltammogram of sample V3 reveals a notable increase in

these two parameters, indicating an enhanced antioxidant activity when compared to samples V and V1.

Cytotoxic effect of V and V3 wines was the lowest on MRC-5 cells, ranging between 106% to 77% compared to control cells (Figure 1B). Conversely, the cytotoxic impact on the two cancer cell lines demonstrated higher percentages, reaching 47% to 16% on Bx-PC3, and 27% to 7% on HT29 cells. Notably, the HT29 cells displayed greater sensitivity when compared to Bx-PC3 cells. Additionally, as the volume percentage of V3 wine increased, a corresponding rise in its cytotoxic effect on cancer cells was observed, suggesting a dose-dependent relationship between the volume percentage and cytotoxicity.

3. Conclusions

In summary, both commercial and clonal wines are rich sources of polyphenols that exhibit antioxidative properties *in vitro*. A particularly important result is that the cytotoxic effect of analysed wine on normal cells is far less than on cancer cell lines. The presence of powerful antioxidants in this natural product holds promise for developing effective and low-risk strategies for cancer prevention. By understanding the mechanisms and potential benefits of red wine polyphenols, researchers aim to pave the way for innovative and safer approaches to combatting cancer and improving patient outcomes.

Acknowledgment

This research is funded by the Ministry of Education and Ministry of Science, Technological Development and Innovation, Republic of Serbia (Research Grant No. 451-03-47/2023-01/200017).

References

- [1] I. Buljeta, A. Pichler, J. Šimunović, M. Kopjar., *Viscous resistance to blood flow in solid tumors: Effect of hematocrit on intratumor blood viscosity Beneficial effects of red wine polyphenols on human health: Comprehensive Review*, Current Issue in Molecular Biology, 45 (2023) 782-798.
- [2] D. Pintać, K. Bekvalac, N. Mimica-Dukić, M. Rašeta, N. Anđelić, M. Lesjak, D. Orčić., *Comparison study between popular brands of coffee, tea and red wine regarding polyphenols content and antioxidant activity*, Food Chemistry Advances, Vol. 1, (2022)100030.
- [3] C. Rodríguez-García, C. Sánchez-Quesada, J. J. Gaforio., *Dietary flavonoids as cancer chemopreventive agents: An update review of human studies*, Antioxidants, 8 (2019) 137.
- [4] N. Đorđević, M. Novaković, B. Pejin, M. Živković, A. Savić, J. Mutić, V. Tešević., *An insight into chemical composition and biological activity of Montenegrin Vranac red wine*, Scientia Horticulturae, 230 (2018) 142-148.
- [5] N. O. Đorđević, B. Pejin, M. M. Novaković, D. M. Stanković, J. J. Mutić, S. B. Pajović, V. V. Tešević., *Multielement analysis and antioxidant capacity of merlot wine clones developed in Montenegro*, Natural Product Research, 32 (2018) 247-251.

Applied machine learning in exploring key features of crayfish populations

Simona R. Đuretanović^{1*}, Marija M. Jakovljević¹, Aleksandra M. Milošković², Nataša M. Kojadinović¹, Milena D. Radenković¹, Vladica M. Simić¹, Ivana Maguire³

¹ University of Kragujevac, Faculty of Science, Department of Biology and Ecology, Radoja Domanovića 12, 34000 Kragujevac, Serbia; e-mail: simona.djuretanovic@pmf.kg.ac.rs, marija.jakovljevic@pmf.kg.ac.rs, natasa.kojadinovic@pmf.kg.ac.rs, milena.radenkovic@pmf.kg.ac.rs, vladica.simic@pmf.kg.ac.rs,

² University of Kragujevac, Institute for Information Technologies, Jovana Cvijića bb, 34000 Kragujevac, Serbia; e-mail: aleksandra@uni.kg.ac.rs

³ University of Zagreb, Faculty of Science, Department of Biology, Roosevelt trg 6, 10000 Zagreb, Croatia; e-mail: ivana.maguire@biol.pmf.hr

* Corresponding author

DOI: 10.46793/ICCBi23.184DJ

Abstract: Uniform Manifold Approximation and Projection (UMAP) is a nonlinear dimension reduction technique based on manifold learning. It is specifically designed to achieve a balance between the global and local structure when embedding data points. We applied this method to morphometric features in populations of the noble crayfish, a freshwater species recognized as both a keystone species and an ecosystem engineer, as well as an indicator of good water quality, with unquestionable cultural and economic value to humans. Our results show that the CLL parameter most contributed to the differences and grouped the investigated specimens into seven clusters, along with ROL and ABL parameters. The parameters associated with the claws also exhibited a considerable influence on differentiation.

Keywords: machine learning, Uniform Manifold Approximation and Projection (UMAP), freshwater crayfish

1. Introduction

Freshwater crayfish are physiologically, ecologically, and behaviorally remarkable animals residing in a wide range of habitats [1]. They are a very important group of aquatic invertebrates, especially in terms of ecosystem integrity retention [2]. At the same time, these invertebrates are particularly sensitive to changes in aquatic ecosystems and are among the most vulnerable, with 32% of species listed as globally threatened by the IUCN [3, 4].

This study aims to deploy the Uniform Manifold Approximation and Projection approach with the Decision Tree algorithm on the noble crayfish *Astacus astacus*

(Linnaeus, 1758) from distinct populations to explore which morphometric parameters contribute most to overall differences.

2. Materials and Methods

A total of 192 noble crayfish from ten ecosystems in Serbia, Slovenia, and Albania were caught with baited LiNi traps or collected by hand. Each specimen was measured for 21 morphometric parameters (adopted from Sint et al. 2005 [5]) and weighed to the nearest 0.01g.

We used the unsupervised dimensionality reduction learning model UMAP (i.e., Uniform Manifold Approximation and Projection). The input matrix contained 192 rows (one row represented each measured specimen) and 21 columns (each column referred to one morphometric parameter). Prior to dimensional reduction modeling, the data were Hellinger-transformed [6, 7]. In the initial stage of machine learning, the weight of crayfish specimens was extracted and further excluded from the training set.

3. Results and discussion

The obtained results (Fig. 1 and Fig. 2) showed a clear differentiation between males and females. The Decision tree algorithm extracted a CLL parameter as a key feature for ordination, which most contributed to the differences, and grouped the investigated specimens into seven clusters. The parameters ROL and ABL also contribute significantly to differentiation. This is in accordance with a previous study by Đuretanović et al. (2017) [8].

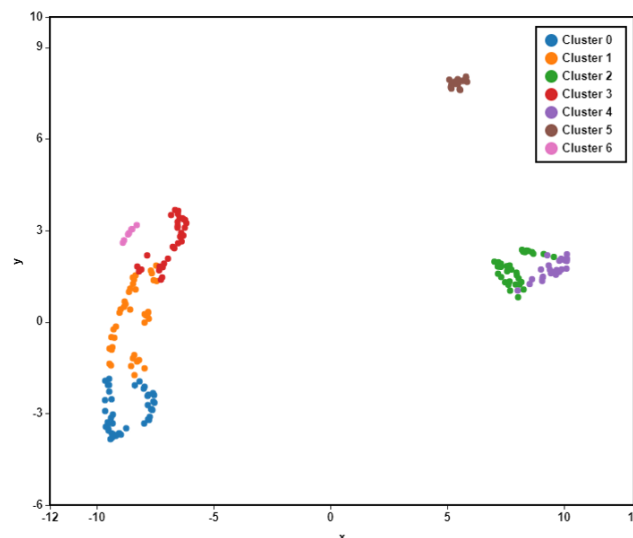


Figure 1. Ordination of morphometric parameters using the UMAP model. Colors stand for different seven clusters of parameters identified by the Decision Tree algorithm. Each point on the 2D UMAP space presents different specimens of crayfish.

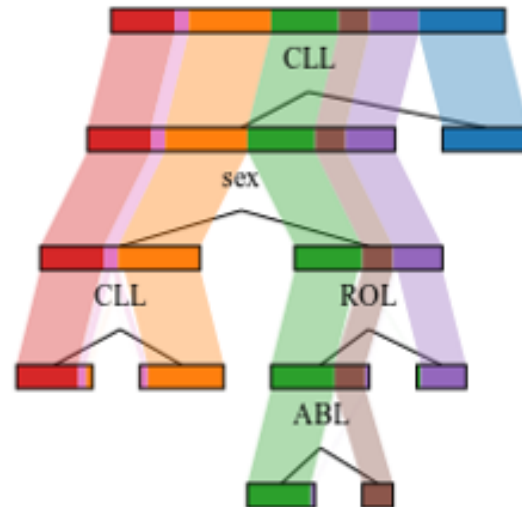


Figure 2. The Decision Tree algorithm was used to determine the most significant parameters for clustering.

Although the Decision Tree determines the key parameters (Fig. 2) it should be noted that the parameters related to the claws also contribute to the differentiation.

3. Conclusions

UMAP technique aims to retain as much variation from the original dataset as possible, surpassing the limitations of traditional reduction techniques. Data mining using the Decision Tree algorithm has proven to be an effective tool, demonstrating a highly predictive performance in exploring complex datasets and identifying representative variables for previously divided clusters.

Acknowledgment

This research was funded by the Serbian Ministry of Science, Technological Development and Innovation under grant no. 451-03-47/2023-01/200122.

References

- [1] J. Kubec, A. Kouba, M. Buřič., *Communication, behaviour, and decision making in crayfish: a review*, *Zoologischer Anzeiger*, 278 (2019) 28-37.
- [2] M.V. Alvanou, D.K. Papadopoulos, A. Lattos, I. Georgoulis, K. Feidantsis, A.P. Apostolidis, B. Michaelidis, I.A. Giantsis., *Biology, distribution, conservation status and stocking perspective of freshwater crayfish in Greece: An updated review*, *Aquaculture Research*, 53, 15 (2022) 5115-5128.
- [3] N.I. Richman, M. Böhm, S.B. Adams, F. Alvarez, E.A. Bergey, J.J. Bunn, Q. Burnham, J. Cordeiro, J. Coughran, K.A. Crandall, K.L. Dawkins, *Multiple drivers of decline in the global*

- status of freshwater crayfish (Decapoda: Astacidea)*, Philosophical Transactions of the Royal Society B: Biological Sciences, 370(1662) (2015) 20140060.
- [4] L.M. Bland, *Global correlates of extinction risk in freshwater crayfish*, Animal Conservation, 20(6) (2017) 532–542.
- [5] D. Sint, J. Dalla Via, L. Füreder., *Morphological variations in Astacus astacus L. and Austropotamobius pallipes (Lereboullet) populations*, Bulletin Français de la Pêche et de la Pisciculture, 376-377 (2005) 637-652.
- [6] M. Jakovljević, M. Nikolić, N. Kojadinović, S. Đuretanođić, M. Radenković, T. Veličković, V. Simić., *Population Characteristics of Spirlin Alburnoides bipunctatus (Bloch, 1782) in Serbia (Central Balkans): Implications for Conservation*, Diversity 15, (2023) 616.
<https://doi.org/10.3390/d15050616D>.
- [7] Dj. Milošević, A.S. Medeiros, M. Stojković Piperac, D. Cvijanović, J. Soinenen, A. Milosavljević, B. Predić., *The application of Uniform Manifold Approximation and Projection (UMAP) for unconstrained ordination and classification of biological indicators in aquatic ecology*, Science of The Total Environment 815 (2022) 152365.
- [8] S. Đuretanođić, M. Jaklič, A. Milošković, N. Radojković, M. Radenković, V. Simić, I. Maguire., *Morphometric variations among Astacus astacus populations from different regions of the Balkan Peninsula*, Zoomorphology, 136 (2017) 19-27.

Dose compensation algorithm in radiotherapy planning

Neda Milosavljević^{1,2*}, Marija Živković Radojević^{1,2}, Darko Stojanović², Marko Spasić³

¹University of Kragujevac, Faculty of Medical Sciences, Department of Clinical Oncology, Kragujevac, Serbia; email: neda.milosavljevic@yahoo.com, makizivkovicmarija@gmail.com.

²University Clinical Center Kragujevac, Kragujevac, Center for Radiation Oncology, Kragujevac, Serbia; email: kgkid.ds@gmail.com

³University of Kragujevac, Faculty of Medical Sciences, Department of Surgery, Kragujevac, Serbia; email: drmspasic@gmail.com

* *Corresponding author*

DOI: 10.46793/ICCBKIG23.188M

Abstract: Pauses in radiotherapy treatment is a significant problem that affects overall treatment time - a predictor of tumor proliferation and definitive patient outcome and demands a decision-making tool for optimizing doses between healthy tissue and target volumes.

During prolonged radiotherapy interruptions, linear-quadratic model showed inadequacy in predicting tumor proliferation. We have developed a radiobiology algorithm applied for dose compensating, providing multiple options for dose compensating due to prolonged pauses. Based on linear-quadratic (LQ) model providing, in specific cases, orientational values for tumors and organs at risk (OAR), we developed a radiobiology calculator that can be used in dose compensation, giving more than one option in correcting biological effective dose (BED) due to prolonged pauses. Generic OAR offers the opportunity to individualize α/β ratio for any organ at risk or tumor. Seven cancer patients who experienced radiotherapy treatment delays, for more than two weeks, are included in this research.

The developed algorithm offers the radiation oncologist optimal modality choice and can be a helpful tool for overcoming long delays, except for patients whose treatment interruptions occur at the end of radiation treatment and for patients with fast proliferating tumors. During this course of treatment, none of the included patients manifested severe acute radiotherapy adverse events.

The dose compensating algorithm can be a useful tool for dose calculations with optimal healthy tissue sparing, but large prospective studies are necessary to confirm the benefit.

Keywords: radiotherapy, dose compensation, algorithm

1. Introduction

Radiotherapy is an integral part of the multidisciplinary treatment of oncological patients, where over 50% of oncology patients undergo radiotherapy during their treatment [1, 2]. For local control of the disease, compliance in treatment, as well as the development of acute and chronic adverse events, it is necessary that radiotherapy treatment be carried out in an adequate time frame depending on the goal of radiotherapy (neoadjuvant, adjuvant, radical or palliative approach) and fractionation regime [2]. Deviations from the recommended regimens can lead to inadequate local control of the disease, which affects the time to disease progression (Disease free survival, DFS), or overall survival (OS) [3]. Fowler et al showed that prolonging radiotherapy treatment in patients with head and neck cancer reduces local tumor control by 1.4% per day of missed treatment [4]. Pauses in radiotherapy treatment are not rare, and the most common reasons for this are of a technical nature (device failure), personal reasons of the patient or manifestations of acute radiation toxicity, grade 3 and higher [5-7].

The current recommendations for overcoming this, regardless of the type and intention of the radiotherapy treatment, according to the recommendations of The Royal College of Radiologists (RCR), are an increase in the daily tumor dose or use of hyperfractionated regimes [8]. Although the mentioned methods are adequate in reimbursing the dose to the target volumes, the surrounding healthy tissues receive a higher dose than recommended [8]. In the previous years, models have been developed for the assessment and recalculation of the effects of delaying radiotherapy, where most of them relied only on $\alpha\beta$ ratio, the relationship between the tumor and surrounding healthy tissues in response to the applied radiotherapy dose [9], where it should be borne in mind that the $\alpha\beta$ value differs between different healthy and tumor tissues.

In the era of the Covid-19 pandemic, it has become clear that there are also unforeseen circumstances that would cause prolonged breaks in the implementation of radiotherapy, which is why it is necessary to define guidelines for the compensation of missed therapeutic doses and the correction of the total time required for the delivery of a radiotherapy dose [10].

2. Material and method

The linear quadratic (LQ) model, which represents the correlation between cell survival and delivered dose, is widely used to analyze and predict responses to ionizing

radiation in vivo and in vitro, but not designed to provide responses to cell proliferation during prolonged intervals. This model can provide orientational parameters for tumor proliferation [11]. Based on the LQ model disadvantages to predict tumor proliferation, during prolonged radiotherapy interruptions, but providing, in certain cases, orientative values for tumors and organs at risk (OAR), a collaboration between radiation oncologists and medical physicists developed a radiobiology calculator that can be used to compensate radiotherapy dose - more than one option in correcting biological effective dose (BED) due to pauses more than two week period, with the possibility to individualize α/β ratio for any organ at risk or tumor.

2. Results

In a newly created algorithm, we included all cancer patients who experienced radiotherapy treatment delays, for more than two weeks, regardless of primary malignancy. During the period of one year, there have been seven patients whose characteristics, as well as data on the planned radiotherapy treatment, are shown in Table 1.

Table 1. Patient and treatment characteristics

	Patient 1	Patient 2	Patient 3	Patient 4	Patient 5	Patient 6	Patient 7
Malignancy	Lung	Laryngs	Breast	Breast	Breast	Prostate	Prostate
Radiotherapy intention	P	R	P	P	P	P	R
Planned dose (Gy)	60	70	50	42.56	42.56	66	72
Pause in days	28	42	34	21	15	18	40
Compensating dose (Gy)	82.34	109.9	78.75	61.86	47.7	80.2	121.1
OAR affection %	121.67	201.66	206.67	99.69	104.1	161.67	201.67

Abbreviations: P- postoperative; R - radical

The calculator offers a radiation oncologist an optimal modality choice, that includes dose per fraction and number of fractions, administering dose in hyperfractionated regiment, especially in patients where $\alpha\beta$ is low ($\alpha\beta$ 3 for breast cancer) (Figure 1, left image). In patients with fast proliferating tumors regardless of tumor characteristics, the

dose compensating algorithm is not applicable (Table 1; an example for one patient is shown in Figure 2, right image).

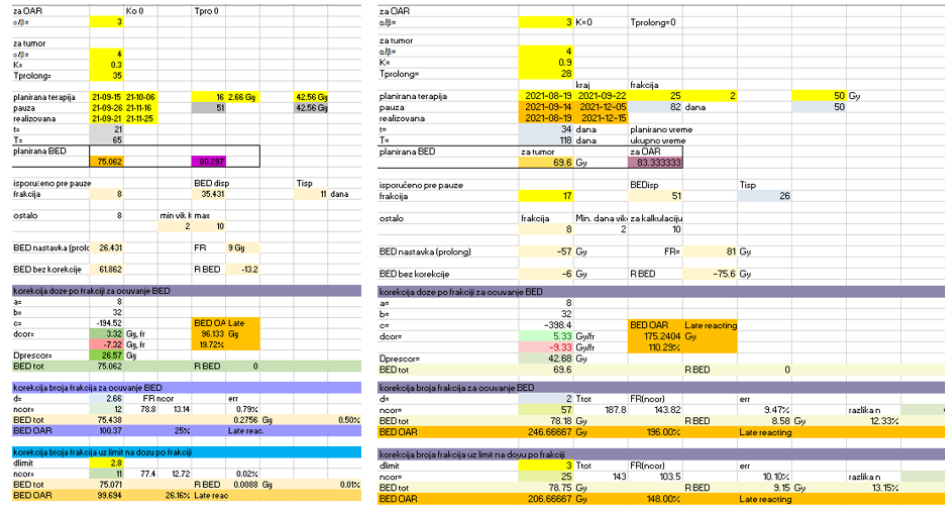


Figure 1. Example for adequate usage of dose compensating algorithm in decision making (left side) where the dose coverage is appropriate to target volumes, according to current guidelines for radiotherapy treatment; Example for patient, in which treatment delays algorithm is not useful (right side).

In collaboration with a medical physicist, the final decision is up to the radiation oncologist, to accept or decline proposed alterations in radiotherapy for each patient. As shown in Table 1, due to the high percentage of OAR affection, not all patients continued with compensated treatment. During this course of treatment, none of the included patients manifested severe acute radiotherapy adverse events and in one-year follow-up, no disease recurrence was detected.

4. Conclusions

Currently, there are no adequate recommendations or prospective studies for dose compensation for pauses that last longer than two weeks, which are individualized according to the characteristics of the patient and his primary malignancy, while taking into account all the parameters that affect the effectiveness of radiotherapy treatment.

This algorithm can be a useful tool to a radiation oncologist for dose compensation with appropriate OAR spare and it is applicable in any situation with treatment delays, but further prospective studies are needed to prove the benefit.

References

- [1] Yang Y, Cameron J, Humphris G. The relationship between cancer patient's fear of recurrence and radiotherapy: a systematic review and meta-analysis. *Psychooncology* 2017;26(6):738-46.
- [2] Siegel RL, Miller KD, Jemal A. 2020. Cancer statistics, 2020. *CA: A Cancer Journal for Clinicians* 70 7–30.
- [3] Fietkau R, Rödel C, Hohenberger W, Raab R, Hess C, Liersch T, Becker H, Wittekind C, Hutter M, Hager E, Karstens J, Ewald H, Christen N, Jagoditsch M, Martus P, Sauer R; German Rectal Cancer Study Group. Rectal cancer delivery of radiotherapy in adequate time and with adequate dose is influenced by treatment center, treatment schedule, and gender and is prognostic parameter for local control: results of study CAO/ARO/AIO-94. *Int J Radiat Oncol Biol Phys.* 2007 Mar 15;67(4):1008-19.
- [4] Fowler JF, Lindstrom MJ. Loss of local control with prolongation in radiotherapy. *Int J Radiat Oncol Biol Phys.* 1992;23(2):457-67.
- [5] Osei E, Francis R, Mohamed A, Sheraz L, Soltani-Mayvan F. Impact of COVID-19 pandemic on the oncologic care continuum: urgent need to restore patients care to pre-COVID-19 era. *J Radiother Pract.* 2021 Apr 19:1–11.
- [6] Cox JD, Stetz J, Pajak TF. Toxicity criteria of the Radiation Therapy Oncology Group (RTOG) and the European Organization for Research and Treatment of Cancer (EORTC). *Int J Radiat Oncol Biol Phys* 1995;31(5):1341-6.
- [7] National Cancer Institute, National Institutes of Health USD. U.S. Department of health and human services. Common Terminology Criteria for Adverse Events (CTCAE). U.S. Department of Health and Human Services. Common Terminology Criteria for Adverse Events (CTCAE) Version 5.0 Published: November 27, 2017.
- [8] Royal College of Radiologists. The timely delivery of radical radiotherapy: standards and guidelines for the management of unscheduled treatment interruptions. 2008. (Third edition).
- [9] Putora PM, Schmuecking M, Aebersold D, Plasswilm L. Compensability index for compensation radiotherapy after treatment interruptions. *Radiat Oncol.* 2012 Dec 8;7:208.
- [10] Abolfath R, Khalili M, Senejani AG, Kodery B, Ivker R. The Dependence of Compensation Dose on Systematic and Random Interruption Treatment Time in Radiation Therapy. *Onco.* 2022; 2(3):264-281.

A protocol for thoracic radiation therapy in patients with cardiac implantable electronic devices

Neda Milosavljević^{1,2*}, Marija Živković Radojević^{1,2}, Darko Stojanović², Katarina Janković^{2,3*}, Tatjana B. Miladinović⁴

¹University of Kragujevac, Faculty of Medical Sciences, Department of Clinical Oncology, Kragujevac, Serbia; email: neda.milosavljevic@yahoo.com, makizivkovicmarija@gmail.com,

²University Clinical Centre Kragujevac, Kragujevac, Centre for Radiation Oncology, Kragujevac, Serbia; email: kgkid.ds@gmail.com

³University of Kragujevac, Faculty of Medical Sciences, Kragujevac, Serbia, email: k.jankovic1991@gmail.com

⁴University of Kragujevac, Institute for Information Technologies, Department of Science, Kragujevac, Serbia; email: tanja.miladinovic@uni.kg.ac.rs

* *Corresponding author*

DOI: 10.46793/ICCB23.193M

Abstract: Prolonged lifespan and improved diagnostic and treatment modalities have led to significant progress in the diagnosis and treatment of cardiovascular disease and cancer. A substantial number of patients with malignancies also have cardiovascular disease at the time of cancer treatment. Per literature, over one million implantable cardiac devices are inserted annually.

Ionizing radiation, especially in the thoracic area is related to cardiac implantable electronic device (CIED) damage and malfunction. Besides that, CIED can interfere with radiotherapy planning and delivery, as well as patient motivation to undergo radiotherapy treatment.

Management of oncology patients, undergoing radiotherapy, for any indication, with a CIED is essential, and safe radiotherapy practice requires minimizing the risk to patients as much as possible, from pretherapy planning to posttherapy follow-up. A collaborative multidisciplinary approach, tailor-made for every single radiotherapy center is imperative to provide effective and safe radiotherapy for these patients.

A collaboration of radiation oncologists, medical physicists and cardiologists from the University Clinical Center Kragujevac has created a local protocol for radiotherapy treatment and follow-up for patients receiving radiotherapy at the Center for Radiation Oncology University Clinical Center Kragujevac, which provides safe and efficient delivery of an adequate radiotherapy dose to target volumes with appropriate cardiac monitoring.

Keywords: radiotherapy, CIED, cancer, cardiology

1. Introduction

Patients with malignancies are treated with radiotherapy due to different intentions (preoperative, postoperative, radical or palliative intent). Pretreatment preparation starts with a computed tomography simulation where the organs at risk (OAR) and target volumes are identified [1]. The treatment intention, duration and radiation dose, as well as technique, are determined by several clinical parameters and it is carried out following the current guidelines for the given oncology patient [2].

In a patient with CIED, radiotherapy planning and treatment requires minimizing the risk to patients as much as possible, from pretherapy planning to posttherapy follow-up. A collaborative multidisciplinary approach, including but not limited to radiation oncologists, medical physicists and cardiologists, should provide tailor-made personalized radiotherapy treatment [3].

Types of implantable devices for treating cardiovascular diseases are called cardiac implantable electronic devices (CIEDs). A pacemaker (PM) is indicated for bradyarrhythmias, where symptoms vary from asymptomatic to repeating syncope. An implantable cardioverter-defibrillator (ICD) is indicated for high-risk patients in preventing sudden cardiac death, due to ventricular fibrillation or ventricular tachycardia [3].

Malfunctions of CIEDs can cause a variety of cardiovascular symptoms [4], but these events can rarely be life-threatening.

The CIED tolerance dose, in order to prevent malfunction has not been precisely determined, but CIED manufacturers specified device dose limits of <1–5 Gy. However, the dose limit varies depending on the manufacturer, model and the presence or absence of ICD functions and a significant number of manufacturers do not assume direct irradiation to the main body.

That is why, our multidisciplinary team, consisting of a radiation oncologist, a medical physicist and a cardiologist, following current recommendations based on Japanese Society for Radiation Oncology (JASTRO) Guidelines for radiotherapy in patients with cardiac implantable electronic devices [3] and AAPM TG-203 report - Management of radiotherapy patients with implanted cardiac pacemakers and

Defibrillators [4] created a local protocol for treating and monitoring of patients with CIED undergoing radiotherapy at the Center for Radiation Oncology, University Clinical Center Kragujevac.

2. Local protocol for patients with CIED, undergoing radiotherapy

After obtaining a recommendation from the multidisciplinary tumor team (MDT), for radiotherapy treatment, the first step in treatment planning is risk stratification to low risk patients (not pacemaker dependent, no radiotherapy to the chest region, estimated dose to CIED <5 Gy, without a history of ventricular tachycardia); medium risk (a case that is not in the low or high risk classification) and high risk patient (Pacemaker dependent, electron beam energy ≥ 20 MeV, CIED dose estimated to be >10 Gy, history of ICD intervention and a history of ventricular fibrillation).

During the first interview with a patient, in order to obtain informed consent, information must be given to the patient on possible CIED malfunction due to radiotherapy. The patient must undergo consultation with a cardiologist. CIED identification book of the manufacturer's contact information, model and settings, must be obtained and copied into the medical history.

A checklist (Figure 1) is completed by a radiation oncologist, medical physicist and cardiologist, after which radiotherapy planning and patient follow-up are approached, relying on recommendations for the given risk group.

Lista za pacijente sa ugrađenim pejsmejerima i defibrilatorima

Šifra pacijenta: _____
Pacijent: _____
Datum: _____

Potpisi: _____

1. Početna konsultacija:
a) CIED označen na kartonu pacijenta _____
b) Kopija CIED kartice napravljena i dodata kartonu pacijenta _____
c) Sastanak sa kardiološkom elektrofiziologijom zakazan/nije potreban _____
d) Kardiolog odredio da je magnet potreban/nepotreban _____

2. Simulacija:
a) Pacijent je zavisian/nije zavisian od CIED _____
b) CIED je označen na kartonu pacijenta _____
c) Lekar je popunio uputstva vezna za planiranje _____
d) Dodato upozorenje da se ne koriste energije iznad 10MV i wedge _____
e) Dozni limiti dobijeni od dobavljača CIED _____

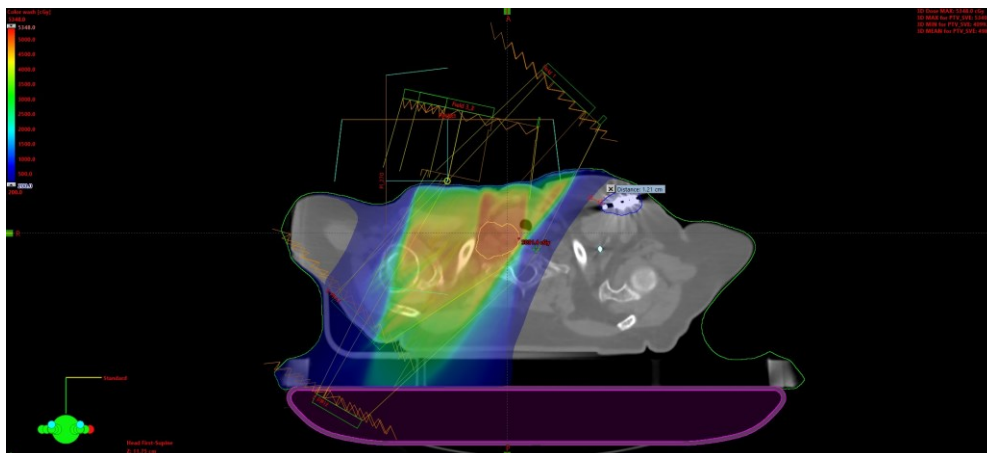
3. Planiranje:
a) verifikovano da nema energije iznad 10MV niti wedge _____
b) Procenjena doza po frakciji i kumulativna doza: _____
c) Potvrdi najmanju udaljenost CIED od iverice polja: _____
Ako je udaljenost manja od 10 cm nastavi sa listom:
d) Po potrebi dodaj naznaku za in-vivo dozimetriju na prvoj frakciji _____
e) Podesi imidžing polja da ne pogađaju uređaj _____

4. Prvi dan tretmana:
a) In-Vivo dozimetar postaviti na CIED na tačkun najbližu polju _____
b) potvrditi da imidžing doze ne pogađaju CIED _____
c) Pročitaj dozimetar posle tretmana i generiši sumarni izveštaj _____

Figure 1.: Patient Check list in Serbian language for patient with CIED undergoing radiotherapy.

2.1. Real time treatment and patient monitoring

Given that patients with neck and thoracic radiotherapy have increased risk for CIED malfunctioning, their planning on target volumes, organs at risk and especially on CIED (Figure 2), as well as the implementation of radiotherapy is carried out according to a described regime. Also, special attention is paid to the daily verification of the position during the radiotherapy treatment, by the medical staff on the device itself, as well as by the radiation oncologist and cardiologist, once a week and more often if indicated.



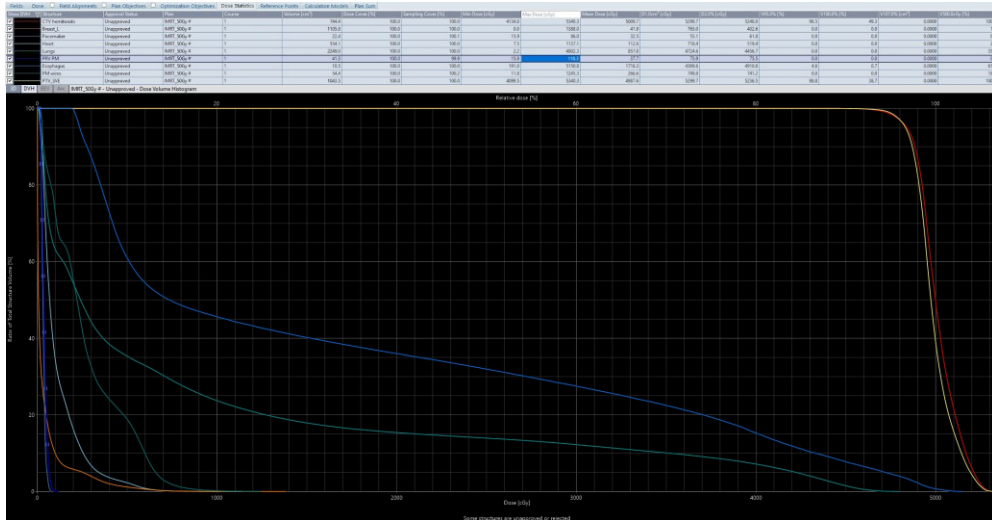


Figure 2.: Radiotherapy planning in patients with pacemaker, dose volume histogram and OAR and target volume constraints.

After the treatment of patients with CIED, of medium and high risk, it is necessary to control the functioning of the CIED weekly at least 1 month and once a month for the next 6 months after treatment.

4. Conclusions

Management of oncology patients, undergoing radiotherapy, for any indication, with a CIED is essential and safe radiotherapy practice requires minimizing the risk to patients as much as possible. A collaborative multidisciplinary approach, tailor-made for every single radiotherapy center is imperative to provide effective and safe radiotherapy for these patients.

References

- [1] Fradley MG, Lefebvre B, Carver J, Cheung JW, Feigenberg SJ, Lampert R, Liu J, Rajagopalan B, Lenihan DJ. How to Manage Patients With Cardiac Implantable Electronic Devices Undergoing Radiation Therapy. *JACC CardioOncol.* 2021 Sep 21;3(3):447-451.
- [2] NCCN Clinical Practice Guidelines in Oncology (NCCN Guidelines®). Available at: https://www.nccn.org/guidelines/category_1
- [3] Toshiki Ohno and al, JASTRO/JCS Guidelines for radiotherapy in patients with cardiac implantable electronic devices, *Journal of Radiation Research*, Volume 62, Issue 1, January 2021, Pages 172–184.
- [4] Miften M, Mihailidis D, Kry SF, Reft C, Esquivel C, Farr J, Followill D, Hurkmans C, Liu A, Gayou O, Gossman M, Mahesh M, Popple R, Prisciandaro J, Wilkinson J. Management of radiotherapy patients with implanted cardiac pacemakers and defibrillators: A Report of the AAPM TG-203†. *Med Phys.* 2019 Dec;46(12):e757-e788.

Distribution of doses to organs at risk in Cervical Cancer High Dose Rate Brachytherapy using Tandem and Ovoids or Vaginal Cylinder

Tatjana B. Miladinović^{1*}, Jasmina Obradović¹, Marija Živković Radojević^{2,3}, Neda Milosavljević^{2,3}, Aleksandar Miladinović⁴, Milena Živković⁵, Dragana Krstić⁵

¹ University of Kragujevac, Institute for Information Technologies, Department of Science, Jovana Cvijića bb, 34000 Kragujevac, Serbia; e-mail: tanja.miladinovic@uni.kg.ac.rs

² University of Kragujevac, Faculty of Medical Sciences, Department of Clinical Oncology, Svetozara Markovića 69, 34000 Kragujevac, Serbia; e-mail: makizivkovicmarija@gmail.com, neda.milosavljevic@yahoo.com

³ University Clinical Center Kragujevac, Centre for Radiation Oncology, Zmaj Jovina 30, 34000 Kragujevac, Serbia; e-mail: makizivkovicmarija@gmail.com, neda.milosavljevic@yahoo.com

⁴ University Clinical Center Kragujevac, Medical Physics Department, Zmaj Jovina 30, 34000 Kragujevac, Serbia; e-mail: miladinovic.al@gmail.com

⁵ University of Kragujevac, Faculty of Sciences, Department of Physics, Radoja Domanovića 12, 34000 Kragujevac, Serbia; e-mail: dragana.krstic@pmf.kg.ac.rs, milena.zivkovic@pmf.kg.ac.rs

DOI: 10.46793/ICCB23.197M

Abstract: Brachytherapy is an integral part of the treatment of cervical cancer. In brachytherapy, the dose delivered to the tissue is determined primarily by the inverse square law thus the dose decreases rapidly as the distance from the source increases. Therefore, an important role in dose distribution is the geometry of the applicator. A patient's anatomy as well as the fact that the patient may have been operated on must also be taken into account when selecting the applicator. The aim of this study was to assess the influence of the type of cervical cancer brachytherapy applicators (tandem and ovoids or vaginal cylinder) on the dose delivered to adjacent organs, urinary bladder, and rectum. The treatment plans of 10 patients with cervical cancer treated by intracavitary brachytherapy were reviewed, and dose distribution data was collected. Prescribed doses were 7 Gy (or 8 Gy)/fractions, and the number of fractions was from 3 to 5, thus cumulative target EQD2 was between 85-90 Gy. Deliveries of doses to the rectum and bladder were controlled within the tolerance ranges. It was found that the selection of the applicator and the doses administered to the bladder and rectum were correlated. Tandem and ovoid applicators produced lower doses in the bladder and rectum by approximately 20% than the vaginal cylinder. The results of this analysis may potentially enable the optimization of dose distribution for organs at risk in each individual clinical situation.

Keywords: brachytherapy, cervical cancer, applicators, tandem and ovoids, vaginal cylinder

1. Introduction

The fourth most common malignant tumor in women is uterine cervix cancer, with 604.127 new cases identified in 2020 [1]. According to the clinical stage and pathology type of cervical cancer, treatment may include surgery, radiotherapy, and chemotherapy

[2]. Brachytherapy (BT) is a method of treatment developed in the early 1950s and is used to give the majority of the dose to the central tumor of the cervix cancer with a reduction of the dose to organs at risk due to rapid dose decreasing. Iridium-192, which has a half-life of 73.8 days, is the radionuclide most frequently used for HDR BT [3, 4]. Due to this, this radionuclide can be applied to radiotherapy systems relatively affordably because it requires replacing the source approximately four times a year, and this is enough to maintain a high dose rate of at least 12 Gy/h [5]. With this technique, in order to avoid insufficient underdosing, proper selection of the applicator is necessary. Many vaginal applicators are available, some of them are suitable for low-dose-rate brachytherapy [6], whereas the tandem and cylinder applicator effectively delivers 100% isodose of brachytherapy to the tumor without raising the danger of toxicity for high-dose-rate brachytherapy (HDR B) [7, 8]. Thus, the aim of this study was to evaluate organs at risk (OAR) doses estimated in patients with cervical cancer treated with HDR BT in the case when two types of applicators (tandem and ovoids or vaginal cylinder) are used.

2. Methods and results

A sample of 10 cervical cancer patients treated at the Centre of Radiation Oncology, the University Clinical Center Kragujevac was observed. At the time of diagnosis, the patient's average age was 65.6 (range 56-79). Patients with locally advanced cervical cancer are treated with definitive radiotherapy (transcutaneous (External Beam Radiotherapy (EBRT)) and brachytherapy) with or without chemopotiation. The total dose prescribed during EBRT and brachytherapy to the tumor volume (Gross Tumor Volume (GTV)) ranged from 85-90 Gy, calculated based on the application of the EQD2 model for dose calculation where α/β for the tumor is 7, and for organs at risk 3 [9]. EBRT was performed with 3D-conformal radiotherapy (3D-CRT), intensity modulated therapy (IMRT) or volumetric modulated arc radiotherapy (VMAT).

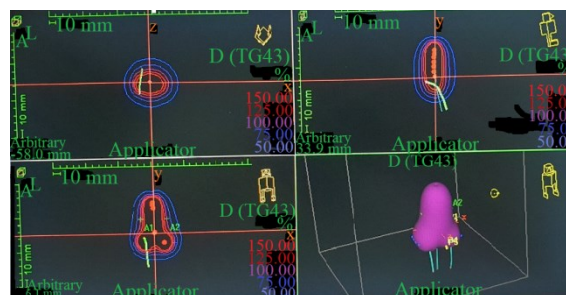


Figure 1. Dose distribution calculated by Oncentra brachytherapy treatment planning software for carcinoma cervix with tandem and ovoids applicator.

Half of the studied patients were treated with HDR brachytherapy using tandem and ovoids, and the other half with vaginal cylinders. CT scanning and delineation of the target and organs at risk (bladder and rectum) were done as a standard procedure. Optimization was then performed in order to deliver the prescribed dose to the target

while maintaining the dose at the organs at risk within tolerance limits all in order to obtain the best treatment plan that satisfies all input criteria (Figures 1 and 2).

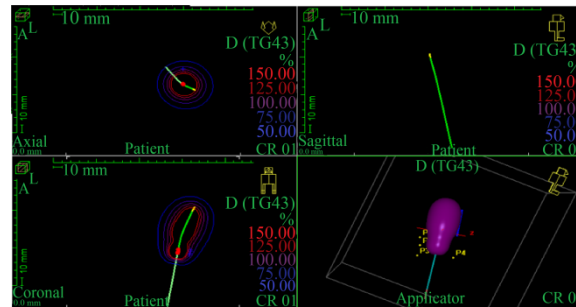


Figure 2. Dose distribution calculated by Oncentra brachytherapy treatment planning software for carcinoma cervix with vaginal cylinder applicator.

In comparing dose distributions for organs at risk, it can be concluded that tandem and ovoid applicators deliver lower doses. It can be observed from Table 1 and Figure 3 that these doses are approximately 20 % lower.

Table 1. The dosimetry results of the two types of applicators used in the study.

Patient	Type of the brachytherapy applicator	Age (year)	Prescribed dose [cGy] and No. of fraction	Number of rectal reference points	Number of bladder reference points	Dose to rectal point [cGy]	Dose to bladder point [cGy]
1	vaginal cylinder	77	800 (3)	7	1	552.16	567.07
2	vaginal cylinder	59	700 (5)	10	3	502.18	527.89
3	vaginal cylinder	79	800 (4)	12	3	605.17	575.41
4	vaginal cylinder	71	700 (5)	7	1	515.66	497.48
5	vaginal cylinder	67	700 (5)	3	1	398.46	243.05
6	tandem and ovoids	74	700 (5)	4	1	293.72	372.97
7	tandem and ovoids	56	700 (5)	5	2	328.58	232.42
8	tandem and ovoids	56	700 (5)	4	2	487.88	366.64
9	tandem and ovoids	60	700 (5)	5	2	448.40	493.10
10	tandem and ovoids	57	700 (5)	4	2	422.09	548.55

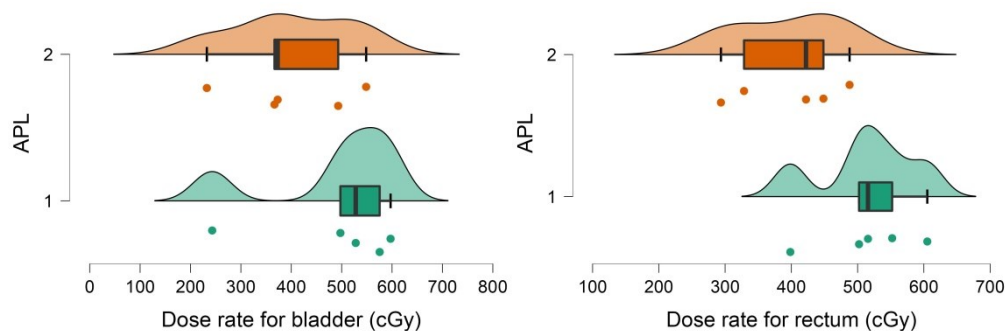


Figure 3. Distribution of high dose rate values for organs at risk (bladder and rectum) according to the type of applicator (APL: 1- vaginal cylinder, 2- tandem and ovoids applicators).

Independent samples T test showed a significance of $p=0.045$ for HDR for the rectum and choice of the applicator. The analysis was performed using JASP computer software (Version 0.16) [10].

3. Conclusions

According to this study, tandem and ovoid applicators provide a lower dose distribution to the bladder and rectum than vaginal cylinder applicators. The differences in dosimetric characteristics as well as the advantages and disadvantages of the applicators themselves may account for these obtained results. In order to improve clinical outcomes, it is necessary to analyze all of these aspects in more detail.

Acknowledgment

This research is funded by the Ministry of Education and Ministry of Science, Technological Development and Innovation, Republic of Serbia, Grants: No. 451-03-47/2023-01/200378 and No. 451-03-47/2023-01/200122.

References

- [1] <https://cutt.ly/KCeMB11>
- [2] C.A. Burmeister, S.F. Khan, G. Schäfer, N. Mbatani, T. Adams, J. Moodley, S. Prince., *Cervical cancer therapies: Current challenges and future perspectives*, *Tumour Virus Res*, 13 (2022) 200238.
- [3] J.F. Williamson., *Brachytherapy technology and physics practice since 1950: a half-century of progress*, *Phys. Med. Biol.*, 50 (2006) R303–R325.
- [4] Y. Roussakis, G. Anagnostopoulos., *Physical and Dosimetric Aspects of the Iridium-Knife*, *Frontiers in Oncology*, 11 (2021) 728452.
- [5] https://www-pub.iaea.org/mtcd/publications/pdf/te_1257_prn.pdf
- [6] C. Baker, S.A. Dini, M. Kudrimoti, S.B. Awan, A.S. Meigooni., *Dosimetric evaluation of a newly designed low dose rate brachytherapy applicator for treatment of cervical cancer with extension into the lower vagina*, *J Appl Clin Med Phys.*, 8 (2007) 37–46.
- [7] A.A. Khan, A. Vijay, S. Qamar Wani, M.M. Haq., *Dosimetric analysis of intracavitary brachytherapy applicators: a practical study*, *Radiat Oncol J.*, 40(3) (2022) 180-191.
- [8] M. Jreij, A. El Ahmar, P. Finianos., *Applicators used for vaginal high dose rate brachytherapy: Effect of type and shape on dose distribution and toxicity, a literature review*, *Cancer/Radiothérapie*, 27 (1) (2023) 80-85.
- [9] S.M. Bentzen, W. Dörr, R. Gahbauer, R.W. Howell, M.C. Joiner, B. Jones, D.T. Jones, A.J. van der Kogel, A. Wambersie, G. Whitmore., *Bioeffect modeling and equieffective dose concepts in radiation oncology-terminology, quantities and units*, *Radiother Oncol*, 105(2) (2012) 266-268.
- [10] JASP Team (2021). JASP (Version 0.16)[Computer software].

Assessment of radioactivity levels in soil samples on Zlatibor mountain

Milena P. Živković¹, Nenad M. Zlatić¹, Tatjana B. Miladinović², Milan S. Stanković¹,
Dragana Ž. Krstić^{1*}

¹ University of Kragujevac, Faculty of Science, R. Domanovica 12, 34000 Kragujevac,
Republic of Serbia

e-mail: milena.zivkovic@pmf.kg.ac.rs, dragana.krstic@pmf.kg.ac.rs,
nenad.zlatic@pmf.kg.ac.rs, milan.stankovic@pmf.kg.ac.rs

² University of Kragujevac, Institute for Information Technologies, Jovana Cvijića bb,
34000 Kragujevac, Serbia

e-mail: tanja.miladinovic@uni.kg.ac.rs

* *Corresponding author*

DOI: 10.46793/ICCB23.201Z

Abstract: This study aimed to investigate the presence and activity concentrations of natural radionuclides and cesium in soil samples collected from the Zlatibor region. A total of ten soil samples were collected from various locations across the Zlatibor area. The analysis was performed using gamma spectrometry to measure the activity concentrations of ²²⁶Ra, ²³²Th, ⁴⁰K, and ¹³⁷Cs. Additionally, ¹³⁷Cs was found in big amounts in some of the samples, indicating its dispersion in the environment. The activity concentrations of the detected radionuclides were calculated, and their potential radiological implications were assessed. The obtained data from this study contributes to the baseline information on the natural radioactivity levels in the Zlatibor region, which is essential for environmental monitoring and radiation protection purposes. Furthermore, the presence of ¹³⁷Cs highlights the importance of continued monitoring to assess potential radiological risks to the local population and environment.

Keywords: natural radionuclides, soil samples, Zlatibor

1. Introduction

In recent years, the investigation of natural radionuclides and anthropogenic radionuclides has become a crucial area of research due to their potential implications for human health and the environment. Radionuclides are radioactive isotopes that emit radiation as they decay, and their presence in the environment can arise from both natural and human-made sources. Among the anthropogenic radionuclides, cesium-137 (¹³⁷Cs) has gained particular attention due to its association with nuclear accidents and nuclear weapons testing [1, 2, 3].

The Zlatibor region, known for its scenic landscapes and environmental significance, has also been subject to scrutiny concerning potential radionuclide contamination.

Understanding the distribution and levels of radionuclides in this area is essential for assessing the radiological risk to the local population and ecosystems. Consequently, gamma spectrometry, a powerful and non-destructive analytical technique, has been widely employed for the detection and quantification of radionuclides in environmental samples [4].

The presence of ^{137}Cs in the soil can lead to its uptake by plants and subsequent transfer through the food chain, ultimately reaching humans and wildlife. Long-term exposure to elevated levels of ^{137}Cs can increase the risk of cancer, especially in organs that accumulate radiation, such as the thyroid and gastrointestinal tract. Moreover, exposure to gamma radiation from ^{137}Cs can also cause other health effects, including genetic mutations and damage to cells.

The significance of this research lies in providing comprehensive data on radionuclide contamination in the Zlatibor region. Such information is critical for the development of effective environmental monitoring strategies and the implementation of appropriate remediation measures, if necessary.

2. Material and methods

2.1 Collection and preparation of samples

Ten soil samples were collected from various locations in the Zlatibor region to ensure representativeness of different soil types. The collected samples were air-dried to remove any moisture content and ground into a fine powder using a mill. The powdered soil samples were then sieved to obtain a homogenous particle size distribution. Subsequently, the homogenized samples were divided into ten separate aliquots, with each aliquot carefully labeled and stored in airtight containers to prevent contamination. To achieve a secular equilibrium between ^{226}Ra and its short-lived decay products, the samples were hermetically sealed for a period of four-to-six weeks.

2.2 Gamma spectrometry

The activity concentrations of ^{226}Ra , ^{232}Th , ^{40}K , and ^{137}Cs were measured using a coaxial HPGe detector (GEM30-70, ORTEC) with an energy resolution (FWHM) of 1.85 keV at 1.33 MeV (^{60}Co) and a relative efficiency of 30%. To minimize background interference, the detector was housed within a 10 cm lead shield during measurements. Each sample was exposed to the detector for a timed duration of 172,800 seconds, and background corrections were applied. Data analysis was conducted using the computer software MAESTRO 2. For the determination of ^{226}Ra activity concentration, gamma lines of ^{214}Pb and ^{214}Bi (at 351.9 keV, 609.3 keV, and 1764.5 keV) were utilized. The specific activity of ^{232}Th was estimated by examining gamma lines at 338.3 keV, 911.1 keV, and 583.0 keV (corresponding to ^{228}Ac and ^{208}Tl). For ^{137}Cs activity concentration, the gamma line at 661.6 keV was monitored. Moreover, the photopeak at 1460.7 keV was utilized to estimate the activity concentration of ^{40}K in the soil samples.

2.3 Activity concentration of soil samples

Specific activity of radionuclides can be calculated as [5]:

$$AC = \frac{N_L}{\varepsilon \cdot m \cdot t \cdot P_\gamma}, \quad (1)$$

where: AC is the activity concentration (Bq kg⁻¹)

N_L is the net area of the photopic

m is the sample mass (kg)

ε is counting efficiency for a specific energy

P_γ is the emission probability of the measured gamma-ray

t is the counting time (s).

3. Results and discussion

Activity concentrations of natural radionuclides (²²⁶Ra, ²³²Th, and ⁴⁰K) and anthropogenic ¹³⁷Cs measured in soil samples are presented in Table 1.

Table 1. Table of Radionuclide Activity Concentrations in Soil Samples from Zlatibor Region (in Bq kg⁻¹).

Sample No	²²⁶ Ra	²³² Th	⁴⁰ K	¹³⁷ Cs
S1	3.6 ± 0.2	5.2 ± 0.3	72.6 ± 3.6	610 ± 30
S2	5.5 ± 0.3	7.2 ± 0.4	118.7 ± 5.9	870 ± 40
S3	3.3 ± 0.2	5.2 ± 0.3	89.0 ± 4.5	660 ± 30
S4	3.9 ± 0.2	6.4 ± 0.3	115.8 ± 5.8	490 ± 30
S5	4.9 ± 0.2	6.9 ± 0.3	102.4 ± 5.1	780 ± 40
S6	3.8 ± 0.2	6.0 ± 0.3	95.1 ± 4.8	590 ± 30
S7	6.2 ± 0.3	7.8 ± 0.4	120.1 ± 6.0	930 ± 50
S8	4.3 ± 0.2	6.2 ± 0.3	98.8 ± 4.9	720 ± 40
S9	4.0 ± 0.2	5.5 ± 0.3	81.3 ± 4.1	660 ± 30
S10	5.9 ± 0.3	7.6 ± 0.4	116.9 ± 5.8	890 ± 50

The measured activity concentrations of ²²⁶Ra ranged from 3.3 Bq kg⁻¹ (Sample S3) to 6.2 Bq kg⁻¹ (Sample S7). These values are within the typical range found in soil samples from various geological regions. The presence of ²²⁶Ra in soil can be attributed to the natural decay series of uranium and its abundance in the Earth's crust. For ²³²Th, the activity concentrations varied from 5.2 Bq kg⁻¹ (Sample S3) to 7.8 Bq kg⁻¹ (Sample S7). The activity concentrations of ⁴⁰K were found to be in the range of 81.3 Bq kg⁻¹ (Sample S9) to 120.1 Bq kg⁻¹ (Sample S7). Furthermore, the anthropogenic radionuclide ¹³⁷Cs was detected in all samples, with activity concentrations ranging from 490 Bq kg⁻¹ (Sample S4) to 930.0 Bq kg⁻¹ (Sample S7). The observed elevated activity concentrations of ¹³⁷Cs in the soil samples from the Zlatibor region can potentially represent a radiological risk to the environment and human health. The radiological risk associated with ¹³⁷Cs stems from its long half-life of approximately 30 years. This means that even though it is considered

a short-term hazard due to its high radioactivity, it can persist in the environment for an extended period. ^{137}Cs emits gamma radiation, which can penetrate the body and pose a risk to human tissues and organs if exposure levels are significant [6].

3. Conclusion

The analysis of soil samples from the Zlatibor region revealed the presence of both natural radionuclides (^{226}Ra , ^{232}Th , and ^{40}K) and anthropogenic radionuclide ^{137}Cs . The elevated levels of ^{137}Cs indicate a potential radiological risk to the environment and human health. Continuous monitoring and mitigation strategies are crucial to ensure the safety and sustainable development of the region, minimizing the potential impacts of ^{137}Cs on the ecosystem and local population. Public awareness and education on radiological risks are essential in fostering responsible practices and safeguarding the well-being of the community.

Acknowledgment

This work was supported by the Ministry of Education, Science and Technological Development of Serbia through Agreements No. 451-03-47/2023- 01/200122 and 451-03-47/2023-01/200378.

References

- [1] SRBATOM (2021) <http://www.srbatom.gov.rs/srbatommm/posledice-akcidenta-u-fukusimi-na-srbiju/?lang=en>
- [2] G. Steinhauser, A. Brandl, T.E. Johnson, *Comparison of the Chernobyl and Fukushima nuclear accidents: a review of the environmental impacts*, Science of The Total Environment, 470–471 (2014) 800–817.
- [3] UNSCEAR (2008) Report to the general assembly. Sources and effects of ionizing radiation, vol II. United Nations, New York
- [4] M. M. Janković, Rajačić, M., Jelić, I., Krneta-Nikolić, J. D., Vukanac, I., Dimović, S., Sarap, N., M.Ž. Šljivić-Ivanović, *Distribution of Natural Radionuclides and ^{137}Cs in Urban Soil Samples from the City of Novi Sad, Serbia - Radiological Risk Assessment*, Toxics, 11(4) (2023) 345.
- [5] A. Jose, J. Jorge, M. Cleomacio, V. Sueldo, D.S. Romilton, *Analysis of the ^{40}K levels in soil using gamma spectrometry*, Brazilian Archives of Biology and Technology 48 (2005) 221-228.
- [6] Kabata-Pendias A., Trace elements in soils and plants, 4th edn. CRC Press, (2011) New York

Influence of different production systems and tomato genotypes on the content of macroelements in tomato fruits

Vojin Cvijanović¹, Beka Sarić², Marija Bajagić³, Petar B. Stanić^{4*}, Nenad Đurić⁵, Gordana Dozet⁶, Gorica Cvijanović⁴

¹ Institute for Science Application in Agriculture, 68b Blvd. despota Stefana, Belgrade, Serbia; e-mail: vcvijanovic@ipn.bg.ac.rs

² Maize Research Institute "Zemun Polje", Slobodana Bajića 1, 11185 Belgrade, Serbia;

³ University of Bijeljina, Faculty of Agriculture, Pavlovića put bb, Bijeljina, BiH;

⁴ University of Kragujevac, Institute for Information Technologies, Jovana Cvijića bb., Kragujevac, Serbia; e-mail: petar.stanic@uni.kg.ac.rs, cvijagor@yahoo.com

⁵ Institute of Vegetable Growing, Karađorđeva 71, Smederevska Palanka, Serbia; e-mail: nenad.djuric@outlook.com

⁶ Megatrend University Belgrade, Faculty of Biofarming, Bačka Topola, Serbia; e-mail:

* Corresponding author

DOI: 10.46793/ICCBi23.205C

Abstract: Agriculture has managed to produce enough food for the accelerated population growth, which has led to environmental transformation and increasingly intensive exploitation of both renewable and non-renewable natural resources. The use of synthetic plant protection agents and fertilizers can lead to negative consequences in food production. Identification of agricultural food production systems is gaining importance in order to protect human health and the environment. Interest in the cultivation of certain plant species with an innovative approach to cultivation and technology has grown significantly. Organic and integrated agriculture implies the use of natural products while limiting or completely eliminating the use of synthetic resources. Knowledge of the mineral composition in tomato samples can be used as a potent tool in the identification of chemical markers as potential indicators of the farming system. The goal of the research is to determine the impact of different production systems on the content of macroelements in the fruits of different types of tomatoes.

Keywords: tomato, organic and integrated, macroelement, growing systems

1. Introduction

Tomato (*Lycopersicon esculentum* L.) is an important vegetable in daily feeds to enrich our foods with a number of contents such as organic acids, vitamins, carotene, lycopene, sugars, amino acids, and minerals that are essential in human health and proper functioning [1]. Tomatoes are rich in vitamins C, E and B, copper and iron, and minerals such as potassium, sodium, magnesium and calcium [2]. Vitamin E (α -tocopherol), carotenoids, lycopene in particular, and various phenolic compounds are among the chief components of tomato fruit that have beneficial health properties. Mineral

elements are essential substances which are required for proper physiology and anatomy of humans and animals [3]. Magnesium is an essential element required as a cofactor for over 300 enzymatic reactions and is therefore necessary for the biochemical functioning of numerous metabolic processes [4]. Sodium is vital in the human body for regulating blood pressure, stimulating nerves and muscles; calcium has some very important life-supporting functions because it is a structural component of bones, teeth, and soft [5,6]. Phosphorus is a basic unit in DNA, and RNA and serves as an energy store in metabolic reactions of biological systems [7,8]. To ensure food and ecosystem security, it is necessary to design a model and produce future crops for sustainable agriculture by maximizing production and minimizing adverse environmental impacts [9].

The aim of the work was to determine the content of macroelements in tomato fruits of different types, as well as which type of tomato has a higher content of the examined macroelements.

2. Material and method

The research was conducted during one growing season in 2020, in controlled microclimate conditions, in order to examine the influence of integrated and organic cultivation systems on the content of macroelements in tomato fruits. The research was conducted on the sample of the company "Zeleni hit", in "13. May", in the vicinity of Zemun Polje. The experiment was set up in a closed facility, the total area of 320 m² (8 m x 40 m), a ridge height of 5 m.

The experimental parts of the research were designed as a two-factor experiment:

- Factor A: growth system
 - o integrated
 - o organic;
- Factor B: selected tomato genotypes, a total of 4 hybrids, two from each of the dominant tomato species
 - o Cherry (hybrids: Sakura and Tomagino)
 - o Beef (hybrids: Rally and Velocity)

In both systems, researchers have used bio-pesticides, beneficial microorganisms and predators, as well as pheromone traps and mass trapping systems to protect crops from pests and diseases. Everything was done to harvest the final product without pesticide residues, which was confirmed by certified laboratories Faculty of Chemistry in Belgrade. The determination of trace element content in the tomato sample was carried out by elemental analysis using an ICP-OES device. When it comes to weed control, researchers used silver polyethylene mulch in the integrated farming system, and a layer of organic matter for covering in the organic system, which allows for high thermal stability, as well as preservation of soil moisture and accessible nutrients in the soil.

3. Results

Table 1 shows the results of the analysis of the content of seven macroelements in the fruits of the tomato hybrids tested. Based on the average values from both production systems, tomato fruits from the integral production system had a higher content of Ca by 2,44%, P by 8.53% and S by 5.71%. The obtained results can be explained by the fact that mineral fertilizers based on these elements can be used in integral production, which is not allowed in the organic system.

The content of K was higher in the organic system by only 0.89% and Mg by 3.13%. In both production systems, according to the number of identified macroelements, hybrids of the type that stood out were Beef.

Table 1. The content of macroelements in the fruits of tomato hybrid grown in both production systems.

	Hybrids	Type		Ca	Fe	K	Mg	Na	P	S
Integrated	Tomagino	Cherry	1	1380	1130	17900	1310	540	4430	1680
	Sakura		2	704	142	21700	1780	543	4680	1890
	Average 1-2			1042	636	19800	1545	541	4555	1785
	Velocity	Beef	3	1990	67	25100	1950	918	4870	1690
	Rally		4	1620	80	25400	1720	482	3470	1180
	Average 3-4			1805	73	25250	1835	700	4170	1435
Average 1-4			1424	355	22525	1690	621	4363	1610	
Organic	Tomagino	Cherry	1	1040	889	19800	1420	668	4340	1410
	Sakura		2	389	1530	19300	1350	809	3280	915
	Average 1-2			714	1209	19550	1385	738	3810	1162
	Velocity	Beef	3	1730	1540	27300	2160	1300	4360	1780
	Rally		4	2400	296	24500	2040	798	4100	2000
	Average 3-4			2065	918	25900	2100	1049	4230	1890
Average 1-4			1390	1064	22725	1743	893	4020	1526	

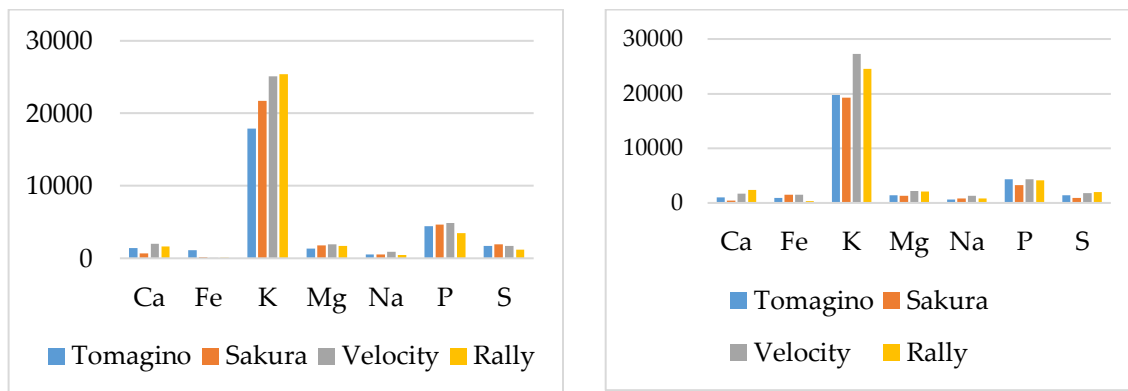


Figure 1. Content of macroelements in the fruits of tomato hybrids grown in an integral system and organic system ($\text{mg}\cdot\text{kg}^{-1}$ dry matter).

3. Conclusions

The content of certain elements, the concentrations of which are higher in integrally produced tomato fruits than in organically produced fruits, may be the result of the application of fertilizers that, in addition to macroelements, also contain microelements. Beef type hybrids had a higher concentration of examined macroelements in both production systems.

Acknowledgment

This paper is a result of the research conducted within the contract on the implementation and financing of scientific research in 2023, between the Institute for Science Application in Agriculture, Belgrade and the Ministry of Science, Technological Development and Innovation of the Republic of Serbia, contract numbers: 451-03-47/2023-01/ 200045 and 451-03-47/2023-01/ 200378.

References

- [1] F. Qu, J. Zhang, X. Ma, *Effects of different N, P, K, and Ca levels on tomato yield, quality and fertilizer use efficiency*, *Plant, Soil and Environment* 6 (2020) 569-75.
- [2] S. Setiarti, I. Heru. L. Shinta, S. Nita, *The Effects of Tomato Concentration on Sensory and Chemical Properties of Jelly Drink*, *The 6th International Conference of Food, Agriculture, and Natural Resource (IC-FANRES 2021)*, *Advances in Biological Sciences Research* 16 (2022) 184-189.
- [3] Md Yousuf Ali, Abu A.I. Sina, S. Saif Khandker, L. Neesa, E.M. Tanvir, A. Kabir, Md Ibrahim Khalil, Siew Hua Gan, *Nutritional Composition and Bioactive Compounds in Tomatoes and Their Impact on Human Health and Disease: A Review*, *Foods* 10 (2021) 45.
- [4] G.K. Schawalfenberg S.J. Genuis, *The Importance of Magnesium in Clinical Healthcare*, *Scientifica* (2017) 4179326.
- [5] C. Véronique, *Current Data with Inulin-Type Fructans and Calcium, Targeting Bone Health in Adults*, *Journal of Nutrition* 137 (2007) 2527S-2533S.
- [6] S. Kumar, P.H.R. Gowda, N.M. Mallikarjuna, *Evaluation of selected F6 tomato lines for extended shelf life*, *SABRAO Journal of Breeding and Genetics* 47 (2015) 326-34.
- [7] M. Oves, I.M.I. Iqbal, *Phosphate availability and importance in a living system*, *Acta Scientific Microbiology* 2 (2019) 40-41.
- [8] J. Serna, C. Bergwitz, *Importance of dietary phosphorus for bone metabolism and healthy aging*, *Nutrients* 12 (2020) 1-44.
- [9] Z. Tian, J. Wang, J. Li, B. Han, *Designing future crops: challenges and strategies for sustainable agriculture*, *The Plant Journal* 105 (2022) 1165-1178.

Challenges in radiotherapy planning in patients with synchronous rectal and prostate cancer and hip prosthesis

Marija Živković Radojević^{1,2*}, Neda Milosavljević^{1,2}, Slađana Aćimović Talijan²,
Tatjana B. Miladinović³, Aleksandar Miladinović², Miloš Grujić^{2,4}

¹University of Kragujevac, Faculty of Medical Sciences, Department of Clinical Oncology, Kragujevac, Serbia; email: makizivkovicmarija@gmail.com, neda.milosavljevic@yahoo.com

²University Clinical Centre Kragujevac, Centre for Radiation Oncology, Radiotherapy Department, Kragujevac, Serbia; email: sladjana.acimovic84@gmail.com, miladinovic.al@gmail.com

³University of Kragujevac, Institute for Information Technologies, Department of Science, Kragujevac, Serbia; email: tanja.miladinovic@uni.kg.ac.rs

⁴University of Kragujevac, Faculty of Medical Sciences, Kragujevac, Serbia; email: grujcmilos10@gmail.com

* Corresponding author

DOI: 10.46793/ICCBi23.209ZR

Abstract:

Background. Prostate and rectal carcinomas, although among the most common malignancies in males, rarely exhibit synchronous diagnosis and treatment of both malignancies. This paper presents a case of a patient with synchronous prostate and rectal carcinoma and an artificial right hip, which complicates the creation of a radiotherapy plan.

Case Report. A 76-year-old male was diagnosed with synchronous mucinous infiltrating adenocarcinoma of the rectum (T3N0M0) and adenocarcinoma of the prostate (T3aN0M0), confirmed by immunohistochemistry. He had a history of testicular carcinoma previously treated with orchiectomy, chemotherapy, and radiotherapy. The treatment approach involved neoadjuvant chemotherapy with 5-fluorouracil and leucovorin, following the protocol for rectal carcinoma, and concurrent radiotherapy for both rectal and prostate carcinoma. The presence of an artificial metal right hip prosthesis made the creation of the radiotherapy plan more challenging. The plan was developed by defining four target volumes and delineating artifacts in the soft tissue and bony structures. It was designed to deliver the prescribed dose using 6 MV photon energy during 25 radiotherapy sessions, applying a simultaneous integrated boost. The best dose delivery was achieved with the VMAT plan, and the analysis of dose-volume histograms (DVH) indicated satisfactory contributions to organs at risk.

Conclusion. Individualized approaches in treating patients are particularly important in cases of synchronous tumors. As oncology patients tend to have longer overall survival, special attention must be given to the patient's quality of life, necessitating organ sparing during radiotherapy treatment. The complexity of treatment planning due to the presence of comorbidities and metal implants is overcome through excellent collaboration between radiation oncologists and medical physicists.

Keywords: prostate cancer, rectal cancer, hip prosthesis, radiotherapy

1. Introduction

Prostate and rectal carcinomas are the most common malignancies in males, accounting for 7.3% and 6% of the overall cancer incidence, respectively [1]. Although they are frequently encountered in clinical practice, the synchronous diagnosis and treatment of both malignancies are rare [2]. According to current recommendations, rectal carcinoma is initially treated with neoadjuvant chemoradiation, followed by surgical treatment, while patients with high-risk prostate cancer are treated with definitive radical radiotherapy combined with androgen deprivation therapy (ADT) [3,4]. Radiation therapy for synchronous malignancies in the pelvic region poses a significant challenge for radiation oncologists [5]. Treating prostate and rectal cancer requires the use of highly sophisticated radiotherapy techniques that ensure precise dose delivery to the target volumes while sparing the surrounding healthy tissues. The presence of artificial metal hip prostheses greatly complicates the creation of a radiotherapy plan as it affects the dose distribution within the target volumes and organs at risk (OAR) [6,7].

The aim of this study is to present a patient with synchronous rectal and prostate carcinoma and an artificial titanium prosthesis in the right hip, which hinders the development of the radiotherapy plan.

2. Case report

The patient, 76 years old, was diagnosed synchronously with mucinous infiltrating adenocarcinoma of the rectum (T3N0M0) and adenocarcinoma of the prostate (T3aN0M0), with an initial PSA level of 100 ng/ml. Immunohistochemical analysis revealed that these malignancies have different origins. Diagnostic imaging (multislice scan (MSCT) of the chest, abdomen and pelvis, and bone scintigraphy) indicated that both diseases are localized. The urology multidisciplinary tumor board (MDT) decided to proceed with radical radiotherapy for prostate cancer without androgen deprivation therapy (ADT). The digestive MDT decided to initiate treatment with neoadjuvant chemotherapy using the 5-fluorouracil-leucovorin regimen along with preoperative radiotherapy. In the patient's personal medical history, there is a reported presence of abdominal aortic aneurysm, and past testicular cancer treated with orchiectomy, chemotherapy, and radiotherapy (although medical documentation was not provided). The patient is also being treated for hypertension and is regularly using medication therapy.

2.1 Challenges in radiotherapy treatment planning

Before initiating the treatment, the patient underwent an examination and informative interview with a radiation oncologist at the Center for Radiation Oncology, University Clinical Center Kragujevac. An initial CT simulation was performed on the

G Discovery CT machine. The patient was positioned in a prone position with belly board immobilization. Co-registration with the pre-treatment MSCT imaging was performed.

Initially, the delineation of organs at risk (OAR) was carried out, followed by the delineation of the metal hip prosthesis. Since the CT simulator did not have software for metal artifact reconstruction, tissue density optimization was necessary for accurate dose calculation. For this reason, the delineation of artifacts in the soft tissue and bone structures was performed (Figure 1). As the precise tissue density in the artifact region was not known, auxiliary structures named "soft tissue" and "bone" were created in artifact-free regions, based on which the radiotherapy planning system calculated tissue density. Thus, the artifacts in the soft tissue were assigned a density of 50 Hounsfield units (HU), while the bone was given a density of -110 HU.

Integrating the recommendations for delineating target volumes for preoperative radiotherapy of rectal and prostate cancer led to the creation of four target volumes for irradiation [3,4]: PTV 45 Gy (regional lymph nodes, both carcinomas, mesorectum, prostate, and seminal vesicles); PTV 60 Gy (prostate and seminal vesicles); and PTV 63.5 Gy (prostate) (Figure 1). The prescribed dose was intended to be delivered using 6 MV photon energy during 25 radiotherapy sessions, applying simultaneous integrated boost, enabling simultaneous irradiation of multiple target volumes with different therapeutic doses.

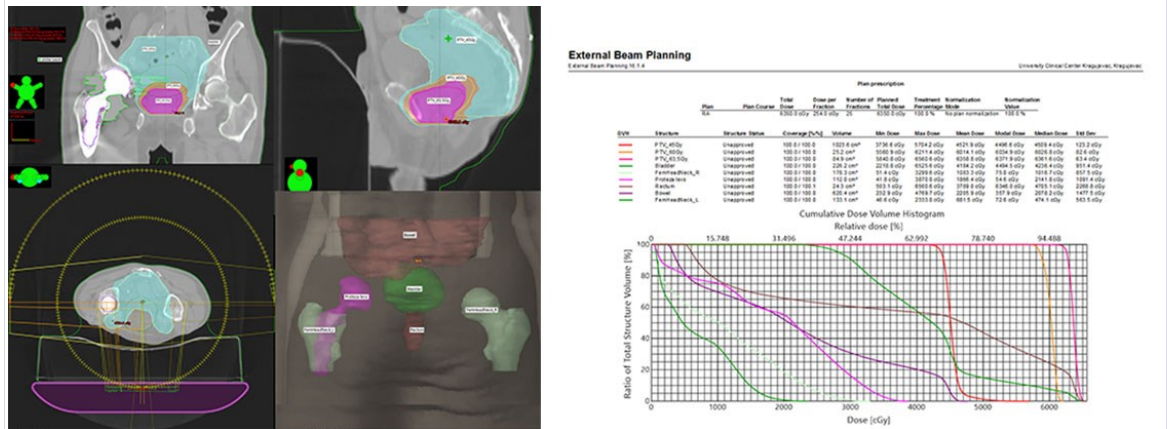


Figure 1. VMAT plan for patient with a metal hip prosthesis and simultaneous rectal and prostate cancer and dose volume distribution.

Multiple radiotherapy plans were initially created using 3D-CRT, IMRT, and VMAT techniques, with the VMAT plan using two partial arcs and two full arcs providing the best dose delivery (Figures 1 and 2). The assessment of dose distribution on OAR was performed after analyzing the DVH (Figure 2). The contributions to dose on OAR were satisfactory [3,4]. During the planning process, the optimizer utilized an option to avoid angles passing directly through the artificial hip prosthesis, ensuring an adequate dose distribution.

After evaluating the radiotherapy plan and analyzing the dose-volume histogram (DVH), and ensuring accuracy and verification, the patient was properly positioned in the therapeutic position. Throughout all radiotherapy sessions, regular quality assurance (QA) procedures were conducted, including verification of the

patient's position and target volumes using Cone Beam CT imaging. Once a week, the patient was monitored by the radiation oncologist, including checking laboratory analyses, conducting a physical examination, and assessing the presence and intensity of radiation toxicity. In the patient's case, mild genitourinary toxicity of grade one was verified, in accordance with CTCAE v.5 criteria [8].

3. Conclusions

Since there are no recommendations for simultaneous radiotherapy treatment of rectal and prostate cancer, it is necessary to approach the treatment of each patient individually. Considering the presence of large target volumes for irradiation, special attention must be given to sparing organs at risk (OAR). Oncology patients now exhibit longer overall survival, making the approach to specific oncological treatment significantly more complex in situations involving comorbidities and metal implants. Effective collaboration between radiation oncologists and medical physicists allows for overcoming challenges in radiotherapy planning for patients with a metal hip prosthesis and simultaneous rectal and prostate cancer.

References

- [1] H. Sung, J. Ferlay, R.L. Siegel, M. Laversanne, I. Soerjomataram, A. Jemal, F. Bray, *Global Cancer Statistics 2020: GLOBOCAN Estimates of Incidence and Mortality Worldwide for 36 Cancers in 185 Countries*, *CA Cancer J Clin*, 71 (2021) 209-249.
- [2] N.A. Lavan, D.O. Kavanagh, J. Martin, C. Small, M.R. Joyce, C.M. Faul, et al., *The curative management of synchronous rectal and prostate cancer*, *Br J Radiol*, 89 (2016) 20150292.
- [3] NCCN Clinical Practice Guidelines in Oncology. Prostate Cancer Version: 2.2023. Available at: www.nccn.org/guidelines/category_1
- [4] NCCN Clinical Practice Guidelines in Oncology. Rectal Cancer Version: 4.2023. Available at: www.nccn.org/guidelines/category_1
- [5] A. Doussot, D. Vernerey, E. Rullier, J.H. Lefevre, H. Meillat, E. Cotte, et al; French Research Group of Rectal Cancer Surgery (GRECCAR)., *Surgical Management and Outcomes of Rectal Cancer with Synchronous Prostate Cancer: A Multicenter Experience from the GRECCAR Group*, *Ann Surg Oncol*, 11 (2020) 4286-4293.
- [6] D. To, I. Khaferllari, M. Liu, J. Liang, C. Knill, S. Nandalur, et al., *Evaluation of VMAT Planning Strategies for Prostate Patients with Bilateral Hip Prosthesis*, *Technol Cancer Res Treat*, 20 (2021) 15330338211038490.
- [7] A.M. Fischer, P.J. Hoskin., *Radiotherapy-induced toxicity in prostate cancer patients with hip prostheses*, *Radiat Oncol*, 17 (2022) 9.
- [8] National Cancer Institute, National Institutes of Health USD. U.S. Department of health and human services., *Common Terminology Criteria for Adverse Events (CTCAE)*. U.S. Department of Health and Human Services, Common Terminology Criteria for Adverse Events (CTCAE) Version 5.0 Published: 2017.

Exploring the Pharmacokinetic Properties of $(\text{NH}_4)_4[\text{Fe}(\text{idadtc})_2]$: *In Silico* Biological screening and ADMET analysis

Marko Antonijević¹, Milica Kosović Perutović², Zorica Leka^{2*}, Zoran Marković¹

¹ University of Kragujevac, Institute for Information Technologies, Department of Science, Jovana Cvijića bb, 34000 Kragujevac, Serbia; e-mail: mantonijevic@uni.kg.ac.rs, zmarkovic@uni.kg.ac.rs

² University of Montenegro, Faculty of Metallurgy and Technology, Džordža Vašingtona bb, 81000 Podgorica, Montenegro, e-mail: zorica@ucg.ac.me, mkosovic@ucg.ac.me

* Corresponding author

DOI: 10.46793/ICCB23.213A

Abstract: Carbonic anhydrases (CA) have been identified in the early '50s as potential targets for the treatment of numerous diseases, including cancer, glaucoma, epilepsy, etc. Current inhibitors, i.e., treatment options, offer high efficacy coupled with a high probability of various side-effects. On the other hand, dithiocarbamates and their metal complexes are known for being good CA inhibitors. In this paper, a novel Fe (II) dithiocarbamate complex was investigated for its biological and pharmacological properties using a combination of different *in silico* methodologies. It was found that this water soluble, almost non-toxic (LD_{50} values around 4860 mg/kg), druglike compound shows high inhibitory potential towards CA II. However, it also shows slow gastro-intestinal absorption, which means that, if ever used as a pharmacological agent, in its present form cannot be orally administrated. Binding energies with the value of $-7.8 \text{ kcal mol}^{-1}$ indicate reversible binding to human serum albumin, which can serve as a delivery system for the investigated compound. Overall, the obtained results indicate a high potential of $(\text{NH}_4)_4[\text{Fe}(\text{idadtc})_2]$ to be an effective CA II inhibitor.

Keywords: Dithiocarbamates, Carbonic anhydrases, Albumin, ADMET, Acetazolamide

1. Introduction

Carbonic anhydrase II (CA II) is an enzyme from the family of carbonic anhydrases, which catalyses the reversible hydration of carbon dioxide. It is a zinc-containing metalloenzyme found in high concentrations in red blood cells, where it serves a crucial role in the transport of carbon dioxide from tissues to the lungs. In addition, this enzyme has been linked to several other physiological processes, including acid-base regulation, bone resorption, and fluid secretion. Additionally, CA II has been identified as a potential drug target for a variety of diseases, including glaucoma, epilepsy, and cancer [1-2]. Since the 1950s, CA inhibitors have been the subject of extensive research for the treatment of epilepsy, heart disease, cancer, and altitude illness. The medication known as acetazolamide was one of the first and most important carbonic anhydrase inhibitors. It is commonly used to treat, among other conditions, altitude sickness, glaucoma,

epilepsy, edema, etc. Additionally, it is used to treat metabolic alkalosis, a condition characterized by excess concentrations of bicarbonate ions in the organism. This medication reduces the production of cerebrospinal fluid, thereby reducing intracranial pressure, and providing relief to patients with hydrocephalus and pseudotumor cerebri. As with all medications, acetazolamide can cause adverse effects including nausea, dizziness, tingling in the extremities, etc. [2-3].

Dithiocarbamates are a class of chemical compounds which consist of a carbon atom bonded to two sulphur atoms and an additional nitrogen atom. Due to their diverse properties and prospective applications, these customizable compounds have proven to be of great use in different fields. They have shown promising antifungal, antibacterial, and antiviral activities, making them valuable candidates for the development of novel antimicrobial agents. In addition, their potential function as anticancer agents has been investigated due to their ability to induce apoptosis and inhibit tumour cell proliferation via a variety of cellular mechanisms. As chelating compounds that form stable complexes with various metal ions, dithiocarbamates have been utilized in medicinal chemistry for metalloenzyme inhibition [4-6]. Despite their pharmacological potential, the adverse effects and toxicity profiles of dithiocarbamates must be thoroughly evaluated to ensure their safe and effective use in the pharmaceutical industry [3-6].

In this paper, a comprehensive biological screening, including ADMET (*Absorption, Distribution, Metabolism, Excretion and Toxicity*) analysis of (NH₄)₄[Fe(idadtc)₂] was performed. Since this compound in our previous endeavours was found to be highly soluble in water, and dithiocarbamate derivatives are known for being bioactive compounds, it was reasonable to perform a scan of its biological properties and investigate its potential pharmacological application [7].

2. Materials and Methods

The SwissTargetPrediction [8] was used to predict the potential protein/enzyme targets for the examined compound. Further, the AutoDock4.2 software package was used to run molecular docking simulations (MD) to acquire more precise parameters and binding affinities of examined complexes towards the selected targets, following the methodology described in detail in our previous work [9]. The protein structure under IDs: 2BDX (*Human Serum Albumin-HSA*) and 2EU2 (*Carbonic Anhydrase II - CA II*) were obtained from the RCSB Protein Data Bank. BIOVIA Discovery Studio 2020 was used to prepare and visualize the results. Finally, ADMET analysis was performed using ADMETlab 2.0, and toxicological assessment was further confirmed by ProToxII [8, 9].

3. Results and discussions

According to the results obtained through the SwissTargetPrediction website, (NH₄)₄[Fe(idadtc)₂] is a possible inhibitor of CA II. These findings are strongly supported by the literature data [10-12]. To assess the inhibitory potential of the investigated compound towards the CA II, MD techniques were employed. Obtained results

presented in Table 1, show excellent inhibitory activity of the investigated compound towards this enzyme. Moreover, if we compare the results with the data obtained for acetazolamide, as well as ligand (ammonium-amino-diacetato-dithiocarbamate-idadtc), we can conclude that investigated compounds show higher binding potential, indicating better inhibitory activity.

Table 1. Thermodynamic parameters describing inhibitory potential of (NH₄)₄[Fe(idadtc)₂]

Compound	acetazolamide	idadtc	(NH ₄) ₄ [Fe(idadtc) ₂]
Gr _{ind} (kcal mol ⁻¹)	-6.39	-5.74	-8.67
K _i (μM)	21.08	62.02	0.44

In order for the investigated compound to demonstrate its inhibitory potential, it must possess the appropriate pharmacokinetic and toxicological profiles. Since the first parameter which eliminates the highest percentage of potential pharmacological agents is a toxicological effect, (NH₄)₄[Fe(idadtc)₂] was subjected to the toxicological analysis. Obtained results suggest that the investigated compounds are low in overall toxicity, with LD₅₀ values 4860mg/kg, which puts it in Class V (*may be harmful if swallowed*), almost Class VI (*non-toxic*) (LD₅₀ > 5000 mg/kg) on the toxicity scale. However, further ADMET analysis showed low gastro-intestinal (GI) absorption, moving the investigated compound towards Class IV: *harmful if swallowed*. The same data was obtained for the idadtc, while acetazolamide had LD₅₀ values of 4300 mg/kg. However, ProToxII indicated the potential carcinogen potential of acetazolamide, which was not the case for the other compounds within this study. Other ADMET parameters indicated that (NH₄)₄[Fe(idadtc)₂] is highly water soluble, has no blood-brain barrier permeability, shows no affinity towards P450 enzymes and according to Pfizer and Lipinski rules represents a drug-like structure.

However, because of the low GI absorption, this compound could not be administrated orally. Because of that, HSA binding was investigated, by utilization of the MD once more. According to the obtained results, (NH₄)₄[Fe(idadtc)₂] shows excellent binding to the HSA, with binding energies of -7.8 kcal mol⁻¹. The combination of good inhibitory activity towards the CA II, high water solubility, low toxicity and good HSA binding potential makes (NH₄)₄[Fe(idadtc)₂] a suitable candidate for further pharmacological testing.

4. Conclusions

In conclusion, this paper explored the pharmacological and biological properties of a (NH₄)₄[Fe(idadtc)₂], as a potential inhibitor of CA II. The results revealed that the investigated complex exhibits significant inhibitory activity against CA II, making it a promising candidate for the treatment of various diseases, including cancer, glaucoma, and epilepsy. Despite its high inhibitory potential, the compound displayed slow gastrointestinal absorption, which limits its feasibility for oral administration as a pharmacological agent. However, the compound's water solubility and low toxicity make it an attractive candidate for alternative delivery methods, with human serum

albumin (HSA) identified as a potential delivery system for this compound due to its reversible binding affinity. Further studies and optimizations are necessary to enhance its bioavailability and identify suitable administration routes, thereby unlocking the full therapeutic potential of this dithiocarbamate complex.

Acknowledgment

This research is funded by the Ministry of Education and Ministry of Science, Technological Development and Innovation, Republic of Serbia, Grants: No. 451-03-47/2023-01/200378.

References

- [1] C. T. Supuran, *Carbonic anhydrases-an overview*. *Current pharmaceutical design*, 14(7) (2008) 603-614.
- [2] M. B. Stokes, W. P. A. Chan, M. I. Worthley, & P. T. Coates, *Acetazolamide—another tool in the congestion battle?* *Kidney International*, 103(6) (2023) 1012-1014.
- [3] C. T. Supuran, *Emerging role of carbonic anhydrase inhibitors*. *Clinical Science*, 135(10) (2021) 1233-1249.
- [4] J. W. D. F. Oliveira, H. A. O. Rocha, W. M. T. Q. de Medeiros, M. S. Silva, *Application of dithiocarbamates as potential new antitrypanosomatids-drugs: Approach chemistry, functional and biological*. *Molecules*, 24(15) (2019) 2806.
- [5] Wei, M.X., Zhang, J., Ma, F.L., Li, M., Yu, J.Y., Luo, W. and Li, X.Q., *Synthesis and biological activities of dithiocarbamates containing 2 (5H)-furanone-piperazine*. *European Journal of Medicinal Chemistry*, 155 (2018) 165-170.
- [6] Ahmed, A.J., *Metal complexes of dithiocarbamate derivatives and its biological activity*. *Asian J. Chem*, 30 (2018) 2595-2602.
- [7] Z.Leka, D.Čikić, A.Gežović, *Examination of the mechanochemical reaction of Fe(II)- salt with iminodiacetatodithiocarbamate-ligand (idadc³⁻)*. 59th Meeting of the Serbian Chemical Society, Novi Sad, June 2023, Book of Abstracts, 90
- [8] Gfeller, D., Grosdidier, A., Wirth, M., Daina, A., Michielin, O., & Zoete, V. *SwissTargetPrediction: a web server for target prediction of bioactive small molecules*. *Nucleic acids research*, 42(W1), (2014) W32-W38.
- [9] Jovanović, J. Đ., Antonijević, M., Vojinović, R., Filipović, N. D., & Marković, Z. *In silico study of inhibitory capacity of sacubitril/valsartan toward neprilysin and angiotensin receptor*. *RSC advances*, 12(46), (2022) 29719-29726.
- [10] Carta, F., Aggarwal, M., Maresca, A., Scozzafava, A., McKenna, R., Masini, E. and Supuran, C.T., *Dithiocarbamates strongly inhibit carbonic anhydrases and show antiglaucoma action in vivo*. *Journal of medicinal chemistry*, 55(4), (2012) 1721-1730.
- [11] Winum, J.Y. and Supuran, C.T., *Recent advances in the discovery of zinc-binding motifs for the development of carbonic anhydrase inhibitors*. *Journal of enzyme inhibition and medicinal chemistry*, 30(2), (2015) 321-324.
- [12] Hogarth, G., *Metal-dithiocarbamate complexes: chemistry and biological activity*. *Mini reviews in medicinal chemistry*, 12(12), (2012) 1202-1215.

The influence of different plasticizers on the mechanical properties of active edible bilayer films

Tamara Erceg^{1*}, Olja Šovljanski¹, Ana Tomić¹, Nevena Vukić², Dejan Kojić³, Senka Popović¹, Vesna Teofilović¹

¹ University of Novi Sad, Faculty of Technology Novi Sad, Serbia, tamara.erceg@uns.ac.rs, oljasovljanski@uns.ac.rs, anav@uns.ac.rs, madjarev@uns.ac.rs, vesnateofilovic@uns.ac.rs

² University of Kragujevac, Faculty of Technical Sciences, Čačak, Serbia, nevena.vukic@ftn.kg.ac.rs

³ PIM University Banja Luka, Technical Faculty, Despota Stefana Lazarevića bb, Banja Luka, Bosnia and Herzegovina, dejan.kojic@univerzitetpim.com

* Corresponding author

DOI: 10.46793/ICCBi23.217E

Abstract: In addition to potentially resolving environmental issues that come from plastic and food waste, active biodegradable packaging is being developed to increase the shelf life, quality, and safety of packaged food. In order to overcome the drawbacks of monolayer hydrocolloid-based coating, such as poor mechanical and barrier properties, the design of bilayer hydrocolloid-based coating has been structured using pullulan and gelatin. Sugar alcohols are widely used for the plasticizing of biopolymer-based films. The aim of this work is to investigate the influence of different sugar alcohols – xylitol, mannitol, and glycerol on the mechanical properties of pullulan/gelatin bilayer films. Among investigated plasticizers, glycerol has demonstrated the best plasticizing effect, giving a bilayer film with the value of elongation at break which is 66.5 and 88.4% greater than the same values for the bilayer films prepared using xylitol and mannitol. The formulation with glycerol has been applied for the preparation of active edible coating using the mixture of two hydrolats – lemongrass and curry plant. Obtained coatings have shown great potential for the improvement of packaged cheese shelf-life.

Keywords: active edible bilayer coating, Pullulan, Gelatin, sugar alcohols

1. Introduction

Edible films can be effective barriers that prevent unwanted mass transfers in foods and are also a *green* alternative to synthetic petroleum-based polymer packaging materials [1, 2]. In that way, they can help extend the shelf life of certain food products by providing a protective barrier against moisture and gases [3, 4]. Some edible packaging materials may contain added nutrients or functional compounds that make them active. Recently, there has been growing interest in research into the use of edible films containing natural preservatives in food protection [5]. The active compounds mostly are a variety of antioxidants, antimicrobials, probiotics, or other incorporated ingredients [1]. The

development of edible packaging is still in its early stages, and there may be things to overcome to find the right balance between the packaging's durability and its edibility. The development of bilayer edible packaging films involves addressing various challenges, such as optimizing its mechanical strength, improving gas barrier properties, and ensuring it remains safe for consumers. The bilayer approach usually involves two edible materials with different functions. This paper aims to study the effect of various plasticizers (glycerol, xylitol, and mannitol) on the mechanical properties of active edible films based on pullulan and gelatin. Gelatin is an edible animal-originated protein with remarkable film-forming ability, biocompatibility, nontoxicity, and biodegradability which makes it ideal for food packaging applications [6]. Pullulan is an exopolysaccharide obtained from the fermentation of black yeast and is considered a promising material for edible films due to its film-forming properties, biodegradability, and biocompatibility. The interest in the use of pullulan for edible packaging is growing due to several advantages such as the lack of taste and odor, and the ability to create transparent, shiny, and flexible films with relatively low oxygen and lipid permeability. Both pullulan and gelatin are biodegradable materials and compatible with different food products, making the packaging environmentally friendly and safe for consumption.

2. Experimental part

2.1. Materials

Pullulan ($M_w \sim 574\ 570$ g/mol) was acquired from Avena Lab (Vršac, Srbija). Xylitol and mannitol were purchased from Sigma Aldrich, USA, while gelatin and glycerol were purchased from Centrohem.

2.2 Methods

The film-forming solutions were prepared by dissolving pullulan (10 wt%) and gelatin (4 wt%) in a mixture of curry plant (*Helichrysum italicum*) and lemongrass (*Cymbopogon citratus*) in a ratio of 1:1. The solutions were prepared with the addition of different types of plasticizers (xylitol, mannitol and glycerol) in the amount of 30 wt% per biopolymer weight. The bilayer film was produced using a solution-casting technique. After drying of pullulan-based film, the gelatin-based solution with the same plasticizer type was poured onto the surface of the pullulan film.

The chemical structure of obtained films was analyzed by Fourier-transform infrared spectroscopy (FTIR) (Thermo Fisher Scientific, MA, USA) operating in total reflectance attenuation (ATR) mode.

Mechanical properties of obtained bilayer films were investigated using the Instron Universal Testing Instrument Model 4301 (Instron Engineering Corp., Canton, MA) according to the ASTM standard D882-18. All tests were performed at a temperature of 23 ± 2 °C with an initial grip spacing set to 50 mm and a crosshead speed of 10 mm/min. In order to investigate the ability of an active edible coating to prolong the storage time of cheese slices, the same were contaminated by inoculation with bacterial suspension after application of the edible coating in order to simulate the contamination during the

storage and distribution. The coating was applied by spraying on the cheese surface. Sampling and analysis were performed at regular time intervals during the 28 days.

3. Results and discussion

Figure 1 shows the FTIR spectra of Pull, Gel, and bilayer Pull/Gel film with incorporated hydrolats. The broad peak with the center at 3342 cm^{-1} in the FTIR spectrum of neat Pull is attributed to OH stretching. The overlapping of N-H and OH stretching vibrations of amino acids in gelatin results in a broad absorption band between 3600 and 3000 cm^{-1} (Figure 1b). Two peaks between 2900 and 2800 cm^{-1} in spectra of neat biopolymers are attributed to C-H stretching. In the spectrum of bilayer film with hydrolats and plasticizers (Figure 1c), there are three peaks in this range. A peak at 1646 cm^{-1} corresponds to an O-C-O bond in Pull, while the absorption band at 1631 cm^{-1} in the spectrum of Gell corresponds to CO stretching. The band at 1547 in the spectrum of Gel and bilayer film is attributed to NH bending and C-N stretching. Stretching of the COO-group appears as a weak peak at 1453 cm^{-1} in both spectra (Figure 1b and c).

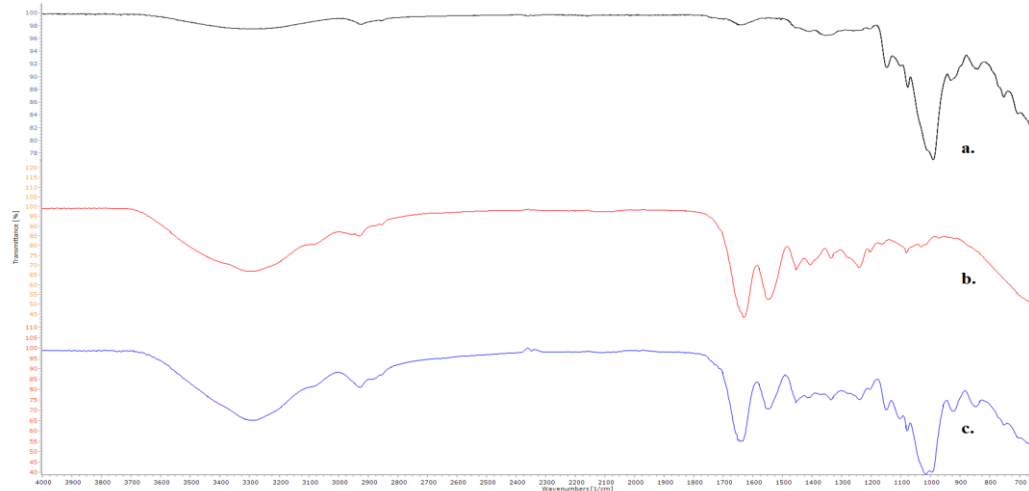


Figure 1. FTIR spectra of a) Pull, b) Gel, c) bilayer Pull/Gel-g film.

In comparison to the monolayer films (Pull and Gel), bilayer films possess improved values of tensile strength (TS), and elongation of break (EB) in comparison to the neat Gel (Table 1). Among investigated plasticizers, glycerol has demonstrated the best plasticizing effect, resulting in the bilayer film (Pull/Gel-g) with an EB value that is 65.8% greater than the EB value of bilayer film prepared with xylitol as plasticizer (Pull/Gel-x), and even 88.4% higher EB value in comparison to the EB value of bilayer film prepared with mannitol (Pull/Gel-m).

Table 1. Tensile strength (TS) and elongation at break (EB) for edible bilayer films with different plasticizer type.

Samples	Tensile strength (N/mm ²)	Elongation at break (%)
Pull	14.23	25.60

Gel	15.34	8.23
Pull/Gel-x	32.20	9.12
Pull/Gel-m	30.45	8.6
Pull/Gel-g	31.45	15.12

Pull/Gel active coating exhibited a reduction in bacterial concentration for 50% at day 3, and complete elimination of *S. aureus* cells at day 14, demonstrating the efficiency against this pathogen and the potential to be applied for prolongation of cheese slices' shelf-life.

3. Conclusions

Bilayer active edible films based on Pull and Gel with glycerol as a plasticizer have shown the best mechanical properties (the greatest EB value) in comparison to the films prepared with xylitol and mannitol as plasticizers. The obtained formulation has demonstrated potential in the application for the packaging of cheese slices, enabling the prolongation of the shelf-life of this food product.

Acknowledgment

This research is funded by the Ministry of Science, Technological Development and Innovation, Republic of Serbia, project number 451-03-47/2023-01/ 200134.

References

- [1] T. Erceg, N. Vukić, O. Šovljanski, et al. Preparation and characterization of biodegradable cellulose acetate-based films with novel plasticizer obtained by polyethylene terephthalate glycolysis intended for active packaging. *Cellulose* 30 (2023) 5825–5844.
- [2] N. Vukić, T. Erceg, M. Hadnađev, The investigation of edible packaging films based on pullulan and alginate, 11th International Symposium on Graphic Engineering and Design, November 2022, Novi Sad, Serbia, 447-452.
- [3] T. Erceg, N. Vukić, O. Šovljanski, et al. Characterization of Films Based on Cellulose Acetate/Poly(caprolactone diol) Intended for Active Packaging Prepared by Green Chemistry Principles. *ACS Sustainable Chemistry & Engineering*. 10 (28) (2022) 9141-9154.
- [4] M. Gniewosz, K. Pobiega, K. Kraśniewska, A. Synowiec, M. Chaberek, S. Galus, Characterization and Antifungal Activity of Pullulan Edible Films Enriched with Propolis Extract for Active Packaging. *Foods* (2022) 11, 2319.
- [5] A. Trajkovska Petkoska, D. Daniloski, N. Kumar et al. Active Edible Packaging: A Sustainable Way to Deliver Functional Bioactive Compounds and Nutraceuticals. In: Muthu, S.S. (eds) *Sustainable Packaging. Environmental Footprints and Eco-design of Products and Processes*. Springer (2021) Singapore.
- [6] T. Erceg, O. Šovljanski, A. Stupar et al. A comprehensive approach to chitosan-gelatine edible coating with beta-cyclodextrin/lemongrass essential oil inclusion complex - Characterization and food application. *International Journal of biological Macromolecules* (2023), 228, 400-410.

Patch clamp pipette giga seal forming success on the nanosurgery-obtained filamentous fungi protoplasts

Katarina Stevanović¹, Tanja Pajić^{1*}, Aleksandar Krmpot², Mihailo Rabasović², Milan Žižić^{3,4}, Miroslav Živić¹, Nataša V Todorović⁵

¹ University of Belgrade, Faculty of Biology, Institute of Physiology and Biochemistry, Studentski trg 16, 11158 Belgrade, Serbia; e-mail: katarina.stevanovic@bio.bg.ac.rs; tpajic@bio.bg.ac.rs; mzivic@bio.bg.ac.rs

² University of Belgrade, National Institute of the Republic of Serbia, Institute of Physics Belgrade, Pregrevica 118, 11080 Belgrade, Serbia ; e-mail: krmpot@ipb.ac.rs; rabasovic@ipb.ac.rs

³ University of Belgrade, Institute for Multidisciplinary Research, Kneza Višeslava 1, 11030 Belgrade, Serbia

⁴Elettra - Sincrotrone Trieste, Strada Statale 14, km 163.5 in Area Science Park, 34149 Basovizza, Trieste, Italy; e-mail: mzizic1004@gmail.com

⁵ University of Belgrade, National Institute of the Republic of Serbia, Institute for Biological Research "Sinisa Stankovic", Bulevar Despota Stefana 142, 11000 Belgrade, Serbia; e-mail: nara@ibiss.bg.ac.rs

* Corresponding author

DOI: 10.46793/ICCBi23.221S

Abstract: The success of patch-clamp giga-ohm seal formation on filamentous fungi *Phycomyces blakesleeanus* protoplasts was investigated to evaluate their usefulness in ion channel studies on filamentous fungi. Protoplasts were obtained by laser-mediated nanosurgery of the cell wall stained with Calcofluor White. To enable a successful seal formation, it is critical to prevent cell wall regeneration. Since wall integrity responses in fungi involve kinase-dependent pathways, we aimed to sufficiently reduce intracellular ATP availability using the respiratory inhibitor azide. The effect of azide on phosphate metabolites of *Phycomyces blakesleeanus*, as determined by ³¹P NMR spectroscopy, was a reduction in intracellular ATP accompanied by a decrease in long chain polyphosphates. Subsequently, all seal formation measurements were performed in the presence of azide, and protoplast viability was confirmed by cytoplasmic streaming. The success of seal formation depends on the size of the protoplasts, as larger protoplasts are more prone to successful seal formation. It was also found that the laser power used in nanosurgery could influence the success of seal formation, as higher values were associated with a lower success rate. The protoplasts released by laser nanosurgery produced by our newly developed method are a good model system for patch clamp on filamentous fungal membranes because their plasma membrane can easily form high-quality seals with the patch pipette.

Keywords: *Phycomyces*, azide, laser surgery

1. Introduction

Filamentous fungi (FF) hyphae perform important functions in most ecosystems based on their ability to excrete, transport, and exchange signals with the environment. Although FF plasma membrane ionic currents are thought to play an essential role in their excreting/transporting/signaling functions, they remain insufficiently explored because of technical difficulties in accessing the plasma membrane of FF, which is covered by a cell wall that has a distinct regenerative capacity [1]. The patch-clamp method, the gold standard for electrophysiological measurements, can only be applied to a healthy, clean plasma membrane accessible to the patch pipette. We developed a laser nanosurgery-based method of FF cell wall removal to obtain naked fungal cells (protoplasts) with a healthy and clean plasma membrane [2]. Briefly, the principle of the method was as follows: 1. Plasmolysed hyphae were subjected to laser sectioning of the cell wall stained with Calcofluor White; 2. Hyphae were partially deplasmolyzed. Cell wall regeneration was inhibited throughout the procedure. Successful formation of a gigaohmic resistance ($G\Omega$) seal between the patch-clamp pipette and protoplast plasma membrane is a prerequisite for the patch-clamp current recording. Here, we investigated whether azide is a good wall regeneration inhibitor and which parameters in our new method affect the formation of the $G\Omega$ -seal.

2. Material and Methods

The culture of the filamentous fungus *Phycomyces blakesleeanus* (Burgeff) wt. (NRRL 1555(-)) was grown from the spore stock according to the standard protocol [3]. The ^{31}P NMR spectra were recorded from a control culture and an age-matched culture treated acutely with 5 mM azide. The details of the procedure, experimental setup and quantification of peak intensity were as previously described [3]. For the nanosurgery patch-clamp experiments, the cultures were grown with the following modifications: Spore cultures were plated on glass coverslips coated with 50% collagen type I and grown in media with glucose reduced to 10 g/l. Cultures (19-30 hours old) were stained with 1% Calcofluor White dye (Sigma Aldrich) in nominally isosmotic solution (ISOSOL, contains in mM: 60 KCl, 65 K-glutamate, 2 MgCl₂, 1 CaCl₂, 2 mM azide, 10 HEPES pH 7, supplemented with sucrose to 495 mOsm) with the addition of 10 μM brefeldin A for 10 min at 20°C. Subsequently, the stained cultures were washed and plasmolyzed in hyperosmotic solution (HYPERSOL, composed as ISOSOL, with $[\text{Ca}^{2+}]$ increased to 30 mM and sucrose replaced with sorbitol to bring the osmolarity to 620 mOsm). Details of the experimental setup for Nonlinear Laser Scanning Microscope for Two Photon Excitation Fluorescent (TPEF) imaging and laser nanosurgery were previously described [2, 4]. The nanosurgical pattern was positioned in the empty hyphal section (where the hyphal protoplast had retracted from the area due to plasmolysis) (Fig. 1a, left). After laser nanosurgery, the resulting cell wall incision was verified by TPEF and bright-field imaging (Fig. 1a, middle and right, respectively). The release of protoplasts through the wall incision was monitored by bright field microscopy. Subsequently, the fungal culture was transferred to the patch-clamp setup (an EPC8 amplifier connected to an

Istrutec 1600 digitizer, along with Pulse software (all from HEKA)). The $\frac{1}{4}$ of the solution was carefully replaced with an appropriate solution to bring the final osmolarity of the chamber bath solution to 595 mOsm. The pipettes for the patch clamp, pulled on a Sutter p-97 puller had a resistance of 10-20 M Ω . Statistical comparisons were performed using ANOVA with multiple comparisons and Holm-Sidak correction, and an unpaired two-tailed t-test with Welch's correction for unequal variances. Confidence levels for statistical significance were 0.05 (*), 0.01 (**), and 0.005 (***)

3. Results and Discussion

To enable successful seal formation, it was critical to prevent cell wall regeneration, both at the hypha prior to protoplast release and at the released protoplasts. Since wall integrity responses in fungi involve kinase-dependent pathways [1], we aimed to reduce intracellular ATP availability by using the respiratory inhibitor azide. The effect of azide on phosphate metabolites of *P. blakesleeanus*, as determined by ^{31}P NMR spectroscopy (Fig. 1B), was a decrease in intracellular ATP (measured as a $20 \pm 8\%$ decrease in the

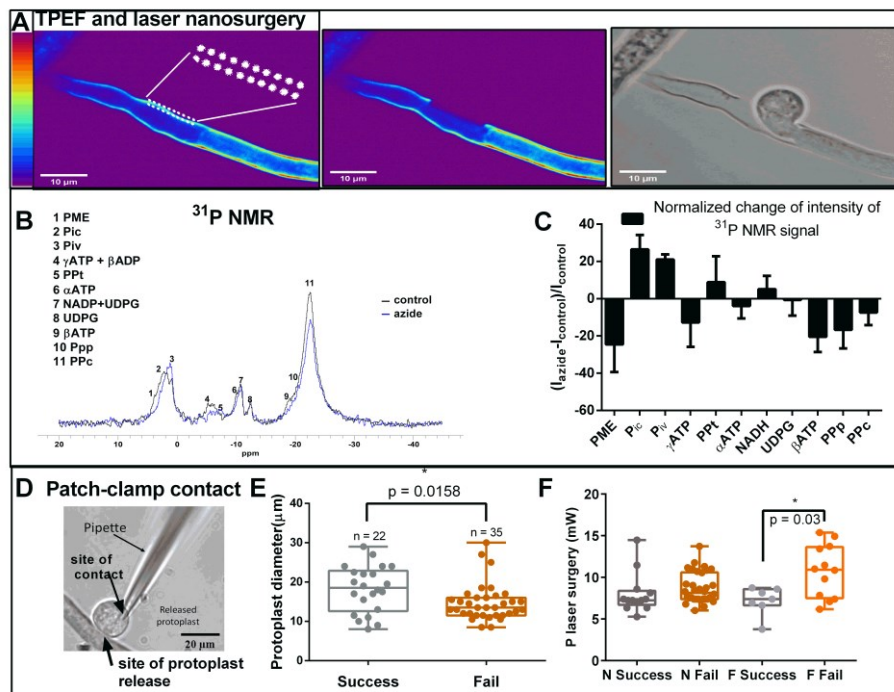


Figure 1. Success of patch-clamp pipette contact with the membrane of protoplasts released by laser nanosurgery. **A.** The procedure of obtaining protoplasts by laser nanosurgery. Left and middle: TPEF images before and after laser nanosurgery of hypha cell wall; Right: brightfield image of protoplast crawling through laser-made incision. Color bar for TPEF images is on the far left **B.** Overlapped ^{31}P NMR spectra of *P. blakesleeanus*, obtained in control conditions and after azide addition. Peaks (annotated by numbers) can be assigned to corresponding phosphate-containing molecules: 1. sugar phosphate (PME); 2. inorganic phosphate cytoplasmatic (Pic); 3. Inorganic phosphate vacular (Piv); 4. γ -ATP and β -ADP (γ ATP); 5. terminal phosphate residues of polyphosphates (PolyP) and pyrophosphate (PPT); 6. α -ATP; 7. NAD(H) and uridine diphosphoglucose (UDPG); 8. UDPG second resonance; 9. β -ATP; 10. penultimate phosphates of PolyP (PPp); 11. central PolyP residues (PPc). **C.** Normalized change of intensity of ^{31}P NMR signal, calculated for each peak as $(I_{\text{azide}} - I_{\text{control}}) / I_{\text{control}}$. Values shown are mean \pm SD (n=3). **D.** Brightfield image of the patch-clamp pipette on the nanosurgery-released protoplast during forming G Ω contact (seal). **E.** Diameters

of the nanosurgery-released protoplasts, sorted according to failure or success in forming the seal. T-test with Welch's correction. F. Laser surgery power at the sample, used for nanosurgeries performed in a close proximity ($<3 \mu\text{m}$) of retracted protoplast (N-"near") and for nanosurgeries at distance larger than $3 \mu\text{m}$ from the retracted protoplast in hypha (F-"far"), sorted according to failure or success in forming the seal. ANOVA with Holm-Sidak correction.

signal intensity of the β -phosphate group of ATP) accompanied by acidification of cytoplasm reflected through upfield shift of Pic signal and decrease of long-chain polyphosphates (Fig. 1C). The desired inhibition of wall regeneration by azide during nanosurgery and patch clamp was confirmed by 1. the released protoplasts; 2. formed $G\Omega$ -contacts at the protoplast plasma membrane (as shown in Fig. 1D). In addition, the viability of hyphae and the obtained protoplasts was confirmed by observing the presence of cytoplasmic streaming in bright field microscopy. Protoplasts obtained after nanosurgery exhibited a range of diameters, with a significant difference ($p=0.016$) between groups sorted by $G\Omega$ -seal formation success (in μm): $d_{\text{succ}} = 18 \pm 6$ ($n=22$), $d_{\text{fail}} = 15 \pm 5$ ($n=35$) (Fig. 1E). It is possible that a skilled patch-clamp operator could improve the success rate on smaller protoplasts, with further practice. Variation in the laser power applied during nanosurgery showed that it is safer to use lower values, as a significant difference in laser power was found for nanosurgery sorted by $G\Omega$ -sealing success, that was performed farther from the hyphal protoplast (Fig. 1F).

3. Conclusions

The protoplasts released by our newly developed laser nanosurgery method are a good model system for the patch-clamp method on filamentous fungal membranes because their plasma membrane can easily form high-quality seals with a patch pipette.

Acknowledgment

The authors acknowledge funding provided by the Ministry of Science Technological Development and Innovation, Republic of Serbia through the Grants: No. 451-03-47/2023-01/200007, 451-03-47/2023-01/200178, 451-03-47/2023-01/ 200053; by Science Fund of the Republic of Serbia, grant number 4545 [BioPhysFUN]; by the Institute of Physics Belgrade, through the grant provided by the Ministry of Science Technological Development and Innovation.

References

- [1] A. Yoshimi, K. Miyazawa, et al. *Cell Wall Integrity and Its Industrial Applications in Filamentous Fungi*. J. Fungi. 8 (2022) 435.
- [2] T. Pajić, K. Stevanović, N.V. Todorović, et al. *Laser nano-surgery of fungal cell wall to enable patch clamping*. 18th European Molecular Imaging Meeting, Saltzburg, 2023. PW36#1095.
- [3] M. Živić, J. Zakrzewska, et al. *31P NMR study of polyphosphate levels during different growth phases of *Phycomyces blakesleeanus**. Antonie Van Leeuwenhoek 91(2) (2007)169-177.
- [4] T. Pajić, N.V. Todorović, M. Živić, et al. *Label-free third harmonic generation imaging and quantification of lipid droplets in live filamentous fungi*. Sci Rep. 12(1) (2022) 18760.

Analysis of heavy metals in the soil in the Ibar river valley in the district of Kosovska Mitrovica

Svetlana Belošević^{1*}, Maja Đukić², Marija Ristić², Ljubomir Milentijević¹, Slavica Jovanović¹, Katarina Mačenovski Gagnon¹, Jakov Danilović¹

¹ University of Priština in Kosovska Mitrovica, Faculty of Technical Sciences, Knjaza Miloša 7, 38220 Kosovska Mitrovica, Republic of Serbia; e-mail: svetlana.belosevic@pr.ac.rs, bubosivi028@gmail.com, slavicaj1982@hotmail.com, katarinamacenovski@gmail.com, jakovd74@gmail.com

² University of Kragujevac, Faculty of Science, Radoja Domanovića 12, 34000 Kragujevac, Republic of Serbia; e-mail: maja.djukic@pmf.kg.ac.rs, marija.jeremic@pmf.kg.ac.rs

* *Corresponding author*

DOI: 10.46793/ICCBi23.225B

Abstract: Soil, air, and water pollution is emerging as a major problem in many cities because of industrialization and fast-paced lifestyles. The main sources of pollution in such environments are combustion products originating from industry, traffic, city heating plants, individual fireplaces, and construction activities, but also improper storage of industrial and communal waste. Soil is a complex and specific layer of the earth's crust that represents a geochemical "accumulator" of pollutants and plays an important role in environmental processes where it acts as a natural buffer that controls the transport of chemical elements and compounds to the atmosphere, hydrosphere, and the living world. Most of the industry in its production processes uses various mineral resources, the burning and melting of which results in the emission of dust, smoke, and suspended particles containing heavy metals, which are deposited in the soil from the air. The greening of urban areas through the construction of parks and green oases is of great importance for the reduction of soil pollution and the rest of the environment and for the preservation of urban ecosystems.

Keywords: soil pollution, heavy metals, environmental

1. Introduction

Intensive urbanization and industrialization led to the development of new and expansion of existing cities and industrial basins, where today, for the first time in history, more than half of the human population lives. Even though cities occupy only 2% of the Earth's surface, they are responsible for as much as 75% of resource consumption globally [1]. Pollution of air, water, soil, and vegetation occurs as a basic problem in cities and industrial zones, which are most often in or near large cities. The main sources of pollution in such environments are combustion products originating from industry, traffic, city heating plants, individual fireplaces, construction activities,

but also improper storage of industrial and communal waste. The conditions of emission of pollutants, climatic conditions and the method of greening have a great influence on soil pollution with various organic and inorganic pollutants and on changing its physical and chemical characteristics.

Soil is a complex and specific layer of the earth's crust created because of the joint and mutual action of the lithosphere, atmosphere, hydrosphere, and biosphere. [2] In addition to being a geochemical "accumulator" of pollutants, soil plays an important role in environmental processes where it acts as a natural buffer that controls the transport of chemical elements and compounds to the atmosphere, hydrosphere, and living world. [3] Of all natural bodies, the soil is the most inert, but in cities, it is constantly exposed to various anthropogenic influences, and direct and indirect human activity, which is why compared to soil in natural environments, it often has a damaged structure, altered physical and chemical characteristics, including a reduced content of nutrients, but also depleted fauna.

Soil quality is of crucial importance for the environment, which in urban and industrialized environments is damaged due to the release of various pollutants originating from mobile and stationary sources. Without a doubt, traffic represents one of the main sources of pollutants in urban areas that negatively affect the condition and quality of land, vegetation, and population. Heavy metals (HMs) are a special type of pollutant in urban soils. [4] The risk of HMs pollution lies in the fact that they are persistent and do not undergo biological degradation, which is why when they reach the soil they remain there for a very long time and are available for uptake by plants.

HMs in natural soils mainly originate from rocks and minerals that make up the Earth's crust, while in urban soils they are often of anthropogenic origin. [5] In urban soils, the main anthropogenic sources of HMs are pollutants originating from industry, traffic, and industrial and urban waste. Traffic-related activities also lead to the emission of metals in the form of dust and suspended particles from car exhaust or particles created by the wear and tear of various vehicle parts and the friction of tires on road surfaces. [6] Metals whose origin in urban soils is related to traffic and whose concentrations are most often measured and monitored are Pb, Cu, Zn, Cd, and Cr. [7] Municipal waste has a heterogeneous chemical composition and often contains large amounts of Cd, Pb, Zn, and Cu. Careless disposal of municipal waste in small areas can lead to the accumulation of very high concentrations of HMs in the soil. Due to all the above, numerous studies have been conducted on the topic of determining their overall content and behavior in the soil, as well as their potential impact on the environment [8-9]. The results of such research contribute to the characterization of contamination and enable the finding of adequate ways to protect and restore polluted urban soils.

2. Study area and sample collection

The Ibar is a river in the southwestern part of Serbia and the eastern part of Montenegro, with a total length of 276 km and a catchment area of 8,059 km². The Ibar springs from a strong spring under Mount Hajla in eastern Montenegro, 10 km upstream

from Rožaj, then flows east to Kosovska Mitrovica in Kosovo, then north to Kraljevo where it flows into West Morava. The basin lies between 42°21' and 43°44' north latitude and 19°55' and 21°29' east longitude. Relief, altitude, climate, and geological composition played a significant role in the formation of the pedological cover. The study area is located in Northern Kosovo in the district of Kosovska Mitrovica in the lower flows of the Ibar River.

2.1 Preparation of soil samples for analysis

The preparation of a representative sample was carried out using the method of random squares, which were taken from several measurement points, and then a composite sample was prepared. 5-10 g of soil was weighed on an analytical scale and poured with 20 mL of aqua regia. The sample was left to stand for 24 h, then heated in a water bath at 95 °C for 2 h. The cooled sample was strained into a volumetric flask of 100 mL and topped up with water to the line. The test was performed using the NITRON XRF ANALYZER method.

2.2 Results of measurements of HMs in the soil

The results of the measurement of HMs in the soil are shown in the Table 1. Measurements were made at four measuring points: Measuring point 1 “Žitkovac”, Measuring point 2 “Vojni remont”, Measuring point 3 “Česmin lug” and Measuring point 4 “Kablar”.

Table 1. Results of measuring HMs at four different measuring points.

	Measuring point 1	Measuring point 2	Measuring point 3	Measuring point 4
HMs	Measured value (ppm)	Measured value (ppm)	Measured value (ppm)	Measured value (ppm)
Mo	Ø	Ø	Ø	2.3
Zr	137.74	250.24	296.58	Ø
Sr	172.96	147.71	168.86	298.6
Rb	36.37	23.71	73.8	Ø
Pb	16811.97	9829.06	2100.26	27152.14
As	408.18	540.76	36.22	825.0
Hg	Ø	Ø	Ø	Ø
Zn	4426.38	2351.8	552.54	4998.08
Cu	1491.12	147.64	38.32	6894.65
Ni	537.68	163.98	162	Ø
Co	36.64	Ø	Ø	Ø
Fe	51543.82	35455.25	31458.01	11836.99
Mn	469.21	653.92	252.13	797.2
Cr	646.63	282.04	340.22	89.6

The measured values are in accordance with the expected results for this area and type of soil, as well as with the degree of its pollution.

3. Conclusions

The most abundant elements are lead, zinc, and iron, which are in accordance with anthropogenic sources of soil pollution originating from industry, traffic, industrial and urban waste. The presence of the most dangerous HMs such as mercury, molybdenum, and chromium are at minimum values, which indicates that the pollution is at a level where there is a possibility of recultivating the soil in order to return it to an uncontaminated form.

Acknowledgment

This research is funded by the Ministry of Education and Ministry of Science, Technological Development and Innovation, Republic of Serbia, Grants: No. 451-03-47/2023-01/200122.

References

- [1]. Y. M. Galitskova, A. I. Murzayeva, *Urban soil contamination*, *Procedia Engineering* 153 (2016) 162-166.
- [2]. B. J. Alloway, *Heavy metals in soils*, Springer Dordrecht (1995) 368 pp.
- [3]. A. Kabata-Pendias, H. Pendias, *Trace elements in soils and plants*, CRC Press LLC, Boca Raton, London, New York, Washington (2001) 413 pp.
- [4]. M. Biasioli, R. Barberis, F. Ajmone-Marsan, *The influence of a large city on some soil properties and metals content*, *Science of the Total Environment* 356 (2006) 154-164.
- [5]. C. Y. Chang, H.Y. Yu, J. J. Chen, F. B. Li, H. H. Zhang, C. P. Liu, *Accumulation of heavy metals in leaf vegetables from agricultural soils and associated potential health risks in the Pearl River Delta, South China*, *Environmental Monitoring and Assessment* 186 (2014) 1547-1560.
- [6]. J. C. Akan, S. I. Audu, Z. Mohammed, V. O. Ogugbuaja, *Assessment of heavy metals, pH, organic matter and organic carbon in roadside soils in Makurdi metropolis, Benue State, Nigeria*, *Journal of Environmental Protection* 4(6) (2013) 18-628.
- [7]. P. B. Tchounwou, C. G. Yedjou, A. K. Patlolla, D. J. Sutton, *Heavy metals toxicity and the environment*, *Molecular, Clinical and Environmental Toxicology* 101 (2012) 133-164.
- [8]. D. Cakmak, V. Perović, M. Kresović, D. Jaramaz, V. Mrvić, S. Belanović Simić, E. Saljnikov, G. Trivan, *Spatial distribution of soil pollutants in urban green areas (a case study in Belgrade)*, *Journal of Geochemical Exploration* 188 (2018) 308-317.
- [9]. N. Barać, *Mobilnost i biodostupnost odabranih elemenata u poljoprivrednom zemljištu aluviona reke Ibar*, Doktorska disertacija, Tehnološko-metalurški fakultet, Univerzitet u Beogradu (2017).

Water quality analysis in the district of Kosovska Mitrovica

Svetlana Belošević^{1*}, Maja Đukić², Marija Ristić², Ljubomir Milentijević¹, Slavica Jovanović¹, Katarina Mačenovski Gagnon¹, Jakov Danilović¹

¹ University of Priština in Kosovska Mitrovica, Faculty of Technical Sciences, Knjaza Miloša 7, 38220 Kosovska Mitrovica, Republic of Serbia; e-mail: svetlana.belosevic@pr.ac.rs, bubosivi028@gmail.com, slavicaj1982@hotmail.com, katarinamacenovski@gmail.com, jakovd74@gmail.com

² University of Kragujevac, Faculty of Science, Radoja Domanovića 12, 34000 Kragujevac, Republic of Serbia; e-mail: maja.djukic@pmf.kg.ac.rs, marija.jeremic@pmf.kg.ac.rs

* Corresponding author

DOI: 10.46793/ICCB123.229B

Abstract: Water is extremely important for the continuation of life. Water is life. Water is an essential substance not only for humans but for all living things. The demand for water, whose usage areas are expanding with the change in living conditions, is increasing day by day. Water, soil, and air, which are the basic components of the earth, constitute the basic components that ensure the continuity of life. Using and protecting the natural composition of soil, water, and air without disturbing it is an absolute necessity for sustainable living and the natural environment. In addition, for a sustainable natural environment, economic decisions and natural environment decisions should be evaluated together and together in accordance with the purpose of sustainable development. As a matter of fact, in order to protect the natural environment and transfer this value to future generations in the same way, all the elements that make up the natural environment should be considered as an inseparable whole and the perception and awareness that the negative effects that may occur in any of them will affect the other elements in sequence. Since ensuring the sustainability of water and resources is very important for life, benefiting from water resources in various fields should be seamlessly sustainable in the future as in the past and today.

Keywords: water analysis, environmental, drinking water

1. Introduction

Water covers more than two-thirds of the planet, but readily available freshwater – found in rivers, lakes, wetlands, and aquifers – accounts for less than 1 percent of the world's water supply. As the global population grows, so do the demands for water – for drinking, sanitation, agriculture, and energy production, among many other uses. At the same time, human activity and climate change are disrupting natural water cycles, putting the source of our water, our freshwater ecosystems, under pressure. [1]

Pollution, infrastructure development, and exploitation of resources represent additional challenges. Poor water management, pollution, infrastructure development, and resource extraction further exacerbate the negative impacts on our freshwater systems.

Water, as an irreplaceable foodstuff, occupies a special place among environmental factors, on which the life and health of people, as well as the economic and cultural development of society, depend [2]. Water is a good of general interest, it represents the wealth of every country, it is socially owned, and it serves to satisfy general and individual needs [3]. Water is essential for maintaining life in general and makes up 60-70% of body weight [4].

From a hygienic point of view, water is important not only as a basic foodstuff and an environment in which complex biochemical processes take place but also because the causative agents of many infectious diseases and chemical toxic substances can be transmitted with it.

The epidemiological importance of water is great, every year around 3 million people die worldwide due to the use of improper drinking water [5]. Due to the importance of water and its multipurpose use, it enjoys special protection and is used in the manner prescribed by law. Water of unsanitary quality can endanger health in several ways.

2. Water analysis

The beginning of the organized supply of drinking water in Kosovska Mitrovica dates back to 1938. The basic raw material for providing drinking water is the Ibar Lepenac canal, water intake from Lake Gazivode.

Water quality control was carried out from the central and city water supply systems in the north and south of Kosovo and Metohija: 988 samples for physical and chemical analysis and 989 samples for bacteriological analysis. The percentage of defective samples is 3.64% in physical-chemical testing and 5.86% in bacteriological testing of water quality. Since the end of 2019, Kosovska Mitrovica has been supplied with water from the new water supply system and the old water supply system located on the south side of the city. Drinking water in the municipality of Kosovska Mitrovica is chemically correct and safe for health, and the percentage of defective samples in the 2022 physicochemical test was 1.62% and in the bacteriological test 3.24%. Increased turbidity, the presence of KMnO_4 , and the presence of *E. coli* bacteria are the causes of defective water samples.

Tests were conducted in accordance with ISO standards *JUS ISO 9001* and *JUS/ISO/IEC 17025* in the accredited laboratories of the Institute for Health Protection of Kosovska Mitrovica.

Table 1. The results of testing the hygienic correctness of drinking water and other waters presented as an annual cumulative report.

	Chemical correctness of water			Biological correctness of water		
	Total number of samples	Correct	Defective	Total number of samples	Correct	Defective
Kosovska Mitrovica central water supply	431	424	7 (1.62%)	432	418	14 (3.24%)
Kosovska Mitrovica surface, waste, and other waters	30	29	1 (3.33%)	30	29	1 (3.33%)

Comparing the number of correct samples in relation to the number of defective ones, which is very small, indicates a high level of drinking water quality in the area of Kosovska Mitrovica.

3. Conclusions

Water is one of the most essential needs for life. Water shortages already exist in many regions, with more than one billion people without adequate drinking water. This situation is one of the most important indicators of why we should be very sensitive and conscious towards our water resources. As the world population increases, the need for water also increases. However, as a result of different effects and especially human activities, water resources are decreasing, polluted and still used unconsciously. Therefore, it is necessary to take and implement measures as soon as possible and we have to use water resources carefully. We must act in the awareness that the lives of future generations are in our hands. The prerequisite for this is to leave potable water and a livable environment to future generations.

Acknowledgment

This research is funded by the Ministry of Education and Ministry of Science, Technological Development and Innovation, Republic of Serbia, Grants: No. 451-03-47/2023-01/200122.

References

- [1]. D. Pimentel, B. Berger, D. Filiberto, M. Newton, B. Wolfe, E. Karabinakis, S. Clark, E. Poon, E. Abbett, S. Nandagopalet, *Water Resources, Agriculture, and the Environment*. Ithaca (NY): New York State College of Agriculture and Life Sciences, Cornell University. Environmental Biology Report. (2004) 1–46.
- [2]. Z. Kiliç, *The importance of water and conscious use of water*. Int J Hydro. 4(5) (2020) 239-241.
- [3]. I. A. Shiklomanov, J.C. Rodda, *World Water Resources at the Beginning of the Twenty-first Century*, Cambridge (United Kingdom): Cambridge University Press, 2003.
- [4]. Riebl SK, Davy BM. The Hydration Equation: Update on Water Balance and Cognitive Performance. ACSMs Health Fit J. 2013 Nov;17(6):21-28.
- [5]. <https://www.who.int/news-room/fact-sheets/detail/drinking-water>

The effect of consumer ethnocentrism on the competitiveness of the economy of the Republic of Serbia

Ana Spasojević ^{1*}, Stefan Zdravković ²

¹ University of Kragujevac, Faculty of Economics, e-mail: ana.spasojevic@kg.ac.rs

² University MB, Faculty of Business and Law in Belgrade, e-mail: szdravkovic034@yahoo.com

* *Corresponding author*

DOI: 10.46793/ICCB23.232S

Abstract: The goal of the research is to determine whether consumer ethnocentrism has a positive impact on the competitiveness of companies at the micro level, as well as whether the aforementioned implies an improvement in competitiveness at the macro level, i.e., the state's ability to place its products on the international market and thus ensure economic growth and an increase in the standard of living of citizens. Research was conducted using the survey method in which 128 citizens of the Republic of Serbia and 37 managers employed in domestic companies participated, and their answers were analyzed using the SPSS statistical program. The results showed that there is a high degree of consumer ethnocentrism among consumers in Serbia, as well as that the managers of domestic companies claim that such a purchase pattern improves the competitiveness of companies on a micro level. After that, on the basis of the Diamond Model of National Advantages by Michael Porter, as well as the Global Competitiveness Index of The World Economic Forum, the conclusion is drawn that the competitiveness of companies (micro level) improves the competitiveness of the state (macro level).

Keywords: consumer ethnocentrism, microeconomic competitiveness, macroeconomic competitiveness, economy, Republic of Serbia

1. Introductory considerations and literature review

Ethnocentrism is a concept that has a sociological genesis and is based on the belief of members of one society that their culture is dominant compared to any culture of another society [1]. From the basic concept of ethnocentrism, consumer ethnocentrism has developed, which represents an economic component and is based on people's belief that buying domestic products and services is an ethical issue, because it contributes to the increase in the employment rate of the population and the standard of living of citizens, while on the other hand, the import of goods causes certain economic consequences for the national economy [2]. Analyzes of the results of previous studies [1,2] show that a high degree of consumer ethnocentrism implies the purchase of domestic products and services by consumers. The first research hypothesis can be formulated:

H1: Consumer ethnocentrism has a statistically significant positive influence on the intention of consumers in the Republic of Serbia to buy domestic products and services.

Previous studies [3,4] have determined that consumer ethnocentrism is a cohesive factor that unites citizens in the intention that in crisis situations it is necessary to buy domestic products in order to support the domestic economy. The pandemic of the COVID-19 virus and the war in Ukraine caused geopolitical tensions and at the same time certain deglobalization processes, because the governments of certain countries, within the framework of their marketing campaigns, appealed to citizens to buy domestic products and services, as well as to spend their vacations in domestic tourist destinations, in order to preserve the stable functioning of the domestic economy. Based on the above, the second research hypothesis can be formulated:

H2: Managers employed in domestic companies in the territory of the Republic of Serbia believe that the purchase of domestic products and services by consumers improves competitiveness and the position of their companies on the market (micro level).

The microeconomic competitiveness of the company represents its ability to compete, to achieve a relative advantage over the competition, position itself on the market, and in the last instance to achieve the appropriate profit that will enable its further growth and development. Michael Porter (1990) defined the Diamond Model of National Advantages [5], which consists of four determinants and is shown in Figure 1.

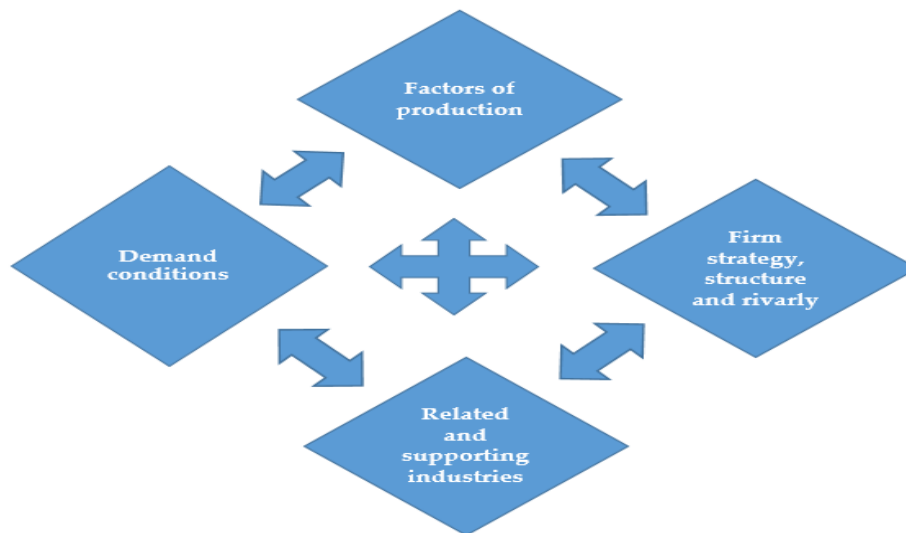


Figure 1. Diamond Model of National Advantages

Factors of production include infrastructure, human resources, and intellectual capital. *Demand conditions* imply that there is a demand for the company's products, as well as that the given products meet the wishes and needs of consumers on the domestic market. *Related and supporting industries* refer to the presence of interrelated competitive industries. *Firm strategy, structure and rivalry* refer to the formulation and implementation of appropriate strategies, which will enable a relative advantage over competing companies. If domestic companies are successful in their operations (micro level), the aforementioned implies an improvement in the state's competitiveness (macro

level). The Global Competitiveness Index which is published in reports of The World Economic Forum [6] is used as the main indicator of a country's macroeconomic competitiveness (Figure 2).

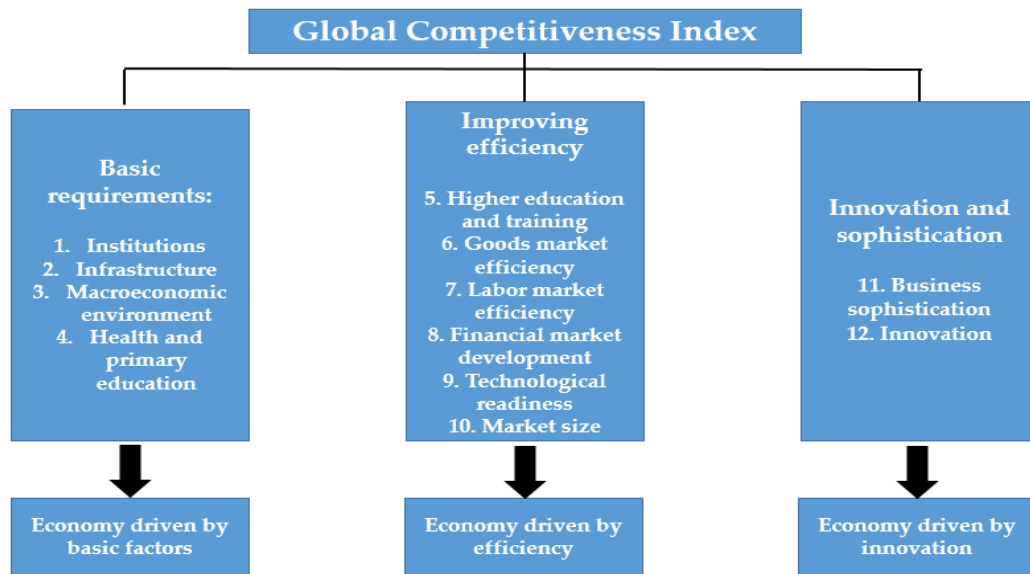


Figure 2. Global Competitiveness Index

In the first phase, the economy is driven by basic factors, which is a characteristic of the least developed countries. In the second phase, the focus shifts to efficiency factors, which primarily imply a higher level of education, as well as greater efficiency of the goods and services market and the financial market, and Serbia also belongs to this group. The third phase refers to technological sophistication and innovation, which is characteristic of countries with the highest GDP per capita. Based on the above, the third research hypothesis and research model (Figure 3) can be formulated:

H3: The competitiveness of domestic companies (micro level) improves the competitiveness of the state (macro level).

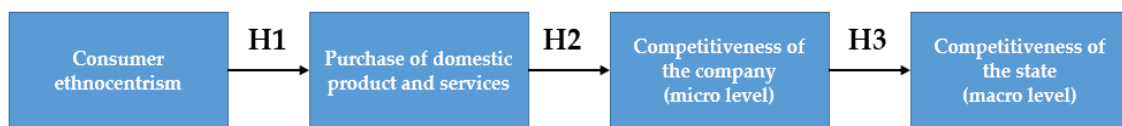


Figure 3. Research model

2. Data and Methodology

Empirical research using the survey method was conducted on the territory of the Republic of Serbia, in which 128 consumers and 37 managers employed in domestic companies participated. Respondents' responses (Likert scale 1-7) were analyzed using SPSS statistical software. Table 1 shows the statements that were used in the questionnaire. Regression analysis (next section) was applied, and the results are shown in Table 2.

Table 1. Overview of the statements used in the questionnaire.

<p>1. The purchase of domestic products implies an increase in the standard of living of citizens. 2. The purchase of domestic products implies an increase in the employment rate. 3. Consumers who buy domestic products help strengthen the domestic economy. (consumers)- consumer ethnocentrism H1</p>	<p>1. I believe that buying domestic products is a moral obligation. 2. I will recommend family members and friends to buy local products. 3. I will continue to buy domestic products in the future. (consumers) –purchase of domestic products H1</p>
<p>1. I believe that the citizens of Serbia have pronounced ethnocentric tendencies. 2. Citizens of Serbia accept the Government's recommendation to buy domestic products. 3. Consumers in Serbia understand that it is necessary to buy domestic products, for that is how the domestic economy functions stably. (managers)- consumer ethnocentrism H2</p>	<p>1. The purchase of domestic products by consumers increases the competitiveness of domestic companies. 2. Buying domestic products enables better positioning of companies on the market. 3. A high degree of consumer ethnocentrism enables domestic companies to profit. (managers)- competitiveness, micro level H2</p>

3. Results, Discussion and Concluding remarks

Table 2. Regression analysis

	β coefficient	T test	Sig
consumer ethnocentrism → purchase of domestic product H1	0.501**	6.475**	0.000
purchase of domestic product → company (micro level) H2	0.506**	6.503**	0.000

Consumer ethnocentrism has a positive effect on the purchase of domestic products ($\beta=0.501$; T test= 6.475; Sig= 0.000), and the purchase of domestic products has a positive effect on the competitiveness of domestic companies ($\beta =0.506$; T test= 6.503; Sig= 0.000), **so H1 and H2 are confirmed based on empirical quantitative research.** Through *qualitative research* and analysis of Michael Porter's Diamond Model and Global Competitiveness Index, it can be concluded that the *microeconomic competitiveness of the company* improves the *macroeconomic competitiveness of the state*, so the **H3 is also confirmed.**

References

- [1] Cleveland, M., Papadopoulos, N. & Laroche, M. (2022). Global consumer culture and national identity as drivers of materialism: an international study of convergence and divergence. *International Marketing Review*, 39(2), 207-241.
- [2] Marinković, V. (2017). Effects of the Republic of Serbia's citizens' patriotism and animosity towards the EU on consumer ethnocentrism. *Economics Horizons*, 19(1), 3-15.
- [3] Balbanis, G. & Siamagka, N.T. (2022). A meta-analysis of consumer ethnocentrism across 57 countries. *International Journal of Research in Marketing*, 39 (2022), 745-763.
- [4] Rojas-Méndez, J.I., Massi, M. & Gallito, E. (2022). Consumer pandemic animosity: scale development and validation. *International Marketing Review*, 39(6), 1417-1442.
- [5] Porter, M.E. (1990). *The competitive advantage of nations*. Free Press, New York.
- [6] Schwab, K. & Zahidi, S. (2020). The global competitiveness report: How countries are Performing on the road to recovery. World Economic Forum, Special Edition, 2020.

The role of socially responsible business in improving the company's market positioning

Ana Spasojević^{1*}, Stefan Zdravković²

¹University of Kragujevac, Faculty of Economics, e-mail: ana.spasojevic@kg.ac.rs

²University MB, Faculty of Business and Law in Belgrade, e-mail: szdravkovic034@yahoo.com

* *Corresponding author*

DOI: 10.46793/ICCB123.236S

Abstract: The concept of corporate social responsibility (CSR) refers to a constant commitment to business that contributes to the economic development of the company while simultaneously improving the quality of life of the company's employees, their families, as well as the community and society in general. The main segment of the analysis in this paper indicates the effects of applying the concept of socially responsible business on the market positioning of the company's brand. The main contribution study is the implementation of empirical research using the survey method in which 122 consumers from the territory of the Republic of Serbia participated, as well as 28 managers who are employed in companies of various activities (production, banking sector, telecommunications). Respondents' answers about the importance of socially responsible business were analyzed using the SPSS statistical program. This research may interest certain entities, that is, business entities on the domestic/foreign market to see the benefits and serious opportunities that the application of the CSR concept can bring.

Keywords: socially responsible business, business image of the company, brand management, market positioning of the brand

1. Introduction

The concept of corporate social responsibility (CSR) has gained more and more importance in the public eye over the last few decades. Although there are numerous definitions of this concept, its unique interpretation cannot be determined. What has changed over time is the company's reason for implementing CSR activities. In the beginning, the application of this concept was an imposed obligation of the regulatory authorities of the country where the company operates. Today, companies are increasingly resorting to this concept themselves, because it can represent a serious source for gaining competitive advantage and success in the market positioning of the brand. Every modern company should have and implement a specific corporate social responsibility policy, as well as publish an annual report detailing its activities. Therefore, the company is expected to be able to distinguish between organizational

behavior that is socially responsible, and socially conscious, and activities that do not fit into that concept [1] The concept of CSR implies the way in which companies integrate social, environmental and economic problems into their values, culture, decision-making, strategy and business, in a transparent and responsible manner, establishing better practices in the company, creating wealth, improving society, positioning itself as successfully as possible on the market. That is exactly why the concept of CSR, successful market positioning of the brand, and their mutual relationship are the starting point for the analysis in this paper [2].

2. The effects of applying the concept of socially responsible business on the market positioning of the company's brand

CSR includes the following four key domains [3]:

- Employee-oriented CSR corresponds to company initiatives that ensure the well-being of its employees, for example, through organizational fairness, as well as opportunities for career advancement.
- Customer-oriented CSR is the company's responsibility to its customers, for example, through ensuring product safety beyond legal provisions and customer care.
- Environmentally oriented CSR represents the company's responsibility towards the natural environment, for example, through the protection of natural resources and animals.
- Philanthropy-oriented CSR means the responsibility that a company shows to society, for example, through contributions to education, culture or sports.

Brand positioning with the help of CSR generally requires significant strategic changes in the company's way of thinking, about itself and its activities, initiatives, communication with internal and external stakeholders. CSR is still a "voluntary action", but stakeholders expect it from companies. Implementing the concept of CSR means that the company has already integrated CSR into its corporate culture and activities. Businesses need to fully understand their behavior and activities, aimed at solving social issues, and be able to justify their actions, but also to use them. This further enables proactive external use with the aim of actions influencing brand positioning. Market positioning of the brand with the help of CSR creates the effects of a better position of the company on the market, as well as the effect of improved consumer perception of product quality [4].

Charitable donations have a greater effect on the consumer's evaluation of the company than business sponsorship. They influence consumers and their continued willingness to buy, which improves consumers' perception of corporate reputation and the company's position in the market. Similarly, volunteering activities of companies also have a positive impact on corporate image. Companies effectively cross society, economy, and employees, by organizing and implementing volunteer activities, where they also advertise the brand. Therefore, companies should actively organize and implement CSR activities, so that consumers understand that the company is honest and transparent

about CSR initiatives, which has a positive impact on the image of the corporate brand, and on the market position of the company [5].

Professor Akbari and colleagues from the University of Tehran indicate that CSR initiatives play a significant role in positioning corporate brands in the market (Figure 1). Consumers try to establish a connection with the brand, which is in fact a substitute for contact between the organization and the customers. Satisfied consumers are more willing to recommend the brand to others, are less willing to switch to other alternative brands, and are willing to buy its products repeatedly. When consumers have a positive experience with a brand, they would buy that brand repeatedly and recommend it to others and are less likely to buy an alternative brand. Therefore, when a brand evokes multiple dimensions of user experience, a higher level of experiential value is expected. The value for consumers is developed, potential risks are reduced, information search costs are reduced, and satisfying attitudes are created [6].

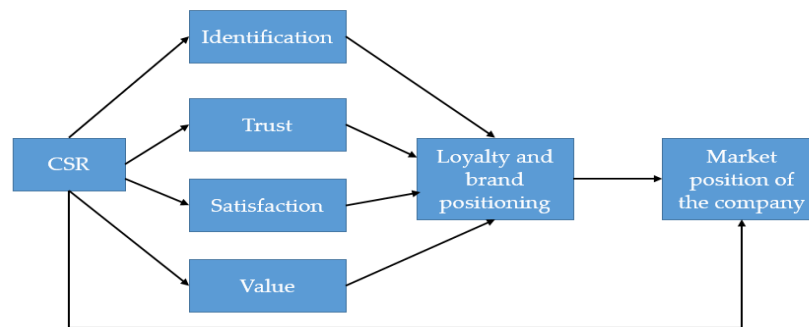


Figure 1. The impact of CSR on brand positioning and the company's position on the market.

Based on the mentioned model, subject and research objectives, the conceptual model of this study (Figure 2) and the research hypothesis are formulated.



Figure 2. Conceptual model

H1: Consumers in Serbia buy brands of companies that operate in a socially responsible way.

H2: Socially responsible business improves the company's market position.

3. Research results

Empirical research was conducted on the territory of the Republic of Serbia, in which 122 consumers and 28 managers who are employed in companies of various activities (production, banking sector, telecommunications). Respondents' responses (Likert scale 1-7) were analyzed using SPSS statistical software. Table 1 shows the statements that

were used in the questionnaire and Table 2 shows the results of regression analysis.

Table 1. Overview of the statements used in the questionnaire.

1. Companies need to invest in socially responsible business. 2. It is necessary for companies to respect environmental norms and standards. 3. Companies need to sponsor cultural and music events. (consumers)- CSR H1	1. I prefer buying the brands of those companies that are socially responsible. 2. I will recommend my friends to buy the brands I use. 3. I will recommend family members to buy the brands I use. (consumers) –brands of company H1
1. The company where I work invests money in socially responsible businesses. 2. The company where I work pays attention to charitable and humanitarian actions. 3. The company where I work sponsors sport events. (managers)- CSR H2	1. Socially responsible business improves the image of the company. 2. Socially responsible business improves the company's market position. 3. The concept of socially responsible business enables a competitive advantage. (managers)- company's market position H2

Table 2. Regression analysis

		β	T	Sig
corporate social responsibility ▼	baying brands of company H1	0.472**	5.848**	0.000
corporate social responsibility ▼	company's market position H2	0.445**	5.201**	0.000

4. Concluding considerations

Corporate social responsibility has a positive significant effect on consumers' decision to buy brands of companies that are socially responsible ($\beta=0.472$; T test= 5.848; Sig= 0.000), and also corporate social responsibility has a positive significant effect on the company's market position ($\beta =0.445$; T test= 5.201; Sig= 0.000), **so H1 and H2 are confirmed**, so the research provides important practical implications for marketing managers.

References

- [1] A. Abubakar, S. Belwal, N. Mohammed & U.D. Mohammed (2022). Sustainable Competitive Advantage through Corporate Social Responsibility (CSR) and Green Behavior Strategies. *Discrete Dynamics in Nature and Society*, Volume 2022, 1-8.
- [2] P. Kotler & N.R. Lee (2004). *Corporate Social Responsibility*, John Wiley & Sons.
- [3] S. D. Schaefer, R., R. Terlutter & S. Diehl (2020). Talking about CSR matters: employees' perception of and reaction to their's company' CSR communication in four different CSR domains. *International Journal of Advertising*, 39(2), 191-212.
- [4] J. Lee & Y. Lee (2018). Effects of multi-brand company's CSR activities on purchase intention through a mediating role of corporate image and brand image. *Journal of Fashion Marketing and Management*: 22(3), 387-403.
- [5] J. Lu, L. Ren, C. Zhang, C. Wang, Z. Shahid, & J. Streimikis (2020). Influence of a Firm's CSR initiatives on Brand loyalty and Brand image. *Competitiveness*, 12(2), 106–124.

- [6] M. Akbari, M. Meherali, N.S. Amiri, N. Rezaei, & A. Pourjam (2020). Corporate social responsibility, customer loyalty and brand positioning. *Social Responsibility Journal*, 16(5), 671-689

Chemometric approach to the investigation of microelements and potentially toxic elements in the soil

Jelena D. Božović^{1*}, Zoran D. Miletić², Ilija Đ. Đorđević³, Dragana Z. Živojinović⁴

¹ Institute of Forestry, Laboratory of Soil , Plant Material and Water analysis, Belgrade, Serbia; e-mail: jbozovic@tmf.bg.ac.rs jelena.bozovic@forest.org.rs

² Institute of Forestry, Department of Forest Establishment, Silviculture and Ecology, Laboratory of Soil , Plant Material and Water analysis, Belgrade, Serbia; e-mail: zoran.miletic@forest.org.rs

³ Institute of Forestry, Department of Spatial regulation, GIS and Forest Policy, Belgrade, Serbia; e-mail: djordjevic_ika@yahoo.com

⁴ Faculty of Technology and Metallurgy, Department of Analytical Chemistry and Quality Control, Belgrade, Serbia; e-mail: gaga@tmf.bg.ac.rs

* *Corresponding author*

DOI: 10.46793/ICCB123.241B

Abstract: The goal of this investigation was to assess the presence, content and limit concentrations of macro, trace elements, and potentially toxic elements in the soil. The research was carried out in Kopaonik, Crni vrh, and Mokra Gora during the period 2020-2022 on different depths. Samples were prepared by microwave digestion with a mixture of mineral acids. The concentration of extracted elements was measured by Inductively Coupled Plasma Optical Emission spectroscopy (ICP-OES). The method of sample preparation is very important for the successful determination of elements because it is a very complex matrix. A chemometric approach was applied to explain the distribution of elements and potentially toxic elements in the soil by location and sampling depth. Principal Component Analysis and Cluster Analysis have proven to be excellent tools for reducing the number of measurements and for grouping data by parameters and sampling location. Research has shown that there was no major soil contamination with toxic metals in the selected areas.

Keywords: microwave digestion, trace metals, ICP-OES, PCA, HCA

1. Introduction

Forest ecosystems contain pools of microelements, as well as toxic elements in virtually all forest compartments: forest floor, vegetation (trees, shrubs, ground vegetation), fauna, micro-organisms, soil and soil solution. Fluxes of these trace metals cycle along with carbon and nutrients and water (e.g., leaching). This labor focuses on microelements and toxic elements concentrations and stocks in the forest soil, i.e., the mineral or organic (peat) soil including the ecto-organic layer (forest floor), without considering elements in the soil solution. The objective of this experiment was to assess the presence, content and limit concentrations of trace elements and potentially toxic elements in the soil. The research was carried out in Kopaonik, Crni vrh, and Mokra Gora, by sampling and soil analysis.

2. Materials and Methods

In 2020 on Kopaonik, in 2021 on Crni vrh and in 2022 on Mokra Gora, soil sampling and laboratory analyzes of physical and chemical parameters were carried out. The sampling was performed on the observation plot established for soil analysis. It was performed using a probe at 30 different spots and making average samples. Probing was performed at depths of 0-10 cm, 10-20 cm, and 20-40 cm.

The surface soil layer of 0–10 cm depth was sampled from 30 pits, and the deeper layers from 30 individual samples were collected using a probe. An average sample was made for each layer. There were three average samples, each composed of 10 individual samples. The following parameters were determined in the samples: exchangeable acid cations: aluminium (Al), iron (Fe), manganese (Mn), exchangeable base cations: calcium (Ca), magnesium (Mg), potassium (K), sodium (Na), oxalate soluble iron and aluminium, elements soluble in aqua regia, macroelements of plant nutrition, essential microelements of plant nutrition, useful elements, toxic elements. Samples for soil analysis were prepared in the Testing Laboratory of the Department of Soil, Plant Material and Water Analysis of the Institute of Forestry.

Elements that are soluble in aqua regia are processed by wet digestion. Wet digestion is carried out in the Microwave Digestion System - Milestone Ethos LEAN, EASY in a mixture of nitric acid (HNO₃) and hydrochloric acid (HCl). A sample weighing about 0.2 grams of air-dry soil was poured with 7.5 ml of HCl and 2.5 ml of HNO₃. The resulting extract was filtered through filter paper into a normal vessel and filled up to 50 ml. The amounts of the analyzed elements were determined by the ICP-OES spectrometer VARIAN VISTA-PRO and calculated to an absolutely dry sample [1].

3. Results and Discussion

Of the micronutrients extracted in the aqua regia, manganese, iron, copper, and zinc were determined on Kopaonik. The amounts of iron and manganese are high, but these two elements do not have a defined limit and remediation values, because there are always sufficient amounts of these elements in the soil, and their high concentrations do not affect plants. Copper and zinc are essential microelements, which are necessary for plant nutrition. In no collective samples, the amounts of copper and zinc do not exceed the remediation value, i.e., there are sufficient quantities of these elements in the soil. Among the potentially toxic nutritional elements that can be extracted in Aqua regia are mercury, cadmium, lead, arsenic, and chromium [1]. The amounts of mercury, arsenic and chromium are extremely low and were below the detection limit, both in the organic layer and in the soil layer of 0-10 cm depth. In the horizon of the organic layer, the amount of cadmium was below the detection limit. Small amounts of cadmium were found in the surface layer of the soil 0-10 cm thick, however, they are far below the remediation value and even the lower limit value. This means that the amounts of this toxic element do not endanger plants on the sample plot. Small amounts of lead were found, both in the organic layer and in the surface layer of 0-10 cm of soil. However, the

concentrations of this element are far below the remediation value, and also below the lower limit value, which means that they are far below the toxic concentrations.

Table 1 shows the results of mean values of concentration of microelements and potentially toxic elements from soil sampled from Kopaonik, Mokra Gora, and Crni Vrh.

Table 1. The concentration of microelements and potentially toxic elements from soil - Kopaonik, Mokra Gora, and Crni Vrh.

Sampling site	Depth cm	Ca	Mg	K	Mn	P	Cu	Pb	Cd	Zn	Fe	Al
		mg/kg										
Kopaonik	-4.5-0	625.1	70.1	46.8	121.4	104.6	3.4	22.3	<0.1	3.1	1238.9	69.3
	0-10	106.1	139.9	51.6	44.2	80.5	5.07	23.9	0.2	3.3	2621.4	637.5
	10-20	<0.1	<0.1	<0.1	<0.1	<0.1	<0.1	<0.1	<0.1	<0.1	<0.1	<0.1
	20-40	<0.1	<0.1	<0.1	<0.1	<0.1	<0.1	<0.1	<0.1	<0.1	<0.1	<0.1
Mokra Gora	-4.5-0	7074.4	8324.4	497.5	543.5	1374.2	5.1	<0.1	<0.1	32.5	<0.1	<0.1
	0-10	1671.2	40135.9	330.3	1321.5	333.6	8.1	<0.1	<0.1	28.7	10.97	11.4
	10-20	1519.6	40907.3	296.8	1355.5	349.4	8.3	<0.1	<0.1	31.7	18.8	13.8
	20-40	1837.1	42572.5	325.1	1476.1	343.1	16.9	<0.1	<0.1	53.9	18.8	9.6
Crni Vrh	-4.5-0	1061.9	625.98	474.9	178.3	31.93	25.0	<0.1	23.2	3031.6	4614.9	3031.6
	0-10	1250.7	653.89	487.7	164.6	24.16	26.4	<0.1	17.2	3222.2	4866.9	3222.2
	10-20	983.2	692.19	528.9	190.1	32.82	18.5	<0.1	4920.9	136.4	3127.1	136.4
	20-40	1061.9	625.98	474.9	178.3	31.93	25.0	<0.1	23.2	3031.6	4614.9	3031.6

The most abundant element on Mokra Gora in the extract in aqua regia is magnesium. Its concentrations are the lowest in the organic horizon, but they sharply increase with the transition to the organomineral part of the solum. It is the result of biological accumulation. The increased presence of potassium in the organic layer compared to the deeper parts of the soil is also a result of the biological accumulation of this nutrient macroelement. Manganese content in Mokra Gora is the lowest in the organic horizon and increases strongly with depth. Copper soluble in aqua regia is poorly represented on Mokra Gora, both in the organic horizon and in the surface soil layers. The amount of lead and cadmium in the organic horizon and in the deeper layers of the soil on Mokra Gora is below the detection limit. The predominance of iron over aluminum is understandable because serpentinites are ferromagnesian silicates. The lowest concentrations of aluminum were found in the surface layers, but they slightly increase with the depth of the soil [2].

The most abundant elements on Crni Vrh extracted in aqua regia are aluminum and iron, which is understandable because it is an acidic brown soil. The second most abundant element extracted in aqua regia are the alkaline earth elements calcium and magnesium. The amounts of toxic elements in the soil extracted in aqua regia – mercury, cadmium, and arsenic are below the detection limit. Only certain amounts of

lead were found, but they are also less than the lower limit values.

By applying PCA analysis, a strong correlation was established between most of the examined elements. However, the grouping of elements according to their appearance at different depths in the soil was made into three main components, of which most of the elements are in the first component (PC1), which includes the largest part of the variance, as shown in Figure 1.

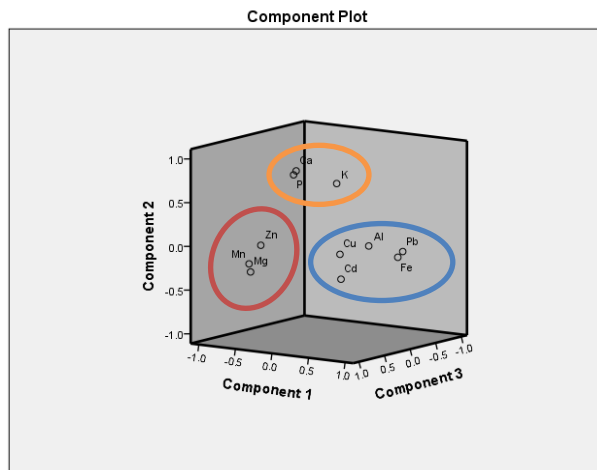


Figure 1. PCA plot of loadings of elements in soil

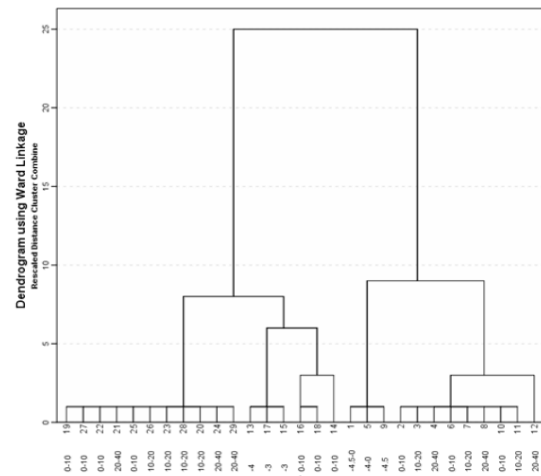


Figure 2. Dendrogram of soil samples

Using hierarchical cluster analysis (HCA), the samples were grouped according to the sampling location and on the basis of the measured concentrations of elements. Three clusters can be seen on the dendrogram, the first two of which are Crni Vrh (samples marked with numbers 19-29) and Kopaonik (samples marked with numbers 13-18) at a very close Euclidean distance and continue to connect into one cluster. Mokra Gora (samples numbered from 1 to 12) is a special cluster (Figure 2).

3. Conclusions

Research has shown that there was no major soil contamination with toxic elements in the selected areas. As for the grouping of elements, three groups were distinguished using the PCA method: I (Fe, Al, Cu, Cd, and Pb), II (Mn, Mg, and Zn) and III (K, P, and Ca), while the cluster analysis grouped the samples by location and depth of sampling in two clusters.

References

- [1] L. Madrid, E. Diaz-Barrientos, E. Ruiy-Cortés, R. Reinoso, M. Biasioli, C. M. Davidson, A. C. Duarte, H. Grčman, I. Hossack, A. S. Hurshouse, T. Kralj, K. Ljung, E. Otabbong, S. Rodrigues, G. J. Urquhart and F. Ajmone-Maesano, *Variability in concentrations of potential toxic elements in urban parks from six European cities*, *Journal of Environmental Monitoring*, 8 (2006) 1158-1165.
- [2] S. Albanese, P. Ebrahimi, A. Aruta, D. Cicchella, B. De Vivo, A. Lima, *Potentially toxic elements in the soils of Campi Flegrei (south Italy) and the immediate surroundings: Spatial distribution, origin and probabilistic human health risk*, *Chemosphere*, 313 (2023): 137297.

Application of chemometrics in monitoring of spatial and temporal variations in river water quality and water classification

Dragana Z. Živojinović¹, Dušan V. Trajković¹, Jelena D. Božović^{2*}

¹ Faculty of Technology and Metallurgy, Department of Analytical Chemistry and Quality Control, Belgrade, Serbia, Karnegijeva 4; e-mail: gaga@tmf.bg.ac.rs

² Institute of forestry, Belgrade, Kneza Višeslava 3, Serbia; e-mail: jbozovic@tmf.bg.ac.rs

* Corresponding author

DOI: 10.46793/ICCB23.245Z

Abstract: The Topčiderska River is the right tributary of the Sava River, with the length of its course of 31 km, and the catchment area of about 147 km². It represents one of the most polluted urban waters in the territory of the Republic of Serbia. Soil erosion, as well as the discharge of wastewater from certain parts of the city and from industrial zones located in its catchment, to the greatest extent cause the pollution of this river. Within this work, representative samples of Topčiderka River water sampled in different time periods and from different locations were analyzed. Over ten physico-chemical parameters were selected that best indicate the current quality of the river water. The obtained measurement results were subjected to chemometric analysis, using chemometric methods (HCA and PCA). Water quality was analyzed from two aspects, temporal and locational. Based on the results of statistical data processing, insight was gained into the variation in the water quality of the Topčiderska River and the causes of the resulting variation were revealed. Based on these conclusions, the water of this river was classified in accordance with the Regulation on limit values of pollutants in surface and underground waters and the Regulation on water classification. The obtained results show that the water of the Topčiderska River is highly polluted, and that according to the degree of pollution and purpose, it is classified as IV class.

Keywords: Topčiderska River, pollution, chemometric methods, classification

1. Introduction

The surface water quality control program in the territory of the City of Belgrade includes 24 watercourses with 30 control profiles, with water, sediment and hydrobionts (shellfish, fish) as the medium of the freshwater ecosystem. The monitoring is carried out in order to: assess the quality of watercourses, monitor the trend of pollution, the convenience of using them for the irrigation of agricultural areas, the convenience of using them for water supply, the health safety of citizens, monitoring the deposition of organic and inorganic micropollutants in the sediment, and their bioaccumulation in hydrobionts, the assessment of the ability of self-purification and eutrophication, preservation of water quality, rehabilitation, protection and improvement of watercourses.

The water of the Topčiderska River is tested in the laboratory for human ecology and ecotoxicology of the City Institute for Public Health Belgrade, once a month on the profile of the bridge near the Hippodrome, by sampling directly from the shore.

2. Material and methods

During the three-year period of monitoring the water quality of the Topčiderska River, samples from the water intake of the bridge near the Hippodrome were analyzed. Water quality and seasonal variation of quality parameters were examined, and the water class was determined according to the Regulation on limit values of pollutants in surface and underground waters [1]. 13 physico-chemical parameters were selected for regular monitoring. Samples were collected and analyzed once a month (except in January and February). The sample size was 30.

The water of the Topčiderska River was tested from the source to the mouth by sampling at 13 measuring points as shown in Figure 1.

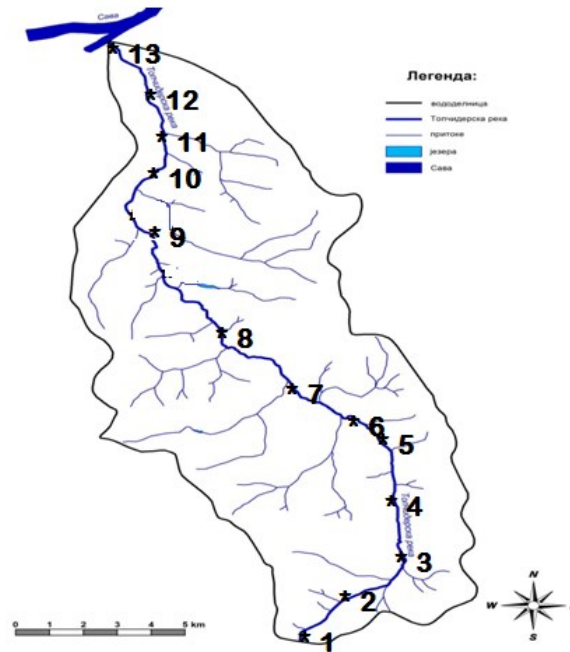


Figure 1. Description of study area – Topčiderska River basin and sampling sites.

Legend:

- | | |
|--|---|
| 1. The source of the Topčiderska River | 8. Entrance to the Rakovica engine factory |
| 2. Dućevac | 9. The exit from the Rakovica industrial zone |
| 3. Palanački potok | 10. Lisički potok |
| 4. Ripanj | 11. Topčiderski park |
| 5. Resnik (center) | 12. Topčider Barracks |
| 6. Settlement of Kijevo (Knezevac) | 13. Mouth of Topčiderska River |
| 7. Entrance to the industrial zone | |

Hierarchical cluster analysis (HCA) and principal component analysis (PCA) were used in order to reveal the sources of pollution and to group locations according to the

similarity in the distribution of pollutants and to reduce the database i.e., reduced the number of variables required for monitoring.

3. Results and discussion

Basic statistical parameters were calculated for all selected parameters, and Table 1 shows the mean value, minimum and maximum value and standard deviation.

Table 1. Descriptive statistics of the results of the analysis of the physical and chemical parameters of water quality of the Topčiderska River in three years of monitoring.

Parameter	Number of samples	Max	Min	Mean	Standard deviations, %
Temperature, °C	30	26.0	5.4	16.69	6.30
pH value	30	8.5	7.8	8.1	0.18
Electrical conductivity, µS/cm	30	980	580	761.7	67.01
Alkalinity, mg/l	30	358.2	246.8	320.12	26.12
Total hardness, mg/l CaCO ₃	30	493.9	274.0	382.23	37.43
Suspended matter, mg/l	30	52	2	22.77	14.47
Total organic carbon, TOC, mg/l	30	16.2	4.85	7.63	2.79
Dissolved oxygen, mg/l O ₂	30	3.1	11.4	7.67	2.52
Chemical oxygen demand, COD, mg/l O ₂	30	75	3.5	17.89	15.02
Biochemical oxygen demand, BOD ₅ , mg/l O ₂	30	18.5	3.1	9.54	4.11
Nitrite nitrogen, mg/l N	30	0.805	0.002	0.34	0.20
Nitrate nitrogen, mg/l N	30	4.5	0.5	3.03	0.96
Total phosphates, mg/l	30	1.45	0.268	0.73	0.31

In this way, by applying multivariate chemometric methods, temporal/spatial variations in the water quality were performed. The classification and categorization of the water of the Topčiderska River at the sampling sites was carried out. The grouping of measurement sites by similarity and Euclidean distance is shown in Figure 2.

As can be seen from the dendrogram (Figure 2), 4 clusters were formed from 13 measurement locations. The first cluster includes five locations (8-12), the second, also, 5 measurement locations (2, 4-7), the third only one measuring point (3), and two locations (1,13) are grouped in the fourth cluster. The first cluster represents the measuring points next to the industrial zone and the surrounding area (8-12). The second cluster consists of populated places (2, 4-7). The third cluster represents only one location, Palanački potok (3) which is singled out as highly polluted. In the fourth cluster, they grouped samples from the source and mouth of the Topčiderska River (1 and 13), according to the measured very high values of conductivity and hardness, concentrations of chloride and bicarbonate, which indicates a high content of ionic species in the water. It is worth noting that the content of organic matter has increased in all locations, which means that this river is quite polluted because most of the parameters are above the maximum allowed concentration (MAC) parameters for water surfaces [1].

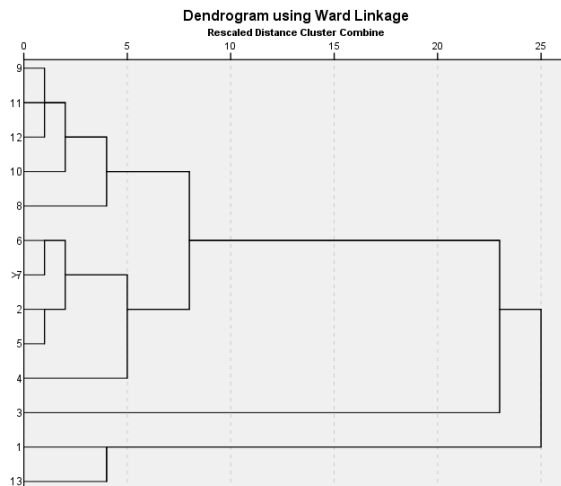


Figure 2. Dendrogram of sampling location grouping using HCA, *Ward Linkage* method.

Based on the PCA after Varimax rotation and the correlation matrix with the corresponding factors, hardness (UT), alkalinity and conductivity belong to the first component, with a very high factor loading over 0.7. The second component has the highest load of oxygen, phosphates and pH. Temperature and BOD belong to the third component, while the parameters HPK and TOC and total suspended matter, with a very high coefficient of 0.87 now belong to the fourth factor. Nitrates and nitrites are equally represented in all components.

3. Conclusions

The results obtained from this research show the great importance of multivariate statistical techniques for the analysis and interpretation of complex data sets obtained through multi-year monitoring. Using these chemometric statistical methods, the identification and distribution of pollution sources and factors responsible for the variability of parameters in water was carried out, which contributed to a better understanding of temporal/spatial variations in water quality, with the aim of more efficient management of water resources and adequate water classification [2, 3].

Acknowledgment

This research is funded by the Ministry of Education and Ministry of Science, Technological Development and Innovation, Republic of Serbia, Project III43009.

References

- [1] Закон о водама („Службени Гласник РС“, бр. 30/10 и 93/12)
- [2] P.R. Kannel, S. Lee, S.R. Kanel, S.P. Khan, *Chemometric application in classification and assessment of monitoring locations of an urban river system*, *Analytica Chimica Acta* 582 (2007) 390–399
- [3] S. Shrestha, F. Kazama, *Assessment of surface water quality using multivariate statistical techniques: A case study of the Fuji river basin, Japan*, *Environmental Modelling and Software* 22 (2007) 464–475

Mechanochemistry: optimization of the synthesis of dithiocarbamate derivatives

M. Kosović Perutović^{1*}, Z. Leka¹, M. Bigović², J. Mišurović¹, V. Medojević¹

¹University of Montenegro, Faculty of Metallurgy and Technology, Cetinjski put, 81000 Podgorica, Montenegro, mkosovic@ucg.ac.me, zorica@ucg.ac.me, janam@ucg.ac.me, medojevicvalentina@gmail.com

² University of Montenegro, Faculty of Science and Mathematics, Džordža Vašingtona bb, 81000 Podgorica, Montenegro, miljan@ucg.ac.me

DOI: 10.46793/ICCBi23.249KP

Abstract: As a continuation of our research in the field of synthesis and characterization of dithiocarbamate (DTC), we are developing mechanochemical protocols for the synthesis of new compounds with potential biological activity. Optimizing the methods of obtaining desired compounds is of special importance for a completely eco-friendly science, and one of the prospective strategies is mechanochemistry, recognized as a green, sustainable synthesis method. Herein we present the mechanochemical reactions of homopiperazine and CS₂. The aim was to obtain homopiperazine dithiocarbamate derivative through mechanochemical synthesis. The optimization of the process was carried out through mechanochemical grinding in the planetary ball-mill using zirconium oxide grinding media (jars and balls), under various reaction conditions. The selected reactions were conducted using a one-pot method. Chemical and spectral characterization revealed that the product was obtained in the form of a dimer with a good yield. Water and NaHCO₃ were generated as by-products. Homopiperazine-1,4-bis-carbodithioate was synthesized for the first time in a ball-mill under mechanochemical and solvent-free conditions. This protocol is promising and thus constitutes an appealing alternative both in academic research and in practical processes, being simple to perform, cheap, scalable, and occurring under mild conditions.

Keywords: mechanochemistry, dithiocarbamates, homopiperazine, green synthesis

1. Introduction

IUPAC identified mechanochemistry as one of the 10 future technologies in chemistry that positively contributes to sustainable development of the planet. Mechanochemistry enables the reduction or complete elimination of solvents, while ensuring increased yields compared to products obtained through conventional solution-based synthesis. It offers higher product purity and the possibility of obtaining compounds that can only be achieved under mechanical activation conditions.

Recent studies have shed light on the interactions of DTCs with enzymes, intracellular metal concentrations, and oxidative processes, which represent important targets in various disease states. DTC derivatives have shown encouraging research

results in multiple clinical trials for applications in cancer, infectious diseases and substance abuse [1]. Significant number of biologically active compounds contain heterocyclic rings. Azepanes are a prime example of such compounds. The flexibility of the seven-membered ring allows functional groups attached to it to adopt a wide range of positions, increasing the potential for forming hydrogen bonds and other types of interactions [2].

We will utilise the advantages of these methods for the synthesis of homopiperazine dithiocarbamate derivative (HPDTC). The synthesis of homopiperazine-1,4-bis-carbodithioate from a solution has already been published [3]. In the described reaction of CS₂ incorporation into the homopiperazine ring, 50 mL of ethanol is used. One of the objectives of our research is to reduce the use of ethanol as a solvent while maintaining a satisfactory reaction yield.

2. Experimental section

All mechanochemical reactions were carried out using a XQM Planetary Ball Mill, equipped with a zirconium oxide jar. IR spectra were recorded with a Perkin Elmer FT-IR Spectrometer Spectrum Two in the range 400–4000 cm⁻¹, with attenuated total reflection (ATR) technique on diamond crystal with 4 cm⁻¹ resolution.

2.1 Synthesis of HPDTC1 (homopiperazine-1,4-bis-carbodithioate, without rinsing)

The mixture of homopiperazine (0.005 mol), CS₂ (0.01 mol) and 0.005 mol Na₂CO₃ was introduced into a 100 mL zirconium oxide jar. The reaction vessel was closed and fixed on the vibration arms of a ball-milling apparatus, along with 20 stainless balls of 5.0 mm diameter using a second parallel jar to equilibrate the system. Then, both vessels were vibrated vigorously at a frequency of 25 Hz at room temperature, 30 min.

2.1 Synthesis of HPDTC2 (homopiperazine-1,4-bis-carbodithioate, rinsed with ethanol)

The reaction was done by placing reactants (0.01 mol homopiperazine, 0.02 mol CS₂ and 0.01 mol Na₂CO₃) in a 100 mL zirconium oxide jar, containing 70 zirconium oxide balls (ø 5mm). The mill was operated at 50 Hz for 30 min. The resulting pale-yellow product was collected by vacuum filtration and washed with C₂H₅OH (2 × 1 mL).

3. Results and discussion

In order to optimize the synthesis of HPDTC, a large number of mechanochemical reactions were conducted. We chose as a model the stoichiometric reaction homopiperazine and CS₂ in the presence of sodium carbonate.

The first milling process (synthesis of HPDTC1) was monitored using FT-IR spectroscopy. The process was stopped after 20, 25 and 30 min, and the spectra were

recorded without any additional sample preparation (**Figure 1**). The spectra of HPDTC1 indicated that binding of CS₂ to the N in homopiperazine occurred, but the yield was low. Due to the larger size of the available reaction vessels requiring larger quantities of reagents, the synthesis was repeated with slight variations.

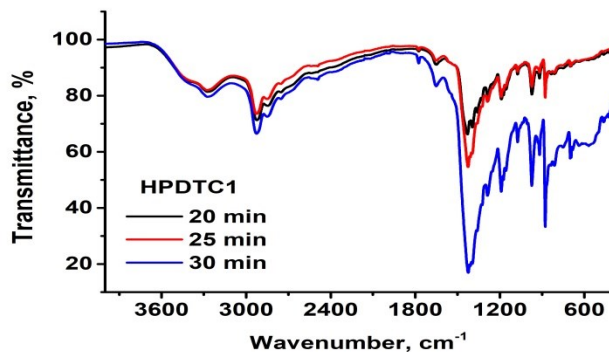
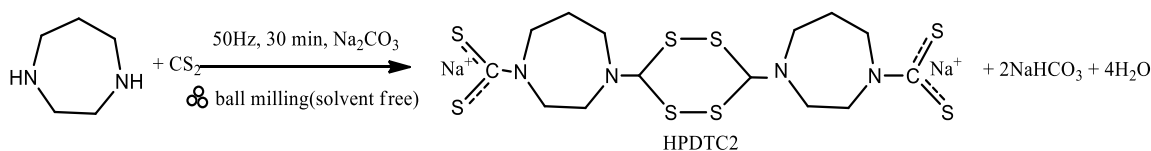


Figure 1. IR spectra of HPDTC1

The synthesis of the HPDTC2 is shown at **Scheme 1**. The precipitate was filtered under vacuum washed with small amount of C₂H₅OH (2x1 mL). After drying in the desiccator, the mass of the obtained product was 1.895 g (yield = 64.02 %).



Scheme 1. Synthesis of homopiperazine-1,4-bis-carbodithioate (HPDTC2, dimer form).

Relevant IR bands for HPDTC2 are given in Table 1 and Figure 2. The absorption at 1444 cm⁻¹ was assigned to stretching vibration mode $\nu(\text{C-N})$ from NCS group (thioamide band II). The thioamide I stretching vibration appears at 1382 cm⁻¹. The position of C=S stretching vibration of NCS₂ group at 957 cm⁻¹[4]. Peak positions: 835, 977, 1195, 1353, 1651, 1686 cm⁻¹ correspond to HCO₃⁻(H₂O)₄ [5].

Table 1. Selected infrared frequencies of HPDTC2

IR frequencies/cm ⁻¹					
$\nu(\text{OH})$	$\nu(\text{N-CS})$ (thioamide band I)	$\nu(\text{NC=S})$ (thioamide band II)	$\nu(\text{C=S})$	Peak positions in the HCO ₃ ⁻ (H ₂ O) ₄	
3459	1444	1382	957	835	(CO ₃ out of plane mode)
				977	(C-OH)
				1195	(COH)
				1353	(CO ₂ symmetric)
				1651	(Water bend)
				1686	(Water bend)

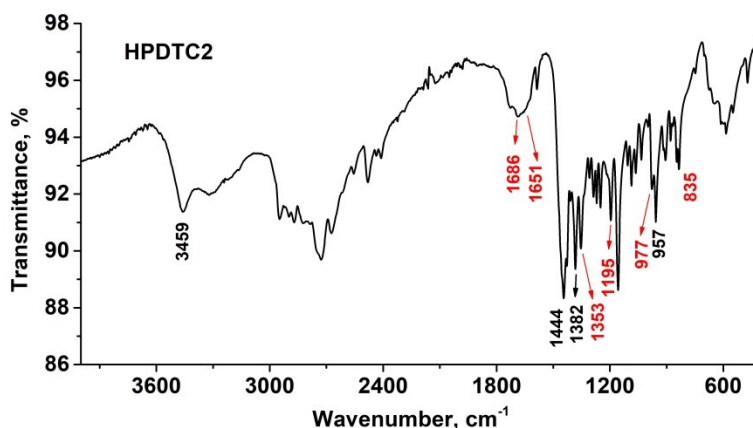


Figure 2. IR spectrum of HPDTC2

Elemental CHN analysis confirmed the presence of $\text{NaHCO}_3 \cdot 4\text{H}_2\text{O}$ in the product, but also indicated that the DTC derivative is formed in the form of a dimer. The presumed structural formula of HPDTC2 is provided in Scheme 1. Analysis, found: C, 24.99; H, 4.32; N, 6.94 %, calculated for $[\text{Na}_2(\text{S}_2\text{CN})_4(\text{C}_5\text{H}_{10})_2] \times 2\text{NaHCO}_3 \times 4\text{H}_2\text{O}$: C, 24.48; H, 3.89; N, 7.11.

4. Conclusions

Mechanochemical syntheses enable the formation of dithiocarbamate derivative of homopiperazine. Homopiperazine-1,4-bis-carbodithioate is obtained as a dimer, representing a novel compound. Further research aims to optimize synthesis for a purer product and conduct additional characterization. Its coordination with transition metals and potential biological activity will also be explored.

References

- [1] L.Kaul, R. Suss, A. Zannettino, K. Richter., The revival of dithiocarbamates: from pesticides to innovative medical treatments, *iScience*, 24(2)(2021)102092
- [2] S. Singh, J. Goo, V. Gajulapati, T.S. Chang, K. Lee, Y. Choi., Recent Advances in Anticancer Chemotherapeutics Based upon Azepine Scaffold, *Anti-Cancer Agents in Medicinal Chemistry* 16(2016)539–557
- [3] A. M. C.Villegas, M. Pérez-Redondo, M. L.Cardoso, A. Toscano, R. Cea-Olivares., *Organotin(IV) azepane dithiocarbamates: Synthesis and characterization of the first organotin(IV) complexes with seven-membered cyclic dithiocarbamate*, *Phosphorus, Sulfur, and Silicon and the Related Elements*, 159(2020)498-506J.
- [4] V.Uivarosi, M. Badea, V. Aldea, L.Chirigiu, R.Olar., *Thermal and spectral studies of palladium(II) and platinum(IV) complexes with dithiocarbamate derivatives*, *J Therm Anal Calorim*, 111 (2013) 1177-1182
- [5] E. Garand, T. Wende, D. J. Goebbert, R.Bergmann, G. Meijer, D. M. Neumark, K. R. Asmis., *Infrared Spectroscopy of Hydrated Bicarbonate Anion Clusters: $\text{HCO}_3^-(\text{H}_2\text{O})_{1-10}$* , *JACS*, 132(2010) 849-856

Capacitive behaviour of biomass-derived activated carbon in Al-ion-containing electrolytes

Jana Mišurović^{1*}, Aleksandra Gezović¹, Veselinka Grudić¹, Milica Vujković²

¹ University of Montenegro, Faculty of Metallurgy and Technology, Podgorica, Montenegro, Cetinjski put, bb; e-mail: janam@ucg.ac.me, gezovic.a@ucg.ac.me, grudicv@ucg.ac.me

² University of Belgrade, Faculty of Physical Chemistry, Belgrade, Serbia, Studentski trg 12-16; e-mail: milica.vujkovic@ffh.bg.ac.rs

* Corresponding author

DOI: 10.46793/ICCBi23.253M

Abstract: Vine shoots, abundant by-products of the wine industry, were used as biomass resources for obtaining activated carbon (AC_{vs}) through a simple two-step activation/carbonization process with ZnCl₂ as an activator. The physicochemical characterization including N₂ physisorption, FTIR and XRD analysis, revealed that the resulting carbon exhibits a high specific surface area and has low surface functionality. Carbon electrochemistry was investigated in three different non-conventional Al-ion containing aqueous electrolytes – sulphate, nitrate, and chloride. Through a comparative analysis it was observed that anion type had a major influence on the electrochemical behaviour of activated carbon. AC_{vs} showed excellent charge storage properties in all three electrolytes in a wide operating voltage of 1,35 V, reaching the best value of specific capacitance of 235 F g⁻¹ at 20 mV s⁻¹ in 1 M Al(NO₃)₃. Apart from contributing to the fundamental understanding of carbon interfacial processes in unconventional electrolytes, these findings open up exciting possibilities for advancing aqueous supercapacitor technology using sustainable and easily available biomass resources like vine shoots.

Keywords: biomass-derived activated carbon, Al-based carbon electrochemistry, supercapacitors

1. Introduction

Given the evident consequences of extensive fossil fuels exploitation, there is a strong focus on transitioning toward clean and renewable energy sources. Sustainable biomass, which is readily available, affordable, and considered environmentally friendly, is gaining attention in the circular economy as an excellent choice for converting into high-value products. Researchers are addressing the global challenge of agricultural waste disposal, and extensive studies are underway to optimize biomass resources.

One particularly promising "green" approach involves using various by-products of the grape processing industry, such as vine shoots, grape stalks, seeds, etc., for the

production of activated carbon (AC) [1–6]. AC is a valuable material used in energy storage devices such as batteries and supercapacitors. This is achieved through either chemical or physical activation methods. Chemical activation, in particular, has been shown to result in highly developed surface porosity, up to $2000 \text{ m}^2 \text{ g}^{-1}$, unlike physical activation, which typically reaches about $1000 \text{ m}^2 \text{ g}^{-1}$ [4]. Such high surface area is crucial for obtaining high specific capacitance electrodes for supercapacitors, reaching about 300 F g^{-1} for chemically activated, and 150 F g^{-1} for physically activated carbon [4]. This research focuses on turning abundant agricultural waste, vine shoots, into activated carbon with excellent charge storage capacity, contributing to sustainable and eco-friendly energy solutions. Specifically, the paper investigates the use of novel electrolytes based on Al-ions as a method of widening the workable voltage window of aqueous supercapacitors.

2. Experimental

Vine shoots (VS) of the Vranac grape variety, collected from a vineyard near Podgorica, Montenegro, were used to synthesize activated carbon (AC_{vs}) according to the scheme presented at Figure 1 [7]. The VS precursors were firstly washed, chopped, and air-dried overnight at room temperature. The AC synthesis involved a two-step process: first, pre-carbonization at $300 \text{ }^\circ\text{C}$ under Ar atmosphere for 2 hours (biochar), and then chemical activation with ZnCl_2 at $700 \text{ }^\circ\text{C}$ under the same other conditions (activated carbon, AC_{vs}).

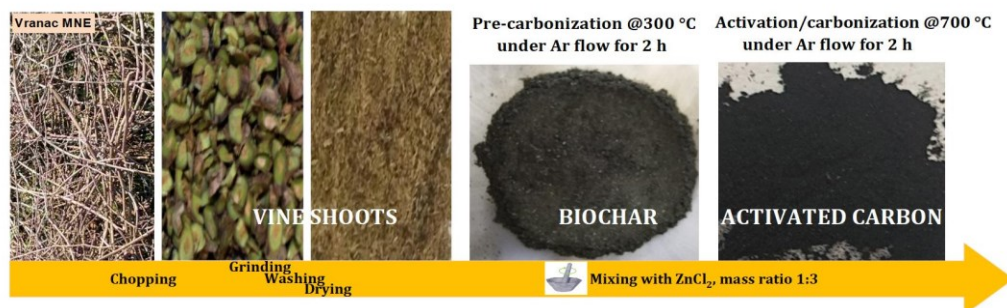


Figure 1. Schematic representation of AC_{vs} synthesis.

The prepared carbon was investigated by Fourier transform infrared spectroscopy (FTIR, using Perkin Elmer FT-IR Spectrometer Spectrum Two with KBr technique in $4000\text{--}400 \text{ cm}^{-1}$ wavenumber range and resolution of 4 cm^{-1}) and X-ray powder diffraction (XRPD, Rigaku Miniflex 600, Cu- $K\alpha$ radiation ($\lambda = 1.5406 \text{ \AA}$), D/teX Ultra2 MF detector, the instrument worked under 600 W and the diffractogram was recorded in the $10\text{--}80^\circ$ 2θ angle range, with a step of 0.01° , at a data acquisition rate of $10.00^\circ/\text{min}$). The specific surface area of AC_{vs} was estimated by Brunauer-Emmet-Teller (BET) method applied to the N_2 adsorption–desorption isotherm obtained with a Sorptomatic 1990 Thermo Finnigan device. The capacitive behavior of AC_{vs} was investigated in 1 M aluminium sulphate, nitrate and chloride aqueous solutions by cyclic voltammetry. The measurements were done on a Gamry 1010E Potentiostat/Galvanostat in a three-

electrode cell configuration. AC_{vs} was supported on glassy carbon as working electrode, the reference was a saturated calomel electrode (SCE), and platinum served as the counter electrode.

3. Results and discussion

Structural characterization of AC_{vs} is presented in **Figure 2a)** and **b)**. FTIR spectrum of AC_{vs} (**Figure 2a)** indicates the complete carbonization of the vine shoots precursor and the presence of two weak bands attributed to aromatic C=C (1551 cm⁻¹) and C–O (1120 cm⁻¹) stretching vibrations [8]. The XRPD diffractogram of AC_{vs}, shown in **Figure 2b)**, revealed the amorphous structure of the material evidenced by two broad diffraction peaks centered at 23° and 44° 2θ. The absence of other diffraction peaks confirms the high purity of the synthesized AC_{vs}. The applied synthetic procedure yielded highly porous carbonaceous material as confirmed by considerably high BET estimated specific surface area of 1494 m² g⁻¹.

Investigations of electrochemical behavior of AC_{vs} revealed extremely good carbon electrochemistry in different Al-ion containing electrolytes. Cyclic voltammograms (CVs) measured in 1 M aqueous solutions of Al sulphate, nitrate and chloride at the scan rate 20 mV s⁻¹ are presented at **Figure 2c)**. The results have shown better pseudocapacitive behaviour of AC_{vs} in aluminium nitrate and chloride solutions, with more pronounced redox peaks at 0,23/0 V vs SCE.

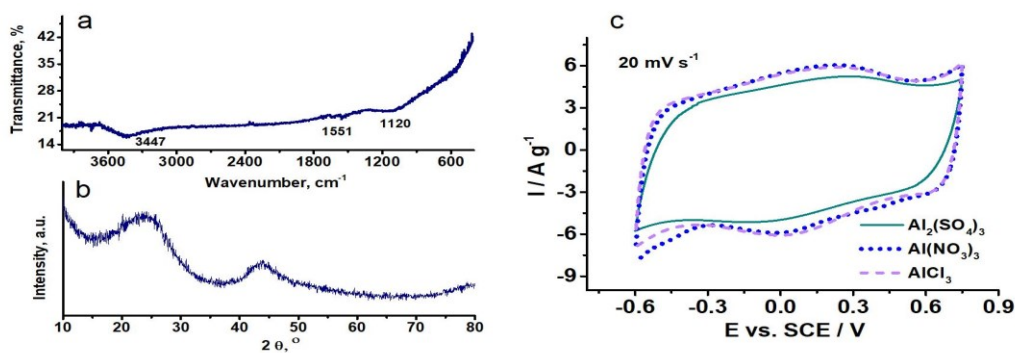


Figure 2. FTIR spectra a) XRPD pattern b) and comparative CVs of AC_{vs} measured in 1 M Al-based electrolytes at 20 mV s⁻¹ c).

Average specific capacitances of AC_{vs} in Al-ion-containing aqueous electrolytes reached high values of 193, 235 and 233 F g⁻¹ in 1 M Al₂(SO₄)₃, Al(NO₃)₃ and AlCl₃, respectively. Such high charge storage ability is strongly related to the high specific surface area of synthesized AC_{vs}.

3. Conclusions

Structural and textural characterization of the prepared AC_{vs} showed that the as synthesized material is activated carbon of high purity and low surface functionality, but of high specific surface area amounting to 1494 m² g⁻¹.

Electrochemical investigations in different Al-ion containing aqueous electrolytes revealed extremely good pseudocapacitive behavior of AC_{vs} and high specific capacitances were obtained, reaching 235 F g⁻¹ in nitrate solution.

This research opened wide possibilities for enhancing aqueous charge storage technology through innovative carbon electrochemistry designs and introduction of alternative electrolyte solutions.

Acknowledgment

This research was supported by the NATO Science for Peace and Security Programme under grant G5836-SUPERCAR. Authors gratefully acknowledge the financial support from the bilateral project Montenegro-Slovenia "Biomass-derived carbons as anodes in sodium-ion batteries."

References

- [1] D. Jiménez-Cordero, F. Heras, M.A. Gilarranz, E. Raymundo-Piñero, *Grape seed carbons for studying the influence of texture on supercapacitor behaviour in aqueous electrolytes*, Carbon N. Y. 71 (2014) 127–138.
- [2] L. Guardia, L. Suárez, N. Querejeta, V. Vretenár, P. Kotrusz, V. Skákalová, T.A. Centeno, *Biomass waste-carbon/reduced graphene oxide composite electrodes for enhanced supercapacitors*, Electrochim. Acta. 298 (2019) 910–917.
- [3] L. Alcaraz, A. Adán-Más, P. Arévalo-Cid, M. de F. Montemor, F.A. López, *Activated Carbons From Winemaking Biowastes for Electrochemical Double-Layer Capacitors*, Front. Chem. 8 (2020) 1–10.
- [4] L. Suárez, T.A. Centeno, *Unravelling the volumetric performance of activated carbons from biomass wastes in supercapacitors*, J. Power Sources. 448 (2020) 227413.
- [5] J. Zhang, H. Chen, J. Bai, M. Xu, C. Luo, L. Yang, L. Bai, D. Wei, W. Wang, H. Yang, *N-doped hierarchically porous carbon derived from grape marcs for high-performance supercapacitors*, J. Alloys Compd. 854 (2021) 157207.
- [6] L. Guardia, L. Suárez, N. Querejeta, C. Pevida, T.A. Centeno, *Winery wastes as precursors of sustainable porous carbons for environmental applications*, J. Clean. Prod. 193 (2018) 614–624.
- [7] A. Gezović, J. Mišurović, B. Milovanović, M. Etinski, J. Krstić, V. Grudić, R. Dominko, S. Mentus, M.J. Vujković, *High Al-ion storage of vine shoots-derived activated carbon: New concept for affordable and sustainable supercapacitors*, J. Power Sources. 538 (2022) 231561.
- [8] V. Gomez-Serrano, J. Pastor-Villegas, A. Perez-Florindo, C. Duran-Valle, C. Valenzuela-Calahorro, *FT-IR study of rockrose and of char and activated carbon*, J. Anal. Appl. Pyrolysis. 36 (1996) 71–80

The interdependence of structural properties and pseudocapacitive behavior of biomass-derived activated carbon

Minea Kapidžić¹, Sonja Kastratović¹, Milica Vujković², Veselinka Grudić¹, Jana Mišurović^{1*}

¹ University of Montenegro, Faculty of Metallurgy and Technology, Podgorica, Montenegro, Cetinjski put, bb; e-mail: kapidzicminea126@gmail.com, sokikastratovicss@gmail.com, grudicv@ucg.ac.me, janam@ucg.ac.me

² University of Belgrade - Faculty of Physical Chemistry, Belgrade, Serbia, Studentski trg 12-16; e-mail: milica.vujkovic@ffh.bg.ac.rs

* Corresponding author

DOI: 10.46793/ICCB123.257K

Abstract: Montenegro produces a significant amount of grapes annually for both commercial and domestic purposes. Wooden biowaste that is left after grooming poses an environmental issue as it calls for an adequate management plan. This study investigates hydrothermal treatment as an efficient strategy to convert this abundant waste into a high-quality, carbon-based energy storage material. The activation process took place in a hydrothermal reactor with ZnCl₂ aqueous suspension under 200°C. The material was further carbonized at 700 °C until lignin, cellulose, and hemicellulose completely decomposed. The structure of the obtained materials was investigated by means of FTIR spectroscopy. The carbonized sample was analyzed as an electrode material for supercapacitors in typical aqueous electrolytes. Cyclic voltammograms were recorded in different pH environments. The results showed that AC reached the maximum specific capacity of 104.3 F g⁻¹ in H₂SO₄. This implicates thus obtained electrode material to be a promising candidate for use in energy storage systems.

Keywords: biomass-derived carbon, hydrothermal activation, supercapacitors

1. Introduction

Agricultural residues pose an environmental risk due to the lack of sustainable management solutions. The waste of the organic industry, such as wine production, is particularly challenging to dispose of. In Montenegro, around 22000 tons of grapes are produced for both consumption and fermentation for beverages [1]. Roughly 11 million tons year⁻¹ of vine are produced worldwide. Traditionally, vine shoots are either burnt or abandoned in the fields [2]. Due to its interesting chemical composition, rich in bioactive compounds such as phenols, this abundant waste is an attractive feedstock for the extraction of useful chemicals such as resveratrol [3–5]. On the other hand, thermal conversion is considered optimal for adequate management as it yields energy-dense biochar [6,7]. Carbonaceous materials derived from biomass are frequently used as

catalyst support [8], sorbent for contaminants and valuable chemicals [9], etc. Because of its high porosity and large specific surface area, it makes a promising electrode material [10]. However, more research is needed to find optimal conditions for increasing porosity and surface area to improve the electrochemical properties of the material.

Tailoring hydrochar in an efficient and sustainable way may be possible using hydrothermal co-carbonization. Hydrothermal carbonization alters the chemical structure of the material under autogenous pressure and moderate temperatures, up to 220°C. Co-carbonization with metal salts may contribute to the breakdown of biomass during the hydrothermal process, producing hydrochar with increased surface area and porosity [8]. According to Loow et al., the metal salts operate specifically as Lewis acids, assisting in the breakage of the glycosidic bonds and catalyzing the degradation of biomass resulting in a structure with micro- and mesopores [11].

This study aims to investigate the effect of activation via one-pot synthesis of biomass with a common activating agent, zinc chloride. To our knowledge, no research was conducted on single-step activation of vine shoots for the production of highly porous carbon used in energy systems.

2. Materials and methods

Vine shoots were collected from the local grape producer nearby Podgorica, Montenegro. They were cut, meshed in the particles uniform in size, and stored in the airtight containers until the experimentation. The reaction mixture with ZnCl₂ as an activator was placed in the laboratory batch reactor and carbonized at 200°C. Further carbonization of the resulting hydrochar (HTC) was at 700 °C in an Ar environment (AC700). To get rid of the inorganic residues, carbonized sample was ultimately rinsed with 1 M HCl solution and distilled water.

Both samples were structurally characterized with Fourier transform infrared spectroscopy (FTIR) by attenuated total reflection (ATR) technique on diamond crystal with 4 cm⁻¹ resolution, in 4000-400 cm⁻¹ wavenumber range, using Perkin Elmer FT-IR Spectrometer Spectrum Two. The electrochemical behavior of AC700 was investigated by cyclic voltammetry in aqueous electrolytes of three different pH using Gamry Potentiostat/ Galvanostat. Measurements were done in a three-electrode cell with glassy carbon supported working electrode, saturated calomel electrode (SCE) as a reference and Pt as a counter electrode.

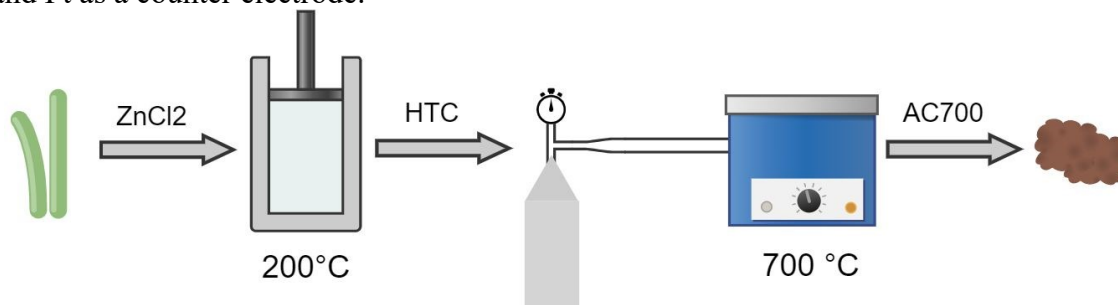


Figure 1. Activated carbon synthesis scheme.

3. Results and discussion

FTIR spectroscopy revealed the changes in the material structure during different synthesis stages (**Figure 2a**). HTC spectrum shows several strong bands indicating that lignin and cellulose structures are still present in the material, while the spectrum of carbonized sample AC700 exhibits only two weak bands which prove the complete decomposition of organic compounds and are ascribed to aromatic C=C and C–O stretchings.

Cyclic voltammograms (CVs) of the AC700 sample obtained at a rate of 20 mVs^{-1} in common aqueous electrolytes (1 M H_2SO_4 , 6 M KOH, and 1 M Na_2SO_4) are shown at **Figure 2b**. The capacitance behavior of activated carbon was observed across a wide pH range. In acidic or alkaline solutions, the typical CV shape of pseudocapacitance is evident, while in neutral electrolyte, the pure double layer dominates [12]. The pseudofaradaic reactions are mainly attributed to quinone and hydroxyl groups [12].

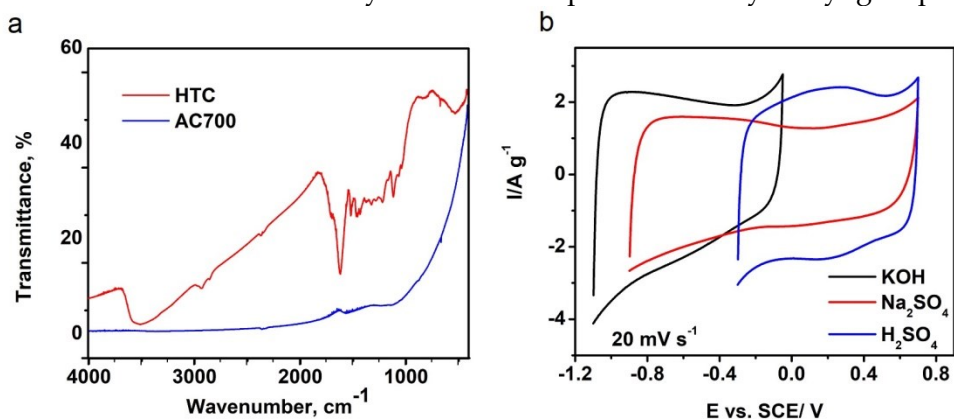


Figure 2. FTIR spectra of HTC and AC700 a) and CVs of AC700 in 6 M KOH, 1 M Na_2SO_4 and 1 M H_2SO_4 at 20 mV s^{-1} b).

Specific capacitances in 1 M H_2SO_4 , 6 M KOH, and 1 M Na_2SO_4 were calculated to be 104.3 F g^{-1} , 95.40 F g^{-1} , and 72.5 F g^{-1} , respectively. As previously reported, due to a higher ionic conductivity, H_2SO_4 and KOH provide higher capacitance than Na_2SO_4 [12].

3. Conclusions

Promising carbonaceous electrode material was obtained via hydrothermal ZnCl_2 -assisted synthesis using vine shoots as precursor. FTIR spectroscopy was used to detect and analyze the changes in the material structure after carbonisation. In conventional aqueous electrolytes, AC700 showed good capacitive behavior making it favorable for application in aqueous supercapacitors.

Acknowledgment

This work is sustained by NATO Science for Peace and Security (SPS) Programme (project G5836-SUPERCAR). M.K. is grateful to the CEEPUS network for the mobility to

the Institute of Chemical and Energy Engineering, University of Natural Resources and Life Sciences, Vienna, Austria.

References

- [1] Statistical Office of Montenegro - MONSTAT, (n.d.). <https://monstat.org/eng/page.php?id=62&pageid=62> (accessed July 31, 2023).
- [2] R. Sánchez-Gómez, G.L. Alonso, M.R. Salinas, A. Zalacain, 4 - *Reuse of Vine-Shoots Wastes for Agricultural Purposes*, in: C.M. Galanakis (Ed.), *Handbook of Grape Processing By-Products*, Academic Press, 2017: pp. 79–104.
- [3] E. Karacabey, G. Mazza- *Optimization of Solid–Liquid Extraction of Resveratrol and Other Phenolic Compounds from Milled Grape Canes (Vitis vinifera)*, *J Agric Food Chem.* 2008 Aug 13;56(15):6318-25.
- [4] M.S. Jesus, Z. Genisheva, A. Romaní, R.N. Pereira, J.A. Teixeira, L. Domingues, *Bioactive compounds recovery optimization from vine pruning residues using conventional heating and microwave-assisted extraction methods*, *Industrial Crops and Products.* 132 (2019) 99–110.
- [5] M.P. Delgado-Torre, C. Ferreiro-Vera, F. Priego-Capote, P.M. Pérez-Juan, M.D. Luque de Castro, *Comparison of Accelerated Methods for the Extraction of Phenolic Compounds from Different Vine-Shoot Cultivars*, *J. Agric. Food Chem.* 60 (2012) 3051–3060.
- [6] R. Al Afif, C. Pfeifer, T. Pröll, *Bioenergy Recovery from Cotton Stalk*, in: M.-R. Ansari (Ed.), *Advances in Cotton Research*, IntechOpen, 2020.
- [7] S.Y. Lee, R. Sankaran, K.W. Chew, C.H. Tan, R. Krishnamoorthy, D.-T. Chu, P.-L. Show, *Waste to bioenergy: a review on the recent conversion technologies*, *BMC Energy.* 1 (2019) 4.
- [8] F. Li, A.R. Zimmerman, X. Hu, Z. Yu, J. Huang, B. Gao, *One-pot synthesis and characterization of engineered hydrochar by hydrothermal carbonization of biomass with ZnCl₂*, *Chemosphere.* 254 (2020) 126866.
- [9] G. Padovani, C. Pintucci, P. Carlozzi, *Dephenolization of stored olive-mill wastewater, using four different adsorbing matrices to attain a low-cost feedstock for hydrogen photo-production*, *Bioresource Technology.* 138 (2013) 172–179.
- [10] Z. Gao, Y. Zhang, N. Song, X. Li, *Biomass-derived renewable carbon materials for electrochemical energy storage*, *Materials Research Letters.* 5 (2017) 69–88.
- [11] Y.-L. Loow, T.Y. Wu, K.A. Tan, Y.S. Lim, L.F. Siow, J. Md. Jahim, A.W. Mohammad, W.H. Teoh, *Recent Advances in the Application of Inorganic Salt Pretreatment for Transforming Lignocellulosic Biomass into Reducing Sugars*, *J. Agric. Food Chem.* 63 (2015) 8349–8363.
- [12] A. Gezović, J. Mišurović, B. Milovanović, M. Etinski, J. Krstić, V. Grudić, R. Dominko, S. Mentus, M.J. Vujković, *High Al-ion storage of vine shoots-derived activated carbon: New concept for affordable and sustainable supercapacitors*, *Journal of Power Sources.* 538 (2022) 231561.

Elucidating Health-Enhancing Properties of Natural Products: A Journey from Extract Isolation to Quantum Mechanics (QM) Calculations

Gregor Hostnik¹, Anja Petek¹, Sara Štumpf¹, Franjo Frešer¹, Zala Kolenc¹, Matej Keber¹, Jelena Tošović¹, Urban Bren^{1,2,3*}

¹ University of Maribor, Faculty of Chemistry and Chemical Technology, Laboratory for Physical Chemistry and Chemical Thermodynamics, Smetanova ulica 17, SI-2000 Maribor, Slovenia; e-mail: gregor.hostnik@um.si, anja.petek@um.si, sara.stumpf@um.si, franjo.freser@um.si, matej.keber@student.um.si, jelena.tosovic@um.si, urban.bren@um.si

² University of Primorska, Faculty of Mathematics, Natural Sciences and Information Technologies, Glagoljaška 8, SI-6000 Koper, Slovenia

³ Institute of Environmental Protection and Sensors, Beloruska 7, SI-2000, Slovenia

* Corresponding author

DOI: 10.46793/ICCB23.261H

Abstract: Natural extracts are a promising source of compounds with health-enhancing properties. However, the challenge lies in understanding the relationships between the composition of extracts, and the connection between the structure and activity of its constituents, given that the extracts are a complex mixture. Typically, researchers adopt two main methods to tackle this: experimental examination of the biological activity of the extracts and computational chemistry to obtain insights into the properties of the molecules. There are, however, inherent challenges in drawing comparisons between the results of these methods, particularly because of the potential antagonistic and synergistic effects of compounds present within the natural extracts. This task is significantly simplified when pure compounds are used for experimental work.

This study exemplifies the process of isolating pure compounds from hop and chestnut wood extracts using preparative High-Performance Liquid Chromatography (HPLC). The pKa values, chelation ability and antibacterial activity of isolated compounds were examined experimentally. Moreover, the experimental results were further elucidated with computational findings, an approach made possible using pure compounds. This comprehensive approach significantly enhances our understanding of these natural compounds.

Keywords: Purification, chelation, protolytic equilibrium, hop extract, chestnut extract

1. Introduction

Plants are promising sources of new compounds with health-enhancing properties. However, the beneficial effects are relatively weak in several cases and often observed only in epidemiologic studies [1]. To better design the studies, the information on which compound in the extract is responsible for its biological activity and an

understanding of the mechanism of action is essential. The experiments performed on the pure compounds are crucial in getting this information. The information obtained from these experiments varies from understanding the mechanism of action to obtaining structure-to-activity relationships and finally understanding the possible synergistic or antagonistic effects of various compounds in the extract.

On the other hand, computational calculations are practically always performed on pure compounds. And while the advantage of calculations is that they provide insight into processes on the molecular level, the results largely depend on the computational method used. Consequently, by performing calculations as well as experiments on pure compounds, one can obtain information on (i) which compounds in the raw natural extracts are responsible for the biological activity; (ii) by studying structurally similar compounds, the contribution of structural elements of studied compounds to their activity can be observed; (iii) by comparison of the activity of mixture with controlled composition to the results for pure compound possible synergistic or antagonistic effects of these compounds can be confirmed and last but not least (iv) by combining experimental and computational results the information on the mechanism of action on the molecular level can be obtained [1]. The following study will demonstrate the synergistic effects of computational and experimental studies on two systems – the compounds isolated from the hop extract and the ellagitannins isolated from the aqueous chestnut extract.

2. Experimental

In all cases, isolation was performed by several consecutive isolation steps using flash chromatography (PF-50C18HP-F0025 C18 flash column, AdvisionInterchim Scientific, Montluçon, France) and preparative chromatography (US10C18HQ-250/212 C18 chromatographic column, AdvisionInterchim Scientific, Montluçon, France). The isolation was performed using a puriFlash 5.250 preparative chromatograph with UV/Vis and ELSD detectors (AdvisionInterchim Scientific, Montluçon, France). The mobile phase was composed of 0.1 % formic acid aqueous solution and 0.1 % solution of formic acid in acetonitrile. All the UV/Vis measurements were performed on Varian Cary 50 UV/Vis spectrophotometer (Varian Inc., Mulgrave, Australia) with cuvettes with optical path lengths of 0.1, 0.2, 0.5, and 1 cm. The chelation ability was examined at five pH values (3.5–5.5) controlled using acetate buffer.

The antibacterial activity of the isolated compound was determined by the determination of MIC values. These values were determined using the dilution method, where bacterial growth was observed using optical density measurements and by applying the INT dye.[2]

The structure of molecules, their respective energies and UV/Vis spectra were calculated using the Gaussian 09 program package. The level of theory used was B3LYP/6-311++G(d,p) with PCM implicit water model ($\epsilon=78.3553$). The UV/Vis spectra were calculated by subjecting the obtained ground state TDDFT calculations to estimate the excited singlet state properties. In all the cases, enough transitions were considered that the calculated transitions reached slightly below 200 nm [3].

3. Results and Discussion

3.1 Isolation of pure compounds

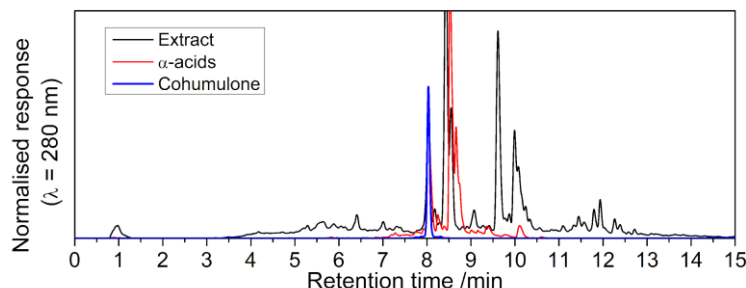


Figure 1. Comparison of chromatographic purity in various stages of isolation of cohumulone. Four compounds were isolated from the aqueous chestnut extract: vescalin, castalin, vescalagin and castalagin. From the hop extract, seven compounds were isolated (xanthohumol, cohumulone, adhumulone, n-humulone, colupulone, adlupulone, n-lupulone). The chromatographic purity of all isolated compounds was higher than 95 %. In Figure 1, the chromatograms for cohumulone isolation after each isolation step are depicted with a blue line presenting the chromatogram of the final product.

3.2 Spectrum of cohumulone

According to the literature, the cohumulone can be present in two tautomeric forms, depicted as structures C0 and Ct0 in Figure 2 [4]. The cohumulone was isolated from hop extract, and its UV/Vis spectrum was measured to confirm which form is prevalent in the aqueous solution. In Figure 2, the comparison of the experimental and calculated spectrum of cohumulone is depicted. The structure C0 has lower energy, while its calculated spectrum is in much better agreement with the experimental data. Both facts indicate that C0 is the prevailing species in an aqueous solution. Finally, from the pH dependence of absorbance, we determined the pKa value of cohumulone to be 3.9.

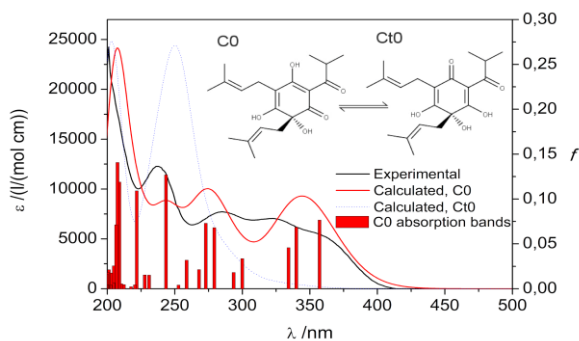


Figure 2. Comparison of experimental and calculated spectrum of cohumulone.

3.3 Chelation of metal ions and antibacterial activity

Gallic acid, vescalin and vescalagin are the major constituents of aqueous chestnut extract. The MIC values of vescalagin, vescalin, and gallic acid were measured, and it was determined that the MIC values of vescalin and vescalagin are approx. 20 % lower than the MIC value of the extract, while the MIC value of gallic acid is significantly higher – indicating that the contribution of gallic acid to the antibacterial activity of the extract is

relatively small. It was shown that gallic acid chelate one Fe(II) ion, while QM calculations confirmed that Fe(II) is rapidly oxidised into Fe(III) after chelation with gallic acid.[5] Additionally, vescalin and vescalagin can chelate two and three Fe(II) ions, respectively. Because the molar mass ratio of vescalin/vescalagin is 0.66, this results in similar MIC values of both compounds when expressed in.

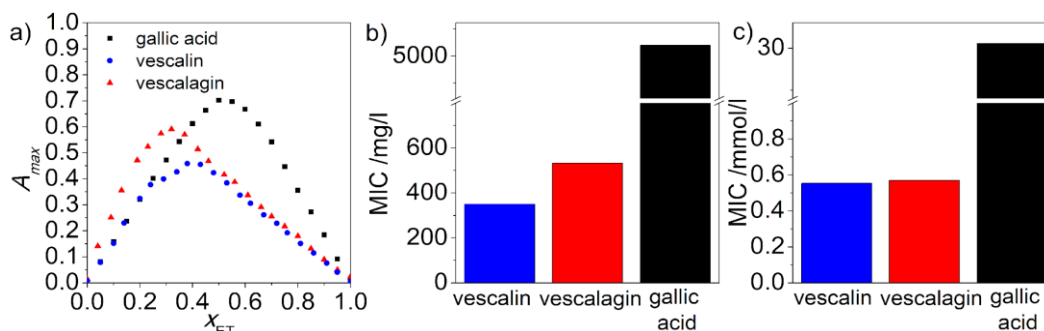


Figure 3. Job plots for Fe(II) chelation ability (a) and MIC values (b,c) of gallic acid, vescalin and vescalagin.

4. Conclusions

Several pure compounds were isolated from the chestnut extract and hop extract. Afterwards, the pKa values of cohumulone were determined experimentally, while the QM calculations enabled us to determine which tautomer was prevalent in the solution. It was also demonstrated that gallic acid has a minor contribution to the chestnut extract's antibacterial activity, while other compounds' contribution was more pronounced. Finally, their antibacterial activity was correlated with their ability to chelate Fe(II) ions.

Acknowledgement

This work was supported by the Slovenian Research Agency (ARRS) through program and project grants J1-2471, P2-0046, L2-3175, J4-4633, J1-4398, L2-4430, J3-4498, J7-4638, J1-4414, J3-4497, P2-0438, and I0-E015.

References

- [1] S. Sauer, A. Plauth, *Health-Beneficial Nutraceuticals-Myth or Reality?*, Appl. Microbiol. Biotechnol. 101 (2017), 951–961.
- [2] S. Štumpf, G. Hostnik, T. Langerholc, M. Pintarič, Z. Kolenc, U. Bren, *The Influence of Chestnut Extract and Its Components on Antibacterial Activity against Staphylococcus aureus*, Plants, 12 (2023) 2043.
- [3] G. Hostnik, J. Tošović, S. Štumpf, A. Petek, U. Bren, *The influence of pH on UV/Vis spectra of gallic and ellagic acid: A combined experimental and computational study*, Spectrochim. Acta A, 267 (2022), 120472.
- [4] D. E. Briggs, C. A. Boulton, P. A. Brookes, R. Stevens, *Brewing Science and Practice*, Cambridge: Woodhead Publishing Limited, 2004.
- [5] F. Frešer, G. Hostnik, J. Tošović, U. Bren, *Dependence of the Fe(II)-Gallic Acid Coordination Compound Formation Constant on the pH*, Foods, 10 (2021) 2689

A computational model of the left ventricle – application in cardiomyopathy disease

Miljan Milosevic^{1,2,3*}, Bogdan Milicevic^{2,4}, Vladimir Simic^{1,2}, Milos Kojic^{2,5,6}, Nenad Filipovic^{2,4}

¹ University of Kragujevac, Institute for Information Technologies, Kragujevac, Serbia (Jovana Cvijica bb, 34000 Kragujevac); e-mail: miljan.m@kg.ac.rs, vsimic@kg.ac.rs

² BioIRC, Bioengineering Research and Development Center, Kragujevac, Serbia (Prvoslava Stojanovica 6 34000 Kragujevac); e-mail: mkojic42@gmail.com

³ Metropolitan University, Belgrade, Serbia (Tadeša Koščuška 63, 11000 Belgrade);

⁴ University of Kragujevac, Faculty for Engineering Sciences, Kragujevac, Serbia (Sestre Janjic 6, 34000 Kragujevac); e-mail: bogdan.milicevic@uni.kg.ac.rs, fica@kg.ac.rs

⁵ Methodist Research Institute Houston, The Department of Nanomedicine, Houston USA (6670 Bertner Ave, Houston, TX 77030, United States);

⁶ Serbian Academy of Sciences and Arts, Belgrade, Serbia (Kneza Mihaila 35, Beograd 11000);

* *Corresponding author*

DOI: 10.46793/ICCB23.265M

Abstract: Cardiomyopathy or structural and functional abnormalities of the ventricular myocardium is a common cardiac disease. It can be commonly classified as hypertrophic (HCM) and dilated (DCM) cardiomyopathy. A computational model was developed to simulate drug effects on heart behavior during the heartbeat cycle. The model includes parametric left ventricle geometry supported with the finite element (FE) code PAK with the implemented methodology for loose coupling fluid-structure interaction (FSI) and coupled electromechanics which enables investigation of the influence of different drugs on the conditions of virtual cardiomyopathy patients. Passive mechanical stresses are calculated using a recently introduced orthotropic material model based on an experimental investigation of passive material properties of the myocardium. Active stresses are calculated using the Hunter excitation model. The basic equations for solid mechanics, fluid dynamics, and excitation are summarized, and the applicability of this model is illustrated on a simple model of the left ventricle which includes inlet mitral and outlet aortic valve cross-sections. The presented computational model can serve as a basis for the in-silico simulation of the drug effects in the common types of cardiomyopathy.

Keywords: cardiac cycle, cardiomyopathy, finite element method, left ventricle model

1. Introduction

Cardiomyopathy is a general name for all anomalies of the ventricular endocardium leading to the stretched, thickened, or stiff heart chamber. Treatment of symptoms of cardiomyopathy using existing types of therapies can only partially affect the

improvement of treatment outcomes, but it is still necessary to introduce new types of treatment that could have a more significant effect on this type of disease.

Testing of drugs for cardiomyopathy can be done by using *in-silico* clinical trials that employ computational modeling and a variety of simulation techniques. In this work, we present the application of finite element (FE) numerical procedure for the simulation of the cardiomyopathy diseased left ventricle model.

2. Materials and Methods

The FE code PAK [1] is used to solve coupled solid mechanics and fluid dynamics fields using the loose coupling procedure. For solid mechanics, two types of stresses are accounted for - passive and active. The determination of passive stresses is based on the recently published experimental investigation of Professor Holzapfel and his research group [2]. For the active stresses in solid material, calcium concentration relation for the heart muscle formulated in [3] is used in our model [4]. Fluid flow is considered as Newtonian and is based on the continuity equation and differential Navier-Stokes equations [6]. The loose coupling procedure is used to solve the solid-fluid interaction: first, we solve the fluid field, then calculate the forces of fluid acting on the surrounding solid domain, and determine the solid deformation. Finally, when solving for a solid domain, we transfer the velocities of the solid to the corresponding fluid nodes. A usual iterative procedure [6] is used for both solid and fluid models.

2. Results

The parametric FE model consists of a fluid domain surrounded by a solid wall (Figure 1a), with prescribed velocities at the inlet (mitral; Figure 1b) and outlet (aortic; Figure 1c) valves.

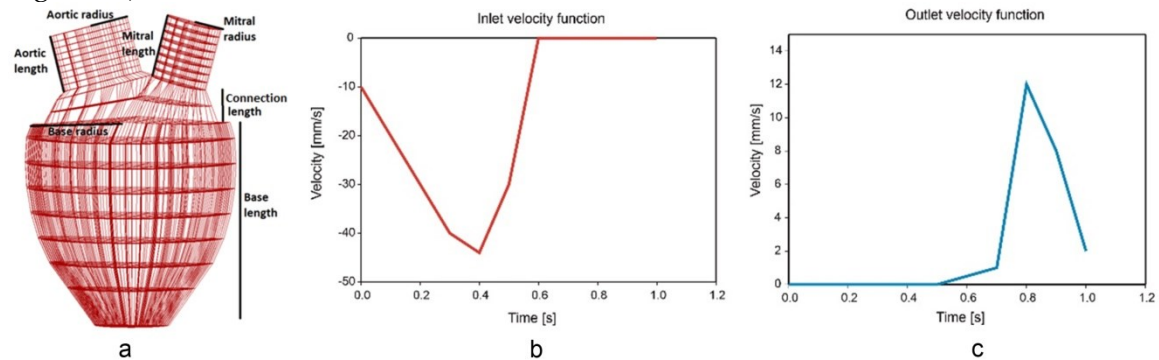


Figure 1. a) Parametric model of the left ventricle with structural mesh. Base, connecting part, and valves (mitral and aortic) parameters noted [7]; Prescribed blood velocities as functions of time: b) Inlet velocity, at mitral valve cross-section, and c) outlet velocity, at aortic valve cross-section.

Velocity and pressure distribution inside the model, during one heartbeat cycle of 1.0s duration, for four different time moments are shown in Figures 2a and 2b. In Figure 2c shows how the displacements are distributed over the ventricle wall.

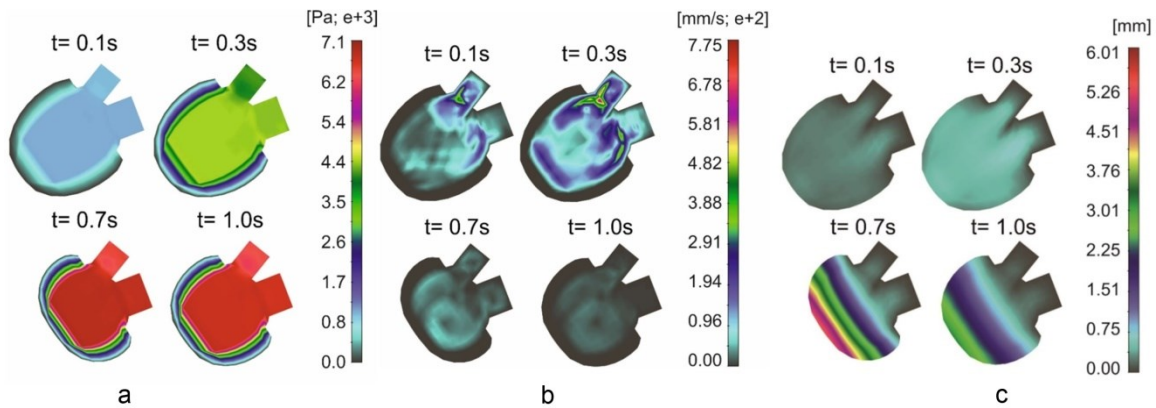


Figure 2. Results for parametric left ventricle model for four different time steps, a) field of velocities within the fluid part, b) pressures inside of the left ventricle, and c) field of displacements for the left ventricle wall.

A computed pressure vs. volume (pV) diagram and a commonly accepted pV diagram for one full cycle is shown in Figures 3a and 3b, while Figure 3c displays a vectorial representation of velocities inside the fluid part of the ventricle.

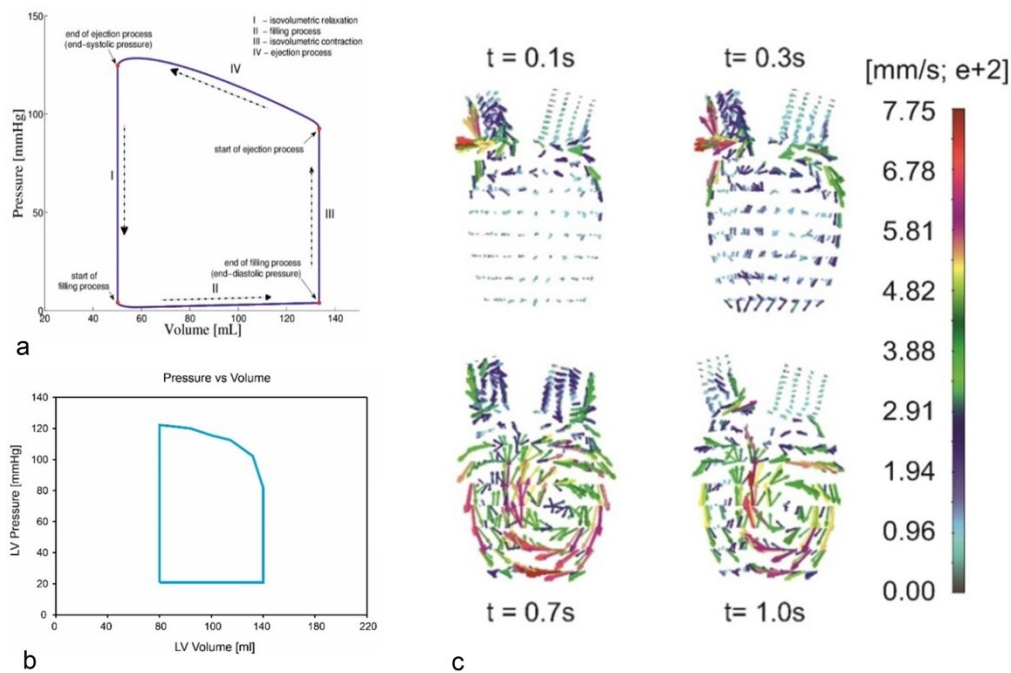


Figure 3. a) Pressure vs Volume diagram for left ventricle with an explanation of notable steps during one full cycle. b) Pressure vs Volume (pV) diagram for left ventricle structural model. Prescribed cycle duration- 1.0 s, 10 time steps. c) Vectorial representation of velocities in a parametrical model of the left ventricle; four different time steps.

3. Conclusions

We have demonstrated that the coupled solid-fluid mechanical model can be used for the simulation of the heartbeat. The calculation was executed using our PAK solver while the model generation was performed by the in-house CAD software. The presented computational model serves as a basic tool for the in-silico simulation of the drug effects in the common types of cardiomyopathy.

Acknowledgment

This paper is supported by the SILICOFCM project that has received funding from the European Union's Horizon 2020 research and innovation programme under grant agreement No 777204. This article reflects only the author's view. The Commission is not responsible for any use that may be made of the information it contains. This research is funded by Serbian Ministry of Education, Science, and Technological Development [451-03-47/2023-01/200378 (Institute for Information Technologies, University of Kragujevac)] and [451-03-68/2023-14/200107 (Faculty of Engineering, University of Kragujevac)]. The authors acknowledge support from the City of Kragujevac, Serbia.

References

- [1] M. Kojic, R. Slavkovic, M. Zivkovic, N. Grujovic, N. Filipovic, M. Milosevic, PAK - Finite Element Program for Linear and Nonlinear Analysis, Univ Kragujevac and R&D Center for Bioengineering, Kragujevac, Serbia, 2010.
- [2] Gerhard Sommer, Andreas J. Schriefl, Michaela Andrä, Michael Sacherer, Christian Viertler, Heimo Wolinski, Gerhard A. Holzapfel, Biomechanical properties and microstructure of human ventricular myocardium, *Acta Biomaterialia* 24 (2015) 172–192.
- [3] P.J. Hunter, A.D. McCulloch, H.E.D.J. ter Keurs, "Modelling the mechanical properties of cardiac muscle", *Progress in Biophysics & Molecular Biology*, Vol 69, pp. 289-331, 1998.
- [4] M. Kojic, M. Milosevic, V. Simic, B. Milicevic, V. Geroski, S. Nizzero, A. Ziemys, N. Filipovic, M. Ferrari, Smearred multiscale finite element models for mass transport and electrophysiology coupled to muscle mechanics, *Frontiers in Bioengineering and Biotechnology*, Vol 7, 2019, DOI: 10.3389/fbioe.2019.00381, ISSN: 2296-4185.
- [5] Milos Kojic, Miljan Milosevic, Bogdan Milicevic, Vladimir Simic, Heart mechanical model based on Holzapfel experiments, *Computational Bioengineering and Bioinformatics, ICCB 2019*, ISBN: 978-3-030-43657-5, *Learning and Analytics in Intelligent Systems*, vol. 11, Springer Cham, pp 12-21, 2020.
- [6] M. Kojic, N. Filipovic, B. Stojanovic, N. Kojic, "Computer Modelling in Bioengineering Theory, Examples and Software", J. Wiley and Sons, 2008.
- [7] M. Anic, S. Savic, A. Milovanovic, M. Milošević, B. Milicevic, V. Simic, N. Filipovic. Solution of fluid flow through left heart ventricle, *Applied Engineering Letters: Journal of Engineering and Applied Sciences*, Vol. 5 (2020) No. 4, Article 2 (p. 120-125), <https://doi.org/10.18485/aeletters.2020.5.4.2>

Status and quality of life of people with celiac and people on a gluten-free diet

Jasna Frljak¹, Senita Isaković², Enver Karahmet^{2*}, Almir Toroman², Ervina Bečić³, Fahir Bečić³, Zoran Marković⁴

¹ University of Tuzla, Faculty of Technology, University 8, 75000 Tuzla, Bosnia and Herzegovina

² University of Sarajevo, Agricultural and Food Sciences Faculty, Zmaja od Bosne 8, 71000 Sarajevo Bosnia and Herzegovina, email: e.karahmet@ppf.unsa.ba

³ University of Sarajevo, Faculty of Pharmacy, Zmaja od Bosne 8, 71000 Sarajevo, Bosnia and Herzegovina

⁴ University of Kragujevac, Institute for Information Technologies Kragujevac, Jovana Cvijića bb, 34000 Kragujevac, Serbia

DOI: 10.46793/ICCB23.269F

*Corresponding author

Abstract: Celiac disease is defined as an autoimmune disorder that is the result of a reaction of adaptive immune response of sensitive individuals, to gluten-containing cereals. The aim of this study was to assess the nutritional habits of patients with the diagnosis and people without the diagnosis, to evaluate the importance of adhering to a strict gluten-free diet, recognizing properly declared gluten-free products and to assess the quality of life of people diagnosed with celiac disease. Anthropometric and dietary tests were conducted through a survey by a total of 96 people, 56 respondents were diagnosed with celiac disease, while the remaining 40 respondents were undiagnosed, and of whom 32 were on a gluten-free diet. The majority of respondents (58.92%) have an adequate level of nutrition; however, 30.37% of respondents are overweight, including the degree of obesity in four cases. The most consumed cereals are rice, corn and white ready-made gluten-free flour mixtures, while the respondents consume the least pseudo-cereals, whole grains and micro-cereals. Within the survey CD-QOL (Celiac Disease Quality of Life) we assessed the quality of life, general the attitude of patients according to the given claims related to celiac disease. The obtained results led us to the conclusion that the dietary habits of celiac patients are somewhat worse than those of the undiagnosed group, although these are very small differences. It has been found that there is some confusion among people diagnosed regarding properly declared and certified gluten-free products, while most respondents believe that a strict gluten-free diet is the only effective treatment for the disease.

Keywords: celiac disease, gluten-free diet, nutritional status, quality of life

1. Introduction

Celiac disease is a serious autoimmune disease that occurs in genetically predisposed individuals in which gluten ingestion leads to damage in the small intestine. Gluten is naturally found in common wheat (*Triticum aestivum* L.) and in all its species whose Latin name begins with *Triticum* L., and this includes e.g., spelt, emmer, durum wheat, einkorn, in rye (*Secale cereale* L.) and barley (*Hordeum vulgare* L.). It is estimated that 1% of adults and children have celiac disease [1]. There is a wide range of symptoms manifested by the disease, from

classic digestive problems and malnutrition to dental anomalies, underdevelopment, osteopenic diseases of the bone system, lactose intolerance, infertility, and non-specific abdominal pain [2].

Celiac disease can be classified as a classic or typical celiac disease with signs and symptoms: malabsorption, diarrhea, steatorrhea, weight loss or growth retardation, and as non-classic or atypical in which the patient does not suffer from malabsorption but has other symptoms or complaints, e.g. patient with constipation and abdominal pain, but without malabsorption [3]. This can include disorders such as gluten ataxia, DH (Dermatitis herpetiformis), NCGS (Non-celiacs gluten sensitiviti), and celiac disease itself [3, 4]. All blood tests for celiac disease require a gluten-containing diet to be accurate. Antibodies to tissue transglutaminase (tTG-IgA) – test will be positive in about 98% of celiac patients on a gluten-containing diet. This same test will be negative in about 95% of healthy people without celiac disease, indicating its high sensitivity [5]. Among the first more precise data, celiac disease as a disease is mentioned in records from 1888, by Samuel Gee in a detailed description of the disease as a chronic disease of the digestive system, which can appear at any age but especially affects children between one and five years old [6, 7].

2. Material and Methods

In the research were included 96 respondents, members of various associations for people with celiac disease. The respondents were divided into two groups. The first group of respondents was made up of people with a diagnosis of celiac disease (56 respondents), while the second group was made up of people who are not on a gluten-free diet for some other health reasons, that is, people who do not have a diagnosis of celiac disease (40 respondents).

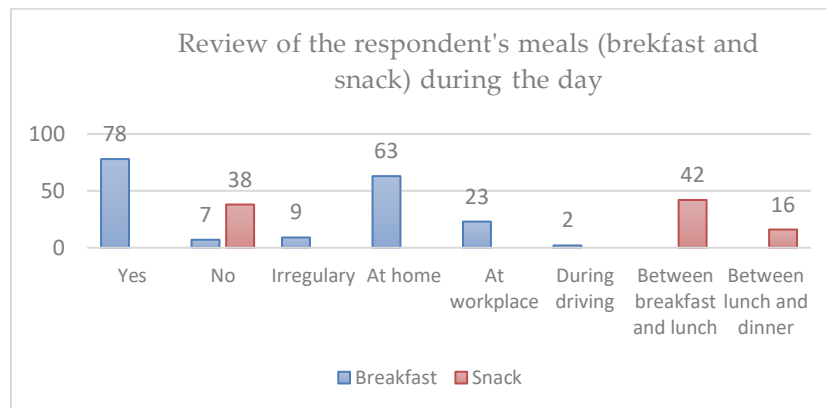
The survey was conducted using a free online survey questionnaire created on the Google Forms page. The research was conducted anonymously. The survey was divided into five categories. The first category included questions related to the respondents' general data, the second category to data on physical activity and lifestyle, the third category to data on dietary habits, the fourth to additional data related to the concept of celiac disease, and the last category is a survey on the quality of life in which it is emphasized that only people with a diagnosis of celiac disease should fill it out. The quality of life of the persons involved in the research was assessed by the CD-QOL (Celiac Disease Quality of Life) form.

Statistical analysis was performed using an electronic program that is part of the Google questionnaire, which includes graphs and tables, and using Microsoft Office Excel 2017.

3. Results and discussion

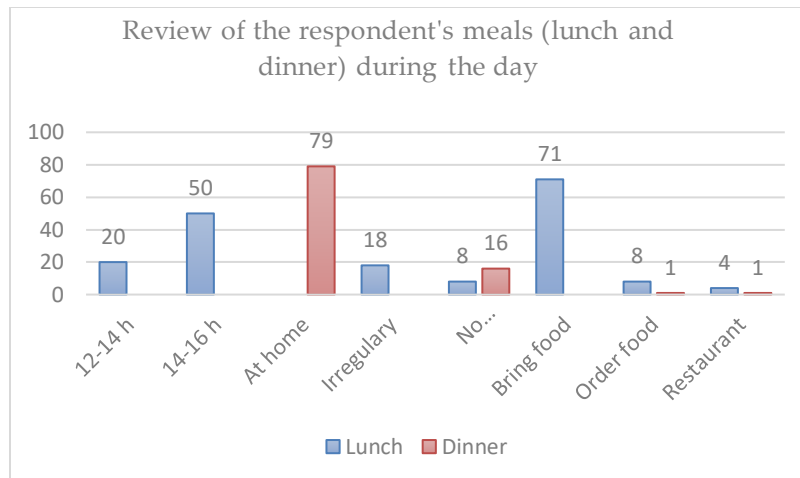
The group consisted of 76 (85.4%) women and 11 (14.6%) men. Of these, there were 4 children, 3 boys and one girl, whose information was entered by their custodians. 48 respondents have completed a high level of education, 36.5% of them (35 respondents) have a secondary vocational education, and 13.5% (13 respondents) have completed a vocational education. Out of 96 respondents, 67.7% (65 respondents) have the status of employed, 11.5% (11 respondents) are unemployed, 11.5% (11) are studying, 8.3% (8 respondents) are unable to work and 1% (1 respondent) is retired. Within the group of 31 respondents who did not have a diagnosis of celiac disease, 6 (19.35%) respondents were malnourished, 18 (58.06%) had an adequate BMI, 5 (16.13%) were overweight, and four were obese (6.46%). Out of 96 respondents, 21 (21.8%) respondents walk once a week, 47 (49%) respondents walk twice a week or more, 11 respondents walk every day, 10 respondents never walk (10.41%), and 10 respondents walk per month (10.41%).

Out of 96 respondents, 81.3% (78 respondents) eat breakfast regularly, 7.3% (7 respondents) do not have breakfast and 11.5% of respondents eat breakfast but irregularly. Breakfast at home had 71.6% (63 respondents), 26.1% (23 respondents) have breakfast at work/college and 2% (2 respondents) while going to work/college as shown in Graph 1.



Graph 1. Review of the respondent's meals (breakfast and snack) during the day.

As it is shown on Graph 2., 50 respondents have a lunch between 2-4 p.m., 20 respondents between 12-2 p.m., 18.8% (18 respondents) have lunch irregularly, while 8 respondents do not have lunch at all, 71 of them bring lunch, 8 respondents order lunch, and 4 eat in a restaurant. 79 respondents have dinner at home, 16 respondents do not have dinner, 1 of them orders dinner, and 1 goes to a restaurant for dinner.



Graph 2. Review of the respondent's meals (lunch and dinner) during the day.

According to the answers given in the survey to assess the impact of celiac disease on the quality of life, the average answer score was 3.7, 10% of respondents completely agree with the given statements, 13% agree with the statements, 14% of respondents are undecided, 23% disagree with the statements, and 43% showed complete disagreement with the given statements.

According to the available data, celiac disease is very common in Europe. The frequency varies widely in individual European countries; by age 30 to 64, it is eight times higher in Finland (2.4%) than in Germany (0.3%), which is probably additionally influenced by genetic and environmental factors [8, 9, 10].

3. Conclusions

The results of this research showed an unsatisfactory frequency in the consumption of fish, dairy products with probiotic cultures, pseudocereals, micro- and whole grains as well as their products. The frequency is satisfied in the consumption of fruits, vegetables and proteins. Based on the given results, people diagnosed with celiac disease consume more baked goods and products based on white flour and fast food, which contain a lot of undesirable fats. The respondents are aware of the importance of following a strict gluten-free diet. Respondents agree that a strict gluten-free diet does not lead to the development of anxiety, depression, dissatisfaction and a generally worse quality of life.

References

- [1] Mustalahti K, Catassi C, Reunanen A, Fabiani E, Heier M, Mcmillan S, et al. *Project Epidemiology. The prevalence of celiac disease in Europe: results of a centralized, international mass screening project.* *Ann Med.* 2010, 42(8):587–95.
- [2] Murray Joseph A. The widening spectrum of celiac disease, *The American Journal of Clinical Nutrition*, Volume 69, Issue 3, March 1999, Pages 354–365.

- [3] Ludvigsson JF, Leffler DA, Bai JC, et al. *The Oslo definitions for coeliac disease and related terms*. *Gut*. 2013; 62:43–52.
- [4] Parsons K, Brown L, Clark H, Allen E, McCammon E, Clark G, Oblad R, Kenealey J. *Gluten cross-contact from common food practices and preparations*. *Clin Nutr*. 2021;40(5):3279-3287.
- [5] Al-Toma A, Volta U, Auricchio R, Castillejo G, Sanders DS, Cellier C, et al. *European Society for the Study of Coeliac Disease (ESsCD) guideline for coeliac disease and other gluten-related disorders*. *United European Gastroenterol J*. 2019;7(5):583–613.
- [6] Losowsky MS. *A history of coeliac disease*. *Dig Dis*. 2008; 26(2):112-20.
- [7] Guennouni M, Admou B, El Khoudri N, Bourrhout A, Zogaam LG, Elmoumou L, et al. *Gluten contamination in labelled gluten-free, naturally gluten-free and meals in food services in low-, middle- and high-income countries: a systematic review and meta-analysis*. *Br J Nutr*. 2021;1–15.
- [8] Lohi S, Mustalahti K, Kaukinen K, Laurila K, Collin P, Rissanen H, Lohi O, Bravi E, Gasparin M, Reunanen A, Mäki M. *Increasing prevalence of coeliac disease over time*. *Aliment Pharmacol Ther*. 2007 Nov 1;26(9):1217-25.
- [9] Cabrera-Chávez F, Dezar GVA, Islas-Zamorano AP, Espinoza-Alderete JG, Vergara-Jiménez MJ, Magaña-Ordorica D. *Prevalence of self-reported gluten sensitivity and adherence to a gluten-free diet in Argentinian adult population*. *Nutrients* [Internet]. 2017;9(1):81. Available from: <http://dx.doi.org/10.3390/nu9010081>.
- [10] Gaesser, Glenn & Angadi, Siddhartha, *Navigating the gluten-free boom*. *JAAPA: official journal of the American Academy of Physician Assistants*. 2015;28.1-7.

Modeling of circulating tumor cell (CTC) and platelet interaction in capillaries

Aleksandar Nikolić¹, Miljan Milošević^{2,3,4,*}, Vladimir Simić^{2,3} and Miloš Kojić^{2,5,6}

¹ Institute for Artificial Intelligence of Serbia, Novi Sad, Serbia; e-mail: aleksandar.nikolic@ivi.ac.rs

² Bioengineering Research and Development Center, BioIRC Kragujevac, Serbia; e-mail: miljan.m@kg.ac.rs, vsimic@kg.ac.rs

³ University of Kragujevac, Institute for Information Technologies, Kragujevac, Serbia; e-mail: miljan.m@kg.ac.rs, vsimic@kg.ac.rs

⁴ Belgrade Metropolitan University, Belgrade, Serbia; e-mail: miljan.m@kg.ac.rs

⁵ Houston Methodist Research Institute, Department of Nanomedicine, Houston, USA; e-mail: mkojic42@gmail.com

⁶ Serbian Academy of Sciences and Arts, Belgrade, Serbia; e-mail: mkojic42@gmail.com

* Corresponding author

DOI: 10.46793/ICCB23.274N

Abstract: The main function of platelets is to bind to the sites of the damaged vessels to stop bleeding. However, in cancer patients, activated platelets adhere to circulating tumor cells and accelerate metastatic spreading. To examine the biophysical conditions needed for CTC arrest, we use a custom-built viscoelastic solid–fluid 2D computational model that enables us to calculate, under physiological conditions, the limiting cases for which CTC will pass through the narrowed capillary with platelet attached to the capillary wall. By exploring the parameter space, a relationship between the CTC material properties (Young’s modulus) and the platelet size, the time in contact between the CTC and platelet will be determined.

Keywords: solid-fluid interaction, finite element analysis, CTC-platelet interaction

1. Introduction

Metastasis is a highly coordinated, multistep process, whereby cancerous cells detach from a primary tumor, penetrate the bloodstream or lymphatics, adhere to the vascular endothelium of distant organs, and exit and colonize these sites. Even when CTCs survive their first hours in the bloodstream, their ability to metastasize is entirely reliant on forming stable interactions with the vascular wall, followed by extravasation [1].

Most CTCs arrest in capillaries, where they can be trapped due to size restriction, but they can also be found adhered to pre-capillary arteries and portal venules, which are larger in diameter, suggesting the existence of active receptor-ligand interactions [2]. When CTCs leave the circulation and enter the tissue, appropriate factors from activated

platelets can promote angiogenesis and stimulate growth at the site of metastasis [3]. Almost every step of the metastatic process has been linked to platelet involvement [4].

2. Materials and methods

The computational model implemented in PAK [5] is with a strong-coupling method that enables direct coupling of the solid properties (e.g., stiffness) to the fluid conditions (e.g., pressure) in order to solve for the resulting deformations.

For the fluid, we have the basic equations of the balance of linear momentum, known as the Navier–Stokes equations with continuity (mass balance) equation [6]:

$$\rho_f \left(\frac{\partial v_i}{\partial t} + \frac{\partial v_i}{\partial x_k} v_k \right) = - \frac{\partial p}{\partial x_i} + \mu \frac{\partial^2 v_i}{\partial x_k \partial x_k} + f_i^V \quad i = 1, 2, 3; \quad (1)$$

sum on $k : k = 1, 2, 3$

$$\frac{\partial v_i}{\partial x_i} \equiv \frac{\partial v_x}{\partial x} + \frac{\partial v_y}{\partial y} + \frac{\partial v_z}{\partial z} = 0 \quad (2)$$

By implementing a weighted procedure within an incremental-iterative computational scheme (Galerkin method [6]), a weak form of the above equations can be derived related to one finite element.

For the solid, following the approach in modeling incompressible plastic deformation and fluid model, we are using the mixed formulation which is convenient for incompressible bodies moving in an incompressible fluid [7]. Therefore, the stress tensor σ_{ij} can be decomposed into the deviatoric stress σ'_{ij} and the mean stress p ,

$$\sigma_{ij} = \sigma'_{ij} + p \quad (5)$$

$$p = (\sigma_{11} + \sigma_{22} + \sigma_{33}) / 3 \quad (6)$$

Then, the differential equation of balance of linear momentum is:

$$\rho_s \frac{\partial v_i}{\partial t} = \frac{\partial \sigma_{ik}}{\partial x_k} + f_i^V \quad i = 1, 2, 3; \quad \text{sum on } k : k = 1, 2, 3 \quad (7)$$

3. Results and discussion

The model (Fig. 1a) consists of a simple vascular system, which branches into two vessels. The undeformed CTC is initially positioned in the tunnel at the left entrance of the system (segment L1). The CTC then enters the narrowing, passes the bifurcation, and enters the lower branch. Thus deformed, the CTC is trying to break through an even smaller gap between the platelet and the wall of the blood vessel.

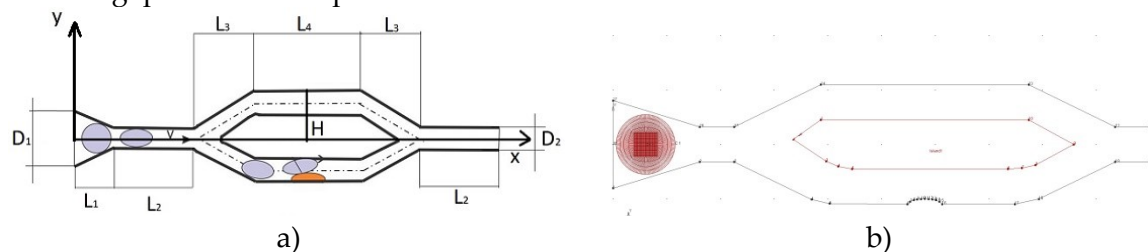


Figure 1. Circulating tumor cell (CTC) in a capillary branching: a) parametric model, b) computational model with CTC FE mesh.

The effect of platelet stiffness due to time in contact is investigated, between the CTC and the platelet in channel. In the computational model (Fig. 1b), for the fluid FE mesh, a remeshing procedure is performed at the end of each time step of the simulation. The average number of time steps used is 500, each lasting 0.002 s. On Fig. 2 the characteristic snapshots of a simulation of CTC motion are shown. For this case, the platelet thickness is 1.5 μm , the CTC diameter is 17 μm , and the Young's modulus of CTC is 24 kPa. The platelet in this model is rigid type. Figure 3 shows diagrams of Time in contact (in seconds) vs. Young's modulus of CTC for different platelet thicknesses: 1.5 μm , 2.0 μm , 2.5 μm and 3.0 μm .

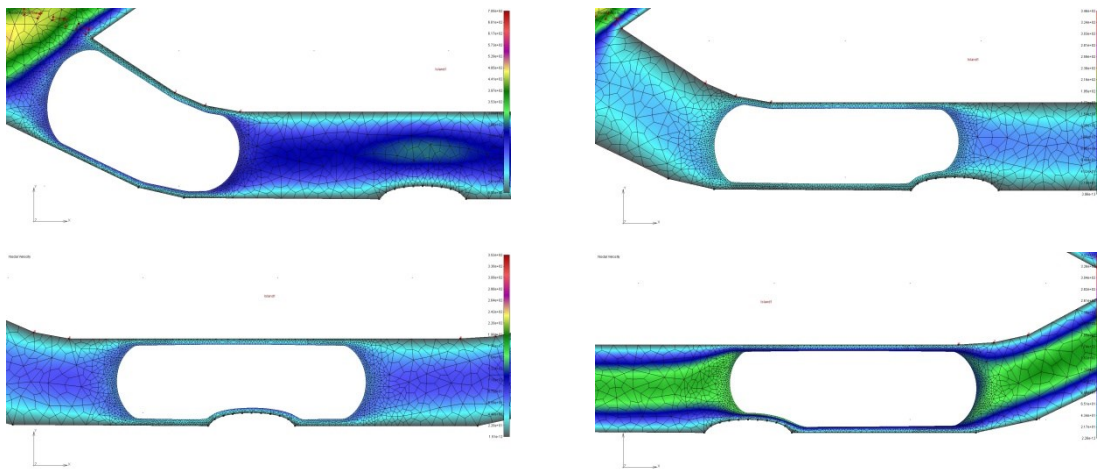


Figure 2. Field of fluid velocity for four random time steps; $t = 0.16\text{s}$ - CTC passing through the lower branching channel, $t = 0.32\text{s}$ - CTC approaching contact with platelet, $t = 0.56\text{s}$ - contact between the CTC and attached platelet, and $t = 0.72\text{s}$ - CTC going further after platelet.

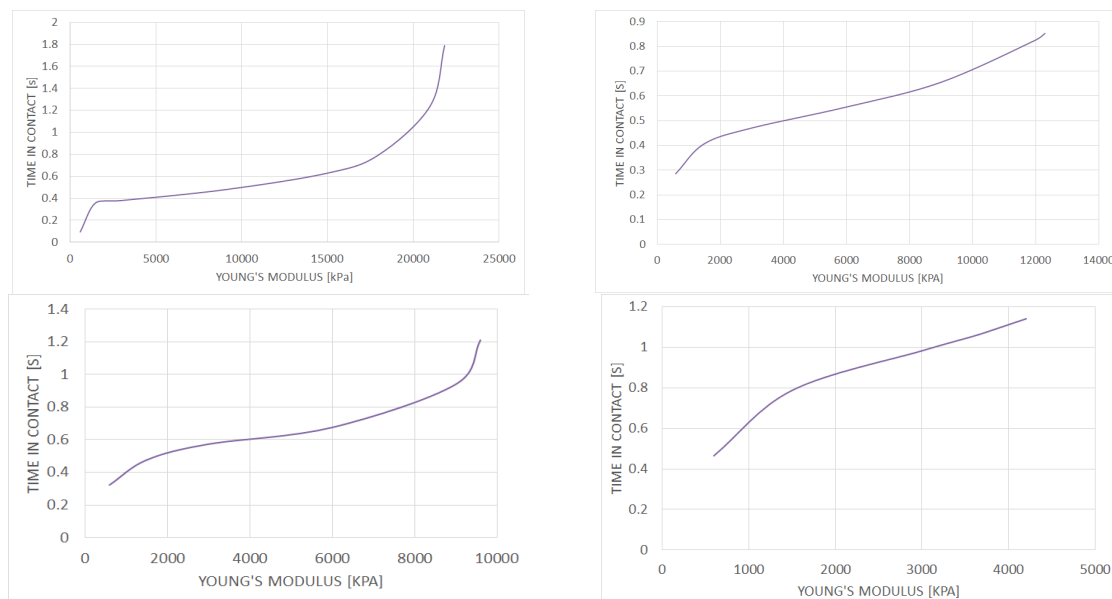


Figure 3. Comparison of the time in contact between CTC 17 μm diameter and platelet with respect to Young's modulus of CTC; results for platelet thicknesses 1.5, 2.0, 2.5 and 3.0 μm respectively.

Young's modulus of CTC is used in the range between 0.5 kPa until the critical Young's modulus values for which the CTC is stuck in the gap between platelet and upper wall of the channel. From the results in Fig. 3 we can conclude that the time in contact falls together with a CTC Young's modulus and the platelet thickness, respectively.

3. Conclusions

In this paper we used a computational model to study the motions of CTCs in the plasma flow, influenced by the platelet attached to the capillary wall. For modeling the motion of bodies in fluids, the most robust and accurate approach consists of a strong coupling (balance equations for solid and fluid form one system of equations and are solved simultaneously), and a remeshing procedure. The goal of this work is to retain a better understanding of the underlying mechanisms of metastasis, and interaction between CTC and platelets.

Acknowledgment

Research project was funded by the Ministry of Science, Technological Development and Innovation of the Republic of Serbia, contract number 451-03-47/2023-01/200378 (Institute for Information Technologies Kragujevac, University of Kragujevac), Center for Scientific Research of the Serbian Academy of Sciences and Arts and the University of Kragujevac [Project MODELETS]. We also appreciate the support from The Institute for Artificial Intelligence Research and Development of Serbia, and the City of Kragujevac, Serbia.

References

- [1] Lucotti S., M.J.R., Platelets and Metastasis: New Implications of an Old Interplay. *Frontiers in Oncology*, 2020. 10.
- [2] Chambers AF, Groom AC, Macdonald IC. Dissemination and growth of cancer cells in metastatic sites. *Nat Rev Cancer*. (2002) 2:563–72. doi: 10.1038/nrc865.
- [3] Pinedo HM, Verheul HM, D'Amato RJ, Folkman J. 1998. Involvement of platelets in tumour angiogenesis? *Lancet* 352:1775–77.
- [4] Konstantopoulos, K., & Thomas, S. N. (2009). Cancer cells in transit: the vascular interactions of tumor cells. *Annual review of biomedical engineering*, 11, 177–202.
- [5] Kojic M., Zivkovic M., Filipovic N., Milosevic M., PAK – Finite Element Program for Engineering Analysis, Coupled and Biomechanical Problems. 2020., University of Kragujevac, Bioengineering R&D Center, Kragujevac.
- [6] Kojic M., Filipovic N., Stojanovic B., Kojic N., *Computer Modeling in Bioengineering – Theoretical Background, Examples and Software*. 2008, Chichester, England: John Wiley and Son.

- [7] M.Kojic, Simple concepts in computational mechanics – do they really work? J. Serb .Soc. Comput. Mech. 7(2013)1–15.

Bioinformatics and Applied Biology

Abundance, species richness and diversity of earthworms (lumbricidae) in several habitats of the northern part of Jastrebac Mountain

Filip J. Popović^{1*}, Tanja B. Trakić¹, Mirjana M. Stojanović¹, Jovana M. Sekulić²

¹University of Kragujevac, Faculty of Science, Institute of Biology and Ecology, Radoja Domanovića 12, 34000 Kragujevac, Serbia;

e-mail: tanjatrakic@pmf.kg.ac.rs, mirjana.stojanovic@pmf.kg.ac.rs

²University of Kragujevac, Institute for Information Technologies Kragujevac, Department of Science, Jovana Cvijića bb, 34000 Kragujevac, Serbia;

e-mail: jovanas034@gmail.com

DOI: 10.46793/ICCBi23.280P

* *Corresponding author*

Abstract: The aim of this study was to investigate the diversity of earthworms in different habitats (meadow, humid meadow, oak and beech forest). A total of nine earthworm species belonging to six genera were found in the studied habitats. In the studied habitats, the earthworm fauna was found to be different: the beech forest was richer in earthworms (6 taxa), while the oak forest was poorest in earthworms (3 taxa). The earthworm abundance was higher in the humid meadow (34 individuals), while was lower in the beech forest (17 individuals). A combination of the alpha diversity index (Shannon-Weaver, Evenness, and Berger-Parker) and beta diversity (Jaccard's coefficient of similarity) were used to determine the impact of studied habitats on the earthworm fauna. Shannon's diversity and Shannon's evenness indices had higher values in the beech forest/humid meadow, while the Berger-Parker index of dominance had higher values in oak forests. Jaccard's index of similarity showed the earthworm fauna was clearly separated between the oak forest, meadow, humid meadow and beech forest. The results of these indices confirmed that vegetation cover strongly influences the diversity of earthworm fauna.

Keywords: earthworm, diversity, habitats, indices, Jastrebac Mountain

1. Introduction

Jastrebac Mountain is located in the central part of Serbia and belongs to the Rhodopes Mountain range. It has a total length of about 45 km and is composed of two mountain massifs. The first of them is Veliki Jastrebac (in the west) and Mali Jastrebac (in the east). In a geological sense, the enigmatic area of Jastrebac Mt. in central Serbia is characterized by a complex geological structure with its wider environment, which is related to its position within the transit zone – the Vardar zone, between the units of the Adriatic and European plates, as well as to multiphase tectonic activity from the Mesozoic to the present day [1]. On the other hand, earthworms can act as useful

biodiversity indicators, as their abundance and richness may reflect the diversity of other arthropods [2]. Species diversity has two parts. In contrast to abundance, which refers to the overall number of individuals of each species present in a community, richness refers to the number of species present. During the last years, earthworm studies in Serbia gained new momentum and several papers added new data on the earthworm diversity of regions such as the Kopaonik Mountain [3, 4].

In this paper, we compare the earthworm fauna of different habitats in the Jastrebac Mt. Our objectives were: a) to determine species richness and abundance of earthworm fauna in studied habitats b) calculate alpha and beta diversity indices as well as to examine the impact of vegetation cover on the species richness and abundance of earthworm fauna in the studied habitats.

2. Material and Methods

The earthworm fauna was sampled on the northern part of Jastrebac Mt. (43° 23' 31"N; 21° 26' 57"E) during the course of two months in 2021 (from May and June, which coincided with the rainy season), in secondary oak forest (OF) (village Naupare 380 a.s.l.), primary beech forest (BF) (village Buci 450 a.s.l.), meadow (M) (village Naupare 380 a.s.l.) and humid meadow (HM) (near Lomnička River 300 a.s.l.). We sampled eight samples of 50 x 50 cm from each of the sampling units (plots). Earthworms were collected by the diluted formaldehyde method, complemented by digging and hand-sorting. The specimens were killed and fixed in 75% ethanol or 4% formaldehyde. The specimen identification was carried out based on the works of Stojanović et al. [5] using a stereo microscope. The material is deposited in the Earthworm Collection of the University of Kragujevac, Serbia (CEKUS).

Species richness (S) was represented by the number of species in the habitats, and total abundance (Ab) by the total number of individuals of each species in the habitats. We used alpha diversity (Shannon-Weaver (H'), Evenness (J'), and Berger-Parker (D_{BP}) indices) to describe the diversity of communities within habitats, while for diversity between habitats, we used cluster analysis (UPGMA) based on Jaccard's coefficient of similarity. Paleontological statistics software (PAST) was utilized for calculating the alpha and beta diversity indices in the studied habitats [6].

3. Results and Discussion

The present study resulted in reporting altogether nine earthworm species (*Aporrectodea caliginosa* (Savigny 1826), *Aporectodea rosea* (Savigny 1826), *Cernosvitovia dofeini* (Ude, 1922), *Lumbricus polyphemus* (Fitzinger, 1833), *Lumbricus rubellus* Hoffmeister, 1843, *Lumbricus terrestris* Linnaeus, 1758, *Octolasion lacteum* (Örley, 1881), *Panionia leoni* (Michaelsen, 1891) and *Proctodirlus antipai* (Michaelsen, 1891)) belonging to six genera of the family Lumbricidae. The most abundant taxon in the BF and HM was *L. rubellus* (N = 10; 58.8%/N = 23; 67.6% of all observed individuals in mentioned habitats), while in OF and M (N = 17; 68%/N = 19; 70.3% of all observed individuals in

mentioned habitats) as well in the overall study *Ap. rosea* (N = 36; 34.9% of all observed individuals) was most abundant. It is not surprising that *Ap. rosea* is the species that dominates the investigated habitats. According to Stojanović et al. [7], one of the most represented earthworm species in Serbia is the peregrine species *Ap. rosea*. According to Lee [8], earthworm communities typically contain two to five taxa. Nevertheless, some studies indicated earthworm communities are reported to be able to have from one to 11 taxa [3, 9]. Our results showed BF and M were richer in earthworm species, while OF and HM were poorer in earthworm species. The xerothermic character of oak forests is caused by a small depth of useful soil layer, the skeleton presence on the surface and in profile and by water permeability, which is very unfavorable for earthworm species. The H' and J' indicated that the BF/HM had a higher species diversity/uniformity than the other habitats. In contrast, the D_{BP} index showed higher dominance species in OF (Table 1).

Table 1. Alpha diversity index of earthworm fauna in the studied habitats.

Alpha diversity	OF	M	HM	BF
S	3	5	4	6
Ab	25	27	34	17
H'	0.65	1.25	1.1	1.28
J'	0.64	0.7	0.75	0.6
D_{BP}	0.76	0.48	0.44	0.64

The cluster analysis showed a clear separation of earthworm fauna in studied habitats (Figure 1). Essentially, rankings in the cluster analysis of the select habitats confirm the obvious vegetation and earthworm relationship at the ecosystem level [2, 10].

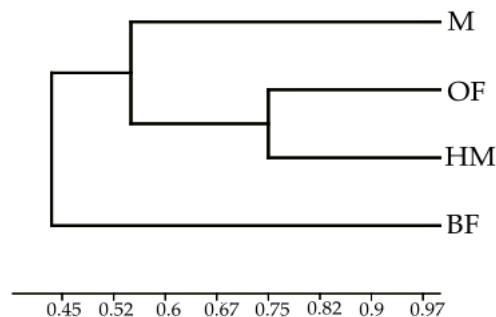


Figure 1. Cluster analysis (UPGMA) using Jaccard's index of similarity among the studied habitats.

3. Conclusions

This study indicates that species richness and abundance in studied habitats are different. The spatial distribution of earthworm fauna depends on a variety of factors, including the amount of food available and the characteristics of the soil (i.e., moisture, pH concentration, temperature, and organic matter). Actually, Lavelle & Spain [11]

established that earthworm diversity depends on the relative significance of different ecological categories of a region, climatic factors, phylogenetic and biogeographic history, and regional parameters such as vegetation type or soil characteristics. *Aporrectodea caliginosa*, *Ap. rosea* and *L. rubellus* were recorded in the studied habitats. These species have a wide ecological valence (peregrine species) and high tolerance when it comes to fluctuations in environmental factors. Overall, earthworms have important roles in the functioning of a variety of ecosystems and have high potential as model organisms for this type of study.

Acknowledgment

This work was supported by the Serbian Ministry of Education, Science and Technological Development (Agreement No. 451-03-47/2023-01/200122; Agreement No. 451-03-47/2023-01/200378).

References

- [1] D. Erak., *Tektono-termalna evolucija kontakta Dinarida i Karpato-Balkanida u području Jastrepca*, Универзитет у Београду (2019).
- [2] E. Klemens, T. Stierhof, J. Dauber, K. Kreimes, V. Wolters., *On the quality of soil biodiversity indicators: abiotic and biotic parameters as predictors of soil faunal richness at different spatial scales*, *Agro Ecosystem Environment*, 98 (2003) 273-283.
- [3] F. Popović, M. Stojanović, S. Radosavljević, T. Trakić, J. Sekulić., *Earthworm community structure along altitudinal gradients on the western slopes of Kopaonik Mountain in Serbia*, *Turkish Journal of Zoology*, 46, no. 1 (2022) 103-114.
- [4] F. Popović, M. Stojanović, J. Sekulić, T. Trakić., *Comparison of earthworm fauna in oak and spruce forests on the Western slope of Kopaonik Mountain in Serbia*, *Biologia Serbica*, 44 (2) (2022) 109-115.
- [5] M. Stojanović-Petrović, T. Trakić, J. Sekulić., *Kišne gliste (Oligochaeta: Lumbricidae) Srbije*, *Univerzitet u Novom Sadu*, (2020) p. 276.
- [6] Ø. Hammer, D. Harper, P. Ryan., *PAST: Paleontological statistics software package for education and data analysis*, *Palaeontologia Electronica*, 4 (1) (2001) 1-9.
- [7] M. Stojanović, J. Sekuić, T. Trakić., *Checklist of earthworms (Oligochaeta: Lumbricidae) from Serbia: a review*, *Zootaxa*, 4496 (1) (2018) 124-155.
- [8] K. Lee., *Earthworms: Their Ecology and Relationships with Soils and Land Use*, Sydney (AU): Academic Press, (1985).
- [9] D. Hackenberger, B. Hackenberger., *Earthworm community structure in grassland habitats differentiated by climate type during two consecutive seasons*, *European Journal of Soil Biology*, 61: (2014) 27-34.
- [10] V. Pop., *Earthworm-vegetation-soil relationships in the Romanian Carpathians*, *Soil Biology and Biochemistry*, 29 (3-4) (1997) 223-229.
- [11] P. Lavelle, A. Spain., *Soil Ecology*, Dordrecht (NL): Kluwer Academic Publishers.J. (2001).

A new record of *Dendrobaena Serbica* karaman, 1973 (Clitellata; Lumbricidae) from Serbia

Filip J. Popović^{1*}, Tanja B. Trakić¹, Mirjana M. Stojanović¹, Jovana M. Sekulić²

¹University of Kragujevac, Faculty of Science, Institute of Biology and Ecology, Radoja Domanovića 12, 34000 Kragujevac, Serbia;

e-mail: tanjatrakic@pmf.kg.ac.rs, mirjana.stojanovic@pmf.kg.ac.rs

²University of Kragujevac, Institute for Information Technologies Kragujevac, Department of Science, Jovana Cvijića bb, 34000 Kragujevac, Serbia;

e-mail: jovanas034@gmail.com

DOI: 10.46793/ICCBi23.284P

* Corresponding author

Abstract: The new records of the little-known Balkan endemic species *Dendrobaena serbica* Karaman, 1973 from Kopaonik Mountain, Serbia, are reported. So far, the species has been recorded at four localities: three localities in Serbia (Čakor, Kragujevac, Niš) and one locality in Montenegro (Prokletije Mountain). The first records were from 1973 from the locality in southwestern Serbia (Čakor, Prokletije). A review of the geographical distribution of *D. serbica* is presented. The confirmed geographical distribution of the species includes only the territories of the Republic of Serbia and Montenegro. Also, its distinction from the taxonomic similar congeners *Dendrobaena illyrica* (Cognetti de Martiis, 1906), *Dendrobaena sasensis* Šapkarev 1983 and *Dendrobaena vej dovskyi* (Černosvitov, 1935) is discussed. Further, the habitats of this species are restricted to the uppermost litter layer in forest soil and humid forests near stream banks. This paper summarized the knowledge of the taxonomy, ecology, and distribution of a little-known Balkan endemic species *D. serbica*.

Keywords: a new record, *Dendrobaena serbica*, earthworm, Serbia

1. Introduction

The total number of the species within the genus *Dendrobaena* Eisen, 1873 is estimated at about 92 species [1], of which 25 are endemics of the Balkan Peninsula [2]. Previous faunistic studies have revealed 14 species of the genus *Dendrobaena* in Serbia, of which only four are endemic– *Dendrobaena kozuvensis* (Šapkarev 1971), *Dendrobaena rhodopensis* (Černosvitov 1937), *Dendrobaena serbica* Karaman 1973 and *Dendrobaena zicsi* Karaman 1973. *Dendrobaena serbica* is one of the smallest earthworms known only in a few localities in Serbia [3], was first recorded in Serbia in the early 1970s from the Prokletije Mountain [4].

In this article, we summarise data on the distribution of *D. serbica* in Serbia and provide information on some taxonomic and ecological characteristics of the species.

2. Material and Methods

Dendrobaena serbica was recorded twice during the sampling on the eastern slopes of Kopaonik Mountain: in 2020 and 2021. The samples were collected on the forest soil. Earthworms were collected by digging (0.4 × 0.4 m²), hand sorting (by turning over rocks, debris, and logs) and then fixed in 96% alcohol. Species identification was done in accordance with the key by Karaman [4] and Stojanović et al. [3]. The specimens were deposited at the Earthworm Collection of the University of Kragujevac, Serbia (CEKUS). The main taxonomic differences between *D. serbica* and its Balkan congeners (*Dendrobaena illyrica* (Cognetti de Martiis, 1906), *Dendrobaena sasensis* Šapkarev, 1983 and *Dendrobaena vejvodskyi* (Černosvitov, 1935)) are presented according to their original descriptions and the features mentioned in the different identification keys. The map of the distribution of the species was created with Google Maps.

3. Results and Discussion

Dendrobaena serbica Karaman, 1973

(Figure 1)

Dendrobaena serbica Karaman, 1973: 180.

Dendrobaena serbica Šapkarev, 1993: 17; Stojanović et al., 2008: 60; Csuzdi, 2012: 97–99; Trakić et al., 2016: 263; Stojanović et al., 2018: 139; Stojanović-Petrović et al., 2020: 163–164.

Material examined. CEKUS/2806, CEKUS/2807, CEKUS/2808, CEKUS/2809 CEKUS/2810, 5 exp., Serbia, Kopaonik Mt. (Lukovska Banja), 43.16 N 21.03 E, beech forest, M. Stojanović, T. Trakić, J. Sekulić and F. Popović, 11.03.2020; CEKUS/2812, CEKUS/2813, CEKUS/2814, CEKUS/2815 4 exp., Serbia, Kopaonik Mt. (Kuršumlijska Banja), 43.25 N 20.69 E, oak forest, M. Stojanović, T. Trakić, J. Sekulić and F. Popović, 04.05.2021; CEKUS/2818, CEKUS/2819 2 exp., Serbia, Kopaonik Mt. (Metode), 43.3 N 20.85 E, river bank, M. Stojanović, T. Trakić, J. Sekulić and F. Popović, 21.06.2021.



Figure 1. A living specimen of *Dendrobaena serbica*

The species *D. serbica* was found and described by Karaman [4] and our studied specimens fully agree with her description. During this study, 11 specimens of *D. serbica*

were examined and three records were mapped (four from the literature) (Figure 2). *Dendrobaena serbica* is a broad-range Balkan endemic, characteristic of the Balkan part of Serbia and Montenegro [3, 5]. Based on literature data, the species *D. serbica* inhabits pastures and meadows [3, 4]. However, we found this species lives in the uppermost litter layer in forest soil and humid forests near stream banks. According to Bouché's ecological characterization, *D. serbica* belongs to the epigeic group.

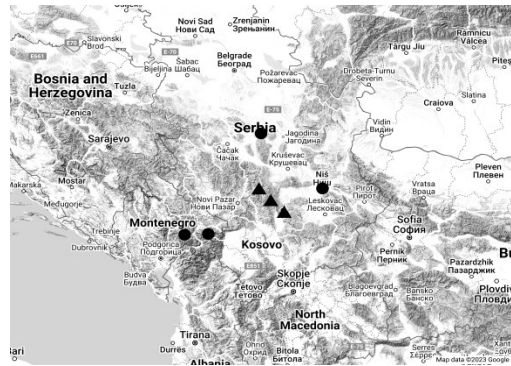


Figure 2. Distribution of *Dendrobaena serbica* (triangle: author's data; circle: literature data)

Dendrobaena serbica is taxonomically different from the similar species *D. illyrica* and *D. sasensis* by the absence of a tubercle, while it differs from the species *D. vej dovskiji* by the absence of a tubercle and the number of seminal vesicles (Table 1).

Table 1. Comparison of some taxonomic characteristics of the Balkan endemic species *Dendrobaena serbica* with its Balkan congeners.

T. characters	<i>D. serbica</i>	<i>D. illyrica</i>	<i>D. sasensis</i>	<i>D. vej dovskiji</i>
Body size	53–89	76–112	65–76	20–50
Body color	dark violet	dark violet	dark violet	dark violet
Prostomium	Epilobous	epi/tanilobous	Epilobous	Epilobous
S. vesicles	9–12	9–12	9–12	11,12
Spermathecae	9/10, 10/11	9/10, 10/11	9/10, 10/11	9,10
Clitellum	½ 29, 29–33, ½ 34, 34	½ 28, 28, 29–33, 34	29–34	½ 28, 29–33
Tubercle	Absent	(30)31–32(33)	31–32	31–32

3. Conclusions

According to Csuzdi & Zicsi [6], the genus *Dendrobaena* is heterogeneous very much and urgently needs a revision. Balkanic taxonomists of earthworms are taxonomically similar species that are difficult to distinguish; they have been described as new species, which raises doubts about their identity. On the other hand, it is known that earthworms absent some taxonomic characters and secondary sexual organs in varying degrees of development [7]. Some authors [8, 9] consider that the absence of tubercula indicates a form of parthenogenesis. Basically, little is known about the origin of parthenogenetic earthworms. The question arises: is the species *D. serbica* actually a parthenogenetic form

of the species *D. illyrica*? The molecular-phylogenetic analysis will be very useful in elucidating this topic in the near future. Also, the current earthworm species checklist for the whole of Kopaonik Mt. was updated by recording 29 taxa [10, 11]. We expect despite understudied the eastern slopes of Kopaonik Mt., future samplings will likely yield many more species, among them many endemic ones.

Acknowledgment

This work was supported by the Serbian Ministry of Education, Science and Technological Development (Agreement No. 451-03-47/2023-01/200122; Agreement No. 451-03-47/2023-01/200378).

References

- [1] C. Csuzdi., *Earthworm species, a searchable database*, Opuscula Zoologica Budapest, 43 (1) (2012) 97–99.
- [2] T. Trakić, H. Valchovski, M. Stojanović., *Endemic earthworms (Oligochaeta: Lumbricidae) of the Balkan Peninsula: a review*, Zootaxa, 4189 (2016) 251-274.
- [3] M. Stojanović-Petrović, T. Trakić, J. Sekulić., *Kišne gliste (Oligochaeta: Lumbricidae) Srbije*, Univerzitet u Novom Sadu, (2020) p. 276.
- [4] S. Karaman., *Drugi prilog poznavanju kišnih glista Srbije*, Zbornik radova, 1 (1973) 177-182.
- [5] T. Szederjesi., *Allolobophora ruzsai sp. n., a new earthworm species and new records from Montenegro (Oligochaeta: Lumbricidae)*, North-Western Journal of Zoology, 10 (2014) 48-52.
- [6] C. Csuzdi, A. Zicsi., *Earthworms of Hungary (Annelida: Oligochaeta: Lumbricidae)*. In: C. Csuzdi, S. Mahunka (eds.), *Pedozoologica Hungarica*. Vol. 1, Hungarian Natural History Museum, Budapest, (2003) pp. 1-271.
- [7] C. Edwards, P. Bohlen., *Biology and ecology of earthworms*, 3rd ed. Chapman & Hall, London, (1996).
- [8] G. Gates., *Burmese earthworms. An introduction to the systematics of megadrile oligochaetes with special references to southeast Asia*, Transactions of the American Philosophical Society, 62 (1972) 1-326.
- [9] E. Christian, A. Zicsi., *Ein synoptischer Bestimmungsschlüssel der Regenwürmer Österreichs (Oligochaeta: Lumbricidae)*, Bodenkultur, 50 (1999) 121-131.
- [10] F. Popović, M. Stojanović, T. Trakić, J. Sekulić, S. Sekulić, T. Ralitsa., *New Records of Earthworms (Annelida: Clitellata) from the Kopaonik Mountain, with the First Finding of Allolobophora treskavicensis (Mršić, 1991) in Serbia*, Acta Zoologica Bulgarica Supplement, 15 (2020) 61-70.
- [11] F. Popovic, M. Stojanovic Petrović, T. Trakić, J. Sekulić., *Earthworms (Annelida: Oligochaeta, Lumbricidae) of the Kopaonik National Park (Serbia)*, Kragujevac Journal of Science, (2022) 219-230.

Potentially toxic elements in the edible part of trout (*Salmo trutta* L.) from the upper reaches of the Raška and Studenica rivers

Aleksandra M. Milošković^{1*}, Milena D. Radenković², Simona R. Đuretanić², Nataša M. Kojadinović², Tijana Z. Veličković², Vladica M. Simić²

¹University of Kragujevac, Institute for Information Technologies Kragujevac, Department of Sciences, Jovana Cvijića bb, 34000 Kragujevac, Serbia, e-mail: aleksandra@uni.kg.ac.rs

²University of Kragujevac, Faculty of Science, Department of Biology and Ecology, Radoja Domanovića 12, 34000 Kragujevac, Serbia, e-mail: vladica.simic@pmf.kg.ac.rs

DOI: 10.46793/ICCB23.288M

* Corresponding author

Abstract: This paper reports the accumulation of potentially toxic elements (PTEs) in trout (*Salmo trutta* L.) sampled from rivers Raška and Studenica in Serbia, which are assumed to be free of pollutants. The presence of PTEs, essential elements and heavy metals, in aquatic ecosystems is usually a consequence of anthropogenic activities such as mining, agricultural drainage, sewage discharge, industrial effluent discharge, gasoline leakage from fishing boats, and accidental chemical waste spills. The appearance of these elements in water and aquatic biota can also be a consequence of natural processes such as atmospheric deposition and weathering, earth's crust erosion, and volcanic eruption. Since trout inhabits pristine upper reaches of the river, this species represents an appealing model to assess the biological impact of environmental and geochemical contamination in freshwater ecosystems. The concentrations of 14 PTEs in the edible part (EP, muscle + skin) of trout were evaluated. The data obtained in this study confirmed that freshwater, even if far from industrial and anthropogenic activities, can lead to the accumulation of PTEs related to the site's geochemical morphology.

1. Introduction

The presence of potentially toxic elements (PTEs), essential elements and heavy metals, in aquatic ecosystems is usually a consequence of anthropogenic activities such as mining, agricultural drainage, sewage discharge, industrial effluent discharge, gasoline leakage from fishing boats, and accidental chemical waste spills [1]. The appearance of these elements in water and aquatic biota can also be a consequence of natural processes such as atmospheric deposition and weathering [2], earth's crust erosion, and volcanic eruption [3].

The trout (*Salmo trutta* L.) inhabit watercourses located in mountainous and sparsely populated areas, which guarantee good water quality [4]. Since it inhabits pristine upper reaches of the river, trout species represent an appealing model to assess the biological impact of environmental and geochemical contamination in freshwater ecosystems [5].

This paper reports a contamination study of a profile of 14 PTEs of the edible part (EP) (muscle and skin) in trout (*Salmo trutta* L.) collected from pristine upper reaches of the rivers Studenica and Raška in Serbia. Furthermore, the potential risk to human health resulting from the consumption of trout was assessed.

2. Material and methods

The field study was conducted at upper reaches of the rivers Studenica and Raška in summer of 2011. Sampling sites (Raška River: 43.114391N, 20.377664E; Studenica River: 43.466234N, 20.548036E) are given in Figure 1.



Figure 1. Sampling sites on Studenica and Raška rivers.

The trout were sampled using the Aquatech DC electrofisher IG 1300 (2.6 kW, 80-470 V). Ten specimens were selected from each river catch, sacrificed by a quick blow to the head and transferred on ice in a hand-held refrigerator to the laboratory.

In the laboratory, fish were measured for their total body length (to the nearest cm), weighed (to the nearest g), and subsequently dissected with a decontaminated ceramic knife. The right dorsal muscle with the skin below the dorsal fin of each specimen was dissected. Following dissection, the samples were weighed using an electronic scale (accuracy ± 0.01 g).

Before digestion in microwave Christ Alpha 2-4 LD, Harz, Germany, samples are dried in a lyophilizer Christ Alpha 2-4 LD, Harz, Germany, and measured one more time. Dried sample portions between 0.3 and 0.5 g were digested with a mixture of 65% nitric acid and 30% hydrogen peroxide (Suprapur®, Merck, Darmstadt, Germany, 10:2, v/v) at 200 °C for 20 min. After cooling to room temperature and without filtration, the solution was diluted to a fixed volume of 25 ml with ultrapure water. Fish free samples were analyzed with each batch of samples to observe contamination by the reagents used. The concentrations of Al, As, Cd, Co, Cr, Cu, Fe, Hg, Mn, Ni, Pb, Se, Sn, and Zn were analyzed with inductively coupled plasma optical emission spectrometry (ICP-OES), using a Thermo Fisher Scientific iCAP 6500 Duo ICP (Cambridge, United Kingdom).

The mean values and standard deviations were calculated for each group, and PTEs were expressed as mg kg⁻¹ wet weight (ww). Concentrations were compared with the maximum permitted concentrations (MPCs) for available elements in fish meat for utilization in the human diet, according to the national [6] and European Union [7] legislations.

3. Results and discussion

The average weight of the examined specimens from Raška River was 155.33 ± 6.6 g while the average length was 21.4 ± 2.05 cm. The average weight of the examined specimens from Studenica River was 184 ± 9.5 g while the average length was 25.3 ± 2.8 cm.

In Table 1 concentrations of PTEs in trout from Raška and Studenica rivers are shown. Except for Cr and Hg, all other PTEs were recorded in higher concentrations in the edible part of the trout sampled from the Studenica River. As expected, fish samples examined had no concentrations of PTEs above the MPC prescribed by the EU [6] and national legislation [7].

Table 1. The average PTEs concentrations and standard deviation in (EP) (muscle and skin) in trout (*Salmo trutta* L.) from Raška and Studenica rivers in mg kg⁻¹ ww.

PTEs	Studenica River	Raška River
Al	0.23 ± 0.26	nd*
As	0.19 ± 0.02	0.16 ± 0.04
Cd	0.010 ± 0.005	0.005 ± 0.001
Co	0.010 ± 0.004	0.002 ± 0.003
Cr	0.13 ± 0.05	0.14 ± 0.04
Cu	0.4 ± 0.1	0.34 ± 0.19
Fe	3.52 ± 0.59	2.75 ± 0.98
Hg	0.003 ± 0.005	0.09 ± 0.07
Mn	0.26 ± 0.16	0.11 ± 0.09
Ni	0.11 ± 0.05	0.02 ± 0.02
Pb	0.31 ± 0.09	0.12 ± 0.10
Se	0.34 ± 0.07	0.32 ± 0.03
Sn	0.004 ± 0.003	0.004 ± 0.005
Zn	4.7 ± 1.8	3.38 ± 0.87

*nd – not detected

Bioaccumulation of PTEs in living organisms depends on pollution in situ, rate of detoxification and metabolism [8]. Anthropogenic activities are considered the primary source of PTEs pollution in aquatic ecosystems [9]. Bearing in mind that the trout is sampled from pristine upper parts of rivers Raška and Studenica, the presence of some PTEs can be explained by the geomorphology of the studied sites, which could have led to the release of many PTEs [9].

4. Conclusions

The data obtained in this study confirmed that freshwater, even if far from industrial and anthropogenic activities, can lead to the accumulation of PTEs related to the site's geochemical morphology.

Acknowledgment

This research is funded by the Ministry of Education and Ministry of Science, Technological Development and Innovation, Republic of Serbia, Grants: No. 451-03-47/2023-01/200378.

References

- [1] G. Gómez, R. Baos, B. Gómara, B. Jiménez, V. Benito, R. Montoro, E. Hiraldo, M.J. González., *Influence of a mine tailing accident near Doñana National Park (Spain) on heavy metals and arsenic accumulation in 14 species of waterfowl (1998 to 2000)*. Archives of Environmental Contamination and Toxicology 47 (2004) 521-529.
- [2] E. Has-Schön, I. Bogut, I. Strelec., *Heavy metal profile in five fish species included in human diet, domiciled in the end flow of river Neretva (Croatia)*. Archives of Environmental Contamination and Toxicology 50 (2006) 545-551.
- [3] Y. Fakhri, A. Nematollahi, Z. Abdi-Moghadam, H. Daraei, S.M. Ghasemi, V.N. Thai., *Concentration of potentially harmful elements (PHEs) in trout fillet (rainbow and brown) fish: a global systematic review and meta-analysis and health risk assessment*. Biological Trace Element Research 199 (8) (2021) 3089-3101.
- [4] A. Carosi, L. Ghetti, R. Padula, M. Lorenzoni., *Population status and ecology of the Salmo trutta complex in an Italian river basin under multiple anthropogenic pressures*. Ecology and Evolution 10 (14) (2020) 6867-7947.
- [5] Z. Bajc, K.S. Gačnik, V. Jenčič, D.Z. Doganoc., *The contents of Cu, Zn, Fe and Mn in Slovenian freshwater fish*. Slovenian Veterinary Research 42(1/2) (2005) 15-21.
- [6] *Regulation on the maximum permitted residue levels of pesticides in food and animal feed for which maximum quantities of residues of pesticides are permitted. Anex 5 – Regulation on maximum allowed amounts of certain contaminants in food and feed for animals of plant and animal origin* Oficial Gazette Of the Republic of Serbia 2018 Nos. 22/2018-3, 90/2018-22, 76/2019-35, 81/2019-17 (2018).
- [7] EU Commission Regulation (EC) No. 1881/2006 of 19December 2006, *Setting maximum levels for certain contaminants in food stuufs (Text with EEA relevance)*. Official Journal of the European Union No. 1881/2006 364 (2006) 5-24.
- [8] A. Jakimska, P. Konieczka, K. Skóra, J. Namieśnik., *Bioaccumulation of metals in tissues of marine animals, Part I: The role and impact of heavy metals on organisms*. Polish Journal of Environmental Studies 20(5) (2011) 1117-1125.
- [9] A. Alberto, C. Francesco, A. Atzei, A. Sabatini, F. Palmas, C. Lai, M. Russo., *Heavy metal and metalloid accumulation in wild brown trout (Salmo trutta L., 1758 complex, Osteichthyes: Salmonidae) from a mountain stream in Sardinia by ICP-OES*. Environmental Monitoring and Assessment 193 (2021) 448.

Diet composition and feeding habits of common bleak (*Alburnus alburnus* L.) in the Gruža and Gazivode reservoirs

Milena D. Radenković¹, Aleksandra M. Milošković^{2*}, Nataša M. Kojadinović¹, Simona R. Đuretanić¹, Tijana Z. Veličković¹, Marija M. Jakovljević¹, Vladica M. Simić¹

¹ University of Kragujevac, Faculty of Science, Department of Biology and Ecology, Radoja Domanovića 12, 34000 Kragujevac, Serbia, e-mail: milena.radenkovic@pmf.kg.ac.rs

² University of Kragujevac, Institute for Information Technologies Kragujevac, Department of Sciences, Jovana Cvijića bb, 34000 Kragujevac, Serbia, e-mail: aleksandra@uni.kg.ac.rs

DOI: 10.46793/ICCB23.292R

* Corresponding author

Abstract: This paper presents the feeding habits of specimens of the fish *Alburnus alburnus* (L.) that inhabit the Gruža and Gazivode reservoirs. The diets of 37 specimens from Gruža reservoir and 44 specimens from Gazivode reservoir were analyzed. The common bleak from Gazivode reservoir fed more diversely on eight different prey items, while six different prey items were identified in specimens from Gruža reservoir. The most common prey in the diet of specimens from both reservoirs is *Bosmina* sp., which was present in every digestive tract studied. Very common prey items are also *Daphnia* sp. and Cladocera. In contrast to the specimens from Gruža reservoir, the specimens from Gazivode reservoir feed on both *Leptodora kindtii* and insects. The specimens from Gazivode reservoir also feed on Ostracoda at a much higher percentage than the specimens from Gruža reservoir. Numerous reports in the literature have confirmed that common bleak feed mainly on zooplankton and often on insects, as shown by our results.

Keywords: planktivorous fish, natural diet, zooplankton

1. Introduction

Knowledge of fish diet is necessary to determine the trophic status of the ecosystem and the ecological niche of fish within that ecosystem [1]. It is also useful in understanding the ecology of species so that they can be managed sustainably, and measures can be developed to conserve and protect specific species [2]. Fish diet analysis based on digestive tract content analysis is a common practice [3, 4]. Detailed analysis of fish diet contributes to the understanding of trophic interactions in aquatic ecosystems and food chains of aquatic organisms. In addition, fish diet includes very important ecological components such as behaviour, fitness, habitat characteristics, energy consumption, and inter- and intra-species relationships [5].

The common bleak *Alburnus alburnus* (Linnaeus, 1758), inhabiting the rivers, lakes and estuaries of the Danube and the Aegean Basin [6], is common in the waters of Serbia. It lives in shoals near the water surface and feeds mainly on zooplankton, but also frequently ingests insects from the surface [7].

The objective of this study was to investigate the diet of common bleak, which is an important link in the food chains of the reservoirs studied.

2. Material and methods

Field studies were conducted in the summer of 2011 at the Gruža and Gazivode reservoirs. Gruža reservoir is located in central Serbia, near the town of Kragujevac, and was created by building a dam on the Gruža river. Its main purpose is water supply. Gazivode reservoir is located on the upper reaches of the Ibar river near the village of Ribariće. It is a multipurpose reservoir.

Fish samples were collected using nets with a mesh size of 10 x 10 mm. After capture, the total length (TL, to the nearest cm) and weight (W, to the nearest g) of the specimens were measured. Fish were then dissected, and their digestive tract was removed, which was immediately preserved with 4% formaldehyde to stop the digestion process. The material was bagged, labeled and transported to the laboratory, where the contents of the digestive tract were examined under a binocular microscope (Nikon SMZ800). Depending on the level of digestion reached, the prey was identified to the lowest possible taxonomic level.

Frequency of occurrence (%FO) is numerical method that represents the number of digestive tracts containing particular food relative to the total number of digestive tracts containing any food [4]. It is determined separately for each category of prey.

3. Results and discussion

Although common bleak has no economic importance today due to its small size, it remains an important link in the trophic webs of aquatic ecosystems. It feeds on zooplankton, insect larvae, and imagoes captured from the water surface, and is a food competitor for adult and juvenile forms of many valuable fishes [8]. The composition of the diet of 37 specimens from Gruža reservoir and 44 specimens from Gazivode reservoir is shown in Table 1.

Table 1. Assessment of diet composition of common bleak expressed as frequency of occurrence (%FO).

	Gruža reservoir	Gazivode reservoir
Ostracoda	26.66	92.68
Cladocera	100.00	85.36
<i>Daphnia</i> sp.	100.00	95.12
<i>Bosmina</i> sp.	100.00	100.00
<i>Leptodora kindtii</i>	-	24.39
Calanoida (Copepoda)	66.66	85.36
Cyclopoida (Copepoda)	73.33	48.78

The common bleak is an obligate planktivore and a specialized open-water feeder [9, 10], feeding on small planktonic crustaceans and insects from the water surface [11]. The diet of common bleak described in this paper is largely consistent with other studies on this species. Eight different categories of prey have been identified in their diet from these two reservoirs. The common bleak from Gazivode reservoir fed more diversely on eight different prey items, while six different prey items were identified for those from Gruža reservoir. *Bosmina* sp. were present in every examined digestive tract of specimens from both reservoirs (%FO = 100), while in specimens from Gruža reservoir this is also the case for Cladocera and *Daphnia* sp. Although present in the diet of specimens from both reservoirs, Copepoda are less represented in the diet than Cladocera. This is due to the ability of copepods to develop strategies against predators to avoid becoming prey [12]. The results also show that the common bleak from Gazivode reservoir use much more Ostracoda in their diet than the specimens from Gruža reservoir. Specimens from Gazivode reservoir, unlike specimens from Gruža reservoir, also consume insects and large Cladocera *Leptodora kindtii*. The low proportion of *Leptodora kindtii* in the diet is a consequence of its pronounced transparency, which is why planktivorous fish, visual predators, have difficulty hunting it [13]. Mehner et al. [7] noted that the main component of the diet of the common bleak is zooplankton, but they also make extensive use of insects in their diet. Although most claim that the common bleak is an obligate planktivore, there are also (fewer in number) those who claim that the main component of the common bleak diet is zoobenthos [14], but our results do not confirm this.

4. Conclusions

In summary, this study offers valuable insights into the dietary strategies of common bleak. Numerous reports in the literature have confirmed, and our results are consistent with the fact that common bleak feeds primarily on zooplankton and often on insects.

Acknowledgment

This research is funded by the Ministry of Education and Ministry of Science, Technological Development and Innovation, Republic of Serbia, Grants: No. 451-03-47/2023-01/200122.

References

- [1] R.J. Wootton., *Ecology of Teleost Fishes*, Chapman and Hall, London, (1990) 404 p.
- [2] G. La Mesa, M. La Mesa, P. Tomassetti., *Feeding habits of the Madeira rockfish *Scorpaena maderensis* from central Mediterranean Sea*, *Marine Biology*, 150 (2007) 1313-1320.

- [3] H.B.N. Hynes., *The food of freshwater sticklebacks, (Gasterosteus aculeatus and Pygosteus pungitius) with a review of methods used in studies of the food of fishes*, Journal of Animal Ecology, 19 (1950) 36-58.
- [4] E.J. Hyslop., *Stomach content analysis: a review of methods and their applications*, Journal of Fish Biology, 17 (1980) 411-429.
- [5] P.U. Zacharia, K.P. Abdurahiman., *Methods of stomach content analysis of fishes*, Winter School on Towards Ecosystem Based Management of Marine Fisheries – Building Mass Balance Trophic and Simulation Models, 1 (2004) 148-158.
- [6] P. Simonović., *Ribe Srbije*, NNK International, Beograd, (2001) 247 p.
- [7] T. Mehner, J. Ihlau, H. Dörner, F. Hölker., *Can feeding of fish on terrestrial insects subsidize the nutrient pool of lakes?*, Limnology and Oceanography, 50 (2005) 2022-2031.
- [8] A. Kompowski., *Morphological features of the bleak Alburnus alburnus (L. 1758) from Miedzyodrze*, Acta Ichthyologica et Piscatoria, 18 (1998) 15-26.
- [9] M. Vinni, J. Horppila, M. Olin, J. Ruuhijärvi, K. Nyberg., *The food, growth and abundance of five co-existing cyprinids in lake basins of different morphometry and water quality*, Aquatic Ecology, 34 (2000) 421-431.
- [10] A. Specziár, E.T. Rezsű., *Feeding guilds and food resource partitioning in a lake fish assemblage: An ontogenetic approach*, Journal of Fish Biology, 75 (2009) 247-267.
- [11] P. Biro, B. Musko., *Population dynamics and food of bleak (Alburnus alburnus L.) in the littoral zone of Lake Balaton, Hungary*, Hydrobiologia, 310 (1995) 139-149.
- [12] K. Karus, T. Paaver, H. Agasild, P. Zingel., *The effect of predation by planktivorous juvenile fish on the microbial food web*, European Journal of Protistology, 50 (2014) 109-121.
- [13] D.O. Hassen., *Selective zooplankton predation by pre-adult roach (Rutilus rutilus): the size-selective hypothesis versus the visibility-selective hypothesis*, Hydrobiologia, 124 (1985) 73-79.
- [14] B. Losos, M. Penaz, J. Kubičková., *Food and growth of fishes of the Jihlava river*, Acta scientiarum naturalium Academiae scientiarum Bohemicae – Brno, 14 (1980) 1-46.

Identification of protein target molecules for [Pd(dach)Cl₂] complex in HeLa cervical carcinoma cells

Vanja Ralić^{1*}, Branislava Gemović², Maja D. Nešić¹, Iva Popović¹, Milutin Stepić¹,
Marijana Petković¹

¹ University of Belgrade, National Institute of the Republic of Serbia, Vinča Institute of Nuclear Sciences, COHERENCE-Center for light-based science and technologies, Department of Atomic Physics, Mike Petrovića Alasa 12-14, 11000 Belgrade, Serbia; e-mail: vanja.ralic@live.com (VR), maki@vin.bg.ac.rs (MN), ivavukicevic@vin.bg.ac.rs (IP), mstepic@vin.bg.ac.rs (MS), petkovic.marijana.71@gmail.com (MP)

² University of Belgrade, National Institute of the Republic of Serbia, Vinča Institute of Nuclear Sciences, Department of Theoretical Physics and Condensed Matter Physics, Belgrade, Mike Petrovića Alasa 12-14, 11000 Belgrade, Serbia; e-mail: gemovic@vin.bg.ac.rs (BG)

DOI: 10.46793/ICCB23.296R

Abstract: In this work, we have applied the Informational Spectrum Method (ISM) to discover a potential protein target in the HeLa cervical cancer cell line for [Pd(dach)Cl₂] complex. Since Pd complexes are considered an alternative to traditionally used Pt complexes in anti-cancer therapy, it is essential to elucidate the mechanism of their action. A detailed analysis that also involves screening the known protein databases revealed the proteins of the SOSS complex as the most probable [Pd(dach)Cl₂] targets. Since this protein maintains genomic stability, this result shows the potential of the Pd(II) complex as an anti-cancer drug.

Keywords: Informational Spectrum Method, Cervical Cancer, palladium complex, SOSS protein

1. Introduction

Computational methods in drug discovery are helpful tools to elucidate the signaling pathways affected by a drug [1]. In our previous work [2], we have identified signaling pathways that can be affected mainly by the interaction of ovarian cancer (A2780 cell line) and osteosarcoma (CAL72) cell lines with carbon-based nanoparticles (carbon dots, CDs) loaded with Ru-complex. The genes with abundant expression in one of these cell lines are analyzed using specific tools, and the proteins, which are associated with individual signaling pathways and specific secondary structures, are recognized as the most probable cell-specific target for the interaction with CDs loaded with Ru complex.

An additional possibility that can accelerate the drug discovery process is to calculate the informational spectrum of a drug, which enables more precise identification of specific target molecules [3]. ISM analysis can predict protein-protein interactions [4,5], but it was also successfully applied for discovering new therapeutic targets [6]. Recently,

ISM was applied during the COVID-19 outbreak as a strategy for *in-silico* drug repurposing approach [3].

Cervical cancer is women's fourth most frequently diagnosed malignant disease [7]. Current treatments for cervical cancer include radiotherapy and platinum-based chemotherapy, which can cause severe side effects. Palladium(II) complexes are one of the leading contenders for replacing cisplatin due to the similarity of their metal center to platinum(II) complexes [8], but with less toxicity. Therefore, in this work, we wanted to discover a protein in the HeLa cervical cancer cell line that will be most likely targeted by Pd(II) complex metallodrug, dichloro(1,2-diaminocyclohexane)palladium(II) ([Pd(dach)Cl₂]).

Our results show that a DNA-binding protein complex named SOSS is the most probable target for HeLa cells for Pd(dach)Cl₂. These results encourage further development of anti-cervical cancer therapeutic agents based on Pd.

2. Methods

The Informational Spectrum Method (ISM) was focused on the cross-spectral analysis of the informational spectrum of the Pd(II) complex and informational spectra of all gene products expressed as a baseline in the HeLa cells [9,10]. With this goal, several steps were conducted: 1. Molecules were presented as a series of numbers based on Electron-Ion Interaction Potential (EIIP) [11]; in proteins, each amino acid in the sequence of the protein's primary structure is replaced by the value of EIIP for that amino acid; 2. This numerical sequence was transformed into an Informational Spectrum (IS) using Fourier Transform; 3. The spectra of two molecules were multiplied to obtain cross-spectrum (CS). Modification of ISM applied to small molecules (ISM-SM) was used to generate IS of the Pd(II) complex [13].

The list of Ensemble identifiers of genes (TPM \geq 2.0) that encode HeLa cell baseline expression was retrieved from Expression Atlas [9]. The FASTA format of protein sequences needed for further ISM analysis was obtained using UniProt Retrieve/ID mapping tool [10]. Accession numbers of proteins the ISM gave were analyzed using the bioinformatics resource for gene enrichment analysis, DAVID [12].

3. Results and discussion

Potential targets for the Pd(II) complex in the HeLa cells are investigated using the ISM method. As the first step, the informational spectrum of the complex was analyzed. The structure of the Pd(II) complex and its IS are given in Fig. 1. An IS of the Pd(II) complex generated by the ISM showed a dominant peak at the frequency 0.402, which was used for further cross-spectral analysis [3]. HeLa cell's 9462 baseline proteins, more precisely, their sequences, were screened for potential interactions with the Pd(II) complex using cross-spectral analysis [6].

Cross-spectral analysis recovered 106 proteins that were analyzed using the bioinformatics resource for gene enrichment analysis, DAVID, to determine which pathways/GO terms were enriched in this list [12]. Functional Annotation Chart revealed that the GO terms with the highest statistical significance were nucleoplasm and SOSS complex, which is involved in maintaining genomic stability [13]. Three

proteins, out of 106 predicted as Pd complex interactors, in the SOSS complex are SOSS C (gene name: INIP), SOSS B1 (gene name: NAPB2), and SOSS B2 (gene name: NAPB1).

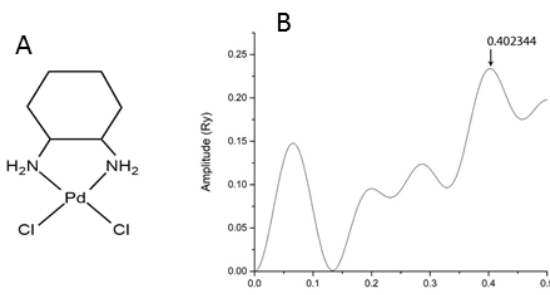


Figure 1. The structure of [Pd(dach)Cl₂] complex (A) and its informational spectrum (B). An arrow and number in the figure indicate the peak position for finding potential interactions with HeLa cell protein sequences.

Fig. 2 shows the interaction network of these proteins. These proteins vary in their secondary structure regarding the content of α -helices and β -secondary structures. The computational method applied in this work implied that the SOSS complex could be a protein target of the inspected Pd(II) complex. The SOSS complex is a protein complex involved in maintaining genomic stability. Therefore, the interaction with Pd(II) complex can affect the function of the SOSS complex, as it responds to DNA double-strand breaks. In addition, the interaction network of SOSS complex proteins predicted as Pd interactors includes TP53 and EP300. Since these proteins are involved in the cellular response to DNA damage, programmed cell death [14,15], and regulation of the cell migration process, treatment of HeLa cells with the Pd(II) complex might inhibit cell migration, as well [16]. The latter demonstrates the anti-metastatic potential of the tested Pd(II) complex.

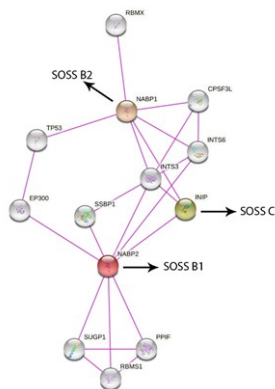


Figure 2. Interaction network of NAPB1, INIP, and NAPB2, retrieved from the STRING database, only including experimentally verified interactions.

The SOSS complex subunit A is a central assembly factor of the entire complex and holds together the other subunits, SOSS-B1, SOSS-B2, and SOSS-C [13]. SOSS-B1 can localize at sites of DNA breaks, and cells deficient in this protein exhibit increased sensitivity to DNA damage and a diminished capacity for DNA repair [17].

3. Conclusions

In this work, we have applied the bioinformatics approach to identify the most probable target in HeLa cells for [Pd(dach)Cl₂] complex, which can be further tested as a potential anti-cervical cancer metallodrug. The results are promising, as the protein complex

SOSS, which is involved in the maintenance of genomic stability, indicates a potential interference of [Pd(dach)Cl₂] with the cancer cell cycle and triggering apoptosis.

Acknowledgement

This research is funded by the Ministry of Education and Ministry of Science, Technological Development and Innovation, Republic of Serbia, Grant: No. 451-03-47/2023-01/200017.

References

- [1] C. Fotis, A., Antoranz, D. Hatzivramidis, et al., *Network-based technologies for early drug discovery*, Drug Discovery Today, 23 (2018) 62-635.
- [2] M. Nešić, T. Dučić, M. Gonsalves, et al., *Biochemical changes in cancer cells induced by photoactive nanosystem based on carbon dots loaded with Ru-complex*, Chemico-Biological Interactions, 360 (2022) 109950.
- [3] M. Senčanski, V. Perović, S. Pajović, et al., *Drug Repurposing for Candidate SARS-CoV-2 Main Protease Inhibitors by a Novel In Silico Method*, Molecules 25 (2020) 3830.
- [4] R. V. Srinivasa, K. Srinivasa, G. N. Sujini, et al., *Protein-Protein Interaction Detection: Methods and Analysis*, International Journal of Proteomics, 17(2014) 1-12.
- [5] K. Jha, S. Sriparna, S. Hiteschi, *Prediction of Protein-Protein Interaction Using Graph Neural Networks*, Scientific Reports, 12 (2022) 8360.
- [6] N. Veljković, S. Glišić, J. Prlić, et al., *Simple and general criterion for "in silico" screening of candidate HIV drugs*. Current Pharmaceutical Biotechnology, 14(2013) 561-569.
- [7] F. Bray, J. Ferlay, I. Soerjomataram, et al., *Global cancer statistics 2018: GLOBOCAN estimates of incidence and mortality worldwide for 36 cancers in 185 countries*, CA: A Cancer Journal for Clinicians 68 (2018) 394-424.
- [8] M. P. M. Marques, *Platinum and Palladium Polyamine Complexes as Anti-cancer Agents: The Structural Factor*, ISRN Spectrosc 2013 (2013) 1-29.
- [9] I. Papatheodorou, P. Moreno, J. Manning, et al. *Expression Atlas Update: From Tissues to Single Cells*, Nucleic Acids Research, 48 (2020) D77-83.
- [10] The UniProt Consortium, "UniProt: The Universal Protein Knowledgebase in 2021," *Nucleic Acids Research* 49, no. D1 (January 8, 2021) D480-89
- [11] V. Veljković, *A Theoretical Approach to the Preselection of Carcinogens and Chemical Carcinogenesis*, Gordon and Breach Science Publishers, 1980
- [12] B.T. Sherman, M. Hao, J. Qiu, et al., *DAVID: A Web Server for Functional Enrichment Analysis and Functional Annotation of Gene Lists (2021 Update)*, Nucleic Acids Research 50, no. W1 (2022) W216-21
- [13] H. Jun, G. Zihua, G. Gargi, et al., *SOSS Complexes Participate in the Maintenance of Genomic Stability*, Molecular Cell, 35, no. 3 (2009) 384-93.
- [14] W. Hanel and U. M. Moll, *Links between Mutant P53 and Genomic Instability*, Journal of Cellular Biochemistry 113 (2012) 433-39.
- [15] H. Yang, T. Salz, M. Zajac-Kaye, et al., *Overexpression of Histone Deacetylases in Cancer Cells Is Controlled by Interplay of Transcription Factors and Epigenetic Modulators*, FASEB Journal: Official Publication of the Federation of American Societies for Experimental Biology 28 (2014) 4265-79.
- [16] Y. Bi, P. Kong, L. Zhang, et al., *EP300 as an Oncogene Correlates with Poor Prognosis in Esophageal Squamous Carcinoma*, Journal of Cancer 10 (2019) 5413-26.
- [17] D. J. Richard, E. Bolderson, L. Cubeddu, et al., *Single-Stranded DNA-Binding Protein HSSB1 Is Critical for Genomic Stability*, Nature 453 (2008) 677-81.

Edible mushrooms as promising antioxidants

Jovana D. Todorović^{1*}, Aleksandra D. Vesić², Nevena N. Petrović², Marijana M. Kosanić²

¹ University of Kragujevac, Institute for Information Technologies, Department of Science, Jovana Cvijića bb, 34000 Kragujevac, Republic of Serbia; e-mail: jovana.todorovic@pmf.kg.ac.rs

² University of Kragujevac, Faculty of Science, Department of Biology and Ecology, Radoja Domanovića 12, 34000 Kragujevac, Republic of Serbia; e-mail: 1070-2020@pmf.kg.ac.rs , nevena.n.petrovic@pmf.kg.ac.rs , marijana.kosanic@pmf.kg.ac.rs

DOI: 10.46793/ICCB23.300T

* Corresponding author

Abstract: Antioxidant activity of the acetone extracts of the mushrooms *Macrolepiota procera* and *Chlorophyllum rhacodes* has been screened *in vitro* by using different methods (DPPH radical scavenging and reducing power assay), and also it has been determined the total phenolic compounds as total flavonoid content. The research findings indicate that the acetone extract of *M. procera* demonstrated superior antioxidant activities when compared to *C. rhacodes*. Similarly, the mushroom *M. procera* displayed a more pronounced effect on reducing power. In addition, the total content of phenol and flavonoid in extracts were determined as pyrocatechol equivalent, and as rutin equivalent, respectively. A higher content of total phenols and flavonoids was detected in the extract of *M. procera*. The strong relationships between total phenolic and flavonoid contents and the antioxidative activities of tested extracts imply that these compounds have a significant impact on antioxidant activity. The present study highlights that the tested mushroom species exhibit potent antioxidant properties and can be regarded as valuable sources of natural antioxidants.

Keywords: mushrooms, acetone extract, antioxidant activity

1. Introduction

Edible mushrooms are extensively consumed in numerous countries. Their consumption has experienced a substantial rise due to their delectable flavor, convenient availability, and appeal as functional foods. Aside from their nutritional benefits, mushrooms have the potential to be utilized for therapeutic intentions as they can generate a wide array of secondary metabolites, including organic acids, alkaloids, terpenoids, steroids, and phenolic compounds [1]. In the past few years, there has been an increasing focus on edible mushrooms as a viable resource of antioxidants in the commercial sphere.

This study evaluated the antioxidant activity of two closely related edible mushroom species *Macrolepiota procera* (Scop.) Singer 1948 (commonly referred to as the

parasol mushroom) and *Chlorophyllum rhacodes* (Vittad.) Vellinga 2002 (known as the shaggy parasol) that are widely consumed in Serbia because of their availability and appealing flavor.

Despite the extensive research conducted on edible mushrooms across various countries, only a limited number of studies have investigated the antioxidant properties of these specific two species of edible mushrooms [1, 2, 3]. Therefore, the aim of the present work is to evaluate the antioxidant activity of the acetone extract of *M. procera* and *C. rhacodes* found in Serbia.

2. Materials and Methods

Mushroom samples of *M. procera* and *C. rhacodes* were collected from Kragujevac, Serbia, in October of 2020. Finely dry ground dried thalli of the examined mushrooms (100 g) were extracted using acetone (500 mL) in a Soxhlet extractor, Quickfit, England. The dry extracts were dissolved in 5% dimethyl sulfoxide (DMSO).

The antioxidant activity of mushroom extracts was assessed using the 1,1-diphenyl-2-picryl-hydrazil (DPPH) method. Although the method was slightly modified, it was similar to approaches employed by other researchers [4, 5]. The absorbance was measured at 517 nm using a spectrophotometer. The DPPH radical concentration was calculated using the following equation (1):

$$DPPH \text{ scavenging ability} (\%) = \frac{[A_0 - A_1] \times 100}{A_0} \quad (1)$$

where A_0 is the absorbance of the negative control and A_1 is the absorbance of the reaction mixture or standards.

The determination of the reducing power of the extracts followed the methodology established by Oyaizu [6]. The absorbance of the resulting solution was measured at 700 nm using a spectrophotometer. A blank sample was prepared with all the reaction agents without extract. Ascorbic acid was used as a positive control.

The phenolic compounds in the mushroom extracts were determined with Folin-Ciocalteu reagent, following the method described by Slinkard and Singleton [7]. Pyrocatechol was used as a standard phenolic compound. The absorbance of the solution was measured at 760 nm using a spectrophotometer. The total concentration of phenolic compounds in the extracts was determined in micrograms of pyrocatechol equivalent (PE) per milligram of dry extracts.

The determination of total flavonoid content followed the Dowd method, as described by Meda *et al.* [8]. Absorbance of the solutions was measured at 415 nm using a spectrophotometer, comparing against blank samples. The total flavonoid content was quantified as micrograms of rutin equivalent (RE) per milligram of dry extracts.

3. Results and Discussion

The DPPH radical scavenging and reducing power of the examined extracts are presented in Table 1. Acetone extracts of the tested mushrooms exhibited moderate scavenging activity against DPPH radicals. The results in these tables indicate that the extract derived from *M. procera* exhibited higher antioxidant activities compared to *C. rhacodes*. The antioxidant activities of the tested samples were also compared to ascorbic acid, which demonstrated stronger activity as a standard antioxidant. The results of the reducing power assay demonstrate that the reducing capability of the extracts varies with concentration.

Table 1. DPPH radical scavenging (%) activity of acetone extracts of *M. procera* and *C. rhacodes*

Mushroom species	DPPH radical scavenging (%)					Reducing power		
	2 mg/mL	1 mg/mL	0.5 mg/mL	0.25 mg/mL	0.125 mg/mL	1000 µg/mL	500 µg/mL	250 µg/mL
<i>M. procera</i>	48.47	31.60	16.36	8.89	3.27	0.144	0.093	0.047
<i>C. rhacodes</i>	10.33	10.94	6.34	4.09	0.31	0.097	0.056	0.041
Ascorbic acid	-	-	-	-	-	2.113	1.654	0.096

The total phenolic and flavonoid contents of the mushroom extracts are given in Table 2. Acetone extract of *M. procera* has greater values of phenolic content (13.12 µg PE/mg extract), while higher amounts of flavonoid compounds were found in the extract of *C. rhacodes* (33.42 µg RE/mg extract).

Table 2. Total phenolic and flavonoid content of acetone extracts of acetone extracts of *M. procera* and *C. rhacodes*

Mushroom species	Phenolic content (µg PE/mg extract)	Flavonoid content (µg RE/mg extract)
<i>M. procera</i>	13.12	5.76
<i>C. rhacodes</i>	8.53	33.42

In the literature there are several data for the antioxidant activity of *M. procera* and *C. rhacodes* [1, 2, 3]. They determined antioxidant activity for these species but for other extraction solvents used. Kosanić *et al.* [1] reported that the antioxidant activity of the methanol extract of *M. procera* showed the most potent reducing power and total phenolic content. Akata *et al.* [2] reported the proximate composition of *C. rhacodes* and the highest content of proteins of all other tested species.

Varying outcomes have been observed in studies investigating the antioxidant effects of mushrooms belonging to the same genera. Various factors such as strain differences, developmental stage, age of mushrooms, storage conditions, and the extraction method, particularly the choice of solvent, can influence the concentrations of substances which are responsible for the antioxidant properties [9].

4. Conclusion

The utilization of mushrooms offers several advantages compared to the use of various chemical compounds, primarily due to their varied bioactive properties. This study has provided evidence that the acetone extracts of *M. procera* and *C. rhacodes* exhibit moderate antioxidant effects. Due to the widespread availability and abundance of these edible species, it is strongly recommended to include them in one's diet, and in the pharmaceutical industry. Further investigation is necessary to identify the specific active compounds responsible for the bioactive observed in the selected mushroom species.

Acknowledgment

This research is funded by the Ministry of Education and Ministry of Science, Technological Development and Innovation, Republic of Serbia, Grants: No. 451-03-47/2023-01/200378 and No. 451-03-47/2023-01/200122.

References

- [1] M. Kosanić, B. Ranković, A. Rančić, T. Stanojković., *Evaluation of metal concentration and antioxidant, antimicrobial, and anticancer potentials of two edible mushrooms Lactarius deliciosus and Macrolepiota procera*, Journal of Food and Drug Analysis, 24 (2016) 477-484.
- [2] I. Akata, B. Ergonul, F. Kalvoncu., *Chemical compositions and antioxidant activities of 16 wild edible mushroom species grown in Antolia*, International Journal of Pharmacology, 8 (2012) 134-138.
- [3] A. Fernandes, L. Barros, J.C.M. Barreira, A.L. Antonio, M.B.P.P. Oliveira, A. Martins, I.C.F.R. Ferreira., *Effects of different processing technologies on chemical and antioxidant parameters of Macrolepiota procera wild mushroom*, LWT - Food Science and Technology, 54 (2013) 493-499.
- [4] E. Ibanez, A. Kubatova, F.J. Senorans, S. Cavero, G. Reglero, S.B. Hawthorne., *Subcritical water extraction of antioxidant compounds from rosemary plants*, Journal of Agricultural and Food Chemistry, 51 (2003) 375-382.
- [5] H.J. Dorman, O. Bachmayer, M. Kosar, R. Hiltunen., *Antioxidant properties of aqueous extracts from selected Lamiaceae species grow in Turkey*, Journal of Agricultural and Food Chemistry, 52 (2004) 762-770.
- [6] M. Oyaizu., *Studies on products of browning reaction prepared from glucoseamine*, Japanese Journal of Nutrition, 44 (1986) 307-314.
- [7] K. Slinkard, V.L. Singleton., *Total phenol analysis: Automation and comparison with manual methods*, American Journal of Enology and Viticulture, 28 (1977) 49-55.
- [8] A. Meda, C.E. Lamien, M. Romito, J. Millogo, O.G. Nacoulma., *Determination of the total phenolic, flavonoid and proline contents in burkina fasan honey, as well as their radical scavenging activity*, Food Chemistry, 91 (2005) 571-577.
- [9] K.K. Mishra, R.S. Pal, R. Arunkumar, C. Chandrashekara, S.K. Jain, J.C. Bhatt., *Antioxidant properties of different edible mushroom species and increased bioconversion efficiency of Pleurotus eryngii using locally available casing materials*, Food Chemistry, 138 (2013) 1557-1563.

Antimicrobial potential of mushrooms *Macrolepiota procera* and *Chlorophyllum rhacodes*

Jovana D. Todorović^{1*}, Aleksandra D. Vesić², Nevena N. Petrović², Marijana M. Kosanić²

¹ University of Kragujevac, Institute for Information Technologies, Department of Science, Jovana Cvijića bb, 34000 Kragujevac, Republic of Serbia; e-mail: jovana.todorovic@pmf.kg.ac.rs

² University of Kragujevac, Faculty of Science, Department of Biology and Ecology, Radoja Domanovića 12, 34000 Kragujevac, Republic of Serbia; e-mail: 1070-2020@pmf.kg.ac.rs , nevena.n.petrovic@pmf.kg.ac.rs , marijana.kosanic@pmf.kg.ac.rs

DOI: 10.46793/ICCBi23.304T

* Corresponding author

Abstract: The aim of this study is to investigate the *in vitro* antimicrobial properties of the acetone extracts of the mushrooms *Macrolepiota procera* and *Chlorophyllum rhacodes*. The microdilution method was used to determine the minimum inhibitory concentration (MIC) and assess the antimicrobial effects against three bacterial and ten fungal species. Overall, the tested mushroom extracts had relatively strong antimicrobial activity against the tested microorganisms. The minimum inhibitory concentration for both extracts related to the tested bacteria and fungi was 0.625 - 20 mg/mL. Extract of *C. rhacodes* exhibited more powerful antimicrobial properties, with ranged MIC values from 0.625 mg/mL to 10 mg/mL. The Acetone extract of *C. rhacodes* has shown the most antibacterial activity against *S. aureus*, while the extract of *M. procera* has not shown activity against *S. aureus* as against *G. candidum*. In comparison to the standard antibiotics as positive controls, the antimicrobial activity of studied extracts was less expressed. The results suggest that mushroom species may be used for pharmaceutical purposes in treating various diseases.

Keywords: mushrooms, acetone extract, antimicrobial activity

1. Introduction

Presently, the global community is confronting noteworthy difficulties in contemporary healthcare provisions as numerous antimicrobial substances have become less potent in combatting infectious diseases predominantly attributable to the emergence of microbial resistance [1]. Searching for bioactive compounds that can effectively treat drug-resistant pathogenic microorganisms is incredibly beneficial. At present, there is an increasing focus on the exploration of novel antimicrobial agents derived from natural sources like bacteria, fungi, and plants [2]. Mushrooms release a range of bioactive compounds, including terpenoids, flavonoids, tannins, alkaloids, and

polysaccharides. They possess abundant bioactive compounds that remain largely unexplored but hold significant potential as valuable natural resources.

Only a few studies describe the antimicrobial properties of mushrooms *Macrolepiota procera* (Scop.) Singer 1948., and *Chlorophyllum rhacodes* (Vittad.) Vellinga 2002. could be found in literature [3, 4, 5].

Thus, the aim of the present work is to evaluate the antimicrobial potential of the acetone extract of mushrooms *M. procera* and *C. rhacodes*.

2. Materials and Methods

Fungal samples of *M. procera* and *C. rhacodes* were collected from Kragujevac, Serbia in October 2020. The demonstration samples are preserved in the facilities of the Department of Biology and Ecology, Faculty of Science, Kragujevac. The fresh fungal material was ground using an electrical mill and then subjected to extraction with acetone. After filtration, the extracts were concentrated under reduced pressure using a rotary evaporator. Before the test, the extracts were dissolved in 5% dimethyl sulphoxide (DMSO).

The antibacterial activity of acetone extracts of *M. procera* and *C. rhacodes* was tested on three species of bacteria: *Staphylococcus aureus* (ATCC 25923), *Escherichia coli* (ATCC 25922), and *Proteus mirabilis* (ATCC 12453), and ten species of fungi: *Trichophyton mentagrophytes* (ATCC 9533), *Fusarium oxysporum* (ATCC 62506), *Geotrichum candidum* (ATCC 34614), *Trichoderma viride* (ATCC 13233), *Cladosporium cladosporioides* (ATCC 11680), *Penicillium italicum* (ATCC 10454), *Mucor mucedo* (ATCC 20094), *Aspergillus flavus* (ATCC 9170), *Aspergillus niger* (ATCC 16888) and *Candida albicans* (ATCC 10259).

Cultures of tested species of microorganisms are provided from the American Type Culture Collection (ATCC). Bacterial cultures were maintained on Müller-Hinton agar. Suspensions were prepared with sterile distilled water and were adjusted to contain approximately 10^8 CFU/mL. Fungal cultures were maintained on potato dextrose (PD) agar and Sabourad dextrose (SD) agar (Torlak, Belgrade). Fungal spores were rinsed with sterile distilled water, used to determine turbidity spectrophotometrically at 530 nm, and then further diluted to approximately 10^6 CFU/mL according to the procedure recommended by the National Committee for Clinical Laboratory Standards (NCCLS) [6].

The minimum inhibitory concentration (MIC) was determined by the broth microdilution method using 96-well microtiter plates [7]. A series of dilutions with concentrations ranging from 40 to 0.019 mg/mL for extracts were used in the experiment against every microorganism tested. Resazurin was used for the evaluation of bacterial growth. The MIC was determined by establishing the visible growth of microorganisms. The boundary dilution without any visible growth was defined as the MIC for the tested microorganism at the given concentration. The MIC for antifungal activity was determined by establishing the visible growth of microorganisms.

Standard antibiotics (streptomycin for bacteria and ketoconazole for fungi) were used as positive controls and DMSO was used as negative control.

3. Results and Discussion

The results of testing the antimicrobial activity are presented in Table 1.

Table 1. Minimum inhibitory concentration of acetone extracts of *M. procera* and *C. rhacodes*.

Mushroom species	<i>M. procera</i>	<i>C. rhacodes</i>	Streptomycin	Ketoconazole
<i>S. aureus</i>	-	0.625	0.039	-
<i>E. coli</i>	20	20	0.039	-
<i>P. mirabilis</i>	20	20	0.078	-
<i>T. mentagrophytes</i>	5	2.5	-	0.078
<i>F. oxysporum</i>	10	2.5	-	0.078
<i>G. candidum</i>	-	5	-	0.078
<i>T. viride</i>	10	10	-	0.078
<i>C. cladosporoides</i>	10	5	-	0.039
<i>P. italicum</i>	5	5	-	0.156
<i>M. mucedo</i>	10	5	-	0.156
<i>A. flavus</i>	20	10	-	0.156
<i>A. niger</i>	20	20	-	0.078
<i>C. albicans</i>	10	10	-	0.039

*Values given as mg/mL for extract and as µg/mL for antibiotics.

MIC values for *M. procera* ranged from 5 to 20 mg/mL, while for *C. rhacodes* they ranged from 0.625 to 20 mg/mL. However, *C. rhacodes* exhibited stronger and more effective antimicrobial activity compared to *M. procera*. *M. procera* has not shown activity against *S. aureus* and *G. candidum*. In general, gram-positive bacteria *S. aureus* was more susceptible than Gram-negative bacteria. Overall, fungi were more resistant than bacteria. The lowest MIC values for fungal species were for *C. rhacodes* against *T. mentagrophytes* (2.5 mg/mL), and against *F. oxysporum* (2.5 mg/mL). Our results showed that in comparison to standard antibiotics as positive controls, the antimicrobial activity of studied extracts was less expressive.

In our experiments, the tested mushroom extracts showed significant antimicrobial activity. The strength of the antimicrobial effect depended on the species of mushroom, its concentration, and the tested organism. Interestingly, when compared at the same concentrations, the examined mushroom displayed stronger antifungal than antimicrobial activity. The reason for the different sensitivity between the fungi and bacteria can be found in the different transparency of the cell wall [8].

While there is limited information available regarding the antimicrobial activity of *M. procera* and *C. rhacodes*, some authors have previously confirmed their antimicrobial properties [3, 4, 5].

The dissimilarities in our results, when compared to theirs, can be attributed to the disparity in the extraction technique, extraction solvent, and tested organisms.

4. Conclusion

In conclusion, it can be affirmed that mushroom extracts that were tested exhibit potent antimicrobial properties *in vitro*. These findings suggest that mushrooms can serve as valuable natural antioxidants and may have implications in the treatment of human ailments, as well as diseases in animals and plants. Additional research is needed to investigate the extraction and identification of novel compounds from mushrooms that are responsible for their antimicrobial effects.

Acknowledgment

This research is funded by the Ministry of Education and Ministry of Science, Technological Development and Innovation, Republic of Serbia, Grants: No. 451-03-47/2023-01/200378 and No. 451-03-47/2023-01/200122.

References

- [1] M. Balouiri, M. Sadiki, S.K. Ibnsouda., *Methods for in vitro evaluating antimicrobial activity*, Journal of Pharmaceutical Analysis, 6 (2016) 71–79.
- [2] M. Alves, I.F.R. Ferreira, J. Dias, V. Teixeira, A. Martins, M. Pintado., *A review on antimicrobial activity of mushroom (Basidiomycetes) extracts and isolated compounds*, Planta Medica, 78 (2012) 1707-1748.
- [3] I. Adamska, G. Tokarczyk., *Possibilities of using Macrolepiota procera in the production of prohealth food and in medicine*, International Journal of Food Science, 2022 (2022).
- [4] M. Kosanić, B. Ranković, A. Rančić, T. Stanojković., *Evaluation of metal concentration and antioxidant, antimicrobial, and anticancer potentials of two edible mushrooms Lactarius deliciosus and Macrolepiota procera*, Journal of Food and Drug Analysis, 24 (2016) 477-484.
- [5] I. Akata, B. Ergonul, F. Kalvoncu., *Chemical compositions and antioxidant activities of 16 wild edible mushroom species grown in Antolia*, International Journal of Pharmacology, 8 (2012) 134-138.
- [6] National Committee for Clinical Laboratory Standards., *Reference method for broth dilution antifungal susceptibility testing of conidium-forming filamentous fungi*, Proposed Standard M38-P, Wayne, PA, USA, 1998.
- [7] S.D. Sarker, L. Nahar, Y. Kumarasamy., *Microtitre plate-based antibacterial assay incorporating resazurin as an indicator of cell growth, and its application in the in vitro antibacterial screening of phytochemicals*, Methods, 42 (2007) 321-324.
- [8] Y. Yang, E.J. Anderson., *Antimicrobial activity of a porcine myeloperoxidase against plant pathogenic bacteria and fungi*, Journal of Applied Microbiology, 86 (1999) 211-220.

Obesity as a risk factor for Covid- 19 mortality: an overview of published meta-analyses

Jasmina Obradovic ^{1*}, Jelena Mladenovic ², Vladimir Jurisic³

¹ University of Kragujevac, Institute for Information Technologies Kragujevac, Department of Science, Jovana Cvijića bb, 34000 Kragujevac, Serbia; e-mail: jasmina.obradovic@uni.kg.ac.rs

² University of Kragujevac, Faculty of Education in Jagodina, Milana Mijalkovica 14, 35000 Jagodina, Serbia; e-mail: jelena.mladenovic@pefja.kg.ac.rs

³ University of Kragujevac, Faculty of Medical Sciences, Svetozara Markovica 69, 34000 Kragujevac, Serbia; e-mail: jurisicvladimir@gmail.com

* Corresponding author

DOI: 10.46793/ICCBi23.3080

Abstract: Obesity and Covid-19 affected the world in the form of pandemics. With this brief review was investigated whether obesity is a risk factor for Covid-19 mortality. The search procedure was performed in the PubMed database with restrictions on meta-analysis (MAs), systematic reviews (SRs), and papers published in the English language. A total of 326 papers were obtained, 11 of which were eligible for analysis according to the aim of this study. The reported odds ratio (OR) range was 1.05-3.76, and the reported hazard ratio (HR) was 2.1, but significant heterogeneity was evidenced by I^2 values up to 89.1%. Eight MAs and SRs reported an association between obesity and an increased risk of Covid-19 mortality or severe disease, while two studies found no association. One study reported that the risk of Covid-19 mortality is related to morbid obesity with body mass index (BMI) ≥ 40 kg/m². Good quality MAs and SRs requires good quality of the included studies, which was a great challenge during the Covid-19 pandemic.

Keywords: Obesity, Covid-19, Mortality

1. Introduction

Obesity is a major health problem worldwide and is associated with epidemic proportions [1]. According to a report published by the World Health Organization (WHO), almost one-third of the world's population is obese or overweight, with approximately 2.8 million people deaths per year [2]. Various chronic diseases are associated with obesity or being overweight [3]. Moreover, obesity is a predisposing factor for poor prognosis in viral diseases [4]. WHO classifies obesity according to body mass index (BMI). Obese individuals are classified according to BMI into class I (30-35 kg/m²), class II (35-40 kg/m²), and class III (≥ 40 kg/m²) [2]. WHO announced the global pandemic of COVID-19 on February 11, 2020 [5]. Even nowadays, a quick Pub Med search ending with July 14, 2023, revealed 373,914 papers published on the "Covid 19" term. This study aimed to descriptively summarize the main findings from available

systematic reviews (SRs) and meta-analyses (MAs) referring to obesity (overweight) as a risk factor for Covid- 19 mortality.

2. Search procedure and discussion

The search procedure was performed on June 21, 2023, in the PubMed database using the following search query: (((obesity) AND (Covid 19)) AND (mortality)) AND (prognosis) with activated filters restricted to MAs, SRs, and papers published in English. A total of 326 papers were obtained, 21 of which were SRs and MAs. Ten studies were excluded because they did not address the aim of this study and 11 studies were analyzed [6-16]. The reasons for exclusion were gravidity, kidney injury, thyroid disorders, no reported mortality, Candida auris infections, and age below 18 years etc. Odds ratios (OR) or hazard ratios (HR) were used as measures of the associations [18]. The reported OR range was 1.05-3.76, and the reported HR was 2.1 [6-16]. Heterogeneity, which might introduce a certain bias, was measured using Cochran's Q and I² statistics. Levels that correspond to low, medium, and high heterogeneity follow I² values of 25%, 50%, and 75% [17]. Reported I² values varied from 7.49%-89.1% [6-16]. Due to the constraints of this paper format, this brief review omitted formal statistical measurements, and the main findings are explained descriptively. In addition to this short form of review, we acknowledge certain limitations.

The emergence of SARS-CoV-2 has changed people's lives in many ways. During the COVID-19 pandemic, in addition to sedentary behavior, changes in diet, poor nutrition, and increased BMI were observed during the pandemic compared to the period before the pandemic [19]. Of the 11 studies reviewed, eight reported that obesity is a risk factor for Covid-19 mortality [6-13], seven studies for severe disease [6-8, 10-12, 16], and two reported no association [15, 16]. One study reported that the risk of Covid-19 mortality was related to morbid obesity (BMI≥40 kg/m²) (three studies included in MA; OR 3.76, 95% CI 2.67-5.28, I²=0%, p=0.665) [14].

It was assumed here potential sources of the heterogeneity and proposed recommendations for further MAs and SRs. At the beginning of the pandemic, it was difficult to draw precise conclusions because there were many uncertainties about the virus; however, they were urgently needed for patient care. MAs or SRs published close to the beginning of the pandemic had small (two or more) numbers of studies included in MA and SR [6, 14, 15]. Even though two studies are required to perform MA, more quality papers included in MA produce more certainty about the summary results [18]. Even larger numbers of the studies were included in the MA, the smaller number of studies were included in the formal MA, where mortality was the endpoint (i.e., 88/3 and 40/10) [9, 13]. The majority of studies confirmed the association between Covid-19 mortality and obesity, but the presence of medium or high levels of heterogeneity according to the I² values ≥50% and ≥75%, and p values ≤0.05, were observed [6-16]. This should be considered when accepting or rejecting the main findings of particular MAs or SRs. Heterogeneity is always present, according to the Cochrane Handbook for Systematic Reviews of Interventions [18]. A rapid pace in publications during the Covid-

19 pandemic, prevented constant updating during work on the particular MA. Procedures in MA require a statement about their limitations. All of the studies investigated here [6-16] had statements about their limitations, which we extracted and summarized [Table 1]. However, papers in non-English languages are usually rejected. Most studies reported hospital mortality. Mortality out of the hospital was hard to identify and report. Obesity is associated with other comorbidities; thus, it is difficult to interpret obesity as an independent risk factor for Covid-19 mortality. Although, morbid obesity is a risk factor for mortality with or without Covid-19 [2].

Table 1. Reported main limitations from the studies.

<i>Finding</i>	<i>Author, year</i>
<i>Limited number of studies included in the MA</i>	Deng 2014
<i>Lack of definition for obesity and the severity of the disease in COVID-19</i>	Deng 2014
<i>Not uniform definition of the obesity: national cut-points (BMI>25 kg/m²), or WHO definition (BMI>30 kg/m²)</i>	Raiesi,2022; Zhao,2020
<i>Recall bias; reporting bias</i>	Hoong, 2021
<i>Hospitalisation may differ between hospitals-not uniform population of included studies</i>	Hoong 2021;
<i>Overlap of some participants included in the MA</i>	Huang 2020;
<i>Differences between self-reported and measured BMI</i>	Najafabady,2023
<i>Independent risk for mortality of comorbidities, other than Covid- 19</i>	Ng, 2021;
<i>The confounders other than pooled adjusted OR/HR might be accounted for.</i>	Pranata, 2021;
<i>Majority retrospective studies which is less reliable compared to prospective studies</i>	Pranata, 2021
<i>Omitted comorbidities of the obese patients. The included studies varied in their differentiation of patients' disease severity according to the clinical definition.</i>	Raiesi, 2022;
<i>Alpha and Beta variants were considered, without the risk factors within the post-Omicron strain (B.1.1.529) context</i>	Vardavas, 2022
<i>Cross sectional, and retrospective studies. Some studies had small sample sizes.</i>	Aghilli,2021; Zhao, 2020

Our findings are consistent with those of previous reports [20]. The authors pointed to caution in interpretation of the results since the evidenced and proven low quality of MAs and SRs [20]. True significance in the relationship between obesity and Covid 19 mortality is a challenge for future MA with good quality of included studies, following strict rules and procedures.

3. Conclusions

The majority of MAs and SRs investigated here have reported an association between obesity and an increased risk of severe disease and Covid- 19 mortality. Some studies found no relationship between obesity patients with Covid- 19 mortality. Others found that during the pandemic, persons with BMI> 40 kg/m² were more vulnerable to mortality than other obesity classes. According to WHO recommendations, obesity is preventable. Even evidence of considerable heterogeneity in the MAs and SRs, Covid-19 mortality and obesity should be investigated in future MAs and SRs by following strict methodological procedures with included high-quality papers.

Acknowledgment

This work was supported by the Ministry of Science, Technological Development and Innovation, Republic of Serbia, Agreements Numbers: 451-03-47/2023-01/200378 and 451-03-47/2023-01/200111.

References

- [1] M. Blüher., *Obesity: global epidemiology and pathogenesis*, Nature reviews. Endocrinology, 15 (2019) 288–298.
- [2] World Health Organization. Obesity and overweight. www.who.int/news-room/fact-sheets/detail/obesity-and-overweight (Accessed on 14 July 2023).
- [3] L. La Sala, A. E. Pontiroli., *Prevention of Diabetes and Cardiovascular Disease in Obesity*. International journal of molecular sciences, 21(2020) 8178.
- [4] M. Smith , R. Honce, S. Schultz-Cherry, *Metabolic Syndrome and Viral Pathogenesis: Lessons from Influenza and Coronaviruses*. Journal of virology, 94 (2020) e00665-20.
- [5] World Health Organization. Tracking SARS-CoV-2 variants. www.who.int/en/activities/tracking-SARS-CoV-2-variants/ (Accessed: 14 July 2023).
- [6] R. Pranata, M.A. Lim, E. Yonas, R. Vania, A.A. Lukito, B.B. Siswanto, M. Meyer., *Body mass index and outcome in patients with COVID-19: A dose-response meta-analysis*, Diabetes & metabolism, 47 (2021) 101178.
- [7] C.W.S. Hoong, I. Hussain, V.M. Aravamudan, E.E. Phyu, J.H.X. Lin, H. Koh., *Obesity is Associated with Poor Covid-19 Outcomes: A Systematic Review and Meta-Analysis*, Hormone and metabolic research = Hormon- und Stoffwechselforschung = Hormones et métabolisme 53 (2021) 85-93.
- [8] J.S.Y. Ho, D.I. Fernando, M.Y. Chan, C.H. Sia., *Obesity in COVID-19: A Systematic Review and Meta-analysis*, Annals of the Academy of Medicine, Singapore 49 (2020) 996-1008.
- [9] C.I. Vardavas, A.G. Mathioudakis, K. Nikitara, K. Stamatelopoulos, G. Georgiopoulos, R. Phalkey, J. Leonardi-Bee, E. Fernandez, D. Carnicer-Pont, J. Vestbo, J.C. Semenza, C. Deogan, J.E. Suk, P. Kramarz, F. Lamb, P. Penttinen., *Prognostic factors for mortality, intensive care unit and hospital admission due to SARS-CoV-2: a systematic review and meta-analysis of cohort studies in Europe*, European respiratory review : an official journal of the European Respiratory Society, 31(2022) 220098.
- [10] T. Raeisi, H. Mozaffari, N. Sepehri, M. Darand, B. Razi, N. Garousi, M. Alizadeh, S. Alizadeh., *The negative impact of obesity on the occurrence and prognosis of the 2019 novel coronavirus (COVID-19) disease: a systematic review and meta-analysis*, Eating and weight disorders: EWD, 27 (2022) 893-911.
- [11] B. Tadayon Najafabadi, D.G. Rayner, K. Shokraee, K. Shokraie, P. Panahi, P. Rastgou, et al., *Obesity as an independent risk factor for COVID-19 severity and mortality*, Cochrane Database Systematic Reviews, 5 (2023) CD015201.
- [12] Y. Huang, Y. Lu, Y.M. Huang, M. Wang, W. Ling, Y. Sui, H.L. Zhao., *Obesity in patients with COVID-19: a systematic review and meta-analysis*, Metabolism, 113 (2020) 154378.
- [13] S.M.M. Aghili, M. Ebrahimpur, B. Arjmand, Z. Shadman, M. Pejman Sani, M. Qorbani, B. Larijani, M. Payab., *Obesity in COVID-19 era, implications for mechanisms, comorbidities, and prognosis: a review and meta-analysis*, International journal of obesity, 45 (2021) 998-1016.
- [14] X. Zhao, X. Gang, G. He, Z. Li, Y. Lv, Q. Han, G. Wang., *Obesity Increases the Severity and Mortality of Influenza and COVID-19: A Systematic Review and Meta-Analysis*, Frontiers in endocrinology, 11 (2020) 595109.
- [15] W.H. Ng, T. Tipih, N.A. Makoah, J.G. Vermeulen, D. Goedhals, J.B. Sempa, F.J. Burt, A. Taylor, S. Mahalingam., *Comorbidities in SARS-CoV-2 Patients: a Systematic Review and Meta-Analysis*, mBio, 12(2021) e03647-20.
- [16] L. Deng, J. Zhang, M. Wang, L. Chen., *Obesity is associated with severe COVID-19 but not death: a dose-response meta-analysis*, Epidemiology and infection, 149 (2021) e144.
- [17] J.P.T. Higgins, S.G. Thompson, J.J. Deeks, D.G. Altman., *Measuring inconsistency in meta-analyses*. BMJ 327 (2003) 557-560.
- [18] J.P.T. Higgins, J. Thomas, J. Chandler, M. Cumpston, T. Li, M.J. Page, V.A. Welch (editors). Cochrane Handbook for Systematic Reviews of Interventions version 6.3 (updated February 2022). Cochrane, 2022. Available from www.training.cochrane.org/handbook. (Accessed: 17 July 2023)
- [19] G. Bennett, E. Young, I. Butler, S. Coe., *The impact of lockdown during the COVID-19 outbreak on dietary habits in various population groups: a scoping review*, Frontiers in nutrition 8 (2021) 626432.
- [20] F.M. Silva , J. Lima, P.P. Teixeira, G.B. Grezzana, M. Figueiro, T. Colombo, K. Souto, A.T. Stein., *Risk of bias and certainty of evidence on the association between obesity and mortality in patients with SARS-COV-2: An umbrella review of meta-analyses*, Clinical nutrition ESPEN 53 (2023) 13–25.

Classification and analysis of key parameters in predicting the state of facultative oligotrophs in two different reservoirs

Ivana Radojević^{1*}, Nenad Stefanović², Aleksandar Ostojić¹

¹ University of Kragujevac, Faculty of Science, Institute of Biology and Ecology, 34000 Kragujevac, Radoja Domanovića 12, Republic of Serbia; e-mail: ivana.radojevic@pmg.kg.ac.rs

² University of Kragujevac, Faculty of Technical Sciences Čačak, Department of Information Technologies, Svetog Save St., 65, 32102 Čačak, Republic of Serbia;

* *Corresponding author*

DOI: 10.46793/ICCB23.312R

Abstract: This study analyzes the condition, influence and dependence of facultative oligotrophs, with different physico-chemical and biological parameters determined in the routine monitoring of the status of natural water quality. The SeLaR database was used for advanced data analysis - statistical methods and data mining. Data were analyzed for reservoirs of different morphometric qualities, different positions, trophic status and dominant bacterial communities, Gruža and Grošnica. Classification and analysis of key influencing factors were applied in this research. The results indicate that the designed data mining system can successfully analyze the condition and impact of facultative oligotrophs in open waters, thus providing new information and knowledge valuable for research investigation and decision making.

Keywords: data mining, reservoirs, facultative oligotroph, classification, influential parameters

1. Introduction

For a long time, the world has been faced with the fact that there is a contradiction between different needs in drinking water and relatively clean water resources. One way to solve the problem is to build and use reservoirs. That is why there is a need to maintain the condition of the reservoirs at a satisfactory level. Continuous monitoring of water conditions, i.e., water monitoring, includes monitoring of various physical, chemical, and biological parameters. Many microbiological parameters, either from a strictly sanitary or a wider ecological aspect, indicate the nature and intensity of pollution, as well as whether the impact of the pollutant is immediate or permanent.

Various tools and techniques of information technologies, as well as methods of data analysis such as data mining, become an important part in monitoring the state of water quality, enable the prediction of changes and are important in the processes of sustainable management of water resources. Classification, modeling, and interpretation of a large amount of data is an important step when observing water quality [1]. These techniques and methods have been applied and validated as tools for monitoring microbiological quality indicators in aquatic ecosystems [2].

Therefore, the subject of this research is the application of a specialized data mining model of the SeLaR information system in the ecological analysis of the bacterial community of facultative oligotrophs (FO) in reservoirs with different morphometric qualities, positions, trophic status, and dominant bacterial community.

2. Materials and Methods

This research was performed using the SeLaR IS, which combines relevant data on reservoirs in Serbia and enables advanced methods of analysis. For the analysis of data, two reservoirs with different morphometric properties, trophic status, and dominant microbial community Gruža and Grošnica, intended for water supply, were selected. The material in this research are data sets standard routine and broader scientific hydrobiological tests from certain periods selected reservoirs. The data include physico-chemical, biochemical, microbiological and other biological parameters. Gruža - data set 3 (VI 2003. - VII 2009) and Grošnica - data set 2 (V 1997 - X 1998) were analyzed [3]. The units of measurement of all parameters are according to the standards of routine water testing and are given in section 5.1. Basic statistical overview and created models [3].

For the realization of the goal the descriptive methods, classification, and analysis of influencing factors, were used. The methods use different algorithms: a decision tree is used for classification and naïve bayes for key impacts [4].

3. Results and discussion

3.1 Classification and analysis of key influencing factors

Gruža - data set 3 has 1181 objects and Grošnica - data set 2 has a total of 182 objects. Existing values are classified into five classes. The first classes of data are the most common for both reservoirs. The classification, class values, and the number of data with probabilities are given in Table 1.

Table 1. Classification of values of facultative oligotrophs in the reservoir Gruža - data set 3 and Grošnica - data set 2.

Gruža - data set 3			
Class	Value	Number of data	Probability
1.	< 2876	771	64.63%
2.	2876-13912	150	12.75%
3.	13912-27088	26	2.39%
4.	27088-54152	13	1.31%
5.	≥ 54152	2	0.39%
-	-	219	18.52%
Grošnica - data set 2			
1.	< 307	63	33.16%
2.	307-673	42	22.56%
3.	673-1267	31	17.00%
4.	1267-1852	10	6.40%
5.	≥ 1852	8	5.39%
-	-	28	15.49%

The review of the results of the analysis of key influence parameters with impact

over 50, as well as the review of the classes with values is given in Table 2.

Table 2. Key parameters and their impact on the values of the facultative oligotrophs (FO) in the reservoir Gruža - data set 3 and Grošnica - data set 2.

Gruža - data set 3			
Parameter	Value	Class FO	Relative influence of the parameter
heterotroph psihrophile (Hp)	< 2872	< 2876	100
heterotroph mesophile (Hm)	< 1418	< 2876	50
Hp	2872-9363	2876-13912	100
depth	27	2876-13912	50
Hp	9363-20742	13912-27088	100
Hm	1418-6997	13912-27088	57
location	22-27	13912-27088	20
	20742-		
Hp	39809	27088-54152	100
Hp	≥ 39809	27088-54152	88
total coliform	≥ 1500	27088-54152	50
nitrites	0.29-0.52	≥ 54152	100
Hp	≥ 39809	≥ 54152	85
electrical conductivity	≥ 672	≥ 54152	67
Fe	0.39-1.16	≥ 54152	56
Grošnica - data set 2			
electrical conductivity			
y	≥ 458	< 307	100
Hp	< 181	< 307	96
chlorophyll			
l a	< 3.22	< 307	60
month	VI	< 307	52
Phosphatase activity index	1.42-2.94	673-1267	100
Fe	0.05	673-1267	76
Hp	181-475	673-1267	58
Cladocera	306-491	673-1267	50
Phosphatase activity index	< 1.42	1267-1852	100
ammonia	2.61-3.13	1267-1852	85
month	II	1267-1852	72
Copepoda	345-689	≥ 1852	77
Fe	0.08	≥ 1852	51
depth	3	≥ 1852	51

For reservoir Gruža for most classes of facultative oligotrophs, the most influential parameter is heterotroph psychrophile (Hp). The exception is the fifth class, where the

most influential nitrites are in higher values. For this class, high values for electrical conductivity and Fe content have a significant relative influence, but these influences can be questioned due to the extremely small number of this class. Extremely high influence, as well as the phenomenon that low values of Hp follow low values of FO, and vice versa, is consistent with the high degree of correlation between these two parameters in this data set. Among other parameters whose relative influence is greater than 50, the following stand out: lower and medium values of heterotroph mesophile (Hm) for the first and third classes; depths over 25 m for the second class; total coliform in low values for the first class and in high values for the other classes. The analysis shows the importance of the spatial distribution with higher values at the tributaries and lower values from the dam to the bridge.

In the Grošnica reservoir, the first class is most influenced by high values for electrical conductivity and low values of Hp. Average and lower values of chlorophyll a and environmental conditions in June show a high degree of influence. The second class of facultative oligotrophs is characterized by the fact that there is no high influencing parameter. For the third class of FO, there are high influences of average and lower values of phosphatase activity index and Hp, average and higher values of Fe, as well as higher values of Cladocera. In the fourth class of FO, the impacts are relatively highly significant. This class is highly influenced by low phosphatase activity index, high ammonia values and environmental conditions in February. The fifth class is highly influenced by the greater abundance of Copepoda. The highest values of FO occur in February, the lowest in July, and a depth of 3 m. High abundance of FO is conditioned by low ammonia content and vice versa.

Facultative oligotrophs have a spatial distribution in the Gruža reservoir, and a seasonal distribution in the Grošnica reservoir.

3. Conclusions

The results of this research show that developed data mining models for classification and analysis of key influencing parameters can be used in monitoring the microbiological quality of aquatic ecosystems, like reservoirs. The results provide a clear classification of the values for the FO.

Acknowledgment

This research is funded by the Ministry of Education and Ministry of Science, Technological Development and Innovation, Republic of Serbia, Grants: No. 451-03-47/2023-01/ 200122.

References

- [1] H. Boyacioglu, H. Boyacioglu, *Surface Water Quality Assessment by Environmetric Methods*. Environmental Monitoring and Assessment, 131 (2007) 371-376.
- [2] T.C. Ogwueleka, F.N. Ogwueleka, *Data mining application in predicting Cryptosporidium spp. oocysts and Giardia spp. cysts concentrations in rivers*. Journal of Engineering Science and Technology, 5 (2010) 342-349.
- [3] И.Д. Радојевић, Микробиолошки аспекти примене информационих система у мониторингу акумулација и језера, Докторска дисертација, Природно-математички факултет, Универзитет у Крагујевцу, (2012) 218 pp.

- [4] D. Harts, *Microsoft Office 2007 Business Intelligence*, McGraw_Hill, (2008). ISBN-13: 978-0071494243; ISBN-10: 00714942

Ecological applications based on bacterial community abundance in reservoirs using an artificial neural network approach

Ivana Radojević^{1*}, Aleksandar Ostojić¹, Vesna Ranković²

¹ University of Kragujevac, Faculty of Science, Institute of Biology and Ecology, 34000 Kragujevac, Radoja Domanovića 12, Republic of Serbia; e-mail: ivana.radojevic@pmg.kg.ac.rs

² University of Kragujevac, Faculty of Engineering, Department for applied mechanics and automatic control, 34000 Kragujevac, Sestre Janjić 6, Republic of Serbia

* *Corresponding author*

DOI: 10.46793/ICCB23.317R

Abstract: The objective of this study is to analyze the influence and predict abundance the heterotrophic bacteria (psychrophile; mesophile) and facultative oligotrophic bacteria as a reflection of ecological relationships in reservoirs and water quality. We used artificial neural networks (ANNs) to develop models based on input variables derived from two different reservoirs. The neural network models were developed using experimental data which is collected for ten years. Although reservoirs have a different position, different morphometric qualities, trophic state and dominant bacterial community there is a possibility of predicting these bacterial communities with the same input parameters. Comparing the modeled values by ANN with the experimental data indicates that neural network models provide accurate results. The important conclusion of this work is that ANNs can provide a flexible and applicable tool in monitoring water quality across bacterial communities in reservoirs.

Keywords: ecological application, feedforward neural network, reservoir, water quality

1. Introduction

The microbiological properties of water represent a significant and valid indicator of its quality. Heterotrophic bacteria show a high level of metabolic activity and contribute to a large extent to the process of decomposition of organic matter and its transformation. Contrary to heterotrophic bacteria the dominance of facultative oligotrophic bacteria in waters with a small amount of dissolved organic matter which favors their development as autochthonous community is confirmed. The basic problem in the case of water quality monitoring is the complexity associated with analyzing a large number of variables. The artificial neural networks (ANNs) have been successfully used as tools in the fields of water quality prediction and forecasting [1]. Much less common are the examples of the application of ANN networks as tools for predicting ecological status in aquatic systems based on the knowledge of heterotrophic and oligotrophic communities. LOBOVA et al. [2] studied the anthropogenic impact on the

prediction of community heterotrophic bacteria, and RADOJEVIC et al. [3] applied a neural network for predicting the facultative oligotrophic bacteria in two reservoirs with different trophic states. Due to the significance of heterotrophic and facultative oligotrophic bacteria in analyzing complex microbiological relations, and as indicators of water quality and ecological conditions, the objective of this study is the development of different ANN models used for the prediction of their abundance.

2. Materials and methods

2.1 Study area and water quality data

The city of Kragujevac (in the central part of Serbia) is supplied with water from Gruža and Grošnica reservoirs. The data set used in this study was generated by monitoring of the water quality of Gruža and Grošnica reservoirs. The data set includes the data of the laboratory for water quality inspection of the public utility company for water supply in Kragujevac. Monthly sampling was carried out during the period of ten years (1998 to 2008). Three permanent sampling sites were selected for qualitative and quantitative sampling for Grošnica reservoir and five sampling sites for Gruža reservoir. Samples were taken at every 5 m of depth. The data set for Gruža reservoir includes 455 data samples. The available set of data was divided into training, validation, and test subsets. In the training process of the FNN 273 samples were used. The ANN model was tested by using 91 randomly selected data. 91 data was taken for the validation set. The data set for Grošnica reservoir includes 199 data samples. In the training process of the FNN, 121 samples were used. 39 randomly selected data were taken for the validation set. The ANN model was tested by using 39 selected data. The variables of those data sets is: water temperature (T), dissolved oxygen (DO), pH, manganese (Mn), iron (Fe), electrical conductivity (EC), m-alkalinitet (m-alk.), total phosphate (TP), nitrites (NO₂⁻), ammonia (NH₄⁺), chlorophyll-a (Chl-a), chemical oxygen demand (COD), 5-day biochemical oxygen demand (BOD₅), number of heterotroph (psychrophile) (Hp), heterotroph (mesophile) (Hm) and facultative oligotroph (FO). Basic statistics of the measured water quality variables in Gruža Reservoir and Grošnica Reservoir during this period are given in the paper RADOJEVIC et al. [3].

2.2 Performance criteria and sensitivity analysis

The sensitivity analysis is based on the correlation of change percentages between inputs and outputs, where the least sensitive input is identified and deleted [4]. Pearson's correlation coefficient is one of the most used when choosing appropriate inputs for an artificial neural network. The correlation coefficient is defined as the degree of correlation between measured and modeled values:

$$R = \frac{\sum_{i=1}^{N_o} (y_i - \bar{y})(y_{mi} - \bar{y}_m)}{\sqrt{\sum_{i=1}^{N_o} (y_i - \bar{y})^2 \sum_{i=1}^{N_o} (y_{mi} - \bar{y}_m)^2}} \quad (1)$$

where \hat{y}_i and y_i represent network output and the measured value of i -th element and \bar{y} represent their average and n represent the number of observations.

2.3 Artificial neural network: model and training algorithm

To predict the condition of bacterial communities in reservoirs, there has been used non-recurrent neural network (feed-forward neural network, FNN) with different numbers of variables, depending on which bacterial community had been modeled. Levenberg-Marquardt backpropagation (LMA) was used in this study. MATLAB Neural Network Toolbox was used for the implementation of neural networks. ANN model, training algorithm, and performance criteria are given in the previous paper [5].

3. Results and discussion

3.1 Modeling and predicting H , H_m and FO using ANNs

The first phase of modeling was designed to determine suitable sets of input parameters for modeling H_p , H_m , and FO . Based on the correlation coefficient for the whole data set, the initial input parameters for a particular model were selected. The second phase of modeling used only the sets of input parameters yielding good results in the first phase and was targeted at finding the most suitable set of input parameters and the best-performing network structure. The number of hidden neurons increased stepwise to a maximum of 35. Table 1 shows the obtained models with the best performances. The reservoirs, models, selected inputs, outputs, network architecture, correlation coefficients for the whole data set, are shown. It is obvious from Table 1 that only modeling and predicting of H_p was not possible with the same input parameters in both reservoirs. In Gruža Reservoir model ANN-1- H_p shows the best qualities with the smallest number of inputs.

Table 1. Summary of artificial neural networks developed for predicting different bacteria community levels in reservoirs in Serbia.

Reservoir	ANN - output	Input variables selected	Architecture ¹	r (for all data)
Gruža	ANN-1- H_p	FO, H_m , COD	3-30-1	0.970
Grošnica	ANN-2- H_p	FO, T, TP, Fe	4-30-1	0.944
Grošnica	ANN-3- H_p	FO, T, pH, Chl- <i>a</i>	4-10-1	0.915
Gruža	ANN-4- H_m	H_p , FO, T, DO, COD, BOD5	6-30-1	0.881
Gruža	ANN-5- H_m	H_p , FO, T, DO, EC, Fe, Mn	7-30-1	0.944
Grošnica	ANN-6- H_m	FO, H_p , T, DO, EC, Fe, Mn	7-30-1	0.935
Gruža	ANN-7-FO	H_p , T, NO_2^-	3-30-1	0.947
Grošnica	ANN-8-FO	H_p , T, NO_2^-	3-30-1	0.945

¹The architecture of an ANN model is the ANN structure that presents the number of neurons in each of three layers—input, hidden, and output; ² r is the linear correlation between predicted values and measured values.

LOBOVA et al. [2] with help of artificial neural networks, and over a number of heterotrophic bacteria, successfully predict the condition of the ecosystem of a lake exposed to anthropogenic influence. Modeling and predicting Hm in two reservoirs were possible with the same input parameters. For Gruža Reservoir model ANN-5-Hm and Grošnica Reservoir model ANN-6-Hm, have the same input parameters, whereby the correlation coefficients (r) for all data are almost the same for both models. Predicting and modeling of Hm in Gruža Reservoir is possible with a smaller number of input parameters (ANN-4-Hm). RADOJEVIC et al. [3], showed that in both reservoirs modeling and predicting of FO with the same input parameters is possible (11). Table 1 shows that the number of input parameters was reduced from 11 to 3 (ANN-7-FO and ANN-8-FO). The parameters were selected according to sensitivity analysis, whereby, the top three parameters were selected. Correlation coefficients (r) for all data are better in new models (Table 1) than in the previous [3].

3. Conclusions

The models with the same inputs can predict, equally well, the number and the dynamics of bacterial communities in reservoirs with different positions, morphometric characteristics, trophic status, and dominant bacterial community. The gained knowledge contributes to a better understanding of relations, to ecological correlation and causality of the bacterial community, to more effective control, as well as to the reduction of expenses needed for monitoring the state and managing the water resources.

Acknowledgment

This research is funded by the Ministry of Education and Ministry of Science, Technological Development and Innovation, Republic of Serbia, Grants: No. 451-03-47/2023-01/ 200122.

References

- [1] K. CHAU, *A review on integration of artificial intelligence into water quality modeling*, Marine Pollution Bulletin, 52 (2006): 726-733.
- [2] T.I. Lobova, Yu.P. Lankin, L.Yu. Popova, *Assessing the anthropogenic impact on Lake Shira from antibiotic resistance of heterotrophic bacteria by neural networks methods*, Mikrobiologiya, 76 (2007) 263-270.
- [3] Radojevic I., Lj. Comic, V. Rankovic, A. Ostojic, M. Topuzovic, *Applying Neural Networks for Predicting the Facultative Oligotrophic Bacteria in Two Reservoirs with Different Trophic State*, Journal of Ecological Protection and Ecology, 14 (2013): 55-63.
- [4] Maier, H.R., Dandy, G.C. (1996): *The use of artificial neural networks for the prediction of water quality parameters*. Water Resources Research. 32 (4): 1013-1022.
- [5] V. Ranković, J. Radulović, I. Radojević, A. Ostojić, Lj. Čomić, *Neural network modeling of dissolved oxygen in the Gruža reservoir, Srbija*, Ecological modeling, 221 (2010) 1239-1244.

Oxidative DNA damage preventive activity of essential oils of three *Pinus* species: *P. mugo*, *P. sibirica*, and *P. silvestre*

Sanja Lj. Matić¹, Tamara M. Mladenović^{1*}, Milan P. Mladenović², Nevena M. Tomašević², Roberto Capobianco³, Alessio Ragno³, Filippo U. Sapienza⁴, Roberta Astolfi⁴, Rino Ragno⁴

¹ University of Kragujevac, Institute for Information Technologies Kragujevac, Department of Science, Jovana Cvijića bb, 34000, Kragujevac, Serbia; sanjamatic@kg.ac.rs, tamara.mladenovic@uni.kg.ac.rs

² University of Kragujevac, Faculty of Science, Kragujevac Center for Computational Biochemistry, Department of Chemistry, Radoja Domanovića 12, 34000, Kragujevac, Serbia; e-mail: milan.mladenovic@pmf.kg.ac.rs, nevena.tomasevic@pmf.kg.ac.rs

³ Sapienza University of Rome, Department of Computer, Control and Management Engineering "Antonio Ruberti", Via Ariosto 25, 00186 Rome, Italy; e-mail: capobianco@diag.uniroma1.it, alessio.ragno@uniroma1.it

⁴ Sapienza University of Rome, Rome Center for Molecular Design, Department of Drug Chemistry and Technology, Piazzale Aldo Moro 5, 00185 Rome, Italy; e-mail: rino.ragno@uniroma1.it, filippo.sapienza@uniroma1.it

* Corresponding author

DOI: 10.46793/ICCB23.321M

Abstract: Pharmacological properties of essential oils of *Pinus* species are mainly associated with antimicrobial, antioxidant, anticancer, anti-aging, and anti-inflammatory potencies. However, only limited scientific information has been gathered regarding the genotoxic and antigenotoxic activities of *Pinus* essential oils. Therefore, the aim of the present study was to investigate the *in vitro* DNA protective activities of three commercial essential oils of *Pinus* species: *P. mugo*, *P. sibirica*, and *P. silvestre*, against the oxidative damage induced by hydroxyl and peroxy radicals. The tested essential oils significantly reduced the DNA damage caused by the free radicals. Due to its capacity to decrease DNA damage, essential oils of *Pinus* species can be of great importance in clinical applications.

Keywords: essential oils, DNA damage, free radicals, antigenotoxicity, *Pinus*

1. Introduction

Essential oils (EOs) obtained from medicinal plants have been known to possess a number of beneficial pharmacological properties and are widely used in traditional medicine for the treatment of different disorders [1]. Also, EOs are considered to be less toxic and with fewer side-effects compared to synthetic chemicals [2], which makes them safe to be used as medicinal ingredients [3]. Reports indicate the beneficial properties of *Pinus* species such as anti-inflammatory, antioxidant [4], antineoplastic and immuno-

modulatory [5]. The *Pinus* species EOs have been used in the food and pharmaceutical industries [6] and for medicinal purposes in aromatherapy worldwide.

P. mugo Turra, *P. sibirica* Du Tour, and *P. silvestre* L. are a species of the genus *Pinus* of the Pinaceae family from the Gymnospermae class. *P. mugo*, also known as dwarf mountain pine, is used in traditional medicine for treating various illnesses such as respiratory diseases [7], coughs and throat inflammation [8]. Several studies reported anti-inflammatory, cytotoxic [9], analgesic, cardioprotective, and neuroprotective activities of *P. mugo* EO [10]. On the other hand, *P. sibirica*, known as cedar nuts, is traditionally used in folk medicine for the prevention and treatment of various diseases such as infections, wounds, rheumatism and arthritis, and for liver and kidney dysfunction [11]. Finally, *P. sylvestre*, also known as scots pine, is a traditional remedy with antibacterial, antifungal, anti-inflammatory, antioxidant, antiseptic, anti-parasitic, anti-viral, anti-allergenic, antispasmodic, and anti-hyperglycemic activities [12]. Besides, there have been studies on the potential therapeutic value of *P. mugo*, *P. sibirica*, and *P. silvestre* EOs, but not sufficient literature data has been published regarding their genotoxic and/or antigenotoxic properties. Therefore, this study aims to evaluate their *in vitro* antigenotoxic effects using two antioxidative assays. To the best of our knowledge, this report is the first to investigate the antigenotoxic properties of these three *Pinus* species.

2. Materials and methods

2.1. Essential oils

Essential oils (Farmalabor srl, Assago, Italy) were dissolved in dimethyl-sulfoxide (DMSO) at 50 mg/mL to obtain complete solubilization and further diluted in the medium for *in vitro* experiments.

2.2. The protective activity of essential oils against hydroxyl and peroxy radicals induced DNA damage

The protective effect of commercial essential oils (25, 50, 100, 200, and 400 µg/mL) against hydroxyl and peroxy radicals induced DNA damage was assessed *in vitro* using the salmon sperm DNA [13, 14]. In both assays, quercetin (100 µg/mL) was used as a standard drug [15]. DNA bands on the agarose gels were visualized under UV light (UV transilluminator, Vilber Lourmat, France) at 365 nm, photographed and analyzed using ImageJ software (version 1.48 for Windows, Softonic International, Barcelona, Spain).

2.3. Statistical analysis

Results were expressed as mean±SD and statistical evaluation of data was analyzed with one-way analysis (ANOVA) using SPSS statistical software package, version 13.0 for Windows. The significance level was set at $p < 0.05$.

3. Results and Discussion

To explore the potential DNA protective activities of three commercial EOs against the hydroxyl radicals, formed in a Fenton-type decomposition of H₂O₂ catalysed by

FeSO₄, as well as against the peroxy radicals, formed after the *in situ* oxidation of 2,2'-azobis(2-amidinopropane) dihydrochloride (AAPH) with molecular oxygen, two oxidative DNA damage protective activity assays were performed.

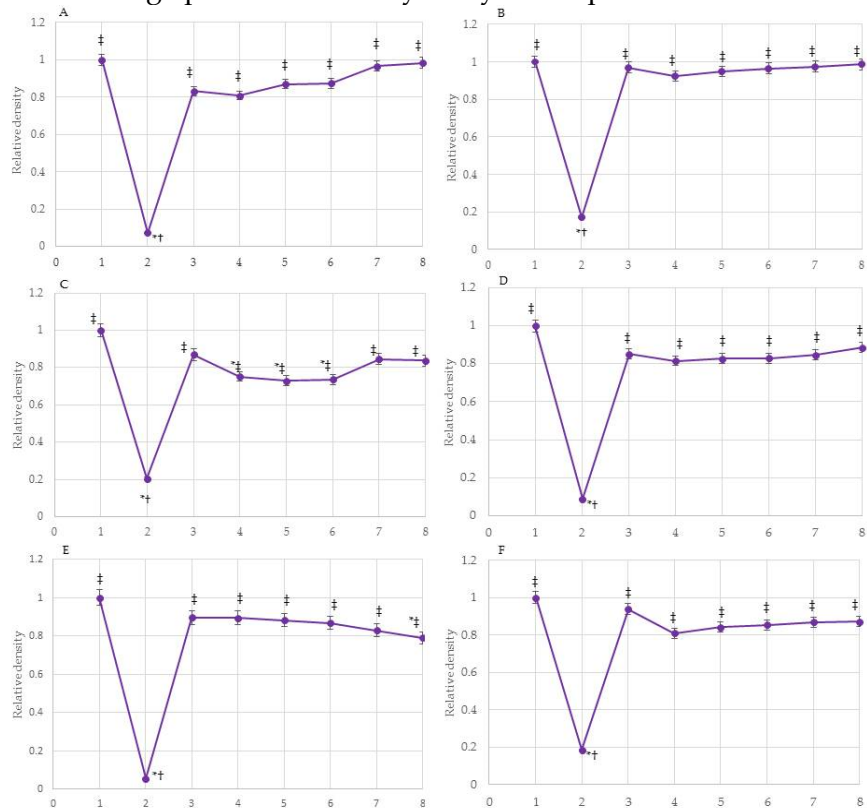


Figure 1. Protective effect of essential oils of *P. mugo* (A and B), *P. sibirica* (C and D), and *P. silvestre* (E and F) against hydroxyl and peroxy radicals-induced DNA damage. DNA from salmon sperm (1, negative control), DNA damage control (2, positive control), quercetin (3, 100 µg/mL, standard), essential oil in concentrations of 25, 50, 100, 200, and 400 µg/mL (4, 5, 6, 7, and 8). **p* < 0.05 when compared with the negative control, †*p* < 0.05 when compared with the standard, ‡*p* < 0.05 when compared with the positive control.

The DNA protective activity against the damage induced by hydroxyl (Figure 1A) and peroxy (Figure 1B) radicals of different concentrations of *P. mugo* EOs has been dose-dependent, increasing with the rise of concentrations applied. In concentrations from 25 to 400 µg/mL, *P. sibirica* essential oil showed effective and concentration-dependent reduction in the DNA damage induced by both radicals, which was better as the administered doses increased (Figure 1C and D). Distinct EO at high concentrations (200 and 400 µg/mL) showed better DNA protective activity against DNA damage induced by peroxy than for hydroxyl radicals. *P. silvestre* EO at high concentrations (200 and 400 µg/mL) had a weak scavenging activity on hydroxyl radicals (Figure 1E) and was significantly more effective in scavenging peroxy radicals (Figure 1F). According to the experimental findings, the highest DNA protective activity against free radicals was found in *P. mugo* EO, and the lowest DNA protective potential against peroxy radicals was determined in *P. sibirica* and *P. silvestre* EOs.

4. Conclusions

The results from the present study indicated that the tested essential oils are valuable natural agents with a high degree of hydroxyl radical scavenging activity and ability to scavenge peroxy radicals.

Acknowledgment

This research is funded by the Ministry of Science, Technological Development, and Innovation, Republic of Serbia, Grants: Nos. 451-03-47/2023-01/200122 and 451-03-47/2023-01/200378.

References

- [1] M. Basholli-Salih, R. Schuster, A. Hajdari, D. Mulla, H. Viernstein, B. Mustafa, M. Mueller., *Phytochemical composition, anti-inflammatory activity and cytotoxic effects of essential oils from three Pinus spp.*, *Pharmaceutical Biology*, 55 (2017) 1553-1560.
- [2] M. Paw, R. Gogoi, N. Sarma, S.K. Pandey, A. Borah, T. Begum, M. Lal., *Study of anti-oxidant, anti-inflammatory, genotoxicity, and antimicrobial activities and analysis of different constituents found in rhizome essential oil of Curcuma caesia Roxb., collected from north east India*, *Current Pharmaceutical Biotechnology*, 21 (2020) 403-413.
- [3] S. Garzoli, V.L. Masci, V. Caradonna, A. Tiezzi, P. Giacomello, E. Ovidi., *Liquid and vapor phase of four conifer-derived essential oils: comparison of chemical compositions and antimicrobial and antioxidant properties*, *Pharmaceuticals* 14 (2021) 134.
- [4] A. Guri, P. Kefalas, V. Roussis., *Antioxidant potential of six pine species*, *Phytotherapy Research*, 20 (2006) 263-266.
- [5] K. Li, Q. Li, J. Li, D. Gao, T. Zhang, Z. Han, F. Zheng., *Effect of procyanidins from Pinus koraiensis bark on growth inhibition and expression of PCNA and TNF- α in mice with U14 cervical cancer*, *Therapy*, 4 (2007) 685-690.
- [6] E. Sezik, U. Osman, B. Demirci, K.H.C. Baser, *Composition of the essential oils of Pinus nigra Arnold from Turkey*, *Turkish Journal of Chemistry*, 34 (2010) 313-325.
- [7] E. Dumitru, R. Dumitru., *Terapia naturistă. incursiune in farmacia naturii*; Editura Științifică: Bucharest, Romania, 1992.
- [8] S. Vitalini, M. Iriti, C. Puricelli, D. Ciuchi, A. Segale, G. Fico., *Traditional knowledge on medicinal and food plants used in Val San Giacomo (Sondrio, Italy)—An Alpine ethnobotanical study*, *Journal of Ethnopharmacology*, 145 (2013) 517-529.
- [9] M. Basholli-Salih, R. Schuster, A. Hajdari, D. Mulla, H. Viernstein, B. Mustafa, M. Mueller., *Phytochemical composition, anti-inflammatory activity and cytotoxic effects of essential oils from three Pinus spp.*, *Pharmaceutical Biology*, 55 (2017) 1553-1560.
- [10] M. Bottoni, F. Milani, L. Colombo, K. Nallio, P.S. Colombo, C. Giuliani, P. Bruschi, G. Fico., *Using medicinal plants in Valmalenco (Italian Alps): from tradition to scientific approaches*, *Molecules*, 25 (2020) 4144.
- [11] A.N. Shikov, V.G. Makarov, V.E. Ryzhenkov., *Plant fixed oils and oil extracts: Technology, standardization, properties*, Moscow: Publishing house Russian Doctor, (2004) 177-185,
- [12] G.K. Silori, N. Kushwaha, V. Kumar., *Essential oils from Pines: chemistry and applications*. In: S. Malik (ed) *essential oil research, trends in biosynthesis, analytics, industrial applications and biotechnological production*. Springer, Cham., 2019.
- [13] Y.W. Lin, Y.T. Wang, H.M. Chang, J.S.B. Wu., *DNA protection and antitumor effect of water extract from residue of jelly fig (Ficus awkeotsang Makino) achenes*, *Journal of Food and Drug Analysis*, 16 (2008) 63-69.

- [14] L.L. Zhang, L.F. Zhang, J. G. Xu, Q. P. Hu., *Comparison study on antioxidant, DNA damage protective and antibacterial activities of eugenol and isoeugenol against several foodborne pathogens*, Food and Nutrition Research, 61 (2017), 1353356.
- [15] C.A. Poorna, M. Resmi, E. Soniya., *In vitro antioxidant analysis and the DNA damage protective activity of leaf extract of the Excoecaria agallocha linn Mangrove plant*. In: Stoytcheva, M. (Ed.), Agricultural Chemistry. Intech, UK, 2013.

Comparative assessment of fish diversity indices in protected Vlasina Reservoir and unprotected Gruža Reservoir

Marija M. Jakovljević^{1*}, Simona R. Đuretanović¹, Marijana D. Nikolić¹, Nataša M. Kojadinović¹, Milena D. Radenković¹, Predrag M. Simović¹, Vladica M. Simić¹

¹ University of Kragujevac, Faculty of Science, Department of Biology and Ecology, Kragujevac, Serbia

DOI: 10.46793/ICCB23.326J

* *Corresponding author*

Abstract: The species diversity indices, namely the Shannon Index (H), Reciprocal Simpson's Index (1/D), Fisher's Alpha Diversity Index (A), and Pielou's Evenness Index (J), were calculated for both the protected Vlasina Reservoir and the unprotected Gruža Reservoir. A total of 15 fish species were identified in the Vlasina Reservoir during the investigation period from 2003 to 2022, while the Gruža Reservoir revealed 10 fish species within the period from 2013 to 2021. The obtained values of the H, 1/D, and A indices, were not considerably high, sometimes even lower than expected, showing a slight increase in recent years for both reservoirs. In Vlasina Reservoir, the J Index was in a range from 0.2488 to 0.3348, while in Gruža Reservoir it varied from 0.1834 to 0.3832, indicating the low homogeneity in terms of well-balanced fish assemblage structure. Moreover, an increasing trend in recent years has been observed, which favors the dominance of some fish species against the balanced fish structure. Our results provide valuable information about fish diversity and evenness in the investigated areas under high anthropogenic threats, considering the importance of both reservoirs in Serbia.

Keywords: fish diversity indices, fish assemblage structure, Serbia

1. Introduction

The Vlasina Reservoir is ranked among the largest and highest artificial lakes in Serbia, with a system of four hydroelectric power, while Gruža Reservoir is the most important artificial lake in Central Serbia, mainly used for the water supply of Kragujevac. Both reservoirs have been faced with strong anthropogenic threats, even though Vlasina has been protected in Serbia [1]. Some of the main anthropogenic pressures are the development of unplanned urbanization which leads to the spreading of agricultural lands and waste depots, agricultural discharge, as well as sewage discharge. Additionally, the considerable water level regulation, boosting tourism and recreational fishing, construction of roads, etc. significantly impact both reservoirs [2]. From the aspect of the fish species diversity in fish assemblage structure, the most severe anthropogenic impact has been the inadequate fish introduction in both reservoirs [1,3].

This study aimed to assess the fish diversity and evenness indices in some protected and unprotected areas under severe anthropogenic threats, without the intention to compare these two reservoirs due to their different origin, and hydrological, geological, and morphological characteristics.

2. Material and methods

2.1 Sampling collection

The fish specimens were collected during the five-field sampling from the Vlasina Lake Reservoir spanning the period 2003–2022, and from the Gruža Reservoir covering the period 2013–2021, following the standard procedure (Figure 1). The ichthyological research on both reservoirs was conducted to develop fisheries management plans for the protection and sustainable use of fish stocks.

2.2 Fish Diversity Indices

The basic diversity indices of the fish community were determined: species richness (S), Shannon Diversity Index (H), and Alpha Diversity Index (A) or Fisher's Alpha diversity index (A) [2]. The Simpson's Index (D) was used to measure the probability that two randomly chosen specimens from a sample will belong to different fish species. Due to the potential errors during the reverse interpretation of the obtained results, Simpson's Index was expressed as Reciprocal Simpson's Index (1/D) because its value increased with greater diversity [2]. Additionally, the link between the number of species and their abundances is determined with Fisher's Alpha diversity index (A) [2,4]. Pielou's evenness (J) was used to compare the actual diversity value (H index) to the maximum possible diversity value (ln S). It is constrained between 0 and 1 and the more variation in abundances between different fish species within the community, the lower J [4]. All fish diversity indices were calculated using BioDiversityPro version 2 software.

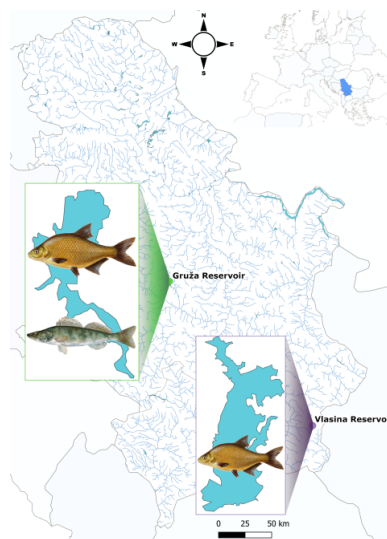


Figure 1. The map of the investigated reservoirs with highlighted dominant fish species.

3. Results and discussion

The obtained results of fish diversity and evenness indices in investigated reservoirs were summarized and presented in Table 1.

Table 1. Diversity indices were calculated based on sampled fish species at individual localities of the Vlasina Reservoir and the Gruža Reservoir.

Localities	Species richness S	Shannon Index H	Reciprocal Simpson's Index 1/D	Alpha Index A	Evenness Index J
Vlasina Reservoir 2022	7	0.6515	3.5906	1.4702	0.3348
Vlasina Reservoir 2019	7	0.6038	3.4340	1.1239	0.3102
Vlasina Reservoir 2016	8	0.5426	2.4950	1.3415	0.2609
Vlasina Reservoir 2014	6	0.5892	3.0845	0.9113	0.3288
Vlasina Reservoir 2003	8	0.5175	2.0889	1.5118	0.2488
Gruža Reservoir 2021	5	0.6047	3.6683	1.1550	0.3757
Gruža Reservoir 2020	7	0.7457	4.7258	1.4576	0.3832
Gruža Reservoir 2019	5	0.4914	2.3963	0.7882	0.3053
Gruža Reservoir 2017	9	0.4107	1.8608	1.2559	0.1869
Gruža Reservoir 2013	5	0.2953	1.5186	0.6616	0.1834

A total of 15 fish species were identified during the investigation period in the Vlasina Reservoir, while the Gruža Reservoir had 10 fish species identified. The species richness diversity for both reservoirs is presented in Table 1. According to the available literature on the Vlasina Reservoir, a total of 16 fish species have been previously documented [1,3]. Comparing with these data, our results indicate the changes in the composition and structure of the fish community since we did not register the *Salmo trutta* L. and *Barbus peloponessius* (Valenciennes, 1842) but there were abundant *Abramis brama* L. as well as *Carassius gibelio* (Bloch, 1782), while the *Alburnus albidus* (Costa, 1838; Vulnerable according to IUCN) and *Rutilus pigus* (Lacepède, 1803) have not been registered since 2003. According to Simić et al. [1], *A. brama* was introduced to the Vlasina Reservoir between 1998 and 2010. Personal observation suggests that *Esox lucius* L. and *Silurus glanis* L. have been present in recent years, likely due to frequent catches by fishermen. On the other side, in the Gruža Reservoir *A. brama* stood out as the dominant fish species, along with *Sander lucioperca* L. and *Rutilus rutilus* L. It has been observed the stagnation of previously dominant fish *C. gibelio* in the last year.

The Shannon Index (H) values in the Vlasina Reservoir have varied from 0.5175 to 0.6515, while in the Gruža Reservoir were in the range of 0.2953 to 0.7457 (Table 1). Although we obtained the moderate and lower values of the H index, interestingly an increasing trend in recent years in both reservoirs has been observed. Generally, the values of Shannon Index, Reciprocal Simpson's Index, as well as Fisher's Alpha Index were not considerably high and sometimes were even lower than expected, which could be a consequence of the strong anthropogenic pressure [2]. Both reservoirs faced

inadequate anthropogenic introduction of attractive fish species for recreational fisheries improvement, which led to the disappearance of native species and changes in fish species' relative abundances [1,3]. Consequently, of the native species' reduction in abundance, the tendency toward non-native fish species dominance has been observed. Moreover, in both reservoirs, we registered the occurrence of invasive fish species (*Lepomis gibbosus* L. and *Ameiurus nebulosus* Lesueur, 1819) [5]. In the Vlasina Reservoir, the Pielou's Evenness Index ranged from 0.2488 to 0.3348, whereas in the Gruža Reservoir, it varied between 0.1834 and 0.3832. Evenness indices show how homogeneous the fish community is, it can be even seen as an ecosystem, considering different fish species' abundances [4]. To be more precise, the evenness index represents the distribution of specimens among different fish species. Our results, obtained for both reservoirs, indicated a low level of homogeneity in terms of a well-balanced fish assemblage structure. Moreover, an increasing trend in recent years has been observed, favoring the dominance of certain fish species over a balanced fish structure.

4. Conclusions

Our results provide valuable information about fish diversity and evenness in the investigated areas under high anthropogenic threats, considering the importance of both reservoirs in Serbia.

Acknowledgment

This research is funded by the Ministry of Education and Ministry of Science, Technological Development and Innovation, Republic of Serbia, Grants: No. 451-03-47/2023-01/200122.

References

- [1] V. Simić, S. Simić, M. Paunović, P. Simonović, N. Radojković, A. Petrović., *Scardinius knezevici* Bianco & Kottelat, 2005 and *Alburnus scoranza* Bonaparte, 1845: New species of ichthyofauna of Serbia and the Danube basin, *Archives of Biological Science*, 64 (2012) 981-990.
- [2] I. Buj, S. Pleše, L. Onorato, Z. Marčić, P. Mustafić, D. Zanella, M. Čaleta, L. Ivić, L. Novoselec, N. Renić, S. Horvatić, R. Karlović, G. Tvrđinić., *The ichthyofauna of the Bednja River, ichthyological „hot spot“ in the Danube Basin—Exceptional diversity under strong threats*, *Water* 15 (2023) 311.
- [3] P. Simonović, V. Nikolić., *Ichthyofauna of the Vlasinsko jezero reservoir (Serbia, Yugoslavia)*, *Archives of Biological Science* 47 (1995) 71-74.
- [4] M. Ulfah, S.N. Fajri, M. Nasir, K. Hamsah, S. Purnawan., *Diversity, evenness and dominance indeks reef fish in Krueng Raya Water, Aceh Besar*, *IOP Conf. Series: Earth and Environmental Science* 348 (2019) 012074.
- [5] Z. Marinović, J. Lujić, V. Bolić-Trivunović, G. Marković., *Comparative study of growth in *Carassius gibelio* (Bloch, 1782) and *Rutilus rutilus* (L., 1758) from two Serbian reservoirs: Multi-model analysis and inferences*, *Fisheries Research* 173 (2016) 11–16.

Assessment of different machine learning tools employed in lipidomics

David Pirić^{1*}, Romana Masnikosa¹

¹ University of Belgrade, Vinča Institute of Nuclear Sciences - National Institute of the Republic of Serbia, Department of Physical Chemistry, Mike Petrovića Alasa 12-14, 11000 Belgrade, Serbia; e-mail: david.piric@vin.bg.ac.rs, romana@vin.bg.ac.rs

* *Corresponding author*

DOI: 10.46793/ICCB23.330P

Abstract: Herein we present the potential of four machine learning (ML) algorithms: Partial Least Squares - Discriminant Analysis (PLS-DA), Random Forests (RF), Support Vector Machines (SVM) and Decision Trees (DT) to classify human plasma samples into cancer or control group, using a lipidomic dataset retrieved from the research article "Lipidomic profiling of human serum enables detection of pancreatic cancer" by Wolrab et al. [1]. Our main objective was to assess and compare, for the four ML techniques, the performance metrics, that is accuracy, precision, sensitivity, F1 score and ROC-AUC, with those computed by Orthogonal Projections to Latent Structures (OPLS)-DA in [1]. Our findings suggest that SVM and RF offer a superior performance as binary classifiers, making these two promising candidates for future use in the discovery of potential lipidomic biomarkers.

Keywords: machine learning, lipidome, classification, random forests, support vector machines

1. Introduction

In recent years lipidomics has emerged as an influential scientific field that provides a deep insight into the intricate lipidomic landscape of biological systems. A vast area of interest is the study of lipidomic alterations in the plasma of diseased individuals, due to the availability of this biological liquid. The primary goal of many lipidomic studies is to discover a lipid signature of a disease that can be further developed into a potential diagnostic or prognostic biomarker. A typical lipidomic experiment produces a big dataset, consisting of hundreds of lipids measured in hundreds of samples. Powerful machine learning (ML) algorithms are wanted if one wants to extract the biological meaning out of lipidomics data. To assess the biomarker potential of lipid species, lipidomics dataset is often combined with orthogonal projections to latent structures discriminant analysis (OPLS-DA). One such example is the pancreatic cancer lipidomic study, where concentrations of 168 lipids in plasma samples from 262 cancer patients and 102 healthy controls were measured, as published in the article of Wolrab et al. [1]. The aim of the original study was to investigate the lipid marker patterns in this cancer. OPLS arrives at a linear transformation that

converts the data to a lower dimensional space, while trying to keep as much information contained in the original dataset as possible. However, when the relationship between input variables and the response is non-linear, as is often the case in biology, linear models perform sub-optimally. Herein, we examined the potential of non-linear ML techniques: random forests (RF) and decision trees (DT) as binary classifiers, working on the testing set retrieved from the ref. [1], in parallel with the partial least squares discriminant analysis (PLS-DA), often used in the lipidomics community and support vector machines (SVM). We evaluated metrics of our PLS-DA, RF, SVM and DT binary classifiers in comparison to that originally used, that is OPLS-DA.

2. Materials and methods

For the present study, molar concentrations [nmol/mL] of lipid species measured in human plasma using Ultrahigh-Performance Supercritical Fluid/Mass Spectrometry were retrieved from ref [1]. The dataset format 364 x 168 was divided into a training and testing set (80/20), by random choice. The models were built using the training set and verified using the testing set. Four different ML algorithms: PLS-DA, DT, RF and SVM were used to compute binary classifiers. The PLS-DA model was built from unit-variance-scaled data. In RF and SVM, set.seed was 1. In RF, mtry and ntree were selected to minimize the class-separated (cancers vs. controls) errors. In SVM, for the sake of simplicity, a linear kernel and type C-classification were chosen, while the cost was set to 10. An automatic search for the best combination of parameter values was used by iterating over a range of possible values and testing each combination against a performance metric to find one that produces the best results. ML modeling was performed in the R software environment and its packages (<https://www.r-project.org>, v 4.3.1).

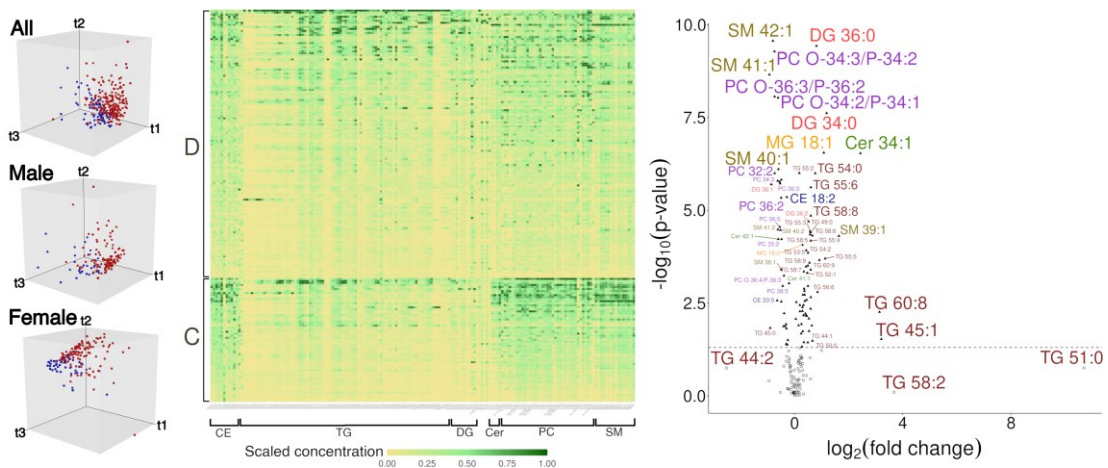
3. Results and discussion

PLS-DA was a better classifier of cancer and healthy control samples when the lipidomic dataset was gender-separated, in comparison to non-separated dataset (Figure 1, left). From this point on, we displayed the single-gender lipid status, plots and models, specifically those for females. The plasma lipidomic landscape (132 cases + 61 controls) is depicted as a heatmap, whereas the most significantly altered lipid species can be seen in the Volcano plot (Figure 1).

Knowing that ML models operate in a high-dimensional space defined by a large number of variables, by RF and SVM, we computed new variables/dimensions so that the dataset can be plotted in a low-dimensional space. That was a 3D space for our RF models, where dimensions Dim1, -2 and -3 still kept a great deal of information contained in the original lipid dataset (Figure 2, left). Figure 2. displays four different binary classifiers, which enabled a distinction between plasma levels of lipid species in cases and controls: supervised and unsupervised RF, SVM and DT model. The model

scores calculated for test samples were further used to calculate the predictive power of models in terms of accuracy, sensitivity, F1 score, receiver operating characteristic (ROC) and area-under-the-ROC-curve (AUC), all listed in Table 1. The main complaint of life scientists is that a typical ML model is a “black box”, i.e., no one understands the real nature of derived variables, or how to go from scores/dimensions/principal components back to the originally measured variables and draw the biological meaning. The only exception is DT (see Figure 2, right), where the lipids whose plasma levels had the greatest effect on the binary classification were obvious. Although the simplest to comprehend, DTs are the weakest learners. Apart from the binary classification, we extracted the importance of individual features – plasma levels of lipid species, in building the classifiers. As an example, in Figure 3, we show the significant lipid variables recognized by three supervised ML models: PLS-DA, RF and SVM. Finally, Table 1 shows the performance of four binary classifiers from the present study in parallel to the original OPLS-DA, all built using the same lipidomic dataset from [1].

Figure 1. from left to right: PLS-DA score plots representing all samples, only males, and only



females, cases are displayed as red circles, while controls are blue circles, t1, t2 and t3 are PLS-computed variables; Heatmap shows concentrations of plasma lipid species measured in cases (D) and controls (C), the concentrations were min-max scaled and shown from the lowest to the highest average scaled concentration; Volcano plot displayed as $-\log_{10}(p\text{-value})$ against $\log_2(\text{FC})$, p -values were from between-groups (cases vs. controls) comparisons of the means of lipid levels, fold change (FC) is the ratio of mean concentrations in cases and controls, triangles represent significantly altered lipid species ($p\text{-value} < 0.05$), whereas circles all others.

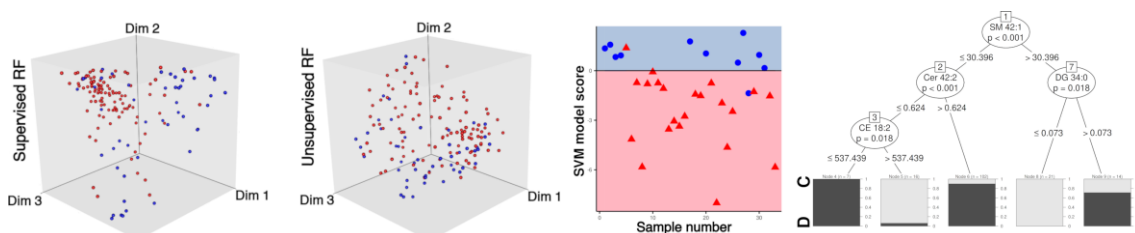


Figure 2. from left to the right: Supervised and unsupervised RF scatter plots, cases are in red, controls in blue; SVM model score for the testing set, cases are red triangles, controls are blue circles; DT model for cases(D) and controls (C), with adjusted p -values based on multiplicity (“Bonferroni”).

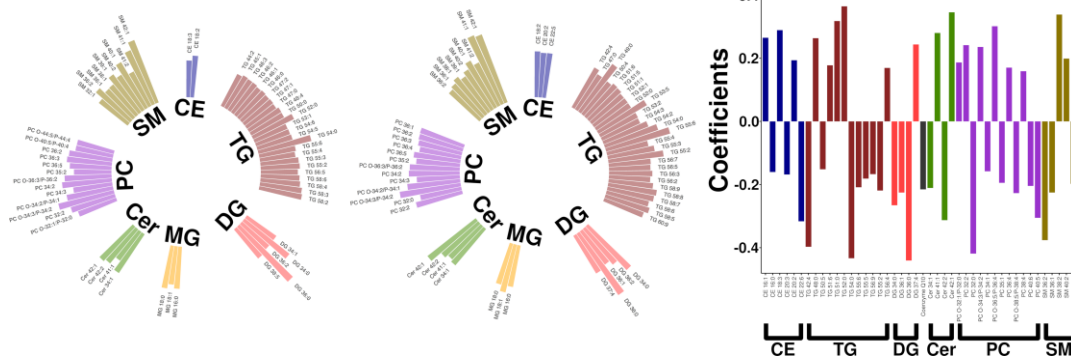


Figure 3. from left to right: Variable Importance in Projection (VIP) from PLS-DA (> 1 are shown); Mean decrease in Gini from the supervised RF (> 0.3 are shown); Coefficients from SVM with absolute values greater than 0.15. The RF parameters were mtry = 21 and ntree = 250.

Table 1. Comparison of different binary classifiers.

Model	Accuracy	Precision	Sensitivity	F1_score	AUC_ROC
PLS-DA	0.879	0.875	0.954	0.913	0.841
OPLS-DA	0.879	0.875	0.954	0.913	0.841
DT	0.818	0.786	1.000	0.880	0.727
RF	0.879	0.875	0.954	0.913	0.841
SVM	0.939	0.954	0.954	0.954	0.932

4. Conclusions

To sum up, although not intuitive at first glance, RF and SVM proved to be pretty good models for the binary classification in the pancreatic cancer lipidomic dataset retrieved from [1]. However, in order to extract the biological knowledge from RF and SVM, one needs to combine knowledge-based data mining, connect variable importance with metabolic/signaling pathways, and conduct deep feature and pathway enrichment analyses.

Acknowledgment

This research is funded by the Ministry of Science, Technological Development and Innovation, Republic of Serbia, Grants: No. 451-03-47/2023-01/200017.

References

[1] D. Wolrab et al., *Lipidomic profiling of human serum enables detection of pancreatic cancer*, Nature communications, 13 (2022), 124, doi: 10.1038/s41467-021-27765-9.

Slight cooling during growth induced changes in filamentous fungi hypha mitochondrial morphology

Aleksandra Vitkovac¹, Tanja Pajić^{1*}, Marta Bukumira², Marina Stanić³, Mihailo Rabasović², Nataša Todorović⁴

¹ University of Belgrade, Faculty of Biology, Department for General Physiology and Biophysics, Belgrade, Serbia (Studentski trg 16, 11158); e-mail: b1039_2022@stud.bio.bg.ac.rs, tpajic@bio.bg.ac.rs

² University of Belgrade, Institute of Physics, Laboratory for Biophysics, Belgrade, Serbia (Pregrevica 118, 11080); e-mail: marta@ipb.ac.rs, rabasovic@ipb.ac.rs

³ University of Belgrade, Institute for Multidisciplinary Research, Department of Life Sciences, Belgrade, Serbia (Bulevar despota Stefana 142, 11060); e-mail: mstanic@imsi.rs

⁴ University of Belgrade, Institute for Biological Research "Siniša Stanković", Department of Neurophysiology, Belgrade, Serbia (Bulevar despota Stefana 142, 11060); e-mail: nara@ibiss.bg.ac.rs

* Corresponding author

DOI: 10.46793/ICCBi23.334V

Abstract: Adaptive changes in mitochondrial morphology are associated with changes in the mitochondrial function and metabolic fitness of eukaryotic cells. We previously described in young hyphae of the filamentous fungus *Phycomyces blakesleeanus* a dramatic effect of an increase in ambient temperature during growth: a 3°C warmer environment compared with a control temperature of 22°C resulted in the appearance of long elongated ("tubular") mitochondria accompanied by an increase in lipid droplet density. Here, we examined how cooler ambient temperature (18°C) during growth affects mitochondrial morphology in *P. blakesleeanus* compared with the control grown at 22°C. We used two-photon fluorescence imaging (TPEF) of live hyphae stained with the vital mitochondrial dye rhodamine 123. Extraction of relevant parameters (number, size, and shape of mitochondria) from TPEF images was performed using the Ilastik machine learning-based software. The suitability of the Ilastik analysis was compared with the Particle Analysis (ImageJ). Cold treatment resulted in the appearance of tubular mitochondrial morphology that was absent in the control group. Tubular mitochondrial morphology appears to be an adaptive feature that occurs in both warmer and colder conditions and is likely part of the stress response.

Keywords: *Phycomyces*, Imaging, TPEF, Machine-learning, Ilastik

1. Introduction

Mitochondria are very plastic organelles capable of morphologically adapting in order to meet cellular needs. The conditions that require more efficient quality control or greater respiratory capacity lead to fragmentation or fusion of mitochondria,

respectively [1]. We have previously shown that a 3°C warmer environment induces the appearance of tubular mitochondria in the filamentous fungus *Phycomyces blakesleeanus* [2]. Here we investigate the effects of a 3°C cooler environment on mitochondrial morphology.

2. Methods

Hyphal cells of the unicellular filamentous fungus *Phycomyces blakesleeanus* (Burgeff), wt (NRRL 1555(-)), were grown in illuminated stationary plates at 22°C for 16-21 h, as described previously [3], or at 18°C for cold treatment. Mitochondria stained with 5 μM rhodamine123 (Rhd123) were imaged *in vivo* by two-photon fluorescence microscopy (TPEF) of hyphae. Images were obtained from five separate cultures. For two-photon excitation of Rhd123, we used a Ti:Sa laser tuned to 800 nm (160 fs pulse duration, 76 MHz repetition rate) focused with the Zeiss Plan Neofluar 40x1.3 objective. The signal was detected through a MF530/43 bandpass interference filter (ThorLabs, USA). Details of the experimental setup for TPEF were described in [4]. Raw images were analyzed in both Ilastik and ImageJ Particle Analysis software packages using individually thresholded images to achieve high-quality segmentation of the bright structures representing mitochondria. Only images with a sufficiently high signal-to-noise ratio (to clearly distinguish the structures from the background) were analyzed. Statistics: ANOVA with multiple comparisons and Holm-Sidak correction, and an unpaired two-tailed t test with Welch's correction for unequal variances. Confidence levels for statistical significance were: 0.05 (*), 0.01 (**), 0.005 (**).

3. Results and Discussion

TPEF images showed that Rhd123-stained mitochondria of different shapes and sizes were distributed throughout the control hyphae (n = 6) and that there was no conspicuous region of high density in the growing hyphal tip (Fig. 1a, left). In cold-treated hyphae (n = 12), there was a similar range of mitochondrial shapes and sizes as in the control group, except for some longer mitochondria (Fig. 1a, right). To quantify mitochondrial morphology in an efficient and accurate manner, we trained a machine learning-based software routine in Ilastik to sort them into groups: round, ellipsoid, and elongated. The classifications obtained, such as the example shown in Fig. 1b (a colored mask superimposed on the image), matched well with the initial images. The same images were subjected to ImageJ Particle Analysis (Fig. 1c), and the obtained morphological measures were compared with the Ilastik-derived data for each hypha (Fig. 1d,e). The number of mitochondria determined by ImageJ was significantly lower than the number counted by Ilastik ($p < 0.0001$) (Fig. 1d left), while the total area occupied by mitochondria was similar in ImageJ and Ilastik ($p=0.46$) (Fig. 1d right). Visual inspection of the ImageJ-generated masks confirmed that many individual mitochondria were not well separated. Therefore, we analyzed the Ilastik-generated dataset in more detail. The results are shown in Fig. 2.

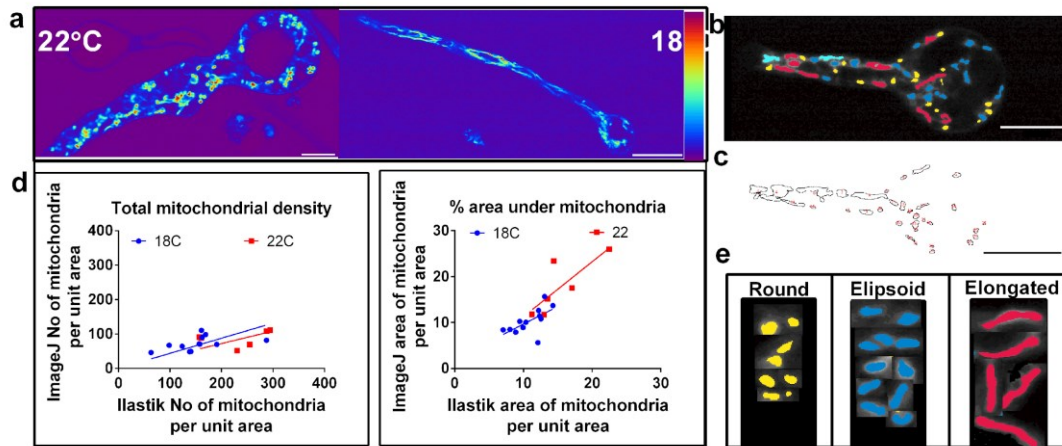


Figure 1. Mitochondrial morphology analysis from *P. blakesleeanus* hypha TPEF images. a.) Representative TPEF images of Rhd123-stained hypha grown in control (22°C) and cool (18°C) conditions. The color bar on the right, blue indicates lowest signal values. b-c.) Results of segmentation during image analysis using Ilastik (b) and Particle Analysis in ImageJ (c). d.) Comparison of values obtained by Ilastik and ImageJ analysis: Mitochondrial density (left) and percent of hyphal area occupied by mitochondria (right). All points are shown, with obtained linear fit coefficients: for mitochondrial density, $k = 0.44 \pm 0.04$ (18°C) and $k = 0.36 \pm 0.05$ (22°C); for % area under mitochondria, $k = 0.76 \pm 0.3$ (18°C) and $k = 1.2 \pm 0.4$ (22°C). e.) Representative examples of shapes of mitochondria for each of the main morphology groups: round, ellipsoid and elongated. Scales are shown in the bottom of images: a.) 10 μm (left) and 20 μm (right); b.) 10 μm ; c.) 10 μm .

We found that the number of mitochondria per unit area of hyphae (Fig. 2a) was lower in the 18°C group, which is consistent with the expected changes in mitochondrial morphology toward greater connectivity during adaptation to stress. On the other hand, the finding that the total area under the mitochondria (Fig. 2b) decreased with cooling suggests an increase in mitophagy, or alternatively, that increased fragmentation of mitochondria resulted in a portion of very small structures below the detection limit (submicron size). Overall, these results suggest that the dynamic restructuring of the mitochondrial network occurs in cooled hyphae. We examined a subset of representative hyphae from both groups in more detail. The density of each morphological type was similar in both groups, so the data were pooled (Fig. 2c). The length of the mitochondria in each morphological group is shown in Fig. 2d for the 22°C group and in Fig. 2e for the 18°C group. Significantly longer elongated (tubular) mitochondria were found in the 18°C group compared with the 22°C group (Fig. 2f).

3. Conclusions

The tubular morphology of mitochondria is an adaptive feature that occurs under colder conditions, similar to the changes previously observed in warmer environments, and is likely part of the stress response. Slight changes in ambient temperature can elicit a mitochondrial response, that is, dynamic changes in morphology.

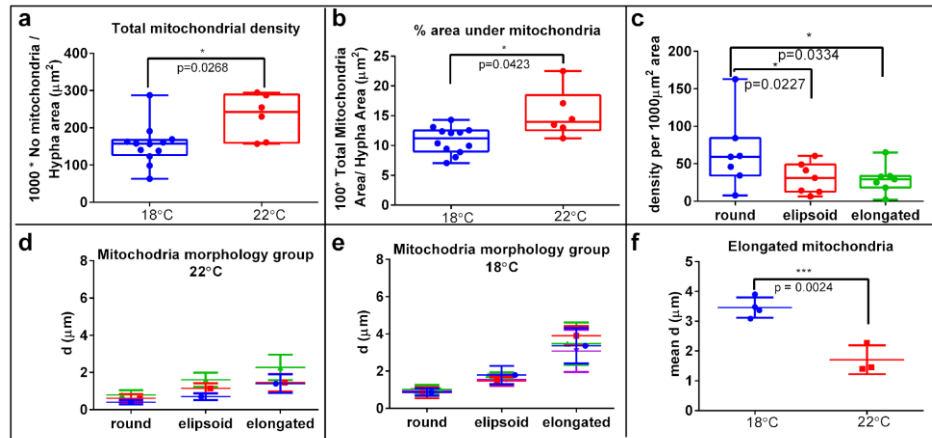


Figure 2. Parameters of mitochondrial morphology obtained from Ilastik image analysis, shown as box and whiskers plots enclosing the 25th and 75th percentile range with the line representing the median and the whiskers extending to the minimal and maximal value, all points shown. (a.,b.,f.) Comparison of hypha grown at 18°C (n=12) and at 22°C (n=6). T-test with Welch’s correction: a.) Mitochondrial density (defined as the number of mitochondria per 1000 μm^2 of hypha area). b.) Mitochondrial area in a hypha normalized to the area of that hypha (% area under mitochondria). c.) The density of mitochondria belonging to each morphological type (round, ellipsoid, elongated) from pooled subsets of Control (n=3) and Cold-treated (n=4) hypha images. Anova with Holm-Sidac correction. d-e.) The length (d) of mitochondria belonging to each morphological type in hypha grown at 22°C (graph in 2d.) and 18°C (graph in 2e.) shown as average value and SD in each hypha (18°C group, n=4 and 22°C group, n=3). f.) Average length of elongated mitochondria. T-test with Welch’s correction.

Acknowledgment

The authors acknowledge funding provided by the Ministry of Science Technological Development and Innovation, Republic of Serbia through the Grants: No. 451-03-47/2023-01/200007, 451-03-47/2023-01/200178, 451-03-47/2023-01/ 200053; by Science Fund of the Republic of Serbia, grant number 4545 [BioPhysFUN]; by the Institute of Physics Belgrade, through the grant provided by the Ministry of Science Technological Development and Innovation.

References

- [1] A.R. Fenton, T.A. Jongens, E.L.F. Holzbaur. *Mitochondrial dynamics: Shaping and remodeling an organelle network*. *Curr Opin Cell Biol.* 68 (2021) 28-36.
- [2] T. Pajić, S. Kozakijević, A.J. Krmpot, et al. *In vivo multiphoton imaging of a filamentous fungus *Phycomyces blakesleeanus*: the effect of small ambient temperature increase on mitochondrial morphology and lipid droplets density*. IX International School and Conference on Photonics, PHOTONICA 2023, August 28 – September 1, 2023, Belgrade-Serbia.
- [3] M. Stanić, J. Zakrzewska, M. Hadžibrahimović, et al. *Oxygen regulation of alternative respiration in fungus *Phycomyces blakesleeanus*: connection with phosphate metabolism*. *Res Microbiol.* 164(7) (2013) 770-8.
- [4] T. Pajić, N.V. Todorović, M. Živić, et al. *Label-free third harmonic generation imaging and quantification of lipid droplets in live filamentous fungi*. *Sci Rep.* 12(1) (2022) 18760.

Structural simulations predicting protein folding in Alzheimer's disease

Marios Krokidis¹, Aristidis Vrahatis¹, George Dimitrakopoulos¹, Konstantina Skolariki¹, Panagiotis Vlamos¹, Themis Exarchos^{1*}

¹ Ionian University, Department of Informatics, Bioinformatics and Human Electrophysiology Laboratory, Corfu, Greece; e-mail: mkrokidis@ionio.gr, aris.vrahatis@ionio.gr, dimitrakopoulos@ionio.gr, skolariki@ionio.gr, vlamos@ionio.gr, exarchos@ionio.gr

* *Corresponding author*

DOI: 10.46793/ICCB23.338K

Abstract: Proteins assume a suitable spatial structure to effectively execute their intracellular functions. The occurrence of protein misfolding, resulting from single point mutations or external influences, along with the consequent buildup of protein aggregates, can lead to diverse pathological processes like neurodegenerative disorders. Protein misfolding serves as a risk indicator for Alzheimer's disease (AD), the prevailing cause of neurodegenerative dementia in the elderly, characterized by gradual cognitive impairment. Several structure prediction algorithms and computational approaches have been developed to address this challenge. The present work focuses on specific proteins related to AD and aims to verify their conformation through ColabFold which utilizes the MMseqs2 algorithm to quickly provide multiple sequence alignments. The predicted models were then compared to selected PDB structures, a superposition was created and the TM-score and RMSD metrics were assessed. In addition, a comprehensive look into the superposed structures was performed to observe any potent deviations between pairs of residues. These notable findings encompass precise direct sequence-to-structure patterns found in individual AD polypeptides motifs and well-folded domains.

Keywords: protein folding, Alzheimer's disease, functional analysis, multiple sequence alignments, structure prediction

1. Protein misfolding and aggregates formation

Protein functionality is intimately linked to its three-dimensional structure, revealing that the determination of this structure is vital for comprehending biological processes and tackling various health and life science challenges [1]. The conformational transition of protein misfolding greatly enhances the assembly of protein molecules into various morphologies of aggregates. Initially, it was thought that specific aggregate formation, mainly amyloid fibrils, was restricted to proteins associated with amyloidoses.

Nevertheless, recent evidence indicates that, under certain conditions, the majority of proteins undergo structural transitions, giving rise to amyloidogenic intermediates and subsequent aggregate formation [2]. The accumulation of aggregates has been associated with several neurodegenerative disorders, such as Alzheimer's and Parkinson's diseases.

In each of these pathological conditions, a particular protein or protein fragment undergoes a transformation from its native, soluble state to insoluble aggregates, which accumulate in diverse organs and tissues [3]. Numerous algorithms and computational methods have been developed in this direction of enhancing protein structure prediction. AlphaFold's exceptional precision has revolutionized the fields of computational and structural biology while similarly, ColabFold speeds up single predictions with the 40–60-fold faster MMseqs2 [4,5]. This groundbreaking advancement enables the attainment of remarkably accurate protein structure predictions, comparable to experimental accuracy, for numerous proteins.

2. Structural analysis of selected protein models in Alzheimer's disease

2.1 Structural superpositions of the predicted models

Using the ColabFold implementation of AlphaFold, structure prediction of particular proteins associated with AD is provided. The resulting superimposed structures for these protein molecules, as illustrated in Figure 1, are consistent with the observed results and contribute to the enhanced optimization of the outcomes. The predicted structure of TREM2 is showcased in Figure 1a, superimposed with 5UD8. The alignment is remarkably precise, except for the 67-81 region, which lacks definition in the experimental structure, limiting further investigation. Notably, ColabFold's prediction includes a very small beta strand at residues 86-87, fitting accurately within the "Immunoglobulin-like beta-sandwich" fold. Figure 1b presents the structure of APP695, with the green chain corresponding to entry 4PQD, the orange chain to 2FMA, and the purple chain to 1TKN. The structural alignment of the predicted model with 4PQD demonstrates remarkable accuracy. Minor deviations are observed near both ends of the reference chain, along with a small deviation involving two consecutive residues within a loop, namely G 101 and R 102, with pair distances measuring 4.2 Å and 5.6 Å, respectively. Additionally, the alignment with 2FMA is exceptional, showing no significant deviations. The alignment with 2FMA is outstanding, revealing no notable deviations. However, it is worth noting that the experimental structure comprises residues 171-173 at the end of a beta strand, whereas ColabFold's model predicts this beta strand ending at residue 170. Regarding the reference 1TKN, it is an NMR structure with 20 submitted conformations. In this specific superposition, conformation 8/20 is depicted, and the overall alignment with 1TKN is satisfactory.

Presenilin 1 (PSN1), displayed with the reference structure 7D8X, exhibits an accurate alignment with minor deviations, potentially attributed to its length (Figure 1c). Notably, a region encompassing approximately residues 421-434 shows deviations reaching up to 6.2 Å. The four-helical-bundle of APOE is prominently displayed in Figure 1d. The green conformation corresponds to PDB entry 7FCR, and the alignment is generally satisfactory, with one exception: the loop connecting the third and fourth major helices of the bundle. This loop comprises four residues in the order of L, G, Q, S (positions: 144-147) with distances between residue pairs measuring 3.4 Å, 6.6 Å, 5.0 Å, and 3.3 Å, respectively.

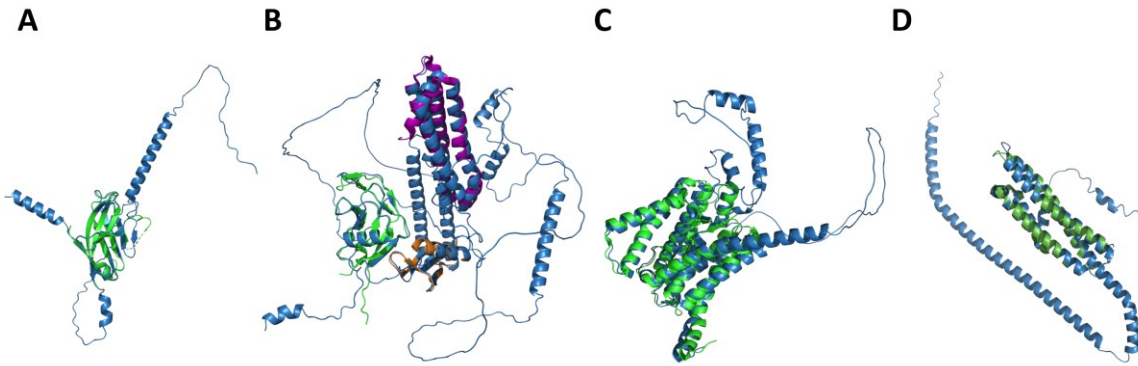


Figure 1. Structural superpositions of the models by ColabFold (in blue) and the corresponding reference structures fetched from the PDB (in green, orange and purple). (a) TREM2 – 5UD8; (b) APP695 – 4PQD, (c) PSN1 – 7D8X, (d) APOE – 7FCR.

2.2 Sequence parameters and Predicted Aligned Error matrices

Shedding light on the predicted conformation of TREM2, it was revealed that the first region of confidence is oriented as a domain consisting of 9 beta strands and the small region near the C-terminal end is predicted as a single alpha-helix (TM-score 0.94-0.98, RMSD 0.60-1.54 Å). For PSEN1 two regions are also predicted with high accuracy in their relative positions. Both of the regions identified in the plots can be seen in the predicted model as a complex formation of alpha-helices. These helices compose the transmembrane part of the protein (TM-score 0.94, RMSD 1.80 Å). The PAE matrix for APOE indicates that the relative positions of these smaller regions are also predicted with high confidence while on the predicted model four alpha-helices are highlighted, connected to each other by turns and a small helix (TM-score 0.96, RMSD 1.09 Å). Lastly, the relative positions of APP695 residues within each of the two aforementioned regions are predicted with high accuracy according to the PAE matrix, and a very small region of high confidence is found at residues 628-648 (TM-score 0.77-0.85, RMSD 1.18-2.61 Å). Alignment length and sequence identity parameters are highlighted in Table 1.

Table 1. Alignment length and sequence identity parameters for the studied protein models.

Protein	Alignment length	Sequence Identity	Reference (PDB)
APP695	97	1.00	4PQD
	59	0.97	2FMA
	109	0.97	1TKN
PSN1	306	0.98	7D8X
APOE	137	0.99	7FCR
TREM2	104	0.94	5UD8
	112	1.00	5ELI

3. Conclusions

Dissecting the three-dimensional protein structure is crucial for understanding protein function, which, accordingly, plays a critical role in comprehending biological processes and addressing various health and life science challenges such as in neurodegenerative disorders and particularly AD. According to our results, predictions provided by ColabFold in the set of specific proteins involved in AD were highly accurate and most of the aforementioned deviations depicted between predicted and reference models were mainly located around residues that form loops. The recent advancements in protein structure prediction and provided algorithms have demonstrated a significant contribution in enhancing our understanding of protein folding challenges, however, there is a need for enhancements to address certain limitations, including the prediction of novel structures, intrinsically disordered regions and the capacity to predict only a single conformer without ligands.

Acknowledgment

This research has been co-financed by the European Union and Greek national funds through the Operational Program Competitiveness, Entrepreneurship and Innovation, under the call Regional Excellence (Research Activity in the Ionian University, for the study of protein folding in neurodegenerative diseases) (FOLDIT) MIS 5047144.

References

- [1] R. Pearce, Y. Zhang., 2021. *Toward the solution of the protein structure prediction problem*, *Journal of Biological Chemistry*, 297 (2021) 100870.
- [2] Z.L. Almeida, R.M. Brito., *Structure and aggregation mechanisms in amyloids*, *Molecules*, 25 (2020) 1195.
- [3] F. Chiti, C.M. Dobson., *Protein Misfolding, Amyloid Formation, and Human Disease: A Summary of Progress Over the Last Decade*. *Annual review of biochemistry*, 86 (2017) 27–68.
- [4] J. Jumper, R. Evans, A. Pritzel, T. Green, M. Figurnov, O. Ronneberger, K. Tunyasuvunakool, R. Bates, A. Žídek, A. Potapenko, A. Bridgland., *Highly accurate protein structure prediction with AlphaFold*, *Nature* 596 (2021) 583-589.
- [5] M. Mirdita, K. Schütze, Y. Moriwaki, L. Heo, S. Ovchinnikov, M. Steinegger., *ColabFold: making protein folding accessible to all*, *Nature methods* 19 (2022) 679-668.

A Machine Learning approach combining omics data for Alzheimer's Disease analysis

Georgios N. Dimitrakopoulos¹, Konstantinos Lazaros¹, Aristidis G. Vrahatis¹, Marios Krokidis¹, Konstantina Skolariki¹, Panagiotis Vlamos¹, Themis Exarchos^{1*}

¹ Ionian University, Department of Informatics, Bioinformatics and Human Electrophysiology Lab (BiHELab), Corfu, 49100, Greece; e-mail: dimitrakopoulos@ionio.gr, konlazaros@gmail.com, aris.vrahatis@ionio.gr, mkrokidis@ionio.gr, c19skol@ionio.gr, vlamos@ionio.gr, exarchos@ionio.gr

* *Corresponding author*

DOI: 10.46793/ICCBIG23.342D

Abstract

Alzheimer's disease (AD) is a complex neurological disorder whose underlying mechanisms remain elusive to this day. Molecular biology methodologies, especially techniques like single-cell RNA sequencing (scRNA-seq), offer unparalleled granularity in deciphering the disease's cellular intricacies. However, despite the potential of scRNA-seq, comprehensive machine-learning analyses are yet to be fully harnessed. Emphasizing the multi-omics machine-learning-based approaches, which integrate diverse single-cell omics datasets, could highlight novel therapeutic targets and deepen our understanding of AD's intricate nature. In this work, we propose a machine-learning-based method to embed gene expression into a protein interaction graph. Specifically, we model each interaction with a regression model on the participating genes and we use the R² score as edge weight. Our aim is to detect parts of the PPI graph that differentiate between control and disease conditions. Application on a scRNA-seq AD dataset managed to identify interactions forming small subgraphs, which consisted of genes involved with biological processes related to neurons.

Keywords: Machine learning, scRNA-seq, integration, Alzheimer's disease, PPI graph

1. Introduction

Alzheimer's disease (AD), a neuro-degenerative condition predominantly affecting the elderly, is marked by the accumulation of amyloid-beta plaques and tau protein aggregates, leading to progressive cognitive decline. Despite extensive research, effective treatments remain out of reach, largely due to the disease's complex and diverse nature, which spans multiple biological pathways and cell types.

Single-cell RNA sequencing (scRNA-seq) can offer insights into the heterogeneity of AD by analyzing gene expression patterns in individual cells [1]. This technique, in conjunction with broader omics data, provides a refined understanding of the disease's cellular nuances, thereby highlighting potential biomarkers and therapeutic targets [2].

In recent years, a large number of single-cell datasets has been published, enabling integrative analyses across diverse scRNA-seq datasets. The goal of data integration is to account for technical differences between data and to combine multiple single-cell datasets into a single, cohesive object [3]. By combining data, the robustness of downstream analyses has increased and the comprehension of biological phenomena is enhanced.

Network modeling has perennially served as an effective tool in decoding the intricacies of multifaceted biological systems. Herein, biological systems are delineated as an ensemble of nodes and edges: the former symbolizing biological entities ranging from genes, proteins, and metabolites, while the latter characterizes their interrelations, be it through regulatory dynamics, statistical affiliations, physical engagements, or other biological processes [4].

Here, we propose a method to combine dynamic data, such as gene expression in different conditions with protein-protein interactions (PPI) network, in order to detect subgraphs that play a role in a disease. This was performed by training a regression random forest model for each interaction, using the two genes as input and output, and utilizing the R^2 score as weight. Parts of the graphs presenting large differences in score were further examined to establish their relationship with AD.

2. Methods

2.1 Data and pre-processing

For the scope of this analysis, two AD-related single-cell datasets were sourced from the scREAD database [5]. This public data repository comprises scRNA-seq and snRNA-seq datasets originating from postmortem human brain tissues demonstrating AD pathology, as well as from AD mouse models. These datasets encompass human brain cells from the superior frontal gyrus region, with one dataset representing healthy control cells and the other cells from AD cases, collectively accounting for 66,612 cells.

To perform data integration and batch effect correction, we used SCANORAMA [3]. Functionally, it projects cells within a low-dimensional embedding space, subsequently identifying cells exhibiting the highest similarity across different batches. Leveraging these identified anchors, the algorithm proficiently rectifies batch effects, ensuring the cohesive integration of the datasets.

The protein-protein interaction (PPI) network was downloaded from PICKLE (www.pickle.gr) [6] and specifically, the gene-normalized network at a cross-checked level was used. PICKLE is a meta-database integrating primary information from various databases on experimentally validated PPIs performing cross-checking to eliminate possible false positives. The final dataset includes 3301 PPIs between 1063 genes.

2.2 Graph weighting and analysis

For each condition, health and disease, we aim to create a weighted graph, representing the strength of each PPI. Hence, for each known pair of interacting proteins, we perform regression with a Random Forest model, using the gene expression of one gene as input and the second as output. For each model, the R^2 score is estimated, based on out-of-bag samples, showing the degree of the prediction matching the actual output. Thus, we obtain one graph for each condition, with identical structure but different weights. Next, the corresponding PPIs are compared, and the largest differences are examined in further detail. The difference in score shows that the function governing the interaction has changed, probably as an effect of the disease (i.e., there is an increment/decrement of the expression in one of the two proteins that does not happen in the second protein).

3. Results and discussion

The interactions that show the largest differences in score between the two conditions are presented in Table 1. Of note, in all cases the disease condition has the largest score, showing that it is easier for the model to predict gene expression in this condition, i.e., the two interacting proteins might have more similar patterns.

Table 1. Largest score differences in PPIs.

Interactor A	Interactor B	Control	Disease	Difference
MBP	PLP1	0.245	0.507	0.261
CALM3	MBP	0.015	0.191	0.175
STMN2	CTNNA3	0.015	0.18	0.165
MGST3	PLP1	0.023	0.184	0.161
RAN	MBP	0.013	0.172	0.159
IFITM3	PLP1	0.021	0.176	0.155
TNNI2	CTNNA3	0.013	0.168	0.155
CSF1R	INPP5D	0.043	0.194	0.151
NDUFB7	CTNNA3	0.014	0.164	0.150
STMN3	CTNNA3	0.014	0.159	0.145

Of note, the genes of Table 1 are connected in 3 subgraphs (Fig. 1). This shows that in such complex diseases, groups of interacting genes and proteins are affected. Finally, we performed enrichment analysis using DAVID (<https://david.ncifcrf.gov>) based on the genes involved in the most differentiated PPIs, as shown in Table 1. The significant Biological Process Gene Ontology terms found were (in parenthesis the p-value): GO:0021762~substantia nigra development (3.9E-4), GO:0031175~neuron projection development, (2.6E-3) GO:0008366~axon ensheathment (3.7E-3), GO:0031110~regulation of microtubule polymerization or depolymerization (9.2E-3), GO:0007019~microtubule depolymerization (9,8E-3), GO:0071902~positive regulation of protein serine/threonine kinase activity (2,6E-2). We highlight that a pure data-driven procedure is provided as output genes related with biological mechanisms related with neurons. For example, the

substantia nigra (involving PLP1, CALM3, MBP genes) is critical in the development of many diseases and syndromes, including Parkinson's disease and AD [7]. The terms neuron projection development (involving STMN2, PLP1, STMN3) and axon ensheathment (involving PLP1, MBP) are also related with processes in the neurons and might be related with AD [8]. These results show that our method is able to provide biologically relevant results, which might act as network biomarkers for disease diagnosis, as well as candidate drug targets for therapeutic treatment.

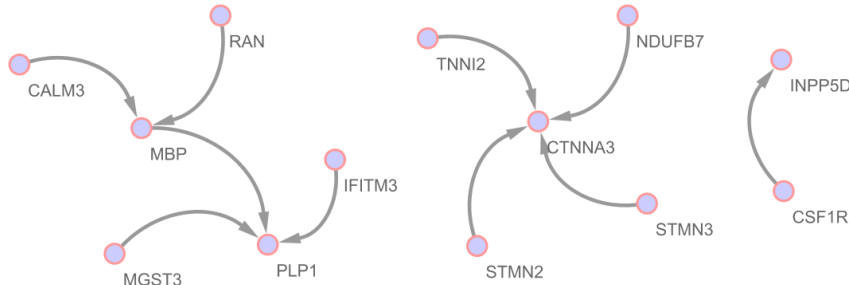


Figure 1. Three subgraphs derived from the important genes identified within the dataset, serving as potential network biomarkers for Alzheimer's disease.

Acknowledgment

This research has been co-financed by the European Union and Greek national funds through the Operational Program Competitiveness, Entrepreneurship and Innovation, under the call Regional Excellence (Research Activity in the Ionian University, for the study of protein folding in neurodegenerative diseases) (FOLDIT) MIS 5047144.

References

- [1] T. Nawy., *Single-cell sequencing*, Nat Methods 11, 18 (2014).
- [2] H. Mathys, J. Davila-Velderrain, Z. Peng, et al., *Single-cell transcriptomic analysis of Alzheimer's disease*. Nature 570, 332–337 (2019).
- [3] B. Hie, B. Bryson, B. Berger., *Efficient integration of heterogeneous single-cell transcriptomes using Scanorama*, Nat Biotechnol 37, 685–691 (2019).
- [4] M. Blencowe, D. Arneson, J. Ding, et al., *Network modeling of single-cell omics data: challenges, opportunities, and progresses*. Emerg Top Life Sci 16; 3 (4): 379–398 (2019).
- [5] J. Jiang, W. Cankun, Q. Ren, F. Hongjun, M. Qin., *ScREAD: a single-cell RNA-Seq database for alzheimer's disease*. IScience 23(11), 101769 (2020).
- [6] G. N. Dimitrakopoulos, M. I. Klapa, N. K. Moschonas., *How Far Are We from the Completion of the Human Protein Interactome Reconstruction?* Biomolecules, 12, 140 (2022).
- [7] J. M. Burns, J. E. Galvin, C. M. Roe, et al., *The pathology of the substantia nigra in Alzheimer disease with extrapyramidal signs*. Neurology, 64(8), 1397-1403 (2005).
- [8] M. Chen, H. K. Lee, L. Moo, et al., *Common proteomic profiles of induced pluripotent stem cell-derived three-dimensional neurons and brain tissue from Alzheimer patients*. Journal of proteomics, 182, 21-33 (2018).

Biomedical Engineering

Numerical modeling of new 4,7-dihydroxycoumarin derivative diffusion within finite element liver model

Vladimir Simić^{1*}, Miljan Milošević^{1,2,4}, Žiko Milanović¹, Miloš Kojić^{2,3,5}

¹ University of Kragujevac, Institute for Information Technologies, Department of Technical-Technological Sciences, Jovana Cvijica bb, 34000 Kragujevac, Serbia.; e-mail: vsimic@kg.ac.rs, miljan.m@kg.ac.rs, ziko.milanovic@uni.kg.ac.rs

² Bioengineering Research and Development Center (BioIRC), Prvoslava Stojanovića 6, 34000 Kragujevac, Serbia

³ Houston Methodist Research Institute, The Department of Nanomedicine, 6670 Bertner Ave., R7 117, Houston, TX 77030, USA.; e-mail: mkojic42@gmail.com

⁴ Belgrade Metropolitan University, Tadeuša Košćuška 63, 11158, Belgrade, Serbia

⁵ Serbian Academy of Sciences and Arts, Kneza Mihaila 35, 11 000, Belgrade, Serbia

* *Corresponding author*

DOI: 10.46793/ICCBi23.347S

Abstract: Blood coagulation, also known as blood clot formation, is an essential biochemical process which occurs when a blood vessel is damaged and requires repair [1]. Blood clot development, inevitable to exclude excessive bleeding and damaged area healing, can be detrimental if clots form in blood vessels improperly, leading to various problems- thrombosis, pulmonary embolism, etc. In order to prevent those scenarios, there is a certain need for the development of novel drugs. For that purpose, we have performed computational modeling of a diffusion process of a newly investigated and synthesized 4,7-dihydroxycoumarin derivative. Also, for the purpose of the diffusion modeling process, a smeared modeling concept for gradient-driven mass transport and formulation of a new composite smeared finite element (CSFE) is introduced in [2] and generalized in [3]. CSFE is composed of multiple domains: capillary, extracellular space, cells and organelles, with pressure and concentration for each domain. The domains are coupled by connectivity elements at each node. Here, we implemented this concept to a 3D liver model, which illustrates the applicability of the CSFE element and smeared concept to large biological systems. Special emphasis was placed on the distribution of the potential drug, which was monitored by the flow through the liver and blood vessel network via a purposely developed computational model of the liver. The main goal of the application of computational models is to reduce the financial costs of in vivo experiments, as well as to avoid the direct use of drugs on animals as well as humans.

Keywords: diffusion, smeared model, composite smeared finite element, liver model

1. Introduction

Transport of particles and molecules from the blood to tissue and from tissue back to blood is a complex process. Transport within tumors has additional complexities due to irregular blood vessel branching and variability of vessel diameters and lengths. It is not feasible to model each capillary, cell and organelles, even in small domains. Here, we implement a smeared modeling concept in order to provide models for large domains which can effectively be used for transport in the capillary system and tissue, with a focus on the diffusion process of the potential anticoagulation drug. Anticoagulants are drugs which extensively used to treat conditions in which a blood clot (thrombus) forms in the blood vessels. In addition, they are used to prevent the formation of new or growth of existing blood clots in patients who suffer from illnesses and disorders associated with an increased risk of clot formation.

2. Composite smeared finite element formulation

To introduce the smeared methodology, we consider a ‘detailed model’ of a composite medium. Fig. 1a shows a schematic of a medium composed of continuum domains- compartments and a network of fiber-like 1D domains. The continuum domains include extracellular space, cells and organelles. First, it is necessary to transform the 1D balance equations into the corresponding continuum format. Also, each domain has its own field within the corresponding volume of the CSFE. Finally, we include connectivity elements to couple the corresponding domains, at each node of the CSFE (equations are given in [2] and [3]).

There are the following physical fields within the element: pressure and concentration in capillaries, within extracellular space and cytosol of cells; and concentration within organelles. These fields are mutually dependent. Schematics of a finite element with elementary volumes and connectivity element are shown in Fig. 1c [3].

3. Computational finite element liver model

The geometry of the liver and blood vessel network, shown in Fig. 1d, is generated at R&D Center BIOIRC from micro-CT scan of a mouse liver. The computational model consists of three parts: one-dimensional finite elements for larger vessels (7216 elements), three-dimensional composite smeared finite elements (36 243 elements) representing surrounding tissue, and connectivity elements (689 elements) necessary to connect large vessels and continuum nodes of smeared finite elements. The complete procedure is explained in [4], where it is noted how micro-computed tomography (micro-CT) was used to scan the vascular structure.

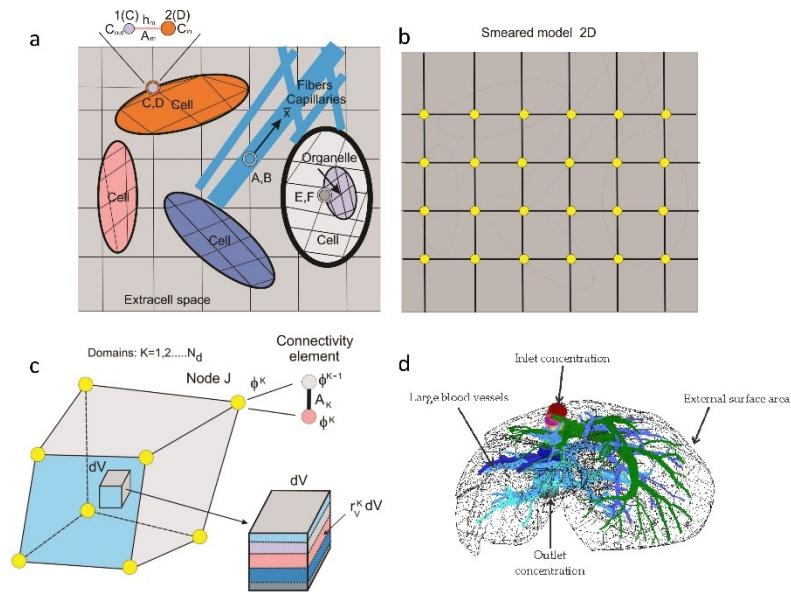


Fig.1. Schematic of detailed, smeared and liver model. a) Detailed model of tissue as composite medium, 2D representation, with 1D and connectivity elements; b) Smeared FE representation of the detailed model; c) Composite smeared finite element (CSFE) with subdomains and connectivity element at a FE node J; d) Geometry and boundary conditions of the liver model.

Material data applied in this computational model are used as in [5] with the addition of different diffusion coefficients for two different compounds (WF and L), used for representing the concentration field. The diffusion coefficient of the first compound, WF, is $D_{WF} = 4.52 \times 10^{-4} \text{ mm}^2 \text{ s}^{-1}$ while for L, the diffusion coefficient used is $D_L = 4.34 \times 10^{-4} \text{ mm}^2 \text{ s}^{-1}$. Both values were estimated using the Stokes-Einstein equation. The simulation lasts for 400 s, divided into 40 equal time steps. The concentration field for three different time steps, in the vertical plane, within the capillary domain for both WF and L compounds is shown in Figure 2.

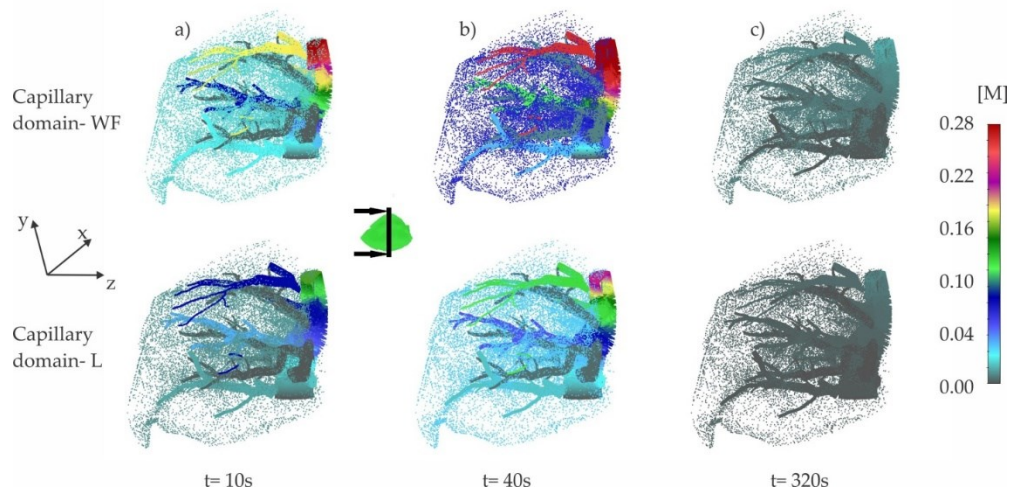


Fig.2. Mean concentration evolution inside the capillary and tissue domain within the liver, represented for both **WF** and **L** compound, for a) t= 10s, b) t= 40s and c) t= 320s.

4. Conclusions

In this study we summarized smeared methodology for field problems as a general concept for modeling gradient-driven field problems in complex biological media. The smeared model for transport offers a possibility to simulate *in silico* transport of small molecules and particles used in biomedical applications to improve drug delivery and therapeutics. Therefore, this computational model can serve as a basis for potential patient-specific drug delivery models, which can contribute to a better understanding of pharmacokinetic characteristics and the potential of novel anticoagulant compounds.

Acknowledgment

This research was funded by the Ministry of Science, Technological Development and Innovation of the Republic of Serbia, contract number 451-03-47/2023-01/200378 (Institute for Information Technologies Kragujevac, University of Kragujevac).

References

- [1] Milanović Ž., Antonijević M., Avdović E., Simić V., Milošević M., Dolićanin Z., Kojić M., Marković Z., *In silico* evaluation of pharmacokinetic parameters, delivery, distribution, and anticoagulative effects of new 4,7-dihydroxycoumarin derivative, *Journal of Biomolecular Structure and Dynamics*, <https://doi.org/10.1080/07391102.2023.2245071>, ISSN: 0739-1102, 2023.
- [2] Kojic M., Milosevic M., Simic V., Koay E.J., Fleming J.B., Nizzero S., Kojic N., Ziemys A., Ferrari M., A composite smeared finite element for mass transport in capillary systems and biological tissue. *Comput. Methods Appl. Mech. Engrg*, Vol. 324, pp. 413-437, ISSN : 0045-7825, 2017.
- [3] Kojic M., Smeared concept as a general methodology in finite element modeling of physical fields and mechanical problems in composite media, *J. Serb. Soc. Comp. Mech.*, Vol 12, No.2, 1-16, 2018.
- [4] Zagorchev, L.; Oses, P.; Zhuang, Z. W.; Moodie, K.; Mulligan-Kehoe, M. J.; Simons, M.; Couffinhal, T. Micro computed to-mography for vascular exploration. *J. Angiogenes Res.*, Vol. 2, 1-11. 2010.
- [5] Kojic, M.; Milosevic, M.; Simic, V.; Koay, E. J.; Fleming, J. B.; Nizzero, S., Kojic, N.; Ziemys, A.; Ferrari, M. A composite smeared finite element for mass transport in capillary systems and biological tissue. *Comput. Methods Appl. Mech. Eng.*, Vol 324, 413-437, 2017.

UV-blocking sustainable food packaging based on polyhydroxyalkanoate and bacterial pigment prodigiosin

Marijana Ponjavic^{1*}, Ivana Malagurski¹, Ana Salevic-Jelic², Jelena Lazic¹, Jasmina Nikodinovic-Runic¹

¹ University of Belgrade, Institute of Molecular Genetics and Genetic Engineering, Laboratory for Molecular Genetics and Ecology of Microorganisms, Vojvode Stepe 444a, 11042 Belgrade, Serbia; e-mail: mponjavic@imgge.bg.ac.rs, ivana.malagurski@imgge.bg.ac.rs, jasmina.nikodinovic@imgge.bg.ac.rs

² University of Belgrade, Faculty of Agriculture, Department of Food Technology and Biochemistry, Nemanjina 6, 11080 Belgrade, Serbia; e-mail: ana.salevic@agrif.bg.ac.rs

DOI: 10.46793/ICCB23.351P

Abstract: New film materials based on bacterial biomolecules polyhydroxyalkanoate (poly(3-hydroxybutyrate-co-3-hydroxyvalerate) PHBV) and prodigiosin (PG) were produced by solvent casting as a potential food packaging material. Film precursors were obtained in a sustainable manner via microbial fermentation using waste stream-based substrates (cooking oil and second-grade canned meat, after the expiry date). The incorporation of PG into the PHBV has influenced the morphology and functionality of the obtained materials. PG acted as a nucleating agent, affecting in turn PHBV/PG film surface morphology. The films were intensively colored, transparent and blocked UV-light. An increase in PG content decreased film transparency but it did not affect UV-blocking ability. Migration experiments have shown that films possess the potential to release PG into lipophilic food simulant media where it has exhibited antioxidative action. The obtained results suggest that PHBV/PG films can be potentially used as sustainable and active food packaging materials.

Keywords: prodigiosin, polyhydroxyalkanoate, food packaging, solvent casting, UV-blocking

1. Introduction

As a major consumer of worldwide plastic production, with a product that has one of the shortest mean lifetimes (0.5 years), the packaging industry contributes significantly to the plastic waste generation. To address this, significant efforts have been put into developing biopolymer-based food packaging materials as eco-friendly alternatives to petroleum-based materials.

Polyhydroxyalkanoates (PHAs) are biodegradable thermoplastic biopolyesters produced by a wide range of bacteria as intercellular storage of carbon and energy. They are structurally heterogeneous and exhibit a variety physicochemical properties, some of which are comparable to the conventional plastics [1].

Prodigiosin (PG) is a biopigment produced as a secondary metabolite in Gram-positive and Gram-negative bacteria. The remarkable properties (*e.g.*, UV protective,

antioxidative and antimicrobial activity) made it the subject of many studies [2]. Combining these two bacterial biomolecules can lead to improved PHA-based materials which are biodegradable, sustainable and functional. The presented study proposed the PHBV-PG as a new active food packaging material with improved UV-blockage, migration and antioxidative activity that can further be successfully tuned by the concentration of prodigiosin as an active compound.

2. Materials and methods

2.1. Fabrication of PHBV/PB films

Film precursors were obtained in a sustainable manner via microbial fermentation using waste stream-based substrates. Poly(3-hydroxybutyrate-co-3-hydroxyvalerate) (PHBV, M_w 5.4×10^5 kDa) was obtained using *Cupriavidus necator* DSM 428 and cooking oil as a carbon source [3]. Prodigiosin was produced in a bioreactor (Bio4, EDF-5.4_1, Biotehniskais centras AS, Riga, Latvia) using *Serratia marcescens* ATCC 27117 (American Type Culture Collection, ATCC, Manassas, VA, USA) and second-grade canned meat waste (Takovo d.o.o., Serbia) as a substrate [4].

PHBV/PB films were produced using solvent casting method according to the procedure described in our previous study [5]. In brief, PHBV and PB were dissolved in CHCl_3 and the obtained film solution was cast into a glass Petri dish (diameter of 6 cm). The samples were left to dry for 14 days at room temperature. In order to investigate the effect of PB content on the obtained films properties, multiple films solutions with fixed PHBV content (150.0 mg) and increasing PB content (2.5, 5.0 and 10.0 mg) were made and cast. The control was the pure PHBV film. The obtained samples were denoted as PHBV, 2.5-PHBV/PB, 5-PHBV/PB and 10-PHBV/PB, for the control and the samples with increasing PB content, respectively.

2.1. Characterization of PHBV/PB films

Morphology. PHBV/PB film surface morphology was investigated using an optical microscope using Olympus SZX10 attached to a digital imaging system.

Transparency and UV-blockage. Film strips ($1 \times 4 \text{ cm}^2$) were placed perpendicularly to the light beam, transmission and absorption were measured in the ultraviolet and visible spectra. In addition, a qualitative assessment of the samples' contact transparency was conducted visually.

Migration evaluation. Migration of PB from the samples into the food was evaluated in accordance with the European Commission requirements using 10 % and 95 % aqueous ethanol solutions (v/v) as food simulant media with hydrophilic and lipophilic characteristics, respectively.

Antioxidative activity. Following the migration test, the food simulant media with migrated PB were analyzed for antioxidant activity against using 2,2-diphenyl-1-picrylhydrazyl (DPPH•) free radicals scavenging assay.

2.2. Results

Prodigiosin was successfully incorporated into PHBV biopolymer to obtain films using the solvent casting method. All samples appeared uniform, with no visible defects or phase separation, Figure 1A.

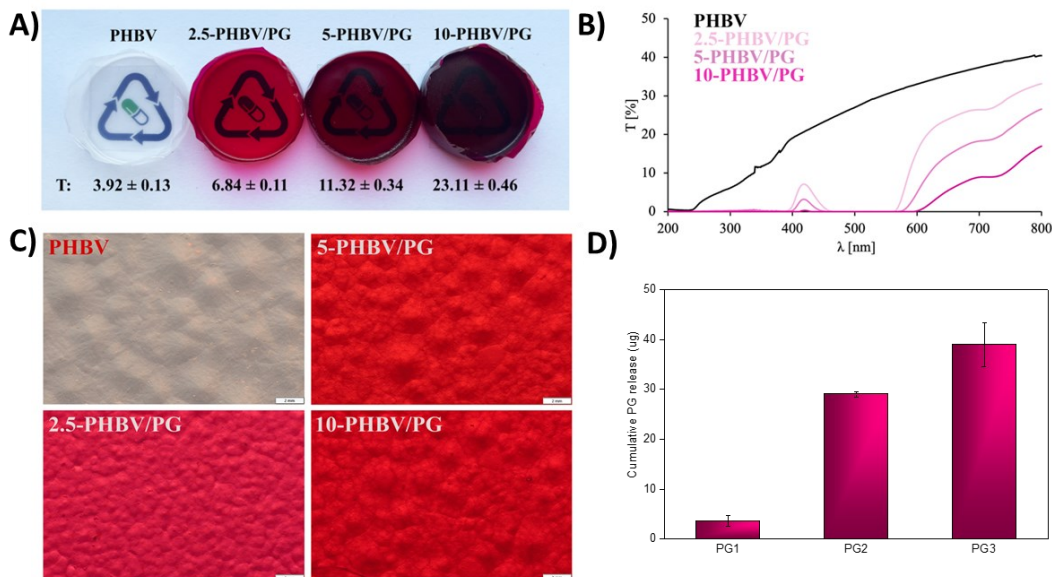


Figure 1. Characterization of the PHBV/PG films with increasing PG content: (A) Contact transparency and corresponding transparency value (T , mm^{-1}) at $\lambda = 600$ nm; (B) Light transmission in the UV-VIS spectrum and (C) Surface morphology; (D) Migration test: cumulative prodigiosine release in lipophilic medium.

Optical properties are important characteristics of food packaging materials. Packaging material should allow visual observation of packed products, but at the same time prevent photodegradation during storage. Evaluation of light transparency and transmission indicated that the presence of PG within PHBV has significantly decreased light transmission of the obtained film materials, especially in the UV region (Figure 1A and 1B). The increase in the PG content has resulted in more intensively colored films which appeared less transparent (Figure 1A). However, all PG-containing formulations were equally efficient in UV blockage, irrespective of the PG loading.

In addition to the obvious difference in color and transparency, the film samples exhibited different surface morphology with clearly visible macroscopic spherulites (Figure 1C). The biggest spherulites were observed on the surface of the control (PHBV) sample, in contrast to the smaller and more numerous ones that appeared in PHBV/PG samples, indicating that PG acts as a nucleating agent for biopolymer crystallization. There was also a difference among the PHBV/PG samples: the lower the PG loading, the smaller and more numerous the spherulites were. PHBV has been widely recognized in the field of active packaging materials, but preferentially other active ingredients, such as eugenol, carvacrol, phenolic acid, ferulic acid, etc., have been used [6, 7, 8]. The incorporation of PG into PHBV as a polymer matrix has been reported for the first time

in our previous study [5] where the biological benefits of this system (its cytotoxicity) have been proved.

Cumulative release experiments were conducted to evaluate migration of PG from PHBV/PF films into food in potential applications as food packaging materials (Figure 1D). No PG migration was detected in the hydrophilic medium, however when placed in lipophilic medium, the release was significant, and it was directly proportional to the PG content in the films. In addition, the migrated PG exhibited antioxidant activity.

3. Conclusions

Bacterial biomolecules, PHA and PG, were successfully combined to produce film materials as potential sustainable and active food packaging material alternatives to conventional plastics. The incorporation of PG into the biopolymer matrix has improved the optical properties and antioxidative potential of the obtained films rendering them as suitable alternatives for packaging applications.

Acknowledgment

This research was funded by The Science Fund of the Republic of Serbia, IDEJE, 7730810, BioECOLogics and the Ministry of Science, Technological Development and Innovations of the Republic of Serbia, Project No. 451-03-47/2023-01/200042.

References

- [1] M. Keller., *The handbook of polyhydroxyalkanoates, Volume 3*, Taylor & Francis Group, LLC (2021) 285-313.
- [2] T. Paul, et al., *A comprehensive review on recent trends in production, purification, and applications of prodigiosin*, *Biomass Convers. Biorafinery*, 12 (2022) 1409-1431.
- [3] M.V. Cruz, et al. *Online monitoring of P(3HB) produced from used cooking oil with near-infrared spectroscopy*. *J Biotechnol* 194 (2015) 1–9.
- [4] J. Lazic., *Structure optimization of biopigment prodigiosin from Serratia marcescens ATCC 27117 and antimicrobial and anticancer properties of novel halogenated derivatives*, PhD Thesis, (2022)
- [5] M. Ponjavic et al., *Advancing PHBV biomedical potential through incorporation of bacterial biopigment prodigiosin*, *Int J Mol Sci*, 24 (2023), 1906.
- [6] R. Requena et al., *Eugenol and carvacrol migration from PHBV films and antibacterial action in different food matrices*, *Food Chem*, 277 (2019), 38-45.
- [7] E. Moll et al., *Release and antibacterial action of phenolic acids incorporated into PHBV films*, *Food Pack Shelf Life*, 38 (2023), 101112.
- [8] R. Requena et al., *Release kinetics of carvacrol and eugenol from poly(hydroxybutyrate-co-hydroxyvalerate) (PHBV) films for food packaging applications*, *Eur Polym J*, 92 (2017), 185-193.

Using numerical modeling to analyze the behavior of cancer cells after diverse co-treatments

Tijana Djukić^{1,2*}, Dragana Seklić¹, Milena Jovanović¹, Marko Zivanović^{1,2}, Nenad Filipović³

¹ Institute for Information Technologies, University of Kragujevac, Jovana Cvijića bb, 34000 Kragujevac, Serbia; e-mail: tijana@kg.ac.rs , dragana.seklic@uni.kg.ac.rs , milena.jovanovic@pmf.kg.ac.rs

² Bioengineering Research and Development Center, BioIRC, Prvoslava Stojanovica 6, 34000 Kragujevac, Serbia; e-mail: zivanovicmkg@gmail.com

³ University of Kragujevac, Faculty of Engineering, Sestre Janjić 6, 34000 Kragujevac, Serbia; e-mail: fica@kg.ac.rs ,

* Corresponding author

DOI: 10.46793/ICCBi23.355DJ

Abstract: It is important to analyze a variety of treatments for colorectal cancer and the effects of possible co-treatments, in order to find the most efficient ones. Experimental results using cancer cell lines provide valuable information, but in combination with numerical simulations, additional quantitative information can be obtained. In this study, the viability of SW-480 cancer cells was analyzed experimentally after cotreatments of *Phellinus linteus* extract and chemical compound (Cisplatin drug). Numerical simulations are afterward applied to analyze the effect of diverse cotreatments on the numerical parameters of the model that are related to both cell proliferation and cell death. This approach can provide valuable insight into the quantitative effect these considered treatments have on the behavior of cancer cell lines. Similar analyses could be also performed using numerical simulations to predict the values of parameters for diverse cases that were not studied experimentally, and this would be an additional benefit for the exploration of the effects of various possible treatments.

Keywords: numerical model, SW-480 cancer cell line, parameter estimation

1. Introduction

One of the most common cancers with significant mortality rates worldwide is the colorectal carcinoma (CRC). It is therefore very important to analyze a variety of possible treatments and co-treatments, in order to find the most efficient ones. Experimental results using cancer cell lines provide valuable information, but in combination with numerical simulations, additional quantitative information can be obtained, that can be used to additionally analyze the benefits of considered treatments. There are several numerical models proposed in the literature that were applied to

model cancer progression [1,2] and the model proposed by Breward et al. [2] is used within this study.

In this paper, the effect of *P. linteus* extract and chemical compound (Cisplatin drug) in cotreatments was analyzed for a colorectal cancer cell line – SW-480. The viability of cells was measured experimentally after cotreatments, and afterward numerical simulations were performed to analyze the effect of these cotreatments on the numerical parameters related to cell proliferation and cell death.

2. Materials and Methods

In this Section, the experimental setup is explained and information about the numerical model and parameter estimation are provided.

2.1 Experimental setup

Colorectal cancer cell line SW-480 was obtained from ATCC (Manassas, USA), seeded in 96-well plates, and propagated according to standard culturing procedure [3]. *P. linteus* methanol extract was prepared as previously described [3]. Two types of co-treatments were performed: cells were treated with extract which was added simultaneously with cisplatin – 0 h; or the addition of cisplatin was done 6 h after the initial treatment of cells with *P. linteus* extract – 6 h. Either way, the final concentration of cisplatin in wells was 10 μM , and for *P. linteus* extract: 10, 25, 50 and 250 $\mu\text{g}/\text{mL}$. Cytotoxic effects of these co-treatments were evaluated by the MTT method [and obtained results were analyzed 24 or 72 h after treatment.

2.2 Numerical model

The numerical model proposed by Breward et al. [2] was used in this study. Details of the numerical model are provided in the literature [4]. If the concentration of cancer cells is denoted by α and the oxygen concentration is denoted by C , then the change of concentration over time can be described using the following relation:

$$\frac{\partial \alpha}{\partial t} = \frac{(1 + s_1)\alpha(1 - \alpha)C}{1 + s_1 C} - \frac{(s_2 + s_3 C)\alpha}{1 + s_4 C} \quad (1)$$

The parameters of the model are denoted by s_1 (related to cell proliferation) and s_2 , s_3 and s_4 (related to cell death).

The change in oxygen concentration within the observed domain can be described using the following relation:

$$\frac{\partial^2 C}{\partial x^2} = \frac{Q\alpha C}{1 + Q_1 C} \quad (2)$$

The parameters Q and Q_1 are related to the oxygen consumption rate.

The incremental-iterative form of eqs. (1) and (2) is solved numerically using the finite element method [5] and the in-house developed software.

2.3 Parameter estimation

As it was discussed in Section 2.2, there are overall 6 parameters of the numerical model - s_1, s_2, s_3, s_4, Q and Q_1 . It was demonstrated in literature [4] that for the considered experimental setup (where the aerobic conditions can be presumed) it can be assumed that unlimited supply of oxygen is available. For this reason, the parameters related to the oxygen consumption rate have almost no influence on the percentage of viable cells and are therefore estimated only for the control cancer cell lines and assumed equal for all considered cotreatments. The remaining 4 parameters vary for each considered cotreatment, so they are estimated for each considered treatment using the experimental data.

The estimation procedure was carried out in Matlab. The minimization function used for the estimation of parameters considers the percentages of cells obtained in experiment and simulation, 24 and 72 hours after treatment. The function can be described using the following relation:

$$SE = (V_{24}^e - V_{24}^s)^2 + (V_{72}^e - V_{72}^s)^2 \tag{3}$$

3. Results

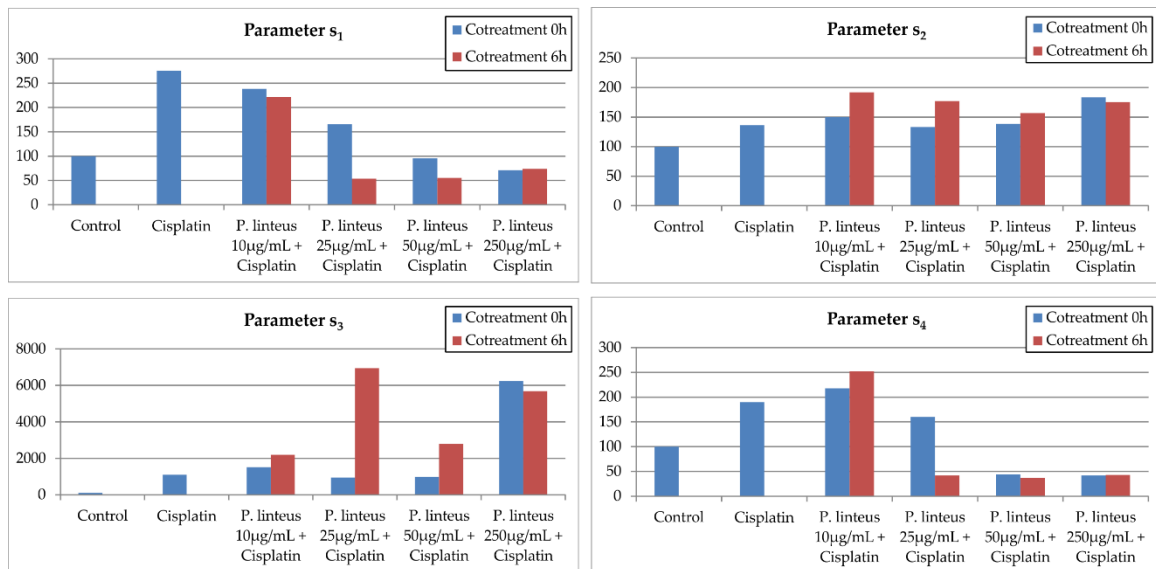


Figure 1. Values of estimated parameters for all considered cotreatments.

Figure 1 shows the results of the parameter estimation. The relative values of parameters are shown in order to ensure easier analysis of the influence of considered cotreatments. As it can be observed, the values of parameter s_1 that is related to cell proliferation decrease when the insertion of *P. linteus* treatment occurs 6 hours after the treatment with chemical compound. This means that cell proliferation is smaller for these cotreatments. Similarly, the values of parameters s_2 and s_3 related to cell death increase for the cotreatments after 6 hours, indicating that for these cases more cells die. It can be concluded that the cotreatment after 6 hours is more effective than the immediate administration of both treatments.

3. Conclusions

In this study, numerical simulations are applied to analyze the effect of diverse cotreatments of *P. linteus* extract and chemical compound (Cisplatin drug) on the numerical parameters of the model. This approach can provide valuable insight into the quantitative effect these considered treatments have on the behavior of cancer cell lines. Similar analyses could be also performed using numerical simulations to predict the values of parameters for diverse cases that were not studied experimentally, and this would be an additional benefit for the exploration of the effects of various possible treatments.

Acknowledgment

This research is funded by the Ministry of Science, Technological Development and Innovation, Republic of Serbia, Grants: No. 451-03-47/2023-01/200378 (Institute for Information Technologies, University of Kragujevac) and 451-03-47/2023-01/200107 (Faculty of Engineering, University of Kragujevac).

References

- [1] K. R. Swanson, C. Briggde, J. D. Murray, A. C. Jr. Ellsworth, *Virtual and real brain tumors: using mathematical modeling to quantify glioma growth and invasion*, J. Neurol. Sci. 216 (2003) 1-10.
- [2] C.J.W. Beward, H.M. Byrne, C.E. Lewis, *The role of cell-cell interactions in a two-phase model for avascular tumour growth*, J. Math. Biol. 45 (2002) 125-152.
- [3] D. S. Šeklić, M. S. Stanković, M. G. Milutinović, M. D. Topuzović, A. Š. Štajn, S. D. Marković, *Cytotoxic, antimigratory and pro/antioxidative activities of extracts from medicinal mushrooms on colon cancer cell lines*, Arch. Biol. Sci. 68 (2016) 93–105.
- [4] M. Živanović, M. Gazdić Janković, A. Ramović Hamzagić, K. Virijević, N. Milivojević, K. Pecić, D. Šeklić, M. Jovanović, N. Kastratović, A. Mirić, T. Đukić, I. Petrović, V. Jurišić, B. Ljujić, N. Filipović, *Combined Biological and Numerical Modeling Approach for Better Understanding of the Cancer Viability and Apoptosis*, Pharmaceutics. 15 (2023) 1628
- [5] M. Kojic, N. Filipovic, B. Stojanovic, N. Kojic, *Computer modeling in bioengineering, Theoretical Background, Examples and Software*, John Wiley and Sons, Chichester, England, 2008.

Overview of Left Ventricular Segmentation in Ultrasound Images

Bogdan Milićević^{1,2,*}, Miljan Milošević^{2,3,4}, Mina Vasković Jovanović¹, Vladimir Milovanović¹, Nenad Filipović^{1,2}, Miloš Kojić^{2,5,6}

¹ University of Kragujevac, Faculty of Engineering, Sestre Janjić 6, 34000 Kragujevac, Serbia; e-mail: bogdan.milicevic@uni.kg.ac.rs, mina.vaskovic.jovanovic@kg.ac.rs, vlada@kg.ac.rs, fica@kg.ac.rs

² Bioengineering Research and Development Center (BioIRC), Prvoslava Stojanovića 6, 34000 Kragujevac, Serbia; e-mail: miljan.m@kg.ac.rs, mkojic42@gmail.com

³ University of Kragujevac, Institute for Information Technologies, Jovana Cvijića bb, 34000 Kragujevac, Serbia

⁴ Belgrade Metropolitan University, Tadeuša Košćuška 63, 11000 Belgrade, Serbia

⁵ Serbian Academy of Sciences and Arts, Knez Mihailova 35, 11000 Belgrade, Serbia

⁶ Houston Methodist Research Institute, The Department of Nanomedicine, 6670 Bertner Ave., R7 117, Houston, TX 77030

DOI: 10.46793/ICCB23.359M

Abstract: Due to its great temporal resolution and quick acquisition periods, two-dimensional echocardiography, or shorter 2D echo, is the most used non-invasive approach for assessing heart disease. It offers a grayscale image that anatomical details can be extracted from to evaluate heart functioning. The initial stage in quantifying cardiac function in 2D echo is the segmentation of the left ventricular (LV) walls. The primary boundary identification methods used for 2D echo at the moment are semi-automatic or manual delineation carried out by professionals. However, manual or semi-automatic approaches take a lot of time and are subjective, which makes them vulnerable to both intra- and inter-observer variability. Many researchers have tried to automate the process of left ventricle segmentation. The extensive use of deep learning algorithms has lately changed medical image analysis. The revolution has primarily been powered by supervised machine learning with convolutional neural networks. In this paper, we will provide a short overview of some of the popular deep-learning techniques for left ventricular segmentation in two-dimensional echocardiography.

Keywords: echocardiography, left ventricle, image segmentation, convolutional neural networks

1. Introduction

The most popular non-invasive imaging technique for the detection of abnormalities within the heart is a two-dimensional echocardiogram (2D echo), which has a quick acquisition time, a low cost, and a high temporal resolution [1]. The initial stage in calculating clinical characteristics is boundary detection of the left ventricle (LV) in 2D echo, also known as image segmentation. LV segmentation in 2D echo is now mostly done semi-manually. More work must be done to segment the LV wall totally

automatically. Deep learning techniques can aid in automating the annotation process, but their effectiveness is constrained by the quantity and caliber of labeled training data, which can be hard to come by since annotating the raw data is laborious. Self-supervised learning can use unlabeled data that does not require input from clinical professionals. Contrastive pretraining on unlabeled data demonstrated considerable increases in performance for comparable tasks [2].

For biomedical image segmentation, UNet [3] and DeepLabV3 [4] are often used, and they have shown great performance in numerous segmentation issues. UNet is a fully convolutional network with a U-shaped design that comprises of a contracting path (encoder) and an expanding path (decoder). With skip connections between corresponding layers in the contracting and expanding paths, features are retrieved by the contracting path and then incrementally upsampled by the expanding path. To handle the problem of segmenting objects at multiple scales, DeepLabV3 was designed using modules that employ atrous convolution in cascade or in parallel to capture multi-scale context by adopting multiple atrous rates.

2. Methods

In this section, we will give a short description of commonly used neural network architectures for left ventricle image segmentation: UNet, SegAN, and DeepLabV3.

UNet comprises of an expanded path on the right and a contracting path on the left [3]. The contracting path adheres to the standard convolutional network architecture. It entails applying two 3x3 convolutions (unpadded convolutions) repeatedly, followed by a rectified linear unit (ReLU), a 2x2 max pooling operation, and a stride 2 downsampling operation for each convolution. We quadruple the number of feature channels with each downsampling step. Every step in the expansive path entails upsampling the feature map, followed by a 2x2 convolution (also known as an "up-convolution") that cuts the number of feature channels in half, a concatenation with the correspondingly cropped feature map from the contracting path, and two 3x3 convolutions, each followed by a ReLU. The cropping is necessary due to the loss of border pixels in every convolution. At the final layer, a 1x1 convolution is used to map each 64-component feature vector to the desired number of classes. In total, the network has 23 convolutional layers. To allow a seamless tiling of the output segmentation map, it is important to select the input tile size such that all 2x2 max-pooling operations are applied to a layer with an even x- and y-size.

The segAN, a neural network architecture for medical image segmentation is based on a generative adversarial model [5]. A generator (a network that learns how to sample from the sample's underlying distribution) and discriminator (a network that aids in enhancing the quality of the data points sampled by the generator) make up a generative adversarial network model (GAN). In the segAN design, the segmentor (which also serves as a generator) uses an encoder-decoder architecture to produce anticipated segmentation images from original images. The segmentor and the ground truth pictures serve as the discriminator's two inputs, which computes the loss between the

two input images. During the training, the segmentor aims to minimize the loss, whereas the discriminator aims to maximize the same loss.

DeepLabV3 offers an Atrous Spatial Pyramid Pooling (ASPP) module [4] that makes use of atrous (dilated) convolutions at various speeds to address the issue of object scale fluctuations as well as enlarge the receptive field while maintaining the spatial dimensions of the feature maps. The ASPP consists of a series of parallel, dilated convolutions with varying rates, followed by a concatenation of the outputs of those convolutions. Before upsampling back to the original resolution, the ASPP module processes features from the encoder. In [2], DeepLabV3 was chosen to train on a large publicly available EchoNet-Dynamic dataset [6], containing 20,060 annotated images from 10,030 patients. Random samples of echocardiographic images and corresponding masks from the EchoNet-Dynamic dataset are shown in Figure 1.

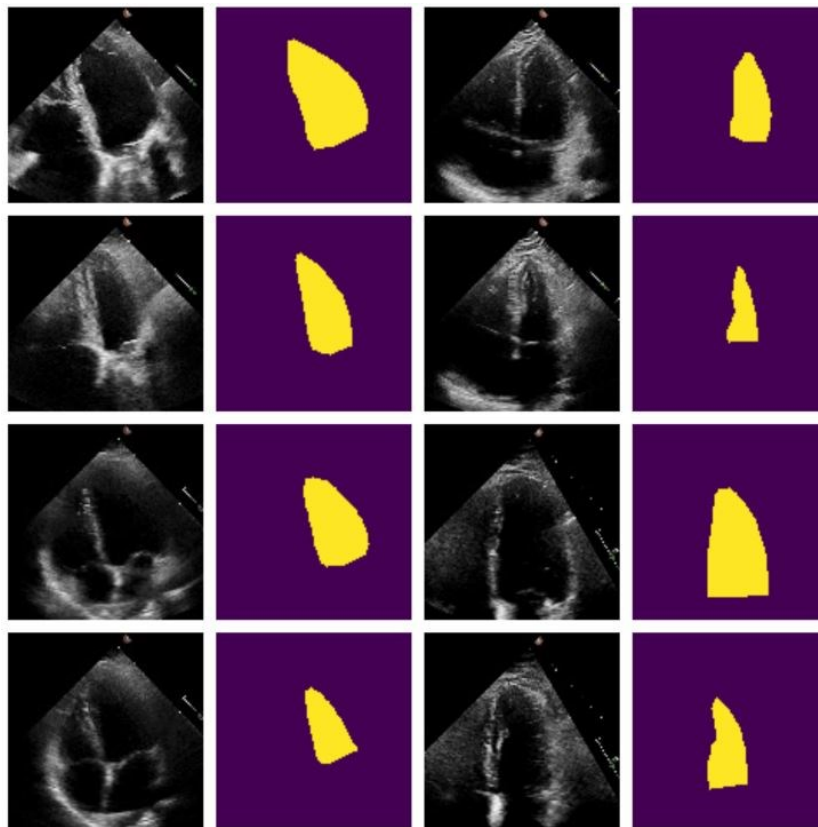


Figure 1. Random samples of echocardiographic images and corresponding masks from the EchoNet-Dynamic dataset.

3. Conclusions

Different CNN models, UNet, segAN, and DeepLabV3, have been employed to segment the LV from 2D echo images automatically by researchers. The assessment metrics and segmented images show that all of these methods achieve high performance on LV segmentation. While contrastive learning is an open research problem, it can be concluded that it could lead to an improvement in cardiac ultrasound segmentation, especially when annotated data for the downstream task is limited.

Acknowledgment

This research was supported by the European Union's Horizon 2020 research and innovation programme under grant agreement No 952603 (<http://sgabu.eu/>). This article reflects only the author's view. The Commission is not responsible for any use that may be made of the information it contains. Research was also supported by the SILICOFCM project that has received funding from the European Union's Horizon 2020 research and innovation programme under grant agreement No 777204. This article reflects only the authors' views. The European Commission is not responsible for any use that may be made of the information the article contains. The research was also funded by the Ministry of Education, Science and Technological Development of the Republic of Serbia, contract numbers [451-03-68/2022-14/200107 (Faculty of Engineering, University of Kragujevac) and 451-03-68/2022-14/200378 (Institute for Information Technologies Kragujevac, University of Kragujevac)].

References

- [1] T. Kim, M. Hedayat, V. V. Vaitkus, M. Belohlavek, V. Krishnamurthy, and I. Borazjani, "Automatic segmentation of the left ventricle in echocardiographic images using convolutional neural networks," *Quantitative Imaging in Medicine and Surgery*, vol. 11, no. 5. AME Publishing Company, pp. 1763–1781, May 2021. doi: 10.21037/qims-20-745.
- [2] M. Saeed, R. Muhtaseb, and M. Yaqub, "Contrastive Pretraining for Echocardiography Segmentation with Limited Data" *arXiv*, 2022. doi: 10.48550/ARXIV.2201.07219.
- [3] O. Ronneberger, P. Fischer, and T. Brox, "U-Net: Convolutional Networks for Biomedical Image Segmentation" *arXiv*, 2015. doi: 10.48550/ARXIV.1505.04597.
- [4] L.-C. Chen, G. Papandreou, F. Schroff, and H. Adam, "Rethinking Atrous Convolution for Semantic Image Segmentation" *arXiv*, 2017. doi: 10.48550/ARXIV.1706.05587.
- [5] Y. Xue, T. Xu, H. Zhang, L. R. Long, and X. Huang, "SegAN: Adversarial Network with Multi-scale L1 Loss for Medical Image Segmentation," *Neuroinformatics*, vol. 16, no. 3–4. Springer Science and Business Media LLC, pp. 383–392, May 03, 2018. doi: 10.1007/s12021-018-9377-x.
- [6] D. Ouyang et al., "Video-based AI for beat-to-beat assessment of cardiac function," *Nature*, vol. 580, no. 7802. Springer Science and Business Media LLC, pp. 252–256, Mar. 25, 2020. doi: 10.1038/s41586-020-2145-8.

Finite element analysis of stress distribution in 3D tooth model with extensive cavities restored with direct and indirect composite restoration

Ivana R. Kantardžić^{1*}, Bojana D. Ramić¹, Karolina Vukoje¹, Tijana Z. Lainović¹, Darko M. Vasiljević², Larisa Blažić¹

¹ University of Novi Sad, Faculty of Medicine, Department of Dental Medicine, Hajduk Veljkova 12, 21000 Novi Sad, Serbia; e-mail: ivana.kantardzic@mf.uns.ac.rs , bojana.ramic@mf.uns.ac.rs , karolina.vukoje@mf.uns.ac.rs , tijana.lainovic@mf.uns.ac.rs , larisa.blazic@mf.uns.ac.rs

² University of Belgrade, Institute of Physics, Photonics Centre, Pregrevica 118, 11080 Belgrade, Serbia; e-mail: darko@ipb.ac.rs

DOI: 10.46793/ICCBi23.363K

Abstract: Restoring a tooth with extensive loss of biological structures is a major challenge for any clinician, as it affects biomechanical properties and survival rate of the restored tooth. Using numerical simulation with finite element analysis (FEA), this study aimed to determine the influence of two types of extensive cavities (MOD - mesio-occlusal-distal cavity, MODBP - mesio-occlusal-distal cavity with buccal and palatal cusp reduction) and two different restorations (CRd-direct composite restoration, CRi-indirect composite restoration) on the stress distribution in 3D tooth models. First, a 3D model of an intact tooth was generated based on the CT scans of an extracted maxillary premolar. Then, four additional models were created with a combination of each cavity and restoration type. All 3D tooth models were subjected to a static occlusal load of 200 N to simulate masticatory forces. The results showed that CRi with MODBP cavity provides the most favourable stress distribution in the remaining tooth structures, thus suggesting that cusp reduction and a restorative material with a higher modulus of elasticity biomechanically protect the remaining tooth structures.

Keywords: finite element analysis, stress distribution, tooth, composite restoration

1. Introduction

In recent years, finite element analysis (FEA) and numerical simulations have been widely used as a research method in biomedical sciences [1-3]. By calculating stress and strain values in the biomedical three-dimensional (3D) models, this method allows a better understanding of the biomechanics of human structures. This is of great value, especially because such calculations are hardly possible *in vitro* and *in vivo* experiments. In addition, numerical simulations using FEA allow researchers to explore an infinite number of possibilities, helping to determine critical variables that can then be evaluated in a laboratory and clinical setting [4, 5].

Teeth are complex biostructures composed of multiple tissues (enamel, dentin, cementum and pulp) with different biomechanical properties. In the oral environment, they are affected by masticatory forces that result in stresses in each tissue. Intact teeth can withstand these forces [6, 7]. However, if there is a cavity in the tooth crown,

whether as a result of caries or other reasons, the fracture resistance of the tooth is reduced [6, 8]. To strengthen the tooth with a cavity, a restorative procedure should be performed. Various techniques and materials are available for this purpose, all of which have different effects on the stress distribution in the remaining tooth structures [9, 10]. The aim of this study was to create a 3D tooth model and to determine the influence of two types of extensive cavities (MOD - mesio-occlusal-distal cavity, MODBP - mesio-occlusal-distal cavity with buccal and palatal cusp reduction) and two different restorations (CRd-direct composite restoration, CRi-indirect composite restoration) on the stress distribution in the tooth structures using FEA.

2. 3D tooth model generation and FEA

An intact maxillary second premolar was used to create the 3D tooth model (Fig. 1a). After extraction, the tooth was cleaned of soft tissue debris and scanned with a multilayer CT scanner (SOMATOM Sensation 64 Cardiac, Siemens, Germany). A total of 110, 88 and 47 slices were acquired with a resolution of 0.5 mm along the *x*, *y*, and *z*-axis, respectively (Fig. 1b). The 42 slices from the *z*-axis that contained useful information were imported into AMIRA software (Visage Imaging Inc., USA) for tooth structure (enamel, dentin, pulp) segmentation (Fig. 1c). Then, the obtained counters were imported into SolidWorks software (Dassault Systèmes SolidWorks, USA) (Fig. 1d), where a 3D tooth model was generated (Fig. 1e). In addition, based on literature data [6], the periodontal ligament and alveolar bone around the tooth were created using the same software.

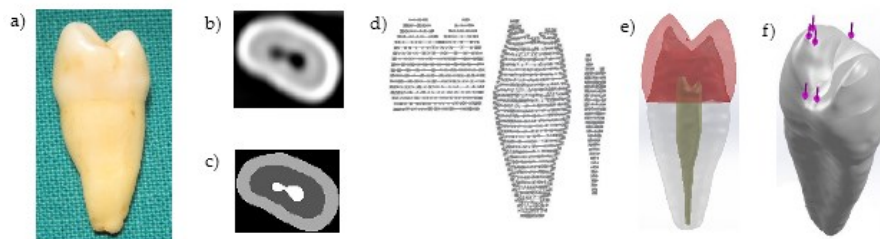


Figure 1. 3D tooth model generation: a) intact maxillary premolar, b) DICOM slice, c) segmented tooth structures in AMIRA, d) counters of enamel, dentin and pulp in SolidWorks, e) 3D model of intact premolar, f) loading conditions.

Afterwards, two types of cavities were generated (MOD and MODBP). Both cavities had a width of $\frac{1}{2}$ the intercuspal distance and a gingival wall located 1 mm above the enamel-cement junction. In the MODBP cavity additional buccal and palatal cusp reduction of 2 mm was performed. For CRd restoration, the buccal and palatal walls of the cavities were parallel to the tooth axis. In models with CRi restoration, the buccal and palatal walls had an occlusal divergence of 6° , and a 0.1 mm layer of adhesive cement was added between the cavity walls and the restoration.

All tooth structures and restorative materials were modelled as linear, elastic and isotropic with defined mechanical properties (Table 1). Boundary conditions were set at the outer surface of the alveolar bone, and a static occlusal load of 200 N was applied to

the occlusal surface of the tooth (Fig. 1f). FEA was used to determine the distribution of von Mises stress values in the restored 3D tooth model.

Table 1. Mechanical properties assigned to dental tissues and restorative materials [9].

Material	Young's modulus (MPa)	Poisson's ratio
Enamel	84100	0.20
Dentin	18600	0.31
Pulp	2	0.45
Periodontal ligament	70	0.45
Cortical bone	15000	0.30
Cancellous bone	1500	0.30
Direct composite restoration	6700	0.22
Indirect composite restoration	50000	0.30
Adhesive cement	6000	0.30

3. Results

The maximum von Mises stress values for the remaining tooth structures and restorative materials are presented in Table 2.

Table 2. Maximum von Mises stress values in all models (MPa).

Model	Enamel	Dentin	Restoration
MOD + CRd	126.5	35.7	129.8
MOD + CRi	125.7	36.6	146.1
MODBP + CRd	105.0	38.7	126.2
MODBP + CRi	100.0	34.2	121.1

The maximum von Mises stresses in enamel and dentin were similar for models with MOD cavity for both restorations. However, for models with MODBP cavities, there is a slight decrease in stress values in the remaining tooth structures when CRi is used. For the restoration, the highest stress values are registered in CRi in the model with MOD cavity.

The stress distribution is shown in Figure 2. CRi in the MODBP cavity resulted in the most favourable stress distribution in the remaining tooth structures, while the stress distribution was the same for all restorations.

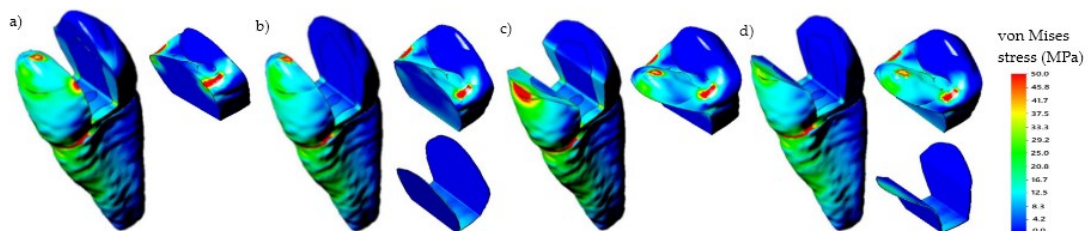


Figure 2. Stress distribution: a) MOD + CRd, b) MOD + CRi + adhesive cement c) MODBP + CRd, d) MODBP + CRi + adhesive cement.

4. Conclusions

The presented numerical simulation, with the FEA application showed that both the type of cavity and the restorative material influence the stress distribution in the 3D restored tooth model. According to the results, it could be suggested that premolars with extensive cavity should be prepared with MODBP cavity and restored with indirect composite restoration in order to achieve the optimal biomechanical properties.

Acknowledgment

This research is funded by the Ministry of Education and Ministry of Science, Technological Development and Innovation, Republic of Serbia, Grants: III45016 and TR35020; and the Office of Naval Research Global through the Research Grant N62902-22-1-2024.

References

- [1] T. Maravić, A. Comba, C. Mazzitelli, L. Bartoletti, I. Balla, E. di Pietro et al., *Finite element and in vitro study on biomechanical behaviour of endodontically treated premolars restored with direct or indirect composite restorations*, *Scientific Reports*, 12 (2022) 1-11.
- [2] Y. Huang, W.A. Fokkinga, Q. Zhang, N.H.J. Creugers, Q. Jiang., *Biomechanical properties of different endocrown designs on endodontically treated teeth*, *Journal of the Mechanical Behavior of Biomedical Materials*, 140 (2023) 1-9.
- [3] K. Zelić, A.M. Vukićević, G. Jovičić, S. Aleksandrović, N. Filipović, M. Đurić., *Mechanical weakening of devitalized teeth: three-dimensional Finite Element Analysis and prediction of tooth fracture*, *International Endodontic Journal*, 48 (2015) 850-863.
- [4] P. Magne., *Efficient 3D finite element analysis of dental restorative procedures using micro-CT data*, *Dental Materials*, 23 (2007) 539-548.
- [5] P. Magne, T. Oganesyanyan., *CT scan-based finite element analysis of premolar cuspal deflection following operative procedures*, *International Journal of Periodontics and Restorative Dentistry*, 29 (2009) 361-369.
- [6] P.V. Soares, P.C. Santos-Filho, L.R. Martins, C.J. Soares., *Influence of restorative technique on the biomechanical behavior of endodontically treated maxillary premolars. Part I: Fracture resistance and fracture mode*, *Journal of Prosthetic Dentistry*, 99 (2008) 30-77.
- [7] P.V. Soares, P.C. Santos-Filho, L.R. Martins, C.J. Soares., *Influence of restorative technique on the biomechanical behavior of endodontically treated maxillary premolars. Part II: strain measurement and stress distribution*, *Journal of Prosthetic Dentistry*, 99 (2008) 114-122.
- [8] N.A. Taha, J.E. Palamara, H.H. Messer., *Fracture strength and fracture patterns of root filled teeth restored with direct resin restorations*, *Journal of Dentistry*, 39 (2011) 527-535.
- [9] I. Kantardžić, D. Vasiljević, O. Lužanin, T. Maravić, L. Blažić., *Influence of the restorative procedure factors on stress values in premolar with MOD cavity: a finite element analysis*, *Medical & Biological Engineering & Computing*, 56 (2018) 1875-1886.
- [10] A. Merdji, R. Mootanah, B.A. Bouiadjra, A. Benaissa, L. Aminallah, E.B. Chikh et al., *Stress analysis in single molar*, *Materials Science and Engineering C*, 33 (2013) 691-698.

Multiscale Modelling of the Effects of Temperature on Cardiac Twitches

Momcilo Prodanovic^{1,2*}, Srboljub M. Mijailovich²

¹ University of Kragujevac, Institute for Information Technologies, Department of technical and technological sciences, Kragujevac, Serbia; e-mail: momcilo.prodanovic@kg.ac.rs

² FilamenTech, Inc., Newton, 02458 MA, USA; e-mail: smijailo@gmail.com

* *Corresponding author*

DOI: 10.46793/ICCB23.367P

Abstract: Functional changes in cardiac muscle, caused by mutations in sarcomere proteins, are significant for understanding cardiac pathophysiology. Experimental investigations of mechanical responses in cardiac tissue, especially in humans, are limited due to challenges in obtaining suitable samples. Trabeculae from transgenic rodent models serve as a common experimental model for studying cardiac function. However, differences in temperature between experimental settings and physiological conditions, as well as differences in myosin α and β isoform content, can complicate the interpretation and translation of findings from rodents to humans. To bridge this gap, we present a novel methodology utilizing the MUSICO computational simulation platform for multiscale modeling of cardiac twitch contractions. MUSICO integrates crossbridge cycling, calcium regulation of thin and thick filaments, explicit 3D sarcomere geometry, and species-specific mixtures of myosin isoforms. In this study, we quantitatively estimated the impact of temperature variations on twitch transients in rat trabeculae using MUSICO simulations. Model predictions were compared with a consistent set of experimental data from rat trabeculae. Our results demonstrated that the temperature of the experiments plays a significant role in force generation during cardiac muscle twitch, since it affects intracellular calcium concentrations, but also influences several crossbridge cycle kinetic rates which had to be adjusted in simulations for accurate predictions of twitch responses. By accounting for species-specific physiological variations and the temperature sensitivity of cardiac responses, this approach offers insights into a more comprehensive understanding of cardiac dynamics, ultimately leading to the prediction of human cardiac muscle responses under physiological conditions. Through improved predictive capabilities, MUSICO will open new opportunities for the development of novel therapeutics and treatments targeting cardiomyopathies.

Keywords: cardiac muscle, rat trabecula, temperature effect, twitch contraction, MUSICO simulation

1. Introduction

The complexities of cardiac muscle function, modulated by sarcomere proteins, are pivotal for understanding cardiovascular health. Mutations in these proteins can lead to significant functional changes, with profound implications for cardiac pathophysiology.

Experimental models like rodent trabeculae offer insights into heart mechanics, yet translating these findings to human physiology requires considering factors such as temperature dependence and species-specific protein isoforms.

Investigating cardiac mechanical responses requires a comprehensive approach. Temperature, often overlooked, fundamentally influences biochemical reactions and protein function. The significant study by Janssen et al. [1] points out the connection between temperature, muscle tension and intracellular calcium concentrations in cardiac muscle, emphasizing the need for precise temperature control in experiments.

Computational models, such as MUSICO (Muscle Simulation Code) platform [2], complement multiscale experiments and provide a comprehensive framework for understanding cardiac function. Recent studies by Mijailovich et al. [2] emphasize the significance of temperature in accurately characterizing mechanical responses in rat cardiac tissue. This study showed that temperature has the effect of changing several acto-myosin crossbridge cycle kinetic rates. However, the simulations included a single (equivalent) myosin isoform, instead mixture of 75% α and 25% β myosin isoforms observed in rat ventricular muscles. In our following study, Prodanovic et al. [3], we included the observed mixture of the isoforms, however simulation were done at single temperature of 25°C exclusively using dataset acquired from Chung et al. [4].

In this study we investigate implications of a range of temperatures on rat cardiac twitch contractions. By synergizing experimental data with computational simulations we aim to unravel the relationship between temperature and cardiac twitch dynamics.

2. Methods

The experimental data for examining the temperature dependence of cardiac twitches were obtained from the study by Janssen et al. [1]. In this study, temperature was gradually increasing between 22.5°C and 37.5°C in 2.5°C intervals, while simultaneously recording force and calcium transients during twitches in rat trabeculae preparations at 0.5 Hz stimulating frequency.

The computational simulations were conducted using the MUSICO platform, which enables simulation of cardiac muscle twitch contractions by accounting for all interactions between sarcomere proteins in the explicit 3D sarcomere geometry. The crossbridge model contains five biochemical states of the chemomechanical cycle, and a “parked” state associated with thick filament regulation by calcium [2]. The model of thin filament regulation by $[Ca^{2+}]$ consists of four states [2]. Furthermore, model accounts for species-specific mixtures of myosin fast (α) and slow (β) isoforms [3]. Simulation parameters were primarily derived from the studies of cardiac muscle contractions in rodents and humans by [3], while $[Ca^{2+}]$ transients were taken from the experimental observations [1]. However, due to differences in experimental conditions in Janssen et al. [1] and Chung et al. [4], a few adjustments of the crossbridge cycle kinetic rates from [3] were essential to obtain good match with the observations in Janssen et al. [1] at 25°C. Particularly, myosin binding and detachment to actin rates, k_{+A} and k_{-A} respectively, were increased 1.5 times, myosin reverse powerstroke cap rates, k_{-pi}^{cap} , for fast and slow

myosin isoforms were increased 2-fold, while ADP release rates, k_{+D} , for both myosin isoforms were decreased 2-fold compared to the values reported in Prodanovic et al. [3].

These adjusted parameters, alongside the observed patterns of temperature-induced changes in crossbridge kinetic rates used in simulations of rat trabeculae with a single myosin isoform [2], served as a basis for creating a translation matrix (Figure 1). This matrix enables quantitatively connecting the effects of temperature on twitch contractions in rat cardiac trabeculae allowing simulation of cardiac muscle behavior at physiologically relevant temperatures, as well as cross-species translation.

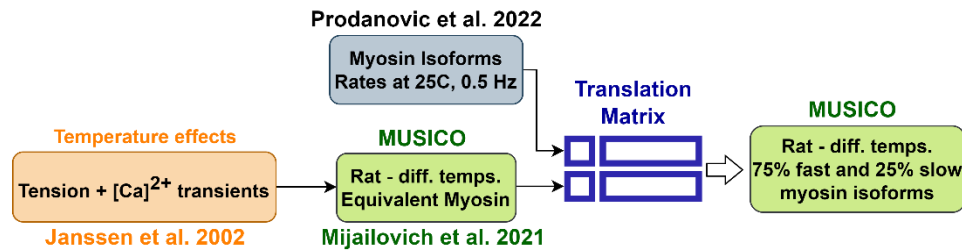


Figure 1. Workflow for predicting twitches in rat cardiac muscle at various temperatures.

3. Results

Using MUSICO platform and translation matrix, the proposed workflow for predicting twitches at various temperatures demonstrated good simulation fits to the experimental twitch data (Figure 2A). As observed, increase of temperature affects calcium transients (inset in Figure 2A) which consequently increases twitch responses.

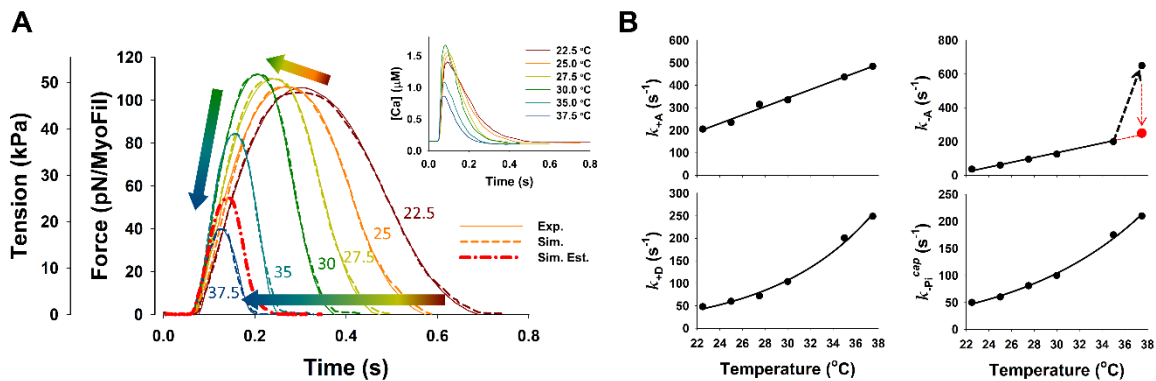


Figure 2. MUSICO simulations of temperature dependence on rat cardiac twitch. A) Simulations (dashed lines) compared to experimental observations [1] (thin lines). Inset: $[Ca^{2+}]$ transients from [1] used as the inputs for simulations. B) Temperature dependence of acto-myosin crossbridge cycle kinetic rates in MUSICO.

Moreover, twitch duration is decreasing, while peak of the twitch is rising until temperature reaches 30°C and then progressively declines. Beside intracellular calcium transients, simulations show that temperature strongly affects kinetic rates of acto-myosin crossbridge cycle by progressively increasing myosin to actin binding and

detachment rates (k_{+A} and k_{-A}), ADP release rate (k_{+D}) and reverse powerstroke cap rates, k_{-Pi}^{cap} , (Figure 2B).

However, it should be noted that rapid decline in observed twitch tension at 37.5°C could potentially originate from inconsistencies in the recording of tension and calcium transients. This is reflected in the drastic increase in myosin detachment rate (Figure 2B). Following the pattern of twitch peak decline with increasing the temperature above 30°C, it was expected that the peak tension at 37.5°C would be between 25-30 kPa. Assuming this, simulations predicted expected physiological peak tension of 25.4 kPa for $k_{-A} = 250s^{-1}$ (red dotted line in Figure 2A), based on the linear increase of the rate by temperature (red point in Figure 2B).

4. Conclusions

MUSICO simulation showed that temperature plays a significant role in tension generation during cardiac muscle twitch. Besides observed effects on intracellular calcium concentrations, simulations revealed that temperature affects several crossbridge cycle kinetic rates. Because numerous recorded observations fall beyond the physiological temperature range, translating data across scales and species becomes a formidable challenge. However, our translational matrix approach, as demonstrated, effectively integrates various datasets to provide valuable insights even in data-scarce scenarios. To deepen our understanding, collecting detailed experimental data across the full physiological temperature range holds promise for uncovering novel cardiac phenomena. By accounting for species-specific physiological variations and the temperature sensitivity of cardiac responses, this approach offers insights into a more comprehensive understanding of cardiac dynamics, ultimately leading to prediction of human cardiac contractions more accurately under physiological conditions.

Acknowledgment

This research is funded by the Ministry of Science, Technological Development and Innovation, Republic of Serbia, Grant: No. 451-03-47/2023-01/200378.

References

- [1] P. M. Janssen, L. B. Stull, and E. Marban, "Myofilament properties comprise the rate-limiting step for cardiac relaxation at body temperature in the rat," *Am J Physiol Heart Circ Physiol*, vol. 282, pp. H499-507, Feb 2002.
- [2] S. M. Mijailovich, M. Prodanovic, Poggesi, C., M. A. Geeves, and M. Regnier, "Multiscale Modeling of Twitch Contractions in Cardiac Trabeculae," *Journal of General Physiology*, vol. 153 p. e202012604, 2021.
- [3] M. Prodanovic, M. A. Geeves, C. Poggesi, M. Regnier, and S. M. Mijailovich, "Effect of Myosin Isoforms on Cardiac Muscle Twitch of Mice, Rats and Humans," *Int J Mol Sci*, vol. 23, Jan 20 2022.
- [4] C. S. Chung, C. W. Hoopes, and K. S. Campbell, "Myocardial relaxation is accelerated by fast stretch, not reduced afterload," *J Mol Cell Cardiol*, vol. 103, pp. 65-73, Feb 2017.

Analytically Computed Fractional Flow Reserve based on Coronary CT Angiography

Aleksandar Milovanović^{1*}, Velibor Isailović², Igor Saveljić¹, Nenad Filipović²

¹ University of Kragujevac, Institute for Information Technologies, 34000 Kragujevac, Serbia; e-mail: acakg85@hotmail.com, isaveljic@kg.ac.rs

² University of Kragujevac, Faculty of Engineering, 34000 Kragujevac, Serbia; e-mail: velibor@kg.ac.rs, fica@kg.ac.rs

* Corresponding author

DOI: 10.46793/ICCB23.371M

Abstract: Invasively determined Fractional Flow Reserve (FFR) has been recognized as a reliable tool for assessing coronary artery stenosis severity. Since the invasive method is associated with a risk of vessel injury due to pressure wire manipulation several non-invasive techniques have been developed. The objective of this paper is to propose an alternative, much less time-consuming, analytical solution based on Computed Tomography Angiography (CTA) images and the overall pressure drop calculation across the stenosis in the coronary artery.

The results obtained using this method are validated by comparing them with the clinical data for patients who underwent invasive coronary angiography as well as with the results obtained by using CFD simulation. FFR determined using the analytical method compared with the clinical and CFD ones differs by 4.5% and 3.9% respectively. This confirms that the analytically determined FFR can be reliable for the physiological assessment of coronary artery stenosis.

Keywords: coronary artery stenosis, fractional flow reserve, analytical method, CTA images

1. Introduction

Cardiovascular diseases (CVDs) refer to any type of disturbance in the normal functioning of the heart and blood vessels [1] whose frequency has dramatically increased in the modern world as a consequence of overall global trends (social, economic, demographic, etc.) [2]. Coronary artery disease (CAD) represents the most common type of cardiovascular disease. The cause of this disease in more than 95% of cases is atherosclerosis, which occurs in coronary arteries as a result of the deposition of cholesterol, fibrous tissue, calcium and other substances contained in the blood [3]. This results in the appearance of atherosclerotic plaque inside blood vessels (Fig. 1) which forms a barrier (stenosis) that restricts the blood flow to the heart and causes myocardial ischemia, the most prevalent risk factor associated with adverse clinical outcomes.

A number of methods, such as *Invasive Coronary Angiography (ICA)*, *Myocardial scintigraphy (MS)*, *Magnetic Resonance Imaging (MRI)* and *Computed Tomography Coronary Angiography (CTCA)* can be used for the diagnosis and monitoring of coronary artery

disease. However, all these methods rely on visual assessment of coronary artery obstruction and are unable to directly assess its hemodynamic significance.



Figure 1. Coronary artery disease [4]

In order to overcome these shortcomings additional algorithms have been developed to enhance the assessment of coronary stenoses severity and make the best possible decisions about further steps in the treatment of patients (medical therapy or percutaneous or surgical revascularization) [5].

2. Determination of Fractional flow reserve (FFR)

Fractional flow reserve (FFR), first proposed by Pijls [6], represents a significant advance in assessing the functional significance of coronary artery stenosis. FFR is based on the fact that stenosis causes a pressure drop proportional to the narrowing of the cross-section caused by the formed plaque. FFR is calculated as [7]:

$$FFR = \frac{P_a - \Delta P}{P_a} \quad (1)$$

where P_a is proximal arterial pressure (equal to aortic pressure) and ΔP is the overall pressure loss along the vessel segment.

The overall pressure loss consists of four losses (due to flow convection, constriction at the entrance of stenosis, flow diffusion and expansion post-stenosis).

The pressure drops due to flow convection can be expressed as [8]:

$$\Delta P_{conv} = \frac{\rho}{2} (V_{out}^2 - V_{in}^2) = \frac{\rho Q^2}{2} \left(\frac{1}{A_{out}^2} - \frac{1}{A_{in}^2} \right) \quad (2)$$

where ρ , V and Q are blood density, blood velocity and flow rate, while A_{in} and A_{out} represent the cross sectional areas proximal and distal to stenosis.

In the case of fully developed flow, the pressure drop due to constriction is [9]:

$$\Delta P_{contr} = \frac{\rho Q^2}{2} \frac{1}{2} \left(\frac{1}{A_{sten}^{8/3}} - \frac{1}{A_{prox} A_{sten}^{5/3}} \right)^{3/4} \quad (3)$$

where A_{sten} and A_{prox} the sectional areas of stenosis and artery proximal to stenosis.

The pressure drop due to flow diffusion which is caused by viscosity, initiates flow acceleration. If we suppose an inviscid flow core (with a uniform velocity) at the entrance of stenosis defined by a dimensionless radius ϕ which can be calculated by [10]:

$$\frac{\pi\mu L_{sten}}{4\rho Q} = \frac{1}{4} \int_{\varphi}^1 \frac{(1-\varphi)(6+\varphi)(1+4\varphi+9\varphi^2+4\varphi^3)}{5\varphi(3+2\varphi)(3+2\varphi+\varphi^2)^2} d\varphi \quad (4)$$

In case $\varphi < 0.05$, that is usual for coronary artery, the pressure drop due to diffusion is:

$$\Delta P_{diff}^{vess} = \frac{\rho Q^2}{2A_{sten}^2} \frac{96}{5} \int_{\varphi}^1 \frac{(1+4\varphi+9\varphi^2+4\varphi^3)}{\varphi(3+2\varphi)(3+2\varphi+\varphi^2)^2} d\varphi + \int_0^{L_{vess}-L_{entr}} \frac{8\pi\mu Q}{A_{in}^2} dx \quad (5)$$

while the pressure drop due to sudden expansion is:

$$\Delta P_{exp}^{par} = \rho Q^2 \left[\left(\frac{1}{A_{sten}} - \frac{1}{A_{dist}} \right) \left(\frac{1}{A_{sten}} - \frac{1}{3} \frac{1}{A_{dist}} \right) \right] \quad (6)$$

The total pressure drop is calculated as the sum of (2), (3), (4) and (6):

$$\Delta P = \Delta P_{conv} + \Delta P_{contr} + \Delta P_{diff} + \Delta P_{exp} \quad (7)$$

All needed anatomic parameters (diameters, lengths, areas, etc.) were taken from the corresponding artery models reconstructed from CTA images.

3. Results

Using the presented analytical model, FFR values were computed for 20 patients. These values are compared with the corresponding medical (experimental) values obtained by the invasive method. Figure 1 shows the relationship between the medical results (mFFR) and the results obtained by the proposed analytical method (aFFR). A linear least-squares fit method gave the relation $mFFR = 0.041 + 0.972 \cdot aFFR$. The coefficient of determination is $R^2 = 0.854$. A relatively small deviation of the results in relation to the regression line is observed.

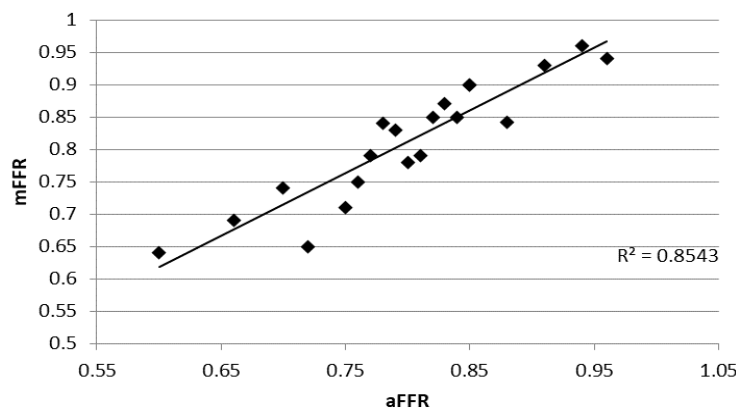


Figure 1. A relationship between medical and analytical FFR.

4. Conclusion

The presented analytical model is based on conservation of energy, which takes into account various energy (pressure) losses along the stenosis. It calculates non-invasive aFFR from CTA images data. This method was validated for 20 models of coronary arteries using the corresponding experimental data obtained by “gold standard” invasive measurement. A very good coefficient of determination (0,926) is observed in the entire range of FFR values. This confirms that the presented analytical model can reliably assess the physiological significance of the stenosis, and accordingly, suggest further treatment of the patient. At the same time, this method requires significantly lower computation time.

Acknowledgment

This research is funded by the Ministry of Science, Technological Development and Innovation, Republic of Serbia, Grants: No. 451-03-68/2022-14/200378.

References

- [1] P. Libby, R.O. Bonow, D.L. Mann, et al., *Braunwald's Heart Disease, Single Volume: A Textbook of Cardiovascular Medicine*, Elsevier, 12th edition (2022) p2032.
- [2] G.A. Roth, G.A. Mensah, C.O. Johnson, et al., *Global Burden of Cardiovascular Diseases and Risk Factors*, *Journal of American College of Cardiology*, 76(25) (2020) 2982–3021.
- [3] N.V.K.Pothineni, S. Subramany, K. Kuriakose, et al., *Infections, atherosclerosis, and coronary heart disease*, *European Heart Journal*, 38(43) (2017) 3195-3201.
- [4] V.L. Roger, A.S. Go, D.M. Lloyd-Jones, et al., *Heart disease and stroke statistics-2011 update: A report from the American Heart Association*, *Circulation*, 123 (2011) e18-e209.
- [5] P.D. Morris, R. Al-Lamee & C. Berry, *Coronary physiological assessment in the catheter laboratory: haemodynamics, clinical assessment and future perspectives*, *Heart*, 108 (2022) 1737-1746.
- [6] N.H. Pijls, J.A. van Son, R.L. Kirkeeide et al., *Experimental basis of determining maximum coronary, myocardial, and collateral blood flow by pressure measurements for assessing functional stenosis severity*, *Circulation*, 86(4) (1993) 1354-1367.
- [7] A. Milovanovic, I. Saveljic. & N. Filipovic., *Numerical vs Analytical Comparison with Experimental Fractional Flow Reserve Values of Right Coronary Artery Stenosis*. *Technology and Health Care*, 31(3) (2023) 977-990.
- [8] G. Хајдин., *Mehanika fluida, knjiga prva, šesto izdanje*, Građevinski fakultet, Univerzitet u Beogradu (2021).
- [9] S. Sisavath, X. Jing, C.C Pain, & R.W. Zimmerman., *Creeping flow through an axisymmetric sudden contraction or expansion*, *Journal of Fluids Engineering*, 124 (2002) 273-278.
- [10] Y. Huo, M. Svenson, J.S. Choy et al., *A validated predictive model of coronary fractional flow reserve*, *Journal of the Royal Society Interface*, 9 (2012) 1325-1338.

A finite element model for structural optimization of parametrized lattice scaffolds

Jovan Z. Arandjelović^{1*}, Rajko M. Turudija¹, Nikola D. Korunović¹, Miloš S. Stojković¹, Jelena R. Stojković¹

¹ University of Niš, Faculty of Mechanical Engineering, Department of Production Information Technologies, Niš, Serbia (Aleksandra Medvedeva 14); e-mail: jovan.arandjelovic@masfak.ni.ac.rs, rajko.turudija@masfak.ni.ac.rs, nikola.korunovic@masfak.ni.ac.rs, milos.stojkovic@masfak.ni.ac.rs, jelena.stojkovic@masfak.ni.ac.rs

DOI: 10.46793/ICCB23.375A

Abstract: In modern biomedical engineering, scaffold development has become an important direction of research. Multiple research papers have covered this topic, considering mechanical performance, production methods, etc. Nevertheless, to the author's knowledge, no study has considered creating a numerical meta model that links several lattice scaffold design parameters with the stress-strain behavior of the scaffold. In this paper, we start to address this topic. A novel approach to generic parametrized lattice scaffold model design, proposed by the authors previously, is improved. A corresponding model for finite element analysis (FEA) based structural optimization of lattice scaffold is presented, which is derived from a flexible and robust parametric computer aided design (CAD) model. A bidirectional link between the CAD and FEA models is established enabling model changes to be transferred in both directions, which is a prerequisite for automatic performance of sensitivity and structural optimization studies.

Keywords: Finite Element Method (FEM), Biomedical engineering, Scaffold, Structural optimization

1. Introduction

Scaffolds are used to replace missing parts of bones in cases where a large part of the bone is lost (a part large enough that the bone cannot heal naturally) [1]. More specifically, they are used to guide bone growth and provide mechanical support for bone fractures [2]. Based on their geometry, scaffolds can be divided into two groups: porous scaffolds (that have geometry like that of spongy bone tissue and are divided into unit cells) and lattice scaffolds (that are created through the distribution of 3D struts in a volume, usually by repeating pattern) [2]. Out of these two groups, less attention has been given to research on lattice scaffolds due to their complex design [3]. For this reason, lattice scaffolds have been chosen for this study.

This paper focuses on the preparation of the computer aided design (CAD) that serves as the basis for finite element model creation, finite element model setup and testing of the flexibility and robustness of CAD and finite element analysis (FEA) models through a sensitivity analysis. As a result of sensitivity analysis, a response surface that predicts the effects that changes in scaffold structural parameters have on mechanical behavior is created. The resulting finite element (FE) model can be used for the structural optimization of the scaffold and the determination of the functions that link the dimensions of the scaffold to its mechanical behavior, which are important for the scaffold design process.

2. Methodology

The CAD model was created in SolidWorks using a procedure described in [3]. The model is defined through 12 parameters and multiple formulas that link some of them together. For this study, 5 parameters were chosen as structural parameters (Figure 1): **outer strut diameter** (OSD, diameter of green struts), **inner strut diameter** (ISD, diameter of yellow struts), **outer strut angle** (OSA, angle between the green struts and vertical axis), **inner strut angle** (ISA, angle between the yellow struts and vertical axis) and **number of outer struts** (NOOS, number of green struts in one direction, equal to half of all outer struts, must be a whole even number for the model to be flexible and robust).

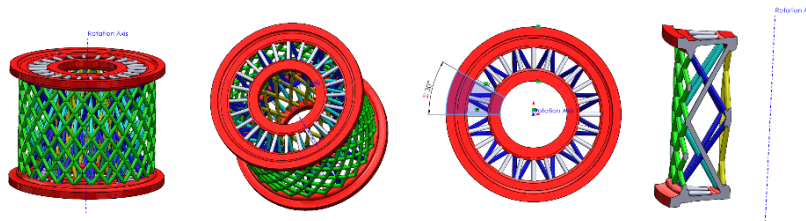


Figure 1. CAD model of the scaffold.

The values of model parameters other than structural ones are set in the following way (Figure 1): **number of inner struts** is equal to a half of the number of outer struts (this is done to create comparable variations of the model where the cross struts always connect to the same points on inner and outer struts), **outer ring diameter** (big red ring) is set to 36 mm, **inner ring diameter** (small red ring) is set to 18 mm, while **height** is set to 30 mm. These dimensions were determined approximately based on a simulated subtrochanteric fracture of the standardized composite femur [4]. The **arc distance** between two outer struts is calculated based on the formula:

$$\text{arc distance} = \text{outer ring diameter} \cdot \frac{\pi}{\text{number of outer struts}} \quad (1)$$

the **base strut diameter** (grey struts, Figure 1) and **cross strut diameters** (turquoise and blue struts, Figure 1) are set to 1 mm, the minimal diameter that can be produced successfully on a selective laser sintering (SLS) additive manufacturing (AM) machine (this is done because the inner and outer struts will take the brunt of the load).

By defining the model parameters in the described way, a finite element model based on cyclic symmetry can be created, as the model can be cut into multiple identical portions using radial planes. The number of these portions, a.k.a. symmetry regions, is equal to the number of outer struts. A formula is added to determine the angle (between the axes of the base struts) of the symmetry region cut (Figure 1):

$$\text{symetry angle} = \frac{360^\circ}{\text{number of outer struts}} \quad (2)$$

Using cyclic symmetry significantly decreases the size of the finite element model and thus reduces the needed computing time and enables the use of a much finer FE mesh.

To define the FE model presented in this paper, the parametric CAD model was imported into ANSYS. Typical material properties of SLS produced PA12 (Young's Modulus 1780 MPa, Poisson's Ratio 0.4, Tensile Yield Strength 21.2 MPa and Tensile Ultimate Strength 30 MPa) were applied to the model [5]. A default mesh element size of 0.1 mm was used for the struts, while the outer and inner rings (red rings, Figure 1) were set to 0.4 mm. The number of elements varied depending on the dimensions of the scaffold, taking values between 290000 and 360000 elements.

A cylindrical coordinate system was created to define the cyclic symmetry region (this was possible because the symmetry of material, boundary conditions and geometry existed). For the cyclic region to be fully defined, start and end surfaces that can be regenerated for any combination of structural parameters must be defined. To do so, a local coordinate system was created on a cross-strut surface, which is present in every variation of the model. This made it possible to automatically select all surfaces that lie in these planes (by setting the selection distance to 0 mm in the normal direction of the local coordinate system, Figure 2) for every variation of the model.

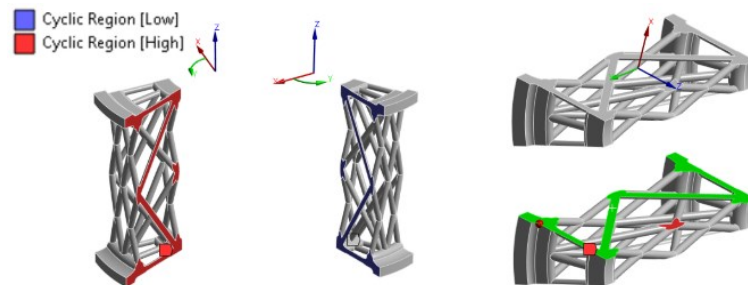
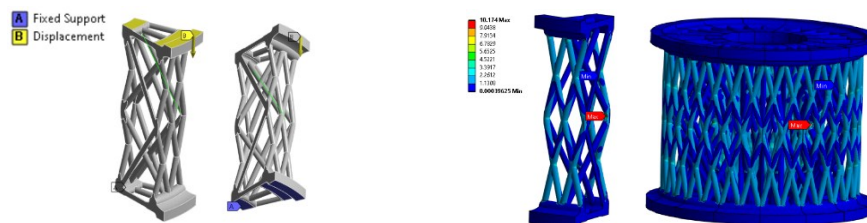


Figure 2. A portion of CAD model of the scaffold obtained using cyclic symmetry.

Compression of the scaffold was modeled by applying a 0.025 mm displacement on the top faces and a fixed support on the bottom faces (Figure 3 a). The typical von Mises stress field obtained by FEA is shown in Figure 3 b.



a) b)
Figure 3. a) Scaffold boundary conditions and b) von Mises stress results

3. Conclusions

The developed CAD and FEA models could successfully be regenerated for any combinations of input parameters: OSD and ISD (from 1 to 1.8mm with an 0.1 increment), OSA (from 30° to 70° with an 1° increment), ISA (from 30° to 40° with an 1° increment), and discrete values of 20, 22, 24, 26, 28 and 30 for NOOS. This makes the model ideal for future sensitivity analyses and structural optimization studies, the results of which will model the relationship between the dimensions of lattice scaffolds and its mechanical behavior. An example of one such relationship is shown in Figure 4.

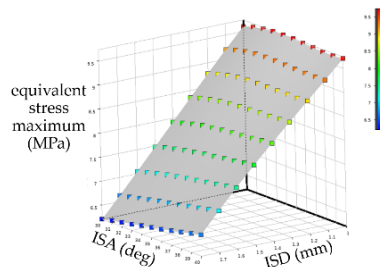


Figure 4. Response surface example: effect of inner strut diameter and angle on maximum von Mises stress

Acknowledgment

This research was financially supported by the Ministry of Science, Technological Development and Innovation of the Republic of Serbia (Contract No. 451-03-47/2023-01/200109).

References

- [1] J. R. Milovanovic, M. S. Stojkovic, K. N. Husain, N. D. Korunovic, and J. Arandjelovic, "Holistic Approach in Designing the Personalized Bone Scaffold: The Case of Reconstruction of Large Missing Piece of Mandible Caused by Congenital Anatomic Anomaly," *J Healthc Eng*, vol. 2020, 2020, doi: 10.1155/2020/6689961.
- [2] J. Milovanović, M. Stojković, M. Trifunović, and N. Vitković, "REVIEW OF BONE SCAFFOLD DESIGN CONCEPTS AND DESIGN METHODS," *Facta Universitatis, Series: Mechanical Engineering*, vol. 21, no. 1, pp. 151–173, Apr. 2023, doi: 10.22190/FUME200328038M.
- [3] R. Turudija, J. Arandelović, M. Stojković, N. Korunović, and J. Stojković, Novel approach to generic parametrized lattice scaffold model design. Information Society of Serbia - ISOS, 2022. Accessed: Aug. 09, 2023. [Online]. Available: <http://www.eventiotic.com/eventiotic/library/paper/706>
- [4] M. Viceconti, "The 'Standardised Femur' model," Aug. 2016, doi: 10.15131/shef.data.3839766.v1.
- [5] A. Lindberg, J. Alftan, H. Pettersson, G. Flodberg, and L. Yang, "Mechanical performance of polymer powder bed fused objects – FEM simulation and verification," *Addit Manuf*, vol. 24, pp. 577–586, Dec. 2018, doi: 10.1016/J.ADDMA.2018.10.009.

Application of Machine Learning Algorithms in Medical Data Processing

Tijana Geroski^{1,2,*}, Nenad Filipović^{1,2}

¹ University of Kragujevac, Faculty of Engineering, Sestre Janjić 6, 34000 Kragujevac, Serbia

² Bioengineering Research and Development Center (BioIRC), Prvoslava Stojanovića 6, 34000 Kragujevac, Serbia

e-mails: tijanas@kg.ac.rs, fica@kg.ac.rs

* *Corresponding author*

DOI: 10.46793/ICCB23.379G

Abstract: Machine learning (ML) leverages sophisticated computation and inference to generate insights, enables the system to reason and learn, and empowers clinician decision making. Starting from data (medical images, biomarkers, patients' data) and using powerful tools such as convolutional neural networks, classification and regression models, etc., it aims at creating personalized models, adapted to each patient, which can be applied in real clinical practice as a decision support system to doctors.

Keywords: image processing, deep learning, data mining, medical expert systems

1. Introduction

Advances in computational power paired with massive amounts of data generated in healthcare systems make many clinical problems ripe for Machine Learning (ML) applications. Machine Learning has been successfully applied in the automation of the process of analysis of medical data, shortening the time for diagnosis, as well as ensuring high accuracy and repeatability of results. Algorithms can be applied to automatically diagnose diseases based on MRI/CT/X-ray images, predict patient survival rates more accurately, estimate treatment effects on patients using data from randomized trials and automate the task of labeling medical datasets using natural language processing. Algorithms in medicine have so far demonstrated several potential benefits to both physicians and patients.

2. Application of Machine Learning in Medical Data Processing

ML has found application in several fields of medicine. One example is the stratification of patients with carotid artery disease by analysing clinical and personalized data, plaque and cerebral image processing and novel biomarkers [1]. Convolutional neural network U-net was used in plaque components segmentation (semantic segmentation) (Figure 1).

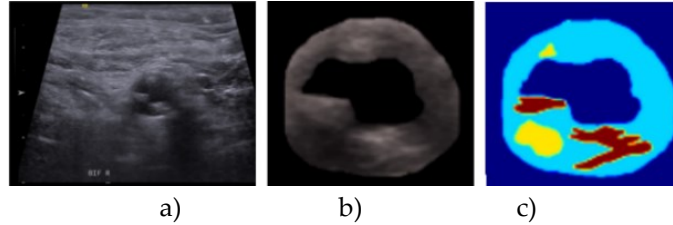


Figure 1. Original ultrasound image (a), extracted carotid artery (b), annotated plaque (c).

Another interesting area of ML application is the analysis of patient-specific data and the development of patient-specific models for monitoring and assessment of patient conditions with familiar cardiomyopathy [2]. Ultrasound images are processed in order to segment the Left ventricle and reconstruct a 3D model of the heart (**Figure 2**).

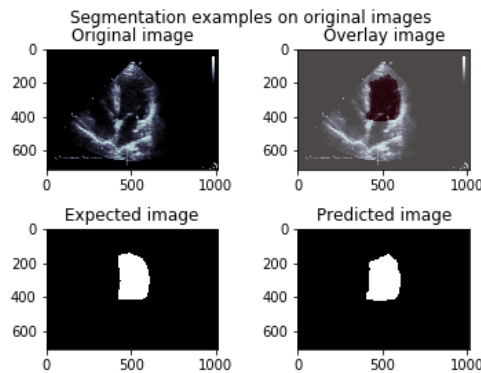


Figure 2. Segmentation of Left Ventricle in apical view images performed by U-net.

Other areas include the integration of different machine learning algorithms into one multiscale platform to investigate cancer, cardiovascular, bone disorders and tissue engineering [3], prediction of coating thickness to increase the lifespan of biomaterial susceptible to corrosion [4] or even contribute to developing drug-eluting devices to combat the burden of peripheral artery disease (PAD) [5]. Machine Learning also plays its role in the development of personalized models for COVID-19 prediction in patients or epidemiological models for monitoring of number of people infected with COVID-19 [6].

3. Conclusions

The astonishing capacity of machine learning to analyse massive quantities of data, make sense of images, and discover patterns that even the most expert human eye

misses, has inspired hope that technology may improve medicine. Finally, ML holds the promise of “making health care human again” by bringing the physician closer to the patient by creating personalized models.

Acknowledgment

The research was funded by the Ministry of Science, Technological Development and Innovation of the Republic of Serbia, contract number [451-03-47/2023-01/200107 (Faculty of Engineering, University of Kragujevac)]. This research is also supported by the project that has received funding from the European Union’s Horizon 2020 research and innovation programmes under grant agreement No 952603 (SGABU project). This article reflects only the author's view. The Commission is not responsible for any use that may be made of the information it contains.

References

- [1] TAXINOMISIS project: A multidisciplinary approach for the stratification of patients with carotid artery disease, <https://taxinomisis-project.eu/>
- [2] SILICOFCM project: In Silico trials for drug tracing the effects of sarcomeric protein mutations leading to familial cardiomyopathy, <https://silicofcm.eu/>
- [3] SGABU project: Increasing scientific, technological and innovation capacity of Serbia as a Widening country in the domain of multiscale modelling and medical informatics in biomedical engineering, <http://sgabu.eu/>
- [4] PANBIORA project: Personalised and generalised integrated biomaterial risk assessment, <https://www.panbiora.eu/>
- [5] DECODE project: Drug-coated balloon simulation and optimization system for the improved treatment of peripheral artery disease, <https://www.decodeitn.eu/>
- [6] COVIDAI project: Use of Regressive Artificial Intelligence (AI) and Machine Learning (ML) Methods in Modelling of COVID-19 Spread, <http://www.covidai.kg.ac.rs/>

**Bioorganic, bioinorganic and
medicinal chemistry**

Structural, spectroscopic, and molecular docking analysis of isoproterenol

Marija Milosavljević¹, Aleksandra Rakić², Dušan Dimić^{1,*}

¹ University of Belgrade, Faculty of Physical Chemistry, Belgrade, Serbia; e-mail: milosavljevic.fh@gmail.com, saska@ffh.bg.ac.rs, ddimic@ffh.bg.ac.rs

DOI: 10.46793/ICCB23.383M

Abstract: Isoproterenol (ISO) is a non-selective β adrenoceptor agonist structurally similar to epinephrine and norepinephrine. In this contribution, the structure of ISO was optimized by several common functionals (B3LYP, CAM-B3LYP, B3PW91, M06-2X, and M05-2X) in conjunction with 6-311++G(d,p) level of theory. The appropriate level of theory (M05-2X/6-311++G(d,p)) was determined by a comparison between experimental bond lengths and angles. The experimental and theoretical IR spectra were obtained, and a high resemblance between them was observed, with the positions of the most intense bands being well reproduced. The differences in these values were explained by the physical state of a sample that was used for the experimental spectra. The experimental and theoretical wavenumbers of the most prominent transition in UV-Vis spectra were very similar, and this transition was assigned as HOMO→LUMO. The scavenging activity towards DPPH was determined by UV-Vis spectroscopy. The antiradical potency of ISO was comparable to standard antioxidants due to the presence of catechol moiety. These structural parameters were also important for the interactions of β_1 adrenergic receptors.

Keywords: isoproterenol, DFT, IR, molecular docking

1. Introduction

Isoproterenol (isoprenaline, ISO) is a non-selective β adrenoceptor agonist and analog of epinephrine with an isopropyl group attached to amino nitrogen of the aliphatic chain. It belongs to catecholamines and contains two hydroxyl groups attached to the aromatic ring. When bound to the receptors, it mimics the effects of neurotransmitters. It is used to treat heart block and, in emergency cases, for cardiac arrest until electric shock can be applied. The adverse effects of this compound include tachycardia which can possibly dispose people taking it to cardiac arrhythmias.

In this contribution, the structure of ISO was optimized by Density functional theory (DFT) methods, and theoretical IR and UV-VIS spectra were predicted and compared to the experimental ones. The antioxidant activity towards DPPH• was determined and compared to the standard antioxidants. The molecular docking study was performed on a β_1 adrenergic receptor (PDB: 2Y02).

2. Materials and methods

2.1. Chemicals and instruments

Used chemicals, including isoproterenol, absolute alcohol, DPPH•, and methanol, were obtained from Merck. The electronic spectra were recorded on a Thermo Scientific Evolution 220 spectrophotometer in the range between 250 and 600 nm. The DPPH• reduction capacity was determined by the spectrophotometric method based on the reduction of DPPH• absorbance at 517 nm in the presence of radical scavengers. The percentage of reduction was calculated as the relative difference between the absorbance of pure DPPH• and DPPH• in the presence of a scavenger divided by the absorbance of pure DPPH•. The concentration of DPPH• was held constant at 10⁻⁴ M and the amount of ISO ranged from 0 to 100 μM. The spectra were recorded 30 min after adding ISO. The IR spectra of ISO were obtained on an Avatar 370-Thermo Nicolet FTIR spectrometer between 4000 and 40 cm⁻¹ with 32 scans and a resolution of 2 cm⁻¹.

2.2. Theoretical methods

The crystallographic structure of ISO was optimized in the Gaussian 09 Program package by employing different common functionals (B3LYP, M06-2X, M05-2X, CAM-B3LYP, and B3PW91) with 6-311++G(d,p) basis set. The optimization was performed without any geometrical constraints, and the crystallographic and optimized structures were compared by calculating the mean absolute error (MAE) and correlation coefficient between two sets of data. The electronic transitions were calculated by Time Dependent-Density Functional Theory (TD-DFT). The solvent model used to mimic the experimental conditions was Conductor-like Polarizable Continuum Model (CPCM). The optimized structure was later included in the molecular docking simulations with β₁ adrenergic receptor (PDB: 2Y02). The remaining solvent molecules and ligands were removed from the crystallographic structure in BIOVIA Discovery studio. The receptor and ligand were prepared in AutoDockTools4, while a docking study was performed on the whole surface of the protein in AutoDockVina. The visual inspection of the interactions was done in BIOVIA Discovery Studio.

4. Results and Discussion

The crystallographic structure of ISO (CSD: 1291900, [3]) was optimized by employing common functionals in conjunction with the 6-311++G(d,p) level of theory. The crystallographic and optimized structures were compared by examining the mean absolute error and correlation coefficients of bond lengths and angles. Based on these results, the lowest MAE (0.018 Å and 1.52°) and highest correlation coefficients (0.95 for bond lengths and 0.94 for bond angles) were obtained for structure optimized at M05-2X/6-311++G(d,p) level of theory. The optimized structure of protonated ISO is shown in Figure 1. This structure contains several structural parameters that can be important for antioxidant activity and protein binding, such as two hydroxyl groups attached to the aromatic ring, a hydroxyl group, and a secondary amino group on the aliphatic chain.

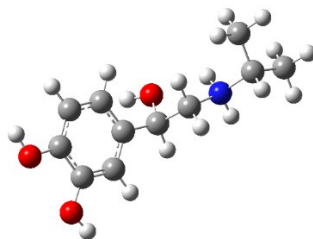


Figure 1. Optimized structure of isoproterenol at M05-2X/6-311++G(d,p) level of theory.

The experimental and theoretical IR spectra are presented in Figure 2. As ISO is a low-symmetry molecule, all of the vibrational modes were active in the IR spectrum. The most notable bands in the higher wavenumber part of the spectrum were assigned to O-H and N-H vibrations at 3105 and 3453 cm^{-1} . These bands were widened due to the formation of hydrogen bonds between molecules in the solid state. In the theoretical spectrum, these vibrations are located at 3919 and 3500 cm^{-1} . This difference is expected as the theoretical spectra were calculated for an isolated compound in a vacuum, while the experimental one was obtained for the compound in the solid phase. High-intensity bands were assigned to C-H stretching vibrations above 3000 cm^{-1} for aromatic ring carbon atoms and below for aliphatic chain carbon atoms. The band belonging to C-O stretching vibration was also well reproduced in the theoretical spectrum (1108 and 1085 cm^{-1}) thus proving the applicability of the chosen level of theory.

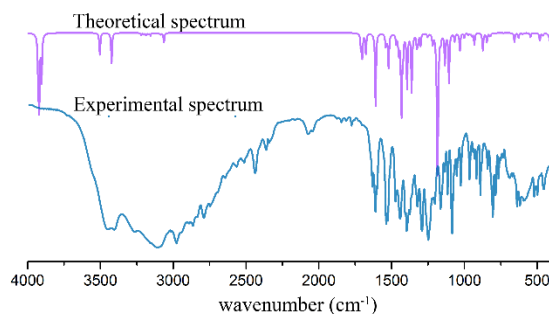


Figure 2. Experimental and theoretical (at M05-2X/6-311++G(d,p) level of theory) spectra of ISO.

The electronic spectrum of ISO consists of a single peak at 280 nm in the investigated range. This value in the theoretical spectrum is located at 279 nm, and it can be assigned to the HOMO→LUMO transition. The position of the absorption peak is important for the determination of the DPPH• scavenging potency, as the spectra of ISO and radical do not overlap. The reduction of the radical was concentration-dependent and formed a sigmoidal curve that had an increase in the first part and a plateau at the higher concentration range. This curve allowed the determination of the IC₅₀ value, which represents a concentration of ISO required to reduce half of the present radical. The obtained value was 13 μM which is comparable to the other catecholamines such as dopamine, epinephrine, and norepinephrine [1]. This result proves the importance of catechol moiety in the structure of these compounds for their antioxidant activity [2]. The stoichiometric factor (SF) of ISO is 3.84 which marks its good antioxidant activity (SF>2). The other functional groups on the aliphatic chain do not influence radical scavenging activity significantly. Catechol moiety allows better delocalization of electron

density upon radical formation due to the elongated delocalization throughout the structure.

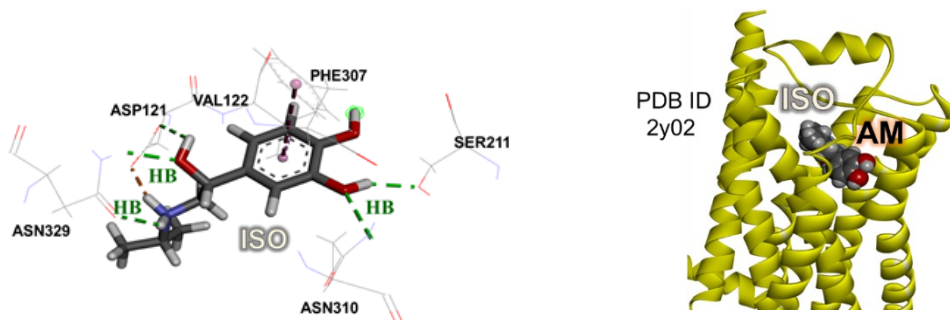


Figure 3. The active pocket of protein and detailed view of interactions between ISO and surrounding amino acids.

The docking study showed that ISO was located in the active pocket of the protein. The lowest value of the free energy of binding was $-31.4 \text{ kJ mol}^{-1}$, while epinephrine and norepinephrine had higher binding energies of -28.0 and $-27.2 \text{ kJ mol}^{-1}$, respectively. These binding energy values proved the reversibility of the binding process, and differences in these values could be attributed to present substituents. Present hydroxyl and amino groups within the structure form hydrogen bonds with ASN329, ASP121, and SER215 within the active pocket. The aromatic ring formed π - π interactions with PHE307. The salt bridge was formed between the protonated amino group of ISO and surrounding amino acids. Further studies on these interactions are advised.

3. Conclusions

In this contribution, isoproterenol (ISO) was investigated, and the highest resemblance between the experimental and optimized structure was obtained for the structure optimized at M05-2X/6-311++G(d,p). The experimental wavenumbers in the IR spectrum and wavelength in the UV-Vis spectrum were well reproduced. ISO molecule proved to be a good antioxidant with reactivity towards DPPH comparable to other catecholamines. The hydrogen bonds, salt bridges, and π - π interactions are the most important for the binding to β_1 adrenergic receptor.

Acknowledgment

The authors gratefully acknowledge financial support from the Science Fund of the Republic of Serbia (Serbian Science and Diaspora Collaboration Program: Knowledge Exchange Vouchers: Project TumorSelCoum 6388843).

References

- [1] D. Dimić, D. Milenković, J. Dimitrić Marković, Z. Marković, *Antiradical activity of catecholamines and metabolites of dopamine: theoretical and experimental studies*, Physical Chemistry Chemical Physics 19 (2016), 12970-12980
- [2] D. Dimić, D. Milenković, J. Ilić, B. Šmit, A. Amić, Z. Marković, J. Dimitrić Marković, *Experimental and theoretical elucidation of structural and antioxidant properties of vanillylmandelic acid and its carboxylate anion*, Spectrochimica Acta A 198 (2018), 61-70.
- [3] R. Kingsford-Adaboh, E. Hayashi, M. Haisa, S. Kashino, *Crystal Structures and Molecular Conformations of Isoprenaline Hydrochloride and (S)-Isoprenaline Hydrogen (2R,3R)-Tartrate*, BCSJ 66 (1993) 2883.

Molecular docking study of ruthenium-*p*-cymene complexes with isothiazole derivatives as SARS-CoV-2 main protease inhibitors

Marko Radovanović^{1,*}, Ignjat Filipović¹, Maja Đukić¹, Marija Ristić¹, Ivan Jakovljević¹
Zoran D. Matović¹

¹ University of Kragujevac, Faculty of Science, Department of Chemistry, Radoja Domanovića 12, 34000 Kragujevac, Serbia; e-mail: marko.radovanovic@pmf.kg.ac.rs, ignjat.filipovic@pmf.kg.ac.rs, maja.djukic@pmf.kg.ac.rs, marija.jeremic@pmf.kg.ac.rs, ivan.jakovljevic@pmf.kg.ac.rs, zoran.matovic@pmf.kg.ac.rs

* Corresponding author

DOI: 10.46793/ICCBi23.387R

Abstract: Since proper treatment for COVID-19 still has not been developed, exploration of novel options is required. Activities of different metal complexes, promising results gained from examining different thiazole derivatives, and research in the field of natural products like *p*-cymene, produced an idea to test piano stool ruthenium *p*-cymene complexes with isothiazole derivatives as ligands. *In silico* methods are often used as the first step in a series of experiments during the development of new drugs, and docking simulations are a quick way to determine the feasibility of novel compounds as potential inhibitors of target enzymes. Existing compounds of ruthenium with published crystal structures were tested against the main protease of SARS-CoV-2. All of the tested compounds show a potential ability to bind to the target enzyme, while the compound with phenyl and morpholinyl substituents in isothiazole ligand shows the best activity among tested compounds. Authors feel confident that further research on this topic will yield compounds with even better potential activities against the main protease of the SARS-CoV-2.

Keywords: ruthenium, *p*-cymene, isothiazole, docking, SARS-CoV-2

1. Introduction

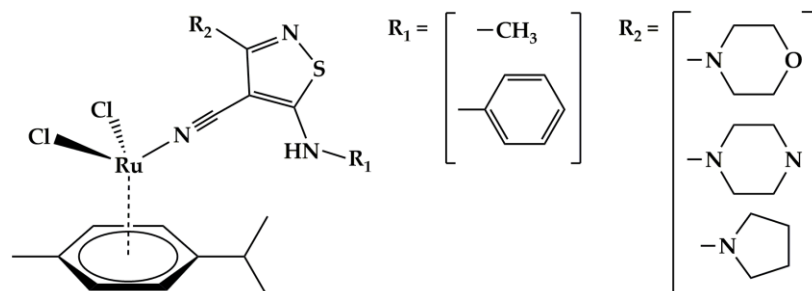
Severe acute respiratory syndrome coronavirus 2 (SARS-CoV-2) is a virus responsible for 2019 pandemic of disease COVID-19 [1]. In the early stages of pandemic, it seemed that vaccine development was in the spotlight, overshadowing therapeutic means of controlling this outbreak which can be seen from the extensive number of potential vaccines that were developed [2].

The use of metals as cures for ailments has a long history, while in modern medicine metal complexes were sometimes first-to-be-found or only effective treatments for certain diseases, like in the case of cisplatin with some types of cancer. Naturally, in the

fight against SARS-CoV-2 there was an effort to study established metallodrugs that already showed activities against viral diseases, like auranofin and bismuth citrate [3].

Large number of organic molecules were tested against SARS-CoV-2, selected from databases of known drugs and active compounds. The first step is usually *in silico* study of the select active compound like *p*-cymene [4] that is sent to later *in vitro* studies if the compound shows promise. Design of the novel drugs often starts from the promising small-molecule moiety present in many active compounds, like thiazole, from which potentially active derivatives are made by introducing diverse functional groups [5].

The search for effective therapy against COVID-19 is not over [6]. Considering promising results shown by metal complexes, *p*-cymene, and thiazole derivatives we decided to use molecular docking to examine the potential inhibitory power of existing [7, 8] piano stool *p*-cymene ruthenium complexes with isothiazole derivatives towards the active site of main protease of SARS-CoV-2 (M^{Pro}). Scheme 1 describes selected compounds.



Scheme 1.

2. Methods

Structures of selected compounds were modeled following instructions in previously published work [8]. Structures are based on Scheme 1 and named according to Table 1.

Table 1. Naming convention of selected compounds.

Compound	R ₁	R ₂
1	methyl	morpholinyl
2	methyl	piperazinyl
3	methyl	pyrrolidinyl
4	phenyl	morpholinyl
5	phenyl	pyrrolidinyl

Structures of selected compounds were prepared for docking using AutoDockTools (ADT) [9] using previously calculated partial charges. Parameters for ruthenium interactions had to be added to the parameter file. The crystal structure of SARS-CoV-2 main protease with pdb code 6lu7 [10] was used as a docking target and was also prepared using ADT by removal of co-crystallized substrates and water, calculating Gasteiger charges, assigning atom types, and merging non-polar hydrogens. The structure of the compound designated as N3 from the 6lu7 file was used for method

validation. Docking simulations were performed using AutoDock 4 (AD4) [9]. Lamarckian AD4 hybrid genetic algorithm – local search method was used with 20 runs per tested structure, with maximum of $2.5 \cdot 10^7$ energy evaluations per run.

3. Results

After performing docking simulations, results were scored based on the estimated free energy of binding (ΔE_b), where lower energy indicates stronger binding and potentially higher potency of inhibitory effect. Derived results are presented in Table 2 with energy units as kilocalories per mole (kcal mol^{-1}) as is default for AD4.

Table 2. Docking results for each compound scored by estimated free energy of binding.

Compound	ΔE_b [kcal mol^{-1}]
1	-6.33
2	-6.07
3	-6.37
4	-7.21
5	-6.46

Compound N3 is potent inhibitor of M^{pro} with $\Delta E_b = -8.88 \text{ kcal mol}^{-1}$ obtained from AD4 experiment used for validation. Compared to N3, tested compounds do not perform as well, but scores are good enough to indicate the possibility of binding at the active site of the enzyme. The best-scoring compound is compound 4. Every tested compound had access to the catalytic cavity of the enzyme and could be positioned adjacent to the HIS41 and CYS145 residues that are generally considered to be carriers of the enzyme's catalytic function [11]. Figure 1 shows the best scoring conformation of compound 4 in proximity of the catalytic dyad.

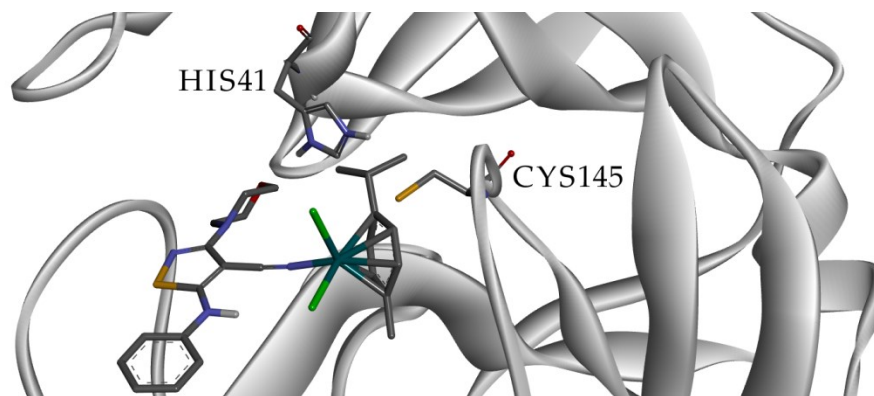


Figure 1. Best docking hit for compound 4 near catalytic dyad of M^{pro} .

4. Conclusions

Based on the results of docking experiments, isothiazole derivatives as ligands in piano stool ruthenium complexes show promising activity in *in silico* studies as

inhibitors of M^{pro}. Further modification of these ligands and their metal complexes may prove a fruitful endeavor during the search for treatment of the COVID-19.

Acknowledgment

This research is funded by the Ministry of Education and Ministry of Science, Technological Development and Innovation, Republic of Serbia, Grants: No. 451-03-47/2023-01/ 200122.

References

- [1] X. Yang, Y. Yu, J. Xu, H. Shu, H. Liu, Y. Wu, L. Zhang, Z. Yu, M. Fang, T. Yu, Y. Wang., *Clinical course and outcomes of critically ill patients with SARS-CoV-2 pneumonia in Wuhan, China: a single-centered, retrospective, observational study*, *Lancet Respiratory Medicine*, 8 (2020) 475-481.
- [2] L. Dai, G.F. Gao., *Viral targets for vaccines against COVID-19*, *Nature Reviews Immunology*, 21 (2021) 73-82.
- [3] K. Ioannou, M.C. Vlasίου., *Metal-based complexes against SARS-CoV-2*, *Biometals*, 35 (2022) 639-652.
- [4] A. Panagiotopoulos, M. Tseliou, I. Karakasiliotis, D. Kotzampasi, V. Daskalakis, N. Kesesisidis, G. Notas, C. Lionis, M. Kampa, S. Pirintzos, G. Sourvinos, E. Castana., **p*-cymene impairs SARS-CoV-2 and Influenza A (H1N1) viral replication: In silico predicted interaction with SARS-CoV-2 nucleocapsid protein and H1N1 nucleoprotein*, *Pharmacology Research & Perspectives*, 9 (2021) e00798.
- [5] R.W. Elsayed, M.A. Sabry, H.I. El-Subbagh, S.M. Bayoumi, S.M. El-Sayed., *Thiazole-based SARS-CoV-2 protease (COV M^{pro}) inhibitors: Design, synthesis, enzyme inhibition, and molecular modeling simulations*, *Archiv der Pharmazie*, 355 (2022) e2200121.
- [6] M.K. Looi., *What are the latest covid drugs and treatments?*, *BMJ*, 381 (2023) p872.
- [7] M.B. Djukić, M.S. Jeremić, I.P. Filipović, O.R. Klisurić, R.M. Jelić, S. Popović, S. Matić, V. Onnis, Z.D. Matović., *Ruthenium(II) Complexes of Isothiazole Ligands: Crystal Structure, HSA/DNA Interactions, Cytotoxic Activity and Molecular Docking Simulations*, *ChemistrySelect*, 5 (2020) 11489.
- [8] M.B. Đukić, M.S. Jeremić, I.P. Filipović, O.R. Klisurić, V.V. Kojić, D.S. Jakimov, R.M. Jelić, V. Onnis, Z.D. Matović., *Synthesis, characterization, HSA/DNA interactions and antitumor activity of new [Ru(η^6 -*p*-cymene)Cl₂(L)] complexes*, *Journal of Inorganic Biochemistry*, 213 (2020) 111256.
- [9] G.M. Morris, R. Huey, W. Lindstrom, M.F. Sanner, R.K. Belew, D.S. Goodsell, A.J. Olson., *Autodock4 and AutoDockTools4: automated docking with selective receptor flexibility*, *Journal of Computational Chemistry*, 16 (2009) 2785-2791.
- [10] Z. Jin, X. Du, Y. Xu, Y. Deng, M. Liu, Y. Zhao, B. Zhang, X. Li, L. Zhang, C. Peng, Y. Duan, J. Yu, L. Wang, K. Yang, F. Liu, R. Jiang, X. Yang, T. You, X. Liu, X. Yang, F. Bai, H. Liu, X. Liu, L.W. Guddat, W. Xu, G. Xiao, C. Qin, Z. Shi, H. Jiang, Z. Rao, H. Yang., *Structure of M^{pro} from SARS-CoV-2 and discovery of its inhibitors*, *Nature*, 582 (2020) 289-293.
- [11] C. Huang, P. Wei, K. Fan, Y. Liu, L. Lai., *3C-like Proteinase from SARS Coronavirus Catalyzes Substrate Hydrolysis by a General Base Mechanism*, *Biochemistry*, 43 (2004) 4568-4574.

Synthesis, spectroscopic, and quantum-chemical analysis of mononuclear Ru(II)-naphthylhydrazine complex

Marta Kosanović¹, Thomas Eichhorn², Dejan Milenković³, Goran Kaluđerović²,
Jasmina Dimitrić Marković¹, Dušan Dimić^{1,*}

¹ University of Belgrade, Faculty of Physical Chemistry, Belgrade, Serbia; e-mail: 20220205@student.ffh.bg.ac.rs, markovich@ffh.bg.ac.rs, ddimic@ffh.bg.ac.rs

² University of Applied Sciences Merseburg, Department of Engineering and Natural Sciences, Merseburg, Germany; e-mail: thomas.eichhorn@hs-merseburg.de, goran.kaluderovic@hs-merseburg.de

³ University of Kragujevac, Institute for Information Technologies, Department of Science, Kragujevac, Serbia; e-mail: dejanm@uni.kg.ac.rs

DOI: 10.46793/ICCBIG23.391K

Abstract: Ruthenium(II) complexes have become increasingly recognized and utilized as potent anticancer agents in recent years. These compounds possess unique capabilities in targeting cancer cells and interfering with vital cellular processes, offering new hope in the relentless battle against cancer. This research study focuses on the characterization of a newly synthesized Ru(II)-naphthylhydrazine complex by IR and NMR spectroscopies. NMR spectral data have revealed the presence of different chemical environments within **1** based on the chemical shifts observed in the ¹H and ¹³C NMR spectra. The infrared spectra were recorded in the region ranging from 400 cm⁻¹ to 4000 cm⁻¹, capturing a comprehensive range of vibrational modes of the studied compound with the main chemical groups outlined. The quantum-chemical optimization of **1** at B3LYP/6-31+G(d,p)(H,C,N,Cl)/LanL2DZ(Ru) level of theory allowed the prediction of structural parameters and analysis of intramolecular interactions governing stability through Natural Bond Orbital approach. The future biological investigation of this compound is advised.

Keywords: Ru(II), DFT, IR, NMR

2. Introduction

Ruthenium, a transition metal in group 8, exists in oxidation states of Ru(II) and Ru(III), with the possibility of Ru(IV) compounds, which are usually unstable due to higher oxidation states. Ruthenium ions have a hex-coordinated structure with octahedral coordination geometries and Ru(II) complexes are more stable [1]. Ruthenium complexes disrupt critical cellular processes in cancer cells, like apoptosis, by forming coordination bonds with essential biomolecules, such as nucleic acids [2]. First-generation ruthenium compounds ([η⁶-arene]ruthenium(II) complexes) in the 1980s showed promise as anticancer agents [3]. Later, drugs like NAMI-A and KP1019 demonstrated remarkable potential in clinical trials against solid tumors, selectively accumulating in tumor tissues while managing toxicity [4]. This research includes

synthetic procedure and spectral characterization of ruthenium(II)-naphthylhydrazine complex, **1**, along with the quantum-chemical optimization.

2. Materials and methods

2.1. Procedure for synthesis of **1**

The ruthenium salt $[\{\text{RuCl}_2(\eta^6\text{-}p\text{-cymene})\}_2]$ was dissolved in methanol and stirred in a nitrogen atmosphere for 15 minutes until fully dissolved. Then, lithium hydroxide and the ligand were added, followed by 15 minutes of stirring in a nitrogen atmosphere. The mixture was left to stir overnight (20 hours). The next day, the solution was placed in a freezer at -25°C for 2 hours, filtered, and washed off with 10 ml of diethyl ether. The filtrate appeared bright ochre yellow.

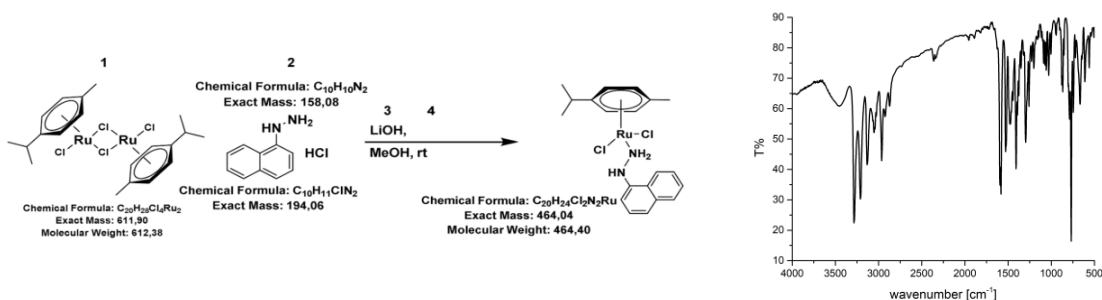


Figure 1. Synthesis of **1** (left) and IR spectrum of **1** (right).

2.2. Analytical methods

The infrared (IR) spectrum was obtained using the FTIR spectrometer - Avatar 370, Thermo Nicolet, covering the range from 400 cm^{-1} to 4000 cm^{-1} . The procedure involved recording a blank sample spectrum with a KBr pellet, followed by the **1** spectrum using a sample pellet containing 100 mg of KBr powder and 1 mg of the complex.

NMR spectra were acquired using a Bruker AvanceTM 400 MHz spectrometer with a Bruker wide bore magnet operating at 300 MHz, referencing chemical shifts to tetramethylsilane. The analysis used 6 mg of the ruthenium complex dissolved in 3 ml of deuterated chloroform.

2.3. Theoretical analysis

The structure of **1** was optimized in the Gaussian 09 Program Package at B3LYP/6-31+G(d,p)(H,C,N,Cl)/LanL2DZ level of theory. The optimization was performed without any geometrical constraints and the absence of imaginary frequencies proved that the stable structure was obtained. The intramolecular interactions were analyzed by the Natural Bond Orbital theory approach.

5. Results and Discussion

4.1. Analysis of IR and NMR spectra of **1**

Infrared spectroscopy was utilized for the qualitative structural analysis of a newly synthesized ruthenium complex. Figure 1 presents the IR spectrum of **1**. The IR spectrum of **1** shows bands at 3452 and 3284 cm^{-1} , indicating free and associated stretching N-H vibrations of amines. A strong band at 1595 cm^{-1} is assigned to the deformation vibrations of amines. Also, a peak at 1296 cm^{-1} with moderate intensity corresponding to the stretching vibration of C-N bond is noticed. The spectrum contains bands of sp^3 hybridized C-H vibrations at 2964 cm^{-1} . The existence of an aromatic ring and sp^2 hybridized C-H groups are shown at 3051 cm^{-1} . A peak at 1473 cm^{-1} corresponds to CH_2 group vibrations. At lower wavenumbers (665 cm^{-1}) band associated with Ru-Cl vibration is observed.

The ^1H NMR spectrum of **1** exhibits distinct peaks representing specific proton environments with unique chemical shifts (Figure 2). Doublet at 1.33 ppm belongs to hydrogen atoms of isopropyl moiety. Peaks at 2.29 ppm and 3.03 ppm correspond to protons of methyl group and CH group of isopropyl moiety. A peak at 5.56 ppm denotes hydrogen atom of NH group. The rest of peaks are located between 6.9 and 8.1 ppm which is characteristic of the hydrogen atoms within aromatic rings. Distinct carbon environments are observed in the ^{13}C NMR spectrum (Figure 2). Isopropyl and methyl groups display the lowest shifts (22.16, 22.41, and 30.97 ppm). Chemical shifts of the other carbon atoms are between 108.94 and 134.05 corresponding to the carbon atoms of the aromatic ring. The highest value of chemical shift was observed for the carbon atom attached to the hydrazine group (143.76 ppm) which is expected due to the electronegativity of the mentioned group. The most intense signal at 77.03 ppm corresponds to deuterated chloroform, the solvent used.

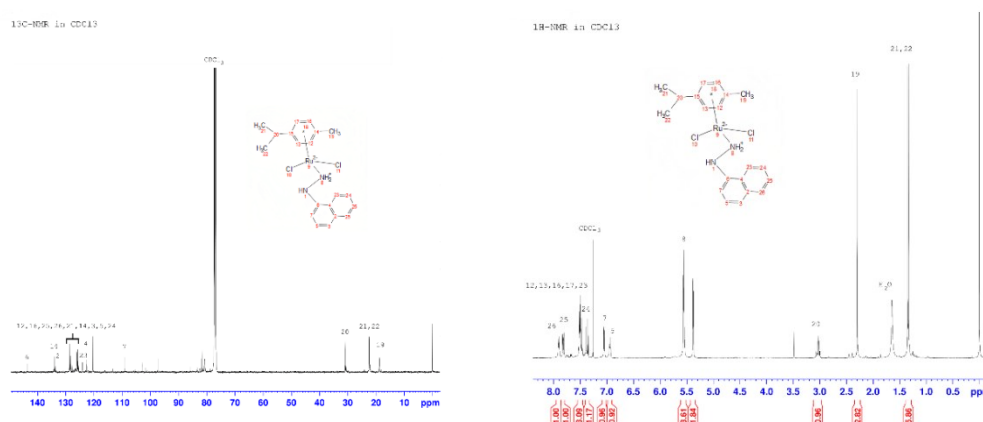


Figure 2. ^1H (left) and ^{13}C (right) NMR spectra of **1**.

4.2. Optimized structure of **1** and intramolecular interactions

The optimized structure of **1** is shown in Figure 3. The structure consists of a p-cymene moiety directly attached to Ru(II), naphthylhydrazyl moiety and two chlorido

ions. The Ru-Cl bonds are 2.441 and 2.453 Å which is in the expected range based on the comparison with similar compounds. The Ru-N bond length is 2.176 Å. The angle Cl-Ru-Cl is 90.479°. The optimization of the compound restores the pseudo-octahedral geometry as three positions are occupied by *p*-cymene moiety. The most abundant interactions include $\pi(\text{C-C}) \rightarrow \pi^*(\text{C-C})$ of *p*-cymene and naphthylhydrazyl rings with energies between 30.6 and 33.1 kJ mol⁻¹. Different stabilization interactions are formed between the aromatic ring and hydrazine group through positive resonant effect of nitrogen atoms. The electron donation from chlorido ligands is very strong, LP(Cl) \rightarrow LP*(Ru) with a stabilization energy of 350 kJ mol⁻¹. The rest of interactions with the metal ion are much weaker.

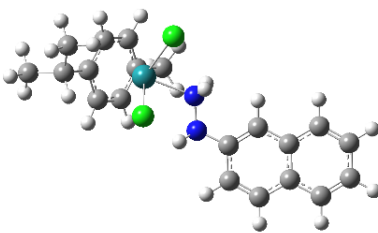


Figure 3. Optimized structure of **1** (at B3LYP/6-31+G(d,p)(H,C,N,Cl)/LanL2DZ(Ru) level of theory)(hydrogen-white, carbon-grey, nitrogen-blue, chlorine-green, ruthenium-teal).

3. Conclusions

This research study focused on characterizing the newly synthesized Ru(II)-naphthylhydrazine complex, **1**, using NMR and IR spectroscopies. The IR spectrum showed characteristic vibrational modes of functional groups, including amines, aromatic rings, and halogens. The NMR allowed the elucidation of the structural properties of **1**. The most important stabilization interactions include $\pi(\text{C-C}) \rightarrow \pi^*(\text{C-C})$ and interactions between donor atoms and Ru.

Acknowledgment

The authors gratefully acknowledge financial support from the Science Fund of the Republic of Serbia (Serbian Science and Diaspora Collaboration Program: Knowledge Exchange Vouchers: Project TumorSelCoum 6388843).

References

- [1] L. Zeng, P. Gupta, Y. Chen, E. Wang, L. Ji, H. Chao, and Z.S. Chen, *The development of anticancer ruthenium(ii) complexes: from single molecule compounds to nanomaterials*, Chemical Society Reviews, 46 (2017), 5771–5804.
- [2] K. Lin, Z.Z. Zhao, H.B. Bo, X.J. Hao and J.Q. Wang, *Applications of Ruthenium Complex in Tumor Diagnosis and Therapy*, Frontiers in Pharmacology, 9 (2018), 1323.
- [3] A.R. Simović, R. Masnikosa, I. Bratsos, and E. Alessio, *Chemistry and reactivity of ruthenium(II) complexes: DNA/protein binding mode and anticancer activity are related to the complex structure*, Coordination Chemistry Reviews, 398 (2019), 113011.
- [4] E. Alessio, and L. Messori, *NAMI-A and KP1019/1339, Two Iconic Ruthenium Anticancer Drug Candidates Face-to-Face: A Case Story in Medicinal Inorganic Chemistry*, Molecules, 24 (2019), 1995.

Synthesis, spectroscopic, and theoretical analysis of Ru(II)-phenylhydrazine complex

Ana Atanasković¹, Thomas Eichhorn², Dejan Milenković³, Dušan Dimić¹, Goran Kaluđerović², Jasmina Dimitrić Marković^{1,*}

¹ University of Belgrade, Faculty of Physical Chemistry, Belgrade, Serbia; e-mail: 20220220@student.ffh.bg.ac.rs, ddimic@ffh.bg.ac.rs, markovich@ffh.bg.ac.rs

² University of Applied Sciences Merseburg, Department of Engineering and Natural Sciences, Merseburg, Germany; e-mail: thomas.eichhorn@hs-merseburg.de, goran.kaluderovic@hs-merseburg.de

³ University of Kragujevac, Institute for Information Technologies, Department of Science, Kragujevac, Serbia; e-mail: dejanm@uni.kg.ac.rs

* Corresponding author

DOI: 10.46793/ICCBIGK23.395A

Abstract: In recent decades, metal-based chemotherapeutics have attracted considerable attention and excitement within the oncology research community, with ruthenium(II) complexes emerging as a particularly promising class of anticancer agents. In this study, the synthesis of a new ruthenium complex was performed, followed by its structural characterization using NMR and IR spectroscopy. The compound's infrared spectrum reveals characteristic bands corresponding to N-H and C-H stretching vibrations from sp² and sp³ hybridized carbon atoms, vibrations of aromatic rings and additional vibrations related to CH₃, C-N, and chloride species at various wavenumbers. The ¹H NMR spectrum of the Ru140 complex reveals distinct peaks corresponding to different atomic environments, including protons attached to sp³ hybridized C-atoms, nitrogen atoms, and protons involved in aromatic rings, as well as signals from deuterated chloroform and water. The ¹³C NMR spectrum displays peaks for saturated carbon atoms in methyl and isopropyl groups at lower, and aromatic carbons at higher chemical shifts. The structure of the complex was optimized at B3LYP/6-31+G(d,p)(H,C,N,Cl)/LanL2DZ level of theory and intramolecular interactions were analyzed through the Natural Bond Orbital approach.

Keywords: ruthenium, DFT, NBO, NMR

3. Introduction

Ruthenium compounds present promising anticancer agents due to the biocompatibility of ruthenium and its similarity to iron [1]. One of the notable features of ruthenium(II) complexes is their ability to interact with biomolecules, including nucleic acids, which are crucial for the survival and growth of cancer cells. By forming coordination bonds with nucleic acids, ruthenium(II) complexes can disrupt essential cellular processes, resulting in cell cycle arrest and programmed cell death (apoptosis),

specifically in cancer cells [2]. In this study, a Ru(II)-phenylhydrazine complex, **C1**, has been synthesized and characterized by IR and NMR spectroscopies. Density functional theory (DFT) and Natural Bond Orbital (NBO) approaches were used for the theoretical analysis of this compound.

2. Materials and methods

2.1. Procedure for synthesis of **C1**

The synthesis of **C1** is shown in Figure 1. Ruthenium salt, $[\{\text{RuCl}_2(\eta^6\text{-}p\text{-cymene})\}_2]$, was dissolved in chloroform under a nitrogen atmosphere and stirred until a clear and reddish solution was obtained. Phenylhydrazine was added in four portions (33 μl each). Upon the addition of the fourth portion, the solution turned orange and became cloudy. After one hour of stirring in nitrogen, the solution was transferred to a freezer at -25°C and filtered after two hours. The flask was washed with 5 ml of chloroform. The resulting filtrate was bright yellow.

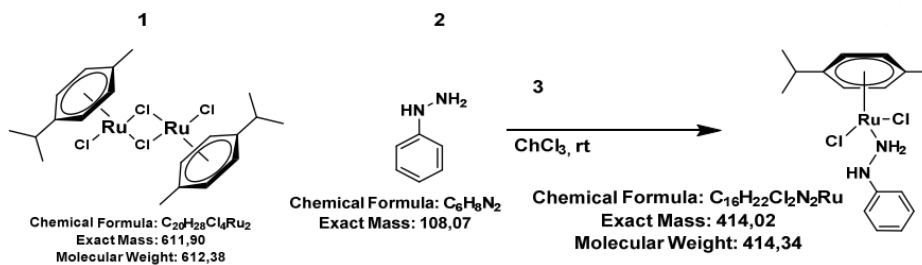


Figure 1. Synthesis of **C1** complex.

2.2. Instrumental methods

IR spectra were recorded on an FTIR spectrometer (Avatar 370 - Thermo Nicolet). The sample was recorded in the form of a potassium bromide (KBr) pellet in the wavenumber range between 400 cm^{-1} and 4000 cm^{-1} . NMR spectra were recorded on Bruker AvanceTM 400 MHz spectrometer with Bruker wide bore magnet at 300 MHz with NMR console Tecmag Apollo. Chemical shifts for ^1H and ^{13}C NMR spectra were referenced to internal standard TMS. The probes were prepared in deuterated chloroform. Peak assignment was done using the MastReNova software.

2.3. Theoretical methods

The structure of **C1** was optimized based on the previously determined level of theory that was suitable for Ru(II)-based compounds, namely B3LYP/6-31+G(d,p)(H,C,N,Cl)/LanL2DZ(Ru), in the Gaussian 09 Program Package. The intermolecular interactions governing the stability of the formed complex were assessed by the Natural Bond Orbital (NBO) approach.

6. Results and Discussion

In the IR spectrum of **C1** (Figure 2), starting from the highest wavenumbers, a band of medium intensity attributed to the stretching vibration of N-H bonds is observed at 3330 cm^{-1} . The presence of aromatic rings in the compound leads to a very intense band at 3180 cm^{-1} . The intense band of C-H stretching vibrations from sp^2 hybridized carbon atoms appears at 3070 cm^{-1} , while the presence of sp^3 hybridized carbon atoms is confirmed by bands at 2990 , 2960 , 2930 , and 2870 cm^{-1} . High-intensity bands corresponding to the deformation vibrations of amine groups are observed at 1600 and 1500 cm^{-1} . Medium-intensity peaks at 1450 and 1390 cm^{-1} are associated with the deformation vibrations of the CH_3 group. Vibrations corresponding to C-N bonds are present at 1280 and 1250 cm^{-1} and are also of medium intensity. Finally, the very intense band at 760 cm^{-1} is characteristic of vibrations associated with chloride species.

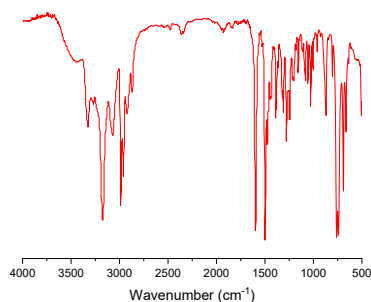
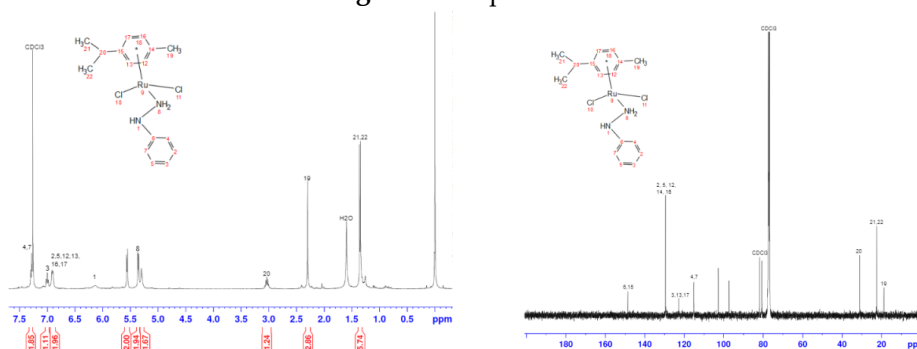


Figure 2. IR spectrum of **C1**



The optimized structure is presented in Figure 4. It has been previously shown that the selected level of theory can be used for the optimization of the crystal structure of similar compounds and the prediction of IR and NMR spectra. The structure of C1 consists of *p*-cymene moiety in the vicinity of Ru(II), phenylhydrazine that is bound to the metal ion through an amino group and two chlorido ligands. These ligands surround central metal ion in a pseudo-octahedral geometry. The electron donation occurs through π electron cloud and lone pairs on nitrogen and chlorine. Various intramolecular interactions stabilize the structure of C1. The aromatic rings of *p*-cymene and phenyl moieties are stabilized by the interactions between neighboring C-C bonds. The interactions between *p*-cymene and Ru occur through $\pi(\text{C-C})\rightarrow\text{LP}(\text{Ru})$ interactions with stabilization energy of 470 kJ mol^{-1} which proves the assumption that the *p*-cymene moiety is important for the complex formation. Nitrogen and chlorido ligands form stabilization interactions with Ru with stabilization energies of 370 and 350 kJ mol^{-1} , respectively. Additionally, there is an interaction between chlorido ligand and amino group through a weak hydrogen bond.

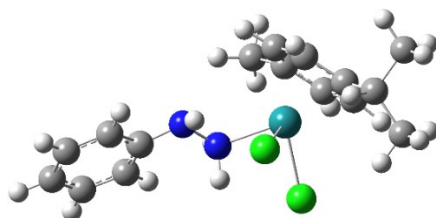


Figure 4. IR spectrum (left) and optimized structure of C1 (at B3LYP/6-31+G(d,p)(H,C,N,Cl)/LanL2DZ(Ru) level of theory)(right).

3. Conclusions

In this study, the synthesis of a new Ru(II)-phenylhydrazyl complex was conducted. The infrared spectrum of the compound confirmed the presence of certain functional groups. The ^1H and ^{13}C NMR spectra provided important information about the chemical environment of the atoms, confirming the successful synthesis of the compound. The most important stabilization interactions were determined from the optimized structures. The obtained results confirmed the expected structure of the compound.

Acknowledgment

The authors gratefully acknowledge financial support from the Science Fund of the Republic of Serbia (Serbian Science and Diaspora Collaboration Program: Knowledge Exchange Vouchers: Project TumorSelCoum 6388843).

References

- [1] S.Y. Lee, C.Y. Kim, and T.G. Nam, *Ruthenium Complexes as Anticancer Agents: A Brief History and Perspectives*, Drug Design, Development and Therapy, 14 (2020), 5375-5392.
- [2] K. Lin, Z.Z. Zhao, H.B. Bo, X.J. Hao and J.Q. Wang, *Applications of Ruthenium Complex in Tumor Diagnosis and Therapy*, Frontiers in Pharmacology, 9 (2018), 1323.

DNA/BSA binding study of mononuclear gold(III) complexes with clinically used azoles

Bojana V. Pantović¹, Nevena Lj. Stevanović¹, Tina P. Andrejević¹, Darko P. Ašanin², Miloš I. Djuran³, Biljana Đ. Glišić^{1*}

¹ University of Kragujevac, Faculty of Science, Department of Chemistry, Radoja Domanovića 12, 34000 Kragujevac; e-mail: bojana.pantovic@pmf.kg.ac.rs, nevena.stevanovic@pmf.kg.ac.rs, tina.andrejevic@pmf.kg.ac.rs, biljana.glicic@pmf.kg.ac.rs

² University of Kragujevac, Institute for Information Technologies Kragujevac, Department of Science, Jovana Cvijića bb, 34000 Kragujevac; e-mail: darko.asanin@uni.kg.ac.rs

³ Serbian Academy of Sciences and Arts, Knez Mihailova 35, 11000 Belgrade, Serbia; e-mail: milos.djuran@pmf.kg.ac.rs

DOI: 10.46793/ICCBi23.399P

Abstract: In the present study, we investigated the interactions of three mononuclear gold(III) complexes of the general formula $[\text{AuCl}_3(\text{azole})]$, azole is clotrimazole (ctz, **Au1**), tioconazole (tcz, **Au2**) and voriconazole (vcz, **Au3**) with calf thymus DNA (ct-DNA) and bovine serum albumin (BSA) by fluorescence emission spectroscopy. A significant decrease in fluorescence intensity of BSA in the presence of the complexes and high values of the calculated binding constants have indicated their good binding affinity toward this model protein. Besides that, the investigated **Au1-3** complexes have shown a significant binding affinity toward ct-DNA-EthBr system (EthBr is ethidium bromide, which behaves as an intercalator between DNA base pairs). The best binding affinity towards the studied biomolecules has been shown by **Au3** complex, which contains a monodentately coordinated voriconazole. The findings from this study could be important for the further development of metal-based antimicrobials, as well as anticancer agents, with favourable activity and therapeutic profile in respect to the parent organic ligands.

Keywords: gold(III) complexes, antifungal azoles, DNA interactions, protein interactions

1. Introduction

The pharmacological properties of gold and its compounds have been known since antiquity, and to date, gold compounds have been studied against the causative agents of various diseases [1]. Although they are currently used only for the treatment of rheumatoid arthritis, numerous gold compounds are currently being investigated as potential antitumor, antibacterial, antifungal and antiparasitic agents [2]. In our previous study, mononuclear gold(III) complexes of the general formula $[\text{AuCl}_3(\text{azole})]$, where azole stands for clotrimazole (ctz, **Au1**), tioconazole (tcz, **Au2**) and voriconazole (vcz, **Au3**) were synthesized, characterized and biologically evaluated [3]. In all these complexes, the corresponding azole ligand is monodentately coordinated to the Au(III)

via the imidazole or triazole nitrogen atom, while the remaining coordination sites are occupied by chloride anions leading to the square-planar arrangement [3]. In a continuation, herein we investigated the interaction of **Au1-3** complexes with bovine serum albumin (BSA) and calf thymus DNA (ct-DNA) by fluorescence emission spectroscopy to check their binding affinity towards these biomolecules.

2. Material and Methods

2.1 Chemicals

Potassium tetrachloridoaurate(III) ($K[AuCl_4]$), clotrimazole (ctz), tioconazole (tcz), voriconazole (vcz), phosphate-buffered saline (PBS), bovine serum albumin (BSA), calf thymus DNA (ct-DNA) and ethidium bromide (EthBr) were obtained from commercial suppliers (Sigma-Aldrich and Acros Organics). The complexes **Au1-3** were synthesized according to the previously published procedure [1].

2.2 BSA and DNA interaction assay

The interactions of the synthesized gold(III) complexes (**Au1-3**) with BSA and DNA were investigated by fluorescence emission spectroscopy on a Shimadzu RF-6000 spectrofluorometer. Fluorescence spectra for BSA interactions were recorded at ambient temperature in the range of 300 – 500 nm, with an excitation wavelength of 295 nm. Fluorescence titration experiments were carried out in PBS (pH = 7.4) by keeping the concentration of BSA constant (10 μ M), while varying the concentration of gold(III) complexes (0 – 122 μ M). The DNA binding experiments were also carried out in PBS by keeping $[DNA]/[EthBr] = 10$, while increasing the concentration of the gold(III) complexes. Measurements were performed in the wavelength range of 525 – 750 nm with an excitation wavelength of 520 nm.

3. Results and Discussion

3.1 BSA binding study

Serum albumin is one of the most abundant proteins in blood plasma and plays a role in the transport of various drugs [4]. The fluorescence emission spectra of BSA of constant concentration were recorded in the presence of increasing concentrations of **Au1-3** complexes. As can be seen from Figure 1, the fluorescence intensity of BSA decreases by increasing the concentration of the complex, indicating its interactions with this protein. The values of binding constants (K_A) for **Au1-3** complexes (Table 1) are high enough to indicate their binding to BSA, which can transport them to the corresponding biological targets [5].

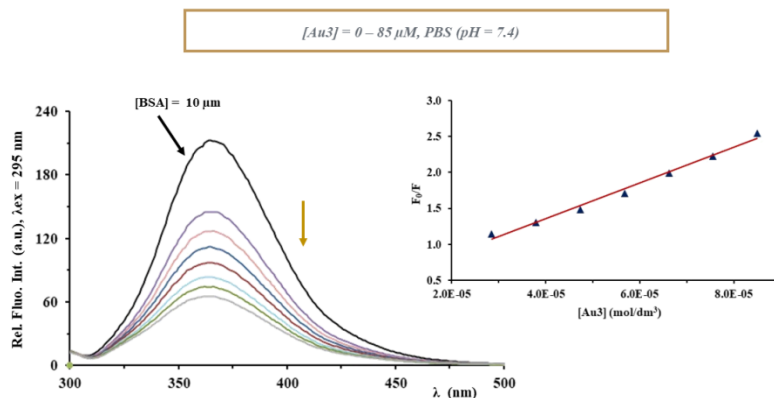


Figure 1. Fluorescence emission spectra of BSA in the presence of an increasing amount of **Au3**.
Inserted graph: Stern-Volmer plot of F_0/F vs. $[Au3]$.

Table 1. Values of the binding constants of **Au1-3** complexes with BSA.

	$K_{SV} (M^{-1})$	Hypochromism (%)	$K_q (M^{-1}s^{-1})$	$K_A (M^{-1})$	n
Au1	$(2.93 \pm 0.05) \times 10^4$	67.4	2.93×10^{12}	4.05×10^5	1.36
Au2	$(8.24 \pm 0.02) \times 10^3$	44.2	8.24×10^{11}	2.00×10^4	1.12
Au3	$(6.93 \pm 0.07) \times 10^4$	69.3	6.93×10^{12}	1.91×10^6	1.46

3.2 DNA binding study

The emission spectra of the EthBr-DNA system were recorded in the absence and presence of an increasing amount of the investigated **Au1-3** complexes. In all cases, upon addition of the gold(III) complexes, a decrease in the fluorescence intensity was observed, indicating their ability to interact with DNA. The **Au3** complex was most reactive toward this biomolecule. The calculated binding constants for **Au3** (K_A , Table 2) are higher than that for EthBr ($K_A = 2 \times 10^6 M^{-1}$), indicating that this complex could bind to DNA through the intercalative mode [6].

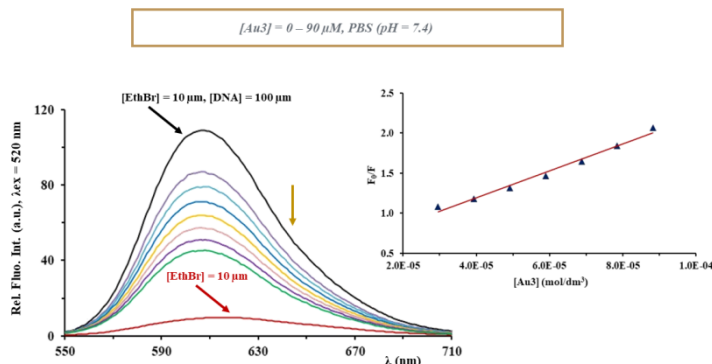


Figure 2. Fluorescence emission spectra of EthBr-DNA system in the presence of an increasing amount of **Au3** complex. Inserted graph: Stern-Volmer plot of F_0/F vs. $[Au3]$.

Table 2. Values of the binding constants of **Au1-3** complexes with DNA.

	K_{sv} (M^{-1})	Hypochromism (%)	K_q ($M^{-1}s^{-1}$)	K_A (M^{-1})	n
Au1	$(2.80 \pm 0.007) \times 10^3$	29.4	2.80×10^{11}	2.29×10^5	1.53
Au2	$(3.30 \pm 0.006) \times 10^3$	27.8	3.30×10^{11}	4.15×10^4	1.30
Au3	$(3.20 \pm 0.05) \times 10^4$	58.3	3.20×10^{12}	2.76×10^6	1.55

4. Conclusions

The presented results have indicated that gold(III)-azole complexes **Au1-3** interact with DNA and BSA. They can be bound by BSA and transported to the target cells. Inside the cell, these complexes could interact with DNA and exert their mode of action. Among the investigated complexes, **Au3** has the highest affinity toward DNA, and it presents a potential DNA intercalator.

Acknowledgment

This research has been financially supported by the Ministry of Science, Technological Development and Innovation of the Republic of Serbia (Agreements No. 451-03-47/2023-01/200122 and 451-03-47/2023-01/200378) and by the Serbian Academy of Sciences and Arts (project F128).

References

- [1] S.J. Berners-Price, A. Filipovska., *Gold compounds as therapeutic agents for human diseases*, Metallomics, 3 (2011) 863-873.
- [2] B.Đ. Glišić, M.I. Djuran., *Gold complexes as antimicrobial agents: an overview of different biological activities in relation to the oxidation state of the gold ion and the ligand structure*, Dalton Transactions, 43 (2014) 5950-5969.
- [3] N.Lj. Stevanović, J. Kljun, I. Aleksic, S. Skaro Bogojevic, D. Milivojevic, A. Veselinovic, I. Turel, M. I. Djuran, J. Nikodinovic-Runic, B. Đ. Glišić., *Clinically used antifungal azoles as ligands for gold(III) complexes: the influence of the Au(III) ion on the antimicrobial activity of the complex*, Dalton Transactions, 51 (2022) 5322-5334.
- [4] H. Zhang, Y. Wang, H. Zhu, Z. Fei, J. Cao., *Binding mechanism of triclocarban with human serum albumin: Effect on the conformation and activity of the model transport protein*, Journal of Molecular Liquids, 247 (2017) 281-288.
- [5] A. Tarushi, E. Potatoglou, J. Kljun, I. Turen, G. Psomas, D. P. Kessissoglou., *Interaction of Zn(II) with quinolone drugs: Structure and biological evaluation*, Dalton Transactions, 40 (2011) 9461-9473.
- [6] Y. Shi, C. Guo, Y. Sun, Z. Liu, F. Xu, Y. Zhang, Z. Wen, Z. Li, *Interaction between DNA and Microcystin-LR Studied by Spectra Analysis and Atomic Force Microscopy*, Biomacromolecules 12 (2011) 797-803.

DNA/BSA interaction of platinum(II) complexes with phenothiazine and *N*-methylphenothiazine

Tina P. Andrejević¹, Darko P. Ašanin², Bojana V. Pantović¹, Nevena Lj. Stevanović¹, Violeta R. Marković¹, Miloš I. Djuran³, Biljana Đ. Glišić^{1*}

¹ University of Kragujevac, Faculty of Science, Department of Chemistry, Radoja Domanovića 12, 34000 Kragujevac; e-mail: tina.andrejevic@pmf.kg.ac.rs, bojana.pantovic@pmf.kg.ac.rs, nevena.stevanovic@pmf.kg.ac.rs, violeta.markovic@pmf.kg.ac.rs, biljana.glisic@pmf.kg.ac.rs

² University of Kragujevac, Institute for Information Technologies Kragujevac, Department of Science, Jovana Cvijića bb, 34000 Kragujevac; e-mail: darko.asanin@uni.kg.ac.rs

³ Serbian Academy of Sciences and Arts, Knez Mihailova 35, 11000 Belgrade, Serbia; e-mail: milos.djuran@pmf.kg.ac.rs

DOI: 10.46793/ICCBi23.403A

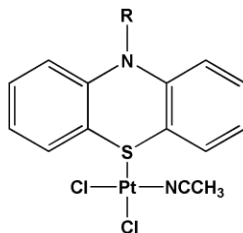
Abstract: In the present study, the interactions of two platinum(II) complexes of the general formula *cis*-[PtCl₂(L)(CH₃CN)], L is phenothiazine (phtz, **Pt1**) and *N*-methylphenothiazine (*N*-Mephtz, **Pt2**) with calf thymus DNA (ct-DNA) and bovine serum albumin (BSA) were studied by fluorescence emission spectroscopy to check their binding affinity towards these biomolecules for possible insights into the mode of their biological activity. A remarkable decrease in BSA fluorescence intensity after the addition of the complexes **Pt1** and **Pt2** and high values of the binding constants are in accordance with their high affinity toward this protein. On the other hand, the low binding affinity of the studied platinum(II) complexes to ct-DNA-EthBr system (EthBr is ethidium bromide, a well-known DNA intercalator) was observed. This has indicated that proteins could be more favorable binding sites for these platinum(II) complexes in comparison to the nucleic acids. Interestingly, **Pt1** complex has shown a higher binding affinity toward DNA than **Pt2**, while the latter complex is a more efficient BSA binder.

Keywords: platinum(II) complexes, phenothiazine, *N*-methylphenothiazine, DNA interactions, protein interactions

1. Introduction

In the last few decades, a large number of platinum(II) complexes have been synthesized and evaluated for their antitumor activity [1]. It is proposed that the interactions of platinum(II) complexes with DNA are responsible for their antitumor effects [2]. Besides that, the ability of platinum(II) complexes to bind serum proteins efficiently and to be transported to the target cells is an equally important factor for their mode of action [3]. Considering this, in the present study, we have investigated the interactions of two

platinum(II) complexes, *cis*-[PtCl₂(phtz)(CH₃CN)] (**Pt1**) and *cis*-[PtCl₂(N-Mephtz)(CH₃CN)] (**Pt2**) (phtz is phenothiazine and N-Mephtz is N-methylphenothiazine; Figure 1) with calf thymus DNA (ct-DNA) and bovine serum albumin (BSA) by fluorescence emission spectroscopy.



R = H (**Pt1**), CH₃ (**Pt2**)

Figure 1. Structural formula of the studied platinum(II) complexes **Pt1** and **Pt2**.

2. Material and Methods

2.1 Chemicals

Platinum(II) complexes, *cis*-[PtCl₂(phtz)(CH₃CN)] (**Pt1**) and *cis*-[PtCl₂(N-Mephtz)(CH₃CN)] (**Pt2**) were synthesized according to the method previously described in the literature [4]. Both complexes were pure based on elemental microanalysis and NMR spectroscopy. Dimethyl sulfoxide, phosphate-buffered saline (PBS), bovine serum albumin (BSA), calf thymus DNA (ct-DNA) and ethidium bromide (EthBr) were obtained from the commercial suppliers (Sigma-Aldrich and Acros Organics).

2.2 DNA/BSA interaction assay

Fluorescence spectra for BSA interactions were recorded on a Shimadzu RF-6000 spectrofluorometer at ambient temperature in the range of 285 – 500 nm, with an excitation wavelength of 280 nm. Fluorescence titration experiments were carried out in PBS (pH = 7.4) by keeping the concentration of BSA constant (17 μM), while varying the concentration of platinum(II) complexes (0 – 56 μM). The DNA binding experiments were also carried out in PBS by keeping [ct-DNA]/[EthBr] = 10, while increasing the concentration of the platinum(II) complexes. Measurements were performed in the wavelength range of 525 – 750 nm with an excitation wavelength of 520 nm.

3. Results and Discussion

3.1 BSA binding study

The fluorescence emission spectra of BSA of constant concentration were recorded in the presence of increasing concentrations of **Pt1** and **Pt2** complexes. As can be seen from Figure 2, the fluorescence intensity of BSA decreases by increasing the concentration of

the complexes, indicating their interactions with this protein. The values of binding constants (K_A) for **Pt1** and **Pt2** complexes (Table 1) are high enough to indicate their binding to BSA, which can transport them to the corresponding biological targets.

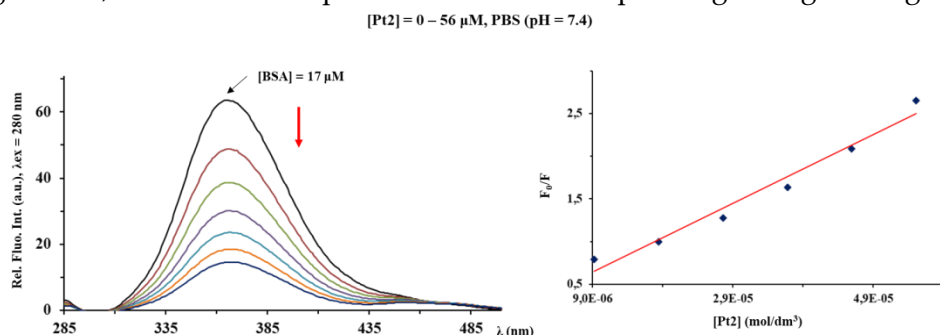


Figure 2. Fluorescence emission spectra of BSA in the presence of an increasing amount of **Pt2**.
Inserted graph: Stern-Volmer plot of F_0/F vs. **[Pt2]**.

Table 1. Values of the binding constants of **Pt1** and **Pt2** complexes with BSA.

	K_{sv} (M^{-1})	Hypochromism (%)	K_q ($M^{-1}s^{-1}$)	K_A (M^{-1})	n
Pt1	$(6.94 \pm 0.02) \cdot 10^4$	74.2	$6.94 \cdot 10^{12}$	$3.30 \cdot 10^5$	1.19
Pt2	$(1.44 \pm 0.02) \cdot 10^5$	77.1	$1.44 \cdot 10^{13}$	$1.58 \cdot 10^6$	1.34

3.2 DNA binding study

The emission spectra of the ct-DNA-EthBr system were recorded in the presence of an increasing amount of the investigated **Pt1** and **Pt2** complexes. After the addition of these complexes, no significant decrease in the fluorescence intensity of the EthBr-DNA system was observed (Figure 3). Moreover, the calculated values of the binding constants and the percentage of hypochromism for both complexes indicate that these complexes do not act as DNA intercalators (Table 2) [5].

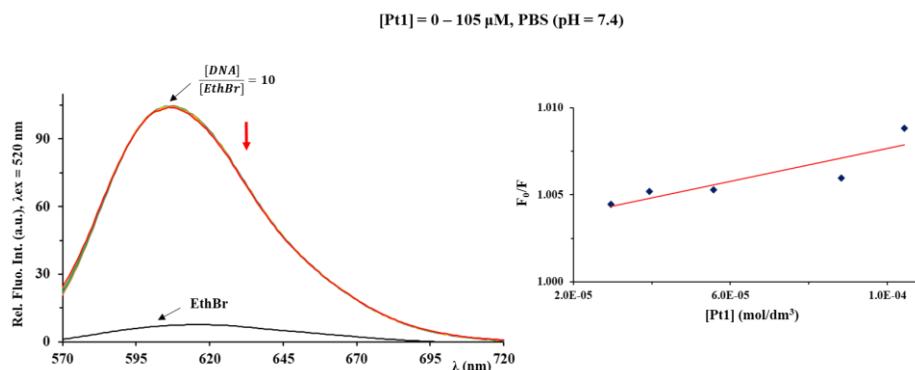


Figure 3. Fluorescence emission spectra of ct-DNA-EthBr system in the presence of an increasing amount of **Pt1** complex. Inserted graph: Stern-Volmer plot of F_0/F vs. **[Pt1]**.

Table 2. Values of the binding constants of **Pt1** and **Pt2** complexes with ct-DNA.

	$K_{sv} (M^{-1})$	Hypochromism (%)	$K_q (M^{-1}s^{-1})$	$K_A (M^{-1})$	n
Pt1	47.10 ± 0.10	0.7	4.71 · 10 ⁹	8.45	0.77
Pt2	32.90 ± 0.10	1.6	3.29 · 10 ⁹	1.10	0.42

4. Conclusions

The presented results have shown that platinum(II) complexes **Pt1** and **Pt2** interact with BSA, which can transport them to the target cells. On the other hand, their low affinity toward ct-DNA is observed, suggesting that this biomolecule is not the primary target for the mode of action of this type of platinum(II) complexes.

Acknowledgments

This research was supported by the Science Fund of the Republic of Serbia, Grant No. 7730810, Value-added biologics through eco-sustainable routes – BioECOLOGics. This research has also received funding from the Ministry of Science, Technological Development and Innovation of the Republic of Serbia (Agreements No. 451-03-47/2023-01/200122 and 451-03-47/2023-01/200378) and by the Serbian Academy of Sciences and Arts (project F128).

References

- [1] J. Qing, H. Daghriri, P. Beale., *Affinity of two novel five-coordinated anticancer Pt(II) complexes to human and bovine serum albumins: a spectroscopic approach*, Journal of Inorganic Biochemistry, 98 (2004) 1261-1270.
- [2] S. Komeda., *Unique platinum–DNA interactions may lead to more effective platinum-based antitumor drugs*, Metallomics, 3 (2011) 650-655.
- [3] B.P. Esposito, R. Najjar., *Interactions of antitumoral platinum-group metallodrugs with albumin*, Coordination Chemistry Reviews, 232 (2002) 137-149.
- [4] D.P. Ašanin, S. Vojnovic, T.P. Andrejević, V.R. Marković, F. Perdih, I. Turel, M.I. Djuran, J. Nikodinovic-Runic, B.Đ. Glišić., *Structural characterization and antitumor activity of platinum(II) complexes with phenothiazine and N-methylphenothiazine*, 16th International Symposium on Applied Bioinorganic Chemistry, Ioannina, Greece, June 11 – 14, 2023, p. 192.
- [5] Y. Shi, C. Guo, Y. Sun, Z. Liu, F. Xu, Y. Zhang, Z. Wen, Z. Li, *Interaction between DNA and Microcystin-LR Studied by Spectra Analysis and Atomic Force Microscopy*, Biomacromolecules 12 (2011) 797-803.

The interaction studies of novel diaminophenazine gold(III) complex and Bovine Serum Albumin (BSA-ibuprofen and BSA-Eosin Y)

Ana S. Kesić^{1,*}, Snežana R. Radisavljević², Jovana V. Bogojeski², Biljana V. Petrović²

¹ University of Kragujevac, Institute for Information Technologies, Jovana Cvijica bb, 34000 Kragujevac, Serbia, e-mail: akesic@uni.ac.kg.rs

² University of Kragujevac, Faculty of Science, R. Domanovica 12, 34000 Kragujevac, Serbia

DOI: 10.46793/ICCBi23.407K

Abstract: It is well known that gold(III) complexes have found applications in medicinal inorganic chemistry. Considering this, the right choice of inert ligands in the structure of Au(III) complexes is crucial for predicting their properties and reactivity, especially towards biomolecules. Here are presented the results of the study of the interactions between the new gold(III) complex [Au(DAP)Cl₃], with 2,3-diaminophenazine (DAP) as an inert ligand, and BSA. Specifically, serum albumin is the main soluble protein in the circulatory system of humans. The metabolism of drugs, their distribution, free concentration, and effectiveness strongly depend on the drug-albumin interaction. Investigation of the interactions of the [Au(DAP)Cl₃] complex with bovine serum albumin (BSA) under physiological conditions was performed by fluorescence spectroscopy. This method was also used to identify the binding site on the BSA molecule, with eosin Y as a marker for site I (subdomain IIA), and ibuprofen as a marker for site II (subdomain IIIA). The results have shown that the complex moderately reacts with the BSA molecule with just one binding site for the complex on the protein. Additionally, based on the results with site markers, especially with eosin Y, it can be concluded that the studied complex binds to site I of the BSA molecule.

Keywords: gold(III), complex, Bovine Serum albumin, interactions, Ibuprofen, Eosin Y

1. Introduction

Many studies have shown that the stability of Au(III) complexes can be achieved by proper choice of ligands during complexation [1]. Published results also confirmed that the proper choice of ligands is crucial for the good biological properties and reactivity of Au(III) complexes [2]. In the human bloodstream, the most abundant protein is serum albumin. The most significant role of serum albumin in the human organism is to transport various matters (hormones, fatty acids, ions, drugs, etc.) through the blood plasma to the organs and tissues. Metal ion complexes, with antitumor activity, often interact with proteins, both as part of their mechanism of action as well as for their transport and metabolism. Bovine serum albumin (BSA) is the most studied albumin due to its structural similarity to human serum albumin (HSA) [3]. Therefore, it is

important to examine the interactions between serum albumin protein, BSA, and transition metal complexes as potential anticancer drugs. Bovine serum albumins are heart-shaped proteins divided into three (I–III) domains, with each domain containing two subdomains (A and B) [4]. In the albumin molecule, transition metal complexes can bind at two sites within the BSA molecule, the site in the subdomain IIA and/or the site in the subdomain IIIA [5]. The fluorescence titration methods were used to identify the binding location of complexes on the BSA molecule, with eosin Y as a marker for site I (subdomain IIA) and ibuprofen as a marker for site II (subdomain IIIA). In the context of this study, we looked at how bovine serum albumin (BSA) interacted with the newly discovered complex, $[\text{Au}(\text{DAP})\text{Cl}_3]$ (where DAP = 2,3-diaminophenazine) (Figure 1).

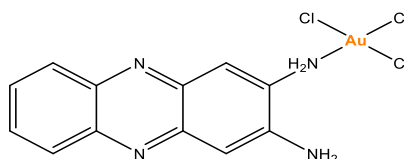


Figure 1. The structural formula of the investigated gold(III) complex.

2. Material and Methods

2.1 Chemicals and Apparatus

The initial potassium-tetrachloridoaurate(III) complex, $\text{K}[\text{AuCl}_4]$, was purchased from ABCR GmbH & Co. KG, 98%. Ligand 2,3-diaminophenazine (DAP), bovine serum albumin (BSA) and phosphate-buffered saline (PBS) were purchased from Sigma-Aldrich Chemical. Eosin Y and ibuprofen were commercially available and used as received. Doubly distilled water was used throughout the experiments. The stock solutions of BSA were prepared by dissolving the corresponding solid in PBS buffer at $\text{pH} = 7.4$. All stock solutions were stored at 277 K and used within 3–5 days. Fluorescence spectra were collected on an RF-6000 spectrofluorometer (Shimadzu, Japan). The widths of the excitation and emission slits were both fixed at 10 nm.

2.2 Albumin binding studies

The quenching of the emission intensity of the solution with a fixed concentration of BSA (2 μM) and increasing concentration of the complex up to 9.09×10^{-6} M as a quencher was monitored at 365 nm. Fluorescence spectra were recorded at an excitation wavelength of 295 nm in the range between 300 - 500 nm. The Stern–Volmer and Scatchard equations [6,7] and graphs have been used to determine the strength of the interactions of the complex with BSA and to calculate the corresponding constants. The values of the dynamic quenching constant (K_{sv}) and the quenching rate constant (K_q) were calculated using the Stern-Volmer quenching equation. The association binding constant (K_b) and the number of the binding sites per albumin (n) were calculated using the Scatchard equation.

In addition, the competitive interactions of site markers (eosin Y, as a marker for site I of subdomain IIA, and ibuprofen, as a marker for site II of subdomain IIIA) and

complex towards BSA were studied using fluorescence emission spectroscopy. The excitation wavelength was set at 295 nm, with the fluorescence emission range between 300 and 500 nm. The solutions of BSA and markers were added in equimolar concentrations (2.0×10^{-6} M). Gold complex is added with increasing concentrations up to 9.09×10^{-6} M.

3. Results and discussion

Fluorescence spectroscopy measurements for the investigation of the interactions of the studied complex and bovine serum albumin, BSA, were performed. By adding the gold(III) complex solution to the BSA solution, a decrease in fluorescence emission appears at about 365 nm. The decrease in fluorescence (Figure 2a) can be attributed to the changes in the tertiary structure of the albumin (changes in the environment of the tryptophan) because of the binding of the complex to BSA. The Stern-Volmer constant (K_{sv}), bimolecular quenching constant (K_q) and other parameters (K_b and n) for the interaction of complex $[\text{Au}(\text{DAP})\text{Cl}_3]$ with BSA are given in Table 1.

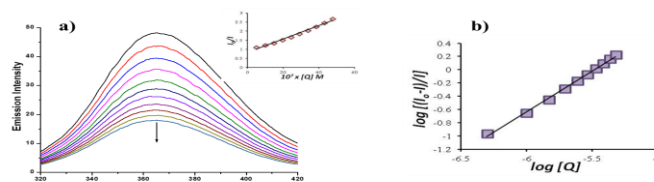


Figure 2. a) Emission spectra observed for the titration of BSA with $[\text{Au}(\text{DAP})\text{Cl}_3]$, insert plots of I_0/I vs. $[\text{Q}]$ (b) Scatchard plots for the $[\text{Au}(\text{DAP})\text{Cl}_3]$ complex and BSA.

Table 1. Stern–Volmer constants (K_{sv}), bimolecular quenching constants (k_q) and the other parameters (K_b and n) for the interactions of complex $[\text{Au}(\text{DAP})\text{Cl}_3]$ with BSA in the absence and presence of the site markers (ibuprofen and eosin Y).

System	K_{sv} (M^{-1})	K_q ($\text{M}^{-1} \text{s}^{-1}$)	K_b ($\text{M}^{-1} \text{s}^{-1}$)	n
Complex-BSA	$(3.70 \pm 0.08) \times 10^5$	$(3.70 \pm 0.08) \times 10^{13}$	$(5.61 \pm 0.06) \times 10^6$	1.23
Complex-BSA- ibuprofen	$(13.46 \pm 0.04) \times 10^5$	$(13.46 \pm 0.04) \times 10^{13}$	$(2.11 \pm 0.01) \times 10^6$	1.16
Complex-BSA- eosin-Y	$(3.14 \pm 0.03) \times 10^5$	$(3.14 \pm 0.03) \times 10^{13}$	$(1.49 \pm 0.09) \times 10^6$	1.13

Competitive experiments with BSA and site markers: The excitation wavelength for the fluorescence titration was 295 nm, and the emission was followed in the range of 300–500 nm. Changes in the emission of BSA solutions with the addition of the increasing concentration of the tested complex were monitored in the presence of the markers eosin Y and ibuprofen (Figures 3 and 4). According to the obtained values of constants ($2.11 \pm 0.01 \times 10^6$ and $1.49 \pm 0.09 \times 10^6$), obviously complex may bind both sites, but preferentially to site I/sub-domain IIA of BSA.

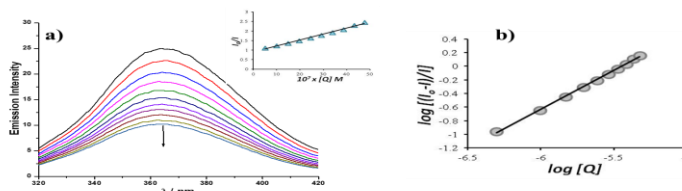


Figure 3. (a) Emission spectra of the titration of BSA in the presence of site marker eosin Y and complex $[\text{Au}(\text{DAP})\text{Cl}_3]$, insert plots of I_0/I vs. $[\text{Q}]$ (b) Scatchard plot for $[\text{Au}(\text{DAP})\text{Cl}_3]$ complex

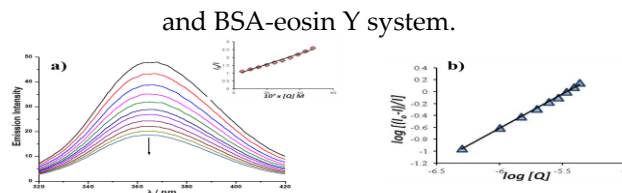


Figure 4. (a) Emission spectra of the titration of BSA in the presence of site marker ibuprofen and complex [Au(DAP)Cl₃], insert: plots of I₀/I vs. [Q]. (b) Scatchard plot for the [Au(DAP)Cl₃] complex and the BSA-ibuprofen system.

4. Conclusions

Based on the calculated values of the constant K_b can be confirmed that the studied complex moderately reacts with the BSA molecule. Also, the results of this study showed that Au(III) complex has a single binding site on the BSA molecule, which means that the complex can bind to either site I or site II of the protein, but not both. Additionally, based on the calculated values of the binding constants it can be concluded that the presence of the eosin Y site marker has a greater influence. However, in the presence of ibuprofen, only a slight change in the value of the constant was observed. These results indicate that the binding of the investigated complex should be located within site I of the BSA molecule.

Acknowledgment

This research is funded by the Ministry of Education and Ministry of Science, Technological Development and Innovation, Republic of Serbia, Grants No. 451-03-47/2023-01/200378 and 451-03-47/2023-01/200122.

References

- [1] B. Bertrand, A. Casini., *A golden future in medicinal inorganic chemistry: the promise of anticancer gold organometallic compounds*, Dalton Trans, 43 (2014) 4209-4219.
- [2] S. Radisavljević, A. Kesić, D. Čočić, R. Puchta, L. Senft, M. Milutinović, N. Milivojević, B. Petrović., *Studies of the stability, nucleophilic substitution reactions, DNA/BSA interactions, cytotoxic activity, DFT and molecular docking of some tetra- and penta-coordinated gold(III) complexes*, New J Chem, 44 (2020) 11172-1187.
- [3] B. Wu, C. Qu, Y. Wang, J. Zhao, H. Du., *Comparison of the Quenching Effects of Two Main Components of Ziziphi Spinosa Semen on Serum Albumin Fluorescence*, J Fluoresc, 29 (2019) 1113-11.
- [4] Y. Song, Y. Liu, W. Liu, F.A. Villamena, J.L. Zweier., *Characterization of the binding of the Finland trityl radical with bovine serum albumin*, RSC Adv, 4 (2014) 47649-47656.
- [5] X.M. He, D.C. Carter., *Atomic structure and chemistry of human serum albumin*, Nature, 353 (1992) 209-2015.
- [6] F. Dimiza, F. Perdih, V. Tangoulis, I. Turel, D.P. Kessissoglou, G. Psomas., *Interaction of copper(II) with the non-steroidal anti-inflammatory drugs naproxen and diclofenac: Synthesis, structure, DNA- and albumin-binding*, J Inorg Biochem, 105 (2011) 476-489.
- [7] D.S. Raja, N.S. Bhuvanesh., *Effect of N(4)-Phenyl Substitution in 2-Oxo-1,2-dihydroquinoline-3-carbaldehyde Semicarbazones on the Structure, DNA/Protein Interaction, and Antioxidative and Cytotoxic Activity of Cu(II)*, Natarajan Inorg Chem., 50 (2011) 12852-12866.

The influence of structural modification of Pd(II) pincer-type complexes on the kinetics of substitution reactions

Snežana Jovanović Stević¹, Snežana Radisavljević², Aleksandar Mijatović³, Biljana Petrović², Ana Kesic^{4,*}

¹ University of Kragujevac, Faculty of medical science, Department of pharmacy, 34000 Kragujevac, Serbia, S. Markovića 69; e-mail: snezana.j@kg.ac.rs

² University of Kragujevac, Faculty of science, 34000 Kragujevac, Serbia, R. Domanovića 12, e-mail: snezana.radisavljevic@pmf.kg.ac.rs, biljana.petrovic@pmf.kg.ac.rs

³ University of Belgrade, Faculty of mining and geology, 11000 Belgrade, Serbia, Djušina 7, e-mail: aleksandar.mijatovic@rgf.bg.ac.rs

⁴ University of Kragujevac, Institute for information technologies, 34000 Kragujevac, Serbia, J. Cvijića bb, e-mail: akesic@uni.kg.ac.rs

DOI: 10.46793/ICCB23.411JS

Abstract: This mini-review summarizes the kinetic data obtained for the substitution reactions of some palladium(II) complexes containing *bis*-pyrazolylpyridine derivatives as pincer-type ligands with biologically significant nitrogen- and sulfur-donor biomolecules as nucleophiles. Three structurally different palladium(II) complexes were selected: [Pd(L1)Cl]⁺ (Pd1), [Pd(L2)Cl]⁺ (Pd2) and [Pd(L3)Cl]⁺ (Pd3) (where L1 = bis(2-(1H-pyrazol-1-yl)ethyl)amine, L2 = 2,6-bis(5-(tert-butyl)-1H-pyrazol-3-yl)pyridine, and L3 = 2,6-bis(5-(tert-butyl)-1-methyl-1H-pyrazol-3-yl)pyridine, while for the entering nucleophiles thiourea (Tu), L-methionine (L-met), and guanosine-5'-monophosphate (5'-GMP) were used. Kinetic measurements were carried out for all systems as *pseudo*-first order reactions (at least 10 times the ligand in excess relative to the complex) under physiological conditions using a stopped-flow UV-Vis spectrophotometer. By comparing the published results for the second-order rate constant, the relationship between the structural properties of the complexes and their reactivity towards selected nucleophiles was established. This overview shows that by tuning the lability of the inert ligands through steric and electronic (σ -donor and π -acceptor) effects, the biological behavior of the complexes can be significantly changed.

Keywords: Pd(II), structural modification, kinetics

1. Introduction

The application of transition metal ion complexes in chemotherapy is widely known [1]. Over the past decades, numerous Pt complexes have been designed and tested as potential antineoplastic agents [2]. Among them, cisplatin, carboplatin, and oxaliplatin entered the clinical trial, and today they are successfully used in the treatment of various types of cancers, such as testicular, ovarian, bladder, colon, head, neck, and small-cell

lung cancers [3]. However, serious side effects such as emesis, nephrotoxicity, neurotoxicity, ototoxicity, and drug resistance may occur during the application of these drugs as chemotherapeutics. These limitations have stimulated investigations for the improvement of existing platinum antitumor drugs and the development of new derivatives that display better therapeutic properties.

Special attention is directed towards palladium(II) complexes, which show higher kinetic reactivity and better solubility than platinum(II) compounds [4]. It is believed that palladium(II) complexes may possess an enhanced curative effect on cancers relative to platinum analogs. Thus, a huge number of structurally different palladium(II) complexes were synthesized and their influence on the tumor cells was examined, while the results indicated a better antitumor effect compared to analogous platinum compounds [5].

Mostly, the antitumor activity of some metallodrugs is based on their interactions with DNA molecules, while interactions with sulfur-containing biomolecules are responsible for the occurrence of toxic effects [6]. By studying the behavior of Pd-complexes in the presence of small biomolecules under physiological conditions, we can obtain key information that improves our understanding of the biochemical processes which occur in the body during the application of metal complexes as antitumor drugs.

2. Substitution reactions of complexes Pd1-Pd3 with different biomolecules

This mini review includes the results of testing the rate of substitution reactions of complexes Pd1-Pd3 (Figure 1) with nucleophiles, such as Tu, L-met and 5'-GMP by stopped-flow method [7, 8]. All kinetic measurements were carried out under the *pseudo*-first order conditions by monitoring the change in absorbance as a function of nucleophile concentration with time. The experiments were performed under physiological conditions at pH 7.2 and 25 °C in the presence of 50 mM NaCl to suppress the hydrolysis of complexes. The same reaction mechanism was reported for all systems, in which the labile chloride ligand from the inner coordination sphere of the starting complex was replaced by a nucleophile. This reaction is characterized by a second-order reaction rate constant, k_2 . Calculated values for k_2 are given in Table 1 [7, 8].

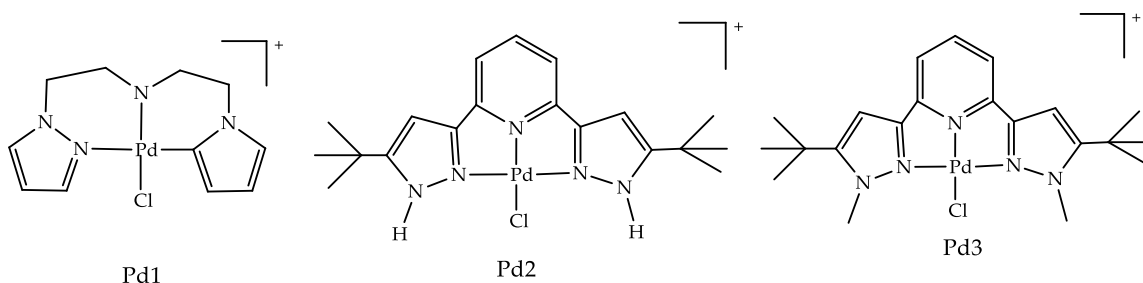


Figure 1. The structures of complexes.

Table 1.	Complex	Ligand	k_2 [$M^{-1} s^{-1}$]		Second-constants
order rate for the	Pd1	Tu	432 ± 4	Ref [7]	
		L-met	186 ± 4		
		5'-GMP	30 ± 1		
	Pd2	Tu	23100 ± 700	Ref [8]	
		L-met	12200 ± 100		
		5'-GMP	760 ± 20		
	Pd3	Tu	18400 ± 200	Ref [8]	
		L-met	10100 ± 100		
		5'-GMP	650 ± 20		

substitution reactions of Pd1-Pd3 complexes with selected nucleophiles.

The reactivity of complexes towards nucleophiles decreases in the order: Pd2 > Pd3 > Pd1 (Table 1). A significant greater reactivity of Pd2 and Pd3 than Pd1 is caused by the electronic effect, due to the π -acceptor ability of the pyridine moiety, by which the electron density on the palladium center is reduced. On the other hand, slightly higher reactivity of Pd2 compared to Pd3 was observed. The presence of additional methyl groups on nitrogen atoms in L3 causes steric hindrance, so the approach of the entering ligands to the metal ion is more difficult. Additionally, methyl group is a good σ -donor and donates electrons to the metal center, increasing the electron cloud on the palladium center leading to a slower substitution reaction. The entering nucleophiles Tu, L-met and 5'-GMP, were selected due to their varied electronic and steric demands, binding abilities and biorelevance [7, 8]. Nucleophiles Tu and L-met were used as models for sulphur-containing molecules, which are plentiful in the blood plasma. The molecule 5'-GMP (nitrogen donor) was utilised as a representative for nucleobases binding. The reactivity of nucleophiles decreases in order: Tu > L-met > 5'-GMP. A much higher reactivity of sulfur-donor molecules (Tu, L-met) compared to 5'-GMP as nitrogen-donor was noticed. It can be attributed to the fact that soft acid such as Pd(II) ion prefers to coordinate with sulfur atom. Thiourea has the highest reactivity since it combines the ligand properties of thiolates as π -donors, and thioethers as σ -donors and π -acceptors. In addition, thiourea is the least sterically demanding molecule from used ligands. The least reactivity of 5'-GMP can also be accounted for by its steric bulkiness in comparison to the other two nucleophiles. Overall, the selected ligands represent good entering nucleophiles for the studied substitution reactions, while the Pd1-Pd3 complexes exhibit a very high affinity towards chosen small biomolecules.

3. Conclusions

We have shown that the rate of the substitution reactions of metallocomplexes with biologically important molecules can be controlled by the suitable choice of inert chelating ligand. Thus, the chemical nature of inert tridentate ligands that combine

electronic and steric effects has a very important role in the prediction of the kinetic behavior of some transition metal ion complexes. The information presented here can provide deeper insights into the possible use of kinetic studies as tools for the development of new metallodrugs.

Acknowledgment

This research is funded by the Ministry of Education and Ministry of Science, Technological Development, and Innovation, Republic of Serbia, Grants: No. 451-03-47/2023-01/200111; 451-03-47/2023-01/200122; 451-03-47/2023-01/200126; and 451-03-47/2023-01/200378.

References

- [1] U. Ndagi, N. Mhlongo, M.E. Soliman, *Metal complexes in cancer therapy – an update from drug design perspective*, *Drug Design, Development and Therapy*, 11 (2017) 599-616.
- [2] M. Fanelli, M. Formica, V. Fusi, L. Giorgi, M. Micheloni, P. Paoli, *New trends in platinum and palladium complexes as antineoplastic agents*, *Coordination Chemistry Reviews*, 310 (2016) 41-79.
- [3] N.P. Farrell, *Multi-platinum anti-cancer agents. Substitution-inert compounds for tumor selectivity and new targets*, *Chemical Society Reviews*, 44 (2015) 8773-8785.
- [4] Ž.D. Bugarčić, J. Bogojeski, R. van Eldik, *Kinetics, mechanism and equilibrium studies on the substitution reactions of Pd(II) in reference to Pt(II) complexes with bio-molecules*, *Coordination Chemistry Reviews*, 292 (2015) 91-106.
- [5] A.R. Kapdi, I.J.S. Fairlamb, *Anti-cancer palladium complexes: a focus on PdX₂L₂, palladacycles and related complexes*, *Chemical Society Reviews*, 43 (2014) 4751-4777.
- [6] B. Petrović, S. Jovanović, R. Puchta, R. van Eldik, *Mechanistic insight on the chemistry of potential Pt antitumor agents as revealed by collaborative research performed in Kragujevac and Erlangen*, *Inorganica Chimica Acta* 495 (2019) 118953.
- [7] R.O. Omondi, A.O. Fadaka, A.A. Fatoku, D. Jaganyi, S.O. Ojwach, *Synthesis, substitution kinetics, DNA/BSA binding and cytotoxicity of tridentate N^EN (E=NH, O, S) pyrazolyl palladium(II) complexes*, *Journal of Biological inorganic chemistry*, 27 (2022) 653-664.
- [8] D. Čović, S. Jovanović, S. Radisavljević, J. Korzekwa, A. Scheurer, R. Puchta, D. Baskić, D. Todorović, S. Popović, S. Matić, B. Petrović, *New monofunctional platinum(II) and palladium(II) complexes: Studies of the nucleophilic substitution reactions, DNA/BSA interaction, and cytotoxic activity*, *Journal of Inorganic Biochemistry*, 189 (2018) 91-102.

In vitro cytotoxic activity of a monolacunary Wells-Dawson nanocluster against cervical carcinoma HeLa cells

Mirjana B. Čolović^{1,*}, Jelena J. Žakula², Lela B. Korićanac², Nada Savić³, Tatjana Parac-Vogt³, Danijela Z. Krstić⁴

¹ University of Belgrade, "Vinča" Institute of Nuclear Sciences-National Institute of the Republic of Serbia, Department of Physical Chemistry, M. Petrović 12-14, 11351 Belgrade, Republic of Serbia; e-mail: colovicm@vin.bg.ac.rs

² University of Belgrade, "Vinča" Institute of Nuclear Sciences-National Institute of the Republic of Serbia, Department of Molecular Biology and Endocrinology, M. Petrović 12-14, 11351 Belgrade, Republic of Serbia; e-mail: pozegaj@vin.bg.ac.rs, lela@vin.bg.ac.rs

³ KU Leuven, Department of Chemistry, Celestijnenlaan 200F, 3001 Leuven, Belgium; e-mail: nada.savic@kuleuven.be, tatjana.vogt@kuleuven.be

⁴ University of Belgrade, Faculty of Medicine, Institute of Medical Chemistry, Višegradska 26, 11000 Belgrade, Republic of Serbia; e-mail: danijela.krstic@med.bg.ac.rs

* Corresponding author

DOI: 10.46793/ICCBi23.415C

Abstract: The aim of this study was to assess *in vitro* cytotoxic activity of a monolacunary Wells-Dawson nanocluster, α_2 -K₁₀P₂W₁₇O₆₁·20H₂O (lacunary WD) against cervical carcinoma HeLa cells as a commonly used model system for the evaluation of antitumor properties. After HeLa cells had been exposed to the investigated polyoxotungstate (the concentration range of 0.001 - 1 mM) for 24, 48, and 72 h, relative cell viability (expressed as a percentage of control) was determined. The obtained results showed that lacunary WD affected HeLa cell viability in a concentration- and time-dependent manner. IC₅₀ values (in μ M), calculated using sigmoidal fitting experimental plots, were as follows: 24.11 ± 9.95 , 12.74 ± 0.096 , and 11.48 ± 0.12 for 24, 48, and 72 hours treatment, respectively. In comparison with cisplatin, (positive control), IC₅₀ values (μ M) for 24 hours treatment were similar – 24.11 (lacunary WD) *vs.* 24.49 (cisplatin). However, after 48 and 72 hours IC₅₀ obtained for cisplatin were found to be lower – 8.81 and 4.93 μ M, respectively. Accordingly, the studied WD polyoxotungstate could not be regarded as a superior anticancer agent in comparison with the standard chemotherapeutic. Nevertheless, this studied nanocluster deserves attention as a promising antitumor therapeutic and as a good platform for the design of next-generation metal-based anticancer agents.

Keywords: antitumor metallodrug, HeLa cells, *in vitro* cytotoxicity, monolacunary Wells-Dawson, polyoxotungstate

1. Introduction

Polyoxotungstates are versatile, metal-based compounds containing tungsten ions in their high oxidation state bridged by oxygen [1]. In recent decades, these negatively charged nanoclusters have been found to demonstrate promising cytotoxic properties against different malignant cells and thus could be studied as a potential platform for the development of next-generation metallodrugs [2].

The objective of this study was to *in vitro* evaluate the antitumor potential of a monolacunary Wells-Dawson polyoxotungstate, $\alpha_2\text{-K}_{10}\text{P}_2\text{W}_{17}\text{O}_{61}\cdot 20\text{H}_2\text{O}$ (lacunary WD). With this aim, *in vitro* cytotoxicity was tested using cervical carcinoma HeLa cells as a model system that has been widely used for research purposes.

2. Experimental

Lacunary WD was synthesized according to the literature [3]. A stock aqueous solution of lacunary WD (1 mM) was prepared by vigorous mixing and heating at 30-40 °C, and working solutions were prepared by diluting the stock solution with water up to desired concentrations.

Cervical carcinoma HeLa cells were obtained from the American Tissue Culture Collection (ATCC, Manassas, VA, USA) and cultured in high-glucose DMEM medium (Sigma-Aldrich, Steinheim, Germany) supplemented with 10% fetal bovine serum (Sigma-Aldrich, Steinheim, Germany), and penicillin/streptomycin (Sigma-Aldrich, Steinheim, Germany) in a humidified atmosphere of 5% CO₂ at 37 °C (Heraeus, Hanau, Germany).

Exponentially growing cells, seeded into flat-bottom 96-well plates at a density of 2×10^3 cells per well, were treated with the selected concentrations of lacunary WD and cisplatin (*cis*-diamminedichloridoplatinum(II)). The cytotoxicity was determined using a sulforhodamine B (SRB) assay based on the measurement of cellular protein content. The assay was performed according to the method of Skehan *et al.* [4] 24 -72 h after the treatment. Cell monolayers were fixed with 10% trichloroacetic acid (TCA) (Carlo Erba, Milan, Italy) for 1 h at 4 °C and stained with 0.4% SRB (Sigma-Aldrich, Steinheim, Germany). The unbound color was removed, and the plates were washed with 1% acetic acid before air-drying. Protein-bound dye was dissolved in 10 mM Tris base (Sigma-Aldrich, Steinheim, Germany). Absorbance was measured at 550 nm and a reference wavelength of 690 nm using a microplate reader (Wallac, VICTOR2 1420 Multilabel counter, PerkinElmer, Turku, Finland). The obtained results were expressed as relative cell viability, calculated as a percentage of control.

3. Results and discussion

In vitro antitumor action of lacunary WD polyoxotungstate towards cervical carcinoma HeLa cells was evaluated by monitoring relative cell viability expressed as a percentage of control (cell viability obtained in the presence of water). Previously, the investigated cell line was *in vitro* exposed to the selected concentrations of the tested compound (the concentration range of 0.001 - 1 mM) for 24, 48, and 72 h. The obtained

results are presented in Figure 1. In addition, the lacunary WD-induced cytotoxic activity was compared with the antitumor activity of cisplatin against cervical carcinoma HeLa cells under the same conditions, which has been used as a gold standard among metal-based chemotherapeutics.

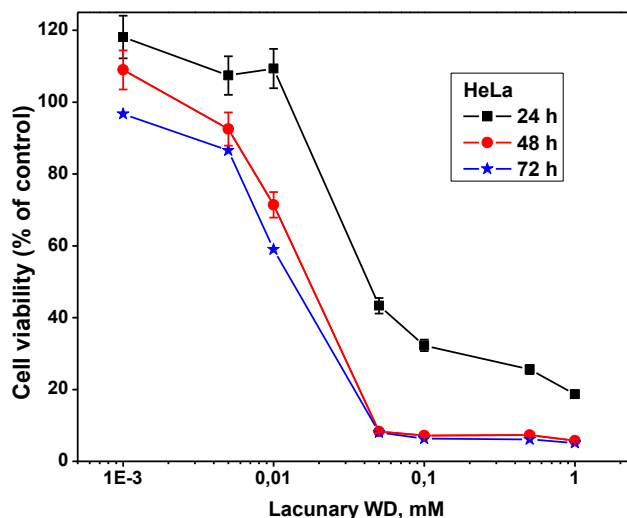


Figure 1. The effect of lacunary WD on the viability of cervical carcinoma HeLa cells. The cells were treated with various lacunary WD concentrations for 24 (square), 48 (circle), and 72 (asterisk) hours. The viability of treated cells was expressed as % of untreated (control) cells (100%). Results are expressed as mean \pm S.E.M. from at least 2 independent experiments done in triplicates.

IC₅₀ values, used as an indicator of antitumor potency, were calculated using sigmoidal fitting the experimental plots. Calculated IC₅₀ values (in μ M) were determined as follows: 24.11 ± 9.95 , 12.74 ± 0.096 , and 11.48 ± 0.12 for 24, 48, and 72 hours treatment, respectively. The obtained results (Figure 1) show that the studied lacunary WD induced HeLa cell cytotoxicity in a concentration - and time-dependent manner. Significant cytotoxic effects were achieved at low micromolar concentrations for all exposure times, whereas concentrations higher than 50 μ M resulted in almost complete cell viability reduction after 48 and 72 hours exposure.

In comparison with cisplatin, which was used as a positive control, IC₅₀ values (μ M) for 24 hours treatment were similar – 24.11 (lacunary WD) *vs.* 24.49 (cisplatin). However, after 48 and 72 hours IC₅₀ obtained for cisplatin were found to be lower – 8.81 and 4.93 μ M, respectively. This indicates that the studied WD polyoxometalate could not be considered a superior anticancer agent in comparison with the standard chemotherapeutic.

4. Conclusions

The results of this *in vitro* study on the potential antitumor activity of lacunary WD polyoxometalate demonstrated that the synthesized polyoxotungstate induces

significant cytotoxic effects on cervical carcinoma HeLa cells at low micromolar concentrations, which are comparable with the cytotoxic properties of cisplatin, the gold standard chemotherapeutic. Thus, this studied nanocluster deserves attention as a potential antitumor therapeutic and as a good base for the design of novel metal-based anticancer agents.

Acknowledgment

This research is funded by the Ministry of Science, Technological Development and Innovation and Ministry of Education, Republic of Serbia, Grants: No. 451-03-9/2023-14/200017 and 451-03-9/2023-14/200110. The authors are also thankful to the Science Fund of the Republic of Serbia (POMCACT Project No. 6526393).

References

- [1] M.B. Čolović, M. Lacković, J. Lalatović, A.S. Mougharbel, U. Kortz, D.Z. Krstić, *Polyoxometalates in biomedicine: update and overview*, *Current Medicinal Chemistry*, 27 (2020) 362-379.
- [2] A. Bijelic, M. Aureliano, A. Rompel, *Polyoxometalates as potential next-generation metallodrugs in the combat against cancer*, *Angewandte Chemie International Edition*, 58 (2019) 2980–2999.
- [3] A.P. Ginsberg, *Inorganic Syntheses*, Wiley, 1990.
- [4] P. Skehan, R. Storeng, D. Scudiero, A. Monks, J. McMahon, D. Vistica, J.T. Warren, H. Bokesch, S. Kenney, M.R. Boyd, *New colorimetric cytotoxicity assay for anticancer-drug screening*, *Journal of the National Cancer Institute*, 82 (1990) 1107-1112.

The influence of Fe(III) incorporation on anti-cancer potential of a Wells-Dawson nanocluster

Mirjana B. Čolović^{1,*}, Lela B. Korićanac², Jelena J. Žakula², Nada Savić³, Tatjana Parac-Vogt³, Danijela Z. Krstić⁴

¹ University of Belgrade, "Vinča" Institute of Nuclear Sciences-National Institute of the Republic of Serbia, Department of Physical Chemistry, M. Petrović 12-14, 11351 Belgrade, Republic of Serbia; e-mail: colovicm@vin.bg.ac.rs

² University of Belgrade, "Vinča" Institute of Nuclear Sciences-National Institute of the Republic of Serbia, Department of Molecular Biology and Endocrinology, M. Petrović 12-14, 11351 Belgrade, Republic of Serbia; e-mail: lela@vin.bg.ac.rs, pozegaj@vin.bg.ac.rs

³ KU Leuven, Department of Chemistry, Celestijnenlaan 200F, 3001 Leuven, Belgium; e-mail: nada.savic@kuleuven.be, tatjana.vogt@kuleuven.be

⁴ University of Belgrade, Faculty of Medicine, Institute of Medical Chemistry, Višegradska 26, 11000 Belgrade, Republic of Serbia; e-mail: danijela.krstic@med.bg.ac.rs

* Corresponding author

DOI: 10.46793/ICCB23.419C

Abstract: The objective of this study was to evaluate *in vitro* the antitumor properties of Fe(III)-substituted monolacunary Wells-Dawson polyoxotungstate, $K_7[Fe^{III}(\alpha_2-P_2W_{17}O_{61})(H_2O)]$ (FeWD) using cervical carcinoma HeLa cells as a model system. HeLa cells were exposed *in vitro* to FeWD within the concentration range from 0.001 to 1 mM, for 24, 48, and 72 hours. The studied Fe(III)-substituted polyoxotungstate affected HeLa cell viability in a concentration- and time-dependent manner. The obtained IC_{50} values (μM), as an indicator of the cytotoxic potential of FeWD, were: 16.64 ± 0.49 , 10.75 ± 0.97 , and 9.64 ± 0.19 for 24-, 48-, and 72-hour treatment, respectively. FeWD exhibited a stronger antitumor potential against HeLa cells than the structurally similar monolacunary Wells-Dawson polyoxotungstate, $K_{10}P_2W_{17}O_{61} \cdot 20H_2O$ (lacunary WD). Lacunary WD achieved IC_{50} at 24,11 μM after 24-hour exposure, which is about 44% higher concentration compared to the corresponding IC_{50} obtained for FeWD. This indicates that incorporating Fe(III) might be a new strategy for improving the antitumor efficacy of polyoxometalates as promising candidates for next-generation chemotherapeutics.

Keywords: Fe(III)-substituted polyoxotungstate, HeLa cells, *in vitro* cytotoxicity, metallodrugs, Wells-Dawson

1. Introduction

Polyoxometalates are negatively charged metal-oxo nanoclusters consisting of early *d*-block metal ions in their high oxidation states and bridged oxygen [1]. The number of studies on the biological activities of this class of metal-based compounds has

been increasing in recent years, which include *in vitro* and *in vivo* antitumor investigations on a variety of model systems [2].

In this study the antitumor potency of Fe(III)-substituted monolacunary Wells-Dawson polyoxotungstate, $K_7[Fe^{III}(\alpha_2-P_2W_{17}O_{61})(H_2O)]$ (FeWD) was assessed *in vitro* on cervical carcinoma HeLa cell line as a model system. In addition, the cytotoxic activity of FeWD was compared with the antitumor action of its parent compound, $\alpha_2-K_{10}P_2W_{17}O_{61}\cdot 20H_2O$ (lacunary WD).

2. Material and methods

FeWD was prepared according to the previously reported procedure [3]. A stock aqueous solution (1 mM) was prepared by mixing at room temperature, whereas working solutions were prepared by diluting the stock solution with water up to investigated concentrations.

Cervical carcinoma HeLa cells were obtained from the American Tissue Culture Collection (ATCC, Manassas, VA, USA) and cultured in high-glucose DMEM medium (Sigma-Aldrich, Steinheim, Germany) supplemented with 10% fetal bovine serum (Sigma-Aldrich, Steinheim, Germany), and penicillin/streptomycin (Sigma-Aldrich, Steinheim, Germany) in a humidified atmosphere of 5% CO₂ at 37 °C (Heraeus, Hanau, Germany).

Exponentially growing cells, seeded into flat-bottom 96-well plates at a density of 2×10^3 cells per well, were exposed to the various concentrations of FeWD. The cell viability was determined using a sulforhodamine B (SRB) assay based on the measurement of cellular protein content. The assay was performed according to the method of Skehan *et al.* [4] 24–72 h after the treatment. Cell monolayers were fixed with 10% trichloroacetic acid (TCA) (Carlo Erba, Milan, Italy) for 1 h at 4 °C and stained with 0.4% SRB (Sigma-Aldrich, Steinheim, Germany). The unbound color was removed, and the plates were washed with 1% acetic acid before air-drying. Protein-bound dye was dissolved in 10 mM Tris base (Sigma-Aldrich, Steinheim, Germany). Absorbance was measured at 550 nm and a reference wavelength of 690 nm using a microplate reader (Wallac, VICTOR2 1420 Multilabel counter, PerkinElmer, Turku, Finland).

3. Results and discussion

HeLa cells were treated *in vitro* with FeWD within the concentration range from 0.001 to 1 mM, for 24, 48, and 72 hours. It is observed (Figure 1) that the investigated polyoxotungstate resulted in a cytotoxic effect on malignant HeLa cells in a concentration- and time-dependent manner. A significant decrease in cell viability is noticeable at 5 μ M FeWD, whereas FeWD concentrations higher than 50 μ M (48- and 72-hour treatment) reduced the starting cell viability almost completely.

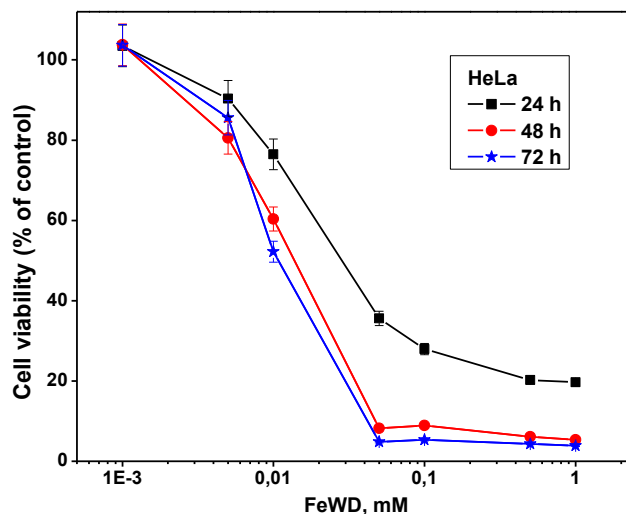


Figure 2. The influence of FeWD on the viability of cervical carcinoma HeLa cells after 24 (square), 48 (circle), and 72 (asterisk) hours exposure towards different FeWD concentrations. Cell viability is expressed as % of (untreated) control (100%). Results are expressed as mean \pm S.E.M. from at least 2 independent experiments done in triplicates.

The cytotoxic potencies of FeWD as a function of time exposure towards HeLa cells were assessed using IC_{50} values that were determined from sigmoidal fitting the experimental plots. Calculated IC_{50} (μ M) were: 16.64 ± 0.49 , 10.75 ± 0.97 , and 9.64 ± 0.19 for 24-, 48-, and 72-hour treatment, respectively.

Compared to the structurally similar lacunary WD, which does not contain Fe, FeWD exhibited a stronger antitumor potential against HeLa cells *in vitro*. Indeed, the most expressed difference between IC_{50} values (μ M) was obtained for 24-hour treatment – 16.64 (FeWD) *vs.* 24,11 (lacunary WD), whereas after 48 and 72 hours of exposure IC_{50} for lacunary WD were about 18% higher than the corresponding values for FeWD.

The FeWD-induced lower IC_{50} values suggest that incorporating Fe into lacunary WD structure results in improving its cytotoxic properties against tumor HeLa cells.

4. Conclusions

The *in vitro* evaluation of the cytotoxic action of Fe(III)-containing lacunary WD polyoxotungstate showed significant antitumor activity at low micromolar concentrations against cervical carcinoma HeLa cells. Moreover, the investigated metal – substituted polyoxometalate exhibited a more potent cytotoxic activity against the tumor cell line in comparison with its structural analog, lacunary WD. This implies that incorporating Fe(III) might be a new strategy for improving the antitumor efficacy of polyoxometalates as promising next-generation metallotherapeutics.

Acknowledgment

This research is funded by the Ministry of Education and Ministry of Science, Technological Development and Innovation, Republic of Serbia, Grants: No. 451-03-9/2023-14/200017 and 451-03-9/2023-14/200110. The authors also thank the Science Fund of the Republic of Serbia (POMCACT Project No. 6526393).

References

- [1] M.B. Čolović, M. Lacković, J. Lalatović, A.S. Mougharbel, U. Kortz, D.Z. Krstić, *Polyoxometalates in biomedicine: update and overview*, *Current Medicinal Chemistry*, 27 (2020) 362-379.
- [2] A.M. Isakovic, M.B. Čolović, T. Ma, X. Ma, M. Jeremic, M. Gerić, G. Gajski, S. Misirlic-Dencic, U. Kortz, D. Krstić, *Selected polyoxopalladates as promising and selective antitumor drug candidates*, *Journal of Biological Inorganic Chemistry*, 26 (2021) 957–971.
- [3] D.K. Lyon, W.K. Miller, T. Novet, P.J. Domaille, E. Evitt, D.C. Johnson, R.G. Finke, *Highly oxidation resistant inorganic-porphyrin analog polyoxometalate oxidation catalysts. 1. The synthesis and characterization of aqueous-soluble potassium salts of $\alpha_2\text{-P}_2\text{W}_{17}\text{O}_{61}(\text{Mn}^+\text{OH}_2)(n-10)$ and organic solvent soluble tetra-*n*-butylammonium salts $A_2\text{-P}_2\text{W}_{17}\text{O}_{61}(\text{Mn}^+\text{Br})(n-1)$ ($M=\text{Mn}^{3+}$, Fe^{3+} , Co^{2+} , Ni^{2+} , Cu^{2+}).* *Journal of the American Chemical Society*, 113 (1991) 7209–7221.
- [4] P. Skehan, R. Storeng, D. Scudiero, A. Monks, J. McMahon, D. Vistica, J.T. Warren, H. Bokesch, S. Kenney, M.R. Boyd, *New colorimetric cytotoxicity assay for anticancer-drug screening*, *Journal of the National Cancer Institute*, 82 (1990) 1107-1112.

DFT approach of the redox properties of brimonidine and varenicline

Marija R. Popović-Nikolić^{1*}, Katarina Nikolić¹, Mara Aleksić²

¹ University of Belgrade, Faculty of Pharmacy, Department of Pharmaceutical Chemistry, Vojvode Stepe 450, 11221 Serbia; e-mail: majap@pharmacy.bg.ac.rs, katarina.nikolic@pharmacy.bg.ac.rs

² University of Belgrade, Faculty of Pharmacy, Department of Physical Chemistry and Instrumental Methods, Vojvode Stepe 450, 11221 Serbia; e-mail: mara.aleksic@pharmacy.bg.ac.rs

* Corresponding author

DOI: 10.46793/ICCB123.423PN

Abstract: The redox properties of two quinoxaline derivatives, brimonidine and varenicline, previously studied electrochemically, were evaluated by performing a computational study. On the basis of some useful quantum chemical parameters the differences and similarities between their redox features were explained. The obtained results support the experimental findings that the redox processes of both compounds are under strong influence of the solution pH, whereas the reduction of brimonidine occurs easier than the reduction of varenicline, at corresponding pH values.

Keywords: brimonidine, varenicline, redox process, molecular orbital energy, quantum chemical parameters

1. Introduction

The redox properties of brimonidine and varenicline, quinoxaline derivatives with different pharmacological effects (antiglaucoma and smoking cessation agent, respectively), were previously examined electrochemically [1-3]. Electrochemical studies showed similarities and differences due to the different molecular structures. The redox processes were shown to be under the strong influence of the solution pH and the substituents/condensed ring on the quinoxaline core, contented in both drugs (**Figure 1**). The reduction process, presented as a two-electron process involving two H⁺, occurred at the quinoxaline moiety (reduction of the C=N bond of the pyrazine ring within the quinoxaline core), in a wide pH range (2.0 – 12.0), since the additional two-electron reduction step involving two 2 protons was strongly influenced by the pH of solution and was observed only in acidic media [1-3]. With the aim of confirming and explaining the comparison of the electrochemically studied redox mechanisms of two quinoxaline derivatives, a computational study was performed.

2. Computation calculation

The geometric structures (**Figure 1**) of brimonidine and varenicline, their corresponding forms which are formed by reduction or oxidation, both in molecular and ionized forms, were optimized at the B3LYP/6-31G (d,p) level of DFT in the gas phase using the Gaussian 03 program [4]. The *Polarizable Continuum Model* (PCM) [5], was applied with B3LYP/6-31G (d,p)^{water} basis set to compute the energies of the *Highest Occupied Molecular Orbital Energy* (E_{HOMO}) and the *Lowest Unoccupied Molecular Orbital Energy* (E_{LUMO}), which were used to calculate quantum chemical based reactivity molecular descriptors: chemical potential (μ), electronegativity (χ), hardness (η), global softness (S), and electrophilicity index (ω) [6]. This methodology has already been successfully implemented in investigations of the electrochemical behavior of compounds [3, 7].

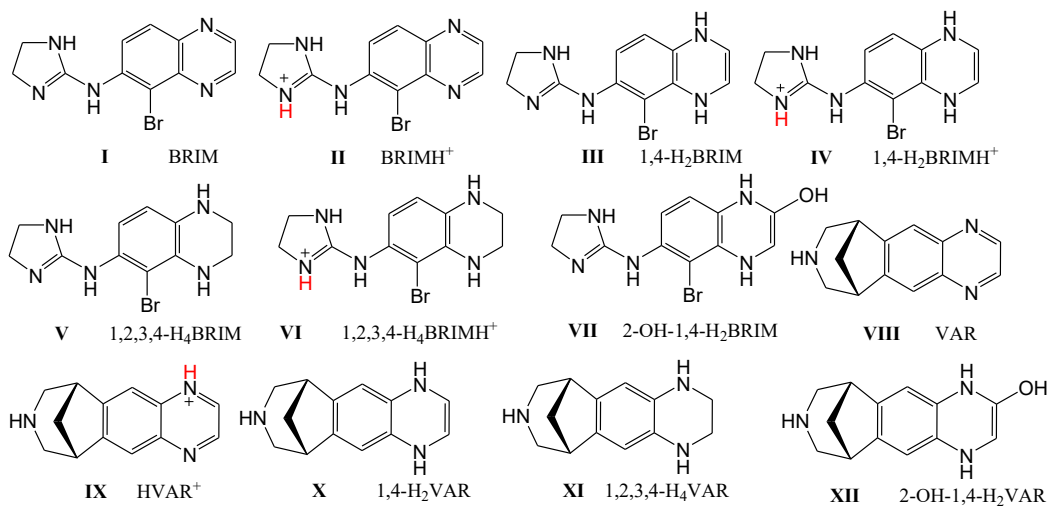


Figure 1. Chemical structures of investigated compounds.

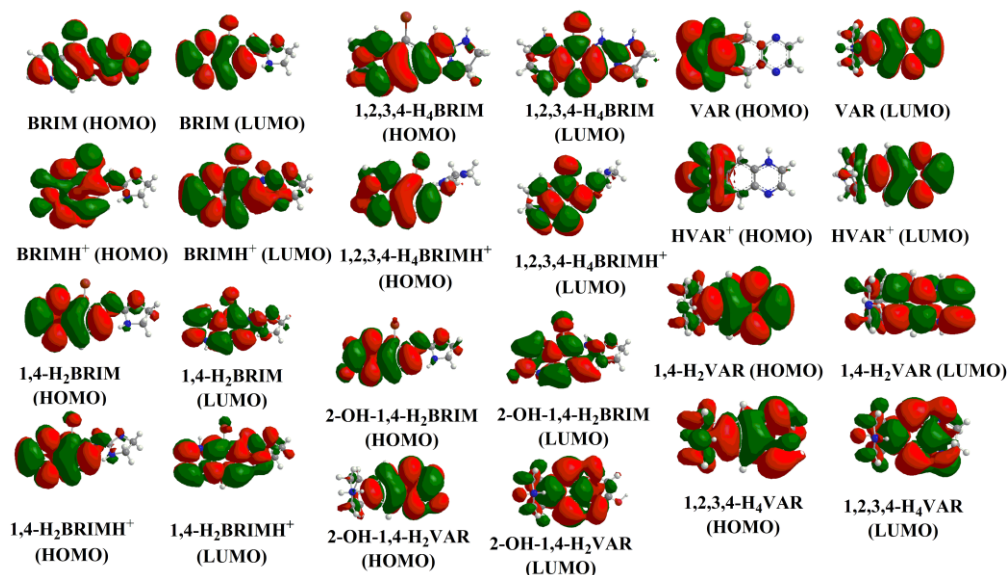
3. Results and discussion

To consider the similarities and differences in redox behavior in pH dependent manner, in addition to the molecular forms present in the neutral/basic conditions (I, III, V, VII, VIII, X, XI, XII), the protonated forms of brimonidine (II, IV, VI) present in the acidic experimental conditions ($\text{pH} \leq 3$), as well as the protonated form of varenicline (IX), were examined. The results of the DFT study are shown in **Table 1**. The E_{HOMO} and E_{LUMO} molecular orbitals, calculated using the PCM approach, are shown in **Figure 2**. Both frontier orbitals are dominantly distributed at the quinoxaline moiety in brimonidine and varenicline, indicating that the electron transfer reactions will occur at the quinoxaline core. A higher E_{HOMO} value indicates the ability of a molecule to donate electrons to the acceptor and thus to be more easily oxidized. A lower E_{LUMO} value reflects the ability of a molecule to accept the electrons and a greater tendency to be reduced [3, 7]. The E_{LUMO} value (**Table 1**) of the protonated brimonidine form IV (-0.720), formed in the first reduction step, is more than twice lower than the value of the corresponding nonprotonated form III (-0.310), as well as the E_{LUMO} value of II (-5.26), in a relation to corresponding nonprotonated form I (-2.09)

Table 1. Quantum mechanical parameters of investigated compounds calculated at B3LYP/6-31G (d,p)PCM level.

	I	II	III	IV	V	VI	VII	VIII	IX	X	XI	XII
E_{LUMO}	-2.09	-5.26	-0.31	-0.72	3.01	-0.26	-0.32	-1.94	-3.33	0.03	0.12	0.29
E_{HOMO}	-5.72	-9.76	-4.27	-4.31	-2.33	-5.15	-4.34	-5.86	-5.84	-4.11	-4.93	-3.32
ΔE gap	3.63	4.50	3.96	3.59	5.33	4.90	4.02	3.93	2.51	4.14	5.05	3.61
μ	-3.91	-7.51	-2.29	-2.52	0.34	-2.71	-2.33	-3.90	-4.59	-2.04	-2.40	-1.52
χ	3.91	7.51	2.29	2.52	-0.34	2.71	2.33	3.90	4.59	2.04	2.40	1.52
η	1.82	2.25	1.98	1.80	2.67	2.45	2.01	1.96	1.26	2.07	2.52	1.81
S	0.28	0.22	0.25	0.28	0.19	0.20	0.25	0.25	0.40	0.24	0.20	0.28
ω	4.20	12.53	1.32	1.76	0.02	1.50	1.35	3.87	8.37	1.01	1.14	0.64

In the case of varenicline, the E_{LUMO} value of IX (-3.330), is lower compared with nonprotonated VIII (-1.936). In both cases, the lower E_{LUMO} values of the protonated forms indicate that the reduction process of brimonidine and varenicline is easier under acidic conditions. The E_{HOMO} values of completely reduced forms of brimonidine which could be formed in the second, V (-2.325) and VI (-5.154), indicate a higher tendency of the nonprotonated form V to the reverse oxidation process, suggesting that the redox equilibria would be more shifted toward the reduction process in the case of the protonated form VI, which is present in solution at the pH of the experiments (pH \leq 3) [1-3]. These results support the experimental findings that the reduction process is affected by pH of the solution since the second reduction step is experimentally detected only in acidic conditions [1-3].

**Figure 2.** B3LYP/6-31G (d,p) calculated HOMO and LUMO orbitals for investigated compounds.

The highest values (Table 1) for the electrophilicity index (ω) [6] were observed for the protonated forms II (12.533) and IX (8.337), indicating that the reduction process

occurs more easily in acidic conditions. The differences in ω values between brimonidine and varenicline confirm the experimental findings that the reduction of brimonidine occurs easier than the reduction of varenicline, at corresponding pH values [2]. For IX the highest value for softness (S) (0.389) and the lowest value for chemical hardness (η) (1.255) are observed suggesting that IX has the most pronounced tendency for polarization of electron density and change of electronic configuration [6], which could explain the difference in the redox behavior between varenicline and brimonidine.

3. Conclusions

The obtained computational results supported and strengthened experimental findings that the redox processes of brimonidine and varenicline are strongly pH dependent, with the reduction of brimonidine being easier than that of varenicline, at corresponding pH values.

Acknowledgment

This research was funded by the Ministry of Science, Technological Development and Innovation, Republic of Serbia through Grant Agreement with University of Belgrade-Faculty of Pharmacy No: 451-03-47/2023-01/ 200161. The authors thank the COST Actions CA18240 and CA18133 of the European Community for support.

References

- [1] M.M. Aleksic, V. Radulovic, N. Lijeskić, V. Kapetanovic., *Electrochemical response and determination of varenicline at boron doped diamond, glassy carbon and hanging mercury electrodes*, *Curr. Anal. Chem*, 8 (2012) 133-142.
- [2] M.M. Aleksic, V. Radulovic, D. Agbaba, V. Kapetanovic., *An extensive study of electrochemical behavior of brimonidine and its determination at glassy carbon electrode*, *Electrochim. Acta*, 106 (2013) 75– 81.
- [3] J. Rupa, M.M. Aleksic, K. Nikolic, M.R. Popovic-Nikolic., *Comparative electrochemical studies of kinetic and thermodynamic parameters of Quinoxaline and Brimonidine redox process*, *Electrochim. Acta*, 271 (2018) 220-231.
- [4] Gaussian 03 (Revision C.02.), Gaussian, Inc, Wallingford, 2004.
- [5] M. Cossi, G. Scalmani, N. Rega, V. Barone., *New developments in the polarizable continuum model for quantum mechanical and classical calculations on molecules in solution*, *J. Chem. Phys*, 117 (2002) 43.
- [6] R.G. Parr, W. Yang., *Density-functional Theory of Atoms and Molecules*, Oxford University Press, New York, 1989.
- [7] A.H. Shah, W. Zaid, A. Shah, U.A. Rana, H. Hussain, M.N. Ashiq, R. ah, M.A. Zia, H.-B. Kraatz., *pH Dependent electrochemical characterization, computational studies and evaluation of thermodynamic, kinetic and analytical parameters of two phenazines*, *J. Electrochem. Soc*, 162 (2015) H115

Theoretical and experimental study of bilastine ionization

Marija R. Popović-Nikolić^{1*}, Gordana Popović², Slavica Oljačić¹, Katarina Nikolić¹

¹ University of Belgrade, Faculty of Pharmacy, Department of Pharmaceutical Chemistry, Vojvode Stepe 450, 11221 Serbia; e-mail: majap@pharmacy.bg.ac.rs, slavica.oljadic@pharmacy.bg.ac.rs, katarina.nikolic@pharmacy.bg.ac.rs

² University of Belgrade, Faculty of Pharmacy, Department of General and Inorganic Chemistry, Vojvode Stepe 450, 11221 Serbia; e-mail: gpopovic@pharmacy.bg.ac.rs

* Corresponding author

DOI: 10.46793/ICCB23.427PN

Abstract: The protolytic equilibria of bilastine were studied experimentally and theoretically. The pK_a values were determined potentiometrically at a constant ionic strength (0.1 M NaCl) and temperature 25 °C. Energy calculation of the optimized structures of the equilibrium forms was performed at the B3LYP/6-31G (d,p) level of the Density Functional Theory (DFT). The results of the theoretical study helped to define the ionization profile of bilastine and to assign the experimentally determined pK_a values to the corresponding ionizable groups.

Keywords: bilastine, protolytic equilibria, molecular orbital energy, quantum chemical parameters

1. Introduction

Bilastine is a second-generation oral H_1 antihistamine approved for use in symptomatic treatment of allergic rhinoconjunctivitis and urticaria with the advantage of its favourable tolerability profile and the long duration of action [1]. For the assessment of the optimal dose in the pediatric population, it is required to specifically characterize the safety and tolerability [2, 3]. To give better insight into pharmacokinetics and safety of bilastine it is important to consider its physico-chemical properties such as the ionization constant [4]. Chemical structure of bilastine (**Figure 1**) contains three ionizable centers, one acidic (carboxylic group) and two basic centers (nitrogens in benzimidazol and piperidinyl groups). To additionally clarify results obtained in experimental investigations of bilastine protolytic equilibria, the theoretical study has been performed.

2. Experimental and computational methods

The pK_a values of bilastine were determined potentiometrically using a titration system 798 MPT Titrino with a combined electrode (LL unitrode Pt1000; Metrohm). Bilastine, 2-[4-(2-{4-[1-(2-Ethoxyethyl)-1H-benzimidazol-2-yl]-1-piperidinyl}ethyl)phenyl]-2-methylpropanoic acid, was kindly donated from ALIMIS. All titrations were carried out at 25°C with continuous magnetic stirring. Constant ionic strength was adjusted to 0.1 M with NaCl. The apparent ionization constants (pK_a^*) were obtained in the different methanol-water mixtures (20% - 40 % wt/wt). 40 mL solutions of bilastine (5×10^{-4} M) in the methanol-water mixtures, were titrated with the 0.02 mL aliquots of standard NaOH solution (0.1017 M). On the basis of the data obtained by potentiometric titrations, the pK_a^* values were calculated using a computer program Hyperquad, which enables determination of equilibrium constants in complex systems containing the overlapped acid-base equilibria.

The chemical structures of 4 equilibrium forms of bilastine that can exist in solution (**Figure 1**) were optimized at the B3LYP/6-31G (d,p) level of DFT in the gas phase using the Gaussian 03 program. The *Polarizable Continuum Model* (PCM) [5], was applied with B3LYP/6-31G (d,p)^{water} basis set to compute the energies of the *Highest Occupied Molecular Orbital Energy* (E_{HOMO}) and the *Lowest Unoccupied Molecular Orbital Energy* (E_{LUMO}), which were used to calculate quantum chemical based reactivity molecular descriptors: chemical potential (μ), electronegativity (χ), hardness (η), global softness (S), and electrophilicity index (ω) [6].

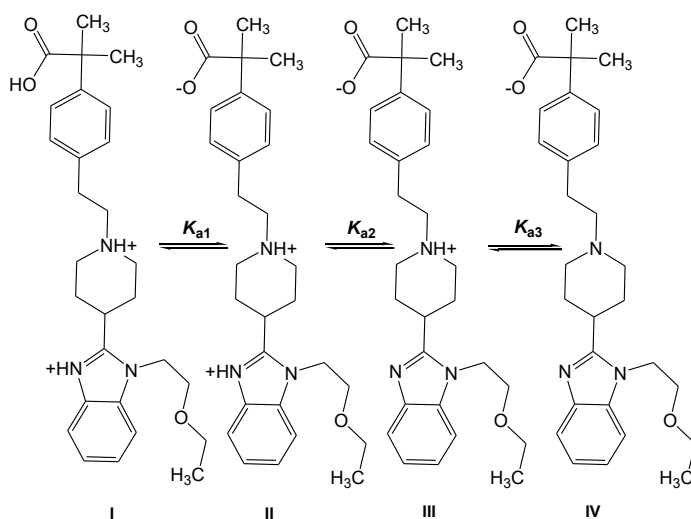


Figure 1. Equilibrium forms of bilastine: (I) dicationic, (II) cationic-zwitterionic, (III) zwitterionic, (IV) anionic.

3. Results and discussion

Due to poor water solubility of bilastine, its aqueous pK_a values ($pK_{a1}=5.72$ for carboxyl group; $pK_{a2}=7.86$ for benzimidazol nitrogen; $pK_{a3}=9.68$ for piperidin nitrogen) were obtained indirectly from the pK_a^* values potentiometrically determined in different methanol/water mixtures (20%-40% methanol, wt/wt) by extrapolation of the pK_a^*

values to 0% of methanol. To additionally clarify the order of bilastine ionization and estimate the properties of its equilibrium forms, the theoretical study was performed, and results are shown in **Table 1**. Among the calculated parameters, the electronegativity (χ) expressed the greatest importance in predicting the order of ionization [7]. It is defined as the ability of the atom in a molecule to attract electrons [7,8]. The higher values of this parameter correspond to the molecules that can be described as stronger Lewis acids, as they have a higher affinity for deprotonation [7]. Calculated χ values of bilastine equilibrium forms (**Table 1**) decrease in the order in which is assumed the ionization takes place (I > II > III > IV).

Table 1. Quantum mechanical parameters of bilastine equilibrium forms calculated at B3LYP/6-31G (d,p)PCM level.

Descriptor (eV)	I	II	III	IV
HOMO	-6.043	-3.528	-5.493	-0.693
LUMO	-1.404	-2.462	-0.488	1.199
ΔE gap	-4.639	-1.066	-5.005	-1.892
μ (chemical potential)	-3.724	-2.995	-2.990	0.253
χ (electronegativity)	3.724	2.995	2.990	-0.253
η (chemical hardness)	-2.319	-0.533	-2.502	-0.946
S (softness)	-0.216	-0.938	-0.200	-0.529
ω (electrophilicity index)	-2.989	-8.415	-1.787	-0.034

To consider the properties of the equilibrium forms in water [7] as a high dielectric solvent ($\epsilon=78.3$) the PCM approach was applied and calculated E_{HOMO} and E_{LUMO} molecular orbitals are shown in **Figure 2**.

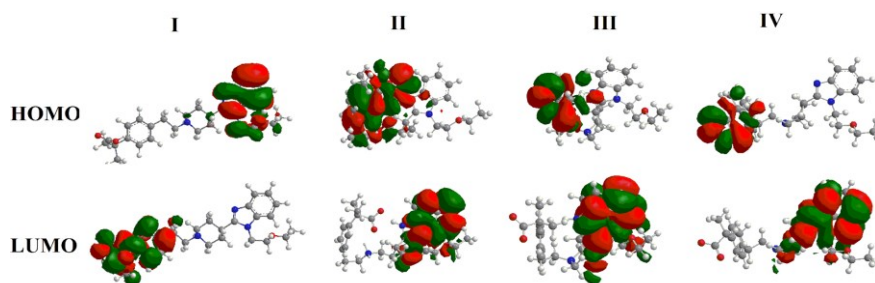


Figure 2. B3LYP/6-31G (d,p) calculated HOMO and LUMO orbitals for investigated compounds.

The lower values of the E_{LUMO} energy indicate high affinity of the compounds to accept electrons, while the high E_{HOMO} energy values indicate high affinity of the compounds to donate electrons, and vice versa [7]. Obtained distribution of the E_{HOMO} energy can confirm assumed order of ionization. In each equilibrium form the E_{HOMO} energy is localized mostly on the part of the molecule which includes carboxyl group as an acidic center (**Figure 2**). In form II, the E_{HOMO} energy is also distributed on benzimidazol nitrogen.

3. Conclusions

The ionization constants of bilastine were determined experimentally and assumed profile of the ionization were investigated in computational study. Localization of molecular orbital energy and the values of quantum mechanical parameters calculated at B3LYP/6-31G (d,p)PCM level were used to estimate the order of ionization and the properties of equilibrium forms of bilastine.

Acknowledgment

This research was funded by the Ministry of Science, Technological Development and Innovation, Republic of Serbia through Grant Agreement with University of Belgrade-Faculty of Pharmacy No: 451-03-47/2023-01/200161. The authors thank the COST Actions CA18240 and CA18133 of the European Community for support.

References

- [1] A. Singh Randhawa, N. Mohd Noor, M. K. Md Daud, B. Abdullah., *Efficacy and safety of bilastine in the treatment of allergic rhinitis: a systematic review and meta-analysis*, *Front. Pharmacol*, 12 (2022) 731201.
- [2] N.G.Papadopoulos, T. Zuberbier., *The safety and tolerability profile of bilastine for chronic urticaria in children*, *Clin. Transl. Allergy*, 9 (2019) 1-7.
- [3] Z. Novák, A. Yáñez, I. Kiss, P. Kuna, M. Tortajada-Girbés, R. Valiente., *Safety and tolerability of bilastine 10 mg administered for 12 weeks in children with allergic diseases*, *Pediatr. Allergy Immunol*, 27 (2016) 493-498.
- [4] D. T. Manallack, R. J. Prankerd, E. Yuriev, T I. Oprea, D.K. Chalmers., *The significance of acid/base properties in drug discovery*. *Chem. Soc. Rev*, 42 (2013) 485-496.
- [5] M. Cossi, G. Scalmani, N. Rega, V. Barone., *New developments in the polarizable continuum model for quantum mechanical and classical calculations on molecules in solution*, *J. Chem. Phys*, 117 (2002) 43.
- [6] R.G. Parr, W. Yang., *Density-functional Theory of Atoms and Molecules*, Oxford University Press, New York, 1989.
- [7] M.R. Popović-Nikolić, G.V. Popović, M. Grujić, K.M. Nikolić, D.D. Agbaba., *A theoretical study on ionization of sartans in aqueous media and on interactions with surfactant micelles*. *J. Mol. Graph. Model*, 82 2018 67-73.
- [8] S. Filipic, K. Nikolic, I. Vovk, M. Krizman, D. Agbaba., *Quantitative structure-mobility relationship analysis of imidazoline receptor ligands in CDs-mediated CE*, *Electrophoresis*, 34 (2013) 471e482.

New vanadium complexes with potential biological activity

Miroslava Matiková Maľarová^{1*}, Alexandra Bilá¹, Mária Vilková², Erika Samolová³,
Zuzana Jendželovská⁴, Viktória Buľková⁴

¹P. J. Šafarik University in Košice, Faculty of Science, Institute of Chemistry, Moyzesova 11, 04154 Košice, Slovakia; e-mail: miroslava.matikova.malárova@upjs.sk, alexandra.bila@student.upjs.sk

²P. J. Šafarik University in Košice, Faculty of Science, NMR Laboratory, Moyzesova 11, 04154 Košice, Slovakia; e-mail: maria.vilkova@upjs.sk

³Czech Academy of Science, Institute of Physics, Na Slovance 2, 182 21 Prague 8, Czech Republic; e-mail: samolova.erika@gmail.com

⁴P. J. Šafarik University in Košice, Institute of Biology and Ecology, Šrobálová 2, 04154 Košice, Slovakia; e-mail: zuzana.jendzelovska@upjs.sk, viktoria.bulkova@student.upjs.sk

* *corresponding author*

DOI: 10.46793/ICCB23.431MM

Abstract: Two slightly different manner of syntheses lead to the formation of four molecular complexes with two type of coordination arrangement; brown complexes VO(iPrO)(dBrQ)₂ (**1**), VO(iPrO)(5I7BrQ)₂ (**2**) and dark green VO(Cl)(dBrQ)₂ (**3**), VO(iPrO)(5I7BrQ)₂ (**4**). The presence of water and isopropanol in synthesis plays a crucial role in the formation of these two types of complexes. Otherwise also some dinuclear oxo-bridged complexes with four quinoline-8-ol derivatives coordinated to vanadium (V) were obtained in this reactions scheme. The mononuclear complexes were characterized by elemental analysis, infrared spectroscopy and X-ray structure analyses. The stability was tested by UV-VIS and NMR spectroscopy and showed some differences in accordance of solvent and also structure of complexes. The first results of biological activity will be reported, too.

Keywords: vanadium complexes, biological activity, crystal structure

1. Introduction

An extended interest in vanadium coordination chemistry is attributed to the importance of these compounds due to biochemical, pharmacological, and catalytic activity. The most studied and active vanadium compounds are associated with such cores as [VO]²⁺, [VO]³⁺, [VO₂]⁺, [V₂O₃]ⁿ⁺ (n = 2–4), and [V₂O₄]²⁺. All these moieties exhibit especially strong affinity toward N, O-donor ligands. The electronic properties of the metal central in the resulting complexes can be tuned by the use of organic ligands of different basicity.

Quinoline-8-ol (HQ = C₉H₇NO) and its derivatives have been widely used as analytical reagents; however, research on vanadium complexes with 8-HQ ligands or its derivatives is almost all on vanadium in oxidation state V. Takano and co-workers prepared series of mononuclear and dinuclear complexes in oxidation state IV where oxygen atom from quinoline made a bridge between vanadium atoms [1]. In the synthesis of these complexes the amount of water or HCl solution play also an important role.

Some vanadium complexes with quinoline-8-ol derivatives were studied as a catalyst in alkaline oxidation with hydrogen peroxide with very promising results [2].

A series of six-coordinate vanadium(V) complexes with chelate bonded 8-hydroxyquinolate ligands (-N,-O) were studied, in order to determine the impact of substituents introduced into 8-hydroxyquinoline core on the antiproliferative efficiency towards HCT116 and A2780 cancer cell lines. These compounds showed lower cytotoxicity for normal human primary fibroblast compared to the widely used chemotherapeutic *cisplatin* [3].

2. Syntheses and characterisation

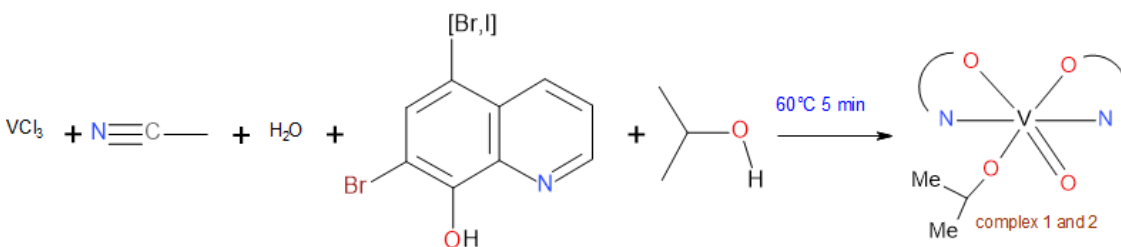
Elemental (C, H, N) analyses were done on a CHNS Elemental Analyzer vario MICRO instrument (Elementar Analyser system GmbH).

Infrared spectra were recorded on Shimadzu FTIR Tracer 100 using ATR technique with DLATGS detector on diamond plate in the range 4000–400 cm⁻¹.

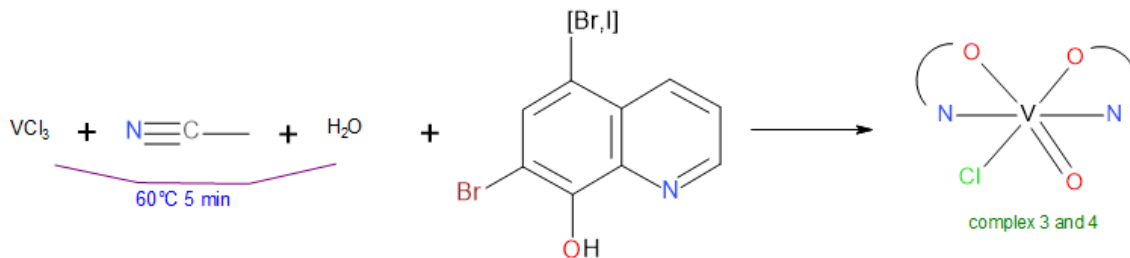
Electronic spectra of the solid samples were taken using a Nujol technique (270–900 nm) and solution spectra in methanol or isopropanol, DMSO and mixture DMSO/H₂O were recorded on a Specord 250 Spectrometer (300–600 nm).

2.1 Syntheses

The reaction of vanadium chloride (0.125 mmol) with chinoline-8-ol derivatives (0.250 mmol) (Scheme 1 and 2) in different conditions and solutions leads to the formation of four new complexes: dark brown VO(iPrO)(dBrQ)₂ (**1**), VO(iPrO)(5I7BrQ)₂ (**2**) and dark green VO(Cl)(dBrQ)₂ (**3**), VO(Cl)(5I7BrQ)₂ (**4**). All prepared complexes were washed with a small amount of ether and dried on air. All used reagents were in analytical grade.



Scheme 1



Scheme 2

2.2 Crystal structure

The X-ray diffraction data for complexes **1-4** were collected using four-circle diffractometer SuperNova Dual with Atlas CCD using graphite monochromated CuK α radiation ($\lambda = 1.5418 \text{ \AA}$) at 100 K. Perspective view of the molecular structure of **1** and **2** together with the atom numbering is depicted in Figure 1. Both compounds are neutral molecular complexes with vanadium atom in oxidation state V. Vanadium (V) is hexacoordinated by two chelate molecules of 8-HQ derivatives 5,7-dibromoquinoline-8-ol (*dBrQ*) for **1** and 5-iodo, 7-bromoquinoline-8-ol (*5I7BrQ*) for **2**. The octahedral environment is completed with O-donor isopropoxy ligand and oxido ligand in *cis* position to alkoxy ligand.

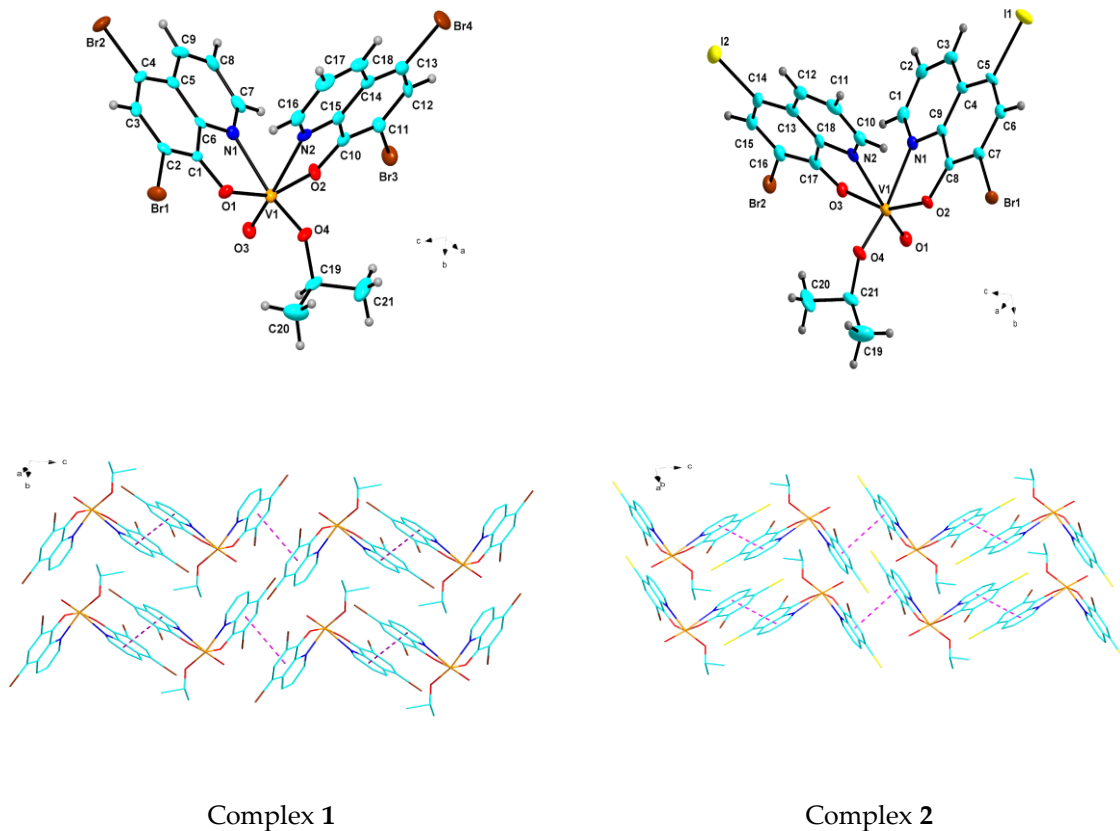


Figure 1. Crystal structure and the system of π - π interactions in *c* direction for complex **1** and **2**.

Vanadium atom (V) in the complexes **3** and **4** is octahedrally coordinated by two chelate (-N, -O) *dBrQ* and *5I7BrQ* ligands respectively. The hexacoordination is completed by one oxido and one chlorido ligand which are disordered together with vanadium atom (Figure 2). The significant deformation of the octahedral geometry of the vanadium(V) ion in all complexes is induced by the multiple bonding terminal oxo ligand and formation of five-member chelate rings due to the coordination of quinoline-8-ol derivatives. This fact is reflected in the values of the angles O–V–O and O–V–N or O–V–Cl which are significantly different from 90°.

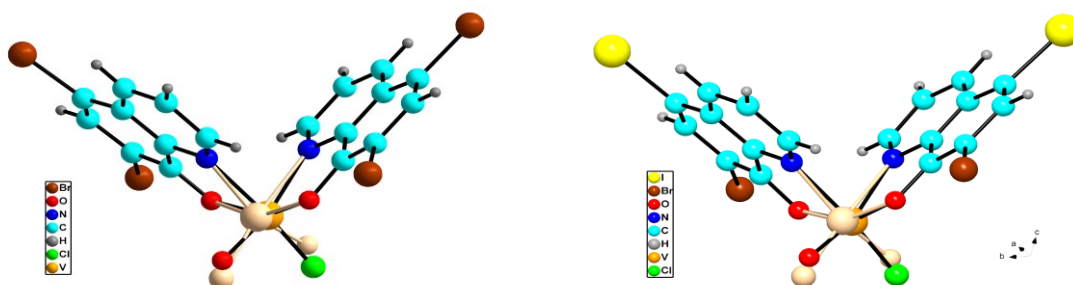


Figure 2. The disordered molecular structure of complexes **3** and **4**.

3. Conclusions

A series of six-coordinate vanadium(V) complexes with 8-hydroxyquinolate ligands (-N, -O) were prepared in order to determine the impact of solvent on the creation of octahedral arrangement. The stability of all complexes in different solvents were tested mainly by UV-Vis spectroscopy and the influence of the solvent on the stability and composition of the complexes in solution was demonstrated.

Acknowledgment

This research is funded by the Slovak Grant Agencies, Grants: No. VEGA 1/0126/23.

References

- [1] K. Takano, Y. Sunatsuki, M. Kojima, I. Kinoshita, T. Shobahara., *Synthesis and characterization of 8-quinolinolato vanadium(IV) complexes*, *Inorganica Chimica Acta*, 362 (2009) 3201-3207.
- [2] I. Gryca, K. Czewinska, B. Machura, A. Chrobok, L.S. Shulpina, M.L.Kuznetsov, D.S. Nesterov, Y.N. Kozlov, A.J.L.Pombeiro, I.A.Varyan, G.B.Shulpin., *Inorganic Chemistry*, 57 (2018) 1824-1831.
- [3] K.Choroba, L.R.Rapaso, J. Palion-Gazda, E.Malicka, K.Erfurt, B.Machura, A.R.Fernandez., *In vitro antiproliferative effect of Vanadium complexes bearing 8-hydroxyquinoline-based ligands*, *Dalton Transaction*, 49 (2020) 6596-6607.

Synthesis of Schiff bases between some five-membered heterocyclic aldehydes and thiocarbohydrazide (TCH) and optimization of reaction conditions

Miljan Bigović^{1*}, Marija Kaluđerović², Jovana Jovanović³, Haris Majstorović⁴,
Milica Kosovic-Perutović⁵

¹ University of Montenegro, Faculty of Natural Sciences and Mathematics, G. Washington Street bb, Podgorica, Montenegro; e-mail: miljan@ucg.ac.me

² University of Montenegro, Faculty of Natural Sciences and Mathematics, G. Washington Street bb, Podgorica, Montenegro; e-mail: marijakaludjerovic.9@gmail.com

³ University of Montenegro, Faculty of Medicine, Krusevac bb, 81 000 Podgorica, Montenegro; e-mail: jokicajoka1212@gmail.com

⁴ University of Montenegro, Faculty of Medicine, Krusevac bb, 81 000 Podgorica, Montenegro; e-mail: harisnedakusi@gmail.com

⁵ Faculty for Technology and Metallurgy, University of Montenegro, G. Washington street bb, Podgorica, Montenegro; e-mail: mkosovic@ucg.ac.me

DOI: 10.46793/ICCB23.435B

Abstract: The usual way of synthesizing imines (Schiff bases) between carbonyl compounds – aldehydes and ketones - with thiocarbohydrazide (TCH) involves heating them for 3 hours in a mixture of water solvents and ethanol with the addition of a catalytic amount of concentrated hydrochloric acid. Heating in the presence of acid catalysts over a long period of time may be unsuitable for acid-sensitive, labile, reactive or thermally unstable aldehydes, which are prone to polymerization under these conditions. We tested the condensation reaction at room temperature with a series of aldehydes, while maintaining the described ratios (equimolar ratio of aldehydes and TCH), with the addition of a few drops of 36% HCl. The course and completion of the reaction were monitored using infrared spectroscopy (FTIR). The reaction time is longer compared to the heating conditions, while the yields are comparable. We obtained a series of compounds of high degree of purity, satisfactory yield varying from 50-90%, whose structure and purity were confirmed by NMR spectroscopy.

Keywords: Schiff bases, aldehydes, NMR, carbohydrazides, FTIR

1. Introduction

Schiff bases (imines) have been known since the middle of the 19th century when they were first synthesized by Hugo Schiff. Because of the wide spectrum biological activities as well as synthetic simplicity represent attractive synthetic targets and occupy a lot of attention of scientists [1,2]. They show antitumor, antioxidant and antimicrobial

properties activity, and therefore have a serious potential application in biomedical [3]. Due to their physicochemical characteristics, they are used in analytics as well as in materials science. The aim of this work was to synthesize new Schiff bases of heterocyclic aldehydes and aromatic ketones in high yield and high degree of purity. Depending on the structure, i.e., from the starting carbonyl compound, can be considered secondary aldimines or secondary ketimines [3]. By exposing aldehydes and ketones to primary amines, hemiaminals, nitrogen analogues, are formed hemiacetal (half acetal). Hemiamines of primary amines readily lose water and form carbon-nitrogen double bond (C=N). In this way, an imine (azomethine) functional group is formed, which represents the nitrogen analogue of the carbonyl group [4]. The formation of imines is a typical example of a condensation process, in which the joining of two molecules (in this case of primary amine and carbonyl compound) separates one smaller molecule (water in this reaction). The mechanism of imine synthesis from a carbonyl compound and an amine is presented in Figure 1.

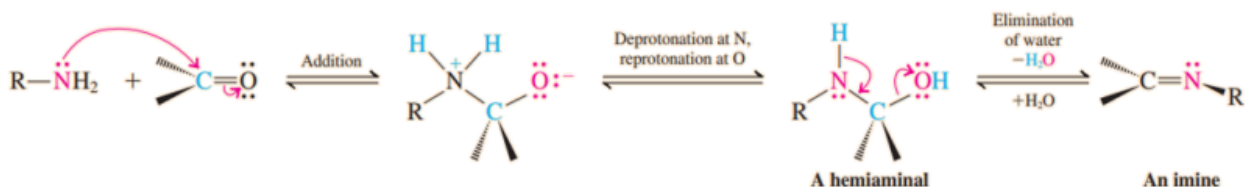


Figure 1. Imine formation from carbonyl compound and amine

Imine formation is fastest at pH 4-6 at lower pH values, the amine is protonated and the first step of the reaction is slower, and at pH values higher than this range, protonation of the OH group is difficult [4].

2. Instructions

In the synthesis reactions of Schiff bases covered in this paper, thiocarbohydrazide (TCH) was used as a reagent, which exhibits pronounced nucleophilic properties and contributes to the diversity of chemical reaction products, since monosubstituted and disubstituted Schiff bases can be formed. Thiocarbohydrazide can be synthetically obtained from hydrazine and carbon disulfide in a basic medium (Figure 2) [5, 6]:

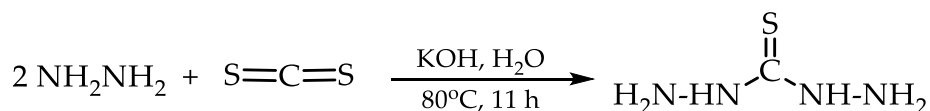


Figure 2. Reaction of synthesis of TCH from hydrazine and carbon-disulfide.

The synthesis of Schiff bases is based on the nucleophilic addition of primary amines to the starting carbonyl compound, where in this work the starting carbonyl compound is a heterocyclic aldehyde, and the carrier of the primary amino group is thiocarbohydrazide (TCH). The reaction takes place at 80°C, with concentrated HCl as a catalyst and in a mixture of ethanol and water as a solvent [7]. Figure 3 shows the synthesis of both types

of Schiff bases: symmetrical (II, figure 3) and asymmetrical (I, figure 3), starting from starting from aromatic five-membered aldehydes with sulfur and oxygen, where the aldehyde group is located at position 2.

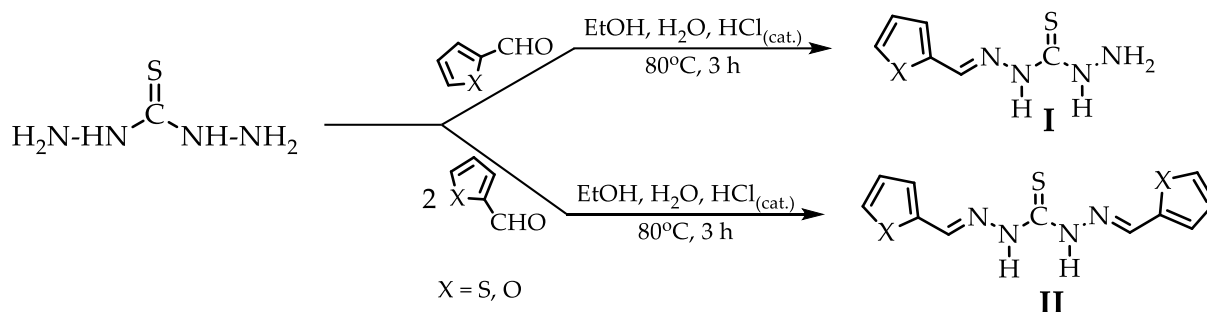


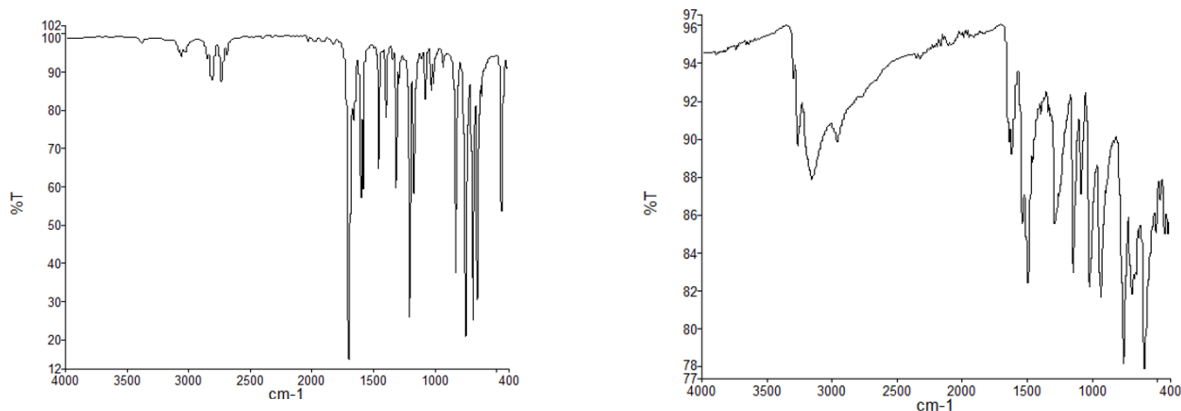
Figure 3. Synthesis of Schiff bases from heterocyclic aldehydes and TCH.

In the first group of reactions, syntheses were carried out according to the usual procedure, with heating of the reaction mixtures, while the second group of reactions was carried out at room temperature. As shown in Table 1, the yields are comparable, but the reactions at room temperature are observed to be complete only after 5 hours.

Table 1. Yields of Schiff bases from heterocyclic aldehydes and TCH

Schiff base	Yield (heating, 3 h)	Yield (room temperature, 5 h)
	60.2 %	58.5 %
	83.4 %	75.0 %
	50.1 %	50.0 %
	80.5 %	78.5 %

The course of the reactions was monitored using infrared spectrophotometry (FTIR). For example, in the reaction of aldehyde with TCH, the main product is Schiff base carbohydrazide. On the spectrum of carbohydrazide synthesized with heating as well as on the spectrum carbohydrazide synthesized at room temperature, during the reaction the peak at 1700 cm^{-1} (originating from the aldehyde group) disappears, and a band appears at $1500\text{-}1600\text{ cm}^{-1}$ which is a characteristic of the $\text{C}=\text{N}$ bond from imine. Figure 4 shows the infrared spectra of aldehyde (a) and Schiff base (b).



a)

b)

Figure 4. FTIR spectrum of a) heterocyclic aldehyde; b) Schiff base from aldehyde and TCH.

3. Conclusions

In our work, we obtained a series of compounds of high degree of purity, satisfactory yield varying from 50-90%, whose structure and purity confirmed by NMR spectroscopy. The synthesized Schiff bases are ready for further examination of their biological activity or for complexation with transition metals, then testing biological activity of the complex, which we certainly expect to be larger than Schiff bases themselves. In order to optimize the reaction conditions, the reactions were carried out at room temperature, without heating, whereby the bases were obtained in yields that are comparable to the reactions that were carried out thermally, but the reaction time was extended. Further optimizations will be carried out in order to avoid the use of strong acid as a catalyst.

References

- [1] H. Schiff H. *A new series of organic base*, *Annalen der Chemie und Pharmacie* (in German), 131 (1864) 118-119.
- [2] S. Laxman, *Introduction to Schiff base. Schiff Base in Organic, Inorganic and Physical Chemistry*. Published online 2022. (link: <https://www.intechopen.com/chapters/84758>)
- [3] B. Chopra, A. K. Dhingra, R. P. Kapoor, D. N. Parsad, *Synthesis and antimicrobial activity of naphthylamine analogs having Azetidinone and thiazolidinone moiety*. *Journal of Exploratory Research in Pharmacology*, 2/4 (2017) 105-112.
- [4] J. Clayden, N. Greeves, S. Warren, *Organic Chemistry*. 2nd edition Oxford University Press; 2001.
- [5] A. Metwally, E. Khalifa, M. Koketsu, *Thiocarbohydrazides: Synthesis and reactions*, *American Journal of Chemistry*, 2 (2012) 38-51.
- [6] J. Zhou, D. Wu, J. Gou, *Optimization of the production of thiocarbohydrazide using the Taguchi method*. *Chemistry Technology Biotechnologu* 85 (2010) 1402-1406.
- [7] K. Gangarapu, S. Manda, A. Jallapally, S. Thota, S. Karki, J. Balzarini, E. Clercq, H. Tokuda, *Synthesis of thiocarbohydrazide and carbohydrazide derivatives as possible biologically active agents*, *Medical and Chemical Research* 23 (2014) 1046-1056.

Synthesis, structure and anticancer activity of Zr(IV) complexes with Schiff bases derived from 8-hydroxyquinoline

Michaela Harmošová^{1*}, Martin Kello², Mária Vilková³, Erika Samolová⁴, Ivan Potočňák¹

¹ Pavol Jozef Šafárik University in Košice, Faculty of Science, Institute of Chemistry, Moyzesova 11, 041 54 Košice, Slovakia; e-mail: michaela.krescankova@upjs.student.sk, ivan.potocnak@upjs.sk

² Pavol Jozef Šafárik University in Košice, Faculty of Medicine, Department of Pharmacology, Trieda SNP 1, 040 11 Košice, Slovakia; e-mail: martin.kello@upjs.sk

³ Pavol Jozef Šafárik University in Košice, Faculty of Science, NMR Laboratory, Moyzesova 11, 041 54 Košice, Slovakia; email: maria.vilkova@upjs.sk

⁴ Czech Academy of Science, Institute of Physics, Na Slovance 2, 182 21 Prague, Czech Republic; e-mail: samolova@fzu.cz

* Corresponding author

DOI: 10.46793/ICCBi23.439H

Abstract: The Schiff base 2-[(2-hydroxyphenyl)imino]methyl}quinolin-8-ol (HLH) and its 5,7-dibromo- (HBrLH) and 5,7-diiodo-derivatives (HILH), which were prepared by multi-step organic synthesis, were used to synthesize [Zr(L)₂]-2DMF (**1**), [Zr(BrL)₂]-DMF (**2**), and [Zr(IL)₂]-2DMF (**3**) complexes. The prepared products were characterized by elemental analysis, IR and NMR spectroscopy, which also monitored the stability of the prepared substances in DMSO, and in the case of HBrLH, HILH and **3**, also by single crystal X-ray structural analysis. In the complex **3**, two IL ligands are tetradentately bound to the central zirconium(IV) atom *via* two oxygen and two nitrogen atoms. DMF molecules are outside the coordination sphere. In complexes **1** and **2**, we assume an analogous structure. Due to poor solubility, the *in vitro* cytostatic activity of only complex **2** and its ligand HBrLH was studied against 8 cancer cell lines of different origin (cervix, colon, pancreas, skin, breast, lung, liver and blood) and their selectivity was studied against healthy cell line BJ-5t (human dermal fibroblasts). HBrLH is comparably active to the reference drug, cisplatin, but complex **2** showed lower biological activity. Selectivity of **2** or HBrLH was not observed.

Keywords: zirconium, 8-hydroxyquinoline, cytotoxic activity

1. Introduction

Important milestones in cancer treatment include the discovery of the antiproliferative activity of cisplatin. However, its serious side effects such as hepatotoxicity, nephrotoxicity or reduced immunity must not be neglected, and in addition, one of the main problems when repeating the treatment is the formation of cell resistance to the drug [1,2]. In order to minimize side effects and prevent resistance, it is

necessary to focus on the preparation of new drugs. 8-Hydroxyquinoline (HQ) as well as its derivatives (HXQ) are known to exhibit anticancer, antifungal, antimicrobial, anti-SARS CoV-2, anti-inflammatory and antioxidant activities [3-5]. Since complexes with commercially available ligands have already been extensively studied, we decided to prepare new Zr(IV) complexes of the Schiff base type.

2. Results and discussion

The Schiff base ligands were prepared by multistep modified synthetic route (Figure 1) described in literature [6-8].

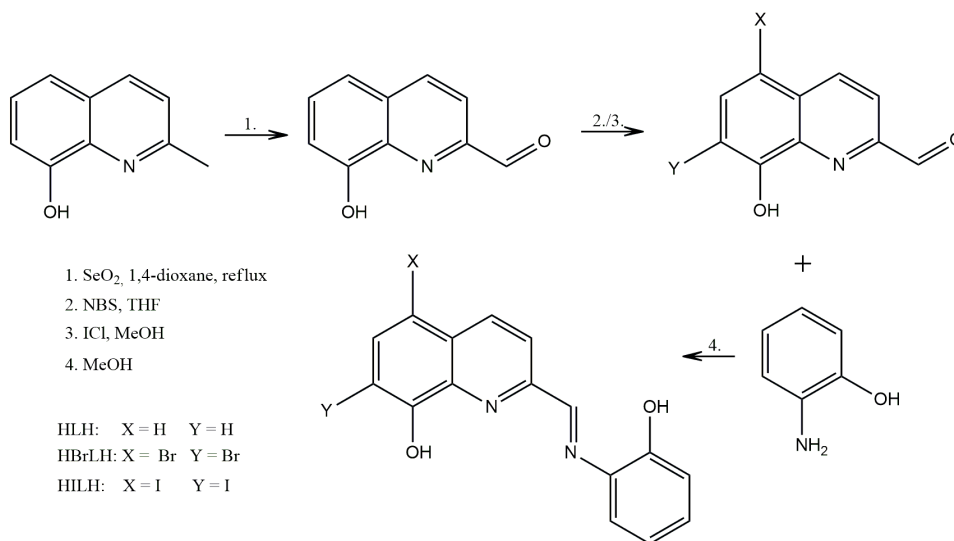


Figure 1. Synthetic route of ligands HLH, HBrLH and HILH.

Zr(IV) complexes, $[\text{Zr}(\text{L})_2] \cdot 2\text{DMF}$ (**1**), $[\text{Zr}(\text{BrL})_2] \cdot \text{DMF}$ (**2**), and $[\text{Zr}(\text{IL})_2] \cdot 2\text{DMF}$ (**3**), were prepared by slow diffusion of ethanol vapor into the reaction mixture in DMF consisting of ZrOCl_2 and the corresponding ligand according to the Figure 2.

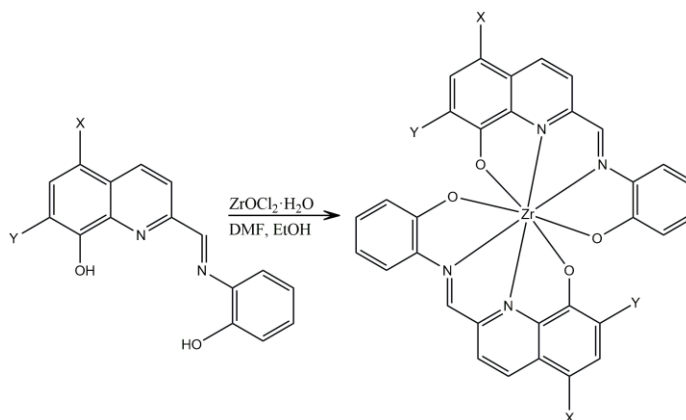


Figure 2. Synthetic route of complexes **1**, **2** and **3**.

Ligands and complexes were characterized by infrared and NMR spectroscopy in DMSO solution and elemental analysis confirming their composition in solid state. X-ray structure analysis showed that ligands HBrLH and HILH are isostructural and crystallized in the monoclinic $P2_1/c$ space group (Figure 3).

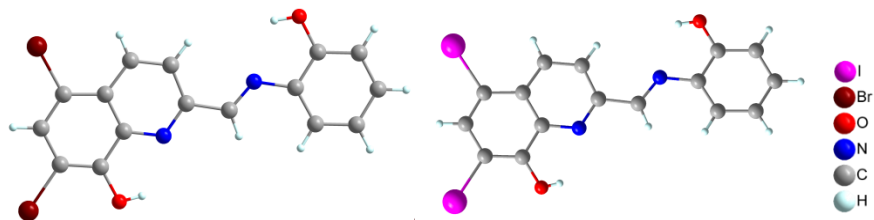


Figure 3. Structure of HBrLH and HILH.

In the structure of **3**, two IL ligands are tetradentately bound to the Zr(IV) atom *via* two oxygen and two nitrogen atoms (Figure 4). DMF molecules are outside the coordination sphere. In microcrystalline complexes **1** and **2**, we assume an analogous structure.

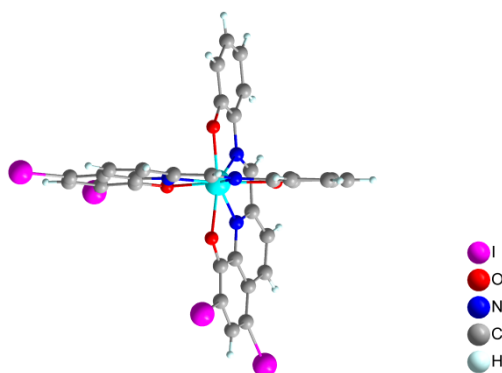


Figure 4. Structure of **3**.

Only *in vitro* antiproliferative activity of **2** and its ligand HBrLH was studied (Table 1), because of poor solubility of **1** and **3**. HBrLH is comparably active to the cisplatin, on the other hand **2** showed lower cytotoxic activity. Selectivity of **2** or HBrLH was not proven.

Table 1. IC₅₀ values [μM] of **2** and HBrLH in the various cell lines.

	HeLa	HCT116	PaTu 8902	A2058	MDA-MB-231	A549	HepG2	Jurkat	BJ-5ta
HBrLH	33.3	9.0	20.1	26.3	19.5	22.2	23.1	18.7	21.2
2	118.4	35.9	64.4	51.8	51.9	72.6	57.0	37.1	65.5
CisPt	30.4	14.5	20.7	18.8	26.7	17.3	14.0	6.2	31.0

3. Conclusions

We have prepared two new Schiff bases, HBrLH and HILH, and three new complexes [Zr(L)₂] \cdot 2DMF (**1**), [Zr(BrL)₂] \cdot DMF (**2**), and [Zr(IL)₂] \cdot 2DMF (**3**) in which two Schiff base ligands are tetradentately bound to the Zr(IV) atom. Complexes **1** and **3** have

poor solubility so only **2** and its ligand HBrLH were studied against 8 different cancer cell lines and their selectivity was studied against healthy cell line. Similar cytotoxic activity of HBrLH compared to cisplatin was observed. Selectivity of **2** or HBrLH was not demonstrated.

Acknowledgment

This research is funded by VEGA 1/0126/23 and VVGS-2022-2182.

References

- [1] L. Kelland., *The resurgence of platinum-based cancer chemotherapy*, Nature Reviews Cancer, 7(8) 2007 573–584).
- [2] F. Bray, J. Ferlay, I. Soerjomataram, R. L. Siegel, L. A. Torre, A. Jemal., *Global cancer statistics 2018: GLOBOCAN estimates of incidence and mortality worldwide for 36 cancers in 185 countries*, CA: A Cancer Journal for Clinicians, 68(6) 2018 394–424.
- [3] R. Gupta, V. Luxami, K. Paul., *Insights of 8-hydroxyquinolines: A novel target in medicinal chemistry*, Bioorganic Chemistry, 108 (2021) 104633.
- [4] X. Zhou., *Insights of metal 8-hydroxyquinolinol complexes as the potential anticancer drugs*, Journal of Inorganic Biochemistry, 238 (2023) 112051.
- [5] H. Saadeh, K. Sweidan, M. Mubarak., *Recent Advances in the Synthesis and Biological Activity of 8-Hydroxyquinolines*, Molecules, 25 (2020) 4321.
- [6] M. Y. Wu, G. Esteban, S. Brogi, M. Shionoya, L. Wang, G. Campiani, M. Unzeta, T. Inokuchi, S. Butini, J. Marco-Contelles., *Donepezil-like multifunctional agents: Design, synthesis, molecular modeling and biological evaluation*, European Journal of Medicinal Chemistry, 121 2016 864–879.
- [7] A. Basak, Y. Abouelhassan, V. M. Norwood, F. Bai, M. T. Nguyen, S. Jin, R. W. Huigens., *Synthetically Tuning the 2-Position of Halogenated Quinolines: Optimizing Antibacterial and Biofilm Eradication Activities via Alkylation and Reductive Amination Pathways*, Chemistry - A European Journal, 22(27) 2016 9181–9189.
- [8] D. González, R. Arrué, E. Matamala-Cea, R. Arancibia, P. Hamon, O. Cador, T. Roisnel, J. R. Hamon, N. Novoa., *Homoleptic CoII, NiII, CuII, and ZnII Complexes Based on 8-Hydroxyquinoline Schiff Base Derivative: a Combined Synthetic, Spectral, Structural, and Magnetic Study*, European Journal of Inorganic Chemistry, 2018(43) (2018) 4720–4730.

Ionic palladium(II) complexes with nitro and halogen derivatives of 8-hydroxyquinoline

Martina Kepeňová^{1*}, Michaela Benediková¹, Mária Vilková², Miroslava Litecká³, Ivan Potočňák¹

¹ Pavol Jozef Šafárik University in Košice, Faculty of Science, Institute of Chemistry, Moyzesova 11, 041 54 Košice, Slovakia; e-mail: martina.kepenova@upjs.student.sk, michaela.benedikova@upjs.student.sk, ivan.potocnak@upjs.sk

² Pavol Jozef Šafárik University in Košice, Faculty of Science, NMR Laboratory, Moyzesova 11, 041 54 Košice, Slovakia; email: maria.vilkova@upjs.sk

³ Institute of Inorganic Chemistry of the CAS, Department of Materials Chemistry, Husinec-Řež 1001, 250 68 Řež, Czech Republic; e-mail: litecka@iic.cas.cz

* Corresponding author

DOI: 10.46793/ICCB23.443K

Abstract: Four commercially unavailable derivatives of 8-hydroxyquinoline with different functional groups (nitro and halogen) in positions 5 and 7 were prepared: 5-nitro-7-iodo-8-hydroxyquinoline (HNIQ), 5-nitro-7-bromo-8-hydroxyquinoline (HNBrQ), 5-iodo-7-bromo-8-hydroxyquinoline (HIBrQ) and 5-chloro-7-bromo-8-hydroxyquinoline (HClBrQ). Their characterization was performed by IR and NMR spectroscopy, elemental analysis and in the case of HIBrQ and HClBrQ by single crystal X-ray structure analysis. Prepared compounds were used for the synthesis of new palladium(II) complexes $\text{NH}_2(\text{CH}_3)_2[\text{PdCl}_2(\text{XQ})]$, where XQ = NIQ (1), NBrQ (2), IBrQ (3) and ClBrQ (4). IR and NMR spectroscopy, elemental and X-ray structure analysis were used for their characterization. Bidentate chelate coordination of one molecule of XQ through nitrogen and oxygen atoms in square planar complexes was found. These complexes represent a group of compounds in which biological activities were found and will be used for the following biological study.

Keywords: palladium(II) complexes, 8-hydroxyquinoline, nitro and halogen derivatives of 8-hydroxyquinoline

1. Introduction

8-Hydroxyquinoline (H8-HQ) belongs to the large group of quinolines, which are abundantly represented in nature and for which a broad spectrum of biological activity was observed [1]. Quinolines found their part as commercially used drugs or as a part of clinical treatment [2]. Antimicrobial, antifungal, antiviral, and anticancer activities of H8-HQ and its derivatives were found [3]. Their effect in the treatment of malaria and neurological diseases was also described [4].

A huge number of complexes with derivatives of H8-HQ were prepared, described and studied as potential anticancer drugs. Compared to uncoordinated derivatives of H8-HQ, better activity in the case of complexes was observed [5].

2. Synthesis and characterization of derivatives of H8-HQ and their Pd(II) complexes

2.1 Synthesis

Commercially unavailable derivatives of H8-HQ were prepared according to the literature [6-9]. The synthetic route described in Figure 1 was used to prepare the complexes 1-4.

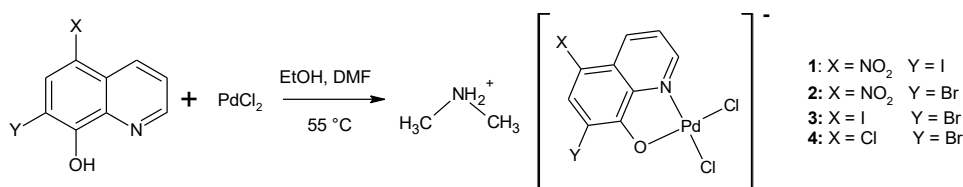


Figure 1. Synthetic route of complexes 1-4. A dimethylammonium cation is a product of the decomposition of dimethylformamide.

2.2 Characterization

All ligands and complexes were initially characterized by infrared spectroscopy and elemental analysis. The infrared spectra of studied compounds (Figure 2) are in agreement with the literature [10]. The presence of dimethylammonium cation in the structure of complexes was confirmed by vibrations in the range 3122-3075 cm⁻¹ for $\nu(\text{N-H})$ and in the range 2783-2780 cm⁻¹ for $\nu(\text{C-H})$.

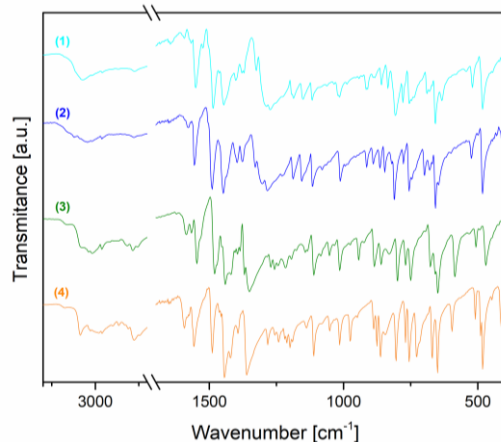


Figure 2. Infrared spectra of 1-4.

Compounds HClBrQ and HIBrQ are isostructural and crystallized in *P2/c* space group (Figure 3). Prepared complexes 1, 3 and 4 (Figure 4) crystallized as square planar complexes in which ligands XQ are bound as chelates to Pd(II) atom *via* oxygen and nitrogen donor atoms. The remaining two coordination sites are occupied by chlorido

ligands in *cis*-positions. The negative charge of the complex is balanced by the dimethylammonium cation (product of decomposition of dimethylformamide) that is outside the coordination sphere.

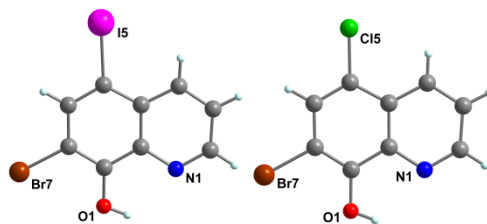


Figure 3. Crystal structure of HIBrQ and HCIBrQ.

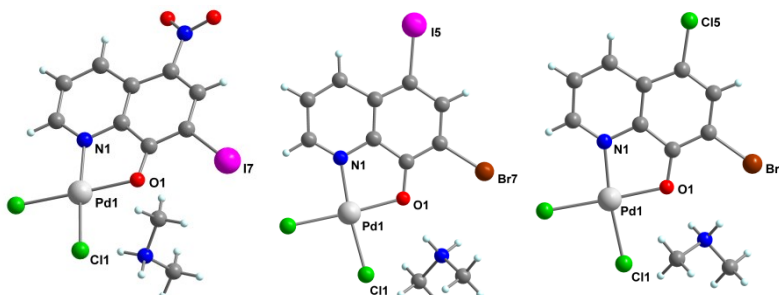


Figure 4. Crystal structure of 1, 3 and 4.

In the crystal structure of **2**, the same coordination of NBrQ was observed. Contrary to the previous crystal structures of the complexes, an asymmetric unit of **2** contains two units of $\text{NH}_2(\text{CH}_3)_2[\text{PdCl}_2(\text{NBrQ})]$ with pseudocentrosymmetric orientation to each other (Figure 5).

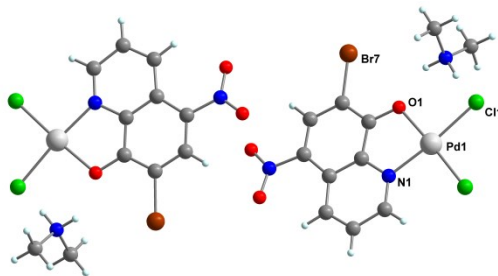


Figure 5. Crystal structure of **2**.

Crystal structures of the ligands and the complexes are stabilized by hydrogen bonds and π - π interactions and will be described as a part of the poster.

3. Conclusions

To conclude, synthesis of commercially unavailable derivatives of H8-HQ and their four palladium(II) complexes $\text{NH}_2(\text{CH}_3)_2[\text{PdCl}_2(\text{XQ})]$, where XQ is deprotonated form of 5-nitro-7-iodo-8-hydroxyquinoline (HNIQ) (**1**), 5-nitro-7-bromo-8-hydroxyquinoline (HNBrQ) (**2**), 5-iodo-7-bromo-8-hydroxyquinoline (HIBrQ) (**3**) and 5-chloro-7-bromo-8-hydroxyquinoline (HCIBrQ) (**4**) was described. Prepared compounds were characterized

by IR and NMR spectroscopy, elemental and X-ray structure analysis. In the case of complexes, square planar coordination of palladium(II) atom was found. Described compounds represent an interesting group of ionic complexes, in which high biological activity is supposed. In the future, these compounds will be tested on selected cancer cell lines. Cation exchange for more bioavailable cations (K^+ and Na^+) is planned, too.

Acknowledgment

This research is funded by the Ministry of Education, Science, Research and Sport of the Slovak Republic, Grant: No. VEGA 1/0126/23.

References

- [1] K. B. Patel, P. Kumari., *A review: Structure-activity relationship and antibacterial activities of Quinoline based hybrids*, Journal of Molecular Structure, 1268 (2022) 133634.
- [2] M. Ilakiyalakshmi, A. Arumugam Napoleon., *Review on recent development of quinoline for anticancer activities*, Arabian Journal of Chemistry, 15 (2022) 104168.
- [3] H. Saadeh, K. Sweidan, M. Mubarak., *Recent Advances in the Synthesis and Biological Activity of 8-Hydroxyquinolines*, Molecules, 25 (2020) 4321.
- [4] R. Gupta, V. Luxami, K. Paul., *Insights of 8-hydroxyquinolines: A novel target in medicinal chemistry*, Bioorganic Chemistry, 108 (2021) 104633.
- [5] X. Zhou., *Insights of metal 8-hydroxyquinolinol complexes as the potential anticancer drugs*, Journal of Inorganic Biochemistry, 238 (2023) 112051.
- [6] Z. Wang, W. Li, Y. Wang, X. Li, L. Huang, X. Li. *Design, synthesis and evaluation of clioquinol-*eb*selen hybrids as multi-target-directed ligands against Alzheimer's disease*, RSC Advances, 6 (2016) 7139-7158.
- [7] D. L. Boger, S. R. Duff, J. S. Panek, M. Yasuda., *Inverse Electron Demand Diels-Alder Reactions of Heterocyclic Aza Dienes. Studies on the Total Synthesis of Lavendamycin: Investigative Studies on the Preparation of the CDE β -Carboline Ring System and AB Quinoline-5,8-quinone Ring System*, The Journal of Organic Chemistry, 50 (1985) 5782-5789.
- [8] H. Jianbo, Z. Tingting, C. Yongjing, Z. Yuanyuan, Y. Weiqing, M. Menglin. *Study on Relationship Between Fluorescence Properties and Structure of Substituted 8-Hydroxyquinoline Zinc Complexes*, Journal of Fluorescence, 28 (2018) 1121-1126.
- [9] H. Gershon, M. W. McNeil, R. Parmegiani, P. K. Godfrey., *Antifungal Activity of 7- and 5,7-Substituted 8-Quinolinols*, Journal of Medicinal Chemistry, 15 (1972) 987-989.
- [10] P. Vranec, I. Potočňák, D. Sabolová, V. Farkasová, Z. Ipóthová, J. Pisarčíková, H. Paulíková., *Low-dimensional compounds containing bioactive ligands. V: Synthesis and characterization of novel anticancer Pd(II) ionic compounds with quinolin-8-ol halogen derivatives*, Journal of Inorganic Biochemistry, 131 (2014) 37-46.

A novel silver complex with 4-hydroxycoumarin derivative: Synthesis, structure, and biological activity

Jakub Kurjan^{1,*}, Rastislav Jendželovský², Zuzana Jendželovská², Viktória Buľková², Mária Vilková³, Miroslava Litecká⁴, Ivan Potočňák¹

¹ Pavol Jozef Šafárik University in Košice, Faculty of Science, Institute of Chemistry, Moyzesova 11, 041 54 Košice, Slovakia; e-mail: jakubkurjan@student.upjs.sk, ivan.potocnak@upjs.sk

² Pavol Jozef Šafárik University in Košice, Faculty of Science, Department of Molecular Biology, Moyzesova 11, 041 54 Košice, Slovakia; email: rastislav.jendzelovsky@upjs.sk, zuzana.jendzelovska@upjs.sk, viktoria.bulkova@student.upjs.sk

³ Pavol Jozef Šafárik University in Košice, Faculty of Science, NMR Laboratory, Košice, Moyzesova 11, SK-041 54 Slovakia; email: maria.vilkova@upjs.sk

⁴ Institute of Inorganic Chemistry of the CAS, Department of Materials Chemistry, Husinec-Řež 1001, 250 68 Řež, Czech Republic; e-mail: litecka@iic.cas.cz

* *Corresponding author*

DOI: 10.46793/ICCB23.447K

Abstract: In this contribution, a novel coumarin-derivative ligand, and its silver(I) complex are reported. Ligand 3-(1-(2-pyridylamino)ethylidene)-2H-chromene-2,4-dione (HL) was prepared by reaction of 3-acetyl-4-hydroxycoumarin with 2-picoyl amine. Further, complex $[Ag(HL)_2]NO_3$ was prepared and both compounds were characterized by physico-chemical methods such as IR and NMR spectroscopy, elemental analysis, and structure of the ligand and the complex was confirmed by X-ray analysis. The stability of both compounds was measured by NMR spectroscopy. MTT assay and cell proliferation assay on human lung adenocarcinoma cell line A549 and human colorectal adenocarcinoma cell line HT-29 showed that complex was more active than free HL ligand.

Keywords: coumarin, silver, anticancer

1. Introduction

Coumarins are an important class of chemicals in synthesis of transitional metal complexes. In many cases, complexes show enhanced biological activity in comparison with free coumarins [1]. Also, there are many complexes of coumarin derivatives with metals such as platinum, palladium, or copper, however complexes with silver are not as well documented as previous ones. It is believed that silver can bond DNA by formation of disulphide bonds. Also, silver is well known for its antibacterial properties [2]. Thus, silver complexes are suitable candidates for potential pharmaceutical use.

It has been shown that some derivatives like *scopoletin* and *esculetin* had significant antiproliferative activity [3]. Since silver complexes with coumarin derivatives have not been widely studied yet, we wanted to investigate this area further. Herein we report synthesis, characterization and anticancer activity over two cancerous cell lines of novel coumarin derivative 3-(1-(2-pyridylamino)ethylidene)-2H-chromene-2,4-dione (HL) and its silver(I) complex $[\text{Ag}(\text{HL})_2]\text{NO}_3$ (AgL2).

2. Results and discussion

2.1 Synthesis and crystal structure of the ligand and the complex

3-acetyl-4-hydroxycoumarin (1) was prepared according to published procedure [4]. Then by the condensation reaction with 2-picolyl amine the new coumarin derivative HL was prepared (Figure 1). Complex AgL2 was simply prepared by mixing ethanolic solution of HL and water solution of AgNO_3 in molar ratio 2:1. The stability of AgL2 was studied by NMR spectroscopy.

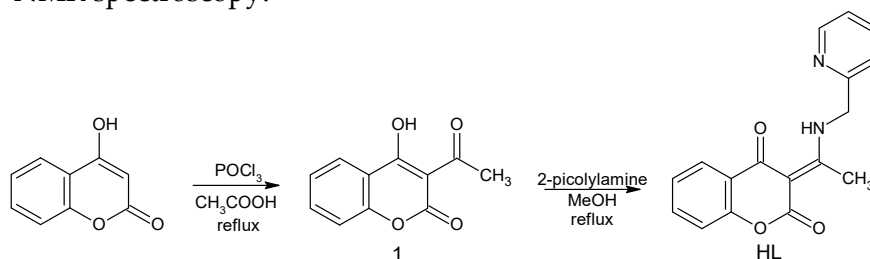


Figure 1. Synthetic pathway of ligand HL.

The crystal structures of HL and AgL2 are shown in Figure 2. In the structure of HL there is an intramolecular hydrogen bond, which leads to the formation of a six-membered ring $\text{O4}=\text{C4}-\text{C3}=\text{C11}-\text{N13}-\text{H13}$ and the molecule is in keto-tautomeric form. Due to the formation of the ring, flattening of $\text{C4}-\text{C3}$ (1,4392(17) Å) and $\text{C3}=\text{C11}$ (1,4413(17) Å) bonds is observed. In the complex, two molecules of the ligand HL are coordinated to the central atom Ag(I) *via* N20 of 2-pyridyl fragment and the shape of coordination polyhedron is linear. As ligands are non-deprotonated, the nitrate anion compensates the charge of the complex cation.

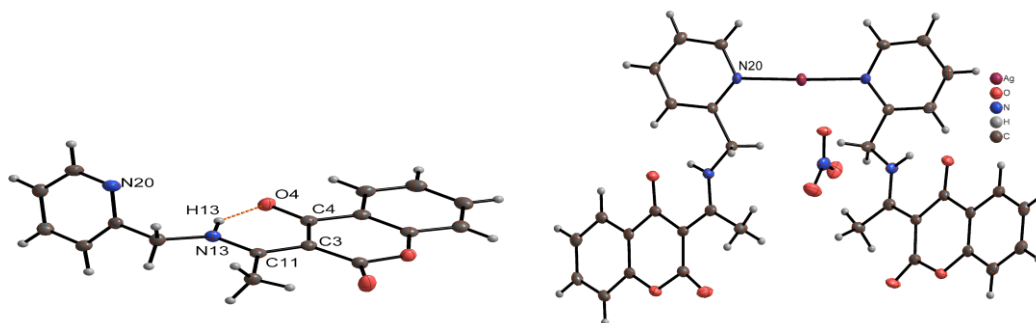


Figure 2. Crystal structure of HL (left) and AgL2 (right).

2.2 Anticancer activity

HL did not inhibit metabolic activity of A549 (Figure 3A) and HT-29 cells (Figure 3C). On the other hand, AgL2 showed time- and dose-dependent inhibitory effect on the metabolic activity of the both cancer cell lines (Figure 3B, D). In the case of A549 cells, significant inhibition in metabolic activity was observed in the experimental groups treated with 50 μM , 75 μM and 100 μM AgL2 (Figure 3B). Moreover, the inhibitory effect of AgL2 against HT-29 cells was even more pronounced (Figure 3D).

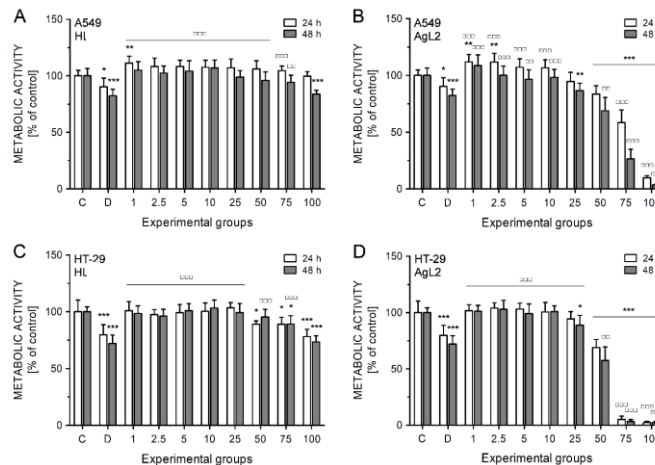


Figure 3. The effect of HL (left, A, C) and AgL2 (right B, D) on metabolic activity of A549 (top A, B) and HT-29 cells (bottom C, D).

HL did not inhibit the proliferation of HT-29 cells, as the confluence was continuously increasing in all treated experimental groups equally to untreated control throughout the whole duration of monitoring. In the case of A549 cells, 75 μM and 100 μM HL slightly but significantly delayed the rate of cell growth, as the percentage of confluence was lower compared to the untreated control group (Figure 4A).

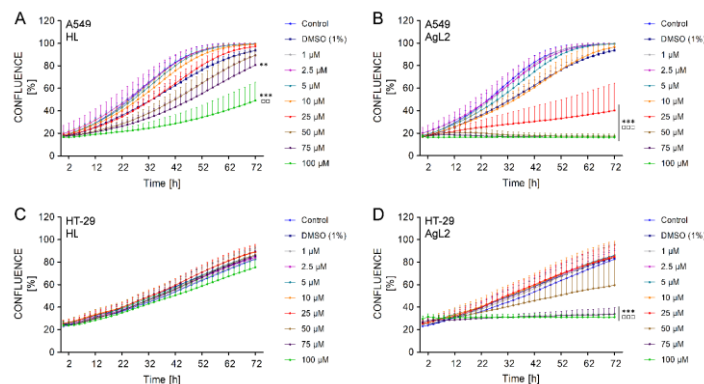


Figure 4. The effect of HL (left, A, C) and AgL2 (right B, D) on proliferation of A549 (top A, B) and HT-29 cells (bottom C, D).

On the other hand, higher concentrations of AgL2 inhibited the proliferation of A549 and HT-29 carcinoma cells, as the confluence of both cell lines was not increasing in time. In the case of A549 cells, the confluence even slightly decreased after the treatment with 50, 75 and 100 μM AgL2 below the percentage of confluence at 0 h (Figure 4B). Moreover, 25 μM AgL2 in A549 cells (Figure 4B) and 50 μM AgL2 in HT-29 cells (Figure 4D) also significantly delayed the rate of cell proliferation, as the percentage of confluence was lower compared to the untreated control group.

3. Conclusions

The synthesis and characterization of novel coumarin derivative 3-(1-(2-pyridylamino)ethylidene)-2H-chromene-2,4-dione (HL) and its silver(I) complex $[\text{Ag}(\text{HL})_2]\text{NO}_3$ (AgL2) were carried out. Both compounds were fully characterized by IR and NMR spectroscopy, elemental analysis, and their crystal structures have been solved. MTT assay and cell proliferation assay of HL and AgL2 have been done. The obtained results suggest that AgL2 has inhibitory potential towards the metabolic activity of cancer cells. However, the drop in the metabolic activity of the cells may either be the consequence of cytotoxic and/or cytostatic action of tested compound on the cancer cells, or may just reflect the inhibitory potential of the compound towards cellular metabolism. Thus, more specific analysis will be needed to elucidate the effect of AgL2 on A549 and HT-29 cells. Also, AgL2 inhibited not only the metabolic activity, but also the proliferation of A549 and HT-29 cells.

Acknowledgment

This research is funded by the Ministry of Education, Science, Research and Sport of the Slovak Republic, Grant: No. VEGA 1/0126/23.

References

- [1] E. H. AVDOVIĆ, et al., *Synthesis, Characterization and Cytotoxicity of a new Palladium(II) Complex with a Coumarin-Derived Ligand 3-(1-(3-hydroxypropylamino)ethylidene)chroman-2,4-dione. Crystal structure of the 3-(1-(3-hydroxypropylamino)ethylidene)-chroman-2,4-dione*, *Inorganica Chimica Acta*, 466 (2017) 188-196.
- [2] R. S. KUMAR, et al., *Silver Complexes as Anticancer Agents: A Perspective Review*, *German J Pharm Biomaterials*, 1 (2022) 6-28.
- [3] BALCIOĞLU, S. et al., *Therapeutic potential of coumarin bearing metal complexes: Where are we headed?*, *Bioorganic and Medicinal Chemistry letters*, 30 (2020) 1135-1146.
- [4] S. SUKDOLAK, et al., *Hantzsch reaction of 3-(2-bromoacetyl)-4-hydroxy-chromen-2-one. Synthesis of 3-(thiazol-4-yl)-4-hydroxy coumarines.*, *Journal of Heterocyclic Chemistry*, 41 (2004) 593-596

Anticancer gallium(III) complexes with halogen- and nitroderivatives of 8-hydroxyquinoline

Ivan Potočňák^{1,*}, Miroslava Litecká², Jitka Prachařová³, Monika Hreusová³, Jana Kašpárková³

¹ Pavol Jozef Šafárik University in Košice, Faculty of Science, Institute of Chemistry, Moyzesova 11, 041 54 Košice, Slovakia; e-mail: ivan.potocnak@upjs.sk

² Institute of Inorganic Chemistry of the CAS, Department of Materials Chemistry, Husinec-Řež 1001, 250 68 Řež, Czech Republic; e-mail: litecka@iic.cas.cz

³ Palacký University in Olomouc, Faculty of Science, Department of Biophysics, 17. listopadu 12, 771 46 Olomouc, Czech Republic; e-mail: pracharova.jitka@seznam.cz, monca.hreusova@gmail.com, jana@ibp.cz

* Corresponding author

DOI: 10.46793/ICCBi23.451P

Abstract: Six gallium(III) complexes with halogen- or nitroderivatives of 8-hydroxyquinoline, [Ga(ClIQ)₃] (**1**), [Ga(BrQ)₃] (**2**), [Ga(dIQ)₃] (**3**), [Ga(CQ)₃] (**4**), [Ga(NQ)₃] (**5**) and [Ga(CINQ)₃].MeOH (**6**) were prepared as possible anticancer drugs (HClQ = 5-chloro-8-hydroxyquinoline, HBrQ = 7-bromo-8-hydroxyquinoline, HdIQ = 5,7-diiodo-8-hydroxyquinoline, HCQ = 5-chloro-7-iodo-8-hydroxyquinoline, HNQ = 5-nitro-8-hydroxyquinoline and HCINQ = 5-chloro-7-nitro-8-hydroxyquinoline). X-ray single crystal structure analysis of [Ga(ClIQ)₃].MeOH (**1** – MeOH) and **5** showed that both complexes are molecular complexes with Ga(III) coordinated in *mer*-fashion by N- and O-donor atoms of three ClIQ and NQ ligands, respectively. The *in vitro* antiproliferative activity of **1** and **5** was evaluated against the human ovarian carcinoma cisplatin-sensitive A2780, breast carcinoma MDA-MB-231, and human colorectal carcinoma HCT-116 cell lines and their selectivity was verified on MRC5 pd30 cells from normal lung tissue. Complexes **1** and **5** display higher antiproliferative activity (IC₅₀ values in the range 2.1–7 μM) compared to the respective ligands, used Ga(III) salts, cisplatin and oxaliplatin, and a significant selective antiproliferative potency (IC₅₀ = 149 and 32 μM, respectively for MRC5pd30 cell line).

Keywords: gallium(III), 8-hydroxyquinoline derivatives, structure, antiproliferative activity

1. Introduction

Gallium is regarded as the second metal after platinum used for cancer treatment [1]. The preclinical and clinical studies revealed the evident potential of anticancer activity of Ga(III), although some disadvantages of simple Ga(III) salts are also apparent [1].

To avoid these disadvantages, new Ga(III) complexes consisting of organic ligands, such as 8-hydroxyquinolate (KP46) [2] or maltolate [3] have been prepared and tested. These complexes display greater antitumor efficacy, a broader spectrum of activity, and better bioavailability and have reached clinical trials as anticancer agents and encouraging results of these trials have been reported. Thus, the coordination of gallium with organic ligands proves to be a promising strategy for designing therapeutic agents with a number of advantages over the metal-based drugs currently used in the clinic.

Therefore, we have decided to study the antiproliferative activity of Ga(III) complexes with derivatives of 8-hydroxyquinoline (HXQ). Herein we present the preparation of [Ga(ClQ)₃] (**1**), [Ga(BrQ)₃] (**2**), [Ga(dIQ)₃] (**3**), [Ga(CQ)₃] (**4**), [Ga(NQ)₃] (**5**) and [Ga(CINQ)₃]·MeOH (**6**) complexes (HClQ = 5-chloro-8-hydroxyquinoline, HBrQ = 7-bromo-8-hydroxyquinoline, HdIQ = 5,7-diiodo-8-hydroxyquinoline, HCQ = 5-chloro-7-iodo-8-hydroxyquinoline, HNQ = 5-nitro-8-hydroxyquinoline and HCINQ = 5-chloro-7-nitro-8-hydroxyquinoline), which were fully characterized by necessary physicochemical methods. The *in vitro* antiproliferative activity of **1** and **5** was investigated against human ovarian carcinoma cisplatin-sensitive A2780, breast carcinoma MDA-MB-231, and human colorectal carcinoma HCT-116 cell lines while their selectivity was verified on MRC5 pd30 cell line from normal lung tissue and compared to cisplatin and oxaliplatin. Crystal structures of [Ga(ClQ)₃]·MeOH (**1** – MeOH) and **5** are presented, too.

2. Experimental part

The corresponding HXQ ligand (1.5 mmol) was suspended in ethanolic/water mixture (2:1, 30 mL) and the aqueous solution of GaCl₃ (88 mg, 0.5 mmol, 10 mL) was added into the mixture. The pH of the mixture was adjusted to 5–6 by an excess of sodium acetate. A formed reaction mixture was then refluxed for 3 h and afterward was cooled down to room temperature, the precipitated complex was filtered off, purified by repeated washing with a large amount of hot water and ethanol and dried in air. Crystals of [Ga(ClQ)₃]·MeOH (**1** – MeOH) were obtained by a recrystallization of **1** from methanol, while crystals of **5** were obtained by a diffusion of liquid methanol into a solution of **5** in DMSO.

X-ray data collection for **1** – MeOH and **5** was carried out on a Bruker D8 VENTURE diffractometer using CuK α radiation and the structures were solved and refined by the SHELX program suite [4]. Antiproliferative effects of Ga(III) complexes and corresponding ligands and salts were evaluated by using the standard 3-(4,5-dimethylthiazol-2-yl)-2,5-diphenyltetrazolium bromide (MTT) assay.

3. Results and discussion

Crystals of **1** – MeOH and **5** crystallize in the triclinic *P*-1 and in the monoclinic *P*2₁/*c* space groups, respectively. In their molecular structures, Ga atoms are tris-coordinated by corresponding XQ ligands with nitrogen and oxygen donor atoms coordinated in *mer*

fashion (Figure 1). Coordination polyhedra of Ga atoms are distorted octahedral. The Ga–O distances are slightly shorter than Ga–N distances (Table 1), which is in consonance with smaller covalent radius and higher electronegativity of oxygen atoms.

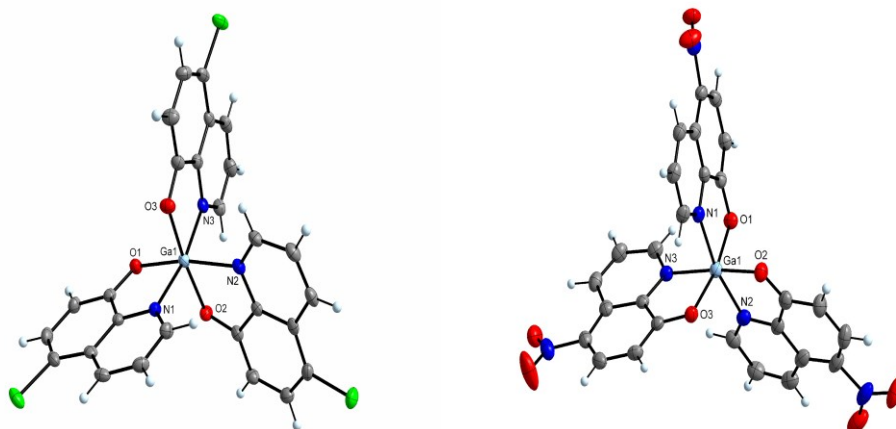


Figure 1. Crystal structure of **1** – MeOH (left; the methanol solvate is not involved for the sake of clarity) and **5** (right).

Table 1. Selected bond lengths [Å] for **1** – MeOH and **5**.

Bond	1 – MeOH	5
Ga1–O1	1.953(2)	1.953(2)
Ga1–O2	1.942(2)	1.946(2)
Ga1–O3	1.948(2)	1.945(2)
Ga1–N1	2.091(2)	2.077(3)
Ga1–N2	2.104(2)	2.070(3)
Ga1–N3	2.064(2)	2.088(3)

The antiproliferative activity of **1** and **5**, and for comparative purposes, of gallium nitrate, ligands (HClQ and HNQ), cisplatin and carboplatin, was studied by commonly used MTT assay after 72 h of incubation with a set of human cancer cell lines of various origin – ovarian, breast and colon. Moreover, the human noncancerous lung fibroblasts were also included in the study. As indicated from IC₅₀ values (Table 2), both complexes showed good activity against the whole panel of cancer cell lines tested in this work, with IC₅₀ values in the range of low micromolar concentrations. Complexes displayed comparable potency to clinically used cisplatin in cisplatin-sensitive A2780 cells; however, they were significantly more active in colon and breast cancer cells inherently resistant to cisplatin, including the hardly treatable highly metastatic MDA-MB-231 cell line; the same is true in the case of comparison with carboplatin. Importantly, the experiments also confirm very low activity in noncancerous lung fibroblasts, which were affected only at concentrations 21–71 times higher than cancer cells for complex **1** (6–9-times higher for complex **5**) thus indicating superior selectivity of **1** for cancer over noncancerous human cells.

Table 2. IC₅₀ values [μ M] for studied compounds in the various cell lines.

Compounds	A2780	MDA-MB-231	HCT116	MRC5pd30
[Ga(ClQ) ₃] (1)	2.1 ± 0.7	7 ± 3	3.2 ± 0.6	149 ± 11
HClQ	6.5 ± 0.7	12 ± 4	16 ± 2	76 ± 6
[Ga(NQ) ₃] (5)	3.6 ± 0.8	5 ± 1	3.8 ± 0.9	32 ± 4
HNQ	2.1 ± 0.7	10 ± 1	8.4 ± 3	62 ± 5
Ga(NO ₃) ₃	ND	> 200	> 200	ND
Cisplatin	3.0 ± 0.3	23 ± 3	5 ± 1	11.7 ± 0.8
Carboplatin	ND	198 ± 45	295 ± 7	148 ± 13

4. Conclusions

We prepared six gallium(III) complexes, [Ga(ClQ)₃] (**1**), [Ga(BrQ)₃] (**2**), [Ga(dIQ)₃] (**3**), [Ga(CQ)₃] (**4**), [Ga(NQ)₃] (**5**) and [Ga(ClNQ)₃]·MeOH (**6**) (HClQ = 5-chloro-8-hydroxyquinoline, HBrQ = 7-bromo-8-hydroxyquinoline, HdIQ = 5,7-diiodo-8-hydroxyquinoline, HCQ = 5-chloro-7-iodo-8-hydroxyquinoline, HNQ = 5-nitro-8-hydroxyquinoline and HCINQ = 5-chloro-7-nitro-8-hydroxyquinoline). Complexes [Ga(ClQ)₃]·MeOH (**1** – MeOH) and **5** were characterized by X-ray single crystal structure analysis which revealed molecular structures with *mer*-isomeric surrounding around gallium(III) atoms. *In vitro* studies revealed that complex **1** displayed comparable potency to clinically used cisplatin in cisplatin-sensitive A2780 cells; however, it was significantly more active in colon and breast cancer cells inherently resistant to cisplatin, including the hardly treatable highly metastatic MDA-MB-231 cell line. Importantly, **1** showed also a distinct selectivity for tumor cells over non-malignant lung fibroblasts, making this complex a perspective candidate for further biological testing.

Acknowledgment

This research is funded by the Ministry of Education, Science, Research and Sport of the Slovak Republic, Grant: No. VEGA 1/0126/23.

References

- [1] P. Collery, B. Keppler, C. Madoulet, B. Desoize., *Gallium in cancer treatment*, Critical Reviews in Oncology/Hematology, 42 (2002) 283-296.
- [2] P. Collery, M.A. Jakupec, B. Kynast, B.K. Keppler., *Preclinical and early clinical development of the antitumor gallium complex KP46 (FFC11)*, Metal Ions in Biology and Medicine, 9 (2006) 521-524.
- [3] L.R. Bernstein, T. Tanner, C. Godfrey, B. Noll., *Chemistry and pharmacokinetics of gallium maltolate, a compound with high oral gallium bioavailability*, Metal-Based Drugs, 7 (2000) Article ID 324842.
- [4] G.M. Sheldrick., *SHELXT-Integrated space-group and crystal-structure determination*, Acta Crystallographica A, 71 (2015) 3-8 and *Crystal structure refinement with SHELXL*, Acta Crystallographica C, 71 (2015) 3-8.

***In silico* Drug-Likeness, Pharmacokinetic and other ADME properties of 2-(aminomethyl)cyclopropane-1,1-dicarboxylic acid**

Marina D. Kostić^{1*}, Jovana S. Marjanović², Sven Mangelinckx³, Vera M. Divac²

¹ University of Kragujevac, Institute for Information Technologies, Department of Science, Kragujevac, Serbia e-mail: marinak@uni.kg.ac.rs

² University of Kragujevac, Faculty of Science, Department of Chemistry, Kragujevac, Serbia; e-mail: vera.divac@pmf.kg.ac.rs, jovana.marjanovic@pmf.kg.ac.rs

³ Ghent University, Faculty of Bioscience Engineering, Department of Green Chemistry and Technology; e-mail: sven.mangelinckx@ugent.be

* *Corresponding author*

DOI: 10.46793/ICCBi23.455K

Abstract: Herein we present the results of *in silico* determination of Drug-Likeness, Pharmacokinetic and other ADME properties of 2-(aminomethyl)cyclopropane-1,1-dicarboxylic acid as an example constrained γ -amino dicarboxylic acid. The results of *in silico* screening of drug-likeness, pharmacokinetic and other ADME (absorption, distribution, metabolism and elimination) properties of 2-(aminomethyl)cyclopropane-1,1-dicarboxylic acid have revealed that this compound is not able to cross the blood-brain barrier, but it shows good solubility and gastrointestinal absorption. The possible target screening has indicated the family C G protein-coupled receptors as the most probable physiological targets. More specifically, the 2-(aminomethyl)cyclopropane-1,1-dicarboxylic acid has the highest structural similarity with the known compounds that act on metabotropic glutamate receptor, excitatory amino acid transporter and betaine transporter. Taking all the above into consideration, it can be concluded that our investigated compound could be considered as a candidate molecule for further structural transformations that could enable better pharmacological performance and physiochemical properties.

Keywords: amino acids; ADMET; pharmacology

1. Introduction

Taking into consideration that drug discovery can be time-consuming and very expensive process, the application of different predictors for the determination of a potential drug's *in vivo* studies and properties necessary for the administration under physiological conditions, is today a recognizable concept for successful drug design and synthesis. ADME properties (absorption, distribution, metabolism and elimination) are excellent predictors of the potential drug's success. Numerous different *in silico* ADME tools have been developed, all based solely on the use of chemical structures [1-3]. Herein we present the results obtained by

the application of SwissADME tool for the evaluation of pharmacokinetics, drug-likeness and other ADME properties of 2-(aminomethyl)cyclopropane-1,1-dicarboxylic acid as an example of sterically constrained amino acids.

2. Results and Discussions

2-(Aminomethyl)cyclopropane-1,1-dicarboxylic acid **1** (Figure 1) as an example of the unnatural amino acids, previously synthesized by us [4], as an example of sterically constrained gamma amino acids. Taking into consideration that our previous work was directed to the resolution of the synthetic pathway for approaching this compound and that compound has never been screened for pharmacological potential, herein we present the results of it *in silico* determination of Drug-Likeness, Pharmacokinetic and other ADME properties. For this purpose, the SwissADME online tool [3] was used to evaluate pharmacokinetics, drug-likeness and other ADME properties and the obtained data are presented in Table 1. According to the data given in Table 1 it can be noticed that the compound has good water solubility and high gastrointestinal absorption, but no possibility to cross the blood-brain barrier.

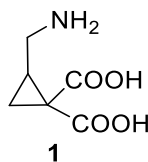


Figure 1. 2-(Aminomethyl)cyclopropane-1,1-dicarboxylic acid.

Table 1. Predicted Drug-Likeness, Pharmacokinetic and other ADME properties calculated by SwissADME web tool for 2-(aminomethyl)cyclopropane-1,1-dicarboxylic acid .

Substrate: 2-(aminomethyl)cyclopropane-1,1-dicarboxylic acid			
Physicochemical Properties		Pharmacokinetics	
Formula	C ₁₃ H ₁₄ NO ₄	GI absorption	High
Molecular weight	159.14 g/mol	BBB permeant	No
Fraction Csp3	0.67	P-gp substrate	No
Num. rotatable bonds	3	CYP1A2 inhibitor	No
Num. H-bond acceptor	5	CYP2C19 inhibitor	No
Num. H-bond donors	3	CYP2C9 inhibitor	No
Molar Refractivity	34.83	CYP2D6 inhibitor	No
TPSA ^{a)}	100.62 Å ²	CYP3A4 inhibitor	No
		Log Kp (skin permeation)	-9.75 cm/s
Lipophilicity		Drug-Likeness	
Log Po/w (iLOGP)	0.32	Lipinski	Yes; 0 violation
Log Po/w (XLOGP3)	-3.49	Ghose	No; 3 violations ^{c)}
Log Po/w (WLOGP)	-0.88	Veber	Yes
Log Po/w (MLOGP)	-0.98	Egan	Yes
Log Po/w (SILICOS-IT)	-0.088	Muegge	No; 2 violations ^{d)}
Log Po/w ^{b)}	-1.18	Bioavailability Score	0.56
Water Solubility		Medicinal Chemistry	
Log S (ESOL)	1.57	PAINS	0 alert
Solubility	5.91e+03 mg/mL; 3.72e+01 mol/L	Brenk	1 alert: β-keto anhydride
Class	Highly soluble	Leadlikeness	No; 1 violation ^{e)}
Log S (Ali)	1.96	Synthetic accessibility	1.79
Solubility	1.44e+04 mg/mL; 9.06e+01 mol/L		
Class	Highly soluble		
Log S (SILICOS-IT)	0.75		
Solubility	3.95e+02 mg/mL; 5.62e+00 mol/L		
Class	Soluble		

a) topological polar surface area; b) average of all 5 predictions; c) MW<160, WLOGP<-0.4, MR<40
d) MW<200, XLOGP3<-2 e) molecular weight <250

The possible intracellular targets of 2-(aminomethyl)cyclopropane-1,1-dicarboxylic acid are given in Figure 2. As it can be seen, our compound has appeared to act on family C G protein-

coupled receptors. C G protein-coupled receptors are transmembrane proteins of the mammalian genome that became pharmaceutically interesting due to the fact that they represent targets of the many approved drugs. More specifically, the 2-(aminomethyl)cyclopropane-1,1-dicarboxylic acid has the highest structural similarity with the known compounds that act on metabotropic glutamate receptor, excitatory amino acid transporter and betaine transporter.

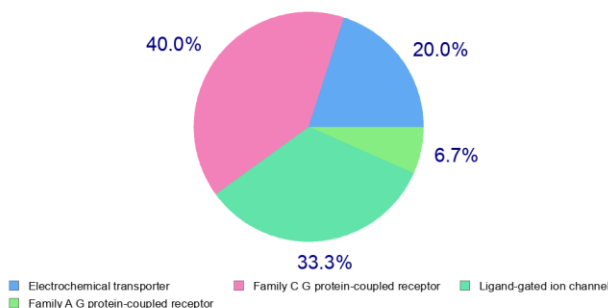


Figure 2. Target prediction of 2-(aminomethyl)cyclopropane-1,1-dicarboxylic acid.

3. *In silico* Drug-Likeness, Pharmacokinetic and other ADME properties study

The physicochemical, ADME, and drug-likeness parameters were computed using the SwissADME online program [3]. This software was used to calculate basic physicochemical properties including topological polar surface area (TPSA) and molecular refractivity. Lipophilicity was estimated through iLOGP, XLOGP3, WLOGP, MLOGP, and SILICOS-IT models from which an average value of all five predictions $\log P_{o/w}$ was determined. The solubility ($\log S$) was calculated by three different models: ESOL, Ali, and SILICOS-IT. Drug-likeness evaluation was based on Lipinski, Ghose, Veber, Egan and Muegge rules of 5. The Abbot Bioavailability scores were computed to predict the probability of a compound having at least 10% oral bioavailability by relying on total charge, TPSA, and violation of the Lipinski's filter. From pharmacokinetic properties gastrointestinal (GI) absorption, blood-brain barrier (BBB) permeation, inhibition of the cytochrome P450 system, permeability glycoprotein (P-gp) substrate and the skin permeation coefficient (k_p) were calculated. Also, tested compounds are screened through PAINS and Brenk filters and Lead likeness potential and synthetic accessibility are calculated.

4. Conclusions

The results of *in silico* screening of drug-likeness, pharmacokinetic and other ADME properties of 2-(aminomethyl)cyclopropane-1,1-dicarboxylic acid have revealed that this compound is not able to cross the blood-brain barrier, but it shows good solubility and gastrointestinal absorption. The possible target screening has indicated the family C G

protein-coupled receptors as the most probable physiological targets. Taking all the above into consideration, it can be concluded that our investigated compound could be considered as a candidate molecule for further structural transformations that could enable better pharmacological performance and physiochemical properties.

Acknowledgment

This research is funded by the Ministry of Education and Ministry of Science, Technological Development and Innovation, Republic of Serbia, Grants: (Agreement No. 451-03-47/2023-01/ 200122 and 451-03-47/2023-01/200378).

References

- [1] A. Effinger, C.M. O'Driscoll, M. McAllister, N. Fotaki., *In Vitro and In Silico ADME Prediction*, in: A. Talevi, P. Quiroga (Eds.), *ADME Processes in Pharmaceutical Sciences*, Springer, 2018.
- [2] S. Kar, J. Leszczynski., *Open access in silico tools to predict the ADMET profiling of drug candidates*, *Expert Opin Drug Discov* 15 (2015) 1473–1487.
- [3] A. Daina, O. Michielin, V. Zoete., *SwissADME: A free web tool to evaluate pharmacokinetics, drug-likeness and medicinal chemistry friendliness of small molecules*, *Sci Rep* 7 (2017) 42717.
- [4] S. Mangelinckx, M. Kostic, S. Backx, B. Petrovic, N. De Kimpe., *Synthesis of racemic 2-(aminomethyl)cyclopropane-1,1-dicarboxylic acid as a new constrained γ -amino dicarboxylic acid bypassing alkyl 3-aza-2-oxobicyclo[3.1.0]hexane-1-carboxylates*, *Eur J Org Chem*, 31 (2019) 5187-5189.

BSA binding of 2-(aminomethyl)cyclopropane-1,1-dicarboxylic acid

Marina D. Kostić^{1*}, Vera M. Divac², Sven Mangelinckx³, Jovana S. Marjanović²

¹ University of Kragujevac, Institute for Information Technologies, Department of Science, Kragujevac, Serbia e-mail: marinak@uni.kg.ac.rs

² University of Kragujevac, Faculty of Science, Department of Chemistry, Kragujevac, Serbia; e-mail: vera.divac@pmf.kg.ac.rs, jovana.marjanovic@pmf.kg.ac.rs

³ Ghent University, Faculty of Bioscience Engineering, Department of Green Chemistry and Technology; e-mail: sven.mangelinckx@ugent.be

* Corresponding author

DOI: 10.46793/ICCB23.459K

Abstract: Herein, we present the results of the study devoted to the exploration of BSA binding of 2-(aminomethyl)cyclopropane-1,1-dicarboxylic acid, as an example of constrained γ -amino dicarboxylic acid, and, taking into consideration that the effectiveness of a potential drug depends on its ability to bind to a protein carrier and in that way enable transfer through the blood stream. For the investigation of binding properties, we used the fluorescence emission titration of BSA with a synthesized compound. Considering that the BSA solution shows an intensive fluorescence emission around 360 nm, a decrease in emission intensity at $\lambda = 366$ nm with the addition of a solution of 2-(aminomethyl)cyclopropane-1,1-dicarboxylic acid indicated the binding of the tested compound. According to the results obtained, our compound binds to the BSA in a molar ratio 1:1 ($n \approx 1$). The optimal values of binding constant K_a are between 10^4 and 10^6 M⁻¹, which indicates to us that the K_a value of the tested compound is in the favorable range.

Keywords: amino acids, cyclopropanes, BSA

1. Introduction

The amino acids have gained important relevance in the research world particularly their unnatural counterparts as constituents of molecules with promising pharmaceutical potential [1]. The replacement of natural amino acids in peptides with non-proteinogenic examples has inspired the development of different studies directed to the better understanding of interactions of small molecules with biological targets such as enzymes or receptors [2, 3]. One of the most important fields in drug development is the design and synthesis of peptidomimetic molecules that should have the same pharmaceutical properties as their natural counterparts, but much better metabolic stability. For this purpose, one of the widely accepted methodologies is the use of conformationally constrained amino acids and dipeptides as entities that mimic parts of natural peptidic substrates and that enable us to understand the relationships between

peptide conformation and biological activity. All these circumstances have caused the development of the synthetic methodologies devoted to the preparation of different examples of conformationally constrained amino acids and their analogs [4]. The examples of rigid cyclic amino acids have played an important role in therapeutic development due to their ability to, upon incorporation into peptides or peptidomimetics, induce conformational restrictions and enable significant structural effects [4]. Herein, we present the results of the *in vitro* study devoted to the exploration of BSA binding of 2-(aminomethyl)cyclopropane-1,1-dicarboxylic acid 1 (Figure 1), as an example of sterically constrained amino acid derivatives and taking into consideration that the effectiveness of a potential drug depends on its ability to bind to a protein carrier and in that way enable transfer through the bloodstream.

2. Experimental section

2.1. Synthesis of 2-(aminomethyl)cyclopropane-1,1-dicarboxylic acid

The synthesis of racemic 2-(aminomethyl)cyclopropane-1,1-dicarboxylic acid 1 was achieved using the previously described procedure in the literature [5].

2.2. Albumin-binding studies

The protein-binding studies were made in accordance with the method described in the literature [6-8].

3. Results and Discussions

Since the effectiveness of a potential drug depends on its ability to bind to a protein carrier, which plays a key role in the transfer of substances through the blood stream, the binding affinity of compound 1 to bovine serum albumin (BSA) has been examined.

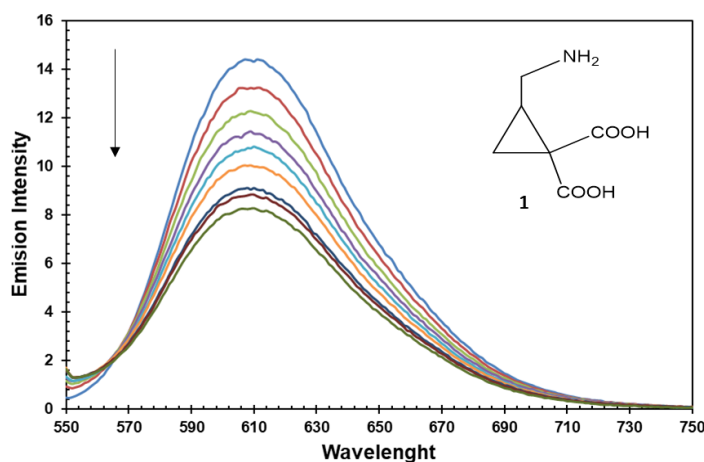


Figure 1. Emission spectra of BSA in the presence of 2-(aminomethyl)cyclopropane-1,1-dicarboxylic acid. [BSA] = 2 μ M, [Acid]/ [BSA] = 0-10, λ_{ex} = 295 nm. Arrows show the intensity changes upon increasing the concentrations of the examined compound.

For the investigation of binding properties, we used the fluorescence emission titration of BSA with synthesized compounds. The spectra were observed in the range between 300 and 500 nm at an excitation wavelength of 295 nm. Considering that the BSA solution shows an

intensive fluorescence emission around 360 nm, at the mentioned wavelength [9], decrease in emission intensity at $\lambda = 366$ nm (Figure 1) with the addition of a solution of 2-(aminomethyl)cyclopropane-1,1-dicarboxylic acid indicated binding of tested compound to the BSA molecule.

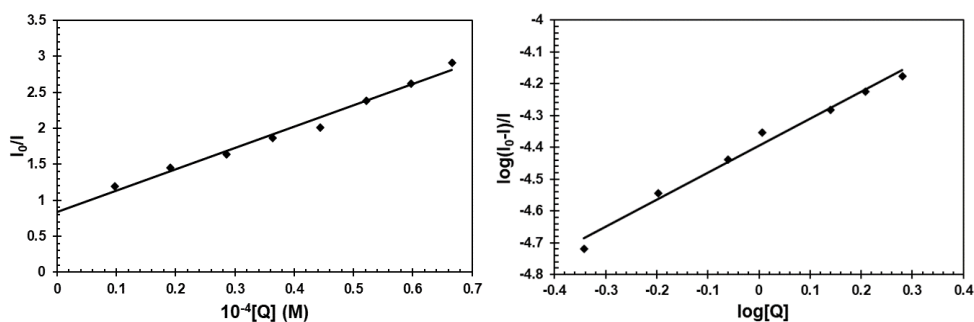


Figure 2. left: Plots of I_0/I versus $[Q]$ in mol/dm³; right: lots of $\log(I_0-I)/I$ versus $\log [Q]$.

The fluorescence quenching data such as Stern-Volmer constant (K_{sv}) were defined from the linear dependence of I_0/I to the concentration of the tested compound (Figure 2, left) using the Stern-Volmer quenching equation and number of binding sites per BSA molecule (n) were acquired by using the Stern-Volmer equation (1)

$$I_0/I = 1 + K_{sv}[Q] \quad (1)$$

where I_0 and I are the emission intensities in the absence and in the presence of the quencher (tested compound), $[Q]$ is the quencher's concentration.

Binding constant (K_a) can be calculated from the equation 2, which represents the relationship between fluorescence quenching intensity and the concentration of quencher [8]

$$\log[(I_0 - I)/I] = \log K_a + n \cdot \log[Q] \quad (2)$$

where n is the number of binding sites per BSA. The value for K_a can be calculated through the linear dependence of $\log [(I_0 - I)/I]$ versus $\log [Q]$ (Figure 2, right), where K_a can be calculated from the slope, while the n represents the intercept.

The calculations of all parameters were performed, and the obtained values are presented in Table 1.

Table 1. Binding parameters (K_{sv} , K_a , n) and the correlation coefficient (R) for interactions of the tested compound with BSA.

	$10^4 K_{sv}$ BSA (M ⁻¹)	K_a [M ⁻¹]	R	n
Acid 1	5.7 ± 0.1	1.8×10^5	0.99	1.02

If we look at the K_a value in Table 1, we can conclude that the tested compound has a very good binding affinity to BSA molecules, knowing that the optimal values of binding constant K_a are between 10^4 and 10^6 M^{-1} [9]. Also, we can conclude that our compound binds to the BSA in molar ratio 1:1 ($n \approx 1$). The optimal values of binding constant K_a are between 10^4 and 10^6 M^{-1} [9], which indicates to us that the K_a value of the tested compound is in the favorable range.

4. Conclusions

According to the results obtained in the screening of binding affinity of 2-(aminomethyl)cyclopropane-1,1-dicarboxylic acid toward BSA, we can conclude that our compound has a very good binding affinity toward BSA molecules and that it binds to the BSA in molar ratio 1:1.

Acknowledgment

This research is funded by the Ministry of Education and Ministry of Science, Technological Development and Innovation, Republic of Serbia, Grants: (Agreement No. 451-03-47/2023-01/ 200122 and 451-03-47/2023-01/200378).

References

- [1] S. Hanessian, G. McNaughton-Smith, H.-G. Lombart, W. D. Lubell., *Design and Synthesis of Conformationally Constrained Amino Acids as Versatile Scaffolds and Peptide Mimetics*, Tetrahedron, 53 (1997) 12789-12854.
- [2] J. Gante., *Peptidomimetics - Tailored Enzyme Inhibitors*, Angew Chem Int Ed Engl, 33 (1994) 1699-1720.
- [3] A. Giannis, T. Kolter., *Peptidomimetics for Receptor Ligands - Discovery, Development and Molecular Perspectives*, Angew Chem Int Ed Engl, 32 (1993) 1244.
- [4] K-H. Parka, M. J. Kurth., *Cyclic amino acid derivatives*, Tetrahedron, 58 (2002) 8629-8659.
- [5] S. Mangelinckx, M. Kostić, S. Backx, B. Petrović, N. De Kimpe., *Synthesis of racemic 2-(aminomethyl)cyclopropane-1,1-dicarboxylic acid as a new constrained γ -amino dicarboxylic acid bypassing alkyl 3-aza-2-oxobicyclo[3.1.0]hexane-1-carboxylates*, Eur J Org Chem, 31 (2019) 5187-5189.
- [6] J.R. Lakowicz, G. Weber., *Quenching of fluorescence by oxygen. A probe for structural fluctuations in macromolecules*, Biochem, 12 (1973) 4161.
- [7] J.R. Lakowicz, I. Gryczynski, Z. Gryczynski, J.D. Dattelbaum., *Anisotropy-based sensing with reference fluorophores*, Anal Biochem, 267 (1999) 397-405.
- [8] Schrödinger Suite, GlideSchrödinger, LLC, New York, NY, 2015.
- [9] A.R. Timerbaev, C.G. Hartinger, S.S. Aleksenko, B.K. Keppler., *Interactions of antitumor metallodrugs with serum proteins: advances in characterization using modern analytical methodology*, Chem Rev, 106 (2006) 2224-2248.

Investigation of binding mode of novel 2,4-diketo esters to BSA

Emilija Milović^{1*}, Kristina Mihajlović², Nenad Joksimović², Jelena Petronijević²,
Nenad Janković¹

¹ University of Kragujevac, Institute for Information Technologies Kragujevac, Department of natural and mathematical sciences, Kragujevac, Serbia, Jovana Cvijića bb; e-mail: emilija.milovic@pmf.kg.ac.rs , nenad.jankovic@uni.kg.ac.rs

² University of Kragujevac, Faculty of Science, Institute of Chemistry, Kragujevac, Serbia, Radoja Domanovića 12; e-mail: kristina.mihajlovic@pmf.kg.ac.rs , nenad.joksimovic@pmf.kg.ac.rs , jelena.petronijevic@pmf.kg.ac.rs

* Corresponding author

DOI: 10.46793/ICCBi23.463M

Abstract: 2,4-Diketo esters are well-known for their wide pharmacological activities as well as their usage in a lot of synthetic transformations. The specific structure of 2,4-diketo esters with many carbonyl groups and the presence of keto-enol tautomerism give suitable chemical properties for many applications. Therefore, an affinity for one of the binding sites of bovine serum albumin (BSA) of 2,4-diketo esters possessing good antimicrobial activity, was examined. Binding modes of compounds **A** and **B** were determined using fluorescence spectroscopy. Eosin Y was used as a marker for Sudlow's Site I (subdomain IIA), while ibuprofen was used as a marker for Sudlow's Site II (subdomain IIIA). Obtained values of K_a suggested that both compounds reversibly bind to BSA. Due to the values of K_a in the presence of site markers, the site II is more likely to be occupied by compound **A**, and compound **B** uses other binding modes. The presented results will help to improve the research of the mechanism of the interaction between transport proteins and similar compounds.

Keywords: 2,4-Diketo esters, BSA, eosin Y, ibuprofen

1. Introduction

2,4-Diketo esters are an essential part in the structures of pharmacological and therapeutically important drugs, and are also common scaffolds in the naturally occurring molecules [1]. The presence of keto-enol tautomerism and several carbonyl groups in the molecule of 2,4-diketo ester are the characteristics that have been significant reasons for their application in many chemical syntheses. Therefore, 2,4-diketo esters are widely used as precursors in many reactions for obtaining different biologically active compounds such as 2,4-diketobutanoic acid derivatives, pyrazoles, isoxazoles, pyrrolidinones, quinoxalinones, benzoxazin-2-ones, and various other

compounds [1]. Besides that, the presence of many oxygens and a highly electrophilic environment makes this type of compound excellent for coordination with different metals [1].

The research of the interaction with transport proteins helps in understanding the ability of the investigated compound to reach the target and it is an important first step during drug development. For that purpose, bovine serum albumin (BSA) is a widely used molecule as a representative transport protein that has similar physico-chemical properties to human serum albumin (HSA). Due to its low cost and easy availability, it is often used instead of HSA.

There are the three most important drug-binding sites on HSA: Sudlow's Site I (subdomain IIA), Sudlow's Site II (subdomain IIIA), and Heme site (subdomain IB) [2]. Drugs are placed at two main binding sites located in subdomain IIA (site IIA) and IIIA (site IIIA). Depending on drug properties, one of the two sites is favored. Bulky heterocyclic compounds with negative charge delocalized near the unpolar fragment usually bind to site IIA, while IIIA (indole-benzodiazepine site) binds the compounds that contain a peripheral negative charge [4].

2. Results and Discussions

The interaction with BSA for previously synthesised 2,4-diketo esters containing vanillin fragments that possess good antibacterial activity was investigated [3]. In this paper, we tried to explain and examine which binding site of BSA is preferred by selected compounds **A** and **B** (Figure 1). Experiments were performed using fluorescence emission titration and ibuprofen and eosin Y as site markers. Eosin Y is known as a marker for Sudlow's Site I (subdomain IIA), while ibuprofen is known as a marker for Sudlow's Site II (subdomain IIIA) [6].

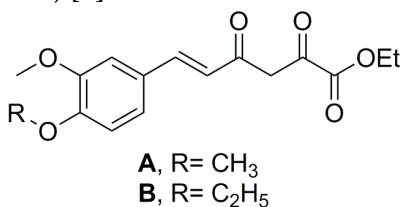


Figure 1. Structures of selected compounds.

2.1 Determination of the binding site in the BSA

Fluorescence spectroscopy is a frequently used technique in the investigation of the binding mode because it is quite simple and has good results in the examination of interaction between small organic molecules and macromolecules such as proteins and DNA.

The tryptophan (Trp) residues of BSA showed fluorescent emission near 360 nm while excited at a 295 nm wavelength and the decrease of intensity of tryptophan emission spectrum was detected while the concentration of investigated compounds was increasing (Figure 2). Competitive experiments with site markers (eosin Y or ibuprofen)

were performed in an identical way as the experiments with BSA and compounds **A** and **B**, while concentration of site marker was the same as the concentration of BSA [4]. After the addition of site markers, they bind to BSA molecule, and the fluorescence intensity decreases.

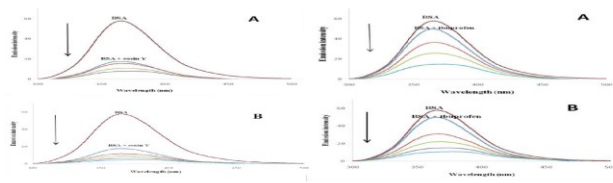


Figure 2. Emission spectra of BSA, BSA + eosin Y/ibuprofen in the absence and the presence of compounds **A** and **B**; [**A**] = 0–15 μM , [**B**] = 0–20 μM , [BSA] = [eosin Y] = [ibuprofen] = 10 μM ; λ_{ex} = 295 nm.

By examining the dependence of $\log[(F_0 - F)/F]$ versus $\log[Q]$, we obtained the values of the binding constant (K_a) and the number of binding sites (n) (Figure 3). The values are presented in Table 1.

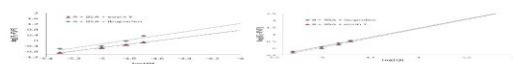


Figure 3. $\log[(F_0 - F)/F]$ dependence of $\log[Q]$.

When the **A** or **B** is added to the ibuprofen–BSA system, the compound must compete with ibuprofen in order to bind to BSA. A similar phenomenon can be observed with eosin Y. According to the results from Table 1, the binding constant is mostly affected in the presence of ibuprofen in comparison with eosin Y for compound **A**, thus compound

A occupies site II of BSA [5]. In the case of compound **B** results suggested that **B** probably binds *via* some different mechanism and can bind to both sites.

Table 1. Binding parameters (K_a and n) for **A** and **B**

system	K_a [M^{-1}]	n	R
A + BSA [4]	1.9×10^6	1.37	0.998
A + BSA + eosin Y	6.25×10^5	1.26	0.998
A + BSA + ibuprofen	1.51×10^7	1.60	0.942
B + BSA [4]	5.0×10^5	1.20	0.996
B + BSA + eosin Y	5.43×10^6	1.33	0.988
B + BSA + ibuprofen	4.5×10^6	1.30	0.993

3. Conclusions

Both compounds reversibly bind to BSA and obtained values for the K_a when site markers are added, suggest that compound **A** binds in the site II, while **B** binds using some other mechanism. The presented results will help in explaining the mechanism of distribution in mimicking physiological conditions and are a good starting point for our further research.

Acknowledgment

This research is funded by the Ministry of Education and Ministry of Science, Technological Development and Innovation, Republic of Serbia, Grants: No. 451-03-47/2023-01/200378.

References

- [1] N. Joksimović, N. Janković, G. Davidović, Z. Bugarčić., *2,4-Diketo esters: Crucial intermediates for drug discovery*, Bioorg. Chem., 105 (2020) 104343-104380.
- [2] F. Zsila., *Subdomain IB Is the Third Major Drug Binding Region of Human Serum Albumin: Toward the Three-Sites Model*, Mol. Pharmaceutics, 10 (2013) 1668–1682.
- [3] B. Lemli, Z. Lomozová, T. Huber, A. Lukács, M. Poór., *Effects of Heme Site (FA1) Ligands Bilirubin, Biliverdin, Hemin, and Methyl Orange on the Albumin Binding of Site I Marker Warfarin: Complex Allosteric Interactions*. Int. J. Mol. Sci., 23 (2022) 14007.
- [4] K. Mihajlović, N. Joksimović, N. Janković, E. Milović, J. Petronijević, I. Filipović, J. Muškinja, N. Petrović, M. Kosanić., *Synthesis, characterization, and biological activity of some 2,4-diketo esters containing dehydrozingerone fragment: DNA and protein binding study*, Bioorg. Med. Chem. Lett., 93 (2023) 129413.
- [5] R. Esteghamat-Panah, H. Hadadzadeh, H. Farrokhpour, J. Simpson, A. Abdolmaleki, F. Abyar., *Synthesis, structure, DNA/protein binding, and cytotoxic activity of a rhodium(III) complex with 2,6-bis(2-benzimidazolyl)pyridine*, Eur. J. Med. Chem. 127 (2017) 958–997.

SR FTIR spectroscopy investigation of Pd@S-CD nanocomposite system effects on biomolecules in cervical carcinoma cells

Vanja Ralić^{1*}, Maja Nešić¹, Anamarija Abu el Rub¹, Tanja Dučić², Branislava Gemović³, Manuel Algarra⁴, Milutin Stepic¹, Lela Korićanac⁵, Jelena Žakula⁵, Marijana Petković¹

¹ University of Belgrade, National Institute of the Republic of Serbia, Vinča Institute of Nuclear Sciences, COHERENCE-Center for light-based science and technologies, Department of Atomic Physics, Mike Petrovića Alasa 12-14, 11000 Belgrade, Serbia; e-mail: vanja.ralic@live.com (V.R.), maki@vin.bg.ac.rs (M.N.), mstepic@vin.bg.ac.rs (M.S.), petkovic.marijana.71@gmail.com (M.P.)

² ALBA-CELLS Synchrotron, Cerdanyola del Vallès, Barcelona, Spain; e-mail: tducic@cells.es (T.D.)

³ University of Belgrade, National Institute of the Republic of Serbia, Vinča Institute of Nuclear Sciences, Department of Theoretical Physics and Condensed Matter Physics, Mike Petrovića Alasa 12-14, 11000 Belgrade, Serbia; e-mail: gemovic@vin.bg.ac.rs (B.G.)

⁴ INAMAT2-Institute for Advanced Materials and Mathematics, Public University of Navarre, Edificio Jerónimo de Ayanz, Campus de Arrosadia, 31006 Pamplona-Iruña, Spain; manuel.algarra@unavarra.es (M.A.)

⁵ University of Belgrade, National Institute of the Republic of Serbia, Vinča Institute of Nuclear Sciences, Department of Molecular Biology and Endocrinology, Mike Petrovića Alasa 12-14, 11000 Belgrade, Serbia; lela@vin.bg.ac.rs (L.K.), pozegaj@vin.bg.ac.rs (J.Z.)

* *Corresponding author*

DOI: 10.46793/ICCB23.467R

Abstract

Nanocomposite system formulated from surface-modified S-doped carbon dot (S-CD) nanoparticle with a potential metallodrug, palladium(II) complex, dichloro(1,2-diaminocyclohexane)palladium(II), [Pd(dach)Cl₂] (Pd@S-CD), was investigated as a model system for the treatment of cervical carcinoma (HeLa) cells. To examine the intracellular biochemical effects induced by the Pd@S-CD, we used Synchrotron Radiation-based Fourier-transform infrared spectroscopy (SR FTIR). SR FTIR spectroscopy was employed to investigate the alterations in cellular components' biochemical composition and secondary structure upon exposure to Pd@S-CD. Spectral analysis, complemented by statistical techniques, revealed changes in biomolecules, lipids, proteins, nucleic acids, and carbohydrates caused by the treatment with Pd@CDs. These results and the increased cytotoxicity of the system demonstrate its high anti-cervical cancer therapeutic potential.

Keywords: transition metal complex, Synchrotron Radiation, Fourier Transform Infrared Spectroscopy, nanocomposite

1. Introduction

Palladium(II) complexes are one of the leading contenders for replacing cisplatin in cancer treatment due to the similarity of their metal center to platinum(II) complexes. The Pd(II) complexes with different ligands can interact with biomolecular targets in diverse ways, thus providing a high potential for developing new and more efficient anticancer drugs. Substituted polyamines have been shown to coordinate efficiently with both Pd(II) and to act as modulators of the hydrophilic/lipophilic properties of the resulting chelates, thus improving their administration and bioavailability [1]. To improve the efficacy of applied metallodrug, they can be combined with various nanocarriers, which preserve the activity of a drug or can affect the intracellular target molecules [2]. As nanocarriers, various nanoparticles are tested. Among them, those based on carbon, such as carbon dots (CDs), are good candidates because of their physicochemical properties and biocompatibility, which can increase the cellular uptake of a drug. For instance, cisplatin combined with S- or N-doped CDs (cis-Pt@S, N-CDs) was demonstrated to overcome cisplatin resistance in cis-Pt-resistant ovarian cancer cells [3]. The intracellular effects that transition metal complexes induce in cells, which lead to their cytostatic effects, which include the entire cellular regulatory system, have yet to be fully elucidated. Synchrotron Radiation Fourier Transform Infrared Spectroscopy (SR FTIR) has a high potential, spatial resolution, and sensitivity, a highly brilliant infrared light source that provides higher quality spectra at a cellular level [4]. Therefore, SR FTIR can provide information about the drug's effect on individual cellular biomolecules without their isolation from the cells, and we have applied this approach to elucidate biochemical changes in cervical cancer, HeLa, cells induced by Pd@S-CD.

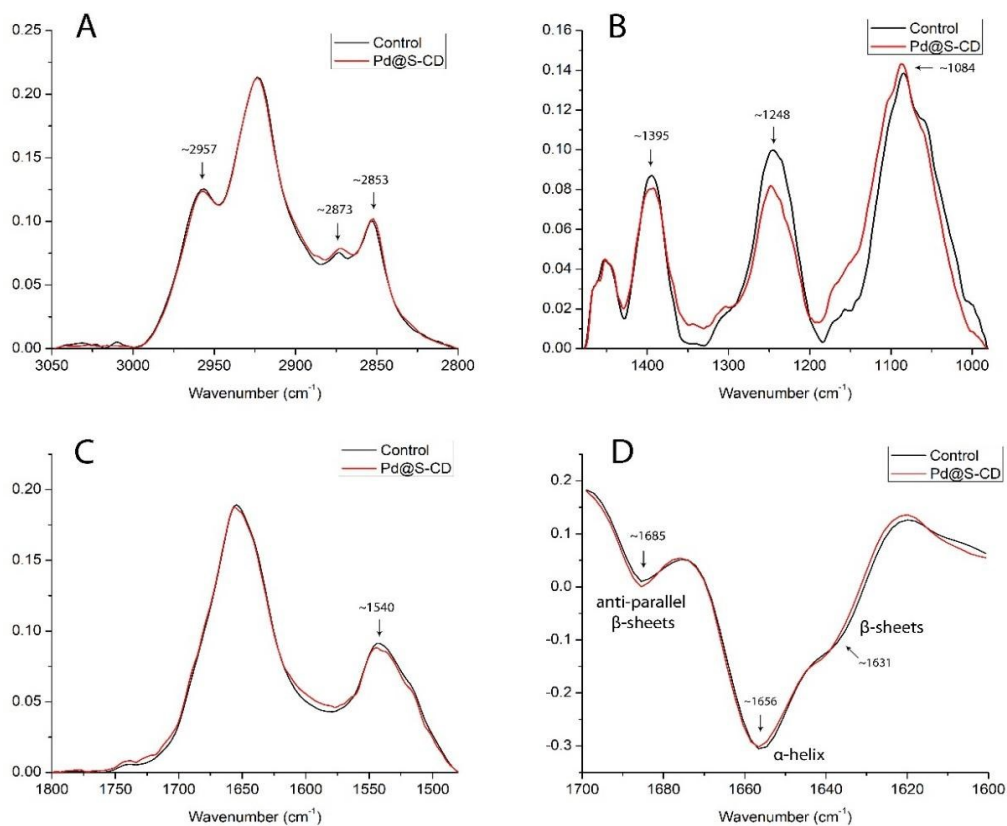
2. Methods

HeLa cells were treated with Pd@S-CD for 48 h. Pd(II) complex concentration was 85 μM , and S-CD 20 $\mu\text{g/mL}$. After the treatment, cell cytotoxicity was determined by the Sulforhodamine B (SRB) assay. Changes in cell biomolecules were analyzed by SR FTIR spectroscopy (Synchrotron ALBA, MIRAS beamline, Barcelona, Spain) with cells seeded and lyophilized on CaF_2 glass support [5]. Spectra for treated and control cells were collected in the 4000–900 cm^{-1} mid-infrared range. Spectral analysis, including rubber band baseline correction and vector normalization for every single cell, was implemented for three different areas: 3050–2800 cm^{-1} lipid area, 1800–1480 cm^{-1} proteins and esters, and 1480–900 cm^{-1} nucleic acids and carbohydrate region. The second derivative (17 smoothing points, third polynomial order, and vector normalization) was determined for the Amide I protein region (1700–1600 cm^{-1}). The principal component analysis (PCA) for each data set was performed.

3. Results and discussion

Pd@SCD treatment of HeLa cells left 70% viable cells after 48 h. This viability was targeted to enable the study of intracellular biochemical changes in viable cells.

Significant spectral differences were present in all inspected areas: lipids, proteins, nucleic acids, and carbohydrates. The average spectra of those regions and the second derivative of the Amide I average spectra are shown in Figure 1, whereas the most affected signals are listed in Table 1. The lipid region is affected in CH₂ and CH₃ stretching assigned bands, while the protein region differs in all main secondary



structure bands, as indicated in Table 1.

Figure 1. The average FTIR spectra of Pd (II) treated (red) and control (black) HeLa cells in the lipid (A), nucleic acid and carbohydrate (B), and protein (C) regions are presented. The second derivative and vector-normalized spectra of the averaged FTIR spectra of Amide I in the 1700-1600 cm⁻¹ region is shown (D).

The most remarkable differences can be seen in the carbohydrate and nucleic acid region (1480–980 cm⁻¹), implying that Pd@S-CD affects these macromolecules the most. In this region, bands that contributed the most to the overall spectral differences were assigned to phosphate and P-O-C stretching and COO⁻ symmetric stretching. These changes could be a consequence of direct nanocomposite-nucleic acid interactions, or a result of downstream changes caused by nanocomposite-protein interactions.

Table 1. Vibration frequencies and band assignments of the regions with the most significant differences between Pd@S-CD treated and control HeLa cells.

Region	Wavenumber (cm ⁻¹)	Band assignment
Lipid	2957	asymmetric CH ₃ stretching
	2873	symmetric CH ₃ stretching
	2853	symmetric CH ₂ stretching
Protein	1685	anti-parallel β -sheets
	1656	α -helix
	1631	β -sheets
	1540	Amide II α -helix
Carbohydrates and nucleic acids	1395	COO ⁻ symmetric stretching
	1248	asymmetric phosphate stretching
	1106	symmetric P-O-C stretching
	1084	symmetric phosphate stretching

3. Conclusions

In this work, we have emphasized the complexity of the intracellular interactions of the transition metal complexes and identified intracellular biochemical processes that might lead to tumor elimination. Conformational modifications in the main classes of macromolecules were experimentally documented.

Acknowledgement

The research was funded by the Ministry of Science, Technological Development and Innovation of the Republic of Serbia (451-03-47/2023-01/200017), the Spanish Ministry of Science and Innovation (MCIN/AEI/10.13039/501100011033) through project PID2021-122613OB-I00. SR FTIR experiment was granted at the MIRAS beamline at ALBA Synchrotron with the collaboration of ALBA staff (experiment No. 2022025758).

References

- [1] M.L. González, J.M. Tercero, A. Matilla, J. Niclós-Gutiérrez, M.T. Fernández, M.C. López, C. Alonso, S. González, cis-Dichloro(α,ω -diamino carboxylate ethyl ester)palladium(II) as Palladium(II) versus Platinum(II) Model Anticancer Drugs: Synthesis, Solution Equilibria of Their Aqua, Hydroxo, and/or Chloro Species, and in Vitro/in Vivo DNA-Binding Properties, *Inorg. Chem.* 36 (1997) 1806–1812.
- [2] C. Azevedo, M.H. Macedo, B. Sarmento, Strategies for the enhanced intracellular delivery of nanomaterials, *Drug Discov. Today*. 23 (2018) 944–959.
- [3] T. Dučić, C.S. Alves, Ž. Vučinić, J.M. Lázaro-Martínez, M. Petković, J. Soto, D. Mutavdžić, M. Valle Martínez de Yuso, K. Radotić, M. Algarra, S, N-doped carbon dots-based cisplatin delivery system in adenocarcinoma cells: Spectroscopical and computational approach, *J. Colloid Interface Sci.* 623 (2022) 226–237.
- [4] I. Martínez-Rovira, O. Seksek, J. Puxeu, J. Gómez, M. Kreuzer, T. Dučić, M.J. Ferreres, M. Artigues, I. Yousef, Synchrotron-based infrared microspectroscopy study on the radiosensitization effects of Gd nanoparticles at megavoltage radiation energies, *Analyst*. 144 (2019) 5511–5520.
- [5] I. Yousef, L. Ribó, A. Crisol, I. Šics, G. Ellis, T. Ducic, M. Kreuzer, N. Benseny-Cases, M. Quispe, P. Dumas, S. Lefrançois, T. Moreno, G. García, S. Ferrer, J. Nicolas, M.A.G. Aranda, MIRAS: The Infrared Synchrotron Radiation Beamline at ALBA, *Synchrotron Radiat. News*. 30 (2017) 4–6.

The effects of a selected methoxy substituted chalcone in human melanoma cells irradiated with γ -rays

Otilija Keta^{1,*}, Vladana Petković¹, Neda Đorđević¹, Miloš Đorđević¹, Branka Ivković², Vladimir Dobričić²

¹ University of Belgrade, Vinča Institute of Nuclear Sciences - National Institute of the Republic of Serbia, Department of Molecular Biology and Endocrinology, Mike Petrovića-Alas 12-14, 11001 Belgrade, Serbia; e-mail: otilijak@vin.bg.ac.rs, vladanap@vin.bg.ac.rs, neda@vin.bg.ac.rs, mdjordjevic@vin.bg.ac.rs

² University of Belgrade, Faculty of Pharmacy, Department of Pharmaceutical Chemistry, Vojvode Stepe 450, 11000 Belgrade, Serbia; e-mail: branka.ivkovic@pharmacy.bg.ac.rs, vladimir.dobricic@pharmacy.bg.ac.rs

* Corresponding author

DOI: 10.46793/ICCBIG23.471K

Abstract: Given the well-established potential of chalcones in modulating the response of cancer cells to therapeutic interventions, coupled with the growing imperative to enhance their biological attributes, the objective of this study was to synthesize a methoxy-substituted chalcone (OCH₃) and assess its capacity to amplify the inhibitory effects of radiation in melanoma cells known for their resistance to radiotherapy. The A375 melanoma cells were subjected to a clinically relevant dose of 2 Gy gamma irradiation. OCH₃ was employed either as a standalone treatment or in conjunction with irradiation. The obtained results unveiled the substantial radiosensitizing potential of OCH₃ within this specific cell line. Our subsequent investigations will be designed to investigate the underlying mechanisms that contribute to the radiosensitizing properties of OCH₃. Moreover, we intend to evaluate the efficacy of OCH₃ against other types of radioresistant cancer cells. The presented data not only illuminates the enhanced therapeutic possibilities offered by OCH₃ but also highlights its potential as a valuable agent in addressing a wider array of challenging malignancies.

Keywords: methoxy substituted chalcone, melanoma, irradiation

1. Introduction

Effective anti-cancer treatments necessitate a comprehensive assessment through drug screening protocols to ensure their safety and efficacy [1]. Over recent years, there has been a significant focus on phytochemicals, including chalcones, owing to their cost-effectiveness, relatively low toxicity, and ability to target molecular pathways implicated in carcinogenesis [2]. Moreover, chalcones extend beyond their anti-tumor properties and have demonstrated a versatile range of beneficial effects. These encompass anti-

inflammatory, antioxidant, anti-microbial, antidiabetic, and neuroprotective potentials, as documented [3, 4], in addition to their established anti-tumor activities.

To increase the biological potency of chalcones, enhancing their chemical attributes continues to be a relevant approach [5]. The combination of medical therapies can heighten the effectiveness of treatments and is frequently necessary in real-world medical scenarios. Our prior research has shown promising inhibitory effects of recently developed methoxy-substituted chalcone in melanoma cells. In this work, our objective was to explore the potential of the synthesized chalcone to enhance the sensitivity to radiation therapy, thereby investigating its radiosensitizing potential.

2. Experimental

2.1 Synthesis of OCH3

The synthesis of metoxychalcone was achieved by ClaisenSchmidt condensation of 2-hydroxyacetophenone with the 2-methoxybenzaldehyde (Figure 1). The reaction is a base-catalyzed aldol condensation that takes place at room temperature.

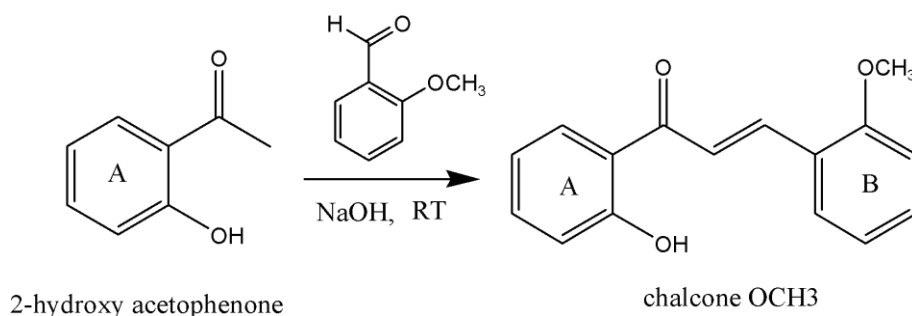


Figure 1. The synthesis of OCH3 metoxychalcone.

2.2 Cell cultivation, OCH3 treatment and irradiation conditions

The human A375 malignant melanoma cell line was obtained from the American Type Culture Collection (ATCC, Rockville, MD, USA). These cells were cultivated in RPMI 1640 medium, supplemented with 10% fetal bovine serum (FBS), penicillin/streptomycin, and L-glutamine. The cell cultures were maintained at a temperature of 37°C within a humidified atmosphere containing 5% CO₂ (Heraeus, Hanau, Germany). Prior to exposure to treatments, the cells were allowed to grow in the culture medium for a period of 24 hours. After incubation with OCH3 for an additional 24 h cells were exposed to irradiation with γ -rays. Stock solutions of the chalcone compound were appropriately diluted in the culture medium to achieve the desired final concentration. The concentration of dimethyl sulfoxide (DMSO) in the treated samples did not exceed 0.1% [6].

In experiments involving irradiation, the cells were exposed to ⁶⁰Co γ -rays (CIRUS-Cis Biointernational) while positioned vertically at room temperature. These irradiation

procedures were carried out at the Vinca Institute of Nuclear Sciences in Belgrade, Serbia. Across all experiments, clinically relevant irradiation dose of 2 Gy was employed [7], with a dose rate of approximately 1 Gy per minute.

2.3 Survival of A375 melanoma cells after combined treatment with OCH3 and γ -irradiation

The procedure for clonogenic assay was performed according to the standard procedure [8]. The results have shown that OCH3 exhibited a notable inhibitory effect on the viability of A375 cells, observed 14 days following the treatment. The survival rate of A375 cells exposed to OCH3 was approximately 40% as compared to the untreated control (Figure 2A). Furthermore, the application of irradiation treatment also yielded a significant decrease in colony count, resulting in a cell survival rate of around 60%. This observation aligns with previously reported data that underscores the heightened radioresistance of these cells, as documented in studies [9,10].

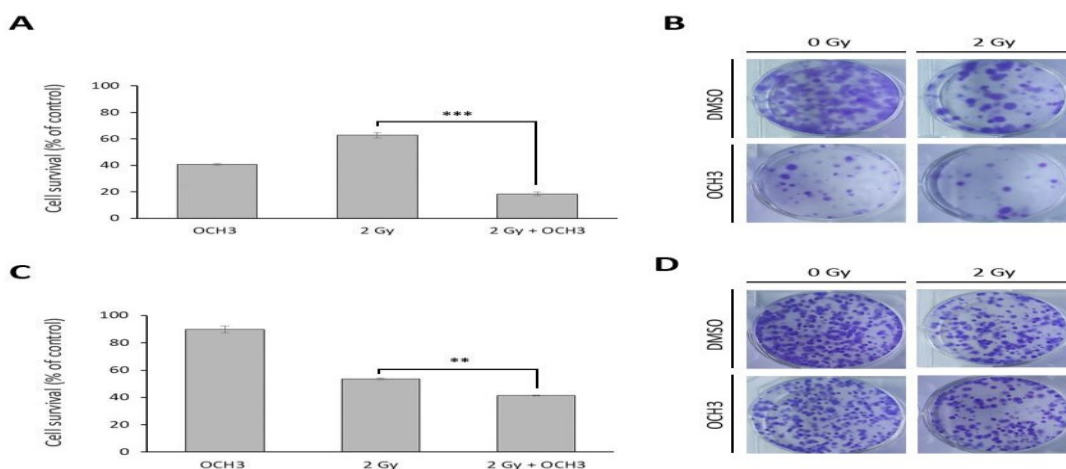


Figure 2. Effects of OCH3 and 2 Gy γ -irradiation on survival of A375 melanoma cells (A, B). Clonogenic survival was evaluated 14 days after the treatments. Statistical significance was determined by Student's t-test and expressed as: * $p < 0.05$; ** $p < 0.01$; *** $p < 0.001$. (*- Statistical significance compared to irradiation).

The combination treatment of OCH3 and irradiation invoked an even more robust, statistically significant decrease in colony count, being less than 20% of the control value. The decline in cell survival was significant when compared to irradiation alone ($p < 0.001$) Moreover, there was a distinct diminution in the size of the colonies subsequent to treatment with both agents, as depicted in Figure 2B.

3. Conclusions

The findings from this preliminary study have illuminated the promising radiosensitizing capabilities of the recently developed methoxy-substituted chalcone within melanoma cells. Future experiments will aim to investigate the radiosensitizing potential of this compound across diverse types of cancer cells as well as the mechanisms underlying the observed radiosensitizing effects.

Acknowledgment

This research is funded by the Ministry of Education and Ministry of Science, Technological Development and Innovation, Republic of Serbia, Grants: No. 451-03-47/2023-01/ 200161 and 451-03-47/2023-01/200017.

References

- [1] H.Y.K. Yip, A., *Signaling Pathways in Cancer: Therapeutic Targets, Combinatorial Treatments, and New Developments*, Cells, 16 (2021) 659.
- [2] C. Zhuang, W. Zhang, C. Sheng, W. Zhang, C. Xing, Z. Miao., *Chalcone: A Privileged Structure in Medicinal Chemistry*, Chemical Reviews, 117 (2017) 7762-7810.
- [3] Y.F. Chen, S.N. Wu, J.M. Gao, Z.Y. Liao, Y.T. Tseng, F. Fülöp, F.R. Chang, Y.C. Lo., *The Antioxidant, Anti-Inflammatory, and Neuroprotective Properties of the Synthetic Chalcone Derivative AN07*, Molecules, 25 (2020) 2907.
- [4] B. Salehi, C. Quispe, I. Chamkhi, N. El Omari, A. Balahbib, J. Sharifi-Rad, A. Bouyahya, M. Akram, M. Iqbal, A.O. Docea, C. Caruntu, G. Leyva-Gómez, A. Dey, M. Martorell, D. Calina, V. López, F. Les., *Pharmacological Properties of Chalcones: A Review of Preclinical Including Molecular Mechanisms and Clinical Evidence*, Frontiers in Pharmacology, 11 (2021) 592654.
- [5] R. Michalkova, L. Mirossay, M. Kello, G. Mojziso, J. Baloghova, A. Podracka, J. Mojzis., *Anticancer Potential of Natural Chalcones: In Vitro and In Vivo Evidence*, International Journal of Molecular Sciences, 24 (2023) 10354.
- [6] M. Moskot, J. Jakóbkiewicz-Banecka, A. Kloska, E. Piotrowska, M. Narajczyk, M. Gabig-Cimińska., *The Role of Dimethyl Sulfoxide (DMSO) in Gene Expression Modulation and Glycosaminoglycan Metabolism in Lysosomal Storage Disorders on an Example of Mucopolysaccharidosis*, International journal of molecular sciences, 20 (2019) 304.
- [7] Y. Kuwahara, T. Oikawa, Y. Ochiai, M.H. Roudkenar, M. Fukumoto, T. Shimura, Y. Ohtake, Y. Ohkubo, S. Mori, Y. Uchiyama, M. Fukumoto., *Enhancement of autophagy is a potential modality for tumors refractory to radiotherapy*, Cell death & disease, 2 (2011) e177.
- [8] N.A. Franken, H.M. Rodermond, J. Stap, J. Haveman, C. van Bree., *Clonogenic assay of cells in vitro*, Nature protocols, 1 (2006) 2315-2319.
- [9] F. Buontempo, E. Orsini, I. Zironi, L. Isolan, A. Cappellini, S. Rapino, A. Tartari, D. Mostacci, G. Cucchi, A.M. Martelli, M. Sumini, G. Castellani, *Enhancing radiosensitivity of melanoma cells through very high dose rate pulses released by a plasma focus device*, PLoS One, 13 (2018) e0199312. Erratum in: PLoS One. 13 (2018) e0204692.
- [10] M. Pedrosa-Rivera, M.J. Ruiz-Magaña, P. Álvarez, I. Porras, J. Praena, M.P. Sabariego, U. Köster, M. Haertlein, V.T. Forsyth, T. Soldner, J.C. Ramírez, C. Jover, D. Jimena, J.L. Osorio, I. Postuma, C. Ruiz-Ruiz, *Applied radiation and isotopes : including data, instrumentation and methods for use in agriculture, industry and medicine*, 163 (2020) 109205.

***In silico* estimation of COX-2 and 5-LOX inhibitory potential of some novel thiourea derivatives of naproxen**

Nikola V. Nedeljković^{1*}, Vladimir D. Dobričić², Marina Ž. Vesović¹, Ana S. Živanović¹, Gordana P. Radić¹, Zorica B. Vujić², Miloš V. Nikolić¹

¹ University of Kragujevac, Faculty of Medical Sciences, Department of Pharmacy, Svetozara Markovića 69, 34000 Kragujevac, Serbia; e-mail: nikola.nedeljkovic@medf.kg.ac.rs, marina.mijajlovic@medf.kg.ac.rs, ana.zivanovic@medf.kg.ac.rs, vasic_gordana@yahoo.com, milos.nikolic@medf.kg.ac.rs

² University of Belgrade, Faculty of Pharmacy, Department of Pharmaceutical Chemistry, Vojvode Stepe 450, 11221 Belgrade, Serbia; e-mail: vladimir.dobricic@pharmacy.bg.ac.rs, zorica.vujic@pharmacy.bg.ac.rs

* *Corresponding author*

DOI: 10.46793/ICCB123.475N

Abstract: Design of dual COX-2/5-LOX inhibitors can be considered an adequate approach in the development of new anti-inflammatory drugs with less pronounced side effects. The aim of the present research was to examine the binding potential of the seven newly designed thiourea derivatives of naproxen towards COX-2 and 5-LOX. The binding analysis of ligand conformations was performed by OEDocking 3.2.0.2 software. The binding potential assessment revealed that thiourea derivatives of naproxen exhibited a comparable binding affinity as naproxen towards COX-2. The highest number of key binding interactions with 5-LOX was formed by compound **5**, whereas compound **6** established the most stable complex (-9.29 kcal/mol). According to the obtained results, derivatives **5** and **6** can be considered as dual COX-2/5-LOX inhibitors with potential anti-inflammatory activity. However, none of the investigated compounds were able to form three hydrogen bonds with the binding site of COX-2, as well as three key hydrogen bonds with the active site of 5-LOX.

Keywords: naproxen, thiourea, OEDocking, COX-2, 5-LOX

1. Introduction

Naproxen and other aroyl propionic acid derivatives cause significant gastrointestinal toxicity due to non-selective inhibition of the cyclooxygenase enzymes (COX-1 and COX-2), so it is important to mask the free carboxyl group of the parent drug [1]. 5-lipoxygenase (5-LOX) is also involved in the metabolism of prostaglandins and catalysis of lipid peroxidation by producing lipid peroxides that lead to inflammatory response [2]. Therefore, the design of dual COX-2/5-LOX inhibitors can be considered an adequate

approach in the development of new anti-inflammatory drugs with less pronounced side effects.

Encouraged by the results of previously published research [3], we decided to design seven new thiourea derivatives of naproxen with aromatic amines and amino acids. The aim of this research was to use a molecular docking analysis to examine the binding potential of these molecules towards COX-2 and 5-LOX.

2. Materials and Methods

Crystal structures obtained from the Protein Data Bank (<http://www.rcsb.org/>) were 3NT1 (naproxen bound to COX-2) and 6N2W (NDGA bound to 5-LOX). For the preparation of target enzymes MAKE Receptor 3.2.0.2 software was used [4]. The multiconformer data sets for each tested compound were prepared using OMEGA 2.5.1.4 [5,6]. Then, the binding analysis of ligand conformations into the active sites of target enzymes was performed by OEDocking 3.2.0.2 software [7–9] with the fast rigid exhaustive docking (FRED) tool.

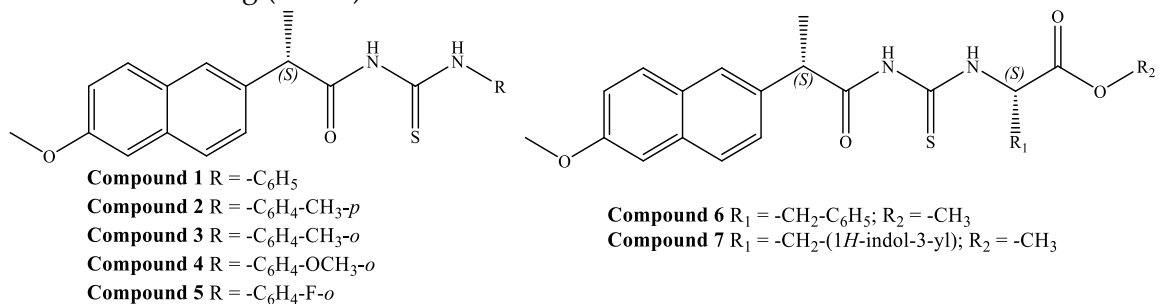


Figure 1. Structures of tested compounds.

3. Results and Discussion

Carbonyl and hydroxyl oxygen atoms of naproxen's carboxyl group interact as proton acceptors with a guanidine group of residue ARG120. Also, residue TYR355 with its phenolic group as hydrogen bond donor establishes hydrogen bond with carbonyl oxygen atom of the naproxen's carboxyl group. It can be observed that carbonyl and thiocarbonyl groups of aromatic amine derivatives **1-3**, and **5** (proton acceptors) establish a double hydrogen bond with residue ARG120 (Figure 2A). Carbonyl oxygen atom of derivative **4** (hydrogen bond acceptor) forms a double hydrogen bond with residue ARG120, whereas methoxy group attached to benzene ring in the side chain of the compound is involved in the formation of an additional hydrogen bond (proton acceptor) with ARG120. The phenylalanine methyl ester derivative (**6**) via thiocarbonyl group forms a single hydrogen bond (proton acceptor) with residue TYR355, while the thiourea nitrogen atom of tryptophan methyl ester derivative (**7**) as proton acceptor establishes a hydrogen bond with TYR355.

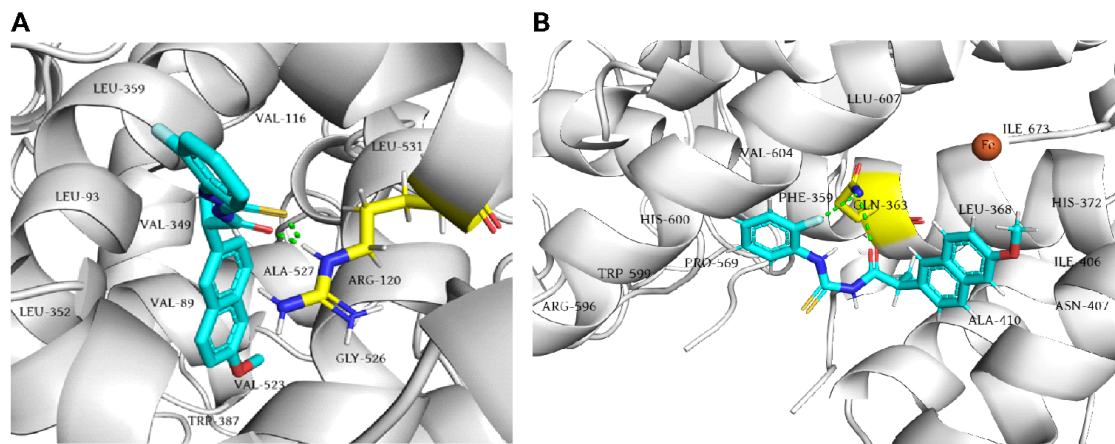


Figure 2. Molecular docking of compound **5** into the COX-2 (**A**) and 5-LOX (**B**) enzymes.

Taking into consideration the docking scores of aromatic amine derivatives (**1**: -14.53 kcal/mol; **2**: -14.57 kcal/mol; **3**: -14.27 kcal/mol; **4**: -12.77 kcal/mol; **5**: -14.62 kcal/mol), it can be observed that their values are lower but comparable to naproxen (-13.13 kcal/mol), with the exception of derivative **4**. Comparable docking score can be associated with the ability of aromatic rings of the tested compound's side chains to form additional binding interactions, whereby methoxynaphthalene core of these derivatives was docked into the active site of COX-2 in a similar fashion to naproxen. In contrast, ester derivatives have significantly higher docking scores (**6**: -11.28 kcal/mol; **7**: -8.99 kcal/mol) in comparison to naproxen. Regardless of the hydrogen bond formed by derivatives **6** and **7** with TYR355, the occurrence of sterically unfavorable interactions with VAL116, and in particular with ARG120 affects the higher value of docking scores. The results of this *in silico* research showed that none of the tested molecules have the ability to chelate the iron ion in the binding site of the 5-LOX enzyme, so they can be considered as potential competitive non-chelating inhibitors. It was observed that none of the tested molecules was able to achieve the key hydrogen interactions that the co-crystal NDGA forms with the residues ARG596, ILE673, and HIS600. Namely, all derivatives form one hydrogen bond via the carbonyl oxygen of the amide group with GLN363, except for derivatives **2** and **3**, which failed to form any hydrogen bond. The highest number of key binding interactions was formed by compound **5** (14 interactions) (Figure 2B). Namely, the naphthalene nucleus of compound **5** forms a double π -alkyl type interaction with the ALA410 residue. The same structural component of the tested ligand established simultaneously one π -alkyl contact with the tertiary carbon and one π - σ contact with the methyl group of the LEU368 side chain. The benzene ring of *o*-fluoroaniline formed a double π - π interaction with the π -electrons of the PHE359 and TRP599 aromatic cores. In terms of free binding energy values, all tested compounds (except derivatives **2** and **7**) achieved energies comparable to NDGA (-8.77 kcal/mol), but not to zileuton (-10.67 kcal/mol). This showed that molecules with the ability to chelate iron ion form more stable complexes with 5-LOX. Based on the free binding energy values, compound **6** established the most stable complex with the target

enzyme (-9.29 kcal/mol).

3. Conclusions

Molecular docking simulations suggest high binding potential of derivatives **5** and **6** towards COX-2 and 5-LOX. However, none of the investigated compounds were able to form three hydrogen bonds with ARG120 and TYR355 of COX-2, as well as three key hydrogen bonds with the active site of 5-LOX, like co-crystallized ligands.

Acknowledgment

This research is funded by the Ministry of Education and Ministry of Science, Technological Development and Innovation, Republic of Serbia, Grants: No. 451-03-47/2023-01/200111 and No. 451-03-47/2023-01/200161.

References

- [1] A.A. Elhenawy, L.M. Al-Harbi, G.O. Moustafa, M.A. El-Gazzar, R.F. Abdel-Rahman, A.E. Salim., *Synthesis, comparative docking, and pharmacological activity of naproxen amino acid derivatives as possible anti-inflammatory and analgesic agents*, *Drug design, development and therapy*, 13 (2019) 1773-1790.
- [2] P. Krieg, G. Fürstenberger., *The role of lipoxygenases in epidermis*, *BBA Molecular and Cell Biology of Lipids*, 1841 (2014) 390–400.
- [3] N. Nedeljković, V. Dobričić, J. Bošković, M. Vesović, J. Bradić, M. Anđić, A. Kočović, N. Jeremić, J. Novaković, V. Jakovljević, Z. Vujić, M. Nikolić., *Synthesis and Investigation of Anti-Inflammatory Activity of New Thiourea Derivatives of Naproxen*, *Pharmaceutics*, 16 (2023) 666.
- [4] MAKE Receptor 3.2.0.2: OpenEye Scientific Software, Santa Fe, USA. Available online: https://docs.eyesopen.com/applications/oedocking/make_receptor/make_receptor_setup.html (accessed on 24 July 2023).
- [5] OMEGA 2.5.1.4: OpenEye Scientific Software, Santa Fe, NM. Available online: <http://www.eyesopen.com/> (accessed on 24 July 2023).
- [6] P.C.D. Hawkins, A.G. Skillman, G.L. Warren, B.A. Ellingson, M.T. Stahl., *Conformer Generation with OMEGA: Algorithm and Validation Using High Quality Structures from the Protein Databank and the Cambridge Structural Database*, *Journal of Chemical Information and Modeling*, 50 (2010) 572–584.
- [7] FRED 3.2.0.2: OpenEye Scientific Software, Santa Fe, NM. Available online: <https://www.eyesopen.com/> (accessed on 24 July 2023).
- [8] M. McGann., *FRED pose prediction and virtual screening accuracy*, *Journal of Chemical Information and Modeling*, 51 (2011) 578–596.
- [9] M. McGann., *FRED and HYBRID docking performance on standardized datasets*, *Journal of Computer-Aided Molecular Design*, 26 (2012) 897–906.

Molecular docking study of designed N-myristoyl transferase inhibitors

Andela D. Gogić¹, Marina Ž. Vesović², Miloš V. Nikolić², Andriana M. Bukonjić²,
Dušan Lj. Tomović², Nikola V. Nedeljković^{2*}

¹ University of Kragujevac, Faculty of Medical Sciences, Department of Medical statistics and informatics, Svetozara Markovića 69, 34000 Kragujevac, Serbia; e-mail: andjelica97@hotmail.com

² University of Kragujevac, Faculty of Medical Sciences, Department of Pharmacy, Svetozara Markovića 69, 34000 Kragujevac, Serbia; e-mail: marina.mijajlovic@medf.kg.ac.rs, milos.nikolic@medf.kg.ac.rs, andriana.bukonjic@medf.kg.ac.rs, dusantomovic@medf.kg.ac.rs, nikola.nedeljkovic@medf.kg.ac.rs

* Corresponding author

DOI: 10.46793/ICCB123.479G

Abstract: N-myristoyl transferase has a key role in the myristoylation of vital proteins and is necessary for the growth and synthesis of material for the survival of various fungi. Due to the difference in the structure of fungal and mammalian N-myristoyl transferase, the crystal structure of the N-myristoyl transferase originating from *Candida albicans* was used as the target molecule. The present *in silico* study aims to design compounds, benzofuran derivatives, and simulate the interactions of the compounds and the amino acid sequences of the active center N-myristoyl transferases from *Candida albicans* using the molecular docking method. The highest number of significant binding interactions is realized by the derivative **4**. Affinity toward the N-myristoyl transferase active site was very similar to the co-crystallized ligand, and important hydrogen interactions were retained. Based on the obtained results of molecular docking, it can be concluded that derivative **4** has the potential to inhibit N-myristoyl transferase, on which future research of its antifungal activity can be based.

Keywords: N-myristoyl transferase, molecular docking, benzofuran derivatives

1. Introduction

N-myristoyl transferase (NMT) is a member of the GNAT (Guanine nucleotide-binding protein) or G-protein superfamily and consists of an N-terminal and C-terminal region. The N-terminal region forms the myristoyl-CoA binding site while the C-terminal region forms the major part of the peptide binding site [1]. N-myristoyl transferase is a ubiquitous enzyme in eukaryotes that catalyzes the transfer of a myristoyl group from myristoyl-CoA to the N-terminal glycine of a protein substrate. Myristoylation occurs in two steps: methionine aminopeptidase removes the methionine initiator residue on the peptide substrate. Then, the resulting peptide with a terminal

glycine moiety becomes the substrate for NMT activity (Figure 1). Genetic experiments have shown that many fungal species such as *Candida albicans* and *Cryptococcus neoformans* cannot survive without NMT [2].

In recent years, infections caused by pathogenic fungi are becoming more common, especially in immunocompromised patients. *Candida albicans* is the most frequently identified *Candida* species and is one of the leading causes of hospital-acquired infections. Currently, conventional antifungal agents have a very limited spectrum of action with an inadequate pharmacokinetic profile and serious interactions with other drugs. Hence, research and development of new drugs with a more attractive mode of action are being pursued [3].

The purpose of the present *in silico* study was to design benzofuran derivatives, based on the results of SAR (structure-activity relationship) studies, and then to simulate their binding interactions with the active site of N-myristoyl transferases using the molecular docking method.

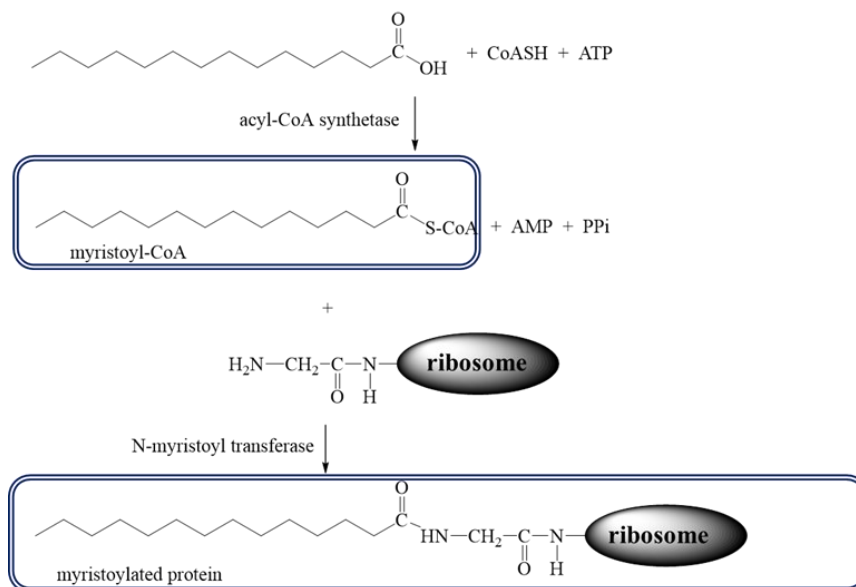


Figure 1. Mechanism of action N-myristoyl transferase.

2. Materials and methods

Optimizing energy of the design compounds was carried out using the program Chem3D Ultra 7.0.[4]. The crystal structure of N-myristoyl transferase in a complex with a non-peptide inhibitor (PDB ID: 1IYL) was downloaded from the Protein Data Bank. The preparation of the target molecule was performed in the Discovery Studio Visualizer 17.2.0.16349 [5], by removing units B, C, and D, whereas unit A was used in this molecular docking study. A focused semi-flexible molecular docking method was carried out using the AutoDockVina software [6]. The search area was set as a grid box size of 30 x 28 x 32 points and a spacing of 0.375 Å, based on the position of the co-crystallized ligand. The best fitted conformation of the design compounds was visualized using Discovery Studio Visualizer and PyMol 2.4.1. [7].

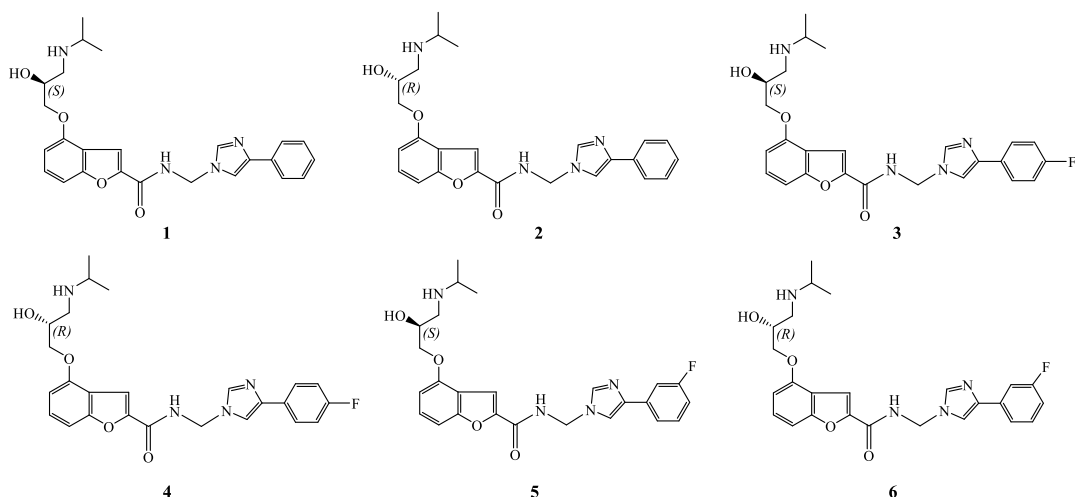


Figure 2. The structures of the design compounds.

3. Results and discussion

N-myristoyl transferase plays an important role in the myristoylation of vital proteins and is necessary for the growth and synthesis of material for the survival of various fungi. Due to the difference in the active sites of fungal and mammalian N-myristoyl transferase, and the difference in the binding manner of the potential inhibitor, the crystal structure of the N-myristoyl transferase originating from *Candida albicans* was used as the target molecule in this research.

The free binding energy values of all six designed compounds were negative, indicating that all compounds (1-6) spontaneously bind to the target enzyme (-9.2 kcal/mol, -9.3 kcal/mol, -9.4 kcal/mol, -9.5 kcal/mol, -9.4 kcal/mol, and -9.3 kcal/mol, respectively). The binding potency, in addition to the Gibbs free energy of binding, is influenced by the number and type of significant interactions that investigated compounds establish with the residues of the N-myristoyl transferase active site. The results of the molecular docking indicate the largest number of formed interactions were hydrophobic in nature, with all compounds forming interactions with Leu394, Tyr225, and Tyr354. The highest number of key interactions was realized by the derivative 4 (Figure 3). The phenyl core of derivative 4 formed hydrophobic interactions including π -alkyl type with Leu394 and π - π T shaped with residue Tyr354, while residue Leu415 participates in the formation of significant π - σ interaction with triazole heterocycle of this compound. Triazole heterocycle also formed π - π stacked interaction with Tyr225. Affinity toward the N-myristoyl transferase active site was very similar to co-crystallized ligand and important hydrogen bonds were retained. Namely, the amide linker group of derivative 4 formed a conventional hydrogen bond with Tyr225 as an H-acceptor and also formed an additional π -donor hydrogen bond. The obtained complex was additionally stabilized by the formation of a π - σ interaction of the residue Tyr225 with the side chain and a π - π T-shaped interaction with the benzofuran core of the tested compound. On the basis of the Gibbs free energy of binding, derivative 4 forms a more stable complex with N-

myristoyl transferase (-9.5 kcal/mol), compared to other design compounds, which makes it particularly interesting for future research.

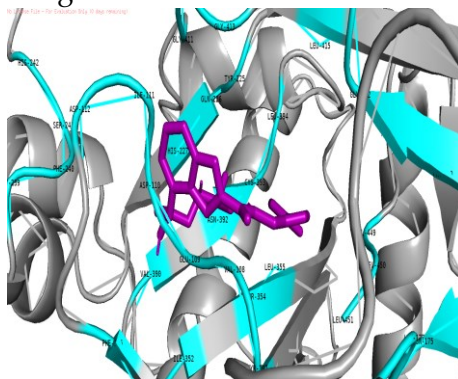


Figure 3. Molecular docking of derivative 4 into the active site of N-myristoyl transferase.

3. Conclusions

According to obtained results of molecular docking, it can be concluded that derivative 4 has the potential of inhibiting N-myristoyl transferase, on which future research of its antifungal activity can be based.

Acknowledgment

This research is funded by the Ministry of Education and Ministry of Science, Technological Development and Innovation, Republic of Serbia, Grants: No. 451-03-47/2023-01/200111

References

- [1] Farazi TA, Waksman G, Gordon JI. *The biology and enzymology of protein N-myristoylation*. J Biol Chem, 276 (2001) 39501-4.
- [2] Yuan M, Song ZH, Ying MD, et al. *N-myristoylation: from cell biology to translational medicine*. Acta Pharmacol Sin, (2020) 1-11.
- [3] Kim JY. *Human fungal pathogens: Why should we learn?* J Microbiol, 54 (2016) 145-8.
- [4] E. R. Buntrock, *ChemOffice Ultra 7.0*. J. Chem. Inf. Model, 42 (2002) 1505-1506.
- [5] BIOVIA, *Dassault Systèmes, Discovery Studio Visualizer, 17.2.0.16349, San Diego: Dassault Systèmes* (2016).
- [6] O. Trott, A.J. Olson, *AutoDockVina: improving the speed and accuracy of docking with a new scoring function, efficient optimization, and multithreading*. J. Comput. Chem, 31 (2010) 455-461.
- [7] L. Schrödinger, W. DeLano. PyMOL. <https://www.pymol.org/pymol>.

Platinum(II) complexes with epoxide derivative of 1,10-phenanthroline in interaction with human serum albumin

Andela A. Franich^{1*}, Marija D. Živković², Snežana Rajković¹

¹ University of Kragujevac, Faculty of Science, Department of Chemistry, R. Domanovića 12, 34000 Kragujevac, Serbia, andjela.franich@pmf.kg.ac.rs

² University of Kragujevac, Faculty of Medical Sciences, Department of Pharmacy, S. Markovića 69, Kragujevac, Serbia

DOI: 10.46793/ICCB23.483F

Abstract: In order to investigate the nature of binding drugs to HSA interaction of mononuclear [Pt(5,6-epoxy-1,10-phen)Cl₂] and [Pt(mal)(5,6-epoxy-1,10-phen)] complexes with HSA were followed by fluorescence emission and UV-Vis spectroscopy. To determine the preferred site of the complex binding to the HSA competitive experiments with site markers eosin Y and ibuprofen were performed. Obtained results showed that the examined complexes bind to HSA and primary interaction is at site II.

Keywords: Platinum(II) complexes, HSA, Eosin Y, Ibuprofen

1. Introduction

Due to the toxic effects exhibited by platinum(II) drugs in chemotherapy, exponential growth has been observed in the development of alternative platinum(II) complexes with other inorganic and organic ligands. 1,10-Phenanthroline (phen), with its rigid structure of three fused aromatic rings with the two nitrogen donors is one of the most commonly used ligands in modern coordination chemistry [1]. We investigated the influence of 5,6-epoxy-5,6-dihydro-1,10-phenanthroline (5,6-epoxy-1,10-phen) as the derivative of 1,10-phenanthroline and malonic acids on the nature of mononuclear platinum(II) complexes [2]. These complexes showed good anticancer activity on human and murine cancer cell lines and good antitumor activity on breast and colorectal cancer in *in vivo* and *in vitro* experiments. In this work, we investigated the interaction of a representative of the previously investigated mononuclear complexes [Pt(5,6-epoxy-1,10-phen)Cl₂] (**Pt1**) and [Pt(mal)(5,6-epoxy-1,10-phen)] (**Pt2**) with HSA. Fluorescence measurement experiments as well as UV-Vis spectroscopy were used to investigate these interactions and to determine the influence of malonic acid on binding to HSA as one of the most important biomolecules.

2. Experimental

Mononuclear complexes [Pt(5,6-epoxy-1,10-phen)Cl₂] (**Pt1**) and [Pt(mal)(5,6-epoxy-1,10-phen)] (**Pt2**) were synthesized by the procedure previously published [2]. Phosphate

buffered saline (PBS, 10 mM, pH = 7.4), human serum albumin (HSA), ibuprofen and eosin Y were purchased from the Aldrich Chemical Co (Merck).

Fluorescence measurements were carried out on a RF-1501 PC spectrofluorometer (Shimadzu, Japan). The experiments involving the interaction of **Pt1** and **Pt2** complexes with HSA were performed at room temperature in 10 mM PBS buffer solution (pH = 7.40) to keep the physiological conditions. The concentration of HSA was kept fixed at 8 μM while the concentration of investigation Pt(II) complexes increased up to 160 μM so that the molar ratio (r) was from 0 to 20. The fluorescence emission spectra of HSA were recorded in the scanning range 300–500 nm at an excitation wavelength of 295 nm in the absence and presence of different concentrations of **Pt1** and **Pt2** complexes. The fluorescence quenching data were analyzed using the Stern–Volmer equation:

$$\frac{F_0}{F} = 1 + K_{sv}[\text{complex}] = 1 + k_q\tau_0[\text{complex}]$$

$$F_0/F = 1 + K_{sv}[\text{complex}] = 1 + k_q\tau_0[\text{complex}] \quad (1)$$

where F and F₀ are the fluorescence intensities of HSA with and without complex, respectively, k_q is the quenching rate constants of the biomolecule, K_{sv} is the dynamic quenching constant, τ_0 is the average lifetime of the biomolecule without a quencher (around 10⁻⁸ s) and [complex] is the concentration of **Pt1** and **Pt2** complexes.

The fluorescence intensities in this were corrected for absorption of the exciting light and reabsorption of the emitted light to decrease the inner filter effect using the following equation:

$$F_{cor} = F_{obs} e^{(A_{ex} + A_{em})/2} \quad F_{cor} = F_{obs} e^{(A_{ex} + A_{em})/2}$$

$$F_{cor} = F_{obs} e^{(A_{ex} + A_{em})/2} \quad F_{cor} = F_{obs} e^{(A_{ex} + A_{em})/2} \quad F_{cor} = F_{obs} e^{(A_{ex} + A_{em})/2}$$

$$(2)$$

The binding constant of the complex with BSA was calculated by the Scatchard equation:

$$\log[(F_0 - F)/F] = \log K_a + n \cdot \log[\text{complex}]$$

$$\log[(F_0 - F)/F] = \log K_a + n \cdot \log[\text{complex}] \quad (3)$$

where K_a is the association binding constant and n is the number of binding sites which have been obtained from the plot of log[(F₀-F)/F] versus log[complex].

Competitive experiments were carried out using two site markers (eosin Y and ibuprofen) by keeping the concentration of HSA and the site markers constant at 8 μM . Then **Pt1** and **Pt2** complexes were gradually added to HSA/marker mixtures so that r was from 0 to 20. Fluorescence spectra of the above systems were recorded from 300 to 500 nm at an excitation wavelength of 295 nm.

The UV–Vis spectra were recorded on a Shimadzu double-beam spectrophotometer equipped with thermostated 1.00 cm quartz Suprasil cells over the wavelength range of 200–500 nm. Electronic absorption spectra were recorded in the presence and absence of **Pt1** and **Pt2** complexes at room temperature. The concentration of HSA was constant (8 μM) while the concentration of investigated Pt(II) complexes increased from 0 - 120 μM .

3. Results and discussion

In order to investigate the structural changes in HSA caused by the addition of Pt(II) complex and determine the binding constant (K_a) and the number of binding sites (n) for the complex formed between platinum(II) complexes and HSA, fluorescence spectra

were measured (**Figure 1**). As can be seen from **Fig 1**, the addition of the complexes **Pt1** and **Pt2** to a solution of HSA provoked a significant decrease in the fluorescence intensity of HSA. The changes in the emission spectra of HSA protein indicate the occurrence of the binding of each complex to albumin. The fluorescence of HSA comes from tryptophan (Trp), tyrosine (Tyr) and phenylalanine (Phe) residues. Trp214, located in the depth of subdomain IIA is largely responsible for the intrinsic fluorescence of HSA, because the fluorescence of tyrosine is almost completely quenched if it is ionized or in the vicinity of an amino group, a carbonyl group, or a tryptophan residue while phenylalanine quantum yield is very low quantum yield [3]. It can be concluded that the addition of **Pt1** and **Pt2** complexes resulted in concentration-dependent quenching of Trp214 fluorescence.

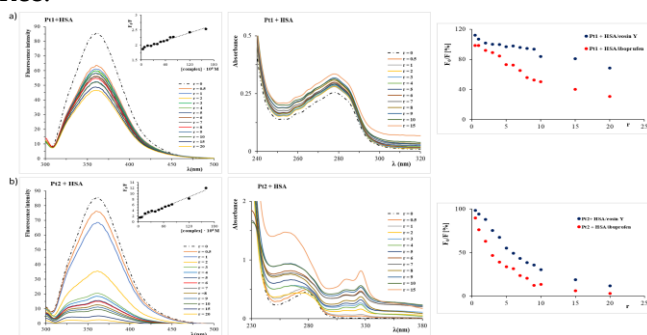


Figure 1. Emission, UV-Vis absorption spectra of the HSA and the relative intensity of the fluorescence emission of HSA/eosin Y or HSA/ibuprofen in the absence and in the presence of **Pt1** (a) and **Pt2** (b) complexes.

The values of K_{sv} ($4.3 \cdot 10^4 \text{ M}^{-1}$ for **Pt1** and $1.9 \cdot 10^5 \text{ M}^{-1}$ for **Pt2**) and k_q ($4.3 \cdot 10^{12} \text{ kJ/mol}$ for **Pt1** and $1.9 \cdot 10^{13} \text{ kJ/mol}$ for **Pt2**) for the interaction of **Pt1** and **Pt2** complexes with HSA indicate a good HSA-binding tendency of the complexes. The **Pt2** complex showed a higher value for K_{sv} in relation to **Pt1** complex which can be attributed to the presence of malonic acid as the bidentate coordinated ligand. Moreover, the k_q values for investigated complexes are higher than for different kinds of quenchers for biopolymer and point evidently to the presence of static quenching. The calculated K_a value ($5.4 \cdot 10^5 \text{ M}^{-1}$ for **Pt1** and $7.4 \cdot 10^6 \text{ M}^{-1}$ for **Pt2**) indicated that a strong affinity existed between HSA and platinum(II) complexes. The value of n (0.9 for **Pt1** and 1.0 for **Pt2**) suggested that there was one independent class of binding site on HSA for investigated platinum(II) complexes. The fluorescence quenching titration was used to determine the binding constants of **Pt1** and **Pt2** complexes interaction with HSA in the presence of eosin Y and ibuprofen as site probes for sites I and II (**Figure 1**).

Table 1. The binding constants of the interaction between HSA and platinum(II) complexes in the presence of site markers.

System		K_{sv} (1/M)	K_a (1/M)	n
HSA/eosinY	Pt1	$6.9 \cdot 10^3$	$2.4 \cdot 10^3$	1.1
	Pt2	$4.7 \cdot 10^4$	$1.8 \cdot 10^5$	0.6
HSA/ibuprofen	Pt1	$2.4 \cdot 10^3$	$2.7 \cdot 10^3$	0.9
	Pt2	$1.8 \cdot 10^5$	$6.1 \cdot 10^4$	0.7

With the increasing concentration of investigated platinum(II) complexes fluorescence intensity of HSA/eosin Y or HSA/ibuprofen system decreases. From **Table 1** it is obvious that there was a competitive interaction between complexes and both site markers, which means that complexes can bind at both sites [4]. Accordingly, complexes displace ibuprofen more easily than eosin Y, so it can be concluded that the primary interaction is at site II. From **Fig. 1**, it can be observed that with increasing amounts of **Pt1** and **Pt2** complexes added to the HSA solution, the intensity of the absorption peak of HSA at 278 nm increases. In the UV-Vis spectra of HSA and **Pt1** complex, there are no changes so it can be concluded that the interaction of the formation ground state complex is done via static process. On the other hand, in the UV-Vis spectra of HSA and **Pt2** complex there is an evident red shift of peak at 278 nm so it can be concluded that the interaction between complex and HSA is a dynamic process [5].

3. Conclusions

In this work we investigated the interaction of two mononuclear [Pt(5,6-epoxy-1,10-phen)Cl₂] and [Pt(mal)(5,6-epoxy-1,10-phen)] complexes with HSA using different spectra techniques. The complex **Pt2** showed a higher value for K_{sv} and K_a constants in relation to the **Pt1** complex which is a consequence of presence of malonic acids in the coordination sphere in the Pt2 complex. Both investigated complexes bind to one place of HSA. Also, competitive experiments with two site markers eosin Y and ibuprofen as site probes for sites I and II showed that investigated platinum(II) complexes bind to HSA at both sites but the primary interaction is at site II. Absorption measurements confirm the binding of mononuclear platinum(II) complexes to HSA. From these experiment results we can conclude that the Pt1 complex binds to HSA through a static process while the Pt2 complex prefers a dynamic process.

Acknowledgment

This research is funded by the Ministry of Education and Ministry of Science, Technological Development and Innovation, Republic of Serbia, Agreement No. 451-03-47/2023-01/200122, 451-03-47/2023-01/ 200111.

References

- [1] C.R. Luman, F.N. Castellano, *Phenanthroline ligands*, Compr. Coord. Chem. II 1 (2004) 25–39.
- [2] M.N. Dimitrijević Stojanović, A.A. Franich, M.M. Jurišević, N.M. Gajović, N.N. Arsenijević, I.P. Jovanović, B.S. Stojanović, S.Lj. Mitrović, J. Kljun, S. Rajković, M.D. Živković, *Platinum(II) complexes with malonic acids: Synthesis, characterization, in vitro and in vivo antitumor activity and interactions with biomolecules*, Journal of Inorganic Biochemistry 231 (2022) 111773–111785.
- [3] A. Sulkowska, *Interaction of drugs with bovine and human serum albumin*, Journal of Molecular Structure 614 (2002) 227–232.
- [4] N. Seedher, P. Agarwal, *Complexation of fluoroquinolone antibiotics with human serum albumin: a fluorescence quenching study*, Journal of Luminescence 130 (2010) 1841–1848.
- [5] E. Mrkalić, R. Jelić, S. Stojanović, M. Sovrlić, *Interaction between olanzapine and human serum albumin and effect of metal ions, caffeine and flavonoids on the binding: A spectroscopic study*, Spectrochimica Acta Part A: Molecular and Biomolecular Spectroscopy 249 (2021) 119295.

Analytical values of beeswax from Montenegro and detection of adulteration

V. Kastratović^{1*}, M. Kapidžić², B. Knežević³

¹ University of Montenegro, Faculty of Natural Sciences and Mathematics, Department of Biology, Podgorica, Montenegro, G. Washington Street, P. O. Box 5455; e-mail: vlatkok@ucg.ac.me

² University of Montenegro, Faculty of Metallurgy and Technology, Podgorica, Montenegro; kapidzicminea126@gmail.com

³ Center for Ecotoxicological Research of Montenegro, Podgorica, Montenegro; bojana.r.knezevic@gmail.com

* Corresponding author

DOI: 10.46793/ICCBi23.487K

Abstract: Beeswax, produced by honeybees by excreting from the abdominal glands, is a complex mixture of organic compounds. According to its chemical composition and properties, it belongs to the group of lipids. Waxes are, for the most part, monoesters of higher fatty acids with higher monohydroxyl alcohols. Determining the physico-chemical properties of beeswax is necessary for examining its quality and authenticity. The recommendation of the International Honey Commission (IHC) is that the basic physicochemical parameters for quality assessment and detection of possible adulteration are: melting point, acid value, saponification value, ester value and ester/acid ratio. In this paper, we examined the basic physical and chemical properties of authentic beeswax from domestic producers from three locations in Montenegro. The melting point of the investigated beeswax is in the range of 61.5-67.2 °C. The solubility of waxes at room temperature in organic solvents was the highest in chloroform and the lowest in acetone. The minimum and maximum value of the acid number of the tested beeswax was 18.2 and 28.6, respectively. The saponification value of the tested samples of beeswax was determined from 3 measurements and was: $SV = 90.8 \pm 16.1$.

Keywords: beeswax, esters, saponification value, acid value

1. Introduction

Wax is a product that bees secrete from special glands, the wax glands, located on the underside of their abdomens. [1].

According to its chemical structure, beeswax is a complex mixture that includes over three hundred different substances. There is considerable variation in the chemical composition of beeswax. This is expected considering that the chemical composition of the wax depends on the geographical and climatic conditions, the species and genetics of the bees, the age of the wax and the like. Waxes are, for the most part (35-45 %), monoesters of higher fatty acids with higher monohydroxyl alcohols. The most

abundant constituent is myricyl-palmitate, $C_{15}H_{31}CO-O-C_{30}H_{61}$. In addition to monoesters, beeswax contains more than 10 % hydrocarbons, free fatty acids, diesters and free polyesters. Less than 10 % contain hydroxy monoesters, hydroxy polyesters, free higher alcohols, triesters, acid polyesters, acid esters and other substances [1,2]. The properties of natural waxes are not determined by the properties of the esters that make them up, but rather by the properties of the impurities, most notably in terms of their share [3].

Due to the high demand for beeswax, unscrupulous manufacturers often mix it with other cheaper and wax-like substances. Among them, paraffin waxes represent the most significant problem, due to their wide availability and low cost. Occasionally, other unwanted substances, such as stearic acid, stearin, tallow, microcrystalline wax, and others, are also noticed in beeswax.

The most reliable way to determine the quality of beeswax is laboratory testing because all other methods are less reliable. Determining the physico-chemical properties of beeswax is necessary to determine both its quality and authenticity. The recommendation of the International Honey Commission (IHC) is that the basic physicochemical parameters for quality assessment and the detection of possible adulteration are the melting point, the acid value, the saponification value, the ester value and the ester/acid ratio.

The examined beeswax was taken from rural domestic producers from 3 locations in Montenegro: Bjelopavlići (S1), Vranjske njive (S2) and Piperi (S3).

2. Methods

2.1 The determination of the melting point

The melting point was determined automatically using an instrument based on a capillary tube (Melting-Point Meter KSPII).

2.2 The determination of the acid value (AV)

The acid value (AV) of the wax is the number of milligrams of KOH required to neutralize the free fatty acids in 1 g of beeswax.

The acid value was calculated according to the equation:

$$AV = \frac{C_{KOH} \times V_{KOH} \times 56.1}{w_{beeswax}}$$

where: C_{KOH} is the concentration of the KOH solution in mol dm^{-3} , V_{KOH} is the volume of the used KOH solution in cm^3 and w is the mass of the measured wax in grams.

2.3 The determination of the saponification value

The saponification value (SV) is the number of milligrams of KOH required to neutralize the total fatty acids in 1g of wax.

The saponification value was calculated according to the equation:

$$SV = \frac{c_{HCl} \times (B - S) \times 56.1}{w_{beeswax}}$$

where c is the molarity of the HCl solution, in mol dm⁻³, B is the number of cm³ of HCl solution used for the control sample, S is the number of cm³ of HCl solution used for the sample, and w is the weight of the sample in grams.

2.4 The ester value (EV) and the ester/acid ratio

The ester value is defined as the amount of KOH in milligrams needed to neutralize 1 g of ester-linked acids of beeswax, being calculated by subtracting the saponification value from the acid value: $EV = SV - AV$.

The ester/acid ratio is the quotient of the ester and acid values of individual measurements.

3. Results and discussion

Table 1 shows the basic physical and chemical properties of the examined beeswax samples from three localities: Bjelopavlići (S1), Vranjske njive (S2) and Piperi (S3).

Table 1. Physico-chemical properties of beeswax examined.

Sample	Melting point (°C)	Solubility in chloroform (%)	Acid value (AV)	Saponification value (SV)	Ester value (EV)	Ester/acid value
S1	61.8	97.2	23.8	81.6	57.8	2.43
S2	64.5	95.3	28.6	109.4	80.8	2.83
S3	65.3	96.0	18.2	81.5	63.3	3.48

Melting point determination is not a reliable analytical method for determining adulteration of beeswax. For example, paraffin wax is often added to beeswax for adulteration, because it has a similar melting point as beeswax. In our work, the melting point of the examined waxes was determined from 3 measurements and is in the range of 61.8-65.3 °C. The measured melting point value is in the range of other literature reports for authentic beeswax [4,5].

In our tests, the solubility of the tested wax samples at room temperature in chloroform decreases in the order: S1 (97.2%) > S3 (96.0%) > S2 (95.3%). Beeswax is practically insoluble in water, partially soluble in hot alcohol (90% V/V) and soluble in weakly polar organic solvents. The solubility of waxes is highly dependent on temperature. At room temperature, beeswax is not completely soluble in organic solvents.

Determining the acid number is a reliable method for determining the contamination of wax by both paraffin and stearic acid. In the case of the falsification of beeswax with the addition of paraffin, the acid value decreases, while the acid value increases with an increase in the content of stearic acid. Based on a comparative review of the quality parameters of beeswax according to FAO (2005), European legislation (2009/10/EC; EP,

2007) and the IHC [6], the generally accepted range of acid number values is 17-24(22). In our research, the result of sample S2 was above the limits of this range.

Based on a comparative review of beeswax quality parameters according to FAO (2005), European legislation (2009/10/EC; EP, 2007) and the International Honey Commission [6], the range of saponification values should be 87-102(104). In our research, the results of samples S1 and S3 were slightly below and sample S2 slightly above the limits of this range. In waxes and lipids in general, the saponification value can be a measure of the average molecular weight of the esters present in the sample. The lower the saponification value, the higher the average molecular weight of the wax esters.

According to European legislation (2009/10/EC; EP, 2007) the range of ester number values should be 70-80, while according to the International Honey Commission (IHC, 2016) the permissible range is 70-90. In our research, the results of samples S1 and S3 were below and sample S2 was within the limits of this range.

According to the International Honey Commission (IHC, 2016), the ester/acid ratio should be in the range of 3.3-4.3. The results of samples S1 and S2 were below and of sample S3 within this range.

3. Conclusions

All the obtained results are not in the range of values given based on a comparative review of the quality parameters of beeswax according to FAO, European legislation and the International Honey Commission. The deviations of the obtained results of the chemical parameters can be partially explained by the exposure to high temperatures during the processing of beeswax for the production of honeycombs. Certain variations in the range of values can be explained by the different origins of the beeswax.

References

- [1] H.R. Hepburn, C.W.W. Pirk, O. Duangphakdee, *Honeybees nests: Composition, structure, function*, New York, NY: Springer. 2014.
- [2] N. Garnier, C. Cren-Olive, C. Rolando, M. Regert, *Characterization or archaeological beeswax by electrospray ionization and electrospray ionization mass spectrometry*, *Analytical Chemistry*, 74 (2002) 4868-4877.
- [3] L. Svečnjak, L.A. Chesson, A., Gallina, M. Maia, M. Martinello, F. Mutinelli, F.M.N. Muz, F.M. Nunes, F. Saucy, B.J. Tipple, K. Wallner, E. Waś, T.A. Waters, *Standard methods for Apis mellifera beeswax research*, *Journal of Apicultural Research*, 58 (2019) 1-108.
- [4] J.S. Serra Bonvehí, F.J. Orantes Bermejo, *Detection of adulterated commercial Spanish beeswax*. *Food Chemistry*, 132 (2012) 642-648.
- [5] M. Maia, F.M. Nunes, *Authentication of beeswax (Apis mellifera) by high-temperature gas chromatography and chemometric analysis*. *Food Chemistry*, 136 (2013) 961-968.
- [6] S. Bogdanov, (2016). *Beeswax: Production, properties, composition and control*. *Beeswax book* (Chapter 1). *Bee Product Science*, pp. 1-18.

Phenolic *N*-acyl hydrazone derivatives: *In silico* assessment of potential antibacterial activity against selected G⁺ and G⁻ strains

Jovica Branković^{1*}, Zorica D. Petrović¹, and Vladimir P. Petrović¹

¹ University of Kragujevac, Faculty of Science, Department of Chemistry, R. Domanovića 12, 34000 Kragujevac, Serbia; e-mail: jovica.brankovic@pmf.kg.ac.rs

* Corresponding author

DOI: 10.46793/ICCB23.491B

Abstract: In this work, a series of phenolic *N*-acyl hydrazones was investigated *in silico* against six selected *E. coli* and *S. aureus* bacterial proteins. Generally, the obtained molecular docking results revealed significantly higher binding affinities of analogs **a–n** towards selected enzymes in comparison to standard compounds. In the case of *E. coli* proteins **1hnj**, **1c14**, and **6ntw**, the lowest binding energies were calculated for derivatives **l** (-8.5 kcal/mol), **d** (-9.0 kcal/mol), and **k** (-8.2 kcal/mol), respectively. On the other hand, the highest binding affinity towards the *S. aureus* **3u2d**, **1mwu**, and **1jjj** enzymes was expressed by derivatives **a**, **d**, and **j**, with binding energies of -8.3, -8.4, and -9.4 kcal/mol, respectively. The obtained *in silico* results indicate the potential inhibitory activity of selected phenolic *N*-acyl hydrazone derivatives against *E. coli* and *S. aureus* bacterial proteins and represent a valuable ground base for future *in vitro* experiments.

Keywords: phenolics, hydrazone, antibacterial activity, molecular docking

1. Introduction

Bacterial drug resistance represents a serious public concern. The emergence of drug-resistant bacteria was considerably affected by inadequate use of antibiotics, improper hygiene, and inadequate prevention and control of bacterial infections in health care [1]. Particularly, *E. coli* and *S. aureus* bacterial strains are recognized for their ability to develop multidrug resistance to antibiotics [2], [3]. Such an outcome triggered the necessity for novel antibacterial agents expressing diverse modes of action [4]. In the endeavor to discover efficient antibacterial agents, fruitful research exposed diverse hydrazone hybrids exerting activity against various bacterial strains [5], [6]. Moreover, the presence of multiple hydrogen-bond donor and acceptor sites enables the hydrazone core to interact with amino acid residues, thus expressing the inhibitory activity on many enzymes [7]. These virtues of hydrazone-type compounds prompted us to evaluate *in silico* inhibitory activity of a series of phenolic *N*-acyl hydrazones against selected *E. coli* and *S. aureus* proteins as multiple targets, particularly those involved in the DNA, protein, and fatty acid biosynthesis, bacterial cell wall, and drug resistance.

2. Results and Discussion

Fourteen hydrazone derivatives **a–n** derived from 2,3-dihydroxybenzoic acid and 2,3,4-trihydroxybenzoic acid bearing different ring B substitution (Figure 1) were subjected to molecular docking with *S. aureus* GyrB ATPase (PDB: **3u2d**), methicillin acyl-Penicillin binding protein 2a (PDB: **1mwu**), and tyrosyl-tRNA synthetase (PDB: **1jjj**), and *E. coli* beta-ketoacyl-acyl carrier protein synthase III (PDB: **1hnj**), enoyl reductase (PDB: **1c14**), and L,D-transpeptidase YcbB (PDB: **6ntw**). Molecular docking was performed using AutodockVina software. The grid box was set to embrace the active sites, which were initially confirmed by employing CASTp software.

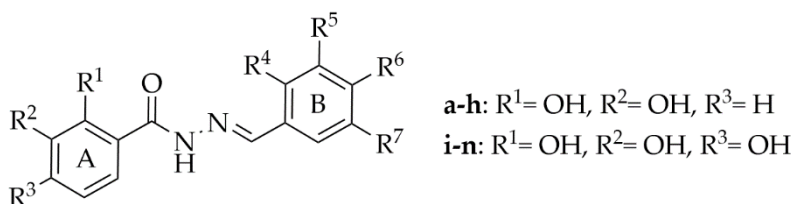


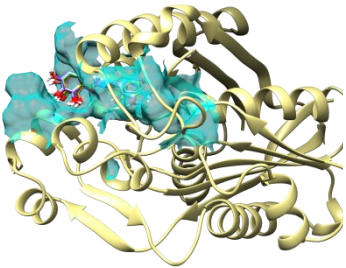
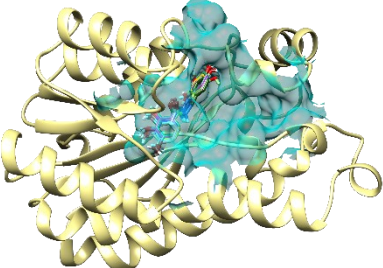
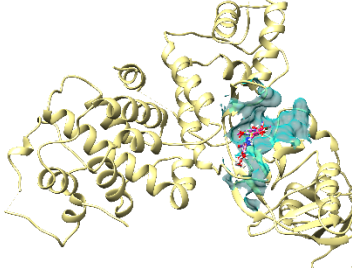
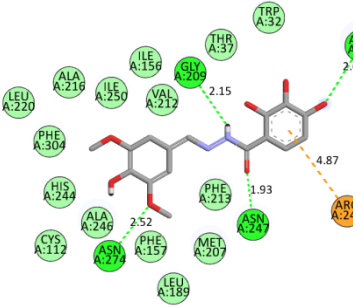
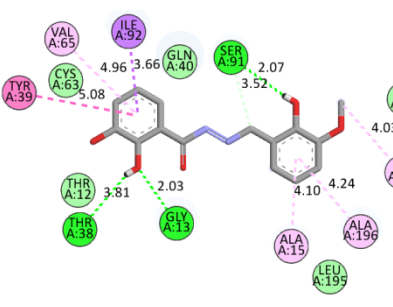
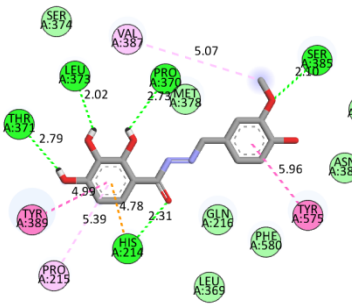
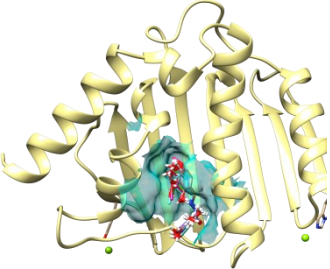
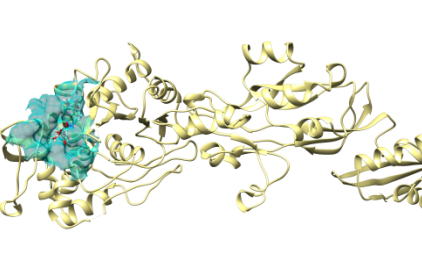
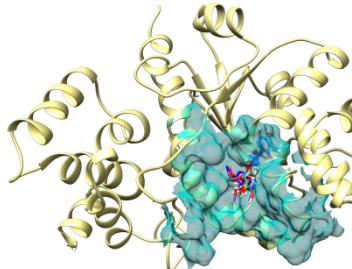
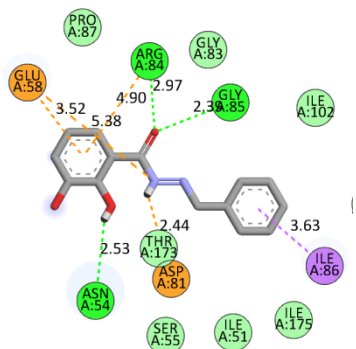
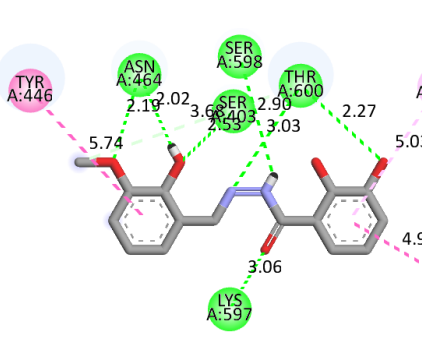
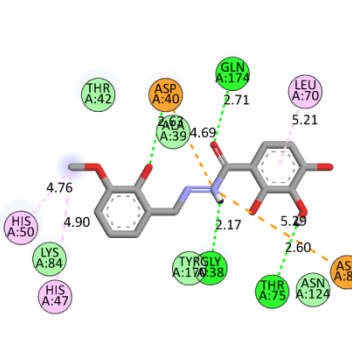
Figure 1. The skeleton of the investigated hydrazone derivatives **a–n**.

Based on the results presented in Table 1, all analogs expressed higher binding affinities towards selected proteins in comparison to standard inhibitors (SI). Here, all investigated compounds were docked within predicted active sites in all cases (Table 2). The most favorable interactions with *S. aureus* **3u2d**, **1mwu**, and **1jjj** enzymes were observed for derivatives **a** (R⁴, R⁵, R⁶, R⁷=H) **d** (R⁴=OH; R⁵=OCH₃; R⁶, R⁷=H), and **j** (R⁴=OH; R⁵=OCH₃; R⁶, R⁷=H), whereas for *E. coli* **1hnj**, **1c14**, and **6ntw** analogs **l** (R⁴=H; R⁵, R⁷=OCH₃; R⁶=OH), **d**, and **k** (R⁴, R⁷=H; R⁵=OCH₃; R⁶=OH) were identified as those with the highest binding affinity, respectively. The insight into the potential bioactive conformations and 2D diagrams for the highest affinity compounds revealed multiple established hydrogen bonds (green); and Van der Waals interactions (light green); alkyl, π -alkyl, π - π , π -amide, and π -sigma interactions (purple); as well as π -anion, π -cation, and salt bridges (orange) (Table 2), with both A and B moieties. Generally, the presence of *o*-vanillin, vanillin, and syringaldehyde moieties on the B side was identified as most favorable for interaction establishment.

Table 1. Calculated binding affinities (kcal/mol) of compounds **a–n** against selected proteins.

	a	b	c	d	e	f	g	h	i	j	k	l	m	n	SI
3u2d	-8.3	-8.3	-8.2	-8.1	-8.2	-7.1	-8.2	-8.2	-8.3	-8.1	-8.1	-7.1	-8.2	-8.1	-7.6
1mwu	-7.8	-8.1	-7.8	-8.4	-8.0	-8.0	-8.1	-8.0	-7.8	-8.4	-8.0	-7.8	-8.2	-8.1	-7.8
1jjj	-8.7	-9.0	-8.7	-9.2	-8.7	-8.9	-9.0	-8.8	-8.8	-9.4	-8.9	-8.8	-9.2	-9.1	-8.4
1hnj	-7.7	-7.6	-7.9	-8.0	-8.3	-8.4	-7.8	-8.1	-7.7	-8.0	-8.3	-8.5	-7.9	-8.2	-7.2
1c14	-8.2	-8.5	-8.2	-9.0	-8.6	-8.5	-8.6	-8.3	-8.3	-8.7	-7.8	-7.9	-7.7	-7.8	-7.7
6ntw	-7.5	-7.6	-7.7	-7.7	-8.0	-7.8	-7.9	-7.8	-7.7	-7.9	-8.2	-7.9	-8.1	-8.1	-6.6

Table 2. Selected *E. coli* and *S. aureus* proteins presented with potential bioactive conformations of compounds **a-n** and 2D interaction diagrams for the highest binding affinity compounds.

PDB: 1hnj	PDB: 1c14	PDB: 6ntw
		
		
analog l	analog d	analog k
PDB: 3u2d	PDB: 1mw	PDB: 1jjj
		
		
analog a	analog d	analog j

3. Conclusions

In the present work, molecular docking analysis was performed with selected phenolic-N-acyl hydrazones and bacterial proteins of *E. coli* and *S. aureus* strains. The obtained results exposed notably higher binding affinities of compounds **a–n** towards selected proteins in comparison to standard compounds. In the case of *E. coli* **1hnj**, **1c14**, and **6ntw** proteins, derivatives **l** (-8.5 kcal/mol), **d** (-9.0 kcal/mol), and **k** (-8.2 kcal/mol) were identified as those with the highest binding affinities, respectively. For *S. aureus* proteins **3u2d**, **1mwu**, and **1jjj**, the lowest binding energy values were calculated for analogs **a**, **d**, and **j** (-8.3, -8.4, and -9.4 kcal/mol, respectively). Insight into the potential bioactive conformations exposed multiple favorable interactions responsible for the enhanced binding affinity towards investigated proteins. The presence of *o*-vanillin, vanillin, and syringaldehyde moieties on the B side of the molecule was identified as most favorable for interaction establishment.

Acknowledgment

This research is funded by the Ministry of Education and Ministry of Science, Technological Development and Innovation, Republic of Serbia, Grants: No. 451-03-47/2023-01/200122.

References

- [1] A. Pormohammad, M. J. Nasiri, and T. Azimi., *Prevalence of antibiotic resistance in Escherichia coli strains simultaneously isolated from humans, animals, food, and the environment: A systematic review and meta-analysis*, Infection and Drug Resistance, 12 (2019) 1181–1197.
- [2] L. Poirel et al., *Antimicrobial Resistance in Escherichia coli*, Microbiology Spectrum, 6 (2018).
- [3] H. F. Chambers and F. R. DeLeo., *Waves of resistance: Staphylococcus aureus in the antibiotic era*, Nature Reviews Microbiology, 7 (2009) 629–641.
- [4] N. Jebli, S. Hamimed, K. Van Hecke, J. F. Cavalier, and S. Touil., *Synthesis, Antimicrobial Activity and Molecular Docking Study of Novel α -(Diphenylphosphoryl)- and α -(Diphenylphosphorothioyl)cycloalkanone Oximes*, Chem Biodivers, 17 (2020) e2000217.
- [5] Ł. Popiołek, *Hydrazide–hydrazones as potential antimicrobial agents: overview of the literature since 2010*, Medicinal Chemistry Research, 26 (2017) 287–301.
- [6] Ł. Popiołek, *Updated Information on Antimicrobial Activity of Hydrazide–Hydrazones*, Int J Mol Sci, 22 (2021) 9389.
- [7] L. Y. Li et al., *Potent hydrazone derivatives targeting esophageal cancer cells*, Eur J Med Chem, 148 (2018), 359–371.

***In silico* antibiofilm potency of phenolic *N*-acyl hydrazones against selected bacterial strains**

Jovica Branković^{1*}, Zorica D. Petrović¹, and Vladimir P. Petrović¹

¹ University of Kragujevac, Faculty of Science, Department of Chemistry, R. Domanovića 12, 34000 Kragujevac, Serbia; e-mail: jovica.brankovic@pmf.kg.ac.rs

* Corresponding author

DOI: 10.46793/ICCBi23.495B

Abstract: In the present work, fourteen phenolic hydrazone derivatives were evaluated for their *in silico* inhibitory activity against selected *P. aeruginosa* and *S. maltophilia* proteins involved in drug resistance and biofilm formation. Molecular docking analysis revealed the highest binding affinity of analogs **n** (-8.4 kcal/mol) and **h** (-7.3 kcal/mol) towards *P. aeruginosa* **7m1m** and **7m1l** proteins, respectively. In the case of *S. maltophilia*, analog **k** (-8.4 kcal/mol) expressed the highest binding affinity to **6qw7**, whereas for **6uaf**, the lowest binding energy was calculated for derivative **d** (-8.1 kcal/mol). The obtained *in silico* results highlight the potential inhibition potency of the selected hydrazone analogs against investigated proteins and represent a good basis for future *in vitro* antibiofilm investigations.

Keywords: phenolics, hydrazone, antibiofilm activity, molecular docking

1. Introduction

The inhibition of biofilm formation has been recognized as a novel target for developing efficient broad-spectrum antibiotics and overcoming bacterial drug resistance [1]. Biofilm bacterial communities express higher resistance to drugs for multiple reasons, such as reduced antimicrobial penetration, slower metabolic state, easier resistance gene exchange between cells, etc. [2]. Among diverse bacteria species, *P. aeruginosa* and *S. maltophilia* are notorious for their ability to form biofilms, enabling their persistence and infectiousness, especially in hospitals and clinical settings [3], [4]. To overcome these concerns, targeting biofilm-related proteins is identified as a route for discovering effective antimicrobial agents [1]. Within numerous chemical entities, hydrazone-type derivatives are renowned for their antimicrobial virtues [5], as well as for their broad enzyme inhibition ability [6]. Bearing this in mind, fourteen phenolic hydrazone derivatives were subjected to molecular docking analysis with biofilm-related *P. aeruginosa* caseinolytic serine proteases (ClpPs) [7], as well as with *S. maltophilia* β -lactamases L1 and L2 involved in the antibiotic resistance [8].

2. Results and Discussion

A series of differently substituted phenolic *N*-acyl hydrazone derivatives (Figure 1) were subjected to molecular docking analysis using AutodockVina. The crystal structures of the selected proteins were acquired from the RSC protein data bank: *P. aeruginosa* ClpP1 (PDB: **7m1m**), *P. aeruginosa* ClpP2 (PDB: **7m1l**), *S. maltophilia* L2 complexed with relebactam (PDB: **6qw7**), and *S. maltophilia* metallo-beta-lactamase L1 in the complex with hydrolyzed imipenem (PDB: **6uaf**). The CASTp tool was used for the prediction of protein active sites. The cuboid grid box was set to embrace the whole protein in all cases.

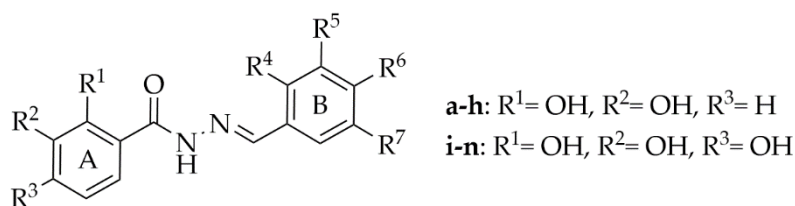


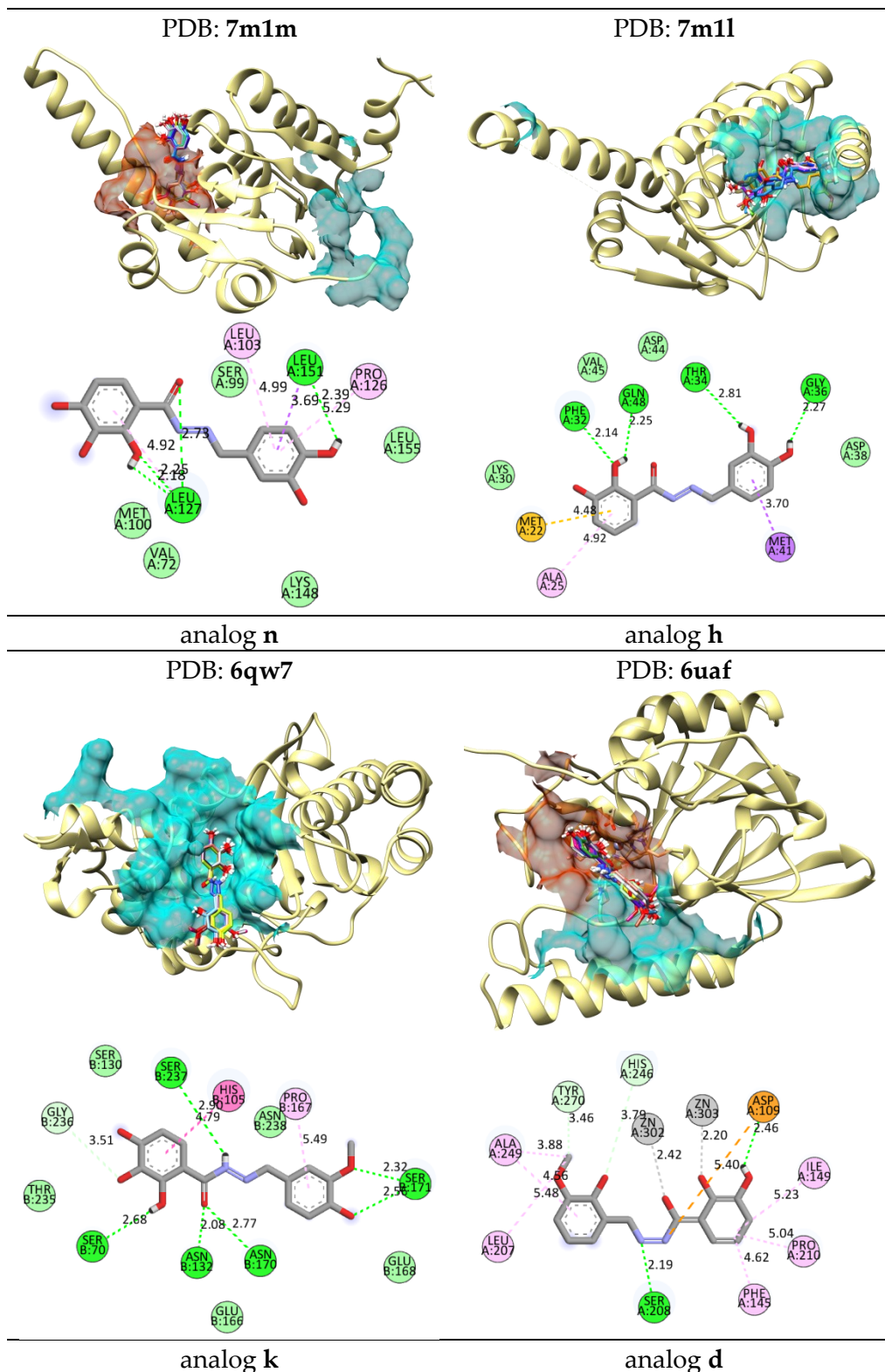
Figure 1. The general structure of the investigated compounds **a-n**.

The obtained binding affinity values exposed derivatives **n** (R⁴, R⁷=H; R⁵, R⁶= OH; -8.4 kcal/mol) and **h** (R⁴, R⁷=H; R⁵, R⁶= OH; -7.3 kcal/mol) as most prominent binders of *P. aeruginosa* **7m1m** and **7m1l**, respectively (Table 1). Excellent agreement with the CASTp was achieved in all cases since all ligands were docked within the predicted active sites (Table 2). In the case of beta-lactamases **6qw7** and **6uaf**, almost all investigated compounds expressed higher binding affinities in comparison to standard inhibitors (SI). Molecular docking exposed derivative **k** (R⁴, R⁷=H; R⁵=OCH₃; R⁶=OH) with the lowest binding energy to **6qw7** of -8.4 kcal/mol. Significantly lower binding energies were obtained for **a-n** with **6uaf** in comparison to SI imipenem, revealing analog **d** (R⁴=OH; R⁵=OCH₃; R⁶, R⁷=H) as the most prominent binder of metallo-beta-lactamase L1 with the binding energy of -8.1 kcal/mol. Potential bioactive conformations of compounds **a-n** and 2D diagrams for the highest affinity compounds (Table 2) provided insight into the binding modes and multiple established interactions with both A and B moieties (hydrogen bonds (green); Van der Waals interactions (light green); alkyl, π -alkyl, π - π , and π -sigma interactions (purple); attractive charges and π -sulfur interactions (orange); as well as metal-acceptor (gray)). Particularly, the presence of catechol, vanillin, *o*-vanillin, and syringaldehyde moiety on the B side of the molecule was identified as most favorable for interaction establishment in all cases.

Table 1. Calculated binding affinities (kcal/mol) of compounds **a-n** against selected proteins.

	a	b	c	d	e	f	g	h	i	j	k	l	m	n	SI
7m1m	-8.2	-8.2	-8.2	-8.3	-8.0	-8.2	-8.2	-8.4	-8.1	-8.2	-8.0	-7.4	-8.1	-8.4	/
7m1l	-6.9	-6.9	-7.1	-7.0	-7.1	-6.0	-7.3	-7.3	-6.4	-6.4	-6.6	-5.8	-6.7	-6.9	/
6qw7	-7.8	-7.4	-7.9	-7.5	-8.3	-8.2	-7.8	-8.1	-8.0	-7.8	-8.4	-8.3	-7.9	-8.2	-7.7
6uaf	-7.6	-7.9	-7.3	-8.1	-7.4	-7.4	-7.9	-8.1	-7.4	-7.2	-6.7	-6.7	-7.1	-7.6	-5.2

Table 2. Selected *P. aeruginosa* and *S. maltophilia* proteins presented with potential bioactive conformations of compounds **a-n** and 2D interaction diagrams for the highest binding affinity compounds.



3. Conclusions

In this research, a series of phenolic *N*-acyl hydrazones were subjected to molecular docking analysis with *P. aeruginosa* and *S. maltophilia* biofilm-related and drug-resistance proteins. The obtained results revealed analogs **n** (-8.4 kcal/mol) and **h** (-7.3 kcal/mol) with the highest binding affinity towards *P. aeruginosa* caseinolytic serine proteases **7m1m** and **7m1l**, respectively. Molecular docking performed on *S. maltophilia* beta-lactamases exposed significantly lower values of binding energies for compounds **a–n** in comparison to standard inhibitors. Here, derivative **k** (-8.4 kcal/mol) was identified as the most effective binder of **6qw7**, whereas in the case of **6auf**, the lowest binding energy was calculated for derivative **d** (-8.1 kcal/mol). Insight into the binding modes exposed multiple favorable interactions responsible for the enhanced binding affinity towards selected proteins. The presence of catechol, vanillin, *o*-vanillin, and syringaldehyde moiety on the B ring was recognized as most beneficial for interaction establishment in all cases.

Acknowledgment

This research is funded by the Ministry of Education and Ministry of Science, Technological Development and Innovation, Republic of Serbia, Grants: No. 451-03-47/2023-01/200122.

References

- [1] S. Islam *et al.*, *Cell-Free Supernatants (CFSs) from the Culture of Bacillus subtilis Inhibit Pseudomonas sp. Biofilm Formation*, *Microorganisms*, 10 (2022) 2105.
- [2] H. Zamani, S. Rahbar, S. R. Garakoui, A. A. Sahebi, and H. Jafari, *Antibiofilm potential of Lactobacillus plantarum spp. cell free supernatant (CFS) against multidrug resistant bacterial pathogens*, 3 (2017) 39.
- [3] M. T. T. Thi, D. Wibowo, and B. H. A. Rehm, *Pseudomonas aeruginosa biofilms*, *International Journal of Molecular Sciences*, 21 (2020) 1–25.
- [4] T. A. Hafiz *et al.*, “*Stenotrophomonas maltophilia* Epidemiology, Resistance Characteristics, and Clinical Outcomes: Understanding of the Recent Three Years’ Trends,” *Microorganisms*, 10 (2022) 2506.
- [5] Ł. Popiołek, *Hydrazide–hydrazones as potential antimicrobial agents: overview of the literature since 2010*, *Medicinal Chemistry Research*, 26 (2017) 287–301.
- [6] J. Branković *et al.*, *Evaluation of antioxidant and cytotoxic properties of phenolic N -acylhydrazones: structure–activity relationship*, *R Soc Open Sci*, 9 (2022) 211853.
- [7] G. D. Mawla *et al.*, *ClpP1P2 peptidase activity promotes biofilm formation in Pseudomonas aeruginosa*, *Mol Microbiol*, 115 (2021) 1094–1109.
- [8] G. García, J. A. Girón, J. A. Yañez, and M. L. Cedillo, *Stenotrophomonas maltophilia and Its Ability to Form Biofilms*, *Microbiology Research*, 14 (2023) 1–20.

TiO₂ nanoparticles and TiO₂ nanoparticles surface modified with salicylic acid affect neurological functions and oxidative stress markers in the eyes of adult rats

K. Bobić^{1*}, A. Todorović¹, S. Pejić¹, F. Veljković², S. Veličković², S. Pajović¹, D. Drakulić¹

¹ University of Belgrade, VINČA Institute of Nuclear Sciences - National Institute of the Republic of Serbia, Department for Molecular Biology and Endocrinology, Mike Petrovića Alasa 12-14, Belgrade, Republic of Serbia; e-mail: katarina.bobic@vin.bg.ac.rs, anato@vin.bg.ac.rs, sneczana@vin.bg.ac.rs, pajovic@vin.bg.ac.rs, drakulic@vin.bg.ac.rs

² University of Belgrade, VINČA Institute of Nuclear Sciences - National Institute of the Republic of Serbia, Department for Physical Chemistry, Mike Petrovića Alasa 12-14, Belgrade, Republic of Serbia; e-mail: filipveljkovic@vin.bg.ac.rs, vsuzana@vin.bg.ac.rs

* *Corresponding author*

DOI: 10.46793/ICCB23.499B

Abstract: Titanium dioxide nanoparticles (TiO₂NPs) are widely used in pharmaceuticals, food products and cosmetics. Besides numerous beneficial outcomes, they also induce toxic effects in different organs, including the eyes. The recent findings report that some surface modifications can attenuate TiO₂NPs toxicity. Thus, the aim of this study was to compare the effects of acute oral treatment with commercially available, bare TiO₂NPs and TiO₂NPs surface modified with salicylic acid (SA-TiO₂NPs) using adult Wistar rats as model organisms. Control animals were gastrically intubated with vehicle (0.01 M HCl), while others were treated with either TiO₂NPs or SA-TiO₂NPs (1000mg/kg dissolved in vehicle). Afterward, the mortality rate as the acute toxicity parameter and parameters of neurological function were assessed. Animals were sacrificed on the 14th day following treatment. In the eye crude synaptosomal fraction, the effects of treatments on oxidative stress markers such as prooxidant/antioxidant balance (PAB) and lipid peroxidation (LPO) were compared. According to the obtained results, the mortality was 0 in all experimental groups. TiO₂NPs and SA-TiO₂NPs treatments displayed mild effects on spontaneous activity and pacing and had no impact on the visual placing reflex. Moreover, TiO₂NPs and SA-TiO₂NPs exposure significantly elevated PAB levels, when compared to controls. Animals treated with SA-TiO₂NPs had similar LPO levels as controls, while in TiO₂NPs group LPO levels were significantly increased. The presented data showed that both examined nanoparticles exerted similar outcomes referring to most of the investigated parameters, however, surface binding of SA decreased the level of LPO and thus, mitigated some of TiO₂NPs toxicity in the eyes.

Keywords: Titanium dioxide nanoparticles (TiO₂NPs) and surface modification with salicylic acid (SA-TiO₂NPs), neurological function, oxidative stress, eye, rat

1. Introduction

Titanium dioxide nanoparticles (TiO₂NPs) are widely used as a white pigment in daily consumer products, like food, toothpaste, sun cream, cosmetics, and plastics. They are also exploited in surgery, dentistry, and pharmacy; in antimicrobial and antibiotic therapies; as photosensitizers in photodynamic cancer therapy; and can potentially be used as a drug delivery system [1]. Unfortunately, toxic impacts of TiO₂NPs, provoked by oxidative stress (OS) and inflammation, are recognized in the brain, liver, kidneys, spleen, and eyes [2]. Their toxicity might be reduced by various modifications, including surface bounding of naturally occurring compounds with a wide range of biological activities and therapeutic applications. Since previous studies showed that some surface modifications can attenuate TiO₂NPs toxicity [3], we compared the effects of bare TiO₂NPs and SA-TiO₂NPs (TiO₂NPs surface modified with salicylic acid, SA) in the eyes of adult Wistar rats.

2. Materials and methods

For the purpose of the experiment, we used commercially available, bare TiO₂NPs (Sigma Aldrich Co., USA, sized 25 nm) with maximum absorption wavelength of 380 nm and SA-TiO₂NPs, synthesized and characterized at the Department for Radiation Chemistry and Physics, VINČA Institute of Nuclear Sciences - National Institute of the Republic of Serbia, University of Belgrade, with maximum absorption of 600 nm. The estimated concentration of SA bound to the surface of TiO₂NPs was 5 %.

All procedures were approved by the Ministry of Agriculture, Forestry and Water Management - Veterinary office of the Republic of Serbia (protocol 323-07-03626/2021-05). Adult Wistar rats, maintained under standard conditions, were randomly divided into 3 groups (n = 4 per group): controls treated with vehicle (2.5 ml, 0.01 M HCl) (V); animals treated with either TiO₂NPs or SA-TiO₂NPs (1000 mg/kg dissolved in 2.5 ml vehicle). All treatments were applied intragastrically in a single dose. During the 14-day rest period, the mortality rate as the acute toxicity parameter was monitored daily. On the last day, sensory-motor parameters, including spontaneous activity, pacing and visual placing reflex were assessed, as indicators of neurological function. Animals were then sacrificed, and their eyes were isolated on ice and stored at -80°C for further processing. Whole eyes were homogenized in 5 volumes of solvent (50 mM Tris-HCl, 0.25 M sucrose, 1 mM EDTA, pH 7.4) to isolate crude synaptosomal fraction [4]. Evaluation of eyes' oxidative status was conducted using modified spectrophotometrical methods for prooxidant/antioxidant balance (PAB) and lipid peroxidation (LPO) [5]. Obtained results are presented as a percentage of V and expressed as mean ± SEM. The GraphPad Prism 5 (GraphPad Software, Inc., USA) was used for statistical analysis, with one way analysis of variance (ANOVA) and Tukey's multiple-comparison post hoc test (statistical significance was p < 0.05).

3. Results and discussion

During the 14-day rest period, the mortality was 0 in all experimental groups, pointing to nonlethal effect of applied NPs (data not shown). As shown in Table 1., the investigated neurological parameters were unaffected by vehicle treatment. Both TiO₂NPs and SA-TiO₂NPs treatments caused noticeable, but mild effects on spontaneous activity and pacing, indicating neurological deficits that tempered animal behavior. The visual placing reflex was unchanged and showed no difference between groups, suggesting that the eye function probably remained intact following TiO₂NPs and SA-TiO₂NPs treatments.

Table 1. Assessment of neurological parameters of rats subjected to acute oral treatment with vehicle (V), bare titanium dioxide nanoparticles (TiO₂NPs) or titanium dioxide nanoparticles surface modified with salicylic acid (SA-TiO₂NPs).

Neurological parameters/groups	V	TiO ₂ NPs	SA-TiO ₂ NPs
Spontaneous activity	-	+	+
Pacing	-	+	+
Visual placing reflex	-	-	-

"- " no effect; "+" mild effect

In the eye crude synaptosomal fraction, the treatments' effect on OS markers: PAB and LPO were tested. As illustrated in Figure 1 both TiO₂NPs treatments significantly elevated PAB levels compared to V ($p < 0.05$), while the LPO level was significantly increased only in the TiO₂NPs group ($p < 0.001$). Animals treated with SA-TiO₂NPs had decreased LPO levels when compared to TiO₂NPs ($p < 0.001$).

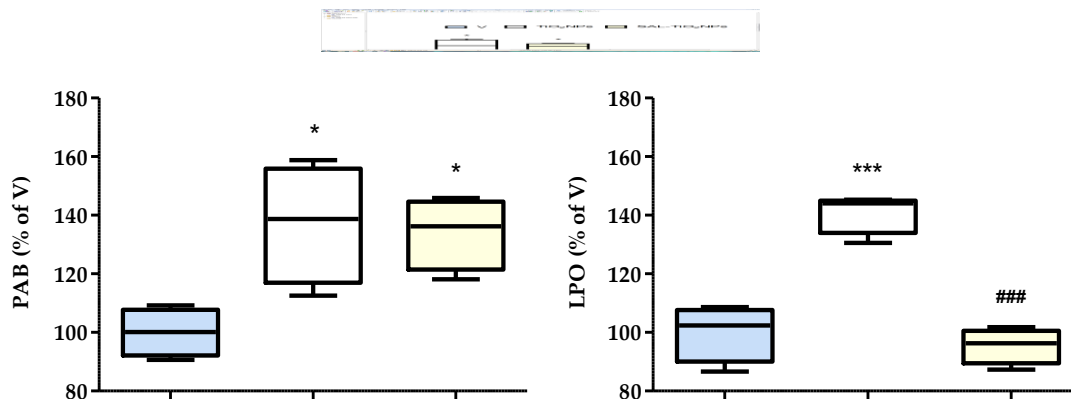


Figure 1. Levels of oxidative stress markers: prooxidant/antioxidant balance (PAB) (left) and end lipid peroxidation products (LPO) (right) in the eye crude synaptosomal fraction of rats, subjected to acute oral treatment with vehicle (V), bare titanium dioxide nanoparticles (TiO₂NPs) or surface modified with salicylic acid (SA-TiO₂NPs). Values are presented as percentage of V and expressed as mean \pm SEM, with ANOVA and Tukey post hoc test statistical analysis.

Statistically significant difference between V and other experimental groups is represented as * (* $p < 0.05$, *** $p < 0.001$) and between TiO₂NPs and SA-TiO₂NPs as # (### $p < 0.001$)

Based on presented results, it can be assumed that TiO₂NPs and SA-TiO₂NPs have different mechanisms of OS induction. TiO₂NPs-induced OS is associated with oxidative

changes of lipids, as also previously reported [6], while SA-TiO₂NPs in the eyes of rats do not affect lipids, but most likely their effects are accomplished through some other mechanisms of action.

3. Conclusions

Although TiO₂NPs and SA-TiO₂NPs exert similar outcomes referring to most of the investigated parameters, surface binding of SA reduces the level of lipid peroxidation and thus, at least partially, suppresses TiO₂NPs toxic effects in the eyes. Further research is needed to reveal unknown mechanisms of TiO₂NPs and SA-TiO₂NPs actions and to investigate the benefits associated with positive outcomes resulting from the implementation of other TiO₂NPs modifications.

Acknowledgment

This research is funded by the Ministry of Education and Ministry of Science, Technological Development and Innovation, Republic of Serbia, Grant: No. 451-03-47/2023-01/200017. We gratefully acknowledge the effort of dr Jovan Nedeljkovic for providing synthesized and characterized surface-modified nanoparticles.

References

- [1] D. Ziental, B. Czarczynska-Goslinska, D.T. Mlynarczyk, A. Glowacka-Sobotta, B. Stanisiz, T. Goslinski, L. Sobotta., *Titanium dioxide nanoparticles: prospects and applications in medicine*, *Nanomaterials*, 10(2) (2020) 387.
- [2] S. Zhu, L. Gong, Y. Li, H. Xu, Z. Gu, Y. Zhao., *Safety assessment of nanomaterials to eyes: an important but neglected issue*, *Advanced Science*, 6(16) (2019) 1802289.
- [3] D. Dekanski, B. Spremo-Potparević, V. Bajić, L. Živković, D. Topalović, D.N. Sredojević, V. Lazić, J.M. Nedeljković., *Acute toxicity study in mice of orally administrated TiO₂ nanoparticles functionalized with caffeic acid*, *Food and Chemical Toxicology*, 115 (2018) 42-48.
- [4] M. Stanojlović, A. Horvat, I. Guševac, I. Grković, N. Mitrović, I. Buzadžić, D. Drakulić., *Time course of cerebral hypoperfusion-induced neurodegenerative changes in the cortex of male and female rats*, *Folia Biologica*, 60 (2014) 123-132.
- [5] S. Đurašević, G. Nikolić, A. Todorović, D. Drakulić, S. Pejić, V. Martinović, D. Mitić-Ćulafić, D. Milić, T.J. Kop, N. Jasnić, J. Đorđević, Z. Todorović., *Effects of fullerene C60 supplementation on gut microbiota and glucose and lipid homeostasis in rats*, *Food and Chemical Toxicology*, 140 (2020) 111302.
- [6] Z. Chen, S. Han, P. Zheng, D. Zhou, S. Zhou, G. Jia., *Effect of oral exposure to titanium dioxide nanoparticles on lipid metabolism in Sprague-Dawley rats*, *Nanoscale*, 12(10) (2020) 5973-5986.

Synthesis and cytotoxic activity of selected dual COX-2 and 5-LOX inhibitors in HeLa and MIA PaCa-2 human cancer cell lines

Otilija Keta^{1*}, Jelena Bošković², Vladana Petković¹, Neda Đorđević¹, Vladimir Dobričić², Olivera Čudina², Snežana B. Pajović¹

¹ University of Belgrade, Vinča Institute of Nuclear Sciences - National Institute of the Republic of Serbia, Department of Molecular Biology and Endocrinology, Mike Petrovića-Alas 12-14, 11001 Belgrade, Serbia; e-mail: otilijak@vin.bg.ac.rs, vladanap@vin.bg.ac.rs, neda@vin.bg.ac.rs, pajovic@vin.bg.ac.rs

² University of Belgrade, Faculty of Pharmacy, Department of Pharmaceutical Chemistry, Vojvode Stepe 450, 11000 Belgrade, Serbia; e-mail: jelena.boskovic@pharmacy.bg.ac.rs, vladimir.dobricic@pharmacy.bg.ac.rs, olivera.cudina@pharmacy.bg.ac.rs

* Corresponding author

DOI: 10.46793/ICCB23.503K

Abstract: Among novel cancer chemotherapy approaches, the use of cyclooxygenases (COXs) and lipoxygenases (LOXs) inhibitors represents a promising mean for cancer treatment showing lesser toxicity comparing to the currently used cytotoxic drugs. This study detailed the synthesis of three novel compounds: 1ME, BHTK-AA, and IBU-Ac, each with the capability to concurrently inhibit both COX-2 and 5-LOX. Subsequently, we assessed their effectiveness in inhibiting the proliferation of HeLa cervical and MIA PaCa-2 pancreatic cancer cells. The IC₅₀ values for both examined cell lines were approximately 40 μM, indicating the promising inhibitory potential of the IBU-Ac compound in both types of cancer cells. This finding is positioned to stimulate further investigation into the potential application of IBU-Ac against these particular types of cancers, while also advocating its use in combination with standard anti-cancer protocols, i.e., chemotherapeutics or radiation therapy. The results of this work are also advocating the development and refinement of dual COX-2 and 5-LOX inhibitors, thus improving their efficacy and safety.

Keywords: cancer, dual COX-2 and 5-LOX inhibitors, cytotoxicity

1. Introduction

In the context of tumor microenvironment, inflammation is currently acknowledged as one of the fundamental characteristics of cancer. Epidemiological studies have shown that individuals afflicted with chronic inflammatory conditions face an elevated likelihood of developing cancer, suggesting that inflammation is, to some extent, a causative factor rather than a consequence of cancer development [1]. The enzyme families cyclooxygenase (COX) and lipoxygenase (LOX) are accountable for the metabolism of arachidonic acid. During this metabolic pathway, secondary products such as eicosanoids, encompassing prostaglandins and leukotrienes can serve as potent agents in fostering inflammation [2,3]. Both COX-2 and 5-LOX are co-expressed, up-

regulated and the eicosanoids generated by these enzymes perform pivotal functions in the progression of cancer such as proliferation, angiogenesis, invasion and metastasis [2].

Dual COX-2 and 5-LOX inhibitors are being considered as promising and innovative anti-inflammatory agents, representing a potential strategy in cancer therapy. This approach of combined inhibition addresses certain limitations associated with selective COX-2 inhibitors, while also sparing the gastrointestinal mucosa [4, 5]. The primary objective of this study was to synthesize and assess the cytotoxic potential of novel compounds capable of simultaneously inhibiting both COX-2 and 5-LOX. The focus of this research was on investigating the inhibitory effects of three inhibitors on two types of cancer cells: cervical and pancreatic carcinoma.

2. Experimental

2.1 Synthesis of 1ME

1ME (Figure 1A) was synthesized through a series of three sequential steps. In the initial phase, 2-sulfobenzoic anhydride (0.01357 mol) was dissolved in 8 ml of methanol, followed by the addition of 6 ml of methanolic ammonia. The resulting product was collected, air-dried overnight, and subsequently utilized in the next step without any additional purification. The compound obtained from the preceding step (0.0129 mol) was dissolved in 2 ml of dimethyl formamide, and subsequently, 16 ml of thionyl chloride was introduced. The reaction mixture was subjected to reflux heating overnight, cooled within an ice bath, and then combined with crushed ice (approximately 200 ml). The ensuing product was extracted using dichloromethane, with subsequent evaporation to yield the acid chloride. To a solution of the acid chloride (0.004 mol) in 13 ml of tetrahydrofuran, a solution of hydroxylamine hydrochloride (0.008 mol) in 4 ml of water was added. The final product (1ME) was extracted using dichloromethane and then subjected to recrystallization from ethyl acetate.

2.2 Synthesis of BHTK-AA

A solution of 3,5-di-tert-butyl-4-hydroxybenzoic acid (0.42 mmol) was prepared by dissolving it with allylamine (0.5 mmol, 1.2 eq) in dimethylformamide (6 mL) at room temperature. Following this, EDC (0.63 mmol), HOBt (0.63 mmol), and TEA (0.84 mmol) were introduced into the reaction mixture. The resulting mixture was stirred overnight at room temperature. Subsequently, the product was subjected to further purification using preparative thin-layer chromatography (TLC) with a solvent mixture of dichloromethane and methanol in a ratio of 9.5:0.5 v/v. The chemical structure of BHTK-AA is presented in Figure 1B.

2.3 Synthesis of IBU-Ac

The synthesis of IBU-Ac (Figure 1C) was carried out in the following manner. 4'-isobutylacetophenone (17 mmol) and hydroxylamine hydrochloride (35 mmol) were dissolved in a mixture of ethanol (25 mL) and pyridine (25 mL), then heated at 50°C for 2 hours. The solution was evaporated to yield an oxime compound. This oxime (5 mmol)

was dissolved in ethanol (10 mL) and cooled to 0°C. Borane-pyridine complex (15 mmol, 3 eq) was added via syringe under a nitrogen, followed by the addition of 6M HCl (5 mL) after 10 minutes. The resulting mixture was subjected to ethyl acetate extraction, yielding compound C. To a solution of TEA (7.8 mmol) and compound C (2.6 mmol) in dichloromethane (10 mL) at 0°C, acetyl chloride (5.73 mmol) was added. The mixture was then introduced to 2M HCl (10 mL), and the organic layer was evaporated to obtain compound D. Compound D (0.36 mmol) was dissolved in 2-propanol (1 mL), and a solution of lithium hydroxide (207 mg/mL) in water (0.5 mL) was added. The resulting product was extracted using 2M HCl (5 mL) and ether (10 mL), followed by further purification through preparative TLC using an ethyl acetate – cyclohexane solvent mixture with a ratio of 15:1 v/v.

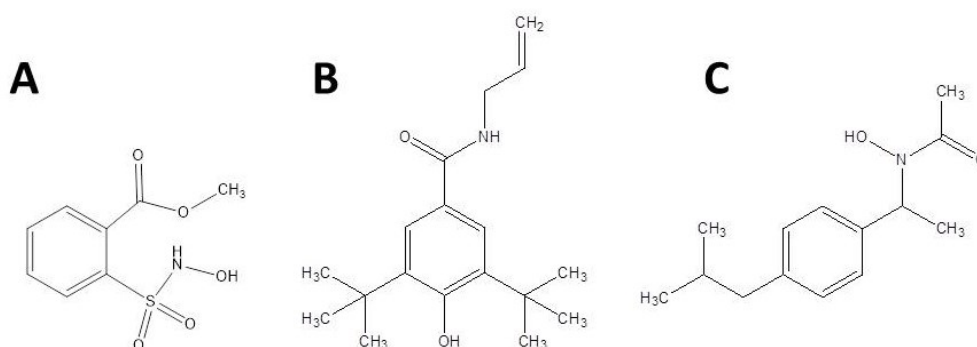


Figure 1. Chemical structure of 1ME (A), BHTK-AA (B) and IBU-Ac (C).

2.4 Cytotoxic activity of 1ME, BHTK-AA and IBU-Ac

For the evaluation of cytotoxic activity of synthesized compounds the MTT (3-[4,5-dimethylthiazol-2-yl]-2,5 diphenyl tetrazolium bromide) assay was applied according to procedure described elsewhere [6]. Briefly, HeLa and MIA PaCa-2 cells (ATCC, Manassas, VA, USA) were grown in 96-well plates, treated with increasing concentrations of tested compounds for 72 h and then incubated with MTT (Sigma-Aldrich Chemie GmbH, Steinheim, Germany) until blue formazan crystals were formed. The water-insoluble formazan produced is then solubilized by a dimethyl sulfoxide (DMSO). Subsequently, the absorbance was measured by a microplate reader (Wallac, VICTOR2 1420 Multilabel counter, PerkinElmer, Turku, Finland) at a wavelength of 550 nm. The IC_{50} values of each inhibitor are given in Table 1. The results have shown that only after application of IBU-Ac 50% inhibition in both cell lines can be achieved. However, the observed IC_{50} values did not differ much between HeLa and MIA PaCa-2 cells being around 40 μ M. As presented in Table 1, 1ME and BHTK-AA did not have a significant impact on the viability of tested cell lines.

Table 1. Cytotoxic activity of 1ME, BHTK-AA and IBU-Ac estimated by MTT assay with corresponding IC₅₀ values.

Cell line	1 ME IC ₅₀ (μM)	BHTK-AA IC ₅₀ (μM)	IBU-Ac IC ₅₀ (μM)
HeLa	>100	>100	39.89±0.61
MIA PaCa-2	>100	>100	46.80±0.29

3. Conclusions

The results of this preliminary study suggest that among three newly synthesized dual COX-2 and 5-LOX inhibitors, IBU-Ac acts as a potent inhibitor against cervical and pancreatic carcinoma. The aim of future experiments will be to investigate more deeply the mechanisms that underlie the response to this agent and to test its utility in conjunction with other anti-cancer modalities.

Acknowledgment

This research is funded by the Ministry of Education and Ministry of Science, Technological Development and Innovation, Republic of Serbia, Grants: No. 451-03-47/2023-01/ 200161 and 451-03-47/2023-01/200017.

References

- [1] E.R. Greene, S. Huang, C.N. Serhan, D. Panigrahy., *Regulation of inflammation in cancer by eicosanoids, Prostaglandins and other lipid mediators*, 96 (2011) 27-36.
- [2] L. Goossens, N. Pommery, J.P. Hénichart., *COX-2/5-LOX dual acting anti-inflammatory drugs in cancer chemotherapy*, *Current topics in medicinal chemistry*, 7 (2007) 283-296.
- [3] X.H. Che, C.L. Chen, X.L. Ye, G.B. Weng, X.Z. Guo, W.Y. Yu, J. Tao, Y.C. Chen, X. Chen., *Dual inhibition of COX-2/5-LOX blocks colon cancer proliferation, migration and invasion in vitro*, *Oncology reports*, 35 (2016) 1680-1688.
- [4] M. Rudrapal, W.A. Eltayeb, G. Rakshit, A.A. El-Arabey, J. Khan, S.M. Aldosari, B. Alshehri, M. Abdalla., *Dual synergistic inhibition of COX and LOX by potential chemicals from Indian daily spices investigated through detailed computational studies*, *Scientific reports*, 13 (2023) 8656.
- [5] J. Bošković, V. Dobričić, M. Mihajlović, J. Kotur-Stevuljević, O. Čudina., *Synthesis, Evaluation of Enzyme Inhibition and Redox Properties of Potential Dual COX-2 and 5-LOX Inhibitors*, *Pharmaceuticals (Basel)*. 16 (2023) 549.
- [6] M. Ghasemi, T. Turnbull, S. Sebastian, I. Kempson., *The MTT Assay: Utility, Limitations, Pitfalls, and Interpretation in Bulk and Single-Cell Analysis*, *International journal of molecular sciences*. 22 (2021) 12827.

Synthesis, characterization and HSA interactions of a new piano-stool ruthenium(II) complex containing a thioamide-type ligand

Danijela Stojković^{1*}, Maja Đukić², Marija Ristić², Marina Ćendić Serafinović², Svetlana Belošević³, Emina Mrkalić¹, Ivan Jakovljević²

¹ University of Kragujevac, Institut for Information Technologies, Department of Science, Jovana Cvijića bb, 34000 Kragujevac, Republic of Serbia; e-mail: danijela.stojkovic@kg.ac.rs, emina.mrkalic@pmf.kg.ac.rs

² University of Kragujevac, Faculty of Science, Radoja Domanovića 12, 34000 Kragujevac, Republic of Serbia; maja.djukic@pmf.kg.ac.rs, marija.jeremic@pmf.kg.ac.rs, marina.cendic@pmf.kg.ac.rs, ivan.jakovljevic@pmf.kg.ac.rs

³ University of Priština in Kosovska Mitrovica, Faculty of Technical Sciences, Knjaza Miloša 7, 38220 Kosovska Mitrovica, Republic of Serbia; svetlana.belosevic@pr.ac.rs

* Corresponding author

DOI: 10.46793/ICCB23.507S

Abstract: The synthesis and characterization of a newly synthesized piano-stool [Ru-(η^6 -*p*-cymene)Cl₂L] complex with a ligand 3-amino-2-cyano-*N*-phenyl-3-(4-phenyl-1-piperazinyl)-2-propenethioamide are presented. The complex was obtained in good yield as an ochre powder and was characterized by elemental analysis, ¹H and ¹³C NMR, IR, conductometry, and melting point. The fluorescence binding studies showed that the interaction of the complex with albumin occurs by a static quenching mechanism and that the complex showed a very high value of the binding constant with one binding site ($K_b = 1.68 \times 10^7$; $n = 1.37$). In order to identify the binding location in the HSA molecule, competitive experiments with site markers (eosin Y (site I) and ibuprofen (site II)) were performed. Obtained results showed that the examined complex binds to the site I of subdomain IIA (for eosin Y: $K_b = 5.94 \times 10^2$; $n = 0.65$ vs. for ibuprofen: $K_b = 1.38 \times 10^7$; $n = 1.34$).

Keywords: ruthenium(II) complex, thioamide, synthesis, HSA interactions

1. Introduction

The success of cisplatin as an antitumor agent has encouraged many research groups worldwide to direct their efforts toward the synthesis of other clinically important metal complexes [1,2]. An ideal anticancer drug must be able to destroy tumor cells while leaving adjacent healthy tissue unharmed. Great attention is paid to platinum group metals, i.e., their complexes, including ruthenium(II)-*p*-cymene complexes. Over the last few years, our research group has reported several scientific papers and described in

detail a structure-activity relationship and *in vitro* cytotoxicity of imidazole and isothiazole piano-stool Ru(II) complexes [3-5]. Since thioamides are precursors in the synthesis of isothiazoles, which were already the subject of our research and showed good antitumor activity [3,4], we have synthesized and characterized a new Ru(II) complex containing thioamide. Additionally, we have studied the binding affinity of complex toward human serum albumin (HSA).

2. Experimental

All chemicals were purchased from Sigma-Aldrich and used as received. Elemental analysis was performed on a Carlo Erba Elemental Analyser 1106. ^1H and ^{13}C NMR spectra were recorded on a Varian Gemini 2000 spectrometer. IR spectra were recorded on a Perkin Elmer FT-IR spectrophotometer. Fluorescence spectra were performed using an RF-1501 PC spectrofluorometer. Molar conductivity was made using an EC-metre BASIC 30+ conductometer. The melting point was measured on the Stuart melter.

2.1 Synthesis of the complex $[\text{Ru}(\eta^6\text{-}p\text{-cymene})\text{Cl}_2\text{L}]$

The complex was synthesized according to the method described elsewhere [3], where L = 3-amino-2-cyano-*N*-phenyl-3-(4-phenyl-1-piperazinyl)-2-propenethioamide [6]. Yield: 73%. Anal. Calcd. for $(\text{C}_{30}\text{H}_{35}\text{Cl}_2\text{N}_5\text{RuS})$ C: 53.81; H: 5.27; N: 10.46. Found: C: 53.72; H: 5.35; N: 10.39. ^1H NMR (200 MHz, CDCl_3): δ = 7.52-7.44 (m, Ar-CH, 3H), 7.29-6.94 (m, Ar-CH, 8H), 6.82-6.70 (m, Ar-CH, 3H), 3.59 (t, $-\text{CH}_2-$, 4H), 3.14 (t, $-\text{CH}_2-$, 4H), 3.01-2.86 (sept, $1\text{-CH}(\text{CH}_3)_2$, 1H), 1.92 (s, Ar- CH_3 , 3H), 1.28 (d, CH_3 , 6H). ^{13}C NMR (50 MHz, CDCl_3): 178.92, 162.52, 149.25, 143.86, 136.28, 131.73, 127.88, 124.19, 119.83, 113.08, 111.26, 62.32, 45.03, 43.62, 31.25, 21.83, 19.52. IR (KBr, 4000-400 cm^{-1}): ν (cm^{-1}) 3412 ($\nu=\text{CH}$), 3059 (νCH), 2187 ($\nu\text{C}\equiv\text{N}$), 1578 ($\nu\text{C}=\text{C}$). Mol. Cond. (DMSO , $\Omega^{-1}\text{ cm}^{-1}\text{ mol}^{-1}$): Λ_m 12. Melting point: 221 °C.

2.3 Albumin-binding studies

Protein binding studies have been performed using human serum albumin (HSA, 2 μM) in buffer (10 mM PBS, pH 7.4). The quenching of the emission intensity of HSA tryptophan residues at 361 nm was monitored using the investigated complex as a quencher with increasing concentration (up to 2.0×10^{-5} M). Fluorescence spectra were recorded from 300 to 500 nm at an excitation wavelength of 295 nm. Besides, we have studied the competitive interactions of the site markers (eosin Y, as a marker for site I of subdomain IIA, and ibuprofen, as a marker for site II of subdomain IIIA) [7] and complex toward HSA using the same method as above ($[\text{HSA}] : [\text{markers}] = 1:1$).

3. Results and discussion

The HSA solutions exhibit strong fluorescence emission with a peak at about 350 nm, which is due to the tryptophan residues when excited at 295 nm [8]. The addition of complex to the solution of HSA results in a decrease of the intensity of the peak (Figure 1a). The Stern-Volmer constant (K_{sv}) and quenching rate constant (k_q) were calculated using the Stern-Volmer quenching equation (1):

$$\frac{F_0}{F} = 1 + k_q \tau_0 [Q] = 1 + K_{sv}[Q] \quad (1)$$

where F_0 and F are the emission intensity in the absence and presence of the $[Q]$, K_{sv} is the Stern-Volmer constant, k_q is the quenching rate constant, τ_0 is the average fluorescence lifetime of HSA without a quencher. The k_q is higher than the different quenching types for biopolymer fluorescence ($10^{10} \text{ M}^{-1} \text{ s}^{-1}$), indicating a static quenching mechanism. The binding constant (K_b) and the number of binding sites per HSA (n), were calculated using the Scatchard equation (2):

$$\log \frac{F_0 - F}{F} = \log K_b + n \log [Q] \quad (2)$$

The values of K_b and n were obtained from the intercept and slope of the plots of $\log (F_0 - F)/F$ versus $\log [Q]$ (Table 1). The obtained values for K_b and n indicate the ability of the complex to strongly bind to HSA occupying one binding site.

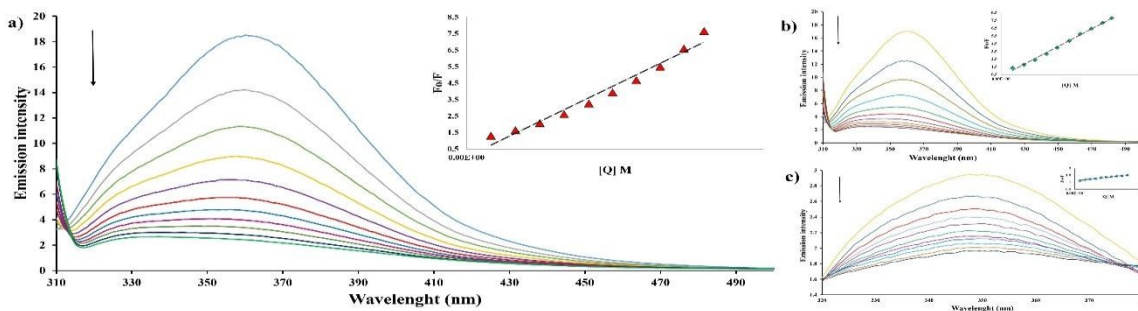


Figure 1. Emission spectra of: complex-HSA (a), complex-HSA-ibuprofen (b) and complex-HSA-eosin Y. $[HSA] = [ibuprofen] = [eosin Y] = 2 \mu\text{M}$, $[Q] = 0\text{-}20 \mu\text{M}$. Insert: plots of F_0/F vs. $[Q]$.

Table 1. The values of K_{sv} , k_q , K_b , and the possible number of binding sites (n) for various systems.

System	$K_{sv} [\text{M}^{-1}]$	$k_q [\text{M}^{-1} \text{ s}^{-1}]$	$K_b [\text{M}^{-1}]$	n
Complex-HSA	3.49×10^5	3.49×10^{13}	1.68×10^7	1.37
Complex-HSA-ibuprofen	3.76×10^5	3.76×10^{13}	1.38×10^7	1.34
Complex-HSA-eosin Y	2.11×10^4	2.11×10^{12}	5.94×10^2	0.65

Competitive experiments with site markers were performed to determine the preferred binding site of the complex to the HSA (Table 1 and Figure 1(b, c)). The decrease in the fluorescence intensity of the HSA solution after the addition of site markers indicates that the marker molecules bind to HSA. If the complex binds to the same site as the corresponding marker the complex must compete with the marker in order to bind to HSA, leading to a significant change in the constant value. In Table 1 it can be seen that the presence of eosin Y significantly decreased values of K_b and n , which

means that the complex binding should be mainly located in site I (subdomain IIA) of HSA, occupying a single binding site.

4. Conclusions

In this work we have synthesized and characterized a new piano-stool $[Ru(\eta^6\text{-}p\text{-cymene})Cl_2L]$ complex, $L = 3\text{-amino-2-cyano-N-phenyl-3-(4-phenyl-1-piperazinyl)-2-propenethioamide}$. The complex was obtained in good yield as an ochre powder. The results of elemental microanalysis, molar conductivity, melting point, and spectroscopic characterization (IR, 1H and ^{13}C NMR) are in agreement with the assumed structure of the complex. The obtained fluorescence results show that the quenching mechanism is static and that the complex strongly binds to one site for HSA (site I of subdomain IIA), which enables the safe transport of the complex to biological targets.

Acknowledgment

This research is funded by the Ministry of Education and Ministry of Science, Technological Development and Innovation, Republic of Serbia, Grants: No. 451-03-47/2023-01/200122, and No. 451-03-47/2023-01/200378.

References

- [1] E. Wong, C.M. Giandomenico., *Current Status of Platinum-Based Antitumor Drugs*, Chemical Reviews, 99 (1999) 2451-2466.
- [2] R.B. Weiss, M.C. Christian., *New cisplatin analogues in development. A review*, Drugs, 46 (1993) 360-377.
- [3] M.B. Đukić, M.S. Jeremić, I.P. Filipović, O.R. Klisurić, V.V. Kojić, D.S. Jakimov, R.M. Jelić, V. Onnis, Z.D. Matović., *Synthesis, characterization, HSA/DNA interactions and antitumor activity of new $[Ru(\eta^6\text{-}p\text{-cymene})Cl_2(L)]$ complexes*, Journal of Inorganic Biochemistry, 213 (2020) 111256.
- [4] M.B. Djukić, M.S. Jeremić, I.P. Filipović, O.R. Klisurić, R.M. Jelić, S. Popović, S. Matić, V. Onnis, Z.D. Matović., *Ruthenium(II) Complexes of Isothiazole Ligands: Crystal Structure, HSA/DNA Interactions, Cytotoxic Activity and Molecular Docking Simulations*, 5 (2020) 11489-11502.
- [5] M. Djukić, M.S. Jeremić, R. Jelić, O. Klisurić, V. Kojić, D. Jakimov, P. Djurdjević, Z.D. Matović., *Further insights into ruthenium(II) piano-stool complexes with N-alkyl imidazoles*, Inorganica Chimica Acta, 483 (2018) 359-370.
- [6] M.T. Cocco, V. Onnis., *An improved procedure for the preparation of substituted thiazoles*, Synthesis (1993) 199-201.
- [7] R. Esteghamat-Panah, H. Hadadzadeh, H. Farrokhpour, J. Simpson, A. Abdolmaleki, F. Abyar., *Synthesis, structure, DNA/protein binding, and cytotoxic activity of a rhodium(III) complex with 2,6-bis(2-benzimidazolyl)pyridine*, European Journal of Medicinal Chemistry, 127 (2017) 958-971.
- [8] J.R. Lakowicz, G. Weber., *Quenching of fluorescence by oxygen. A probe for structural fluctuations in macromolecules*, Biochemistry, 12 (1973) 4161-4170.

HPLC/UV profile and determination of total phenolic and flavonoid contents of lichen *Umbilicaria crustulosa* growing in Serbia

Jovica Tomović¹, Perica Vasiljević², Aleksandar Kočović¹, Nedeljko Manojlović^{1*}

¹ Department of Pharmacy, Faculty of Medical Sciences, University of Kragujevac, 34000 Kragujevac, Serbia; e-mail: jovicatomovic2011@gmail.com, salekkg91@gmail.com, mtnedeljko@gmail.com

² Department of Biology and Ecology, Faculty of Sciences and Mathematics, University of Niš, 18000, Niš, Serbia; e-mail: pericavasiljevic@gmail.com

* Corresponding author

DOI: 10.46793/ICCB23.511T

Abstract: The lichens synthesize a large number of secondary metabolites and most of these compounds are unique to lichen. The present study provides data concerning the chemical characterization and determination of total phenolic and flavonoid contents of lichen extracts of *Umbilicaria crustulosa*. Chemical profiling of the extracts was done by high-performance liquid chromatography coupled with a UV detector (HPLC/UV), while the determination of total phenolic and flavonoid contents was done by the spectrophotometric method. HPLC analysis of the acetone and methanol extracts of *U. crustulosa* lichen revealed the presence of the methyl-orselinate, lecanoric acid, crustinic acid, haematommic acid, gyrophoric acid, methyl lecanorate, physodic acid, atranorin and chloroatranorin as the main compounds. The most abundant compounds of the acetone and methanol extracts were the tri-depside gyrophoric acid (59.27 % and 58.32 %) and didepside lecanoric acid (7.41 % and 11.43 %). The results of the total phenolic content (TPC) and total flavonoid content (TFC) show that the acetone extract had higher values of TPC (205.46 mg GA/g) and TFC (290.18 mg RE/g; 160.50 mg QE/g). The investigated extracts of the lichen *U. crustulosa* can be used as a significant source of biologically active compounds.

Keywords: Lichens, Phenols, HPLC, *Umbilicaria*

1. Introduction

Lichens are a group of organisms that are numerous and represented, but very little known. The lichens synthesize a large number of secondary metabolites and most of these metabolites are unique to lichen [1]. These are mainly monoaromatics, depsides, depsidones, depsones, pulvinates, dibenzofurans, anthraquinones, and xanthonones. These compounds are generally insoluble in water and can be extracted with organic solvents. [2]. The genus *Umbilicaria* includes foliose lichens that are used in folk medicine as purgatives (laxatives). Due to its specific chemical composition, the genus *Umbilicaria*

has shown significant biological activity [3]. For this reason and due to the lack of data on the *Umbilicaria crustulosa* species, we performed a chemical analysis and examination of the total polyphenols and flavonoid contents of the methanolic and acetone extracts.

2. Materials and Methods

Lichen was collected at the site of the mountain Stara Planina. Specimen of the lichen *U. crustulosa* was determined using the relevant key and monographs. The dried lichen material is crushed to a fine powder using a mill. Thereafter, a separate extraction was performed with the acetone and methanol using maceration.

HPLC analyses were performed on the Agilent 1200 Series (Agilent Technologies, Santa Clara, CA, USA) using the C18 column (ZORBAX Eclipse XDB-C18; 25cm×4.6mm; 5 µm). Separate dot detection was performed using a Diode Array Detector (DAD). Identification of individual constituents of the extracts was made by comparing the retention times (t_R) and UV spectra of the compounds with standards ($\lambda = 200\text{--}400$ nm).

The total content of polyphenols in the two extracts was determined with the Folin-Ciocalte reagent, by the spectrophotometric method [4]. The content of the total polyphenols was calculated using an equation obtained from a standard gallic acid calibration curve, and the results were expressed in mg equivalents of gallic acid per g of dry extract (mg GA/g).

The content of total flavonoids in the extracts was determined according to the method described by Sushant et al. [5]. Rutin and quercetin were used as standards, and the results are expressed in milligrams of quercetin equivalents and milligrams of rutin equivalents per gram of dry extract (mg QE/g dry extract or mg RE/g dry extract).

3. Results and Discussion

The HPLC chromatograms of the acetone and methanol extracts of *U. crustulosa* were recorded at 254 nm (Figure 1). HPLC analysis of the acetone and methanol extracts of *U. crustulosa* lichen revealed the presence of the monoaromatic compounds methylorselinate, lecanoric acid (didepside), crustinic acid (tridepside), haematommic acid (monoaromatic component), gyrophoric acid (tridepside), methyl lecanorate (didepside), physodic acid (depsidone) and β -orcinol depside atranorin and chloroatranorin as the main components. The most abundant compound of the acetone and methanol extract of *U. crustulosa* is the tri-depside gyrophoric acid (59.27 % and 58.32 %). Apart from gyrophoric acid, lecanoric acid was also identified in high abundance in the acetone and methanol extract (7.41 % and 11.43 %, respectively). The combined occurrence of gyrophoric and lecanoric acids could indicate that lecanoric acid may be a hydrolysis product of gyrophoric acid [6,7]. Crustinic acid is a very common component of *Umbilicaria* species [6], but in our sample, it was found only in the acetone extract (3.23 %). The reason for this may be the greater presence of methyl orsellinate in the methanol extract (5.24 %) than in the acetone extract (2.89 %) due to the hydrolysis process. Physodic acids have previously been reported from the lichen *Hypogymnia physodes* and other lichens genus [8], but this is the first time to confirm the presence and isolate of this metabolite in the lichen *U. crustulosa*. The composition of the acetone extract is

different due to the presence of atranorin and chloratranorin, which were not identified in the methanol extract.

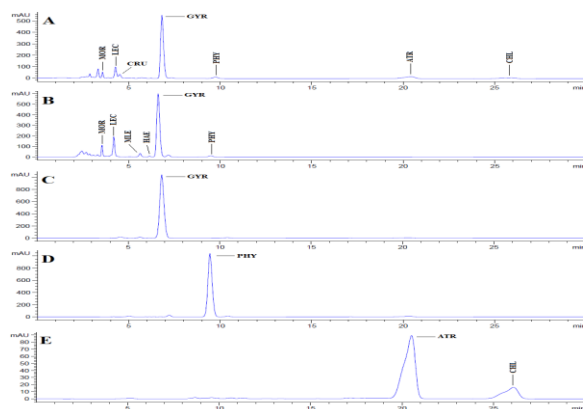


Figure 1. HPLC chromatograms of the acetone and methanol extracts of the lichen *Umbilicaria crustulosa* obtained at 254 nm. (A) the chromatogram of *Umbilicaria crustulosa* acetone extract; (B) the chromatogram of *Umbilicaria crustulosa* methanolic extract; (MOR-methyl orsellinate; LEC-lecanoric acid; CRU-crustinic acid; GYR-gyrophoric acid; PHY-physodic acid; ATR-atranorin; CHL-chloroatranorin; MLE-methyl lecanorate; HAE-haematommic acid.

In *Umbilicaria* species atranorin and chloratranorin could be found in small amounts [7]. Haematommic acid was also found in a very small amount in our methanolic extract (0.49 %). Detailed data on the retention time, absorption maxima, and content of the identified secondary metabolites are presented in Table 1.

Table 1. Retention time, absorbance maxima, and relative abundance of the examined substances.

Compound	Retention time ($t_R \pm SD$)* (min)	Absorbance maxima (nm)	Relative abundance %	
			Acetone	Methanol
Methyl orsellinate	3.54±0.02	218, 270, 308	2.89	5.24
Lecanoric acid	4.22±0.04	220, 270, 312	7.41	11.43
Crustinic acid	4.51±0.01	220, 268, 308	3.23	ND
Methyl lecanorate	5.62±0.01	228, 270, 308	ND	2.63
Haematommic acid	6.13±0.01	202, 236, 258, 280, 344	ND	0.49
Gyrophoric acid	6.70±0.10	214, 270, 304	59.27	58.32
Physodic acid	9.61±0.18	212, 263, 314	1.95	1.70
Atranorin	20.43±0.01	210, 252, 321	6.65	ND
Chloroatranorin	25.90±0.01	213, 252, 315, 350	3.34	ND

*Values are the means of three determinations±SD, ND-not detected.

The results of the total phenolic content (TPC) and total flavonoid content (TFC) are presented in Table 2. It can be observed that the acetone extract had higher values of TPC (205.46 mg GA/g) and TFC (290.18 mg RE/g; 160.50 mg QE/g;), both when quercetin

was used as the standard and when rutin was used as the standard. The examined extracts showed a higher amount of total phenols and flavonoids than the extracts of *Umbilicaria* species by other researchers [3]. The reason for this may be the influence of the extraction method or environmental factors.

Table 2. The total polyphenols and flavonoids content of the extracts of the lichen *U. crustulosa*.

Lichen extracts	Phenolics content (mg GA/g)	Flavonoids content (mg RE/g)	Flavonoids content (mg QE/g)
Acetone	205.46±0.39	290.18± 0.91	160.50 ± 0,56
Methanol	156.36±0.59	253.52± 0.53	138.09±0.32

*Values are expressed as mean ± SD of triplicate measurements; GA – gallic acid equivalents; RE - rutin equivalents; QE - quercetin equivalents.

3. Conclusions

This is the first report of the chemical analysis of the lichen *U. crustulosa* collected from S tara Planina and the identification of physodic acid from this lichen. Both investigated extracts contain a high amount of phenolic and flavonoid compounds. Future investigations will be focused on isolation compounds and the determination of their biological activities.

Acknowledgment

This work was supported by the Ministry of Education, Science and Technological Development of the Republic of Serbia (Agreement Nos. 451-03-47/2023-01/200111), and by the Science Fund of the Republic of Serbia, Grant No. 7743504, NES.

References

- [1] M.P. Nelsen, A. Gargas., *Phylogenetic distribution and evolution of secondary metabolites in the lichenized fungal genus Lepraria (Lecanorales: Stereocaulaceae)*, Nova Hedwigia, 86 (2008) 115–131.
- [2] B. Ranković., *Lichen Secondary Metabolites: Bioactive properties and pharmaceutical potential*, Springer, 1 (2014) 1-26.
- [3] M. Kosanić, B. Ranković, T. Stanojković., *Antioxidant, antimicrobial, and anticancer activity of 3 Umbilicaria species*, Journal of food science, 77 (2012) 20-25.
- [4] V.L. Singleton, R. Orthofer, R.M. Lamuela-Raventós., *Analysis of total phenols and other oxidation substrates and antioxidants by means of Folin-Ciocalteu reagent*. Methods in Enzymology, 299 (1999) 152-178.
- [5] S. Aryal, M.K. Baniya, K. Danekhu, P. Kunwar, R. Gurung, N. Koirala., *Total phenolic content, flavonoid content and antioxidant potential of wild vegetables from Western Nepal*, Plants, 8 (2019) 96.
- [6] B. Posner, G.B. Feige, S. Huneck., *Studies on the chemistry of the lichen genus Umbilicaria Hoffm*, Zeitschrift für Naturforschung C, 47 (1992) 1-9.
- [7] J.A. Elix, K.L. Gaul., *The interconversion of the lichen depsides para-and meta-scrobiculin, and the biosynthetic implications*, Australian Journal of Chemistry, 39 (1986) 613-624.
- [8] B. Ranković, M. Kosanić, N. Manojlović, A. Rančić, T. Stanojković., *Chemical composition of Hypogymnia physodes lichen and biological activities of some its major metabolites*. Medicinal Chemistry Research, 23 (2014) 408-416.

Lichenochemical analysis and *in vitro* antioxidant activity of extracts and gyrophoric acid from lichen *Umbilicaria grisea*

Miroslav Sovrlić¹, Nedeljko Manojlović^{1*}, Marijana Kosanić², Aleksandar Kočović¹, Jovica Tomović, Perica Vasiljević³

¹ University of Kragujevac, Faculty of Medical Sciences, Department of Pharmacy, Svetozara Markovića 69, 34000 Kragujevac, Serbia; msovrlic@medf.kg.ac.rs

² University of Kragujevac, Faculty of Science, Department of Biology, Radoja Domanovića 12, 34111 Kragujevac, Serbia; marijana.kosanic@pmf.kg.ac.rs

³ University of Niš, Faculty of Sciences and Mathematics, Department of Biology and Ecology, Višegradska 33, 18000 Niš, Serbia; pericavasiljevic@gmail.com

* Corresponding author

DOI: 10.46793/ICCB23.515S

Abstract: This research investigates the chemical composition, total phenolic and flavonoid content, and antioxidant activity of acetone, methanol, and ethanol extracts of the lichen *Umbilicaria grisea*, and its major secondary metabolite, gyrophoric acid. The extracts were analyzed using high-performance liquid chromatography (HPLC-UV) and spectrophotometric assays. The results showed significant levels of phenolic compounds and flavonoids, which contribute to the lichen's antioxidant potential. The antioxidant activity was evaluated using *in vitro* assays such as DPPH and ABTS radical scavenging activity. The extracts demonstrated potent antioxidant activity, suggesting their potential as natural antioxidants. The identification of bioactive compounds, high phenolic and flavonoid content, and significant antioxidant activity support the potential use of *U. grisea* as a natural source of therapeutic agents. Further studies are needed to elucidate the underlying mechanisms responsible for these biological activities and evaluate the efficacy and safety of these extracts for potential pharmaceutical applications.

Keywords: *Umbilicaria grisea*, gyrophoric acid, lichen bioactive compounds, antioxidant activity, natural product discovery.

1. Introduction

Lichens, symbiotic organisms with fungus and photosynthetic partners like algae or cyanobacteria, are gaining attention for their chemical diversity, biological activities, and potential therapeutic applications. They are rich sources of secondary metabolites with diverse structures and properties [1]. Due to more synonyms and misidentifications, the number of species from the lichen genus *Umbilicaria* varies between authors, who suggest about 70-80 species [2]. *Umbilicaria grisea* Hoffm. is a temperately distributed species found on siliceous, granite, and steep rock surfaces. The thallus is foliose, with a diameter of 1-5 cm and is attached to the substrate via the umbilicus. Gyrophoric acid is a tridepside, while lecanoric acid, a biosynthetic-related

depside, occurs in a lower concentration (90:1) [3]. Umbilicatic, hiascic, crustinic and ovoic acids are also present *Umbilicaria* tridepsides as well as depsidone norstictic acid [4]. *U. grisea* is understudied in its chemical composition and potential bioactivities. Understanding its antioxidant activity can provide valuable insights into its potential applications in pharmaceutical and biomedical fields.

The aim of this research was to identify the main bioactive secondary metabolites of the acetonic, methanolic and ethanolic extracts of the lichen *Umbilicaria grisea* Hoffm. by the HPLC–UV analysis and to determine total phenolic and flavonoid content, and antioxidant (DPPH and ABTS assays) activity of these three extracts.

2. Materials and methods

U. grisea lichen is collected from Mt. Kopaonik in Serbia. The lichen was identified using standard methods. The lichen material was ground in a laboratory mill and extracted using acetone, methanol, and ethanol as solvents. The extracts were filtered and evaporated to dryness in a vacuum evaporator. The dry extracts were poured into opaque glass bottles and stored in a refrigerator for future analyses.

Gyrophoric acid, obtained from the acetone extract of *U. grisea*, was isolated through a series of steps which included recrystallization, extraction with benzene and centrifugation. Identification was performed by comparing chromatographic and spectroscopic data with the standard.

The extracts were analyzed using an Agilent 1200 Series Gradient HPLC System coupled with a photodiode array detector. The mobile phase consisted of methanol, water, and phosphoric acid (80:20:0,9 %). The analysis time was 30 minutes, with a 1.0 ml/min flow, and 10 µl injected sample amount [5]. Standard compounds were isolated from various sources, and their structures were confirmed through mass spectrometry, ¹H, and ¹³C-NMR data. The *in-vitro* antioxidant activity of the lichen extracts was determined spectrophotometrically using DPPH and ABTS methods [6, 7]. The antioxidant capacity of the tested extracts was expressed as an inhibitory concentration (IC50). The total phenolic content was determined using the Folin-Ciocalteu method, with gallic acid (GA) as a standard and total flavonoid content was determined using a colorimetric method based on the reaction of flavonoids with AlCl₃, and rutin and quercetin were used as standards [5].

3. Results and discussion

The extraction yield and occurrence of individual compounds are shown in Table 1, and the total phenolic content and the total flavonoid content in each extract are presented in Table 2. The results indicate that different solvents used for lichen extraction had varying effects on the flavonoid content. Acetone extraction yielded the highest flavonoid content. Additionally, the results highlight the importance of solvent selection in the lichen extraction protocols to maximize the recovery of specific compounds of interest. The presence of secondary metabolites in the acetone, methanol and ethanol extracts was analyzed using the HPLC–UV method. Lecanoric acid, umbilicatic acid and gyrophoric acid were identified in all three extracts along with

depsidone norstictic acid and the depside atranorin which were reported for the first time in this species. The retention time of the examined lichen substances and their absorbance maxima are presented in Table 3.

Table 1. Yield of lichen extracts and presence of secondary metabolites in the *U. grisea* extracts.

Extracts	Used Eluent	Yields (%)	NOR	LEC	UMB	GYR	ATR
UGA	acetone	12,37 ± 1.33	+	+	+	+	+
UGM	methanol	14,2 ± 2.74	+	+	+	+	-
UGE	ethanol	8,75 ± 1.26	-	+	+	+	-

UGA- *U. grisea* acetonic extract; UGM- *U. grisea* methanolic extract; UGE- *U. grisea* ethanolic extract

Table 2. Total phenolic and flavonoid contents of *U. grisea* extracts (mean ± SD, n=3).

Sample	Total Phenolic Content (mg GAE/g Dry Extract)	Total Flavonoid Content (mg QE/g Dry Extract)	Total Flavonoid Content (mg RU/g Dry Extract)
UGA	56.615 ± 0.385	62.657 ± 0.160	116.303 ± 0.262
UGM	67.128 ± 0.222	54.324 ± 0.893	102.667 ± 1.461
UGE	44.821 ± 0.801	28.213 ± 0.424	59.939 ± 0.694

GAE- Gallic acid equivalent; QE- quercetin equivalent; RU- rutin equivalent.

Table 3. Retention time of the examined lichen substances and their absorbance maxima (nm)

Secondary metabolite	Substance class	Retention time ($t_R \pm SD$)* (min)	UV spectrum Absorbance maxima (nm)
Norstictic acid (NOR)	depsidone	3.21± 0.10	212, 239, 320
Lecanoric acid (LEC)	depside	4.06±0.20	212, 270, 304
Umbilicarinic acid (UMB)	tridepside	6.29± 0.20	210, 254, 292
Gyrophoric acid (GYR)	tridepside	6.34± 0.10	212, 270, 304
Atranorin (ATR)	depside	18.97± 0.10	212, 278, 312 ^m

* Values are the means of three determinations ± SD, m – minor absorbance maximum.

These compounds were identified based on the retention times and UV spectra compared with standard substances previously isolated from lichens and identified by spectroscopic methods in our laboratory. Depside lecanoric acid, tridepsides umbilicarinic acid and gyrophoric acid have been previously detected in *U.grisea*, while depsidone norstictic acid and depside atranorin were found for the first time in this species [6].

The chromatographic analysis showed that atranorin was not found in the methanol and the ethanol extracts, while norstictic acid was not identified in the ethanol extract. In addition, gyrophoric acid was isolated from the acetone extract of the lichen *U.grysea*. The gyrophoric acid purity was confirmed by HPLC (98.77 %). The different chemical compositions of these extracts and isolated gyrophoric acid made it possible to further use them in the investigation of the antioxidant activity (presented in Table 4). The acetone extract showed slightly better antioxidant activity compared to the other two extracts in all tests used. This may be related to the higher content of the flavonoid compounds in this extract. Also, gyrophoric acid shows significantly better antioxidant activity compared to all extracts, but weaker compared to ascorbic acid and Trolox.

Table 4. Results of *in vitro* antioxidant activity test.

Sample	DPPH (IC ₅₀ µg/ml)	ABTS (IC ₅₀ µg/ml)
UGA	3261.00 ± 141.38	2441.53 ± 142.71
UGM	3298.00 ± 50.24	2103.58 ± 156.69
UGE	3419.33 ± 108.58	2689.24 ± 197.78
GYR	354.17 ± 12.15	246.99 ± 11.88
AA	10.53 ± 1.57	8.28 ± 0.24
Trolox	15.59 ± 3.31	12.40 ± 0.40

3. Conclusions

The lichen *U. grisea* species studied in this research can be attractive as a source of bioactive substances with potential health benefits. This research contributes to general knowledge about this lichen species and the genus *Umbilicaria*. Furthermore, this research can provide valuable insights into the potential use of *U. grisea* extracts in the development of new therapeutic agents for combating oxidative stress-related disorders.

Acknowledgment

This work was supported by the Ministry of Education, Science and Technological Development of the Republic of Serbia (Agreement Nos. 451-03-47/2023-01/200111), and by the Science Fund of the Republic of Serbia, Grant No. 7743504, NES.

References

- [1] M. Goga, J. Elečko, M. Marcinčinová, D. Ručová, M. Bačkorová, M Bačkor., Lichen metabolites: an overview of some secondary metabolites and their biological potential, Co-evolution of secondary metabolites, (2020) 175-209.
- [2] G. Hestmark., Lectotypification of *Umbilicaria torrefacta* (Lightf.) Schrad., *The Lichenologist*, 49 (2017) 167-169.
- [3] B. Posner, G. B. Feige, S. Huneck., Studies on the Chemistry of the Lichen Genus *Umbilicaria* Hoffm., *Zeitschrift für Naturforschung C*, 47 (1992), 1-9.
- [4] T. Narui, K. Sawada, S. Takatsuki, T. Okuyama, C. F. Culberson, W. L. Culberson, S. Shibata., NMR assignments of depsides and tridepsides of the lichen family Umbilicariaceae, *Phytochemistry*, 48 (1998), 815-822.
- [5] N. Manojlovic, A. Rancic, R. Décor, P. Vasiljevic, J. Tomovic., Determination of chemical composition and antimicrobial, antioxidant and cytotoxic activities of lichens *Parmelia conspersa* and *Parmelia perlata*, *Journal of Food Measurement and Characterization*, 15 (2020) 686–696.
- [6] H. Dorman, O. Bachmayer, M. Kosar, R. Hiltunen., Antioxidant Properties of Aqueous Extracts from Selected Lamiaceae Species Grown in Turkey, *Journal of Agricultural and Food Chemistry*, 52 (2004) 762–770.
- [7] S. Tabassum, S. Ahmad, K.U. Rehman Khan, F. Tabassum, A. Khursheed, Q.U. Zaman, et al. Phytochemical profiling, antioxidant, anti-inflammatory, thrombolytic, hemolytic activity in vitro and in silico potential of *Portulacaria afra*. *Molecules*, 27 (2022) 2377.

Biological activity of thienyl-terpyridine Ru(II) complex in the presence of biocompatible ionic liquids

Ana Rilak Simović^{1*}, Milica Međedović², Dejan Lazić³, Milan Vraneš⁴, Ghodrat Mahmoudi⁵, Biljana Petrović²

¹ University of Kragujevac, Institute for Information Technologies, Department of Natural Science, 34000 Kragujevac, Serbia, Jovana Cvijića bb; e-mail: anarilak@kg.ac.rs

² University of Kragujevac, Faculty of Science, Department of Chemistry, 34000 Kragujevac, Serbia, Radoja Domanovića 12; e-mail: milica.medjedovic@pmf.kg.ac.rs, biljana.petrovic@pmf.kg.ac.rs

³ University of Kragujevac, Faculty of Medical Sciences, Department of Surgery, 34000 Kragujevac, Serbia, Svetozara Markovića 69; e-mail: dlazic.kg@gmail.com

⁴ University of Novi Sad, Faculty of Sciences, Department of Chemistry, Biochemistry and Environmental Protection, 21000 Novi Sad, Serbia, Trg Dositeja Obradovića 3; e-mail: milan.vranes@dh.uns.ac.rs

⁵ University of Maragheh, Faculty of Science, Department of Chemistry, Maragheh, Iran, e-mail: ghodratmahmoudi@gmail.com

* Corresponding author

DOI: 10.46793/ICCB23.519RS

Abstract: New mononuclear Ru(II)-thienyl-terpyridine complex [Ru(thienyl-tpy)(bpy)Cl]Cl (where thienyl-tpy = 4'-(2-thienyl)-2,2':6',2''-terpyridine, bpy = 2,2'-bipyridine) has been synthesized and then characterized through elemental analysis, followed by various spectroscopic (IR, UV-vis, ¹H and ¹³C NMR) and mass spectrometric technique (ESI Q-TOF MS). Furthermore, the interactions with CT DNA were performed both in the absence and presence of biocompatible ionic liquids 1-amino-2-propanol-lactate (IL1), 1-amino-2-propanol-oxalate (IL2) and 1-amino-2-propanol-citrate (IL3).

Keywords: Ruthenium(II), thienyl-terpyridine, ionic liquids, DNA

1. Introduction

The primary purpose of discovering new metallodrugs is to create and implement novel medicines with better efficacy and tolerance. Scientists are still working on developing new transition metal ion complexes for cancer therapy that have fewer side effects, are more resistant to drugs, and are more biocompatible than the compounds used so far [1]. Ruthenium-based pharmaceuticals have shown encouraging results as potential

anticancer agents due to their unique features such as biological, photophysical, optical, electronic, and catalytic properties, which provide advantageous therapeutic application opportunities [2]. Among the several reported Ru complexes with anticancer therapeutic potential, the Ru(II) polypyridyl complex (TLD1433) and Ru(III) complexes (NAMI-A and KP1019) have advanced to clinical trials [3-5]. The medicinal chemistry community has not yet identified all pharmacological targets (intracellular or extracellular) of anticancer ruthenium compounds. Most of the ruthenium complexes appear to be multitarget compounds capable of binding to several biological molecules, mainly DNA and proteins, but determining which target is the most relevant for biological activity is difficult and requires extensive studies of their interactions with different biomolecules. In this work, we present the synthesis and characterization of the new thienyl-terpyridine Ru(II) complex $[\text{Ru}(\text{thienyl-tpy})(\text{bpy})\text{Cl}]\text{Cl}$ (where thienyl-tpy = 4'-(2-thienyl)-2,2':6',2''-terpyridine, bpy = 2,2'-bipyridine) and its biological activity with calf-thymus DNA (CT-DNA) in the presence of biocompatible ionic liquids 1-amino-2-propanol-lactate (IL1), 1-amino-2-propanol-oxalate (IL2) and 1-amino-2-propanol-citrate (IL3).

2. Biological activity of thienyl-terpyridine Ru(II) complex

The synthesis of the Ru complex was performed by reacting the neutral Ru(III) precursors *mer*- $[\text{Ru}(\text{thienyl-tpy})\text{Cl}_3]$ with the bpy chelating ligand under the reflux. The complex was characterized by elemental analysis and by various spectroscopic techniques, such as IR, UV-Vis, ^1H and ^{13}C NMR, and ESI-MS. Before examining the biological properties of the mononuclear Ru (II) complex, we studied its stability in an aqueous solution. The intensity of the absorption maxima of the Ru(II) complex decreased over 24 h, which was ascribed to the hydrolysis of Ru(II)-bound chloride.

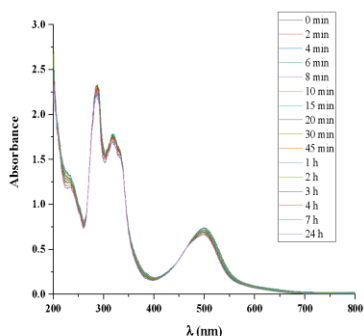


Figure 1. UV-Vis spectra of Ru(II) complex in water over a 24 h period.

2.1 DNA binding investigation

DNA-compound interactions can be established via different modes, including covalent binding, minor groove binding, major groove binding, intercalation and electrostatic interactions [6]. UV-Vis absorption spectroscopy can assess the general interactions (overall binding affinity) between metal compounds and DNA. The binding affinity of

the complex was evaluated by following the changes in the spectra of the compound upon increasing the concentration of the CT-DNA. In the present study, the absorption titration studies were conducted at room temperature using fixed concentration of complex (10 μ M) in PBS and varying amounts of CT-DNA (2–20 μ M).

The intrinsic binding constant, K_b , was determined by monitoring the change in the absorbance at the MLCT band after the addition of growing concentration of the DNA solution, based on the following eqn (1)

$$[DNA]/(\epsilon_A - \epsilon_f) = [DNA]/(\epsilon_b - \epsilon_f) + 1/[K_b(\epsilon_b - \epsilon_f)] \quad (1)$$

K_b is given by the ratio of the slope to the y intercept in plots $[DNA]/(\epsilon_A - \epsilon_f)$ vs. $[DNA]$, where $[DNA]$ is the concentration of DNA in base pairs, $\epsilon_A = A_{\text{obsd}}/[\text{complex}]$, ϵ_f is the extinction coefficient for the unbound complex and ϵ_b is the extinction coefficient for the complex in the fully bound form.

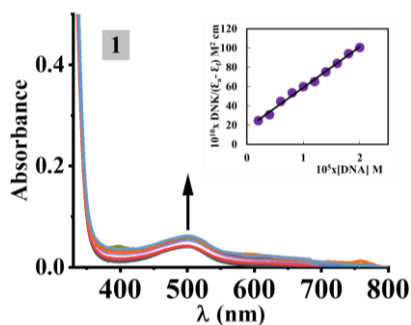


Figure 2. Absorption spectra of complex in 10 mM PBS upon addition of CT DNA.

Interactions of Ru complex and CT-DNA were also examined in the presence of ionic IL1, IL2 and IL3. This was done in order to see if the ionic liquids used as cosolvents have an impact on the interactions between the examined complex and the DNA molecule. Ionic liquids were added in the same amount as the examined complex, e.g., the concentrations were kept the same as the concentration of the complex. Based on the results shown in Table 1, it can be noted that the presence of ionic liquids affects the values of K_b . The highest value was noted in the presence of IL3, while the lowest was in the presence of IL1. In the presence of all three ILs, the values are higher compared to the value obtained in the absence of ILs, implying that the presence of ionic liquids enhances the reactivity of the examined complex with the DNA molecule. Furthermore, it was concluded that applied IL can be used as cosolvents, increasing the solubility of Ru(II)-thienyl-tpy complex. For comparison, ruthenium(II)-terpyridine complexes of the general formula $[\text{Ru}(\text{Cl-tpy}/\text{Cl-Ph-tpy})(\text{N-N})\text{Cl}]^+$ that we previously obtained had similar K_b values of order 10^5 M^{-1} for the interaction with CT DNA [6].

Table 1. The DNA-binding constants (K_b) for the Ru complex.

PBS	IL1	IL2	IL3
$K_b [\text{M}^{-1}]$			

Ru complex	2×10^5	2.22×10^5	2.50×10^5	3.33×10^5
------------	-----------------	--------------------	--------------------	--------------------

3. Conclusions

Here, we described the interactions of Ru(II)-thienyl-tpy complex with CT DNA in the absence and presence of ILs (IL1–IL3), indicating that the IL used as cosolvents significantly affect the binding of the complex to the CT DNA molecule. From the obtained results, it was concluded that applied ILs could be used as cosolvents for the examined complex with the most promising being IL3 (1-amino-2-propanol-citrate).

Acknowledgment

The authors would like to express their gratitude to the Ministry of Science, Technological Development and Innovation of the Republic of Serbia (Agreement No. 451-03-47/2023-01/200378 and Agreement No. 451-03-47/2023-01/200122) for financial support.

References

- [1] A.R. Simović, R. Masnikosa, I. Bratsos and E. Alessio., *Chemistry and reactivity of ruthenium(II) complexes: DNA/protein binding mode and anticancer activity are related to the complex structure*, Coordination Chemistry Reviews, 398 (2019) 113011.
- [2] E. Alessio, *Bioinorganic Medicinal Chemistry*, Wiley-VCH Verlag & Co. KGaA, Weinheim, Germany, 2011 J. Schaff, C.C. Fink, B. Slepohenko, J.H. Carson, L.M. Loew., *A General Computational Framework for Modeling Cellular Structure and Function*, Biophysical Journal, 73 (1997) 1135-1146.
- [3] W. Zheng, Y. Zhao, Q. Luo, Y. Zhang, K. Wu, F. Wang., *Science China Chemistry, Rational design of multi-targeting ruthenium- and platinum-based anticancer complexes*, 59 (2016) 1240–1249.
- [4] S. Leijen, S. A. Burgers, P. Baas, D. Pluim, M. Tibben, E. van Werkhoven, E. Alessio, G. Sava, J. H. Beijnen, J. H. M. Schellens., *Phase I/II study with ruthenium compound NAMI-A and gemcitabine in patients with non-small cell lung cancer after first line therapy*, Investigational New Drugs, 33 (2015) 201–214.
- [5] F. Lentz, A. Drescher, A. Lindauer, M. Henke, R. A. Hilger, C. G. Hartinger, M. E. Scheulen, C. Dittrich, B. K. Keppler, U. Jaehde., *Pharmacokinetics of a novel anticancer ruthenium complex (KP1019, FFC14A) in a phase I dose-escalation study*, Anti-Cancer Drugs, 20 (2009) 97–103.
- [6] M. Međedović, A. Rilak Simović, D. Čočić, L. Senft, S. Matić, D. Todorović, S. Popović, D. Baskić, B. Petrović., *New ruthenium(II) complexes with quinone diimine and substituted bipyridine as inert ligands: synthesis, characterization, mechanism of action, DNA/HSA binding affinity and cytotoxic activity*, Dalton Transactions, 52 (2023) 1323–1344.

Kinetic studies of the Ru(II) polypyridyl complex with biologically relevant ligands

Milica Međedović¹, Dejan Lazić², Milan Vranes³, Ghodrat Mahmoudi⁴, Biljana Petrović¹, Ana Rilak Simović^{5*}

¹ University of Kragujevac, Faculty of Science, Department of Chemistry, 34000 Kragujevac, Serbia, Radoja Domanovića 12; e-mail: milica.medjedovic@pmf.kg.ac.rs, biljana.petrovic@pmf.kg.ac.rs

² University of Kragujevac, Faculty of Medical Sciences, Department of Surgery, 34000 Kragujevac, Serbia, Svetozara Markovića 69; e-mail: dlazic.kg@gmail.com

³ University of Novi Sad, Faculty of Sciences, Department of Chemistry, Biochemistry and Environmental Protection, 21000 Novi Sad, Serbia, Trg Dositeja Obradovića 3; e-mail: milan.vranes@dh.uns.ac.rs

⁴ University of Maragheh, Faculty of Science, Department of Chemistry, Maragheh, Iran, e-mail: ghodratmahmoudi@gmail.com

⁵ University of Kragujevac, Institute for Information Technologies, Department of Natural Science, 34000 Kragujevac, Serbia, Jovana Cvijića bb; e-mail: anarilak@kg.ac.rs

* Corresponding author

DOI: 10.46793/ICCBi23.523M

Abstract: In a group of transition metal complexes that scientists have synthesized to find a good replacement for cisplatin, ruthenium complexes, with various good properties, occupy a very important place. In this group, ruthenium polypyridyl complexes showed promising properties and became leading candidates for use as anticancer agents. In this study, we have synthesized a new ruthenium (II) polypyridyl complex of general formula $[Ru(L)(N-N)Cl]Cl$, where L is 2,2':6',2''-terpyridine with the additional functional group in the 4'-position: 2-thienyl and $N-N$ =bpy (2,2'-bipyridine). The kinetics of the substitution reactions of the studied complex with important biomolecules, the nitrogen-containing ligand 5'-GMP and the S-containing ligand L-Cys, were monitored. The kinetic results showed a faster substitution of the labile aqua ligand with a nitrogen-containing ligand, than a sulfur-containing one.

Keywords: ruthenium(II), polypyridyl, kinetics, 5'-GMP, L-Cys

1. Introduction

Ruthenium complexes with a series of good properties, such as a range of oxidation states (Ru(II), Ru(III), and Ru(IV)), water solubility, slow ligand exchange rates, less toxicity, and anticancer activity, especially toward tumors resistant to cisplatin, became promising non-platinum compounds. A huge number of ruthenium polypyridyl complexes have been synthesized and studied to confirm their activity against cancer

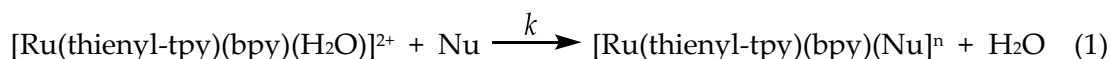
cells. This research has provided confirmation that ruthenium complexes have multiple targets, and a combination of their actions contributes to their observed beneficial properties [1]. Recently, we reported the synthesis of a series of Ru(II) terpyridine compounds, with the general formula $mer-[Ru(L_3)(N-N)(X)][Y]_n$, in which L_3 is either 2,2':6',2''-terpyridine (tpy), 4'-chloro-2,2':6',2''-terpyridine (Cl-tpy) or 4'-(4-chlorophenyl)-2,2':6',2''-terpyridine (Cl-Ph-tpy); N-N is a bidentate chelating ligand (1,2-diaminoethane (en), 1,2-diaminocyclohexane (dach), 2,2'-bipyridine (bpy)); X is a monodentate ligand (Cl or dmsO-S). These compounds, after the hydrolysis of the Cl ligand, form monofunctional adducts with N7 of guanine derivatives (i.e., 9-methylguanine (9MeG) or guanosine-5'-monophosphate (5'-GMP)) with rates and extents that depended strongly on the nature of the chelating ligand [2].

Here, we described the kinetics of the substitution reactions of the complex $[Ru(\text{thienyl-tpy})(\text{bpy})\text{Cl}]\text{Cl}$ with biologically relevant molecules, such as 5'-GMP or amino acid L-Cys. This research confirmed the influence of the nature of entering nucleophiles on the substitution reactions and higher reactivity of the studied Ru(II) complex toward nitrogen-containing nucleophile, 5'-GMP.

2. Kinetic studies of Ru(II) complex with small biomolecules

The substitution kinetics of coordinated water with 5'-GMP and L-Cys in Ru(II) complex were investigated UV-Vis spectrophotometrically. The working wavelengths were previously determined by recording the reaction mixture at the wavelength range of 200 to 800 nm. All kinetic experiments were performed under *pseudo*-first-order conditions (i.e., the concentration of the nucleophile was at least 10-fold that of the complex). The reaction was initiated by mixing a solution of the studied complex (0.3 mL, 1.00 mM) with 2.7 mL of the thermally equilibrated nucleophile solution (5.56 mM) in the UV-Vis cuvette, and the reactions were followed for at least 5 hours. The substitution reactions were monitored in double distilled water as a medium. The observed *pseudo*-first-order rate constants, k_{obsd} , represent an average value of two or three independent kinetic runs for each experimental condition. Reactions were studied with small biomolecules, such as 5'-GMP and L-Cys, at 298 K. The first-order rate constants, k_2 , for the substitution reactions with the studied nucleophiles, were obtained directly from the slopes of k_{obs} plots versus the concentration of the nucleophile. All kinetic data were computer-fitted to the appropriate equation using the programs Microsoft Excel 2016 and Origin 8.

The substitution process of the complex with 5'-GMP and L-Cys was represented by equation (1):



where n depends on the nature of the entering nucleophile Nu, 5'-GMP or L-Cys.

The rate constants for the substitution reaction were determined under *pseudo*-first-order conditions from the plot of the linear dependence of k_{obsd} versus nucleophile according to equation (2):

$$k_{obsd} = k[\text{Nu}] \quad (2)$$

where Nu = 5'-GMP or L-Cys.

The direct nucleophilic attack is characterized by the rate constants k . The first-order rate constant, k , characterizing the formation of the product, can be calculated from a plot of k_{obs} vs. the concentration of entering nucleophiles. A linear dependence on the nucleophile concentration was observed for both nucleophiles, with zero intercepts demonstrating the irreversibility of the reactions (Figure 1).

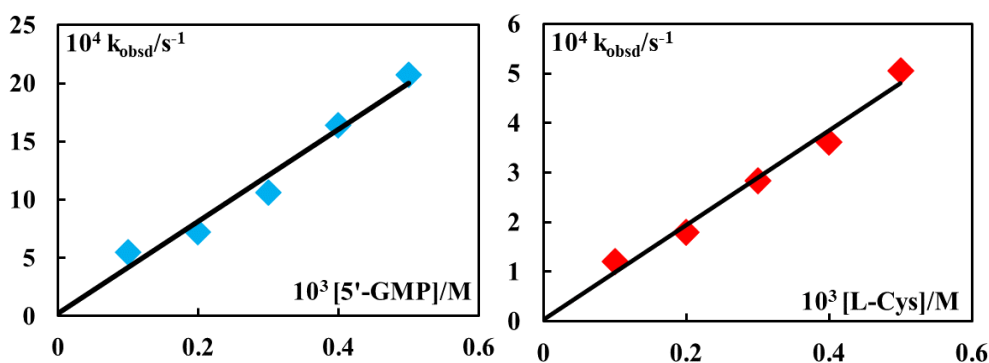


Figure 1. *Pseudo*-first order rate constants, k_{obsd} , as a function of the nucleophile concentration for the substitution reactions of Ru(II) complex with 5'-GMP and L-Cys.

The obtained values of the first-order rate constants for the substitution reactions with 5'-GMP and L-Cys, $k = 4.0 \pm 0.4$ and $0.95 \pm 0.08 \text{ M}^{-1} \text{ s}^{-1}$, respectively, confirm the fact that the rate of the substitution reactions of the ruthenium(II) complex depends on the nature of the entering nucleophile. The Ru-thienyl-tpy complex reacts four times faster with 5'-GMP than with the amino acid L-Cys. Based on the borderline hard-soft acidic properties of ruthenium, it was expected for the ruthenium complex to show a higher affinity for nitrogen-bonding nucleophiles, which also possess borderline hard-soft properties. For comparison, Ru(II) polypyridyl complexes with the general formula $mer\text{-}[\text{RuL}_3(\text{N-N})\text{Cl}]\text{Cl}$, where L is 2,2':6',2''-terpyridine (tpy) or 4'-(4-chlorophenyl)-2,2':6',2''-terpyridine (Cl-Ph-tpy) and N-N is o-benzoquinonediimine (o-bqdi), 2,3-naphthoquinonediimine (nqdi), 4,4'-dimethyl-2,2'-bipyridine (dmbpy), or 2,2'-bipyridine-4,4'-dicarboxylic acid (dcbpy), showed the same trend of reactivity with 5'-GMP and L-Cys [3].

3. Conclusions

The study of the kinetics of the substitution reactions of the selected complex with nitrogen- (5'-GMP) and sulfur-donor nucleophiles (L-Cys) showed higher reactivity of

Ru compound with 5'-GMP. The kinetic data for the reactions of Ru compound with 5'-GMP and L-Cys clearly showed that the rate of the reaction depends on the nature of the entering nucleophile: complex react ca. 4 times faster with 5'-GMP than with L-Cys. The results of the present work represent a further improvement in the structure–pharmacological relationship needed for the design of new antitumor ruthenium drugs and chemotherapeutic strategies.

Acknowledgment

The authors would like to express their gratitude to the Ministry of Science, Technological Development and Innovation of the Republic of Serbia (Agreement No. 451-03-47/2023-01/200378 and Agreement No. 451-03-47/2023-01/200122) for financial support.

References

- [1] E. Antonarakis, A. Emadi, *Ruthenium-based chemotherapeutics: are they ready for prime time?*, *Cancer Chemotherapy and Pharmacology*, 66 (2010) 1.
- [2] A. Rilak Simović, R. Masnikosa, I. Bratsos, E. Alessio, *Chemistry and reactivity of ruthenium(II) complexes: DNA/protein binding mode and anticancer activity are related to the complex structure*, *Coordination Chemistry Reviews*, 398 (2019) 113011.
- [3] M. Međedović, A. Rilak Simović, D. Čoćić, M. Milutinović, L. Senft, S. Matic, D. Todorović, S. Popović, D. Baskić, B. Petrović, *New ruthenium(ii) complexes with quinone diimine and substituted bipyridine as inert ligands: synthesis, characterization, mechanism of action, DNA/HSA binding affinity and cytotoxic activity*, *Dalton Transaction*, 52 (2023) 1323-1344.

Synthesis and physicochemical characterisation of the Ni(II) complex with 3-(4-chlorophenyl)-1H-pyrazole ligand

Marijana S. Kostić^{1,*}, Nikola D. Radnović¹, Ana Radović², David Kočović³, Željko Jaćimović⁴, Berta Barta Holló¹, Mirjana M. Radanović¹

¹University of Novi Sad, Faculty of Sciences, Novi Sad, Serbia, Trg Dositeja Obradovića 3, e-mail: marijana.kostic@dh.uns.ac.rs, nikola.radnovic@dh.uns.ac.rs, berta.hollo@dh.uns.ac.rs, mirjana.lalovic@dh.uns.ac.rs

²Accreditaion Body of Montenegro, Podgorica, Montenegro, Bulevar Džordža Vašingtona 51, e-mail: ana.radovic@atcg.co.me

³Institute for Medicines and Medical Devices of Montenegro, Podgorica, Montenegro, Bulevar Ivana Crnojevića 64a, e-mail: david.kocovic@cinmed.me

⁴University of Montenegro, Faculty of Metallurgy and Technology, Podgorica, Montenegro, Cetinjski put, e-mail: zeljkoj@ucg.ac.me

* Corresponding author

DOI: 10.46793/ICCBIGK23.527K

Abstract: The coordination properties of 3-(4-chlorophenyl)-1H-pyrazole (HL) was investigated and its complex with Ni(II) ion was synthesized. The structure of the ligand was proven using SC-XRD, while both the ligand and the complex were characterized by spectroscopic, and thermogravimetric measurements. The purity and composition of the complex were confirmed by PXRD, elemental analysis, and conductometric measurements. Besides, the search for CSD was made to establish the frequency of different coordination modes of similar compounds. It was found that monodentate coordination of the neutral ligand molecule or the exo-bidentate one in the case of the deprotonation of the pyrazole ring is possible. Based on the results obtained, the formula $[\text{Ni}_2(\mu\text{-L})_2(\text{OH})_2(\text{H}_2\text{O})_2] \cdot 2\text{H}_2\text{O}$ and the bridging bidentate coordination of the monoanionic form of the ligand *via* nitrogen atoms of the pyrazole ring was suggested.

Keywords: pyrazole derivative, metal complex, thermal properties, structure

1. Introduction

The pyrazole derivatives are known for their significant biological and pharmacological activities, which include antimicrobial, anti-inflammatory, antipyretic, and antitumor effects [1, 2]. Due to such a large variety of activities, their coordination abilities toward different metal ions are thoroughly studied. Generally, the pyrazole-type compounds are small and easily coordinate to different metals, mostly to *d*-metals.

Further design and development of biologically active complexes with pyrazole-type ligands are crucial, thus their detailed characterization is of high interest. Here, the structure, IR spectra, and thermal properties of 3-(4-chlorophenyl)-1H-pyrazole (HL), as

well as synthesis, physicochemical, spectral, structural, and thermoanalytical characterization of its complex with Ni(II) ion are presented.

2. Results and discussion

2.1 Experimental

All chemicals used were commercial products of analytical reagent grade.

Hot methanolic solution (3 cm³) of 3-(4-chlorophenyl)-1H-pyrazole (89 mg, 0.50 mmol) is mixed with the hot methanolic solution (3 cm³) of Ni(OAc)₂·2H₂O (63 mg, 0.25 mmol). After three days at room temperature, from the pale blue solution, the green microcrystals of the complex were obtained. Yield: 64 %. Anal. Calcd. for C₁₈H₂₂N₄O₆Cl₂Ni₂ (Mr = 578.28): C, 37.35; H, 3.80; N, 9.68 %. Found: C, 37.04; H, 3.68; N, 9.35 %. $\lambda_M(\text{DMF}) = 44.0 \text{ Scm}^2\text{mol}^{-1}$. IR bands [cm^{-1}]: 3231, 1557, 1488, 1465, 1427, 1346, 1291, 1254, 1187, 1125, 1085, 1045, 1012, 956, 941, 929, 887, 827, 785, 733, 713, 688, 652, 608, 506, 458. IR bands (ligand) [cm^{-1}]: 3237, 3141, 3116, 2969, 1534, 1501, 1473, 1441, 1408, 1361, 1335, 1301, 1293, 1271, 1188, 1115, 1105, 1092, 1074, 1044, 1010, 949, 929, 830, 762, 734, 630, 602, 506, 452.

Elemental analyses (C, H, N) of air-dried compounds were carried out by standard micro-methods. Molar conductivity measurements of freshly prepared solution ($c = 1 \text{ mmol L}^{-1}$) were performed on a Jenway 4010 conductivity meter. IR spectra were recorded on a Thermo Nicolet iS20 FTIR spectrophotometer in ATR mode (range 4000 – 400 cm^{-1}). Thermal data were collected using TA Instruments SDT Q600 thermal analyzer. Temperature range: room temperature to 700 °C; heating rate: 10 °C min^{-1} in the argon carrier gas (flow rate = 50 $\text{cm}^3 \text{ min}^{-1}$). Sample holder/reference: alumina crucible/empty alumina crucible. Sample mass 2.5–3 mg. The X-ray powder diffraction pattern of the complex was measured on a Rigaku MiniFlex 600 diffractometer equipped with a secondary monochromator (graphite) with a Cu-K α source. Samples were mounted on a zero-background silicon single-crystal sample holder. All samples were measured at room temperature in the 2θ range 5 – 55° and these data were compared against simulated patterns from the single crystal data of the ligand that was collected with Gemini S (Oxford Diffraction) diffractometer equipped with a CCD detector Sphire3 at 295 K. *Crystallographic data*: orthorhombic crystal system, *Pbca*, $a = 14.3074(6)$, $b = 5.7946(3)$, $c = 20.2505(8)$ Å, $V = 1678.88(13)$ Å³, $Z = 8$. Refinement based on F^2 (109 parameters): $R_1 = 0.0566$, $wR_2 = 0.1199$, $S = 1.068$, for all data, and $R_1 = 0.0427$ for 1251 reflections with $I \geq 2\sigma(I)$.

2.2 Properties of the compounds

The molecular structure of the neutral form of the ligand HL is shown in Figure 1a. It is interesting to note that this was still unknown even though the ligand is commercially available. All bond lengths are in concordance with those found in similar pyrazole derivatives. Both rings are planar, with the dihedral angle between them at 11.59°. By comparison of the PXRD patterns of HL (simulated) and the complex (measured)

(Figure 1b) it can be concluded that there are no traces of unreacted ligand in the batch of the complex. This is a direct confirmation of complex phase purity.

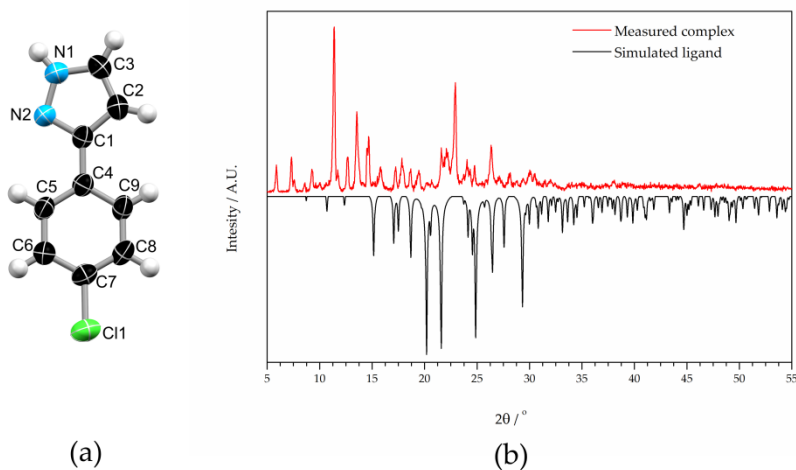


Figure 1. Molecular structure of HL (a) and PXRD patterns for HL (simulated) and the complex (measured) (b).

The reaction of methanolic solution of the ligand and nickel(II)-acetate yielded the formation of green microcrystals of the complex. Due to the presence of acetate ions as deprotonating agent, the coordination of monoanionic ligand form (L) is assumed. The comparison of IR spectra of the ligand and the complex proves the coordination of the ligand. In the spectrum of the complex, the ν OH vibrations are strong and the bands are significantly shifted toward lower frequencies. This suggests that in the complex strong H-bonds are present. In addition, some differences in the middle IR range are also detected. The value of molar conductivity suggests the partial substitution of the anionic ligands with solvent molecules.

To validate the proposed coordination of the ligand, a search of CSD [3] has been made. These results revealed that there are 34 complexes with a similar ligand, i.e., the one without substituents on the phenyl ring. In the majority of these complexes (24 structures), monodentate coordination of the neutral form of the ligand. Among these, the most frequent is the coordination of four monodentate pyrazole ligand molecules to one metal center. On the other hand, in a series of nine complexes, the pyrazole derivative is deprotonated and coordinated in a bridging exo-bidentate manner *via* both nitrogen atoms. Interestingly there is one structure with tridentate NNC coordination pyrazole derivative [4]. In this organometallic iridium complex two ligand monoanions are coordinated in the mentioned NNC manner, one ligand anion is the bridge that connects iridium and boron atoms, while the fourth ligand molecule has the role of a N-monodentate ligand.

Besides, the CSD search was made to find complexes with halogen derivatives of this pyrazole compound. Ten such complexes were found – eight with bromo- and two with fluoro-derivative. In all the complexes with bromo-derivative N-monodentate coordination of the neutral ligand form was found. In both complexes with fluoro-

derivative both neutral and anionic forms are coordinated, in one structure in an N-monodentate manner, while in the other NN bridging coordination mode was proven.

The thermogravimetric curve of L in nitrogen shows that it is stable up to 100 °C. At 101 °C the free pyrazole derivative melts and the melted compound begins to decompose. The decomposition process is the most intensive at 229 °C and finishes at ~240 °C. The nickel(II) complex of this ligand begins to lose mass at room temperature. The differently bonded water molecules and OH groups lead to the partially overlapped steps of water and hydroxide evaporation. In three hardly distinguishable steps with DTG maxima at 84, 118, and 204 °C the total mass loss is 18.1 %, which corresponds well to the calculated H₂O + OH loss (18.33 %). The following steps are well separated with DTG maxima at 258, 334, and 504 °C and partial mass losses of 27.2, 16.9, and 14.3 %. These steps most probably correspond to the decomposition of L molecules.

Based on all the results presented, the proposed formula should be [Ni₂(μ-L)₂(OH)₂(H₂O)₂]:2H₂O.

3. Conclusions

The structure of 3-(4-chlorophenyl)-1H-pyrazole (HL) was determined by SC-XRD and its coordination affinity towards Ni(II) ion was examined. The reaction of nickel(II)-acetate and the ligand in a methanolic solution resulted in the formation of green microcrystals. The complex was characterized by elemental analysis, IR spectroscopy, molar conductivity, thermal analysis, and PXRD measurement. Also, the search of CSD was made to validate the proposed coordination mode of the ligand. Based on all the results gathered it was proposed that the ligand coordinates as monoanion in the bridging exo-bidentate manner.

Acknowledgment

This research is funded by the Ministry of Education and Ministry of Science, Technological Development and Innovation, Republic of Serbia, Grants: No. 451-03-47/2023-01/200125.

References

- [1] D. Matiadis, M. Karagiaouri, B. Mavroidi, K.E. Nowak, G. Katsipis, M. Pelecanou, A. Pantazaki, M. Sagnou., *Synthesis and Antimicrobial Evaluation of a Pyrazoline-Pyridine Silver(I) Complex: DNA-Interaction and Anti-Biofilm Activity*, *BioMetals* 34 (2021) 67–85.
- [2] D. Allison, E. Delancey, H. Ramey, C. Williams, Z.A. Alsharif, H. Al-khattabi, A. Ontko, D. Gilmore, M.A. Alam., *Synthesis and Antimicrobial Studies of Novel Derivatives of 4-(4-Formyl-3-phenyl-1H-pyrazol-1-yl)Benzoic Acid as Potent Anti-Acinetobacter Baumannii Agents*, *Bioorg. Med. Chem. Lett.* 27 (2017) 387–392.
- [3] C.R. Groom, I.J. Bruno, M.P. Lightfoot, S.C. Ward., *The Cambridge Structural Database*, *Acta Crystallogr. B Struct. Sci. Cryst. Eng. Mater.* 72 (2016) 171–179.
- [4] C. Slugove, K. Mereiter, S. Trofimenko, E. Carmona., *Unprecedented pentadenticity of the HB(3-Phpz)₃ (= Tp^{Ph}) ligand*, *Chem. Commun.* (2000) 121-122.

Normal and Reversed Phases Thin-Layer Chromatography of Arylidene 2-Thiohydantoin Derivatives

Petar B. Stanić^{1*}, Biljana Šmit¹, Jovana Muškinja¹, Tanja Soldatović², Marko Ilić³,
Kristian Pastor³, Marijana Ačanski³

¹ University of Kragujevac, Institute for Information Technologies, Department of Science, Jovana Cvijića bb, 34000 Kragujevac, Serbia; e-mail: petar.stanic@uni.kg.ac.rs, biljana.smit@uni.kg.ac.rs, jovana.muskinja@gmail.com

² State University of Novi Pazar, Department of Natural-Mathematical Sciences, Vuka Karadžića 9, 36300 Novi Pazar, Serbia; e-mail: tsoldatovic@np.ac.rs

³ University of Novi Sad, Faculty of Technology Novi Sad, Bulevar Cara Lazara 1, 21000 Novi Sad, Serbia; e-mail: marko.ilic@uns.ac.rs, kristian.pastor@uns.ac.rs, macanski@tf.uns.ac.rs

* Corresponding author

DOI: 10.46793/ICCB23.531S

Abstract: In this paper, the retention behavior of thirteen newly synthesized arylidene derivatives of 2-thiohydantoin was investigated by normal and reversed phases thin-layer chromatography. In normal phase chromatography, thin layers of silica gel and cyano-propyl (CN) silica gel with fluorescent indicator F₂₅₄ were used as the stationary phase. As the mobile phase, binary systems of non-aqueous solvents benzene-ethyl acetate and hexane-ethyl acetate were used, 8:2 (*v/v*). Reversed phase chromatography was performed using a thin layer of octadecyl (C-18) silica gel with fluorescent indicator F₂₅₄ as the stationary phase and a binary solvent mixture of acetonitrile-water in the ratio 7.5:2.5 (*v/v*) as the mobile phase. Observing under a UV lamp, the spots of all tested derivatives were clearly visible. The *R_F* value was determined for each spot. Based on the obtained results the HPLC technique is recommended for further chromatographic examination of the newly synthesized arylidene derivatives of 2-thiohydantoin, using commercial columns with polar chemically bound phases and both non-aqueous and aqueous eluents.

Keywords: arylidene 2-thiohydantoin derivatives, TLC, normal phases, reversed phases, retention behaviour

1. Introduction

2-Thiohydantoin (2-thioxoimidazoline-4-one) is a non-aromatic five-membered heterocyclic compound with a cyclic ureid core [1]. The series of 13 arylidene 2-thiohydantoin derivatives were obtained through a condensation reaction with thiosemicarbazide, utilizing a previously published two-step protocol [2]. The structures of synthesized thiohydantoin derivatives **1-13** are given in Figure 1.

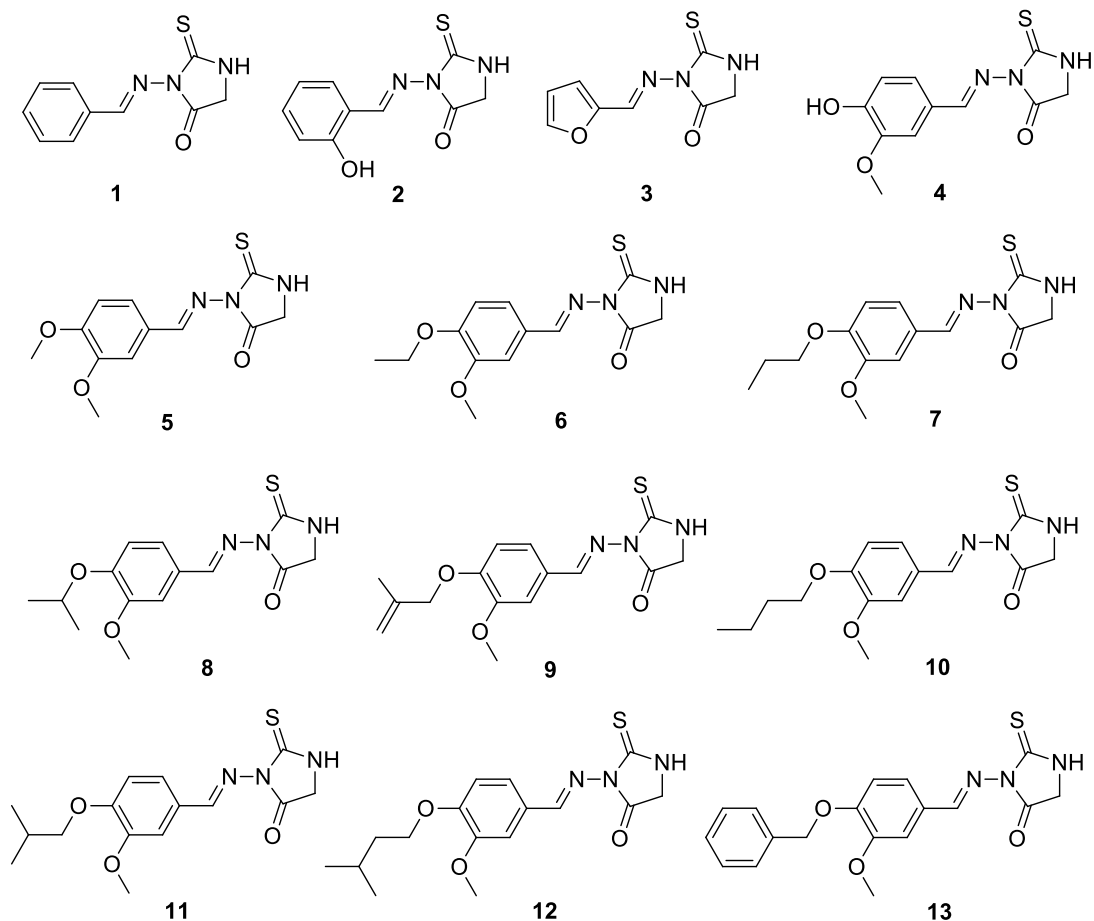


Figure 1. Structures of studied thiohydantoin derivatives 1-13.

The aim of this work was to examine the possibility of chromatographic separation of newly synthesized 2-thiohydantoin derivatives, considering the different character of the functional groups that are introduced into the arylidene part of the molecule. Due to the presence of both polar and non-polar functional groups attached to the benzene ring in the molecule, the retention behavior of the newly synthesized derivatives will be examined by thin-layer chromatography on both normal and reversed chemically bonded phases.

2. Instructions

HPTLC was performed on 10x10 cm plates coated with silica gel 60, cyano propyl (CN) and octadecyl (C-18) silica gel, all with fluorescence indicator (Merck). The compounds were dissolved in acetonitrile (1 mg/ml) and 1 μ l volumes of the solutions spotted randomly on the plates. Silica gel and bonded CN silica gel plates were developed with non-polar mobile phases benzene-ethyl acetate and hexane-ethyl acetate, both in the ratio 8:2 (*v/v*).

Bonded C-18 silica gel plates with fluorescence indicator (Merck) were developed with acetonitrile-water 7.5:2.5 (v/v).

Spots were observed under UV light at $\lambda = 254$ nm and R_F values were determined for all spots, presented in Table 1.

Table 1. R_F values of investigated compounds designated as in Figure 1.

Compound	Silica gel (Bz-EtAc)	Silica gel (Hx-EtAc)	CN (Bz-EtAc)	C-18 (ACN-W)
1	0.43	0.15	0.68	front
2	0.47	0.03	0.71	front
3	0.40	0.14	0.65	front
4	0.24	0.05	0.56	front
5	0.28	0.04	0.63	front
6	0.33	0.06	0.65	front
7	0.38	0.11	0.65	front
8	0.36	0.12	0.67	front
9	0.38	0.11	0.82	front
10	0.40	0.13	0.68	front
11	0.39	0.13	0.70	front
12	0.38	0.13	0.71	front
13	0.35	0.07	0.70	front

Retention of the compounds examined on silica gel using the eluent benzene-ethyl acetate, decreases in the following order:

$$4 > 5 > 6 > 13 > 8 > 7 = 9 = 12 > 11 > 3 = 10 > 1 > 2;$$

while using the eluent hexane-ethyl acetate, decreases in the following order:

$$2 > 5 > 4 > 6 > 13 > 7 = 9 > 8 > 10 = 11 = 12 > 15 > 1.$$

By comparing these two mobile phases it is noticeable that the retention of all examined derivatives on the silica gel is significantly lower if benzene is used as a diluent. Due to the presence of the benzene ring in the molecules, all examined derivatives are more soluble in benzene than in hexane, so the retention is logically lower.

If compared to silica gel, the retention of all examined compounds on CN silica gel is significantly lower using benzene-ethyl acetate as a mobile phase. The retention of the compounds decreases in the following order:

$$4 > 5 > 3 = 6 = 7 > 8 > 1 = 10 > 11 = 13 > 2 = 12 > 9.$$

Based on the obtained results it can be concluded that complete separation of the examined derivatives was not achieved on silica gel nor CN silica gel stationary phases. These results are in accordance with previously published results in normal phase chromatography [3,4].

Although the reversed phase (on C-18 and/or C-8 silica gels) is used in 80% of chromatographic analysis, it is not applicable in this case. Namely, the compounds were examined on C-18 silica gel with acetonitrile-water as an eluent, all compounds were eluting with the front of the mobile phase. This is a consequence of the high polarity of

these newly synthesized compounds, so the application of reverse phase chromatography is not recommended for further chromatographic behaviour examination of arylidene derivatives of 2-hydantione. These results are also in accordance with previously published results [3,4].

3. Conclusions

Based on the obtained results the HPLC technique is recommended for further chromatographic examination of the newly synthesized arylidene 2-thiohydantione derivatives, using commercial columns with polar chemically bound phases and both non-aqueous and aqueous eluents [5,6]. By choosing the appropriate column and mobile phase, it is expected to achieve a complete separation of the newly synthesized arylidene 2-thiohydantione derivatives. Followed by successful chromatographic separation, the corresponding retention constants will be determined and applied in further interpretations of the retention behavior of the examined arylidene 2-thiohydantione derivatives and their biological activity.

Acknowledgment

This research is funded by the Ministry of Education and the Ministry of Science, Technological Development and Innovation of the Republic of Serbia, Grants No.: 451-03-47/2023-01/200378 and 451-03-47/2023-01/200134.

References

- [1] M.A. Metwally, E. Abdel-Latif, *Thiohydantoin: synthetic strategies and chemical reactions*, Journal of Sulfur Chemistry 33 (2012) 229-257.
- [2] B. Šmit, R.Z. Pavlović, A. Radosavljević-Mihailović, A. Došen, M.G. Ćurčić, D.S. Šeklić, M.N. Živanović, *Synthesis, characterization and cytotoxicity of palladium(II) complex of 3-[(2-hydroxy-benzylidene)-amino]-2-thioxo-imidazolidin-4-one*, Journal of the Serbian Chemical Society 78 (2013) 217-227.
- [3] M.M. Ačanski, *Tečna hromatografija derivata estradiola i estrona-monografija*, Tehnološki fakultet, Univerzitet u Novom Sadu, Novi Sad (2007).
- [4] M.M. Ačanski, *Tečna hromatografija derivata benzimidazola*, Tehnološki fakultet, Univerzitet u Novom Sadu, Novi Sad (2010).
- [5] M. Ilić, M. Ačanski, K. Pastor, Lj. Popović, S. Jovanović-Šanta, *New challenge in the lipophilicity determination and separation of biologically active 16,17-secoesterone derivatives by HPLC – Use of pentafluorophenyl-propyl column*, Journal of Liquid Chromatography and Related Technologies 43 (2020) 106-117.
- [6] M. Ilić, K. Pastor, J. Marković, Lj. Grbović, S. Jovanović-Šanta, I. Mitrović, Z. Trivunović, M. Ačanski, *Feasibility study of separation and purification of bile acid derivatives by HPLC on C18 and F5 columns*, Steroids 186 (2022) 109074.

Investigation of the anticancer activity of 2-amino-6-methylbenzothiazole and corresponding Pd(II) complex using molecular docking simulations

Sandra S. Jovičić Milić^{1*}, Marko Antonijević¹, Đorđe S. Petrović², Verica V. Jevtić², Danijela Lj. Stojković¹

¹ University of Kragujevac, Institute for Information Technologies, Department of Science, Kragujevac, Jovana Cvijića bb, 34000, Kragujevac; e-mail: sandra.jovicic@pmf.kg.ac.rs, mantonijevic@uni.kg.ac.rs, danijela.stojkovic@kg.ac.rs

² University of Kragujevac, Faculty of Science, Radoja Domanovića 12, 34000 Kragujevac, Republic of Serbia; e-mail: djordje.petrovic@pmf.kg.ac.rs, verica.jevtic@pmf.kg.ac.rs

* Corresponding author

DOI: 10.46793/ICCBi23.535JM

Abstract: In our prior investigations, it has been established that compound di(2-amino-6-methylbenzothiazole)dichloridopalladate(II) (**C1**) exhibits promising efficacy in inhibiting the growth of colon carcinoma, thereby demonstrating potential as an anticancer agent. To elucidate the underlying mechanism of action against cancer, a comprehensive investigation involving DNA binding analysis and a series of assays to evaluate the inhibitory potential of compound **C1** against key proteins involved in cancer metabolism were conducted. The significant inhibitory potential of **C1** towards Bcl-2, Ki-67, and CDK-4 was determined. In order to investigate the underlying mechanism behind the anticancer properties and to assess the inhibition of various proteins involved in different metabolic pathways of **C1**, molecular docking simulations were conducted. The investigation revealed that the observed lack of similarity between the experimental outcomes and the inhibition of Bcl-2 and CDK-4 by **C1** and 2-amino-6-methylbenzothiazole (**L1**) suggests that the metabolic pathways involving these proteins do not contribute to the anticancer properties of **C1**. The observed correlation between the inhibition of Ki-67 and the experimental outcomes was found to be significant. The inhibition of Ki-67 in cell cycle regulation is a promising approach to the development of anticancer drugs. Further research is required to explore the potential application of **C1** as a Ki-67 inhibitor.

Keywords: Bcl-2, Ki-67, CDK-4, Anticancer agents, Pd(II) complexes

1. Introduction

Thiazoles, as a biologically significant class of compounds, have become very interesting for investigation of their anticancer potential. They represent heterocyclic compounds containing both nitrogen and sulfur atoms as part of an aromatic ring. Because of their structure, derivatives of thiazole are able to bind with transition metals (soft Lewis

acids) such as palladium(II) ion. The thiazole ring is an integral part of penicillin and vitamin B1-thiamine, as well as a large number of already used drugs. Some of them are, ritonavir (medicine for HIV/AIDS) [1], tiazofurin (antitumor effect) [2], bacitracin (antibiotic effect) [3] and many others.

The aim of this paper is to present the results of molecular docking simulations of 2-amino-6-methylbenzothiazole (**L1**) and previously synthesized palladium(II) complex (**C1**) [5] regarding the inhibitory potential towards Bcl-2, Ki-67, and CDK-4. All three examined proteins are important parts of the cell cycle in tumor cells. Ki-67 is an important cancer biomarker, but, according to recent papers, it also has a significant role in cell cycle regulation [4].

2. Methodology

According to the aforementioned paper [5] di(2-amino-6-methylbenzothiazole)dichloridopalladate(II) (**C1**) is expressing its anticancer activity towards colorectal carcinoma by inducing apoptosis. According to the Flow cytometry method, **C1** induced apoptosis via Bcl-2 (B-cell lymphoma 2) inhibition. It was also concluded that **C1** decelerated proliferation of cancer cells by decreasing Cyclin-D, and growth by inhibiting Ki-67. To further investigate the binding potential of 2-amino-6-methylbenzothiazole **L1** and **C1** towards the aforementioned proteins molecular docking studies were performed. Structures of investigated proteins were obtained through RCSB Protein Data Bank with 1G5M (Bcl-2), 1R21 (Ki-67), and 2W96 (Cyclin-dependent kinase-4). Structures of investigated compounds were obtained through the optimization via the Gaussian 16 software package, while molecular docking simulations were done by AMDock platform implementing AutoDock4.2, following the methodology given in our previous work [6].

3. Results and discussion

According to the results of our previous endeavors, [5] **C1** shows good binding potential when it comes to the binding to (circulating tumor DNA) CT-DNA molecules, which indicates that its inhibitory potential towards the specific carcinoma could come as a consequence of CT-DNA binding. However, another investigated complex - di(2-amino-6-chlorobenzothiazole)dichloridopalladate(II) (**C2**) showed better binding affinity towards CT-DNA and at the same time lower cytotoxic activity indicating the possibility of another mechanism of expressing cytotoxic potential. Because of that a series of mechanistic pathways included in cancer expression were investigated. It was determined that Caspase 3 is not involved in the mechanism of cytotoxic activity. However, changes in the expression of Bcl-2, Ki-67, and Cyclin D, were recorded. These proteins were selected according to their role in apoptosis protection (Bcl-2), proliferation (Ki-67), and cell cycle regulation from the G1 to S phase of mitosis (Cyclin D). All three proteins were found to be inhibited by **C1**. To further investigate

interactions with these proteins, molecular docking simulations were performed. Thermodynamic parameters describing these interactions are given in Table 1.

Table 1. Thermodynamic parameters describing interactions between Bcl-2, Ki-67, and Cyclin-dependent kinase-4 (CDK-4) with **C1** and **L1**.

	Bcl-2	Ki-67	CDK-4
C1			
ΔG_{bind} (kcal mol ⁻¹)	-6.45	-6.43	-5.89
k_i (μM)	18.71	22.53	48.15
L1			
ΔG_{bind} (kcal mol ⁻¹)	-6.16	-5.09	-5.34
k_i (μM)	30.53	190.00	120.00

As can be seen from the molecular docking simulations, parameters describing inhibition of Bcl-2 and CDK-4 indicate similar anticancer potential of **C1** and **L1**, which is not in accordance with the experimental results. However, inhibition of Ki-67 follows the trend set by IC₅₀ values (**C1**=12.34 ± 0.74 and **L1**= 389.45 ± 5.14) which is in correlation to binding energies (ΔG_{bind}) and inhibitory constants (k_i) obtained through molecular docking simulations. These findings indicate that out of three investigated proteins, inhibition of Ki-67 is the most probable mechanistic pathway of the anticancer activity of **C1**.

To further explain this phenomenon, the interactions between Ki-67 and **C1/L1** were investigated (Figure 1).

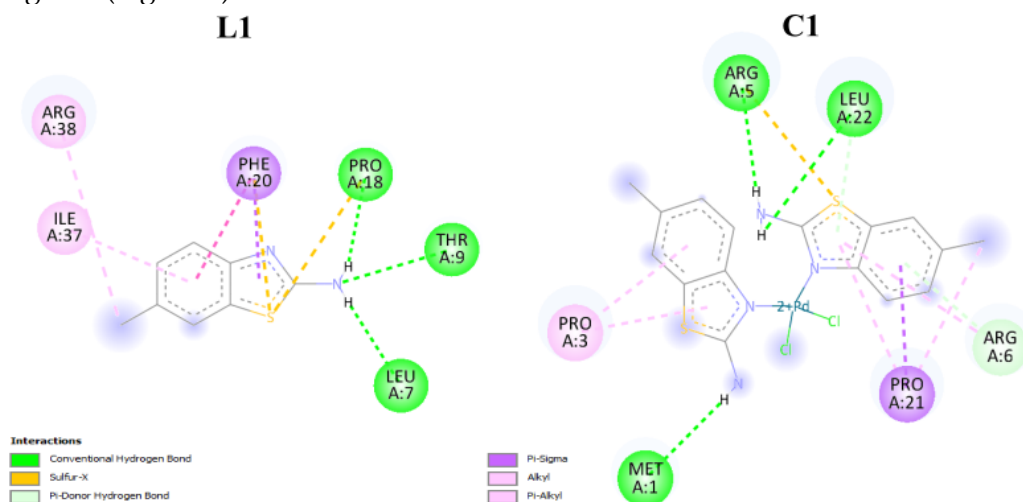


Figure 1. Interactions between Ki-67 and **L1** (left) and **C1** (right).

According to Figure 1, interactions between Ki-67 and **C1** and **L1**, and overall number of hydrogen bonds and other non-covalent interactions do not have an impact on the differences between binding energies, and consequently inhibitory constants, of **C1** and **L1**. However, the layout of the hydrogen bonds and other non-covalent interactions allows for the better stabilization of **C1** in comparison to **L1**, regardless of the higher voluminosity of the **C1**.

4. Conclusions

In our previous endeavors, we have determined that compound **C1** shows good anticancer activity toward colon carcinoma. To determine the mechanistic pathway for anticancer activity also performed the DNA binding analysis, as well as a series of essays investigating inhibitory potential of **C1** towards various proteins important for cancer metabolism. It was found that **C1** shows good inhibitory potential towards Bcl-2, Ki-67, and CDK-4. To further examine inhibition of which of these proteins (describing different metabolic routes) is responsible for the anticancer activity of **C1**, molecular docking simulations were performed. It was found that inhibition of Bcl-2 and CDK-4 by **C1** and **L1** shows no resemblance to the experimental results, indicating that metabolic routes containing these proteins were not responsible for the anticancer potential of **C1**. However, inhibition of Ki-67, showed a good correlation with the experimental results. Preventing the Ki-67 from being involved in cell cycle regulation is one of the novel tactics in the anticancer drug design and development and further investigations are needed for the application of **C1** as a Ki-67 inhibitor.

Acknowledgment

This research is funded by the Ministry of Education and Ministry of Science, Technological Development and Innovation, Republic of Serbia, Grants: No. 451-03-47/2023-01/200378 and No. 451-03-47/2023-01/200122.

References

- [1] M.V.N. de Souza, M.V. de Almeida, *Drugs anti-HIV: past, present and future perspectives*, *Quimica Nova* 26 (2003) 366–372.
- [2] M. Popsavin, L. Torović, M. Svirčev, V. Kojić, G. Bogdanović, V. Popsavin, *Synthesis and antiproliferative activity of two new tiazofurin analogues with 2'-amido functionalities*, *Bioorganic Bioorganic & Medicinal Chemistry Letters*. 16 (2006) 2773–2776.
- [3] T. Moulard, J.F. Lagorce, J.C. Thomes, C. Raby, *Biological Evaluation of Compounds with -NCS- Group or Derived from Thiazole and Imidazole. Activity on Prostaglandin Synthetase Complex*, *Journal of Pharmacy and Pharmacology* 45 (1993) 731–735.
- [4] X. Sun, P.D. Kaufman, *Ki-67: more than a proliferation marker*. *Chromosoma* 127 (2018) 175–186.
- [5] S. S. Jovičić Milić, V. V. Jevtić, S. R. Radisavljević, B. V. Petrović, I. D. Radojević, I. R. Raković, Đ. S. Petrović, D. Lj. Stojković, M. Jurišević, N. Gajović, A. Petrović, N. Arsenijević, I. Jovanović, O. R. Klisurić, N. L. Vuković, M. Vukić, M. Kačaniová, *Synthesis, characterization, DNA interactions and biological activity of new palladium(II) complexes with some derivatives of 2-aminothiazoles*, *Journal of Inorganic Biochemistry* 233 (2022) 111857.
- [6] E.H. Avdović, M. Antonijević, D. Simijonović, S. Roca, D. V. Topić, N. Grozdanić, T. Stanojković, I. Radojević, R. Vojinović, Z. Marković, *Synthesis and Cytotoxicity Evaluation of Novel Coumarin–Palladium(II) Complexes against Human Cancer Cell Lines*. *Pharmaceuticals* 16 (2023) 49.

DNA binding and molecular docking of four palladium(II) complexes with *O,O'*-dialkyl esters of (*S,S*)-propylenediamine-*N,N'*-di-2-(2-benzyl) acetic acid

Dorđe Petrović¹, Maja Đukić¹, Edina Avdović², Danijela Stojković², Verica Jevtić¹, Sandra Jovičić Milić^{2*}, Marina Vesović³

¹University of Kragujevac, Faculty of Science, Department of Chemistry, Radoja Domanovića 12, 34000 Kragujevac, Serbia; e-mail: verica.jevtic@pmf.kg.ac.rs, djordje.petrovic@pmf.kg.ac.rs, maja.djukic@pmf.kg.ac.rs

²University of Kragujevac, Institute for Information Technologies Kragujevac, Department in Science, Jovana Cvijića bb, 34000 Kragujevac, Serbia ; e-mail: danijela.stojkovic@kg.ac.rs; sandra.jovivic@pmf.kg.ac.rs, edina.avdovic@pmf.kg.ac.rs

³University of Kragujevac, Faculty of Medical Sciences, Department of Pharmacy, Svetozara Markovića 69, 34000 Kragujevac, Serbia; e-mail: marina.mijajlovic@medf.kg.ac.rs

* *Corresponding author*

DOI: 10.46793/ICCBi23.539P

Abstract: The antitumor activity of platinum-based complexes still captures the attention of scientists and new potential drugs are being synthesized and investigated. Although complexes of palladium(II) ion show less cytotoxicity compared to platinum(II) complexes due to the high reactivity of the palladium center, research in this field has continued and many authors have found that auxiliary chelating ligands can improve complex stability and their cytotoxicity. As a consequence of rapid ligand exchange, the probability of palladium(II) complexes reaching the biological target in organisms seems to be low. The use of chelating ligands has been proposed as a solution to this problem. In our paper, the interactions of new palladium(II) complexes with ethyl (C1), propyl (C2), buthyl (C3) and pentyl (C4) ester of (*S,S*)-propylenediamine-*N,N'*-di-2-(2-benzyl) acetic acid with calf thymus DNA (CT-DNA) was studied by fluorescence spectroscopy and electronic absorption spectroscopy, while molecular docking simulations were used to examine the inhibitor efficiency of C1-C4 against DNA receptor.

Keywords: DNA binding, molecular docking, Pd(II)complexes

1. Introduction

Palladium is a transition metal from the platinum group of metals. The palladium(II) ion, as a soft Lewis acid, builds stable bonds with nitrogen and sulfur donor atoms. Complexes of palladium(II) ion have been determined to exhibit significant antibacterial activity against gram-positive and gram-negative bacteria [1]. Ligands of edda and edta type represent a distinctive segment of bioinorganic chemistry and they are of fundamental importance within the coordination chemistry due to the fact that some

esters of edda derivatives of amino acids and corresponding transition metal complexes exhibit significant biological activity [2]. Propylenediamine derivatives [3] of amino acids and corresponding complexes, as well as ethylenediamine derivatives of amino acids, have not been sufficiently investigated. In this study, the interactions of palladium(II) complexes with DNA were investigated, as well as molecular docking simulations.

2. Methodology

2.1 Materials and physical measurements

Highly polymerized calf thymus DNA (CT-DNA), ethidium bromide (EB), and DMSO were purchased from Sigma-Aldrich and used as received. PBS solution was prepared by dissolving one tablet in 200 mL deionized water. The phosphate buffer solution was used as the solvent for the preparation of the solutions of DNA, and EB. The stock solution of the complexes was prepared by dissolving in DMSO and diluting with a PBS solution and was kept in the refrigerator at 4 °C for no more than one week.

2.2 DNA-binding experiments

The possible DNA-binding mode was investigated using UV–Vis spectroscopy and the binding constants (K_b) for synthesized complexes and CT-DNA were calculated. The Wolfe-Shimmer equation was used to calculate the value of binding constant (K_b) [4]. Ethidium bromide displacement experiments were performed by fluorescence measurements using emission spectroscopy at room temperature. Fluorescence spectra were recorded from 300 to 450 nm at an excitation wavelength of 295 nm. The fluorescence quenching is described by the Stern–Volmer equation [5]. The K_{sv} value is determined as the slope from the plot of F_0/F versus [Complex] [6].

2.3 Molecular docking

Molecular docking simulations were used to examine the inhibitor efficiency of **C1-C4** against Human DNA Topoisomerase I (Top I) receptors. The AutoDock 4.2 program [7] was used to analyze the binding affinity of the studied drugs. The AMDock software [8] was used to define the pockets and binding sites of the receptor.

3. Results and discussion

Fluorescence spectroscopy was used to study the ability of the newly synthesized compounds **C1-C4** to displace ethidium bromide (EB) from the EB-DNA complexes. The emission spectra of DNA in the absence and presence of the complexes were recorded at room temperature in solution for increasing amounts of each complex. The fluorescence changes indicate that the complexes have interacted with DNA. Emission

spectra of EB bound to DNA in the absence and presence of the complex were recorded for increasing amounts of each complex. Addition of the complex at various values results in a significant decrease in the intensity of the emission band of the DNA-EB system at 618 nm, indicating competition of the complex with EB in binding to DNA. The observed quenching of DNA-EB fluorescence for **C1-C4** indicates that they displace EB from the DNA-EB complex and can interact with DNA probably in an intercalative manner. The quenching parameter can be analyzed using the Stern-Volmer equation [5]. The calculated constants in Table 1 show that all complexes can be inserted between DNA base pairs. These results are consistent with the absorption data.

Table 1. The DNA binding constants (K_b), calculated from UV spectra and the Stern–Volmer constants (K_{sv}) for complexes of **C1-C4**.

Complex	$K_{sv} \times 10^4 (M^{-1})$	$k_q \times 10^{12} (M^{-1} s^{-1})$	R^{2a}	$K_b (M^{-1})$	R^{2a}
C1	4.21	4.21	0.9753	1.29×10^5	0.9751
C2	3.48	3.48	0.9862	7.91×10^4	0.9761
C3	3.26	3.26	0.9874	1.23×10^5	0.9919
C4	2.87	2.87	0.9849	8.75×10^4	0.9703

^a R is the correlation coefficient

Various strategies may be used by potential anticancer medications to cause death. The inhibitory impact on DNA is one of the most significant strategies for creating anti-cancer drugs. In this work, the complex's binding to the molecular target of human DNA topoisomerase I was investigated using a molecular docking approach. Molecular docking simulations were run to investigate the inhibitory action of **C1 - C4** towards DNA-Topoisomerase I. The results are shown in Table 2. To compare the findings, standard naproxen was employed as the substance that had previously shown good cytotoxicity. Results in Table 2 show that the examined complexes inhibit human DNA topoisomerase I, which suggests that there are many different mechanisms by which they might cause cytotoxicity.

Table 2. Thermodynamic parameters ΔG_{bind} (kcal/mol) and k_i (μM) obtained from molecular docking simulation for **C1-C4** with DNA-Topoisomerase I.

Protein/ Complex	C1		C2		C3		C4		Standards	
	ΔG_{bind}	$k_i(\mu M)$	ΔG_{bind}	$k_i(\mu M)$	ΔG_{bind}	$k_i(\mu M)$	ΔG_{bind}	$k_i(\mu M)$	ΔG_{bind}	$k_i(\mu M)$
DNA- Topoisomerase I	-5.97	42.07	-7.34	4.17	-5.84	52.39	-4.67	0.38	-7.7	2.27

The primary factor responsible for the stability of the DNA complex is the establishment of hydrogen bonds. Furthermore, the stability of the DNA-complex is significantly influenced by hydrophobic contacts, which include π - π , π -alkyl, and amide- π interactions with the aromatic and aliphatic components of the compounds under investigation. Complexes **C1-C4** exhibited similar inhibitory action against DNA, as shown by their respective Gibbs energies of -5.97, -7.34, -5.84, and -4.67. The observed

complexes exhibit a decreased inhibitory action in comparison to the established standard.

4. Conclusions

The interactions of CT-DNA with newly synthesized palladium(II) complexes were studied by measuring fluorescence. The high value of the Stern-Volmer quenching constant, K_{sv} , is the result of good binding of the tested complex compounds to CT-DNA. The respective Gibbs energies of investigated complexes showed a similar inhibitory effect against DNA.

Acknowledgment

This research is funded by the Ministry of Education and Ministry of Science, Technological Development and Innovation, Republic of Serbia, Grants: No. 451-03-47/2023-01/200378; 451-03-47/2023-01/200122 and Serbian Science and Diaspora Collaboration Program: Project acronym: TransMeCo.

References

- [1] C. Rîmbu, R. Danac, A. Pui, *Antibacterial Activity of Pd(II) Complexes with Salicylaldehyde-Amino Acids Schiff Bases Ligands*, Chemical and Pharmaceutical Bulletin 62 (2014) 12-15.
- [2] D. Lj, V.V. Stojković, G. P. Jevtić, M. B. Radić, R. M. Đukić, M. M. Jelić, M. V. Zarić, M.S. Anđelković, D. D. Mišić, S. R. Trifunović, D. Baskić, *Stereospecific ligands and their complexes. XXIV. Synthesis, characterization and some biological properties of Pd(II) and Pt(II) complexes with R₂-S,S-eddtyr*, New Journal of Chemistry 42 (2018) 3924-3935.
- [3] A. Savić, S. Misirlić-Denčić, M. Dulović, L.E. Mihajlović-Lalić, M. Jovanović, S. Grgurić Šipka, I. Marković, T.J. Sabo, *Synthesis, characterization and ROS-mediated cytotoxic action of novel (S,S)-1,3-propanediamine-N,N-di-2-(3-cyclohexyl)propanoic acid and corresponding esters*, Bioorganic Chemistry 54 (2014) 73-80.
- [4] E.A. Dolgoplova, A.A. Berseneva, M.S. Faillace, O.A. Ejegbavwo, G.A. Leith, S.W. Choi, H.N. Gregory, A.M. Rice, M.D. Smith, M. Chruszcz, S. Garashchuk, K. Mythreye, N.B. Shustova, *Confinement-Driven Photophysics in Cages, Covalent–Organic Frameworks, Metal–Organic Frameworks, and DNA*, J. Am. Chem. Soc. 142 (2020) 4769–4783
- [5] J. R. Lakowicz, *Principles of Fluorescence Spectroscopy*, Springer, New York, USA, 3rd edn, 2006.
- [6] J. R. Lakowicz, G. Weber, *Quenching of Fluorescence by Oxygen. a Probe for Structural Fluctuations in Macromolecules*, Biochemistry 12 (1973) 4161-4170.
- [7] Morris, G. M., Huey, R., Lindstrom, W., Sanner, M. F., Belew, R. K., Goodsell, D. S., & Olson, A. J., *AutoDock4 and AutoDockTools4: Automated docking with selective receptor flexibility*, Journal of computational chemistry, 2009) 30(16), 2785-2791.
- [8] M.S. Valdés-Tresanco, M.E. Valdés-Tresanco, P.A. Valiente, E. Moreno, *AMDock: a versatile graphical tool for assisting molecular docking with Autodock Vina and Autodock4*, Biology Direct 15 (2020) 1-12.

Macro and microelements in the leaf and extract of nettle from different localities of Montenegro

Bojana Knežević¹, Nataša Bošković², Marija Zorić², Zorica B. Leka^{2*}

¹ Center for Ecotoxicological Research Podgorica, Šarla De Gola 2, 81000 Podgorica, Montenegro, e-mail: bojana.knezevic@ceti.me

² University of Montenegro, Faculty of Metallurgy and Technology, Džordža Vašingtona bb, Podgorica, Montenegro, e-mail: zorica@ucg.ac.me

* Corresponding author

DOI: 10.46793/ICCB23.543K

Abstract: In this study, the content of 11 bioelements and 3 heavy metals in the dry nettle leaf and its water extract was investigated. Nettles were sampled from three different locations in Montenegro (northern, central and southern region). The determination of elements was done using the ICP - OES method. The bioelement content varies with geographic and climatic characteristics. Out of the four macroelements, whose presence was examined in nettle, the highest content is Ca, followed by K, then Mg, and the lowest is Na. Meanwhile, when it comes to microelements, the highest content is Fe, followed by Mn, Zn, and Cu. The amount of Fe as well as Ca and Mg was the most prominent in the sample from the mountain location, while the highest quantities of Cu and K were found in the samples from lower altitudes. The aim of this study was to determine the percentage of daily biometal requirements met through the consumption of nettles, either as a vegetable or as tea. By consuming nettle (5g/d), the greatest fulfilment of daily needs is achieved for Ca, Mg, K, Mn and Fe (52-5%), while the percentage of meeting daily needs for Na is negligible (below 0.04). The high content of K and the low content of Na qualify nettle to maintain a good balance of these electrolytes in the human body, which can be disturbed by an improper diet. The content of toxic metals (Pb, Cd and As) was below the quantification limit of the method.

Keywords: Nettle, extract, macroelements, microelements

1. Introduction

The word “nettle” is said to derive from the Anglo-Saxon word “noedl” meaning “needle”, while its Latin name “urtica” means “to burn”. This refers to the stinging effects of the tiny hairs on the stems and leaves, which when rubbed against the skin cause a burning sensation and temporary rash [1]. In the past, nettle has been primarily used for human consumption and for the production of various pharmaceutical products. Besides that, it is utilized in the textile industry and agriculture. It is exceptionally rich in various beneficial ingredients: proteins, carbohydrates, fibers, minerals. Nettle is traditionally used for the prevention and treatment of nutritional

anemia. Beside iron (Fe) as its most interesting biometal, nettle contains other biometals which are involved with various enzymes and biomolecules [1].

2. Materials and methods

2.1. Materials

For the research, a wild plant species, nettle (*Urtica dioica* L.), was used. It was collected from three locations in Montenegro: Žabljak (L1) - northern region (altitude 1456 m), Danilovgrad (L2) - central region (altitude 48 m), and Herceg Novi (L3) - coastal region of Montenegro (altitude 0 m). Plant harvesting was carried out in November 2022. The locations were far from traffic routes and industrial facilities.

After harvesting, the above-ground parts of the plant were naturally dried in the shade and well-ventilated area. The dried samples were homogenized by grinding in a laboratory mill designed for grinding food samples.

Calibration standards for the determination of macro and microelements were prepared from multicomponent standard solutions of 1000 mg/l (CPA Chem). The quality control of the method was checked using the certified reference material Strawberry leaves - Trace elements LGC7162.

2.2 Methods

The total content of macro- and microelements was determined by optical emission spectrometry technique with inductively coupled plasma after destruction under pressure. Digestion of the samples and reference material (200-300 mg, accurately measured) was performed according to the program recommended by the microwave oven manufacturer (Berghof, SV Xpert) in a mixture of 5 ml nitric acid (Supra 69 %, highpure acid, Carl Roth) and 2 ml hydrogen peroxide ($\geq 30\%$, for trace analysis, Sigma Aldrich). After digestion, the samples were quantitatively transferred to volumetric flasks by adding deionized water, and the content of the elements was analyzed by ICP-OES Thermo iCAP 7400.

The preparation of the water extract was performed by adding 20 ml of hot deionized water to 1 g of homogenized sample, after 10 minutes the samples were filtered through a white ribbon filter paper and the content of elements was determined by ICP-OES.

3. Results

The results of the analyses of selected elements in leaves of nettle, as well as in its water extract, are shown in Table 1. The recommended daily allowance (RDA) of bioelements for adults [2] as well as the percentage of fulfilling daily needs by consuming 5 g of dry nettle (calcul. accor. eq. 1a) and a cup of tea (prepared in the same way as hot water extraction was done) (calcul. accor. eq.1b) are shown in Table 2. In 2019, the National Academy of Medicine (US) updated the Dietary References Intakes (DRI) for sodium and potassium last established in 2005 [3].

$$(\%)_{RDA} = \frac{m(M)_{[kg]}^{[mg]} \times 5 g}{m(M)_{RDA}[mg] \times 1000} \times 100 \quad (\%)_{RDA} = \frac{m(M)_{[kg]}^{[mg]} \times 1 g}{m(M)_{RDA}[mg] \times 1000} \times 100 \quad (\text{Eq.1})$$

Over the years, increasing evidence suggests that sodium and potassium intake patterns of children and adults influence long-term population health mostly through complex relationships among dietary intake, blood pressure and cardiovascular health.

Table 1. The elements content in nettle samples and its extract from localities L1, L2, L3.

	Cr	Co	Cu	Zn	Fe	Mn	Na	K	Ca	Mg	P	Pb	Cd	As
mg/kg dry sample														
Nettle														
L1	<0. 6	<0. 6	3.1 6	13.7 3	161. 2	53.51	103. 2	2211 4	8349 4	1824 5	747 8	1.2 3	<0. 6	<0. 6
L2	<0. 6	<0. 6	4.5 2	17.0 4	142. 6	111.5 7	99.2	4214 8	6520 6	8925	371 9	1.1 8	<0. 6	<0. 6
L3	<0. 6	<0. 6	7.3 3	17.4 5	103. 7	85.41	110. 0	2516 8	4884 9	5273	488 1	1.1 0	<0. 6	<0. 6
Extrac t														
L1	<0. 2	<0. 2	2.6	8.6	3.4	2.4	26	1664 0	8600	7580	326	<0. 2	<0. 2	<0. 2
L2	<0. 2	<0. 2	3.2	11.2	8.0	12.88	74	3500 0	1422 0	4220	152	<0. 2	<0. 2	<0. 2
L3	<0. 2	<0. 2	2.1 4	5.4	2.12	2.22	96	1912 0	8780	2200	224	<0. 2	<0. 2	<0. 2

Table 2. The recommended daily allowance (RDA) for bioelements for adults [2]. The percentage of fulfilling daily needs by consuming 5 g of dry nettle and a cup of tea.

Bioelement	Cu	Zn	Fe	Mn	Na	K	Ca	Mg	P
RDA for adults (mg)	1	10	14	2	1500[3]	2000	800	375	700
% of fulfil. RDA for adul. cons. 5g dry nettle(L 1-3)	1.6-3.6	0.7-0.9	3.7-5.8	13-28	0.03-0.04	5.5-10.5	30-52	7-24	2.7-5.3
% of fulfil. RDA for adul. cons. cup of tea(L 1-3)	0.2- 0.3	<0.1	<0.06	0.1-0.6	<0.006	0.8-1.8	1.1-1.8	0.6-2	<0.05

The content of examined macroelements in nettle varies at three locations. The order of macroelement content in the examined nettle samples changes as follows: Ca > K > Mg > P; while the order of microelement content changes as follows: Fe > Mn > Zn > Cu.

The content of macroelements in nettle extract is in the following order: K > Ca > Mg > P. The content of microelements in the extract varies with the location. The content of Co and Cr is below the instrument's detection limit.

Nettle is a plant traditionally used on the Balkan Peninsula for the prevention and treatment of nutritional anemia. The Fe content in nettle leaves is higher at location L1 than L2 and L3. This may be related to geographical and soil characteristics.

By consuming nettle, the highest fulfilment of daily requirements is achieved for Ca, Mg, K, Mn, and Fe (52-5%), while the percentage of meeting daily Na needs is negligible (below 0.04%). The obtained values do not consider bioavailability and other interactions. A cup of nettle tea contains a significant amount of only Mg, Ca, and K (2 to 0.8%), while Fe and Na are below 0.06% and 0.006% respectively, of daily requirements.

Potassium and sodium are important for the functioning of our body. However, an imbalance of these elements can lead to health risks. Generally, the daily intake of Na in humans is higher than the intake of K. Consuming nettle would provide a higher intake of K than Na, contributing to maintaining a K^+/Na^+ balance. Despite moderately strong evidence that potassium supplementation lowers blood pressure, particularly in hypertensive adults, caution is warranted against high intakes via potassium supplementation for certain population groups, particularly those at high risk for compromised renal function [3].

In addition to bioelements, plants can also contain toxic heavy metals [4]. In the examined samples, the content of Cd and As were below the detection limit and Pb was 1.3 mg/kg. This value is significantly lower than the median lethal dose of lead (76.6 mg per kg of body weight).

3. Conclusions

The results of this study show that the nettle collected from three different locations in Montenegro can be considered a source of valuable bioelements (Fe, Ca, Mg, K, P, Mn, Cu, Zn). The content of Fe is more significant in the plant than in the tea. Nettle tea contains a significant amount of Ca, Mg, and K, while the content of Fe and Na is lower. The favourable ratio of K/Na content gives nettle special importance for maintaining the balance of these two elements, which can be disturbed by improper nutrition.

Namely, consuming more Na than K in the daily diet can lead to an increase in blood pressure and cardiovascular problems. Nettle, which has a positive K/Na ratio, is a natural alternative to potassium supplementation.

Acknowledgement

The authors express their gratitude to the Center for Ecotoxicological Research Podgorica, where the analyses were carried out.

References

- [1] D. Kregiel, E. Pawlikowska, H. Antolak., *Urtica spp.: Ordinary Plants with Extraordinary Properties*, *Molecules*. 23(2018)1664-1685.
- [2] Regulation (EU) no 1169/2011 of the European Parliament and of the Council of 25 October 2011 on the provision of food information to consumers. *Off J Eur Communities*. L304(2011)18-63.
- [3] National Academies of Sciences, Engineering, and Medicine; Health and Medicine Division; M. Oria, A. Virginia, M. Harrison (Eds.) (2019). *Dietary Reference Intakes for Sodium and Potassium*. Washington DC: National Academies Press.
- [4] G. Barboiu, C. Radulescu et al., *Potential health risk assessment associated with heavy metal accumulation in native urtica dioica*, *Romanian Reports in Physics* 72, 711 (2020)

Synthesis and antioxidant activity of novel vanillin-based ferrocenyl chalcones

Violeta R. Marković¹, Jovana M. Muškinja², Tamara Lj. Todorović^{2,*}

¹ University of Kragujevac, Faculty of Sciences, Department of Chemistry, 34000 Kragujevac, Serbia

e-mail: violeta.markovic@pmf.kg.ac.rs

² University of Kragujevac, Institute for Information Technologies, Department of Science, 34000 Kragujevac, Serbia

e-mail: jovana.muskinja@gmail.com, tamara.todorovic@uni.kg.ac.rs

DOI: 10.46793/ICCBIG23.547M

Abstract: A small series of new ferrocenyl chalcones was prepared, starting from the corresponding aldehydes and monoacetyl ferrocene. Di-derivatives of vanillin and ethylvanillin were prepared and used as aldehydes for this synthesis. All new compounds were characterized by IR and NMR spectroscopy and physical data. The antioxidant potential of new compounds was evaluated using the DPPH test and the results showed moderate activity *in vitro*.

Keywords: antioxidant activity, chalcones, ferrocene, synthesis, vanillin

1. Introduction

Chalcones are the core of many biologically interesting compounds from natural sources. They are used as an effective template in medicinal chemistry, and a high percentage of synthesized chalcones showed biological activities, such as anti-inflammatory [1], antitumor [2], antiviral [3], antioxidant [4], and many others.

On the other hand, ferrocene chemistry has revived in recent years. The ferrocenyl group has been incorporated into the structure of many biologically active molecules, such as flavones [5], chalcones [6], quinolinones [7], resulting in increased activities [8]. Different studies have demonstrated an important role for the ferrocene moiety as a structural motif for the enhancement of antioxidant activity [9].

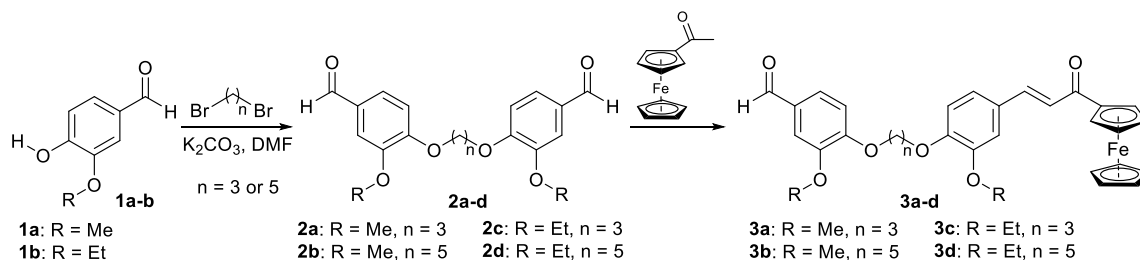
Taking into account our earlier results in the synthesis of bioactive ferrocene chalcones [10], we decided to prepare new chalcones containing ferrocene and vanillin pharmacophores and investigate their antioxidant activity.

2. Results and discussion

2.1. Chemistry synthesis

The novel ferrocenyl chalcones were synthesized in two steps (Scheme 1). For the synthesis of starting aldehydes, the alkylation of the OH group of vanillin **1a** and

ethylvanillin **1b** was performed using corresponding dibromoalkanes in the presence of K_2CO_3 in DMF. The intermediate di-vanillins and di-ethylvanillins (**2a-d**) were obtained in excellent yields. Then, the Claisen-Schmidt condensation of **2a-d** with monoacetylferrocene in the presence of NaOH in ethanol resulted in the formation of ferrocenyl chalcones (**3a-d**).



Scheme 1. Synthesis of vanillin-based ferrocenyl chalcones, **3a-d**.

The new ferrocenyl chalcones were obtained in a crystal form and characterized by their spectral data (IR, 1H and ^{13}C NMR).

2.2. Antioxidant activity

The DPPH radical scavenging activity of **3a-d** is presented in Table 1. The tested ferrocenyl derivatives exhibited moderate activity, with IC_{50} values ranging from 21.36 to 50.51 μM . Compounds that contain a longer linker in their structure (**3b** and **3d**) possess better activity. Additionally, vanillin-derived compounds showed stronger antioxidant capacity than their corresponding ethyl vanillin analogues. Compound **3b** showed the most promising activity ($IC_{50} = 21.36 \mu M$), comparable to reference, ascorbic acid. Further derivatization of these compounds, featuring the incorporation of catechol-containing moieties, may lead to the enhancement of their antioxidant activity.

Table 1. DPPH scavenging activity of compounds 3a-d.^a

Compound	$IC_{50} \pm SD$ (μM)
3a	43.13 \pm 0.61
3b	21.36 \pm 0.79
3c	50.51 \pm 0.84
3d	30.47 \pm 0.17
Ascorbic acid	18.70 \pm 0.86

^a Results are mean values \pm SD from three independent measurements.

3. Material and methods

3.1. Chemistry

All starting chemicals were commercially available and used as received, and the solvents were purified by distillation. IR spectra: PerkinElmer Spectrum One FT-IR

spectrometer with a KBr disc (cm^{-1}); NMR spectra: Varian Gemini 200 MHz spectrometer, using CDCl_3 as the solvent and TMS as the internal standard. ^1H and ^{13}C NMR chemical shifts were reported in parts per million (ppm). The melting points: MelTemp1000 apparatus. UV spectra: Agilent Technologies, Cary 300 Series UV-Vis Spectrophotometer.

3.1.1. General procedure for the synthesis of di-vanillins and di-ethylvanillins

The corresponding aldehyde was dissolved in DMF (36 ml) followed by the addition of anhydrous K_2CO_3 (46 mmol). The resulting suspension was stirred for a few minutes, and to this dibromopropane or dibromopentane was added, and the reaction mixture was allowed to stir at 50-60°C overnight. After that, the reaction mixture was heated to reflux for 2h. Then the reaction mixture was poured slowly into ice-cold water with constant stirring and kept in a refrigerator overnight. The precipitate obtained was filtered, washed, and dried. The obtained aldehydes were isolated as white to yellow powder.

3.1.2. General procedure for the synthesis of ferrocenyl chalcones

To a stirred solution of monoacetyl ferrocene (1.5 mmol) in absolute ethanol (20 ml) NaOH was added (340 mg) slowly. The resulting mixture was stirred at 50-60°C for 30 min. The corresponding aldehyde (1 mmol) was added, and the mixture was heated to reflux 4h. After reaction completion (monitored by TLC), the reaction mixture was poured slowly into ice-cold water and kept in a refrigerator overnight. The precipitate obtained was filtered, washed, dried, and chromatographed on a silica gel column using a dichloromethane-acetone (9:1) mixture as eluent (**3a-d**). All compounds were isolated as red crystalline molecules.

3.2. Antioxidant activity

The DPPH free radical scavenging activity of the studied compounds was determined according to the method described previously [11]. IC_{50} values represent the concentration necessary to obtain 50% of maximum scavenging activity. The results are presented as mean \pm standard deviation (SD) calculated from the independent experiments performed in triplicate using Microsoft Excel software.

4. Conclusions

In this study, four new ferrocenyl chalcones were synthesized in very good yields, and their structures were characterized by spectral data (IR, ^1H NMR, and ^{13}C NMR). Antioxidant activity was evaluated, and the results showed that chalcones containing longer linkers, between two vanillin **3b** or ethylvanillin **3d** fragments, have more prominent *in vitro* activities. These compounds can be a good basis for further derivatization and investigation.

Acknowledgment

This research is funded by the Ministry of Education and Ministry of Science, Technological Development and Innovation, Republic of Serbia, Grants: No. 451-03-47/2023-01/200378 and 451-03-47/2023-01/200122.

References

- [1] Z. Nowakowska, *A review of anti-infective and anti-inflammatory chalcones*, *European Journal of Medicinal Chemistry*, 42 (2007) 125-137.
- [2] W.D. Seo, Y.B. Ryu, M.J. Curtis-Long, C.W. Lee, H.W. Ryu, K.C. Jang, K.H. Park, *Evaluation of anti-pigmentary effect of synthetic sulfonylamino chalcone*, *European Journal of Medicinal Chemistry*, 45 (2010) 2010-2017.
- [3] J.C. Trivedi, J.B. Bariwal, K.D. Upadhyay, Y.T. Naliapara, S.K. Joshi, C.C. Pannecouque, E. De Clercq, A.K. Shah, *Improved and rapid synthesis of new coumarinyl chalcone derivatives and their antiviral activity*, *Tetrahedron Letters*, 48 (2007) 8472-8474.
- [4] R.N. Gacche, N.A. Dhole, S.G. Kamble, B.P. Bandgar, *In-vitro evaluation of selected chalcones for antioxidant activity*, *Journal of Enzyme Inhibition and Medicinal Chemistry*, 23 (2008) 28-31.
- [5] J.-P. Monserrat, G.G. Chabot, L. Hamon, L. Quentin, D. Scherman, G. Jaouen, E.A. Hillard, *Synthesis of cytotoxic ferrocenyl flavones via a ferricenium-mediated 1,6-oxidative cyclization*, *Chemical Communications*, 46 (2010) 5145-5147.
- [6] G. Nabi, Z.Q. Liu, *Radical-scavenging properties of ferrocenyl chalcones*, *Bioorganic and Medicinal Chemistry Letters*, 21 (2011) 944-946.
- [7] A. Pejović, I. Damljanović, D. Stevanović, M. Vukićević, S.B. Novaković, G.A. Bogdanović, N. Radulović, R.D. Vukićević, *Antimicrobial ferrocene containing quinolinones: Synthesis, spectral, electrochemical and structural characterization of 2-ferrocenyl-2,3-dihydroquinolin-4(1H)-one and its 6-chloro and 6-bromo derivatives*, *Polyhedron*, 31 (2012) 789-795.
- [8] N. Metzler-Nolte, M. Salmann, *In ferrocenes ligands, materials and biomolecules*, Stepnicka, P., Ed., Wiley: West Sussex, 13 (2008) 499-639.
- [9] C. Zhao, Z.-Q. Liu, *Modification by ferrocene: An approach to enhance antioxidant ability of aianthoidol to protect DNA*, *Biochimie*, 94 (2012) 1805-1811.
- [10] J. Muškinja, A. Burmudžija, Z. Ratković, B. Ranković, M. Kosanić, G.A. Bogdanović, S.B. Novaković, *Ferrocenyl chalcones with O-alkylated vanillins: synthesis, spectral characterization, microbiological evaluation, and single-crystal X-ray analysis*, *Medicinal Chemistry Research*, 25 (2016) 174-1753.
- [11] C. Kontogiorgis, D. Hadjipavlou-Litina, *Biological evaluation of several coumarin derivatives designed as possible anti-inflammatory/antioxidant agents*, *Journal of Enzyme Inhibition and Medicinal Chemistry*, 18 (2003) 63-69.

A contribution to the knowledge of the species *Dipsacus sylvestris* Huds.

Milica Pavlović^{1*}, Vesna Velicković², Gorica Đelić¹

¹University of Kragujevac, Faculty of Science, Department of Biology and Ecology, Radoja Domnovića 12, 34000 Kragujevac, Serbia; e-mail: milica.novakovic@pmf.kg.ac.rs, gorica.djelic@pmf.kg.ac.rs

²University of Kragujevac, Faculty of Technical Science, Svetog Save 65, 32000 Čačak, Serbia; e-mail: vesna.velickovic@ftn.kg.ac.rs

DOI: 10.46793/ICCBi23.551P

* Corresponding author

Abstract: This study aimed to investigate the content of phenols, flavonoids, and antioxidant activity in *Dipsacus sylvestris* from different localities. Based on the spectrophotometric determination, the extract from the flower Vujan Mountain exhibited the highest phenolic content (98.50 ± 3.18 mg GAE/g), while the leaf extracts from Lake Gruza (48.81 ± 1.76 mg RU/g), contained the highest amount of flavonoids. Additionally, the extract from the root of Vujan Mountain (3.12 ± 0.01 µg/mL) demonstrated the highest capacity to neutralize DPPH radicals. These results suggest that, despite the extensive historical use of the root of *D. sylvestris* as a medical plant, its stem, leaves and flower may also possess valuable biological properties. The presented results may serve as a basis for further research on *D. sylvestris* for potential applications in the pharmaceutical industry.

Keywords: *Dipsacus sylvestris*, Phenols, Flavonoids, Antioxidant activity

1. Introduction

Dipsacus sylvestris Huds. is a herbaceous biennial plant belonging to the Dipsacaceae family, native to Europe, and Asia and it is widespread and invasive. It grows in wet areas, next to swamps, and streams, as well as alongside roads, in dusty and dry areas. [1] The plant can reach a height of up to 2.5 meters, with prickly stems, a distinctive cone-shaped flower head, and leaves downward-pointing prickly. [2] Some of the research has shown that the root plant can be used in the treatment of various conditions, including fibromyalgia, bone fracture, Lyme disease, and especially cancer and Alzheimer's disease [3,4]. It is also known for its use in treating skin diseases such as warts and fistulas. The Infusion made from the plant root is used to strengthen the stomach, stimulate appetite, alleviate liver obstruction, and treat jaundice [5].

However, although there is a wealth of information about the traditional use of *D. sylvestris*, there is no literature data on its chemical composition. So, this study aimed to investigate the total phenols and flavonoid content, and antioxidant activity of the aboveground part and root methanol extracts of *D. sylvestris*.

2. Materials and methods

2.1 Plant material and extracts preparation

The plant material was collected in July 2020 in the flowering phase, (the aboveground parts and roots i.e. herba et radix) in the Vujan Mountain (43°57'54.6"N 20°26'15.9"E), and Lake Gruza (43°55'19.7"N 20°40'30.9"E). Plant material was identified and the voucher specimen of *D. sylvestris* was deposited in the Herbarium at the University of Kragujevac, Faculty of Science, Department of Biology and Ecology. The aboveground part and root were cleaned, separated, and dried at room temperature in a well-ventilated dark room. The dried and finely ground aboveground part and the root were extracted with methanol by the maceration process, and the resulting extract was filtered and evaporated in a vacuum.

2.2 Spectrophotometric determination of total phenols and flavonoid content of the extracts

Total phenols were determined spectrophotometrically by the Folin-Ciocalteu method as described by Peter et al. (2011) [6], and the results were expressed in gallic acid equivalents (mg GAE/g extract). $AlCl_3$ solution was used as a reagent for spectrophotometric determination of total flavonoid content by was described by Quettier-Deleu et al. (2000) [7], whereby results were expressed in rutin equivalents (mg RU/g extract).

2.3 Determination of the antioxidant activity of the extracts

The free radical scavenging activity of samples methanol solutions was analyzed using 2,2-diphenyl-1-picrylhydroxyl (DPPH) according to the Takao et al. (1994) [8], and the results were expressed as ascorbic acid equivalents. The percent DPPH inhibition was calculated by the equation (Eq. 1). Antioxidant activity was expressed as the 50% inhibitory concentration (IC_{50} values in $\mu g/mL$)

$$\% \text{ inhibition} = ((A \text{ of control} - A \text{ of sample}) / (A \text{ of control})) \times 100 \quad (1)$$

3. Results and discussion

Based on the reviewed literature, these are the first results dealing with the examination of the total phenols and flavonoids, aboveground parts, and root methanol extracts of *D. sylvestris*. The results of the spectrophotometric determination of the content of total phenols are shown in Table 1. In this work, the extraction of all *D. sylvestris* samples was performed with methanol. The higher content of total phenols in all parts of the plant

species *D. sylvestris* from the Vujan Mountain was constant in relation to the plant species collected from Lake Gruza. Based on the obtained results, it can be noticed that the extract Vujan Mountain had a high total phenols content (98.50 ± 3.18 mg GAE/g) from the flower and the Lake Gruza extract (51.61 ± 2.99 mg GAE/g) from the stem. The lowest content of total phenols was constant from Vujan Mountain (61.67 ± 1.92 mg GA/g) from the stem and Lake Gruza (31.27 ± 3.91 mg GA/g) from the root.

Table 1. The amount of total phenols determined in methanol *D. sylvestris* extracts presented as equivalents of gallic acid, mg of GA/g extract.

	Root	Stem	Leaf	Flower
Vujan Mountain	67.00 ± 2.73	61.67 ± 1.92	62.67 ± 1.82	98.50 ± 3.18
Lake Gruza	31.27 ± 3.91	51.61 ± 2.99	49.61 ± 3.43	48.28 ± 4.13

Values are mean \pm standard deviation of triplicate analyses.

The results of the spectrophotometric determination of the content of total flavonoids are shown in Table 2. In this work, the extraction of all *D. sylvestris* samples was performed with methanol. Based on the obtained results, it can be observed that the leaf extracts, from both locations contained the highest amount of total flavonoids, Lake Gruza (48.81 ± 1.76 mg RU/g), and Vujan Mountain (42.90 ± 1.85 mg RU/g). The lowest content of total flavonoids was constant in root extracts from both locations, Lake Gruza (1.33 ± 0.22 mg RU/g), and Vujan Mountain (0.93 ± 0.52 mg RU/g).

Table 2. The amount of total flavonoids determined in methanol *D. sylvestris* extracts presented as equivalents of rutin, mg of RU/g extract.

	Root	Stem	Leaf	Flower
Vujan Mountain	0.93 ± 0.52	5.55 ± 0.18	42.90 ± 1.85	6.71 ± 2.77
Lake Gruza	1.33 ± 0.22	10.07 ± 0.50	48.81 ± 1.76	3.71 ± 0.25

Values are mean \pm standard deviation of triplicate analyses.

Both from Vujan Mountain and Lake Gruza, *D. sylvestris* extracts showed a good radical scavenging activity in vitro Table 3.

Table 3. Antioxidant activity of investigated *D. sylvestris* extracts, IC₅₀ values (μ g/mL).

	Root	Stem	Leaf	Flower
Vujan Mountain	3.12 ± 0.01	11.05 ± 0.45	203.09 ± 3.56	350.81 ± 3.56
Lake Gruza	138.68 ± 1.92	75.55 ± 1.21	394.9 ± 3.36	351.76 ± 2.36

Values are mean \pm standard deviation of triplicate analyses.

The lower IC₅₀ value reflects greater activity. The highest antioxidant activity was measured in an extract from Vujan Mountain (3.12 ± 0.01 μ g/mL, from root) and (11.05 ± 0.45 μ g/mL, from the stem), while the lowest capacity to neutralize DPPH radicals was measured in an extract Lake Gruza (519.76 ± 2.36 μ g/mL) from the flower. Compared to

the results published by Witkowska-Banaszczak (2018) [9], our results show much higher IC₅₀ values in the extract of Vujan Mountain ($3.12 \pm 0.01 \mu\text{g/mL}$) from the root, while the mentioned study reported IC₅₀ value of ($86.01 \mu\text{g/mL}$) from the root. However, much lower IC₅₀ values were constant in the extract from Vujan Mountain ($203.09 \pm 3.56 \mu\text{g/mL}$) and Lake Gruza ($394.9 \pm 3.36 \mu\text{g/mL}$) from the leaves, compared to the results of the mentioned study, IC₅₀ ($143.1 \mu\text{g/mL}$).

4. Conclusions

The results of this investigation revealed that *D. sylvestris* methanol extracts from Vujan Mountain and Lake Gruza possess a high amount of total phenols and have significant (extracts root and stem) antioxidant activity. The higher content of total phenols in all parts of the plant species *D. sylvestris* from the Vujan Mountain was constant compared to the plant species collected from Lake Gruza. These results suggest that, while the root of *D. sylvestris* has been extensively used since ancient times, its stem, leaves and flower may also possess valuable biological properties. The presented results may serve as a basis for further research on *D. sylvestris* for potential application in pharmaceuticals.

References

- [1] J.J. Krupa, J.M. Thomas., *Is the common teasel (Dipsacus fullonum) carnivorous or was Francis Darwin wrong?*, Botany, 97 (2019) 321-328.
- [2] J. Oszmiański, A. Wojdyło, P. Juszczak, P. Nowicka., *Roots and Leaf Extracts of Dipsacus fullonum L. and Their Biological Activities*, Plants, 9 (2020) 78.
- [3] T. Liebold, R. Straubinger, H. Rauwald., *Growth inhibiting activity of lipophilic extracts from Dipsacus sylvestris Huds. Roots against Borrelia burgdorferi s. s. in vitro*, Pharmazie, 66 (2011) 628-630.
- [4] Y.M. Zhao, Y.P. Shi., *Phytochemicals and biological activities of Dipsacus species*, Chemistry & Biodiversity, 8 (2011) 414-430.
- [5] A. Chevallier., *Encyclopedia of herbal medicine: the definitive reference to 550 herbs and remedies for common ailments*, New York, USA: DK Publishing, (2000) 336.
- [6] C. Peter, A. Moran, L Ryan., *Stability of the total antioxidant capacity and total polyphenol content of 23 commercially available vegetable juices before and after in vitro digestion measured by FRAP, DPPH, ABTS and Folin-Ciocalteu methods*, Food Research International, 44 (2011) 217-224.
- [7] C. Quettier-Deleu, B. Gressier, J. Vasseur, T. Dine, C. Brunet, M. Luyckx, M. Cazin, J.C. Cazin, F. Bailleul, F Troitin., *Phenolic compounds and antioxidant activities of buckwheat (Fagopyrum esculentum Moench) hulls and flour*, Journal of Ethnopharmacology, 72 (2000) 35-42.
- [8] E.Witkowska-Banaszczak., *Dipsacus fullonum L. leaves and roots - Identification of the components of the essential oils and alpha-amylase inhibitory activities of methanolic extracts*, Acta Poloniae Pharmaceutica-Drug Research, 75 (2018) 951-957.
- [9] T. Takao, N. Watanabe, I. Yagi, K. Sakata., *A simple screening method for antioxidant and isolation of several antioxidants produced by marine bacteria from fish and shellfish*, Bioscience, Biotechnology, and Biochemistry, 58 (1994) 1780-1783.

Qualitative content of selected phenolic compounds in different extracts of plant species *Iris pumila* L.

Gorica Đelić¹, Milica Pavlović¹, Vesna Veličković^{2,*}

¹ University of Kragujevac, Faculty of Science, Department of Biology and Ecology, Radoja Domanovića 12, 34000 Kragujevac, Serbia; e-mail: gorica.djelic@pmf.kg.ac.rs; milica.novakovic@pmf.kg.ac.rs

² University of Kragujevac, Faculty of Technical Science, Svetog Save 65, 32000 Čačak, Serbia; e-mail: vesna.velickovic@ftn.kg.ac.rs

DOI: 10.46793/ICCB23.555DJ

* Corresponding author

Abstract: The aim of this paper is to determine the content of selected phenolic compounds and to find the appropriate optimal extraction agent for the extraction of phenolic compounds from the plant species *Iris pumila* L. The content of total phenols and flavonoids in the rhizome and aboveground parts of the plant was determined by the application of the spectrophotometric method in the examined extracts obtained by the maceration method. By comparatively analyzing the application of two solvents for extraction, we concluded that the application of methanol in the conventional maceration technique contributes to a higher yield of phenolic compounds. Using methanol as a solvent, it was found that the content of selected phenolic compounds in the rhizome (28.57 mg/g extract total phenolic and for total flavonoids 24.21 mg/g extract) compared to ethyl acetate as solvent. Tested extracts of parts of *Iris pumila* L. plant contain high levels of phenolic compounds and are suitable for use as a source of compounds with pronounced antioxidant activity.

Keywords: extraction, maceration, spectrophotometry, phenolics compounds

1. Introduction

Iris pumila L. (bearded dwarf iris) is a perennial herbaceous plant of the family irises (*Iridaceae*). It is a perennial entomophilic plant that inhabits the meadow-steppe regions of Central and Southeastern Europe. [1] The natural habitats of this species in Serbia are its northern and eastern parts, and it is most common in Deliblato sandstone, which consists of a complex of sand dunes in southern Banat. [2] It blooms in April, the flowering period lasts about two weeks. The flowers of the plant are single and distinctly polymorphic in relation to color. [3] The leaves of irises or irises are fleshy, erect, lanceolate, and light green. Ordinary irises inside the flower have clusters of tiny hairs and are therefore often referred to as bearded irises. [3]

Iris pumila as a plant species has been studied in several morphological and cytological studies, but it has not been studied in terms of the content of phenolic compounds. [4, 5, 6] In recent decades, there has been an increase in the interest of the

general scientific public in natural antioxidant compounds and plant species, which are a significant source of these compounds. Numerous scientific studies confirm that natural phenolic compounds (polyphenols) exhibit significant antioxidant potential and are very good antioxidants. [7, 8] Plants are its main source. Given that synthetic antioxidants exhibit a number of side effects and adverse effects due to long-term use, interest and demand for the application of natural antioxidants are on the rise. [9] Among the natural antioxidants, a large and very wide, diverse group of phenolic compounds stands out. These compounds also called natural polyphenols (among which the most important are flavonoids, phenolic acids, anthocyanins, etc.) exhibit a number of positive properties, and due to their antioxidant activity show antiviral [7], antibacterial [8], anticancer effects [9]. Plant antioxidants can be extracted from a variety of plant materials, mainly dried by the extraction process - a method of mass transfer by means of solvents from the solid phase to the liquid. Mass transfer depends on many factors, such as the type of solvent, extraction length, temperature, and polarity of the solvent. [10] This study aimed to investigate selected phenolic compounds and to find the appropriate optimal extraction agent for the extraction of phenolic compounds from the aerial part and rhizome of *Iris pumila*.

2. Materials and methods

2.1 Plant material and extracts preparation

The rhizome and the above-ground part of the iris were collected from the locality Ovcar-Kablar Gorge. Dried parts of the plant are ground in a blender, and as such used in the further procedure. We prepared the extracts by maceration method. 50 ml of solvent and 10 g of herbal drugs were used. Ethyl acetate and methanol (Table 1) were used as solvents. Maceration lasted three days, after which the resulting extracts were dried using a rotary vacuum-evaporator. The extracts are stored in Petri dishes, in the refrigerator at a temperature of + 4 degrees Celsius.

2.2 Spectrophotometric determination of total phenols and flavonoid content of the extracts

The content of the total phenols was determined by the spectrophotometric method according to Folin-Ciocalteu. [11] The method is based on the reduction of Folin-Ciocalteu reagents in the presence of phenolic compounds. Phenolic compounds by dissociation produce a proton and a phenoxide ion that reduces folin-Ciocalteu reagent to phenol-MoW11O40-ion that is colored blue. The intensity of color is measured spectrophotometrically, at the wavelength $\lambda = 765$ nm. The absorbance is measured at $\lambda = 765$ nm. The results of the analysis are shown in Table 1.

The content of total flavonoids was determined by the modified method by Brighente. [12] The method is based on the property of flavonoids to build metalcomplexes with metals, of which the complex with aluminum is particularly

important. [12] The absorbance is measured at $\lambda = 430$ nm. The analysis was done in three repetitions. Gallic acid, a series of standard solutions with a concentration of 0.05-1 mg/mL, was used as standard, the results obtained were expressed as gallic acid equivalents (mg GAE/g \pm SD). All measurements were made on the UV-VIS spectrophotometer, brand DR 3900 Hach Lange produced in 2022. All analyses were done in three repetitions. The results of the analysis are shown in Table 2.

3. Results and discussion

Table 2 presents the results of determining the content of total phenols in the aerial parts and rhizomes of the plant species *Iris pumila* L. by the method of spectrophotometry.

Table 1. The content of total phenols in the various parts of the *Iris pumila* L.

Sample*	A	Total phenolics (mg GAE/g \pm SD)
1.	0.029	25.62 \pm 0.05
2.	0.034	25.66 \pm 0.06
3.	0.088	26.14 \pm 0.17
4.	0.364	28.57 \pm 0.71

*tags :1 -ethyl-acetate-aerial part. 2-ethyl-acetate-rhizome. 3-methanol-above-ground part. 4-methanol rhizome. A- absorbance

The extract obtained by the maceration process where it was used as a solvent methanol contains the largest amount of total phenols (28.57 mg GAE/g). This content is higher in relation to the content of the total phenols of the aboveground part using the same solvent and compared to the rhizome extract in ethyl acetate (25.62 mg GAE/g). where the lowest amount of total phenols was recorded. Methanol is a more efficient solvent for extracting phenolic compounds from plants.

Table 2. The content of flavonoids in the various parts of the *Iris pumila* L.

Sample*	A	Total flavonoids (mg GAE/g \pm SD)
1.	0.009	1.88 \pm 0.02
2.	0.012	2.05 \pm 0.03
3.	0.029	5.87 \pm 0.13
4.	0.121	24.21 \pm 0.67

*tags :1 -ethyl-acetate-aerial part. 2-ethyl-acetate-rhizome. 3-methanol-above-ground part. 4-methanol rhizome. A- absorbance

Based on the results it is noticeable that higher concentrations of flavonoids are represented in extracts in which methanol was used as a solvent in the extraction process. The highest concentration of flavonoids is in rhizome extract in methanol (24.21

mg GAE/g) which is about twelve times higher than the concentration of flavonoids present in the aboveground extract obtained using methanol (5.87 mg GAE/g). The aboveground extract in ethyl acetate shows three times lower content compared to the extract where methanol is used as a solvent (1.88 mg GAE/g).

4. Conclusions

The results obtained in the paper show that extracts of different parts of the plant species *Iris pumila* L. contain significant amounts of total phenols. The content of total phenols is highest in rhizome extract obtained by the maceration process (84.60 mg/g extract) when methanol was used as a solvent. This extract contains the largest amount of total flavonoids (24.21 mg/g extract). Based on the study it can be concluded that methanol has proven to be a better solvent in extraction by maceration process of different parts of plant species *Iris pumila* L. The application of this solvent ensures an increase in efficiency - methanol yields higher concentrations of phenolic compounds in the extract of different parts of the plant species *Iris pumila* L.

References

- [1] L. F. Randolph., *The geographic distribution of European and eastern Mediterranean species of bearded Iris*, Iris Year Book, (1955). 35–46.
- [2] M. Gajić., *Flora Deliblatske pešćare*, Prirodno matematički fakultet OOUR Institut za biologiju. Novi Sad, (1983).
- [3] S. Đ. Budečević., *Morfološko variranje. fenotipska plastičnost i fluktuirajuća asimetrija oblika svetnih organa kod Iris pumila L.*, Doktorska disertacija Beograd, (2018).
- [4] E.G.B. Luscombe., *Iris pumila* L. I. - The Iris Year Book. (1972) 149-157.
- [5] J. Mitra., 1: *Karyotype analysis of bearded iris*, Botanical Gazette, 117 (1956) 265-293.
- [6] L. F. Randolph, K. Heinig., *Cytology and breeding behavior of dwarf and tall-bearded Iris hybrids*, Bulletin of the American Iris Society (1951) 1-8.
- [7] M.R. Loizzo, A.M. Saab, R. Gambari, J. Cinatl, H.W. Doerr, *Phytochemical analysis and in vitro antiviral activities of the essential oils of seven Lebanon species*, Chemistry & Biodiversity, 5 (2008) 461-470.
- [8] B. Khameneh, R. Diab, K. Ghazvini, B.S.F. Bazzaz, *Breakthroughs in bacterial resistance mechanisms and the potential ways to combat them*, Microbial Pathogenesis, 95 (2016) 32-42.
- [9] I. C. Arts, P.C. Hollman *Polyphenols and disease risk in epidemiological studies*, The American Journal of Clinical Nutrition, 81 (2005) 317S-25S
- [10] Q.W. Zhang, L.G. Lin, W.C. Ye., *Techniques for extraction and isolation of natural products. A comprehensive review*, Clinical Medicine, 13 (2018) 20.
- [11] V.L. Singleton, J.A. Rossi, *Colorimetry of total phenolics with phosphomolybdic-phosphotungstic acid reagents*, Enology and Viticulture, 16 (1965) 144-158.
- [12] I.M.C. Brighente, M. Dias, L.G. Verdi, M.G. Pizzolatto, *Antioxidant activity and total phenolics content of some Brazilian species*, Pharmaceutical Biology, (2007) 156-161.

Building a 3D QSAR model with isopropylidene analogs of cytotoxic styryl-lactones

Bojan D. Levovnik¹, Aleksa P. Alargić¹, Miloš M. Svirčev^{1,*}, Goran I. Benedeković¹

¹ University of Novi Sad, Faculty of Sciences, Department of Chemistry, Biochemistry and Environmental Protection, Novi Sad, Serbia, Trg Dositeja Obradovića 3; e-mail: milos.svircev@dh.uns.ac.rs

* Corresponding author

DOI: 10.46793/ICCB23.559L

Abstract: Styryl-lactones are a class of natural products and related analogs that exhibit diverse biological activities, including anticancer, anti-inflammatory, and antimicrobial properties. Since these compounds are routinely obtained in our laboratory from their *O*-isopropylidene precursors, we envisioned the project to examine and compare their respective structures and *in vitro* activities.

This paper presents a basic 3D-QSAR steric model built on a small set of 11 selected *O*-isopropylidene and styryl-lactone (particularly [3.3.0]furofuranone) ligands and their *in vitro* activities against an MCF-7 cell line. It is part of a larger ongoing study that encompasses synthesis as well as *in vitro* and *in silico* testing of a growing library of natural products and their analogs, with the aim to determine their pharmacophores, molecular targets, and cellular mechanisms of action.

Keywords: 3D-QSAR, *O*-isopropylidene, styryl-lactone, ADME

1. Styryl-lactones and their *O*-isopropylidene analogs

The presence of the *O*-isopropylidene/dioxolane moiety is relatively uncommon in bioactive molecules. This is partially due to their susceptibility to hydrolysis under mildly acidic conditions, which simultaneously makes them preferred protective groups in diol chemistry [1,2]. However, the isopropylidene fragment's ability to enhance the lipophilicity of a diol structure makes it a compelling synthetic target for medicinal chemists. Indeed, some dioxolane-endowed structures show inhibitory [3], bactericidal [4], anticancer [5], anti-inflammatory [6], and other intriguing activities [7].

Our group synthesizes cytotoxic styryl-lactones from simple (and inexpensive) monosaccharide precursors, and some form of *O*-isopropylidene intermediate is integral to nearly every synthetic route we use [8]. The persistent problem we face, however, is the lack of insight into the biochemical mechanisms of our compounds.

As a part of ongoing research, we recently envisioned a series of halogenated *O*-isopropylidenes as intermediates (but also potential bioactive molecules themselves) in the synthesis of novel, halogenated thiazole styryl-lactones [9]. In order to better understand the incoming *in vitro* results, we initialized a set of *in silico* tests that (will) include inverse docking, pharmacophore screening, 3D-QSAR and MD.

2. 3D-QSAR model

The 11 molecules with bicyclic furo-dioxolane or furofuranone ring system and their *in vitro* activities against MCF-7 (ER+ breast cancer) cell line were selected for 3D-QSAR (Figure 1). The average Tanimoto coefficient for the molecules was 0.56 (0.32 – 1).

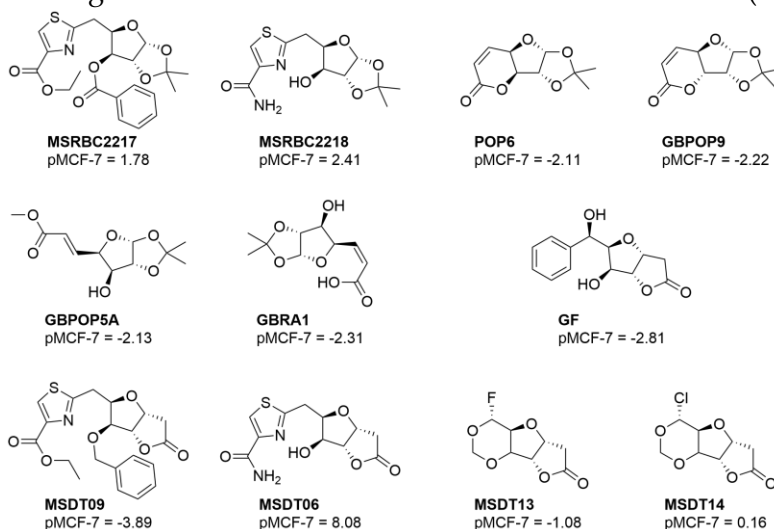


Figure 1. Ligands used for 3D-QSAR.

The 3D-QSAR model (Figure 2) was built using a Py-CoMFA, a Python implementation of the CoMFA method, available via a server (<https://www.3d-qsar.com>) [10]. Only the steric model, 3D-QSAR STE, fulfilled minimal requirements with $q^2 = 0.68$ and $r^2 = 0.997$, but the standard deviation for error in the prediction set was high (SDEP = 2.078), which combined with a low standard deviation in the calibration set (SDEC = 0.2) could indicate limitations in predicting the activities of new compounds due to potential overfitting.

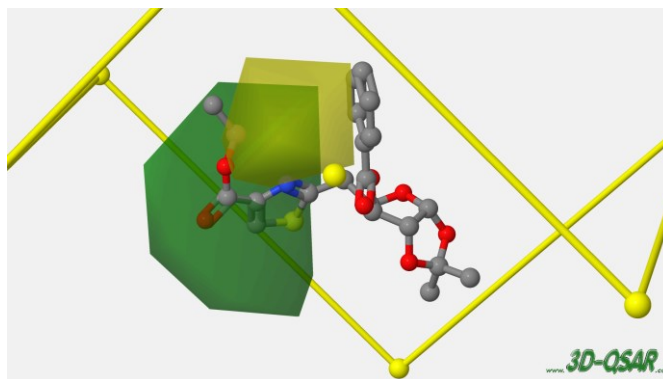


Figure 2. Steric (green: favored, yellow: unfavored) contour map for a compound **MSRBC2217**.

When tested on SwissADME server (<http://www.swissadme.ch/index.php#top>) the compounds showed a moderate *in silico* lipophilicity (Table 1), passed rules of Lipinski, Ghose (1 violation by **MSDT06** and **MSDT13**), Veber, Egan (1 violation by **MSRBC2218** and **MSDT06**) and Muegge, scored good bioavailability (0.55), did not raise PAINS alerts and were predicted a high GI absorption (unfortunately, except the most active compound **MSDT06**).

Table 1. Lipophilicity

Molecule	iLOGP	XLOGP3	WLOGP	MLOGP	Consensus Log P	Silicos-IT LogSw
MSRBC2217	4.12	3.53	2.96	1.58	3.2	-4.72
MSRBC2218	2.18	-0.04	0.02	-0.99	0.46	-1.15
POP6	2.1	0.37	0.34	0.33	0.72	-0.32
GBPOP9	1.99	0.37	0.34	0.33	0.7	-0.32
GBPOP5A	2.62	-0.16	-0.05	-0.19	0.51	0.08
GBRA1	1.61	-0.49	-0.14	-0.48	0.06	0.78
MSDT06	0.84	-0.74	-0.77	-1.36	-0.23	-0.82
MSDT09	3.03	2.64	2.38	1.07	2.61	-4.87
MSDT13	1.26	-0.2	0.16	-0.43	0.24	-0.07
MSDT14	1.48	0.05	0.01	-0.27	0.38	-0.41
GF	1.69	0.43	-0.16	0.18	0.58	-1.41

3. Conclusions

A 3D-QSAR steric model was built based on 11 ligands and their *in vitro* activities against MCF-7 cell line. Although the ligand library is still too small/diverse to give us conclusive results, the obtained model could point our future design in the right direction. More precisely, the chemical space around the thiazole/aromatic ring in the C-5 position (*O*-isopropylidene enumeration) could be further investigated and expanded with novel analogs.

Acknowledgment

This research is funded by the Ministry of Education and Ministry of Science, Technological Development and Innovation, Republic of Serbia, Grants: No. 451-03-68/2022-14/200125 as well as a research project from the Serbian Academy of Sciences and Arts (Grant No. F-130).

References

- [1] T.F. Tam, B. Fraser-Reid., *1,2-O-isopropylidene furanoses as chiral precursors for α -methylene- γ -butyrolactones*, *J. Chem. Soc., Chem. Commun.*, (1980) 556–558.
- [2] K.M. Sun, B. Fraser-Reid, T.F. Tam., *Annulated sugars: the 1,2-O-isopropylidene ring as a stereo-, regio-, and chemoselective agent*, *J. Am. Chem. Soc.*, 104 (1982) 367–369.
- [3] S.B. Ferreira, A.C.R. Sodero, M.F.C. Cardoso, E.S. Lima, C.R. Kaiser, F.P. Silva, V.F. Ferreira., *Synthesis, Biological Activity, and Molecular Modeling Studies of 1 H⁻1,2,3-Triazole Derivatives of Carbohydrates as α -Glucosidases Inhibitors*, *J. Med. Chem.*, 53 (2010) 2364–2375.
- [4] M. Korycka-Machała, A. Brzostek, B. Dziadek, M. Kawka, T. Popławski, Z. Witczak, J. Dziadek., *Evaluation of the Mycobactericidal Effect of Thio-functionalized Carbohydrate Derivatives*, *Molecules*, 22 (2017) 812.
- [5] G. Catelani, F. Osti, N. Bianchi, M.C. Bergonzi, F. D’Andrea, R. Gambari., *Induction of erythroid differentiation of human K562 cells by 3-O-acyl-1,2-O-isopropylidene-D-glucofuranose derivatives*, *Bioorg. Med. Chem. Lett.*, 9 (1999) 3153–3158.
- [6] J. Xing, J. Sun, H. You, J. Lv, J. Sun, Y. Dong., *Anti-Inflammatory Effect of 3,4-Oxo-isopropylidene-shikimic Acid on Acetic Acid-Induced Colitis in Rats*, *Inflammation*, 35 (2012) 1872–1879.
- [7] R.A. Aitken, L.A. Power., *1,3-Dioxoles and 1,3-Oxathioles*, in: *Compr. Heterocycl. Chem. III*, Elsevier, 2008: pp. 841–891.
- [8] M. Svirčev, G. Benedeković, I. Kovačević, M. Popsavin, V. Kojić, D. Jakimov, T. Srdić-Rajić, M. V. Rodić, V. Popsavin., *Conformationally restricted goniofufurone mimics with halogen, azido or benzyloxy groups at the C-7 position: Design, synthesis and antiproliferative activity*, *Tetrahedron*, 74 (2018) 4761–4768.
- [9] B.D. Levovnik, J.D. Kesić, S.M. Đokić, M.M. Svirčev, *A variation in the initial step in the synthesis of halogenated goniofufurone/tiazofurin analogs and in silico search for their receptors*, in: *8th Conf. Young Chem. Serbia*, Serbian Chemical Society, Serbian Young Chemists’ Club, Belgrade, 2019: p. 105.
- [10] R. Ragno., *www3d-qsar.com: a web portal that brings 3-D QSAR to all electronic devices—the Py-CoMFA web application as tool to build models from pre-aligned datasets*, *J. Comput. Aided. Mol. Des.*, 33 (2019) 855–864.

Validation of gravimetric method for determination of clay in soil

Marina Uđilanović^{1,*}, Andrija Ćirić¹

¹ Faculty of Science, Department of chemistry, University of Kragujevac, Radoja Domanovića 12, 34000 Kragujevac, Serbia; e-mail: marinainka95@gmail.com, andrija.ciric@pmf.kg.ac.rs, andrija@kg.ac.rs

* Corresponding author

DOI: 10.46793/ICCB23.563U

Abstract: The requirements for method validation are taken from the method ISO 11277:2020 Soil quality - determination of particle size in soil - by sieving and sedimentation method, Annex C table C.1 [1]. The validation was performed on soil samples and on soil reference material (old PT scheme). Validation includes checking the volume of the pipette i.e., calibration of the pipette, correction for the contribution of the dispersing agent, repeatability (RSD_r), reproducibility (RSD_R), recovery (R), checking bias from the used lab equipment and the bias from purity of use chemicals. As a final part of the validation, the combined measurement uncertainty (U_c) and expanded measurement uncertainty (U) with a confidence level of 95% were calculated. The pipette calibration error is 2.40%. The obtained results are RSR_r = 1.38%, RSD_R = 13.21%, Recovery = 100.66%, laboratory equipment bias is 2.66%, bias from used chemicals is 0.17%, combined uncertainty is 5.08% and expanded measurement uncertainty is 10.17% by gravimetric determination of clay content, using the pipette method.

Keywords: soil composition, clay, method validation

1. Introduction

The mechanical (textural, granulometric) composition of the soil is a key parameter in the study of genesis, evolution, properties and systematics. In the processes of pedogenesis by the effect of physical, chemical, physico-chemical and biological decay and decomposition, mechanical elements (primary particles) are created from the parent substrate. Mechanical elements are elementary (primary) soil particles of different sizes that are under the influence of mild force (under a finger or a jet of water) and cannot be divided or crushed. The percentage of the representation of mechanical elements of different dimensions is called the mechanical composition of soil. From an agronomic point of view, the best soils have a ratio of sand-clay powder fractions of 35%-40%, 35%-40% and 20%-30%. In the processes of connecting primary particles - mechanical elements (sand, powder and clay) create larger secondary particles – micro and macro structural aggregates.

The clay fraction is created by synthesis from the products of chemical decomposition of primary ones, as aluminosilicate or is inherited from the parent substrate, and it is colloidal in nature and has a huge specific surface with which all the essential properties of the soil are connected. With the increased content of the clay fraction, the share of capillary pores and the height of the capillary rise of water increase in the soil.

The mechanical composition has a great influence on other physical, water-physical, physical-mechanical, chemical, biological and ecological-production properties of soil. The water, air, heat and nutrition regime of the soil depend on the mechanical composition. The choice of mechanization for its cultivation depends on the mechanical composition of the soil and on the use of the land.

The clay content contributes significantly to the compaction of the soil, for this reason it is very important to determine as accurately as possible the proportion of clay in the mechanical composition of the soil. Different methods are used to determine the mechanical composition of the soil: fractionation using a series of sieves (for the skeleton and larger fractions) and the pipette method (sedimentation in still water). Large fractions are removed with a set of sieves, while the clay content is determined by dispersion and pipetting.

2. Instructions

Air-dried soil or soil dried in a dryer at 105°C is divided into smaller portions using a Johnson divider, homogenized, and sieved through an ISO sieve with a diameter of 2 mm. Depending on the clay content, 10-30g of soil sample is weighed. The measured mass of the sample is transferred to a vessel with a volume of 500 ml, moistened with 20ml of water, and 30% H₂O₂ is added in portions to remove organic matter. After the reaction is complete, 0.1M HCl is added to remove carbonate interference. After the reaction is finished, add water up to a volume of 500ml and 1-2 drops of aluminum sulfate (may or may not). The next day, the clear part above the solid phase is pumped out with a vacuum system and 25 ml of dispersant and 225 ml of water are added over the solid phase. The suspension is brought to a boil and allowed to boil for 5 minutes and cooled at room temperature. Place a set of sieves with openings of 2 mm, 0.63 mm, 0.063 mm and sift the sand fractions by wet sieving, while collecting the suspension in the sedimentation vessel, taking care that the total volume does not exceed 500 ml. When the 500ml beaker, i.e. the sedimentation vessel, is filled up to the line, stir the suspension. Keep the sedimentation vessel in the middle with a constant temperature and monitor the dependence of the particle size on the temperature so that it is known at what time fractions of dust and clay are pipetted at a depth of 10 cm. After a certain time, the pipetted aliquots are quantitatively transferred into fixed Al containers, and the composition is evaporated to a smaller volume and dried in an oven at 105°C to a constant mass. The working temperature was 25°C where the clay pipetting was done after 6 hours 52 minutes and 37 seconds.

Precision in terms of repeatability and reproducibility is also expressed through the relative standard deviation (RSD, %). The calculation of the combined measurement uncertainty (U_c) includes the contribution from the impurity of chemicals, the error of measuring devices and laboratory equipment, RSD_r , RSD_R , Recovery ie bias according to equation (1) [2-6]:

$$U_c (\%) = \sqrt{(U_{\text{impurity}}^2 + \text{bias}^2 + RSD_r^2 + RSD_R^2 + U_{\text{sampling}}^2)} \quad (1)$$

The summarized results are given in Table 1.

Table 1. Evaluation of obtained validation results

Validation parameter	Experimental results [%]	ISO 11277:2020 Annex C, Table C.1 and AOAC [1, 2] [%]
RSD _r	1.38	5.23
RSD _R	13.21	25.93
Recovery	100.66	98-102
U impurity	0.17	/
bias	2.66	/
U _c	5.08	/
U	10.17	/

3. Conclusions

Based on the obtained validation results of the method, it can be concluded that this procedure satisfies the given criteria for validation in determining the clay content by the gravimetric method with sedimentation. The obtained validation parameters meet the criteria according to the AOAC specifications for accuracy, repeatability and reproducibility.

Acknowledgment

The authors are grateful for the help and support of Miphem d.o.o. laboratory Belgrade and the Ministry of Science. The authors are grateful to the Ministry of Science, Technological Development and Innovation of the Republic of Serbia for contract No. 451-03-47/2023-01/200052.

References

- [1] ISO 11277 (2020). Soil quality — Determination of particle size distribution in mineral soil material — Method by sieving and sedimentation.

- [2] AOAC (2016). Association of Official Agricultural Chemists, Appendix F: Guidelines for Standard Method Performance Requirements.
- [3] Eurachem (2019). Measurement uncertainty arising from sampling: A guide to methods and approaches, second edition.
- [4] Association of Chemical Engineers of Serbia (2021). Seminar SHI, Validation of methods in laboratory practice (in Serbian: Savez hemijskih inženjera Srbije, Seminar SHI (2021), Validacija metoda u laboratorijskoj praksi).
- [5] Association of Chemical Engineers of Serbia (2021). Seminar SHI, Assessment of measurement uncertainty of routine analytical methods (in Serbian: Savez hemijskih inženjera Srbije, Seminar SHI (2021), Procena merne nesigurnosti rutinskih analitičkih metoda).
- [6] International standard ISO/IEC 17025 (2017). General requirements for the competence of testing and calibration laboratories.

Pyrazole/tacrine derivatives as potential cholinesterase inhibitors

Mihajlo J. Krunic¹, Jelena Z. Penjisevic¹, Slađana Kostić-Rajačić¹, Vladimir B. Šukalović¹, Deana B. Andrić², Ivana I. Jevtić^{1*}

¹ University of Belgrade/Institute of Chemistry, Technology and Metallurgy/Department of Chemistry, Belgrade, Republic of Serbia (Njegoševa 12, 11000 Belgrade)

e-mail: jelena.penjisevic@ihm.bg.ac.rs, ivana.jevtic@ihm.bg.ac.rs,
vladimir.sukalovic@ihm.bg.ac.rs, sladjana.kostic@ihm.bg.ac.rs

² University of Belgrade/Faculty of Chemistry, Belgrade, Republic of Serbia (Studentski trg 12-16, 11158, Belgrade). e-mail: deanad@chem.bg.ac.rs

* Corresponding author

DOI: 10.46793/ICCB23.567K

Abstract: Two new tacrine/pyrazole conjugates were designed, synthesized, and pharmacologically evaluated for their inhibitory activity toward acetylcholinesterase (AChE) and butyrylcholinesterase (BuChE). A scalable and cost-efficient synthetic route was developed, and key reaction steps for the synthesis of compounds **4a,b** were nucleophilic substitution of α -aroylketene dithioacetals with tacrine intermediates, followed by cyclocondensation of respective *N,S*-acetals with hydrazine hydrate. The preliminary pharmacological evaluation revealed high inhibitory activities of **4a,b** toward AChE (180 and 259 nM, respectively) and BuChE (51 and 95 nM, respectively) as compared with known inhibitor, tacrine. Overall, both compounds were more efficient BuChE inhibitors while **4a**, with a shorter linker connecting tacrine and phenylpyrazole moieties, showed higher inhibitory activity toward both enzymes. Molecular docking analysis strongly corroborated pharmacological results since both compounds interacted favorably with target enzymes. Calculated pharmacokinetic properties (absorption, distribution, metabolism, and excretion (ADME) showed that **4a,b** obey Lipinski's rule of druglikeness and are promising lead compounds for the development of new drug candidates.

Keywords: Alzheimer's disease, acetylcholinesterase, butyrylcholinesterase, tacrine, pyrazol

1. Introduction

Alzheimer's disease (AD) is a severe, neurodegenerative disease characterized by a progressive loss of cognitive and behavioral functions leading to a fatal outcome. According to the World Health Organisation (WHO), around 55 million people have dementia, with AD contributing to 60-70% of cases. Most of these occur in low-income countries.[1]

Tremendous efforts have been made so far in the discovery of AD mechanisms, nonetheless, the cholinergic hypothesis is still one of the most researched topics. The

decreased level of acetylcholine (ACh) in the central nervous system (CNS) is one of the most recognizable signs of AD, and it is related to cognitive impairment and loss of memory in AD affected people.[2] Acetylcholinesterase (AChE) is the main esterase responsible for cholinergic regulation in the CNS. Butyrylcholinesterase (BuChE) is a non-specific cholinesterase, that was found to contribute to ACh breakdown, especially in the advanced stages of AD, when the activity of AChE is diminished. Three of five currently available AD therapeutics are reversible cholinesterase inhibitors (ChEIs).

Tacrine (Cognex®) was the first ChEI approved for AD treatment. However, due to significant hepatotoxicity, it was withdrawn from the market in 2013. Nevertheless, tacrine is used as a pharmacophore in many multi-target derivatives due to the ease of structural manipulation of the tacrine core. More importantly, tacrine core usually ensures high ChE inhibitory activity of derivatives, devoid of toxic side effects. [3]

As a part of ongoing research, we used computer-aided drug design and literature data to design new potential ChEIs, with tacrine core as a pharmacophore. This approach yielded two new lead compounds, **4a** and **4b**, which were synthesized and pharmacologically evaluated.

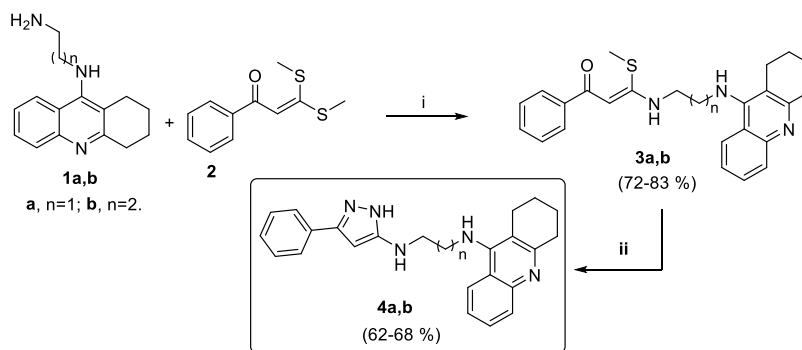
2. Results and discussion

2.1 Chemistry

The efficient and scalable synthesis of new tacrine-pyrazole derivatives **4a** and **4b** was accomplished, starting from readily available precursors (Scheme 1). The diamino tacrine derivatives **1a,b** were prepared by S_NAr of 9-chloro-1,2,3,4-tetrahydroacridine with terminal diamines, while acetophenone condensation with CS₂ afforded α -aroylketene dithioacetals **2**. [4] *N*-substitution of α -aroylketene dithioacetals with diamines **1a,b**, followed by cyclocondensation of the respective *N,S*-acetals **3a,b** with hydrazine, [5] provided final compounds **4a,b** in high overall yields. All compounds were fully spectroscopically characterized.

2.2 ChE inhibitory activity

Preliminary *in vitro* evaluation of the ChE inhibitory activity of compounds **4a,b** was performed according to the modified Ellman method [6] and the results are presented in Table 1. Both compounds showed high inhibitory activity toward AChE and BuChE compared to tacrine and were more efficient toward BuChE, manifesting the influence of the tacrine pharmacophore. The number of methylene groups in alkyl linker between tacrine and phenylpyrazole had some impact since compound **4a** with a shorter linker was more efficient ChEI.



Scheme 1. Reagents and conditions: i) PhMe, reflux, 37-41 h; ii) $N_2H_4 \cdot H_2O$, EtOH, reflux, 24-50 h.

Table 1. Calculated pharmacokinetic properties and experimental IC_{50} values of compounds **4a,b**

Cmpd.	MW	Calculated pharmacokinetic properties						IC_{50} (nM \pm SD)	
		#HBA	#HBD	TPSA	Log P	GI absorption	BBB permeant	eeAChE	eqBuChE
4a	383.49	2	3	65.63	4.3	High	Yes	180 \pm 4	51 \pm 3
4b	397.52	2	3	65.63	4.59	High	Yes	259 \pm 5	95 \pm 2
tacrine	198.26	1	1	38.91	2.59	High	Yes	114 \pm 2	59 \pm 3

2.3 Molecular docking

Schrodinger Maestro software induced fit docking procedure was carried out using standard protocol and flexible ligand/flexible bind site and revealed that both compounds bind well with the target enzymes, interacting with key residues for AChE (TRP86, TRP286, GLU202, ASP74, TYR72, TYR124) and BuChE (TRP82, TRP231, PHE329, ASP70, GLU197, HIS438). Bind mode and calculated binding energies of **4a,b** were comparable to tacrine (Figure 1). Docking results were strongly corroborated by experimentally obtained inhibitory activities. ADME calculations were performed using SwissADME, web-based predication tool, (Table 1) showed that **4a,b** obey Lipinski's rule of druglikeness and are promising lead compounds for the development of new drug candidates.

3. Conclusions

Two new tacrine/pyrazole conjugates were designed, synthesized and pharmacologically evaluated for their inhibitory activity toward AChE and BuChE. The key reaction steps for the synthesis of compounds **4a,b** were nucleophilic substitution of α -aroylketene dithioacetals with tacrine intermediates, followed by cyclocondensation of respective *N,S*-acetals with hydrazine hydrate. The preliminary pharmacological evaluation revealed high inhibitory activities of **4a,b** toward AChE and BuChE compared with a known inhibitor, tacrine. Molecular docking analysis strongly corroborated pharmacological results since both compounds interacted favorably with target enzymes. ADME prediction revealed agreeable druglike properties of **4a,b**

The influence of the methanol extract of *Galium verum* on cardiac oxidative damage in hypertensive rats in a model of global ischemia

Anica M. Petrovic^{1,2*}, Jovana V. Bradic^{1,2}, Vladimir Lj. Jakovljevic^{2,3,4}

¹University of Kragujevac, Faculty of Medical Sciences, Department of Pharmacy, Kragujevac, Serbia; e-mail: jovanabradickg@gmail.com, petkovicanica0@gmail.com

²Center of Excellence for Redox Balance Research in Cardiovascular and Metabolic Disorders, Kragujevac, Serbia; e-mail: jovanabradickg@gmail.com, petkovicanica0@gmail.com, drvladakgbg@yahoo.com

³University of Kragujevac, Faculty of Medical Sciences, Department of Physiology, Kragujevac, Serbia; e-mail: drvladakgbg@yahoo.com

⁴First Moscow State Medical University, I.M. Sechenov, Department of Human Pathology, Moscow, Russia; e-mail: drvladakgbg@yahoo.com

* Corresponding author

DOI: 10.46793/ICCB23.571P

Abstract: *Galium verum* (*G. verum*, Lady's bedstraw) is a perennial herbaceous plant that has been used for centuries as a sedative, an anticancer agent, in the treatment of gout, epilepsy, as antioxidant. Previous studies confirmed cardioprotective properties of this plant species extract in animal models of heart dysfunction, however, the impact of *G. verum* consumption on cardiac redox state in a condition of global ischemia has not been fully clarified. Therefore, our goal was to examine the effect of *G. verum* methanol extract on cardiac redox state in spontaneously hypertensive rats in the model of global ischemia. The study involved 20 Wistar kyoto spontaneously hypertensive rats, divided into a control (CTRL) and an experimental group (GVE). CTRL group included untreated rats, while the GVE group included rats that received 100 mg/kg of the methanol extract of *G. verum* for 14 days. After the treatment protocol, animals were sacrificed, and the hearts of all rats were isolated and subjected to 20-minute ischemia followed by a 30-minute reperfusion period. After accomplishment of the experimental protocol (*ex vivo* ischemia-reperfusion injury), heart tissue samples were used to determine the markers of cardiac oxidative stress such as superoxide dismutase (SOD), catalase (CAT), reduced glutathione (GSH) and index of lipid peroxidation (TBARS). The results have shown that methanol extract of *G. verum* increased the level of GSH and the activity of SOD and CAT in the experimental group, while reduced TBARS levels compared to the CTRL group. It might be concluded that treatment with *G. verum* extract can attenuate oxidative damage resulting from ischemia-reperfusion injury in the hearts of spontaneously hypertensive rats.

Keywords: *Galium verum*, cardiac ischemia-reperfusion injury, oxidative stress, rats

1. Introduction

Galium verum (*G. verum*, Lady's bedstraw) is a perennial herbaceous plant that has been used for centuries as a sedative, an anticancer agent, in the treatment of gout, epilepsy, as antioxidant. Previous studies confirmed cardioprotective properties of this plant species extract in animal models of heart dysfunction. The two most important groups of biomolecules found in the extract of *G. verum* which are responsible for antioxidant activity include phenolic acids and flavonoids. The beneficial effect of *G. verum* extract on the heart is reflected in the ability of this plant to prevent structural damage of the heart after ischemia, to reduce coronary circulation disorders, and to preserve the contractility and systolic and diastolic function of the heart. However, the impact of *G. verum* consumption on cardiac redox state in a condition of global ischemia has not been fully clarified [1, 2]. Therefore, our goal was to examine the effect of *G. verum* methanol extract on cardiac redox state in spontaneously hypertensive rats in the model of global ischemia.

2. Material and methods

This investigation was carried out in the Center for Preclinical and Functional investigations, Faculty of Medical Sciences, University of Kragujevac, Serbia. The study design was approved by the Ethical Committee for the welfare of experimental animals of the Faculty of Medical Sciences. All experiments were performed according to the EU Directive for the welfare of laboratory animals (86/609/EEC) and principles of Good Laboratory Practice (GLP).

2.1 Plant material and extract preparation

The methanol extract of *G. verum* was prepared by extracting the aerial parts of the plant with methanol as solvent by heat reflux extraction method. The dry extract was obtained by evaporation under reduced pressure. Before administration to animals, dry extract was *ex tempore* dissolved in the tap water [1].

2.2 Animal treatment

This study involved 20 spontaneously hypertensive Wistar kyoto rats randomly divided into two groups: CTRL group - control untreated rats and GVE group - rats that received *G. verum* methanol extract for two weeks once daily per os (100 mg/kg). After the accomplishment of two-week treatment, animals were sacrificed, and hearts were isolated and perfused retrogradely on Langendorff apparatus. After achieving stable rhythm, hearts were subjected to 20-minute ischemia (induced by blockage of coronary flow) and 30-minute reperfusion. At the end of *ex vivo* ischemia-reperfusion injury, hearts were collected for spectrophotometric determination of cardiac oxidative stress markers: index of lipid peroxidation, measured as thiobarbituric acid-reactive substances (TBARS), reduced glutathione (GSH), catalase (CAT) and superoxide dismutase (SOD) [3].

3. Results and Discussion

Rats treated with a methanol extract of *G. verum* had significantly lower levels of TBARS compared to the control group. Additionally, the activity of SOD and CAT as well as the level of GSH were markedly increased in rats that received GVE for two weeks (Table 1).

Table 1. The effects of GVE on oxidative stress markers in heart tissue samples

Group	SOD (U/g tissue)	CAT (U/g tissue)	GSH (nmol/g tissue)	TBARS (μ mol/g tissue)
CTRL	12.2 \pm 1,1	13.01 \pm 2.2	76121 \pm 234	2.15 \pm 0.05
GVE	16,3 \pm 0.9*	18.5 \pm 1.6*	96443 \pm 170	1.83 \pm 0.12*

p<0.05 statistical significance at the level p<0.05 compared to CTRL group.

Hypertension, as one of the most important risk factors for cardiovascular diseases, can worsen the ischemia-reperfusion outcome by leading to a significant mechanical load and stress of the myocardium. Oxidative stress is recognized as one of the significant factors that contributes to ischemia-reperfusion damage of the myocardium [4]. Exposure of the isolated heart to ischemia-reperfusion causes increased generation of all cardiac prooxidants. The main source is the mitochondrial respiratory chain and the activation of xanthine oxidase, which results in increased production of reactive oxygen species such as O_2^- and H_2O_2 . Previous research revealed that *G. verum* has the potential to preserve the structure and function of the heart in conditions of ischemia. Additionally, *G. verum* extract may prevent ischemia-induced lipid peroxidation by ensuring adequate cell membrane integrity [1, 2]. In this research, all investigated parameters of antioxidant protection were increased in the group treated with *G. verum* extract compared to the control group. Polyphenols have been recognized as the main constituents of *G. verum* extract responsible for the increase in SOD and CAT, which activate endogenous antioxidant mechanisms, reducing tissue damage caused by oxidative stress [1]. The current results are in line with the previous investigation that revealed the antioxidant capacity of *G. verum* extract in terms of alleviation of cardiac redox damage after 4-week treatment. The current findings indicate that a two-week consumption of *G. verum* methanol extract was sufficient to achieve protective effects on redox signaling in heart tissue. Alleviation of cardiac oxidative damage can contribute to functional recovery of the heart exposed to ischemia [5].

4. Conclusions

It can be concluded that treatment with *G. verum* extract can alleviate oxidative damage that occurs as a result of cardiac ischemia-reperfusion injury in spontaneously hypertensive rats via promotion of antioxidant defense capacity. Further studies are required in order to reveal the role of this extract as a potential antioxidant dietary supplement in various oxidative stress-related pathologies.

Acknowledgment

This research was funded by the University of Kragujevac—Faculty of Medical Sciences No. 451-03-47/2023-01/200111.

References

- [1] J. Bradic, V. Zivkovic, I. Srejovic, V. Jakovljevic, A. Petkovic, T. Nikolic Turnic, et al., *Protective Effects of Galium verum L. Extract against Cardiac Ischemia/Reperfusion Injury in Spontaneously Hypertensive Rats*, *Oxid Med Cell Longev.*, 2019 (2019) 4235405.
- [2] J. Bradic, M. Andjic, J. Novakovic, A. Kocovic, M. Tomovic, A. Petrovic., et al. *Lady's Bedstraw as a Powerful Antioxidant for Attenuation of Doxorubicin-Induced Cardiotoxicity*, *Antioxidants (Basel)*, 12 (2023) 1277.
- [3] A. Milevic, M. Simic, M. Tomovic, M. Rankovic, V. Jakovljevic, J. Bradic. *The effects of methanol extract of Galium verum L on cardiac redox state in hypertensive rats*, *Braz. J. Pharm. Sci.*, 58 (2022) e191062
- [4] M. Xiang, Y. Lu, L. Xin, J. Gao, C. Shang, Z. Jiang, H. Lin, et al., *Role of Oxidative Stress in Reperfusion following Myocardial Ischemia and Its Treatments*. *Oxid Med Cell Longev.*, 2021 (2021) 6614009.
- [5] M. Rankovic, M. Krivokapic, J. Bradic, A. Petkovic, V. Zivkovic, J. Sretenovic, N., et al., *New Insight Into the Cardioprotective Effects of Allium ursinum L. Extract Against Myocardial Ischemia-Reperfusion Injury*, *Front Physiol*, 12 (2021) 690696

Can a three-week administration of methanol extract of wild garlic modulate systemic redox state in hypertensive rats?

Jovana V. Bradic^{1,2*}, Anica M. Petrovic^{1,2}, Vladimir Lj. Jakovljevic^{2,3,4}

¹University of Kragujevac, Faculty of Medical Sciences, Department of Pharmacy, Kragujevac, Serbia; e-mail: jovanabradickg@gmail.com, petkovicanica0@gmail.com

²Center of Excellence for Redox Balance Research in Cardiovascular and Metabolic Disorders, Kragujevac, Serbia; e-mail: jovanabradickg@gmail.com, petkovicanica0@gmail.com, drvladakbg@yahoo.com

³University of Kragujevac, Faculty of Medical Sciences, Department of Physiology, Kragujevac, Serbia; e-mail: drvladakbg@yahoo.com

⁴First Moscow State Medical University, I.M. Sechenov, Department of Human Pathology, Moscow, Russia; e-mail: drvladakbg@yahoo.com

* Corresponding author

DOI: 10.46793/ICCB23.575B

Abstract (150 - 450 words): Wild garlic (*Allium ursinum*) is a widespread perennial herbaceous plant that has wide therapeutic applications and it is used as well as food. Natural preparations based on wild garlic have been used for gastrointestinal tract disorders, as antioxidants, antihypertensive, hypolipidemic agents, etc. Nevertheless, the data related to the effects of chronic wild garlic extract consumption on systemic redox state in hypertensive animals is yet to be understood. Therefore, the main goal of this study was to examine the effects of a three-week application of ethanolic extract from wild garlic on oxidative stress markers in spontaneously hypertensive rats. This was an experimental study conducted in 20 spontaneously hypertensive Wistar Kyoto rats divided into two groups: CTRL group - control untreated rats and wild garlic group - rats treated for three weeks with wild garlic ethanol extract once daily per os (100 mg/kg). After the accomplishment of the treatment protocol, animals were sacrificed, and blood samples were taken for determination of the levels of pro-oxidants and the activity of antioxidant enzymes. Our results indicate that there was a significant reduction in almost all of the measured pro-oxidants and an increase in antioxidant enzyme activity in rats treated with wild garlic extract compared to untreated rats. Ethanolic extract from wild garlic showed promising antioxidant potential in hypertensive conditions, however, future studies are necessary in order to reveal the full therapeutic potential of this plant species in various cardiovascular disorders.

Keywords: wild garlic, oxidative stress, rats

1. Introduction

Wild garlic (*Allium ursinum* L, ramson, or bear garlic, belonging to Alliaceae family) has been widely used as a dietary supplement and food. This plant species has been

traditionally used due to protective effects on the cardiovascular system, mainly due to antioxidants, blood pressure lowering potential, ability to decrease cholesterol levels, etc. Sulfur and phenolic compounds are the main constituents of wild garlic that are responsible for the pharmacological effects [1, 2]. Despite the use of this plant species for centuries in the prevention and treatment of cardiovascular disorders, the influence of chronic consumption on markers of redox state in the presence of hypertension has not been fully clarified. Therefore, the aim of this study was to reveal the impact of three-week wild garlic ethanol extract intake on pro-oxidant and antioxidant parameters in hypertensive rats.

2. Material and methods

This investigation was conducted in the Center for Preclinical and Functional investigations, Faculty of Medical Sciences, University of Kragujevac, Serbia. The study protocol was approved by the Ethical Committee for the welfare of experimental animals of the Faculty of Medical Sciences, University of Kragujevac, Serbia. All experiments were performed according to EU Directive for the welfare of laboratory animals (86/609/EEC) and principles of Good Laboratory Practice (GLP).

2.1 Wild garlic ethanol extract preparation

The ethanol extract of wild garlic was prepared by extracting 100 g of plant leaves with 500 ml of ethanol by heat reflux extraction. The dry extract for animal treatment was obtained by evaporation under reduced pressure and was daily dissolved in the water immediately before application to animals [1].

2.2 Experimental design

The research included 20 spontaneously hypertensive Wistar kyoto rats randomly divided into two groups: CTRL group - control untreated rats and WG group - rats treated for three weeks with wild garlic ethanol extract once daily per os (100 mg/kg). After the accomplishment of the treatment protocol, animals were sacrificed, and blood samples were taken for determination of the level of pro-oxidants and the activity of antioxidant enzymes. Plasma samples and erythrocytes were separated via centrifugation of heparinized venous blood. The concentration of pro-oxidative markers such as the index of lipid peroxidation, measured as thiobarbituric acid-reactive substances (TBARS), nitrites (NO_2^-), superoxide anion radical (O_2^-), and hydrogen peroxide (H_2O_2) was determined spectrophotometrically in plasma samples. On the other hand, in the lysate samples, the activity of non-enzymatic antioxidants such as reduced glutathione (GSH) and the activity of the enzymes such as catalase (CAT) and superoxide dismutase (SOD) was determined [3].

3. Results and Discussion

The levels of most of the measured pro-oxidants such as O_2^- , H_2O_2 and TBARS were significantly decreased in rats treated with WG compared to untreated spontaneously hypertensive rats. On the other hand, the level of NO_2^- had similar values in both groups

(Table 1). Moreover, the activity of SOD and CAT as well as the level of GSH were significantly elevated in the WG group (Table 2).

Table 1. The impact of WG on the level of pro-oxidant markers in plasma samples

Group	O ₂ ⁻ (nmol/ml)	H ₂ O ₂ (nmol/ml)	NO ₂ ⁻ (nmol/ml)	TBARS (μmol/ml)
CTRL	1.6 ± 0.3	4.6 ± 0.2	3.6 ± 0.15	2.2 ± 0.14
WG	1.1 ± 0.12*	3.7 ± 0.17*	3.2 ± 0.1	1.5 4.6 ± 0.12*

p<0.05 statistical significance at the level p<0.05 compared to CTRL group.

Table 2. The impact of WG on the level of antioxidant markers in erythrocyte samples.

Group	SOD (U/g Hb × 10 ³)	CAT (U/g Hb × 10 ³)	GSH (nmol/ml red blood cells)
CTRL	10 ± 0.21	8.3 ± 0.14	86 100 ± 245
WG	14 ± 0.18*	12 ± 0.19*	114 245 ± 311*

p<0.05 statistical significance at the level p<0.05 compared to CTRL group.

It is believed that the antioxidant activity of *Allium* species is due to the presence of various sulfur-containing compounds, polyphenols, dietary fibers and various microelements [4]. Our previous research confirmed the presence of various polyphenols in WG extract such as kempferol 3-O-Glc, p-coumarin acid, ferulic acid, kaempferol and we might assume that the observed benefits in hypertensive rats in the current study are due to the presence of those biomolecules [5]. In brief, an increase in the activity of SOD which acts as the first line of cellular defense against oxidative injury is in accordance with the drop in O₂ level since SOD catalyzes the conversion of O₂⁻ to H₂O₂. Additionally, a reduction in H₂O₂ level may be explained by the higher activity of CAT [3]. Most of previously conducted research confirmed *in vitro* antioxidant activity of wild garlic, however *in vivo* studies are limited. Recently conducted research in our laboratory also showed the antioxidant potential of wild garlic extract in ischemia-reperfusion injury model in rats [1]. Taking into consideration that oxidative stress strongly contributes to the pathogenesis of hypertension, it might be concluded that wild garlic extract can provide a significant contribution to hypertension management due to its potential to regulate redox homeostasis in conditions of elevated blood pressure levels.

4. Conclusions

Three-week application of the ethanol extract of wild garlic led to an improvement in the redox state of hypertensive rats via reduction in the production of pro-oxidants and

enhancement in antioxidant defence system capacity. Promising antioxidant potential in our study can be a basis for future clinical research before implementation of this plant species extract as an adjuvant in hypertension management.

Acknowledgment

This research is funded by the University of Kragujevac—Faculty of Medical Sciences No. 451-03-47/2023-01/200111.

References

- [1] M. Rankovic, M. Krivokapic, J. Bradic, A. Petkovic, V. Zivkovic, J. Sretenovic, N., et al., *New Insight Into the Cardioprotective Effects of Allium ursinum L. Extract Against Myocardial Ischemia-Reperfusion Injury*, *Front Physiol*, 12 (2021) 690696
- [2] M. Bombicz, D. Priksz, B. Varga, R. Gesztelyi, A. Kertesz, P. Lengyel, et al., *Anti-atherogenic properties of allium ursinumliophylisate: impact on lipoprotein homeostasis and cardiac biomarkers in hypercholesterolemic rabbits*, *Int. J. Mol. Sci.*, 17(2016) 1284.
- [3] J. Bradic, V. Zivkovic, I. Srejovic, V. Jakovljevic, A. Petkovic, T. Nikolic Turnic, et al., *Protective Effects of Galium verum L. Extract against Cardiac Ischemia/Reperfusion Injury in Spontaneously Hypertensive Rats*, *Oxid Med Cell Longev.*, 2019 (2019) 4235405.
- [4] M. Krivokapic, J. Bradic, A. Petkovic, M. Popovic., *Phytochemical and Pharmacological Properties of Allium Ursinum*, *Serbian Journal of Experimental and Clinical Research*, 22 (2021) 357-362.
- [5] M. Krivokapic, V. Jakovljevic, M. Sovrljic, J. Bradic, A. Petkovic, I. Radojevic., *Biological activities of different extracts from Allium ursinum leaves*, *Acta Poloniae Pharmaceutica ñ Drug Research*, 77 (2020) 121-129.

**Chemoinformatics, chemogenomics
and molecular design**

High-throughput screening of novel hydrogen storage materials – ML approach

K.Batalović^{1*}, J.Radaković¹, B.Paskaš Mamula¹, M.Medić Ilić¹, B.Kuzmanović¹

¹ University of Belgrade, VINCA Institute of Nuclear Sciences – National institute of the Republic of Serbia, Department of Nuclear and Plasma Physics, CONVINCE - Center of Excellence for Hydrogen and Renewable Energy, Mike Petrovića Alasa 12-14, Belgrade, Serbia; e-mail: kciric@vin.bg.ac.rs

* *Corresponding author*

DOI: 10.46793/ICCB23.580B

Abstract: Hydride formation in metals is a widely studied and applied phenomenon necessary to transition to clean energy solutions and various technological applications. We focus on three perspective applications of these materials, namely near-ambient hydrogen storage, hydrogen storage compressor materials, and alkali metal conversion electrodes, to demonstrate acceleration in the research achieved by utilizing a data-driven approach. Graph neural network was developed using a transfer learning approach from the MEGNet model and data related to the thermodynamics of hydride formation obtained in experimental work. Based on the crystal structure and composition as input features, we apply the MetalHydrideEnth model developed in our previous work to predict hydride formation enthalpy in intermetallic compounds. In this work, we focus on demonstrating how this approach, combined with available crystal information obtained from density functional theory calculations, can be applied for fast and extensive searches of novel metal hydride materials, having in mind the above-listed applications.

Keywords: metal hydride, GNN, hydrogen storage, DFT, conversion-type anode

1. Introduction

The storage of hydrogen, a clean energy vector, is essential in adopting various renewable energy use cases. Storing hydrogen by chemical bounding in the metals is a widely studied and applied method that offers safe and efficient storage [1]. In addition, specific applications, including metal hydride-based compressors and alkali metal hydride electrodes, also depend on tuning the stability of metal hydrides [2]. Metal hydrides form reversibly during hydrogen sorption in the metal/intermetallic compound. The enthalpy change (expressed in kJ/molH₂) in the hydride formation reaction determines the metal hydride's applicability [1].

Data-driven science as the 4th paradigm in materials science [3] has led to the rapid development of materials informatics, and dedicated machine learning approaches for materials design [4]. Although several exciting machine learning models were developed to predict the capacity and thermodynamical features of the metal hydride

materials, in this work, we focus on the model based on the graph neural network implementation for the crystal materials, MEGNet, which demonstrated low prediction errors in a broad array of properties in both molecules and crystals, enabling hydride formation energy prediction with DFT accuracy [5]. Using a transfer learning approach and a combination of DFT crystal structures and experimentally measured enthalpies of hydride formation, the MetalHydrideEnth [6] model was developed in our recent work [7]. We perform a large-scale screen of a Materials Project database [8] for possible metal alloy compositions, predict the enthalpy of hydride formation, and discuss the findings considering these materials' applications.

2. Methodology

Elemental embeddings are adopted from the mp-2019.4.1 model [15] (trained on a data set containing 133,420 data from the Materials Project (MP) [8]). The model comprises 2 MEGNet blocks (each with two dense layers with 12 and 8 nodes per attribute) trained on the dataset containing experimental heats of forming various metal hydrides paired with the composition and crystal structure of the corresponding metal/intermetallic compound [7]. In particular, the structural features and chemical composition of metal/intermetallic compounds are transformed into an index-type graph and used to predict the heat of hydride formation. The model showed an MAE of 9.1 kJ/molH₂ for predicting hydride formation enthalpy of arbitrary intermetallics [7]. We used the Materials Project database [8] to provide the composition and crystal structure of the metal/intermetallic compound; the database was queried using pymatgen API [9].

3. Results

3.1 Near ambient hydrogen storage and conversion type anodes for Li-ion batteries

For hydrides to reach an equilibrium pressure of 1 bar at 300K, classifying them as suitable for near-ambient hydrogen storage, an enthalpy change of -39.2kJ/molH₂ in the hydride formation reaction is required [1]. In addition, high stability of the material and friendly use are desired to maintain multiple sorption cycles. A low intermetallic mass is a starting point for obtaining a high gravimetric density of stored hydrogen. The highest stability of the proposed intermetallics was requested by limiting the search to intermetallics having formation energy per atom at the convex hull of thermodynamics. The second condition is met by adopting restrictions in terms of compositions: we excluded alloys containing exotic, radioactive, or highly toxic elements, and for these applications, we focus on the Mg-containing intermetallics. This narrowed the metal alloy compositions from over 19000 intermetallics containing Mg to 433 stable intermetallics satisfying the above conditions. Fig.1 displays the predicted enthalpy of hydride formation in these intermetallics as a function of the stability of the alloy itself. Thirty-two potential candidates [10] are identified as suitable for near ambient storage (fig.1., orange shaded). At the same time, the stability of corresponding metal alloys,

shown as formation energy per atom of the alloy, is found in the range -0.8eV to 0eV.

We examine the same batch of materials for conversion-type anode materials in Li-ion batteries. MgH₂ conversion electrodes improve capacity and density while alloying Mg improves durability and enables the selection of suitable working potentials.

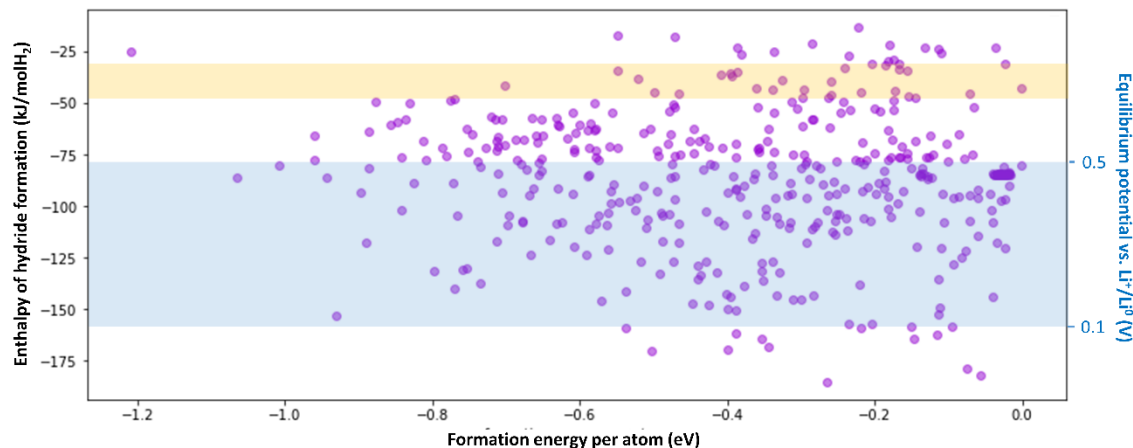


Figure 1. Fig.4. Predicted enthalpy of hydride formation and equilibrium potential vs. Li⁺/Li⁰ as a function of formation energy per atom in the intermetallic compound.

For negative electrodes in Li-ion batteries, the safe potential range is 0.1–0.5 V versus Li⁺/Li⁰. Potential vs. Li⁺/Li⁰ is calculated from the known changes in Gibbs free energy in the formation of LiH and metal hydride [11]. A wide range of potentials related to the Mg-containing intermetallics can be obtained (Fig. 1). Hydrides of the same or higher stability as compared to MgH₂ are needed, and a total of 244 potential candidates [10] are selected for this application (shaded blue, fig.1.).

3.2 Metal hydride compressor materials

An additional search is done for high-pressure hydrogen output materials. In particular, AB₂ intermetallics (A=Ti, Zr and B= Mn, Cr, Co) are assessed for utilization in metal compressors. To be used for this application, the lower stability of hydride is required as compared to storage materials. Table 1 lists predicted enthalpies of hydride formation in these materials, enabling the structural and compositional tuning of hydride stability.

Table 1. Predicted enthalpies of hydride formation for high-pressure hydrogen output materials

A=	ΔH (kJ/molH ₂)	
	Ti	Zr
ACr ₂	-19.9 <i>Laves phase</i>	-41.0 <i>Laves phase</i>
	-19 <i>cubic</i>	-39.4 <i>cubic</i>
AMnCr	-18.3	-35.3
ACo ₂	-15.8 <i>Laves phase</i>	-26.2 <i>cubic</i>
	-14.1 <i>cubic</i>	

3. Conclusions

We demonstrate the application of a dedicated machine learning model for fast screening of intermetallic compounds based on the stability of their hydrides. Based on the structural features and composition of intermetallic compounds we are able to predict their behavior in 3 various systems – near ambient hydrogen storage, high-pressure hydrogen output materials, and conversion-type electrodes in Li-ion batteries.

Acknowledgment

This research is funded by the Ministry of Education and Ministry of Science, Technological Development and Innovation, Republic of Serbia (contract number: 451-03-47/2023-01/200017).

References

- [1] V. Yartys, M. Zhu, *Recent advances in hydrogen storage materials*, *J. Alloys Compds.*, 927 (2022) 166892.
- [2] A. El Kharbachi, E. M. Dematteis, K. Shinzato, S. C. Stevenson, L. J. Bannenberg, M. Heere, C. Zlotea, P. Á. Szilágyi, J.-P. Bonnet, W. Grochala, D. H. Gregory, T. Ichikawa, M. Baricco, B. C. Hauback, *Metal Hydrides and Related Materials. Energy Carriers for Novel Hydrogen and Electrochemical Storage*, *J. Phys. Chem. C*, 124 (2020) 7599–7607.
- [3] G.R. Schleder, A.C.M.Padilha, C.M.Acosta, M.Costa, A.Fazzio, *From DFT to machine learning: recent approaches to materials science—a review*, *J. Phys.: Mater.*, 2 (2019) 032001.
- [4] C.Chen,Y.Zuo,W. Ye,X.Li,Z.Deng,S. Ping Ong, *A Critical Review of Machine Learning of Energy Materials*, *Adv. Energy Mater.*, 10 (2020) 1903242.
- [5] C. Chen, W. Ye, Y. Zuo, C. Zheng, S. Ping Ong, *Graph Networks as a Universal Machine Learning Framework for Molecules and Crystals*, *Chem. Mater*, 31 (2019) 3564–3572.
- [6] K. Batalović, J. Radaković, B. Kuzmanović, M. Medić Ilić, B. Paskaš Mamula, “*MetalHydrideEnth*”, *Mendeley Data*, V1 (2022), doi: 10.17632/4tpmdzxtf6.1.
- [7] K. Batalović, J. Radaković, B. Paskaš Mamula, B. Kuzmanović, M. Medić Ilić, *Predicting the Heat of Hydride Formation by Graph Neural Network - Exploring the Structure–Property Relation for Metal Hydrides*, *Adv. Theory Simul.*, 5 (2022) 2200293.
- [8] A. Jain, S.P. Ong, G. Hautier, W. Chen, W. Davidson Richards, S. Dacek, S. Cholia, D. Gunter, D. Skinner, G. Ceder, K. A. Persson, *Commentary: The Materials Project: A materials genome approach to accelerating materials innovation*, *APL Materials*, 1 (2013) 011002.
- [9] S. Ping Ong, W. D. Richards, A. Jain, G. Hautier, M. Kocher, S. Cholia, D. Gunter, V. Chevrier, K. A. Persson, G. Ceder, *Python Materials Genomics (pymatgen) : A Robust, Open-Source Python Library for Materials Analysis*, *Comput. Mater. Sci.*, 68 (2013) 314–319.
- [10] K. Batalović, J. Radaković, B. Paskaš Mamula, B. Kuzmanović, M. Medić Ilić, *Machine learning-based high-throughput screening of Mg-containing alloys for hydrogen storage and energy conversion applications*, *J. Energy Storage*, 68 (2023) 107720.
- [11] Y. Oumellal, A. Rougier, G. A. Nazri, J.-M. Tarascon, L. Aymard, *Metal hydrides for lithium-ion batteries*, *Nat. Mater.*, 7, 916-921, 2008.

3D-Quantitative Structure-Activity Relationship and design of novel Rho-associated protein kinases-1 (ROCK1) inhibitors

Milan Beljkas^{1*}, Jelena Rebić¹, Milica Radan², Teodora Đikić³, Slavica Oljačić¹, Katarina Nikolic¹

¹ University of Belgrade, Faculty of Pharmacy, Department of Pharmaceutical Chemistry, Serbia (Vojvode Stepe 450, Belgrade, 11000); e-mail: milan.beljkas@pharmacy.bg.ac.rs; jelena.rebic@yahoo.com; slavica.oljacic@pharmacy.bg.ac.rs; knikolic@pharmacy.bg.ac.rs

² Institute for Medicinal Plant Research Dr. Josif Pancic, Tadeusa Koscuska 1, Belgrade, 11000, Serbia e-mail: milica.r994@live.com

³ Laboratoire d'Innovation Thérapeutique, UMR7200, Université de Strasbourg, 74 route du Rhin, Illkirch Cedex, 67401, France e-mail: teodora.djik88@gmail.com

* Corresponding author

DOI: 10.46793/ICCB23.584B

Abstract: Rho-associated coiled-coil kinases (ROCKs) are involved in essential cellular functions such as adhesion, contraction, motility, proliferation, and cell survival/apoptosis. Four ROCK inhibitors have already been approved by the FDA and are used to treat glaucoma (riipasudil and netarsudil), cerebral vasospasm (fasudil), and graft-versus-host disease (belumosudil). Recent studies have focused on exploring the role of ROCK kinase inhibitors in cancer treatment and the development of new ROCK inhibitors. The main objective of this study was to identify critical structural features relevant to the inhibition of ROCK1 using a ligand-based 3D-QSAR (3D quantitative structure-activity relationship) method. The 3D-QSAR model for ROCK1 was created and validated using internal and external validation parameters (R^2 , Q^2 , R^2_{pred} , I_m^2 , r^2_m , $\overline{r_m^2}$ and Δr^2_m). The main structural features that correlate with the inhibition of ROCK1 were identified (e.g., heterocycle with hydrogen donor group like nitrogen atom) and further structural modifications of the ROCK1 inhibitors that contribute to increased activity were proposed (removal of the amino group of the oxadiazole, modification of the substituents of the phenyl ring).

Keywords: ROCK, cancer, 3D-QSAR, design

1. Introduction

Rho-associated protein kinases (ROCKs) belong to the serine-threonine protein kinases family which play an important role in the regulation of actin- and myosin-mediated processes such as cell motility, smooth muscle contraction, adhesion, and phagocytosis [1]. Physiologically, there are two isoforms of ROCK kinases, ROCK1 and ROCK2 [2]. Activation of ROCK leads to phosphorylation of myosin light chains, myosin phosphatase target subunit 1, LIM kinases, adducin and ERM proteins [3]. Besides cell motility, ROCK affects proliferation, differentiation, apoptosis, and oncogenic transmission of the cells. Disruption of ROCK kinase activity can lead to

various diseases [1-3]. For this reason, ROCK inhibitors are promising targets in the therapy of cancer, hypertension, cardiovascular and neurodegenerative diseases, smooth muscle contraction disorders, glaucoma or erectile dysfunction. To date, four ROCK inhibitors were approved by the FDA (fasudil, ripasudil, netarsudil and belumosudil) for the treatment of glaucoma, cerebral vasospasm and graft-versus-host disease [4]. The main objectives of this study were to 1) develop a 3D quantitative structure-activity relationship (3D-QSAR) model with good predictive power; 2) determine the key structural features that positively correlate with ROCK1 inhibition; 3) define the structural changes that lead to improvement in ROCK1 inhibitor activity (design of new ROCK1 inhibitors).

2. Materials and methods

The 3D-QSAR study included 48 ROCK1 inhibitors obtained from the ChEMBL database (<https://www.ebi.ac.uk/chembl/>) [5,6]. All compounds were divided into two clusters based on their structural similarity: pyridine derivatives (pKi: 5.563-8.167) and oxadiazole derivatives (pKi: 5.786-7.070). The Marvin Sketch program (Marvin Sketch v 16.10.24, 2016, www.chemaxon.com/) was used to determine the dominant forms for all tested compounds at a physiological pH of 7.4, while they were optimized with the semi-empirical PM3 method (Parameterized Model revision 3) using the Gaussian 098W software included in Chem3D Ultra7 (Chem3D Ultra v 7.0, 7.0, 2001, <http://www.cambridgesoft.com/>) [7].

The data set of 48 compounds was divided into a training set (34 ligands) and a test set (14 ligands) using Principal Component Analysis (PCA), taking into account that the entire range of pKi values is homogeneously distributed in both the training and test sets. Pentacle software 1.0.7 was used for the calculation of the alignment-independent three-dimensional molecular descriptors (GRIND) and the formation of the 3D-QSAR model [8,9]. The internal and external validation parameters were used to confirm the predictive power of the created 3D-QSAR model [10,11,12].

3. Results and discussion

The created 3D-QSAR model was used to identify structural features crucial for ROCK1 inhibition. The parameters of internal and external validation showed that the formed 3D-QSAR model was reliable and could be used to predict the activity of novel design compounds. The validation parameters for the training set of compounds, $Q^2=0.760$ and $R^2=0.920$, indicate good statistical reliability and internal predictability of the model [10,11]. In order to analyze the external predictability of the model, a test set of 14 compounds was used. The calculated values of R^2_{pred} (0.746), r_m^2 , $\overline{r_m^2}$ greater than 0.5, and Δr_m^2 less than 0.2 indicated the possibility of applying the created 3D-QSAR model for activity prediction of newly designed molecules. Moreover, the close values of Q^2 and R^2_{pred} , as well as RMSEE (0.227) and RMSEP (0.296), confirmed the good robustness and predictive power of the created model [11,12]. The main variables that positively or negatively affected the activity of the compounds are presented by Partial Least Square (PLS) coefficient plot (**Figure 1**).

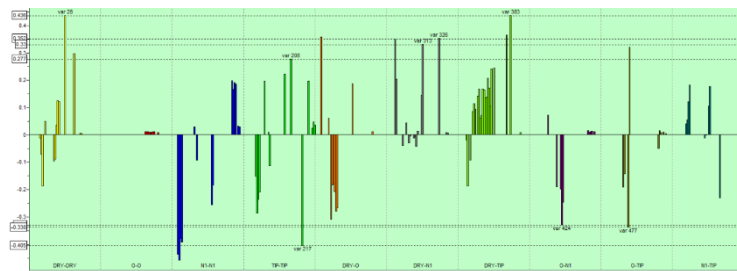


Figure 1. PLS coefficient plot for the 3D-QSAR (ROCK1) model. The most significant variables are labelled.

CHEMBL3581126 ($pK_i=8.100$) is one of the most active compounds belonging to the first cluster. It has all favourable variables that positively correlated with ROCK1 inhibition. The favourable var28 (DRY-DRY: 11.20-11.60 Å) is described between the hydrophobic regions around the pyridine and the 1,3-benzodioxole. The optimal distance between these two groups (pyridine and 1,3-benzodioxole) is also underlined by the favourable var208 (TIP-TIP: 14.80-15.20 Å). The importance of the hydrogen accepting group of pyridine (nitrogen atom) for ROCK1 inhibition is highlighted by the favourable var313 (DRY -N1: 11.20-11.60 Å) and var326 (DRY -N1: 16.40-16.80 Å). Favourable var208, var313 and var28 are also present in the least active molecule of the first cluster, **CHEMBL3581136** ($pK_i=5.600$), but in contrast to **CHEMBL3581126** they are weakly expressed. On the other hand, the unfavourable var424 (O-N1: 10.00 - 10.40 Å) showed the negative influence of the distance between the hydrogen accepting group of pyridine (nitrogen atom) and the hydrogen donating group (nitrogen atom of the amide) on ROCK1 inhibition. It is described for both the most active and the least active molecule of the first cluster. However, besides the unfavourable var424, the unfavourable var217 (TIP-TIP: 18.40-18.80 Å) is also observed in the least active molecule (**CHEMBL3581126**), highlighting the negative correlation of the distance between the steric spots around pyridine and the methoxy group of the phenyl ring on ROCK1 inhibition. This variable is found in all compounds that have a methoxy group as a substituent. The lower activity of the most active compound of the second cluster -**CHEMBL1080071** ($pK_i=7.070$) can be explained by the absence of the favourable var28 probably due to an insufficient distance between two hydrophobic regions of the molecule. Meanwhile, the favourable var313 was found, highlighting the importance of the nitrogen atom of the oxadiazole for the activity of ROCK1 inhibitors. Moreover, the unfavourable variable 424 (O-N1: 10.00-10.40 Å) correlates negatively with the ROCK1 inhibition and is observed between the hydrogen donating group (amino group of benzoimidazole) and hydrogen accepting group (nitrogen atom of 1,3,5-oxadiazole) of **CHEMBL1080071**. In one of the least active compounds of the second cluster, **CHEMBL1079208** ($pK_i=5.720$), the favourable variables are not described, while the presence of unfavourable var477 (O-TIP:8.40-8.80 Å) emphasizes the negative influence of the distance between hydrogen donor group (amino group at position C-3 of oxadiazole) and steric spot around the benzimidazole on ROCK1 inhibition.

4. Conclusion

Taking into account all the previous results, we can assume that:

- 1) the presence of a hydrogen accepting group of the heterocycle (nitrogen atom of pyridine or oxadiazole) is crucial for ROCK1 inhibition due to the positive impact of var313 and var326;
- 2) replacement of the methoxy group with other groups (e.g., electron-withdrawing groups) may correlate positively with ROCK1 inhibition due to the elimination of the influence of unfavourable var217;
- 3) the removal of the amino group of the oxadiazole may positively contribute to the activity of ROCK1 inhibitors by reducing the negative influence of var477
- 4) the optimal distance between two hydrophobic parts of molecules can be crucial for ROCK1 inhibition due to the influence of var28. Therefore, the length of the linker should be taken into account when designing new ROCK1 inhibitors.

In accordance with the previous conclusions, some novel ROCK1 inhibitors were. Designed. Their activities were predicted using created 3D-QSAR models and some of them showed good ROCK1 inhibitory activity, MBT1 (derivative of ChEMBL3581147, which has chloro group instead of methoxy group, predicted pKi=7.520) and MBT2 (derivative of ChEMBL1080071, whose amino group of oxadiazole was removed, predicted pKi=7.340). These compounds will be further synthesized and evaluated by enzyme and cancer cell assays.

Acknowledgments

This research was funded by the Ministry of Science, Technological Development and Innovation, Republic of Serbia through Grant Agreement with University of Belgrade-Faculty of Pharmacy No: 451-03-47/2023-01/200161.

References

- [1] Julian L, Olson M F (2014) Rho-associated coiled-coil containing kinases (ROCK): structure, regulation, and functions, *Small GTPases*, 5(2), e29846.
- [2] Amano M, Nakayama M, Kaibuchi K (2010) Rho-kinase/ROCK: A key regulator of the cytoskeleton and cell polarity. *Cytoskeleton*, 67(9), 545–554.
- [3] Hahmann C, Schroeter T (2009). Rho-kinase inhibitors as therapeutics: from pan inhibition to isoform selectivity. *Cellular and Molecular Life Sciences*, 67(2), 171–177
- [4] Barcelo, J., Samain, R., & Sanz-Moreno, V. (2023). Preclinical to clinical utility of ROCK inhibitors in cancer. *Trends in Cancer*
- [5] Bandarage U, Hare B, Parsons J, Pham L, Marhefka C, Bemis G, ... Green J (2009) 4-(Benzimidazol-2-yl)-1,2,5-oxadiazol-3-ylamine derivatives: Potent and selective p70S6 kinase inhibitors. *Bioorganic & Medicinal Chemistry Letters*, 19(17), 5191–5194
- [6] Green J, Cao J, Bandarage U K, Gao H, Court J, Marhefka C, ... Rodems S (2015) Design, Synthesis, and Structure–Activity Relationships of Pyridine-Based Rho Kinase (ROCK) Inhibitors. *Journal of Medicinal Chemistry*, 58(12), 5028–5037
- [7] Frisch, M. J. (1998). *Gaussian 98 (Revision A.7)*. Pittsburgh, PA: Gaussian, Inc.
- [8] Pastor M, Cruciani G, McLay I, Pickett S, Clementi S (2000) Grid-INdependent Descriptors (GRIND): A novel class of alignment-independent three-dimensional molecular descriptors. *Journal of Medicinal Chemistry*, 43(17), 3233–3243.

- [9] Pentacle, Version 1.0.6, Molecular Discovery Ltd., Perugia, Italy; 2009
- [10] Ojha P K, Roy K (2011) Comparative QSARs for antimalarial endochins: Importance of descriptor-thinning and noise reduction prior to feature selection. *Chemometrics and Intelligent Laboratory Systems.*, 109(2), 146–161
- [11] Tropsha, A. (2010). Best practices for QSAR model development, validation, and exploitation. *Molecular Informatics*, 29(6-7), 476–488
- [12] Roy P P, Roy K (2008) On some aspects of variable selection for partial least squares regression models. *QSAR & Combinatorial Science*, 27(3), 302–313.

Virtual Docking, design and *in silico* ADMET profiling of novel Rho-associated protein kinases-1 (ROCK1) inhibitors

Milan Beljkas^{1*}, Jelena Rebić¹, Milica Radan², Teodora Đikić³, Slavica Oljačić¹, Katarina Nikolić¹

¹ University of Belgrade, Faculty of Pharmacy, Department of Pharmaceutical Chemistry, Serbia (Vojvode Stepe 450, Belgrade, 11000) e-mail: milan.beljkas@pharmacy.bg.ac.rs; jelena.rebic@yahoo.com; slavica.oljadic@pharmacy.bg.ac.rs; knikolic@pharmacy.bg.ac.rs

² Institute for Medicinal Plant Research Dr. Josif Pancic, Tadeusa Kosciuska 1, Belgrade, 11000, Serbia e-mail: milica.r994@live.com

³ Laboratoire d'Innovation Thérapeutique, UMR7200, Université de Strasbourg, 74 route du Rhin, Illkirch Cedex, 67401, France e-mail: teodora.djik88@gmail.com

* Corresponding author

DOI: 10.46793/ICCBi23.589B

Abstract: Overexpression of Rho-associated protein kinases has been associated with various diseases, including tumors. None of the approved ROCK inhibitors are used for cancer treatment. However, some of them have been shown to have anti-tumor potential. The main objective of this study was to develop novel ROCK1 inhibitors using the structure-based method, molecular docking, and prediction of pharmacokinetic properties using the ADMET predictor. The key interactions that strongly correlate with the activity of ROCK1 inhibitors are hydrogen bonds between amino acid residues Met156, Glu154 and the hinge region of the inhibitors, indicating possible structural changes in the hinge region of studied compounds. On the other hand, the lack of interactions between 1,3-benzoxadiol moiety and the enzyme presents a promising approach for further structural modifications in order to design more effective ROCK1 inhibitors.

All the important interactions between the developed ROCK1 inhibitors and the binding site of the enzyme were established. They also showed acceptable pharmacokinetic properties and could be further used for synthesis and evaluation by various biological assays.

Keywords: molecular docking, ADME, design, ROCK1

1. Introduction

Rho-associated protein kinases (ROCKs) are serine-threonine kinases that have been strongly associated with the development and progression of various tumors by regulating the function of several downstream target proteins [1]. Overexpression of ROCKs leads to phosphorylation of myosin light chain, myosin phosphatase target subunit 1, LIM -kinases, ERM proteins, etc [1]. Altogether, it leads to tumorigenesis and increases the motility of cancer cells, which probably promotes the metastasis of various tumors [1]. Four ROCK inhibitors are already in clinical use (fasudil, ripasudil, netarsudil and belumosudil), but none of them is used for cancer treatment. However, some of them, such as fasudil, have shown great antitumor potential in several *in vitro* and *in vivo* studies [2]. The recent research has focused on the development of novel potent ROCK inhibitors with multitarget activity profile. The main objective of this

study was to design novel ROCK1 inhibitors using CADD (computer-aided drug design). Specifically, the structure-based method, molecular docking, and pharmacokinetic properties predicted by ADMET predictor were used to design novel ROCK1 inhibitors with stronger activity and improved pharmacokinetic properties.

2. Materials and methods

The molecular docking study was performed using GOLD 2022 software [3]. The crystal structure of ROCK1 (PDB: 4YVC) was obtained from the Protein Data Bank (PDB) (<https://www.rcsb.org/>). The ROCK1 inhibitors with their pIC₅₀ values were obtained from the ChEMBL database (<https://www.ebi.ac.uk/chembl/>). The dominant microspecies of all compounds at physiological pH were selected using the program Marvin Sketch Sketch 6.1.0 (Chem Axon 2013) [4] and geometrically optimized using the semi-empirical PM3 method [5]. Discovery Studio 2020 was used to visualize the key interactions between the enzyme and ROCK1 inhibitors [6]. Ligands were ranked based on their affinity for ROCK1 using the ChemPLP score function. The virtual docking procedure was validated for further prediction of novel design inhibitors by calculating the Root Mean Square Deviation (RMSD) values, which should be below 2Å. The RMSD value was calculated by comparing the poses of heteroatoms of the co-crystallized ligand with the re-docked ligand. The binding site was defined by default according to the position of the co-crystallized ligand and all atoms within 8.0 Å of the co-crystallized ligand were selected. The Physicochemical and pharmacokinetic properties of all studied compounds were calculated by ADMET Predictor 8.5.0. [7] and were compared to already known ROCK1 inhibitor – fasudil.

3. Results and discussion

According to their chemical structure, all studied compounds can be divided into two clusters: cluster I containing pyridine derivatives and cluster II which contains oxadiazole derivatives.

Figure 1 shows the key interactions between the ROCK1 and the most active compound (CHEMBL3581126, pKi=8.150), as well as the least active compound (CHEMBL3581136, pKi= 5.600) from the cluster I, while the main interactions between the ROCK1 and the most active (CHEMBL1080071, pKi=7.070) and the least active compound (CHEMBL1079208, pKi=5.720) of cluster II are shown in **Figure 2**.

Previous studies have shown the importance of hydrogen bonding between ROCK1 inhibitors and Met156 and Glu154 of the enzyme for optimal binding to the active site of ROCK1 [8]. In the most active compounds of the I cluster, including CHEMBL3581126 (**Figure 1**), hydrogen bond is established only between the nitrogen atom of the pyridine and Met156, while it is not observed in the least active molecule, CHEMBL3581136 (**Figure 1**), suggesting its importance for ROCK1 inhibition. Considering the cluster II, a hydrogen bond between the amino group (benzimidazole part of the molecule) and Glu154 is formed only in the most active molecule (CHEMBL1080071), while it is not described in the least active compounds, including CHEMBL1079208. In addition, the oxadiazole derivatives probably did not anchor adequately in the binding site of ROCK1

because the distance between the two heterocycles was not appropriate, as also shown by the 3D-QSAR study. Based on the results of previous studies, modification of this part of the molecule should be considered to increase the activity of ROCK1 inhibitors- e.g., replacement of the pyridine with other heterocycles such as pyrazole in order to establish hydrogen bonds with Met156 and Glu154.

Numerous Van der Waals interactions have been observed for both clusters between pyridine, thiazole, benzimidazole, oxadiazole and various amino-acid residues (Leu205, Val92, Met153, Ala215, Ala103), and some of them are already described in the literature as significant for anchoring in the active site of ROCK1 [10]. 1,3-benzodioxole did not form an important interaction with the binding site of the enzyme. Therefore, this part presents an opportunity for further structural modifications.

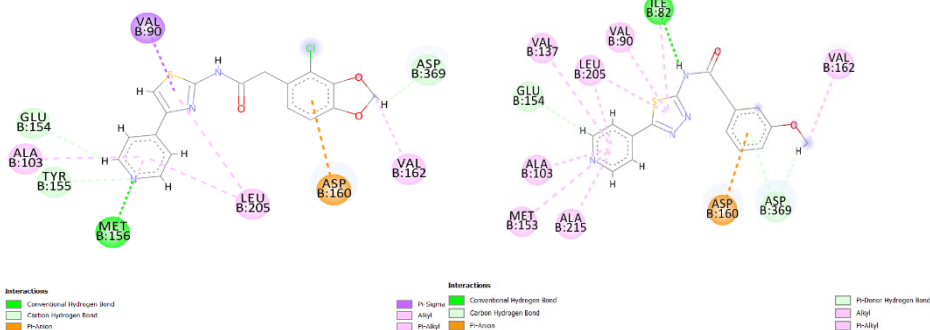


Figure 1. 2D diagram of the most important CHEMBL3581126 – ROCK1 interactions (left) and the most significant CHEMBL3581136 – ROCK1 interactions (right).

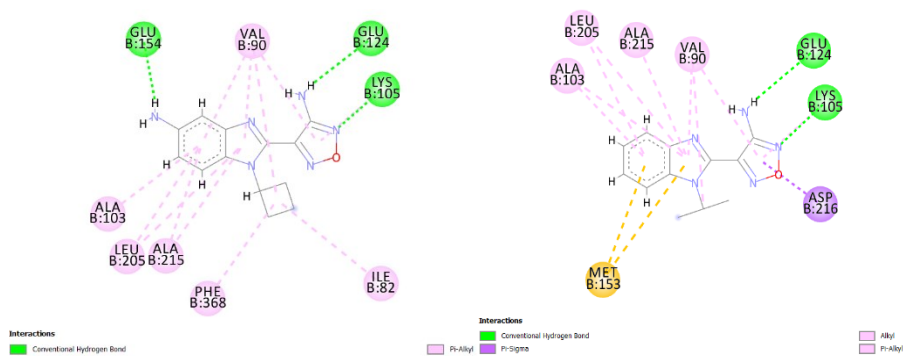


Figure 2. 2D diagram of the most important CHEMBL1080071 – ROCK1 interactions (left) and the most significant CHEMBL1079208– ROCK1 interactions (right).

The ChemPLP score values are mostly consistent with the activity of ROCK1 inhibitors in cluster I (e.g., CHEMBL3581126 – 65.35; CHEMBL3581136 – 60.09 – the lowest score), while there are some exceptions in cluster II.

Based on the results of the molecular docking study and the RMSD value obtained after redocking (0.293 Å) we can conclude that the docking procedure is valid and can be further used for the design of new ROCK1 inhibitors. The key interactions of the most active designed inhibitors according to the ChemPLP Score Values (**MB1** – ChemPLP Score Value 70.38; **MB2** - ChemPLP Score Value 69.23) are shown in **Fig.3**.

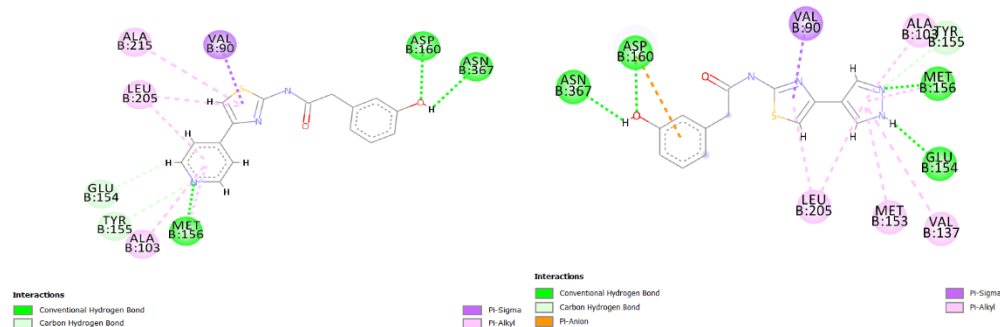


Figure 3. 2D diagram of the most important MB1 – ROCK1 interactions (left) and the most significant MB2 – ROCK1 interactions (right).

In terms of pharmacokinetic properties, designed compound MB1 (89%) is likely to cross the blood-brain barrier (BBB), which is comparable to fasudil (99%) and the most active compound from the dataset (ChEMBL3581126 - 94%), while MB2 has a low potential to cross the BBB (59%). Unlike Fasudil, ChEMBL3581126 and MB2, whose TOX risk is 1, MB1 has no TOX risk (TOX risk=0). Therefore, we can assume that MB1 will have a better safety profile.

4. Conclusion

A molecular docking study was performed, and based on the results of this study, a structural modification of the most active ROCK1 inhibitor (ChEMBL3581126) was proposed. A series of new ROCK1 inhibitors were developed, and MB1 and MB2 showed the best ChemPLP score values and pharmacokinetic properties. These compounds will be used for further synthesis and biological evaluation.

Acknowledgments

This research was funded by the Ministry of Science, Technological Development and Innovation, Republic of Serbia through Grant Agreement with University of Belgrade-Faculty of Pharmacy No: 451-03-47/2023-01/200161.

References

- [1] Wei, Lei, et al. "Novel insights into the roles of Rho kinase in cancer." *Archivum immunologiae et therapiae experimentalis* 64 (2016): 259-278.
- [2] Ying, Han, et al. "The Rho kinase inhibitor fasudil inhibits tumor progression in human and rat tumor models." *Molecular cancer therapeutics* 5.9 (2006): 2158-2164.
- [3] Jones, Gareth, et al. "Development and validation of a genetic algorithm for flexible docking." *Journal of molecular biology* 267.3 (1997): 727-748.
- [4] MarvinSketch 5.5.1.0. ChemAxon, Budapest, Hungary, 2011; software available at <https://www.chemaxon.com>
- [5] Stewart, James JP. "I. Method Ati 2/L5 Z 9" 0." *Journal of Computational Chemistry* 10.2 (1989): 209-220.
- [6] Discovery Studio Predictive Science Application | Dassault Systèmes BIOVIA <https://3dsbiovia.com/products/collaborative-science/biovia-discovery-studio/> (accessed Jun 25, 2023)
- [7] ADMET Predictor, v. 10.3, Simulations Plus Inc., Lancaster, CA, USA, <https://www.simulations-plus.com>
- [8] Shen, Mingyun, et al. "Discovery of novel ROCK1 inhibitors via integrated virtual screening strategy and bioassays." *Scientific reports* 5.1 (2015): 16749

A metric for pairwise similarity analysis of binary cheminformatics data

Izudin Redžepović^{1,*}

¹ State University of Novi Pazar, Vuka Karadžića 9, 36300 Novi Pazar, Serbia; e-mail: iredzepovic@np.ac.rs

* Corresponding author

DOI: 10.46793/ICCB23.593R

Abstract: This paper unveils the findings derived from an in-depth exploration of a novel similarity measure designed to assess pairwise resemblances. Called the Substructure Similarity Index, this measure centers around the comparison of substructures identified within compounds. Through a rigorous evaluation conducted on an extensive dataset of drugs and by juxtaposing it against other commonly employed indices, the study reveals that the Substructure Similarity Index can be adeptly employed for molecular similarity calculations since it provides information that cannot be obtained by available measures.

Keywords: molecular similarity, molecular structure, binary vectors, molecular fingerprints, similarity measure

1. Introduction

Countless chemical procedures have been developed to create molecules that resemble existing ones but exhibit specific, highlighted characteristics. However, the significance of molecular similarity extends beyond the realm of chemistry and finds implementation in diverse fields, including pharmaceuticals, materials design, agriculture, toxicology, and many more [1]. For example, computer-assisted retrosynthesis uses molecular similarity to assist in planning synthetic routes [2], while mass spectrometry-based annotation of natural product compound families relies on it to identify related compounds [3]. These uses underscore the wide-ranging scope and potential impact of molecular similarity across different disciplines.

At the heart of molecular similarity lies the principle that structural similarity leads to similar activity [4]. The significance of choosing different similarity metrics and their impact on the variability of similarity assessment results have been widely acknowledged [5]. In this work, we introduce a novel pairwise similarity measure for binary vectors in order to eradicate the shortcomings of existing measures. To evaluate its performance, we conducted a comparative statistical analysis.

2. Theory

In this part, we define Substructure Similarity Index (*SSI*) and discuss its basic properties. The *SSI* is defined as follows:

$$SSI = \frac{ax + by}{n + m} \quad (1)$$

whereas a and b are the length of the longest string of ones in the fingerprint A (i.e., the substructure of molecule A) and the length of the longest string of ones in the fingerprint B (i.e., the substructure of molecule B), respectively. The x and y denote how many times a and b occur, respectively. The n and m stand for the number of bits one in binary vectors A and B, respectively. From Eq. (1), it is obvious that *SSI* yields similar results in the [0,1]-range. Note that the *SSI* allows the comparison of vectors with different lengths. It is worth emphasizing that *SSI* compares only the biggest substructures of two molecules, preventing false similarity caused by small structural overlaps.

2.1 Molecular library and computational details

To investigate *SSI*, we have performed a comparative statistical analysis of our metric with other similarity indices. More precisely, for this purpose, Tanimoto (*T*), Jaccard (*Ja*), Gleason (*Gle*), Sokal-Sneath (*SS*), and Consonni-Todeschini (*CT*) indices have been employed. In this work, as a case study, we have used the FDA approved drugs available in DrugBank database V. 5.1.10, that consists out of 975 compounds. The Morgan circular fingerprint (1024 bits, radius=2) has been used to represent the chemical structure of each compound.

3. Results and Discussion

The statistical parameters corresponding to the similarity values computed using six distinct similarity measures are outlined in Table 1. Moreover, the visual representation of their distributions can be observed in Figure 1. The first five indices all exhibit a minimum value of zero, in contrast to the *SSI*, which demonstrates a value of 2.38%. This distinctive behavior of *SSI* underscores its superiority among the other measures. Specifically, this dataset comprises a variety of molecules that possess certain structural elements in common, including identical atoms and bonds, as a minimum. So, having zero similarity between some molecules is questionable. A visual representation of this concept is depicted in Figure 2, providing a clear illustrative example. Among all the indices, *CT* consistently yields the highest average values, while *SSI* displays the most pronounced data scattering. This observation regarding *SSI* aligns with the notable diversity present within the compound set.

Table 1. Statistical parameters for the similarity indices: minimal (min), maximal (max), and the mean value (all in %), and the s denotes standard deviation.

Measure	min	max	mean	s
<i>T</i>	0	100	10.37	5.17
<i>Ja</i>	0	100	24.95	9.75

<i>Gle</i>	0	100	18.43	7.94
<i>SS</i>	0	100	5.55	3.17
<i>CT</i>	0	100	47.65	11.59
<i>SSI</i>	2.38	100	32.62	28.63

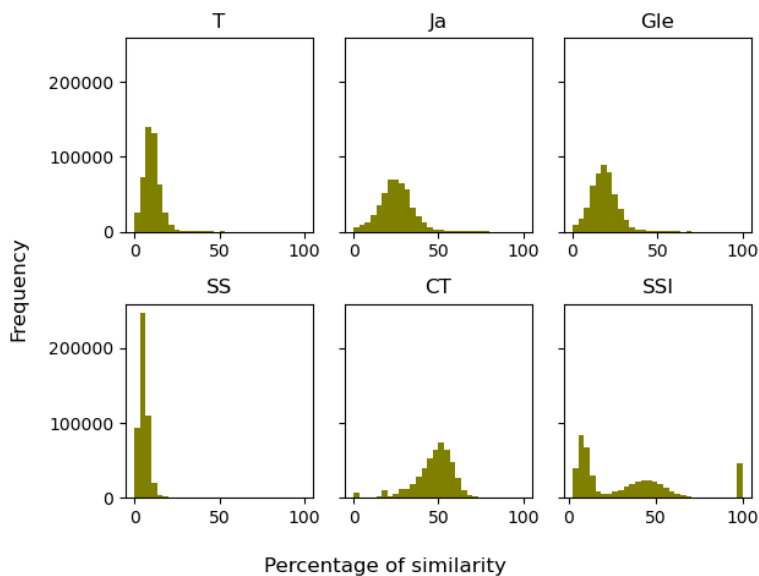


Figure 1. Distribution of 474 825 similarity values calculated by six different similarity measures.

To explore the correlation between *SSI* and other indices, we have computed the Pearson correlation coefficients between the similarity measures. The outcomes of these calculations are showcased in Table 2. As one may see, it is evident that *SSI* shows negligible correlation with other indices. This observation substantiates the rationale behind introducing *SSI*, as it has the potential to offer insights into molecular similarity that existing measures cannot capture.

Table 2. The absolute values of the correlation coefficient between similarity indices.

	<i>T</i>	<i>Ja</i>	<i>Gle</i>	<i>SS</i>	<i>CT</i>	<i>SSI</i>
<i>T</i>	1					
<i>Ja</i>	0.9762	1				
<i>Gle</i>	0.9901	0.9968	1			
<i>SS</i>	0.9880	0.9344	0.9579	1		
<i>CT</i>	0.8643	0.9305	0.9088	0.8082	1	
<i>SSI</i>	0.0455	0.0604	0.0540	0.0397	0.1927	1

The comprehensive findings presented in this study collectively affirm the efficacy of employing *SSI* for molecular similarity calculations. Notably, its definition suggests that *SSI* holds promising potential for successful utilization in substructure searching applications.

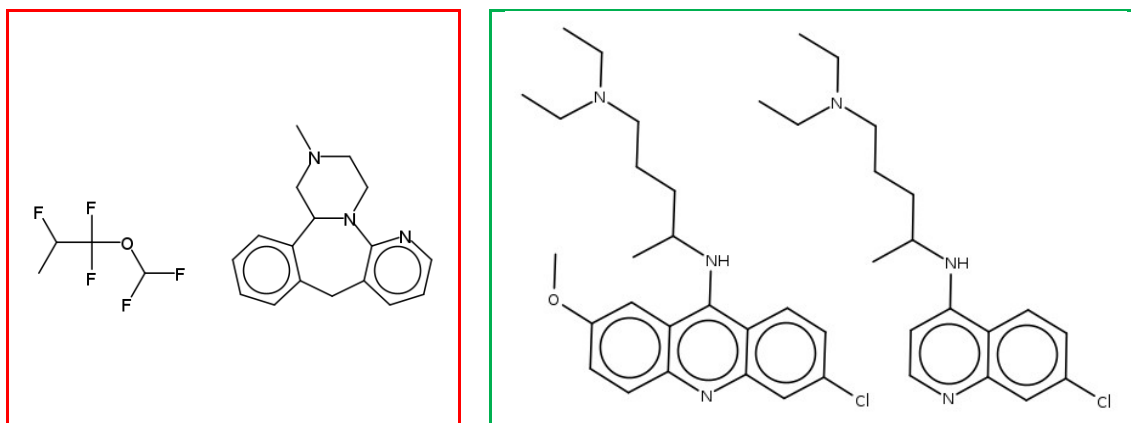


Figure 2. Red box: Two least similar molecules within the dataset. The *SSI* shows 2.38% similarity between two compounds. Other indices estimate it at 0, even though they share some structural details, like the C-C bonds. Green box: A pair of molecules for which *SSI* shows 100% similarity, while other indices yield significantly less percentage of similarity.

4. Conclusions

The Substructure Similarity Index introduces a fresh approach to quantifying pairwise similarity within binary vectors. The outcomes underscore its potential significance in similarity assessments, as it imparts novel insights not covered by existing measures.

Acknowledgment

Izudin Redžepović thanks the Serbian Ministry of Science, Technological Development, and Innovation for its support (Grant No. 451-03-47/2023-01/200122). The author also acknowledges financial support from the State University of Novi Pazar.

References

- [1] A. Bender, R.C. Glen., *Molecular Similarity: A Key Technique in Molecular Informatics*, Organic & Biomolecular Chemistry, 2 (2004) 3204-3218.
- [2] C.W. Coley, L. Rogers, W.H. Green, K.F. Jensen., *Computer-Assisted Retrosynthesis Based on Molecular Similarity*, ACS Central Science, 3 (2017) 1237-1245.
- [3] N.J. Morehouse, T.N. Clark, E.J. McMann, J.A. van Santen, F.P.J. Haeckl, C.A. Gray, R.G. Lington., *Annotation of Natural Product Compound Families Using Molecular Networking Topology and Structural Similarity Fingerprinting*, Nature Communications, 14 (2023) #308.
- [4] M.A. Johnson, G.M. Maggiora., *Concepts and Applications of Molecular Similarity*, John Wiley & Sons, New York, 1990.
- [5] R. Todeschini, V. Consonni, H. Xiang, J. Holliday, M. Buscema, P. Willett, *Similarity Coefficients for Binary Chemoinformatics Data: Overview and Extended Comparison Using Simulated and Real Data Sets*, Journal of Chemical Information and Modeling, 52 (2012) 2884-2901.

Coumarins as promising PPAR α agonists. Novel *in silico* insights

Draginja Radošević^{1,*}, Kristina Stevanović¹, Vladimir Perović¹, Sanja Glišić¹

¹ University of Belgrade, Institute of Nuclear Sciences Vinča, Department for Bioinformatics and Computational Chemistry, Mike Petrovića Alasa 12-14, 11351 Vinča, Belgrade, Serbia; e-mail: draga@vin.bg.ac.rs , kristina.stevanovic@vin.bg.ac.rs , vladaper@vin.bg.ac.rs , sanja@vin.bg.ac.rs

* Corresponding author

DOI: 10.46793/ICCB23.597R

Abstract: The occurrence of metabolic syndrome, which includes several chronic severe diseases such as cardiovascular disease, dyslipidemia, hypertension, stroke, and type 2 diabetes mellitus, is becoming a serious public health concern on a global scale. Peroxisome proliferator-activated receptor alpha (PPAR α) is a ligand-activated transcription factor that are members of the nuclear hormone receptor superfamily. PPAR α plays a crucial function in regulating the expression of genes involved in fatty acid beta-oxidation and glucose homeostasis, making it a potential drug target for treating metabolic syndrome. In experimental models, several coumarins, such as graphene, ostiole, and interruption B, have been found to activate PPAR α . In this study, we focus our attention on exogenous natural ligands known as coumarins. Using *in silico* screening, we searched for the most promising coumarin candidates from the Chemical Synthesis Database. Using a combination of ligand-based virtual screening and molecular docking, we identified (E)-3-[(2-oxo-chromen-3-yl)-methyleneamino]-acrylaldehyde as the most favorable candidate PPAR α agonist and proposed it for subsequent experimental testing.

Keywords: PPAR α , agonists, coumarins, virtual screening, molecular docking

1. Introduction

Atherosclerosis, a metabolic complication, is a significant public health challenge impacting longevity and well-being [1]. In light of this, PPAR α has gathered attention as a crucial lipid sensor capable of regulating the expression of target genes involved in various aspects of lipid metabolism, inflammation, and atherosclerosis [2]. PPAR α is a ligand-activated transcriptional factor crucial in regulating gene expression involved in fatty acid beta-oxidation and maintaining glucose homeostasis. Therefore, PPAR α is a critical potential drug target for treating metabolic syndrome. Evidence suggests that an extensive range of lipophilic molecules encompassing natural and synthetic ligands can activate PPAR α [3]. The coumarin scaffold's simplicity and versatility make it a compelling starting point for various applications in medicinal chemistry. Some coumarins like auraptene [4], ostiole [5], and interruption B [6] have shown their potential to activate PPAR α in experimental models. This study proposes a theoretical criterion for the virtual screening of coumarins as PPAR α agonists.

2. Methods

For finding PPAR α agonist candidates, 158 coumarins from the Chemical Synthesis Database (<https://www.chemsynthesis.com>) were screened. Virtual screening protocol considered the formation of a 3D QSAR (quantitative structure–activity relationships) model for ligand-based screening, followed by molecular docking.

2.1 Ligand-based Screening

In order to define a good predictive criterion learning set was composed of auraptene, the most potent coumarin PPAR α agonist from the literature [4], GW409544 co-crystallized ligand from the PDB structure obtained for the molecular docking [7], as well as 28 literature agonists downloaded from the ChEMBL database (Target ID ChEMBL239). We selected compounds with the lowest EC₅₀ value (0.026 – 1 nM) as the most potent ones. All compounds were converted into the SDF format and then imported, along with candidate compounds into the Pentacle QSAR software [8], protonated at pH 7.4, and oriented according to the principal moments of inertia. Standard GRIND descriptors were calculated and the PCA model was built. We used the centroid distance method as a criteria for similarity between the learning set and candidate compounds.

2.2 Molecular Docking

Molecular docking of the best PCA model candidates into the crystal X-ray structure of PPAR α ligand binding downloaded from RCSB, PDB ID 1K7L [7] domain was carried out. All ligands, waters and ions were removed from the PDB file. Grid boxes with dimensions 16 x 16 x 16 Å were set to span all amino acid residues interacting with co-crystallised inhibitor GW409544. Selected candidates were converted from smiles to 3D SDF and further to PDB files and protonated at physiological pH. After geometrical optimization, molecular docking was carried out in Autodock Vina [9]. Exhaustiveness was set to 50.

3. Results and Discussion

After forming the learning set, we screened the entire coumarin database for promising PPAR α agonist candidates. Table 1 shows the top three candidates obtained after ligand-based screening and ranked according to similarity distance values. We performed molecular docking to identify possible interactions with the ligand binding domain residues. The obtained docking energies are also presented in Table 1.

Table 1. Three best candidates from ligand-based screening, ranked by similarity distance, along with the docking scores.

Candidate compounds	Similarity distance from the centroid	Vina docking score (kcal/mol)
ethyl 5-(2-oxo-2H-chromen-3-yl)pentanoate	0.4933	-8.4
(E)-3-[(2-oxo-chromen-3-yl)-methyleneamino]-acrylaldehyde	1.0304	-8.9
ethyl 6-methyl-8-oxo-8H-chromeno[7,8-d][1,3]oxazole-2-carboxylate	1.4316	-7.4

The docked conformation of the candidate with the lowest binding energy (compared to crystal coordinates of co-crystallized ligand GW409544) is presented in Figure 1. The formation of an extensive hydrogen bond network with the subpocket formed by Ser280, Tyr314, His440, and Tyr464 is essential for the activation of PPAR α . As can be seen, GW409544 adopts a conformation within the receptor that allows the acidic carboxyl group to form hydrogen bonds with these key residues. Thanks to the aldehyde head, the candidate molecule conserves corresponding interactions with Ser280, and the oxo group attached to the benzene ring can form a hydrogen bond with His440. Although hydrogen bonds with Tyr314 and Tyr464 are not realized, there are strong hydrophobic interactions with the corresponding helices. Other compounds did not show similar binding patterns. Therefore (E)-3-[(2-oxo-chromen-3-yl)-methyleneamino]-acrylaldehyde has been identified as the most favorable candidate PPAR α agonist.

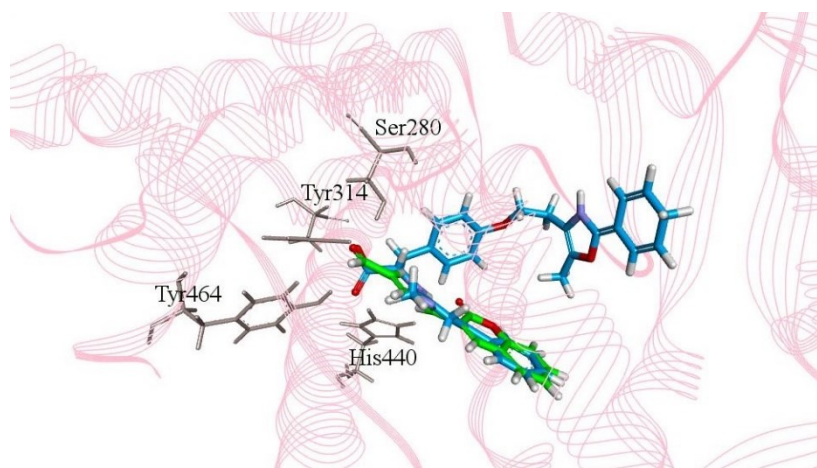


Figure 1. Best ranking docked conformation of the candidate molecule (green carbon atoms) in X-ray structure of PPAR α ligand binding domain (PDB 1K7L), compared to GW409544 coordinates in complex (blue carbon atoms).

3. Conclusions

Based on QSAR model we screened coumarin database for possible PPAR α candidate agonists. After molecular docking was performed on the best ranking candidates we identified (E)-3-[(2-oxo-chromen-3-yl)-methyleneamino]-acrylaldehyde as the most promising candidate.

Acknowledgment

This research is funded by the Ministry of Education and Ministry of Science, Technological Development and Innovation, Republic of Serbia, Grants: No. 451-03-47/2023-01/200017.

References

- [1] R. Ross., *Atherosclerosis--an inflammatory disease*, The New England Journal of Medicine, 340 (1999) 115-126.
- [2] F. Zandbergen, J. Plutzky., *PPAR α in atherosclerosis and inflammation*, Biochimica et Biophysica Acta, 1771 (2007) 972-982.
- [3] D. Rigano, C. Sirignano, O. Tagliatela-Scafati., *The potential of natural products for targeting PPAR α* , Acta Pharmaceutica Sinica, 7 (2017) 427-438.
- [4] N. Takahashi, M.S. Kang, K. Kuroyanagi, T. Goto, S. Hirai, K. Ohyama, J.Y. Lee, R. Yu, M. Yano, T. Sasaki, S. Murakami, T. Kawada., *Auraptene, a citrus fruit compound, regulates gene expression as a PPAR- α agonist in HepG2 hepatocytes*, Biofactors, 33 (2008) 25-32.
- [5] X. Zhao, J. Xue, M. Xie., *Osthole inhibits oleic acid/lipopolysaccharide-induced lipid accumulation and inflammatory response through activating PPAR α signaling pathway in cultured hepatocytes*, Experimental gerontology, 119 (2019) 7-13.
- [6] S. Kaewsuwan, A. Plubrukarn, M. Utsintong, S.H. Kim, J.H. Jeong, J.G. Cho, S.G. Park, J.H. Sung., *Interruptin B induces brown adipocyte differentiation and glucose consumption in adipose-derived stem cells*, Molecular Medicine Reports, 13 (2016) 2078-2086.
- [7] H.E. Xu, M.H. Lambert, V.G. Montana, K.D. Plunket, L.B. Moore, J.L. Collins, J.A. Oplinger, S.A. Kliewer, R.T.Jr. Gampe, D.D. McKee, J.T. Moore, T.M. Willson., *Structural determinants of ligand binding selectivity between the peroxisome proliferator-activated receptors*, Proceedings of the National Academy of Sciences of the United States of America, 98 (2001) 13919-13924.
- [8] A. Duran, I. Zamora, M. Pastor., *Suitability of GRIND-Based Principal Properties for the Description of Molecular Similarity and Ligand-Based Virtual Screening*, Journal of Chemical Information and Modelling, 49 (2009) 2129-2138.
- [9] O. Trott, A.J. Olson., *AutoDock Vina: improving the speed and accuracy of docking with a new scoring function, efficient optimization, and multithreading*, Journal of Computational Chemistry, 30 (2010) 455-461.

Combined *in silico* approach to identify new terpenoid PPAR α agonists

Kristina Stevanović^{1,*}, Draginja Radošević¹, Vladimir Perović¹, Sanja Glišić¹

¹ University of Belgrade, Institute of Nuclear Sciences Vinča, Department for Bioinformatics and Computational Chemistry, Mike Petrovića Alasa 12-14, 11351 Vinča, Belgrade, Serbia; e-mail: kristina.stevanovic@vin.bg.ac.rs , draga@vin.bg.ac.rs , vladaper@vin.bg.ac.rs , sanja@vin.bg.ac.rs

* Corresponding author

DOI: 10.46793/ICCB23.601S

Abstract: In treating atherosclerosis and dyslipidemia, peroxisome proliferator-activated receptor alpha (PPAR α) has been recognized as an interesting drug target. It is a ligand-activated transcriptional factor that controls genes involved in lipid metabolism regulation. The discovery of natural PPAR α agonists may open new perspectives in its targeting. For several terpenoid molecules, it has been shown that they potentially activate PPAR α . Linalool is a terpenoid molecule for which the PPAR α antagonistic effect has been demonstrated *in vivo*. Here, we focused on searching for new terpenoid PPAR α agonist candidates by proposing a simple theoretical criterion for fast virtual screening of TeroKit database. After *in silico* screening by using the EIIP/AQVN filter and through filtering of candidate compounds by ligand based virtual screening, natural monoterpene alcohol geraniol was selected as a promising candidate. Further, molecular docking was conducted to investigate its potential activation mechanisms, along with the reference molecule linalool. Despite observing low binding energies, the molecular docking results revealed potential insights into activation mechanisms of geraniol as well as reference molecule linalool.

Keywords: PPAR α , lipid metabolism, terpenoids, virtual screening, molecular docking

1. Introduction

Peroxisome proliferator-activated receptor PPAR α is a ligand-activated transcriptional factor responsible for the activation of multiple genes associated primarily with lipid metabolism regulation. By means of its activation with many endogenous ligands and environmental factors, PPAR α can help balance dysregulated lipid status and maintain energy homeostasis [1]. Accordingly, it has been recognized as an attractive therapeutic target in the development of drugs to treat atherosclerosis and dyslipidemia [1]. The PPAR α is one of three PPAR isoforms (α , γ , and β/δ). Natural compounds are usually partial PPAR α/γ agonists and exert lower activation potency than specific synthetic activators such as fibrates [2]. However, a healthy diet encompassing different natural sources of PPAR α agonists can be a winning strategy in such conditions. Terpenoids are a promising class of molecules for targeting PPAR α . In an *in-vivo* experimental model, it was found that acyclic monoterpene linalool present in

teas and fragrant herbs acts as a direct ligand of PPAR α [3]. In this study, we wanted to explain the structural basis for this activation, but also to identify new promising candidates and their mechanism of action. We performed a virtual screening protocol that considers both short-and long-range interactions between interacting molecules.

2. Methods

2.1 EIIP/AQVN Filter

First, the electronic molecular descriptors: the average quasi-valence number (AQVN), and the electron-ion interaction potential (EIIP) were applied for *in silico* screening of the TeroKit database (<http://terokit.qmclab.com/>). EIIP value for organic molecules can be determined by the following simple equation derived from the “general model pseudopotential” [4]:

$$EIIP = 0.25Z^* \sin(1.04\pi Z^*)2\pi \quad (1)$$

where Z^* is the average quasi-valence number (AQVN) determined by

$$Z^* = \sum m(n_i Z_i / N) \quad (2)$$

Z_i is the valence number of the i th atomic component, n_i is the number of atoms of the i -th component, m is the number of atomic components in the molecule, and N is the total number of atoms. EIIP values calculated according to the above equations are expressed in Rydberg units (Ry). We performed screening in a narrow range of EIIP/AQVN values around those for reference molecule linalool.

2.2 Ligand-Based Virtual Screening

Selected candidate molecules from the previous step were converted to 3D sdf format from smiles and imported, along with a reference molecule into the Pentacle version 1.06 for Linux software [5]. All compounds were protonated at pH 7.4, and oriented according to the principal moments of inertia. Standard GRIND descriptors were calculated and the PCA model was built. The number of PCA components was set to five. The explained variance of such obtained model was 62.47%.

2.3 Molecular Docking

For molecular docking, we used Auto Dock Vina version 1.2.3 [5]. The X-ray protein crystal structure of human PPAR α with code 1K7L [6] was downloaded from the RCSB Protein Data Bank and preprocessed for calculating protonation states and adding hydrogen atoms. All ions, cofactors, and crystallographic water were removed from the structure. The best candidates from the PCA model as well as the reference molecule linalool were energy-minimized. The grid box with dimensions 16 \times 16 \times 16 Å was set in the center of the ligand binding site, spanning all the amino acid residues involved in binding based on the coordinates of the co-crystallized ligand. The exhaustiveness was set to 50. For comparison, we performed molecular docking of linalool as well.

3. Results and discussion

After *EIIP/AQVN* filtering 400 candidate molecules were selected for the next step. The ligand based screening revealed geranoil, typical isoprenol in many essential oils of fruits, vegetables, and herbs, as the second best-ranked candidate. Although molecular docking was performed for the top 10 candidates, only geranoil molecule was able to enter the subpocket crucial for PPAR α activation (Figure 1).

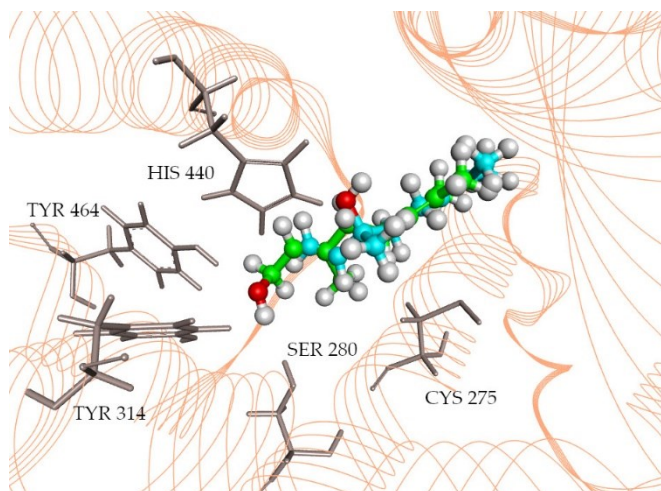


Figure 1. Best ranking docked conformation of Geranoil (green carbon atoms) and Linalool (blue carbon atoms) in X-ray structure of PPAR α ligand binding domain (PDB 1K7L).

It has already been found that isoprenols can act as potential PPAR α/γ dual agonists [8]. Yet, the hydroxy group of geranoil molecule can form only one hydrogen bond with Ser 280. This is consistent with small Vina binding energy of only - 6.1 kcal/mol. In order to form 4 hydrogen bonds with the key amino acids marked in Figure 1, the carboxyl group present in all synthetic agonists, as well as in fatty acids, is necessary. Linalool has also only one hydroxy group oriented toward Hys 440 and the Vina binding score was of the same order of magnitude (- 6.5 kcal/mol). Clearly, for the

activation with such molecules, the existence of one hydrogen bond stabilized by hydrophobic interactions (mostly via Cys 275) is sufficient. Most likely these molecules are partial activators, inducing only some conformational changes compared to full agonists.

3. Conclusions

We identified *in silico* granoil as a promising PPAR α agonist. This result needs to be further experimentally investigated and compared with other isoprenyl monoterpenes.

Acknowledgment

This research is funded by the Ministry of Education and Ministry of Science, Technological Development and Innovation, Republic of Serbia, Grants: No. 451-03-47/2023-01/200017.

References

- [1] A.V. Contreras, N. Torres, A.R. Tovar., *PPAR- α as a Key Nutritional and Environmental Sensor for Metabolic Adaptation*, *Advances in Nutrition*, 4 (2013) 439-452.
- [2] D. Rigano, C. Sirignano, O. Tagliatela-Scafati., *The potential of natural products for targeting PPAR α* , *Acta Pharmaceutica Sinica*, 7 (2017) 427-438.
- [3] H.J. Jun, J.H. Lee, J. Kim, Y. Jia, K.H. Kim, K.Y. Hwang, E.J. Yun, K.R. Do, S.J. Lee., *Linalool is a PPAR α ligand that reduces plasma TG levels and rewires the hepatic transcriptome and plasma metabolome*, *Journal of Lipid Research*, 55 (2014) 1098-1110.
- [4] N. Veljkovic, S. Glisic, V. Perovic, V. Veljkovic., *The role of long-range intermolecular interactions in discovery of new drugs*, *Expert Opinion on Drug Discovery*, 6 (2011) 1263-1270.
- [5] A. Duran, I. Zamora, M. Pastor., *Suitability of GRIND-Based Principal Properties for the Description of Molecular Similarity and Ligand-Based Virtual Screening*, *Journal of Chemical Information and Modelling*, 49 (2009) 2129-2138.
- [6] O. Trott, A.J. Olson., *AutoDock Vina: improving the speed and accuracy of docking with a new scoring function, efficient optimization, and multithreading*, *Journal of Computational Chemistry*, 30 (2010) 455-461.
- [7] H.E. Xu, M.H. Lambert, V.G. Montana, K.D. Plunket, L.B. Moore, J.L. Collins, J.A. Oplinger, S.A. Kliewer, R.T.Jr. Gampe, D.D. McKee, J.T. Moore, T.M. Willson., *Structural determinants of ligand binding selectivity between the peroxisome proliferator-activated receptors*, *Proceedings of the National Academy of Sciences of the United States of America*, 98 (2001) 13919-13924.
- [8] N. Takahashi, T. Kawada, T. Goto, T. Yamamoto, A. Taimatsu, N. Matsui, K. Kimura, M. Saito, M. Hosokawa, K. Miyashita, T. Fushiki, *Dual action of isoprenols from herbal medicines on both PPAR γ and PPAR α in 3T3-L1 adipocytes and HepG2 hepatocytes*, 514 (2002), 315-322.

***In silico* screening of *Solanum lycopersicum* carotenoids from Carotenoids Database for candidates PPAR α agonists**

**Tamara Drljača^{1,*}, Kristina Stevanović¹, Draginja Radošević¹, Jelena Milićević¹,
Nevena Veljković¹, Sanja Glišić¹**

¹ University of Belgrade, Institute of Nuclear Sciences Vinča, Department for Bioinformatics and Computational Chemistry, Mike Petrovića Alasa 12-14, 11351 Vinča, Belgrade, Serbia; e-mail: tamara.drljaca@vin.bg.ac.rs, kristina.stevanovic@vin.bg.ac.rs, draga@vin.bg.ac.rs, jdjordjevic@vin.bg.ac.rs, nevenav@vin.bg.ac.rs, sanja@vin.bg.ac.rs

* Corresponding author

DOI: 10.46793/ICCB23.605D

Abstract: Peroxisome proliferator-activated receptor alpha (PPAR α) is crucial in regulating lipid metabolism. Clinically, PPAR α is significant as a possible therapeutic target for a variety of human disorders, including cardiovascular, neurological, and metabolic syndromes. The wide range of natural compounds provides great opportunities for new approaches in targeting PPAR α . Carotenoids, a large class of natural compounds, have been recognized as PPAR α agonists. Tomatoes (*Solanum lycopersicum*) are one of the most widely grown crops in the world and contain compounds that improve lipid metabolism. Since there is no data on tomato carotenoids as PPAR α agonists in this study, we focused on searching carotenoids from tomatoes as possible PPAR α agonists. The *Solanum lycopersicum* carotenoids from Carotenoids Database were in silico screened using a combined protocol with the Electron-Ion Interaction Potential/Average Quasi Valence Number (EIIP/AQVN) filter and molecular docking to find the most promising candidate compounds. The best resulting compounds may have the promise to be further developed as candidates for PPAR α agonists.

Keywords: PPAR α , virtual screening, EIIP/AQVN, molecular docking, carotenoids

1. Introduction

PPAR α is a ligand-activated transcription factor that is crucial in regulating lipid metabolism. It can be activated by different metabolites of fatty acids and specific agonists, such as fibrates, which trigger PPAR α to exert its transactivating function or repressive functions leading to changes in gene expression. Due to its involvement in lipid metabolism, PPAR α has implications in diverse human diseases [1]. The vast diversity of natural compounds offers promising opportunities for novel approaches in targeting PPAR α . Natural compounds exhibit a lower degree of PPAR α activation when compared to synthetic compounds such as fibrates [2]. Carotenoids have been identified as PPAR α agonists. Research has shown that bixin, a carotenoid derived from the pericarp of the seeds of *Bixa Orellana*, displays a moderate level of PPAR α activation [3].

Tomatoes are one of the most widely grown crops in the world and contain compounds that improve lipid metabolism. There is no data on tomato carotenoids as PPAR α agonists. Therefore, in this study, we investigate carotenoids from tomatoes as possible PPAR α agonists.

2. Methods

2.1. EIIP/AQVN Filter

Specific recognition and targeting between interacting biological molecules at distances $> 5 \text{ \AA}$ are determined by the average AQVN and the EIIP derived from the general model pseudopotential [4]:

$$EIIP = 0.25Z^* \sin(1.04\pi Z^*)2\pi \quad (1)$$

where Z^* is the average quasi-valence number (AQVN) determined by:

$$Z^* = \sum m(n_i Z_i / N) \quad (2)$$

where Z_i is the valence number of the i th atomic component, n_i is the number of atoms of the i th component, m is the number of atomic components in the molecule, and N is the total number of atoms. EIIP values are calculated according to Equations (1) and (2) and are expressed in Rydberg units (Ry).

2.2 Molecular Docking

The molecular docking of *Solanum lycopersicum* carotenoids into the X-ray structure of the PPAR α ligand binding domain (PDB ID 1K7L [5]) was performed in Autodock Vina software [6]. The receptor preparation process considered the removal of all ligands, waters and ions. The candidate compounds were converted to 3D SDF from smiles, protonated at physiological pH and geometrically optimized. A grid box with dimensions $16 \times 16 \times 16 \text{ \AA}$ was positioned at $(-16.5, -15, -4)$. Exhaustiveness was set to 50.

3. Results and Discussion

In this virtual screening (VS) study, we used successive filters to choose PPAR α agonist candidates. Previous research demonstrated that small molecules with similar AQVN and EIIP values have shared therapeutic targets [4,7]. In this study, EIIP/AQVN values of the experimentally proved PPAR α agonists enabled the establishment of criteria for searching the Carotenoids Database [8] to identify compounds with similar therapeutic properties. Results of the application of VS based on the EIIP/AQVN approach have shown that the domain encompassing carotenoids from tomato is inside

the AQVN/EIIP domain of all known terpenes active PPAR α agonists. Therefore, we performed molecular docking on all candidate carotenoids.

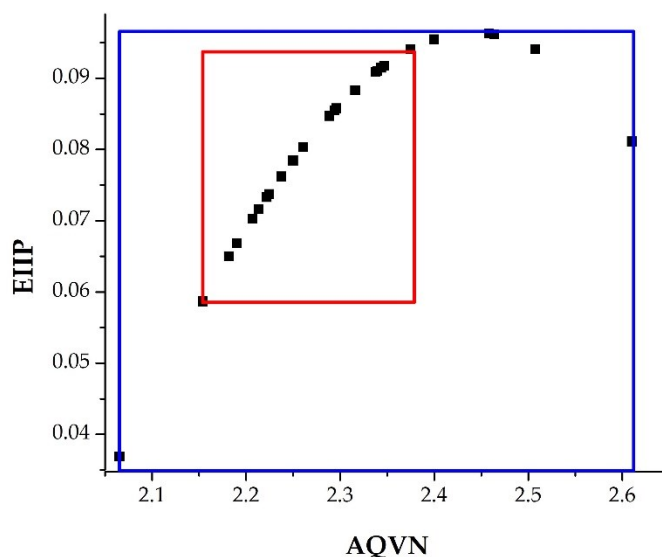


Figure 1. Schematic presentation of the EIIP/AQVN descriptor values for all known terpenes active PPAR α agonists (blue) and for Solanum lycopersicum carotenoids (red).

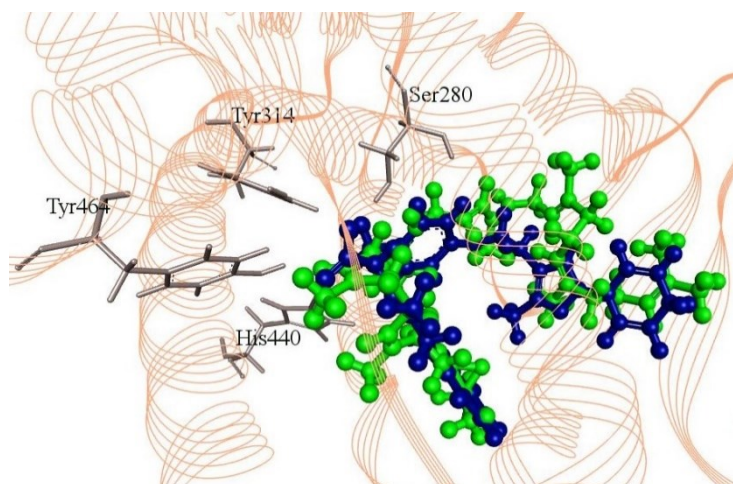


Figure 2. Best ranking docked conformation of the candidate molecule zeta-Carotene epoxide (green) in X-ray structure of PPAR α ligand binding domain (PDB 1K7L), compared to GW409544 coordinates in complex (blue).

Zeta-Carotene epoxide from all tomato carotenoid compounds had the best docking energy of -9.6 kcal/mol. Although it does not form hydrogen bonds with the key amino acid residues marked in Figure 2, it fits perfectly along the entire length of the binding pocket. The stability of this complex comes from hydrophobic interactions. This result shows that it may be possible to activate PPAR α without a hydrogen bonds network, which should be further investigated.

4. Conclusions

Selected carotenoid from *Solanum lycopersicum* represents promising candidate as PPAR α agonists that need to be further experimentally investigated.

Acknowledgment

This research is funded by the Ministry of Education and Ministry of Science, Technological Development and Innovation, Republic of Serbia, Grants: No. 451-03-47/2023-01/200017.

References

- [1] Y. Lin, Y. Wang, P.F. Li., *PPAR α : An emerging target of metabolic syndrome, neurodegenerative and cardiovascular diseases*, *Frontiers in Endocrinology*, 13 (2022) 1074911.
- [2] D. Rigano, C. Sirignano, O. Tagliatela-Scafati., *The potential of natural products for targeting PPAR α* , *Acta Pharmaceutica Sinica*, 7 (2017) 427-438.
- [3] T. Goto, N. Takahashi, S. Kato, Y.I. Kim, T. Kusudo, A. Taimatsu, K. Egawa, M.S. Kang, T. Hiramatsu, T. Sakamoto, T. Uemura, S. Hirai, M. Kobayashi, F. Horio, T. Kawada., *Bixin Activates PPAR α and Improves Obesity-Induced Abnormalities of Carbohydrate and Lipid Metabolism in Mice*, *Journal of Agricultural and Food Chemistry*, 60 (2012) 11952–11958.
- [4] N. Veljkovic, S. Glisic, V. Perovic, V. Veljkovic., *The role of long-range intermolecular interactions in discovery of new drugs*, *Expert Opinion on Drug Discovery*, 6 (2011) 1263–1270.
- [5] H.E. Xu, M.H. Lambert, V.G. Montana, K.D. Plunket, L.B. Moore, J.L. Collins, J.A. Oplinger, S.A. Kliewer, R.T.Jr. Gampe, D.D. McKee, J.T. Moore, T.M. Willson., *Structural determinants of ligand binding selectivity between the peroxisome proliferator-activated receptors*, *Proceedings of the National Academy of Sciences of the United States of America*, 98 (2001) 13919–13924.
- [6] O. Trott, A.J. Olson., *AutoDock Vina: improving the speed and accuracy of docking with a new scoring function, efficient optimization, and multithreading*, *Journal of Computational Chemistry*, 30 (2010) 455-461.
- [7] J. Vucicevic, T. Srdic-Rajic, M. Pieroni, J.M. Laurila, V. Perovic, S. Tassini, E. Azzali, G. Costantino, S. Glisic, D. Agbaba, M. Scheinin, K. Nikolic, M. Radi, N. Veljkovic., *A combined ligand- and structure-based approach for the identification of rilmenidine-derived compounds which synergize the antitumor effects of doxorubicin*, *Bioorganic & medicinal chemistry*, 24 (2016) 3174-3183.
- [8] J. Yabuzaki., *Carotenoids Database: structures, chemical fingerprints and distribution among organisms*, *Database: the journal of biological databases and curation*, (2017) 1-11.

Numerical simulations of the oscillatory dynamics in the Bray-Liebhafsky reaction perturbed by L-tyrosine

Ana Ivanović-Šašić¹, Stevan Maćešić², Jelena Maksimović², Željko Čupić^{1*},
Ljiljana Kolar-Anić²

¹ University of Belgrade, Institute of Chemistry, Technology and Metallurgy, National Institute of the Republic of Serbia, Njegoševa 12, 11000 Belgrade

e-mail: ana.ivanovic.sasic@ihtm.bg.ac.rs, zcupic@ihtm.bg.ac.rs

² University of Belgrade, Faculty of physical chemistry, Studentski Trg 12-16, 11158 Belgrade

e-mail: jelena.maksimovic@ffh.bg.ac.rs, stevan.macesic@ffh.bg.ac.rs

* Corresponding author

DOI: 10.46793/ICCB123.609IS

Abstract: It is well known that almost all living or biological systems are naturally in the oscillatory dynamic states and can be considered as biochemical reaction systems. These oscillatory dynamic states can be caused by internal self-organized phenomena, but also by external periodic variations of temperature, light, food, or seasonal changes. The hypothalamic-pituitary-thyroid (HPT) axis is one such nonlinear system with feedback that is always in an oscillatory dynamic state and L-tyrosine is its main representative.

The biological importance of L-tyrosine interactions with iodine species was the motivation for modelling of the oscillatory dynamics in the Bray-Liebhafsky (BL) reaction perturbed by L-tyrosine. Also, direct experimental investigation of metabolic processes in the human body is extremely complex to be done, and therefore any alternative approach is of great importance. Therefore, the BL reaction has the potential to be used as a model of the biological system due to certain characteristics shared with the considered processes; it is characterized by its oscillatory dynamics and based on the chemistry of hydrogen peroxide and iodine compounds commonly present in the thyroid gland, where L-tyrosine is iodinated.

The impact of L-tyrosine on the dynamics of the Bray-Lienbhafsky oscillatory reaction was investigated numerically using the proposed model. The study was focused on the examination of the sensitivity of the BL reaction to L-tyrosine perturbation. The obtained results indicated possible pathways of influence.

Keywords: Numerical simulation, Bray-Liebhafsky oscillatory reaction, L-tyrosine

1. Introduction

The Bray-Liebhafsky (BL) oscillatory reaction [1], the first homogeneous oscillatory reaction presents hydrogen peroxide decomposition into the water and oxygen in the presence of iodate and hydrogen ions:

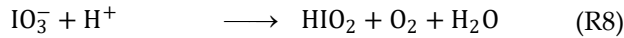
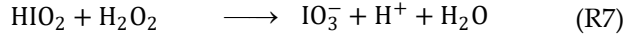
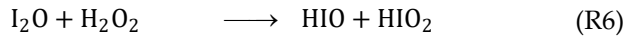
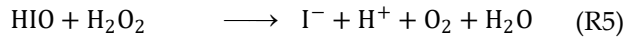
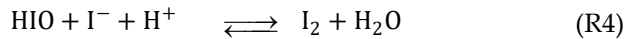
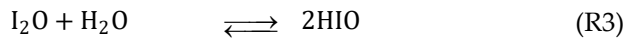
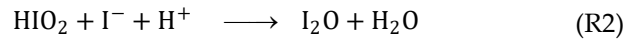


This apparently simple reaction comprises a complex homogeneous catalytic oscillatory process involving periodic changes in concentrations of numerous iodine intermediates such as I_2 , I^- , HIO , I_2O and HIO_2 .

2. Model

To explain L-tyrosine activity, numerical simulations were performed using the proposed model of the BL oscillatory reaction that exists of eight reactions, present in Table 1 [2].

Model of the Bray-Liebafsky oscillatory reaction



The dynamics of the considered system is described by five differential equations:

$$\frac{d[I^-]}{dt} = v_{-1} + v_{-4} + v_5 - v_1 - v_2 - v_4$$

$$\frac{d[HIO]}{dt} = v_1 + 2v_3 + v_{-4} + v_6 - v_{-1} - 2v_{-3} - v_4 - v_5$$

$$\frac{d[HIO_2]}{dt} = v_1 + v_6 + v_8 - v_{-1} - v_2 - v_7$$

$$\frac{d[I_2O]}{dt} = v_2 + v_{-3} - v_3 - v_6$$

$$\frac{d[I_2]}{dt} = v_4 - v_{-4}$$

3. Numerical simulation

Numerical simulations were performed in MATLAB, using the ODE15s solver routine based on the Gear algorithm for the integration of stiff differential equations. The response of the BL matrix to a low concentration of L-tyrosine single pulse

perturbations was investigated. The system was perturbed with various concentrations (1.27×10^{-7} M – 1.27×10^{-5} M) of L-tyrosine in the pre-oscillatory period at the same instant of time (40 min).

4. Results and discussion

Previous experimental investigations show that the BL oscillatory reaction is the well-selected matrix for examination of the chemical activity of L-tyrosine. The mechanism of interaction between the L-tyrosine and BL reaction system constituents is therefore studied here by the numerical simulation of the BL reaction.

As the BL matrix is a very rich reaction system with many intermediate species and numerous reactions between them produce various parallel reaction pathways, and L-tyrosine is a reactive species, the selection of the reactions that describe their interactions was a difficult task. By the examinations of the main kinetic activities of L-tyrosine, we proposed a reaction with the aim of explaining a mechanism of L-tyrosine interaction with the BL matrix.



This reaction was chosen as the most probable pathway for interaction between L-tyrosine and BL reaction system. [3] Products of this reaction step are considered irrelevant for the nonlinear dynamics of BL reaction. Reaction (RT) is consistent with experimentally observed increase of iodide concentration after perturbation since HIO concentration is directly related to iodide concentration through very fast iodine hydrolysis. Therefore, a decrease in HIO concentration leads to an equilibrium shift toward a further increase in iodide concentration, a reaction (R4) from the model presented in Table 1.

Numerically simulated time evolution of the BL reaction was perturbed with various amounts of L-tyrosine. The rate constant of reaction (RT) is estimated to be $k_{\text{RT}} = 5.00 \times 10^5 \text{ min}^{-1}$. Results obtained with the selected value of rate constant k_{RT} show that a very small amount of L-tyrosine produces an important response of the BL matrix. Sensitivity to perturbation by small amounts of L-tyrosine depends on the selected rate constant value.

Based on the results presented in Figure 1, it can be observed that the peak intensity and the length of the oscillogram depend on the value of L-tyrosine concentration. More precisely, with an increase in the concentration of L-tyrosine, both the peak intensity and the length of the oscillogram also increase as well as the period between perturbation and first oscillation. Therefore, it can be concluded that the system is sensitive to low concentrations of perturbators which is in accordance with previous experimental results.

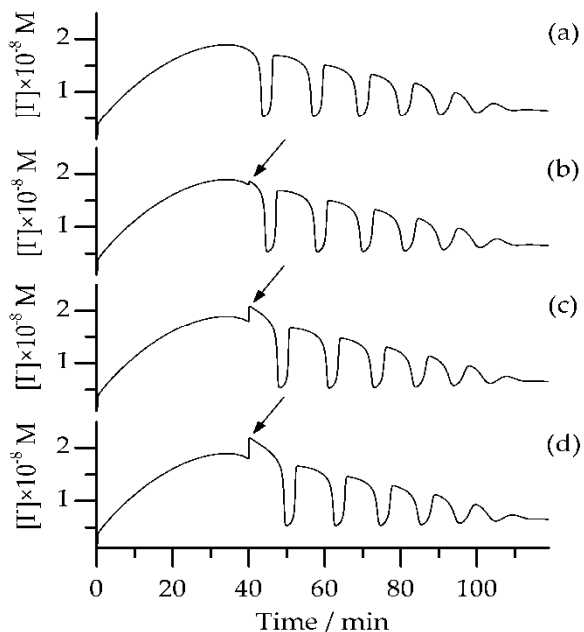


Figure 1. Numerically simulated time evolution of the BL reaction: (a) without perturbation and perturbed with different L-tyrosine concentration: (b) $[Tyr] = 1.27 \times 10^{-6} \text{ M}$, (c) $[Tyr] = 6.33 \times 10^{-6} \text{ M}$, (d) $[Tyr] = 9.50 \times 10^{-6} \text{ M}$. Arrow presents time of perturbation. The rate constant of reaction (RT) is determined to be $k_{RT} = 5.00 \times 10^5 \text{ min}^{-1}$.

5. Conclusion

The impact of L-tyrosine on the dynamics of the Bray-Lienbhafsky oscillatory reaction was investigated numerically using the proposed model. The system was perturbed with various L-tyrosine concentrations. The obtained results show a very good potential of the BL reaction in the analysis of the L-tyrosine and indicated possible pathways of influence.

Acknowledgment

We are grateful to the financial support from Ministry of Science, Technological Development and Innovation of Republic of Serbia (Grant Numbers 172015 and 45001, and Contract numbers 451-03-47/2023-01/200026 and 451-03-47/2023-01/200146. This research was supported by Science Fund of Republic of Serbia #Grant Number. 7743504, NES.

References

- [1] W.C. Bray, H.A. Liebafsky, *Reactions involving hydrogen peroxide, iodine and iodate ion. I Introduction*, J America Chemical Society, 53 (1931)38-44.
- [2] Lj. Kolar-Anić, Đ. Mišljenović, S. Anić, G. Nicolis, *The influence of the reduction of iodate ion by hydrogen peroxide on the model of the Bray-Liebafsky reaction*. Reaction Kinetics Catalysis Letters, 54 (1995) 35–41.
- [3] H.B. Dunford, I.N. Ralston, *On the Mechanism of iodination of tyrosine*, Biochem. Biophys. Res. Commun. 116 (1983) 639-643.

The assessment of the antioxidant capacity of the selected vanillin-based pyrido-dipyrimidines using DPPH assay: *in silico* approach

Svetlana Jeremić^{1*}, Nenad Janković², Jelena Đorović Jovanović², Zoran Marković^{1,2}

¹ The State University of Novi Pazar, Department of Natural Sciences and Mathematics, Vuka Karadžića 9, 36300 Novi Pazar, Serbia; e-mail: sjeremic@np.ac.rs

² University of Kragujevac, Institute for Information Technologies, Jovana Cvijica bb, 34000 Kragujevac, Serbia; e-mail: nenad.jankovic@uni.kg.ac.rs, jelena.djorovic@uni.kg.ac.rs, zmarkovic@uni.kg.ac.rs

* Corresponding author

DOI: 10.46793/ICCBi23.613J

Abstract: It is known that pyridine derivatives possess significant biological activity, and that vanillin is a natural aromatic compound with pharmacoeological properties. Earlier research indicated that among the series of synthesized vanillin-based pyrido-dipyrimidine compounds, two of them show significant antioxidative activity. Based on the thermodynamic parameters obtained using the DFT method, the operative mechanism of the reaction of the investigated antioxidants with the DPPH radical was considered. Calculations are done in water, methanol, and benzene, to imitate real experimental conditions, and to examine the reaction mechanisms under the environment of different polarity. HAT and SPLET mechanisms were identified as operative reaction mechanisms. Which reaction pathway is dominant was found to be independent of the nature of the solvent. A molecule with two O-H groups can react through both O-H groups simultaneously, so it shows a higher antioxidant capacity than a molecule with one O-H group, which is in accordance with the experimentally obtained results.

Keywords: vanillin-based pyrido-dipyrimidine, DPPH, antioxidant mechanisms, thermodynamic parameters, DFT

1. Introduction

Pyrimidine derivatives possess significant biological activity, which is additionally enhanced by the binding of some other heterocyclic molecules to pyrimidine. Thus, it has been proven that molecules with a pyridopyrimidal structure show antimicrobial, anti-inflammatory, antioxidant and anti-carcinogenic activity [1]. Therefore, some of them are officially accepted as drugs in the treatment of some types of cancer [2]. On the other hand, vanillin is a natural compound, which possesses numerous biological and pharmacoeological properties [3]. Due to its specific pleasant aroma, its use in the food and cosmetic industry is large, so today the greatest quantities of vanillin are produced synthetically or biotechnologically. Previously published results indicated remarkably antioxidant activity of vanillin-based pyrido-dipyrimidine [4]. Therefore, the capacity of

selected vanillin-based pyrido-dipyrimidines to neutralize DPPH radical species was investigated, and the obtained results were compared with experimental indicators of antioxidant activity of these compounds determined using the DPPH assay [4].

2. Methodology section

Geometry optimization of investigated pyrido-dipyrimidines, their ionic and radical species, as well as neutral and charged species of DPPH is performed using M06-2X/6-311++G(d,p) method implemented in Gaussian09 program package [5,6]. CPCM solvation model was applied to imitate the solvent effect [7]. To examine the reactivity of the considered molecules towards DPPH in polar and non-polar environments, the calculations were performed in water, methanol, and benzene.

The DPPH radical can be neutralized by a transfer of a hydrogen atom from the antioxidant molecule to the DPPH. This reaction can follow several mechanistic pathways, three of which are discussed here: HAT (Hydrogen Atom Transfer), SPLET (Sequential Proton Loss Electron Transfer), and SET-PT (Single-Electron Transfer followed by Proton Transfer) [4,8]. The probability that the reaction follows the HAT mechanism can be estimated based on the ΔG_{BDE} value (Bond Dissociation free Energy, Eq. 1) as the corresponding thermodynamic parameter. Whether a SPLET mechanism is the most likely reaction pathway can be discussed based on ΔG_{PA} (Proton Affinity, Eq. 2) and ΔG_{ETE} (Electron Transfer free Energy, Eq. 3). The possibility that the reaction follows the SET-PT mechanism can be estimated based on ΔG_{IP} (Ionization Potential, Eq. 4) and ΔG_{PDE} (Proton Dissociation free Energy, Eq. 5).

$$\Delta G_{\text{BDE}} = [G(\text{M}-\text{O}^\bullet) + G(\text{DPPH}_n)] - [G(\text{M}-\text{OH}) + G(\text{DPPH}_r)] \quad (1)$$

$$\Delta G_{\text{PA}} = [G(\text{M}-\text{O}^-) + G(\text{DPPH}_n)] - [G(\text{M}-\text{OH}) + G(\text{DPPH}_a)] \quad (2)$$

$$\Delta G_{\text{ETE}} = [G(\text{M}-\text{O}^\bullet) + G(\text{DPPH}_a)] - [G(\text{M}-\text{O}^-) + G(\text{DPPH}_r)] \quad (3)$$

$$\Delta G_{\text{IP}} = [G(\text{M}-\text{O}^{\bullet+}) + G(\text{DPPH}_a)] - [G(\text{M}-\text{OH}) + G(\text{DPPH}_r)] \quad (4)$$

$$\Delta G_{\text{PDE}} = [G(\text{M}-\text{O}^\bullet) + G(\text{DPPH}_n)] - [G(\text{M}-\text{O}^{\bullet+}) + G(\text{DPPH}_a)] \quad (5)$$

In the previous equations $G(\text{M}-\text{OH})$, $G(\text{M}-\text{O}^\bullet)$, $G(\text{M}-\text{O}^-)$ and $G(\text{M}-\text{O}^{\bullet+})$ denote Gibbs free energies of the neutral molecule of antioxidant, its radical, anionic and radical cation moieties respectively, while $G(\text{DPPH}_n)$, $G(\text{DPPH}_r)$ and $G(\text{DPPH}_a)$ presents Gibbs free energies of protonated, radical and anionic moieties of DPPH respectively.

3. Results and discussions

Geometry optimization of the estimated vanillin-based pyrido-dipyrimidine antioxidants indicated the absence of planarity observing the whole molecule [4]. Earlier investigations indicate a better antioxidant capacity of molecule A than of molecule B, which is explained by the presence of the two O-H groups in molecule A, and only one O-H group in molecule B (Fig. 1), [4].

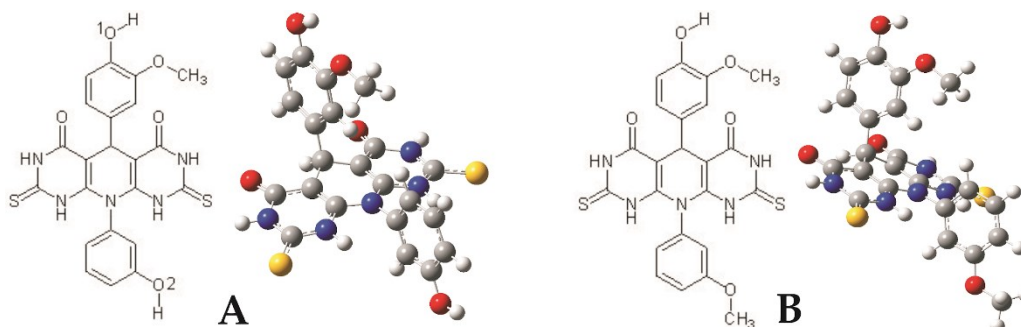


Figure 1. 2D and optimized 3D structures of investigated vanillin-based pyrido-dipyrimidine antioxidants A and B.

Comparing ΔG_{BDE} with ΔG_{GPA} and ΔG_{IP} values, as thermodynamic parameters that determine the first step of the reaction, one can conclude that HAT is the most plausible reaction mechanism for O1 position of A and for molecule B. A molecule in position 2 in all three estimated solvents reacts following SPLET as the most plausible mechanistic pathway. The reactivity of B is almost equal to the reactivity of A-O1, and the reactivity of A-O2 is somewhat lower and predominantly follows the other mechanism compared with A-O1 and B. Considering that the reaction is favorable if its Gibbs free energy is ≤ 40 kJ/mol [8], SET-PT is not an operative reaction mechanism in any of the observed environments.

Table 1. Thermodynamic parameters of investigated mechanisms of antioxidant activity of molecules A and B (see Fig. 1).

Solvent	Molecule	HAT	SPLET		SET-PT	
		ΔG_{BDE}	ΔG_{GPA}	ΔG_{ETE}	ΔG_{IP}	ΔG_{PDE}
water	A-O1	19	64	-45	110	-91
	A-O2	139	27	111	110	28
	B	12	55	-43	103	-91
methanol	A-O1	20	66	-47	116	-96
	A-O2	138	27	112	116	22
	B	12	57	-45	109	-97
benzene	A-O1	23	107	-84	221	-198
	A-O2	131	22	110	221	-89
	B	24	99	-74	222	-198

The experimental results obtained by DPPH assay indicate a higher activity of molecule A compared to molecule B. This can be explained by the fact that molecule A

exerts its antioxidant activity via two O-H groups simultaneously. Based on the thermodynamic parameters, it can be concluded that the reactivity of the investigated mechanisms toward the DPPH radical does not depend on the nature of the solvent.

3. Conclusions

Examining the reaction mechanism of selected vanillin-based pyrido-dipyrimidine antioxidants A and B in the presence of DPPH radical, we concluded that the HAT is the operative mechanism for A in position 1 and for molecule B, in all estimated solvents. The predominant mechanism for the A molecule at position 2 is SPLET. The experimentally determined high antioxidant activity of molecule A compared to molecule B is probably due to two possible reaction positions in molecule A.

Acknowledgment

This research is funded by the Ministry of Education and Ministry of Science, Technological Development and Innovation, Republic of Serbia, Grants: No. 451-03-47/2023-01/200252 and 451-03-47/2023-01/200378.

References

- [1] F. Buron, J.Y. Mérour, M. Akssira, G. Guillaumet, S. Routier, *Recent advances in the chemistry and biology of pyridopyrimidines*, *European Journal of Medicinal Chemistry*, 95 (2015) 76–95.
- [2] S. Wang, X.-H. Yuan, S.-Q. Wang, W. Zhao, X.-B. Chen, B. Yu, *FDA-approved pyrimidine-fused bicyclic heterocycles for cancer therapy: Synthesis and clinical application*, *European Journal of Medicinal Chemistry*, 214 (2021) 113218.
- [3] L. Blaikie, G. Kay, P.K. Thoo Lin, *Synthesis and in vitro evaluation of vanillin derivatives as multi-target therapeutics for the treatment of Alzheimer's disease*, *Bioorganic and Medicinal Chemistry Letters*, 30 (2020) 127505.
- [4] N. Janković, J. Tadić, E. Milović, Z. Marković, S. Jeremić, J. Petronijević, N. Joksimović, T.T. Borović, S.N.A. Bukhari, *Investigation of the radical scavenging potential of vanillin-based pyrido-dipyrimidines: experimental and in silico approach*, *RSC Advances*, 13 (2023) 15236-15242.
- [5] Y. Zhao, D.G. Truhlar, *The M06 suite of density functionals for main group thermochemistry, thermochemical kinetics, noncovalent interactions, excited states, and transition elements: two new functionals and systematic testing of four M06-class functionals and 12 other functionals*, *Theoretical Chemistry Accounts*, 120 (2008) 215-241.
- [6] M.J. Frisch, G.W. Trucks, H.B. Schlegel, et al., *Gaussian 09, Revision A.02*, Gaussian Inc, Wallingford CT, 2009.
- [7] Y. Takano, K.N. Houk, *Benchmarking the Conductor-like Polarizable Continuum Model (CPCM) for Aqueous Solvation Free Energies of Neutral and Ionic Organic Molecules*, *Journal of Chemical Theory and Computation*, 1 (2005) 70–77.
- [8] A. Amić, Z. Marković, J.M. Dimitrić Marković, S. Jeremić, B. Lucić, D. Amić, *Free radical scavenging and COX-2 inhibition by simple colon metabolites of polyphenols: A theoretical approach*, *Computational Biology and Chemistry* 65 (2016) 45-53.

Inhibitory potential of barbarin and its platinum(II) complex towards PBP1a protein

Svetlana Jeremić^{1*}, Milan Dekić¹, Violeta Jakovljević¹, Enisa Selimović¹, Amina Gusinac²

¹ The State University of Novi Pazar, Department of Natural Sciences and Mathematics, Vuka Karadžića 9, 36300 Novi Pazar, Serbia

e-mail: sjeremic@np.ac.rs; mdekic@np.ac.rs; vjakovljevic@np.ac.rs; eselimovic@np.ac.rs

² University of Niš, Faculty of Sciences and Mathematics, Višegradska 33, 18106 Niš, Serbia

e-mail: aminag5667@gmail.com

* Corresponding author

DOI: 10.46793/ICCBi23.617J

Abstract: Some natural compounds and their metal complexes have been proven to show a significant ability to inhibit some proteins. By using *in silico* techniques, we examined how effectively the biologically active natural compound barbarin and its Pt(II) complex inhibit penicillin-binding protein 1A (PBP1a). DFT calculations are used to optimize the geometry of ligands. Molecular docking analysis is used to evaluate the binding positions, inhibition constants, and binding energies of complexes formed between ligands and the PBP1a protein. The inhibitory potency of the investigated ligands is compared to that of lactivicin, an antibiotic that is already utilized in the treatment of Gram-negative and Gram-positive bacteria. Docking research revealed that the Pt(II)-barbarin complex inhibits the PBP1a protein significantly more effectively than lactivicin, while barbarin has a similar inhibitory activity as lactivicin. The theoretically obtained results were also confirmed experimentally, by treating *Escherichia coli*, *Staphylococcus aureus*, and *Bacillus subtilis* bacteria with a solution of barbarin. Based on the obtained results, barbarin and Pt(II)-barbarin complex can be considered as candidates for further investigations with the aim of their potential application in *Streptococcus pneumoniae* therapy.

Keywords: barbarin, Pt(II)-barbarin complex, PBP1a protein, molecular docking, inhibition potency

1. Introduction

Streptococcus pneumoniae (*S. pneumoniae*) is a common respiratory pathogen that causes pneumonia, otitis media, and sepsis. This bacterium is most often treated with antibiotics such as penicillin, amoxicillin, and cephalosporins. Recent research shows that more than 25% of all invasive strains are resistant to these antibiotics, which leads to high mortality of infected patients [1]. The cell wall of Gram-positive bacteria, such as *S. pneumoniae*, is made of peptidoglycan. Penicillin-binding protein (PBP1a) catalyzes formation of the cell septum during the cycle of bacterial division and is involved in the

recombination of homologous DNA, then participates in the repair and segregation of chromosomes [2]. Inhibition of this protein would prevent the development of cells of *S. pneumonia*, which would prevent the development of diseases caused by this bacterium. Barbarin ((R)-5-phenyloxazolidine-2-thione) is a naturally occurring compound found in some *Brassicaceae* and *Resedaceae* taxa that have been commonly consumed by livestock, and occasionally by humans [3,4]. Barbarin possesses immunomodulatory, antithyroid and tyrosinase inhibitory effects [3,4]. Our study here focuses on its potency to act as PBP1a protein. It is known that platinum(II) complexes with 2-phenylpyridine derivatives show significant anticancer activity [5]. Based on this fact, the inhibitory activity of the theoretically assumed structure of the platinum(II) complex with 2-phenylpyridine, which contains barbarine in its structure: $[Pt(C^N)(barbarine)Cl]$, (where C^N = 2-phenylpyridine (ppyH) and barbarine = 5-phenyl-2-oxazolidinethione), was investigated and analyzed. The inhibitory potential of both mentioned ligands was compared with the inhibitory activity of lactivicin, a drug used in the therapy of *S. pneumoniae*, and whose mechanism of action was shown to be based on the inhibition of the PBP1a protein [6]. *E. coli*, *S. aureus* and *B. subtilis* are treated with different concentrations of barbarin solution, and the results obtained by the broth dilution method supported the theoretical results.

2. Methodology section

The structures of all estimated ligands were optimized using M062X/6-311++G(d,p) method implemented in the Gaussian09 program package [7,8]. The three-dimensional (3D) crystal structure of PBP1a was retrieved from the Protein Data Bank (PDB ID: 2C6W) [2]. AutoDock 4.0 software was applied for molecular docking simulations [9]. The used grid box had dimensions of 45 x 59 x 56 number of grid points in -x, -y, and -z directions respectively, and the grid center was at 98.799 Å x 35.214 Å x 55.068 Å coordinates. The used grid spacing was 0.375 Å. Flexible protein-ligand simulations were performed using the Lamarckian Genetic Algorithm (LGA), which treated the ligand as flexible and the protein as rigid. The visualization and analysis of the obtained results was performed using BIOVIA Discovery Studio [10]. The experimental investigation of the antibacterial activity of barbarin was carried out using the broth dilution method [11].

3. Results and discussions

Optimized structures of ligands indicate an absence of planarity. The five-membered ring of barbarin stands at an angle of 91.5° to the aromatic ring. The optimized structure of the Pt(II)-barbarin complex indicates a square-planar geometry, and the intramolecular hydrogen bond formed between the chlorine atom and the hydrogen from the N-H group of barbarin additionally stabilizes the complex.

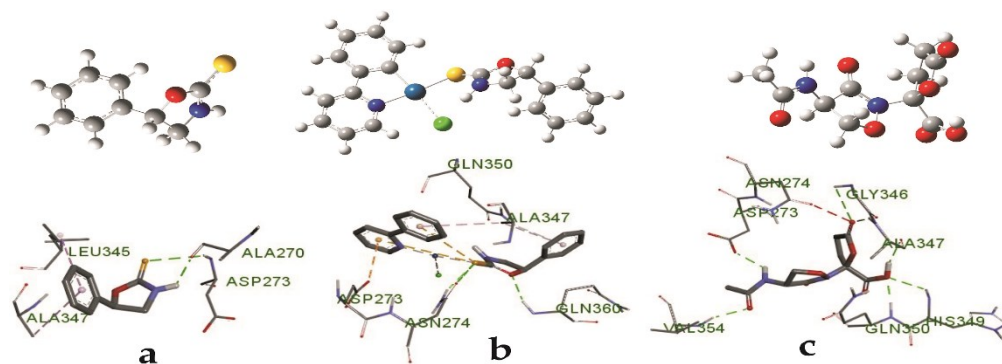


Figure 1. Optimized structures (up) and docking position with the lowest corresponding bonding energy (down) for barbarin (a), Pt(II)-barbarin complex (b), and lactivicin (c).

Molecular docking analysis indicated that all estimated ligands link with PBP1a molecule via Asp273 and Ala347 amino acids. The other bond positions are presented in Fig. 1. Barbarin links to PBP1a over conventional hydrogen bonds and π -alkyl interactions, while the Pt(II) complex achieves π -anion and π -donor hydrogen bond interactions in addition to those mentioned. The only type of bonds by which lactivicin binds to PBP1a are conventional hydrogen bonds. Based on the calculated thermodynamic parameters shown in Table 1 (energy of binding (ΔG_{bind}), intermolecular energy (ΔG_{inter}), energy of dispersion and repulsion (ΔG_{vdw}), hydrogen-bond energy (ΔG_{hbond}), desolvation (ΔG_{desolv}) energy, and inhibition constant (K_i)), it can be concluded that barbarin is an almost equally strong inhibitor of PBP1a protein as lactivicin, while the Pt(II)-barbarin complex shows a significantly higher inhibitory activity than lactivicin. The antimicrobial activity of barbarin was tested on the species *E. coli*, *S. aureus* and *B. subtilis*, and the obtained results showed that barbarin exhibits the strongest inhibitory effect on the growth of *E. coli*, and the weakest on the growth of *B. subtilis*.

Table 1. Labels a, b and c correspond to the structures of the corresponding ligands (see Fig.1). The inhibition constant values (K_i) are presented in μM . Energy values are presented in kcal/mol.

Ligand	ΔG_{bind}	K_i	ΔG_{inter}	$\Delta G_{\text{vdw+hbond+desolv}}$
a	-5.48	95.93	-5.78	-5.77
b	-9.07	0.226	-9.96	-9.97
c	-5.76	59.75	-6.96	-6.90

4. Conclusions

Based on the results of molecular docking analysis, as well as on the experimental analysis, it can be concluded that barbarin has an inhibitory activity towards PBP1a almost equal to lactivicin, while its Pt(II) complex shows significantly stronger inhibitory activity than lactivicin. Since the theoretically assumed Pt(II) complex showed high stability and inhibitory activity, for further research it would be important to synthesize it and investigate its biological activity. Barbarin, and especially its Pt(II)

complex after its detailed investigation, may be further considered as potential agents in the treatment of bacterial infections.

Acknowledgment

The authors gratefully acknowledge financial support from State University of Novi Pazar, Novi Pazar, Republic Serbia. This research is funded by the Ministry of Education and Ministry of Science, Technological Development and Innovation, Republic of Serbia, Grants: No. 451-03-47/2023-01/200252.

References

- [1] C. Doit, C. Loukil, F. Fitoussi, P. Geslin, E. Bingen, *Emergence in France of multiple clones of clinical Streptococcus pneumoniae isolates with high level resistance to amoxicillin*, *Antimicrobial Agents and Chemotherapy*, 43 (1999) 1480-1483.
- [2] C. Contreras-Martel, V. Job, A. M. Di Guilmi, T. Vernet, O. Dideberg, A. Dessen, *Crystal structure of penicillin-binding protein 1a (PBP1a) reveals a mutational hotspot implicated in beta-lactam resistance in Streptococcus pneumoniae*, *Journal of Molecular Biology*, 355 (2005) 684-696.
- [3] M. A. Greer, J. Whallon, *Antithyroid effect of barbarin (phenylthiooxazolidone), a naturally occurring compound from Barbarea*, *Proceedings of the Society for Experimental Biology and Medicine*, 107 (1961) 802-804.
- [4] N. S. Radulović, M. M. Todorovska, D. B. Zlatković, N. M. Stojanović, P. J. Randjelović, *Two goitrogenic 1,3-oxazolidine-2-thione derivatives from Brassicales taxa: Challenging identification, occurrence and immunomodulatory effects*, *Food and Chemical Toxicology* 110 (2017) 94-108.
- [5] L. Niu, G. Ren, T. Hou, X. Shen, D. Zhu, *Synthesis, structure and anticancer activity of three platinum(II) complexes with 2-phenylpyridine derivatives*, *Inorganic Chemistry Communications*, 130 (2021) 108737.
- [6] Y. Nozaki, N. Katayama, S. Harada, H. Ono, H. Okazaki, *Lactivicin, a naturally occurring non-beta-lactam antibiotic having beta-lactam-like action: biological activities and mode of action*, *The Journal of Antibiotics*, 42 (1989) 84-93.
- [7] M.J. Frisch, G.W. Trucks, H.B. Schlegel, et al., *Gaussian 09, Revision A.02*, Gaussian Inc, Wallingford CT, 2009.
- [8] Y. Zhao, D.G. Truhlar, *The M06 suite of density functionals for main group thermochemistry, thermochemical kinetics, noncovalent interactions, excited states, and transition elements: two new functionals and systematic testing of four M06-class functionals and 12 other functionals*, *Theoretical Chemistry Accounts*, 120 (2008) 215-241.
- [9] G.M. Morris, R. Huey, W. Lindstrom, M.F. Sanner, R.K. Belew, D.S. Goodsell, A.J. Olson, *AutoDock4 and AutoDockTools4: Automated docking with selective receptor flexibility*, *Journal of Computational Chemistry*, 30 (2009) 2785-2791.
- [10] D. S. Biovia, *Discovery studio modeling environment*, 2017.
- [11] National Committee for Clinical Laboratory Standard. Reference method for broth dilution antifungal susceptibility testing of yeasts Approved standard M27A. NCCLS, Wayne, PA; 1997.

Modeling ion- π interactions of transition metal complexes

Dušan P. Malenov^{1,*}, Katarina A. Čeranić², Dubravka Z. Vojislavljević-Vasilev²,
Snežana D. Zarić¹

¹ University of Belgrade, Faculty of Chemistry, Studentski trg 12-16, Belgrade, Serbia; e-mail: malenov@chem.bg.ac.rs

² Innovative center of the Faculty of Chemistry in Belgrade, Studentski trg 12-16, 11000 Belgrade, Serbia

DOI: 10.46793/ICCB23.621M

Abstract: Interactions of π -systems with ions are very important for many chemical and biological systems. In this work we show how transition metal coordination strengthens cation- π interactions, and how it makes anion- π interactions of some systems possible. The calculations showed that cation- π interactions between ferrocene and alkali metal ions are stronger than cation- π interactions of benzene. The strongest cation- π interaction is between ferrocene and Li^+ , with interaction energy of -44.0 kcal/mol, while benzene- Li^+ interaction has the energy of -36.1 kcal/mol. Cation- π interactions can also involve transition metal complexes as cations, with $[\text{Co}(\text{NH}_3)_6]^{3+}$ /benzene interaction being very strong (-31.4 kcal/mol), while $[\text{Zn}(\text{H}_2\text{O})_6]^{2+}$ /benzene interaction somewhat weaker (-14.0 kcal/mol). Anion- π interactions of unsubstituted aromatic rings without heteroatoms are possible if they are ligands in organometallic half-sandwich complexes with electron-withdrawing ligands. The anion- π interactions of such transition metal complexes with halides can reach the energy of -25.0 kcal/mol, and they are stronger than anion- π interactions of organic aromatic molecules.

Keywords: anion- π interactions, cation- π interactions, half-sandwich compounds, transition metal complexes, density functional theory

1. Introduction

Interactions of ions with π -systems are of great importance in many areas of science. Cation- π interactions have primarily found their importance in many biological systems [1], while anion- π interactions have found their application in many areas, most notably the design of receptors and materials chemistry [2].

Computational studies have shown that transition metal coordination can lead to strengthening of noncovalent interactions. Coordination of water to transition metals increases the strength of hydrogen bonds [3], while stacking interactions of metal-chelate rings are stronger than stacking interactions of organic aromatic rings [4]. Moreover, stacking interactions of aromatic ligands of sandwich and half-sandwich compounds are stronger than stacking interactions of uncoordinated aromatic rings [5].

In this proceeding, we present computational studies on cation- π and anion- π interactions involving transition metal complexes. We show that cation- π interactions

can be strengthened by transition metal coordination. Moreover, we show an interesting case of anion- π interactions that exist due to transition metal coordination and are comparable in strength with anion- π interactions of organic aromatic molecules.

2. Methodology

The energies of anion- π and cation- π interactions were calculated by keeping the monomer geometries rigid and by changing their mutual orientation to obtain the dimer geometries with the strongest interactions. The choice of methods and basis sets was based on the agreement of the applied level of theory with the gold standard CCSD(T)/CBS for the studied systems. The B97-D3/6-31++G** level was used for anion- π calculations, B3LYP/6-31++G**(C,H,M),DZVP(Fe) for cation- π interactions of ferrocene, while cation- π interactions of benzene with ammine and aqua metal complexes were calculated at B3LYP/631G*(C,H,N),LANL2DZ(Co) and MP2/def2-QZVP levels, respectively.

3. Results and discussion

Benzene cannot form anion- π interactions due to negative electrostatic potentials above its aromatic ring. Introducing heteroatoms and electron-withdrawing substituents produces areas of positive electrostatic potentials above the aromatic ring, which makes anion- π interactions possible [5]. Unsubstituted aromatic moieties without heteroatoms can also form anion- π interactions, provided that they are coordinated to transition metals in half-sandwich compounds with electron-withdrawing ligands. The electron withdrawal makes electrostatic potentials above aromatic ligands positive (Figure 1), and they are available for anion- π interactions (Figure 2) [6].

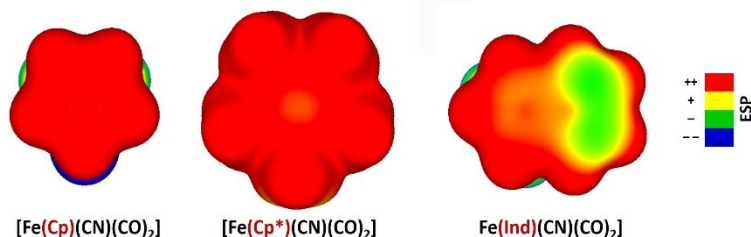


Figure 1. Electrostatic potentials of aromatic ligands in half-sandwich compounds of iron mapped on the isosurfaces defined by electron density 0.001 a.u.

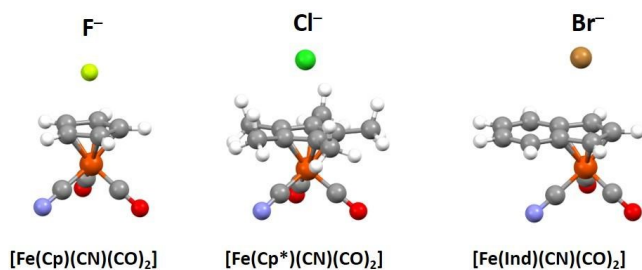


Figure 2. Anion- π interactions of halides and aromatic ligands in half-sandwich compounds.

The calculations show that anion- π interactions between iron half-sandwich compounds and halide anions (Figure 2) are stronger than anion- π interactions of organic aromatic molecules, such as hexafluorobenzene (Table 1) [6]. The anion- π interactions are particularly strong with Cp* ligand – the strongest calculated interaction is for fluoride-Cp* system, with the interaction energy of -25.0 kcal/mol (Table 1).

Table 1. Energies (in kcal/mol) of anion- π interactions of half-sandwich compounds. Interaction energies for hexafluorobenzene are given for comparison.

π -system	F ⁻	Cl ⁻	Br ⁻	Methodology
C ₆ F ₆	-20.2	-14.8	-13.6	CCSD(T)/CBS
Fe(Cp)(CN)(CO) ₂	-21.6	-17.0	-16.0	
Fe(Cp*)(CN)(CO) ₂	-25.0	-21.2	-20.5	B97-D3/6-31++G**
Fe(Ind)(CN)(CO) ₂	-21.2	-15.6	-14.8	

Due to negative electrostatic potentials above its aromatic ring, benzene forms strong cation- π interactions with alkali metal ions. This interaction is the strongest with Li⁺ (36.1 kcal/mol), and weaker, but still substantial with K⁺ (20.0 kcal/mol) [7]. Transition metal coordination increases the strength of cation- π interactions, since cation- π interactions of Li⁺ and Na⁺ with ferrocene (Figure 3) are stronger than interactions with benzene, with particularly strong ferrocene-Li⁺ interaction (-44.0 kcal/mol, Table 2) [7].

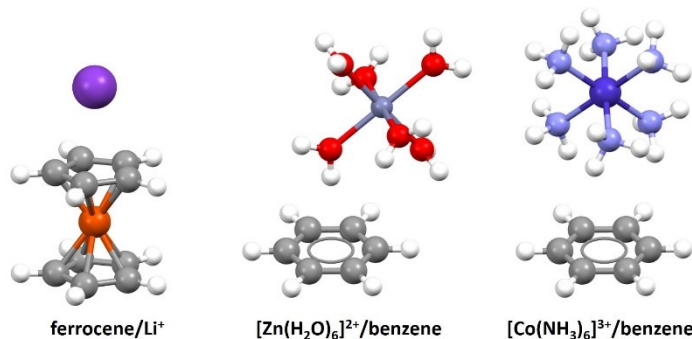


Figure 3. Cation- π interactions of some transition metal complexes.

Table 2. Energies (in kcal/mol) of cation- π interactions of selected transition metal complexes and corresponding systems that do not contain transition metal complexes.

cation	benzene	ferrocene	cation	benzene
Li ⁺	-36.1	-44.0	[Zn(H ₂ O) ₆] ²⁺	-14.0
Na ⁺	-24.2	-30.0	[Co(NH ₃) ₆] ³⁺	-31.3
K ⁺	-20.0	-20.1		

The role of cation in cation- π interactions can be played by the transition metal complex as well. These interactions are called metal-ligand NH- π (MLNH- π) and metal-ligand OH- π (MLOH- π) if N-H or O-H bond is directed toward the π -system. The first calculations were performed on MLNH- π interactions between [Co(NH₃)₆]³⁺ and benzene (Figure 3) and showed quite attractive interaction (-31.3 kcal/mol, Table 2) [8]. Also, substantially strong MLOH- π interaction was calculated between [Zn(H₂O)₆]²⁺ and benzene (Figure 3), with an interaction energy of -14.0 kcal/mol (Table 2) [9].

4. Conclusions

In this proceeding, we showed how transition metal coordination can lead to the formation of strong cation- π interactions, whether the transition metal compound is a cation or contains a π -system. More interestingly, we showed that the anion- π interactions of unsubstituted aromatic species can exist if they are coordinated to transition metal in half-sandwich compounds with electron-withdrawing ligands. Both cation- π and anion- π interactions involving transition metal complexes can be stronger than corresponding ion- π interactions of organic aromatic species.

Acknowledgment

This research is funded by the Ministry of Science, Technological Development and Innovation, Republic of Serbia, contracts 451-03-47/2023-01/200168 and 451-03-47/2023-01/200288. Part of computational resources used in this work were provided by the IT Research Computing Group at Texas A&M University at Qatar.

References

- [1] D.A. Dougherty, *The Cation- π Interaction*, *Accounts of Chemical Research*, 46 (2013) 885-893.
- [2] I.A. Rather, S.A. Qagay, R. Ali, *Emergence of anion- π interactions: The land of opportunity in supramolecular chemistry and beyond*, *Coordination Chemistry Reviews*, 415 (2020) 213327.
- [3] J.M. Andrić, M. Misini-Ignjatović, J.S. Murray, P. Politzer, S.D. Zarić, *Hydrogen Bonding between Metal-Ion Complexes and Noncoordinated Water: Electrostatic Potentials and Interaction Energies*, *ChemPhysChem*, 17 (2016) 2035-2042.
- [4] D.P. Malenov, G.V. Janjić, V.B. Medaković, M.B. Hall, S.D. Zarić, *Noncovalent bonding: Stacking interactions of chelate rings of transition metal complexes*, *Coordination Chemistry Reviews*, 345 (2017) 318-341.
- [5] D.P. Malenov, S.D. Zarić, *Stacking interactions of aromatic ligands in transition metal complexes*, *Coordination Chemistry Reviews*, 419 (2020) 213338.
- [6] D.P. Malenov, S.D. Zarić, *New Type of Aromatic π -Systems for Anion Recognition: Strong Anion- π and C-H \cdots Anion Interactions Between Halides and Aromatic Ligands in Half-Sandwich Compounds*, *Chemistry. A European Journal*, 27 (2021) 17862-17872.
- [7] A.H. Ilkhechi, J.M. Mercero, I. Silanes, M. Bolte, M. Scheibitz, H-W. Lerner, J. M. Ugalde, M. Wagner, *A Joint Experimental and Theoretical Study of Cation- π Interactions: Multiple-Decker Sandwich Complexes of Ferrocene with Alkali Metal Ions (Li^+ , Na^+ , K^+ , Rb^+ , Cs^+)*, *Journal of the American Chemical Society*, 127 (2005) 10656-10666.
- [8] S.D. Zarić, *Cation- π interaction with transition-metal complex as cation*, *Chemical Physics Letters*, 311 (1999) 77-80.
- [9] D.Z. Vojislavljević, G.V. Janjić, D.B. Ninković, A. Kapor, S.D. Zarić, *The influence of water molecule coordination onto the water-aromatic interaction. Strong interactions of water coordinating to a metal ion*, *CrystEngComm*, 15 (2013) 2099-2105.

Substituent effects on stacking interactions of aromatic ligands in organometallic compounds – chemoinformatics and quantum chemical study

Dušan P. Malenov^{1,*}, Jelena P. Blagojević Filipović², Snežana D. Zarić¹

¹ University of Belgrade, Faculty of Chemistry, Studentski trg 12-16, Belgrade, Serbia; e-mail: malenov@chem.bg.ac.rs

² Innovative center of the Faculty of Chemistry in Belgrade, Studentski trg 12-16, 11000 Belgrade, Serbia

DOI: 10.46793/ICCBi23.625M

Abstract: The effects of alkyl substituents on stacking interactions of aromatic ligands in organometallic compounds were studied on two most common ligands with substituents – pentamethylcyclopentadienyl (Cp*) and 1-methyl-4-isopropylbenzene (*p*-cymene). The analysis of geometries of interactions found in crystal structures deposited in the Cambridge Structural Database indicated that substituents are involved in interactions with aromatic rings, indicating the combination of stacking and C-H/ π interactions for both Cp* and *p*-cymene ligands. Quantum chemical calculations on *p*-cymene half-sandwich ruthenium(II) compound showed that additional C-H/ π interactions significantly strengthen stacking interactions, since the B97D2/def2-TZVP interaction energy between two *p*-cymene complexes is -7.56 kcal/mol, while the interaction energy between two corresponding benzene complexes is -3.93 kcal/mol. Ruthenium *p*-cymene complexes can engage in stacking interactions with large horizontal displacements combined with interactions between the substituents, with a significant interaction energy of -4.57 kcal/mol. These studies show that substituents strengthen stacking interactions of coordinated aromatic rings and modulate their geometries by providing additional simultaneous interactions.

Keywords: stacking interactions, C-H/ π interactions, organometallic compounds, crystal structures, density functional theory

1. Introduction

Stacking interactions are abundant in many chemical and biological systems, and they have found many applications in different areas of science. Transition metal coordination strengthens stacking interactions of aromatic molecules [1, 2]. Stacking interactions of both uncoordinated and coordinated aromatic molecules can be quite substantial at large horizontal displacements [1, 3].

Quantum chemical calculations have shown that the substitution of aromatic rings strengthens their stacking interactions, regardless of the substituent type (electron withdrawing or electron donating). This strengthening is ascribed to direct interactions of substituents with aromatic rings, and this effect is transferrable and additive [4].

Here we present our results on the effect of alkyl substituents on stacking interactions of the most common aromatic ligands in transition metal complexes – pentamethylcyclopentadienyl (Cp*) and 1-methyl-4-isopropylbenzene (*p*-cymene). The stacking interactions of these ligands were analyzed in crystal structures deposited in the Cambridge Structural Database (CSD), as well as by means of DFT calculations.

2. Results and Discussion

2.1 Stacking interactions of Cp* ligands in transition metal complexes

Crystal structures from the CSD were searched for the stacking interactions between two Cp* ligands of transition metal complexes [5]. The contact was considered a stacking interaction if the angle between the mean planes of aromatic rings of Cp* ligands was less than 10°, and if the centers of their aromatic rings were within the ellipsoid defined by a horizontal displacement (*r*) of 7.5 Å and normal distance (*R*) of 5.0 Å (Figure 1). The CSD search gave a total of 3632 stacking interactions between Cp* ligands [5]. The analysis revealed two groups of contacts, indicating two preferred stacking geometries (Figure 1).

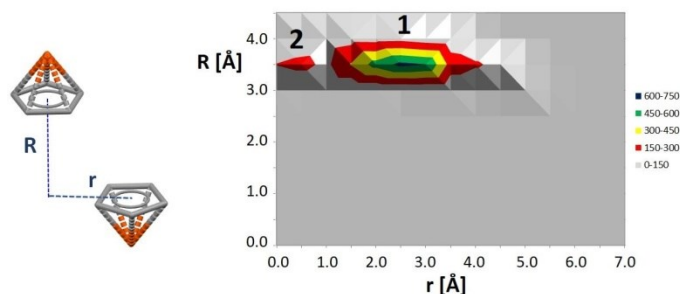


Figure 1. Correlation of horizontal displacement (*r*) and normal distance (*R*) for stacking interactions between Cp* ligands of organometallic compounds found in CSD crystal structures.

The most frequent geometry of Cp* stacking interactions has longer horizontal displacement and longer normal distances than stacking interactions of unsubstituted aromatic rings [1, 2], which indicates that substituents are involved in Cp* stacking arrangements. The most frequent arrangement involves stacking and multiple C-H/ π interactions (1, Figure 2) [5]. The second observed arrangement has very small horizontal displacements, which indicates a significant overlap of aromatic rings. In these geometries, methyl substituents of one Cp* are above the areas between methyl substituents of the other Cp* ligand (2, Figure 2).

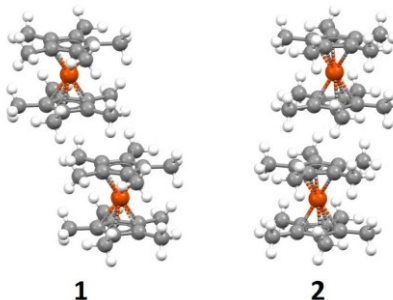


Figure 2. Two most common geometries of stacking interactions between Cp* ligands.

2.2 Stacking interactions of *p*-cymene ligands in ruthenium(II) complexes

The search for stacking interactions between *p*-cymene ligands was performed using the same criteria as for Cp* ligands (Section 2.1). A total of 679 stacking interactions were obtained from the CSD crystal structures [6]. The most frequent geometry has stacking interaction combined with C-H/ π interactions between methyl substituents and aromatic rings (**1**, Figure 3) [6]. The second most frequent is the stacking interaction combined with C-H/ π interactions of methyl groups of isopropyl substituents (**2**, Figure 3) [6]. Somewhat less frequent is the stacking with large horizontal displacement (**3**, Figure 3), which may also involve additional interactions of substituents [6].

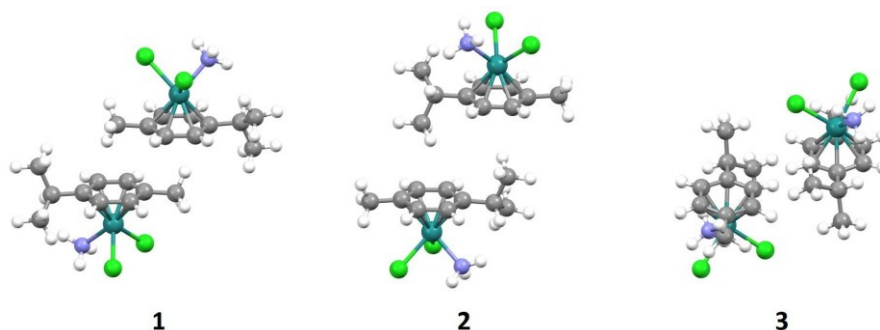


Figure 3. The most common geometries of stacking interactions between *p*-cymene ligands of ruthenium(II) complexes found in the CSD crystal structures. The presented molecule is [Ru(*p*cym)Cl₂(NH₃)], which was used for DFT calculations of interaction energies.

The DFT calculations of interaction energies were performed on [Ru(*p*-cym)Cl₂(NH₃)] complex, since the majority of *p*-cymene complexes are with ruthenium(II). In order to assess the effect of substituents on stacking interactions, additional calculations were performed on a similar complex containing benzene instead of *p*-cymene. The calculations show the significant strengthening of stacking interactions by additional C-H/ π interactions of substituents with aromatic rings (Table 1). Moreover, stacking interactions with large horizontal displacements can be significantly strengthened by additional interactions of substituents.

Table 1. Geometrical parameters (horizontal displacement *r* and normal distance *R*) and B97D2/def2-TZVP interaction energies (ΔE) of the most stable stacking interactions between *p*-cymene ruthenium(II) complexes (Figure 3). The energy of stacking interactions of corresponding benzene complexes with the same geometrical parameters are given for comparison.

system	<i>r</i> [Å]	<i>R</i> [Å]	ΔE [kcal/mol]	
			[Ru(<i>p</i> cymene)Cl ₂ (NH ₃)]	[Ru(<i>benzene</i>)Cl ₂ (NH ₃)]
1	2.5	3.4	-7.56	-3.93
2	1.5	4.6	-5.34	-1.65
3	5.0	2.2	-4.57	-2.24

3. Conclusions

The analysis of crystal structures deposited in the Cambridge Structural Database was performed in order to assess the effect of alkyl substituents on stacking interactions between Cp* and *p*-cymene ligands of organometallic compounds. It was shown that stacking interactions of these ligands are combined with C-H/ π interactions between the substituents and aromatic rings. Moreover, *p*-cymene ligands can form stacking interactions with large horizontal displacements, combined with other interactions of substituents. The DFT calculations on *p*-cymene and corresponding benzene half-sandwich compounds showed that additional C-H/ π interactions modulate interaction geometries and significantly strengthen stacking interactions of substituted aromatic ligands in transition metal complexes.

Acknowledgment

This research is funded by the Ministry of Science, Technological Development and Innovation, Republic of Serbia, contracts 451-03-47/2023-01/200168 and 451-03-47/2023-01/200288. Part of computational resources used in this work were provided by the IT Research Computing Group at Texas A&M University at Qatar.

References

- [1] D.P. Malenov, G.V. Janjić, V.B. Medaković, M.B. Hall, S.D. Zarić, *Noncovalent bonding: Stacking interactions of chelate rings of transition metal complexes*, *Coordination Chemistry Reviews*, 345 (2017) 318-341.
- [2] E.C. Lee, D. Kim, P. Jurečka, P. Tarakeshwar, P. Hobza, K.S. Kim, *Understanding of Assembly Phenomena by Aromatic–Aromatic Interactions: Benzene Dimer and the Substituted Systems*, *Journal of Physical Chemistry A*, 111 (2007) 3446–3457.
- [3] D.B. Ninković, G.V. Janjić, D.Ž. Veljković, D.N. Sredojević, S.D. Zarić, *What Are the Preferred Horizontal Displacements in Parallel Aromatic–Aromatic Interactions? Significant Interactions at Large Displacements*, *ChemPhysChem*, 12 (2011) 3511–3514.
- [4] S.E. Wheeler, *Local Nature of Substituent Effects in Stacking Interactions*, *Journal of the American Chemical Society*, 133 (2011) 10262–10274.
- [5] D.P. Malenov, J.P. Blagojević Filipović, S.D. Zarić, *Stacking interactions of the methylated cyclopentadienyl ligands in the crystal structures of transition metal complexes*, *Acta Crystallographica*, B76 (2020) 252-258.
- [6] D.P. Malenov, S.D. Zarić, *Stacking interactions between ruthenium *p*-cymene complexes: combined crystallographic and density functional study*, *CrystEngComm*, 21 (2019) 7204-7210.

Computational study on the interactions of quercetin 3-O-rutinoside with human DPP III

Dejan Agić^{1*}, Drago Bešlo¹, Bono Lučić², Sanja Tomić³, Bojana Blagojević⁴, Boris M. Popović⁴

¹ Josip Juraj Strossmayer University of Osijek, Faculty of Agrobiotechnical Sciences Osijek, Vladimira Preloga 1, 31 000 Osijek

e-mail: dagic@fazos.hr, dbeslo@fazos.hr

² Ruđer Bošković Institute, NMR Center, Bijenička cesta 54, HR-10000 Zagreb, Croatia

e-mail: lucic@irb.hr

³ Ruđer Bošković Institute, Division of Organic Chemistry and Biochemistry, Bijenička Cesta 54, 10000 Zagreb, Croatia

e-mail: sanja.tomic@irb.hr

⁴ University of Novi Sad, Faculty of Agriculture, Department of Field and Vegetable Crops, Chemistry & Biochemistry Laboratory, Trg Dositeja Obradovića 8, 21000 Novi Sad, Serbia

e-mail: bojana.blagojevic@polj.uns.ac.rs, boris.popovic@polj.uns.ac.rs

* Corresponding author

DOI: 10.46793/ICCB23.629A

Abstract: Human dipeptidyl peptidase III (hDPP III) is a zinc-dependent enzyme that participates in several pathophysiological processes. Recently, we have shown that *Prunus* fruit extracts have the potential to inhibit hDPP III and that its flavonol component, quercetin 3-O-rutinoside (**Q3r**), has the affinity to bind into the active site of the open form of hDPP III. In this study, docking and molecular dynamic (MD) simulations were performed to investigate the possible interactions between **Q3r** and the semi-closed form of hDPP III, a more common form in water. The docking results have shown that **Q3r** has a better binding affinity to the semi-closed form of hDPP III compared to its open form. Results of the MD simulations showed seven H-bonds, as well as several van der Waals and π interactions between **Q3r** and hDPP III active site residues. This computational study provided valuable insight into how this flavonol compound interacts with hDPP III and supports its observed *in vitro* inhibitory activity.

Keywords: quercetin 3-O-rutinoside, dipeptidyl peptidase III, docking, molecular dynamics simulations

1. Introduction

Quercetin 3-O-rutinoside (**Q3r**) or rutin is a polyphenolic compound widely distributed in various fruits and vegetables, and it is assumed that it has a role in enhancing defense against environmental stress in plants [1,2]. This natural product is vital in human nutrition and is of great interest due to its many reported beneficial activities (i.e., antibacterial, antioxidant, antidiabetic, anti-inflammatory,

cardioprotective) [3]. Some studies have shown that **Q3r** has the ability to create non-covalent interactions with the active site of pathologically important enzymes such as SARS-CoV-2 main protease and angiotensin-converting enzyme 2, therefore inhibiting their activity [4,5].

Human dipeptidyl peptidase III (hDPP III) is a zinc enzyme belonging to the metallopeptidase family M49, which sequentially hydrolyzes a number of biologically active peptides by cleaving dipeptides from the N-terminus of its substrates. Its role in various physiological processes, including blood pressure regulation, pain modulation, oxidative stress response and regulation of the Nrf2/KEAP1 signaling has been suggested [6]. To find new specific and potent hDPP III inhibitors (necessary to elucidate the (patho)physiological role of this peptidase) we have studied *Prunus* fruit extracts and shown that they have the potential to inhibit hDPP III and that **Q3r** has the affinity to fit into the active site of the open form of hDPP III [7]. Since the semi-closed form of hDPP III is the most preferable enzymatic form in aqueous solution [8], in this study, docking and molecular dynamic (MD) simulations were performed to explore the intermolecular interactions responsible for the observed inhibitory activity of **Q3r** against this form of hDPP III.

2. Methodology

The starting model for docking and MD simulations was built using the **Q3r** structure downloaded from PubChem, and the semi-closed form of hDPP III obtained earlier [9] by MD simulations of the open form hDPP III (PDB ID: 3FVY). MGL Tools 1.5.6 was used to prepare the structures for docking, while AutoDockVina 1.1.2 [10] was employed to determine the best ligand position at the enzyme active site. The docking site for the ligand on hDPP III was defined by the cubic box of size 80 Å centered on the catalytic zinc cation. The complex with the best docking score was chosen as the initial structure for the MD simulations. The obtained complex was parameterized by the *antechamber* and *leap* modules of the AMBERTools16, using the Amber Force Field (GAFF) and *ff14SB* force fields to parameterize the ligand and the protein, respectively. Prior to the MD simulations, the complex was optimized as described earlier [11] and simulated during 300 ns with the AMBER16 software [12]. Trajectory analysis was carried out by the AmberTools16 *cptraj* module and visually examined using Discovery Studio Visualizer, 20.1.0.19295 and Visual Molecular Dynamics 1.9.3 software.

3. Results and discussion

3.1 Docking

The best binding pose revealed that **Q3r** was located in the area of the central enzyme cleft near the lower β -sheet (residues 389–393) and enzyme active site with the minimum distance between the catalytic Zn cation and **Q3r** (oxygen atom at C2 of glucoside moiety) being ~ 4.5 Å (Figure 1 left). The obtained binding affinity of **Q3r** for

the semi-closed form (-10.0 kcal/mol) is lower than that obtained for the open form (-9.4 kcal/mol) [7], which means a better fit of **Q3r** into the active site of this hDPP III form.

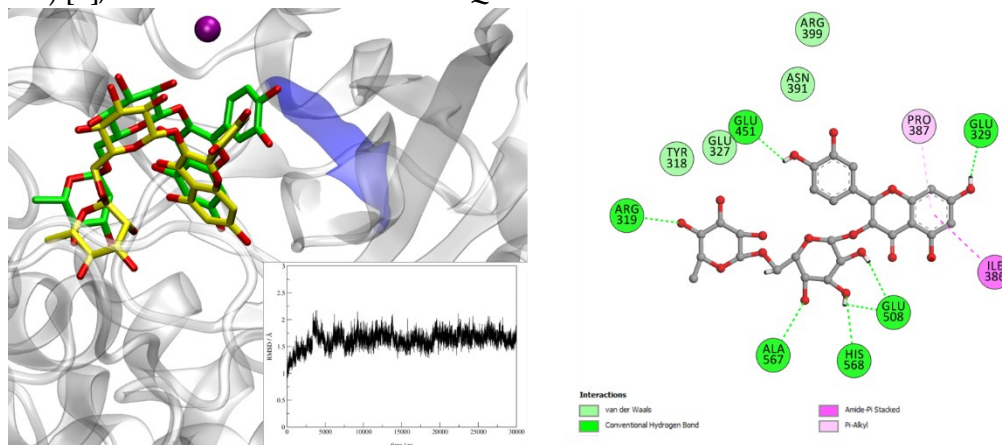


Figure 1. Left: Overlay of the hDPP III-**Q3r** complexes obtained by docking (yellow) and after 300 ns of MD simulations (green), with RMSD of the protein backbone atoms. The lower β sheet is colored in blue, and zinc cation is represented as a purple sphere. Right: 2D diagram of the most important interactions in hDPP III-**Q3r** complex obtained after 300 ns of MD simulations.

3.2 MD simulations

To establish the reliability of the best docking result, productive MD simulations were utilized to investigate the binding mode of **Q3r** in complex with the semi-closed form of hDPP III. According to the RMSD values of the protein backbone atoms, it can be seen (Figure 1 left) that the protein stability is better in the last 100 ns of MD simulations. The results of trajectory hydrogen bonds (H-bonds) analysis (Table 1 and Figure 1 right) showed that the aglycone core of **Q3r** formed H-bonds with GLU329, and GLU451, while rutinosyl moiety formed H-bonds with ARG319, GLU508, ALA567 and HIS568. Additionally, van der Waals interactions were noted between **Q3r** and protein residues TYR318, GLU327, ASN391 and ARG399. Besides, the aglycone core of **Q3r** forms amide- π stacking and π -alkyl interactions with ILE386 and PRO387, respectively, which probably helps in **Q3r** stabilization in the enzyme binding site (Figure 1 right).

Table 1. Detailed analysis of hydrogen bonds (with the occupation time > 30 %) between quercetin 3-O-rutinoside (**Q3r**) and hDPP III residues during last 100 ns of MD simulations.

Acceptor	Donor H	Donor	Fraction	Avg. Dist.	Avg. Angle
GLU_329@OE2	Q3r@H3	Q3r@O14	0.99	2.59	165.76
GLU_508@OE2	Q3r@H8	Q3r@O5	0.97	2.67	165.64
GLU_508@OE2	Q3r@H4	Q3r@O7	0.76	2.69	165.12
GLU_451@OE2	Q3r@H1	Q3r@O16	0.43	2.67	166.49
Q3r@O5	HIS_568@H	HIS_568@N	0.39	2.91	150.74
Q3r@O4	ALA_567@H	ALA_567@N	0.39	2.90	157.80
Q3r@O10	ARG_319@H	ARG_319@N	0.32	2.91	154.81

4. Conclusions

Docking studies showed that **Q3r** has a better affinity to form complex with the active site of semi-closed form of hDPP III compared to the open form. Furthermore, MD simulations indicate that **Q3r** forms seven H-bonds, as well as several van der Waals and π interactions with hDPP III active site residues. These interactions could additionally explain the observed *in vitro* **Q3r** inhibitory activity toward hDPP III.

Acknowledgment

This research is funded by the Science Fund of the Republic of Serbia, APIDES, Grant No. 7731993, and the Croatian Science Foundation, Grant No. IP-2018-01-2936.

References

- [1] M.S. Ganjaji, R.S. Karunakaran, S. Gandham, M. Balaji., *Quercetin-3-O-rutinoside from Moringa oleifera Downregulates Adipogenesis and Lipid Accumulation and Improves Glucose Uptake by Activation of AMPK/Glut-4 in 3T3-L1 Cells*, Revista Brasileira de Farmacognosia, 33 (2023) 334-343.
- [2] T. Suzuki, T. Morishita, S.J. Kim, S.U. Park, S.H. Woo, T. Noda, S. Takigawa., *Physiological roles of rutin in the buckwheat plant*, Japan Agricultural Research Quarterly, 49 (2015) 37-43.
- [3] P.K. Agrawal, C. Agrawal, G. Blunden., *Rutin: A Potential Antiviral for Repurposing as a SARS-CoV-2 Main Protease (Mpro) Inhibitor*, Natural Product Communications, 16 (2021) 1-12.
- [4] S. Das, S. Sarmah, S. Lyndem, R.A. Singha., *An investigation into the identification of potential inhibitors of SARS-CoV-2 main protease using molecular docking study*, Journal of Biomolecular Structure and Dynamics, (2021) 39 3347-3357.
- [5] L. Xiaocao, R. Raghuvanshi, F.D. Ceylan, B.W. Bolling., *Quercetin and Its Metabolites Inhibit Recombinant Human Angiotensin-Converting Enzyme 2 (ACE2) Activity*, Journal of Agricultural and, Food Chemistry, 68 (2020) 13982-13989.
- [6] M. Abramić, D. Agić., *Survey of Dipeptidyl Peptidase III Inhibitors: From Small Molecules of Microbial or Synthetic Origin to Aprotinin*, Molecules, 27 (2022) 3006.
- [7] B.M. Popović, B. Blagojević, A.Z. Kucharska, D. Agić, N. Magazin, M. Milović, A.T. Serra., *Exploring fruits from genus Prunus as a source of potential pharmaceutical agents - In vitro and in silico study*, Food Chemistry, 358 (2021) 129812.
- [8] A. Tomić, M. Berynskyy, R.C. Wade, S. Tomić., *Molecular simulations reveal that the long range fluctuations of human DPP III change upon ligand binding*, Molecular BioSystems, 11 (2015) 3068-3080.
- [9] A. Tomić, M. Gonzalez, S. Tomić, S., *The large scale conformational change of the human DPP III - substrate prefers the "closed" form*. Journal of Chemical Information and Modeling, 52 (2012) 1583-1594.
- [10] O. Trott, A.J. Olson., *AutoDock Vina: improving the speed and accuracy of docking with a new scoring function, efficient optimization, and multithreading*, Journal of Computational Chemistry, 31(2010) 455-461.
- [11] D. Agić, M. Karnaš, D. Šubarić, M. Lončarić, S. Tomić, Z. Karačić, D. Bešlo, V. Rastija, M. Molnar, B. M. Popović, M. Lisjak., *Coumarin Derivatives Act as Novel Inhibitors of Human Dipeptidyl Peptidase III: Combined In Vitro and In Silico Study*, Pharmaceuticals (Basel), 14 (2021) 540.
- [12] D.A. Case, R.M. Betz, D.S. Cerutti, T.E. Cheatham, III, T.A. Darden, R.E. Duke, T.J. Giese, H. Gohlke, A.W. Goetz, N. Homeyer, S. Izadi, P. Janowski, J. Kaus, A. Kovalenko, T.S. Lee, S. LeGrand, P. Li, C. Lin, T. Luchko, R. Luo, B. Madej, D. Mermelstein, K.M. Merz, G. Monard, H. Nguyen, H.T. Nguyen, I. Omelyan, A. Onufriev, D.R. Roe, A. Roitberg, C. Sagui, C.L. Simmerling, W.M. Botello-Smith, J. Swails, R.C. Walker, J. Wang, R.M. Wolf, X. Wu, L. Xiao and P.A. Kollman. (2016), AMBER 2016, University of California, San Francisco.

Noncovalent interactions of halogen atoms in halogenated bipyridines

Bogdan K. Pantelić¹, Snežana D. Zarić¹, Jelena M. Živković^{2*}

¹ University of Belgrade, Faculty of Chemistry, Studenski trg 12-16, 11000 Belgrade, Serbia; email: szaric@chem.bg.ac.rs

² Innovative Centre of Faculty of Chemistry, e-mail: Studenski trg 12-16, 11000 Belgrade, Serbia; andric_jelena@chem.bg.ac.rs

* Corresponding author

DOI: 10.46793/ICCB23.633P

Abstract: Noncovalent interactions of halogen atoms in halogen substituted bipyridines have been studied by analyzing crystal structures in the Cambridge Structural Database (CSD). The study included both non-coordinated and coordinated halogen substituted bipyridines. The analysis has shown that the most frequent interactions of halogens are with hydrogen and carbon atoms from the surroundings. Halogen-halogen interactions are in less than 20% for both coordinated and non-coordinated bipyridines. The distribution of $d(D_A)$ distance for coordinated and non-coordinated bipyridines depends on the position of the halogen atom; at position 1 $d(D_A)$ distance shows maxima at 3.8 – 3.9 Å, at position 2 $d(D_A)$ maxima are 3.7 - 3.8 Å and 3.6 - 3.7 Å, at position 3 $d(D_A)$ maxima are 3.3 - 3.4 Å and 3.7 - 3.8 Å, at position 4 $d(D_A)$ maxima are 3.5 - 3.6 Å and 3.7 - 3.8 Å. The distribution of α angle for all cases shows peaks at 110-120°. Since interactions are quite bent and maxima of $d(D_A)$ distances are greater than 3.3 Å, interactions are expected to be weak. The most frequent metal for coordinated bipyridines with halogens at positions 2, 3 and 4 is ruthenium while with halogens at position 1 is copper.

Keywords: CSD, bipyridines, halogens, noncovalent interactions

1. Introduction

Halogen interactions are a highly debated and important topic in crystal engineering and supramolecular chemistry [1-4]. Because of their high electronegativity halogen atoms are typically considered, in most of their derivatives, as sites of high electron density, with negative electrostatic potential. It is commonly accepted that they can form attractive interactions by functioning as the electron donor site (nucleophilic site). This is the case when they work as hydrogen bond acceptor sites.

In addition to the regions of negative electrostatic potentials, halogen atoms in some compounds can have also regions of positive electrostatic potentials. Interactions of these positive regions (electrophilic sites) are halogen bonds. Halogen bonds are a highly directional class of intermolecular interactions widely employed in chemistry and chemical biology. This linear interaction is commonly viewed to be analogous to the hydrogen bond. A recent paper has shown evidence of π -covalency being operative in

halogen bonds formed between chloride and halogenated triphenylamine-based radical cations [3].

The aim of this work was to study interactions of halogens in halogen substituted bipyridines by analyzing crystal structures in the Cambridge Structural Database (CSD). In this study interactions of halogen atoms were analysed for non-coordinated and coordinated halogen substituted bipyridines.

2. Methodology & Results

In order to get crystal structures of coordinated and non-coordinated halogenated bipyridines the CSD (Cambridge Structural Database) search was done. The halogen interactions with different atoms from surroundings were analysed for four different positions (Figure 1). The geometrical criteria were: (a) the distance between halogen atom (D) and atom from the surrounding (A) ($d(D_A)$) was less than 4.0 Å and (b) α angle (C-D-A) was larger than 110°.

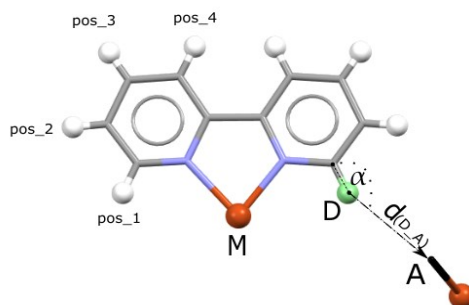


Figure 1. The geometrical parameters used for the CSD search of halogen atom interactions in halogenated bipyridines.

The distribution of $d(D_A)$ distance for coordinated and non-coordinated bipyridines at position 1 shows maxima at 3.8 – 3.9 Å, at position 2 $d(D_A)$ maxima are 3.7 - 3.8 Å and 3.6 - 3.7 Å, at position 3 $d(D_A)$ maxima are 3.3 - 3.4 Å and 3.7 - 3.8 Å, at position 4 $d(D_A)$ maxima are 3.5 - 3.6 Å and 3.7 - 3.8 Å (Figure 2). It can be noticed that the number of contacts is increasing with the increasing $d(D_A)$ distance. The distribution of α angle for all cases shows peaks at 110-120° meaning that the geometry of interaction is very bent (Figure 3).

The halogen-halogen interactions are not very frequent in analyzed D...A interaction. At position 1, the percentage of halogen-halogen interaction is 18% for coordinated and 12% for non-coordinated bipyridines. At position 2, the percentage of halogen-halogen interactions is around 10% and at position 3, the percentage of halogen-halogen interactions for non-coordinated than coordinated is 11% bipyridines. At position 4, halogen-halogen interactions are more frequent for coordinated (18%) than for non-coordinated (3%) bipyridines. The most frequent halogen atom that appears in D...A interaction (D atom) is fluorine while the most frequent A atoms are hydrogen and carbon.

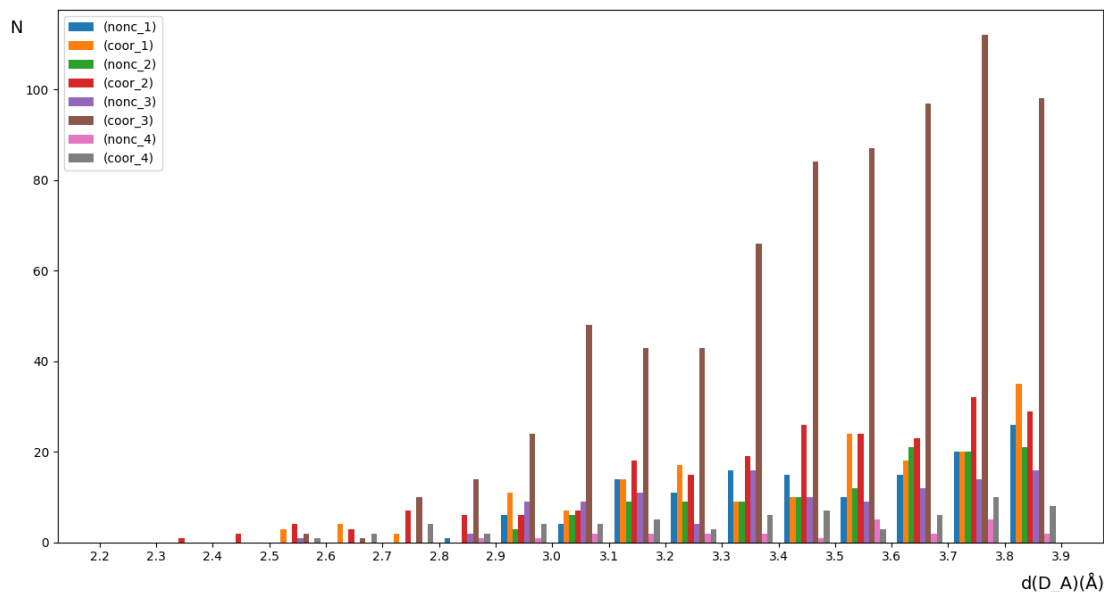


Figure 2. The distribution of $d(D_A)$ (Å) distance for non-coordinated and coordinated bipyridines at four different positions (Figure 1).

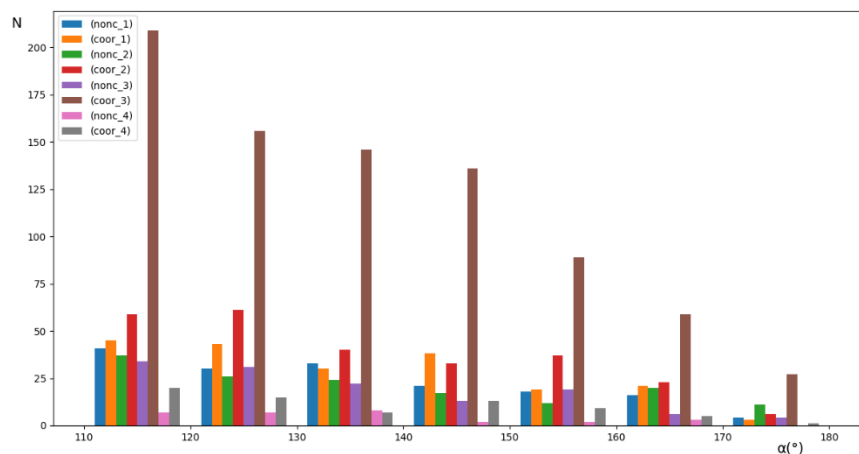


Figure 3. The distribution of α (°) angle for non-coordinated and coordinated bipyridines at four different positions (Figure 1).

The distribution of metal types for coordinated bipyridines is shown in Figure 4. The most frequent metal in complexes with bipyridines with halogen at positions 2, 3 and 4 is ruthenium while with halogens at position 1 that is copper.

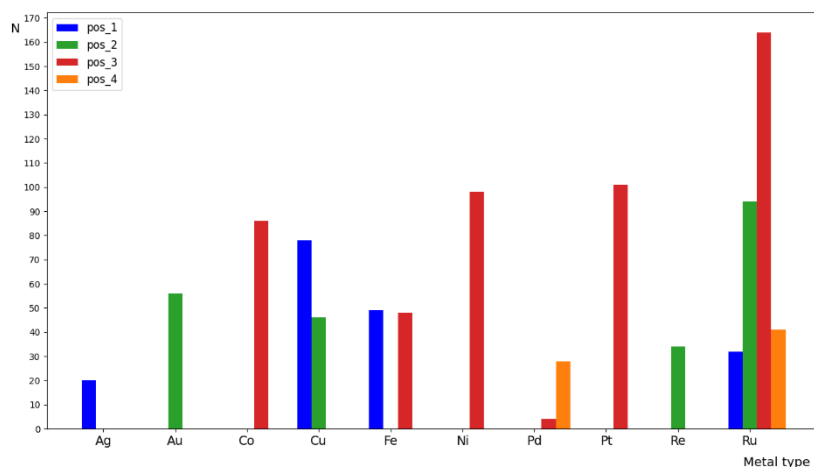


Figure 4. The distribution of metal type for coordinated bipyridines with halogen atom at four different positions (Figure 1).

3. Conclusions

The study of interactions of halogen atoms in halogenated bipyridines in crystal structures in the Cambridge Structural Database showed that the interactions of halogen atoms on halogenated bipyridines are mostly with hydrogen and carbon atoms and in smaller percentages (less than 20%) they form interactions with other halogen atoms. The distribution of $d(D_A)$ (Å) shows a tendency toward large distance while $\alpha(^{\circ})$ angle is mostly bent. This indicates weak interactions of halogens with other atoms from surroundings.

This work was supported by the Serbian Ministry of Education, Science and Technological Development (Contract numbers: 451-03-47/2023-01/200168 and 451-03-47/2023-01/200288).

References

- [1] [B. K. Saha](#), [R. V. P. Veluthaparambath](#), [V. G. Krishna](#), *Halogen...Halogen Interactions: Nature, Directionality and Applications*, Chemistry an Asian Journal, 18 (2023) 1-8.
- [2] G. Cavallo, P. Metrangolo, T. Pilati, G. Resnati, G. Terraneo, *Halogen Bond: A Long Overlooked Interaction*, Topics in Current Chemistry, 358 (2014) 1-17.
- [3] C. W. Kellett, P. Kennepohl, C.P. Berlinguette, *π covalency in the halogen bond*, Nature Communication, 11 (2020) 1-8.
- [4] K. E. Riley, J. S. Murray, J. Fanfrlík, J. Řezáč, R. J. Solá, M. C. Concha, F. M. Ramos, P. Politzer, *Halogen bond tunability II: the varying roles of electrostatic and dispersion contributions to attraction in halogen bonds*, Journal of Molecular Modeling, 19 (2013), 4651–4659.

Repulsive water-water contacts from Cambridge Structural Database

Milan R. Milovanović¹, Jelena M. Živković¹, Ivana M. Stanković², Dragan B. Ninković¹, Snežana D. Zarić^{3,*}

¹ Innovation Center of the Faculty of Chemistry, Studentski trg 12-16, Belgrade 11000, Serbia; e-mail: milovanovic@chem.bg.ac.rs, andric.jelena@chem.bg.ac.rs, dragannin@chem.bg.ac.rs

² University of Belgrade, Institute of Chemistry, Technology and Metallurgy, Njegoševa 12, Belgrade, 11000 Serbia; e-mail: ivana.stankovic@ihtm.bg.ac.rs

³ University of Belgrade, Faculty of Chemistry, Studentski trg 12-16, Belgrade 11000, Serbia; e-mail: szaric@chem.bg.ac.rs

DOI: 10.46793/ICCBi23.637M

Abstract: Water is one of the most important molecules on the Earth. Since water plays a crucial role in many life processes, it is of great importance to understand every aspect of its behavior and interactions with itself and its surroundings. It is known that water molecules can interact via classical hydrogen bonds and antiparallel interactions, with interaction energies of - 5.02 kcal/mol and -4.22 kcal/mol, respectively. Besides these attractive interactions, repulsive interactions were also noticed. In this work, we analyzed repulsive water-water contacts from the Cambridge Structural Database. All interaction energies were calculated at the so-called gold standard, i.e., CCSD(T)/CBS level of theory. It was found that among all water-water contacts, ca. 20% (2035 contacts) are repulsive with interaction energies mainly up to 2 kcal/mol. Most of these repulsive contacts do not belong to two main groups of water-water contacts. Namely, 12.8% of all repulsive contacts can be classified as classical hydrogen bonds, 2.1% to the antiparallel interactions, and the rest (85.3%) as remaining contacts. This study points out that additional attention should be paid when one deals with contacts including water or, eventually, hydrogen atoms in general.

Keywords: water, repulsive interactions, CSD, quantum chemical calculations

1. Introduction

Water is the most abundant molecule. It plays important roles in life processes: transportation of protons, protein solvation, support of polar reactions and hydration of ions. Two water molecules can interact via attractive interactions as hydrogen bonds (- 5.02 kcal/mol) [1]. Besides hydrogen bonds, antiparallel interactions have been recognized as a significant mode of interaction between water molecules. Surprisingly, nearly 20% of all attractive water-water contacts from the Cambridge Structural Database (CSD) form antiparallel interactions [2]. The results

show that the most stable geometry of antiparallel water-water interaction has an interaction energy of -4.22 kcal/mol. Besides attractive interactions between two water molecules, repulsive contacts were also noticed.

Here we present an analysis of repulsive water-water contacts from the CSD. Namely, it was found that more than 20% of all water-water contacts from CSD are repulsive. The results are shown in terms of the above-mentioned classical hydrogen bonds and antiparallel interactions.

2. Experimental section

2.1 CSD methodology

The statistical study was based on the data from the Cambridge Structural Database (CSD) [3]. Crystal structures taken into consideration satisfied the following criteria: (a) distance between two oxygen atoms $d_{OO} \leq 4.0 \text{ \AA}$; (b) a crystallographic R factor $\leq 5\%$; (c) error-free coordinates according to the criteria used in the CSD; (d) O–H bond lengths normalized using the CSD default O–H bond lengths (0.993 \AA); (e) no ionic structures; (f) no polymer structures; (g) no powder structures; (h) no disordered structures; and (i) 3D coordinates determined. An additional restriction that could minimize structures with incorrectly introduced hydrogen atoms was achieved by taking into consideration only structures with bond angles (H–O–H) in the range $96.4\text{--}112.8^\circ$ [4].

2.2 Computational methods

The interaction energies of two interacting water molecules satisfying the criteria described in the CSD methodology (9928 water dimers) were calculated at a very accurate level of theory, i.e., at CCSD(T)/CBS using the Gaussian09 program package.

3. Results and discussion

9928 water-water contacts were obtained as a result of the performed CSD search. A significant part of these contacts, i.e., 2616 contacts, are repulsive. Some repulsive contacts with short H...H or O...O contacts (581 contacts) were excluded from further consideration by applying criteria: $d_{HH} - d_{OH} < -0.6 \text{ \AA}$ or $d_{OO} - d_{HH} < 0$. After applying geometric criteria for classical hydrogen bonds ($\alpha > 120^\circ$, $d_{OH} \leq 3.0 \text{ \AA}$) and antiparallel interactions ($\beta_1 \geq 160^\circ$, $\beta_2 \geq 160^\circ$, $80^\circ \leq \alpha \leq 140^\circ$, $T_{HOHO} > 40^\circ$) [2], it was found that the 12.8% of all repulsive water-water contacts belong to the classical hydrogen bonds, 2.1% to the antiparallel interactions, and 85.3% to remaining contacts (Figure 1). There are 4 contacts that can belong to both groups of contacts. It is important to notice that some of the water-water contacts that satisfy geometrical criteria for classical hydrogen bonds are repulsive. The CCSD(T)/CBS interaction energies of most of these repulsive contacts are up to 2 kcal/mol. Larger repulsive interaction energies

(> 2 kcal/mol) are most probably caused by short H···H contacts. The existence of short H···H contacts might be a consequence of packing of water molecules within crystal structures or poorly determined hydrogen atom positions.

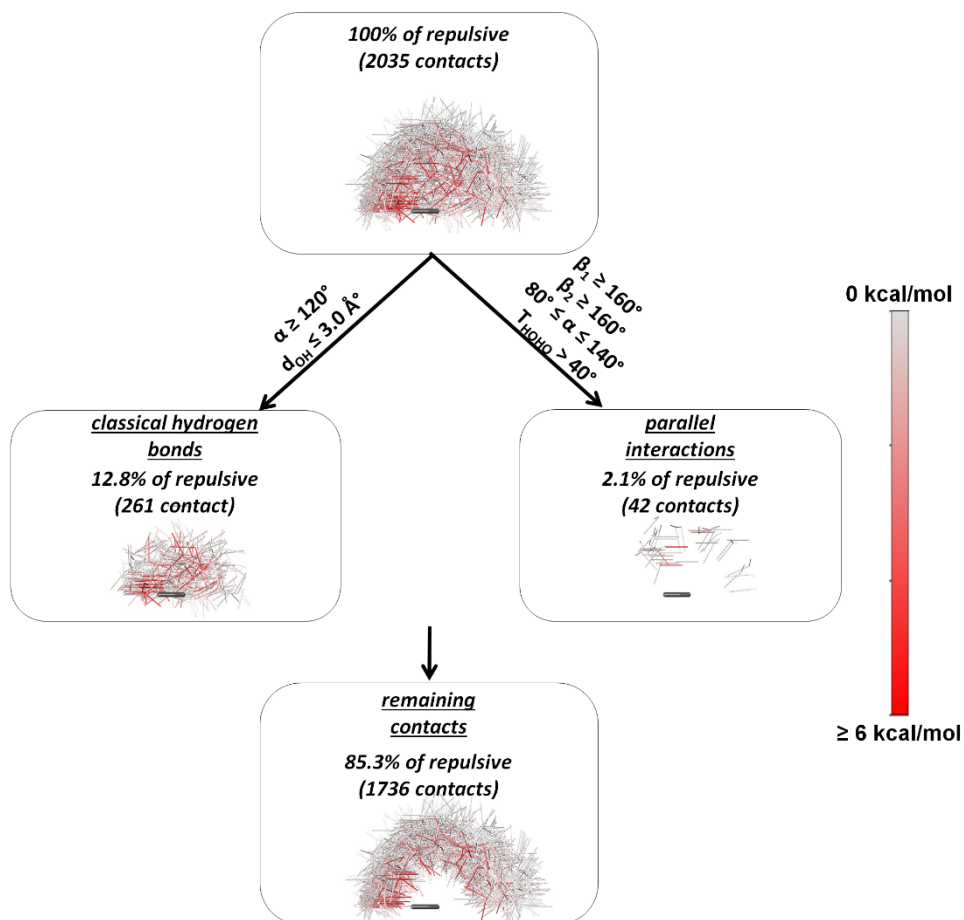


Figure 1. Sets of repulsive water–water contacts found in the CSD. In the graphical representations of water–water contacts, one water molecule was positioned in the centre (shown in dark grey). The other water molecules from every water–water contact are shown in the colour representing the CCSD(T)/CBS interaction energies, as shown in the scale.

4. Conclusions

This study aimed to point out that additional attention should be paid when contacts including hydrogen atoms are being discussed, since it was found that ca. 20% of all water-water contacts are repulsive, mostly with CCSD(T)/CBS interaction energies up to 2 kcal/mol. A cause for the overall repulsive interaction energies of these water-water contacts might be due to the existence of short H···H contacts. However, the repulsiveness of these contacts still remains unclear. On the other hand, since there is a large number of non- classified water-water contacts, one might consider that some

efforts should be dedicated to defining geometric criteria that would describe these contacts.

Acknowledgment

HPC resources and services used in this work were partially provided by the IT Research Computing group in Texas A&M University at Qatar. Authors are thankful to Marina Andrić from Free University of Bozen-Bolzano for help in data analysis. This research is funded by the Ministry of Education and Ministry of Science, Technological Development and Innovation, Republic of Serbia, Grants: Nos. 451-03-47/2023-01/200168 and 451-03-47/2023-01/200288).

References

- [1] W.M. Klopper, J.G.C.M. van Duijneveldt-van de Rijdt, F.B. van Duijneveldt, *Computational determination of equilibrium geometry and dissociation energy of the water dimer*, Phys. Chem. Chem. Phys., 2 (2000) 2227-2234..
- [2] M.R. Milovanović, I.M. Stanković, J.M. Živković, D.B. Ninković, M.B. Hall, S.D. Zarić, *Water: new aspect of hydrogen bonding in the solid state*, IUCrJ, 9 (2022) 639-647.
- [3] C.R. Groom, I.J. Bruno, M.P. Lightfoot, S.C. Ward, *The Cambridge Structural Database*, Acta Cryst., B72 (2016) 171–179.
- [4] M.R. Milovanović, J.M. Živković, D.B. Ninković, I.M. Stanković, S.D. Zarić, *How flexible is the water molecule structure? Analysis of crystal structures and the potential energy surface*, Phys. Chem. Chem. Phys., 22 (2020) 4138–4143.

Computer-aided design of new drugs against breast cancer

Milan P. Mladenović^{1,*}, Nevena M. Tomašević¹, Sanja Lj. Matic², Tamara M. Mladenović², and Rino Ragno³

¹ University of Kragujevac, Faculty of Science, Kragujevac Center for Computational Biochemistry, Department of Chemistry, Radoja Domanovića 12, 34000, Kragujevac, Serbia; e-mail: milan.mladenovic@pmf.kg.ac.rs, nevena.tomasevic@pmf.kg.ac.rs

² University of Kragujevac, Institute for Information Technologies Kragujevac, Department of Science, Jovana Cvijića bb, 34000, Kragujevac, Serbia; sanjamatic@kg.ac.rs, tamara.mladenovic@uni.kg.ac.rs

³ Sapienza University of Rome, Rome Center for Molecular Design, Department of Drug Chemistry and Technology, Piazzale Aldo Moro 5, 00185 Rome, Italy; e-mail: rino.ragno@uniroma1.it

* Corresponding author

DOI: 10.46793/ICCB23.641M

Abstract: Computational medicinal chemistry, if used properly and in accordance with the available experimental data, may provide significant support to rational drug design. Herein, an overview of the computational approaches that have been applied to an estrogen receptor α (ER α) and endowed in the rational design of pM ER α antagonists with profound anti-breast cancer activity either *in vitro* or *in vivo*, will be presented. ER α is a 17 β -estradiol inducible transcriptional regulator that initiates the RNA polymerase II-dependent transcriptional machinery, pointed for breast cancer (BC) development *via* either genomic direct or genomic indirect (*i.e.*, tethered) pathway. To develop innovative ligands, structure-based (SB) 3-D QSAR, ComBinE, and 3-D Pharmacophore studies have been undertaken from experimentally resolved partial agonists, SERMs, and SERDs within either wild-type or mutated ER α receptors. SB and ligand-based (LB) alignments gave rules to align the untested compounds. The protocols led to the development of 3DQs, CBEs, and 3DPQs compounds, further synthesized and submitted to either *in vitro* or *in vivo* assessments, upon which new leads were revealed as candidates for clinical trials.

Keywords: ER α , 3-D QSAR, COMBINE, 3-D Pharmacophore, SB and LB alignment assessment, rational design of new SERMs, synthesis, pharmacological evaluation *in vitro* and *in vivo*

1. Introduction

Breast cancer is one of the leading causes of death in women worldwide. Its development is usually associated with the binding of estrogen receptor α (ER α), as nuclear receptor (NR), to human Estrogen Response Element (*hERE*) sequence, as a promoter, initiated by the interaction of 17 β -estradiol (E₂), as a morphogen, which subsequently endows over-expression of breast proteins and cancer [1-3]. No full structure of ER α has been yet deposited at Protein Data Bank (<https://www.rcsb.org/>),

but only the crystal structures of DNA binding domain (DBD), complexed with *hERE* sequence, and ligand-binding domain (LBD), co-crystallized with a series of partial agonists/antagonists (Figure 1), are available (Table 1) [1-3].

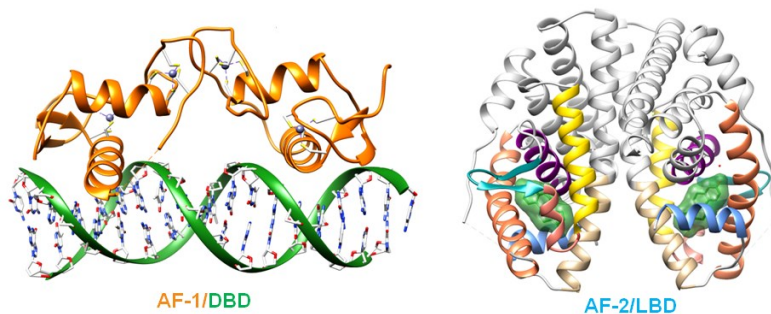


Figure 1. Left: The crystal structure of the ER α DBD domain in complex with human Estrogen Response Element (*hERE*) (PDB ID: **1HCQ**). Right: The crystal structure of the ER α LBD domain E region in complex with 17 β -estradiol (PDB ID: **1ERE**, resolution of 3.1 Å).

The LBD conveys either partial agonists', SERM's, or SERD's potency on the transcription (Table 1) and is considered a target for rational design. All the available data was used in herein-described case studies [1-3] to derive new anti-breast cancer drugs, by combining structure-based (SB) and ligand-based (LB) computational approaches with wet chemistry methods, *viz.* synthesis and pharmacological evaluation *in vitro* and *in vivo*.

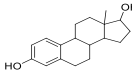
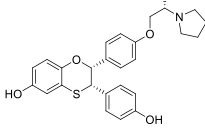
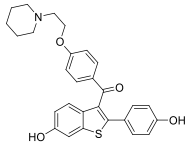
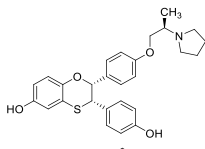
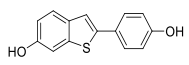
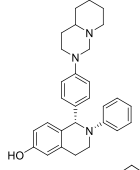
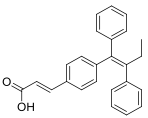
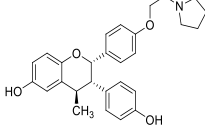
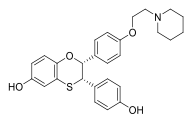
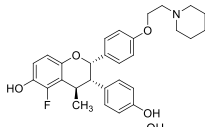
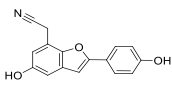
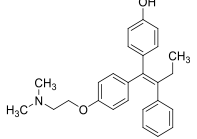
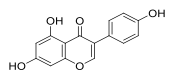
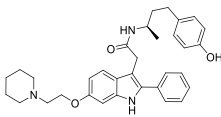
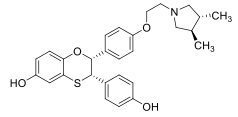
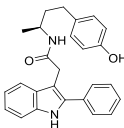
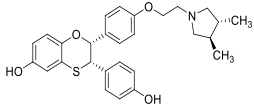
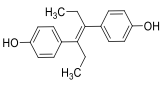
2. Materials and methods

All the experimental details regarding SB 3-D QSAR, SB ComBinE, and 3-D pharmacophore models, SB and LB alignment assessments, design, syntheses, and pharmacological protocols were reported elsewhere [1-3].

3. Results and Discussion

For designing the innovative SERMs, all the available ligand-ER α complexes have been retrieved from PDB (Table 1) and co-aligned. Upon extracting ligands, the pharmacodynamics profiles were obtained by means of generating either SB three-dimensional quantitative structure-relationships (3-D QSAR) (Figure 2), comparative molecular binding energies (ComBinE), or 3-D Pharmacophore models. The yielded molecular determinants further guided the rational design of new SERMs. Their bioactive conformations were generated by applying the consensus SB/LB alignment assessment on crystals, and upon being aligned into the active site of ER α , hits were potency predicted by means of the generated 3-D QSAR, ComBinE, and 3-D Pharmacophore models and prioritized for synthesis and pharmacological evaluation. The designed compounds were promptly synthesized and evaluated against ER α , breast cancer cell lines, and *in vivo* xenograft models, showing pM activity and optimal pharmacological profiles.

Table 1. PDB codes, ligand structures, and pharmacological profile of wild-type (WT) estrogen receptor α complexed with agonists, partial agonists, and antagonists.

PDB	Ligand structure	pIC ₅₀	PDB	Ligand structure	pIC ₅₀
1ERE PA ^a H12: CC ^b		9.24	1XP9 SERM H12: OC		8.80
1ERR SERM ^c H12: OC ^d		9.52	1XPC SERM H12: OC		8.70
1GWQ PA H12: CC		5.85	1XQC SERM H12: OC		7.20
1R5K SERD ^e H12: OC		7.40	1YIM SERM H12: OC		8.80
1SJO SERM H12: OC		9.09	1YIN SERM H12: OC		8.80
1X7E PA H12: CC		5.90	2BJ4 SERM H12: OC		8.60
1X7R PA H12: CC		8.01	2IOG SERM H12: OC		8.09
1XP1 SERM H12: OC		9.30	2IOK SERM H12: OC		9.00
1XP6 SERM H12: OC		9.30	3ERD PA H12: CC		9.48

^aPartial agonist; ^bH12: closed conformation; ^cSERM – mixed agonist/antagonist; ^dH12: open conformation; ^eSERD – full antagonist.

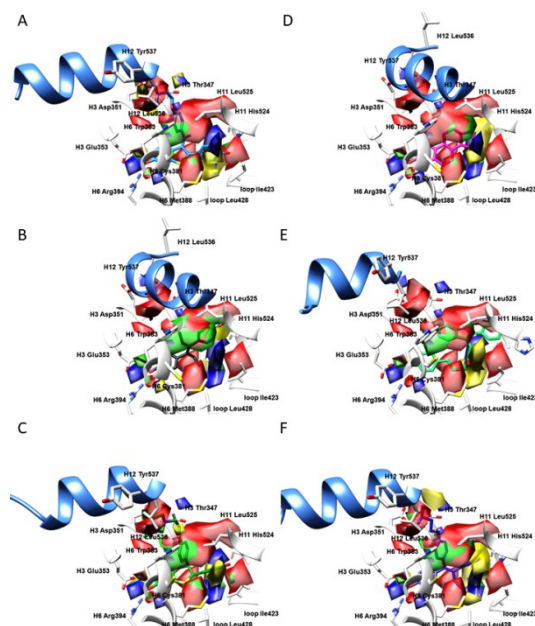


Figure 2. Representative N probe 3-D QSAR model *PLS-coefficients* contour maps (in red positive coefficients, in blue negative ones) and *Actual Activity Contribution* plots (*LACC*, positive green, negative yellow) for **1ERR** (A); **3ERD** (B); **1XP1** (C); **1ERE** (D); **2IOK** (E); **2BJ4** (F).

4. Conclusions

The applied procedures led to the development of three series of compounds, **3DQs**, **CBEs**, and **3DPQs**, characterized with pM potency either *in vitro* or *in vivo*, proving that cheminformatics tools are very useful in the rational design of new anti-breast cancer agents.

Acknowledgment

This research is funded by the Ministry of Science, Technological Development, and Innovation, Republic of Serbia, Grants: Nos. 451-03-47/2023-01/200122 and 451-03-47/2023-01/200378.

References

- [1] N. Kurtanović, N. Tomašević, S. Matic, M.M. Mitrović, D.A. Kostić, M. Sabatino, Lorenzo Antonini, R. Ragno, M. Mladenović, *Human estrogen receptor α antagonists, part 1: 3-D QSAR driven rational design of innovative coumarin-related antiestrogens as breast cancer suppressants through structure-based and ligand-based studies*, *Journal of Chemical Information and Modeling*, 61 (2021) 5028-5053.
- [2] N. Kurtanović, N. Tomašević, S. Matic, M.M. Mitrović, D.A. Kostić, M. Sabatino, Lorenzo Antonini, R. Ragno, M. Mladenović, *Human estrogen receptor α antagonists, part 2: synthesis driven by rational design, in vitro antiproliferative, and in vivo anticancer evaluation of innovative coumarin-related antiestrogens as breast cancer suppressants*, *European Journal of Medicinal Chemistry*, 227 (2022) 113869.
- [3] N. Kurtanović, N. Tomašević, S. Matic, E. Proia, M. Sabatino, L. Antonini, M. Mladenović, R. Ragno, *Human estrogen receptor alpha antagonists, part 3: 3-D Pharmacophore and 3-D QSAR guided brefeldin a hit-to-lead optimization toward new breast cancer suppressants*, *Molecules*, 27 (2022) 2823.

Stacking Interactions at Large Horizontal Displacements—Comparison of Various Ring Types

Jelena P. Blagojević Filipović¹, Dragan B. Ninković¹, Snežana D. Zarić^{2,*}

¹ Innovation Center of the Faculty of Chemistry, Studentski trg 12-16, 11000 Belgrade, Serbia; e-mail: jbfilipovic@chem.bg.ac.rs, dragannin@chem.bg.ac.rs

² University of Belgrade, Faculty of Chemistry, Studentski trg 12-16, 11000 Belgrade, Serbia; e-mail: szaric@chem.bg.ac.rs

* Corresponding author

DOI: 10.46793/ICCB23.645BF

Abstract: Noncovalent interactions at large distances play an important role in molecular recognition processes, early steps of protein folding or the design of supramolecular structures. Plateaus or even shallow minima can occur at potential energy curves of stacking interactions between certain ring types. Stacking interactions at large horizontal displacements are also frequently found in crystal structures of various rings. In this work, we discuss how horizontal displacement affects stacking interactions on the basis of interaction energy calculations and energy decomposition analysis performed by Symmetry-Adapted Perturbation Theory (SAPT). We compared aromatic/aromatic to aromatic/aliphatic stacking as well as stacking interactions involving resonance-assisted hydrogen bridged (RAHB) rings, including RAHB/RAHB and RAHB/aromatic interactions. Among RAHB rings we observed different behavior of polar and nonpolar RAHB molecules. A comparison of aromatic/aromatic and aromatic/aliphatic systems provides an insight into fundamental differences in the nature between these two interaction types. While comparing stacking involving RAHB rings we can observe the difference between polar and nonpolar RAHB rings.

Keywords: stacking at large horizontal displacements, SAPT calculations, RAHB rings

1. Introduction

Stacking interactions between aromatic rings in crystal structures are mostly formed at large horizontal displacements. In spite of being disfavoured in dimer systems, stacking at large horizontal displacement is favoured in crystal structures, since it enables the formation of additional interactions with the faces of aromatic rings [1]. Resonance-assisted hydrogen-bridged (RAHB) rings are very interesting molecules useful in synthesis and material design due to synergistic strengthening between intramolecular hydrogen bond and resonance. The stacking of RAHB rings is confirmed by crystal structure analysis and quantum-chemical calculations of interaction energies [2].

2. Methodology

Interaction energies of aromatic/aromatic and aromatic/aliphatic interactions are calculated for the most stable geometries and the horizontally displaced geometries at 5.0 Å (Figure 1a,b) by Symmetry-Adapted Perturbation Theory (SAPT2+3) method at def2-tzvpd level using PSI4 programme [3].

3. Results

Stacking interactions between benzene and cyclohexane are somewhat stronger than benzene/benzene interactions [1], however, benzene/benzene interactions preserve a much more significant portion of their strength with increasing horizontal displacements (69.6%) than the benzene/cyclohexane interactions (44.2%) (Table 1). This is the advantage of the aromatic/aromatic interactions since two aromatic rings can recognize each other at a larger range of distances. The electrostatic contribution is the main reason for the observed difference between the two systems (89.7% compared to 28.6% of the electrostatic term is preserved in the two systems, Table 1). The other energy contributions (exchange-repulsion, induction and dispersion terms) are similarly conserved in both systems (31–47%, Table 1). Electrostatic term decreases more in benzene/cyclohexane than in the benzene/benzene systems due to the direction of local C-H dipoles in the large displacement geometries which are orthogonal in benzene/cyclohexane system and antiparallel in benzene/benzene system [1].

Malonaldehyde ($\text{H}_4\text{C}_3\text{O}_2$) and two of its analogues, mononitrogen ($\text{H}_5\text{C}_3\text{NO}$) and dinitrogen ($\text{H}_4\text{C}_2\text{N}_2\text{O}$) are particularly frequent in the Cambridge Structural Database (CSD) [2]. These molecules served as model systems for the calculations of RAHB/RAHB and RAHB/benzene interaction energies. It is interesting that one of these molecules, dinitrogen analogue of malonaldehyde ($\text{H}_4\text{C}_2\text{N}_2\text{O}$), does not have a clearly pronounced dipole moment, which can be visualized from electrostatic potential maps [2]. Hence, we can compare RAHB/RAHB (Figure 1c,d) and RAHB/benzene interactions (Figure 1e,f) in case of a polar and a nonpolar RAHB molecule. The potential energy curves of RAHB/RAHB and RAHB/benzene stacking interactions were calculated along several directions. Plateaus or even shallow minima can occur at potential energy curves at large horizontal displacements, depending on the system and the direction observed [4]. A larger portion of the maximum stacking interaction strength is preserved when shifted to large displacement in the case of the nonpolar RAHB molecule ($\text{H}_4\text{C}_2\text{N}_2\text{O}$) than in the case of the polar RAHB molecule (malonaldehyde), 79.5% and 37.3% respectively for RAHB/RAHB interactions and 86.8% and 51.1% respectively for RAHB/benzene interactions. The main reason is the larger preservation of the electrostatic and induction components in the nonpolar systems than in the polar systems. Namely, the electrostatic and induction terms are more favourable at maximum energy geometries for the polar systems (Table 1) but decrease at large displacements.

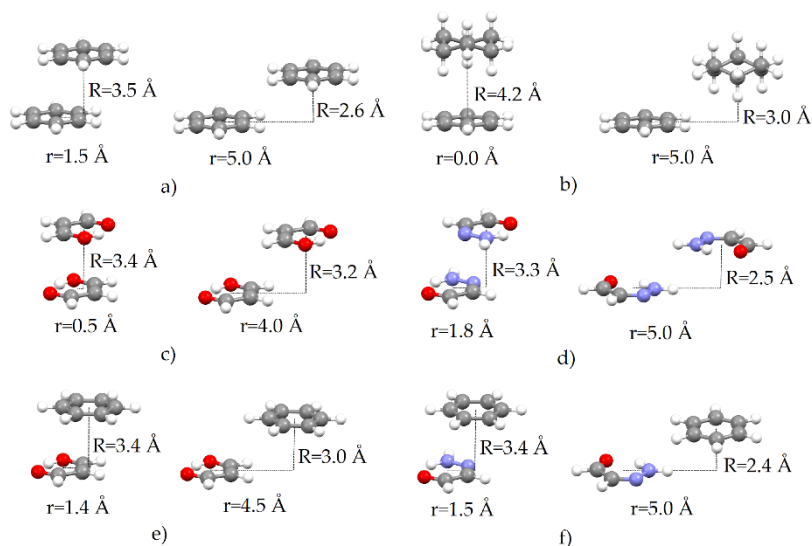


Figure 1. Model systems for the SAPT calculations with the horizontal displacements (r) and distances between the ring planes (R) indicated; the left geometry of each system corresponds to the maximum interaction energy, the right geometry is a large displacement one; a) benzene dimer; b) benzene/cyclohexane dimer; c) $\text{H}_4\text{C}_3\text{O}_2/\text{H}_4\text{C}_3\text{O}_2$ dimer; d) $\text{H}_4\text{C}_2\text{N}_2\text{O}/\text{H}_4\text{C}_2\text{N}_2\text{O}$ dimer; e) $\text{H}_4\text{C}_3\text{O}_2/\text{C}_6\text{H}_6$ dimer; f) $\text{H}_4\text{C}_2\text{N}_2\text{O}/\text{C}_6\text{H}_6$ dimer; large displacement geometries correspond to the plateaus or minima at the potential energy curves for systems c,d,e and f.

Table 1. SAPT2+3/def2-tzvpdp energy decomposition analysis of the interactions given in Figure 1. Total interaction energies and its components (ELST, electrostatics; EXCH, exchange-repulsion; IND, induction; DISP, dispersion) are given in kcal/mol.

system	ELST	EXCH	IND	DISP	TOTAL
$\text{C}_6\text{H}_6/\text{C}_6\text{H}_6$ max energy*	-1.51	6.63	-0.71	-7.22	-2.81
$\text{C}_6\text{H}_6/\text{C}_6\text{H}_6$ large displ.*	-1.36	2.85	-0.31	-3.14	-1.96
Conserved (%)	89.7	43.0	43.1	43.5	69.6
$\text{C}_6\text{H}_6/\text{C}_6\text{H}_{12}$ max energy*	-1.87	4.99	-0.63	-5.68	-3.19
$\text{C}_6\text{H}_6/\text{C}_6\text{H}_{12}$ large displ.*	-0.53	2.04	-0.20	-2.72	-1.41
Conserved (%)	28.6	40.9	31.3	47.8	44.2
$\text{H}_4\text{C}_3\text{O}_2/\text{H}_4\text{C}_3\text{O}_2$ max. energy	-3.20	5.18	-0.54	-5.80	-4.35
$\text{H}_4\text{C}_3\text{O}_2/\text{H}_4\text{C}_3\text{O}_2$ large displ.	-1.19	2.36	-0.26	-2.53	-1.63
Conserved (%)	37.2	45.5	49.1	43.6	37.3
$\text{H}_4\text{C}_2\text{N}_2\text{O}/\text{H}_4\text{C}_2\text{N}_2\text{O}$ max. energy	-1.49	5.27	-0.44	-5.61	-2.27
$\text{H}_4\text{C}_2\text{N}_2\text{O}/\text{H}_4\text{C}_2\text{N}_2\text{O}$ large displ.	-1.85	2.34	-0.39	-1.90	-1.80
Conserved (%)	124.8	44.4	88.7	33.8	79.5
$\text{H}_4\text{C}_3\text{O}_2/\text{C}_6\text{H}_6$ max. energy	-2.79	6.72	-0.81	-6.80	-3.68
$\text{H}_4\text{C}_3\text{O}_2/\text{C}_6\text{H}_6$ large displ.	-1.33	2.32	-0.27	-2.61	-1.88
Conserved (%)	47.6	34.6	33.4	38.3	51.1
$\text{H}_4\text{C}_2\text{N}_2\text{O}/\text{C}_6\text{H}_6$ max. energy	-0.81	3.32	-0.39	-4.92	-2.80
$\text{H}_4\text{C}_2\text{N}_2\text{O}/\text{C}_6\text{H}_6$ large displ.	-2.16	2.95	-0.46	-2.75	-2.43
Conserved (%)	268.2	88.8	119.5	55.8	86.8

*data taken from reference 1

On the other hand, the electrostatic term increases at large displacements of the

H₄C₂N₂O/H₄C₂N₂O dimer since the local N-H dipoles are in antiparallel contact (Figure 1d). The electrostatic term also increases in the H₄C₂N₂O/C₆H₆ dimer at large displacements due to the interaction of the N-H dipole with the electrostatic potential gradient at the edges of the benzene molecule (Figure 1f). The induction term becomes slightly more favourable at large displacement than at the most stable geometry of the H₄C₂N₂O/C₆H₆ dimer. Exchange-repulsion term decreases more in the case of H₄C₃O₂/C₆H₆ than in the case of H₄C₂N₂O/C₆H₆ dimer. Dispersion term decreases in all systems upon shifting to large displacements due to the smaller contact area of the interacting fragments.

4. Conclusions

Significant stacking interactions occur at large horizontal displacements of certain systems and they sometimes correspond to energy minima or the plateaus on the potential energy curves. Comparing benzene/benzene and benzene/cyclohexane systems the benzene/benzene interaction preserves more of its strength upon horizontal displacement due to the slower decrease of electrostatic term. Both RAHB/RAHB and RAHB/benzene interactions are stronger in the case of a polar RAHB molecule but conserve a smaller portion of their strength at large displacements mostly due to the larger decrease of the electrostatics and induction terms.

Acknowledgment

This research is funded by the Ministry of Education and Ministry of Science, Technological Development and Innovation, Republic of Serbia, Grant 172065 and Contract numbers: 451-03-47/2023-01/200168 and 451-03-47/2023-01/200288.

References

- [1] D. B. Ninković, J. P. Blagojević Filipović, M. B. Hall, E. N. Brothers, S. D. Zarić, *What Is Special about Aromatic–Aromatic Interactions? Significant Attraction at Large Horizontal Displacement*, ACS Central Science, 6 (2020) 420–425.
- [2] J. P. Blagojević Filipović, M. B. Hall, S. D. Zarić, *Stacking Interactions of Resonance-Assisted Hydrogen-Bridged rings. A Systematic Study of Crystal Structures and Quantum-Chemical Calculations*, Cryst. Growth Des, 19 (2019) 5619–5628.
- [3] R. M. Parrish et al. *PSI4 1.1: An Open-Source Electronic Structure Program Emphasizing Automation, Advanced Libraries, and Interoperability*, J. Chem. Theory Comput. 13 (2017) 3185–3197.
- [4] J. P. Blagojević Filipović, S. D. Zarić, *Significant Stacking Interactions of Resonance-Assisted Hydrogen-Bridged (RAHB) Rings at Large Horizontal Displacements*, Cryst. Growth Des. 21 (2021) 4947–4958.

Influence of Coordination on OH/ π and NH/ π Interactions

Jelena P. Blagojević Filipović¹, Dubravka Z. Vojislavljević-Vasilev¹, Snežana D. Zarić^{2,*}

¹ Innovation Center of the Faculty of Chemistry, Studentski trg 12-16, 11000 Belgrade, Serbia; e-mail: jbfilipovic@chem.bg.ac.rs, dubravkav@chem.bg.ac.rs

² Faculty of Chemistry, University of Belgrade, Studentski trg 12-16, 11000 Belgrade, Serbia; e-mail: szaric@chem.bg.ac.rs

* Corresponding author

DOI: 10.46793/ICCB23.649BF

Abstract: The interactions of noncoordinated water or ammonia molecules with aromatic rings, as well as coordinated water or coordinated ammonia molecules with aromatic rings have been investigated by searching the Cambridge Structural Database (CSD) and through quantum-chemical calculations. The data from the CSD show that for noncoordinated systems distances between the interacting fragments are the shortest in case of negative C₆-aromatic groups and the longest in case of positive C₆-aromatic groups. In the case of contacts between coordinated water or ammonia molecules and C₆-aromatic group, oppositely charged fragments are mutually closer than the neutral fragments. The DFT calculations for the water/benzene system yield an interaction energy of -2.97 kcal/mol, while for the [Zn(H₂O)₆]²⁺/C₆H₆ system the interaction energy is -14.72 kcal/mol. For the ammonia/benzene system, the DFT calculations yield an interaction energy of -2.28 kcal/mol, while for the [Zn(NH₃)₆]²⁺/C₆H₆ system it is -15.50 kcal/mol. The results show that there is an influence of water or ammonia coordination on OH/ π or NH/ π interactions; the interactions of coordinated species are significantly stronger. OH/ π and NH/ π interactions are comparable in both cases. OH/ π interactions are slightly stronger than NH/ π interactions in the case of noncoordinated molecules due to a higher partially positive charge on the hydrogen atom of the water molecule, but this is not necessarily the case for the coordinated molecules due to additional interactions that can occur between the benzene ring and the other ligands present in the complex.

Keywords: OH/ π interactions, NH/ π interactions, CSD, quantum chemical calculations non-covalent interactions, metal complexes

1. Introduction

Interaction of water molecules with aromatic systems is of large importance in many systems from biological molecules to materials. The results show the influence of water coordination to a metal ion on OH/ π interactions; interactions of coordinated water are significantly stronger even if the aqua complex is neutral [1]. Aromatic ring/ammonia dimers are also well studied systems. NH/ π interactions of the coordinated ammonia

were studied by analyzing crystal structures deposited in the Cambridge Structural Database (CSD) and by quantum chemical calculations [2].

2. Methodology

The Cambridge Structural Database (CSD) was searched for the intermolecular OH/ π and NH/ π interactions of the noncoordinated and coordinated water or noncoordinated and coordinated ammonia with C₆-aryl groups. The structure was considered a hit if the distance (*d*) between the interacting hydrogen atom H_i and the center of the C₆-aryl ring (Ω) was less than 3.5 Å, the angle α was larger than 110° and the angle β smaller than 30° for water/C₆-aryl contacts (Figure 1a), or the distance *d* was smaller than 4.5 Å, the angle α was between 90 and 180° and the angle β was smaller than 50° for ammonia/C₆-aryl contacts (Figure 1b).

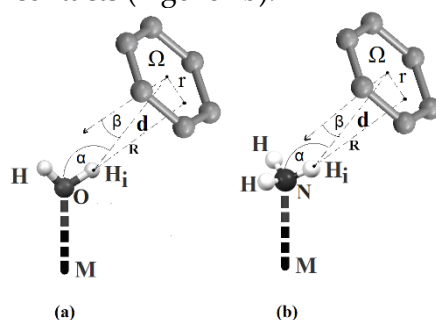


Figure 1. The geometric parameters describing OH/ π and NH/ π interactions of the water and ammonia in case of the noncoordinated molecules and the molecules coordinated to any metal atom (*M*). Ω is the center of the aromatic ring, *d* is the distance between Ω and hydrogen atom H_i of water or ammonia molecule. α is the O–H_i... Ω angle for coordinated and noncoordinated water systems and N–H_i... Ω angle for coordinated and noncoordinated ammonia systems, β is the angle between the H_i... Ω direction and the normal to the C₆-aryl ring passing through the ring center Ω . The offset *r* is the distance between the ring center Ω and the projection of the H_i atom on the ring plane. *R* is the normal distance between H_i atom and the ring plane.

In order to obtain interaction energies of the noncoordinated and coordinated water and ammonia molecules with the benzene ring we performed the calculation of the interaction energy on model structures given in Figure 2. The energies are calculated using a Gaussian series of programs [3] at B3LYP/def2TZVP level with a D3 version of Grimme dispersion with Becke-Johnson damping [4] and the basis set superposition error correction included [5].

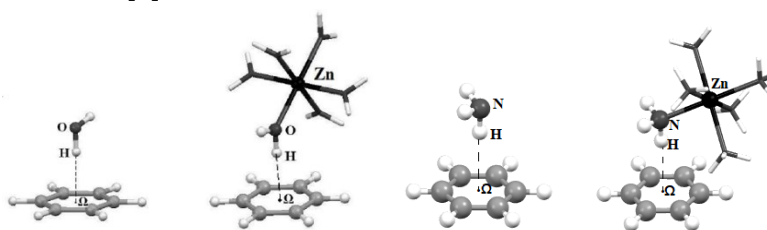


Figure 2. Model systems for OH/ π interactions of the coordinated and noncoordinated water and NH/ π interactions of the coordinated and noncoordinated ammonia used for calculations.

3. Results

Since charge of the interacting species have influence on OH/ π interactions, 644 interactions of noncoordinated water that are found by the CSD search were separated into three groups depending on the charge of the species. There is a tendency towards shorter d distances if the aryl groups are negative. The distances d are the longest for positive aryl groups. The contacts between the coordinated water molecule and the C₆-aryl group were separated into two groups, a group of 71 contacts with neutral species and a group of 54 contacts where both aqua complex and aryl group are charged. Shorter d distances in systems with opposite charge indicate stronger interactions than in the case of neutral species [1].

We found 41 contacts of noncoordinated NH₃ molecule and a C₆-aryl ring and 332 contacts with only one amine ligand interacting with a C₆-aryl ring. The distribution of the distance d for NH/ π interactions indicates that these distances are longer in systems with a neutral aryl group. When the aryl group is a part of a negative species, the distances are shorter. The shortest distance d for the contacts between the coordinated ammonia and the C₆-aryl group are found in the systems with oppositely charged species, which indicates significantly stronger interactions. Comparison of NH/ π of coordinated and noncoordinated ammonia shows that the interacting H_i atoms are closer to the aryl group when the amine group is coordinated [2].

The calculation results show that the coordination of both water and ammonia molecules to a metal substantially strengthens the interactions with benzene. Namely, the interaction energies of noncoordinated water and ammonia molecules are -2.97 kcal/mol and -2.28 kcal/mol, respectively, while for the coordinated water and ammonia the interactions are much stronger, -14.72 and -15.50 kcal, respectively (Table 1). OH/ π interaction in water/benzene and NH/ π interaction in ammonia/benzene systems are of comparable strength, although OH/ π interaction is slightly stronger (Table 1) due to higher electronegativity of the oxygen than the nitrogen atom, which leads to the more partially positive interacting hydrogen atom. Aqua and amine complexes also form similarly strong OH/ π and NH/ π interactions (Table 1), but the interactions are more difficult to compare in this case due to the presence of side interactions between the benzene ring and the other ligands present in the metal complex. The side interactions are more pronounced in the amine complex, which leads to a slightly stronger interaction (-15.50 kcal/mol, Table 1).

Table 1. Interaction energies (ΔE) and normal distances (R) for the most stable dimers of the noncoordinated and coordinated water and ammonia molecules and the benzene molecule.

Model systems	ΔE (kcal/mol)	R (Å)
H ₂ O/C ₆ H ₆	-2.97	2.7
[Zn(H ₂ O) ₆] ²⁺ /C ₆ H ₆	-14.72	2.3
NH ₃ /C ₆ H ₆	-2.28	2.6
[Zn(NH ₃) ₆] ²⁺ /C ₆ H ₆	-15.50	2.4

4. Conclusions

In summary, the results show a significant influence of charge of the interacting fragments on OH/ π and NH/ π contacts in the CSD, since distances between the interacting fragments are the shortest in the case of negative aryl groups interacting with water and ammonia molecules and the longest in case of positive aryl groups. Oppositely charged species are closer than neutral species in the CSD in case of contacts between the coordinated water or ammonia molecules and the aryl group. The calculated interaction energies on dimer model systems are much higher in the case of the coordinated water and ammonia molecules. OH/ π and NH/ π interactions are of comparable strength for the noncoordinated as well as for the coordinated molecules. Partial charge is more positive on hydrogen atoms of the water molecule than the ammonia molecule, which leads to a slightly stronger interaction. Although the interaction is slightly stronger in the case of amine than the aqua complex, these interactions are more difficult to compare due to the additional interactions of the benzene ring with the other ligands present in the metal complex.

Acknowledgment

This research is funded by the Ministry of Education and Ministry of Science, Technological Development and Innovation, Republic of Serbia, Contract numbers: 451-03-47/2023-01/200168 and 451-03-47/2023-01/200288.

References

- [1] D. Z. Vojislavljević, G. V. Janjić, D. B. Ninković, A. Kapor, S. D. Zarić, *The Influence of Water Molecule Coordination onto the Water–Aromatic Interaction. Strong Interactions of Water Coordinating to a Metal Ion*, *CrystEngComm*, 15 (2013) 2099–2105.
- [2] J. P. Blagojević Filipović, D. Z. Vojislavljević-Vasilev, S. D. Zarić, *Crystallographic and Quantum Chemical Study of NH/ π Interactions of Metal Ammine Complexes with Aromatic Rings in the Second Coordination sphere*, submitted.
- [3] M. J. Frisch, G. W. Trucks, H. B. Schlegel, G. E. Scuseria, M. A. Robb, J. R. Cheeseman, G. Scalmani, V. Barone, G. A. Petersson, H. Nakatsuji et al. *Gaussian 09, revision D.01*; Gaussian, Inc. (2016).
- [4] S. Grimme, S. Ehrlich, L. Goerigk, *Effect of the damping function in dispersion corrected density functional theory*, *J. Comput. Chem*, 32 (2011) 1456–1465.
- [5] S. F. Boys, F. Bernardi, *The Calculation of Small Molecular Interactions by the Differences of Separate Total Energies. Some Procedures with Reduced Errors*, *Mol. Phys*, 19 (1970) 553–566.

Relativistic DFT calculation and their effect on the accuracy of results

Marko D. Radovanović^{1*}, Ignjat Filipović¹, Maja Djukić¹, Marija Ristić¹, Matija Zlatar², Zoran D. Matović¹

¹ University of Kragujevac, Faculty of Science, Department of Chemistry, Radoja Domanovića 12, 34000 Kragujevac, Republic of Serbia; e-mail: marko.radovanovic@pmf.kg.ac.rs, ignjat.filipovic@pmf.kg.ac.rs, maja.djukic@pmf.kg.ac.rs, marija.jeremic@pmf.kg.ac.rs, zoran.matovic@pmf.kg.ac.rs

² University of Belgrade – Institute of Chemistry, Technology and Metallurgy, Njegoševa 12, 11000 Belgrade, Republic of Serbia; e-mail matija.zlatar@ihm.bg.ac.rs

* Corresponding author

DOI: 10.46793/ICCB23.653R

Abstract: This study explores the significance of density functional theory (DFT) calculations with relativistic effects for two ethylenediaminetetraacetate (edta) type complexes: *trans*(O₅)-[M(eddadp)]⁻ (M = Rh³⁺, Co³⁺). Relativistic effects affect the electronic structure of a molecule and, thus, its chemical and spectroscopic properties. With the use of scalar relativistic corrections (SR-ZORA), as implemented in the ADF package, with the B3LYP functional, the TZP basis set and the COSMO solvation model, structural analyses show improved predictions for the geometries of both complexes. In the case of the Rh³⁺ complex, the differences in metal-ligand bond lengths with and without the relativistic effects were small. In the case of the Co³⁺ complex, the changes in metal-ligand bond lengths due to the relativistic effects were slightly more pronounced. Compared to experimental values, excitation energies are better when including relativistic corrections, especially for the Rh³⁺ complex. These results indicate the importance of relativistic DFT calculations for heavy element compounds.

Keywords: DFT, Relativistics, ZORA, [Rh(eddadp)]⁻, [Co(eddadp)]⁻

1. Introduction

Chemistry and physics are tightly interconnected, and fundamental ideas and laws of physics often find rapid application in chemistry. Einstein's theory of special relativity, proposed in 1905, was one of the most significant breakthroughs in physics. For a long time, it was thought this theory would not significantly impact chemistry. This view changed in the 1970s when it was realized that (nonrelativistic) Schrodinger quantum mechanics yields results on molecular properties that differ considerably from experimental results, particularly for heavy element compounds [1]. As the atomic number increases, the electron velocities approach a significant fraction of the speed of light, leading to a relativistic increase in mass and by that changing the energies of orbitals [1]. As a result, relativistic effects influence compounds' electronic structure, leading to deviations from nonrelativistic predictions [2]. Irregularities in the trends in

the periodic table of elements, such as the yellow color of gold [3], the melting point of mercury [4], and the voltage of lead batteries [5], are attributed to relativistic effects.

While successful for many chemical systems, traditional nonrelativistic (NR) Density Functional Theory (DFT) calculation falls short in describing the behavior of heavy element-containing compounds by neglecting the relativistic effects [6]. Thus, relativistic corrections for heavy-element compounds are essential to model their properties accurately.

In this study, we aim to highlight the importance of relativistic DFT calculations through a comparative analysis of the structural and spectroscopic properties of two ethylenediaminetetraacetate (edta) - type complexes with respect to the atomic number of the central metal ion. Specifically, we investigated the *trans*(O₅)-[M(eddadp)]⁻ (M = Rh³⁺, Co³⁺; eddadp⁴⁻ = ethylenediamine-N,N-diacetate-N'N'-dipropionat) complexes (**Figure 1**) and compared results with available experimental data.

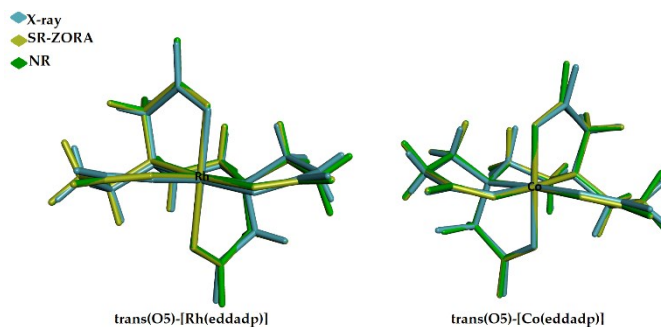


Figure 3. Overlay of X-ray structure, SR-ZORA optimized and NR optimized structures.

2. Methods

All DFT calculations were carried out by using the Amsterdam Density Functional (ADF) code, version 2017.01 [7], incorporating scalar relativistic (SR) corrections via the Zero Order Relativistic Approximation (ZORA) [8]. The hybrid B3LYP functional [9] and the all-electron TZP basis set for all atoms were used. Calculations were carried out with water as a solvent using the Conductor-like Screening solvation model (COSMO) [10].

The Ligand Field Density Functional Theory (LFDFT) [Ref] was used to study the excited state energies. LFDFT calculations were performed on the structures determined by geometry optimizations and X-ray structures. The SR-ZORA-B3LYP/TZP(COSMO-water) level of theory was used for LFDFT calculations.

The calculations were also performed without the SR corrections to see the influence of the relativistic effects (NR calculations).

3. Results and discussions

Structural data for X-ray, SR-ZORA-optimized, and NR-optimized geometries are presented in Table 1. For both complexes, SR-ZORA improves the accuracy of the structural predictions. The metal-ligand (M-L) bond lengths in both complexes are shorter when SR calculations are employed. M-L bond lengths are similar with and without relativistic effects for the Rh³⁺ complex, while these differences are more

pronounced for the Co^{3+} complex. However, the root mean square deviation (RMSD) of all atoms between X-ray and optimized structures, Table 1, indicates that relativistic effects cause slightly more distinct structural changes in the case of the Rh^{3+} complex.

The energies of the excited states calculated by LFDFT corresponding to the spin-allowed transitions are given in Table 2 and compared with the available experimental values. Relativistic effects are important for the accuracy of computed transitions, Table 2. In the case of a unified effect of relativistic on geometry and excited state energies, compared to NR calculations, MAE shows a significant improvement in the case of the Rh^{3+} complex.

Table 1. Comparison of structural data of X-ray and optimized geometries.

	Refs.	X-ray	SR-ZORA	NR	
<i>trans</i> (O5)-[Co(eddadp)]	[11]	average (Co-N)	1.948	1.986	1.992
		average (Co-O) ^[a]	1.926	1.926	1.932
		average (Co-O) ^[b]	1.892	1.910	1.915
		RMSD (Å) ^[c]		0.167	0.168
<i>trans</i> (O5)-[Rh(eddadp)]	[12]	average (Rh-N)	2.022	2.078	2.082
		average (Rh-O) ^[a]	2.045	2.070	2.073
		average (Rh-O) ^[b]	2.008	2.048	2.050
		RMSD (Å) ^[c]		0.199	0.203

[a] Average length of M-O (M = Rh, Co) of equatorial oxygen; [b] Average length of M-O (M = Rh, Co) of axial oxygen [c] RMSD is the root mean square deviation of all atoms overlaid X-ray and DFT optimized geometries.

Table 2. Energies (10^3 cm^{-1}) of the singlet excited states from LFDFT and comparison with available experimental data.

Transition ^[c]	<i>trans</i> (O5)-[Co(eddadp)]					<i>trans</i> (O5)-[Rh(eddadp)]				
	x-ray ^[a]	x-ray ^[b]	Opt ^[a, d]	Opt ^[b, e]	Exp.[13]	x-ray ^[a]	x-ray ^[b]	Opt ^[a]	Opt ^[b]	Exp.[13]
$^1\text{A}_{1g} \rightarrow ^1\text{T}_{1g}$	15.59	15.44	14.94	14.49	18.55	26.18	26.18	23.53	22.54	26.45
	16.36	16.20	15.04	14.60		26.79	26.30	23.95	22.98	
	16.46	16.25	15.16	14.77		28.07	27.73	25.16	24.12	
$^1\text{A}_{1g} \rightarrow ^1\text{T}_{2g}$	23.12	22.93	22.03	21.53	25.64	33.55	33.44	30.67	29.52	33.89
	23.98	23.79	22.76	22.24		34.06	33.82	31.10	30.06	
	24.89	24.67	24.45	23.92		36.27	36.03	33.96	32.80	
MAE ^[f]	2.03	2.22	3.03	3.50		0.85	0.96	3.12	4.17	

[a] SR-ZORA LFDFT calculations; [b] NR LFDFT calculation; [c] Oh point group assignment; [d] SR-ZORA geometry optimization [e] NR geometry optimization; [f] Mean average error in 10^3 cm^{-1} .

3. Conclusions

In conclusion, scalar-relativistic corrections in DFT calculations are crucial for accurately predicting the chemical properties of heavy-element complexes. By taking the effects of relativity into account, we can obtain more accurate results and better understand the properties of these molecules.

Acknowledgment

This research is funded by the Ministry of Science, Technological Development and Innovation, Republic of Serbia, Grants: No. 451-03-47/2023-01/200122, 451-03-47/2023-01/200026. This research was supported by the Science Fund of the Republic of Serbia, #7750288, Tailoring Molecular Magnets and Catalysts Based on Transition Metal Complexes – TMMagCat.

References

- [1] Pyper, N. C., et al., *Relativity and The Periodic Table*, Philosophical Transactions of the Royal Society A: Mathematical, Physical and Engineering Sciences, 378 (2020) no. 2180, 20190305.
- [2] J. Autschbach, *Perspective: Relativistic effect*, The Journal of Chemical Physics, 136 (2012), 150902
- [3] P. Schwerdtfeger, *Relativistic Effect in Properties of Gold*, Heteroatom Chemistry 13 (2002) 6 578-584
- [4] Calvo, F. A., Pahl, E., Wormit, M., Schwerdtfeger, P. (2013). *Evidence For Low-temperature Melting Of Mercury Owing To Relativity*. Angewante Chemie International Edition, 52 (2013), 7583-7585.
- [5] Ahuja, R., Blomqvist, A., Larsson, P., Pykkö, P., Zaleski-Ejgierd, P., *Relativity and The Lead-acid Battery*. Physical Review Letters, 106 (2011) 018301.
- [6] Demissie, T. B. (2017). *Relativistic Effects On the Nmr Parameters Of Si, Ge, Sn, And Pb Alkynyl Compounds: Scalar Versus Spin-orbit Effects*. The Journal of Chemical Physics, 147 (2017) 174301.
- [7] G. te Velde, F. M. Bickelhaupt, E. J. Baerends, C. Fonseca Guerra, S. J. A. van Gisbergen, J. G. Snijders, T. Ziegler, *Chemistry with ADF*, Journal of Computational chemistry 22 (2001) 931–967
- [8] E. van Lenthe, E.-J. J. Baerends, J. G. Snijders, *The zero-order regular approximation for relativistic effects: The effect of spin-orbit coupling in closed shell molecules*, Journal of Chemical Physics 105 (1996), 6505-6516.
- [9] P. J. Stephens, F. J. Devlin, C. F. Chabalowski, M. J. Frisch, *Ab Initio Calculation of Vibrational Absorption and Circular Dichroism Spectra Using Density Functional Force Fields*, The Journal of Physical Chemistry 98 (1994) 11623–11627
- [10] T. Mizuta, T. Yamamoto, N. Shibata, K. Miyoshi, *The molecular structure of the trans(O5) isomer of (ethylenediamine-N,N'-diacetato-N,N'-di-3-propionato)cobaltate(III), trans(O5)-[Co(eddda)]-determined by x-ray analysis and its structural comparison with some metal(III) complexes of related ligands*. Inorganica Chimica Acta 169 (1990) 257;
- [11] D.J. Radanovic, M.I. Djuran, K.D. Gailey, B.E. Douglas, *Circular Dichroism And Electronic Absorption Of Rhodium(Iii) Edta-Type Complexes: Ethylenediamine-N, N'-Diacetato-N, N'-Di-3-Propionatorhodate(Iii) And (S,S)-Ethylenediamine-N, N'-Disuccinotorhodate(III) Ions*, Journal of Coordination Chemistry, 10 (1980) 115–123.
- [12] M.S. Jeremić, M.D. Radovanović, F.W. Heinemann, M.M. Vasojević, Z.D. Matović, *Structural and theoretical investigations of the Rh(III) and Co(III) complexes containing symmetrical edta-type ligands with mixed carboxylate and diamine rings: Quantum-mechanical/NBO insight into stability of geometrical isomers*, Polyhedron. 169 (2019) 89–101

Analysis of prediction of water solubility and lipophilicity of coumarins by free cheminformatics tools

Bešlo Drago^{1*}, Agić Dejan¹, Rastija Vesna¹, Karnaš Maja¹, Šubarić Domagoj¹, Lučić Bono²

¹ University J. J. Strossmayer in Osijek, Faculty of Agrobiotechnical Sciences Osijek, Vladimira Preloga 1, HR 31000 Osijek, Croatia, [e-mail:dbeslo@fazos.hr](mailto:dbeslo@fazos.hr); dagic@fazos.hr; vrastija@fazos.hr; mkarnas@fazos.hr; dsubaric@fazos.hr

² NMR Center, Ruđer Bošković Institute, Bijenička cesta 54, HR 10000 Zagreb, Croatia; [e-mail:lucic@irb.hr](mailto:mail:lucic@irb.hr)

* Corresponding author

DOI: 10.46793/ICCBi23.657D

Abstract Pharmacokinetics of drugs involves the study of the drug's path through the body, from its introduction to its final excretion from the body (Absorption, Distribution, Metabolism, and Excretion (ADME)). The basis of pharmacokinetic tests provides insight into the behavior of the tested substance after it is introduced into the body. They include consideration of the physicochemical properties of the medicinal substance, as well as its biopharmaceutical properties. Experimental measurements are often demanding and take a long time to conclude the continuation of further research, whether it is a natural or synthesized substance that could be used as a medicine. *In silico* testing is resorted to because of the high cost of experimental testing. That is why today more and more research is done theoretically using different cheminformatics tools. Using the results obtained theoretically or *in silico* related to key parameters such as solubility, degree of dissociation, and binding to plasma proteins, it is possible to successfully predict the fate of the drug in the body, i.e., its bioavailability. There is a large number of software that are free to obtain the desired information about solubility, metabolism, distribution, and excretion from the organism. In this work, we decided to examine the solubility and lipophilicity of coumarin with three cheminformatics tools.

Keywords: cheminformatics tool, ADME, $\log P$, $\log S$, enzymes

1. Introduction

Coumarins are a large family of secondary metabolites that are synthesized via the shikimic and chorismic pathways. They were discovered in plants and their fruits, as well as in fungi and various microorganisms [1,2]. Different coumarin derivatives have characteristic properties that enable them to have diverse therapeutic effects [3,4].

To be effective as a drug, a molecule must reach its target in the body in sufficient concentration and remain there in a bioactive form long enough for the expected biological effects to occur. The early stages of drug development include an Absorption, Distribution, Metabolism, and Excretion (ADME) assessment to screen potential candidates, especially when access to physical samples is limited. In this context, computer models represent a valid alternative to experiments.

Lipophilicity is an important parameter in the modeling of new drugs. The optimal range of lipophilicity with low molecular weight and low polar surface area is the main driving force that leads to good absorption of chemicals in the intestines by passive diffusion. Lipophilicity plays a major role in controlling the kinetic and dynamic aspects of drug action [5,6]. Experimental evaluation of octanol/water partition coefficients is an expensive and time-consuming procedure, so theoretical methods of estimating this parameter are often used as a permissible substitute for experimental data. Namely, the drug that has been absorbed is not effective until it reaches the target site of action. Water solubility, $\log S$, is another common physicochemical parameter during drug discovery. It is an important parameter for achieving the desired drug concentration in the circulatory system to obtain a pharmacological response [7-11].

Drug metabolism is carried out by isoenzymes of CYP 450. CYP 450 is a family of heme-containing enzymes that is capable of inactivating and metabolizing many drugs as well as endogenous substances. Compounds that inhibit CYP 450 may cause toxicity by accumulating other substrates.

2. Materials and methods

Using the structure of 7-hydroxy-2-oxo-2H-cromen-4-yl series from Molnar and Čačić (2012)[12], the *in silico* chemo information tool freely available online at www.Swiss ADME; www.ademet SAR and www.ADMET lab 2.0, we will determine to $\log P$, $\log S$ and passage through the blood-brain barrier (BBB).

3. Results and discussion

Absorption of a drug is a key step during a series of events culminating in the target site where it can perform therapeutic purposes [13]. A whole series of factors affect the absorption rate of the drug, such as the size and shape of the molecule, polarity, lipophilicity, degree of ionization, solubility in different media, transport mechanism (active or passive), applied concentration, physicochemical properties of the drug, as well as the medicinal form. Figure 1. shows the linear dependence of $\log P$ obtained by different *in silico* methods.

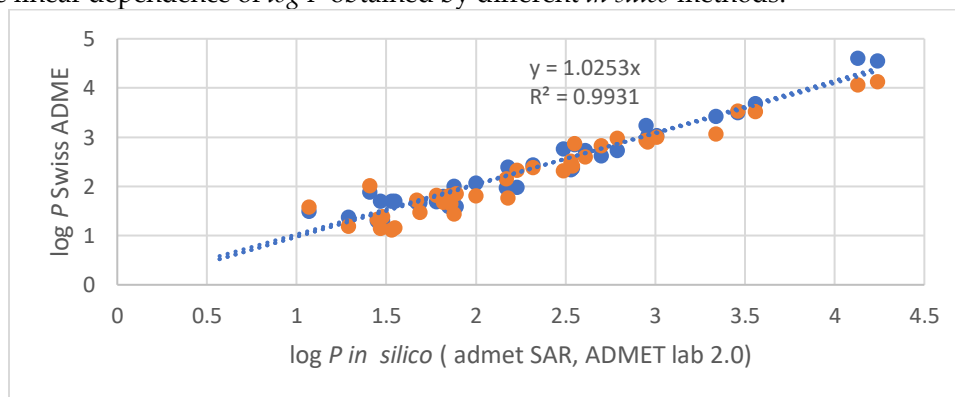


Figure 1. Linear dependence of *in silico* $\log P$ obtained by Swiss ADME on $\log P$ obtained by admet SAR (blue) and ADMETlab 2.0 (orange).

The results obtained by the methods used show a good mutual correlation ($R^2 = 0.941$). The obtained values indicate a good permeability of the tested coumarins through the cell membrane. Molecules with low lipophilicity ($\log P < 0.5$) will not be able to penetrate the membrane compared to those whose lipophilicity value is in the range of $0.5 < \log P > 3.0$. The lipophilicity of most of the tested coumarins is exactly in this range, which indicates that they will pass through

the cell membrane. Solubility in water is another common physicochemical parameter when discovering a compound as a drug. Poor solubility will affect other AMDE analyses. Figure 2 shows the values of $\log S$ obtained by three different online software.

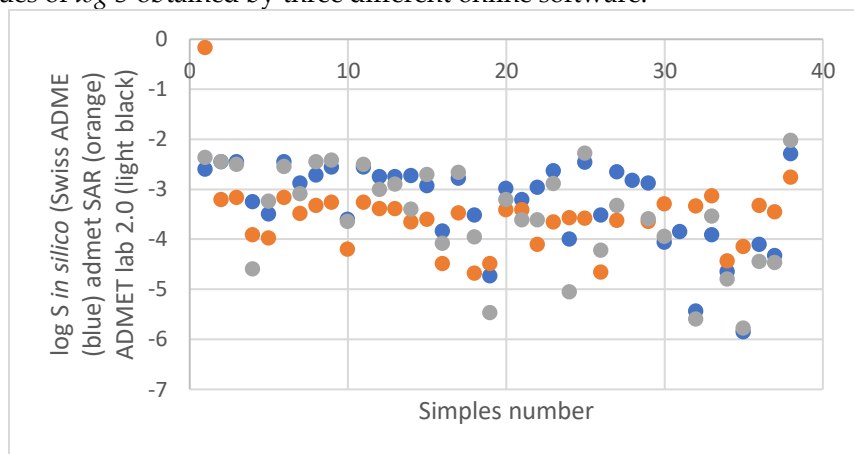


Figure 2. Comparison of $\log S$ of three methods *in silico* Swiss ADME, admet SAR, ADMET lab 2.0.

It should be emphasized that its pharmacological activity, rate of metabolism in the liver, passage through the BBB, rate of excretion, and frequency of interactions with other drugs present in the patient's body depend on the state of binding of the drug to plasma proteins. It is naturally permeable to essential elements and nutrients. It is important to point out that only lipophilic molecules smaller than 600 Da can cross the BBB passively, while it has been assumed that some are transported by transport proteins present on the endothelium such as P-glycoprotein [13,14]. In Figure 3, Egan et al. [15] developed descriptors to distinguish between well-absorbed and poorly absorbed molecules based on their lipophilicity and polarity, n-octanol/water partition coefficient ($\log P$) and polar surface area (TPSA).

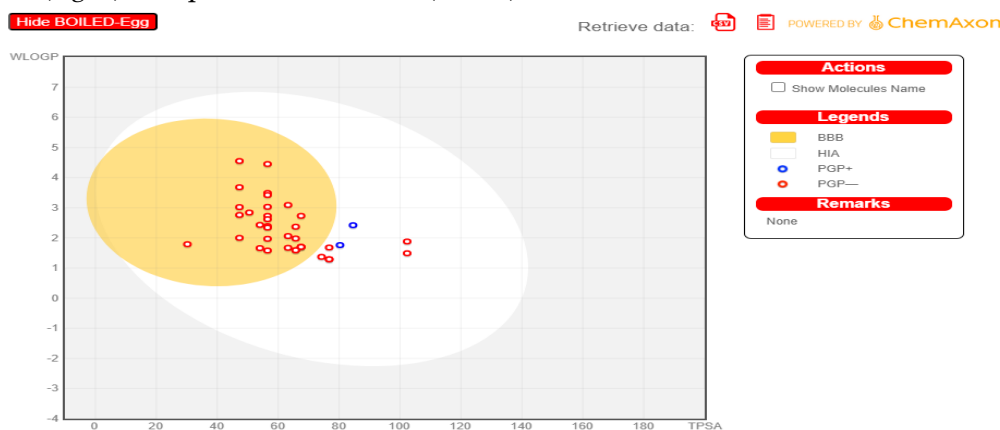


Figure 3. Test and illustrative use of BOILED-Egg. a) points located in the yellow part are predicted to pass through the blood-brain barrier, b) points located in the white part are predicted to be absorbed by the gastrointestinal tract, but will not penetrate the blood-brain barrier, c) blue points that P-glycoprotein will not allow to penetrate the blood-brain barrier, d) P-glycoprotein will not allow to release the molecule from the central nervous system.

Medicines are most often metabolized by the CYP 450 enzyme. The most studied CYP 450 isoenzymes are CYP3A4, CYP2C9, CYP2C19, CYP2E1 and are therefore in focus

when monitoring the metabolism of medicines. By using *in silico* software, the results show that apart from CYP1A2, other enzymes metabolize the tested coumarins.

4. Conclusion

By using *in silico* cheminformatics tools, the desired results are reached faster when testing a substance as a drug. The desired information is obtained on solubility, absorption, passage through the membrane, binding to plasma proteins, distribution, passage through the central nervous system, and distribution to other tissues, including the liver. The optimal range of lipophilicity with low molecular weight and low polar surface area is the main driving force that indicates good drug absorption, i.e., passive diffusion in the intestines. This is why the $\log P$ coefficient is known as one of the main parameters that evaluate drug absorption. Our $\log P$ results using the three cheminformatics tools showed a good correlation ($R^2 = 0.941$). Descriptors developed by Egon et al. showed that most of the tested coumarins can pass through the BBB. It was also confirmed that almost all CYP 450 isoenzymes metabolize the tested coumarins.

References

- [1] F. Borges, F. Roleira, N. Milhazes, L. Santana, [E. Uriarte](#), *Simple coumarins and analogues in medicinal chemistry: Occurrence, synthesis and biological activity*. *Current Medical Chemistry*, 12(8) (2005) 887-916, doi: [10.2174/0929867053507315](https://doi.org/10.2174/0929867053507315)
- [2] J.R.S. Hoult, Miguel Payá., *Pharmacological and biochemical actions of simple coumarins: Natural products with therapeutic potential*. *General Pharmacology: The Vascular System*, 27(4) (1996) 713-722. [https://doi.org/10.1016/0306-3623\(95\)02112-4](https://doi.org/10.1016/0306-3623(95)02112-4)
- [3] P. Govindaiah, N. Dumala, P. Grover, M. J. Prakash., Synthesis and biological evaluation of novel 4,7-dihydroxycoumarin derivatives as anticancer agents. *Bioorganic & Medicinal Chemistry Letters*, 29(14) (2019) 1819-1824. <https://doi.org/10.1016/j.bmcl.2019.05.008>
- [4] [J. Sumorek-Wiadro](#), [A. Zajac](#), [E. Langner](#), [K. Skalicka-Woźniak](#), [A. Maciejczyk](#), [W. Rzeski](#), [J. Jakubowicz-Gil.](#), Antiglioma Potential of Coumarins Combined with Sorafenib. *Molecules*, 25(21) (2020) 5192-5209, doi: [10.3390/molecules25215192](https://doi.org/10.3390/molecules25215192)
- [5] C. A. Lipinski, F. Lombardo, B. W. Dominy, P. J. Feeney., Experimental and computational approaches to estimate solubility and permeability in drug discovery and development settings, *Advanced Drug Delivery Reviews*, 46(1-3) (2001)3-26, [https://doi.org/10.1016/S0169-409X\(00\)00129-0](https://doi.org/10.1016/S0169-409X(00)00129-0)
- [6] [D.A. Smith](#), [B. C. Jones](#), [D.K. Walker](#)., Design of drugs involving the concepts and theories of drug metabolism and pharmacokinetics. *Medicinal Research Reviews* 16(3)(1996)242-266. [https://doi.org/10.1002/\(SICI\)1098-1128\(199605\)16:3<243::AID-MED2>3.0.CO;2-Z](https://doi.org/10.1002/(SICI)1098-1128(199605)16:3<243::AID-MED2>3.0.CO;2-Z)
- [7] [H. van de Waterbeemd](#), [E. Gifford](#)., ADMET *in silico* modelling: towards prediction paradise? *Nature reviews. Drug discovery* 2(3) (2003) 192-204. doi: [10.1038/nrd1032](https://doi.org/10.1038/nrd1032).
- [8] M.T.D. Cronin., The role of hydrophobicity in toxicity prediction. *Current Computer-Aided Drug Desing* 2(4)(2006)405-413. doi: [10.2174/157340906778992346](https://doi.org/10.2174/157340906778992346)
- [9] P. Cozzini, M. Fornabaio, A. Marabutti, D. J. Abraham, G. E. Kellogg, A. Mozzarelli. Lipophilicity Study of New Selenazole Derivatives by RP-HPLC. *Journal of Medicinal Chemistry* 45 (12) (2002) 2469-2483.
- [10] E. Arab Tehrany, F. Fournier, S. Desobry., Simple method to calculate octanol–water partition coefficient of organic compounds. *Journal of Food Engineering* 64 (3) (2004) 315–320, doi: [10.1016/j.jfoodeng.2003.10.015](https://doi.org/10.1016/j.jfoodeng.2003.10.015)

- [11] D. Eros, I. Kövesdi, L. Orfi, K. Takacs-Novak, G. Acsady, G. Keri. Reliability of logP Predictions Based on Calculated Molecular Descriptors: A Critical Review Current Medicinal Chemistry 9 (20) (2002), 1819-1829. <https://doi.org/10.2174/0929867023369042>
- [12] M. Molnar, M. Čačić., Antioxidant activity of some (7-hydroxy-2-oxo-2H-chromen-4-yl) acetic acid derivatives. Croatia Journal of Food AScience and Technology, 4(1)(2012)54-63
- [13] T. Fujita, J. Iwasa, C. Hansch., A New Substituent Constant, π , Derived from Partition Coefficients Journal of the American Chemical Society. 86 (23)(1964), 5175-5180. <https://doi.org/10.1021/ja01077a028>
- [14] Hirtz J. The gastrointestinal absorption of drugs in man: a review of current concepts and methods of investigation. Br J Clin Pharmac 1985, 19 (2) (1985) 77-83. [doi: 10.1111/j.1365-2125.1985.tb02746.x](https://doi.org/10.1111/j.1365-2125.1985.tb02746.x)
- [15] W. J. Egan, K. M. Merz, J. J. Baldwin, Prediction of Drug Absorption Using Multivariate Statistics. Journal of Medicinal Chemistry. 43 (21) (2000) 3867 – 3877. <https://doi.org/10.1021/jm000292e>

Influence of phthalimide substitution on the interaction with carbon nanotube

Sonja S. Zrilić¹, Jelena M. Živković¹, Snežana D. Zarić^{2*}

¹ Innovation Center of the Faculty of Chemistry, Studentski trg 12-16, 11158, Belgrade, Serbia; email: sonjaz@chem.bg.ac.rs, andric_jelena@chem.bg.ac.rs

² University of Belgrade, Faculty of Chemistry, Studentski trg 12-16, Belgrade, Serbia; e-mail: szaric@chem.bg.ac.rs

* Corresponding author

DOI: 10.46793/ICCBIG23.662Z

Abstract: The interaction energy of phthalimide and carbon nanotube calculated at SAPT0/6-31G* level is -17.37 kcal/mol. After the substitution of phthalimide with a hydroxyl group interaction was stronger (-18.64 kcal/mol) because of the larger dispersion followed by an increase in the molecular planar surface and an increased electrostatic term due to the additional electronegative oxygen atom. When a hexafluoroisopropyl group is used as a substituent (ph-6F/CNT), the molecule loses planarity and the dispersion term only slightly increases, but not enough to compensate for the unfavorable shift in the exchange interaction contribution. Thus, the resulting interaction energy in the ph-6F/CNT system is weaker (16.63 kcal/mol) than in the original ph/CNT system. Electrostatic contributions are also significant, with the largest value calculated for ph-OH/CNT (11.32 kcal/mol), because of the additional electronegative oxygen atom in the hydroxyl group. The other two systems, ph/CNT and ph-6F/CNT have electrostatic interactions of 10.14 and 10.05 kcal/mol, respectively. Exchange interaction is more repulsive for ph-OH (+26.60 kcal/mol) and ph-6F (+26.29 kcal/mol) systems than the ph/CNT (+24.86 kcal/mol).

Keywords: phthalimide, SAPT, quantum chemistry, carbon nanotube

7

1. Introduction

Interactions of aromatic rings with other aromatic molecules are important for numerous fields from molecular recognition to catalysis [1]. Aromatic interactions have extensively been studied between two benzene molecules. The calculations for benzene dimer showed two low-energy geometries. In the first geometry, CH groups of one benzene molecule interact with the π system of the other by forming CH- π interaction and the interaction energy is -2.84 kcal/mol. In other geometries, two benzene molecules are parallel at offset 1.51 Å and the interaction energy is -2.73 kcal/mol. Although interactions between two benzenes show minima at lower offset values, in the crystal structure preferred parallel aromatic/aromatic interactions are at large offsets. At large offsets new minimum has been obtained at 4.53 Å with an interaction energy of 2.01 kcal/mol [2].

Here we analyze the interaction of substituted heteroaromatic systems with a planar non-polar carbon nanotube in order to better understand the interactions of aromatic rings.

2. Results

Interactions of phthalimide (ph) and phthalimide molecules substituted with hydroxyl (ph-OH) and hexafluoroisopropyl group (ph-6F) with carbon nanotube (CNT) sheet were investigated. Phthalimides (ph, ph-OH and ph-6F) were optimized at B3LYPD3/6-31G* level using Gaussian 09 program package and their geometries are presented in **Figure 1**.

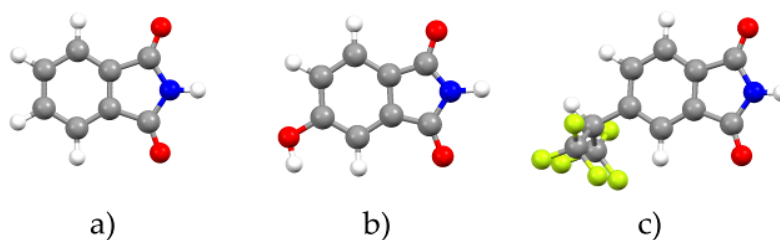


Figure 1. Optimized structures of phthalimide (ph) (a), and phthalimide substituted with hydroxyl (ph-OH) (b) and hexafluoroisopropyl (ph-6F) group (c).

Armchair (222,222) type CNT with a diameter of 30.1 nm was chosen and its atomic coordinates were obtained using VMD Nanotube builder plugin from which an approximately square curved sheet of 82 carbon atoms was cut out and saturated with 24 hydrogens to obtain a CNT sheet. Partial geometry optimization of each system consisting of one phthalimide and a CNT sheet was performed at B3LYPD3/6-31G* level with a frozen CNT sheet. The initial geometry used for optimization was with a phthalimide plane parallel to the CNT sheet. The optimized systems are shown in **Figure 2**.

Symmetry Adapted Perturbation Theory (SAPT) in the Psi4 program package was used for energy decomposition analysis in optimized systems at SAPT0/6-31G* level. Contributions to total SAPT0 energy (ΔE_{SAPT0}) are electrostatic (ΔE_{el}), exchange (ΔE_{ex}), induction (ΔE_{ind}), and dispersion (ΔE_{disp}) interactions. Normal distances (d) and SAPT energy decomposition results are presented in **Table 1**. Normal distance is calculated as the distance between the center of phthalimide C6 ring and a CNT sheet (**Figure 2**).

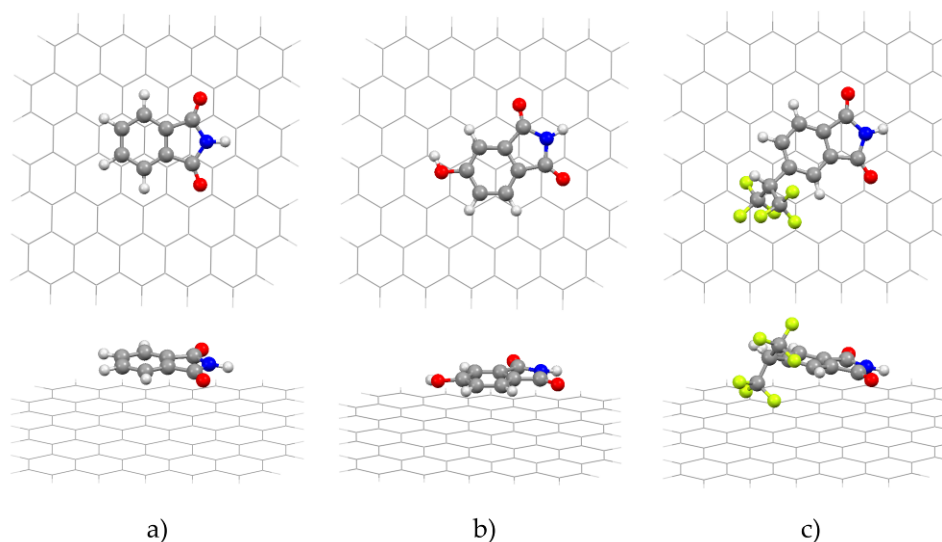


Figure 2. Top and side views of ph/CNT (a), ph-OH/CNT (b), and ph-6F/CNT systems after geometry optimization.

After geometry optimization, ph and ph-OH stayed parallel to the CNT sheet with a normal distance of 3.38 and 3.30 Å (**Table 1**), but this is not the case in ph-6F/CNT system (**Figure 2**). In ph-6F/CNT system, normal distance value (3.86 Å) is larger because of the different position of the ph-6F molecule to the CNT sheet. One CF₃ and the NH group are oriented towards the CNT sheet (**Figure 2**). The atoms of ph-6F with the closest distances to the CNT are one fluorine atom with 2.81 Å and the hydrogen from the NH group with 2.82 Å.

Table 1. Normal distances d (Å) and decomposition of interaction energy ΔE_{SAPT0} at SAPT0/631G* level into electrostatic ΔE_{el} , exchange ΔE_{ex} , induction ΔE_{ind} , and dispersion ΔE_{disp} terms for optimized systems. All energies are in expressed in kcal/mol.

	d	ΔE_{el}	ΔE_{ex}	ΔE_{ind}	ΔE_{disp}	ΔE_{SAPT0}
ph/CNT	3.38	-10.14	+24.86	-2.73	-29.37	-17.37
ph-OH/CNT	3.30	-11.32	+26.90	-2.92	-31.31	-18.65
ph-6F/CNT	3.86	-10.05	+26.29	-2.70	-30.17	-16.63

After the substitution of the phthalimide with the hydroxyl group, the total interaction becomes stronger, while the substitution with hexafluoroisopropyl weakens the interaction (**Table 1**).

The largest contribution to the total SAPT0 energy is dispersion, which is interestingly very similar for all three systems. For ph and ph-OH, this contribution originates from the dispersion interactions of all atoms to the CNT sheet, which makes its value proportional to the molecule surface. This explains the larger ΔE_{disp} for phOH/CNT (-31.31 kcal/mol) than ph/CNT (-29.37 kcal/mol) (**Table 1**). On the other hand, the dispersion in ph-6F/CNT system is not equally distributed among ph-6F atoms because

of their different distances from the CNT sheet. Thus, ΔE_{disp} originates from the atoms closest to the CNT sheet and is calculated to be -30.17 kcal/mol which is interestingly very close to the values in ph/CNT and ph-OH/CNT systems.

Electrostatic contributions are also significant, with the largest value calculated for ph-OH/CNT (-11.32 kcal/mol), because of the additional electronegative oxygen atom in the hydroxyl group (**Figure 2**). The other two systems, ph/CNT and ph-6F/CNT have electrostatic interactions -10.14 and -10.05 kcal/mol, respectively (**Table 1**). Exchange interaction is more repulsive for ph-OH/CNT (+26.60 kcal/mol) and ph-6F/CNT (+26.29 kcal/mol) systems than the ph/CNT (+24.86 kcal/mol), because of the larger surface and smaller normal distance of the ph-OH, and because of the very small distance of some groups of the ph-6F to the CNT sheet (**Figure 2**). The induction term is relatively small in all cases, and values are very similar.

4. Conclusions

Interaction with CNT is strengthened after the substitution of phthalimide with hydroxyl group in ph-OH/CNT system, because of the larger dispersion interaction caused by the increase of the molecule planar surface and an increased electrostatic term caused by the additional electronegative oxygen atom. In the case of the hexafluoroisopropyl substituted phthalimide (ph-6F/CNT), the molecule loses planarity, and the dispersion term only slightly increases, but not enough to compensate for the unfavorable shift in the exchange interaction contribution. Thus, the resulting interaction energy in the ph-6F/CNT system is weaker than in the original ph/CNT system.

Acknowledgment

This research is funded by the Ministry of Education and Ministry of Science, Technological Development and Innovation, Republic of Serbia, Contract numbers: 451-03-47/2023-01/200168 and 451-03-47/2023-01/200288.

References

- [1] K. E. Riley, P. Hobza, *On the Importance and Origin of Aromatic Interactions in Chemistry and Biodisciplines*, *Accounts of Chemical research*, 46 (2013) 927-936
- [2] D. B. Ninković, J. P. Blagojević Filipović, M. B. Hall, E. N. Brothers, S. D. Zarić, *What is Special about Aromatic–Aromatic Interactions? Significant Attraction at Large Horizontal Displacement*, *ACS Central Science*, 6 (2020), 420-425.

Interaction energy and decomposition of interaction energy of halo-substituted phthalimide with carbon nanotube

Sonja S. Zrilić¹, Jelena M. Živković¹, Snežana D. Zarić^{2*}

¹ Innovation Center of the Faculty of Chemistry, Studentski trg 12-16, 11158, Belgrade, Serbia; e-mail: sonjaz@chem.bg.ac.rs, andric_jelena@chem.bg.ac.rs

² University of Belgrade, Faculty of Chemistry, Studentski trg 12-16, Belgrade, Serbia; e-mail: szaric@chem.bg.ac.rs

* Corresponding author

DOI: 10.46793/ICCB23.666Z

Abstract: Interaction energy of phthalimide (ph) with carbon nanotube (CNT) calculated at SAPT0 level with a mixed basis set (6-31G* for CNT and 6-311G* for ph) is -19.51 kcal/mol. Halo-substitution of the phthalimide generally strengthens its interaction with the CNT and interaction energies are in the range from -21.02 kcal/mol to -22.62 kcal/mol going from ph-Cl to ph-I. However, interaction energy for phthalimide substituted with F atom (ph-F) is weaker (-18.81 kcal/mol) than for non-substituted phthalimide. For ph-Cl, ph-Br, ph-I, the total interaction energy increases with the higher halogen atomic number, because of the significant dispersion term and, less pronounced, electrostatic term increase. The smallest dispersion is calculated for ph-F/CNT (-28.72 kcal/mol), while the remaining systems range from -31.51 kcal/mol for ph/CNT to -35.78 kcal/mol for ph-I/CNT. Apart from dispersion, the system with fluorine has a less pronounced electrostatic term than other substituted phthalimides and does not follow trends observed for other systems.

Keywords: phthalimide, SAPT, quantum chemistry, carbon nanotube, halogen

1. Introduction

It has been proposed that aromatic interactions consist of van der Waals and electrostatic forces, as well as hydrophobic effects [1]. The relative ratio of these components is complicated to define due to the fact that aromatic groups interact in one of several geometries, depending on the nature of the rings involved. The solvent studies on aromatic interactions addressed the importance of electrostatic and solvophobic components in aromatic interactions. The influence of substituents on both edge-face and stacking interactions was analyzed. It was found that the position of fluorine on a phenyl ring has a significant influence on its interaction with a flavin ring in chloroform. This system provides a good example of polar interactions influencing the magnitude of aromatic interactions [2].

In this work, we studied the influence of halo-substitution of the phthalimide (ph) on stacking interactions with carbon nanotube (CNT). We performed Symmetry Adapted Perturbation Theory (SAPT) calculations on stacking interaction geometries and energies for ph/CNT, ph-F/CNT, ph-Cl/CNT, ph-Br/CNT, and ph-I/CNT systems.

2. Results

Geometry optimization of phthalimide (ph) and its halo-substituted structures (ph-F, ph-Cl, ph-Br, and ph-I) (**Figure 1**) was performed at ω B97XD/6-311G* level using Gaussian 09 program package. CNT was built using the VMD Nanotube builder plugin by choosing 30.1 nm diameter armchair (222,222) type CNT, cutting out an 82-carbon curved square sheet and saturating it with 24 hydrogen atoms.

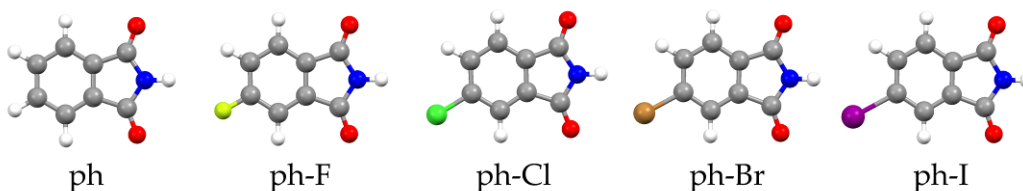


Figure 4. **Optimized structures of phthalimide (ph) and phthalimide substituted with fluorine (ph-F), chlorine (ph-Cl), bromine (ph-Br) and iodine (ph-I).**

Using phthalimides and CNT sheet prepared as explained above, each system was built by placing a phthalimide or a substituted phthalimide above a CNT sheet, parallel to it and performing geometry optimizations starting from this geometry. Geometry optimizations at ω B97XD/6-311G* level were done with frozen CNT coordinates to preserve the CNT curvature and the resulting coordinates are presented in **Figure 2**.

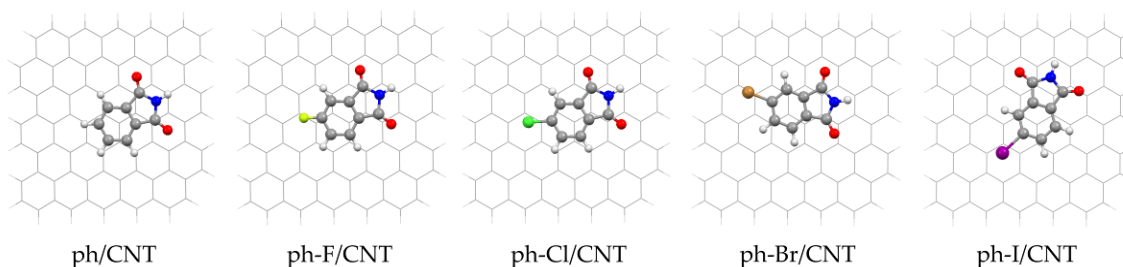


Figure 2. **Optimized geometries of ph/CNT, ph-F/CNT, ph-Cl/CNT, ph-Br/CNT and ph-I/CNT systems.**

Psi4 program was used to perform Symmetry Adapted Perturbation Theory (SAPT) energy decomposition on optimized systems into electrostatic (ΔE_{el}), exchange (ΔE_{ex}), induction (ΔE_{ind}), and dispersion (ΔE_{disp}) interactions at the SAPT0 (ΔE_{SAPT0}) level. Basis set 6-311G* was proven to be too demanding for such large systems, so a mixed basis set was used: 6-31G* on CNT atoms and 6-311G* on the atoms belonging to ph or

substituted phthalimides. **Table 1** represents normal distances (d) between phthalimides and a CNT sheet and the results of SAPT energy decomposition analysis. Normal distances represent the distance from the center of phthalimide C6 ring to the CNT plane.

In all systems, phthalimides stayed parallel to the CNT sheet after geometry optimization. In ph-I/CNT system, iodine is slightly bent away from the CNT sheet because of its large diameter. Normal distances (d) are rising uniformly from hydrogen to iodine in the range from 3.33 to 3.39 Å with an exception for ph-F/CNT system which has a longer d distance (3.37 Å) than ph-Cl/CNT system (3.35 Å) (**Table 1**).

Table 1. Normal distances d (Å) and decomposition of interaction energy ΔE_{SAPT0} , at SAPT0 level with 6-31G* basis on CNT atoms and 6-311G* on the remaining atoms, into electrostatic ΔE_{el} , exchange ΔE_{ex} , induction ΔE_{ind} , and dispersion ΔE_{disp} terms of optimized systems. All energies are expressed in kcal/mol.

	d	ΔE_{el}	ΔE_{ex}	ΔE_{ind}	ΔE_{disp}	ΔE_{SAPT0}
ph/CNT	3.33	-10.96	+25.80	-2.84	-31.51	-19.51
ph-F/CNT	3.37	-8.61	+20.68	-2.16	-28.72	-18.81
ph-Cl/CNT	3.35	-11.32	+26.84	-2.89	-33.65	-21.02
ph-Br/CNT	3.38	-11.43	+27.39	-2.86	-34.63	-21.54
ph-I/CNT	3.39	-11.81	+27.97	-3.00	-35.78	-22.62

The total SAPT0 interaction is becoming stronger with an increased atomic number of the halogen substituent. However, ph-F/CNT system does not follow the trend and its total SAPT0 interaction energy is the weakest (-18.8 kcal/mol) (**Table 1**). The SAPT0 energies of ph, ph-Cl, ph-Br and ph-I with the CNT sheet are -19.51, -21.02, -21.54, and -22.62 kcal/mol, respectively (**Table 1**).

Dispersion interaction has the strongest attractive contribution to the total SAPT0 energy with values having the same trend as ΔE_{SAPT0} . The smallest dispersion is calculated for ph-F/CNT (-28.72 kcal/mol), while the remaining systems range from -31.51 kcal/mol for ph/CNT to -35.78 kcal/mol for ph-I/CNT (**Table 1**). Dispersion interaction is rising because of the larger surface area between a phthalimide molecule and a CNT sheet, even though the distances are also slightly rising. Such a drastic difference between ph-F/CNT and ph/CNT ΔE_{disp} values compared to the other neighboring values could also be caused by a large distance of ph-F from the CNT sheet. The same trend observed in total and dispersion interactions can be noticed for electrostatic terms which is also the second largest attractive contribution. The system with fluorine has a significantly weaker electrostatic interaction (-8.61 kcal/mol) than the ph/CNT system (-10.96 kcal/mol) which could probably be explained in the same manner as for dispersion interactions. Electrostatic terms for ph-Cl/CNT, ph-Br/CNT and ph-I/CNT are -11.32, -11.43 and -11.81 kcal/mol (**Table 1**). Induction terms are very small and have similar values with again fluorine system having the considerably smaller value (-2.16 kcal/mol) than the remaining systems (from -2.84 to -3.00 kcal/mol) (**Table 1**).

Exchange interaction is the only repulsive interaction at the SAPT0 level, and its values also follow the same trend as mentioned above with the fluorine system having the smallest exchange (+20.68 kcal/mol), while the other systems have values from +25.80 for ph/CNT to +27.97 kcal/mol for ph-I/CNT.

4. Conclusions

Halo-substitution of phthalimide generally strengthens its interaction with the CNT with ph-F/CNT being the exception. For other systems, the total interaction increases with the higher halogen atomic number, because of the significant dispersion and less pronounced electrostatic term increase. The system with fluorine does not follow trends observed for other systems and its interaction with CNT is weaker than for ph/CNT system.

Acknowledgment

This research is funded by the Ministry of Education and Ministry of Science, Technological Development and Innovation, Republic of Serbia, Contract numbers: 451-03-47/2023-01/200168 and 451-03-47/2023-01/200288.

References

- [1] C. A. Hunter, K. R. Lawson, J. Perkins, C. J. Urch, *Aromatic interactions*, Journal of the Chemical Society Perkin Transaction, 2 (2001) 651-669.
- [2] A. J. Goodman, E. C. Breinlinger, C. M. McIntosh, L. N. Grimaldi, V. M. Rotello, *Model systems for flavoenzyme activity. Control of flavin recognition via specific electrostatic interactions*, Organic Letters, 3 (2001) 1531-1534.

Identification of small molecule binding sites using CmDock

Marko Jukić^{1,2,3*}, Urban Bren^{1,2,3}

¹ University of Maribor, Faculty of Chemistry and Chemical Engineering, Laboratory of Physical Chemistry and Chemical Thermodynamics, Smetanova Ulica 17, SI-2000 Maribor, Slovenia

² Faculty of Mathematics, Natural Sciences and Information Technologies, University of Primorska, Glagoljaška ulica 8, SI-600 Koper, Slovenia

³ Institute of Environmental Protection and Sensors, Beloruska ulica 7, SI-2000 Maribor, Slovenia
e-mail: marko.jukic@um.si

DOI: 10.46793/ICCBi23.670J

Abstract: Identification of binding sites for small molecules is critical in light of modern *in silico* and experimental methods for structure elucidation such as AlfaFold and CryoEM, respectively. The total number of entries in the PDB database is 208,702 through July 2023, and there are a large number of structural data without similar experimental entries and mechanistic or small molecule data. Herein, we report a simple, rapid, and efficient protocol for the identification of drug-like binding sites of small molecules using extended sampling with the self-developed molecular docking software CmDock. The protocol consists of preparing a docking receptor using the RbtProteinMapper method, which uses a full protein surface as a reference. Then, a series of drug-like interaction sampling probes are docked in an extended sampling of 1000 or more runs. The binding conformations calculated by the probes are analyzed using PacMAP reduction and DBSCAN density clustering to identify binding sites. The protocol is capable of identifying known binding sites of small molecules in a very short time frame. In addition, we demonstrate the application of the method to a known DNA Gyrase as well as to a STAT3 NTD domain system.

Keywords: Binding Site Identification, Drug Design, CmDock, CmD, Small Molecule Binding Site, Molecular Docking, Blind Docking, Structure-Based Drug Design, SBDD

1. Introduction

Small molecule binding site identification is a well-known field of research as reviewed by Sotriffer & Klebe [1]. Given the structural data of a validated protein target, for example, the identification of relevant binding sites is a critical step in structure-based drug design. To elaborate upon the subject, one would also like to decompose an identified binding site into sub-sites and even assess the type of binding site or its druggability making this field still an active research problem [2]. Historically most explored, are the topological or structure-based cavity detection methods. They can also be subdivided into energy-based methods and geometry-based methods.

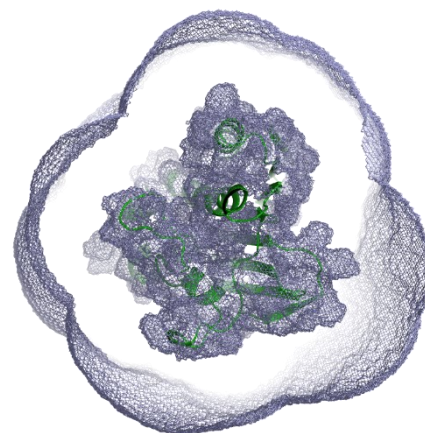
2. Protocol description

We employ CmDock (<https://gitlab.com/Jukic/cmdock>) dock.prm protocol for binding site identification by docking a small set of drug-like probes [3]. Docking protocol (dock.prm) to generate a ligand pose uses three stages of genetic algorithm (GA) search followed by low-temperature Monte Carlo and simplex minimization stages. Scoring function parameters are also varied between the stages to promote efficient sampling (for example 4-8 vdW potential in the first and second genetic algorithm runs to a 6-12 vdW potential in the third, Monte Carlo and and simplex minimisation). The initial population size parameter of the genetic algorithm is 50. The overall procedure is described as follows:

2.1 Generation of a molecular docking receptor

The first step consists of preparing a docking receptor using our newly developed RbtProteinMapper site mapper method that uses the complete protein surface as a reference ligand, effectively designating the complete surface of the examined protein system. Here a key parameter is the radius (in Å) from the protein surface and it is defined by the user.

Figure 1. Defined whole surface grid for the test DNA Gyrase B protein (PDB ID: 4DUH) with radius of 15 Å from the protein surface.



2.2 Molecular probe docking

Standard docking protocol (dock.prm) consisting of three stages of genetic algorithm search followed by Monte Carlo and simplex minimization stages are employed with 1000 runs on each probe. Employed probes consist of 4-[[4'-methyl-2'-(propanoylamino)-4,5'-bi-1,3-thiazol-2-yl]amino}benzoic acid, (2R,3R)-3',4',5,5',7-Pentahydroxyflavan-3-yl 3,4,5-trihydroxybenzoate, 4-Pyridylamine, histidine and 1,3-Dihydro-1,4-benzodiazepin-2-one covering drug-like chemical space and major non-covalent interactions (excepting halogen bonds). A set of drug-like interaction sampling probes are docked in an extended sampling mode of 1000 runs (or more as defined by user; GA population parameter at 50).

2.3 Probe binding mode analysis

Probe set times no. runs (default is 1k runs for binding site identification) of calculated probe binding or docked conformations are analysed in the last step using DBSCAN density-based clustering algorithm [4]. For further subsite classification and detailed analysis, binding mode-aware fingerprints or structural interaction fingerprints are calculated with Schrödinger Small Molecule Discovery Suite (SIFt as implemented by Schrödinger SMD, Release 2022-1, Schrödinger, LLC, New York, NY, 2022). Low variance features are removed and principal component analysis is performed to determine the PCs with the largest variance influence only to be dimensionally reduced

by PacMAP protocol and finally intricately clustered by DBSCAN algorithm [5, 6]. Individual clusters represent binding sites and corresponding subsites. The complete protocol is depicted in Figure 2.

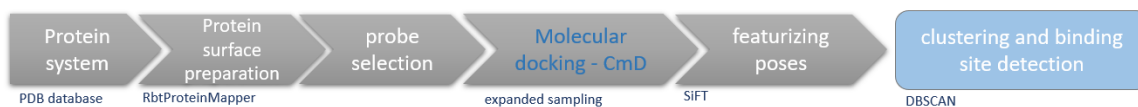
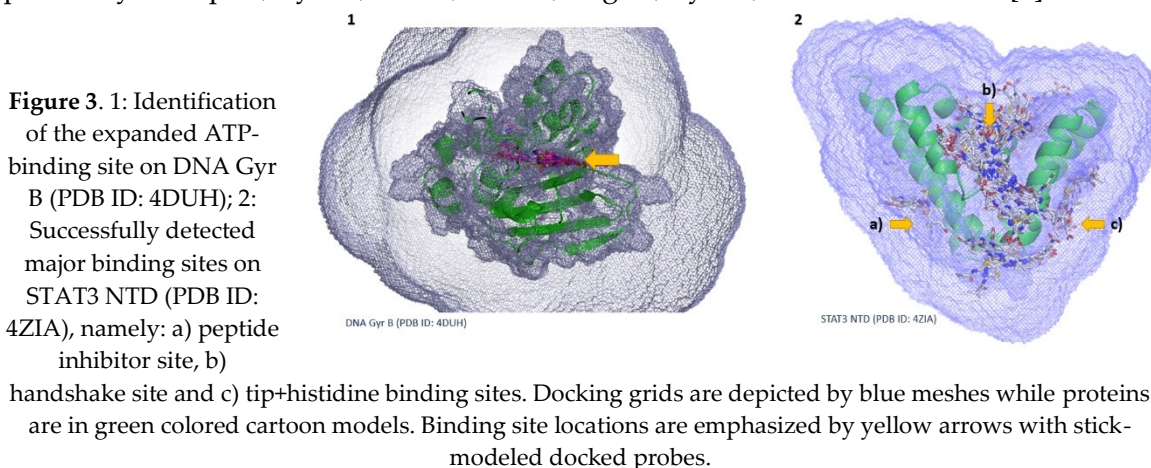


Figure 2. Identification of small-molecule binding sites using CmDock workflow.

3. Results and validation

First, we have employed the workflow on a DNA Gyrase B target (PDB ID: 4DUH) chain A that belongs to the class of topoisomerases and is a subclass of Type II topoisomerases that reduces topological strain in an ATP-dependent manner. Using our protocol, we have successfully identified the DNA gyrase B ATP-binding site, as revealed previously by X-ray crystallography (PDB ID: 1KZN; binding site complex with small-molecule antibiotic clorobiocin; Figure 3, left) [7]. The binding site is defined by residues: Val 43, Asn 46, Ala 47, Glu 50, Val 71, Asp 73, Gly 75, Arg 76, Gly 77, Ile 78, Pro 79, His 83, Ile 94, Leu 98, His 99, Ala 100, Gly 101, Gly 102, Lys 103, Phe 104, Gly 117, Val 118, Gly 119, Val 120, Ser 121, Arg 136, Thr 163, Gly 164, Thr 165 and Val 167. Similarly, three key binding sites were detected on STAT3 NTD (PDB ID: 4ZIA), namely: peptide inhibitor site as defined by proximity of Gln 41, Asp 42, Trp 43, Ala 44, Ala 106, Leu 109, Trp 110, Ser 113, Arg 114, Gln 117, handshake site defined by Trp 4, Gln 8, Leu 18, His 19, Tyr 22, Ser 23, Asp 24, Phe 26, Pro 27, Met 28, Glu 29, Gln 32, Phe 33, Gln 67, Phe 71, Tyr 79, Asn 82, Arg 85, Gln 88 and Phe 89 with final tip and the histidine site in proximity of Asp 65, Tyr 68, Ser 69, Leu 72, Arg 84, Lys 87, Gln 88 and Gln 91 [8].



4. Conclusions

Reputed protocol for binding site detection using CmDock is very fast CPU-wise and efficient. The protocol will be further optimised for the custom set of probes and analysed with the full PDBbind dataset. In addition, we will develop a PyMOL plugin that will allow the end user to quickly and interactively set up the experiments. In conjunction with template-based methods that gain power from data deposition, an

approach such as this can really help to quickly and efficiently identify relevant binding sites and corresponding subsites on protein systems and provide initial clues to ligand type and preference in the expanded probe library docking experiments. The protocol can also be directly integrated with other *in silico* methods such as inverse molecular docking and high throughput virtual screening (HTVS).

Acknowledgment

This research is funded by the Ministry of Education and Ministry of Science, Technological Development and Innovation, Republic of Serbia, Grants: No. xxx-xx-x/2023-xx/xxxxx. Financial support through the Slovenian Research Agency (ARRS) programme and project grants J1-2471, P2-0046, P1-0403, J1-4398, L2-3175, L2-4430, J7-4638, J3-4498, J1-4414, J3-4497, J4-4633, and P2-0438 is gratefully acknowledged.

References

1. Sotriffer, C., & Klebe, G. (2002). Identification and mapping of small-molecule binding sites in proteins: computational tools for structure-based drug design. *Il Farmaco*, 57(3), 243-251.
2. Fauman, E. B., Rai, B. K., & Huang, E. S. (2011). Structure-based druggability assessment—identifying suitable targets for small molecule therapeutics. *Current opinion in chemical biology*, 15(4), 463-468.
3. Jukić, M., Škrlj, B., Tomšič, G., Pleško, S., Podlipnik, Č., & Bren, U. (2021). Prioritisation of compounds for 3CLpro inhibitor development on SARS-CoV-2 variants. *Molecules*, 26(10), 3003.
4. Khan, K., Rehman, S. U., Aziz, K., Fong, S., & Sarasvady, S. (2014, February). DBSCAN: Past, present and future. In *The fifth international conference on the applications of digital information and web technologies (ICADIWT 2014)* (pp. 232-238). IEEE.
5. Tuncer, O., Leung, V. J., & Coskun, A. K. (2015, June). Pacmap: Topology mapping of unstructured communication patterns onto non-contiguous allocations. In *Proceedings of the 29th ACM on International Conference on Supercomputing* (pp. 37-46).
6. Wang, Y., Huang, H., Rudin, C., & Shaposhnik, Y. (2021). Understanding how dimension reduction tools work: an empirical approach to deciphering t-SNE, UMAP, TriMAP, and PaCMAP for data visualization. *The Journal of Machine Learning Research*, 22(1), 9129-9201.
7. Brvar, M., Perdih, A., Renko, M., Anderluh, G., Turk, D., & Solmajer, T. (2012). Structure-based discovery of substituted 4, 5'-bithiazoles as novel DNA gyrase inhibitors. *Journal of medicinal chemistry*, 55(14), 6413-6426.
8. Hu, T., Yeh, J. E., Pinello, L., Jacob, J., Chakravarthy, S., Yuan, G. C., ... & Frank, D. A. (2015). Impact of the N-terminal domain of STAT3 in STAT3-dependent transcriptional activity. *Molecular and cellular biology*, 35(19), 3284-3300.

A comprehensive *in silico* protocol for fast automated mutagenesis and binding affinity scoring of protein-ligand complexes

Sebastjan Kralj¹, Milan Hodošek², Marko Jukić^{1,3,4*}, Urban Bren^{1,3,4*}

¹ University of Maribor, Faculty of Chemistry and Chemical Engineering, Laboratory of Physical Chemistry and Chemical Thermodynamics, Smetanova Ulica 17, SI-2000 Maribor, Slovenia

² National Institute of Chemistry, Theory Department, Hajdrihova ulica 19, SI-1000 Ljubljana, Slovenia

³ University of Primorska, Faculty of Mathematics, Natural Sciences and Information Technologies, Glagoljaška ulica 8, SI-600 Koper, Slovenia

⁴ Institute of Environmental Protection and Sensors, Beloruska ulica 7, SI-2000 Maribor, Slovenia; e-mail: sebastjan.kralj1@um.si, marko.jukic@um.si*

* Corresponding author

DOI: 10.46793/ICCBi23.674K

Abstract: Protein-protein interactions (PPI) are critical for cellular functions, host-pathogen dynamics and are crucial with drug design efforts. The interaction of proteins is dependent on the amino acid sequence of a protein as it determines its binding affinity to various molecules, including drugs, DNA, RNA, and proteins. Polymorphisms, natural DNA variations, affect PPIs by altering protein structure and stability. Computational chemistry is vital for the prediction of ligand-protein interactions through techniques such as docking and molecular dynamics and can elucidate the changes in energy associated with such mutations.

We present a user-friendly protocol that uses the INTE command of CHARMM to predict the effects of mutations on PPIs. This command-line tool automates mutation analysis and interaction energy estimation, is applicable to different ligand types (protein, DNA, RNA, ion, small molecule) and provides various other features. The energy values yield absolute and normalized heat maps that allow rapid identification of stabilizing and destabilizing mutations. Our protocol forms the basis for automated programs that facilitate studies of binding-altering mutations in host-pathogen, protein-protein, and drug-target interactions.

Keywords: Mutations, Drug design, CHARMM, Protein-protein interaction

1. Introduction

At the heart of any drug discovery initiative is the interaction between a drug and its target, usually a protein. Besides being crucial for interactions between drugs and their targets protein-protein interactions (PPI) are also essential in many cell functions and play a critical role in mediating various biological processes, including those involved in host-pathogen interactions. These interactions control the intricate communication between a host organism and a pathogen, influencing the outcome of infections, immune

responses, and the overall dynamics between the two. Understanding these complex PPI networks is critical for developing strategies to combat infectious diseases. They allow proteins to form complexes and aggregates that are involved in a variety of cellular processes [1,2]. The amino acid sequence of a protein determines its binding affinity to other molecules, such as small drugs, DNA, RNA, or other proteins. Therefore, mutations can impact this binding process [2]. Polymorphisms are variations in DNA sequences that occur naturally in the population and can be single nucleotide polymorphisms (SNPs), changes in a single base pair, or major insertions or deletions [3]. As such polymorphisms can affect PPIs in several ways. They alter the amino acid sequence of a protein, changing its structure and binding affinity to other targets. They can also affect a protein's stability, increasing or decreasing the likelihood that it will interact with other proteins. Beneficial polymorphisms can give a person an advantage, such as increased resistance to disease. Harmful polymorphisms can increase the risk of disease or impair the function of a protein [3,4]. Computational chemistry focuses on the search for robust methods to predict ligand binding orientations and affinities that speed up the drug discovery process. Several techniques of various speed and accuracy are available, including docking methods, molecular mechanical Poisson-Boltzmann simulations (MM/PBSA), free energy perturbation (FEP), and others [5]. Recent technological and analytical advances in genomics have opened up opportunities to rapidly identify and interpret the genetic variations underlying individual diseases. These advances offer insight into the patient-specific mechanisms that contribute to disease and promise targeted intervention [6]. At the same time, computational chemistry has made significant advances, providing applicable tools for predicting complicated molecular interactions [7]. One such tool has been the development of our fully automated protocol for comprehensive mutation and subsequent scoring of mutational impact on binding affinity, that is based on our previous work, where a mutagenesis study on the RBD-ACE2 interface was performed [8].

2. Protocol description

The protocol is developed as a command-line tool that can be used to comprehensively mutate individual amino acid positions, estimate interaction energies, and generate a heat map of mutational energy estimation. It allows anyone to quickly estimate how selected mutations on a given protein affect binding with various supported ligands such as proteins, DNA, RNA, small molecules, or various ions. The protocol is based on Python and uses the academic version of CHARMM, which is distributed free to academic users after a license request [9]. It has various features such as automated patching of di-sulfide bonds, automated detection of interacting residues between chains and selection of minimization steps. In essence, the protocol edits PDB files, generates CHARMM input scripts for mutations of PDB files and for estimation of the energy, and generates a heatmap with normalized energies and absolute energies.

2.1 Selection and Mutation

The protocol allows either manual selection of desired amino acids or automated detection with a user-specified cut-off distance. This information is processed and mutated PDB files are formed and saved, making them available for download. Minimization is done in two steps, after generating the mutated chain and after generating the final complex, ensuring the absence of steric clashes.

2.2 Energy calculation

The energy is calculated using the INTE command found in CHARMM [9]. The primary function of the INTE command is to calculate the nonbonded energy and forces between atoms, which arise due to van der Waals interactions and electrostatic interactions. These forces are obtained from the CHARMM force-field equation for the two nonbonded terms, with the van der Waals interactions determined by the Lennard Jones potential and the Coulomb potential for the electrostatic interactions where i represents the atom from the first selection and j from the second:

$$E(r) = \sum_{\text{vdw}} \epsilon_{ij} \left[\left(\frac{R_{\text{min},ij}}{r_{ij}} \right)^{12} - 2 \left(\frac{R_{\text{min},ij}}{r_{ij}} \right)^6 \right] + \sum_{\text{electrostatic}} \frac{q_i q_j}{4\pi\epsilon_0 r_{ij}} \quad (1)$$

2.3 Heatmap generation

After obtaining the energies from the mutated structures we calculated the energetic difference by subtracting the mutated value from the wildtype value. This value shows us how the energy has changed with respect to the wild-type protein (Figure 1). The normalized and the absolute heatmap are generated using a Python script.

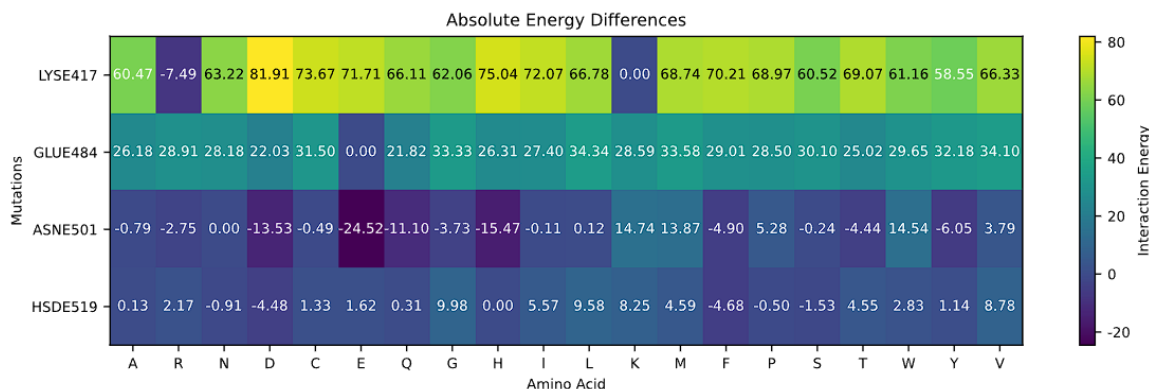


Figure 1. The absolute energy heatmap.

3. Conclusions

The presented protocol provides a basis for the development of a fully automated server that may be useful for studying various interactions where mutations affect the binding of two molecules, such as host-pathogen interaction or a protein-protein/protein-small molecule interaction associated with drug design. A tool like this can pave the way for the development of a holistic approach to pharmacogenomics, as in the

present form we have dubbed it the “molecular docking for mutations”. The protocol can be easily extended with various other *in-silico* methods such as molecular docking and molecular dynamics simulations to improve the accuracy of predicted interactions.

Acknowledgment

This research is funded by the Ministry of Education and Ministry of Science, Technological Development and Innovation, Republic of Serbia, Grants: No. xxx-xx-x/2023-xx/xxxxx. Financial support through the Slovenian Research Agency (ARRS) programme and project grants J1-2471, P2-0046, P1-0403, J1-4398, L2-3175, L2-4430, J7-4638, J3-4498, J1-4414, J3-4497, J4-4633, and P2-0438 is gratefully acknowledged.

References

1. Nicod, C.; Banaei-Esfahani, A.; Collins, B.C. Elucidation of Host–Pathogen Protein–Protein Interactions to Uncover Mechanisms of Host Cell Rewiring. *Current Opinion in Microbiology* **2017**, *39*, 7–15, doi:10.1016/j.mib.2017.07.005.
2. Jubb, H.C.; Pandurangan, A.P.; Turner, M.A.; Ochoa-Montañó, B.; Blundell, T.L.; Ascher, D.B. Mutations at Protein–Protein Interfaces: Small Changes over Big Surfaces Have Large Impacts on Human Health. *Progress in Biophysics and Molecular Biology* **2017**, *128*, 3–13, doi:10.1016/j.pbiomolbio.2016.10.002.
3. Yates, C.M.; Sternberg, M.J.E. The Effects of Non-Synonymous Single Nucleotide Polymorphisms (NsSNPs) on Protein–Protein Interactions. *Journal of Molecular Biology* **2013**, *425*, 3949–3963, doi:10.1016/j.jmb.2013.07.012.
4. Teng, S.; Madej, T.; Panchenko, A.; Alexov, E. Modeling Effects of Human Single Nucleotide Polymorphisms on Protein–Protein Interactions. *Biophysical Journal* **2009**, *96*, 2178–2188, doi:10.1016/j.bpj.2008.12.3904.
5. Williams-Noonan, B.J.; Yuriev, E.; Chalmers, D.K. Free Energy Methods in Drug Design: Prospects of “Alchemical Perturbation” in Medicinal Chemistry: Miniperspective. *J. Med. Chem.* **2018**, *61*, 638–649, doi:10.1021/acs.jmedchem.7b00681.
6. Aronson, S.J.; Rehm, H.L. Building the Foundation for Genomics in Precision Medicine. *Nature* **2015**, *526*, 336–342, doi:10.1038/nature15816.
7. Lin, X.; Li, X.; Lin, X. A Review on Applications of Computational Methods in Drug Screening and Design. *Molecules* **2020**, *25*, 1375, doi:10.3390/molecules25061375.
8. Jukić, M.; Kralj, S.; Nikitina, N.; Bren, U. Bioinformatic and MD Analysis of N501Y SARS-CoV-2 (UK) Variant. In *Computer Science Protecting Human Society Against Epidemics*; Byrski, A., Czachórski, T., Gelenbe, E., Grochla, K., Murayama, Y., Eds.; IFIP Advances in Information and Communication Technology; Springer International Publishing: Cham, 2021; Vol. 616, pp. 1–13 ISBN 978-3-030-86581-8.
9. Brooks, B.R.; Brooks, C.L.; Mackerell, A.D.; Nilsson, L.; Petrella, R.J.; Roux, B.; Won, Y.; Archontis, G.; Bartels, C.; Boresch, S.; et al. CHARMM: The Biomolecular Simulation Program. *J. Comput. Chem.* **2009**, *30*, 1545–1614, doi:10.1002/jcc.21287.

Workflow automation of high-throughput inverse docking using Pharmmapper

Aleksa P. Alargić¹, Bojan D. Levovnik¹, Miloš M. Svirčev^{1,*}

¹ University of Novi Sad, Faculty of Sciences, Department of Chemistry, Biochemistry and Environmental Protection, Novi Sad, Serbia, Trg Dositeja Obradovića 3; e-mail: milos.svircev@dh.uns.ac.rs

* Corresponding author

DOI: 10.46793/ICCBi23.678A

Abstract: In this paper, we present a novel, modular script Pharmmapper-Mass-Docker for the inverse docking workflow automation based on the pharmacophore screening results obtained on the Pharmmapper server. Pharmmapper-Mass-Docker streamlines download, manipulation, and entire inverse docking of the Pharmmapper results, encompassing essential steps like ligand/gridbox/binding site coordinate extraction (via centroid generation) and obtaining the output data ready for further comprehensive data analysis. By automating the entire inverse docking procedure, our modular script potentially enhances data management efficiency during inverse docking and reverse screening, empowering the researchers to efficiently discover and explore novel protein-ligand interactions.

Keywords: reverse screening, inverse docking, automation, Python, script

1. Reverse screening

Computational target fishing, also known as *in silico* reverse screening (isRS), is a drug discovery technique used to identify potential target proteins or other macromolecules (*receptors*) for a given small molecule (*ligand*). Unlike traditional computational methods that abide by the many-ligand-one-receptor paradigm and that usually predict the interactions between novel ligands and known receptors, isRS upends the experimental approach and tackles the problem from the ligand's perspective. By being instrumental in finding the best targets for queried ligand(s) via utilizing various molecular databases and advanced algorithms, isRS plays an important role in repurposing existing drugs, identifying new therapeutic targets, and gaining insights into the mechanisms of action of bioactive compounds. The isRS methodology encompasses three major approaches: fingerprint/shape screening, pharmacophore screening, and reverse (or inverse) docking (ID). Every approach has its own strengths and weaknesses, and it is usually advised to combine them to obtain valid results [1–3].

In this work, we describe and provide a link to [Pharmmapper-Mass-Docker](#), an isRS/ID workflow automation protocol able to take the results of a pharmacophore screening job performed on the freely accessible Pharmmapper[4,5] web server, use them to build a target library (TL; 300 targets by default), calculate and generate all the

input files required for docking and ultimately perform the ID of a queried ligand molecule to all the structures in the TL.

2. Pharmmapper. Pharmmapper-Mass-Docker

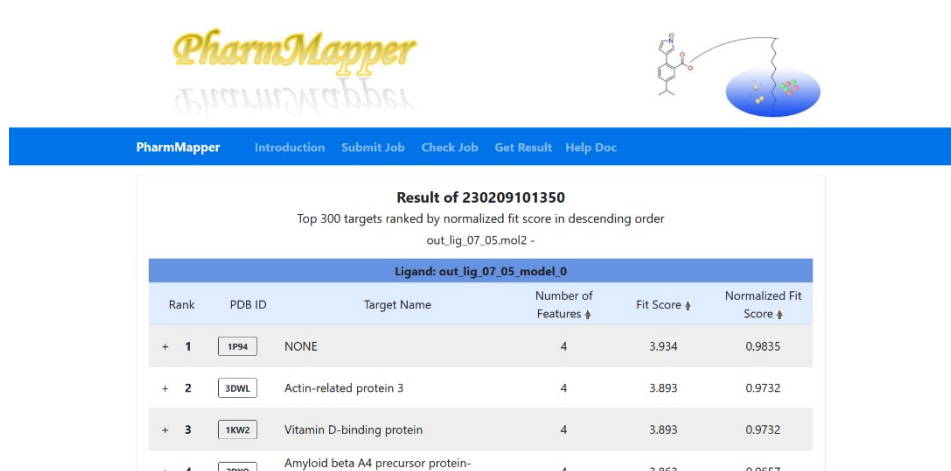
2.1 Pharmmapper

Pharmmapper server is an online tool that employs pharmacophore screening to identify potential target candidates for a queried ligand. The Pharmmapper's in-house database is called PharmTargetDB, and it is annotated from all the target information in other databases such as TargetBank, BindingDB, DrugBank, and PDTD. Pharmmapper (2017 update) currently houses more than 51000 ligandable pharmacophore models for more than 23000 proteins.

The typical Pharmmapper pharmacophore screening job has two parts:

1. The alignment of a queried ligand onto each pharmacophore model of proteins in the PharmTargetDB and assessment of each alignment based on the sequential triangle hashing and genetic algorithm (TriHash/GA) optimization algorithm.
2. The presentation of the aligned pose with the corresponding pharmacophore model and PDB link for the receptor hit as well as ranking of the targets.

After the Pharmmapper job is finished, a unique web page with all the linked results is generated (Figure 1). The obtained list can be used to create a new, filtered target list, ready for another, more versatile session of target fishing via ID.



PharmMapper Introduction Submit Job Check Job Get Result Help Doc

Result of 230209101350
Top 300 targets ranked by normalized fit score in descending order
out_lig_07_05.mol2 -

Ligand: out_lig_07_05.model_0

Rank	PDB ID	Target Name	Number of Features ↓	Fit Score ↓	Normalized Fit Score ↓
+ 1	1P94	NONE	4	3.934	0.9835
+ 2	3DWL	Actin-related protein 3	4	3.893	0.9732
+ 3	1KW2	Vitamin D-binding protein	4	3.893	0.9732
+ 4	7RWO	Amyloid beta A4 precursor protein-	4	3.863	0.9657

Figure 1. The screenshot of the Pharmmapper web page interface showing the results of pharmacophore screening job.

2.2 Pharmmapper-Mass-Docker

ID is performed via our script, [Pharmmapper-Mass-Docker](#), which is uploaded on the GitHub repository of the script's author (AA).[6] The script consists of six modules:

1. wrapper.sh – envelops and calls for all the other scripts and makes an output folder for each docking job in the ID session.

2. `site_parser.py`:
 - a. Creates the `.temp` directory (if it does not exist).
 - b. Downloads the Pharammapper web page with the results and saves it to `.temp/site.html`.
 - c. Finds all the download links for the aligned ligands.
 - d. Extracts each URL for the aligned ligand conformation and downloads it.
 - e. Extracts the PDB ID from each file name and downloads the corresponding PDB file.
3. `ligand_parser.py` – extracts minimum/maximum coordinates for every aligned ligand in order to make a centroid that will correspond to the center of the active site and docking grid box.
4. `generate_config.sh` – uses centroid coordinates obtained from `ligand_parser.py` to generate the Vina configuration file for each receptor file from the list.
5. `convert_prot.sh` – prepares the receptor PDBQT files out of corresponding downloaded PDB files, using *ADFR Suite*.
6. `dock.sh` – performs mass sequential ID session with all ligands and proteins present in master folder. By default, the ligand is a molecule that has been queried in the previous Pharammapper job (although there could theoretically be included multiple ligands), and the receptors are the Pharammapper hits. The script aggregates and organizes the docking output data into folders, generating information ready for comprehensive analysis.

3. Conclusions

The [Pharammapper-Mass-Docker](#), our Vina-using isRS/ID script, docks ligand(s) to the Pharammapper-obtained list of receptors, and offers an automated, streamlined approach to identify potential novel ligand-receptor interactions. The script is modular and allows for further additions and modifications, such as the constructing tables out of the output results, altering the docking tools and/or expanding the target library.

Acknowledgment

This research is funded by the Ministry of Education and Ministry of Science, Technological Development and Innovation, Republic of Serbia, Grants: No. 451-03-68/2022-14/200125 as well as research project from the Serbian Academy of Sciences and Arts (Grant No. F-130).

References

- [1] P.S. Kharkar, S. Warriar, R.S. Gaud., *Reverse docking: A powerful tool for drug repositioning and drug rescue*, *Future Med. Chem.*, 6 (2014) 333–342.
- [2] H. Huang, G. Zhang, Y. Zhou, C. Lin, S. Chen, Y. Lin, S. Mai, Z. Huang., *Reverse Screening Methods to Search for the Protein Targets of Chemopreventive Compounds*, *Front. Chem.*, 6 (2018) 1–28.

- [3] S. Galati, M. Di Stefano, E. Martinelli, G. Poli, T. Tuccinardi., *Recent Advances in In Silico Target Fishing*, *Molecules*, 26 (2021) 5124.
- [4] X. Liu, S. Ouyang, B. Yu, Y. Liu, K. Huang, J. Gong, S. Zheng, Z. Li, H. Li, H. Jiang., *PharmMapper server: a web server for potential drug target identification using pharmacophore mapping approach*, *Nucleic Acids Res.*, 38 (2010) W609–W614.
- [5] X. Wang, Y. Shen, S. Wang, S. Li, W. Zhang, X. Liu, L. Lai, J. Pei, H. Li., *PharmMapper 2017 update: A web server for potential drug target identification with a comprehensive target pharmacophore database*, *Nucleic Acids Res.*, 45 (2017) W356–W360.
- [6] A. Alargić., *Automatizacija procesa za efikasno inverzno dokovanje pomoću PharmMapper-a* (unpublished work), University of Novi Sad, 2023.

Investigating the potential inhibitory effect of the megaphone (molecule) on nasopharyngeal cancer growth factor receptors

Žiko Milanović^{1,*}, Marko Antonijević¹, Dušica Simijonović¹, Jelena Đorović Jovanović¹, Marijana Stanojević Pirković²

¹ University of Kragujevac, Institute for Information Technologies, Department of Science, Kragujevac, Jovana Cvijića bb, 34000 Kragujevac, Serbia; e-mail: ziko.milanovic@uni.kg.ac.rs

² University of Kragujevac, Faculty of Medical Sciences, Svetozara Markovića 69, 34000 Kragujevac, Serbia

* Corresponding author

DOI: 10.46793/ICCBi23.682M

Abstract: Nasopharyngeal cancer (NPC) is a type of cancer that originates in the nasopharynx, which is the upper part of the throat behind the nasal cavity. Like other cancers, the growth and progression of nasopharyngeal cancer are influenced by various proteins involved in cell signaling, growth regulation, and tumor development such as Epidermal Growth Factor Receptor (EGFR), Vascular Endothelial Growth Factor (VEGF), Fibroblast growth factor receptor (FGFR) and Cyclin D1 (CD1). Megaphone ((1'R,5'R,7R,8S)-7-Hydroxy-3,4,5,5'-methoxy-5',6'-dihydro-2'H-8,1'-neolign-8'-en-2'-one, MG) is the main component of the alcohol extract of the ground root of *Aniba megaphylla*, which *in vitro* inhibits the growth of cells derived from human nasopharyngeal carcinoma. Due to the lack of literature data, the main goal of this study was to examine the first step of the mechanisms of anti-carcinogenic activity by examining the inhibitory potential of MG against the above-mentioned cancer cell growth factor receptors.

Keywords: Megaphone, Nasopharyngeal cancer, EGFR, VGFR, FGFR

1. Introduction

The most common form of nasopharynx cancer, also known as **nasopharyngeal carcinoma (NPC)**, is most frequently detected in the postero-lateral nasopharynx or pharyngeal recess (fossa of Rosenmüller). It is essential to differentiate nasopharyngeal cancer from other throat-related malignancies, such as laryngeal and esophageal cancer. In terms of cancer incidence worldwide, nasopharyngeal cancer rates are 22nd among all cancer types. It is the **18th most prevalent cancer in men** and the **22nd most prevalent cancer in women**. There were over **133,000 newly reported cases** of nasopharyngeal cancer in 2020 alone [1].

In the 1960s, research revealed that an alcoholic extract of the ground root of *Aniba megaphylla* inhibited the proliferation of human nasopharyngeal carcinoma cells. In 1978, scientists isolated the active components of the extract using silica gel chromatography, identified them, and named the main compound Megaphone ((1'R,5'R,7R,8S)-7-

Hydroxy-3,4,5,5'-methoxy-5',6'-dihydro-2'H-8,1'-neolign-8'-en-2'-one, $C_{22}H_{30}O_6$, **MG**, solid)). **MG** is a neolignane with considerable cytotoxic properties [2]. Surprisingly, despite its potential, no additional research has been conducted on the mechanisms of anticancer activity of this compound. Determining the inhibitory effects of **MG** on proteins essential for the growth of nasopharyngeal carcinoma cells, namely Epidermal Growth Factor Receptor (**EGFR**), Vascular Endothelial Growth Factor (**VEGF**), Fibroblast growth factor receptor (**FGFR**), and Cyclin D1 (**CD1**), is the purpose of this study (Figure 1).

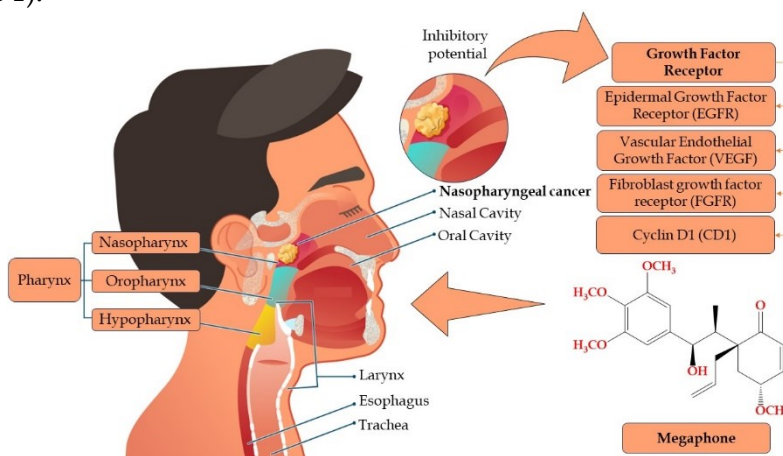


Figure 1. The location of nasopharyngeal carcinoma and the potential mechanism of the anticancer effect of megaphone (a compound isolated from the plant *Aniba megaphylla*) on the receptors for the growth and proliferation of cancer cells.

2. Methodology

In order to study the interactions between the **MG** and EGFR, VEGF, FGFR and CD1 receptor, molecular docking simulations were carried out using the AutoDock 4.2 program package. The three-dimensional crystal structure of the investigated receptors was retrieved from RCSB Protein Data Bank with PDB code: EGFR (1M17) [3], VEGF (4ASD) [4], FGFR (4V05) [5] and CD1 (2W96) [6]. In order to prepare the receptors, the non-protein components (co-crystallized water molecules) were removed, and missing amino acid residues were added. Before docking simulations, the structure of the investigated compound was optimized in *Gaussian 16* at the B3LYP-D3J/6-311++G (d,p) level of theory. The active site definition had been aligned to taken crystal structure co-crystallized with an erlotinib (**EGFR**, $x=22.014$, $y=0.253$, $z=52.724$ Å), sorafenib (**VGFR**, $x=-24.262$, $y=-0.388$, $z=-10.926$ Å), AZD4547 (**FGFR**, $x=85.700$, $y=1.144$, $z=9.265$ Å) and GOL1266 (**CD1**, $x=17.135$, $y=9.905$, $z=59.265$ Å). The other docking parameters have been selected based on standard protocols that have been expanded upon in previous studies. The calculation was performed with the Lamarckian Genetic Algorithm (LGA) technique.

3. Results and discussion

The thermodynamic parameters obtained from the molecular docking simulations are presented in Table 1. Based on the free binding energy (ΔG_{bind}) and the inhibition constant (K_i), the inhibitory activity according to the growth processes of cancerous cells decreases in the following order: **EGFR-MG** < **VEGFR-MG** < **FGFR-MG** < **CD1-MG**. This indicates that **MG** has the greatest inhibitory effect on the transmembrane **EGFR** receptor. By blocking the **EGFR** binding site on the extracellular domain of the receptor, interruption of **EGFR** signaling can prevent the growth of EGFR-expressing tumors and improve the patient's condition. This represents one of the potential mechanisms of anticancer activity of **MG** against nasopharyngeal carcinoma.

Table 1. Thermodynamic parameters (ΔG_{bind} free energy binding, K_i constant of inhibition, ΔG_{total} final total internal energy, ΔG_{tor} torsional free energy, ΔG_{unb} unbound system's energy, ΔG_{elec} electrostatic energy and $\Delta G_{\text{vdw+hbond+desolv}}$ is the sum of dispersion and repulsion (ΔG_{vdw}), hydrogen bond (ΔG_{hbond}), and desolvation (ΔG_{desolv}) energy, kcal mol⁻¹) for the most stable conformations of MG in the different receptors obtained after molecular docking simulations.

Complexes	ΔG_{bind}	K_i (μM)	ΔG_{inter}	$\Delta G_{\text{vdw+h}}$ <i>bond+desolv</i>	ΔG_{elec}	ΔG_{total}	ΔG_{tor}	ΔG_{unb}
EGFR-MG	-7.59	2.73	-10.57	-10.34	-0.23	-1.33	2.98	-1.33
VEGF-MG	-7.54	2.96	-10.52	-10.42	-0.10	-1.95	2.98	-1.95
FGFR-MG	-6.86	9.32	-9.85	-9.65	-0.20	-1.31	2.98	-1.31
CD1-MG	-7.01	7.26	-9.99	-9.34	-0.65	-2.42	2.98	-2.42

Figure 2 presents the amino acid environment of **MG** in the active site of the investigated receptors.

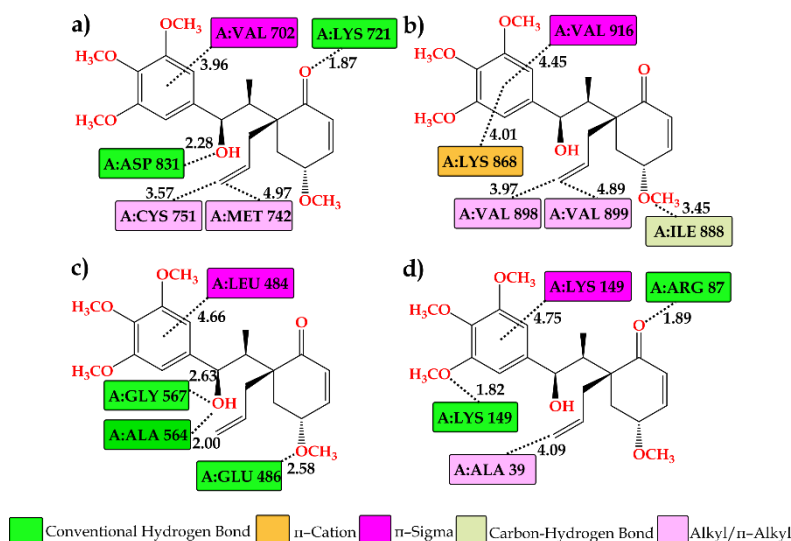


Figure 2. 2D representation of interactions between **MG** and amino acid residues: a) **EGFR-MG**, b) **VEGF-MG**, c) **FGFR-MG**, d) **CD1-MG** complexes with interatomic distance (\AA) obtained after molecular docking simulations.

Through polar functional groups, **MG** establishes the most important type of interactions, conventional hydrogen bonds, with different amino acid residues: LYS, ASP, GLY, ALA, and ARG of investigated receptors. A characteristic π -cation interaction is established between the partially positive $-\text{NH}_3^+$ group of the A:LYS 868 (VGFR receptor) and the aromatic ring of **MG** (4.01Å). **MG** with amino acid residues of different receptors: VAL, CYS, MET, LEU, establish hydrophobic contacts: π -sigma, π -alkyl, alkyl, which contribute to the stabilization of the protein-ligand complex.

3. Conclusions

Based on the presented results, it can be concluded that the **MG** shows significant inhibitory activity toward nasopharyngeal cancer growth factor receptors: **EGFR**, **VGFR**, **FGFR**, **CD1**. According to the study's findings, **MG** has the strongest **EGFR** receptor-inhibitory action. The obtained results and a thorough analysis of the typical intramolecular interactions between **MG** and growth factor receptors serve as a crucial foundation for a further investigation of the mechanisms of **MG**'s anticancer activity.

Acknowledgment

This research is funded by the Ministry of Science, Technological Development and Innovation of the Republic of Serbia, Grants: No. 451-03-47/2023-01/200378.

References

- [1] C.Y.Mimi, J.M.Yuan., Epidemiology of nasopharyngeal carcinoma. *In Seminars in cancer biology, Academic Press*, 12 (2002) 421-429.
- [2] D.A.Whiting., Lignans, neolignans, and related compounds. *Natural Product Reports*, 7 (1990) 349-364.
- [3] J. Stamos, M.X. Sliwkowski, C. Eigenbrot., *Structure of the epidermal growth factor receptor kinase domain alone and in complex with a 4-anilinoquinazoline inhibitor*. *Journal of biological chemistry*, 277 (2002) 46265-46272.
- [4] M. McTigue, B.W.Murray, J.H. Chen, Y.L.Deng, J.Solowiej, R.S. Kania., *Molecular conformations, interactions, and properties associated with drug efficiency and clinical performance among VEGFR TK inhibitors*. *Proceedings of the National Academy of Sciences*, 109 (2012) 18281-18289.
- [5] J.A.Tucker, T.Klein, J. Breed, A.L. Breeze, R. Overman, C. Phillips, R.A.Norman. *Structural insights into FGFR kinase isoform selectivity: diverse binding modes of AZD4547 and ponatinib in complex with FGFR1 and FGFR4*. *Structure*, 22 (2014) 1764-1774.
- [6] P.J.Day, A. Cleasby, I.J. Tickle, M. O'Reilly, J.E.Coyle, F.P.Holding, H. Jhoti., *Crystal structure of human CDK4 in complex with a D-type cyclin*. *Proceedings of the National Academy of Sciences*, 106 (2009) 4166-4170.

Green synthesis of chromeno-pyrimidine derivatives – Part I

Dušica Simijonović^{1*}, Edina Avdović¹, Žiko Milanović¹, Dejan Milenković¹, Zoran Marković¹

¹ University of Kragujevac, Institute for Information Technologies, Department of Science, Kragujevac, Jovana Cvijića bb, 34000, Kragujevac; e-mail: dusicachem@kg.ac.rs; edina.avdovic@pmf.kg.ac.rs; ziko.milanovic@uni.kg.ac.rs; dejanm@uni.kg.ac.rs; zmarkovic@uni.kg.ac.rs

* Corresponding author

DOI: 10.46793/ICCB23.686S

Abstract: Two different chromeno-pyrimidine derivatives were synthesized in the ionic liquid catalyzed reaction of barbituric acid and substituted salicylaldehydes. The product 5-(7-bromo-2,4-dioxo-1,3,4,5-tetrahydro-2H-chromeno[2,3-d]pyrimidin-5-yl)pyrimidine-2,4,6(1H,3H,5H)-trione (CP-1) was obtained in the reaction of barbituric acid and 5-bromo-2-hydroxybenzaldehyde. The second new product 8,9-dihydroxy-2H-chromeno[2,3-d]pyrimidine-2,4(3H)-dione (CP-2) was yielded in the reaction between barbituric acid and 2,3,4-trihydroxybenzaldehyde. These products were isolated in moderate to good yield after 3h reflux in mixture of water: ethanol (1:1v/v) and in presence 20 mol% of catalyst – diethanolammonium chloroacetate. The structure of obtained products was confirmed using ¹H NMR, ¹³C NMR, and IR spectroscopy methods.

Keywords: Chromeno-pyrimidine derivatives, Barbituric acid, Salicylaldehydes, Green synthesis, Structural characterization

1. Introduction

Chromeno and pyrimidine groups possess a wide range of biological and pharmacological activities [1,2]. The combination of chromeno and pyrimidine ring is known to increase biological activity. Therefore, in recent years there has been an increased interest in synthetic procedures for obtaining chromene-pyrimidine derivatives and testing their biological activity [1,3].

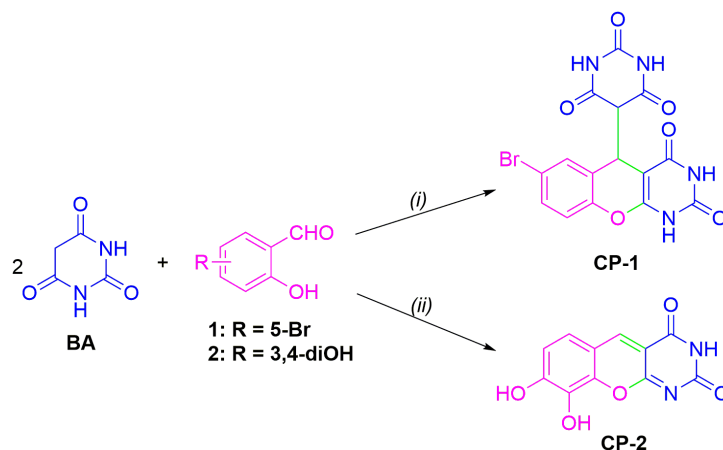
Cascade reactions are an important way for constructing complex chemical compounds from simple and readily accessible constituents. The majority of these reactions are in a one-pot procedure, in which two or more consecutive reactions are performed as a single transformation. [4,5]. These reactions are especially useful in the synthesis of polycyclic compounds using green chemistry conditions. Few methods are known for the synthesis of chromeno[2,3-d]pyrimidin derivatives from salicylaldehydes and barbituric acids. In these reactions both bases and acids are used as catalysts. In base condition the reaction was performed in the presence of piperidine, and in boiling ethanol [6], while as acid reaction mediums were used hydrochloric acid and sulphamic

acid [7,8]. The synthesis of benzopyrano[2,3-d]pyrimidine in non-catalytic reaction in boiling ethanol in literature has also been described but results are limited [9].

The present study reports the green method for the synthesis of two different chromeno-pyrimidine derivatives in presence of ionic liquid diethanolammonium chloroacetate ([HDEA][ClAc]) as catalyst.

2. Results and discussion

The studied reactions and obtained products are depicted in Scheme 1. The reactions were performed by treatment of two different substituted salicylaldehydes (**1** and **2**) with barbituric acid (**BA**) in the presence of 10 mol% [HDEA][ClAc] in water : ethanol (1:1 v/v), under reflux. After cooling and filtration of the reaction mixture products, 5-(7-bromo-2,4-dioxo-1,3,4,5-tetrahydro-2H-chromeno[2,3-d]pyrimidin-5-yl)pyrimidine-2,4,6(1*H*,3*H*,5*H*)-tri-one (**CP-1**) and 8,9-dihydroxy-2H-chromeno[2,3-d]pyrimidine-2,4(3*H*)-dione (**CP-2**) were obtained. In the case of the formation product **CP-1**, this reaction is a pseudo three-component reaction in which twofold equivalents of **BA** to salicylaldehyde participate (**1**). The analogous reactions with aldehyde **2** led to the product **CP-2**. Namely, salicylaldehyde with electron withdrawing group (5-bromosalicylaldehyde) reacted with **BA** producing the final product of the reaction **CP-1**, while aldehyde with electron donating groups such as 2,3,4-trihydroxybenzaldehyde reacted only with one barbituric acid molecule and yielding product **CP-2**. The formed products **CP-1** and **CP-2** were isolated in moderate to good yields (70% and 83%). The structure of the obtained products was confirmed by using ¹H NMR, ¹³C NMR, and IR spectroscopy.

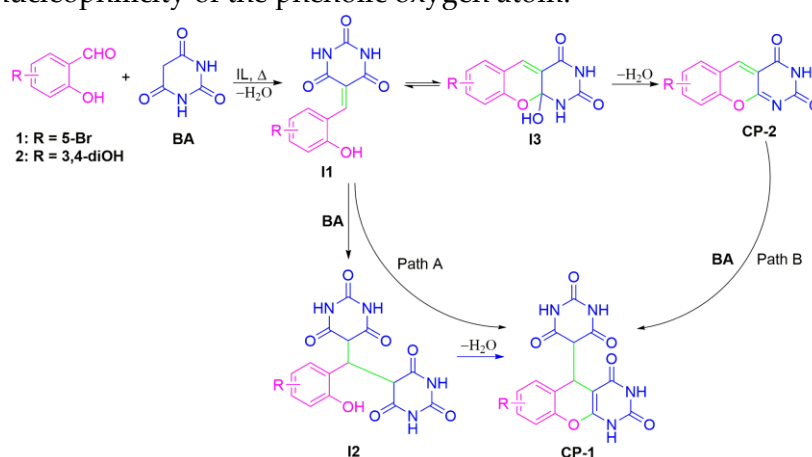


Scheme 1. Synthesis of chromeno-pyrimidine derivatives. Reagents and conditions:

- (i) **BA** (1 mmol), **1** (0.5 mmol), water: ethanol (1:1v/v), 20 mol% [HDEA][ClAc], reflux; (ii) **BA** (1 mmol), **2** (0.5 mmol), water: ethanol (1:1v/v), 20 mol% [HDEA][ClAc], reflux.

The proposed mechanism for the formation of chromeno[2,3-d]pyrimidin derivatives is presented in Scheme 2. For the formation of the final product **CP-1** there are two possible paths. The reaction starts with the Knoevenagel condensation of salicylaldehyde with **BA** and yields the intermediate **I1**. If the reaction occurs via pathway A the next step of the reaction is the formation of the intermediate **I2** by

Michael addition of the second molecule of **BA** to the arylidene intermediate **I1**. Further follows cyclization of **I2** which leads to the final chromeno[2,3-d]pyrimidine **CP-1**. However, if the reaction proceeds via pathway B, cyclization of **I1** and formation of **I3** follows. The next step is dehydration **I3** and formation of product **CP-2**. The formed chromeno-pyrimidine (oxadeazaflavine) **CP-2** reacts with another molecule of **BA** to form product **CP-1**. We assume that in our case the formation of product **CP-1** occurred via pathway A because the formation of product **CP-2** was observed only in the case when the reaction was performed with bulkier 2,3,4-trihydroxybenzaldehyde, which possesses an extremely nucleophilic phenolic oxygen atom in the ortho position. Further reaction of product **CP-2** with another **BA** molecule was not observed. It is most likely that the formation of **I3** does not occur in the case of 5-bromosalicylaldehyde due to insufficient nucleophilicity of the phenolic oxygen atom.



Scheme 2. Suggested mechanism for the formation of chromeno-pyrimidine derivatives.

3. Experimental

The substituted salicylaldehydes and barbituric acid were purchased from Merck and were used without further purification. The NMR spectra were recorded on a Varian Gemini spectrometer (200 MHz for ^1H and 50 MHz for ^{13}C) in DMSO-d_6 . IR spectroscopy was performed on a Perkin-Elmer Spectrum One FT-IR spectrometer using the KBr disc.

3.1 Synthesis of compounds **CP-1** and **CP-2**

To a mixture of salicylaldehydes (1 mmol) and barbituric acid (2 mmol) in a reaction flask equipped with a magnetic stirring bar 20 mol% of $[\text{HDEA}][\text{ClAc}]$ and water: ethanol (1:1 v/v; 5 mL) were added. The resulting reaction mixture was stirred at 80 °C for 3 h. Reaction progress was monitored using thin-layer chromatography (TLC). When the reaction was completed, the resulting mixture was cooled to room temperature and the precipitate was collected by filtration. The products **CP-1** and **CP-2** were characterized with ^1H NMR, ^{13}C NMR, and IR spectra.

5-(7-Bromo-2,4-dioxo-1,3,4,5-tetrahydro-2H-chromeno[2,3-d]pyrimidin-5-yl)pyrimidine-2,4,6(1H,3H,5H)-tri-one (**CP-1**): ^1H NMR (200 MHz, DMSO-d_6) δ : 12.05 (s, 1H), 11.37 (s, 1H), 11.22 (s, 1H), 11.09 (s, 1H), 7.51 (dd, $J = 8.8, 2.3$ Hz, 1H), 7.29 (d, $J = 2.2$ Hz, 1H), 7.08 (d, $J = 8.7$ Hz, 1H), 4.71 (d, $J = 1.7$ Hz, 1H), 3.93 (d, $J = 2.2$ Hz, 1H); ^{13}C NMR (50 MHz,

DMSO-d₆) δ : 169.4, 168.8, 163.5, 149.5, 148.5, 132.0, 130.7, 124.1, 118.8, 117.1, 85.0, 53.7, 33.2; IR (KBr): ν (cm⁻¹): 3424, 3264, 3100, 3086, 2956, 1766, 1704, 1657, 1477, 1355, 1265, 827.

8,9-Dihydroxy-2*H*-chromeno[2,3-*d*]pyrimidine-2,4(3*H*)-dione (**CP-2**): ¹H NMR (200 MHz, DMSO-d₆) δ 11.26 (s, 2H), 9.95 (s, 1H), 8.80 (s, 1H), 7.47 (d, *J* = 8.6 Hz, 1H), 7.02 (d, *J* = 8.6 Hz, 1H); ¹³C NMR (50 MHz, DMSO-d₆) δ 167.7, 161.7, 156.6, 145.7, 143.7, 132.9, 123.3, 115.0, 113.4, 108.7; ν (cm⁻¹): 3530, 3460, 3158, 3036, 2828, 1691, 1627, 1497, 1397, 867.

4. Conclusions

The ionic liquid [HDEA][ClAc] catalysed, the synthesis of chromeno-pyrimidine derivatives **CP-1** and **CP-2** has been reported. This protocol provides isolation of pure products in moderate to good yield without any purification. The obtained compounds were structurally characterized by IR and NMR spectroscopy. It is worth pointing out that the formed chromeno-pyrimidine (oxadeazaflavine) **CP-2** is reported in this study for the first time.

Acknowledgment

This research is funded by the Ministry of Education and Ministry of Science, Technological Development and Innovation, Republic of Serbia, Grants: No. 451-03-47/2023-01/200378.

References

- [1] N.M. Sabry, H.M. Mohamed, E.S.A.E.H. Khattab, S.S. Motlaq, A.M. El-Agrody, *Synthesis of 4*H*-chromene, coumarin, 12*H*-chromeno[2,3-*d*]pyrimidine derivatives and some of their antimicrobial and cytotoxicity activities*, European Journal of Medicinal Chemistry 46 (2011) 765-772.
- [2] C.O. Kappe, W.M.F. Fabian, M.A. Semones, *Conformational analysis of 4-aryl-dihydropyrimidine calcium channel modulators. A comparison of ab initio, semiempirical and X-ray crystallographic studies*, Tetrahedron 53 (1997) 2803-2816.
- [3] L. Moafi, S. Ahadi, A. Bazgir, *New HA 14-1 Analogues: Synthesis of 2-Amino-4-cyano-4*H*-chromenes*, Tetrahedron Letters 51 (2010) 6270-6274.
- [4] L.A. Thompson, *Recent applications of polymer-supported reagents and scavengers in combinatorial, parallel, or multistep synthesis*, Current Opinion in Chemical Biology. 4 (2000) 324-337.
- [5] A. Nefzi, J.M. Ostresh, R. A. Houghten, *The current status of heterocyclic combinatorial libraries*, Chemical Reviews 97 (1997) 449-472.
- [6] F. Eiden, C. Gerstlauer, *Darstellung und reaktionen von formyltetrahydrocannabinol- derivaten*, Archiv der Pharmazie 315 (1982) 551-561.
- [7] H.H. Zooroh, M.M.A.-E. Zahab, M.M. Abdel-Mogib, M.A. Ismail, *Peculiar reaction behaviour of barbituric acid derivatives towards aromatic amines*, Tetrahedron 52 (1996) 10147-10158.
- [8] M.M. Mane, D.M. Pore, *Sulphamic acid: an efficient, cost effective catalyst for facile synthesis of deazaaxaflavin at ambient temperature*, Synthetic Communications, 45 (2015) 868-876.
- [9] R.M.N. Kalla, R.S. Karunakaran, M. Balaji, I. Kim, *Catalyst-Free Synthesis of Xanthene and Pyrimidine-Fused Heterocyclic Derivatives at Water-Ethanol Medium and Their Antioxidant Properties*, ChemistrySelect, 4 (2019) 644 –649.

Chromeno-pyrimidine-type compounds (part II): *in vitro* evaluation of antioxidant potential

Edina Avdović^{1*}, Dušica Simijonović¹, Žiko Milanović¹, Sandra Jovičić Milić¹, Sunčica Roca², Dražen Vikić-Topić³

¹ University of Kragujevac, Institute for Information Technologies, Department of Science, Kragujevac, Jovana Cvijica bb, 34000, Kragujevac; e-mail: edina.avdovic@pmf.kg.ac.rs; dusicachem@kg.ac.rs; ziko.milanovic@uni.kg.ac.rs; sandra.jovicic@pmf.kg.ac.rs;

² NMR Centre, Ruder Bošković Institute, Bijenička 54, 10000 Zagreb, Croatia

³ Department of Natural and Health Sciences, Juraj Dobrila University of Pula, Zagrebačka 30, 52100 Pula, Croatia

* Corresponding author

DOI: 10.46793/ICCBi23.690A

Abstract: The chromeno and pyrimidine classes compounds include a variety of hybrid molecules displaying diverse biological actions. Although they have been examined for many years, these compounds are still of interest due to their facile chemical transformations. The presence of chromeno and pyrimidine structural motifs in many drugs, prompted us to investigate the antioxidant features of compounds 5-(7-bromo-2,4-dioxo-1,3,4,5-tetrahydro-2H-chromeno[2,3-d]pyrimidin-5-yl)pyrimidine-2,4,6(1H,3H,5H)-tri-one (**CP-1**) and 8,9-dihydroxy-2H-chromeno[2,3-d]pyrimidine-2,4(3H)-dione (**CP-2**). In this paper, we investigated *in vitro* antioxidant properties of selected chromeno-pyrimidine derivatives. The percentage activity of the tested compounds **CP-1** and **CP-2**, as well as the quercetin standard, NDGA, against the DPPH radical in concentrations of 25 μ M, 50 μ M and 100 μ M was tested. Compound **CP-2** was found to have an exceptional efficacy of 92% at a concentration of 25 μ M. In addition, the IC₅₀ value confirms a high antiradical power against DPPH radicals for the compound **CP-2** (IC₅₀ = 3.5 μ M) and a moderate activity for the compound **CP-1** (IC₅₀ = 55.4 μ M).

Keywords: Chromeno-pyrimidine derivatives, Antioxidant activity assay, DPPH radical

1. Introduction

Nitrogen-containing heterocyclic pyrimidines and their fused derivatives serve an essential function in medicinal chemistry and have been employed as drug development scaffolds [1–6]. The benzopyrano[2,3-d]pyrimidines is an important pharmacore which contains two fused benzopyran and pyrimidine rings. For this class of compounds, a large spectrum of biological and pharmacological properties is known [7–15]. The benzopyrans (4H-chromene) have shown a wide range of biological activities such as cytotoxic [7], antibacterial [8], antioxidant [9], and antitumorigenic [10]. On the other hand, pyrimidine scaffold is the base of many bioactive molecules [11–13]. Consequently,

synthetic methodologies for the synthesis of novel chromeno-pyrimidines are of particular interest to organic and medicinal chemists. Barbituric acid is a pyrimidine heterocyclic molecule with an active methylene group that can be involved in condensation reactions with aldehydes, ketones and α , β -unsaturated carbonyl compounds forming other heterocycles compounds with an outstanding biological activity.

In this study, the antioxidant features of chromeno-pyrimidine derivatives (CP), 5-(7-bromo-2,4-dioxo-1,3,4,5-tetrahydro-2H-chromeno[2,3-d]pyrimidin-5-yl)pyrimidine-2,4,6(1H,3H,5H)-tri-one (CP-1) and 8,9-dihydroxy-2H-chromeno[2,3-d]pyrimidine-2,4(3H)-dione (CP-2), obtained in ionic liquid catalysed reaction of different substituted salicylaldehydes with barbituric acid are investigated. The synthesis and structural characterization of these compounds is described in the chromene-pyrimidine study part 1.

2. Results and discussion

The 2,2-diphenyl-1-picrylhydrazyl (DPPH) radical scavenging test is one of the most frequently used assays and the first step in evaluating antioxidant activity. Thus, antioxidant molecules can neutralize DPPH free radicals by donating hydrogen atoms or electrons, resulting in a decrease in 517 nm absorbance.

In this work, compounds **CP-1** and **CP-2** (Figure 1) were subjected to *in vitro* antioxidant screening using DPPH assay (Table 1). The obtained DPPH assay results are displayed as an IC_{50} value, which is defined as the effective concentration of antioxidants required to reduce the initial concentration of free radicals by 50 %.

First, the percentage activity of the investigated compounds **CP-1** and **CP-2**, as well as the standards of quercetin, NDGA, on the DPPH radical was tested at concentrations of 25 μ M, 50 μ M and 100 μ M, and for the duration of incubation of 20 and 60 minutes, as shown in Table 1. The Table shows that compound **CP-2** has a remarkable degree of efficacy, with a notable activity level of 92 %, even when administered at low concentrations of 25 μ M. Conversely, compound **CP-1** shows much less activity at the same concentration. In the second step, inhibitory concentrations were determined and expressed as IC_{50} values. The IC_{50} value for compound **CP-2** is 3.5 μ M, indicating excellent antioxidant potential. The activity of this compound is slightly lower than that of the positive control quercetin and NDGA. Chromeno-pyrimidine derivative **CP-1** showed a moderate activity with IC_{50} of 55.4 μ M. The better activity of the compound **CP-2** can be attributed to the presence of the catechol fragment in the structure of this compound.

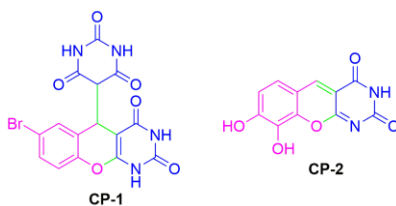


Figure 1. Structure of investigated chromeno-pyrimidine derivatives.

Table 1. *In vitro* interactions of selected compounds CP-1 and CP-2 with DPPH radical.

Compound	DPPH scavenging ability (%)						IC ₅₀ (μM)
	25 μM		50 μM		100 μM		
	20 min	60 min	20 min	60 min	20 min	60 min	
CP-1	40.9 ± 1.4	54.7 ± 3.1	52.2 ± 1.2	69.7 ± 0.5	65.2 ± 1.3	83.1 ± 1.2	55.4 ± 2.5
CP-2	91.3 ± 0.5	91.5 ± 3.0	93.5 ± 0.2	93.9 ± 1.8	96.9 ± 0.8	97.1 ± 1.9	3.5 ± 0.1
NDGA	94.6 ± 0.7	94.6 ± 0.6	94.2 ± 0.7	94.2 ± 0.7	94.5 ± 0.2	94.1 ± 0.7	1.7 ± 0.1
Quercetin	95.3 ± 0.8	95.1 ± 0.9	96.8 ± 1.0	96.5 ± 0.9	95.1 ± 0.9	95.4 ± 0.8	1.9 ± 0.1

3. Experimental

The 2,2-diphenyl-1-picrylhydrazyl (DPPH), nordihydroguaiaretic acid (NDGA), quercetin and methanol were purchased from Merck. The UV-Vis determinations were performed on PerkinElmer, Lambda 365 UV/Vis Spectrophotometer.

3.1 Antioxidant activity of compounds CP-1 and CP-2

The antioxidant potency of chromeno-pyrimidine derivatives was determined using DPPH method [16]. The samples were prepared by mixing the methanolic solution of DPPH radical (0.05 mM, 1 mL) with the tested compound (20 μL of different concentrations in dimethyl sulfoxide (DMSO) and 980 μL of methanol). After the incubation period (twenty and sixty minutes in a dark room at room temperature), the absorbance was determined spectrophotometrically at 517 nm. Quercetin and nordihydroguaiaretic acid were used as reference compounds, whereas methanol was a control solution. All measurements were made in triplicate. The obtained results are presented as mean values ± standard deviation (SD) of three independent measurements.

4. Conclusions

The results of the *in vitro* DPPH examination showed that both investigated compounds, CP-1 and CP-2, expressed antioxidant activity. It should be mentioned that especially compound CP-2, with an activity slightly lower than the reference compounds NDGA and quercetin, acts as an excellent radical scavenger.

Acknowledgment

This research is funded by the Ministry of Education and Ministry of Science, Technological Development and Innovation, Republic of Serbia, Grants: No. 451-03-47/2023-01/200378.

References

- [1] A. Aslam, M. Parveen, K. Singh, M. Azeem, *Green Synthesis of Fused Chromeno-pyrazolo-phthalazine Derivatives with Silica-supported Bismuth Nitrate under Solvent-free Conditions*, *Current Organic Synthesis*, 18 (2021) 1-8.
- [2] T.P. Selvam, C.R. James, P.V. Dniandev, S.K. Valzita, *A mini-review of pyrimidine and fused pyrimidine marketed drugs*, *Journal of Research in Pharmac*, 2 (2012) 1-9.
- [3] K.S. Jain, T.S. Chitre, P.B. Miniyar, M.K. Kathiravan, V.S. Bendre, V.S. Veer, S.R. Shahane, C.J. Shishoo, *Biological and medicinal significance of pyrimidines*, *Current Science*, 90 (2006) 793-803.
- [4] S. Schenone, M. Radi, F. Musumeci, C. Brullo, M. Botta, *Biologically Driven Synthesis of Pyrazolo[3,4-d]pyrimidines as a Protein Kinase inhibitors: An scaffold As a New Tool for Medicinal chemistry and Chemical Biological Studies*. *Chemical Reviews* 114 (2014) 7189-7238.
- [5] J.S. Rane, P. Pandey, A. Chatterjee, R. Khan, A. Kumar, A. Prakash, S. Ray, *Targeting virus-host interaction by novel pyrimidine derivative: An in silico approach towards discovery of potential drug against COVID-19*, *Journal of Biomolecular Structure and Dynamics*, 39 (2021) 5768-5778.
- [6] J. Rani, S. Kumar, M. Saini, J. Mundlia, P.K. Verma, *Biological potential of pyrimidine derivatives in a new era*, *Research on Chemical Intermediates*, 42 (2016) 6777-6804.
- [7] S.C. Ren, F.Y. Sheau, M.L. Chih, G. Amooru, T.K. Damu, C.P. Cheng, F.B. Kenneth, L.K. Hsiung, W.T. Shung, *Anti-HBV and cytotoxic activities of pyranocoumarin derivatives*, *Bioorganic and Medicinal Chemistry*, 17 (2009) 6137-6143.
- [8] A.V. Karnik, A.M. Kulkarni, N.J. Malviya, B.R. Mourya, B.L. Jadhav, *Synthesis and in vitro anti-bacterial evaluation of tetracyclic-ortho-fused 4H-naphtho[1',2'-5,6]pyrano[3,4-d](1,2,3)selenadiazole and its derivatives*, *European Journal of Medicinal Chemistry*, 43 (2008) 2615-2617.
- [9] K.J. Hwan, K.H. Eun, J.J. Kyung, K. Hwajung, C. Jungsook, L. Heesoon, *Synthesis of 7-hydroxy-4-Oxo-4H-chromene- and 7-hydroxychroman-2-carboxylic acidN-alkyl amides and their antioxidant activities*, *Archives of Pharmacal Research*, 29 (2006) 728-734.
- [10] C. Fakher, M. Mehdi, B.M. Hedi, C. Leila, S. Mansour, *Synthesis and antigenotoxic activity of some naphtho[2,1-b]pyrano[3,2-e][1,2,4]triazolo[1,5-c]pyrimidine derivatives*, *European Journal of Medicinal Chemistry*, 42 (2007) 715-718.
- [11] M.B. Deshmukh, S.M. Salunkhe, D.R. Patil, P.V. Anbhule, *A novel and efficient one step synthesis of 2-amino-5-cyano-6-hydroxy-4-aryl pyrimidines and their anti-bacterial activity*, *European Journal of Medicinal Chemistry*, 44 (2009) 2651-2654.
- [12] G. Cecile, D. Douguet, V. Huteau, M. Gilles, M.L. Helene, P. Sylvie, *Substituted benzyl-pyrimidines targeting thymidine monophosphate kinase of Mycobacterium tuberculosis: Synthesis and in vitro anti-mycobacterial activity*, *Bioorganic & Medicinal Chemistry*, 16 (2008) 6075-6085.
- [13] R. Lin, G. Sigmond, P.J. Johnson, S.K. Connolly, E. Wetter, T.V. Binnun, W.V. Hughes, N.B. Murray, S.J. Pandey, M.M. Mazza, A.R. Adams, F. Pesquera, A.M. Steven, *Synthesis and evaluation of 2,7-diaminothiazolo[4,5-d] pyrimidine analogues as anti-tumor epidermal growth factor receptor (EGFR) tyrosine kinase inhibitors*, *Bioorganic and Medicinal Chemistry Letters* 19 (2009) 2333-2337.

For more information, please visit our website:



www.iccbikg2023.kg.ac.rs

and contact as:



+381 34 6100195



iccbikg@uni.kg.ac.rs



Institute for Information Technologies Kragujevac, University of Kragujevac, Jovana Cvijića bb, 34000
Kragujevac, Serbia

